THIESEL 2022
CONFERENCE ON THERMO-AND FLUID DYNAMICS OF
Clean Propulsion Powerplants
13th ~ 16th September 2022

UNIVERSITAT POLITÈCNICA DE VALÈNCIA | cmt | GENERALITAT VALENCIANA

CMT-MOTORES TÉRMICOS

Scientific Editors

Xandra Margot
Raúl Payri
José Ramón Serrano

ORGANISED BY

UNIVERSITAT POLITÈCNICA DE VALÈNCIA

cmt

SPONSORED BY

GENERALITAT VALENCIANA

WELCOME BY
THE RECTOR OF UPV

It is a great honour to welcome you to the **12th Edition of the THIESEL Conference on Thermo-and Fluid Dynamics of Clean Propulsion Powerplants**. As our longing for a return to normality makes its way through steadily, this is the first post-pandemic edition of one of the most renowned conferences on this subject, a proof of how science and human ingenuity can turn the perspectives even in the most challenging situations.

Not only the pandemic, but the risks and threats that geo-political events pose, have speeded up the pace of a steady change towards more sustainable propulsion systems, and not deepening our dependence on fossil fuels will make our societies more sustainable and more resilient, bringing, in the long term, a higher level of wellbeing and freedom. Results from this conference, and its shift towards topics like decarbonisation, hydrogen, and electric mobility, will show the road map to follow, where an entrenched ecosystem of universities, research institutions and companies will make the change we all crave to achieve a sustainable future.

CMT is not only a reference in its field, but one of the most productive institutes, in terms of research and industry cooperation, in our university. Therefore, I can only thank them, and the THIESEL 2022 organisers for taking the responsibility of making possible a new edition of this event.

I wish you the highest success for this conference and that you make the most of your visit to our university, an institution where technology, engineering, arts and business meet, and the highest standards of research and industry collaboration are in place.

José E. Capilla
Rector

OVERVIEW
AND OBJECTIVES

THIESEL 2022, the twelfth edition of this biennial conference, will mark a turning point in its history. Throughout the years, the conference has gained in visibility because it has adapted its topics to the changing conditions imposed by pollutant regulations, with a first significant change in 2012 to include DI gasoline engines. However, it has become clear that the electrification of automobiles is displacing the thermal engine from its primary role, as this is one more component of hybridized powertrains. And this major change will be reflected in the new direction taken for THIESEL 2022, first through a totally renewed Steering and Organizing Committee and, second, with a renewed name to include the complete propulsion system. However, the first part of the conference title does not change, thereby bringing continuity to the conference topics.

The focus of THIESEL 2022 will still be on the thermo-and fluid dynamic processes but adapted to include thermal and noise challenges in electric components, energy optimization in the global electrified propulsion system, new injection/combustion concepts based on hydrogen, ammonia, renewable-fuels and not excluding any other clean propulsion approach.

Since research in all these areas is in full swing, the aim of the THIESEL 2022 Conference is to facilitate the exchange of ideas and experiences between Industry, Universities and Research Centres, as well as to create a discussion forum for the most recent advances and for the identification of future lines of research.

LIST OF CONTENTS

COMMITTEES

STEERING COMMITTEE

Prof. Raúl Payri
CMT. Universitat Politècnica de València – SPAIN

Prof. José Ramón Serrano
CMT. Universitat Politècnica de València – SPAIN

Prof. Choongsik Bae
KAIST - KOREA

Prof. Thomas Koch
IFKM. Karlsruher Institut für Technologie - GERMANY

Prof. Jiro Senda
Doshisha University – JAPAN

Dr. Christian Angelberger
IFP Energies Nouvelles – FRANCE

Dr. Paul Miles
Sandia National Laboratories – USA

Dr. Jim Szybist
Oak Ridge National Laboratory - USA

CONFERENCE COORDINATOR

Dr. Xandra Margot
CMT. Universitat Politècnica de València - SPAIN

LOCAL ORGANISING COMMITTEE

CMT. Universitat Politècnica de València – SPAIN

Prof. Alberto Broatch
Dr. Antonio García
Dr. Xandra Margot
Dr. Ricardo Novella
Dr. Pedro Piqueras
Dr. Benjamín Plá

ADVISORY AND SCIENTIFIC COMMITTEE

Dr. Philipp Adomeit. FEV - Germany

Dr. Rosario Ballesteros. UCLM Ciudad Real - Spain

Dr. Chris Bitsis. Southwest Research Institute - USA

Dr. Tristan Burton – Convergent Science - USA

Dr. Aaron Costall. University of Bath – UK

Dr. Gabin Dober. BorgWarner - Luxembourg

Prof. Pilar Dorado. Universidad de Córdoba - Spain

Dr. Georgios Fontaras. European Commission Joint Research Centre - Italy

Prof. Jinwu Gao. Jilin University - China

Dr. M. Reyes García Contreras. UCLM Toledo - Spain

Prof. Avelina García García. Universidad de Alicante - Spain

Mr. Victor Gordillo. Aramco Overseas Company – France

Dr. Stéphane Guilain. Renault - France

Prof. Viktor Hacker. T.U. Graz - Austria

Mr. Takeshi Hashizume. Toyota - Japan

Dr. Ameya Joshi. Corning Inc. - USA

Prof. Grigoris Koltsakis. Aristotle University Thessaloniki - Greece

Prof. Federico Millo. Politecnico di Torino - Italy

Prof. Eiichi Murase. Kyushu University - Japan

Dr. Omar Noshin. ABEE Group - Belgium

Prof. Hideyuki Ogawa. Hokkaidou University – Japan

Prof. Angelo Onorati. Politecnico di Milano - Italy

Dr. Robert Plank. Horiba Europe - Germany

Mr. Alain Raposo. Hyunday Motor Company - France

Prof. Guillermo Rein. Imperial College London - UK

Prof. Giorgio Rizzoni. Ohio State University - USA

Prof. Christine Rousselle. Université d'Orléans - France

Dr. Antonio Sciarretta. IFP Energies Nouvelles- France

Dr. P. Kelly Senecal. Convergent Science - USA

Prof. Tielong Shen. Sophia University - Japan

Prof. Athanasios Tsolakis. University of Birmingham - UK

Dr. Bianca Vaglieco. CNR-STEMS - Italy

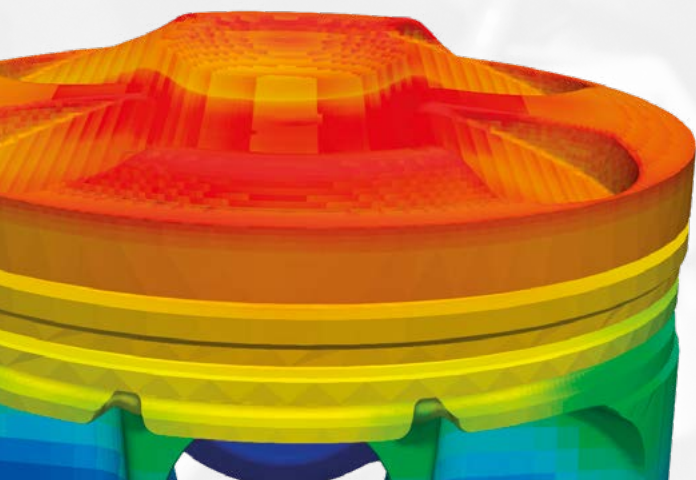Dr. Olivier Varnier. Jaguar Land Rover – UK

Dr. Alberto Vassallo. Punch Torino - Italy

Dr. Timothy Watling. Johnson Matthey - UK

Prof. Margaret Wooldridge. University of Michigan - USA

Dr. Yahui Zhang. Yanshan University - China

Dr. Peng Zhao. University of Tennessee – USA

PRELIMINARY PROGRAMME

TUESDAY 13TH SEPTEMBER 2022

18:00-19:30	**Registration /** Registration also open on 14th September from 7:30 am onwards and 15th-16th September from 8:00 am onwards
19:30–20:00	**Welcome address**
20:00–21:30	**Welcome cocktail**

WEDNESDAY 14TH SEPTEMBER 2022

S1.1	ECOFUELS: NH3-BASED FUELS

8:30-9:00 — **KEYNOTE LECTURE: Energizing mobility transition with low carbon synthetic fuels.**
Amer Amer. Saudi Aramco, Saudi Arabia

9:00-9:25 — **Performances and pollutant emissions of spark ignition engine using direct injection for blends of ethanol/ammonia and pure ammonia**
R. Pelé[1], P. Brequigny[1], J. Bellettre[2], C. Mounaïm-Rousselle[1]
[1]Université d'Orléans, France
[2]UMR Université de Nantes, France

9:25-9:50 — **Effect of compression ratio and ignition energy on ammonia premixed combustion process in a single cylinder engine**
H. Won[1], D. Kumar[1], V. Morel[1], A. Mercier[2], C. Mounaïm-Rousselle[2], J. Bouriot[3], S. Houille[3], C. Dumand[3]
[1]Aramco Overseas Company B.V. Rueil-Malmaison, France
[2]Université d'Orléans, France
[3]Stellantis – Centre Technique Velizy, France

9:50-10:15 — **A study of flame dynamics and structure in premixed turbulent planar NH_3/H_2/air flames**
P. Tamadonfar, S. Karimkashi, O. Kaario, V. Vuorinen
Aalto University, Finland

10:15-10:45 — **Coffee break**

S1.2	ECOFUELS: BIOFUELS

10:45-11:10 — **Performance and exhaust emissions of a Diesel engine fueled with pyrolytic oil from plastic wastes**
J. Tejada-Hernández, M. Carmona-Cabello, J.A. Serrano, S. Pinzi, Mª P. Dorado-Pérez
Universidad de Córdoba, Spain

11:10-11:35 — **Design, vehicle testing and Life Cycle Analysis (LCA) of 100% renewable EN228 gasoline formulation**
C. Esarte, M.D. Cárdenas, R. Miravalles, J. Aríztegui
Repsol Technology Lab., Spain

11:35-12:00 — **Numerical analysis of the combustion of Diesel, dimethyl ether, and polyoxymethylene dimethyl ethers (OMEn, n=1-3) using detailed chemistry**
T. Franken[1], V. Srivastava[2], S.Y. Lee[2], B. Heuser[3], K.P. Shrestha[1], L. Seidel[4], F. Mauß[1]
[1]BTU Cottbus-Senftenberg, Germany
[2]RWTH Aachen University, Germany
[3]FEV Europe GmbH, Aachen, Germany
[4]LOGE Deutschland GmbH, Germany

12:00-12:25 — **Influence of fuel bound oxygen on soot mass and polyaromatic hydrocarbons during pyrolysis of ethanol, methyl acetate, acetone and diethyl ether**
Z.A. Khan[1], P. Hellier[1], N. Ladommatos[1], A.A. Almaleki[2]
[1]University College London, UK
[2]King Abdulaziz City for Science and Technology, Saudi Arabia

12:25-12:50 — **Characterization of waste cooking oil biodiesel as a low carbon fuel for direct injection Diesel engine**
O.A. Kuti[1], S. Bahmanisangesari[1], R. Gilmour[1], A. Albarbar[1], L. Qian[1], K. Nishida[2]
[1]Manchester Metropolitan University, UK
[2]Hiroshima University, Japan

WEDNESDAY 14TH SEPTEMBER 2022

12:50-15:30	**Lunch**
14:00-15:30	**Poster session / Commercial exhibition / Visit to CMT laboratories**

S1.3   H2 - FUNDAMENTAL STUDIES

15:30-16:00	**KEYNOTE LECTURE: Hydrogen as a new energy carrier – what does this mean for the future mobility?** Robert Plank. Horiba Europe, Germany
16:00-16:25	**A fundamental investigation of premixed hydrogen oxy-combustion in carbon dioxide** N. Nasim, B. Nawaz, S.K. Das, A. SubLaban, J.H. Mack University of Massachusetts Lowell, USA
16:25-16:50	**Experimental investigation of hydrogen combustion in a single cylinder PFI engine** L. Buzzi, V. Biasin, A. Galante, D. Gessaroli, F. Pesce, D. Tartarini, A. Vassallo, S. Scalabrini, N. Sacco, R. Rossi PUNCH Torino, Italy
16:50-17:20	**Coffee break**

## S1.4   H2 - ICE EMISSIONS

17:20-17:45	**Examining trade-offs between NOx emissions and hydrogen slip for hydrogen combustion engines** P. Atkins[1], N. Fox[1], A. Saroop[2], J. Hughes[2], Nicolas Coles[2], Trevor Downes[2], A. Thurston[3] [1]University of Brighton, UK [2]Ricardo Ltd., UK [3]Horiba United Kingdom, UK
17:45-18:10	**Emission behavior and aftertreatment of stationary and transient operated hydrogen engines** S. Roiser, P. Christoforetti, E. Schutting, H. Eichlseder Technical University of Graz, Austria
18:10-18:35	**Hydrogen internal combustion engine: viable technology for carbon neutral mobility** Y. H. Chi[1], B. S. Shin[1], S. Hoffmann[2], J. Ullrich[2], P. Adomeit[3], J. Fryjan[3], R. Drevet[4] [1]Hyundai Motor Company, Korea [2]Hyundai Motor Europe Technical Center GmbH, Germany [3]FEV Europe GmbH, Germany [4]BorgWarner France SAS, France

IJER SPECIAL ISSUE

A selection of papers from THIESEL2022 will be published by the International Journal of Engine Research (IJER) in a special issue.

THURSDAY 15TH SEPTEMBER 2022
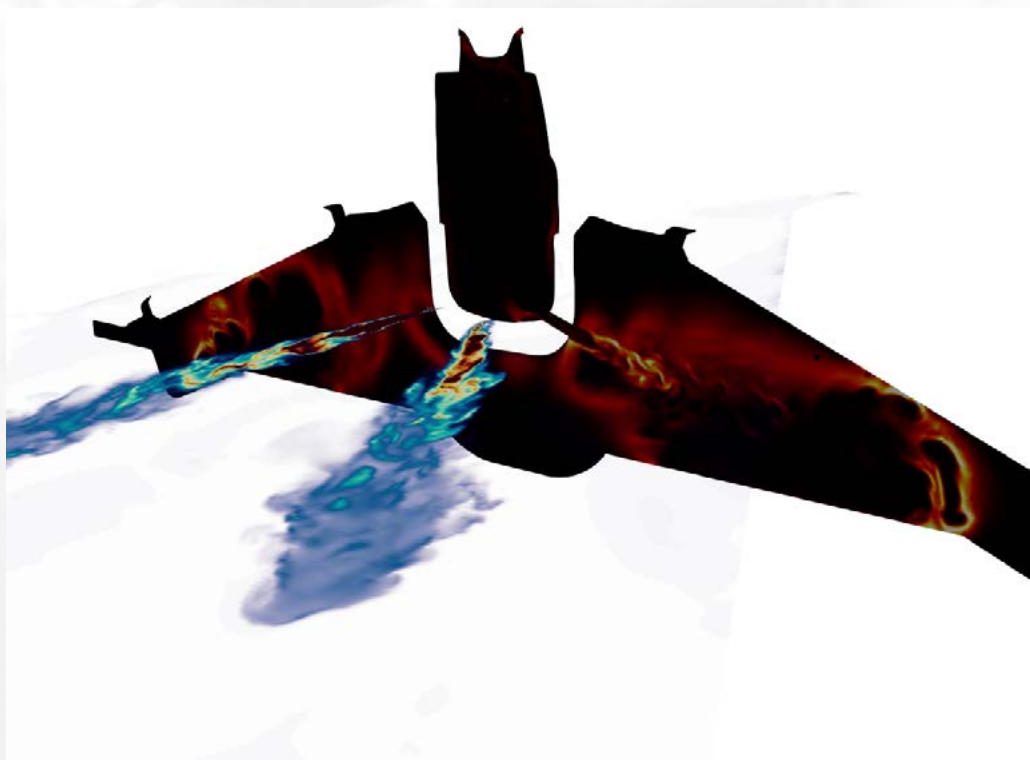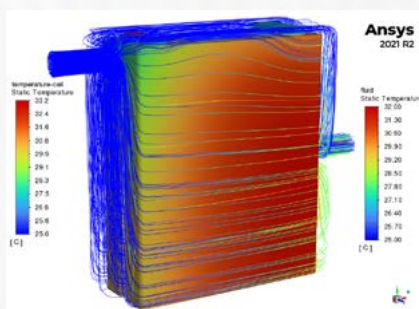
S2.1	THERMAL MANAGEMENT

8:30-9:00 KEYNOTE LECTURE: Battery storage technology in future electrified vehicles.

Noshin Omar. ABEE, Belgium

9:00- 9:25 **Computational investigation on radiation induced Li-ion battery thermal runaway**

L. Zhang[1], Y. Chen[2], H. Ge[3], P. Zhao[1]
[1]University of Tennessee, USA
[2]A123 Systems, USA
[3]Texas Tech University, USA

9:25-9:50 **Battery system lumped thermal model for efficient temperature prediction**

H. Jang, B. Park, T. Kang, J. Yi, W. Kim
Hyundai Motor Company, Korea

9:50h-10:15 **Energy consumption of mobile air-conditioning systems in electrified vehicles under different ambient temperatures**

S. Gil-Sayas[1], G. Di Pierro[2], A. Tansini[2], S. Serra[2], D. Currò[3], A. Broatch[1], G. Fontaras[2]
[1]Universitat Politècnica de València, Spain
[2]European Commission's Joint Research Centre, Italy
[3]Piksel s.r.l. Milano, Italy

10:15-10:45 **Coffee break**

S2.2	FUEL INJECTION AND SPRAYS

10:45-11:10 **Characterization of end of injection events for a high-pressure gasoline direct injection system in a constant volume chamber**

V. Chakrapani[1], J.E. Stolzman[1], E.S. Simoes[2], M. Medina[2], M. Wooldridge[1]
[1]University of Michigan, USA
[2]California State University, USA

11:10-11:35 **Measurement of needle and armature dynamics in a gasoline direct injector by high-speed neutron imaging**

M.L. Wissink, T.J. Toops, D.A. Splitter, E.J. Nafziger, C.E.A. Finney, H.Z. Bilheux, Y. Zhang
Oak Ridge National Laboratory, USA

11:35-12:00 **Investigation on effect of nozzle diameter and inclusion angle to combustion and emissions under high compression ratio heavy-duty Diesel engine**

K. Cung, C. Bitsis, M. Smith, T. Briggs
Southwest Research Institute San Antonio, USA

12:00-12:25 **Parametric evaluation of ducted fuel injection in an optically accessible mixing-controlled compression-ignition engine with two- and four-duct assemblies**

B.F. Yraguen[1], A.M. Steinberg[1], C.W. Nilsen[2], D.E. Biles[2], C.J. Mueller[2]
[1]Georgia Institute of Technology, USA
[2]Sandia National Laboratories, USA

12:25-12:50 **Computational analysis of ducted fuel injection at high-pressure transcritical conditions using large-eddy simulations**

J. Guo, W. T. Chung, M. Ihme
Stanford University, USA
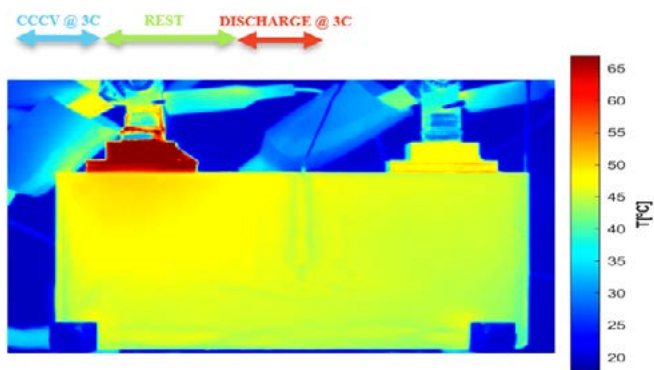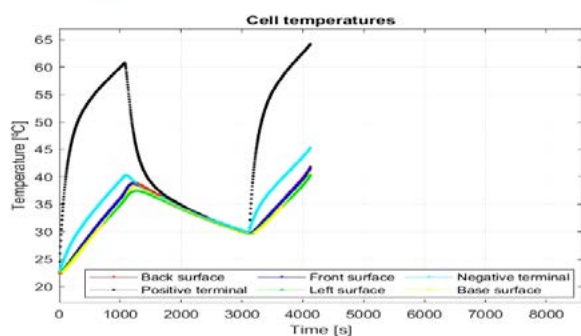
THURSDAY 15ᵀᴴ SEPTEMBER 2022

| 12:50-15:30 | **Lunch** |
| 14:00-15:30 | **Poster session / Commercial exhibition / Visit to CMT laboratories** |

| **S2.3** | **ADVANCES TOWARDS ICE EMISSION REDUCTION** |

| 15:30-16:00 | **KEYNOTE LECTURE: Pathways for near-zero emissions from the transportation sector – an overview of challenges and opportunities.** |
| | Ameya Joshi.   Corning Incorporated, USA. |

16:00-16:25	**Experimental validation of laminar flame model for CH₄/Diesel dual fuel engine applied to H₂/Diesel combustion**
	R. De Robbio[1], E. Mancaruso[1], B.M. Vaglieco[1], S. Artham[2], J. Martin[2]
	[1]STEMS – CNR, Italy
	[2]Universitat Politècnica de València, Spain

16:25-16:50	**The impact of Diesel-hythane dual-fuel combustion on engine performance and emissions in a heavy-duty engine at low-load condition**
	K. Longo, X. Wang , H. Zhao
	Brunel University London, UK

16:50-17:15	**Innovative Diesel piston geometries for soot emissions reduction and cleaner combustion: an optical investigation**
	J.V. Pastor[1], C. Micó[1], F. Lewiski[1], F.J. Tejada[1], A. Vassallo[2], F.C. Pesce[2], G. Belgiorno[2]
	[1]Universitat Politècnica de València, Spain
	[2]PUNCH Torino, Italy

| 17:15-17:45 | **Coffee break** |

| **S2.4** | **NEW CONCEPTS FOR ULTRAEFFICIENT & CLEAN ICEs** |

17:45-18:10	**Developing an accelerated procedure for assessing the injector fouling abatement of different fuel additives**
	G. Brinklow[1], J.M. Herreros[1], S. Zeraati-Rezaei[1], A. Tsolakis[1], F. Oliva[2]
	[1]The University of Birmingham, UK
	[2]Repsol Technology Lab., Spain

| 18:10-18:35 | **A three-stage Arrhenius approach with a coupled 0D-Model to predict ignition delays in a Premixed Charge Compression Ignition (PCCI) Diesel engine** |
	M. Wahl[1], M. Bargende[1], A. Casal Kulzer[1], H.-J. Berner[2], S. Schneider[3]
	[1]University of Stuttgart, Germany
	[2]Forschungsinstitut für Kraftfahrwesen und Fahrzeugmotoren Stuttgart (FKFS), Germany
	[3]MAHLE International GmbH, Germany

18:35-19:00	**CFD modeling of ducted fuel injection compression-ignition combustion**
	T. Lucchini, L. Sforza, Q. Zhou, G. D'Errico, D. Severgnini, A. Onorati
	Politecnico di Milano, Italy
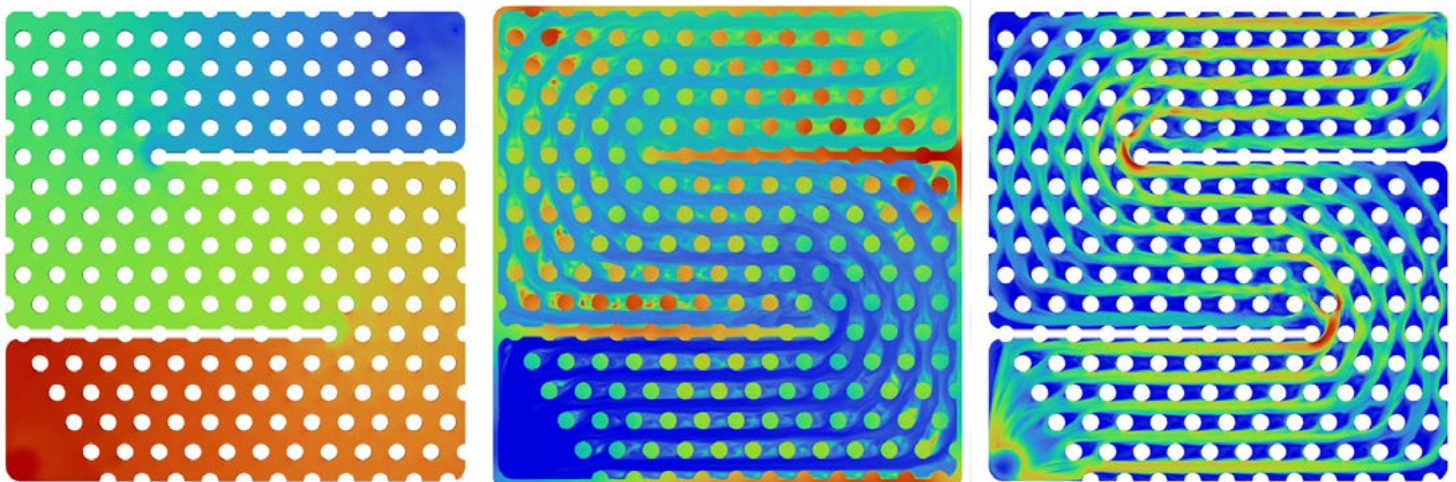
FRIDAY 16TH SEPTEMBER 2022

S3.1	ADVANCED POWERTRAIN

8:30-9:00 — **KEYNOTE LECTURE: Propulsion system contribution to Hyundai Carbon neutrality Road Map.**
Alain Raposo. Hyundai, Korea.

9:00- 9:25 — **Understanding the fuel consumption of plug-in hybrid electric vehicles: a real-world case study**
M.A. Ktistakis, A. Tansini, A. Laverde, D. Komnos, J. Suarez, G. Fontaras
European Commission's Joint Research Centre, Italy

9:25-9:50 — **Development of hybrid electric vehicles in the context of life cycle assessment**
P. Weber, O. Toedter, T. Koch, T. Weyhing
Karlsruhe Institute of Technology, Germany

9:50-10:15 — **Horiba Intelligent Lab – Digitalisation of propulsion system development for emissions compliance**
P. Roberts, K. Tabata, L. Bates, A. Headley, S. Whelan
Horiba Mira, UK

10:15-10:45 — **Coffee break**

S3.2	ADVANCES FOR ULTRAEFFICIENT ICEs

10:45-11:10 — **Optical imaging for understanding of thermal barrier coated piston engine performance**
C. Koci[1], K. Svensson[1], G. Martin[1], C. Kim[1], P. Seiler[1], F. Caliari[2], J. Saputo[2], S. Sampath[2]
[1]Caterpillar Inc. – Technical Center, USA
[2]Stony Brook University, USA

11:10-1135 — **A novel combustion control to achieve higher thermal efficiency for a heavy-duty Diesel engine with high compression ratio**
N. Uchida[1], K. Watanabe[2]
[1]New ACE Institute Co., Japan
[2]Denso Corporation, Japan

11:35h-12:00h — **Experimental optimization of a medium speed dual fuel engine towards RCCI operation**
M. Merts[1,2], J. Hyvönen[3], M. Lundgren[1], P.A. Veenhuizen[2], S. Verhelst[1]
[1]Lund University, Sweden
[2]HAN Automotive Research, The Netherlands   [3]Wärtsilä Finland Oy, Finland

12:00h-12:25h — **Advances in pre-chamber combustion technology for fuel-flexible high efficiency engines**
H.G. Im[1], M. Ben Houidi[1], P. Hlaing[1], F. Almatrafi[1], Q. Tang[1], M.M. Silva[1], H. Aljabri[1], X. Liu[1], K. Hakimov[1], W. Tang[1], I. Gorbatenko[1], J. Turner[1], G. Magnotti[1], A. Farooq[1], S.M. Sarathy[1], B. Mohan[2], A. AlRamadan[2], A. Nicolle[3], E. Cenker[2], A. Amer[2], W.L. Roberts[1]
[1]King Abdullah University of Science and Technology, Saudi Arabia
[2]Aramco Research and Development Center, Saudi Arabia   [3]Aramco Fuel Research Center, France

12:25h-12:50h — **A numerical study of fuel stratification, heat transfer loss, combustion, and emissions characteristics of a heavy-duty RCCI engine fueled by E85/Diesel**
A. Willems[1], P. Rahnama[1,2], B. Somers[1], R. Novella[2]
[1]Technical University of Eindhoven, The Netherlands
[2]Universitat Politècnica de València, Spain

12:50h-15:30h — **Lunch**

14:00h-15:30h — **Poster session / Commercial exhibition / Visit to CMT laboratories**

S3.3	ADVANCED POWERTRAIN CONTROL

15:30h-16:00h — **KEYNOTE LECTURE: Sustainable powertrains for commercial vehicles.**
Nicolas Tourteaux. Volvo GTT Lyon, France.

16:00h-16:25h — **V2X-based engine management and transient control in HEVs with planetary gear unit**
Z. Xu[1], B. Zhang[1], S. Narita[1], F. Xu[2], T. Shen[1]
[1]Sophia University, Tokyo, Japan
[2]Tokyo City University, Japan

16:25h-16:50h — **Economical predictive cruise control-based real-time energy management strategy for connected HEVs**
Y. Zhang[1,2], X. You[1], Z. Wei[1], X. Jiao[1]
[1]Yanshan University, China   [2]Tsinghua University, China

16:50h-17:15h — **Assessment of driving patterns influence on a BEV supercar range using system simulation**
M. Montesinos, M. Rivas, E. Elipe
AVL Ibérica, Spain

17:15h-17:30h — **CLOSURE**

20:00h — **GALA DINNER**

POSTER SESSIONS

Three poster sessions are planned to enable the presentation of interesting work that could not be included in the Conference regular sessions. Extended abstracts of these works are included in the Conference Proceedings.

The poster sessions are planned after lunch every day, between 2:00 pm and 3:30 pm. The exact timetable for the poster presentations will be established once all posters are confirmed.

Conference participants are invited to visit the poster sessions and discuss the issues with their authors.

LIST OF POSTERS TO BE PRESENTED

OH* and NL measurements of two HD Diesel Injectors with identical cetane number fuels, RME and Diesel

H. Fajri, S. Rieß, R. Clemente, M. Wensing

FAU Erlangen-Nürnberg, Germany

Very low soot combustion with modulated liquid length and lift-off length of Diesel spray flame

C. Zhai, K. Nishida, Y. Ogata

Hiroshima University, Japan

Numerical and experimental investigations on the ignition behavior of OME

F. Wiesmann[1], L. Straus[2], S. Rieß[2], T. Lauer[1]

[1]Technische Universität Wien, Austria
[2]FAU Erlangen-Nürnberg, Germany

Effect of injection mass ratio of flat-wall impinging spray on fuel adhesion characteristics

F. Chang[1], H. Luo[1], Y. Hagino[1], T. Tashima[1], K. Nishida[1], Y. Ogata[1], R. Hara[2], K. Uchida[2], W. Zhang[2]

[1]Hiroshima University, Japan
[2]Mazda Motor Corporation, Japan

A simulation and experimental study of the feasibility of a hydrogen fuelled split cycle engine

R.E. Morgan[1], E. Wylie[1], A. Panesar[1], A. Atkins[2], N.J. Owen[2], R. Pickett[2], A. Harvey[2]

[1]University of Brighton, UK
[2]Dolphin N2, UK

Modeling of dual-fuel combustion under different fuel ratios and injection timing conditions

S. Moon, K. Min

Seoul National University, South Korea

A numerical study of hydrogen combustion in Wankel rotary engines

K. Moreno-Cabezas, G. Vorraro, X. Liu, J. Turner, H. Im

King Abdullah University of Science and Technology, Saudi Arabia

Numerical analysis of emissions and operating range of acetone fuel in an homogenous charge compression ignition at different engine speeds

J.M. Garcia[1], J.M. Riesco[2], J.P. Perez[1], A. E. Mendoza[1], O. Rodriguez[1], R. Hernandez[1]

[1]Polytechnic University of Queretaro, Mexico
[2]University of Guanajuato, Mexico

Towards the integration of heavy-duty vehicles in the hydrogen sector: development of a spark ignition engine using hydrogen as fuel

B. Walter[1], D. Serrano[1], F. Foucher[2], J.-M. Neveu[3], F. Duffour[1]

[1]IFP Energies nouvelles, France
[2]Prisme, France
[3]Volvo Group Trucks Technology, France

High performance and Near Zero Emissions H_2 Engine

S. Caprioli, F. Scrignoli, A. Volza, C.A. Rinaldini, E. Mattarelli

University of Modena and Reggio Emilia, Italy

The Argon power cycle: characterization of hydrogen injections

M.M.E. Peters, N.C.J. Maes, N.J. Dam, J.A. van Oi en University of Technology Eindhoven, The Netherlands

The Argon power cycle: Exploring DI-H_2 and DI-O_2 injection strategies using CFD

N. Diepstraten, L.M.T. Somers, J.A. van Oi en
University of Technology Eindhoven, The Netherlands

Spray combustion of fast pyrolysis bio-oil in a constant-volume combustion chamber

Y. Wang, N. Maes, B. Somers

Eindhoven University of Technology, The Netherlands

The influence of hydrogen direct injection on the combustion characteristics of a compression ignition engine

M. Aghahasani[1], A. Gharehghani[1], A. Mahmoudzadeh Andwari[2], J. Könnö[2]

[1]Iran University of Science and Technology, Iran
[2]University of Oulu, Finland

Numerical analysis of the effect of pre-injection strategy on performance and emissions of an opposed-piston two-stroke engine

R. Menaca, G. Vorraro, M. Silva, H.G. Im, J.W.G. Turner

King Abdullah University of Science and Technology, Saudi Arabia

Large eddy simulations (LES) towards a comprehensive understanding of ducted fuel injection concept in non-reacting conditions

F. Millo[1], C. Segatori[1], A. Piano[1], B. Peiretti Paradisi[1], A. Bianco[2]

[1]Politecnico di Torino, Italy
[2]Powertech Engineering, Italy

AUTHORS' LIST OF PAPERS AND POSTERS

Adomeit, P.
Aghahasani, M.
Albarbar, A.
Aljabri, H.
Almaleki, A.
Almatrafi, F.
AlRamadan, A.
Amer, A.
Aríztegui, J.
Artham, S.
Atkins, A.
Atkins, P.
Bahmanisangesari, S.
Bargende, M.
Bates, L.
Belgiorno, G.
Bellettre, J.
Ben Houidi, M.
Berner, H.
Bianco, A.
Biasin, V.
Biles, D.
Bilheux, H.
Bitsis, C.
Bouriot, J.
Brequigny, P.
Briggs, T.
Brinklow, G.
Broatch, A.
Buzzi, L.
Caliari, F.
Caprioli, S.
Cárdenas, M.
Carmona-Cabello, M.
Casal Kulzer, A.
Cenker, E.
Chakrapani, V.
Chang, F.
Chen, Y.
Chi, Y.
Christoforetti, P.
Chung, W.
Clemente Mallada, R.
Coles, N.
Cung, K.
Currò, D.
Dam, N.
Das, S.
De Robbio, R.

D'Errico, G.
Di Pierro, G.
Diepstraten, N.
Dorado-Pérez, M.
Downes, T.
Drevet, R.
Duffour, F.
Dumand, C.
Eichlseder, H.
Elipe, E.
Esarte, C.
Fajri, H.
Farooq, A.
Finney, C.
Fontaras, G.
Fontaras, G.
Foucher, F.
Fox, N.
Franken, T.
Fryjan, J.
Galante, A.
Garcia-Guendulain, J.
Ge, H.
Gessaroli, D.
Gharehghani, A.
Gilmour, R.
Gil-Sayas, S.
Gorbatenko, I.
Guo, J.
Hagino, Y.
Hakimov, K.
Hara, R.
Harvey, A.
Headley, A.
Hellier, P.
Hernández-Alvarado, R.
Herreros, J.
Heuser, B.
Hlaing, P.
Hoffmann, S.
Houille, S.
Hughes, J.
Hyvönen, J.
Ihme, M.
Im, H.
Im, H.
Im, H.
Jang, H.

Jiao, X.
Kaario, O.
Kang, T.
Karimkashi, S.
Khan, Z.
Kim, C.
Kim, W.
Koch, T.
Koci, C.
Komnos, D.
Könnö, J.
Ktistakis, M.
Kumar, D.
Kuti, O.
Ladommatos, N.
Lauer, T.
Laverde, A.
Lee, S.
Lewiski, F.
Liu, X.
Liu, X.
Longo, K.
Lucchini, T.
Lundgren, M.
Luo, H.
Mack, H.
Maes, N.
Maes, N.
Magnotti, G.
Mahmoudzadeh Andwari, A.
Mancaruso, E.
Martin, G.
Martin, J.
Mattarelli, E.
Mauß, F.
Medina, M.
Menaca, R.
Mendoza-Rojas, A.
Mercier, A.
Merts, M.
Micó, C.
Millo, F.
Min, K.
Miravalles, R.
Mohan, B.
Montesinos, M.
Moon, S.
Morel, V.

Moreno-Cabezas, K.
Morgan, R.
Mounaïm-Rousselle, C.
Mounaïm-Rousselle, C.
Mueller, C.
Nafziger, E.
Narita, S.
Nasim, N.
Nawaz, B.
Neveu, J.
Nicolle, A.
Nilsen, C.
Nishida, K.
Nishida, K.
Nishida, K.
Novella, R.
Ogata, Y.
Ogata, Y.
Oliva, F.
Onorati, A.
Owen, N.
Panesar, A.
Park, K.
Pastor, J.
Peiretti Paradisi, B.
Pelé, R.
Pérez-Trujillo, J.
Pesce, F.
Pesce, F.
Peters, M.
Piano, A.
Pickett, R.
Pinzi, S.
Qian, L.
Rahnama, P.
Riesco-Avila, J.
Rieß, S.
Rieß, S.
Rinaldini, C.
Rivas, M.
Roberts, W.
Roberts, P.
Rodríguez-Abreo, O.
Roiser, S.
Rossi, R.
Sacco, N.
Sampath, S.
Saputo, J.
Sarathy, S.

Saroop, A.
Scalabrini, S.
Schneider, S.
Schutting, E.
Scrignoli, F.
Segatori, C.
Seidel, L.
Seiler, P.
Serra, S.
Serrano, J.
Serrano, D.
Severgnini, D.
Sforza, L.
Shen, T.
Shin, B.
Shrestha, K.
Silva, M.
Silva, M.
Simoes, E.
Smith, E.
Somers, B.
Somers, B.
Somers, B.
Splitter, D.
Srivastava, V.
Steinberg, A.
Stolzman, J.
Strauss, L.
Suarez, J.
SubLaban, A.
Svensson, K.
Tabata, K.
Tamadonfar, P.
Tang, Q.
Tang, W.
Tansini, A.
Tansini, A.
Tartarini, D.
Tashima, T.
Tejada, F.
Tejada-Hernández, J.
Thurston, A.
Toedter, O.
Toops, T.
Tsolakis, A.
Turner, J.
Turner, J.
Turner, J.
Uchida, N.

Uchida, K.
Ullrich, J.
Vaglieco, B.
van Oijen, J.
van Oijen, J.
Vassallo, A.
Vassallo, A.
Veenhuizen, B.
Verhelst, S.
Volza, A.
Vorraro, G.
Vorraro, G.
Vuorinen, V.
Wahl, M.
Walter, B.
Wang, Y.
Wang, X.
Watanabe, K.
Weber, P.
Wei, Z.
Wensing, M.
Weyhing, T.
Whelan, S.
Wiesmann, F.
Willems, A.
Wissink, M.
Won, H.
Wooldridge, M.
Wylie, E.
Xu, Z.
Xu, F.
Yi, J.
You, X.
Yraguen, B.
Zeraati Rezaei, S.
Zhai, C.
Zhang, L.
Zhang, W.
Zhang, Y.
Zhang, Y.
Zhang, B.
Zhao, P.
Zhao, H.
Zhou, Q.

Session S1.2 Ecofuels: NH$_3$-Based Fuels

Performances and Pollutant Emissions of Spark Ignition Engine Using Direct Injection for Blends of Ethanol/Ammonia and Pure Ammonia

R. Pelé[1], P. Brequigny[1], J. Bellettre[2], C. Mounaïm-Rousselle[1]

[1]Univ. Orléans, INSA-CVL, EA 4229 – PRISME, F-45072 Orléans, France
[2]Laboratoire de Thermique et Energie de Nantes (LTeN UMR Université de Nantes—CNRS 6607)

E-mail: ronan.pele@etu.univ-orleans.fr (Ronan Pelé)

Abstract. Combustion and emissions characteristics of a spark-ignition engine using direct injection of ethanol blended with ammonia and also pure ammonia were investigated in this study. The experiments were conducted using five different fuel compositions of C_2H_5OH/NH_3: 100/0, 75/25, 50/50, 25/75, and 0/100. Two strategies of injection were conducted to reach homogenous or stratified conditions with three different intake pressures, 0.5, 1.0, and 1.5 bar corresponding to 2.8, 7.9, and 12 bar of IMEP. The performances and the pollutants emissions are compared as a function of fuel compositions at identical IMEP. High stability is observed for all blends and even for pure ammonia. However, operating conditions are more restrictive for pure ammonia: the injection must be made during the intake phase to be in fully premixed mode to guarantee the engine stability. Delaying the injection time for pure am-monia is not possible and requires the split of injections with 50% of the ammonia amount injected during the intake. The thermal efficiency is improved by adding 25% of NH_3 in ethanol but with NOx emissions increase. The stratified strategy for blends improves the combustion duration and the addition of ammo-nia decreases the NOx emission. On the contrary, CO emissions roughly increase for blends. The pres-ence of NH_3 in the fuel composition clearly influences the change of formation of NOx and CO between both strategies.

1. Introduction

Climate change has been one of the greatest challenges in the last decades and is unfortunately still an ongoing concern. Consequently, Europe has decided on a drastic reduction of greenhouse gases emis-sion by 55% in 2030 compared to 1990 [1]. To take up this challenge, the share of renewable energy must reach at least 32% and the use of low carbon fuels and biofuels is necessary. Biofuels are high-lighted as alternative energy sources and bio-ethanol is the most attractive one [2]. It can be produced from a wide variety of sources such as starch, sugarcane, lignocellulosic material derived from agricul-tural waste, and algae [3] reducing its CO_2 footprint.

To limit fossil fuel consumption, the first step of transition has been to blend current fuel as gasoline with bio-fuel. Bio-ethanol blended with gasoline provides positive effects as increasing engine efficiency [4] and decreasing dramatically CO and HC emissions [5]. Elfasakhany [6] explored the ternary blended fuels of bio-ethanol, bio-acetone, and gasoline and the results showed a reduction of CO, CO_2, and Total unburnt HydroCarbons (THC) emissions directly on a tailpipe for the ternary blend compared to ethanol/gasoline and acetone/gasoline. However, in the future decades, fossil fuels will be not available: the oil reserves will run out by 2066 [7].

To do without fossil fuels and mitigate climate challenges, carbon-free fuels such as hydrogen and am-monia are highlighted to be interesting solutions to decarbonize energy, transport, and industrial sectors, especially by considering their production from water electrolysis with green electricity. Hydrogen is an attractive energy carrier [8] but its storage and transport issues, its low ignition energy, and very wide flammability range are the main drawbacks to safety [9]. Ammonia, containing 17.8% by weight of hy-drogen, can be stored in the liquid phase at approximately 9 bar at 20 °C or -34 °C at ambient pressure. Its high auto-ignition temperature and research octane number (RON=130), narrow flammability range, and low laminar flame speed [10] make its combustion difficult. Consequently, ammonia needs to be boosted, i.e. its reactivity could be improved by adding a supplementary fuel, i.e. a promoter. Several studies have addressed the potential of ammonia as fuel in internal combustion engines, mainly blended with another fuel to promote ignition/combustion properties, as reviewed in Mounaïm-Rousselle and Brequigny [11] and Dimitriou and Javaid [12]. Kurien et al. [13] also reviewed the use of ammonia as an alternate fuel in dual-fuel compression ignition engines. This study demonstrates the effectiveness of ammonia combustion using the dual-fuel approach with secondary fuels like diesel, dimethyl ether,

kerosene, and hydrogen. Direct injection of ammonia/dimethyl ether in a compression-ignition engine is feasible [14,15] nevertheless, high cycle to cycle variation is observed when the blend content up to 60% of NH_3. The ignition delay becomes longer and limits the engine load conditions due to its high autoignition temperature and low flame speed. Relative high CO and HC emissions are observed and dedicated exhaust after-treatment is required. The use of ammonia in compression ignition engines is limited by its properties, and mainly by its high autoignition temperature, one of the key parameters of these engines. Nonetheless, in these difficult ignition conditions, the help of a spark can be useful as in [16,17].

The spark-ignition engine has the advantage to optimize combustion by controlling the ignition time. However, fewer studies focused on spark-ignition than on compression ignition engines with ammonia. Recently, Lhuillier et al. [10] confirmed that ammonia/hydrogen is a suitable fuel for current spark-ignition engines with indirect injection and without any design modifications. A numerical work [18], studied the ternary blend of gasoline, ethanol, and ammonia for a spark-ignition engine with port injection and high-lighted an increase of the power engine up to 1.4% for 10% of ammonia content but the CO and HC emissions increase also. The experimental study of Haputhanthri et al. [19] focused on the same ternary blend in a spark-ignition engine with direct injection. The blend of gasoline, ethanol 20%, and ammonia 12.9% by volume was identified as the optimum blend in terms of engine power showing the positive impact of ammonia. The preliminary analysis of this work evaluated the solubility of ammonia in gasoline/ethanol with a vapor-liquid equilibrium cell. The solubility of ammonia in pure gasoline is limited but the addition of ethanol helps to improve the solubility. This improvement is due to the polarities of ethanol and ammonia molecules [20] providing a total solubility between ammonia in ethanol proved in these studies [21,22] while gasoline molecules are not polarized. The direct injection used in [19] has the advantage to inject the liquid blend directly from the tank into the internal combustion chamber. Further-more, the total solubility of ammonia in ethanol in liquid phase and their high difference of vapor pressures [23] will generate an effervescent atomization when the pressure is below the saturation pressure of ammonia during a direct injection improving the fuel vaporization [24]. Moreover, the time of direct injection can be advanced to obtain a homogenous air/fuel mixture or on the contrary, a stratified/heterogeneous mixture by delaying the time of injection; these strategies will influence the performance and the pollutants emissions. The previous studies highlight the feasibility to store a stable homogeneous blend of ammonia and ethanol in the liquid phase providing an efficient way of storing the fuel energy by a unit of volume. Consequently, the direct injection of the liquid fuel into the combustion chamber seems to be the easier solution of injection. The potential of ammonia as a future carbon-free fuel blend to bio-ethanol as an alternative fuel to fossil fuel in a spark-ignition engine needs to be evaluated. This study aims to provide the first data on the performances and pollutants emissions of ethanol blended with ammonia using direct injection.

2. Experimental set-up

The engine experiments were conducted in a single-cylinder long-stroke spark-ignition engine (based on PSA-EP6) with a flat piston and a pent-roof chamber. The engine specifications are indicated in Table 1, and more information can be found in [17]. The engine is driven by an electric motor maintained at 1000 RPM. The main shaft is equipped with a Kubler optical encoder for angular position monitoring with a 0.1 Crank Angle Degree (CAD) resolution. A water-cooled AVL piezoelectric pressure transducer with a 0.1 CAD resolution provides in-cylinder pressure measurements. Its measuring range is 0–25 MPa. Engine intake and exhaust temperature and pressure are monitored using type K thermocouples and piezo-resistive absolute pressure transducers. The absolute cylinder pressure is obtained by equalizing the in-cylinder pressure and the mean absolute intake pressure (Pin), 20 CAD in the middle of the intake stroke.

Table 1: Engine characteristics

	SI (EP6 LC)
Displaced volume (L)	0.535
Stroke (mm)	115
Bore (mm)	77
Connecting rod length (mm)	177
Compression ratio	11.75
Number of valves	4
Coolant and oil temperatures (°C)	80

The spark plug used is the original one with a coil charging time set to 2 ms (~80mJ). Air gaseous flows, preheated to the intake temperature were measured and controlled using Brooks thermal mass flowmeters with +- 0.7% accuracy. The ethanol is blended with ammonia beforehand with a mixture set up and then store in a tank. The liquid fuel is pressured with helium at 120 bar and injected with a current gasoline direct Bosch injector (7 holes of 365 µm diameter) located at the central position. A scheme
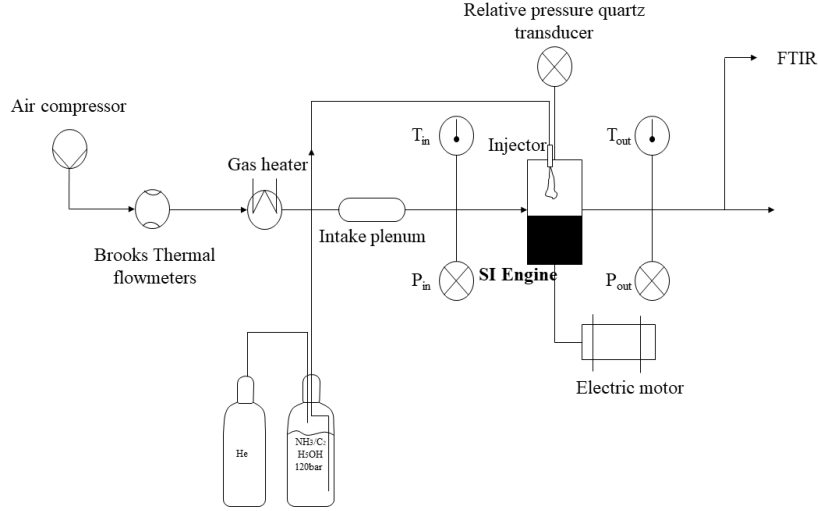
of the experimental setup is shown in Fig.1. The mass injected is deduced with the time of injection controlled and the mass flow rates for each blend were previously estimated in a constant vessel.

Fig. 1. Experimental set-up

The apparent Heat Release Rate (HRR) was computed from pressure trace post-processing with the first law of thermodynamics, as follows:

$$\frac{dQ_{Net}}{d\theta} = \frac{\gamma}{\gamma - 1}.P.\frac{dV_{Cyl}}{d\theta} + \frac{1}{\gamma - 1}.P.\frac{dP_{Cyl}}{d\theta} \tag{1}$$

where γ is the heat capacity ratio, P_{Cyl}, V_{Cyl} and θ, the cylinder pressure, volume, and crank angle respectively. The Burnt Mass Fraction (BMF) is obtained by integrating the heat release using a constant γ. Then the apparent HRR is recalculated using the variable heat capacity ratio computed from the previous BMF. In addition, the wall heat exchange was modeled:

$$\frac{dQ_{Wall}}{d\theta} = \frac{1}{6N}.h_c.S_{Wall}.\left(T_{Wall} - T_{Cyl}\right) \tag{2}$$

Where N is the engine speed, h_c the convection coefficient, S_{Wall} wall surface, T_{Wall} the surface temperature and T_{Cyl} is the temperature in the combustion chamber. The Woshni model was used to estimate the energy fraction lost at the wall and the convection coefficient was optimized by changing only the C_0 value from Eq. (3) as showed in table 2 until the energy balance, Eq. (4), becomes true.

$$h_c = C_0 \left(B^{-0.2}P_{Cyl}{}^{0.8}\left((C_1 C_m) + \frac{C_2 C_u T_{BDC}}{P_{BDC}V_{BDC}}\left(P_{Cyl} - P_0\right)\right)^{0.8} T_{Cyl}{}^{-0.53} \right) \tag{3}$$

with B the cylinder bore, C_m the mean piston speed, C_u the engine displacement and P_0 the cylinder pressure without combustion, BDC the bottom dead center. C_0 is a constant value, function of the fuel and optimised with minimized error function in Matlab subroutine (Table 2), C_1=2.28 and, C_2=3.22e-3 between SIT and CA90 else C_2= 0,

$$\int_{SIT}^{CA90} dQ_{Comb} = \int_{SIT}^{CA90} dQ_{Wall} + \int_{SIT}^{CA90} dQ_{Net} = 0{,}9 . m_{Fuel} . LHV_{fuel} . \eta_{Comb} \tag{4}$$

The different phases of combustion propagation were determined by estimating different characteristic timings, named CAXX, which are the Crank Angle degrees corresponding to XX% of the burnt mass fraction.

The wet exhaust gases were analysed using a Gasmet Fourier Transform Infrared (FTIR) spectrometer to assess H_2O, CO_2, NO, CO, THC, and NH_3 concentrations. The FTIR did not make it possible to measure thresholds <50 ppm of N_2O for the present spectra optimisation: no higher detection was noted.

Table 2: Values of C_0 and the heat capacity ratios for unburned and burned gasses

	CH_4	X_0	X_{25}	X_{50}	X_{75}	X_{100}
C_0	21.13	10.92	9.78	18.18	23.02	31.62
γ_{unburned}	1.37	1.34	1.34	1.34	1.35	1.35
γ_{burned}	1.27	1.27	1.27	1.27	1.28	1.27

2.1 *Operating conditions*

The performances and the pollutants emissions are compared as a function of the different fuel compositions at constant IMEP. Each operating condition is selected with optimum Start Ignition Time (SIT) and a fuel mass injected to obtain the target IMEP with a minimum of Covariance as well as possible. These target IMEP were obtained with the methane conditions (reference case) for the three intake pressures, as indicated in Table 3. Two strategies for the fuel injection were explored: the homogenous condition which corresponds to a fuel injection timing (Start of Injection - SOI) at 175 CAD before Top Dead Center (bTDC) and the stratified condition to a SOI of 90 CAD bTDC. Table 4 sums up the experimental conditions.

Table 3: Equivalence ratio correspondence for the different ethanol/ammonia blend, based on CH4 reference

Inlet Pressure (Bar)	Φ_{CH_4}	PMI_{CH_4}	Φ_{X0}	Φ_{X25}	Φ_{X50}	Φ_{X75}	Φ_{X100}
0.5	1	2.8	0.75	0.8	0.8	0.92	X
1	1	7.9	0.75	0.74	0.75	0.8	1.36
1.5	1	12	0.79	0.74	0.77	0.79	1.27

Table 4: Experimental conditions for both injection strategies

Injection pressure (bar)	120
Intake temperature (°C)	80
Blend (%NH$_3$ in mole)	0, 25, 50, 75, 100
Inlet pressure (bar) / Target IMEP (bar)	0.5; 1.0; 1.5 / 2.8; 7.9; 12
Engine speed (rpm)	1000

From pure ethanol to pure ammonia, the different fuel compositions follow the complete combustion reaction described as:

$$n_{Fuel}\, Fuel + n_{air}\, Air = n_{CO_2}\, CO_2 + n_{H_2O}\, H_2O + n_{N_2}\, N_2 \tag{5}$$
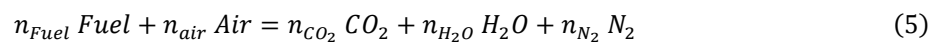
By considering 1 mole of $n_{Fuel} = (1 - X_{NH_3})C_2H_5OH + X_{NH_3}NH_3$ with X_{NH_3}, the mole fraction of ammonia in fresh gases. Therefore, the equivalence ratio (ER) is defined as:

$$ER = \left(\frac{n_{Fuel}}{n_{Air}}\right) \bigg/ \left(\frac{n_{Fuel}}{n_{Air}}\right)_{Stoichiometry} \tag{6}$$

The thermal and combustion efficiencies are defined as:

$$\eta_{Thermal} = \frac{IMEP.V_{Cyl}}{LHV_{Fuel}} \tag{7}$$

$$\eta_{Combustion} = 1 - \frac{LHV_{CO}X_{CO,\ Exhaust} + LHV_{C_2H_5OH}X_{THC,\ Exhaust} + LHV_{NH_3}X_{NH_3,\ Exhaust}}{LHV_{C_2H_5OH}\left(1 - X_{NH_3}\right) + LHV_{NH_3}X_{NH_3}} \tag{8}$$

$$LHV_{Fuel} = (1 - X_{NH_3})LHV_{C_2H_5OH} + LHV_{NH_3}X_{NH_3} \tag{9}$$

With $LHV_{C_2H_5OH} = 1234.8\ kJ/kmol$ and $LHV_{NH_3} = 316.8\ kJ/kmol$.

2.2 *Kinetics modeling*

Two-zones spark-ignition engine model in Chemkin Pro – Ansys was used to simulate the experimental conditions in order to help the analysis. The experimental CA10, CA50, CA90, and SIT are the input data to fit the Wiebe function for the built-in OD simulation. This function describes the mass transfer between the 2 zones. The kinetic model used is CEU from [25], the unique one available currently for ethanol and ammonia blends. As the simulation model considers premixed conditions, therefore, only the homogenous conditions are modelled. Moreover, the heat losses are calculated in the simulation by implementation of the heat transfer coefficient h_c, as function of the crank angle, estimated in the post-processing step of the experimental data with Eq.3.

3. Results and discussions

The results presented correspond to the intake pressure set at 1 bar (IMEP=7.9 bar) for the two strategies homogenous and stratified to limit the number of figures.

3.1 *Homogeneous results*

The homogenous strategy corresponds to a SOI at 175 CAD bTDC to ensure a premixed mixture before ignition. The methane reference points are added to the figures. In the case of pure ammonia, the injection was set earlier at 340 CAD bTDC due to the combustion instabilities.

3.1.1 Performances

The lower heating value of the fuel (Eq.9), plotted in Figure 2.a, decreases strongly with the increase of ammonia content due to the high difference between LHV of ethanol and ammonia, i.e. a ratio of 3.9. Figure 2.b shows the pressure traces as a function of the crank angle for the different fuel compositions. The maximum pressure is in the same order of magnitude for all, reaching around 12 CAD after TDC (aTDC). The small differences are due to the same target of IMEP. The IMEP covariance, in Figure 2.c, highlights the good engine stability, less than 1.5% for pure ethanol and blends and lower than 5%, for pure ammonia. The heat release rate is plotted as a function of the crank angle, in Figure 2.d: the maximum decreases as a function of the ammonia content increase and the combustion duration

increases. 30 CAD is necessary to release almost all the heat for pure ethanol. But for pure ammonia, the maximum is 40% less than for pure ethanol, and a double combustion duration can be noticed. This can be explained by the difference in combustion duration between ethanol and ammonia; the chemical time for carbon in terms of combustion is faster than for nitrogen giving off heat faster.
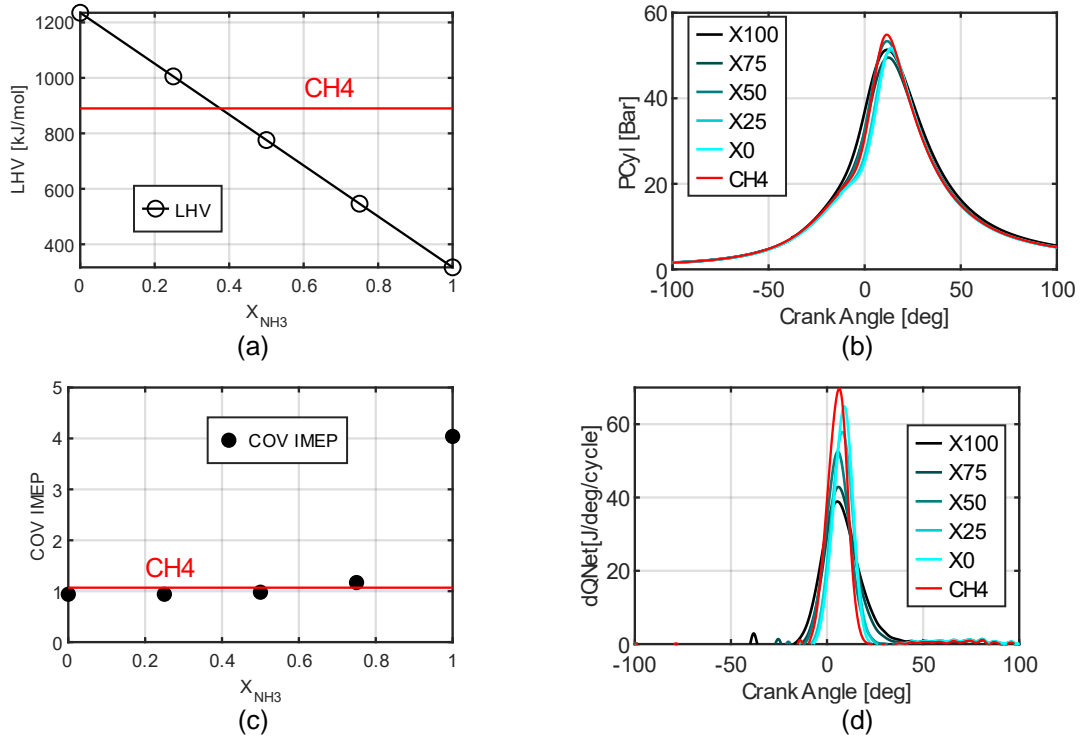
Fig. 2. Combustion specificities as a function of the Ethanol/Ammonia blend, LHV at stoichiometric ratio (a), in-cylinder pressure (b), cycle by cycle stability (c), and heat release rate (d) at 1 bar of intake pressure and homogeneous injection strategy.

These observations are more visible in the characteristic durations as CA90-CA10, the combustion duration, CA10-SIT, the flame kernel development, and CA50-CA10, the self-sustained flame propagation phase. Figure 3.a shows these characteristic timings: they increase non-linearly with ammonia content. CA90-CA10, CA10-SIT, and CA50-CA10 increase by 33%, 31%, and 18% respectively from pure ethanol to X50 and 90%, 147%, and 61% respectively from pure ethanol to pure ammonia.

(c)
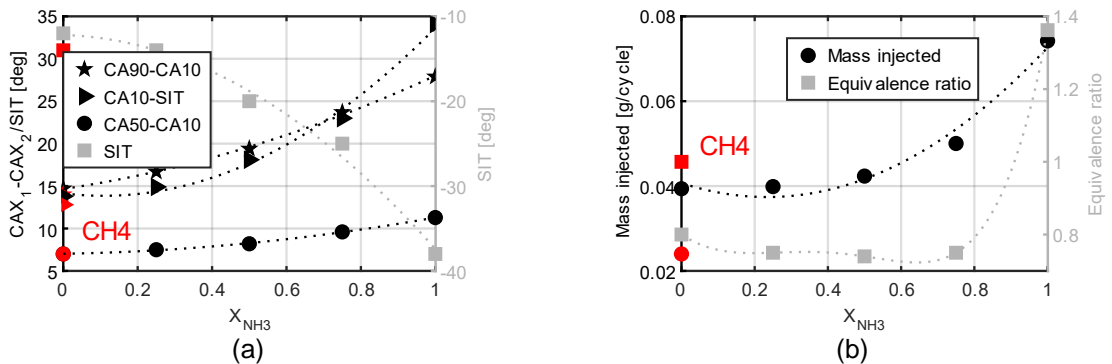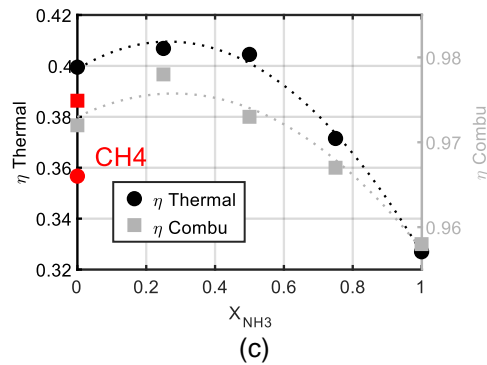
Fig.3. Characteristic of different combustion durations (a), fuel consumption and global equivalence ratio (b), and thermal and combustion efficiencies (c) for all fuel compositions at 1 bar of intake pressure and homogeneous condition.

The change of combustion durations with the ammonia content increases mainly due to the decrease of laminar flame speed with ammonia content, -41% and -86% from pure ethanol to X50 and pure ammonia respectively, at ignition conditions, with CEU mechanism (Figure 4).
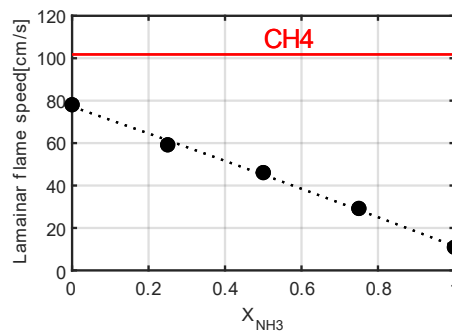
Fig. 4. Laminar flame speed for all fuel compositions at ignition conditions, predicted by CEU mechanism at 1 bar of intake pressure and homogeneous conditions.

Due to these properties of combustion durations, the start of ignition should be advanced by increasing the ammonia content to have the optimal IMEP with minimum fuel consumption. The fuel consumption is shown Figure 3.b and increases with the ammonia content to counterbalance the decrease of the LHV, Figure 2.a, and the combustion efficiency, Figure 3.c. The combustion efficiency is maximum for X25 and then decreases with ammonia increase to reach a minimum at 0.958. The thermal efficiency, Figure 3.c, has the same behaviour as the combustion efficiency and up to 40.5% for X25, providing good performances and a positive effect of ammonia by considering ethanol as the main fuel. It has to be underlined that the global equivalence ratio, Figure 3.b, is lean for pure ethanol and blends but extremely rich for pure ammonia. It can be explained by the injection strategy at 340 CAD bTDC that decreases the intake airflow and consequently increases the global equivalence ratio.

3.1.2 Pollutant emissions

NH3 exhaust, Figure 5.a, increases as a function of the ammonia content, and furthermore pure ammonia reaches the highest value due to the high equivalence ratio. In terms of NOx, the behaviour is completely non-linear with a maximum value 4 times higher than in the case of pure ethanol and obtained for X50. The lean equivalence ratio of blends and ethanol are favourable conditions for NOx formation and the addition of nitrogen from ammonia increases the NOx formation. The same trend was observed for methane/ammonia [26,27] with a maximal NO emission for a 50/50 blend. NOx emissions for pure ammonia are lower by 12% than for pure ethanol, mainly due to the rich global equivalence ratio. Some details about reaction paths are provided in following. The Total unburnt HC (THC) emissions, Figure 5.b, are not linear with the amount of ammonia, always lower for the blends than for pure ethanol with a minimum for X25, and zero THC pure ammonia as expected. CO emission decreases as the decrease of carbon content in the fuel composition. However, in Figure 5.c, CO emissions as a function of the

load (i.e. intake pressures) highlight the non-linear dependence on ammonia content with a maximum for X25. Niki et al. [28] confirmed that CO emissions for blends of diesel and ammonia increase with the NH_3 intake flow rate in a diesel engine. Moreover, Ryu et al. [29] showed a rise in CO emissions for a blend of 60%NH_3/40% DME. As not expected, adding free carbon fuel could not reduce carbon emissions and as a function of the conditions could have a reverse effect. Figure 5.d compares CO_2 emissions measured and CO_2 resulting from the combustion reaction described in Eq.5, the trend is very similar between both. To reduce by a factor 2 the CO_2 emissions, adding 80% of NH_3 is necessary.
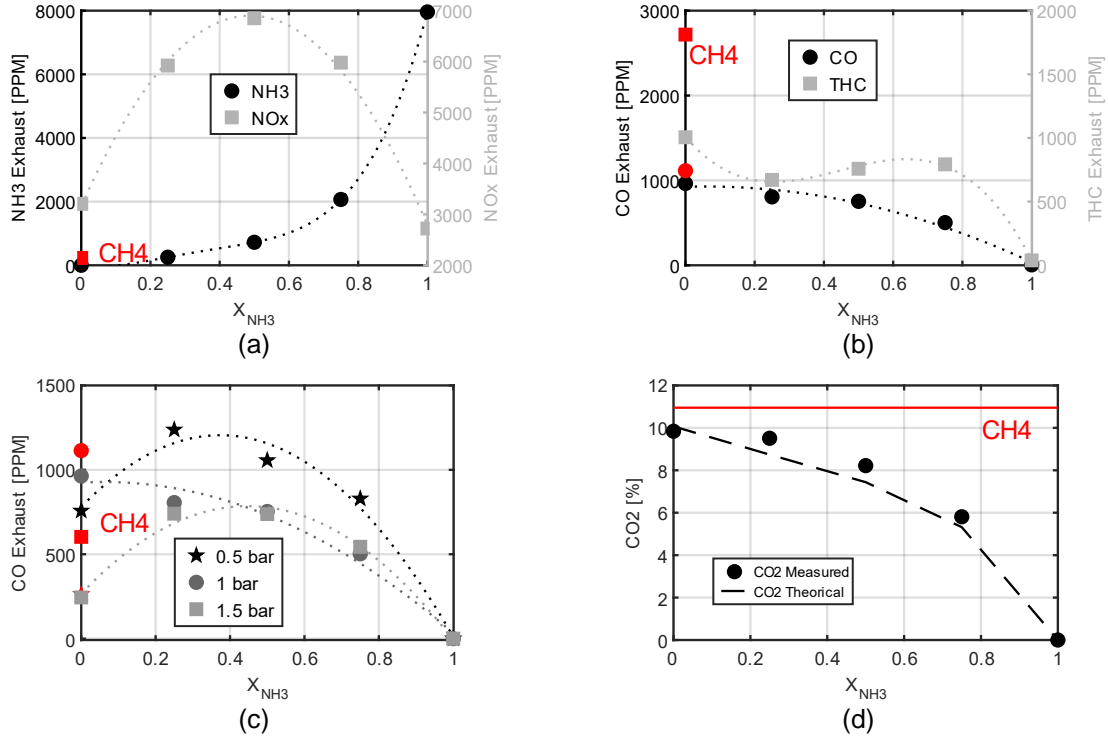
Fig.5. Pollutant emissions as a function of the ethanol/ammonia blends: NH_3 and NOx (a), CO and THC (b), CO_2 (d) at 1 bar of intake pressure, and CO (c) at 0.5,1 and 1.5 of intake under homogeneous condition.

The results of the simulations are shown in Figure 6 for the same previous conditions. The simulated pressure, Figure 6.a, is overestimated by around 10 bar (up to 20 bar for pure ethanol) compared to the experimental results. Due to the inaccurate estimate of the wall heat losses, the estimated in-cylinder temperature reaches 2473K for pure ethanol (X0), as it can be seen in Figure 6.b while only 2088K, for X75. The highest CO and NO mole fractions are obtained for pure ethanol (X0), as it can be seen Figure 6.c. Then, the peaks of CO and NO mole fractions inside the cylinder decrease with ammonia addition, as opposite to the experimental values measured at the exhaust that do not present any trend. But CO is estimated as being totally post-oxidized due also to the high in-cylinder temperature Moreover, the maximum of NO productions seems to be linked to the maximal CO one, as highlighted in Figure 6.d, for the blends and pure ethanol. The relation between the CO and NO production can provide additional information to understand the similarities of experimental trend of NO and CO as a function of ammonia content, Figure 5.c and Figure 5.a.

(c)   (d)
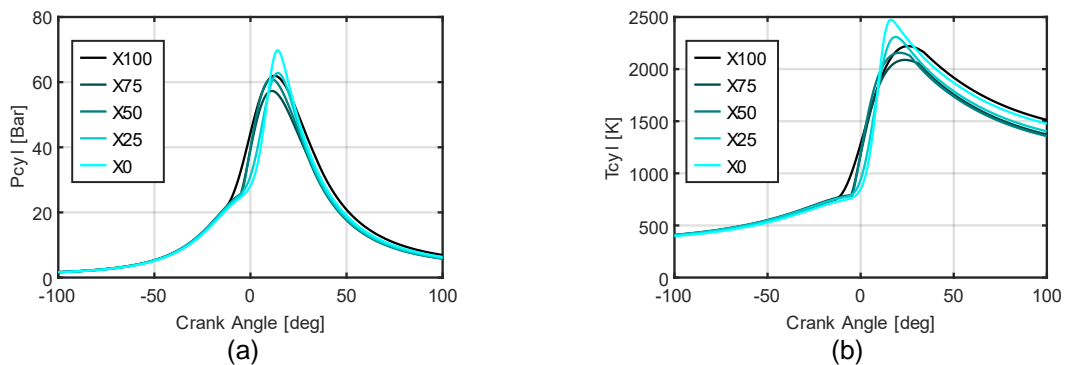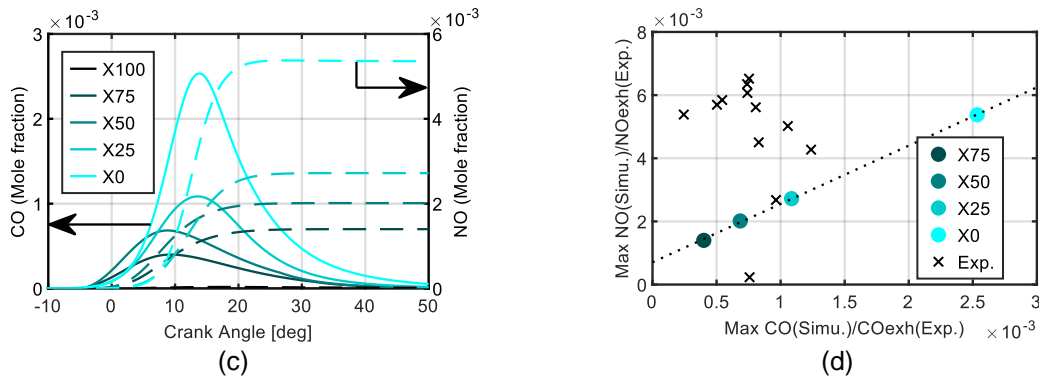
Fig.6. Results from OD kinetics simulations for all fuel compositions: in-cylinder pressure (a), in-cylinder temperature (b), CO (continuous line) and NO (dashed line) mole fraction evolutions (c) and the relationship between maximum of CO and NO mole fractions compared to the experimental data at the exhaust (d) at 1 bar of intake pressure.

The kinetics simulations complete the analysis to better understand the pollutant formation. The 10 reactions that most influenced the production of NO were selected. Their rates of production were integrated during all the time of the simulation and compared to the integrated global rate of production of NO. Figure 7 illustrates the influence of the different pathways on NO production and 3 major pathways are identified.
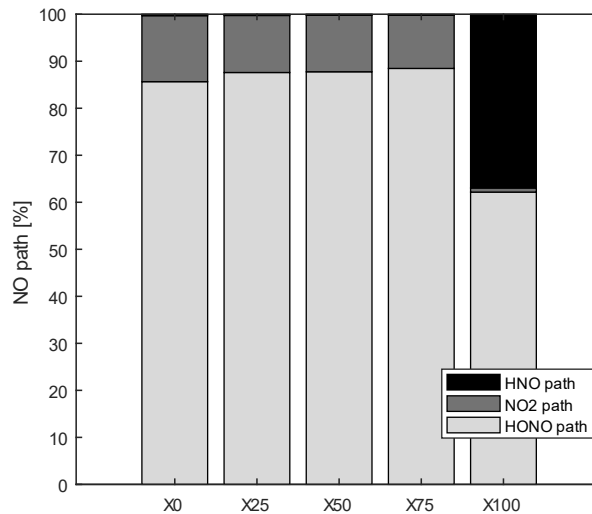
Fig.7. Percentages of the different pathways of NO production at 1 bar of inlet pressure for all fuel compositions with ethanol at 1 bar of intake pressure and homogeneous condition.

The thermal path is not identified in the NO formation, but Figure 7 indicates about 85% of the NO is formed via the HONO path for a carbon fuel while for pure ammonia is about 60%, following this reaction (reverse-path):

NO + OH (+M) <=> HONO (+M)   R1

This reaction occurs above 1060K and this importance increases lowly from X0 to X75. Another path via the NO_2 path is important for fuel composition with carbon 10% of the NO production while only 1% for pure ammonia. The reaction of the NO_2 path becomes important at 1060K and follows:

NO + O (+M) <=> NO_2 (+M)   R2
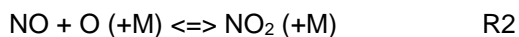
The HNO path is in the minority for pure ethanol and blends while for pure ammonia this HNO path is important as shown also in [30] and contributes to 13% of the production following these reactions:

HNO + O<=>NO + OH   R3
HNO + H<=>NO + H$_2$ R4
HNO + OH<=>NO + H$_2$O   R5
NO + H (+M) <=> HNO (+M)   R6

The R6 contributes to 95% of the NO formation from this kinetic. The sudden change of NO2 to HNO reaction path for blends to pure ammonia is remarkable. This difference can be explained by the high equivalence ratio for pure ammonia (ER=1.36) compare to the other fuel composition (ER~0.75) influencing strongly the reaction paths.

HNO and HONO are also produced in fuel composition with carbon by following theses reactions:

NH + CO$_2$ <=> HNO + CO   R7
HCO + NO<=> HNO + CO   R8
HNO + NO$_2$ <=> HONO + NO   R9

These reactions are mainly produced in burnt gases and can be one of the ways to understand the non-linearity dependence of NO and CO on the amount of NH$_3$. Adding a small quantity of NH$_3$ as X25 increase the quantity of NH pool while the CO$_2$ decrease weakly and consequently HNO and CO productions increase. Then, HNO reacts to give NO via HNO or HONO path.

The trends as a function of the amount of ammonia are identical for the other intake pressures. Figure 8 compares the results for 1 and 1.5 bar relative to 0.5 bar by relative difference calculated as:

$$Relative\ difference = \frac{X|_{Inlet\ pressure=1.0\ or\ 1.5bar} - X|_{Inlet\ pressure=0.5\ bar}}{X|_{Inlet\ pressure=0.5\ bar}} \tag{10}$$

Figure 6.a shows the relative difference in global combustion development characteristics for X50. Rising the inlet pressure increases the maximum in-cylinder pressure due to the heat release increase directly linked to the fuel flow increase, consequently fuel energy. The thermal efficiency increases up to 28% and 24% for 1 bar and 1.5 bar respecti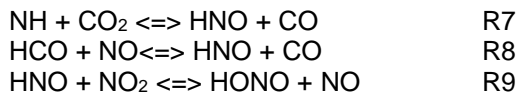vely providing better results at 1 bar. The combustion efficiency increases up to 0.7 and 1.2% respectively as the equivalence ratio becomes leaner by increasing the intake pressure. In terms of pollutants, unburnt NH$_3$ emissions decrease mainly due to the increase in combustion efficiency and in oxygen content (i.e. leaner mixture). On the contrary, NOx emissions increase with the effect of intake pressure while CO and THC decrease.

(a)   (b)
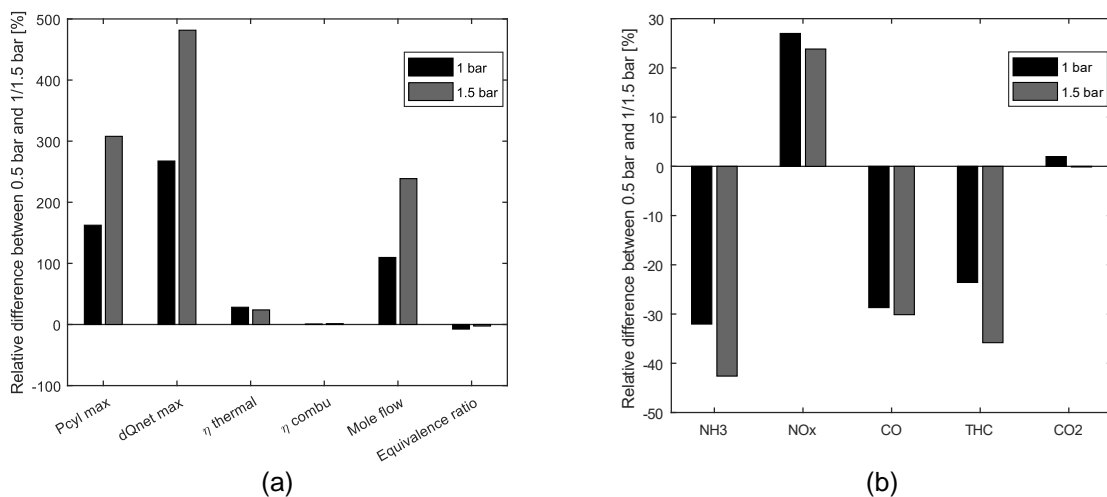
Fig.8. The relative differences as a function of the load (intake pressure) on the performances (a) and pollutants (b) for the X50 and homogeneous strategy.

3.1.3 Focus on pure ammonia performance

Supplementary data for pure ammonia was done to minimize the fuel consumption as a function of the intake pressure, the conditions are detailed in Table 4. The change of injection duration provides a

change of ER from 1.17 to 1.5. It was not possible to burn ammonia only for lower injection duration under homogeneous conditions.

Table 4. Extended conditions for pure ammonia

Injection pressure (bar)	120
Intake temperature (°C)	80
Intake pressure (bar)	1.3 - 1.3 - 1.1 - 1.1 - 1.0 - 1.0 - 0.9
Injection duration (µs)	10600 - 8500 - 8500 - 7500 - 7500 - 6500 - 6000
Global equivalence ratio	1.49 - 1.18 - 1.43 - 1.24 - 1.36 - 1.19 - 1.27
Engine speed (rpm)	1000

Figure 9 focuses on these additional conditions for pure ammonia in a fully premixed strategy with injection at 340 CAD bTDC. The low COV, Figure 9.a, shows very high stability of combustion for pure ammonia, and the thermal efficiency for pure ammonia was observed at about 0.33 for all extended conditions. As expected, NH_3 emissions are almost important due to the rich mixture but seem to be constant; NOx emissions decrease until 1000 ppm for the highest IMEP. The HRR in Figure 9.c shows an increase with equivalence ratio when in Figure 9.b, NOx decrease. These data demonstrate the feasibility of direct liquid injection of ammonia even if a deeper study should be done to fully understand and characterize the performances and pollutant formations.
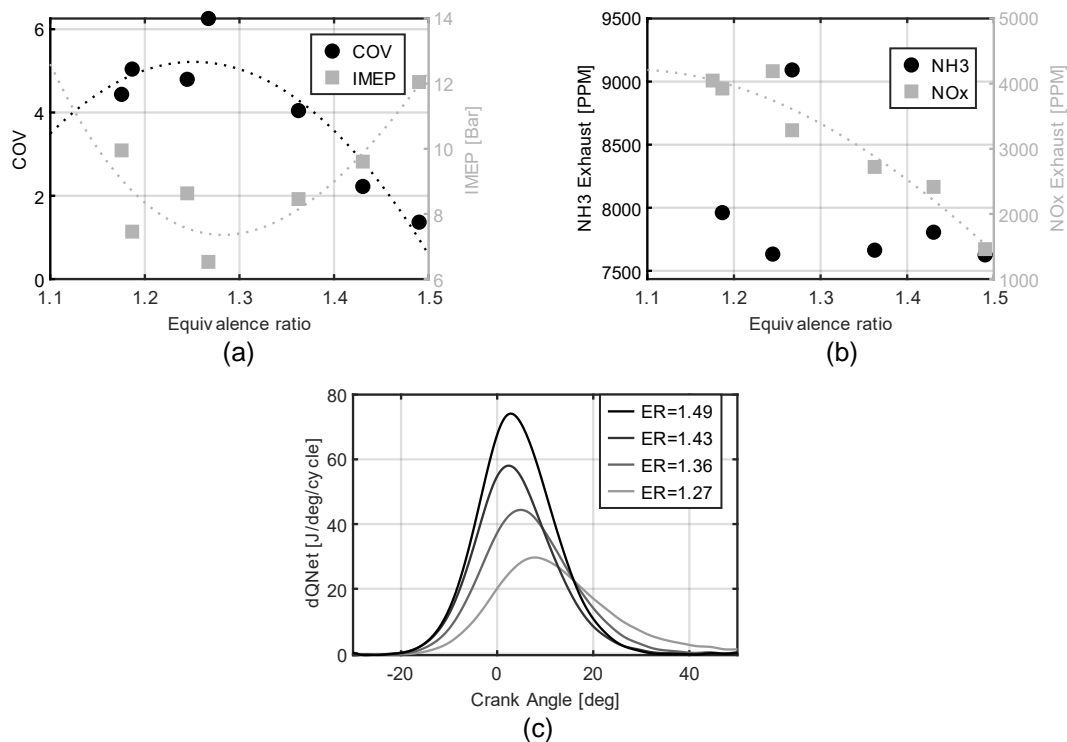
Fig.9. IMEP and COV (a) and unburnt NH_3 and NOx emissions (b) and HRR (c) for extended conditions with pure ammonia at homogeneous conditions.

3.2 *Stratified results*

A second strategy was explored to see the impact of the injection time on the performance and the pollutant emissions. The liquid fuel is injected at SOI 90 CAD bTDC; nevertheless, this strategy was not adapted to pure ammonia.

3.2.1 Performances

Figure 10.a, shows the in-cylinder pressure for the different fuel compositions, the maximal pressure is obtained for X75 and the minimal one for pure ethanol. Figure 11.a highlights the difference between the two injection strategies. The maximal heat release rate, Figure 10.b, is not sorted with the ammonia content, nevertheless, it is higher with a shorter duration for the stratified strategy than the homogeneous one. The higher heat release rate can be explained by the increase of fuel consumption and consequently by the equivalence ratio, consequently, the fuel energy as indicated in Figure 11.a. The fuel consumption is higher while the IMEP is identical (Figure 12.a). Under the conditions, the engine keeps very good stability with COV of less than 1.5% (Figure 10.c).

(a)

(b)

(c)
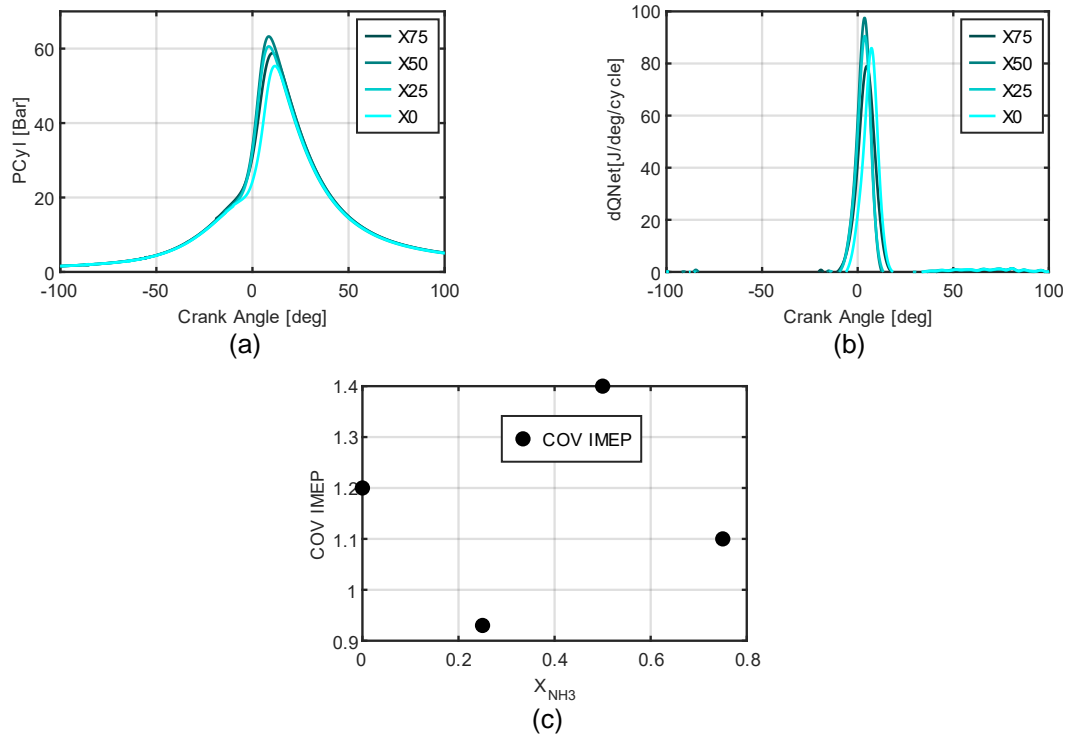
Fig.10. Global characteristics of performances for pure ethanol and blends, in-cylinder pressure (a), heat release rate (b), and stability (c) at 1b of intake pressure for stratified conditions.

(a)

(b)
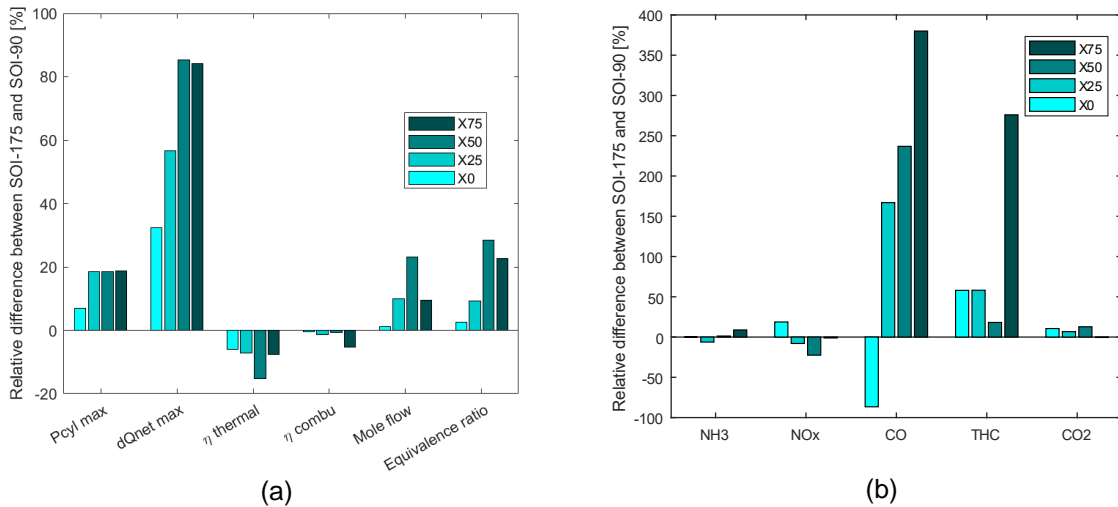
Fig.11. Comparison of performances and pollutant emissions between the homogeneous and stratified strategies for all fuel blends.

Figure 12.b focuses on the characteristic times of combustion: CA50-CA10 and CA90-CA10 are almost similar for all the fuel blends and lower than the homogeneous strategy. However, CA10-SIT, the first stage of combustion, increases with ammonia content increase but is two times lower than for the homogeneous strategy. The stratified strategy accelerates the combustion and the SIT is less advanced, 20 bTDC while 25 CAD bTDC for X75 with homogeneous conditions. However, the thermal and combustion efficiencies decrease (Figure 11.a, Figure 12.c). The maximal thermal efficiency obtained is for X25 as in the homogeneous conditions.
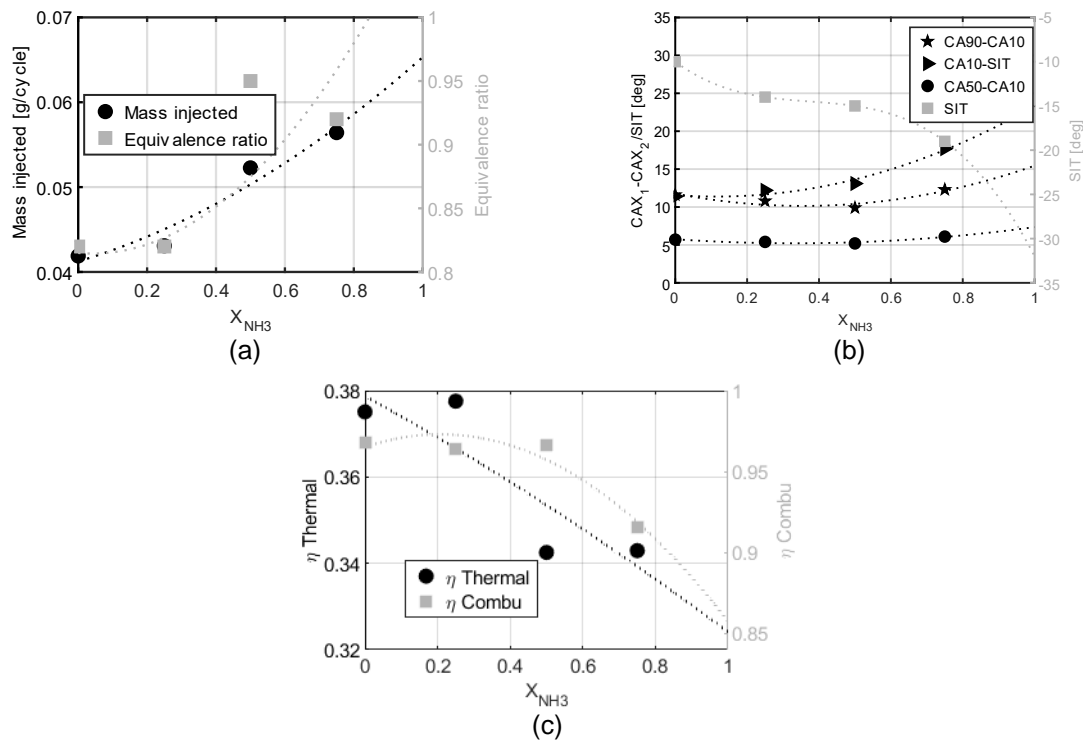
Fig.12. Characteristic timings of combustion (a), fuel consumption and equivalence ratio (b), and efficiencies (c) for pure ethanol and blends at 1b of intake pressure for stratified condition

3.2.2 Pollutant emissions

In terms of pollutants emissions, all trends as a function of ammonia content are similar to the homogeneous strategy (Figure 13). Figure 11.b indicates a decrease of unburnt NH_3 emissions for X25 compared to the homogeneous strategy while for X50 and X75, NH_3 exhaust increases. NOx and CO emissions, Figure 11.b have an interesting trend versus ammonia addition. NOx increases for pure ethanol with this injection strategy but decrease with the ammonia addition. On the contrary, CO emissions decrease for pure ethanol but roughly increase for blends compared to the homogeneous strategy. The presence of NH_3 in the fuel composition clearly influences the change of formation of NOx and CO between both strategies. The difference in THC emissions increases between both strategies and strongly for X75. The CO_2 emissions are also higher for this one.
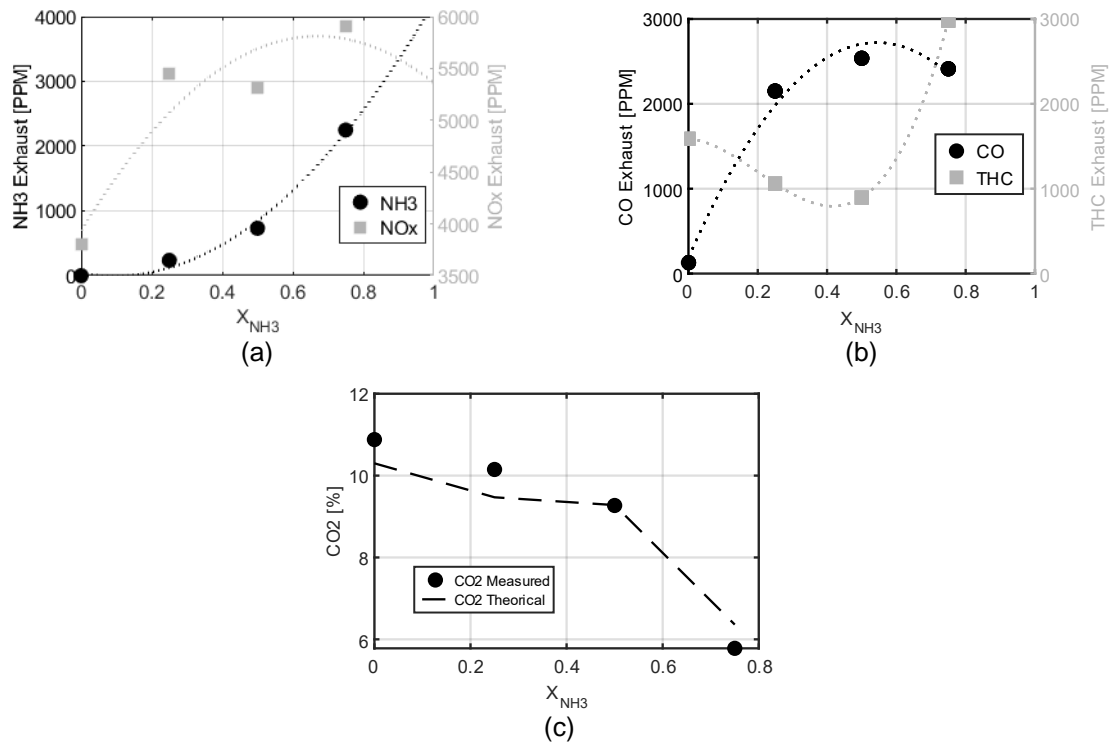
Fig.13. Pollutant emissions of NH_3 and NOx (a), CO and THC (b), and CO_2 (c) at 1 bar of inlet pressure for pure ethanol and blends at 1b of intake pressure for stratified condition

3.2.3 **Pure ammonia injection**

Injection of pure liquid ammonia at 90 CAD bTDC was not feasible, nevertheless, splitting the injection was tested. The ratio between first and second injections, 50%/50% was not possible (instabilities, misfiring), at least more than 50% must be injected during the first injection under homogeneous conditions. Two conditions were done with constant fuel injection, 104.4 mg/cycle, the first injection of 80% and 60% of the load at 340 CAD bTDC with a second one 20% and 40% of the load at 90 CAD bTDC.

Table 5. Extended conditions for the split injection

Injection pressure (bar)	120
Intake temperature (°C)	92
Blend (%NH_3)	100
Intake pressure (bar)	1.5
Engine speed (rpm)	1000

Table 6 compares the fully premixed to the split injection conditions. The COV is low showing high stability and further for the split injection with slightly lower IMEP. However, the thermal and combustion efficiencies are constant, 0.35 and 0.96 respectively for all extended conditions. The equivalence ratio decreases due to the diminution of fuel injected during the intake phase increasing the airflow for the split injection conditions while the fuel mass injected remains constant. The SIT was delayed to maximize the IMEP with the split injection strategy. In terms of pollutants emissions, NH_3 emissions decrease while a slight increase in NOx.

Table 6. Comparison of performances and pollutant emissions between one or double injections conditions

	100%	80%/20%	60%/40%
COV IMEP	3.29	1.58	1.86
IMEP (bars)	12.79	11.98	12.08
Global equivalence ratio	1.27	1.19	1.18
SIT	-36	-31	-24
NH_3 Exhaust (ppm)	8064	6412	6233

NOx Exhaust (ppm)	3732	4265	4211

The in-cylinder pressure and the heat release rate evolutions for the three conditions of injection (Figure 14) indicated that the combustion is delayed with a maximal pressure decrease with the increase of fuel injected during the second injection due to the combustion phasing later in the cycle. However, the heat release rate increases by 3% and 5% with the double injection 80/20 and 60/40 respectively compared to single injection.
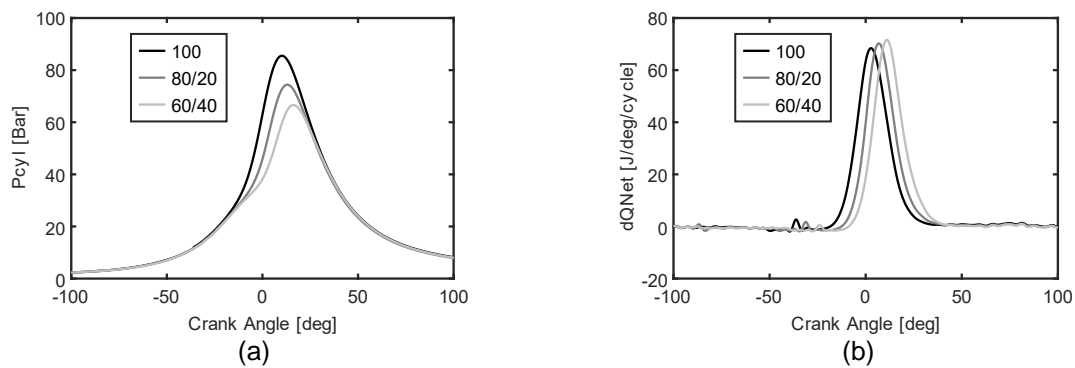
Fig.14. Evolution of In-cylinder pressure (a) and HRR (b) for pure ammonia with single or double injections

Conclusions

This study provides the first information about ethanol blended with ammonia and pure ammonia using a single-cylinder spark-ignition engine with direct injection. Two strategies of injection were investigated, homogeneous and stratified one at different intake pressures. The performances and the pollutants emissions were compared as a function of the fuel compositions and the injection strategies. Due to the low LHV of ammonia compared to ethanol, an increase in fuel consumption is needed to reach same load. Adding 25% of ammonia in ethanol has a positive effect on the thermal and combustion efficiencies. However, NOx and CO emissions are higher for blends than pure fuels (ammonia and ethanol respectively) and are potentially correlated by these reactions: NH + CO$_2$ <=> HNO + CO, HCO + NO<=> HNO + CO, and HNO + NO$_2$ <=> HONO + NO as shown through Chemkin simulations. Blends with ammonia and methane highlight the identical NOx behavior. The major path of NO production is the HONO path and then, the NO$_2$ decomposition or HNO path for blends and pure NH$_3$ respectively. The stratified strategy boosts the combustion time by decreasing the characteristic timings but increasing NH$_3$ exhaust and CO$_2$ and THC emissions. NOx pollutants increase for pure ethanol with the stratified strategy but adding ammonia to the fuel composition decreases the NOx emissions. On the contrary, CO emissions decrease for pure ethanol with the stratified strategy but roughly increase as a function of ammonia increase in the blend. The presence of NH$_3$ in the fuel composition clearly influences the change of formation of NOx and CO between both strategies.

Pure injection of ammonia is more restrictive and to obtain homogeneous conditions ammonia needs to be injected in advance to be fully premixed. In the stratified conditions, the injection starting at 90 CAD bTDC, was not feasible, it needs to split the injection but only if more than 50% of the fuel is injected in homogeneous mode. It is clearly shown from this present study that ethanol/ammonia blends but also pure ammonia can be accurate fuels for standard gasoline direct injection spark-ignition engine with both usual thermal and combustion efficiencies and very good engine stabilities.

References

[1]   United Nation, (2015).
[2]   A. Katoch, A. Millán-Merino, S. Kumar, Fuel 231 (2018) 37–44.
[3]   C.C. Geddes, I.U. Nieves, L.O. Ingram, Curr. Opin. Biotechnol. 22 (2011) 312–319.
[4]   D. Turner, H. Xu, R.F. Cracknell, V. Natarajan, X. Chen, Fuel 90 (2011) 1999–2006.
[5]   W.D. Hsieh, R.H. Chen, T.L. Wu, T.H. Lin, Atmos. Environ. 36 (2002) 403–410.
[6]   A. Elfasakhany, Fuel 274 (2020).

16   R. Pelé, P. Bréquigny, J. Bellettre, C. Mounaïm-Rousselle

[7]   N. Abas, A. Kalair, N. Khan, Futures 69 (2015) 31–49.
[8]   V.T. Sacramento EM, Carvalho P, Lima LC, Energy Pol (2013).
[9]   Y. Li, M. Bi, B. Li, Y. Zhou, L. Huang, W. Gao, Energy 159 (2018) 252–263.
[10]   C. Lhuillier, P. Brequigny, F. Contino, C. Mounaïm-Rousselle, Fuel 269 (2020) 117448.
[11]   C. Mounaim-Rousselle, P. Brequigny, Front. Mech. Eng. (2020).
[12]   P. Dimitriou, R. Javaid, Int. J. Hydrogen Energy 45 (2020) 7098–7118.
[13]   C. Kurien, M. Mittal, Energy Convers. Manag. 251 (2022).
[14]   K. Ryu, G.E. Zacharakis-Jutz, S.C. Kong, Appl. Energy 113 (2014) 488–499.
[15]   C.W. Gross, S.C. Kong, Fuel 103 (2013) 1069–1079.
[16]   C. Mounaïm-Rousselle, P. Bréquigny, C. Dumand, S. Houillé, Energies 14 (2021) 1–13.
[17]   A. Mercier, C. Mounaïm-rousselle, P. Brequigny, J. Bouriot, C. Dumand, 11 (2022) 1–9.
[18]   F. Salek, M. Babaie, A. Shakeri, S.V. Hosseini, T. Bodisco, A. Zare, Appl. Sci. 11 (2021) 1–17.
[19]   S.O. Haputhanthri, T.T. Maxwell, J. Fleming, C. Austin, J. Energy Resour. Technol. Trans. ASME 137 (2015) 1–7.
[20]   M.C. Rehbein, C. Meier, P. Eilts, S. Scholl, Energy and Fuels (2019).
[21]   L.J. Huang, W.L. Xue, Z.X. Zeng, Fluid Phase Equilib. 303 (2011) 80–84.
[22]   Z.X. Zeng, J. Chen, W.L. Xue, L.J. Huang, Ind. Eng. Chem. Res. 50 (2011) 3592–3597.
[23]   R. Pelé, C. Mounaïm-Rousselle, P. Bréquigny, C. Hespel, J. Bellettre, Fuels 2 (2021) 253–271.
[24]   E. Tinon, Etude Expérimentale Des Mécanismes d'atomisation Effervescente. Application à La Sécurité Incendie Dans Les Moteurs Aéronautiques, UNIVERSITÉ DE TOULOUSE, 2018.
[25]   Z. Wang, X. Han, Y. He, R. Zhu, Y. Zhu, Z. Zhou, K. Cen, Combust. Flame 229 (2021) 111392.
[26]   H. Xiao, A. Valera-Medina, P.J. Bowen, Energy 140 (2017) 125–135.
[27]   G. Battista, G. Sorrentino, R. Ragucci, M. De, P. Sabia, 241 (2022).
[28]   Y. Niki, in: Proc. ASME, 2018.
[29]   G.E. Zacharakis-Jutz, MSc Thesis 13032 (2013).
[30]   M.C. Chiong, C.T. Chong, J.H. Ng, S. Mashruk, W.W.F. Chong, N.A. Samiran, G.R. Mong, A. Valera-Medina, Energy Convers. Manag. 244 (2021) 114460.

THIESEL 2022 Conference on Thermo- and Fluid Dynamics of Clean Propulsion Powerplants

Effect of Compression Ratio and Ignition Energy on Ammonia Premixed Combustion Process in a Single Cylinder Engine

H. Won[1], D. Kumar[1], V. Morel[1], A. Mercier[2], C. Mounaïm-Rousselle[2], J. Bouriot[3], S. Houille[3], C. Dumand[3]

[1]Aramco Overseas Company B.V. – Aramco Fuel Research Center, 232 av. Napoléon Bonaparte, Rueil-Malmaison, France.

E-mail: hyunwoo.won@aramcooverseas.com
Telephone: + (31) 88 262 2147

[2]University of Orleans –Laboratoire PRISME, France

E-mail: christine.rousselle@univ-orleans.fr

[3]STELLANTIS – Centre Technique Velizy, France

E-mail: jean.bouriot@stellantis.com

Abstract. Attempts in reducing CO_2 emissions due to greenhouse gas effect with the help of a carbon-free fuel like the hydrogen and its derivate, ammonia, in the transportation sector are expected to increase. However, not only ammonia is toxic and corrosive due to its alkaline properties, but also the narrow flammability limits, the high auto-ignition temperature and the low flame velocity are the challenges to overcome for ammonia (NH_3) fueled internal combustion engine. The combustion instabilities at low loads and / or high engine speed and unburnt NH_3 emissions minimization are the key points to make NH_3 a potential candidate as a fuel for premixed combustion engines.

In this study, the spark ignited combustion of pure NH_3 in a single cylinder engine, based on a compression ignition engine architecture, for different high compression ratios (CR: 16.4, 18.4 and 20) was evaluated as a function of combustion phasing and air fuel ratio in order to improve fuel consumption and engine stability. The experiments were performed over a wide range of operating conditions and the best hardware was defined mainly based on low-load improvement criteria. The experimental results addressed the combustion behavior with the exhaust gases emissions (NO_X, and NH_3) to state about the potential of using pure NH_3 as a sustainable fuel on a diesel-like architecture engine.

1. Introduction

The transport sector is responsible for about a quarter of total GHG emitted, with the road sector accounting for 70% of total transport emissions [1, 2]. Due to the negative GHG effect on the environment, more efficient engines and less tailpipe emissions are trending more than before. For many years, governments around the world have been implementing different legislations to reduce tailpipe pollutant emissions from passenger cars. The existing gasoline and diesel engine vehicles face a critical challenge to adjust to these stringent demands. The European Commission (EC) published its regulatory proposal for post-2020 CO_2 targets for new passenger cars [3]. The proposed regulation would be the third set of mandatory CO_2 standards in the European Union (EU). Under the new EC proposal, the CO_2 emission levels would have to fall by 15% by 2025 and from -37.5% to -55% for new passenger cars and from -31% to -50% for new vans, both relative to a 2021 baseline [4].

Several technological options are being considered as potential solutions for reducing for air pollution and GHG emissions in the transportation sector. Recently, pure battery electric vehicles (BEVs), hybrid electric vehicles (HEVs) and hydrogen fuel cell vehicles (FCEVs) are the main solutions for the environmental issues but the high cost of technologies and the infrastructures for electric charging of vehicles and hydrogen fueling will be the blocking points to expand these technologies rapidly. For that reason, alternative fuels have been the focus of many studies since the increasing concern with air

pollution and greenhouse gas (GHG). The possibility of using NH_3, one promising hydrogen carrier, as a fuel for internal combustion engines (ICEs) appears attractive since NH_3 is carbon free. NH_3 can be liquefied at 20 °C with only around 9 bar of pressure [5]. Liquid NH_3 contains higher energy density by volume than 700 bar pressurized hydrogen itself [6]. In addition, NH_3 is used in many different industries and its production, storage and transportation are already well established worldwide.

Many studies have tried to develop NH_3 as fuel for ICEs in the past, and some of them up to vehicles. The oldest proposal of NH_3 as a fuel for ICE was Sir Goldsworthy Gurney who developed a NH_3 powered engine for a small locomotive. The first pick-up truck with NH_3 and hydrogen ICE was by Norsk Hydro company in 1933 [7]. A previous patent of 1938 deals with the possibility of using NH_3 with hydrogen by Ammonia Casale Ltd [8] and Kroch [9] announced the excellent results by burning NH_3 with coal gas without any loss of power and corrosion. However, due to the difficult ignitability of pure NH_3 under conventional engine operating conditions, most developments were done by blending NH_3 with other fuels. The possibility to use pure NH_3 on ICE or NH_3 as a primary fuel in Spark-Ignition (SI) or Compression Ignition (CI) engine were more scientifically discussed since 1960's. When the occupation forces by destroying any oil refineries and storage depots led to low oil stockpiles in World War II, the feasibility of using NH_3 as an alternative fuel instead of hydrocarbon fuels was dominated [10]. In that time, the US Military funded a project (Energy Depot Project) to develop alternative power source for any future fuel logistic problems [11]. In 1963, Wagner and Domke commented to extend the NH_3 combustion to CI engines and they operated a Cooperative Fuel Research (CFR) engine on pure NH_3. Based on the study, the engine could only run with NH_3 after the warming-up using kerosene at a compression ratio (CR) of 35:1 [11−13]. In 1966, Gray et al. checked the compatibility of NH_3 fuel on CI engine and concluded NH_3-only combustion requires very high CR [14]. NH_3 may be ignited by a promoter fuel (e.g., hydrogen or acetylene) at lower CR. Then, Pearsall and Garabedian investigated anhydrous ammonia fuel on US Army Tank CI engine (with CR, 18.6:1) firstly and then the engine was modified to SI engine with different CRs (12:1, 16:1 and 18.6:1) to use NH_3 as the fuel [15]. However, there were some difficulties and requirements of the NH_3 engine e.g., highly compacted combustion chamber with high peak cylinder pressure, spark plug (SP) design or air-boosting system requirements. Starkan et al. also highlighted that pure NH_3 is able to burn by an adapted spark plug on the engine with a standard CR like in CI engine [16]. In the literature, the research in NH_3 only ICE remains limited but demonstrates some successful operations of NH_3 combustion under specific engine operating conditions as in [17-20]. These recent studies have highlighted some levers to increase the operating range of NH_3 engines, such as increasing the volume ratio and doping with hydrogen or upstream dissociation of NH_3. The NH_3 only combustion is challenging and requires very high CR or adapted engine with an ignitor and fuel injection system.

In the current study, the experimental investigations were performed to characterize the spark ignited combustion of premixed NH_3 and air at variable engine operating conditions (low, medium and higher loads) met on a single cylinder engine with a high CR. The goal of the study is also to address for the first time the limitation of operating boundary of the engine fed with pure NH_3, ignited by spark system. Not only high compression ratio but also high voltage ignition system was investigated for the first time, in the study at mid and low loads, from 1000rpm to 3000rpm. As interesting result, a CR 18.4 engine could be a good solution to avoid the requirement of on-board NH_3 cracker. In addition, the impact of H_2 additives into NH_3 fuel on CR 16.4 engine was investigated and the results were compared with the results of pure NH_3 with different configurations. This study provides new data and insights into the potential of ammonia as a fuel for internal combustion engines, by considering not only performances but also the NO_X and NH_3 emissions trends.

2. Experimental setup

2.1 NH₃ fuel

Table 1 shows the liquid NH_3 fuel specifications compared to other fuels. Among with the storage condition of fuels, NH_3 has a better volumetric energy density than hydrogen and it makes a competitive energy carrier in specific cases. The high heat of vaporization and anti-knocking index (over 120 of research octane number) allows increasing the compression ratio of the engine. However, ammonia deployment as a fuel still faces some challenges since it is corrosive and presents unfavorable combustion properties by its low Laminar Burning Velocity (LBV), high auto-ignition temperature and narrow flammability range. The latter is simultaneously a safety benefit, since accidental ammonia fires or explosions are less likely to happen in case of NH_3 leakage than with conventional fuels or hydrogen.

Table 1. NH₃ Fuel properties and comparison with other fuels

Fuel species	Liquid H₂	Gaseous H₂	Gasoline	Diesel	**Ammonia**
Stoichiometric AFR	34.2	34.2	14.6	14.5	**6.06**
LHV [MJ/kg]	120.1	120.1	42.5	42.6	**18.8**
Approximate RON	>120	>120	95	−	**120**
Storage Temp. [℃]	-253	25	25	25	**25**
Storage Pressure [bar]	1	700	1	1	**10**
Fuel density [kg/m³]	71.1	39.7	698.3	834	**602.8**
Energy density (storage conditions) [MJ/l]	8.5	4.76	29.7	38.6	**11.3**
Flammability limits in air (equivalence ratio)	0.09 − 6.81	0.09 − 6.81	0.6 2− 3.89	-	**0.63 − 1.53**
Heat of vaporization [kJ/kg]	461	461	180-350	450	**1370**
Laminar burning velocity [cm/s]	210	210	40	-	**7**
Auto-ignition Temp. [℃]	537	537	275	210	**651**
Adiabatic flame Temp. [℃]	2519	2519	2392	-	**2107**
Minimum ignition energy [MJ]	0.019	0.019	0.14	-	**8**

2.2 The engine and test bench

The experiments were performed on a 0.5 liter single cylinder compression ignition engine (from a modified four-cylinder engine, DW10F PSA) with CR 16.4:1. The single cylinder engine (SCE) was retrofitted as a SI engine with a classical cold type SP (NGK ILZKR8CG), centrally located instead of the original location of the injector. All engine specifications are presented in Table 2. An original reen-trant combustion chamber with 54 mm throat diameter and 12.7 mm depth length was used in this study.

Table 2. The SCE engine of the NH₃ fuel test

Engine	DW10
Displaced Volume [cm³]	499.4
Stroke [mm]	88
Bore [mm]	85
Connecting rod length [mm]	141
Compression ratio [-]	16.4:1
Number of valves [-]	4
Swirl ratio (50 CAD BTDC)	2.0
Bowl type (baseline)	Re-entrant

The scheme of the engine test bench is shown in Fig. 1. The engine was driven by an electric motor to control the selected engine speed. The in-cylinder pressure measurement was obtained by means of Kistler piezo electric pressure transducer (6045A). The intake and exhaust temperature and pressure were monitored and the fuel and air flow rates were controlled and measured by Brooks thermal mass flowmeters (at the normal condition, 0 ℃ and 1bar). The temperature and the pressure of coolant and oil of the engine were also controlled by means of the automat. NH₃ flowed through a heat exchanger recovering the heat of vaporization in order to avoid freezing of any components and of ammonia itself. NH₃ fuel went thus out of the exchanger in a gaseous state and was premixed with air inside a plenum volume, before entering the cylinder.
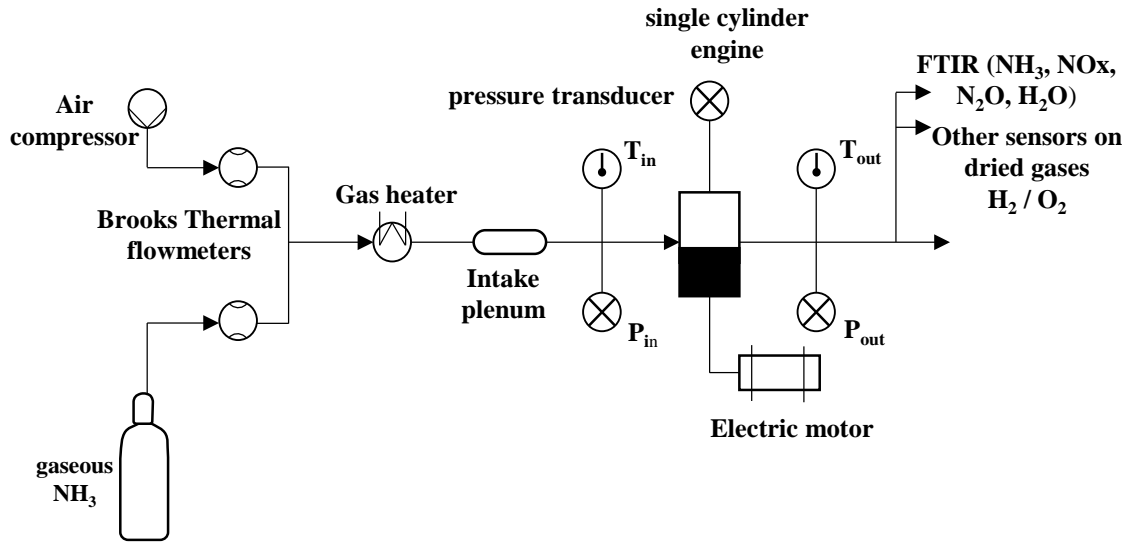
Fig. 1. Layout of the experimental setup

The wet exhaust gases were analyzed using a Gasmet Fourier Transform Infrared (FTIR) spectrometer to assess H_2O, N_2O, NO, NO_2, and NH_3 concentrations. The water vapor is a major interfering compound in infrared wavelengths, and its presence in the exhaust sample is inevitable due to the interest in measuring H_2O itself and NH_3, that would otherwise condensate along with H_2O. Even though its presence is accounted for in the interference corrections, the authors believe that it may lead to some uncertainties in the exhaust gas measurements, in addition with other cross-component interferences. The analysis ranges of the species of interest are more detailed in [17]. The analysis setting-s for the wavelength ranges were as : for H_2O, $3950 - 4240$ cm^{-1}, for N_2O, $2000 - 2250$ cm^{-1}, NO $1840 - 2080$ cm^{-1}, NO_2 $1250 - 1720$ and NH_3 $1000 - 1240$ cm^{-1}. Note that error bars are not plotted consistently in order to improve the readability but it has to be kept in mind that when NH_3 values are higher than 2%, the accuracy is only 20%. A thermal conductivity analyzer for H_2 (XEN-5320) and a paramagnetic analyzer for O_2 were also used on a dry exhaust gas sample, which was without any H_2O and NH_3 content. The water vapor measurement done with the FTIR analyzer was used for wet correction. The accuracy of the H_2 and O_2 analyzers is 6 and 1.5% respectively (range $0 - 20$% H_2 and $0 - 21$% for O_2).

The apparent Heat Release Rate (HRR) was computed from pressure trace post processing with the first law of thermodynamics, as follows:

$$\frac{dQ}{d\theta} = \frac{\gamma}{\gamma - 1} * P * \frac{dV}{d\theta} + \frac{1}{\gamma - 1} V * \frac{dP}{d\theta} \qquad (1)$$

Where, γ is the heat capacity ratio, P, V and θ, the cylinder pressure and volume and crank angle, respectively. Note that heat losses were not considered in the calculation during this study because of the large uncertainties that remain in their estimation. The Burnt Mass Fraction (BMF) was then obtained by integrating the heat release and apparent HRR was then recalculated using the variable heat capacity ratio computed from the previous BMF. The different phases of combustion propagation were determined by estimating different characteristic timings, named CA, which are the Crank Angle degrees corresponding to the percentage of the burnt mass fraction.

$$\int_{SIT}^{CA90} dQ_{Comb} = 0{,}9 * m_{fuel} * LHV_{fuel} * \eta_{Comb} \qquad (2)$$

2.3 Combustion chamber designs

Table 3 summarizes all investigated hardware variations. Regarding the spark ignition system, the standard SP (around 30 mJ baseline SP for SI gasoline engines and 2 ms of coil charge duration) was used first for the hardware variation with different CRs. The high voltage SP (up to 90 mJ, same coil duration, performance spark ignition with a high voltage ignition system) equipped only the reference

bowl design (CR 16.4). The experiments were performed over a wide range of operating conditions and the best hardware was defined mainly based on low-load improvement criteria.

Table 3. The list of new bowl designs and spark plug system for the NH_3 study

Hardware variation	Design of bowl	Compression ratio	Type of spark plug
CR16.4	Reentrant	16.4:1	Standard SP
CR18.4	Reentrant	18.4:1	Standard SP
CR 20.0	Reentrant	20.0:1	Standard SP
CR 16.4_HV	Reentrant	16.4:1	High Voltage SP

2.4 Experimental operating conditions

First, the NH_3 combustion settings, e.g., an optimal combustion phasing, an ideal air-fuel ratio and the inlet condition like the intake temperature, were addressed for some selected operating conditions. In selected operating condition tests, three loads (3, 8 and 15bar of IMEP) and different engine speeds (1000rpm, 1500rpm, 2000rpm and 3000rpm) were chosen as representative of steady state conditions to understand the NH_3 combustion development. Spark ignition timing (SIT) sweeps were investigated to define the optimal combustion phasing of the NH_3 combustion – phasing that gives the lowest fuel consumption but with combustion stability criteria, while the Indicated Mean Effective Pressure (IMEP) was kept constant during the sweeps. Based on the optimal CA50, the air-fuel ratio sweeps (or lambda sweeps) were performed continually while IMEP and CA50 were kept constant. Table 4 summarizes the different testing conditions. In the final stage, the engine load and speed sweeps were performed to create the full map of NH_3 engine based on the achievement of the selected operating conditions. Regarding concerned constrains of the tests, the coefficient of variation of indicated mean effective pressure (COV_{IMEP}) was targeted less than 5% (but recorded the results until 10% of COV_{IMEP} without any misfiring, 10% of IMEP is the criterion for counting a cycle as a misfire) and the maximum in-cylinder pressure was limited to 150bar for the safety of the engine hardware.

Table 4. The engine test conditions (spark ignition timing, air fuel ratio and IMEP sweeps)

Sweeps	Spark ignition	Lambda	T_intake air	P_intake	SP charging
SIT	70 – 20 beforeTDC	1.0	40 ℃	const. IMEP & lambda	2000 µs
A/F	Const. CA50	0.8 – 1.3	40 ℃	const. IMEP	2000 µs
IMEP	Const. CA50	1.0	40 ℃	const. IMEP & lambda	2000 µs

3. Experimental results and discussions

3.1 NH_3 combustion on reference design

3.1.1 Combustion phasing (SIT) sweeps (CR 16.4)

In this section, the NH_3 premixed combustion behaviors on the SCE based on the original combustion bowl design (baseline CI engine hardware with the reentrancy bowl) with spark ignition system are presented for a CR 16.4:1. In selected test operating conditions, the first set of experimental measurement had been gathered to investigate the effects of the combustion phasing on the stability of combustion and engine performances and on the exhaust gases composition. In order to vary one parameter at a time only, the spark advance was varied while IMEP was kept constant for the stoichiometric ammonia/air mixture during these set of experiments. The SIT sweeps were performed at all 11 selected operating conditions and the optimal CA50 when the half mass fraction is burned, was defined by considering different parameters, e.g., the COV_{IMEP}, NO_X and NH_3 exhaust emissions and Indicated Specific Fuel Consumption (ISFC). Since NH_3 has a low laminar flame speed inducing more time to burn, the

use of such fuel requires a higher spark advance compared to gasoline. Fig. 2 shows an example of the SIT sweep results, represented by CA50, at different loads (3, 5.2, 8 and 15bar of IMEP) at a constant engine speed (2000rpm). The range of the spark timing depends on the operating conditions, i.e. the loads: from 45 ~ 30 Crank Angle Degree (CAD) before Top Dead Center (bTDC) at 3bar, and from 60 to 40 CAD bTDC at 5.2, 8bar and 15bar of IMEP. The spark timing must be advanced to guarantee the combustion development. The engine efficiency should increase with an early spark timing before reaching a maximum. For gasoline fuel, the spark advance increases as much as possible while avoiding knocking but in the case of NH_3 thank to very resistant to auto-ignition, the maximum efficiency is reached well before the apparition of knock at all operating conditions. At low load, the lowest COV_{IMEP} reached very early spark timing, but as presented in Fig. 2, the combustion was very instable and incomplete leading to important quantities of unburnt NH_3 emissions in the exhaust gases and modest engine performances. At medium and higher loads, the decrease of the combustion duration induced a better stability (lower COV_{IMEP}) than at low load. However, NO_X emissions were relatively higher compared to engine-out emissions in usual SI engine fueled with gasoline. The unburnt NH_3 emissions were 1.3% at 8bar and 1.1% at 15bar of IMEP with a level as high as 1.47% at low loads due to the lack of stability.
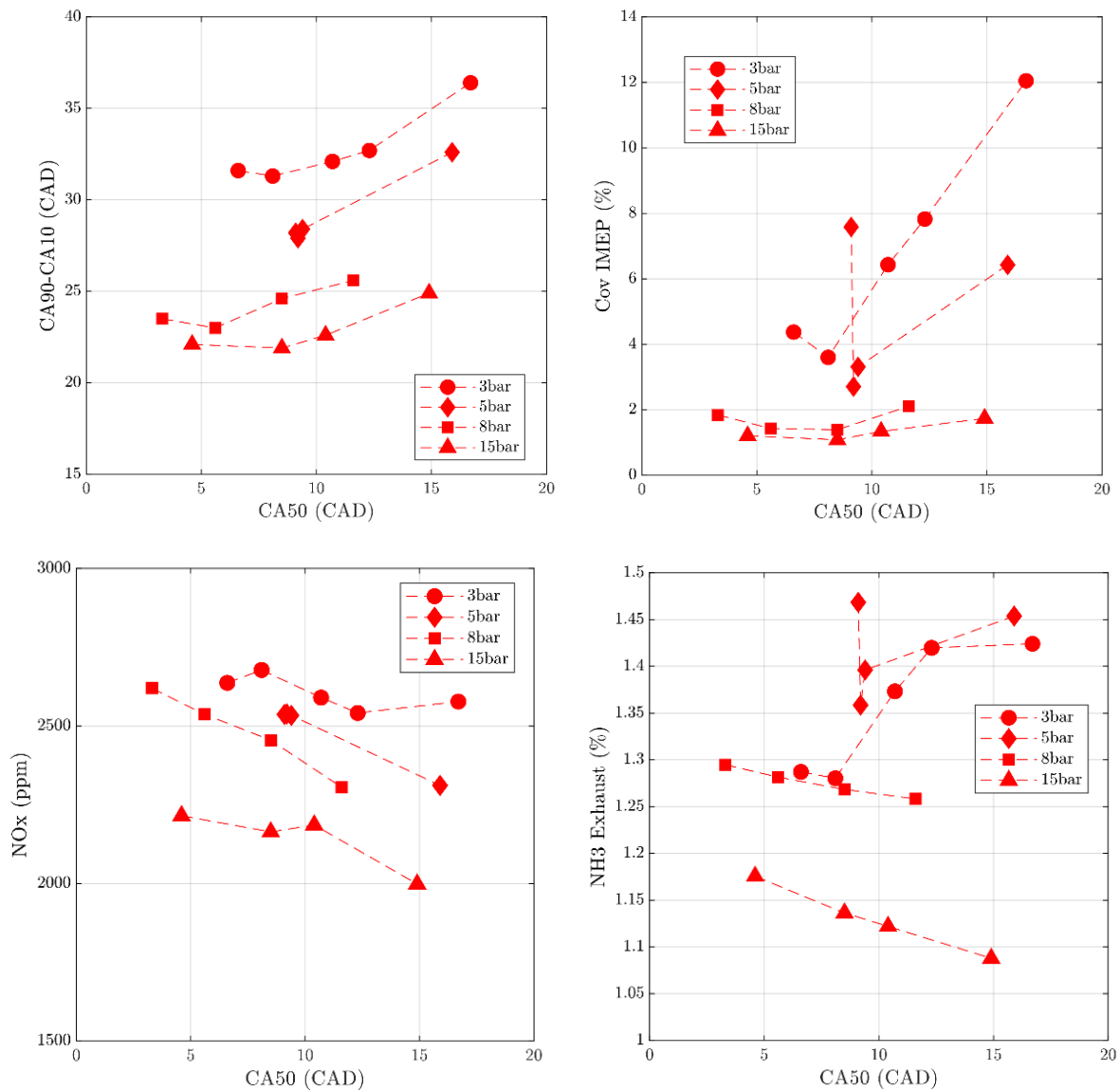
Fig. 2. Effect of Spark-Ignition Timing sweeps on combustion duration, COV_{IMEP}, NO_X and NH_3 emissions at different loads (3, 5.2, 8 and 15bar of IMEP) and a given engine speed (2000rpm)

3.1.2 Air and fuel ratio (lambda) sweeps with reference bowl (CR 16.4)

The second set of experimental tests had the objective to investigate the effect of an equivalence ratio variation. For that, the optimal CA50 (defined by SIT sweeps) was kept constant while the engine runs constant IMEP for each operating condition. Fig. 3 shows the result of the air-fuel ratio sweeps (i.e lambda sweeps) with three different engine speeds (1000rpm, 2000rpm and 3000rpm) at 8bar of IMEP. In general, the trends of all results were very similar by changing engine speeds. Slightly leaner combustions had better thermal efficiency but lead to higher quantity of NO_X emission and COV_{IMEP} and richer combustions implied higher unburnt NH_3 emissions due to the lack of oxygen. It seems that using a slightly lean mixture was an advantage as observed for a lambda 1.08, with a minimum of NH_3 emission and the lowest ISFC, which increased again for very lean side or richer one. Regarding NO_X, the level of emissions was dramatically reduced by increasing equivalence ratio, as for classical hydrocarbon fuel even if NO_X was not only produced from the thermal route but also due to fuel-nitrogen content. Based on the engine out emission results, the ideal lambda should be around 0.95 with lower NO_X and NH_3 and COV_{IMEP} than for the stoichiometric air/fuel ratio. However, the optimized lambda might be discussed when an after-treatment system is designed.
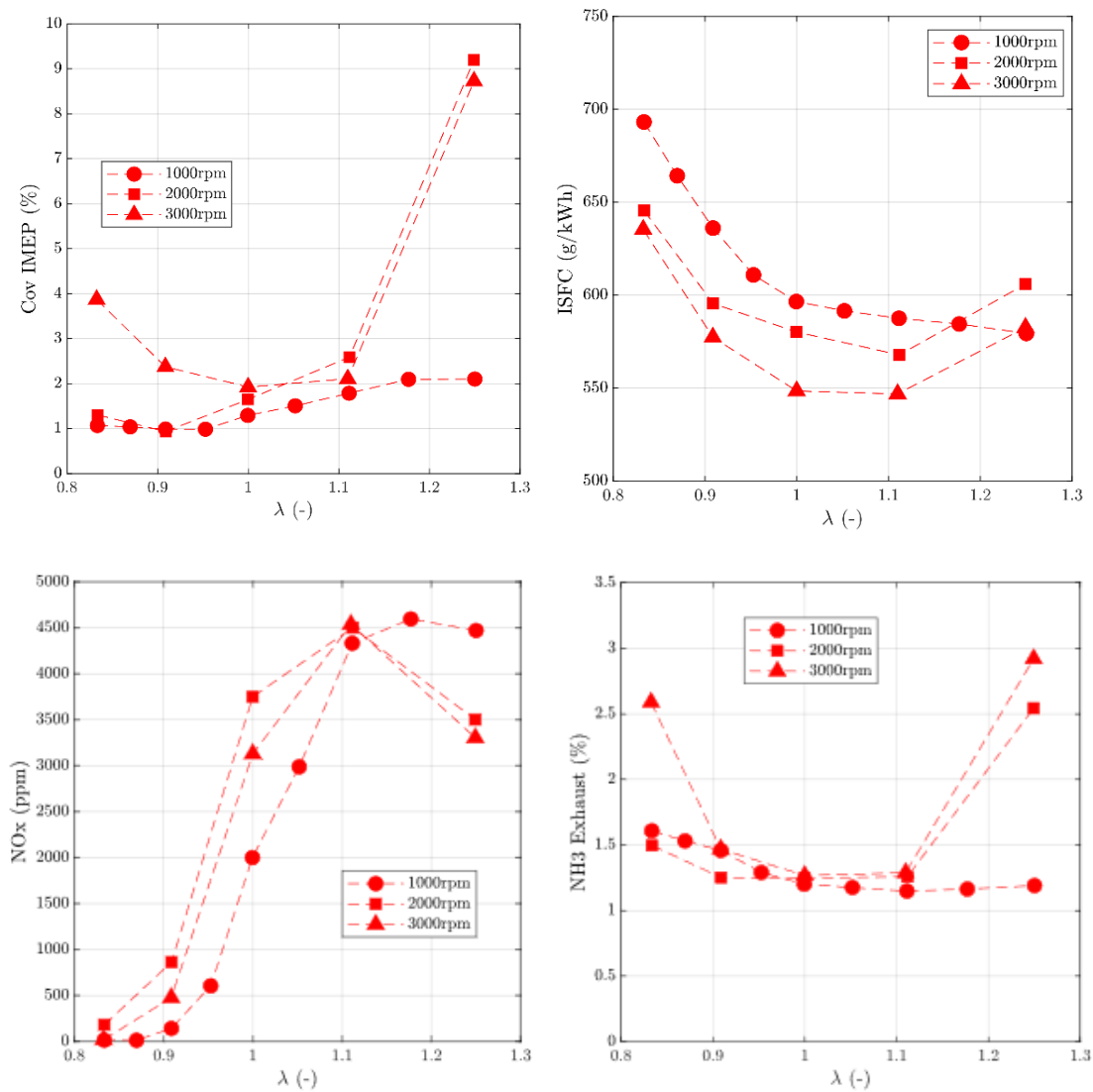
Fig. 3. Effect of Lambda sweeps on COV_{IMEP}, ISFC and NO_X and NH_3 emissions at different engine speeds (1000, 2000 and 3000rpm) and a given load (8bar of IMEP)

3.1.3 Emission trends on NH₃ engine compared to a reference SI engine

Fig. 4 summarizes the emission trends versus lambda for NH₃ fueled SI engine, based on this study, compared to one fueled with Natural Gas (NG) as in [21]. The trend of NO$_X$ emissions for these two very different gaseous fuel engines were very similar since the highest peak was located in slightly lean combustion zone. However, NO$_X$ emission was emitted in a narrower range of lambda with NH₃ as fuel. Due to the thermodynamics conditions related to the high compression ratio, for rich conditions, the NH₃ could be decomposed partially into hydrogen as shown in [18, 19]. As schematized here, the trend of H₂ emission could be considered as the CO emission in NG SI engine. Both emissions were mainly increased at very rich fuel mixture due to the lack of oxygen. Regarding unburnt gases, NH₃ emission was similar trend compared total HC emissions with the lowest emissions near stoichiometric mixture on both rich and lean sides.
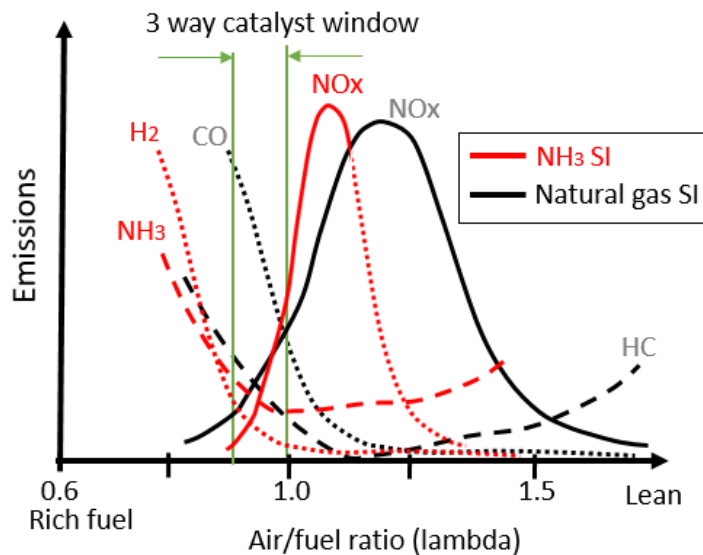
Fig. 4. The emission trade comparison between NH₃ SCE and Natural Gas SCE [21]

3.2 Hardware variations

3.2.1 Compression Ratio comparisons

The following analysis focuses on the comparison of the different compression ratios, achieved by modifying the depth of the bowl as shown in Fig. 5 without any changes in the squish area. The CR were the followings: 16.4, 8.4 and 20. The SIT sweep was varied to determine the best combustion phasing. All graphs in this section report results obtained at 2000rpm and 8bar of IMEP. Increasing the CR had a direct effect on the in-cylinder pressure as plotted in Fig. 5. Consequently, for a same ignition timing (indicated by a spot symbol), due to the increase of the in-cylinder temperature and pressure, the ignition delay (defined by CA10 - SIT) decreased as can be seen in Fig. 6. On the other hand, it seems that an increase in the CR did not necessarily allow faster combustion, it could even be the opposite trend, which was observed where for the same value of CA50, the combustion duration was seen to be lengthened at the highest CR (CR 20.0). One hypothesis would be that a decrease in bowl depth could affect the flame development due to the flow-field.
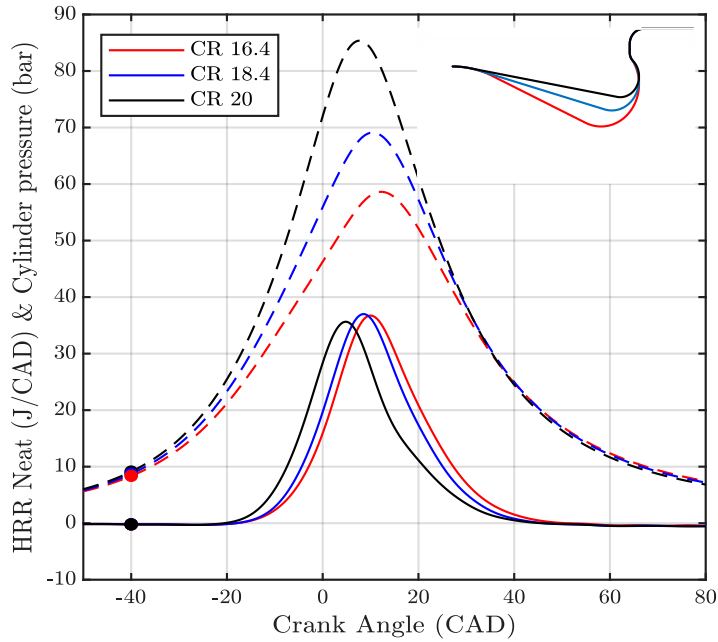
Fig. 5. Evolution of the average pressure (dotted) and heat release rate (continuous) as a function of Compression Ratios (at 2000rpm and 8bar of IMEP)

In Fig. 6, the optimal phasing (i.e. offering the highest engine efficiency) is indicated by the double square symbol. The optimal CA50 angle results from the trade-off between the theoretical optimal phasing, i.e. at TDC according to the Beau De Rochas cycle, and the exchanges that may occur with the walls. Thus, it could be observed a variation of the optimal phasing with an increase of the CR, certainly due to the increase of wall heat exchanges due to the higher in-cylinder pressure. The ISFC, therefore the efficiency seems to be optimal for the intermediate CR, namely 18.4, due to the best trade-off between the combustion development speed and the wall exchanges. In fact, the slow combustion development and the higher level of unburnt emissions with CR 20.0 induce an increase of ISFC.

The unburnt NH_3 emissions seem to be impacted by the change in CR, i.e. they increase with the CR. This was mainly due to the increase in the mass of NH_3 trapped in the dead volumes, a direct consequence of the pressure increased. Finally, the unburned NH_3 emissions were higher in very lean and very rich mixtures owing to the lack of stability and the excess of fuel, respectively, but were far from zero near stoichiometry since nearly 6% by mass of the fuel was found in the exhaust, confirming that an important part of the measured NH_3 should come from the dead zones.
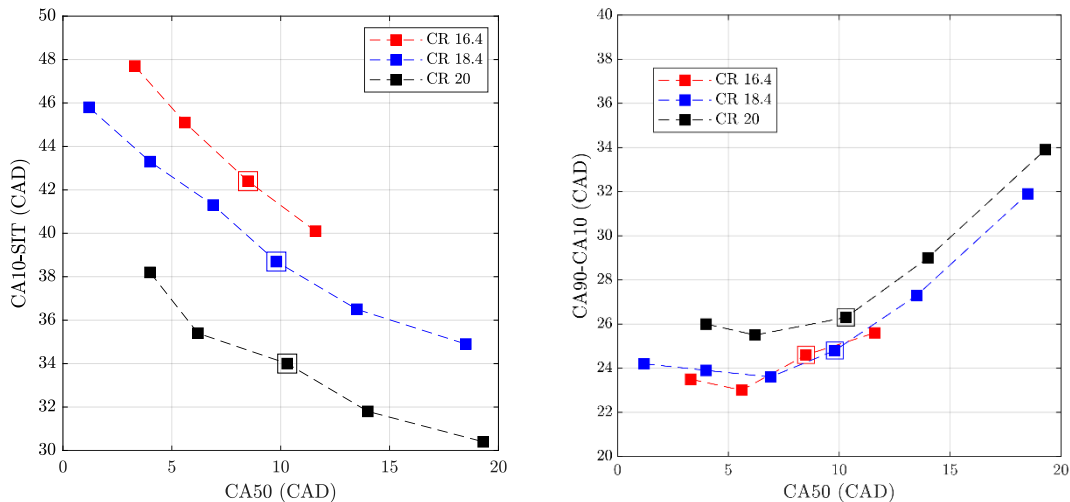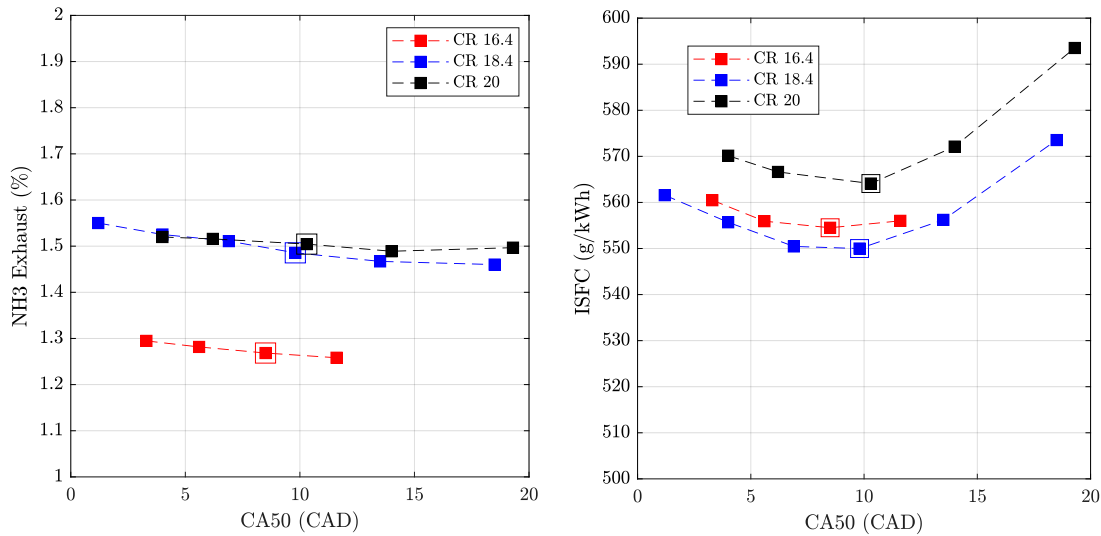
Fig. 6. Effect of SIT sweeps on the ignition duration, combustion duration, ISFC and NH_3 emissions at 2000rpm and 8bar of IMEP with different CR (16.4, 18.4 and 20.0)

Lastly, in Fig. 7, regarding low load operating condition, i.e. 3bar of IMEP, the stability was slightly improved with the compression ratio increase, even though the COV_{IMEP} remains quite similar between CR of 18.4 and 20, for 2000 rpm. However, the combustion behavior was different at higher engine speed due to the decrease of the time available for the combustion. Therefore, more advanced spark ignition angles were needed, which did not allow a consistent ignition of the mixture, especially with low compression ratio due to the longer ignition delay as previously mentioned in Fig. 7. The combination of both, longer ignition delay and less favorable thermodynamic conditions – for same crank angle – made the optimal CA50 impossible to reach for the lowest compression ratio, inducing more instabilities. Furthermore, the optimal CA50 should even be shortened at high engine speed because the time to exchange with the walls was reduced meaning that the optimal feasible setting at CR16 was very far from the theoretical optimal setting.
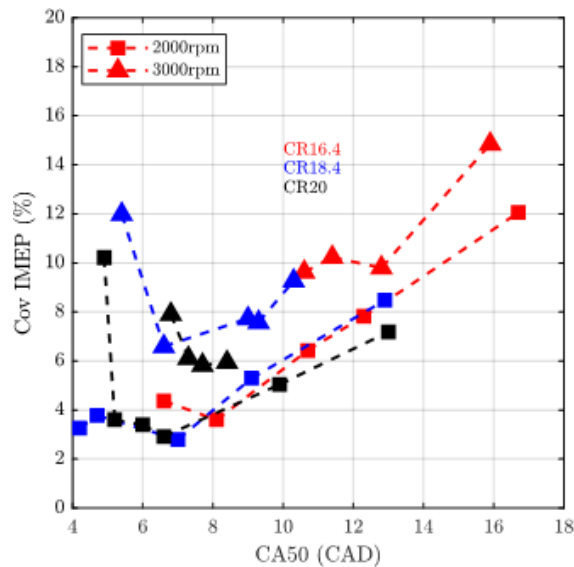
Fig. 7. Effect of SIT sweep on COV_{IMEP} at 2000 and 3000rpm and 3bar of IMEP with different CR (16.4, 18.4 and 20.0)

3.2.2 High voltage spark ignition system

In order to evaluate the relevance of a more efficient ignition system, similar tests were performed with the reference piston (CR16.4) and the high voltage ignition system, at 2000rpm and for two different loads, namely 3 and 8 bars of IMEP. First, Fig. 8 clearly shows the beneficial effect of this high voltage ignition device on the first initiation phase (CA10 - SIT). The decrease of the ignition delays also leads to a rise in thermodynamic conditions at the time of ignition (for the same angle of CA50), which results in a faster combustion process. Thus, less NH_3 emissions were observed at the exhaust, which results, combined with the increase in the combustion speed, in a slight decrease in the specific fuel consumption.
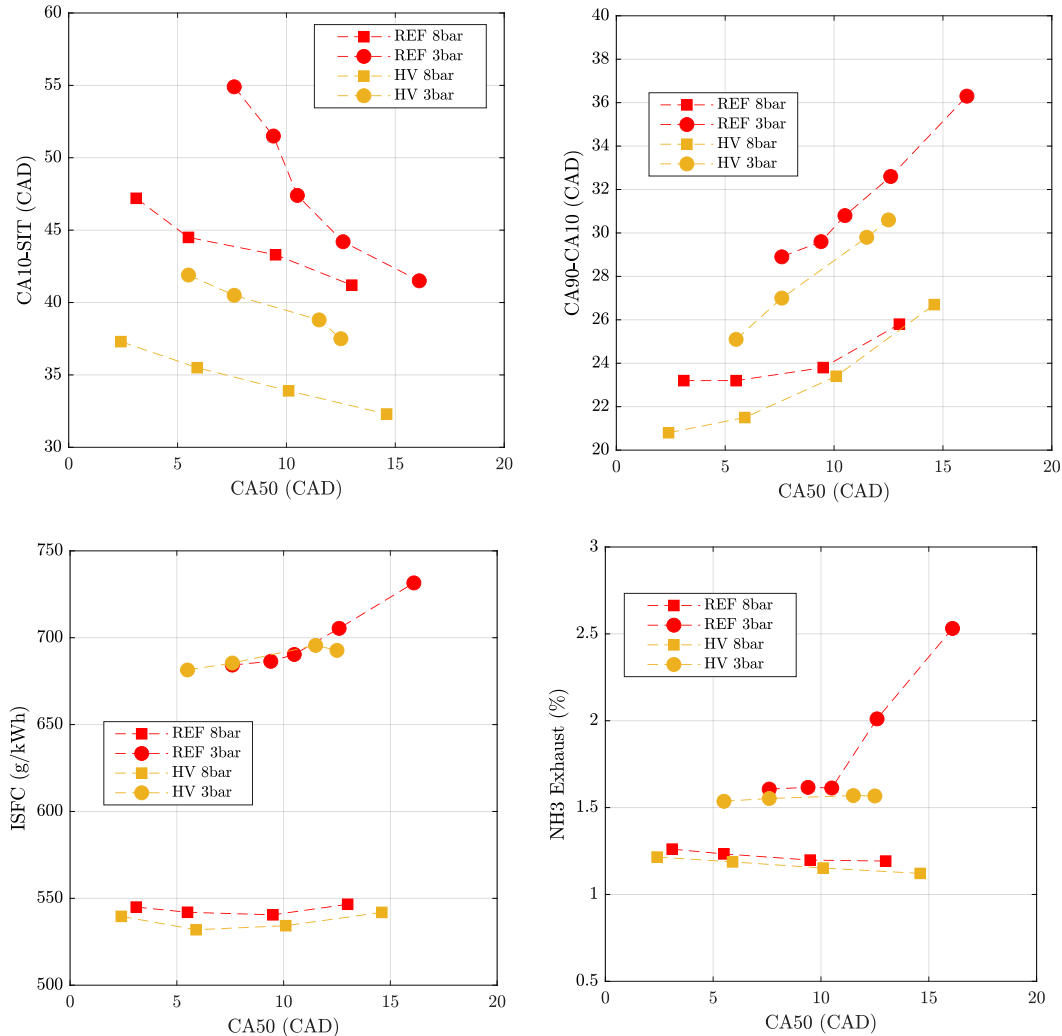
Fig. 8. Effect of SIT sweeps on the ignition duration, combustion duration, ISFC and NH_3 emissions at 2000rpm, 3 and 8bar of IMEP with 2 different spark plugs (REF: reference SP, HV: high voltage SP)

3.3 The lowest IMEPs

In the final stage, the IMEP sweeps were performed at different engine speeds and based on the experimental results (SIT and lambda sweeps). The purpose of the full engine map test was not only to see the global trend of NH_3 combustion on entire engine operating conditions but also to define the boundary of operating range on NH_3 engine by changing hardware configurations. In the NH_3 engine development, the engine operating range (e.g., the stability limit at low load and fuel flow limit at full loads) will be one of key parameters to make NH_3 a potential candidate as a fuel for premixed combustion engines. The experiments were performed over a wide range of operating conditions and during the investigations, we selected a hardware based on low-load improvement criteria. In general, the NH_3 engine was able to run at very low load (below 2bar at all engine speeds) without misfire (10% of IMEP) on all configurations. However, the combustion stability was an important parameter to understand the repeatability and safety of the combustion from engine development's point of view. For example, the

lowest IMEPs were calculated and compared with the different configurations in Fig. 9. The values, which were the interpolated levels on the IMEP sweeps, represent the limit of the lowest load available below 5% of COV_{IMEP} on each configuration. The results of different configurations were compared to the results with different volume of H_2 additives into NH_3 fuel on CR 16.4 reference bowl and the reference spark plug. In general, the lowest IMEPs were high at high engine speeds due to the limited time to complete NH_3 combustion. Based on the results, the higher CR (18.4 and 20.0) gave benefits from the stability point of view at all engine speeds. CR 18.4 enabled to get significant reduction of the lowest IMEP compared to CR 16.4 but there was no additional strong benefit by further increasing of CR (from CR18.4 to CR 20.0). The slow combustion with the highest CR did not bring additional potential in terms of the combustion stability especially at high engine speed. CR16.4 had the highest level of instability with the highest lowest IMEP. As discussed before, the instability could be improved by using high voltage spark plug (CR 16.4_HV). Furthermore, as mentioned before it was possible to extend the low load operating range by means of H_2 addition. One can see that with increasing compression ratio or using high voltage system the minimum IMEPs were similar to those obtained by doping the engine with 2.5% (in vol.) hydrogen. More than 5% vol. of hydrogen content in the fuel (7.5 and 10% vol.) allowed very low IMEPs, which does not really depend on engine speed anymore, but the difference between 7.5 and 10% remains in the margin.
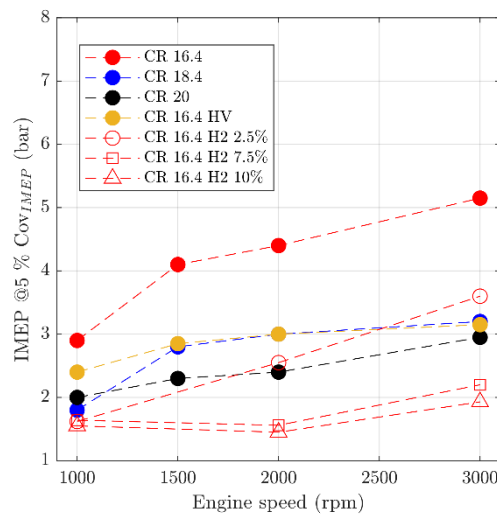
Fig. 9. The lowest IMEPs with below 5% of COV_{IMEP} for different CR at different speeds (compared to the results on CR16.4 with HV SP and some additions of H_2)

Summary and conclusions

This study focused on the potential of using pure NH_3 as fuel in a single cylinder engine with spark igniter, based on a compression ignition engine architecture, over a wide range of operating conditions:

-    Firstly, this study showed the possibility of running pure NH_3 ICE with stable premixed combustion over a wide range of operating conditions, even at low load and high speed. Indeed, for the first time, results are provided for conditions with pure NH_3 at low loads as 3bar of IMEP and for several engine speeds (up to 3000rpm) without any misfire.
-    In accordance with [19], high level of NO_X and especially unburnt NH_3 were measured at the exhaust which mainly came from crevice area that were not optimized for premixed combustion and also from a lack of combustion stability at very low load.
-    To overcome those issues, several hardware variations were investigated, namely compression ratio increase and the use of a high voltage ignition system.
-    CR increase helps to get more stable combustion at low load at the expense of an increase in average unburnt NH_3 emissions due to the increase in in-cylinder pressure that made the unburnt mass of NH_3 in the crevice volumes more important. CR 18.4 seems a promising hardware in terms of the combustion stability and indicated efficiency standpoint.

- On the other side, using a high voltage ignition system provided positive results, such as higher combustion stability at low load but also lower unburnt NH_3 level due to a faster and more efficient combustion. Thus, similar minimum IMEP as CR 18.4 or slight hydrogen doping (<2.5 % vol.) could be reached with high voltage system only on reference hardware (CR 16.4) without any penalty on NH_3 emission and need of on-board NH_3 cracker, respectively.

To go further, more understanding of the flow field effect on the NH_3 flame development would be necessary to design optimized piston shapes that keep allowing pure NH_3 combustion at high speed with a reduced crevice volume to increase the efficiency. For that, CFD study would be useful to help the understanding.

References

[1]   U.S. energy Information Administration, "International energy outlook 2013",DOE/EIA-0484, 2013 http://www. eia.gov/forecasts/ieo/pdf/0484(2013).pdf

[2]   ExxonMobil, 2014 The outlook for energy: A view to 2040 http://corporate.exxonmobil.com/en/energy/energy-outlook/download-the-report/download-the-outlook-forenergy-report (2014 Accessed 13 Jan 2014)Abi Hill, "Global electric and hybrid light vehicles market – forecasts to 2031", 2017 Q1 edition, BUBE by just-auto, 2017

[3]   European Commission: "the European Green Deal", COM (2019) 640 final, 2019.

[4]   ICCT report- The European Commission regulatory proposal for post-2020 CO_2 targets for cars and vans: A summary and evaluation, January 2018, www.theicct.org.

[5]   HW. Xiang "Vapor pressures, critical parameters, boiling points, and triple points of ammonia and trideuteroammonia", J. Phys. Chem. Ref Data 2004, 33(4):1005–1011, 2004.

[6]   C. Zamfirescu, I. Dincer, "Ammonia as a green fuel and hydrogen source for vehicular applications", Fuel Process Technol. 2009, 90(5):729, 2009.

[7]   R. Stevens, "Carbon free ammonia food or fuel?", Japan-Norway hydrogen seminar Tokyo 2017, http://injapan.no/wp-content/uploads/2017/02/12-YARA-Carbon-free-ammonia.pdf.

[8]   M. Zavka, "Device for operating internal combustion engines with mixtures of ammonia, hydrogen, and nitrogen prepared from ammonia", United States Patent. 1937. US13979637.

[9]   E. Kroch, "Ammonia d a fuel for motor buses", J. Inst. Pet 1945, 31:213-223, 1945.

[10]   KP. Werrell, "The strategic bombing of Germany in World War II: costs and accomplishments", J. Am. Hist. 1986, 73(3):702, 1986.

[11]   PG. Grimes, "Energy depot fuel production and utilization" SAE Technical Paper 650051, 1965.

[12]   A. Rosenthal, "Energy depot - a concept for reducing the military supply burden", SAE technical paper 650050, 1965.

[13]   W. Cornelius, LW. Huellmantel, HR. Mitchell, "Ammonia as an engine fuel" SAE Trans. papers, 650001 – 650225, 1966.

[14]   JT. Gray, E. Dimitroff, NT. Merkel, RD. Quillian, "Ammonia Fuel – Engine compatibility and combustion", SAE technical paper 660156, 1966.

[15]   TJ. Pearsall, CG. Garabedian, "Combustion of anhydrous ammonia in diesel engine", SAE Technical paper 670947, 1967.

[16]   ES. Starkman, GE. James, HK. Newhall, "Ammonia as a diesel engine fuel: theory and application", SAE technical paper 670946, 1967.

[17]   Lhuillier C, Brequigny P, Contino F, Rousselle C. "Performance and Emissions of an Ammonia-Fueled SI Engine with Hydrogen Enrichment", SAE Technical Paper 2019-24-0137, 2019. https://doi.org/10.4271/2019-24-0137.

[18]   C. Mounaïm-Rousselle, A. Mercier, P. Brequigny, C. Dumand, J. Bouriot, S. Houillé. "Performance of am-monia fuel in a spark assisted compression Ignition engine", Int. J. Engine Res. 2021:1–12. https://doi.org/10.1177/14680874211038726.

[19]   A. Mercier, C. Mounaïm-Rousselle, P. Brequigny, J. Bouriot, C. Dumand. "Improvement of SI engine combustion with ammonia as fuel: effect of ammonia dissociation prior to combustion", Fuel Commun. 2022;11:100058. https://doi.org/10.1016/j.jfueco.2022.100058.

[20]   F. Westlye, A. Ivarsson, J. Schramm. "Experimental investigation of nitrogen based emissions from an ammonia fueled SI engine", Fuel 2013;111:239–47. https://doi.org/10.1016/j.fuel.2013.03.055.

[21]   L. Hien, "Effects of natural gas composition variations on the operation, performance and exhaust emission of natural gas – powered vehicles", NGV conference paper, Aug., 2002.

A Study of Flame Dynamics and Structure in Premixed Turbulent Planar NH₃/H₂/Air Flames

P. Tamadonfar[1], S. Karimkashi[1], O. Kaario[1], V. Vuorinen[1]

[1] Department of Mechanical Engineering, School of Engineering, Aalto University, Otakaari 4, Espoo 02150, Finland

E-mail: parsa.tamadonfar@aalto.fi
Telephone: +(358) 46 684 5082

Abstract. Ammonia NH_3 has received considerable attention as a near future carbon-free synthetic fuel due to its economic storage/transportation/distribution, and its potential to be thermally decomposed to hydrogen H_2. Since the boiling temperature and condensation pressure of NH_3 is comparable to propane C_3H_8, it could be employed in marine engines running on C_3H_8 making the combustion processes carbon neutral. To promote the low burning velocity and heat of combustion of ammonia, it is required to enrich the pure ammonia with hydrogen. In this study, two quasi direct numerical simulation (quasi-DNS) cases with detailed chemistry (31 species and 203 reactions) and the mixture-averaged transport model are examined to study the planar ammonia/hydrogen/air flames under decaying turbulence. The reactants temperature and pressure are set to $298\,\mathrm{K}$ and $1\,\mathrm{atm}$, respectively. The initial turbulent Karlovitz number is changed from 4.3 to 16.9 implying that all the test conditions are within the thin reaction zones combustion regime. Results indicate that the density-weighted flame displacement speed S_d^*, on average, is higher than the unstrained premixed laminar burning velocity S_L^0 value for both test cases. This suggests that the flame elements propagate faster than its laminar flame counterpart. Furthermore, the flame stretch factor defined as the ratio of the turbulent to the laminar burning velocity divided by the ratio of the wrinkled to the unwrinkled flame surface area is higher than unity, i.e., the Damköhler's first hypothesis is not valid for these flame conditions. This indicates that the local flamelet velocity value, on average, is higher than the unstrained premixed laminar burning velocity. In addition, results show that the mean value of the local equivalence ratio for the turbulent conditions is higher than its laminar counterpart due to the preferential diffusion of hydrogen and the turbulent mixing. Furthermore, the net production rate of hydrogen is negatively correlated with the flame front curvature suggesting that the local burning rate is intensified under positively curved regions.

1. Introduction

Increasing the efficiency of combustion devices as well as using novel carbon-free synthetic fuel blends are considered as of the main targets in order to decrease greenhouse gas emissions. One of the suitable options for attaining this target is to utilize hydrogen which is produced from green-energy origins. However, the economic storage and transportation of hydrogen have not been resolved very well [1]. Therefore, sustainable operation of combustion devices running on pure hydrogen is still a matter of ongoing research. Among all hydrogen carriers, ammonia has received substantial attention as a carbon-free fuel due to its high energy density, and its transportation, storage, handling, and distribution have been very well established [1, 2]. It should be noted that since the condensation pressure and boiling temperature of ammonia is relatively comparable to propane, ammonia could be effortlessly used as an alternative fuel for marine engines running on propane. This helps to decarbonize the whole combustion process. However, the disadvantages of using pure ammonia as a main fuel are its low laminar burning velocity and heat of combustion [1]. It should be mentioned that increasing the reactivity of pure ammonia could be done with enriching it with hydrogen and/or oxygen. Figure 1 shows the variation of the heat release rate with respect to the flame temperature for 1-D premixed laminar ammonia/air, ammonia/hydrogen/air, and methane/air flames. The simulations are performed using the Cantera which is an open-source chemical kinetics software. Results presented in Fig. 1 shows that the heat release rate of pure ammonia is quite negligible, and enriching it with 40% of hydrogen could have a significant effect on its value. With adding hydrogen, the heat release rate value of ammonia/hydrogen/air flame mixture is then comparable with methane/air flames. Since the ammonia has the capability to be thermally decomposed on-board to ammonia and hydrogen, studying the characteristics of ammonia and hydrogen blend is of a particular interest.
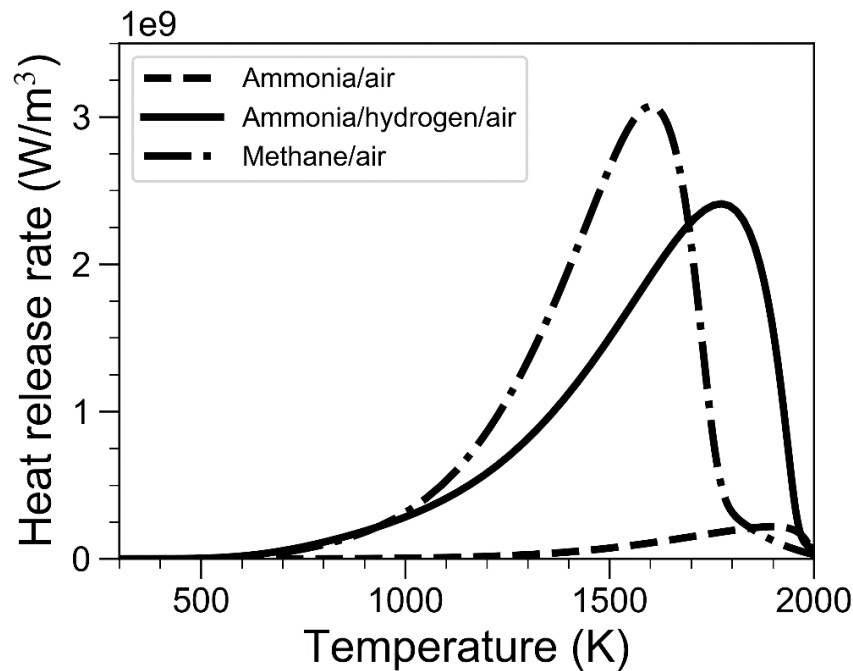
Fig. 1. Heat release rate with respect to the temperature for 1-D premixed laminar ammonia/air, ammonia/hydrogen/air, and methane/air flames. The equivalence ratios for ammonia/air, ammonia/hydrogen/air, and methane/air flames are set to 1.0, 1.0, and 0.85, respectively. The simulations were performed using the Cantera which is an open-source chemical kinetics software

Despite the active research in using novel fuel blends for premixed turbulent combustion, there still exists many unsolved problems for such flames. Among different flame properties, the flame speed is one of the important characteristics for premixed turbulent flames, and comprehending the behaviour of this property is required for the flamelet modelling [3]. The flame displacement speed, the turbulent burning velocity, and the local consumption speed are important flame characteristics, and understanding the behaviour of these quantities is required for less explored novel fuel blends such as ammonia/hydrogen/air flames under different turbulent conditions.

The local turbulence-chemistry interactions could be understood in depth by knowing the flame displacement speed S_d characterizing the speed of an iso-scalar surface relative to the flow field [4-6]. It should be noted that the flame displacement speed has been the subject of various numerical studies. Peters et al. [4] and Echekki and Chen [5] discussed the contributions of the flame front curvature on the flame displacement speed components using direct numerical simulation (DNS) of a 2-D methane/air flame. Chakraborty and Cant [7] showed that the flame displacement speed is negatively correlated with the flame front curvature using 3-D DNS with a simple chemistry, which is consistent with other studies reported in Refs. [4, 5]. Song et al. [6] analysed the density-weighted form of the flame displacement speed for highly turbulent hydrogen/air flames, and they concluded that the most probable values of the local flame displacement speed is relatively equal to the unstrained premixed laminar flame. Chakraborty and Cant [8] discussed the influence of the Lewis number on the flame displacement speed statistics based on 3-D DNS with simple chemistry. They showed that the flame displacement speed, irrespective of the Lewis number, is negatively correlated with the flame front curvature, and the density-weighted flame displacement speed is higher than the unstrained premixed laminar burning velocity when the Lewis number is less than unity. More recently, Chakraborty et al. [9] assessed the performance of various extrapolation relations connecting the density-weighted flame displacement speed to the flame front curvature and flame stretch rate for thermo-diffusively neutral flames using 3-D DNS with detailed chemistry, since the accurate modelling of this quantity is required for the closure of the flame surface density transport equation. They showed that the density-weighted flame displacement speed could be evaluated using the linear model based on the flame front curvature in a very robust manner.

In addition to the flame displacement speed, the turbulent burning velocity S_T is considered as an important parameter for the premixed turbulent combustion, and many attempts have been done over several decades to correlate the turbulent burning velocity data obtained from experimental measurements in terms of various parameters such as the turbulent intensity and turbulent length scale [10-12].

Damköhler [13] hypothesized that the turbulence is responsible for wrinkling the flame front, and the local flamelet consumption velocity is equal to the unstrained premixed laminar burning velocity. According to this hypothesis, the ratio of the turbulent burning velocity to the unstrained premixed laminar burning velocity is equal to the ratio of the wrinkled to the unwrinkled flame surface area. It should be emphasized that the validity of this hypothesis is confirmed based on 2-D and 3-D DNS with simple/detailed chemistry for thermo-diffusively neutral flames (unity Lewis number), see, e.g., Hawkes and Chen [3], Han and Huh [14], Nivarti and Cant [15], Klein et al. [16], Brearley et al. [17], and Song et al. [6]. However, this hypothesis might be no longer valid for thermo-diffusively unstable flames. Chakraborty et al. [18] showed that the ratio of the turbulent to the laminar burning velocity is higher than the ratio of the wrinkled to the unwrinkled flame surface area for thermo-diffusively unstable flames. A similar observation was previously reported by Han and Huh [14] as well using 3-D DNS with simple chemistry. It should be mentioned that Gülder [19] and Tamadonfar and Gülder [20] discussed that the validity of this hypothesis might be disputed under certain experimental conditions for premixed turbulent Bunsen-type flames. More recently, Chakraborty et al. [21] showed that this hypothesis might become invalid for flames with high non-zero mean flame front curvature such as the Bunsen-type flames.

Furthermore, in their comprehensive review paper, Lipatnikov and Chomiak [22] discussed thoroughly about the local flame structure of premixed turbulent flames. They mentioned that the local burning velocity for flames with positive flame front curvature is higher than the corresponding value for negatively curved regions if the Lewis number is less than unity and/or the mass diffusivity of the deficient reactants is higher than the mass diffusivity of the excess reactants. Rutland and Trouvé [23, 24] and Haworth and Poinsot [25] showed a strong correlation between the local burning velocity and the flame front curvature for non-unity Lewis number flame conditions using simple chemistry. Bell et al. [26] reported a positive (negative) correlation between the local burning velocity and the flame front curvature for a premixed turbulent hydrogen/air (propane/air) flame indicating enhanced fuel consumption rate in positive (negative) curvature regions using 2-D DNS with detailed chemistry. They attributed this observation to the thermo-diffusive instability (stable) characteristics of the hydrogen/air (propane/air) flames. Day et al. [27] and Aspden [28] demonstrated a similar correlation between the local burning velocity and the flame front curvature for premixed turbulent lean hydrogen/air flames. More recently, Lee et al. [29] and Rieth et al. [30] showed a positive correlation between the fuel consumption rate and the flame front curvature for highly turbulent premixed lean hydrogen/air and ammonia/hydrogen/air flames developing in the forced turbulence and in a turbulent shear layer, respectively.

To the best of the authors' knowledge, certain aspects of premixed turbulent ammonia/hydrogen/air flames such as the flame displacement speed statistics, the turbulent burning velocity, and the local burning velocity of these flames have been less explored. Therefore, the current study determines on addressing these fundamental properties using quasi direct numerical simulation (quasi-DNS) with detailed chemistry and mixture-averaged transport model to incorporate the preferential diffusion of high diffusivity species accurately. In this respect, the main objectives of the current work is (1) to study the flame displacement statistics, (2) to explore the turbulent burning velocity and the validity of Damköhler's first hypothesis, and (3) to discuss the local flame structure of premixed turbulent planar ammonia/hydrogen/air flames. The remainder of the paper is organized as follows. The numerical methods will be discussed in section 2. This will be followed by results and discussion in section 3, and the concluding remarks in section 4.

2. Numerical methods

2.1. Flame configuration

In this study, the quasi direct numerical simulations of premixed turbulent ammonia/hydrogen/air flames have been performed under the global equivalence ratio of unity. The blending ratio α indicating the amount of hydrogen concentration in the pure ammonia is evaluated as $X_{H_2}/(X_{H_2} + X_{NH_3})$, where X_{H_2} and X_{NH_3} are the mole fractions of hydrogen and ammonia, respectively. The blending ratio is set to 0.4 for the current study. The reactants temperature T_r and pressure p are set to 298 K and 1 atm, respectively. The unstrained premixed laminar burning velocity S_L^0 and the thermal flame thickness δ_T evaluated based on the maximum temperature gradient are 30.37 m/s and 0.604 mm, respectively. The adiabatic flame temperature T_{ad} is then equal to 2146 K.

The Passot-Pouquet spectrum is utilized for generating the homogenous isotropic turbulent flow field on a cube with a domain size of $45\delta_T \times 7\delta_T \times 7\delta_T$. The Python script utilized for generating the turbulent

flow field was originally developed by Saad et al. [31], and they later added the aforementioned spectrum to their script. The non-dimensional turbulence intensity u'/S_L^0 is varied from 4 to 10, and the non-dimensional integral length scale Λ/δ_T is fixed to 3.5. The domain has been discretized on a uniform Cartesian grid of $990 \times 154 \times 154$ and $1100 \times 172 \times 172$ cells for the low and high turbulence intensity test cases, respectively. Flame-turbulence interactions happen under the decaying turbulence. It should be emphasized that such turbulence characteristics without active turbulence generation are essential in internal combustion engine context. The turbulent flow field is then superimposed on a solution of 1-D unstrained premixed reference laminar flame. The grid spacing ensures that at least 22 computational data points exist within the flame thickness, and the initial Kolmogorov length scale $\eta \approx \Lambda Re_\Lambda^{-3/4}$ resides within one computational cell, where Re_Λ is the turbulent Reynolds number. The turbulent Reynolds number Re_Λ, Karlovitz number Ka, and Damköhler number Da are estimated as $u'\Lambda/\nu$, $(u'/S_L^0)^{1.5}(\Lambda/\delta_T)^{-0.5}$, and $\Lambda S_L^0/u'\delta_T$, respectively. The effective Lewis number, using the methodology presented in Ref. [32], is equal to 0.76 for both cases implying that the test cases are thermo-diffusively unstable. Table 1 shows the simulation parameters for the test conditions utilized in this study. Figure 2 shows that all the test conditions studied in this work lie within the thin reaction zones combustion regime since the initial Karlovitz number is higher than unity.
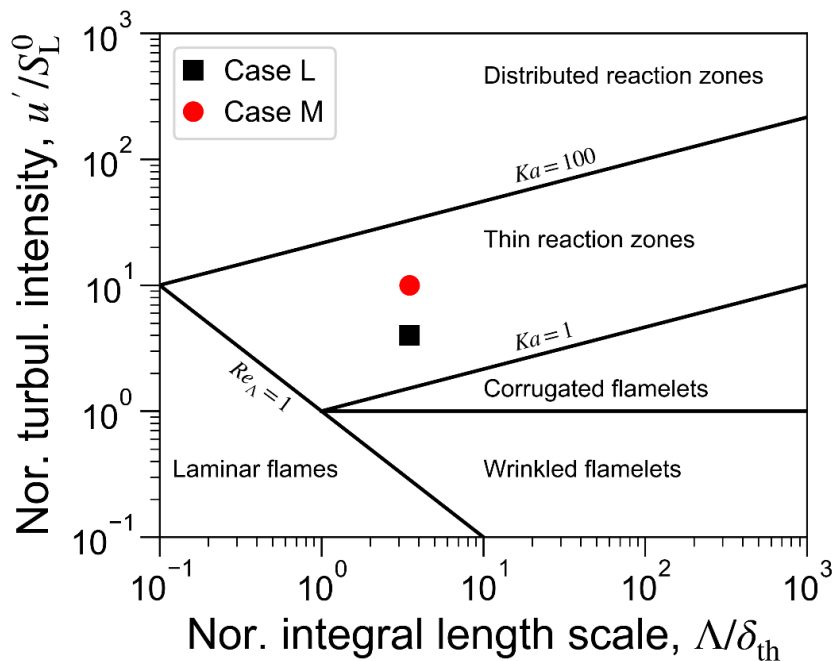
Fig. 2. Numerical data on a Borghi-Peters regime diagram for premixed turbulent combustion regime [33, 34]

2.2. Reacting flow solver

The open-source C++ CFD toolbox OpenFOAM [35], where mass, momentum, species mass fractions, and energy equations are solved with compressible PIMPLE algorithm is utilized to perform quasi direct numerical simulations (quasi-DNS) with detailed chemistry of premixed turbulent planar ammonia/hydrogen/air flames. The chemical kinetic mechanism developed by Stagni et al. [36] consisting 31 species and 203 reactions is used in this study. The reactingDNS solver [37] where the mixture-averaged transport model is used to consider the mass diffusivity of each species evaluated from the binary diffusion coefficients is utilized in this study. This approach leads to more accurate results compared to unity/non-unity Lewis number assumption when simulating the mixtures having high mass diffusivity species such as molecular/atomic hydrogen. This solver is then linked to the open-source library of pyJac, developed by Niemeyer et al. [38]. This library provides C subroutines for generating the analytical Jacobian of a chemical kinetic mechanism which is required for solving a system of ordinary differential equations. The operator-splitting approach is utilized considering the large differences between the chemistry and flow time scales. It should be emphasized that to overcome the computational load imbalance among processors originating from the chemistry problems, a dynamic load balancing model (DLBFoam), developed by Tekgül et al. [39], is used to distribute the chemistry problems equally among all processors using the MPI communication protocol.

Table 1. Simulation parameters for the test cases in this study.

Case	α	u'/S_L^0	Λ/δ_T	Re_Λ	Ka	Da
L	0.4	4.0	3.5	150	4.28	0.875
M	0.4	10.0	3.5	374	16.90	0.35

Inflow and outflow boundary conditions with zero mean inlet velocity in the direction of mean flame front propagation are used. On lateral directions, the periodic boundary conditions are employed indicating an unbounded planar flame brush. For pressure, a non-reflecting boundary condition is applied for both inflow and outflow regions. A second-order implicit backward Euler method for time discretization, and the cubic scheme for spatial discretization have been utilized herein. The simulation runs for 2 (2.85) initial eddy turn over times for case L (M) ensuring that the simulation time is equal/higher than the chemical time scale. The eddy turn over time t_e and the chemical time scale t_{chem} are evaluated as Λ/u' and δ_T/S_L^0, respectively. Figure 3 shows an example of instantaneous flame front surface, cut plane of a temperature field, and the logarithm of enstrophy for cases L and M. It should be noted that the enstrophy values for case M is higher than case L because of higher turbulence intensity. Furthermore, Fig. 4 shows the Lewis number Le fields of ammonia NH_3, molecular hydrogen H_2, atomic hydrogen H, and water H_2O. The Lewis number for each species Le_j is evaluated as α_t/D_j, where α_t and D_j are the thermal diffusivity of the mixture and the mass diffusivity of species j, respectively. Results show that the variation of the Lewis number value across the flame brush is insignificant for NH_3, H_2, and H, while it varies significantly for H_2O. This observation confirms the need for using the mixture-averaged transport model for the current simulations. A similar observation is thoroughly discussed by Poinsot and Veynante [40].
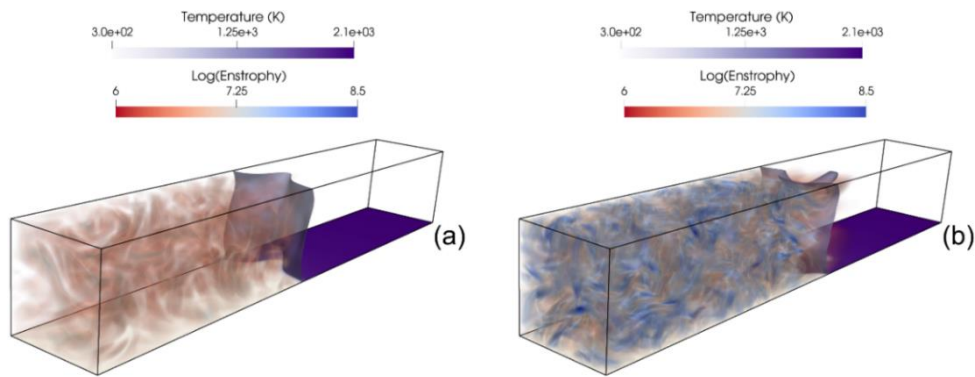
Fig. 3. Instantaneous flame front surface, cut plane of a temperature field, and the logarithm of enstrophy for (a) case L, and (b) case M
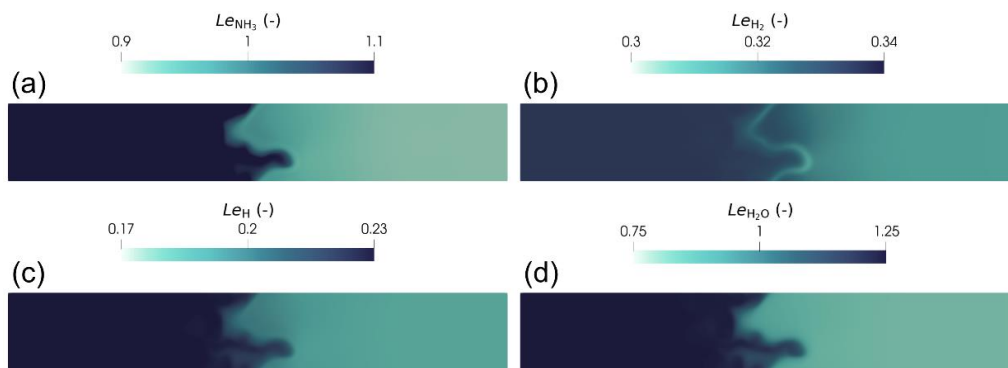
Fig. 4. Lewis number fields for (a) ammonia NH_3, (b) molecular hydrogen H_2, (c) atomic hydrogen H, and (d) water H_2O for case M. These data are captured at 2.85 initial eddy turn over times

3. Results and discussion

Before examining a detailed quantitative analysis on the premixed turbulent ammonia/hydrogen/air flame dynamics, a general overview of the flame front characteristics will be examined. Later in this section, the conditional mean profiles of major species and the atomic hydrogen, the flame displacement speed statistics, the flame stretch factor and the turbulent burning velocity, the local equivalence ratio, the molecular diffusion fluxes of molecular/atomic hydrogen will be discussed. This will be followed by inspecting the fuel net production rate over the curved flame fronts.

3.1. General overview of the flame front characteristics

Figure 5 shows the two-dimensional slices of temperature, enstrophy, mass fractions of H_2O_2, HNO, NH species, and heat release rate for cases L and M from the entire computational domain. The solid lines in the first four rows (from left to right) correspond to the temperature-based reaction progress variable c values of $0.1, 0.2, 0.5, 0.7, 0.8$, where c is evaluated as $(T - T_r)/(T_{ad} - T_r)$. From visual examination of the temperature field, the flame wrinkling, preheat zone layer, and possibly the flame surface area increases with increasing the Karlovitz number. This could be due to the existence of higher enstrophy magnitudes, i.e., stronger turbulence structures, in the preheat zone layer for case M compared to case L. Results indicate that the enstrophy values damped significantly in the reaction zone layer, i.e., $c = 0.8$, due to existence of high heat release region. Therefore, the reaction zone layer is not disrupted for both cases. It should be emphasized that the mass fractions of H_2O_2 and HNO are the proper markers for the preheat and reaction zone layers, respectively, since the maximum value of the former (latter) species happens in the preheat (reaction) zone layer. Results show that the mass fraction of H_2O_2 is disrupted dramatically with increasing the Karlovitz number indicating the local broadening of the preheat zone layer, while the mass fraction of HNO is not altered implying that the reaction zone layer remains relatively intact. Furthermore, results show that the distribution of the mass fraction of NH coincides with the distribution of the heat release rate.
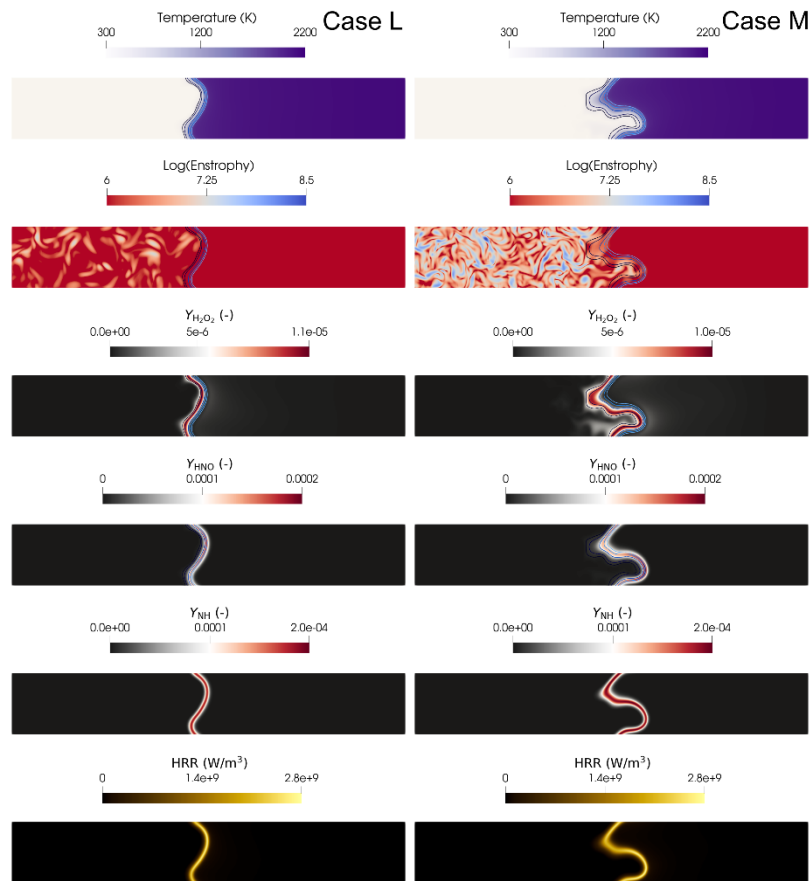
Fig. 5. Two-dimensional slices of temperature, enstrophy, mass fractions of H_2O_2, HNO, NH species, and heat release rate for case L (left) and case M (right). The solid lines in the first four rows (from left to right) correspond to the temperature-based reaction progress variable values of $0.1, 0.2, 0.5, 0.7, 0.8$

3.2. Conditional mean profiles

The conditional mean profiles provide practical information when comparing DNS, LES, and experiments, and evaluating these profiles give more insight than analyzing the mean concentration profiles [41]. Figure 6 shows the conditional mean profiles of major species and the atomic hydrogen for cases L and M as well as the unstrained premixed reference laminar flame. The data has been normalized by the maximum value of the corresponding species obtained from the reference laminar flame. Results indicate that the conditional mean profiles of NH_3 and H_2O for the turbulence cases bears a good resemblance to the counterpart profiles of the reference laminar flame. However, the conditional mean profiles of H_2 and H deviate from the premixed laminar flame profiles. This deviation could be due to the preferential diffusion of these species as well as the turbulent mixing, as discussed by Aspden et al. [42]. A similar observation was previously reported by Aspden et al. [43] and Song et al. [6] for highly turbulent premixed hydrogen/air flames propagating in the forced turbulence. Furthermore, it should be emphasized that the observed deviation is enhanced with increasing the Karlovitz number.
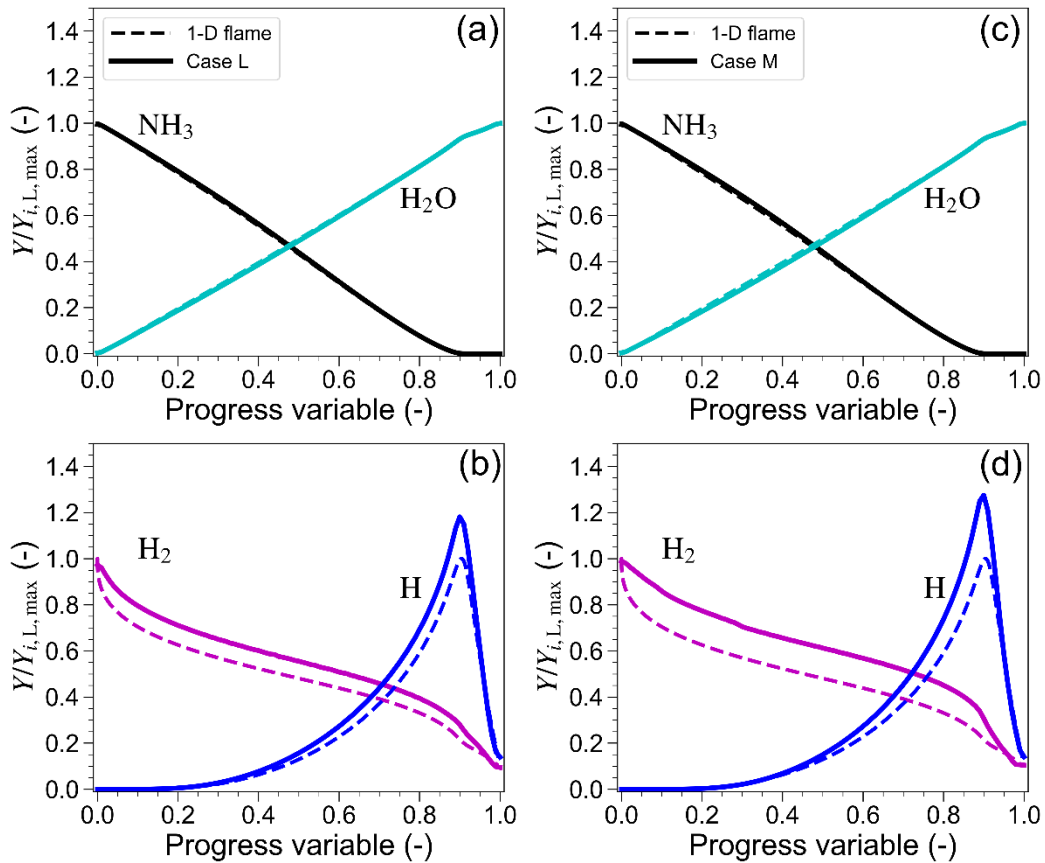
Fig. 6. Conditional mean profiles of NH_3, H_2O, H_2, and H mass fractions (solid lines) compared to the unstrained premixed laminar profiles (dashed lines) for (a-b) case L, and (c-d) case M. The data has been normalized by the maximum value of the reference laminar flame. The dashed lines correspond to the laminar flame, and the solid lines correspond to the turbulent conditions

3.3. Flame displacement speed

As mentioned earlier in Introduction, the flame displacement speed S_d which is the flame speed relative to the local fluid velocity is an important flame property, and it is extensively utilized for modelling the turbulent premixed flames using the flame surface density and G-equation models [40, 44]. Following the methodology presented [4, 5, 45, 46], the flame displacement speed S_d and its components could be estimated as follows:

$$S_d = S_{d,r} + S_{d,n} + S_{d,t} = \frac{\dot{\omega}}{\rho |\nabla c|} + \frac{n.\nabla(\rho \alpha_t n.\nabla c)}{\rho |\nabla c|} - 2\alpha_t \kappa, \tag{1}$$

where $S_{d,r}$, $S_{d,n}$, $S_{d,t}$, $\dot{\omega}$, n, ρ, α_t, and κ are the reaction component of S_d, normal diffusion component of S_d, tangential diffusion component of S_d, reaction rate of the reaction progress variable, unit normal vector to the iso-surface, density, thermal diffusivity of the mixture, and the flame front curvature, respectively. The unit normal vector n and the flame front curvature κ are evaluated as $-\nabla c/|\nabla c|$ and $0.5(\nabla.n)$, respectively. It should be noted that in order to compare between the flame displacement values in a meaningful manner, evaluating the density-weighted form of this quantity is of a great importance [5, 6, 45]. As discussed by Song et al. [6], the velocity acceleration across the flame brush originated due to the thermal expansion is excluded by using the density-weighted form of the flame displacement speed S_d^* evaluated as:

$$S_d^* = \frac{\rho S_d}{\rho_r},$$

(2)

where ρ_r is the reactants density. Each of the flame displacement speed components could be written in their density-weighted format by multiplying their values by ρ/ρ_r. Figure 7 shows the probability density functions (PDFs) of the density-weighted forms of the flame displacement speed and its components for cases L and M. Each component has been normalized by the unstrained premixed laminar burning velocity of the reference flame, and the data are conditioned at $c = 0.8$. Results show that the distribution of S_d^* and its components widens with increasing the Karlovitz number. A similar observation was previously reported by Song et al. [6] for premixed turbulent hydrogen/air flames. It should be noted that all S_d^* values are positive implying that these iso-surfaces moves towards the reactants, and its value, on average, is higher than the laminar flame velocity. This deviation from unity could be due to the preferential diffusion effect. Furthermore, results show that the $S_{d,r}^*$ ($S_{d,n}^*$) are positive (negative) within the reaction zone layer. A similar observation was previously reported in the literature, see e.g. Ref. [47]. It should be added that the negative values for $S_{d,n}^*$ do not occur when conditioning the data near the preheat zone layer (not shown). In addition, the highest probability of $S_{d,t}^*$ is around zero for both turbulent test cases.

In addition, the joint probability density functions (JPDFs) of the density-weighted flame displacement speed with respect to the flame front curvature for both turbulent cases are also shown in Fig. 7. The density-weighted flame displacement speed has been normalized by the unstrained premixed laminar burning velocity, and the flame front curvature has been normalized by the laminar thermal flame thickness. Results show that S_d^* is negatively correlated with the flame front curvature, which is in agreement with previous studies, see e.g., Echekki and Chen [5] for 2-D DNS with detailed chemistry, or Chakraborty and Cant [8] for 3-D DNS using simple chemistry. Furthermore, increasing the turbulence intensity results in generating the flame front with smaller radii, i.e., larger flame front curvature, and the variation of S_d^* promotes significantly. As mentioned earlier, Chakraborty et al. [9] assessed the performance of different extrapolation relations connecting the density-weighted flame displacement speed to the flame front curvature and flame stretch rate using 3-D DNS with detailed chemistry for thermo-diffusively neutral flames. They showed that S_d^* has a negative correlation with the flame front curvature. It should be emphasized that the observed trend in Fig. 7 shows that this negative correlation remains valid for thermo-diffusively unstable flames using detailed chemistry and mixture-averaged transport model as well.

3.4. Flame stretch factor

Assessing the validity of Damköhler's first hypothesis is of a crucial importance for novel fuel blends such as ammonia/hydrogen/air flames. As mentioned earlier, Damköhler [13] hypothesized that the ratio of the turbulent burning velocity to the unstrained premixed laminar burning velocity S_T/S_L^0 is equal to the ratio of the wrinkled flame surface area to the unwrinkled flame surface area A_T/A_L. This means that the local flamelet velocity S_L' is equal to the unstrained premixed laminar burning velocity S_L^0. To examine the validity of this hypothesis, the flame stretch factor I_0 could be used as follows [48]:

$$I_0 = \frac{S_T/S_L^0}{A_T/A_L},$$

(3)

where $S_{\mathrm{T}} = \int_V \dot{\omega}\, \mathrm{d}V / \rho_0 A_{\mathrm{L}}$ and $A_{\mathrm{T}} = \int |\overline{\nabla c}|\, dV$ are the turbulent burning velocity and the wrinkled flame surface area, respectively. The unwrinkled flame surface area A_{L} is the cross sectional area normal to the direction of mean flame propagation. It should be noted that the Damköhler's first hypothesis is valid when the flame stretch factor value is equal to unity.
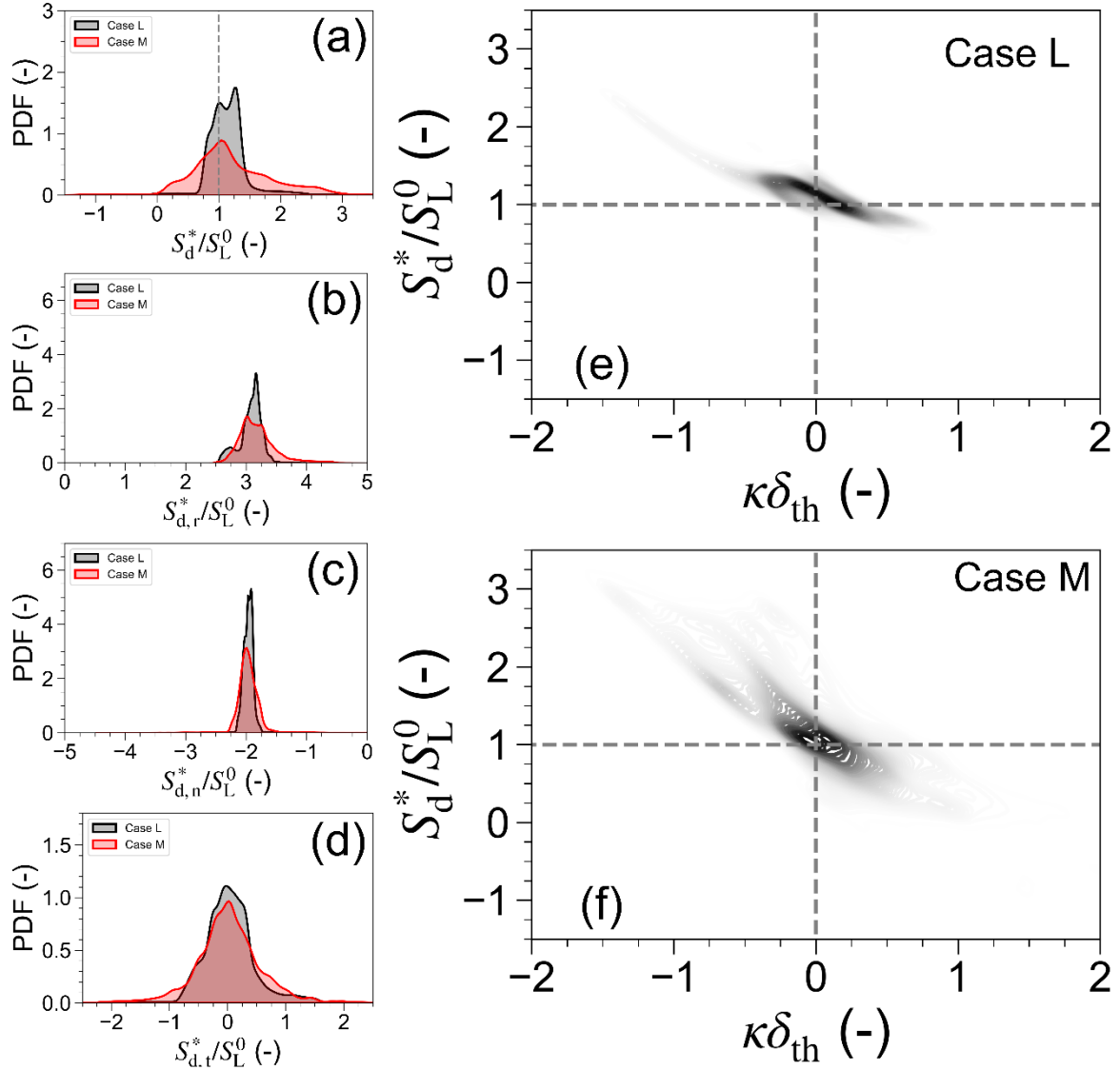
Fig. 7. (a-d) Probability density functions (PDFs) of the density-weighted flame displacement speed and its components for cases L and M. (e-f) The density-weighted flame displacement speed with respect to the flame front curvature for cases L and M. All statistics are conditioned at $c = 0.8$. The flame displacement speed and its components have been normalized by the unstrained premixed laminar burning velocity, and the flame front curvature has been normalized by the thermal flame thickness

Table 2 shows the values of the ratio of the turbulent to the laminar burning velocity, the ratio of the wrinkled to the unwrinkled flame surface area, and the flame stretch factor. Results show that the turbulent burning velocity and the wrinkled flame surface area increases about 35% with increasing the Karlovitz number. This could be due to the enhancement of flame surface area due to the turbulent structures. A similar observation was previously reported in numerous works in the literature, see, e.g., Han and Huh [14], Nivarti and Cant [15], and Song et al. [6]. Furthermore, it is shown that the flame stretch factor values are higher than the unity value for both test cases indicating that the mean flamelet consumption velocity is higher than the unstrained premixed laminar burning velocity for ammonia/hydrogen/air flames. This suggests that the Damköhler's first hypothesis is not valid for these test cases. A similar observation was previously reported in the literature for thermo-diffusively unstable flames based on 3-D DNS with simple chemistry, see, e.g., Han and Huh [14], and Chakraborty et al. [18]. It should be mentioned that increasing the turbulence intensity does not have any effect on the flame stretch factor values for the cases studied herein.

It should be noted that the local flamelet burning velocity is dependent on the local equivalence ratio across the flame brush [27, 49]. The local equivalence ratio ϕ is evaluated as $0.5(Z_F/Z_O)$, where Z_F and Z_O are evaluated as $3X_{NH_3} + 2X_{H_2} + X_H + X_{OH} + X_{HO_2} + 2X_{H_2O_2} + 2X_{H_2O}$ and $2X_{O_2} + X_{H_2O} + X_O + X_{OH} + 2X_{HO_2} + 2X_{H_2O_2} + X_{NO}$, respectively, where X_j corresponds to the mole fraction of species j.

Table 2. Ratio of the turbulent burning velocity to the laminar burning velocity, ratio of the wrinkled flame surface area to the unwrinkled flame surface area, and the flame stretch factor values.

Case	S_T/S_L^0	A_T/A_L	I_0
L	1.444	1.333	1.083
M	2.271	2.097	1.083

The variation of the local equivalence ratio with respect to the progress variable for the turbulent cases as well as the reference laminar flame are shown in Fig. 8(a-b). The dashed line corresponds to the local equivalence ratio for the laminar flame, and the solid line shows the mean value of the local equivalence ratio for the turbulent conditions. The local equivalence ratio is equal to the global equivalence ratio of unity on the unburned and burned regions, and it decreases from unity value across the flame brush. It could be seen that the mean local equivalence ratio values deviate from its laminar counterparts for the turbulent cases, and it promotes slightly with increasing the Karlovitz number. This deviation could be attributed to the enhancement of molecular/atomic hydrogen mass fractions due to the turbulent mixing and preferential diffusion effect, and it could be the underlying reason why the flame stretch factor differs from the unity value. It should be emphasized that the local equivalence ratio varies under curved flame fronts, and understanding its behavior is of a great interest since the local flamelet burning velocity is then affected under curved regions. Figure 8(c-d) shows the joint probability density functions (JPDFs) of the local equivalence ratio with respect to the normalized flame front curvature for both turbulent cases. In this Figure, the flame front curvature has been normalized with the thermal flame thickness of the reference laminar flame. It should be noted that the data are sampled at the reaction zone layer, i.e., $c = 0.8$. Results show the positive correlation between the JPDF of the local equivalence ratio and the flame front curvature. Furthermore, increasing the Karlovitz number results the JPDF to become wider. To unlock the underlying mechanism behind the positive correlation between the local equivalence ratio and the flame front curvature, it is required to investigate the molecular diffusion terms in the transport equation for a species mass fraction. The molecular diffusion flux could be written as follows [29]:

$$\nabla.(\rho D_m \nabla Y_m) = n_m.\nabla(\rho D_m n_m.\nabla Y_m) - \rho D_m |\nabla Y_m| \nabla.n_m, \tag{4}$$

where D_m is the diffusivity of species m evaluated by $D_m = (1 - Y_m)\left(\sum_{j \neq m} X_j / D_{mj}\right)^{-1}$, where Y_m is the mass fraction of species m, and D_{mj} is the binary diffusion coefficient between two species. Here n_m is the unit vector normal to an iso-surface evaluated as $n_m = -\nabla Y_m/|\nabla Y_m|$. The first (second) term on the r.h.s. of Eq. 4 is the normal diffusion (curvature) term. The diffusion flux terms for molecular hydrogen are shown in Figs. 9(a) and 9(c) for cases L and M, respectively. The diffusion fluxes have been normalized with the total diffusion flux values of the reference laminar flame, and the flame front curvature has been normalized with the laminar thermal flame thickness. Results show that for the molecular hydrogen, the curvature and total diffusion flux terms are positively correlated with the flame front curvature, and the normal diffusion term does not have any correlation with the flame front curvature. This shows that the molecular hydrogen diffuses strongly into the positively curved zones from the reactants. It should be noted that the positive correlation between the total diffusion flux term of molecular hydrogen with the flame front curvature could result in having higher molecular hydrogen concentration on positively curved regions (not shown for brevity). This could then explain the trend observed in Fig. 8(c-d). In addition, the curvature and total diffusion flux terms are negatively correlated with the flame front curvature for the atomic hydrogen, while the normal diffusion flux term is not dependent on the flame front curvature (Figs. 9(b) and 9(d)). This shows the enhanced diffusion of the atomic hydrogen to the unburned zone when the flame front is concave towards the reactants. A similar trend was observed very recently by Lee et al. [29] and Rieth et al. [30] for lean premixed turbulent hydrogen/air flames

(located within the thin reaction zones regime) and preheated ammonia/hydrogen/nitrogen/air flames (located within the broken reaction zone regime), respectively.
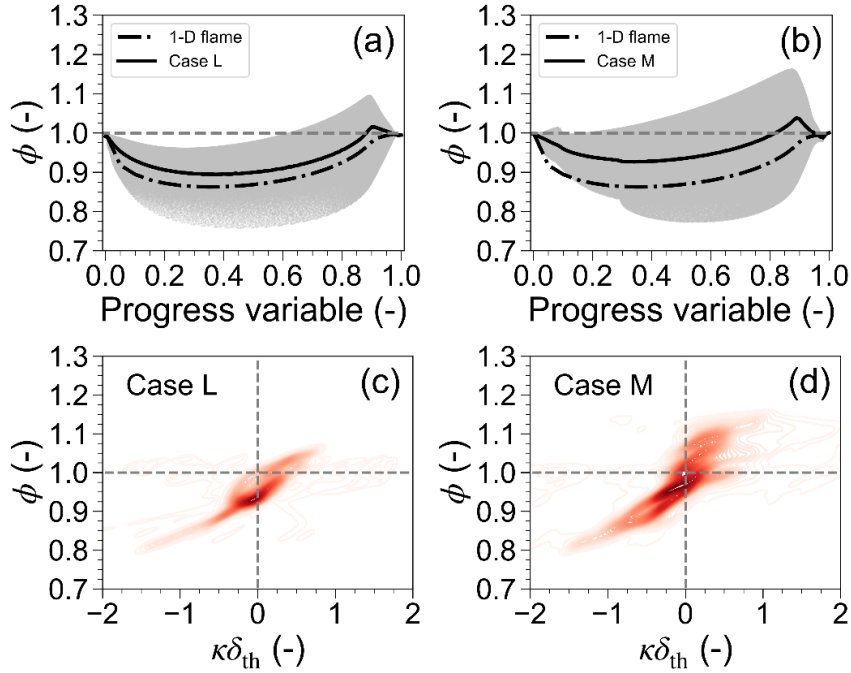
Fig. 8. Local equivalence ratio with respect to the progress variable for (a) case L, and (b) case M. The scatter data and the solid lines are for the turbulent cases, and the dashed lines are for the laminar case. JPDF of the local equivalence ratio with respect to the normalized flame front curvature. The data are conditioned at $c = 0.8$, and the flame front curvature has been normalized by the laminar thermal flame thickness
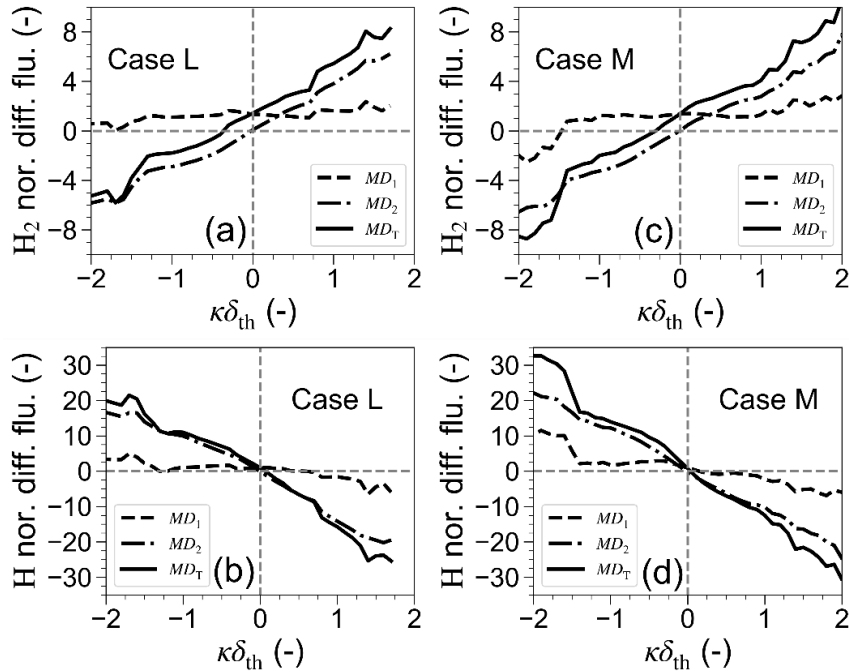
Fig. 9. Diffusion flux terms of molecular hydrogen for (a) case L, and (c) case M, and atomic hydrogen for (b) case L, and (d) case M with respect to the normalized flame front curvature. The fluxes have been normalized by the corresponding values obtained from the reference laminar flame, and the flame front curvature has been normalized by the thermal flame thickness. The normal, curvature, and total diffusion terms are denoted as MD_1, MD_2, and MD_T. The data are conditioned at $c = 0.8$
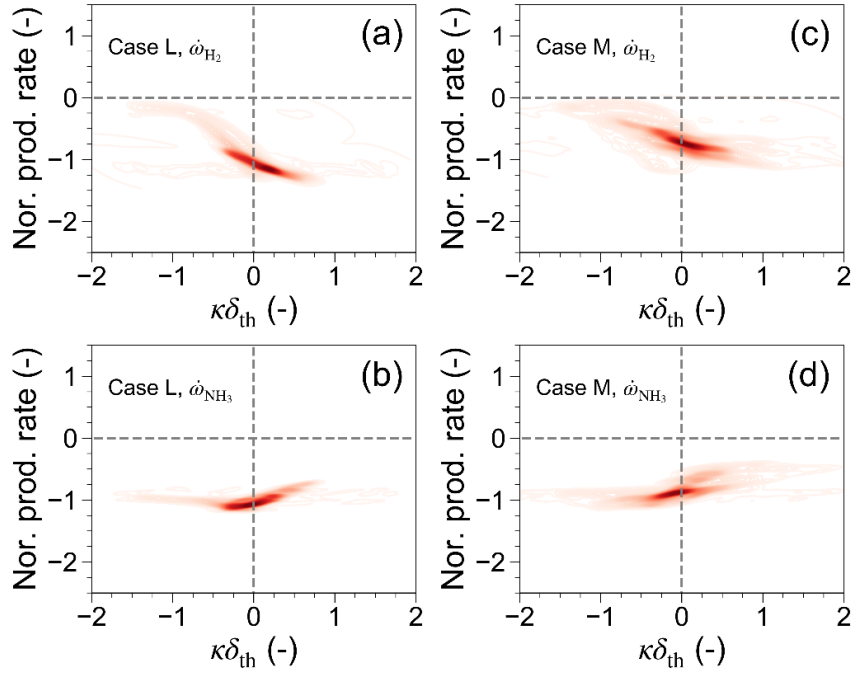
Fig. 10. Production rates of hydrogen and ammonia for (a)-(b) case L, and (c)-(d) case M with respect to the normalized flame front curvature, respectively. The production rates have been normalized by the corresponding values obtained from the reference laminar flame, and the flame front curvature has been normalized by the thermal flame thickness. The data are conditioned at $c = 0.8$

It should be noted that the production rates of molecular hydrogen and ammonia with respect to the flame front curvature are shown in Fig. 10 for both turbulent test cases. The production rates have been normalized with the corresponding values obtained from the reference laminar flame, and the laminar thermal flame thickness has been used to normalize the flame front curvature. The negative (positive) sign of the net production rate implies that the species is consumed (produced). Results show negative correlation of hydrogen production rate with the flame front curvature for both cases, and the absolute values of production rate are higher under positively curved regions compared to the corresponding values under negatively curved zones. Therefore, the hydrogen consumption rate is enhanced under positively curved regions. However, the net production rate of ammonia is not dependent on the flame front curvature. It could be concluded from Figs. 8-10 that the preferential diffusion of molecular hydrogen results in enhanced fuel consumption rate and local equivalence ratio on positively curved regions for the test cases studied in this work. This observation is in line with previous studies showing the enhanced burning rate/fuel consumption rate based on 2-D/3-D DNS using simple/detailed chemistry, see, e.g., Rutland and Trouvé [23, 24], Haworth and Poinsot [25], Day et al. [27], Aspden [28], Lee et al. [29], and Rieth et al. [30].

4. Concluding remarks

The open-source CFD toolbox OpenFOAM was utilized to perform quasi-DNS of premixed turbulent ammonia/hydrogen/air flames with detailed chemistry and mixture-averaged transport model. The blending ratio indicating the amount of hydrogen concentration in the pure ammonia was equal to 0.4. The non-dimensional turbulence intensity was varied from 4 to 10, and the non-dimensional integral length scale was fixed to 3.5. Therefore, the turbulent Karlovitz number was varied from 4.28 to 16.90 indicating that all the test conditions are located within the thin reaction zones combustion regime. The chemical kinetic mechanism developed by Stagni consisting of 31 species and 203 reactions was used, and the recently developed open-source dynamic load balancing model (DLBFoam) was utilized to overcome the computational load imbalance between processors. These simulations should be considered as large-scale simulations in the OpenFOAM framework, and they are completely enabled by the recent DLBFoam package. The main findings are summarized as follows:

1. Under the turbulent conditions, the conditional mean profiles of NH_3 and H_2O were relatively identical to their counterpart profiles of the reference laminar flame, while the conditional mean

profiles of H_2 and H deviated from their reference laminar flame due to the preferential diffusion effect and the turbulent mixing.

2. The averaged value of the density-weighted flame displacement speed was higher than the unstrained premixed laminar burning velocity across the flame brush. Therefore, the flame elements, on average, propagate faster than the unstrained premixed laminar flame.

3. The probability density function of the density-weighted flame displacement speed and its components became wider with increasing the Karlovitz number. The reaction (normal diffusion) component of the density-weighted flame displacement speed was positive (negative) within the reaction zone layer, and the most probable value of the tangential diffusion component was around zero. In addition, the density-weighted flame displacement speed is negatively correlated with the flame front curvature.

4. The turbulent burning velocity and the wrinkled flame surface area increased about 35% with increasing the Karlovitz number from 4.28 to 16.90. In addition, the flame stretch factor was higher than unity indicating that the Damköhler's first hypothesis is not valid for the test cases studied in this work.

5. The mean value of the local equivalence ratio across the flame brush under turbulent conditions deviated from its laminar counterpart. Furthermore, the local equivalence ratio was shown to be positively correlated with the flame front curvature, and this observation could be attributed to the preferential diffusion of hydrogen.

6. The diffusion flux of molecular hydrogen was positively correlated with the flame front curvature indicating the enhanced preferential diffusion of molecular hydrogen from the reactants into the positively curved zones. Furthermore, the diffusion flux of atomic hydrogen was shown to be negatively correlated with the flame front curvature, and it was shown to be intensified towards the unburned region under negatively curved regions.

7. Results show that the net production rate of the molecular hydrogen was strongly dependent on the flame front curvature, and the absolute value of the net production rate of hydrogen was higher under positively curved regions. This could be reflected as the enhanced burning rate under positively curved regions.

Acknowledgments

References

1. Valera-Medina, A., Xiao, H., Owen-Jones, M., David, W. I. F., Bowen, P. J., *Ammonia for power.* Prog. Energy Combust. Sci., 2018. **69**: p. 63-102.
2. Kobayashi, H., Hayakawa, A., Somarathne, K. D. K. A., Okafor, E. C., *Science and technology of ammonia combustion.* Proc. Combust. Inst., 2019. **37**(1): p. 109-133.
3. Hawkes, E.R., Chen, J. H. , *Comparison of direct numerical simulation of lean premixed methane–air flames with strained laminar flame calculations.* Combust. flame, 2006. **114**: p. 112–125.
4. Peters, N., Terhoeven, P., Chen, J. H., Echekki, T., *Statistics of flame displacement speeds from computations of 2-D unsteady methane-air flames.* Proc. Combust. Inst., 1998. **27**: p. 833-839.
5. Echekki, T., Chen, J. H., *Analysis of the contribution of curvature to premixed flame propagation.* Combust. flame, 1999. **118**: p. 308-311.
6. Song. W., H.P., F. E., Tingas, E., Im, H. G., *Statistics of local and global flame speed and structure for highly turbulent H₂/air premixed flames.* Combust. flame, 2021. **232**: p. 111523.
7. Chakraborty, N., Cant, R. S., *Unsteady effects of strain rate and curvature on turbulent premixed flames in an inflow–outflow configuration.* Combust. flame, 2004. **134**: p. 129-147.
8. Chakraborty, N., Cant, R. S., *Influence of Lewis number on curvature effects in turbulent premixed flame propagation in the thin reaction zones regime.* Phys. Fluids, 2005. **17**: p. 105105.
9. Chakraborty, N., Herbert, A., Ahmed, U., Im, H. G., Klein, M., *Assessment of extrapolation relations of displacement speed for detailed chemistry direct numerical simulation database of statistically planar turbulent premixed flames.* Flow Turbul. Combust., 2022. **108**: p. 489–507.
10. Bilger, R.W., Pope, S. B., Bray, K. N. C., Driscoll, J. F., *Paradigms in turbulent combustion research.* Proc. Combust. Inst., 2005. **30**: p. 21-42.

11.   Lipatnikov, A.N., Chomiak, H., *Turbulent flame speed and thickness: phenomenology, evaluation, and application in multi-dimensional simulations.* Proc. Combust. Inst., 2002. **28**: p. 1-74.
12.   Gülder, Ö.L., *Turbulent premixed flame propagation models for different combustion regimes.* Proc. Combust. Inst., 1991. **23**: p. 743-750.
13.   Damköhler, G., *Der Einfluß der Turbulenz auf die Flammengeschwindigkeit in Gasgemischen.* Z. Electrochem., 1940. **46**: p. 601-652.
14.   Han, I., Huh, K. Y., *Roles of displacement speed on evolution of flame surface density for different turbulent intensities and Lewis numbers in turbulent premixed combustion.* Combust. flame, 2008. **152**: p. 194-205.
15.   Nivarti, G., Cant, S., *Direct numerical simulation of the bending effect in turbulent premixed flames.* Proc. Combust. Inst., 2017. **36**: p. 1903-1910.
16.   Klein, M., Herbert, A., Kosaka, H., Böhm, B., Dreizler, A., Chakraborty, N., Papapostolou, V., Im, H. G., Hasslberger, J., *Evaluation of flame area based on detailed chemistry DNS of premixed turbulent hydrogen-air flames in different regimes of combustion.* Flow Turbl. Combust., 2020. **104**: p. 403-419.
17.   Brearley, P., Ahmed, U., Chakraborty, N., *The relation between flame surface area and turbulent burning velocity in statistically planar turbulent statified flames.* Phys. Fluids, 2020. **32**: p. 125111.
18.   Chakraborty, N., Wang, L., Klein, M., *Streamline segment statistics of premixed flames with nonunity Lewis numbers.* Phys. Rev. E, 2014. **89**: p. 033015.
19.   Gülder, Ö.L., *Contribution of small scale turbulence to burning velocity of flamelets in the thin reaction zone regime.* Proc. Combust. Inst., 2007. **31**: p. 1369–1375.
20.   Tamadonfar, P., Gülder, Ö. L., *Effects of mixture composition and turbulence intensity on flame front structure and burning velocities of premixed turbulent hydrocarbon/air Bunsen flames.* Combust. flame, 2015. **162**(12): p. 4417-4441.
21.   Chakraborty, N., Alwazzan, D., Klein, M., Cant, R. S., *On the validity of Damköhler's first hypothesis in turbulent Bunsen burner flames: A computational analysis.* Proc. Combust. Inst., 2019. **37**: p. 2231-2239.
22.   Lipatnikov, A.N., Chomiak, H., *Molecular transport effects on turbulent flame propagation and structure.* Prog. Energy Combust. Sci., 2005. **31**: p. 1-73.
23.   Rutland, C.J., Trouvé, A., *Pre-mixed flame simulations for non-unity Lewis numbers.* 1990, Center for Turbulence Research, Proceeding of the Summer Program: NASA Ames/Stanford University. p. 299-309.
24.   Rutland, C.J., Trouvé, A., *Direct simulations of premixed turbulent flames with nonunity Lewis numbers.* Combust. flame, 1993. **94**: p. 41-57.
25.   Haworth, D.C., Poinsot, T. J., *Numerical simulations of Lewis number effects in turbulent premixed flames.* J. Fluid Mech., 1992. **244**: p. 405-436.
26.   Bell, J.B., Cheng, R. K., Day, M. S., Shepherd, I. G., *Numerical simulation of Lewis number effects on lean premixed turbulent flames.* Proc. Combust. Inst., 2007. **31**: p. 1309-1317.
27.   Day, M., Bell, J., Bremer, P. T., Pascucci, V., Beckner, V., Lijewski, M., *Turbulence effects on cellular burning structures in lean premixed hydrogen flames.* Combust. flame, 2009. **156**: p. 1035-1045.
28.   Aspden, A.J., *A numerical study of diffusive effects in turbulent lean premixed hydrogen flames.* Proc. Combust. Inst., 2017. **36**: p. 1997-2004.
29.   Lee, H.C., Dai, P., Wan, M., Lipatnikov, A. N., *Influence of molecular transport on burning rate and conditioned species concentrations in highly turbulent premixed flames.* J. Fluid Mech., 2021. **928**: p. A5.
30.   Rieth, M., Gruber, A., Williams, F. A., Chen, J. H., *Enhanced burning rates in hydrogen-enriched turbulent premixed flames by diffusion of molecular and atomic hydrogen.* Combust. flame, 2021: p. 111740.
31.   Saad, T., Cline, D., Stoll, R., Sutherland, J. C., *Scalable tools for generating synthetic isotropic turbulence with arbitrary spectra.* AIAA J., 2017. **55**: p. 327-331.
32.   Kobayashi, H., Otawara, Y., Wang, J., Matsuno, F., Ogami, Y., Okuyama, M., Kudo, T., Kadowaki, S., *Turbulent premixed flame characteristics of a $CO/H_2/O_2$ mixture highly diluted with CO_2 in a high-pressure environment.* Proc. Combust. Inst., 2013. **34**: p. 1437-1445.
33.   Borghi, R., *On the structure and morphology of turbulent premixed flames*, in *Recent Advances in the Aerospace Sciences*, C. Casci, Bruno, C., Editor. 1985, Springer: Boston.
34.   Peters, N., *The turbulent burning velocity for large-scale and small-scale turbulence.* J. Fluid Mech., 1999. **384**: p. 107-132.
35.   Weller, H.G., Tabor, G., Jasak, H., Fureby, C., *A tensorial approach to computational continuum mechanics using object-oriented techniques.* Comput. Phys., 1998. **12**: p. 620-631.
36.   Stagni, A., Cavallotti, C., Arunthanayothin, S., Song, Y., Herbinet, O., Battin-Leclerc, F., Faravelli, T., *An experimental, theoretical and kinetic-modeling study of the gas-phase oxidation of ammonia.* React. Chem. Eng., 2020. **5**: p. 696-711.

37. Rocha, R.C., Zhong, S., Xu, L. and Bai, X. S., Costa, M., Cai, X., Kim, H., Brackmann, C., Li, Z., Aldén, M., *Structure and laminar flame speed of an ammonia/methane/Air premixed flame under varying pressure and equivalence ratio.* Energy Fuels, 2021. **35**: p. 7179-7192.

38. Niemeyer, K.E., Curtis, N. J., Sung, C. J., *pyJac: Analytical Jacobian generator for chemical kinetics.* Comput. Phys. Commun., 2017. **215**: p. 188-203.

39. Tekgül, B., Peltonen, P., Kahila, H., Kaario, O., Vuorinen, V., *DLBFoam: An open-source dynamic load balancing model for fast reacting flow simulations in OpenFOAM.* Comput. Phys. Commun., 2021. **267**: p. 108073.

40. Poinsot, T., Veynante, D., *Theoretical and Numerical Combustion.* Second ed. 2005: R.T. Edwards, Inc.

41. Dirscoll, J.F., Chen, J. H., Skiba, A. W., Carter, C. D., Hawkes, E. R., Wang, H., *Premixed flames subjected to extreme turbulence: Some questions and recent answers.* Prog. Energy Combust. Sci., 2020. **76**: p. 100802.

42. Aspden, A.J., Day, M. S., Bell, J. B., *Lewis number effects in distributed flames.* Proc. Combust. Inst., 2011. **33**: p. 1473-1480.

43. Aspden, A.J., Day, M. S., Bell, J. B., *Turbulence–flame interactions in lean premixed hydrogen: transition to the distributed burning regime.* J. Fluid Mech., 2011. **680**: p. 287-320.

44. Veynante, D., Vervisch, L., *Turbulent combustion modeling.* Prog. Energy Combust. Sci., 2002. **28**: p. 193-266.

45. Giannakopoulos, G.K., Gatzoulis, A., Frouzakis, C. E., Matalon, M., Tomboulides, A. G., *Consistent definitions of ''Flame Displacement Speed'' and ''Markstein Length'' for premixed flame propagation.* Combust. flame, 2015. **162**: p. 1249–1264.

46. Im, H.G., Chen, J. H., *Preferential diffusion effects on the burning rate of interacting turbulent premixed hydrogen-air flames.* Combust. flame, 2002. **131**: p. 246-258.

47. Dopazo, C., Cifuentes, L., Alwazzan, D., Chakraborty, N., *Influence of the Lewis number on effective strain rates in weakly turbulent premixed combustion.* Combust. Sci. Technol., 2018. **190**: p. 591-614.

48. Driscoll, J.F., *Turbulent premixed combustion: Flamelet structure and its effect on turbulent burning velocities.* Prog. Energy Combust. Sci., 2008. **34**: p. 91-134.

49. Netzer, C., Ahmed, A., Gruber, A., Løvås, T., *Curvature effects on NO formation in wrinkled laminar ammonia/hydrogen/nitrogen-air premixed flames.* Combust. flame, 2021. **232**: p. 111520.

Session S1.2 Ecofuels: Biofuels

Performance and Exhaust Emissions of a Diesel Engine Fueled with Pyrolytic Oil from Plastic Wastes

J. Tejada-Hernández, M. Carmona-Cabello, J. A. Serrano, S. Pinzi, M.-P. Dorado-Pérez

Dept. Physical Chemistry and Applied Thermodynamics, Universidad de Córdoba, Campus de Excelencia Internacional Agroalimentario, ceiA3, Córdoba, 14071, Spain

E-mail: pilar.dorado@uco.es
Telephone: +(34) 957218332

Abstract. The main objective of this study was to analyze some of the most harmful pollutant gases emitted by a diesel engine fueled with blends of non-recyclable plastic-based pyrolytic fuel (PPF) and ultralow-sulfur diesel fuel. Engine performance was also analyzed, monitoring brake-specific fuel consumption (BSFC) and brake-thermal efficiency (BTE). The test dynamometer was DYNAS3 LI 225 by Horiba (Kyoto, Japan) where 9 stationary tests were programed: low load (50 Nm) at 1400, 2000 and 2600 rpm, medium load (100 Nm) at 1400, 2000 and 2600 rpm and high load (150 Nm) at 1400, 2000 and 2600 rpm. The test bench includes a 190 hp Nissan-Renault twin-turbocharged direct-injection diesel engine. To measure gas emissions, a Horiba MEXA 7100D was used. PPF/diesel fuel blends at 10%, 20% and 30% v/v (P10, P20, P30) were used. Under low-speed conditions, CO emissions increased up to 30% when the blends were used. However, this increase was reduced to 10% when the speed increased from 1400 to 2600 rpm. It was also observed that the higher the load, the lower the CO emissions. In contrast, the higher the PPF content in the blends, the lower the NO_x emissions. At low engine speed, considering low and high load tests, the higher decrease was achieved (36% and 34%, respectively). This trend was repeated for middle speed, decreasing NO_x emissions around 32% for P30 blend. Considering BSFC, a slight reduction was observed with the addition of PPF, since the lower heating value of the pyrolytic fuel was slightly higher than that of diesel fuel. It may be concluded that the production and use of pyrolytic fuel from non-recyclable plastics is a viable option to solve the problem of plastic waste discharge in landfills and oceans.

Notation

BSFC	Brake specific fuel consumption.
BTE	Brake thermal efficiency.
CLD	Chemiluminescence detector.
DOC	Diesel oxidation catalyst
DPF	Diesel particulate filter
HHV	High heating value
LHV	Lower heating value
NDIR	Non-dispersive infrared detector
P10	Fuel/pyrolytic plastic oil blends at 10% v/v
P20	Fuel/pyrolytic plastic oil blends at 20% v/v
P30	Fuel/pyrolytic plastic oil blends at 30% v/v
PPF	Non-recyclable plastic-based pyrolytic fuel
ULSD	Ultra-low sulfur diesel fuel

1. Introduction

Since the 1950s, with the beginning of worldwide plastic production, a new era dawned. Due to its low weight, versatility, physicochemical properties and low production cost, plastic has a fundamental role in packaging, electronic equipment, automotive industry, and construction materials, replacing traditional resources (glass, metal and ceramics) [1]. In Europe, 50.7 million tons of plastic were consumed in 2019. As a result of this demand, 29.1 million tons of post-consumer waste were collected. Around 25% ended up in landfills without the possibility of recycling or being used for energy recovery [2].

Waste plastic management is one of the challenges that society faces today. Mechanical recycling is presented as the least polluting treatment. This process consists in griding the plastic waste to a new feedstock. A series of pre-treatments, such as sorting by color and plastic type, washing, etc. are necessary, which makes it only viable when the raw material is in perfect condition [3].

In Spain, mechanical recycling rate supposes 42% of total plastic waste treatment. However, 39% of post-consumer plastic waste ends up in landfills [2]. Therefore, to achieve the goal of zero discharges of plastic waste to landfills, the rate of energy recovery needs to be increased. The easiest way to obtain energy from plastic waste is by direct incineration, using the waste as fuel in a boiler, to produce electricity. However, the net impact of incineration on climate change is around 60% higher than other energy recovery processes, such as pyrolysis [4]. Pyrolysis consists on thermal degradation (400-600 °C) of plastic waste under an inert atmosphere. The obtained products are composed of a gaseous fraction composed by hydrogen and light hydrocarbons (C1-C5), a liquid fraction with similar properties to traditional fossil diesel fuel (C5-C20) and char, as solid residue [5-6].

One of the main economic activities in Andalusia derives from greenhouse agriculture. More precisely, in Almería area, there are more than 40,000 ha covered with plastic, which produce a large amount of plastic waste with a high degree of soiling [7]. Pyrolysis is shown as a way to recycle this plastic, thus improving this productive process, within the framework of circular economy.

91.2% and 96.3%, considering light and heavy commercial vehicles, respectively, are powered by diesel engines [8]. Therefore, the production of non-recyclable plastic-based pyrolytic fuel (PPF) for compression ignition engines (CIE), would help to achieve the targets set in the European Strategy for Circular Economy [9] while providing a solution to the problem of fuel prices and energy shortages derived from the use of fossil fuels.

Another challenge for the European Government is to reduce pollutant and greenhouse gas emissions in the transport sector [9-10]. For this reason, several research works have studied the performance and emissions of PPF blends in conventional diesel engines. So, waste management would not lead to an increase in air pollution.

To evaluate the effect of PPF and fuel blends, most authors performed stationary tests on a single-cylinder diesel engine. Kumar et al. [12] found a reduction in brake thermal efficiency (BTE) and CO emissions, while brake specific fuel consumption (BSFC) and NO_x emissions increased. In contrast, other researchers observed a decrease in BSFC and an increase in BTE, as a result of the higher PPF high heating value (HHV) compared to conventional diesel fuel [12-13]. The pyrolytic fuel tested by Churkunti et al. [15] showed higher cetane number and kinematic viscosity, which led to the reduction of the most efficient combustion phase (premixed combustion). However, the large pyrolytic fuel lower heating value (LHV) caused BSFC to remain constant. In terms of pollutant emissions, a reduction in NO_x, CO and hydrocarbon (HC) associated with the decrease in aromatic content and the change to saturated bonds was found.

Testing PPF/diesel fuel blends in a four-cylinder diesel engine, Tomar et al. [16] observed a 9.6% and 30% decrease in BSFC and pollutant emissions (NO_x, CO), respectively, and 12.2% increase in the BTE. On the other hand, Kalargaris et al. [17] found that a higher PPF content at lower loads increased ignition delay. As consequence, BTE slightly decreased, but NO_x emissions dramatically increased.

The main objective of this study is to analyze, for the first time, the feasibility of the use of pyrolytic fuel derived from non-recyclable agricultural plastic waste (from Andalusian greenhouses) in conventional 4-cylinder diesel engines. For this purpose, physicochemical properties, most harmful emissions and engine performance of the pyrolytic fuel, straight and blended with diesel fuel, are measured and compared with those derived from the use of straight diesel fuel.

2. Materials and methods

2.1 Fuels

Commercial automotive ultra-low sulfur diesel fuel (ULSD) including 7% biodiesel was acquired from E.S. La Lancha (Cordoba, Spain). Pyrolytic plastic waste fuel (PPF) was supplied by Hintes Oil Europa (Almería, Spain). As pyrolytic fuel come directly from the production plant without any post-treatment, a 50 μm filtration was performed to remove all solid contaminants. Also, 5% v/v was removed from both the head and distillation tail to eliminate part of the volatile and heavy substances that the gross fuel might contain.

Analysis of physicochemical properties was carried out according to the test methods specified in EN 590 standard or its equivalent in American standard (ASTM). To measure the density of fuels at

15°C, the hydrometer method described in ISO 3675 was followed. As the ambient temperature differed by more than 2°C from the test temperature, a cold bath to keep the test conditions was needed. 0.700-0.800 and 0.800-0.900 g/ml Proton (Barcelona, Spain) hydrometers were introduced in a 100 ml measuring cylinder, which guaranteed a free height of at least 25 mm when the hydrometer was floating at the time of measurement.

Kinematic viscosity (ν) was measured with Proton (Barcelona, Spain) Cannon-Fenske viscosimeter. The Series 75 viscometer complied with the test conditions described in ISO 3104, where the test time was set to at least 200 s. According to ASTM D86 standard (test method equivalent to ISO 3405, included in EN 590), the distillation curve was provided. Atmospheric distillation tester OptiDist by PAC (Houston, EEUU) was the equipment used. Cetane index (CI) was calculated by the four-variable equation, Eq. (1), described in ISO 4264. The temperatures of 10, 50 and 90% v/v distillation recovery and the density were the four variables necessary to get the CI.

$$IC = 45.2 + 0.0892T_{10N} + (0.0131 + 0.901B)T_{50N} + (0.0523 - 0.42B)T_{90N} + \cdots \qquad (1)$$
$$\cdots + 0.00049(T_{10N}^2 - T_{90N}^2) + 107B + 60B^2$$

$T_{10N}=$ (Temperature (°C) of 10% v/v distillation recovery) $- 215$
$T_{50N}=$ (Temperature (°C) of 50% v/v distillation recovery) $- 260$
$T_{90N}=$ (Temperature (°C) of 90% v/v distillation recovery) $- 310$
$B=$ $e^{(-0.0035D_N)-1}$
$D_N=$ D-850
$D=$ Density (kg/m^3) at 15°C

To determine of carbon, hydrogen, nitrogen and sulfur (CHNS) content of the tested fuel and blends, the Elemental Analyzer 3100 by EuroVector (Pavia, Italy) was used. This equipment achieves the quantitative analysis of one milligram sample in three steps: in the first step, controlled combustion of the sample at a high temperature takes place, synchronizing the sample admission with the pressurized oxygen injection. Subsequently, combustion gases are separated in the gas-chromatograph (GC) column using helium as carrier gas. Finally, a thermal conductivity detector (TCD) was used to determine the quantity of each combustion product and, consequently, CHNS content.

HCP 842 CFPP+ Herzog by PAC (Houston, EEUU) was the automatic cold filter plugging point analyzer chosen to measure the low temperature operability of fuels, as described UNE-EN 116. IKA C 200 (Staufen, Germany) calorimeter was used to determine HHV, following the measurement method described in ASTM D240. Flash point is an essential property related to shipping and storage of flammable substances. Setaflash Serie 3 by Stanhope-Seta (Chertsey, UK) was the closed cup flash point tester used to determine the flash point for the tested blends, following ISO 2719. The content of highly volatile compounds within PPF resulted in a flash point below ambient temperature. To get a flash point value under the ambient temperature, the fuel and test cup needed to be cooled.

2.2 Experimental setup

To carry out the analysis in DYNAS3 LI 225 test stand by Horiba (Kyoto Japan), nine stationary test points, described in Table 1, were selected. As shown in Table 1, for each engine load (low, medium and high), three engine speed values were selected. Selected engine speed values were in the range between 1400 and 2600 rpm. These points have been chosen covering the most used area of the engine map in both intraurban and extra-urban conditions of a light-duty vehicle. Also, as high load rises temperature inside the cylinder, thus decreasing the PPF influence on performance and emissions, it was important to test the influence over engine speed.

Before starting the measurement of each test point, the engine was warmed up for 20 min, at 2000 rpm and 150 Nm, followed by 20 min of stabilization. Engine speed and load demanded at each point were programmed. Finally, both pollutant gas emissions and fuel consumption were measured in three 300 s stages.

The test bench was equipped whit a four-cylinder, direct-injection, twin-turbocharged diesel engine, provided by Nissan- Renault (Boulogne-Billancourt, France). Its main specifications are described in Table 2.

MEXA 7100D analyzer, by Horiba (Kyoto, Japan) was used to measure the pollutant gas emissions (NO_x and CO). The measuring probe was connected to the exhaust pipe, after the diesel particulate filter (DPF) and diesel oxidation catalytist (DOC). To ensure that hydrocarbons from the exhaust gas were in the gaseous phase at the time of measurement, to transport the sample from the exhaust pipe to MEXA 7100D, a 191°C heated line was used. This instrument is composed of two measuring units. The first unit measures NO_x emissions using a chemiluminescence detector (CLD) which allows

a very accurate NO measurement. In addition, it incorporates a reduction catalyst that converts NO_2 to NO, so that all the NO_x can be detected by CLD. CO is measured by a non-dispersive infrared detector (NDIR), in the second measuring unit. The analyzer is composed of two chambers into which the sample of exhaust gas and the reference gas, respectively, are introduced. An infrared light beam is passed through these two chambers, which causes the expansion of the gases due to light absorption. Measuring the pressure increase in the sample chamber with a pressure transducer and comparing it with the pressure increase in the reference gas chamber, the concentration of CO in the exhaust gas is determined.

Table 1. Test matrix

Test number	Engine speed (rpm)	Torque (N·m)
1	1400	50
2	1400	100
3	1400	150
4	2000	50
5	2000	100
6	2000	150
7	2600	50
8	2600	100
9	2600	150

Table 2. Diesel engine specification

Model	YS23DDTT
Motor type	4-strokes, 4-cylinder, twin-turbocharged intercooled
Fuel injection system	Common rail 2000bar Piezo Injector
Cylinder	4
Bore	85.0 mm
Stroke	103.3 mm
Conrod length	154.5 mm
Displacement	2298 cm^3
Compression ratio	15.4
Maximum power	140 kW at 3750 rpm
Maximum torque	450 Nm at 1500-2500 rpm

FQ-3100DP by Horiba (Kyoto, Japan) was used to measure fuel consumption, ensuring a constant pressure difference (5 bar) between fuel tank outlet and high-pressure pump inlet. For this purpose, a very accurate differential pressure sensor measures the pressure difference and acts on the servomotor coupled to the gear pump, to keep the set point signal. By measuring the speed of the servomotor, the fuel flow rate consumed by the engine is determined.

3. Results and discussions

3.1 Physicochemical properties of the tested blends

As shown in Table 3, most significant physicochemical properties of the proposed blends are within the limits set by the Automotive fuel-Diesel-Requirements and EN 590. However, plastic waste pyrolytic oil properties are highly dependent on the starting feedstock.

Distillation curve allows determining the heavy and light compounds present in fuel from its boiling point. Depending on the distillation curve shape, engine performance and emissions can be predicted. A high percentage of distillation recovery at low temperature is associated with the presence of volatile compounds that can lead to vapor lock problems and poor fuel atomization. [18]. On the other hand, a high boiling temperature at the end of the curve shows the presence of heavy compounds that result in smoke formation and incomplete combustion, decreasing engine performance [19]. As shown in Table 3, all blends fulfill the limit of standard for which 65% of the distillate recovered must be achieved above 250°C. Although the light fraction (up to 20% of distillation recovery) has a low impact on the engine performance, the light hydrocarbon content is crucial for other fuel properties, such as kinematic

viscosity, density, flash point or cold filter plugging point. Regarding standard limitations for the heavier fraction, all blends have a temperature below 350°C for 85% of the distillation recovery; however, the boiling temperature of 95% of distillation recovery is slightly above 360°C. So, to use the pyrolytic fuel blends in automotive diesel engines, 10% of the PPF distillation tail of the PPF needs to be removed to achieve a final boiling point similar to that of diesel fuel.

Density has great importance in the correct operation of the injection system. The injector design is optimized for the strict density limits of automotive diesel fuel (820-845 kg/m^3), so a higher fuel density results in the formation of larger droplets during the injection process, worsening engine performance and emissions [20]. The loop control of the injection system is programmed on a volumetric basis, so if a fuel with a density lower than the minimum standard threshold, as pure pyrolytic fuel (P100=783 kg/m^3) is introduced, the air/fuel ratio demanded by the engine would not be achieved [21]. In addition, fuel is also sold by volume, so fuels with a lower density provide a lower amount of energy for the same price. As shown in Table 3, P30 blend density (821 kg/m^3) is close to the lower limit, so the correct injection system operation is not ensured with a content of PPF above 30% v/v in the blend.

The flash point is very important to ensure the safe transport and storage of liquid fuels. This property measures the lowest temperature at which the vapors of a fuel sample are ignited when an ignition source is approached, under certain test conditions [22]. Results for the three pyrolytic blends (Table 3) show that the higher PPF content in the blend, the lower the flash point. This is due to the high percentage of light hydrocarbon and volatile compounds contained in the waste plastic pyrolytic oils. Results are in agreement with the low values obtained for kinematic viscosity, initial boiling point and density observed for the pyrolytic blend. To improve flash point and increase it above the lower standard threshold, it is necessary to remove the light hydrocarbon content by distillation, keeping only the fraction that has a boiling range equal to that of diesel fuel (160-350°C) [20-21].

As density, kinematic viscosity is a key property for the proper performance of the injection system. Fuels with a high kinematic viscosity provide a higher resistance to flow through the injection system pipes. As a result, a higher pumping power is required, thus reducing the pumping system life-time and decreasing engine performance [25]. On the other hand, lower viscosity fuels can lead to a fuel spill in the fuel pump or fuel injectors, resulting in injector jetting and poor homogenization of the fuel in the combustion chamber [26]. As can be seen in Table 3, all kinematic viscosity values of PPF/diesel blends are within the standard limits. Straight pyrolytic oil (P100) has a kinematic viscosity below the lower standard limit, so the higher the percentage of PPF in the blend, the lower the kinematic viscosity. It is known that kinematic viscosity increases with chain length in aliphatic hydrocarbons [27]. Thus, reduction in kinematic viscosity is associated with the presence of light (short chain) hydrocarbons in PPF. In this case, as all blends complied with the regulation limit, there was no need to improve the kinematic viscosity of pyrolytic fuel. But if PPF content in the blend were to be increased, the light compounds would have to be removed by distillation.

Cold filter plugging point (CFPP) determines the lowest temperature at which proper fuel flow through diesel engine fuel filters is maintained. As shown in distillation curve and CFPP values (Table 3), the presence of heavy hydrocarbons in pyrolytic fuel limits CFPP value of blends. Despite this limitation, all blends comply with CFPP standard for diesel fuel under winter conditions. The presence of a high percentage of light hydrocarbons in the pyrolytic fuel compensates the effect of heavy hydrocarbons, thus keeping CFPP at optimum levels.

One of the most important parameters in CIE combustion control is the ignition delay time (time between injection and auto-ignition points). Fuels with a higher autoignition tendency will result in a shorter ignition delay and, consequently, better combustion performance. The property that measures fuel autoignition tendency and therefore its performance during combustion is cetane number [28]. Given the difficulty to experimentally determine cetane number, cetane index is used to give an approximation of the combustion performance of the tested fuels. According to results described in Table 3, the higher the PPF content in the blend, the improved the combustion performance. Other authors who studied distilled plastic waste oil observed this trend [28-29], but most works with plastic waste oil showed an increase in cetane number, as a result of the high heavy hydrocarbon content [31].

HHV is also closely related to combustion process behavior. HHV refers to the amount of energy per unit mass contained in fuel. Considering experimental HHV values, lower heating values (LHV) are calculated using equation (2).

$$LHV = HHV - (h_{fg} \, m_{H_2O})/m_{C_xH_y} \qquad (2)$$

Where, h_{fg} is the heat of vaporization, $m_{C_xH_y}$ is the fuel mass and m_{H_2O} is the mass of the water produced during combustion, calculated from the stoichiometric equation of the combustion reaction (equation 3).

$$C_xH_y + \left(x + \frac{y}{4}\right)(O_2 + 3.76\,N_2) \rightarrow x\,CO_2 + \frac{y}{2}\,H_2O + \left(x + \frac{y}{4}\right)3.76N_2 \qquad (3)$$
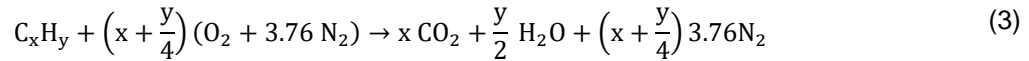
Where, x and y are the number of the atoms of carbon and hydrogen present in the fuel, obtained from the elemental analysis from Table 3.

Thus, a fuel with a higher LHV will have a higher potential to release heat during the complete combustion, which will result in lower BSFC. As can be seen in Table 3, LHV has no limits in EN 590. LHV of pyrolytic fuel is slightly higher than that of diesel fuel, so a slight reduction in BSFC is expected for the blends with a higher percentage of PPF.

From elemental analysis shown in Table 3, it can be deduced that the addition of PPF to diesel fuel leads to a slight reduction in C/H ratio.

Table 3. Properties of tested straight fuels and blends (experimental value)

Properties		ULSD	P10	P20	P30	P100	EN 590 limits
Density at 15°C (kg/m³):	EN 3675	835	828	824	821	783	820 - 845
Kinematic viscosity at 40°C (mm²/s):	EN 3104	3.43	3.05	3.03	2.76	1.99	2.00 - 4.5
Flash point (°C):	EN 2719	58.5	37	36.7	29.7	10	> 55
CFPP (°C): EN 116		-16	-11	-11	-11	-10	
-Winter (31 Oct-31 Mar)							< -10
-Sumer (1 Apr- 30 Sept)							< 0
Distillation temperature (°C):	ASTM D 86						
Initial boiling point		157.3	144.2	121.8	108.2	66.7	
10% of recovery		199.8	189.3	174.3	170.2	135.3	
20% of recovery		220.5	215.7	204.3	195.8	151.5	
30% of recovery		244.7	241.1	233.2	225.8	165.6	
50% of recovery		279	278	274	270.6	231	
65% of recovery		301.1	301.5	299	297.9	276.6	>250
85% of recovery		332	335.8	335.6	336	348.3	<350
90% of recovery		347.5	348.4	349.1	341.6	367.9	
95% of recovery		354.1	366.4	368.6	369.6	380.7	<360
Cetane Index:	EN 4264	53.5	55.7	55.9	56.1	58.1	> 46
LHV (kJ/kg)		45368	45569	45778	45921	47040	
Nitrogen content (%)		0.082	0.077	0.072	0.067	0.033	
Carbon content (%)		85.25	85.14	85.04	84.93	84.19	
Hydrogen content (%)		13.98	14.02	14.06	14.10	14.38	

ULSD ultra-low sulfur diesel fuel; P10, P20, P30 fuel/pyrolytic plastic oil blends at 10%, 20% and 30% v/v; P100 pure pyrolytic plastic oil; *CFPP* cold filter plugging point; *HHV* high heating value

3.2 Pollutant emissions

3.2.1 CO emissions

CO emissions from diesel engines is mainly related to incomplete combustion, lack of oxygen and a poor homogenization of the fuel during the combustion process. Due to the toxicity, the study of the effect of ULSD/PPF blends on the CO emission is needed [32].

Fig. 1 shows a decrease of about 50% in CO emissions when going from low (50 Nm) to medium (100 Nm) load at any engine speed and fuel. CO emission reduction from middle (100 Nm) to high load is not as large, with values slightly lower than the values for medium load. As can be seen in Fig. 1 (A) and (B), CO emissions are directly proportional to PPF content in ULSD/PPF blends, when the engine is running at low to middle engine speed (1400-2000 rpm). It can be found a 30% increase in CO emissions when P30 blend is introduced into the engine, for the operating points where the combustion process is more inefficient (points no. 1 and 4). For high engine speed, Fig. 1 (C), the increase in CO emissions of ULSD with respect to the blend with the highest ratio of PPF (P30) is reduced to 10%.

Poor homogenization of the pyrolytic blends during the injection, due to the reduction of kinematic viscosity [26], can lead to a high fuel/oxygen ratio in certain regions of combustion chamber. Oxygen in these areas is insufficient for oxidation of all hydrocarbons, producing an increased in CO emissions. Also, presence of heavy hydrocarbons in PPF blends observed in distillation curve (Table 3) can be related to CO increase. Mangesh et al. [33] observed that the latent heat of vaporization of C20

hydrocarbons was twice that of C10, as well as that of C30 with respect to C20. Because of the increase in the fuel latent heat of vaporization when heavy hydrocarbons are injected, fuel droplets may appear in cold regions causing an increase in CO emissions. Despite the observed increase in CO emissions with pyrolytic fuel blends, CO is not among the most dangerous diesel engine pollutants. Oxidation catalytic converters (DOC) installed in all vehicles convert most CO into CO_2.
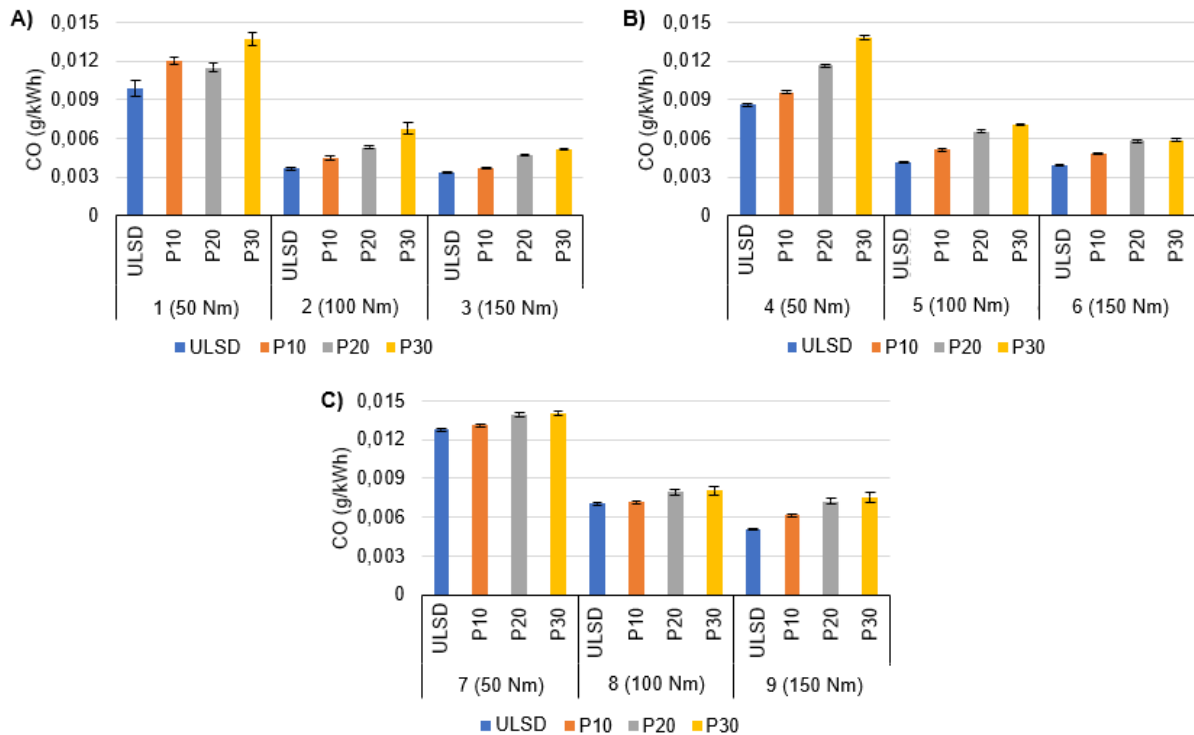
Fig. 1. CO emissions for 9 stationary test points: A) low, middle and high load at low engine speed (1400 rpm); B) low, middle and high load at middle engine speed (2000 rpm); C) low, middle and high load at high engine speed (2600 rpm)
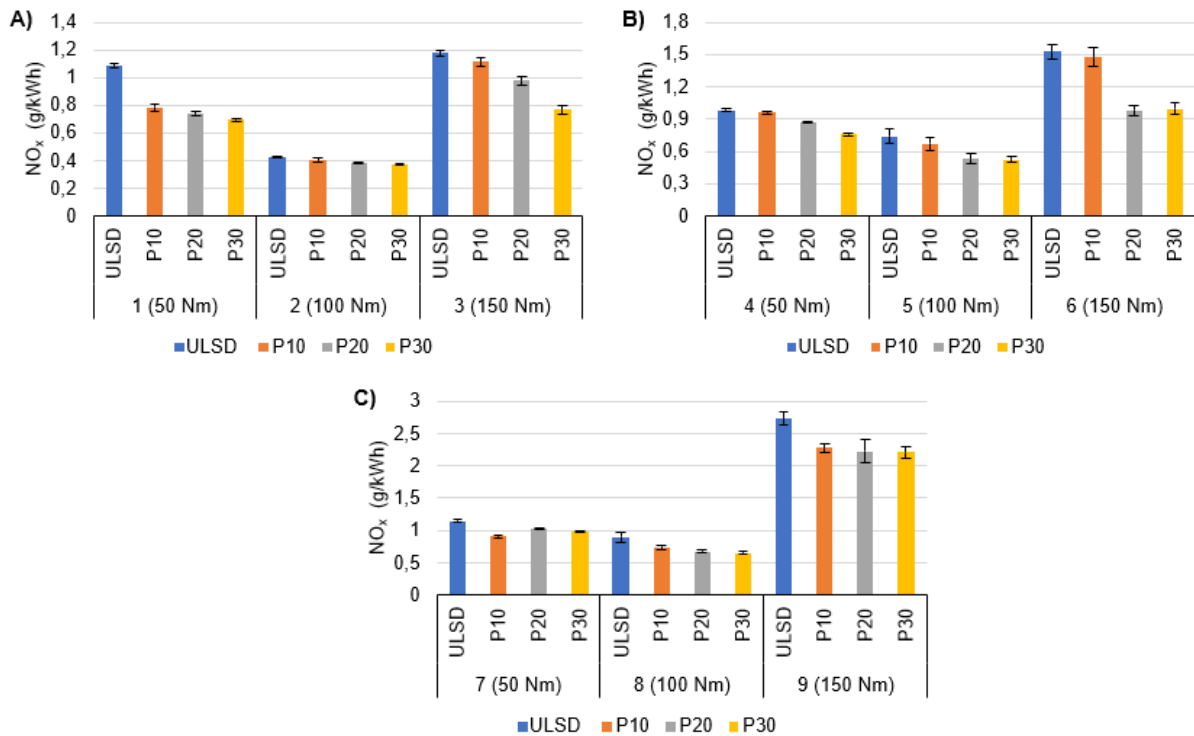
3.2.2 NO_x emissions

With the implementation of higher Euro emission standards, exhaust emission limits for diesel vehicles have been reduced to minimum values. However, periodic technical inspection, which is responsible for verifying compliance with limits, has focused only on black smoke. This has resulted in NOx being the most harmful diesel engine exhaust pollutant today [34]. Due to the dangerousness of this pollutant gas, in this work, the effect of pyrolytic fuels has been studied.

As can be seen in Fig. 2, the higher the pyrolytic fuel content (for any engine speed and load regime), the lower the NO_x emissions. In the case of low-speed tests (Fig. 2 A), the combustion of P30 blend results in a reduction, compared to ULSD, of 34% and 36%, at low and high load, respectively. However, at middle-load, this reduction is only of 13%. The same trend is observed in middle and high engine speed (Fig. 2 B-C). Although at 2000 rpm (Fig. 2 B) there is no difference between ULSD and P10 blend, P30 blend reduces NO_x emissions by about 32% at middle-speed.

An unusual trend in NO_x emissions with respect to load has been observed. For all tested engine speeds, NO_x emissions decrease from low to medium load, and increase again from medium to high load. This behavior can be explained by the Zeldovich formation mechanism, which exponentially relates the NO_x formation to the combustion chamber temperature [35]. As it has been observed by other authors [15, 35], the increase in NO_x emissions at low load is due to the increase in air/fuel ratio. A higher presence of oxygen atoms promote oxidation which increase temperature during combustion.

As shown in Table 3, the cetane index increases with the content of PPF in the blends. As a consequence, the ignition delay time decreases and the heat release rate during the premixed combustion stage is reduced. These changes result in a reduction of the peak temperature in the combustion chamber, thus reducing NO_x formation. Reduction of NO_x emissions and its relationship with the increase of blend cetane number is in agreement with several previous works [28-29, 37].

Fig. 2. NOx emissions for 9 stationary test points: A) low, middle and high load at low engine speed (1400 rpm); B) low, middle and high load at middle engine speed (2000 rpm); C) low middle and high load at high engine speed (2600 rpm)

3.3 Engine performance

3.3.1 Brake Specific Fuel Consumption

BSFC determines the ratio between mass fuel consumption per unit time and brake power [38]. The specific fuel consumption was measured by the FQ-3100 DP by Horiba (Kyoto Japan) and the effective brake power was measured from the power demanded to test stand DYNAS3 LI 225 by Horiba (Kyoto Japan). Ananthakumar et al. [39] showed that the higher the fuel kinematic viscosity, the higher the BSFC, due to poor mixture atomization. Fuel density is also related to BSFC since lower density fuels introduce a lower fuel mass for the same volume [21]. As can be observed in Table 3, both kinematic viscosity and density decrease with the increase in PPF ratio in the blends.

Fig. 3. shows the relationship between BSFC and load for three constant engine speeds. At low engine speed (Fig. 3 A), a progressive reduction in BSFC is seen for all fuels, indicating that the engine becomes more efficient with increasing load. Reduction in BSFC from low to medium load increases for middle and high-speed tests. In these cases, instead of a progressive reduction in load, the specific fuel consumption is reduced by about 25%, remaining constant for tests no. 6 and 9, at high load.

As shown in Fig. 3, BSFC values are similar for ULSD and PPF/ULSD blends at almost all test points. Only at low speed, a slight trend of BSFC reduction is observed with increasing PPF content in the blends. Panda et al. [30] also showed a BSFC reduction when fueled a diesel engine with PPF from waste polypropylene. The observed BSFC reduction is due to the increase in HHV of PPF/ULSD blends.

Fig. 3. Brake Specific Fuel Consumption for 9 stationary test points: A) low, middle and high load at low engine speed (1400 rpm); B) low, middle and high load at middle engine speed (2000 rpm); C) low middle and high load at high engine speed (2600 rpm)
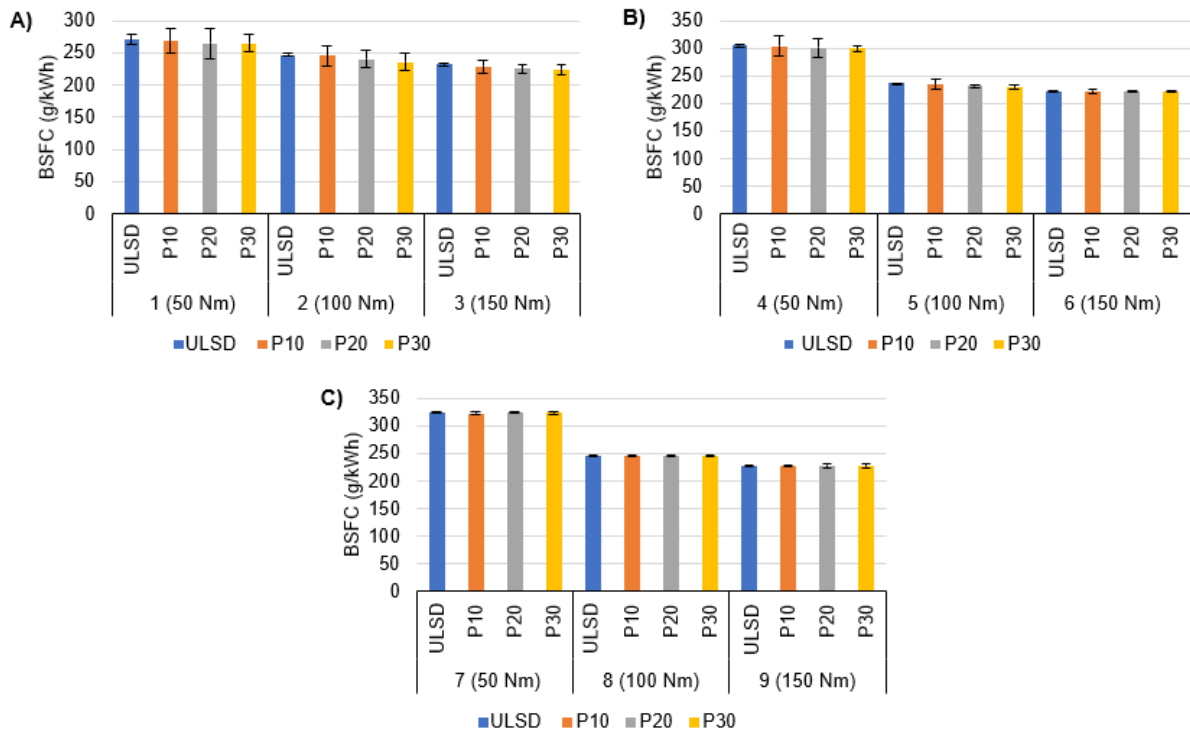
3.3.2 Brake Thermal Efficiency

As expected, Fig. 4 shows an increase in brake thermal efficiency with increasing load for all fuels, inversely proportional to BSFC (Fig. 3). This is because that increasing load, the ratio of mechanical/pumping losses to effective fuel energy decreases [40].

As in Fig. 3, no trend is observed that relates BTE to the pyrolytic fuel content, since both heating value and BSFC are similar for all fuels and test points, respectively. The fact that BTE of ULSD/PPF blends and ULSD is constant regardless PPF content ensures the correct engine performance.
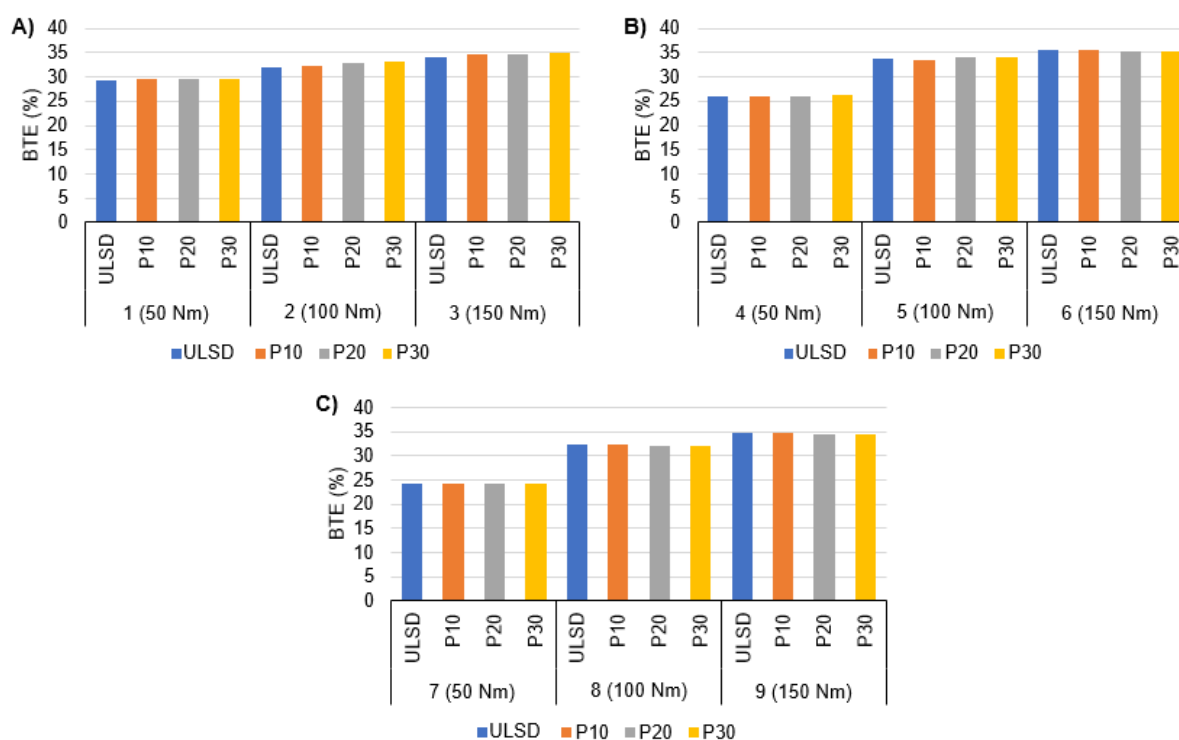
Fig. 4. Brake Thermal Efficiency for 9 stationary test points: A) low, middle and high load at low engine speed (1400 rpm); B) low, middle and high load at middle engine speed (2000 rpm); C) low middle and high load at high engine speed (2600 rpm)

Conclusions

The feasibility of using pyrolyzed plastic residues (from Andalusian greenhouses) as diesel engine fuel has been demonstrated. In fact, this study has shown that the development of alternative fuels from non-recyclable plastic waste (PPF) is a solution to the problem of plastic waste management and plastic waste discharge to oceans. PPF/diesel fuel blends have physicochemical properties like those of straight diesel fuel, besides improved cetane index and increased lower heating value. As a consequence, the higher the PPF content in the blend, the lower the NO_x emissions; engine performance being slightly improved. Thus, a new concept of circular economy for plastics has been proposed.

Acknowledgments

References

[1]   M. Kedzierski, D. Frère, G. Le Maguer, and S. Bruzaud, "Why is there plastic packaging in the natural environment? Understanding the roots of our individual plastic waste management behaviours," *Sci. Total Environ.*, vol. 740, p. 139985, 2020, doi: 10.1016/j.scitotenv.2020.139985.

[2]   PlasticEurope-Association of Plastics Manufactures, "Plastics – the Facts 2020," 2020. [Online]. Available: https://www.plasticseurope.org/en/resources/publications/4312-plastics-facts-2020.

[3]   K. Ragaert, L. Delva, and K. Van Geem, "Mechanical and chemical recycling of solid plastic waste," *Waste Manag.*, vol. 69, pp. 24–58, 2017, doi: 10.1016/j.wasman.2017.07.044.

[4]   H. Jeswani *et al.*, "Life cycle environmental impacts of chemical recycling via pyrolysis of mixed

plastic waste in comparison with mechanical recycling and energy recovery," *Sci. Total Environ.*, vol. 769, 2021, doi: 10.1016/j.scitotenv.2020.144483.

[5]   M. Zeller, N. Netsch, F. Richter, H. Leibold, and D. Stapf, "Chemical Recycling of Mixed Plastic Wastes by Pyrolysis-Pilot Scale Investigations," doi: 10.1002/cite.202100102.

[6]   M. Solis and S. Silveira, "Technologies for chemical recycling of household plastics – A technical review and TRL assessment," *Waste Manag.*, vol. 105, pp. 128–138, Mar. 2020, doi: 10.1016/J.WASMAN.2020.01.038.

[7]   Asociación española de industriales del plástico, "La plasticultura en España," 2018.

[8]   European Automobile Manufacturers' Association (ACEA), "Vehicles in Use Europe 2022," 2022.

[9]   A. European Commission, "A European strategy for plastics in a circular economy," *Communication from the Commission to the European Parliament*. The Council, The European Economic and Social Committee and The Committee af …, 2018.

[10]   European Parliament and Council of the European Union, "Regulation (EU) No. 2019/631 of the European Parliament and of the Council of 17 April 2019 Setting CO2 Emission Performance Standards for NewPassenger Cars and for New Light Commercial Vehicles, and Repealing Regulations (EC) No. 443/2009 and(EU) No. 510/2011. 2011." https://eur-lex.europa.eu/legal-content/EN/TXT/?uri=CELEX%3A32019R0631 (accessed May 03, 2022).

[11]   T. Haas and H. Sander, "Decarbonizing Transport in the European Union: Emission Performance Standards and the Perspectives for a European Green Deal," doi: 10.3390/su12208381.

[12]   Manoj Kumar and J. M. Mallikarjuna, "Experimental Investigation on a Compression Ignition Engine with Blends of Plastic Oil and Diesel as Fuel," in *Lecture Notes in Mechanical Engineering*, Springer Science and Business Media Deutschland GmbH, 2021, pp. 85–97.

[13]   Sunaryo, P. A. Sesotyo, E. Saputra, and A. P. Sasmito, "Performance and fuel consumption of diesel engine fueled by diesel fuel and waste plastic oil blends: An experimental investigation," *Automot. Exp.*, vol. 4, no. 1, pp. 20–26, 2021, doi: 10.31603/ae.3692.

[14]   A. Ramanathan and A. Santhoshkumar, "Feasibility analysis of pyrolysis waste engine oil in CRDI diesel engine," *Energy Procedia*, vol. 158, pp. 755–760, 2019, doi: 10.1016/j.egypro.2019.01.201.

[15]   P. R. Churkunti, J. Mattson, C. Depcik, and G. Devlin, "Combustion analysis of pyrolysis end of life plastic fuel blended with ultra low sulfur diesel," *Fuel Process. Technol.*, vol. 142, pp. 212–218, 2016, doi: 10.1016/j.fuproc.2015.10.021.

[16]   M. Tomar, A. Jain, P. C. Pujari, H. Dewal, and N. Kumar, "Potentials of waste plastic pyrolysis oil as an extender fuel for diesel engine," *Arab. J. Geosci.*, vol. 13, no. 13, 2020, doi: 10.1007/s12517-020-05574-6.

[17]   I. Kalargaris, G. Tian, and S. Gu, "Combustion, performance and emission analysis of a DI diesel engine using plastic pyrolysis oil," *Fuel Process. Technol.*, vol. 157, pp. 108–115, Mar. 2017, doi: 10.1016/j.fuproc.2016.11.016.

[18]   R. Maceiras, V. Alfonsín, and F. J. Morales, "Recycling of waste engine oil for diesel production," *Waste Manag.*, vol. 60, pp. 351–356, Feb. 2017, doi: 10.1016/J.WASMAN.2016.08.009.

[19]   H. Aydin and C. Ilkiliç, "Optimization of fuel production from waste vehicle tires by pyrolysis and resembling to diesel fuel by various desulfurization methods," *Fuel*, vol. 102, pp. 605–612, Dec. 2012, doi: 10.1016/J.FUEL.2012.06.067.

[20]   M. A. Mujtaba *et al.*, "Development of empirical correlations for density and viscosity estimation of ternary biodiesel blends," *Renew. Energy*, vol. 179, pp. 1447–1457, Dec. 2021, doi: 10.1016/J.RENENE.2021.07.121.

[21]   A. Gala, M. Guerrero, B. Guirao, M. E. Domine, and J. M. Serra, "Characterization and Distillation of Pyrolysis Liquids Coming from Polyolefins Segregated of MSW for Their Use as Automotive Diesel Fuel," *Energy and Fuels*, vol. 34, no. 5, pp. 5969–5982, May 2020, doi: 10.1021/ACS.ENERGYFUELS.0C00403/SUPPL_FILE/EF0C00403_SI_002.PDF.

[22]   F. ; Murphy, G. ; Devlin, K. Mcdonnell, F. Murphy, G. Devlin, and K. Mcdonnell, "The Evaluation of Flash Point and Cold Filter Plugging Point with Blends of Diesel and Cyn-Diesel Pyrolysis Fuel for Automotive Engines," doi: 10.2174/1876973X01306010001.

[23]   M. Mikulski, M. Ambrosewicz-Walacik, J. Hunicz, and S. Nitkiewicz, "Combustion engine applications of waste tyre pyrolytic oil," *Prog. Energy Combust. Sci.*, vol. 85, p. 100915, 2021, doi: 10.1016/j.pecs.2021.100915.

[24]   M. Ambrosewicz-Walacik, S. Wierzbicki, M. Mikulski, and T. S. Podciborski, "Ternary fuel mixture of diesel, rapeseed oil and tyre pyrolytic oil suitable for modern CRDI engines," *Transport*, 2018.

[25]   M. Gülüm and A. Bilgin, "Measurements and empirical correlations in predicting biodiesel-diesel blends' viscosity and density," *Fuel*, vol. 199, pp. 567–577, Jul. 2017, doi: 10.1016/J.FUEL.2017.03.001.

12   J. Tejada-Hernández, M. Carmona-Cabello, J. A. Serrano, S. Pinzi, M. P. Dorado

[26]   H. G. Aleme, R. A. Assunção, M. M. O. Carvalho, and P. J. S. Barbeira, "Determination of specific gravity and kinematic viscosity of diesel using distillation curves and multivariate calibration," *Fuel Process. Technol.*, vol. 102, pp. 90–95, Oct. 2012, doi: 10.1016/J.FUPROC.2012.04.016.

[27]   G. Knothe and K. R. Steidley, "Kinematic viscosity of biodiesel fuel components and related compounds. Influence of compound structure and comparison to petrodiesel fuel components," *Fuel*, vol. 84, no. 9, pp. 1059–1065, Jun. 2005, doi: 10.1016/J.FUEL.2005.01.016.

[28]   K. Min *et al.*, "Autoignition of varied cetane number fuels at low temperatures," *Proc. Combust. Inst.*, vol. 37, no. 4, pp. 5003–5011, Jan. 2019, doi: 10.1016/J.PROCI.2018.05.078.

[29]   S. Kumar, R. Prakash, S. Murugan, and R. K. Singh, "Performance and emission analysis of blends of waste plastic oil obtained by catalytic pyrolysis of waste HDPE with diesel in a CI engine," *Energy Convers. Manag.*, vol. 74, pp. 323–331, Oct. 2013, doi: 10.1016/J.ENCONMAN.2013.05.028.

[30]   A. K. Panda, S. Murugan, and R. K. Singh, "Performance and emission characteristics of diesel fuel produced from waste plastic oil obtained by catalytic pyrolysis of waste polypropylene," *Energy Sources, Part A Recover. Util. Enviromental Eff.*, vol. 38, no. 4, pp. 568–576, Feb. 2016, doi: 10.1080/15567036.2013.800924.

[31]   M. Mikulski, M. Ambrosewicz-Walacik, J. Hunicz, and S. Nitkiewicz, "Combustion engine applications of waste tyre pyrolytic oil," *Prog. Energy Combust. Sci.*, vol. 85, p. 100915, Jul. 2021, doi: 10.1016/j.pecs.2021.100915.

[32]   M. Mani, C. Subash, and G. Nagarajan, "Performance, emission and combustion characteristics of a DI diesel engine using waste plastic oil," *Appl. Therm. Eng.*, vol. 29, no. 13, pp. 2738–2744, Sep. 2009, doi: 10.1016/J.APPLTHERMALENG.2009.01.007.

[33]   V. L. Mangesh, S. Padmanabhan, P. Tamizhdurai, and A. Ramesh, "Experimental investigation to identify the type of waste plastic pyrolysis oil suitable for conversion to diesel engine fuel," *J. Clean. Prod.*, vol. 246, p. 119066, 2020, doi: 10.1016/j.jclepro.2019.119066.

[34]   N. Hooftman, M. Messagie, J. Van Mierlo, and T. Coosemans, "A review of the European passenger car regulations – Real driving emissions vs local air quality," *Renew. Sustain. Energy Rev.*, vol. 86, no. March 2017, pp. 1–21, 2018, doi: 10.1016/j.rser.2018.01.012.

[35]   J. B. Heywood, *Internal Combustion Engine Fundamentals*, 2nd editio. New York: McGraw-Hill Education, 2018.

[36]   M. Tomar, A. Jain, P. C. Pujari, H. Dewal, and N. Kumar, "Potentials of waste plastic pyrolysis oil as an extender fuel for diesel engine," *Arab. J. Geosci.*, vol. 13, no. 13, p. 504, 2020, doi: 10.1007/s12517-020-05574-6.

[37]   Y. Kidoguchi, C. Yang, R. Kato, and K. Miwa, "Effects of fuel cetane number and aromatics on combustion process and emissions of a direct-injection diesel engine," *JSAE Rev.*, vol. 21, no. 4, pp. 469–475, Oct. 2000, doi: 10.1016/S0389-4304(00)00075-8.

[38]   D. Saha, A. Sinha, and B. Roy, "Critical insights into the effects of plastic pyrolysis oil on emission and performance characteristics of CI engine," doi: 10.1007/s11356-021-14919-x/Published.

[39]   S. Ananthakumar, · S Jayabal, and · P Thirumal, "Investigation on performance, emission and combustion characteristics of variable compression engine fuelled with diesel, waste plastics oil blends," *J. Brazilian Soc. Mech. Sci. Eng.*, vol. 39, pp. 19–28, 2017, doi: 10.1007/s40430-016-0518-6.

[40]   J. D. Martínez, J. Rodríguez-Fernández, J. Sánchez-Valdepeñas, R. Murillo, and T. García, "Performance and emissions of an automotive diesel engine using a tire pyrolysis liquid blend," *Fuel*, vol. 115, pp. 490–499, 2014, doi: 10.1016/j.fuel.2013.07.051.

Design, Vehicle Testing and Life Cycle Analysis (LCA) of 100% Renewable EN228 Gasoline Formulation

C. Esarte[1], M.D. Cárdenas[1], R. Miravalles[1], J. Aríztegui[1]

[1] Repsol Technology Lab, C/Agustín de Betancourt s/n, 28935, Móstoles (Madrid), SPAIN

E-mail: claudia.esarte@repsol.com
Telephone: +(34) 616371662

Abstract.

In order to accomplish the commitments reached in the Paris Agreement, the European Union has recently published a package of proposals, known as Fit for 55. Among the different proposed measurements, the target of renewable energy in the transport sector has become more challenging by aiming to achieve the 13% GHG (Greenhouse Gases) intensity reduction target for energy in transport. This objective means that it will be necessary to increase the content in renewable components in liquid fuels in the coming years.

In this context, a 100% renewable gasoline fulfilling EN228 has been formulated. The designed gasoline has been adapted to meet Worldwide Fuel Charter requirements.

The performance of the designed gasoline, in comparison to a commercial one, has been tested in a light-duty Euro 6-b vehicle without GPF (Gasoline Particulate Filter) under the WLTC (Worldwide harmonized Light vehicles Test Cycles) cycle and full load acceleration cyles. From this testing, it has been demonstrated that the designed renewable gasoline presents a similar behavior to that of conventional gasoline. No significant differences were found regarding emissions, fuel consumption, spark timing or boost pressure, apart from higher particle emissions when using renewable gasoline, which was attributed to higher aromatic content and poorer volatility as compared to the conventional fuel. Nevertheless, it is supposed that last generation vehicles fitted with GPF will keep particle emissions bellow Euro limits.

Finally, a Life Cycle Analysis (LCA) has been performed to compare GHG emissions levels considering different scenarios. The comparison includes the LCA of an internal combustion engine vehicle (ICEV) using the designed renewable gasoline and conventional gasoline versus battery electric vehicles, considering the current energetic mix for electricity and 100% renewable electricity. On an LCA basis analysis, the use of the designed renewable gasoline in ICEV would lead to an important reduction on GHG emissions compared to the use of mineral fuels. This reduction is potentially higher than the reduction that could be achieved by a BEV using electricity produced under different European electric mix scenarios.

Notation

BEV   *Battery Electric Vehicle*
BtL   *Biomass to Liquid*
ETBE   *Ethyl Tert-Butyl Ether*
EtG   *Ethanol To Gasoline*
FAME   *Fatty Acid Methyl Esthers*
FFV   *Flexi-fuel Vehicles*
GHG   *Greenhouse Gases*
GPF   *Gasoline Particulate Filter*
HVO   *Hydrotreated Vegetable Oil*
ICEV   *Internal Combustion Engine Vehicle*
LCA   *Life Cycle Analysis*
MTBE   *Methyl Tert-Butyl Ether*
OBD   *On-board diagnostics*
RED   *Renewable Energy Directive*
RON   *Research Octane Number*
WLTC   *Worldwide harmonized Light vehicles Test Cycles*
WWFC   *Worldwide Fuel Charter*

1. Introduction

Climate change and the increase in global temperature are mainly attributed to the emission of greenhouse gases (GHG) derived from human activity. In this sense, the Paris Agreement reached in December 2015 at COP21 by the United Nations, established ambitious objectives aiming to stop these phenomena. The participant countries committed to keep the temperature 2ºC below global temperatures in the pre-industrial period and limit the increase to 1,5ºC above such levels.

According to the last data available, the transport sector was directly responsible for almost 25% of greenhouse effect emissions and for the consumption of more than 30% of final energy in the European Union. Within the transport sector, road transport accounts for almost 72% of these emissions due to the consumption of fossil fuels [1].

In this context, the European Commission has recently adopted a package of proposals, called "Fit for 55" to make the European Union's climate, energy, land use, transport and taxation policies fit for reducing net greenhouse gas emissions by at least 55% by 2030, compared to 1990 levels [2,3]. This EU new objectives scenario requires higher shares of renewable energy sources in an integrated energy system than the currently established. The present EU target of at least 32% renewable energy by 2030, set in the Renewable Energy Directive (REDII), is not sufficient and needs to be increased to 38-40%, according to the Climate Target Plan [4,5].

Within this framework, specific targets are proposed for renewable energy in different sectors, being the transport one of the main targets, given the difficulty to the decarbonize such sector. One of the proposals is to replace the 14% objective for renewable energy in transport in 2030 with a 13% GHG intensity reduction target for energy in transport. This change increases the ambition level of the transport target, considering that a greater amount of renewable fuel is needed to achieve a 1% GHG reduction than a 1% of energy [3]. Therefore, a higher amount of renewable fuels will have to be included in the gasoline and diesel blending pools to meet EU targets.

The integration of larger amounts of renewable fuels will not happen immediately, as their incorporation is limited by fuel quality legislation. In Europe, the use of renewable components in fuels is limited by existing regulations, EN228 and EN590 [6,7], for oxygenates in gasoline and FAME (Fatty Acid Methyl Esthers) in diesel, respectively. In the case of gasoline, there is a limitation on the incorporation of oxygenates, including methanol, ethanol, MTBE (Methyl Tert-Butyl Ether) or ETBE (Ethyl Tert-Butyl Ether), which can contribute to the renewable character of the final fuel. In addition, the oxygen content in gasoline is limited to 3,7%m/m, so the final amount of oxygenates that can be incorporated is also restricted by this limitation. In the case of diesel, FAME is limited to a maximum content of 7%v/v. Technical regulations do not limit any other type of biocomponent, nor the type of feedstock or process used to produce fuel biocomponents, being the only requirement that the final fuel meets the technical specification.

On the other hand, it is also important to consider that the availability of renewable fuels and components is currently limited, given that most of such fuels have not reached commercial scale of application due to the limitations in production or consumption processes and technologies. Alternative fuels can be produced from different raw materials and production processes, but they need to be produced through a sustainable and clean procedure, without additional emissions of carbon dioxide [8].

In the case of gasoline, the most used biocomponent is bioethanol, which can be produced from any biological feedstock that contains appreciable amounts of sugar such as starch or cellulose by conventional fermentation [9,10]. As previously mentioned, EN228 [6] limits the maximum content in ethanol to a maximum of 10%v/v; however, ethanol enriched mixtures such as E85 (85%v/v bioethanol/15% v/v conventional gasoline) can be used in cars with specially designed engines, designated as flexible-fuel vehicles (FFVs), which are not commonly used in Europe. E85 mixtures cannot be used in conventional vehicles because ethanol, especially in high concentration blends, can cause corrosion of some metallic components in tanks and deterioration of rubbers and plastics used in internal combustion engines [11]. Bioethanol via catalytic reaction with isobutylene is also used to produce ETBE to be incorporated in gasoline formulation, given that it can be incorporated in higher percentages (up to 22%v/v). Other renewable oxygenated compounds, which content in gasoline is limited by EN228, have been also studied as potential blending components for gasoline, mainly biobutanol [12], but also some research has been done in biomethanol, biopropanol and even bioglycerol [13-15].

The production of other renewable hydrocarbons in the distillation range of gasoline is under development and the best pathway(s) to produce such hydrocarbons is still to be defined.

Methanol-to-Gasoline processes using renewable methanol can be used to the production of renewable gasoline. This process consists of the dehydration of the molecule of methanol to olefins, which are considered the first hydrocarbon products to be further converted to aromatics through dehydrogenation [16]. This type of technology has reached commercial plant scale [17,18].

Similarly, renewable gasoline can be produced from the Ethanol-to-Gasoline (EtG) process. The ethanol molecule is dehydrated to ethylene, followed by oligomerization and dehydrogenation [16,19,20]. The synthetic hydrocarbons obtained in this process meet the quality requirements for motor fuels used in vehicles with spark-ignition engines, from a chemical point of view [20]. Production plant has been built and is operated with an approximate production capacity of 22.500 t/year of synthetic fuels from ethanol, being the main product a mixture of synthetic hydrocarbons in the distillation range of liquid fuels intended for spark-ignition combustion engines [21].

Some processes intended to produce diesel-like renewable fuels, which already count on a technical specification in EN15940 [22], may also lead to products in the distillation range of the gasoline. This is the case of the hydrogenation of vegetable oils, waste and residue fat fractions and non-food grade vegetable oil fractions [23-25]; the BtL (Biomass to Liquid) routes that combine different feedstocks, such as microalgae, tall oil pitch, agricultural/forestry residues or non-food energy crops, with diverse conversion technologies [26,27]; and synthetic fuels, such as e-fuels, that result from the combination of renewable hydrogen and captured CO_2 [28,29]. However, the gasoline-like products from these processes present high paraffinic content, leading to low octane number, potentially limiting the incorporation in the formulation of gasoline [16,28-30]. These products could be of interest to produce renewable gasolines, supposed further cracking and reforming processes, optimized for the conversion of such a feed are developed [16].

Other processes, such as thermal pyrolysis, hydropyrolysis or liquefaction of ligning, as well as pyrolysis of wood and other whole biomass or hydrocarbons production from algae are being developed to produce renewable gasoline [16]. These technologies are at different levels of development, from projects to pilot plants, with no availability of product at commercial or industrial scale.

Unlike HVO for diesel engines, there is not a 100% renewable gasoline-like fuel, supported by an international quality standard, that can be readily used in existing vehicles. Nevertheless, recently a so-called "Blue Gasoline" fulfilling EN228 has been developed [6], with a content up to 33% renewable components [31], and the development of a 95% bio-based gasoline also satisfying the current European Normative for gasoline has been announced [32].
Considering the limitations of the use of conventional biocomponents in gasoline and the difficulty to produce renewable hydrocarbons in the distillation range of gasoline, the objective of this work is to develop a 100% renewable gasoline fulfilling EN 228 [6]. Besides, the present work aims to design a formulation according to the highest quality standards required by the main associations of vehicle manufacturers [33]. Finally, a Life Cycle Analysis (LCA) has been performed in order to compare GHG emissions levels considering different scenarios. The comparison includes an internal combustion engine vehicle (ICEV) using designed renewable gasoline and conventional gasoline and battery electric vehicles, considering the current energetic mix for electricity and 100% renewable electricity.

2. Materials and methods

2.1 Renewable components for gasoline formulation

Different components, preferably renewable, have been used in the present work to design the different formulations to develop a 100% renewable gasoline aiming to fulfill EN228, European Normative which gathers the technical specification for gasoline [6]. The list of selected components is detailed as follows:

- Renewable liquid hydrocarbons from Ethanol-To-Gasoline (ETG) process.
- Bionaphtha from vegetable oil hydrogenation process
- Bioethanol
- Bio ethyl-tert-butyl-ether (ETBE)
- Isopentane

Besides, additives, including octane booster and conventional multifunctional additives for gasoline have been used to achieve the standards and Premium quality as per Worldwide Fuel Charter [33].
Extended information on the quality of renewable components is described below.

2.1.1 Renewable liquid hydrocarbons from Ethanol-to-Gasoline Process

Renewable liquid hydrocarbons in the range of boiling point about 27-260ºC and composition from C_3 to C_{13} are obtained through the Ethanol-to-Gasoline (ETG) process, an innovative technology developed by Ekobenz [20,21]. This process is based on the catalytic conversion of bioethanol to hydrocarbons and is currently the only such technology working in Europe in an industrial scale. The reaction of the catalytic conversion of bioethanol to synthetic biohydrocarbons is carried out in two stages: the dehydration of ethanol and the synthesis of hydrocarbons from ethylene (Equation 1):

$$n \ C_2H_5OH \rightarrow n \ H_2O + n \ C_2H_4 \rightarrow z \ C_xH_y \ \text{(Equation 1)}$$
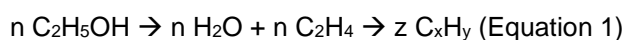
As a result, the process irreversibly converts bioethanol into liquid hydrocarbons, gas hydrocarbons and water. The reaction products from the process are directed to a separator, where they are divided into water, liquid biohydrocarbons and gas biohydrocarbons. The liquid biohydrocarbons are then separated on the distillation column into individual products.

The whole process requires small external electricity supply and due to the exothermic nature of the process, there is no need to supply heat from outside. The process furnaces are also powered by gaseous hydrocarbons obtained from the production process itself. This reduces both the emission of greenhouse gases in the process and significantly improves the process carbon footprint indicators.

The technical specification for the renewable hydrocarbons used in this work is defined by Ekobenz as in Table 1:

Table 1. Technical Specification for Ekobenz Renewable Liquid Hydrocarbons

Property	Units	Values	Test Method
Density at 15ºC	kg/m^3	720-775	ASTM D4052
Distillation curve			ASTM D86
Evaporated at 70ºC, E70	% v/v	15-30	
Evaporated at 100ºC, E100	% v/v	30-50	
Evaporated at 150ºC, E150	% v/v	60-75	
Final Boiling Point	ºC	Max. 210	
Distillation Residue	% v/v	Max. 2,0	
Oxygen content	%m/m	<0,8	EN ISO 22854
Hydrocarbons content			ASTM D5134
Olefins	% v/v	0-10	
Aromatics	% v/v	30-50	
Naphtenes	% v/v	5-10	
n-paraffins	% v/v	5-15	
i-paraffins	% v/v	20-40	
Benzene content	% v/v	< 1,0	
Sulphur content	mg/kg	< 3,0	ASTM D5453
Oxidation Stability	min	>360	ASTM D525
Washed Gums	mg/100 ml	<1	ASTM D381
Copper Strip Corrosion test (3h @50ºC)	Scale	Class 1	ASTM D130
Content of impurities	mg/kg	< 1,0	ASTM D5452
Total halogens content	mg/kg	< 2,0	EN 14077
Phosphorus content	mg/l	< 0,2	ASTM D3231

Considering the technical specification of the renewable liquid hydrocarbons from Ekobenz, special attention must be paid to certain properties considering the requirements to achieve the quality of gasoline fulfilling EN228 quality. The maximum aromatics content in EN228 is limited to 35%v/v, whereas the product from Ekobenz may content up to 50%v/v. Another critical parameter is distillation curve which limits depends on each country climate degrees, in the case of Spanish Regulation RD 1088/2010 [34], required values are E70 from 20 to 54% v/v in winter and from 22 to 56%v/v, E100 from 46 to 74 %v/v and minimum E150 of 75% v/v. The product from Ekobenz would not fulfil Spanish EN228 quality considering distillation curve.

2.1.2 Bionaphtha from vegetable oil hydrogenation process

Renewable naphtha is made from residual oil via hydrotreatment. Lipid-based feedstock is a renewable raw material that is fed together with make-up and recycled hydrogen to the reactor where the chemical structure is modified. Reaction water is separated and directed to wastewater treatment. Remaining hydrogen sulfide and incondensable gases are removed, and the remaining liquid is distilled.

Renewable liquids are separated into renewable diesel (HVO – Hydotreated Vegetable Oil -) and renewable naphtha, which can be used as a biocomponent for gasoline or raw material for bioplastics production. The main characteristics highlighted by the manufacturer of the product are density values, sulphur content and final boiling point according to those of EN228 [6] gasoline. Nevertheless, given the high content in paraffins it is expected that the product presents poor octane number.

2.1.3 Bioethanol and bio-ETBE

Bioethanol and Bio-ETBE are considered conventional renewable components that are usually blended in commercial gasoline. The volume to blend of such biofuels in commercial gasoline is limited by EN228, which allows a maximum 10%v/v ethanol and 22% v/v ETBE; besides, the total amount of oxygenated compounds is limited by the oxygen content, which maximum limit is 3,7 %m/m in oxygen.

Bioethanol is regarded as a 100% renewable fuel since it is normally produced from residual and sustainable raw materials through fermentation processes. However, Bio-ETBE is produced from bioethanol and isobutene (non-renewable origin), thus, it can be considered as 37% e/e renewable [4].

2.2 Additives

Additives are usually added to fossil fuels to improve some properties, aiming to comply with the current technical specification and/or satisfy specific extra quality properties, such as those gathered in "Worldwide Fuel Charter". In the present project, an octane booster additive, based on non-toxic anilines [35], and conventional multifunctional gasoline additives have been tested.

2.3 Characterization of components and gasoline formulations

The tests for characterization and behavior of gasoline tests are referred in the European Standard EN228 [6], as well as in the OEMs document "Worldwide Fuel Charter (WWFC)" (ACEA, Auto Alliance, EMA, JAMA) [33]. In the present work, components and gasoline formulations have been characterized according to such requirements and specific tests are shown in Table 2.

Table 2. Analyses of renewable products and formulations

Property	Test Method
Appearance	ASTM D4176
Density at 15ºC	ASTM D4052
Distillation curve	ASTM D86
Octane Number (RON)	ISO 5164
Vapor Pressure (DVPE)	ASTM D5191
Washed gums	ASTM D381
Oxidation stability	ASTM D525
Aromatics content	EN 22854
Oxygen Content	EN 22854
Olefins content	EN 22854
Benzene content	EN 22854
Ethanol content	EN 22854
Copper Strip Corrosion test (3h @50ºC)	ASTM D130
Demulsion capacity	ASTM D1094
Anti-rust capacity	ASTM D665 A and B

The tests included in Table 2 are those required in EN228 to guarantee the minimum fuel quality to be compatible with current gasoline engines and demulsion and anti-rust capability have been

additionally included. Such properties are critical for premium gasoline quality, as stated in WWFC, since the protection against water in gasoline can be guaranteed, enabling fuel-water separation, and avoiding the rust of materials because of water, including sea water.

2.4 Vehicle tests and performance

Finally, aiming to complete the renewable gasoline behavior assessment, vehicle tests were carried out to compare the performance and emissions to a conventional gasoline. This study was conducted by the GCM Group from University of Castilla-La Mancha.

Tests were carried out using a Euro 6-b homologated vehicle without gasoline particulate filter (GPF) in order to observe possible differences regarding particulate emissions between the tested fuels. An Opel Astra Euro 6-b was selected, which meets both requirements. The main technical data of the engine are: displacement of 1399 cm^3, four cylinders, manual transmission, direct-injection and 150 CV. The installation includes sets of bags for the accumulation of gases extracted during the cycle and its subsequent measurement with Horiba MEXA-ONE C1.

To cover a wide range of driving conditions, two different tests were carried out, the current WLTC cycle used for homologation and a driving cycle composed of very aggressive accelerations (at full load, fixed gear) named toothsaw (plotted in Figure 1) was driven in the chassis dyno test bench. For all tests, the chamber temperature was kept at 23 ⁰C. Determination of the road load coefficients (aerodynamic and rolling resistance of the vehicle) was performed following the methodology proposed by regulation 1151/2017 of the European Commission.
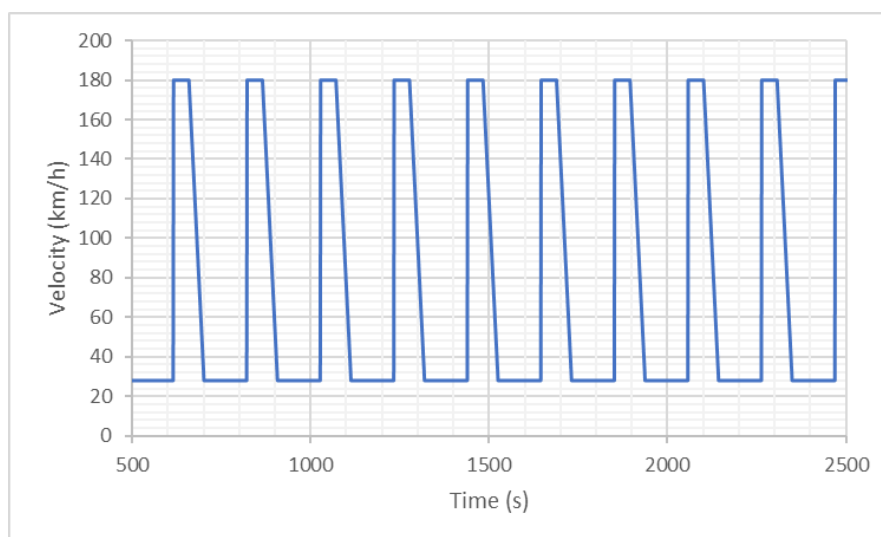

Fig. 1. Toothsaw cycle

WLTC cycle was carried out at cold and warm engine conditions, keeping the chamber temperature at 23 ⁰C. In cold conditions, the soaking period is at least 8 hours whereas in warm conditions, the vehicle has a coolant temperature over 80 ⁰C.

On the other hand, the toothsaw cycle is comprised by 10 full-load accelerations, all carried out in fourth gear (first 5 teeth are considered as "phase 1" whereas the rest are "phase 2" to analyze the results).

Before each acceleration, a two-minute (approximately) period at 28 km/h is driven to ensure that engine parameters are stable before the accelerations at full load. Once the vehicle reaches approximately 180 km/h, it remains at that velocity for approximately 5 seconds. Finally, the vehicle slows down to reach the low-constant-velocity period again. Prior to the 10 toothsaw, a 10-minute warming up at 80 km/h was carried out. First, for each cycle (WLTC cold, WLTC warm and toothcycle), three tests were carried out for the commercial gasoline. Later, the same sequence was repeated with the renewable gasoline. Finally, three more tests with the commercial gasoline were carried out to check time-shifts of the vehicle or the installation.

For the dilution of the total exhaust gas emitted by the vehicle with atmospheric air, a total dilution tunnel Horiba DLT-7040 is required, located horizontally outside the climatic chamber, which has three zones: suction of the exhaust gas and atmospheric air, mixing and sampling. The tunnel is

composed of a heat exchanger to keep the temperature of the exhaust gas diluted at 40 °C, which allows a more accurate control of the flow rate and of the extracted samples.

A Horiba model MEXA-2000SPCS has been used for the counting of particles with a diameter greater than 23 nm (as required by Euro 6 regulation), which includes a previous dilution system and conditioning of the sample. This equipment consists of a primary hot diluter, an evaporation tube, a secondary cold diluter and a particle counter.

For the measurement of continuous diluted gaseous emissions from bags, a Horiba MEXA-ONE C1 analyzer is used, equipped with various modules for the measurement of nitrogen oxides, carbon dioxide and carbon monoxide, and with the necessary components for the switching between gases, filtering and pumping of the sample and communication with the integrated control system.

The main operating parameters of the vehicle during the tests were recorded using the OBD (On-board diagnostics) connection and INCA PC software. Boost pressure, engine speed, vehicle velocity and spark timing are among these parameters.

2.5 Life Cycle Analysis (LCA) Calculations

Different vehicle powertrain technologies do not contribute in the same way to GHG emissions. Life Cycle Analysis of GHG emissions is considered as the adequate tool to compare different vehicle technologies due to differences in production and use patterns. LCA considers GHG emissions during the vehicle life cycle: vehicle and battery manufacturing, energy production, the use phase (tailpipe emissions) and vehicle end of life.

In the present work, two different passenger car powertrain technologies have been analyzed in terms of life cycle GHG emissions: ICEV (Internal Combustion Engine Vehicle) fueled by mineral diesel or gasoline fuel and by low carbon liquid fuels (advanced biofuels and e-fuels) and BEV (Battery Electric Vehicle). A representative case study has been selected in this insight, taking into account the following hypothesis:

- European vehicle segment C (for example, Ford Focus, Renault Megane or Volkswagen Golf)
- Vehicle lifetime of 160.000 km
- Litihium-ion battery of 43,3 kWh (250 km equivalent range) without battery replacement throught BEV lifetime
- ICEV fuelled by the designed gasoline and commercial gasoline blended with 7 %e/e bio-ethanol

Vehicle energy consumptions of each technology are obtained from public database of energy consumption under real driving conditions and no lab certification data are used. However, there are few data available of BEV, and then, the uncertainty derived from the average consumption estimation of these vehicles is higher. Data on emissions and sustainability have been taken from official databases and bibliography [34-41]. CO_2 emissions associated to the production and vehicle use of the designed renewable gasoline are the actual emissions certified by ISCC (International Sustainability and Carbon Certification).

3. Results and Discussion

3.1 Renewable gasoline formulation development

3.1.1 Main components characterization

Renewable liquid hydrocarbons from Ethanol-To-Gasoline process and bionaphtha from vegetable oil hydrogenation process have been chosen as the most adequate products to be considered as main components in the formulations, given their high potential to reduce GHG emissions and their physicochemical properties. These products have been analyzed considering critical parameters and results are shown in Table 3.

Table 3. Analyses of renewable hydrocarbons from ETG process and bionaphtha from oil hydrogenation process

Property	Test Method	Units	Renewable hydrocarbons from ETG	Bionaphtha from oil hydrogenation	Ethanol	ETBE	EN 228 Limits (Spain)
Density at 15ºC	ASTM D4052	kg/m3	763,8	725,6	794	747	720-775
Distillation curve	ASTM D86						
Evaporated at 70ºC, E70		% v/v	25	8,4	n/a	n/a	20-54*/22-56**
Evaporated at 100ºC, E100		% v/v	39,6	35,8	n/a	n/a	46-74
Evaporated at 150ºC, E150		% v/v	66,9	96,7	n/a	n/a	> 75
Final Boiling Point		ºC	202,6	182,2	n/a	n/a	< 210
Distillation Residue		% v/v	1,1	1	n/a	n/a	< 2
Boiling point		ºC	n/a	n/a	78,3	71,7	n/a
Research Octane Number (RON)	ISO 5164	n/a	93	60,34	130	118	> 95
Vapor Pressure (DVPE)	ASTM D5191		54	30,3	17,1	35,7	45-60*/50-80**
Washed Gums	ASTM D381	mg/100 ml	3,3	n/a	n/a	n/a	< 5
Oxidation Stability	ASTM D525	Min	> 1440	n/a	n/a		> 360
Oxygen content	EN ISO 22854	%m/m	0,0	0,0	35	16	< 3,7
Hydrocarbons content	EN ISO 22854						
Olefins		% v/v	3,98	1,72	n/a	n/a	< 18
Aromatics		% v/v	43,5	0,02	n/a	n/a	< 35

*Summer quality **Winter quality

As it can be observed in Table 3, none of the two products satisfy EN228 in all the analyzed parameters. The product coming from ETG process is a heavier product than the bionaphtha coming from oil hydrogenation, presenting higher density, vapor pressure and distillation curve values, except from E150. Products present important differences in composition; whereas aromatics are the main component, together with paraffins, in the hydrocarbons from Ekobenz process, the bionaphtha is mainly composed by paraffins, therefore the content in specified products (olefins and aromatics) is very low.

Regarding octane number, renewable hydrocarbons for ETG process present a RON value near of that in the technical specification for conventional gasoline; however, this is related to its high content in aromatics (over 35%v/v) which exceeds the limit in EN228. On the other hand, bionaphtha, given the high paraffinic content of the product, presents an octane number of 60,43, which is significantly low to prevent this product to be used as the main component to design a gasoline meeting octane number of 95.

Considering all these data and the objective of obtaining a 100% renewable gasoline fulfilling EN228, renewable hydrocarbons from ETG process was the product selected as the main component to design pilot formulations.

3.1.2 Pilot Formulations

26 pilot formulations have been designed using the chosen products, including renewable hydrocarbons from ETG process, bionaphtha from oil hydrogenation process, bioethanol, bio-ETBE and isopentane. Formulations were designed aiming to fulfil critical properties from EN228, specifically density, distillation curve, composition and research octane number, which were found to be key parameters in the characterization of the selected renewable components.

Table 4 shows part of the results of some of the designed formulations which were the closest in quality to a commercial gasoline. The samples included in the table fulfil technical specification EN228 in terms of density and composition (oxygen, olefins, aromatics and benzene content). However, the most critical parameters are those related to the distillation curve, specially E150, that could only be achieved in one formulation (Formulation 6) and the value was within the uncertainty of the measurement. RON values are also slightly far from the specification in some of the formulations.

Table 4. Test results from pilot formulations using renewable hydrocarbons from ETG process as main component

Property	Test Method	Units	Formulation 1	Formulation 6	Formulation 7	Formulation 8	EN 228 Limits (Spain)
Appearance	ASTM D4176	n/a	Bright and clear	Bright and clear	Bright and clear	Bright and clear	Bright and clear
Density at 15ºC	ASTM D4052	kg/m^3	766,5	754,7	763,4	725,6	720-775
Distillation curve	ASTM D86						
Evaporated at 70ºC, E70		% v/v	41,9	20,5	38,1	45,2	20-54*/22-56**
Evaporated at 100ºC, E100		% v/v	48,6	49,4	47	52	46-74
Evaporated at 150ºC, E150		% v/v	69,8	75,1	70,8	70,4	> 75
Final Boiling Point		ºC	202,9	200,2	200,6	202,5	< 210
Distillation Residue		% v/v	1,1	1,1	1,1	1,1	< 2
Research Octane Number (RON)	ISO 5164	n/a	97,2	96	93	92	> 95

*Summer quality **Winter quality

In view of the obtained results, an adjustment of the renewable hydrocarbons from ETG process was proposed and designed aiming to reduce aromatics content and obtaining a heavier distillation curve. Changes in the process were implemented to modify the critical parameters. Table 5 shows the information of the adjusted composition of the Ekobenz product, which is not fulfilling the technical specification EN228, considering several of the selected parameters; specifically, E100, E150 and RON. Gasoline quality was improved by including renewable oxygenates and octane improver additive in Formulations 10 and 11, (Table 5), especially considering Formulation 11 which fulfills EN228 in the analyzed parameters.

Table 5. Test results from pilot formulations using adjusted renewable hydrocarbons from ETG process as main component

Property	Test Method	Units	Adjusted renewable hydrocarbons from ETG	Formulation 10	Formulation 11	EN 228 Limits (Spain)
Appearance	ASTM D4176	n/a	Bright and clear	Bright and clear	Bright and clear	Bright and clear
Distillation curve	ASTM D86					
Evaporated at 70ºC, E70		% v/v	22,1	44,6	44,8	20-54*/22-56**
Evaporated at 100ºC, E100		% v/v	40	52,6	53	46-74

Evaporated at 150ºC, E150		% v/v	70,8	78,5	78,3	> 75
Final Boiling Point		ºC	184	184,7	185,5	< 210
Distillation Residue		% v/v	1,1	1,0	1,1	< 2
Research Octane Number (RON)	ISO 5164	n/a	89,89	94,5	96,6	> 95

*Summer quality **Winter quality

Formulation 11 was analyzed according to all the requirements in EN228, verifying compliance with technical specification (Table 6). Thus, Formulation 11 was selected as the base fuel for the development of premium quality gasoline. Apart from EN228 technical requirements, demulsion and anti-rust properties have been addressed for the design of premium quality gasoline, based on WWFC [33] requirements. These properties are essential from Premium gasoline, since the protection against water in gasoline can be guaranteed, enabling fuel-water separation, and avoiding the rust of materials because of water, including sea water. Finally, biogenic carbon content following ASTM D6866 was determined in Formulation 11, finding that the gasoline is renewable in 99% (additive contribution is considered as negligible given the low used concentration).

Formulation 11 was used as base fuel to include different conventional multifunctional additives to develop a premium gasoline. This way, Formulations 11A, B and C were designed and analyzed. Formulation 11C is the only formulation that achieves both the required quality for gasoline in EN228 and for premium gasoline as established in Worldwide Fuel Charter.

Table 6. Test results from pilot formulations to complete fulfillment of EN228 and Premium gasoline quality tests

Property	Test Method	Units	Formulation 11	Formulation 11A	Formulation 11B	Formulation 11C	EN 228 Limits (Spain)
Appearance	ASTM D4176	n/a	Bright and clear	Bright and clear	Bright and clear	Bright and clear	Bright and clear
Vapor Pressure (DVPE)	ASTM D5191	kPa	54,6	55	54,8	54,6	45-60*/50-80**
Washed Gums	ASTM D381	g/100 ml	1,4	0,1	0,2	0,2	< 5
Non-washed Gums	ASTM D381	g/100 ml	4	15,8	28,6	44,2	n/a
Oxidation Stability	ASTM D525	min	>1440	>1440	>1440	>1440	> 360
Copper Strip Corrosion test (3h @50ºC)	ASTM D130	Scale	1a	1a	1a	1a	Class 1
Demulsion test	ASTM D1094	Scale	2	2	2	2	Max. 2***
Anti-rust (method A)	ASTM D665-A	Scale	C (30%)	A (0%)	A (0%)	A (0%)	Min. B++***
Anti-rust (method B)	ASTM D665-B	Scale	D (70%)	B (20%)	B (20%)	A (0%)	Min. B++***
Biogenic Carbon Content	ASTM D6866	%	99	-	-	-	-

*Summer quality **Winter quality *** Worldwide Fuel Charter and Internal limitations

3.2 Vehicle testing: performance and emissions

To verify the performance of the designed gasoline (Formulation 11C) in use, vehicle testing using an Opel Astra Euro 6-b without GPF homologated vehicle was performed. Test were developed to compare two gasoline fuels: one of them a commercial gasoline sample and, the second one, the designed renewable gasoline (Table 7). The comparison was performed under the WLTC cycle and full-load accelerations cycle, named toothsaw.

Table 7. Characterization of EN228 renewable gasoline and commercial gasoline used in vehicle testing.

Property	Test Method	Units	EN 228 Renewable gasoline	Commercial gasoline	EN 228 Limits (Spain)
Appearance	ASTM D4176	n/a	Bright and clear	Bright and clear	Bright and clear
Distillation curve	ASTM D86				
Evaporated at 70ºC, E70		% v/v	46	39,6	20-54*/22-56**
Evaporated at 100ºC, E100		% v/v	53	62,9	46-74
Evaporated at 150ºC, E150		% v/v	78,6	95,1	> 75
Final Boiling Point		ºC	191,4	178,9	< 210
Distillation Residue		% v/v	1	1	< 2
Research Octane Number (RON)	ISO 5164	n/a	96,6	95,5	> 95
Vapor Pressure (DVPE)	ASTM D5191	kPa	54,6	71,7	45-60*/50-80**
Oxidation Stability	ASTM D525	min	> 1440	> 1440	> 360
Oxygen content	EN ISO 22854	%m/m	< 3,7	1,58	< 3,7
Hydrocarbons content	EN ISO 22854				
Olefins		% v/v	4,6	8,8	< 18
Aromatics		% v/v	28-30	25-27	< 35
Benzene content		% v/v	0,13	0,1	< 1

*Summer quality **Winter quality

Figure 2 shows the results on the average emissions of the 3 repetitions in the WLTC and in the tooth saw cycle. In the case of the tooth saw cycle, the first 5 teeth are labelled as "phase 1" whereas the rest are "phase 2". Error bars are defined as the confidence interval (confidence level 90%).

As it can be observed in Figure 2 (a), CO_2 emissions are independent on the fuel. Figure 2 (b) to (d) reveal that, in the WLTC cycle, the renewable fuel and commercial fuel CO, HC and NO_x emissions do not present significant differences (overlapping of error bars) and are very low. On the other hand, in the tooth saw cycle, the renewable gasoline led to lower CO (Figure 2 (b)), higher HC (Figure 2 (c)) and higher NO_x (Figure 2 (d)). These differences in the case of CO and NO_x are not very relevant and, in most of the cases, fall within the confidence interval.

Also particle emissions are higher for the renewable gasoline, both in number (Figure 2 (e)) and in mass basis (Figure 2(f)), despite of the higher oxygen content as compared to the commercial gasoline. The higher aromatic content of the renewable fuel and, more importantly, its distillation curve, could be responsible for this result, as well as the higher HC emissions registered. As observed in Table 7, the renewable fuel shows lower distilled volumes when temperature is increased (poorer volatility at high temperature), which is often associated with particle formation. Only in the first repetitions of the commercial fuel and the tooth saw cycle, this fuel led to higher particle mass emissions (not in number basis) than the renewable fuel. Probably this was because at the beginning of the test there were soot and deposits stuck in the inner surfaces of the exhaust pipe or even in the engine walls and exhaust valves. The high temperature and high exhaust flowrate reached during the first tooth saw cycles released these deposits, which were collected in the filters and accounted for as particle mass. Contrarily, since the particle number equipment discards large particle prior measuring, these deposits did not affect the result of particle number.

Nevertheless, it is expected that last generation vehicles fitted with GPF will keep particle emissions bellow Euro limits.
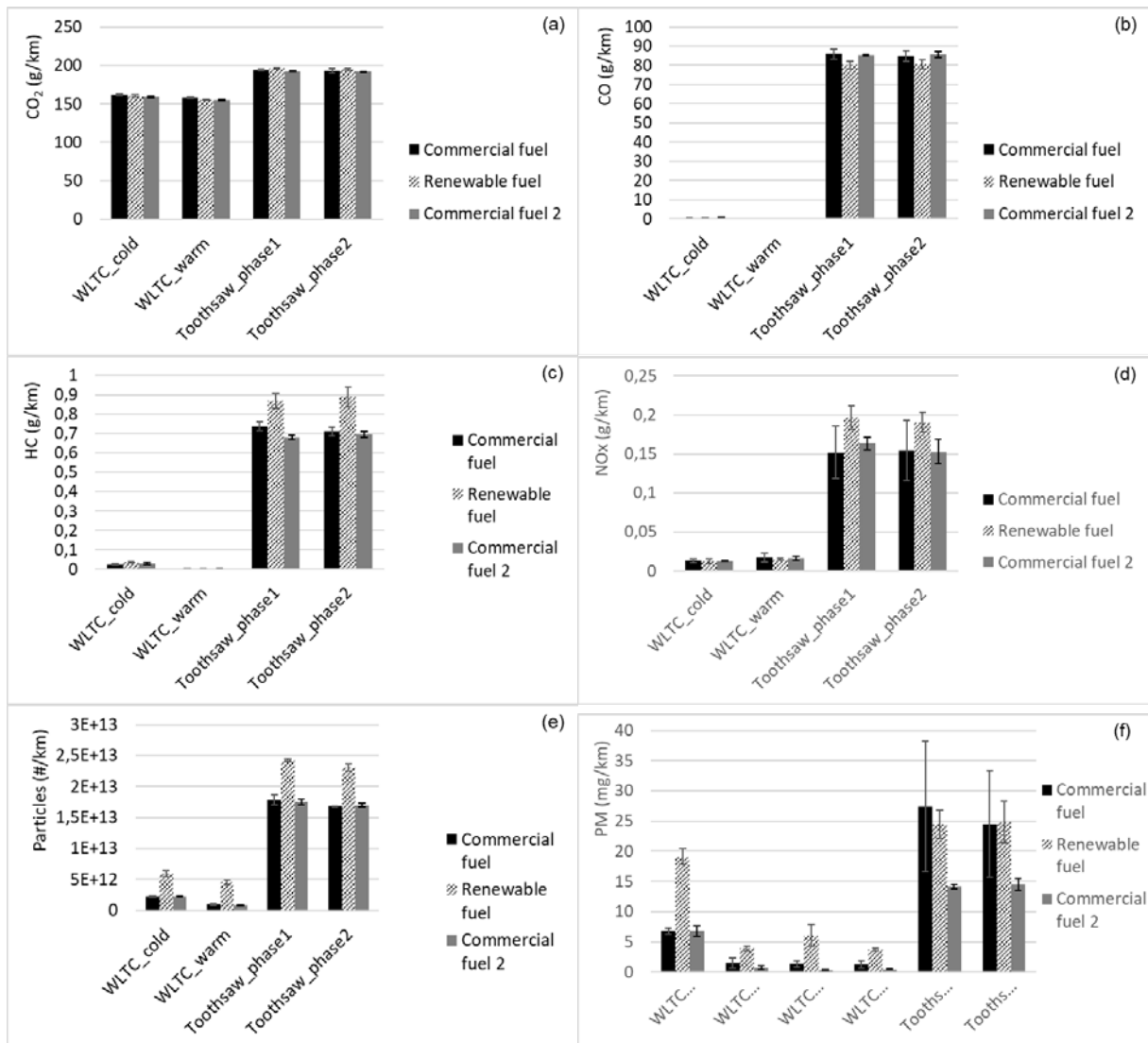
Fig. 2. Gas and particle emissions in vehicle testing

Considering the operating parameters recorded from the OBD, no significant differences were observed in spark timing or boost pressure for the different fuels, which is expectable since the octane number of both fuels are quite similar. It can be remarked that the electronic unit delayed the spark timing during the tooth saw accelerations, specially at the beginning, to prevent knocking. Power and lambda evolution were essentially the same for the two fuels as well during the tooth saw cycle, with lambda output showing an enriched period coinciding exactly with the accelerations.

3.3 Life Cycle Analysis

A comparison of technologies and energy sources in terms of LCA has been performed considering internal combustion engines using mineral gasoline and the 100% renewable gasoline designed in this work and battery electric vehicles. Different scenarios have been analyzed as shown in Table 8.

Table 8. LCA analyzed scenarios.

Vehicle	Energy source scenarios
ICEV	Mineral gasoline
ICEV	Designed 100% renewable gasoline
ICEV	Designed 100% renewable gasoline. Renewable value chain
BEV	Battery manufactured in China. EU electric mix.
BEV	Battery manufactured in China. Spain electric mix.
BEV	Battery manufactured in China. Germany electric mix.
BEV	Battery manufactured in China. Poland electric mix.
BEV	Battery manufactured in China. 100% renewable electric mix.

GHG emissions produced by power sector have been analyzed by means of four different scenarios in terms of electric mix: the average in EU, Germany, Spain and Poland (2018 data) [34]. These scenarios have been selected for this analysis considering that Spain has a very high contribution of renewable electricity generation; Germany is moving from a very coal-based power sector; and Poland is leading the power sector based on coal. Besides, the scenarios considering that the renewable gasoline is produced through a fully renewable value chain and a 100% renewable electric mix have been also included in this analysis.

Data on powertrain technologies and energy production have been retrieved from public sources [35-41], except from the CO_2 emissions associated to the production and vehicle use of the designed renewable gasoline which are the actual emissions certified by ISCC (International Sustainability and Carbon Certification).

CO_2 equivalent emissions calculations for each scenario include the following phases:
- Manufacturing of vehicle battery
- Manufacturing of the rest of the vehicle (named as vehicle manufacturing)
- Production of energy (fuel or electricity) used in the vehicle (named as energy production)
- Use in the vehicle or tailpipe emissions (named as use)
- Vehicle end of life phase.

The results for each scenario are shown in Figure 3. As it can be seen from this figure, the most favorable case, considering CO_2 equivalent emissions, is the ICEV fueled by renewable gasoline produced via renewable value chain. On the other hand, the worst-case scenario is that of ICEV fueled by mineral gasoline. A further analysis of the relevance of the different considered phases is presented as follows.

The GHG emissions during the vehicle manufacturing phase are significantly different when ICEV are compared with BEV. ICEV manufacturing emits around 5,6 t of CO_2 equivalent, whereas BEV manufacturing emissions are around 9,1 t. This difference is based on the different components in the powertrains, such as battery, electronics and electric motor. Battery manufacturing contributes around 45% of CO_2 emissions in the battery electric vehicle manufacturing phase. External references establish a GHG emissions factor for battery manufacturing in the range of 61-106 $kgCO_2eq/kWh$ for the most common lithium-ion batteries in the European market and NMC (Ni-Mn-Co) (93,4 $kgCO_2eq/kWh$). The complete BEV manufacturing phase accounts for 25 - 45 % of total GHG emissions in LCA (depending on the electricity mix considered in the energy production), whereas ICEV manufacturing phase accounts for 15 - 20 % of total GHG emissions.

Analyzing the phases of energy production and vehicle use (tailpipe emissions) it can be observed that ICEV fueled by mineral gasoline presents the highest contribution in these 2 phases. On the other hand, BEV have lower contributions in these phases, regardless the electricity mix scenario considered. This difference is attributed to zero emissions in use and the higher efficiency of the electric vehicle, mainly. Bearing in mind the considered data, the gasoline vehicle requires an energy consumption of 2,35 MJ/km, whereas the battery electric vehicle uses 0,54 MJ/km as electricity. This difference in energy consumption balances the higher GHG emissions in the vehicle manufacturing phase in the BEV case, resulting in a lower total GHG emissions during life cycle under all electricity mix scenarios.
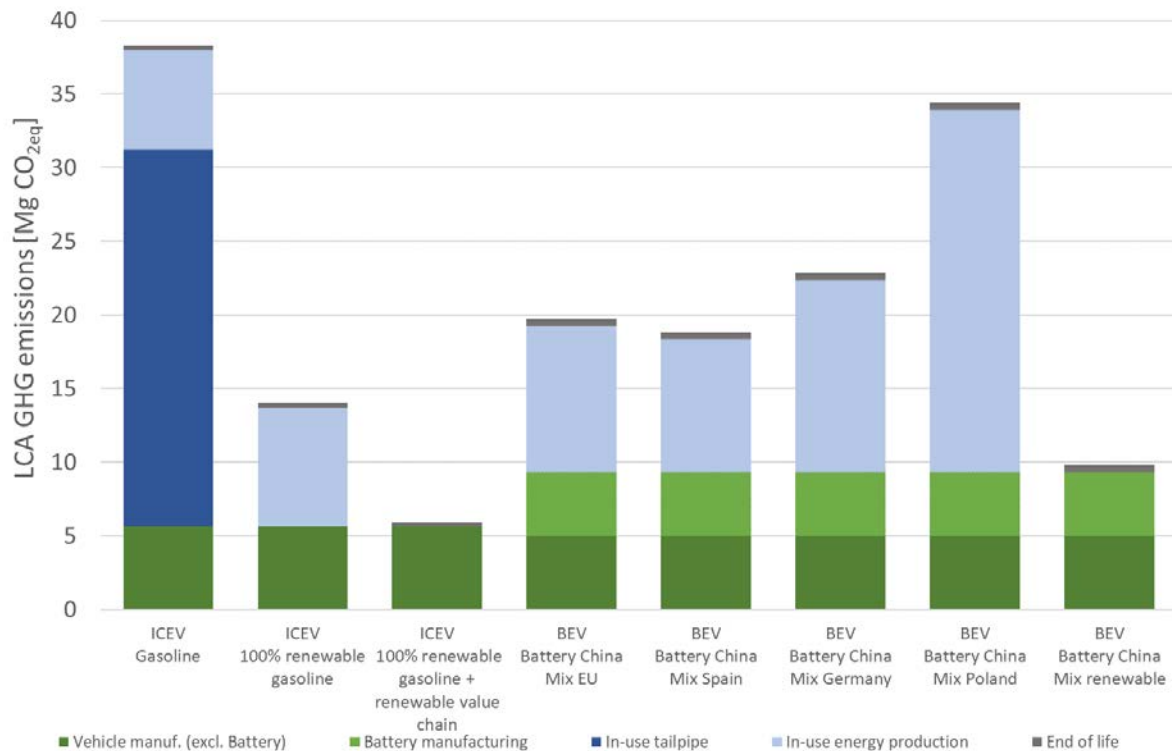
Fig. 3. Different powertrains LCA GHG emissions comparison

In the case of ICEV fueled by mineral fuel, the energy (fuel) production phase contributes around 15-20 % of the GHG emissions in use and tailpipe emissions are around 65 %. For this reason, the potential GHG emissions reduction in the mineral fuel production phase have a lower impact in comparison to tailpipe emissions reduction. On the other hand, the use of the 100% renewable gasoline leads to sifnificant reduction of the tailpipe emissions in an LCA basis as GHG emissions are considered as zero [34,44].

If it is considered that the process of renewable gasoline production might be fully based on renewable sources, the lowest emissions would be achieved in such scenario in which GHG emissions during vehicle manufacturing and end of life would be the only contribution in life-cycle basis. This is the lowest emissions case even considering a 100% renewable electric mix for BEV, in which the emissions associated to vehicle and battery manufacturing are higher than in the case of internal combustion engine vehicles (almost twice).

Conclusions

A one hundred percent renewable gasoline has been designed using as main components: renewable hydrocarbons from Ethanol-to-Gasoline process. Adjustment of the quality of renewable components from ETG process was needed to meet volatility, distillation curve requirements and improve octane number. Besides, octane booster additive was included in the formulation in order to achieve octane number restrictions in EN228. The final product fulfills EN228 gasoline technical specification and Premium gasoline quality as per Worldwide Fuel Charter, guaranteeing high detergency and water protection, and it can be readily used in existing vehicles.

The designed renewable gasoline and a commercial gasoline sample have been subjected to vehicle testing performance. The comparison has been performed in a Euro 6-b spark-ignited light-duty vehicle without GPF under the WLTC cycle and full-load accelerations. Despite the higher oxygen content of the renewable gasoline compared to conventional one, this fuel led to higher particle emissions measured in mass and number. This was explained based on its higher aromatic content and poorer volatility as referred to commercial fuel. Nevertheless, it is supposed that last generation vehicles fitted with GPF will keep particle emissions bellow Euro limits. There were no other differences, or these were minor or within the confidence intervals.

On an LCA basis analysis, the use of the designed renewable gasoline in internal combustion engine vehicles would lead to an important reduction on GHG emissions compared to the use of mineral fuel. This reduction is potentially higher than the reduction that could be achieved by a battery electric vehicle using electricity produced under different European electric mix scenarios.

Acknowledgements

References

[1] European Comission. Statistical Pocket Book. EU Transport in Figures, 2020.

[2] European Green Deal: Commission proposes transformation of EU economy and society to meet climate ambitions. European Commission, 2020

[3] Changes to the Renewable Energy Directive revision and ReFuel EU proposals: Greenhouse gas savings and costs in 2030. Available online. Last retrieved August 2021: https://theicct.org/publications/red-revision-refuel-eu-ghg-sept21.

[4] Directive of the European Parliament and of the Council amending Directive (EU) 2018/2001 of the European Parliament and of the Council, Regulation (EU) 2018/1999 of the European Parliament and of the Council and Directive 98/70/EC of the European Parliament and of the Council as regards the promotion of energy from renewable sources, and repealing Council Directive (EU) 2015/652.

[5] Proposal for a Directive of the European Parliament and of the Council amending Directive (EU) 2018/2001 of the European Parliament and of the Council, Regulation (EU) 2018/1999 of the European Parliament and of the Council and Directive 98/70/EC of the European Parliament and of the Council as regards the promotion of energy from renewable sources and repealing Council Directive (EU) 2015/652. 2021.

[6] EN 228:2013+A1. Automotive fuels. Unleaded petrol. Requirements and test methods. 2017.

[7] EN 590:2014+A1. Automotive fuels. Diesel. Requirements and test methods. 2017.

[8] H. Stančin, H. Mikulčić, X. Wang, N. Duić, A review on alternative fuels in future energy system, Renewable and Sustainable Energy Reviews, Volume 128, 2020, 109927.

[9] Transition towards Low Carbon Fuels by 2050: Scenario analysis for the European refining sector. Concawe Report 7/21. 2021.

[10] Biofuel Technology Handbook. Dominik Rutz and R. Janssen, Published by: WIP Renewable Energies, 2008.

[11] Advanced Biofulels: Using catalytic routes for the conversion of biomass platform molecules, CRC Press, 2015. ISBN 9781771882217.

[12] Arivalagan Pugazhendhi, Thangavel Mathimani, Sunita Varjani, Eldon R. Rene, Gopalakrishnan Kumar, Sang-Hyoun Kim, Vinoth Kumar Ponnusamy, Jeong-Jun Yoon, Biobutanol as a promising liquid fuel for the future - recent updates and perspectives, Fuel,Volume 253,2019, Pages 637-646.

[13] S.D. Minteer,11 - Biochemical production of other bioalcohols: biomethanol, biopropanol, bioglycerol, and bioethylene glycol, In Woodhead Publishing Series in Energy, Handbook of Biofuels Production, Woodhead Publishing, 2011, Pages 258-265, ISBN 9781845696795.

[14] M. Melikoglu, V. Singh, S.-Y. Leu, C. Webb, C.S.K. Lin, 9 - Biochemical production of bioalcohols, Handbook of Biofuels Production (Second Edition), Woodhead Publishing, 2016, Pages 237-258,ISBN 9780081004555.

[15] Roode-Gutzmer, Q.I.; Kaiser, D.; Bertau, M. Renewable Methanol Synthesis. ChemBioEng Rev. 2019,6, 209-236.

[16] Busca, G. Production of Gasolines and Monocyclic Aromatic Hydrocarbons: From Fossil Raw Materials to Green Processes. Energies 2021, 14, 4061.

[17] Available online. Last retrieved December 2021:   https://www.topsoe.com/processes/synthetic-fuels/methane-rich-gas-to-gasoline#:~ {}:text=Gasoline%20from%20synthesis%2

[18] Available online. Last retrieved December 2021: https://www.exxonmobilchemical.com/en/catalysts-and-technology-licensing/synthetic-fuels?utm_source=google&utm_medium=cpc&utm_campaign=cl_downstream_none&ds_k=Methanol+to+gasoline&gclid=EAIaIQobChMIsPT-wtaiJ9QIV1rLVCh29_gCzEAAYASAAEgJ3WPD_BwE&gclsrc=aw.ds

[19] Phung, T.K.; Radikapratama, R.; Garbarino, G.; Lagazzo, A.; Riani, P.; Busca, G. Tuning of product selectivity in the conversion of ethanol to hydrocarbons over H-ZSM-5 based zeolite catalysts. Fuel Process. Technol. 2015, 137, 290–297.

[20] Krzywonos, Małgorzata & Wojdalski, Janusz & Kupczyk, Adam & Sikora, Michał. (2017). Analysis of properties of synthetic hydrocarbons produced using the ETG method and selected conventional biofuels made in Poland in the context of environmental effects achieved. Rocznik Ochrona Srodowiska. 19. ISSN 1506-218X

[21] Available online. Last retrieved December 2021: http://ekobenz.com/index.php

[22] EN 15940:2016+A1:2019+AC. Automotive fuels. Paraffinic diesel fuel from synthesis or hydrotreatment. Requirements and test methods. 2019.

[23] Neste Renewable Diesel Handbook, Neste corporation, 2016.

[24] Available online. Last retrieved December 2021: https://www.eni.com/en-IT/circular-economy/ecofind-biofuel.html.

[25] Available online. Last retrieved December 2021: https://services.totalenergies.fr/pro/produits-services/carburants/carburants-adaptes-professionnels/total-hvo.

[26] Innovation Outlook – Advanced Liquid Biofuels, IRENA 2016.

[27] Laxminarasimhan, C.S. An Introduction to Shell New Energies and IH2 Technology – Drop in Fuel from Waste Biomass. IEU Trade Delegation, March 6-8, 2018.

[28] Yugo, M.; Soler, A. A look into the role of e-fuels in the transport system in Europe (2030-2050) (literature review). Concawe Review, Volume 28, Number 1, October 2019.

[29] Role of e-fuels in the European transport system – Literature Review. Concawe Report 14/19. 2019

[30] Available online: https://www.upmbiofuels.com/traffic-fuels/upm-bioverno-naphtha-for-fuels/ (last retrieved December 2021)

[31] Bosch, Shell and Volkswagen develop renewable gasoline. Published 11/5/2021. Last retrieved December 2021: https://www.bosch-press.be/pressportal/be/en/press-release-24512.html

[32] Neste is testing renewable gasoline in Sweden for possible commercialization internationally. Published 21/5/2021. Last retrieved 29/12/2021: https://www.neste.com/releases-and-news/renewable-solutions/neste-testing-renewable-gasoline-sweden-possible-commercialization-internationally

[33] Worldwide Fuel Charter. Gasoline and Diesel Fuel. 6th Edition. ACEA, Auto Alliance, EMA, JAMA. 2019.

[34] Data retrieved from ENTSO-E. Last retrieved November 2019: https://www.entsoe.eu/

[35] JEC Well to Wheels report v5. Available online. Last retrieved March 2022: https://publications.jrc.ec.europa.eu/repository/handle/JRC121213

[36] Preparing for a Life-Cycle CO2 Measure. Report RD.11/124801.04. Ricardo, 2011.

[37] E. Emilsson, L. Dahllö. Lithium-Ion Vehicle Battery Production. IVL Swedish Environmental Re

[38] World Energy Outlook 2019. International Energy Agency, 2020.

[39] Greenhouse gas emissions for battery electric and fuel cell electric vehicles with ranges over 300 km. Fraunhofer Institute for Solar Energy Systems ISE, 2019.

[40] Data retrieved from Emission Analytics. Last retrieved November 2019: https://www.emissionsanalytics.com/

[41] Data retrieved from Spritmonitor. Last retrieved November 2019: https://www.spritmonitor.de/es/

[42] Spanish Regulation. Real Decreto 1088/2010, de 3 de septiembre por el que se modifica el Real Decreto 61/2006, de 31 de enero, en lo relativo a las especificaciones técnicas de gasolinas, gasóleos, utilización de biocarburantes y contenido en azufre de los combustibles para uso marítimo.

[43] Viayna, A.; Ghashghaei, O.; Vílchez, D.; Estarellas, C.; López, M.; Gómez-Catalán, J.; Lavilla, R.; Delgado, J.; Luque, F.J. Holistic approach to anti-knock agents: A high throughput screening of aniline-like components. Fuel 305, 121518, 2021.

[44] 2006 IPCC Guidelines for National Greenhouse Gas Inventories.

Numerical Analysis of the Combustion of Diesel, Dimethyl Ether, and Polyoxymethylene Dimethyl Ethers (OME$_n$, n=1-3) Using Detailed Chemistry

T. Franken[1], V. Srivastava[2], S.Y. Lee[3], B. Heuser[4], K.P. Shrestha[1], L. Seidel[5], F. Mauß[1]

[1]Chair of Thermodynamics / Thermal Process Engineering. BTU Cottbus-Senftenberg. Siemens-Halske-Ring 8, D-03046 Cottbus, Germany.

E-mail: tim.franken@b-tu.de
Telephone: +(49) 355 69 4333

[2]Chair of Thermodynamics of Mobile Energy Conversion Systems. RWTH Aachen University. Forckenbeckstraße 4, D-52074 Aachen, Germany.

E-mail: srivastava_viv@tme.rwth-aachen.de

[3]Teaching and Research Area Mechatronics in Mobile Propulsion. RWTH Aachen University. Forckenbeckstraße 4, D-52074 Aachen, Germany.

E-mail: lee_sun@mmp.rwth-aachen.de

[4]FEV Europe GmbH, Neuenhofstraße, 181, D-52078 Aachen, Germany.

E-mail: heuser@fev.com

[5]LOGE Deutschland GmbH. Querstraße 48, D-03046 Cottbus, Germany.

E-mail: lars.seidel@logesoft.com

Abstract. New types of synthetic fuels are being used in internal combustion engines to achieve carbon-neutral and ultra-low emission combustion. Dimethyl Ether (DME) and Polyoxymethylene Dimethyl Ethers (OME$_n$) belong to this type of synthetic fuels.

A detailed chemical model for diesel, DME and OME$_n$ (n=1-3) is applied in the zero-dimensional (0D) stochastic reactor model (DI-SRM) to study the non-premixed combustion and species formation in a 2-liter diesel engine. The DI-SRM is validated for two operating points at 1750rpm, 4bar and 12bar IMEP. The engine is operated with neat diesel and a OME$_{3-5}$ blend. The DI-SRM predicts closely the combustion of diesel and the OME$_{3-5}$ blend, and captures the trends of CO_2, NO_x, CO and unburnt hydrocarbon (HC) engine-out emissions.

The combustion and species formation of DME and OME$_n$ (n=1-3) are investigated and compared to diesel. The mixture formation is governed by an earlier vaporization of the DME and OME$_n$, faster homogenization of the respective air-fuel mixture and higher reactivity. At the same injection pressure, OME$_n$ has higher NO_x but lower CO and HC concentrations. High amounts of aromatics, ethene, methane formaldehyde and formic acid are found within the diesel exhaust gas. The DME and OME$_n$ exhaust gas contains higher fractions of formaldehyde and formic acid, and fractions of methane, methyl formate and nitromethane.

1. Introduction

New types of synthetic fuels are being used in internal combustion engines to achieve carbon-neutral and ultra-low emission combustion. Dimethyl Ether (DME) and Polyoxymethylene Dimethyl Ethers (OME$_n$) belong to this type of synthetic fuels and can be produced by methanol synthesis [1–3]. Methanol synthesis can use green hydrogen from water electrolysis and carbon dioxide (CO_2), e.g., from the atmosphere, which makes it an outstanding technology to achieve the CO_2-targets of the Paris Agreement (2015) and the European Green Deal (2019) [4].

The performance of OME_1 and OME_{3-6} blends was studied by Pélerin et al. [5] and Härtl et al. [6] in a diesel engine. They showed that the higher oxygen and hydrogen content of OME_n (see Fig. 1) significantly reduces soot formation, while the NO_x emissions remain at the same level as for diesel. Increasing the exhaust gas recirculation (EGR) rate shows that soot formation with OME_n is less sensitive to EGR, so NO_x-soot tradeoff can be significantly improved. Operation with an OME_{3-6} blend was found to be advantageous because boiling temperature and viscosity are closer to diesel. Pastor et al. [7] conducted an optical study of conventional diesel, Fischer-Tropsch diesel and OME_n in a compression ignition (CI) engine. The results confirmed that OME_n has significantly lower soot concentrations compared to diesel and Fischer-Tropsch diesel.

DME and OME_n have a lower energy content compared to diesel, as shown in Fig. 1. The disadvantages of larger OME_n molecules in the mass-based energy content compared to DME are compensated in the volume-based energy content due to their higher density. Parravicini et al. [8] investigated the influence of different injection geometries on the combustion of diesel OME blends. They increased the number of nozzles with increasing OME content in the blend, to increase the fuel flow at constant rail pressure and constant injection duration. The results show faster diffusion-controlled combustion and a 5.7% reduction in specific fuel consumption compared to diesel operation.
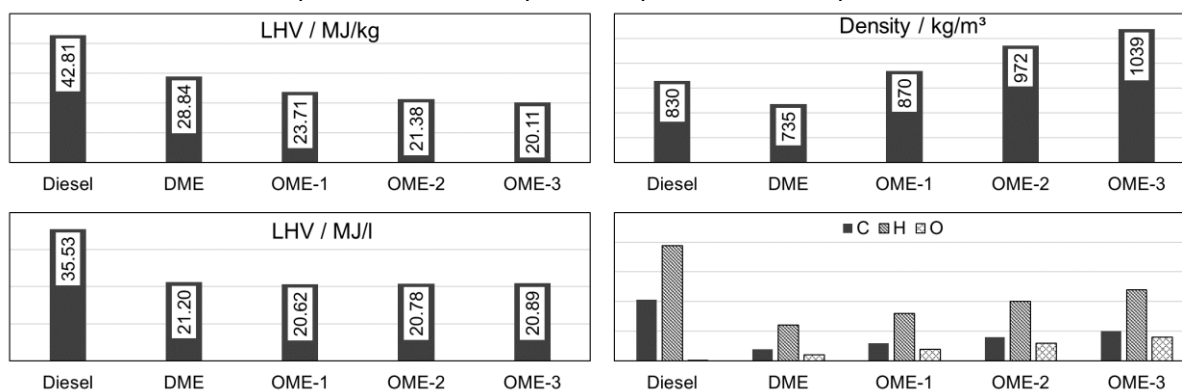
Fig. 1. Lower heating value on mass and volume basis, liquid density, and number of carbon, hydrogen, and oxygen atoms of Diesel, DME, OME_1, OME_2, OME_3.

Recently, Shrestha et al. [9] developed a new detailed chemical model for OME_n (n=1-3) to predict the ignition delay time, laminar flame speed and species formation for different thermodynamic conditions. The detailed chemical model is applied in the zero-dimensional (0D) stochastic reactor model (DI-SRM) to study the non-premixed combustion in a 2-liter diesel engine. In this work, further insight into the formation of unburned hydrocarbons (HC), carbon monoxide (CO), and nitrogen oxides (NO_x) during the combustion of diesel, DME and OME_{1-3} is obtained.

2. Methodology

2.1 Stochastic Reactor Model

The 0D modeling is based on a stochastic approach to predict the in-cylinder processes tailored to the simulation of direct-injection CI engines. The DI-SRM is part of the LOGEengine software [10] and the fundamentals are described in detail in the work of Kraft [11], Tunér [12] and Pasternak [13]. In the work of Franken et al. [14] and Nett et al. [15], the DI-SRM is further developed to predict changing operating conditions in diesel engines. An example for the application of the DI-SRM to predict the performance and emissions of a WLTP drive cycle is shown by Picerno et al. [16].

The DI-SRM is a 0D model of physical and chemical processes occurring during the combustion cycle. It is expressed within the probability density function (PDF) approach for turbulent reacting flows [17] that allows for the precise treatment of chemical reactions. The DI-SRM considers gas contained within the cylinder as an ensemble of notional particles. The notional particles can mix with each other and exchange heat with the cylinder walls. Each notional particle has a chemical composition, enthalpy, and mass that correspond to a point in the gas-phase. These scalars are treated as random variables quantified with probabilities and determine the composition of the gas mixture. Thus, the in-cylinder mixture is represented in gas-phase space by a PDF, and the notional particles are realizations of the distributions. The PDF transport equation provides the solution for scalars, enthalpy, and species mass fractions.

The scalar mixing frequency is the main input parameter for the DI-SRM. It must be modelled because the molecular mixing process cannot be directly calculated by the 0D model. In the current version of the SRM, the mixing frequency is derived from the K-k-based modeling of the turbulence as introduced previously [15].

2.2 Detailed Chemistry and Diesel Surrogate Model

The experiments are conducted for a commercial B7 diesel fuel containing 7 vol% fatty methyl ether (FAME). A three-component surrogate is developed for the simulation, consisting of 71.3 mass % n-decane, 21.3 mass % 1-methylnaphthalene and 7.4 mass % FAME. The 1-methylnaphthalene represents the aromatics portion and shows the strongest soot formation tendency. The comparison between the B7 diesel and the surrogate is shown in Table 1. The experimental cetane number (CN) is determined by the Cooperative Fuel Research (CFR) method and is about 1 point higher compared to the surrogate, which is a good match. Overall, the surrogate represents the main properties of a typical DIN EN 590 diesel fuel.

Table 1. B7 Diesel and surrogate properties

Property	Unit	B7 Diesel	Surrogate
Density	kg/l	0.831	0.83
LHV	MJ/kg	42.76	42.81
C:H:O Ratio	-	13.5:25.1:0.09	10.27:19.4:0.12
L_{st}	-	14.37	14.33
CN	-	54.4 (CFR)	53.5

The detailed chemistry model of the Diesel surrogate is based on the thesis of Wang [18] and contains the important NO$_x$ chemistry pathways based on the work of Shrestha [19] and soot formation pathways. The DME and OME$_{1-3}$ detailed chemistry model is recently developed in [9] based on the work of Shrestha et al. [20,21] and contains the important NO$_x$ chemistry pathways based on the work of Shrestha [19]. The performance of the two detailed chemistry models is shown in Fig. 2 by comparing the ignition delay times at 10bar and isochoric conditions for different air-fuel ratios (λ) and temperatures. For lean mixtures the reactivity of all fuels is reduced compared to stoichiometric mixtures. The Diesel surrogate and DME show a pronounced negative temperature coefficient (NTC) region, where DME ignition delay times are lower. For OME$_1$ the low temperature reactivity is reduced, while at high temperature it shows same reactivity as the Diesel surrogate. OME$_2$ and OME$_3$ show the highest reactivity at low and high temperature.
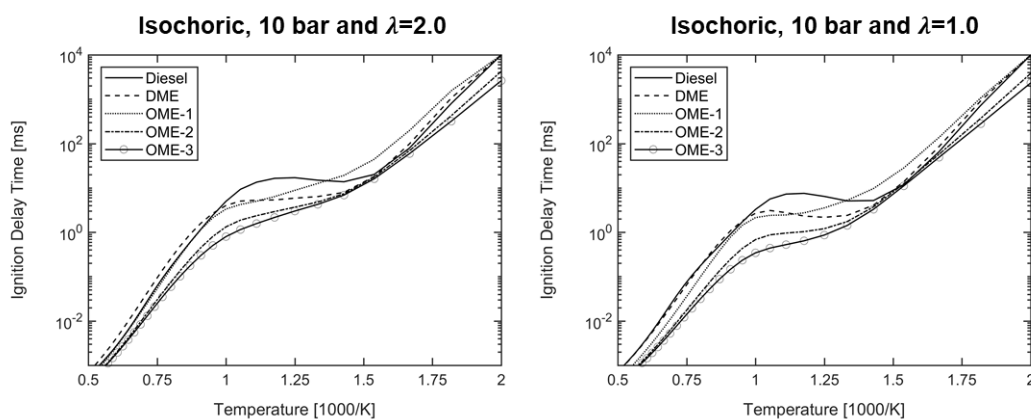
Fig. 2. Ignition delay time for Diesel surrogate, DME, OME$_1$, OME$_2$, and OME$_3$ at isochoric conditions, 10bar and different air-fuel ratio and temperature.

2.3 Thermophysical Property Model

Within the 0D domain of the DI-SRM no spray penetration is calculated, while the vaporization process is treated as a purely statistical process. Hence, no transport properties are required for conducting the simulation. The thermophysical properties of Diesel, DME and OME_{1-3} are represented by saturation temperature, saturation pressure and heat of vaporization. The properties of Diesel, DME, OME_1 and OME_2 are determined based on the NIST database [22] and the work of Himmel et al. [23]. The properties of OME_3 are determined based on the work of Fechter et al. [24]. The results are compared in Fig. 3 for all fuels. For DME the critical temperature is the lowest and the critical pressure is highest, wherefore it starts to vaporize earlier compared to OME_{1-3} and Diesel surrogate. For OME_1, OME_2 and OME_3 the critical temperature is increasing, while the critical pressure is decreasing, which delays the vaporization during the compression stroke. With increasing chain length of OME, the critical properties become closer to the Diesel surrogate. Further, DME shows the highest mass-based heat of vaporization, followed by OME_1, OME_2, OME_3 and Diesel surrogate.
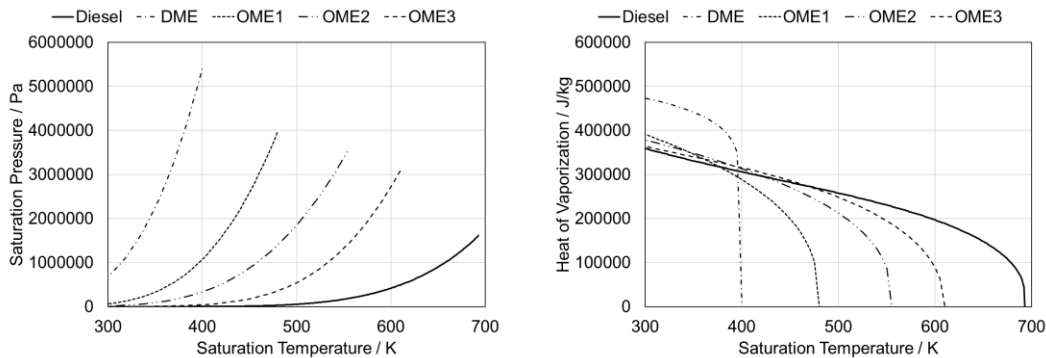
Fig. 3. Saturation temperature, saturation pressure and heat of vaporization of Diesel surrogate, DME, OME_1, OME_2, and OME_3.

3. Numerical Test Case

The experiments for Diesel and OME_{3-5} are conducted on a four-cylinder engine with the specifications outlined in Table 2. To ensure repeatability of results the parameters such as coolant temperature, oil temperature, fuel temperature and pressure, fuel backpressure, charge air temperature, fresh air temperature and pressure and exhaust backpressure are adjusted by their respective conditioning systems. Each cylinder is equipped with pressure transducers to analyze the in-cylinder combustion process, which is measured to a resolution of a tenth of degree crank angle. Exhaust gas analyzers are used to measure raw exhaust gas emissions. Measured CO_2 concentration in the intake manifold is used to estimate EGR rates. More details on the experimental setup and measurement devices can be found in the work of Lee et al. [25,26].

Table 2. Engine specifications.

Parameter	Unit	Value
Bore	mm	75.0
Stroke	mm	88.3
Displacement volume (4-cyl)	cm³	1999
Compression ratio	-	15.5

Four operating points are selected to validate the DI-SRM for Diesel and OME_{3-5} combustion (see Table 3). The operating points are selected at two load conditions at 4bar and 12bar IMEP and 1750rpm engine speed, which are representative for real driving conditions. Since the detailed chemistry model is only validated for OME_{1-3}, the experimental OME_{3-5} fuel mixture is approximated with OME_3 in the simulation.

Table 3. Diesel and OME_{3-5} engine load points.

	OP1-D	OP2-D	OP3-OME	OP4-OME
Fuel	Diesel	Diesel	OME_{3-5}	OME_{3-5}
IMEP [bar]	12.0	4.0	12.0	4.0
Speed [rpm]	1750	1750	1750	1750
CA50 [°CA aTDC]	10.0	9.2	12.0	10.7
Rail pressure [bar]	850	550	930	560
Rel. AFR [-]	1.3	2.0	1.8	2.0
EGR [%]	25.0	41.0	25.0	36.2

The injection rates for Diesel and OME_{3-5}, used for the DI-SRM simulation, are shown in Fig. 4. For Diesel and OME_{3-5} a triple injection strategy is applied, with two pilot injections and one main injection. The injection timings for OME_{3-5} are later compared to Diesel, and the injection duration is longer since more mass must be injected for OME_{3-5} due to the reduced lower heating value (see Fig. 1).
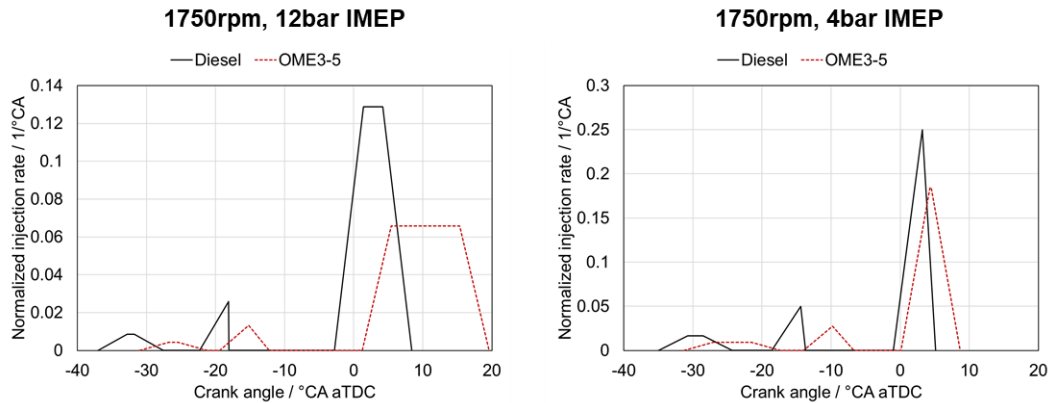
Fig. 4. Normalized injection rate by total injected mass for Diesel and OME_{3-5} at 1750rpm 12bar IMEP and 1750rpm 4bar IMEP.

4. Results and Discussion

4.1 Comparison of Experiment and Simulation for Diesel and OME_{3-5}

The DI-SRM model parameters are set according to the model training in the work of Picerno et al. [16] for the 2-liter diesel engine. Thus, it is possible to predict the effects of different chemical and thermophysical properties of the fuels on combustion and emission formation. The heat release rate, heat losses, and engine temperature of the experiments for diesel and OME_{3-5} are determined using a thermodynamic analysis in LOGEengine [10]. The results of the load point at 1750rpm and 12bar IMEP are shown in Fig. 5. The DI-SRM simulation accurately predicts the pilot and main heat release rates of diesel. For OME_{3-5}, the maximum pilot heat release rate is predicted to be too low, while the main heat release rate agrees. The compression stroke pressure of OME_{3-5} is higher compared to diesel because the air-fuel ratio is higher (see Table 3). Although the injection timing for OME_{3-5} is later compared to diesel, the pilot heat release rate is predicted to be slightly earlier due to faster vaporization and higher reactivity.
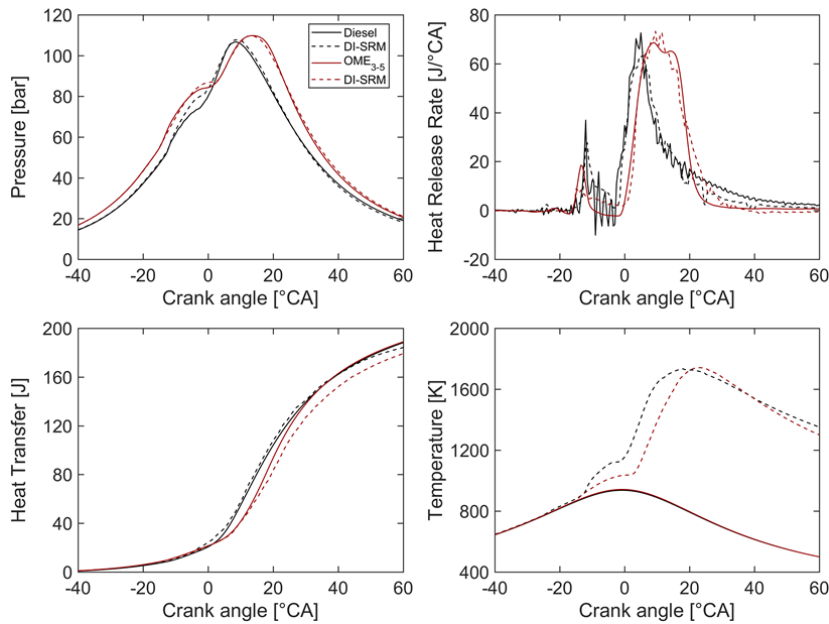
Fig. 5. Cylinder pressure, heat release rate, heat transfer and temperature for Diesel and OME$_{3-5}$ at 1750rpm 12bar IMEP.

The simulation for the load point at 1750 rpm and 4 bar IMEP and diesel in Fig. 6 shows a slight delay in the pilot stage and a delayed main heat release rate compared to the experiments. The experiments for OME$_{3-5}$ indicate a longer delay between the onset of injection and the onset of combustion, therefore more air-fuel mass is premixed, and more energy is spontaneously released when ignition occurs at -5°CA aTDC. The higher reactivity of the OME$_{3-5}$ surrogate results in earlier ignition in the simulation, which is why the air-fuel mixture has less time to premix and the amount of spontaneously released energy is lower for the second pilot injection at -5°CA aTDC. Apart from the differences in the pilot heat release rate, the simulation determines the main heat release rate of the OME$_{3-5}$ experiments to a very good approximation.
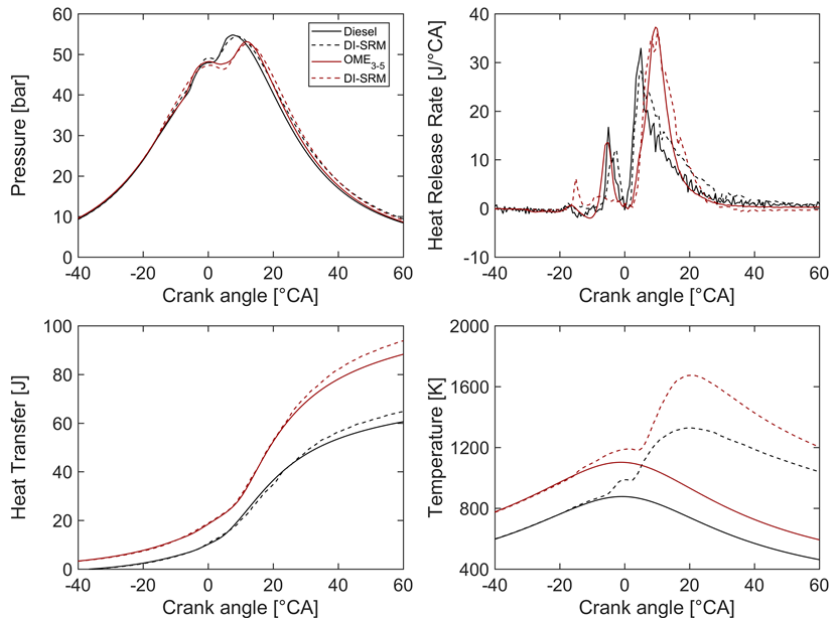
Fig. 6. Cylinder pressure, heat release rate, heat transfer and temperature for Diesel and OME$_{3-5}$ at 1750rpm 4bar IMEP.

The trend of calculated CO_2 emissions is consistent with the experiments, while OP1-D underestimates the experiment and OP4-OME slightly overestimates it (see Fig. 7). The opposite trend is observed for CO emissions, where OP1-D overestimates the experiment and OP4-OME underestimates it. The reason for the differences could be that the local mixture formation for the two operating points is not accurately predicted by the DI-SRM, leading to variations in the local air-fuel mixture and thus

different CO formation. The trends in NO$_x$ and unburned hydrocarbon (HC) emissions are captured by the DI-SRM, while the high HC emissions at low IMEP are underestimated by the DI-SRM. In general, the OME$_{3-5}$ surrogate tends to predict higher NO$_x$ emissions, while the highest concentration for OP3-OME cannot be predicted by the model. A likely cause for these differences is the use of OME$_3$ as a surrogate for the OME$_{3-5}$ mixture used in the experiment. However, this cannot be confirmed at this time because no validated chemical model is available for OME$_4$ and OME$_5$.
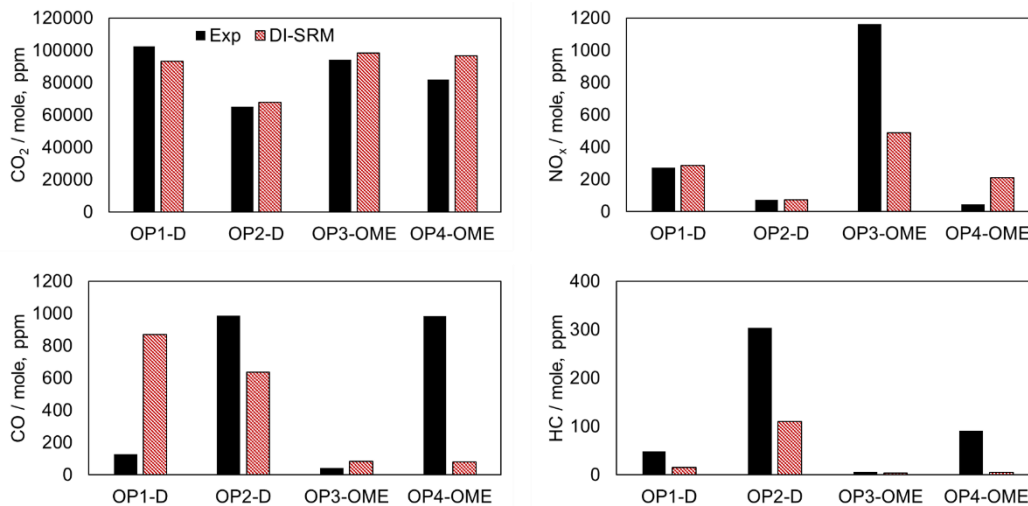
Fig. 7. Engine-out CO$_2$, NO$_x$, CO, and HC emissions on mole-basis for experiments and simulation for Diesel and OME$_{3-5}$.

4.2 Comparison of Diesel, DME, OME$_1$, OME$_2$ and OME$_3$

The operating points OP1-D and OP2-D are used as a starting point for the investigation of diesel, DME, OME$_1$, OME$_2$ and OME$_3$. The injection rate is set as a function of fuel mass and density, as shown in Fig. 8. The fuel mass is adjusted according to the LHV to obtain the same total energy (see Fig. 9). The ratio of pilot injection mass to total injection mass is kept the same for all fuels studied. Therefore, the pilot injection masses are increased for DME, OME$_1$, OME$_2$ and OME$_3$. The timing of pilot injection is earlier for DME, and OME$_{1-3}$ compared to diesel due to the longer injection duration.
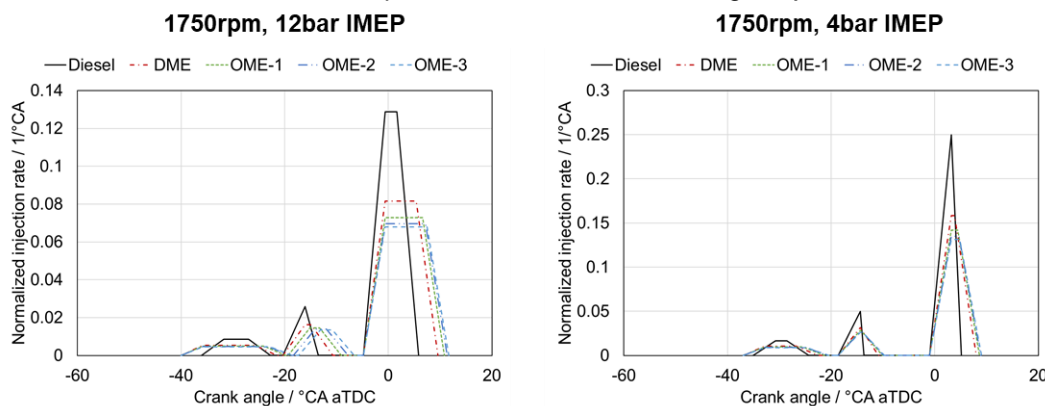
Fig. 8. Normalized injection rate for Diesel, DME, OME$_1$, OME$_{2,}$ and OME$_3$ at 1750rpm 12bar IMEP and 1750rpm 4bar IMEP.

For DME and OME$_1$, the start of combustion after pilot injection is delayed compared to diesel (see Fig. 9) due to the lower reactivity at low temperatures (see Fig. 2). For OME$_2$ and OME$_3$, combustion starts earlier due to higher reactivity compared to diesel (see Fig. 2). The onset of diffusion combustion during main injection is not significantly affected by the change in fuel, while the maximum heat release rate is increased for DME and OME$_{1-3}$ compared to diesel, and the combustion duration between 10% and 90% burned mass is decreased for DME and OME$_{1-3}$ compared to diesel. The faster combustion of DME and OME$_{1-3}$ results in higher heat losses and higher peak cylinder temperature. The temperature at the opening of the exhaust valve is lower for DME and OME$_{1-3}$ due to the earlier center of combustion and shorter combustion duration.
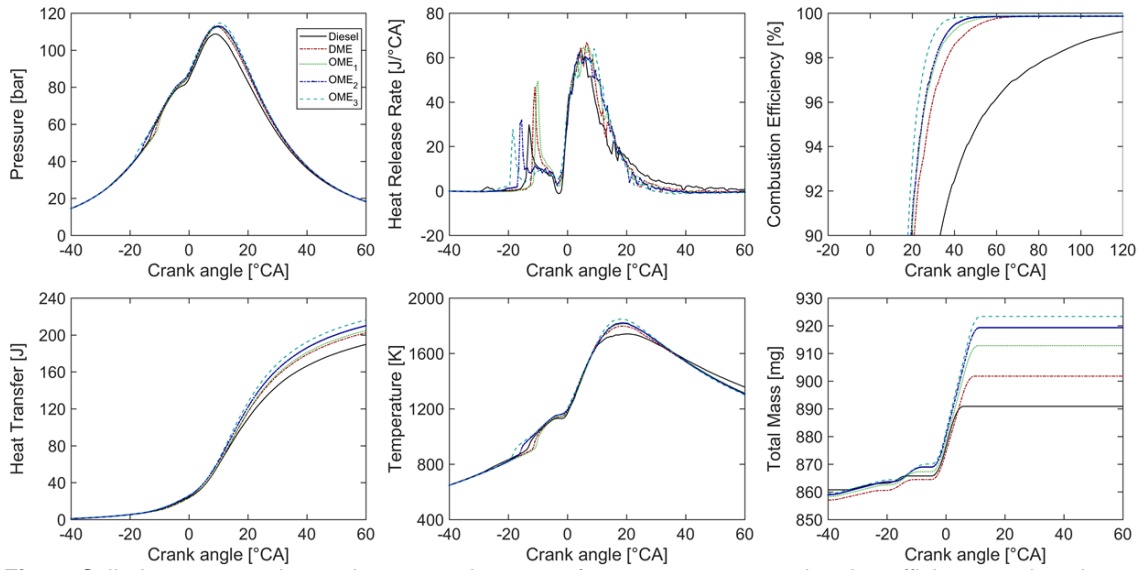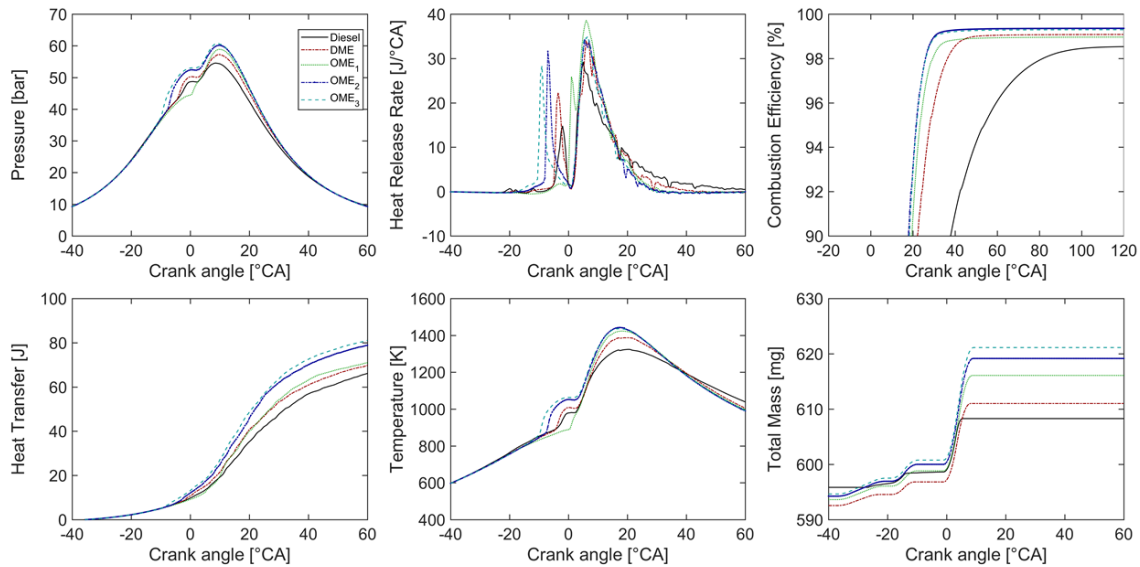
Fig. 9. Cylinder pressure, heat release rate, heat transfer, temperature, combustion efficiency and total mass for Diesel, DME, OME_1, OME_2 and OME_3 at 1750rpm 12bar IMEP.

The higher reactivity of DME and OME_{1-3} at medium and high temperatures is due to higher OH and HO_2 formation, as shown in Fig. 10. This leads to accelerated combustion, bringing the center of combustion forward and increasing the peak cylinder temperature. The higher cylinder temperature for OME_3, OME_2, OME_1 and DME results in a higher NO concentration compared to diesel. During combustion, OME_3 and OME_2 have a higher maximum NO_2 concentration. During the expansion stroke, the NO_2 concentration first decreases and increases again towards 120°CA aTDC, with diesel reaching the highest NO_2 concentration. The maximum CO and unburned HC concentrations are lower for DME, and OME_{1-3} compared to diesel due to the higher oxygen content in the fuel (see Fig. 1). Moreover, the combustion efficiency is higher for DME and OME_{1-3}, as shown in Fig. 9, and as also described by Omari et al. [27,28]. However, the maximum concentrations of oxygenated hydrocarbon (HCO) are higher for DME and OME_1 due to greater formation of formaldehyde and formic acid.
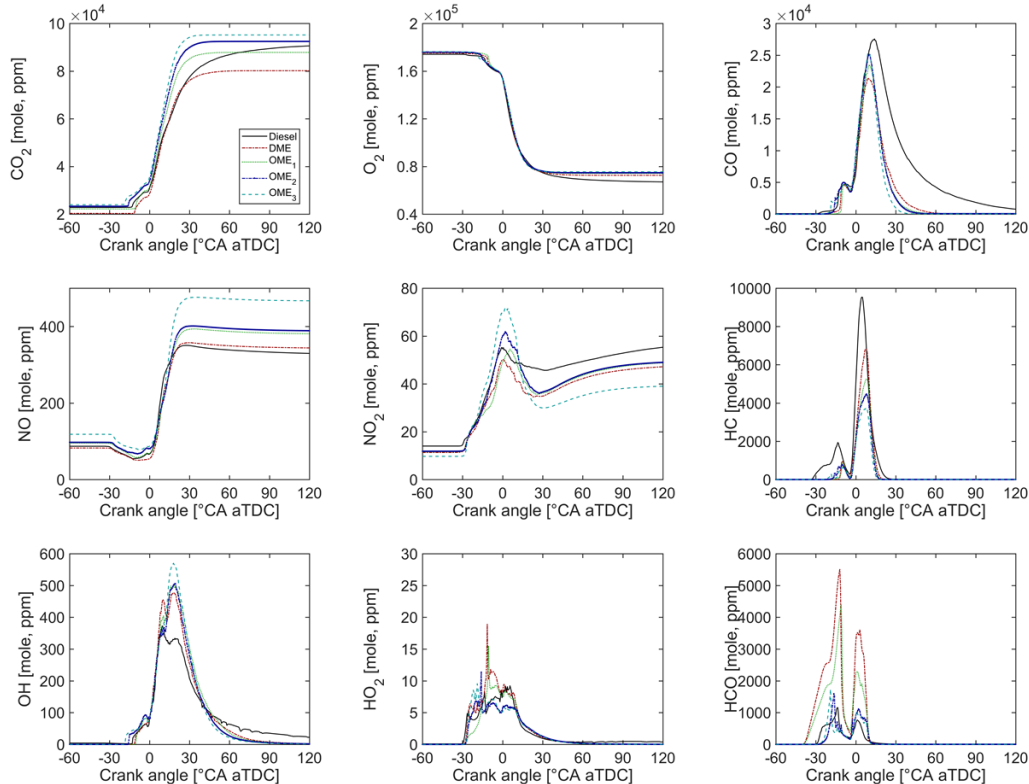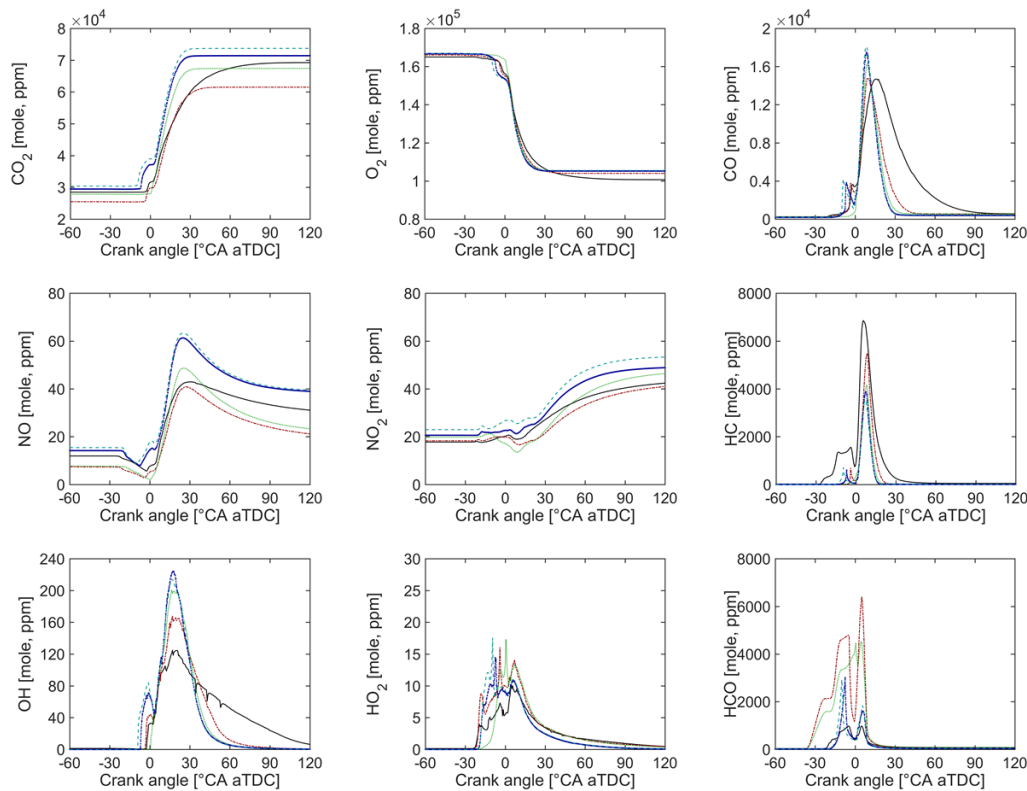

Fig. 10. Instantaneous emissions of CO_2, O_2, CO, NO, NO_2, HC, OH, HO_2 and HCO for Diesel, DME, OME_1, OME_2 and OME_3 at 1750rpm 12bar IMEP.

DME shows a late onset of combustion after pilot injection similar to diesel, while OME$_2$ and OME$_3$ are more advanced. The delayed onset of combustion after pilot injection of OME1 is most pronounced for the low-load operating point at 1750rpm 4bar IMEP (see Fig. 11). The maximum heat release rate is increased for DME, and OME$_{1-3}$ compared to diesel, and the combustion duration is shortened. OME$_1$ reaches the highest maximum heat release rate due to the strong premixed combustion. The peak pressure and peak temperature in the cylinder as well as the heat losses are higher for DME, OME$_1$, OME$_2$ and OME$_3$ compared to diesel.

Fig. 11. Cylinder pressure, heat release rate, heat transfer, temperature, combustion efficiency and total mass for Diesel, DME, OME$_1$, OME$_2$ and OME$_3$ at 1750rpm 4bar IMEP.

The high reactivity of DME and OME$_{1-3}$ compared to diesel is caused by a stronger formation of HO$_2$ and OH radicals as shown in Fig. 12. The increased cylinder temperature due to the faster combustion leads to an increase in the maximum NO concentrations. During the expansion stroke, NO is converted to NO$_2$, with OME$_3$ and OME$_2$ reaching the highest NO$_2$ concentrations at 120°CA aTDC. The maximum CO concentration is elevated for DME and OME$_{1-3}$ but is mostly re-oxidized during the expansion stroke. At 50°CA aTDC, CO oxidation is frozen, so CO concentration remains at a higher level and DME and OME$_{1-3}$ reach values similar to diesel at 120°CA aTDC. The maximum unburned HC emissions decrease, while the maximum unburned HCO emissions increase for DME and OME$_{1-3}$. The highest values of maximum unburned HCO emissions are obtained for DME and OME$_1$ due to a strong formation of formic acid and formaldehyde. At 120°CA aTDC, unburned HC emissions are highest for diesel and OME$_1$, while they decrease for DME, OME$_3$, and OME$_2$ (see Fig. 13). In addition, the combustion efficiency is lower at the low-load operating point compared to the high-load operating point, which is why larger proportions of unburned DME and OME$_1$ are found in the exhaust gas composition (see Fig. 11).

Fig. 12. Instantaneous emissions of CO_2, O_2, CO, NO, NO_2, HC, OH, HO_2 and HCO for Diesel, DME, OME_1, OME_2 and OME_3 at 1750rpm 4bar IMEP.

The composition of the unburned HC emissions is analyzed in more detail for the low-load operating point in Fig. 13. The exhaust gas composition in the cylinder is determined directly when the exhaust valves are opened and neglects post-oxidation in the exhaust manifold. The diesel exhaust shows a diverse composition with large amounts of formaldehyde (13.6%), ethene (12.2%), ethynylbenzene (15.0%), formic acid (12.3%), ketene* (12.1%), and methane (9.3%). The aromatic components are the result of the decomposition of 1-methylnaphthalene, which forms the aromatic moiety in the diesel surrogate (see Section 2.2). The oxygenated HC components are the result of the decomposition of FAME, which forms the biodiesel fraction in the surrogate. The exhaust gas from DME and OME_{1-3} consists of fewer components compared to diesel. The DME exhaust consists mainly of formic acid (32.5%), formaldehyde (21.7%), methane (16.1%), and unburned DME (18.1%). The high percentage of unburned DME is due to the low combustion efficiency at low-load operating points (see Fig. 11). In addition, small amounts of acrolein (7%) are present in the exhaust gas. Compared to DME, the exhaust gas composition of OME_1 contains a lower amount of formic acid (19.8%), while additional methyl formate (16.6%) and unburned OME_1 (10.8%) are present in the exhaust gas. Small amounts of methanol (2.9%), nitromethane (2.3%) and monomethyl ether (1.2%) are also present in the exhaust gas. Due to their higher combustion efficiency, OME_2 and OME_3 have the lowest overall unburned HC emissions compared to the other fuels. For OME_2, the amount of formic acid (32.8%), methyl formate (17.9%), and acrolein (10.8%) is increased compared to OME_1, while small amounts of nitromethane (2.5%) are present. For OME_3, a larger amount of methoxymethyl formate (10%) remains in the exhaust gas, while the amounts of methyl formate (13.8%) and acrolein (7.2%) are lower compared to OME_2. In addition, small amounts of nitromethane (2.4 %) and ketene* (2.1 %) are present in the exhaust gas from OME_3.

The investigation of soot formation is not part of this study due to the lack of a validated soot precursor chemistry for DME and OME_{1-3}. However, a brief analysis of the gas composition with respect to soot formation will be performed. Pastor et al. [29] used fast spectroscopy and 2-color pyrometry to investigate the soot propensity of diesel, OME_x, and diesel-OME_x blends. Diesel has the highest soot concentration, which can be attributed to the high content of aromatic components in the gas mixture. This study shows a high content of 1-methylnaphthalene and ethenylbenzene in the diesel exhaust as well, along with the soot formers ethene and acetylene. DME and OME_{1-3} do not have aromatic components in the gas composition, while the OH concentration is higher compared to diesel (see Fig. 12), which may promote soot oxidation. Schmitz et al. [30] report that the number of small soot nanoparticles increases in OME_{2-4} flames, and that the composition of these particles has oxygenated functionalities. They suggest that aldehydes are responsible for the formation of these functionalities and seek further

research in this area. Such a formation mechanism could also play an important role in this study, as DME and OME$_{1-3}$ have higher concentrations of formaldehyde in the gas composition.
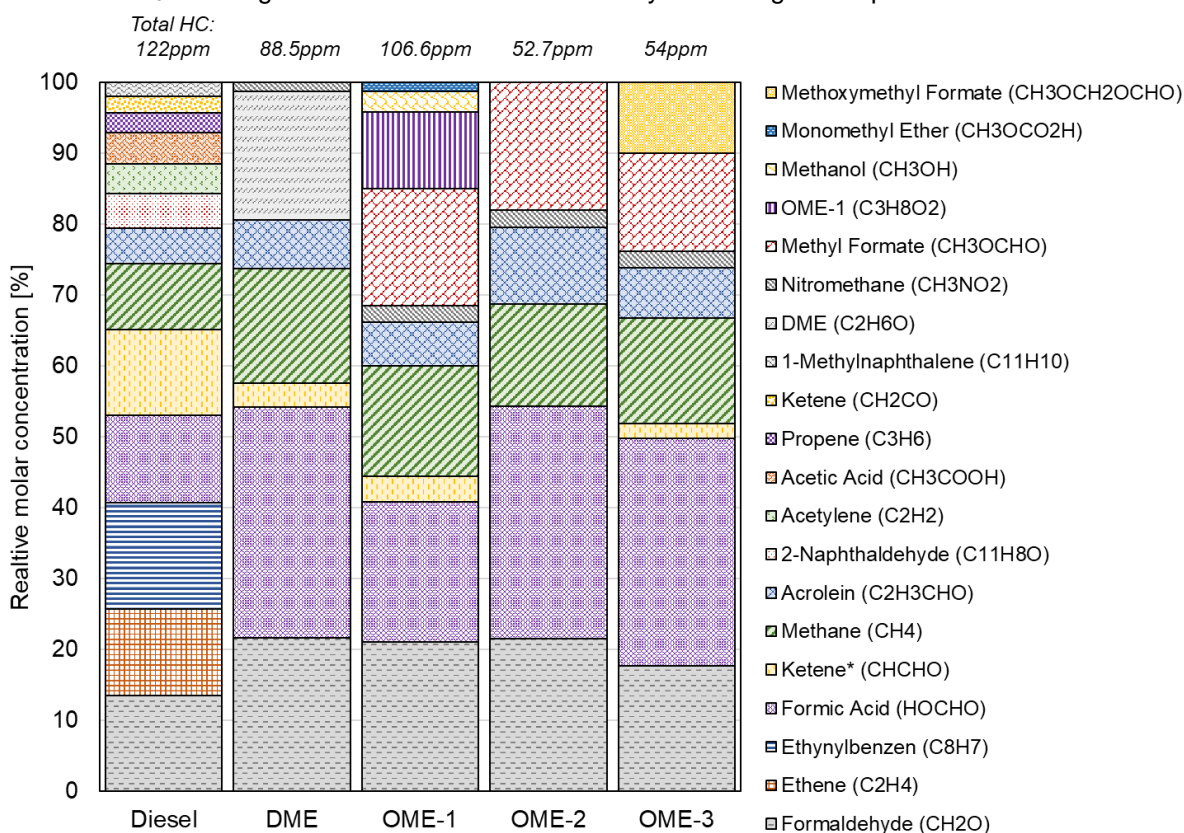
Fig. 13. Relative molar concentration of unburnt hydrocarbons for Diesel, DME, OME$_1$, OME$_2$ and OME$_3$ at 1750rpm 4bar IMEP. On top of the diagram the total HC emissions on mole basis are shown.

5. Conclusions

The combustion process and exhaust gas composition of diesel, DME and OME$_{1-3}$ are numerically investigated using the stochastic reactor model (DI-SRM) and a detailed chemistry model. The DI-SRM is validated using experiments for a 2.0-liter compression-ignition engine fueled by B7 diesel and OME$_{3-5}$. The model is able to accurately predict instantaneous cylinder pressure and heat release rate for various operating conditions and captures the pattern of CO$_2$ and NO$_x$ emissions in the engine. Larger deviations are found for CO and unburned HC emissions in the exhaust.

Finally, the DI-SRM with detailed chemistry is used to study the performance of DME and OME$_{1-3}$ in comparison to Diesel. The results are summarized as follows:
- DME and OME$_1$ show a lower reactivity at low temperature, wherefore start of combustion for pilot injection is delayed compared to Diesel.
- OME$_2$ and OME$_3$ show a higher reactivity at low and high temperature, wherefore start of combustion for pilot injection is advanced compared to Diesel.
- The maximum heat release rate is increasing, and the burn duration is decreasing for DME, OME$_1$, OME$_2$ and OME$_3$.
- The advanced combustion of DME and OME$_{1-3}$ leads to an increase of peak cylinder temperature, and consequently an increase of engine-out NO emissions.
- At high load operating conditions, the NO$_2$, CO and unburnt HC engine-out emissions are decreased for DME, and OME$_{1-3}$ compared to Diesel.
- At low load operating conditions, the NO$_2$ engine-out emissions are higher for OME$_{1-3}$ compared to Diesel and DME. The CO and unburnt HC emissions remain at higher concentrations for DME and OME$_1$ compared to OME$_2$ and OME$_3$.
- The unburnt HC composition of Diesel shows high fractions of formaldehyde (13.6%), ethene (12.2%), ethynylbenzen (15.0%), formic acid (12.3%), ketene* (12.1%) and methane (9.3%).

- The unburnt HC composition of DME shows high fractions of formic acid (32.5%), formaldehyde (21.7%), methane (16.1%) and unburnt DME (18.1%).
- For OME_{1-3} high fractions of formic acid (19.8 − 32.8%), formaldehyde (17.8 − 21.5%), methyl formate (13.8 − 17.9%), acrolein (6.2 − 10.8%) and nitromethane (~2.3%) are present in the exhaust gas.

References

[1]   J. Burger, M. Siegert, E. Ströfer, H. Hasse, Poly(oxymethylene) dimethyl ethers as components of tailored diesel fuel: Properties, synthesis and purification concepts, Fuel. 89 (2010) 3315–3319. https://doi.org/https://doi.org/10.1016/j.fuel.2010.05.014.

[2]   J. Burre, D. Bongartz, A. Mitsos, Production of oxymethylene dimethyl ethers from hydrogen and carbon dioxide—part II: modeling and analysis for OME3--5, Ind. \& Eng. Chem. Res. 58 (2019) 5567–5578.

[3]   S. Deutz, D. Bongartz, B. Heuser, A. Kätelhön, L.S. Langenhorst, A. Omari, M. Walters, J. Klankermayer, W. Leitner, A. Mitsos, others, Cleaner production of cleaner fuels: wind-to-wheel--environmental assessment of CO 2-based oxymethylene ether as a drop-in fuel, Energy \& Environ. Sci. 11 (2018) 331–343.

[4]   E. Commission, European Green Deal, (n.d.). https://ec.europa.eu/info/strategy/priorities-2019-2024/european-green-deal_de.

[5]   D. Pélerin, K. Gaukel, M. Härtl, E. Jacob, G. Wachtmeister, Potentials to simplify the engine system using the alternative diesel fuels oxymethylene ether OME1 and OME3−6 on a heavy-duty engine, Fuel. 259 (2020) 116231. https://doi.org/https://doi.org/10.1016/j.fuel.2019.116231.

[6]   M. Härtl, P. Seidenspinner, E. Jacob, G. Wachtmeister, Oxygenate screening on a heavy-duty diesel engine and emission characteristics of highly oxygenated oxymethylene ether fuel OME1, Fuel. 153 (2015) 328–335. https://doi.org/https://doi.org/10.1016/j.fuel.2015.03.012.

[7]   J. V Pastor, A. García, C. Micó, F. Lewiski, An optical investigation of Fischer-Tropsch diesel and Oxymethylene dimethyl ether impact on combustion process for CI engines, Appl. Energy. 260 (2020) 114238. https://doi.org/https://doi.org/10.1016/j.apenergy.2019.114238.

[8]   M. Parravicini, C. Barro, K. Boulouchos, Compensation for the differences in LHV of diesel-OME blends by using injector nozzles with different number of holes: Emissions and combustion, Fuel. 259 (2020) 116166. https://doi.org/https://doi.org/10.1016/j.fuel.2019.116166.

[9]   K.P. Shrestha, S. Eckart, S. Drost, C. Fritsche, R. Schießl, L. Seidel, U. Maas, H. Krause, F. Mauss, A comprehensive kinetic modeling of oxymethylene ethers (OMEn, n=1-3) oxidation - laminar flame speed and ignition delay time measurements, Combust. Flame - To Be Publ. (2022).

[10]   LOGEsoft, Manual: LOGE engine v3.0, (2015). www.logesoft.com.

[11]   M. Kraft, Stochastic Modeling of Turbulent Reacting Flow in Chemical Engineering, VDI-Verlag, 1998.

[12]   M. Tunér, Stochastic Reactor Models for Engine Simulations, Lund University, 2008.

[13]   M. Pasternak, Simulation of the diesel engine combustion process using the stochastic reactor model, Logos Verlag Berlin, 2016.

[14]   T. Franken, A. Sommerhoff, W. Willems, A. Matrisciano, H. Lehtiniemi, A. Borg, C. Netzer, F. Mauss, Advanced Predictive Diesel Combustion Simulation Using Turbulence Model and Stochastic Reactor Model, SAE Tech. Pap. 2017-March (2017). https://doi.org/10.4271/2017-01-0516.

[15]   O. Nett, M. Pasternak, Q. Yang, F. Mauss, M. Bargende, T. Franken, M. Grill, M. Diezemann, Simulations of combustion and emissions formation in a diesel engine with variable valve actuation, (2020). https://doi.org/10.14279/depositonce-9822.

[16]   M. Picerno, S.Y. Lee, M. Pasternak, R. Siddareddy, T. Franken, F. Mauss, J. Andert, Real-Time Emission Prediction with Detailed Chemistry under Transient Conditions for Hardware-in-the-Loop Simulations, Energies 2022, Vol. 15, Page 261. 15 (2021) 261. https://doi.org/10.3390/EN15010261.

[17]   S.B. Pope, PDF methods for turbulent reactive flows, Prog. Energy Combust. Sci. 11 (1985) 119–192.

[18]   X. Wang, Kinetic mechanism of surrogates for biodiesel, BTU Cottbus-Senftenberg, 2017.

[19]   K.P. Shrestha, Detailed kinetic modeling of ammonia combustion, BTU Cottbus-Senftenberg, 2021.

[20]   K.P. Shrestha, S. Eckart, A.M. Elbaz, B.R. Giri, C. Fritsche, L. Seidel, W.L. Roberts, H. Krause, F. Mauss, A comprehensive kinetic model for dimethyl ether and dimethoxymethane oxidation and NOx interaction utilizing experimental laminar flame speed measurements at elevated pressure and temperature, Combust. Flame. 218 (2020) 57–74. https://doi.org/10.1016/j.combustflame.2020.04.016.

[21]   K.P. Shrestha, B.R. Giri, L. Seidel, A. Farooq, F. Mauss, A Kinetic Modeling Study for the Effect of NOx on Oxymethylene ethers (OMEn, n= 0 and 1) oxidation, in: 10th Eur. Combust. Meet., 2021.

[22]   E.W. Lemmon, I.H. Bell, M.L. Huber, M.O. McLinden, NIST Standard Reference Database 23: Reference Fluid Thermodynamic and Transport Properties-REFPROP, Version 10.0, National Institute of Standards and Technology, Stand. Ref. Data Program, Gaithersbg. (2018).

[23]   D. Himmel, R.J. White, E. Jacob, I. Krossing, Highly correlated ab initio thermodynamics of oxymethylene dimethyl ethers (OME): formation and extension to the liquid phase, Sustain. Energy \& Fuels. 1 (2017) 1177–1183.

[24]   M. H. H. Fechter, P. Haspel, C. Hasse, A.S. Braeuer, Vapor pressures and latent heats of vaporization of Poly(oxymethylene) Dimethyl Ethers (OME3 and OME4) up to the vicinity of the critical temperature, Fuel. 303 (2021) 121274. https://doi.org/https://doi.org/10.1016/j.fuel.2021.121274.

[25]   S.-Y. Lee, J. Andert, D. Neumann, C. Querel, T. Scheel, S. Aktas, M. Miccio, J. Schaub, M. Koetter, M. Ehrly, Hardware-in-the-Loop-Based Virtual Calibration Approach to Meet Real Driving Emissions Requirements, SAE Int. J. Engines. 11 (2018) 1479–1504. https://doi.org/https://doi.org/10.4271/2018-01-0869.

[26]   S.-Y. Lee, J. Andert, S. Pischinger, M. Ehrly, J. Schaub, M. Koetter, A.S. Ayhan, Scalable Mean Value Modeling for Real-Time Engine Simulations with Improved Consistency and Adaptability, in: WCX SAE World Congr. Exp., SAE International, 2019. https://doi.org/https://doi.org/10.4271/2019-01-0195.

[27]   A. Omari, B. Heuser, S. Pischinger, C. Rüdinger, Potential of long-chain oxymethylene ether and oxymethylene ether-diesel blends for ultra-low emission engines, Appl. Energy. 239 (2019) 1242–1249. https://doi.org/https://doi.org/10.1016/j.apenergy.2019.02.035.

[28]   A. Omari, B. Heuser, S. Pischinger, Potential of oxymethylenether-diesel blends for ultra-low emission engines, Fuel. 209 (2017) 232–237. https://doi.org/https://doi.org/10.1016/j.fuel.2017.07.107.

[29]   J. V. Pastor, A. García, C. Micó, F. Lewiski, Simultaneous high-speed spectroscopy and 2-color pyrometry analysis in an optical compression ignition engine fueled with OMEX-diesel blends, Combust. Flame. 230 (2021) 111437. https://doi.org/10.1016/J.COMBUSTFLAME.2021.111437.

[30]   R. Schmitz, C. Russo, F. Ferraro, B. Apicella, C. Hasse, M. Sirignano, Effect of oxymethylene ether-2-3-4 (OME2-4) on soot particle formation and chemical features, Fuel. 324 (2022) 124617. https://doi.org/10.1016/J.FUEL.2022.124617.

Influence of Fuel Bound Oxygen on Soot Mass and Polyaromatic Hydrocarbons during Pyrolysis of Ethanol, Methyl Acetate, Acetone and Diethyl Ether

Z.A. Khan[1*], P. Hellier[1], N. Ladommatos[1], A.A. Almaleki[2]

[1]Department of Mechanical Engineering, University College London, Torrington Place, London, WC1E 7JE, UK

[2]King Abdulaziz City for Science and Technology, Riyadh, Saudi Arabia

*Corresponding author
 Email: zuhaib.khan.17@ucl.ac.uk (Zuhaib Khan)
Telephone: +(44) 07405691444

Abstract. Air pollution has reached critical levels in many major industrial cities, endangering public health, deteriorating the environment, and causing harm to property and landscape. The particulate emissions (PM) from propulsion which contribute to air pollution vary greatly in size and composition, conveying carcinogenic polyaromatic hydrocarbons (PAHs) present on the particle surface. Although it has been found that replacing fossil fuels with renewable oxygen-bearing fuels reduces the mass of PM released, not much is known on how this change in fuel composition affects soot levels, PAH production, and toxicity during the pyrolysis processes that occur in combustion engines. Biofuels such as alcohols, esters, ethers, and ketones are considered to be potentially sustainable alternatives fuels and can be produced by various biological and thermochemical processes from a range of renewable feedstocks. The effects of these oxygenated functional groups on the soot mass and PAHs produced during pyrolysis in a laminar flow reactor were investigated quantitatively in this study. The 16 PAHs identified as priority pollutants by the US Environmental Protection Agency (EPA) were investigated in this research, with particular focus on the probable mechanisms for production of the most carcinogenic PAHs (group B). The oxygenated fuels were pyrolyzed at temperatures ranging from 1050 to 1350 ^{0}C under oxygen-free conditions with a constant carbon atom content in nitrogen of 10,000 ppm and at a consistent residence period. Both soot bound PAH collected on filter papers and gaseous PAHs collected on XAD resin were extracted using accelerated solvent extraction (ASE), with PAH identification and quantification carried out using gas chromatography combined with mass spectroscopy (GCMS). An effect of the oxygenated functional groups on soot mass was readily apparent, with consistently lower production of soot by methyl acetate, and which has a higher oxygen to carbon ratio than ethanol, acetone, and diethyl ether. At all temperatures except 1350 ^{0}C, methyl acetate pyrolysis yielded much lower GP PAH levels than acetone and diethyl ether, but somewhat higher than that from ethanol pyrolysis. The concentration of PP PAH per unit volume of gas is much lower than the corresponding GP PAH, which suggests that PP PAH that condensed onto particulate surface, subsequently experienced surface reaction and were therefore not recoverable during the extraction process. The production of pyrene via acenaphthylene was found to dominate at higher temperatures for all fuels, regardless of molecular structure. At 1150 ^{0}C the relative abundance of the soot particles was low, however, the toxicity of the soot particles formed was substantially higher at lower temperatures, particularly in the case of pyrolysis of methyl acetate soot.

1   Introduction

Air pollution due to combustion process has reached critical levels in many major industrial cities, endangering public health and deteriorating the environment. The particulate emissions (PM) from combustion which contribute to air pollution vary greatly in size and composition, conveying carcinogenic polyaromatic hydrocarbons (PAHs) present on the particle surface. The resultant toxicity of particulate matter from internal combustion engines is therefore a topic of significant scientific and practical importance in the development of sustainable low emission propulsion systems. It is widely accepted that it is the presence of adsorbed PAHs on the surface of soot which are primarily responsible for the toxicity of these particles [1]. The link between polyaromatic hydrocarbons (PAHs) and soot generation has long been known, with PAHs being regarded as the primary soot precursors. Following the development of single aromatic rings, the rings expand into larger polyaromatic hydrocarbons and finally produce soot particles by a variety of processes.

Biofuels such as alcohols, esters, ethers, and ketones are regarded as possible sustainable alternative fuels since they can be produced from a range of potentially renewable feedstocks that can

be found all over the world. [2–6]. The combustion characteristics of biofuels containing oxygen in various forms, such as ethanol, methyl acetate, acetone, and diethyl ether, have been investigated in several experimental and numerical investigations. Ethanol and its blends with other fuels have been previously studied in different combustion systems, such as tube reactors, flames, and IC engines [7–13]. From these studies, it can be concluded that the addition of ethanol to fossil fuel suppressed the sooting tendency and PAHs formation. In recent years, Diethyl ether (DEE) has gathered the attention of many researchers as a potential alternative fuel as, unlike dimethyl ether, DEE is liquid at ambient temperature and thus relatively easy to store [14–16]. In the literature, several studies reported the use of DEE as a pure fuel or diesel additive in compression ignition engines and numerical simulation [14,15,17]. Long chain methyl ketones have been proposed as a possible alternative fuel as these exhibit relatively high cetane numbers. The simplest and the shortest methyl ketone is acetone, also known as dimethyl ketone and has potential as a renewable oxygenated fuel due to latent heat of vaporization similar to that of gasoline, addressing the issue of poor cold start behaviour of SI engines when utilising bioethanol, which has a higher heat of vaporization. The use of acetone in a spark-ignition engine has been reported in the literature [5,6,18], while Wu et al., 2015 [19] reported the effect of acetone fraction in acetone-butanol-ethanol-diesel blends and found that a high percentage of acetone reduced the mass of soot emitted and improved thermal efficiency. In recent years, methyl acetate and ethyl acetate have emerged as competitive alternative fuels as they are non-toxic, less volatile, easy handling, and low production cost as compared to alcohols and ethers. Furthermore, methyl and ethyl acetates have been found not to produce toxic emissions like aldehydes, ketones, and carbon monoxide due to a high proportion of carbon bonded to oxygen within the fuel [20,21]. Methyl acetate could also be used as potential biodiesel additive reducing viscosity [2].

While renewable fuels of various oxygenated functional groups have received interest for the potential of these to displace fossil fuel use, it remains unknown how the presence of oxygen impacts on PAH development during pyrolysis and thus the toxicity emitted particles. Therefore, four distinct oxygenated fuels, ethanol, methyl acetate, acetone and di-ethyl ether have been investigated in this study to increase knowledge of the impact of oxygenated fuel functional groups on soot and PAH production and relative toxicity.

2   Experimental methodology

2.1   Experimental setup and conditions

The high temperature flow reactor facility used in this study has been previously described in detail [22–25], therefore only a short explanation is provided. The laminar flow reactor tube used was electrically heated and vertically positioned with a tube length of 1440 mm and an inner diameter of 104 mm. The selected fuels were premixed with a heated nitrogen stream and pyrolyzed at temperatures ranging from 1050 to 1350 ^{0}C at atmospheric pressure. The fuel inlet concentration was fixed at 10,000 ppm based on a per carbon atom within the fuel. Pure nitrogen was used as a carrier gas with a fixed flow rate of 20 l/min. The soot and gaseous PAHs formed during the pyrolysis of oxygenated fuels were collected on a 70 mm glass microfibre filter paper and XAD-2 resin, respectively. The liquid fuel supply lines, soot and XAD-2 resin sample collection, and reactor tube temperature profiling have all been detailed in great detail before [22,23,25]. A gas residence time for all experiments of t(s) = 4479/T was, and is defined as the ratio of reactor volume to gas flow at a certain temperature.

Particle and gas phases PAHs collected on the filter paper and XAD-2 resin were extracted with dichloromethane using an accelerated solvent extractor (ASE). The extraction process was repeated sequentially three times for each filter paper and resin, yielding a total of 60 ml extract which was subsequently placed on a heated block maintained at 40°C, with pure nitrogen blown over the top of the extraction vial to concentrate the extract to initially 15 ml and finally 1 ml.

The gas chromatography mass spectrometry (GC-MS) method used for the analysis of particulate and gas-phase PAHs has been detailed previously[22]. PAHs were quantified using the EPA Method TO-3A [26], with each of the 16 PAHs allocated to one or more of the deuterated PAHs in the internal standard. The tube reactor utilised in all of the tests is shown schematically in **Fig. 1**, replete with gaseous and liquid fuel supply lines and also sample paths for soot and XAD-2 resin collection.
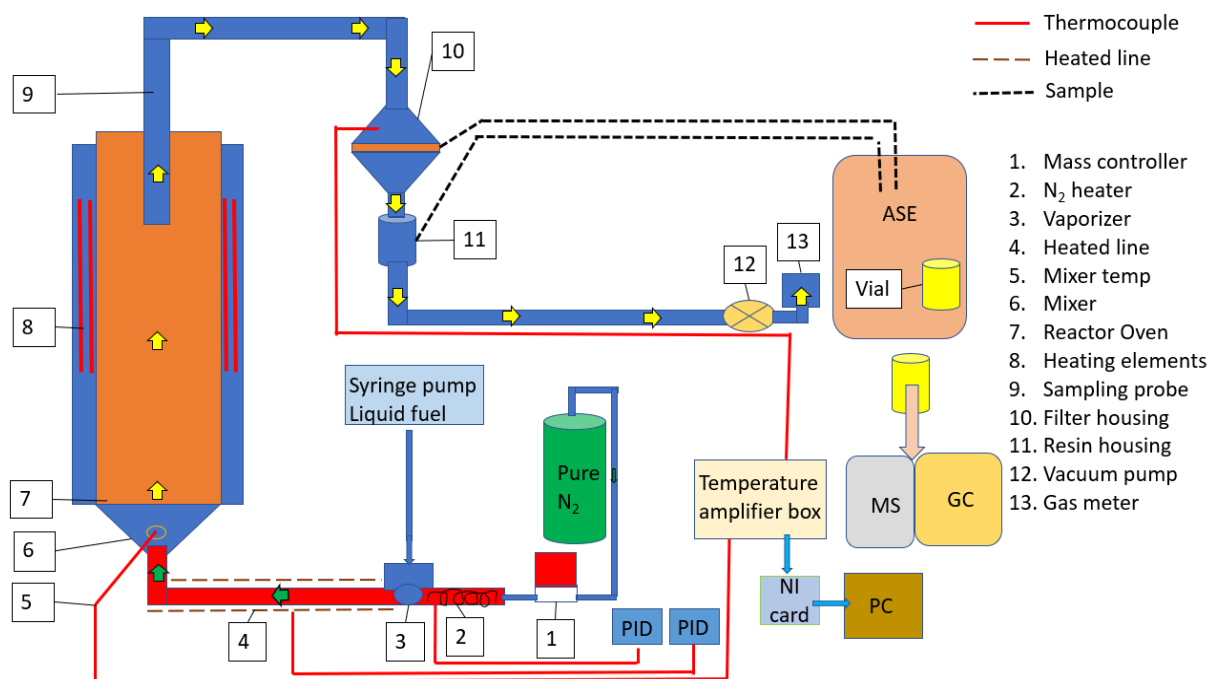
Fig. 1. Schematic diagram of laminar flow tube reactor facility

2.2   Fuels investigated

Ethanol, methyl acetate, acetone, and diethyl ether fuels were all obtained from Sigma Aldrich, at a purity of 99.6 % certified AR grade with the properties of each shown in **Table 1**. **Fig. 2** shows the molecular structure of each of the tests fuels.

Table 1. Tested oxygenated fuels and their properties [27,28]

Fuel	Molecular structure	Oxygen to carbon ratio	Molar mass (g/mol)	Density (Kg/m^3) at 25 $^\circ$C	Boiling point ($^\circ$C)
Ethanol	C$_2$H$_5$OH	0.5	46.07	789	78.37
Methyl acetate	CH$_3$COOCH$_3$	0.66	74.08	934	57.1
Acetone	(CH$_3$)$_2$CO	0.33	58.08	791	56
Diethyl ether	(C$_2$H$_5$)$_2$O	0.25	74.12	706	34.6
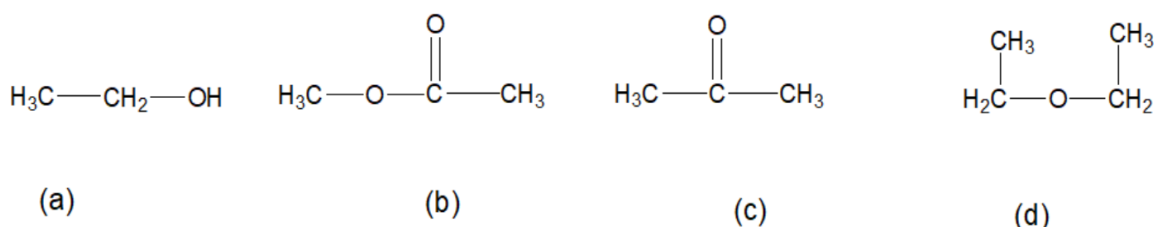
Fig. 2. Fuel molecular structure of (a) Ethanol, (b) Methyl acetate, (c) Acetone, and (d) Diethyl ether

The test fuels were selected so as to provide insight and understanding as to the following during pyrolysis:

- The influence of oxygen to carbon bond types and functional group within a fuel on soot and PAH formation.
- Consideration of the possible mechanisms that lead to individual PAH growth and the formation of the most toxic PAHs in the case of short chain oxygenates.

3   Results and discussion

3.1   Effect of oxygenated fuel on soot mass

The mass of soot extracted from the oxygenated fuels is depicted in **Fig. 3** at various temperatures, where the mass of soot extracted from the filter was normalised with the total volume of gas to have flowed through the filter during sampling. For determining experimental reproducibility, ethanol was employed as the reference fuel, with five repeat collections of soot mass and PAHs obtained. Where error bars are given in Figure 3, and subsequent figures, these show plus and minus one standard deviation from the mean value.

Fig. 3 shows that with the increase in the temperature of the tube reactor from 1050 to 1250°C, the mass of soot produced increased and subsequently decreased marginally at 1350°C for all fuels tested. This increase in the soot mass concentration with increasing temperature is in agreement with previous studies of various short chain hydrocarbon and alcohol fuels [7,10,22,23]. It is evident from **Fig. 3** that, compared to methyl acetate and ethanol, the pyrolysis of acetone and diethyl ether fuels produced a significantly greater soot mass, especially so at the lowest temperature at which soot was observed of 1150 °C. Methyl acetate produced the least mass of soot of all fuels tested and at all temperatures. It is to important to note that methyl acetate contains one more oxygen than the other fuels tested (**Fig. 2**), as in the functional group of methyl acetate, a single carbon atom is attached to two oxygen atoms by a double bond and a single bond respectively. The carbon-oxygen double bond is very strong, and difficult to break [29], therefore, in the context of soot formation, it is important to understand whether the single-bonded oxygen atom will also remain bonded to the same carbon atom.
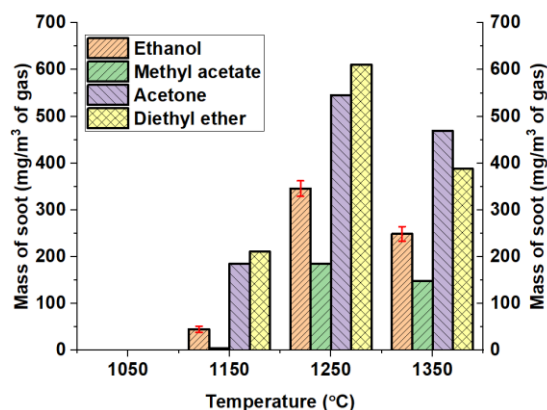
Fig. 3. Mass of soot collected during pyrolysis of oxygenated fuels at a temperature range of 1050 to 1350°C. The error bars denote standard deviation.

Fig. 4 shows two possible decomposition pathways of methyl acetate. Osswald et al. (2007) [30] suggested that ketene formation is more a prominent pathway for direct fuel decomposition. In this case, the carbon-oxygen double bond breaks, resulting in two of the three carbon atoms present
remaining bonded to two different oxygens. Assuming that these two carbon to oxygen bonds do not subsequently break, these two carbon atoms might be considered reserved by the oxygen to which they are bonded and thus unable to participate in soot formation, reducing the overall soot tendency of methyl acetate. The methoxy radical upon unimolecular decomposition forms formaldehyde, which upon further dehydrogenation produces CO [31]. It has been also reported that the thermal decomposition of ketene produces allene and carbon dioxide, with the former further decomposing to methylene and acetylene [32].

Another possible explanation for the low mass of soot produced by methyl acetate might be the higher oxygen to carbon ratio, in a scenario whereby the carbon to oxygen bonds break the resulting free oxygen may subsequently oxidize intermediate species or soot, resulting in a higher concentration of CO and CO_2, thus reducing the carbon availability for soot formation. From **Fig. 3**, comparing the C3 oxygenated fuels, it can be seen that acetone produced a relatively higher mass of soot as compared to methyl acetate. This might be attributable to the low carbon to oxygen ratio for acetone as compared to methyl acetate.
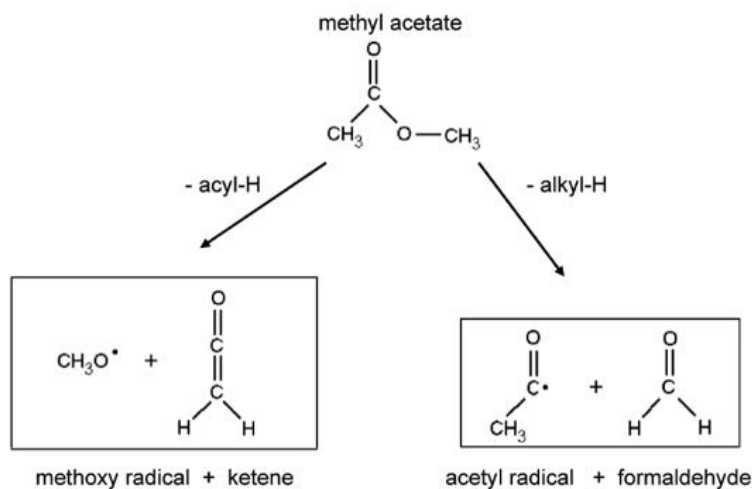
Fig. 4. Methyl Acetate fuel destruction pathways (Osswald et al., 2007 [30])

Agafonov et al. (2019) [33] studied experimentally, and through detailed simulation, the influence of acetone and propane on soot formation during pyrolysis in an acetylene flame behind a reflected shock wave, reporting that the thermal decomposition of acetone produced two methyl radicals and CO. This observation suggested that in acetone only one carbon atom is reserved and prevented from taking part in soot formation. The observed sooting propensity of acetone is in agreement with the study by Agafonov et al. (2019). The methyl radicals could be further consumed by first forming ethane molecules, before decomposition to form acetylene by the following reaction sequence (Eq 1):

$$2CH_3 \rightarrow C_2H_6 \rightarrow C_2H_5 \rightarrow C_2H_4 \rightarrow C_2H_3 \rightarrow C_2H_2. \tag{1}$$
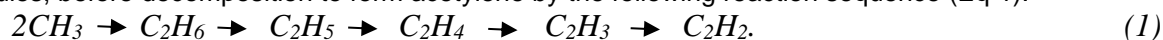
Fig. 3 shows that Diethyl ether formed the highest mass of soot of the four oxygenated fuels at 1150°C and 1250°C. In the functional group of diethyl ether, the oxygen atom is attached to two carbon atoms. It has been reported that the thermal decomposition of diethyl ether produces species including carbon monoxide, methane, ethylene, and acetaldehyde, with the two hydrocarbons able to undergo a progressive dehydrogenation to form soot [34]. Acetaldehyde could also potentially generate methyl radicals which could be consumed via ethane to form acetylene (Eq 1), an important soot precursor.

Fig. 3 shows that ethanol produced the second lowest mass of soot, after methyl acetate, at all temperatures. This can likely be attributed to ethanol possessing the second highest oxygen to carbon ratio (**Table 1**), potentially resulting in a higher concentration of CO and CO_2 as compared to acetone and diethyl ether. A further explanation for low soot mass formed during ethanol is that the C-O bond has been found to remain intact in a majority of instances under similar conditions, reserving a carbon atom and reducing the number available for soot formation [25].

The observed soot propensity trend of Ether> Ketone>Alcohol>Ester is in agreement with studies of the same functional groups during shock tube and jet flames experiments [35–37]. Furthermore, this is the first study to have observed the same trend of sooting tendency under purely pyrolytic conditions.

3.1.1 Effect of oxygenated fuel on gas-phase (GP) and particle-phase (PP) PAHs

Fig. 5 shows the total PAH measured (sum of the 16 US EPA priority PAH speciated) during pyrolysis of ethanol, methyl acetate, acetone, and diethyl ether at varying temperatures, collected from both gas and particle phases.
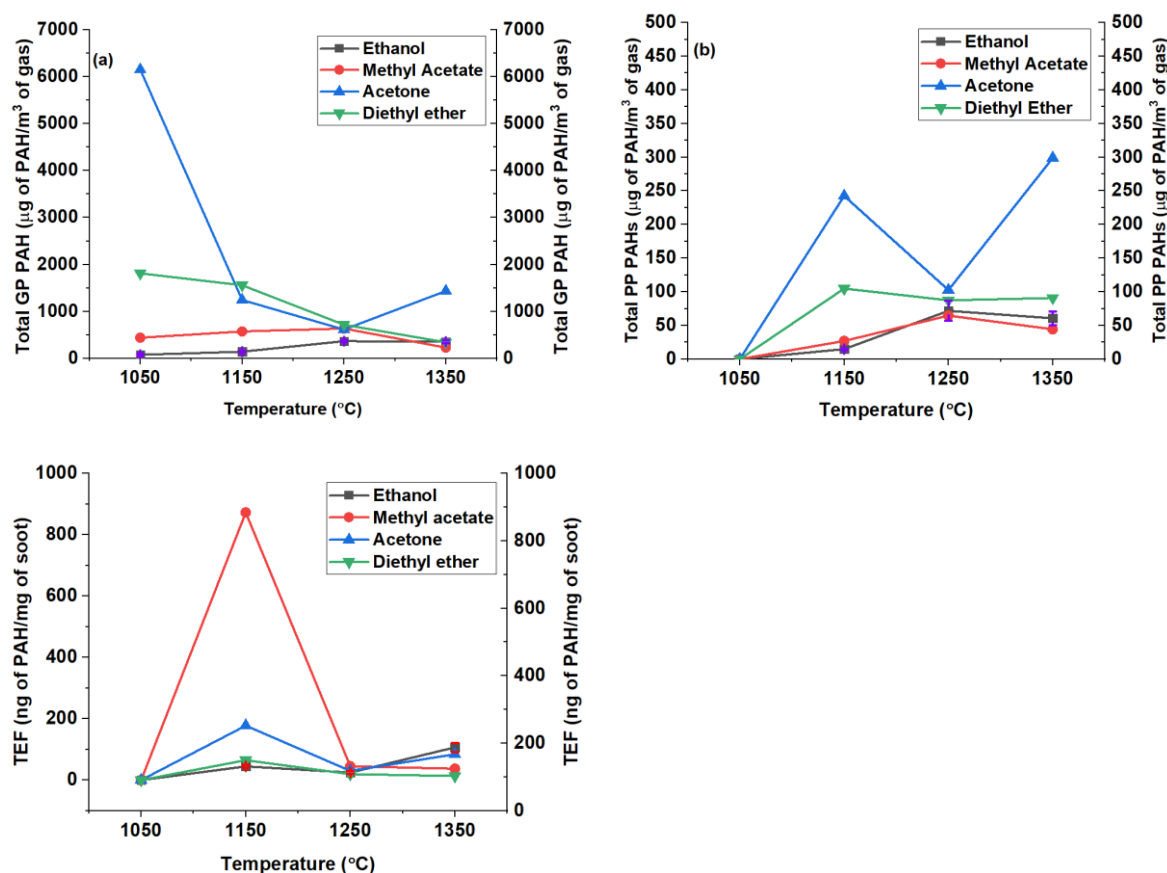
Fig. 5 (a) Total gas-phase PAH per m³ of gas, (b) Total particle-phase PAH per m³ of gas, and (c) Total particle-phase PAH per mg of soot during pyrolysis of ethanol, methyl acetate, acetone and diethyl ether at varying temperature. Error bars are for ethanol fuel repeatability

Fig. 5a shows that the concentration of gas-phase (GP) PAH produced during pyrolysis of diethyl ether and acetone decreased with an increase in temperature of the flow reactor from 1050 to 1250°C. At lower temperatures of 1050 and 1150 °C, methyl acetate and ethanol pyrolysis produced much lower GP PAH concentrations than acetone and diethyl ether fuel (**Fig. 5**a), which is likely due to the delayed formation of intermediate PAH precursors (i.e., acetylene) from methyl acetate and ethanol decomposition due to unavailability of carbon as explained in Section 3.1 . Despite the shorter carbon chain length and higher molecular oxygen content than diethyl ether, pyrolysis of acetone resulted in a larger concentration of GP PAH at the lowest and highest measured temperatures, as shown in **Fig. 5**a. A possible explanation for this is that during pyrolysis of diethyl ether the initial decomposition of DEE is slower than that of acetone, e.g. more unreacted DEE might remain at 1050 °C. produced two methyl radicals which readily formed acetylene and propargyl radicals, major precursors for benzene ring formation and PAHs growth.

It can also be seen from **Fig. 5**a that the relative effects of different functional groups on GP PAH concentration diminishes at 1250°C and above, as was also observed in the case of short-chain alcohols fuels [22]. This can likely be attributed to the very fast reaction rates present at higher temperatures, and thus effects of temperature dominate those of fuel structure. It is interesting however that at 1350°C the concentration of GP PAH is appreciably higher in the case of acetone relative to the other fuels, despite presumably faster rates, perhaps because of a new reaction regime is reached [22,23]. The decrease in the GP PAH concentration of during diethyl ether and acetone in the temperature range of 1050 to 1250 °C might be attributed to the increased rates of conversion of GP to heavier PAH, and then to soot particles, as can be observed in **Fig. 3**.

Fig. 5b shows that for the particle phase (PP) PAH concentration per unit volume of gas of the oxygenated fuels, there is a visible general trend of increasing PP PAH with temperature and a clear impact of DEE and acetone relative to methyl acetate and ethanol. **Fig. 5**b shows that the concentration of PP PAH for all fuels increased with an increase in temperature from 1050 to 1150°C, while at 1250°C all the fuels produced a comparable PP PAH concentration. The increase in PP PAH concentration for all four oxygenates in the temperature range of 1050 to 1150°C, could be due to an increase in the collisions between the PAH which resulted in an increase in the heavier PAHs at higher temperatures

(**Fig. 5**b). It is also interested to note that the concentration of PP PAH during ethanol and methyl acetate pyrolysis at different temperatures was very similar, despite different carbon numbers and oxygen to carbon ratios.

At a temperature of 1150°C, **Fig. 5**c indicates a peak PP PAH concentration per mass of during acetone and methyl acetate pyrolysis on a mass of soot basis, but that this concentration reduced when the temperature was increased to 1250°C. At a temperature of 1250°C, a further decrease in the PAH mass concentrations was observed. A similar effect was reported previously in the case of short-chain alcohols [22]. The small rise in PP PAH in the temperature range of 1250 to 1350°C shows that more PP PAHs were deposited on the soot surface, whereas the amount of soot decreased as the temperature rose (**Fig. 3**). In **Fig. 5**c an effect of the functional group on the PP PAH is most prominent at 1150°C. At a temperature of 1150°C methyl acetate produced approximately 9.8, 4.4, and 11.8 times more PP PAH concentration than ethanol, acetone, and diethyl ether respectively. This can likely be attributed to the very low mass of soot produced by methyl acetate at 1150°C as compared to acetone and diethyl ether (**Fig. 3**). It is interesting to note that methyl acetate produced the lowest PP PAH on a volume gas basis (Figure 5b) but the highest level on a per mass of soot basis (Figure 5c). It is tentatively suggested that during particle growth some surface adsorbed PAH becomes part of the soot structure and can no longer be extracted.

3.2 Influence of oxygenates on the PAH rings distribution

Fig. 6 shows the PAH concentration per volume basis of oxygenated fuels grouped according to the number of aromatic rings present. It can be observed from **Fig. 6** that for all fuels, except ethanol, at the two lowest temperatures of 1050°C and 1150°C, the concentration of 3 ring PAH was greater than that of any other grouping of PAH by number of rings.

As observed from in **Fig. 6** that the pyrolysis of acetone and diethyl ether fuels produced a greater amount of three-ring PAHs (for example, phenanthrene) than 2, 4, 5, or 6 rings in the temperature range of 1050 and 1150 °C. At temperatures of 1050 and 1150°C, for example, diethyl ether produced a significant amount of three-ring PAH, but the concentration of three-ring decreased as the temperature increased, implying that three-ring PAHs are rapidly converted into larger species, such as soot particles, at higher temperatures (**Fig. 6**c). This observation supports the finding from **Fig. 3** that the mass of soot increases with increasing temperature. The three-ring PAHs play an important role in the growth of 4-6 rings PAHs [22]. It can be seen that the concentration of 2 and 3 membered rings PAH formed during diethyl ether pyrolysis decreased with temperature from 1050 to 1350°C while in the case of acetone, between 1250 and 1350°C the concentration of 2, 4, and 5 rings PAH increases. Acetone produced a considerably higher concentration of 2, 3, and 4 member rings at 1350°C relative to the other tested fuels. Despite variations in fuel chemical structure, the concentration of four ring PAHs during pyrolysis of methyl acetate and diethyl ether were similar at all temperatures, as shown in **Fig. 6**b and **Fig. 6**c.
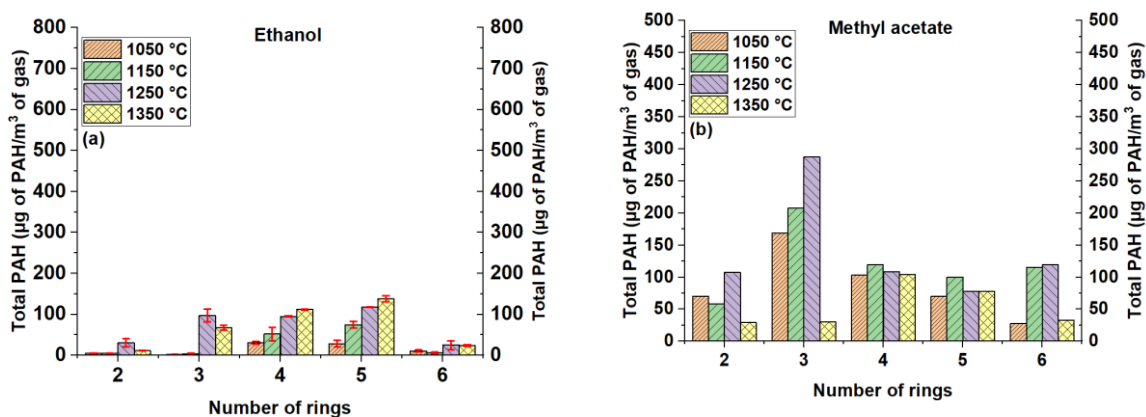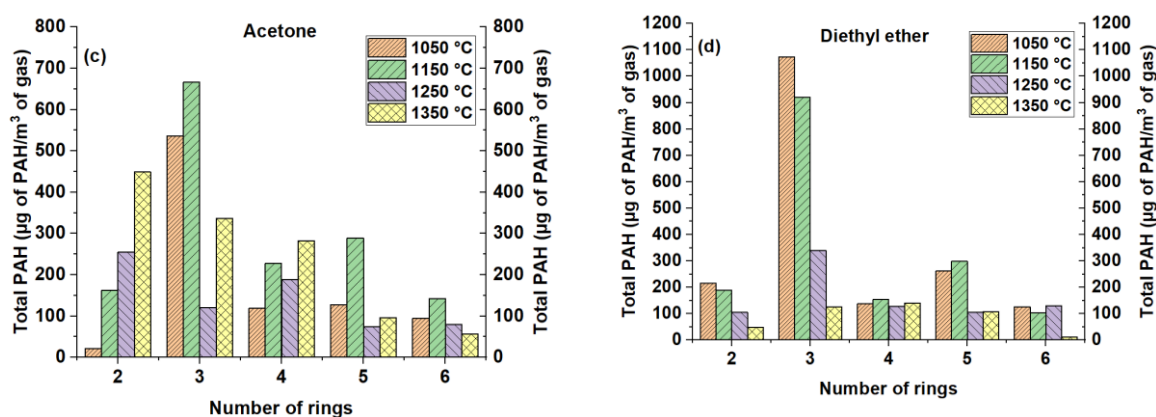
Fig. 6. PAH distribution according to the number of rings during pyrolysis at four different temperatures of 1050°C, 1150°C, 1250°C, and 1350°C (a) Ethanol (b) Methyl acetate (c)Acetone (d) Diethyl ether. Error bars denote standard deviation for ethanol fuel and note the extended y-axis necessary in the case of diethyl ether.

Fig. *6*d demonstrates that the relative abundance of heavier ring PAHs in diethyl ether is higher than in methyl acetate and ethanol when considering the heavier ring PAHs (i.e., 5 and 6 rings) in the temperature range of 1050 and 1150 °C. At temperatures of 1050 and 1150°C, the concentration of 5 ring PAHs in acetone and diethyl ether was higher than that of 6 ring PAHs, although methyl acetate had a slightly higher concentration of six member rings at 1150°C. The difference in concentration of the 5 and 6 ring PAHs might be attributed to the pace at which these rings convert to soot particles. The comparable ratios of 5 and 6 ring PAHs suggests that the formation rate of 5 rings PAHs and subsequent consumption to form 6 ring PAH is approximately equivalent for all fuels in the temperature range of 1250 to 1350°C.

In the temperature range of 1050 to 1150°C, the influence of the various functional groups on the ring distribution is clearly visible (**Fig. *6***). When compared to methyl acetate, ethanol, and acetone at 1150°C, diethyl ether generated 1.3, 211, and 4.4 times more three-ring PAHs. The larger quantity of three-ring PAHs during methyl acetate, acetone and diethyl ether pyrolysis implies that at lower temperatures the conversion rate of three-ring PAH to heavier-ring PAH was reduced and may have been a limiting step.

3.3   Influence of oxygenated structure on growth of individual PAHs

Fig. *7* shows the concentration of Naphthalene (NPH), Acenaphthylene (ACY), Phenanthrene (PHN), Pyrene (PYR), Benzo [a] Pyrene (B[a]P), and Benzo [k] fluoranthene (B[k]F) during the pyrolysis of ethanol, methyl acetate, acetone, and diethyl ether. These individual PAHs of varying size were chosen for further discussion on the basis of the PAH distribution by ring number presented in **Fig. *6***.

Fig. *7*a shows that the concentration of naphthalene decreased with an increase in temperature from 1050 to 1350°C for all the oxygenates tested, except ethanol for which the total concentration of naphthalene increased up to 1250°C but then decreased at 1350°C. This decrease can likely be attributed to the rapid conversion of 2 ring naphthalene to higher ring PAHs, reaction rates of which can be expected to increase with temperature. A relatively low concentration of naphthalene was found at all temperatures during pyrolysis of methyl acetate and ethanol, and it is tentatively suggested that this can be attributed to slower rates of first ring formation, due to the high O: C ratio of methyl acetate and ethanol, which prevents accumulation of naphthalene. **Fig. *7***a shows that at the lowest temperatures of 1050 and 1150°C, diethyl ether produced an appreciably higher concentration of naphthalene than acetone. However, at 1250°C and 1350°C, diethyl ether and acetone produced an approximately equivalent concentration of naphthalene, suggesting a reduced influence of molecular structure at this condition.

As discussed in Section 3.1, C2 and C3 oxygenated fuels are expected to predominately decompose to methyl radicals which are consumed via ethane to form acetylene and subsequently propargyl radicals. Two propargyl radicals bond to form benzene, according to a mechanism proposed in the literature [38,39]. Following this, the benzene ring loses hydrogen atoms, yielding phenyl radicals that may readily generate two-ring naphthalene through the HACA mechanism [40,41]. Although the HACA method is most likely to produce naphthalene, cyclopentadienyl radicals might potentially be recombined to produce naphthalene as well 1], however, it is tentatively suggested that the formation of cyclopentadienyl radicals from the selected oxygenated is less likely. Once two-ring naphthalene has formed, it grows

further to the three ring species acenaphthylene and phenanthrene via the HACA mechanism. In **Fig. 7**b, it can be seen that acetone and diethyl ether produced a comparable concentration of acenaphthylene at 1050 and 1150°C, despite the difference in the levels of naphthalene at these conditions (**Fig. 7**a). **Fig. 7**c shows that diethyl ether produced the highest concentration of phenanthrene in the temperature range of 1050 to 1250°C. An effect of fuel molecular structure on phenanthrene formation is very evident at 1050 and 1150°C. In comparison to acetone, ethanol, and methyl acetate, diethyl ether generated 1.2, 166, and 5.6 times the concentration of phenanthrene at 1150°C, respectively. Pyrene can be formed by either the benzenoid phenanthrene or the three-ring acenaphthylene [42], as shown in **Fig. 7**d, which displays the ratio of acenaphthylene to phenanthrene at various temperatures. The concentration of phenanthrene was larger than that of acenaphthylene for all of the oxygenated fuels at the low-temperature range of 1050 to 1250°C, as shown in **Fig. 7**d, while the converse is true at the maximum temperature.
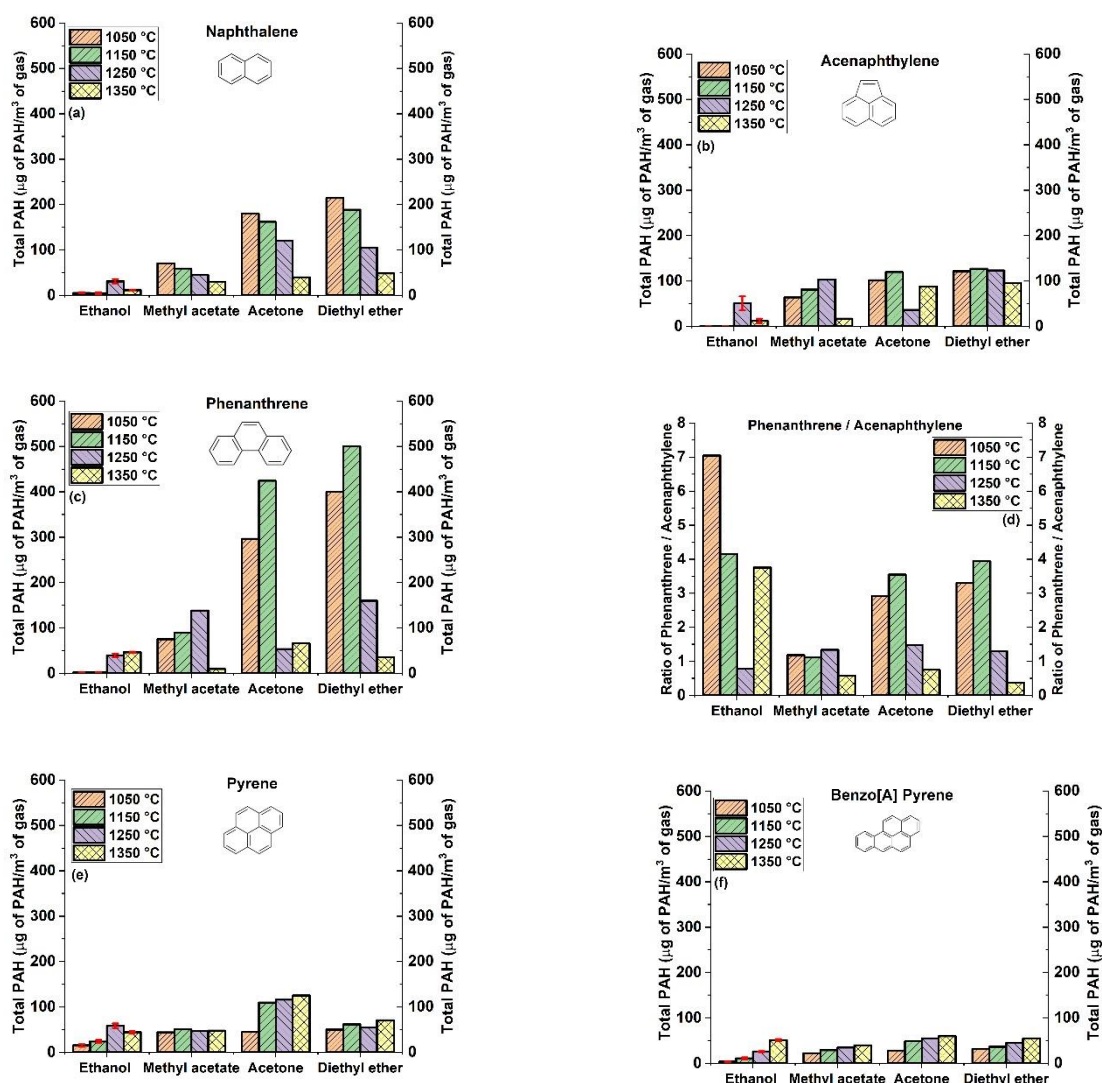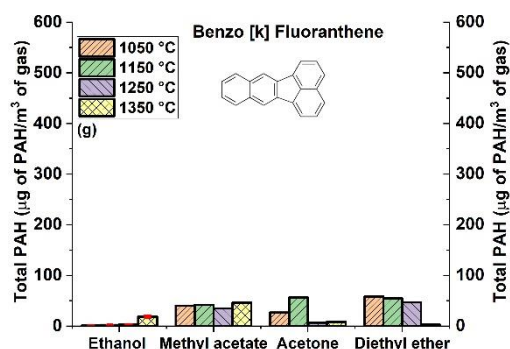
Fig. 7. Measured concentrations of (a) Naphthalene (NPH) (b) acenaphthylene (ACY) (c) phenanthrene (PHN) (d) ratio of acenaphthylene to phenanthrene (e) pyrene (PYR) (f) benzo[a] pyrene (B [A] P) (g) benzo[f] fluoranthene (B [K] F) and during pyrolysis of ethanol, methyl acetate, acetone, and diethyl ether. Error bars denote ethanol fuel repeatability.

It is hypothesised that for all fuels at lower temperatures, pyrene formation is dominated by growth from phenanthrene via the HACA mechanism, but at higher temperatures (except ethanol at 1350 ^{0}C, which exhibited a higher concentration of phenanthrene), pyrene formation is dominated by acenaphthylene due to the larger abundance of the smaller molecule. This hypothesis is in agreement with the previously suggested formation of PAH from alcohol fuels via the HACA mechanism [22]. A similar effect of temperature on pyrene formation was observed during the pyrolysis of a series of alcohol fuels [22]. **Fig. 7**e demonstrates that all oxygenated fuels formed a significant quantity of pyrene at all temperatures, and it is likely that various 2-ring and 3-ring PAHs expanded via pyrene to form heavier PAHs, particularly the B2 group, via HACA or HAVA (Hydrogen Abstraction/Vinylacetylene-Addition) [43]. It is interesting to note that, for all the tested fuels the concentration of pyrene is approximately constant at all temperatures, with the exception of acetone at 1050°C where the measured concentration of pyrene is significantly lower than for the same fuel at higher temperatures.

From **Fig. 7**f, it is interesting to note that for all oxygenated fuels the concentration of benzo[a] pyrene increased linearly with temperatures, which supports the assumption that at higher temperatures the low and medium molecular PAHs were more rapidly converted into heavier weight benzo[a]pyrene.

Fig. 7g shows that the measured concentration of benzo[f] fluoranthene was much less systematically influenced by temperature. It is also interesting to note that during ethanol and methyl acetate pyrolysis the concentration of benzo[f] fluoranthene increased at the highest tested temperature of 1350°C but only very low concentrations were detected in the case of acetone and di-ethyl ether.

3.4   PAH toxicity

This section assesses the potential carcinogenicity of particulate matter produced by oxygenated fuels of various functional groups at a range of temperatures, with a focus on PAHs from the B2 group because of their high toxicity. As indicated in Eq 2, a PAH toxicity index was computed for each particulate sample by adding the products of each PAH concentrations (Ci) and their toxicity equivalent factor (TEF). TEFs were proposed by Nisbet and Lagoy (1992) [44] and are commonly used to evaluate PAH toxicity.

$$\text{Toxicity index} = \sum_{i=1}^{n}(\text{TEFi} * \text{Ci}) \qquad (2)$$

Fig. 8 depicts the PAH toxicity of particulate matter formed during the pyrolysis of the test fuels on a mass basis. As seen in **Fig. 8**, the studied fuels had dramatically different degrees of toxicity at 1150°, however, it is interesting to see how close the TEF are at higher temperatures. At 1150°C, methyl acetate displays a maximum toxicity, 4.9 times that of acetone, 13.45 times that of diethyl ether, and 19.48 times that of ethanol, as shown in **Fig. 8**. The significant toxicity of soot from methyl acetate at 1150°C can be explained by a comparatively large concentration of toxic benzo [a] pyrene condensing onto the soot particles (**Fig. 3** and **Fig. 7**d). Further, it should be noted that methyl acetate produced very little mass of soot at this temperature, and so while the per volume of gas concentration of benzo[a]pyrene
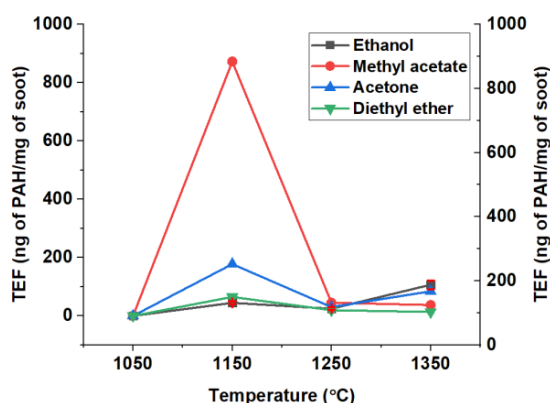
Fig. 8. Calculated toxicity equivalency factor of ethanol, methyl acetate, acetone, and diethyl ether fuels soot particle per mg of soot.

is not especially greater, it is much higher on a per mass of soot basis. Each step of PAH formation from acenaphthylene to benzo [a] anthracene and on to the most hazardous species, benzo[a] pyrene, raises the toxicity level of PAH by a factor of ten. At 1150°C, particulate matter from acetone is the most hazardous, while that from diethyl ether is the least harmful. Acetone has the maximum toxicity at the highest temperature measured, which is due to the presence of benzo[A]pyrene.

Finally, while the quantity of soot mass for all fuels is relatively low at 1150°C, as shown in **Fig. 3**, the toxicity of the extractable PAHs adsorbed on the soot particles was substantially higher than at higher temperatures, as shown in **Fig. 8**. It is also worth noting that at 1150°C, acetone produced the second highest PP PAH as shown in **Fig. 5**, which follows the same patterns as **Fig. 8**, implying that the PM toxicity is most influenced by the total concentration of PAH present rather than any dramatic change in the composition of those PAH when comparing the different fuels.

4   Conclusions

In summary, this paper investigated the sooting tendency and PAHs emissions from pyrolysis of ethanol, methyl acetate, acetone, and diethyl ether and the following conclusions can be drawn:

- Pyrene formation pathways appeared temperature dependent for all four oxygenates and were dominated by phenanthrene at 1050 and 1150°C, while at higher temperatures higher concentrations of acenaphthylene were found.
- At 1150°C the relative abundance of the soot particles was low, however, the toxicity of the soot particles produced was significantly higher than at higher temperatures, especially in the case of soot produced during pyrolysis of methyl acetate.
- An effect of different oxygenated functional groups on soot mass was evident, with consistently lower production of soot by methyl acetate, which has higher oxygen to carbon ratio than ethanol, acetone, and diethyl ether.
- Functional groups had an impact on the GP PAH concentration with methyl acetate pyrolysis resulting in a significantly lower GP PAH concentration relative to acetone and diethyl ether, but slightly higher than ethanol at all temperatures. However, the pyrolysis of acetone resulted in a higher concentration of GP PAH at the lowest and highest temperatures, despite the shorter carbon chain length and higher molecular oxygen content as compared to diethyl ether.
- The concentration of PP PAH per unit volume of gas is much lower than the corresponding GP PAH, which suggests that PP PAH that condensed onto the particulate surface, subsequently experienced surface reaction and were therefore not recoverable during the extraction process, contributing to the formation and emission of particulate matter.
- The concentration of four ring PAHs (which contribute to the formation of heavier molecular weight PAHs comprising 5 or 6 rings) during methyl acetate and diethyl ether pyrolysis were relatively similar, despite different molecular structures and carbon numbers.

5   References

[1]   Richter H, Howard JB. Formation of polycyclic aromatic hydrocarbons and their growth to soot-

a review of chemical reaction pathways. Prog Energy Combust Sci 2000;26:565–608. https://doi.org/10.1016/S0360-1285(00)00009-5.

[2]   Garcı E, Laca M, Pe E, Garrido A. New Class of Acetal Derived from Glycerin as a Biodiesel Fuel Component. Energy and Fuels 2008;22:4274–80. https://doi.org/10.1021/ef800477m.

[3]   Goh EB, Baidoo EEK, Keasling JD, Beller HR. Engineering of bacterial methyl ketone synthesis for biofuels. Appl Environ Microbiol 2012;78:70–80. https://doi.org/10.1128/AEM.06785-11.

[4]   Baeyens J, Kang Q, Appels L, Dewil R, Lv Y, Tan T. Challenges and opportunities in improving the production of bio-ethanol. Prog Energy Combust Sci 2015;47:60–88. https://doi.org/10.1016/j.pecs.2014.10.003.

[5]   Elfasakhany A. Engineering Science and Technology , an International Journal Performance and emissions analysis on using acetone – gasoline fuel blends in spark-ignition engine. Eng Sci Technol an Int J 2016;19:1224–32. https://doi.org/10.1016/j.jestch.2016.02.002.

[6]   Elfasakhany A. Investigations on performance and pollutant emissions of spark-ignition engines fueled with n -butanol – , isobutanol – , ethanol – , methanol – , and acetone – gasoline blends : A comparative study. Renew Sustain Energy Rev 2017;71:404–13. https://doi.org/10.1016/j.rser.2016.12.070.

[7]   Alexiou A, Williams A. Soot Formation in Shock-Tube Pyrolysis of Toluene , Toluene-Methanol,Toluene-Ethanol, and Toluene-Oxygen Mixtures. Combust Flame 1996;104:51–65. https://doi.org/https://doi.org/10.1016/0010-2180(95)00004-6.

[8]   Böhm H, Braun-Unkhoff M. Numerical study of the effect of oxygenated blending compounds on soot formation in shock tubes. Combust Flame 2008;153:84–96. https://doi.org/10.1016/j.combustflame.2008.01.002.

[9]   Esarte C, Millera Á, Bilbao R, Alzueta MU. Gas and soot products formed in the pyrolysis of acetylene-ethanol blends under flow reactor conditions. Fuel Process Technol 2009;90:496–503. https://doi.org/10.1016/j.fuproc.2009.01.011.

[10]   Esarte C, Bilbao R, Alzueta MU, Peg M, Ruiz MP. Pyrolysis of Ethanol : Gas and Soot Products Formed. Ind Eng Chem Res 2011;50:4412–9. https://doi.org/10.1021/ie1022628.

[11]   Viteri F, López A, Ángela Millera, Rafael Bilbao, Alzueta M. Influence of temperature and gas residence time on the formation of polycyclic aromatic hydrocarbons (PAH) during the pyrolysis of ethanol. Fuel 2019;236:820–8. https://doi.org/10.1016/j.fuel.2018.09.061.

[12]   Kass MD, Thomas JF, Storey JM, Domingo N, Wade J, Kenreck G. Emissions from a 5.9 liter diesel engine fueled with ethanol diesel blends. SAE Tech Pap 2001. https://doi.org/10.4271/2001-01-2018.

[13]   Paul A, Bose PK, Panua R, Debroy D. Study of performance and emission characteristics of a single cylinder CI engine using diethyl ether and ethanol blends. J Energy Inst 2015;88:1–10. https://doi.org/10.1016/j.joei.2014.07.001.

[14]   Cinar C, Can Ö, Sahin F, Yucesu HS. Effects of premixed diethyl ether (DEE) on combustion and exhaust emissions in a HCCI-DI diesel engine. Appl Therm Eng 2010;30:360–5. https://doi.org/10.1016/j.applthermaleng.2009.09.016.

[15]   Mohan B, Yang W, Yu W, Tay KL. Numerical analysis of spray characteristics of dimethyl ether and diethyl ether fuel. Appl Energy 2017;185:1403–10. https://doi.org/10.1016/j.apenergy.2016.01.128.

[16]   Semelsberger TA, Borup RL, Greene HL. Dimethyl ether (DME) as an alternative fuel. J Power Sources 2006;156:497–511. https://doi.org/10.1016/j.jpowsour.2005.05.082.

[17]   Rakopoulos DC, Rakopoulos CD, Giakoumis EG, Dimaratos AM. Characteristics of performance and emissions in high-speed direct injection diesel engine fueled with diethyl ether / diesel fuel blends. Energy 2020;43:214–24. https://doi.org/10.1016/j.energy.2012.04.039.

[18]   Meng L, Zeng C, Li Y, Nithyanandan K, Lee TH, Lee C. An Experimental Study on the Potential Usage of Acetone as an Oxygenate Additive in PFI SI Engines. Energies 2016;9:1–20. https://doi.org/10.3390/en9040256.

[19]   Wu H, Nithyanandan K, Zhou N, Lee TH, Lee CF, Zhang C. Impacts of acetone on the spray combustion of Acetone – Butanol – Ethanol (ABE) -Diesel blends under low ambient temperature. FUEL 2015;142:109–16. https://doi.org/10.1016/j.fuel.2014.10.009.

[20]   Pumphrey JA, Brand JI, Scheller WA. Vapour pressure measurements and predictions for alcohol – gasoline blends. Fuel 2000;79:1405–11. https://doi.org/10.1016/S0016-2361(99)00284-7.

[21]   Dabbagh HA, Ghobadi F, Ehsani MR, Moradmand M. The influence of ester additives on the properties of gasoline. Fuel 2013;104:216–23. https://doi.org/10.1016/j.fuel.2012.09.056.

[22] Khan ZA, Hellier P, Ladommatos N. Measurement of soot mass and PAHs during the pyrolysis of C 2 – C 4 alcohols at high temperatures. Combust Flame 2022;236:111803. https://doi.org/10.1016/j.combustflame.2021.111803.

[23] Dandajeh HA, Ladommatos N, Hellier P, Eveleigh A. Effects of unsaturation of C2and C3hydrocarbons on the formation of PAHs and on the toxicity of soot particles. Fuel 2017;194:306–20. https://doi.org/10.1016/j.fuel.2017.01.015.

[24] Dandajeh HA, Ladommatos N, Hellier P, Eveleigh A. In fluence of carbon number of C 1 – C 7 hydrocarbons on PAH formation. Fuel 2018;228:140–51. https://doi.org/10.1016/j.fuel.2018.04.133.

[25] Eveleigh A, Ladommatos N, Hellier P, Jourdan A. An investigation into the conversion of specific carbon atoms in oleic acid and methyl oleate to particulate matter in a diesel engine and tube reactor. Fuel 2015;153:604–11. https://doi.org/10.1016/j.fuel.2015.03.037.

[26] USEPA. Compendium of Methods for the Determination of Toxic Organic Compounds in Ambient Air, Compendium Method TO-13A: Determination of Polycyclic Aromatic Hydrocarbons (PAHs) in Ambient Air Using Gas Chromatography/Mass Spectrometry (GC/MS). Cent Environ Res Inf Off Res Dev US Environ Prot Agency Cincinnati, OH 45268 1999;II:78.

[27] Yacoub Y, Bata R, Gautam M. The performance and emission characteristics of C1-C5 alcohol-gasoline blends with matched oxygen content in a single-cylinder spark ignition engine. Proc Inst Mech Eng Part A J Power Energy 1998;212:363–79. https://doi.org/10.1243/0957650981536934.

[28] Dean JA. Lange's Handbook of Chemistry, 14th edition. McGraw-Hill, New York; 1992.

[29] Osmont A, Catoire L, Gökalp I, Swihart MT. Thermochemistry of C - C and C - H bond breaking in fatty acid methyl esters. Energy and Fuels 2007;21:2027–32. https://doi.org/10.1021/ef070132e.

[30] Osswald P, Struckmeier U, Kasper T, Kohse-Höinghaus K, Wang J, Cool TA, et al. Isomer-specific fuel destruction pathways in rich flames of methyl acetate and ethyl formate and consequences for the combustion chemistry of esters. J Phys Chem A 2007;111:4093–101. https://doi.org/10.1021/jp068337w.

[31] Page M, Lin MC, He Y, Choudhury TK. Kinetics of the methoxy radical decomposition reaction: Theory and experiment. J Phys Chem 1989;93:4404–8. https://doi.org/10.1021/j100348a007.

[32] Tsuda Morizo KK. Thermal Decomposition of Ketene of Ketene in Shock Waves. Chem Soc Japan 1968;41. https://doi.org/10.1246/bcsj.41.53.

[33] Agafonov GL, Vlasov PA, Tereza AM, Garmash AA, Smirnov VN, Shumova V V. An experimental and simulation study of the effect of acetone and propane additives on soot formation in acetylene pyrolysis behind reflected shock waves. J Phys Conf Ser 2019;1147:012044. https://doi.org/10.1088/1742-6596/1147/1/012044.

[34] Russo C, Alfe M, Rouzaud JN, Stanzione F, Tregrossi A, Ciajolo A. Probing structures of soot formed in premixed flames of methane, ethylene and benzene. Proc Combust Inst 2013;34:1885–92. https://doi.org/10.1016/j.proci.2012.06.127.

[35] Lemaire R, Lapalme D, Seers P. Analysis of the sooting propensity of C-4 and C-5 oxygenates: Comparison of sooting indexes issued from laser-based experiments and group additivity approaches. Combust Flame 2015;162:3140–55. https://doi.org/10.1016/j.combustflame.2015.03.018.

[36] Hong Z, Davidson DF, Vasu SS, Hanson RK. The effect of oxygenates on soot formation in rich heptane mixtures: A shock tube study. Fuel 2009;88:1901–6. https://doi.org/10.1016/j.fuel.2009.04.013.

[37] Pepiot-desjardins P, Pitsch H, Malhotra R, Kirby SR, Boehman AL. Structural group analysis for soot reduction tendency of oxygenated fuels. Combust Flame 2008;154:191–205. https://doi.org/10.1016/j.combustflame.2008.03.017.

[38] Singh P, Sung CJ. PAH formation in counterflow non-premixed flames of butane and butanol isomers. Combust Flame 2016;170:91–110. https://doi.org/10.1016/j.combustflame.2016.05.009.

[39] Veloo PS, Egolfopoulos FN. Studies of n-propanol, iso-propanol, and propane flames. Combust Flame 2011;158:501–10. https://doi.org/10.1016/j.combustflame.2010.10.001.

[40] Bittner JD, Howard JB. Composition profiles and reaction mechanisms in a near-sooting premixed benzene/oxygen/argon flame. Symp Combust 1981;18:1105–16. https://doi.org/https://doi.org/10.1016/S0082-0784(81)80115-4.

[41] Frenklach M, Ramachandra MK, Matula RA. Soot formation in shock-tube oxidation of hydrocarbons. Symp Combust 1984;20:871–8. https://doi.org/10.1016/S0082-0784(85)80576-

14   Z.A. Khan, P. Hellier, N. Ladommatos, A.A. Almaleki

2.
[42]   Raj A. PAH growth assisted by five-membered ring: pyrene formation from acenaphthylene. Combust Theory Model 2022;26:91–109. https://doi.org/10.1080/13647830.2021.1991596.
[43]   Shukla B, Koshi M. A novel route for PAH growth in HACA based mechanisms. Combust Flame 2012;159:3589–96. https://doi.org/10.1016/j.combustflame.2012.08.007.
[44]   Nisbet I, Lagoy P. Toxic Equivalency Factors (TEFs) for Polycyclic Aromatic Hydrocarbons (PAHs). Regul Toxicol Pharmacol 1992;16:290–300. https://doi.org/10.1016/0273-2300(92)90009-X.

THIESEL 2022 Conference on Thermo- and Fluid Dynamics of Clean Propulsion Powerplants

Characterization of Waste Cooking Oil Biodiesel as a Low Carbon Fuel for Direct Injection Diesel Engine

O.A. Kuti[1], S. Bahmanisangesari[1], R. Gilmour[1], A. Albarbar[1], L. Qian[2], K. Nishida[3]

[1]Department of Engineering, Manchester Metropolitan University, Manchester, M1 5GD, UK

[2]Department of Computing and Mathematics, Manchester Metropolitan University, Manchester, M1 5GD, UK

E-mail: o.kuti@mmu.ac.uk
Telephone: +(44) 161 247 6281

[3]Department of Mechanical System Engineering, Hiroshima University, Higashi- Hiroshima 739-8527, Japan.
E-mail: nishida@mec.hiroshima-u.ac.jp

Abstract. An increase in biodiesel content in diesel fuel in the EU and UK beyond the current value of 5-7% is imperative in achieving emission control in the heavy-duty transportation sector. Waste cooking oil (WCO) obtained from various sources such as the food industry, restaurants and sewers could provide sustainable means of producing biodiesel. In this research WCO biodiesel and conventional diesel fuels were characterized fundamentally in terms of their spray and gas entrainment qualities under diesel-like engine conditions using the laser-induced fluorescence and particle image velocimetry (LIF-PIV), shadowgraph and chemiluminescence techniques under non-evaporating, evaporating and reacting conditions. The impact of fuel injection parameters such as injection pressure and nozzle diameter on spray and gas entrainment characteristics of the fuel were investigated. Furthermore, WCO biodiesel B100 (100% biodiesel) and its blends with diesel namely B20 (20% biodiesel, 80% diesel) B40 (40% biodiesel, 60% diesel), B60 (60% biodiesel, 40% diesel) alongside conventional diesel fuel (B7) were characterized in a real diesel engine. As a result of higher viscosity and surface tension, it was observed that WCO biodiesel produced longer spray penetration and shorter spray angle than diesel fuel under non-evaporating conditions. Furthermore, the quantity of gas entrained by WCO biodiesel spray was lower. Due to higher distillation temperature and less gas entrainment, WCO biodiesel liquid length was longer. The combined effect of ultra-high injection pressure of 300 MPa with smaller nozzle hole diameter of 0.08mm was observed to enhance gas entrainment processes. Due to higher cetane number WCO biodiesel produced a shorter ignition delay. While higher injection pressure had an influence on the combustion processes, with less air-entrained upstream of the WCO biodiesel lifted flame, it was observed that its higher oxygen atoms (oxygen ratio) played a crucial role in soot formation. From the real engine experiments, due to the lower heating value, as the quantity of biodiesel increased, the peak in-cylinder pressure decreased for biodiesel and its blends in the order B100 < B60 < B40 < B20 < B7. It was also observed that as the quantity of biodiesel increased, ignition delay and peak heat release rate decreased in the order B100 < B60 < B40 < B20 < B7. Emission measurements at the exhaust showed that for all fuels, there was no significant change in CO and CO_2 species. As ignition delay was shortened, hydrocarbon and NO_x were observed to reduce as the quantity of biodiesel increased in the blends.

1. Introduction

The diesel engine plays a key role as an energy source for light and heavy-duty transportation and power generation applications. However, emissions from these applications have been found to be detrimental to health and the environment [1]. In achieving a low carbon economy, stringent emission regulations are being proposed for automakers and power generation industries by policy makers [2]. With the recent COP 26 conference in Glasgow, UK, it is expected that these regulations will become more stringent with time. Also, increase in biodiesel content in diesel fuel in the EU and UK beyond the current value of 5-7% will be crucial in achieving the future emission controls in the transportation sector [3]. Current heavy-duty diesel engine operates between injection pressure of 200 to 250 MPa. Previous

works have been reported that by increasing in injection pressure to 300 MPa, emissions such as particulates can be reduced drastically in diesel engine [4]. In addition, the prospects of using biodiesel fuel as an alternative in achieving emission reductions in diesel engines have been reported [1]. With the notions of feedstock competing with food supply, there have been concerns on biodiesel production [5]. The key solution to mitigate this competition is by recycling used cooking oil from food industries, restaurants and sewage fatbergs. By using these waste materials, feedstock will be made available easily while the production of waste cooking oil (WCO) biodiesel through the esterification processes will be enhanced sustainably. To mention a few, there have been several works on the prospects of using WCO biodiesel in diesel engine. WCO biodiesel has been found to produce lower level of noxious emission such as hydrocarbon (HC) and carbon monoxide (CO) with similar engine performance when compared to diesel [6-7]. Smoke emissions have been observed to decrease with increase in biodiesel concentration with no significant change in engine efficiency when two different cases of WCO-diesel blends were investigated [8]. It was concluded that WCO was better in reducing HC, CO and smoke emissions as injection pressure increased. The performance, emission and combustion characteristics of a single cylinder diesel engine fuelled with WCO-diesel blends at various volumetric concentration were investigated in the work reported by [9]. As the compression ratio increased, it was observed that WCO-diesel blends tend to have longer ignition delay, maximum rate of pressure rise, lower heat release rate and higher mass fraction compared to conventional diesel fuel. The use of optical diesel engine test rig to investigate the spray, combustion and emission characteristics of neat WCO biodiesel and diesel have been reported by [10-11]. It was observed that WCO biodiesel exhibited longer liquid penetration length and narrower spray angle than diesel. Due to poor atomization, WCO displayed longer ignition delay with a slightly lower peak of in-cylinder pressure and heat release rate than diesel with reduction in carbon monoxide, unburned hydrocarbon and particulate matter emissions. Fundamental studies using the constant volume vessel to investigate the spray characteristics of diesel fuel blended with hydrogenated catalytic biodiesel from WCO has been reported in [12]. It was observed that as the quantity of WCO increased in the diesel blends, the fuel density increased, and this further led to longer liquid length. With all the previous research, there is a dearth of information on the air entrainment characteristics of WCO biodiesel sprays in diesel engine. Due to the method fuel is introduced towards the top dead centre, the direct injection (DI) diesel engine depends more on mixture formation. Hence in the DI diesel engine, air entrainment in fuel sprays is expected to have influence on spray formation and the subsequent combustion processes. Since there is a keen interest in the use of low carbon fuels such as WCO biodiesel it becomes imperative to have an in-depth understanding on its spray and combustion characteristics. Therefore, in this work, the synergies between WCO biodiesel air entrainment characteristics and spray formation are investigated fundamentally using high pressure rig with optical diagnostics techniques. Furthermore, the influence these synergies have on WCO biodiesel combustion are investigated. To establish the effect of increasing biodiesel content beyond the current EU and UK levels, the influence WCO biodiesel in diesel fuel blends in an engine test bench is investigated. Inferences deduced from the fundamental research are correlated with data from engine tests.

2. Experimental Set-up

2.1 Fundamental Experiments

Experiments were done in a high-pressure constant volume vessel to investigate spray formation and combustion characteristics of waste cooking oil biodiesel and diesel fuels. Experimental conditions similar to real production at −10° ATDC (After Top Dead Centre) were maintained inside the high-pressure vessel. The high-pressure vessel is set up to focus mainly on fuel-air interactions under turbulent conditions initiated by high injection conditions towards the top dead centre without considering other engine processes such as spray swirl, spray squish and spray-piston interactions. The LIF-PIV (Laser Induced Fluorescence-Particle Image Velocimetry) techniques was used to characterize the spray formation and gas entrainment characteristics of the fuels at non-evaporating conditions. In tracking the gas entrained in the spray, Rhodamine B - water solution was used while capturing spray images through the elastic scattering of droplets by laser beam. Figure 1 presents the experimental set-up for the LIF–PIV optical diagnostics. A double pulsed Nd:YAG laser (New Wave Research, DPIV-N50) at a wavelength of 532 nm and energy of 120 mJ was used to image the spray developed by the fuels and also the fluorescent images of the tracer droplets. A laser sheet of 1 mm thickness was generated with a cylindrical convex lens. The Rhodamine B solution was injected by a swirl type injector at 9 MPa into the injected spray region in the constant volume vessel. In accordance with the Stoke's law, the fuel was injected when the size of the tracer droplets being excited by the laser light reached

an optimum size suitable to track the entrained gas. Two continuous images (tracer and spray images) were captured within a short interval using a CCD (Charge Coupled Device) camera (PCO 1600-PIV). The resolutions of the images were 1600 by 1200 pixels. A long pass filter which allows light of wavelength longer than 560 nm was fitted to the front of the CCD camera to only capture the fluorescence signal of the tracer droplets. The ambient pressure inside the constant volume vessel and tracer accumulator were respectively controlled using a regulator and nitrogen cylinder. Two delay generators (DG535 Stanford Inc.) were synchronized to produce electrical pulses for the tracer injection, fuel injection, laser firing and image capturing.
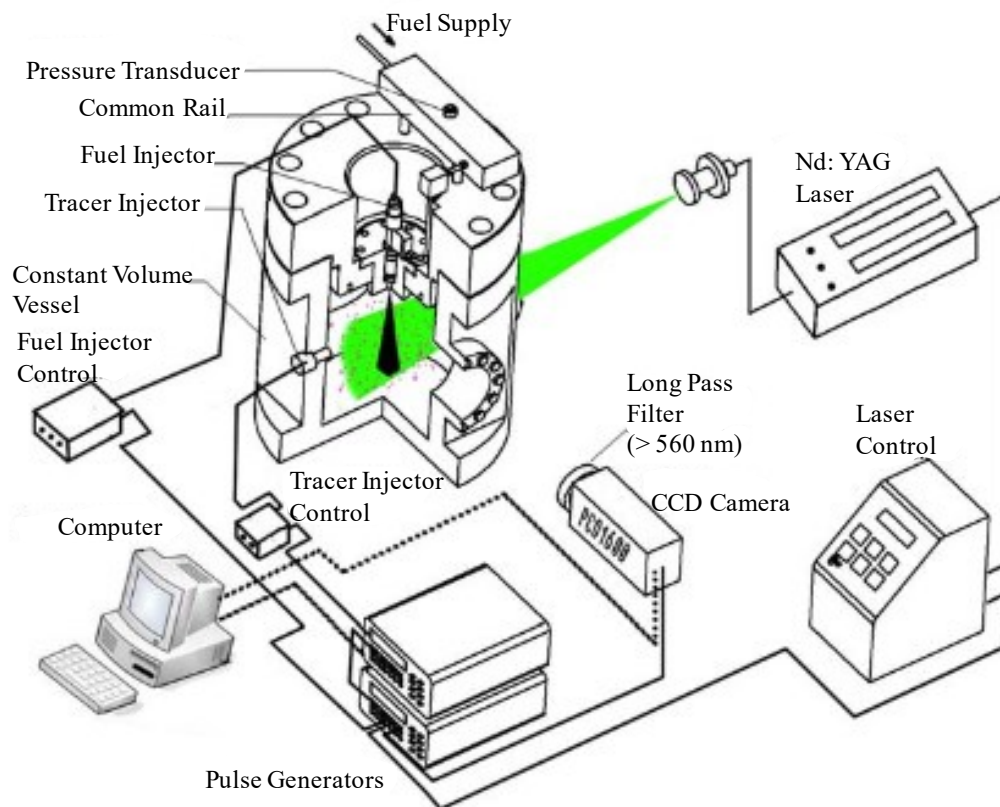
Fig. 1. Experimental set-up for the LIF-PIV measurements

To achieve proper distribution and optimum size for the Rhodamine B droplets, the interval between the tracer and fuel injections was maintained at 1400 ms. In addition to the LIF-PIV set up, the LDSA (Laser Diffraction Size Analyzer) optical system was used to determine the optimum tracer droplet size suitable to track the gas entrained. In predicting the magnitude of the velocity of the gas entrained in the spray, interrogation window size of 16 by 16 pixels (1.55 by 1.55 mm) with 50% overlap and frame time interval. The cross-correlation method was selected as the algorithm for the vector analyses in the double frame/double exposure mode. The two-dimensional ambient gas flow field was calculated based on the displacement of the tracer in the two images by using a commercial PIV analytical software (Koncerto, Seika Inc.). Details about the LIF–PIV techniques and LDSA techniques for the determination of the tracer size suitable for tracking the gas entrained in the sprays can be found in previous works by some of the authors [13-14]. In order to eliminate the effect of shot-to-shot variations, data were acquired from 10 fuel injections. The velocity measurements were then obtained by averaging data from 5 injections with less error vector. In understanding the impact of the gas entrained and fuel oxygen content evaporating sprays and combustion experiments were performed using the high-speed camera (FASTCAM-APX RS, Photron Corp.). Shadowgraphy through Mie Scattering techniques was used to investigate the evaporating sprays. The Xenon lamp with two reflecting mirrors was utilized to illuminate and capture the evaporating sprays. For the reacting sprays, the OH chemiluminescence optical technique was used to investigate the autoignition processes and lifted flame structures . With the aid of the UV-Nikkor lens (Nikon, 105 mm, f/4.5) mounted to an image intensifier (LaVision Inc., HS-IRO) and   attached to the high-speed camera, the OH chemiluminescence images were captured. The OH band-pass filter of wavelength 313 nm (10 nm FWHM) coupled to the UV-Nikkor lens was used to observe the OH chemiluminescence. The two-colour pyrometry technique was used to investigate the

soot propensity of the fuels. A visible lens (Nikon, 105 mm, f/4.5) was mounted to the high- speed camera. The two colour system was calibrated using a tungsten lamp (Polaron Components) before it was used to capture two raw identical flame images at wavelengths of 650 and 800 nm (10 nm FWHM). The Thermera HS4 software (Mitsui Optronics, version 4.61) was used to process the captured raw image data to generate two-dimensional and line-of-sight false-colour maps of soot concentration. Details about the evaporating spray combustion experiments could be found in previous works by the authors [15]. The injector used is a single hole type with nozzle length of 1.2mm and sac volume of 0.488 mm^3. The injection system is a manually operated piston screw pump (High-Pressure Equipment Co. Model 37-5.75.60). It was designed with the capability of generating injection pressure up to 300 MPa in the   common rail. The injector was electronically controlled by an injector driver, while the common rail   pressure was measured with a pressure transducer. A pulse generator (Stanford Inc. DG 535) was used to synchronise the operation of the high-speed camera and injection system. An ambient density of 15 kg/m^3 was used to simulate engine conditions at a crank angle of −10° ATDC. In investigating the effect of injection pressures on spray and combustion, three injection pressures (100, 200 and 300MPa) were utilized. Two fuel injector nozzles with diameters of 0.16 mm (baseline) and 0.08 mm (micro-hole) were selected for the experiments. Biodiesel fuel from waste cooking oil (WCO) and conventional diesel were utilized in the experiments. For the spray experiments, ambient temperature of 293K and pressure of 1.4 MPa (non-evaporating) were maintained in the constant volume vessel. For the evaporating sprays and combustion experiments the ambient temperature and pressure were maintained at 885K and 4.0 MPa. Nitrogen which has similar properties like air was utilized for the spray experiment to create a non-reactive environment inside the constant volume chamber. For the combustion experiments the constant volume vessel was filled with air (21% oxygen gas). Table 1 shows the list of the experimental conditions, while Table 2 presents the physical and chemical properties of the WCO biodiesel and conventional diesel fuels.

**Table 1.** Fundamental experimental conditions

	Spray		Combustion
Ambient conditions			
Density (kg/m^3)	15 (-10° ATDC)		
Pressure. $P_{amb.}$ (MPa)	1.36 (non-evaporating); 4.0 (Evaporating)		4.0
Temperature, $T_{amb.}$ (K)	295 (non-evaporating); 885 (Evaporating)		885
Injection conditions			
Nozzle diameter, d_o (mm)	0.08; 0.16		0.16
Fuel Pressure, P_{inj} (MPa)	100; 300		100
Duration, $t_{inj.}$ (ms)	2.2		1.5
Injection quantity (g/s)	d_o = 0.08mm		d_o = 0.16mm
	100 MPa	**300MPa**	**100 MPa**
WCO biodiesel	1.64	2.85	14.21
Diesel	1.61	2.5	14.2

Table 2. Physical and chemical properties of fuels

Fuel Property	WCO biodiesel	Diesel
Density @ 15°C (kg/m^3)	885	830
Viscosity @ 40°C (mm^2/s)	4.45	3.36
Surface tension @ 20°C (mN/m)	33.1	30.6
Cetane number	51	45
Distillation temperature (°C)	360	320
Heating value (MJ/kg)	39.03	43.1
Sulphur content (ppm)	<3	<19
Carbon content (wt. %)	77.9	86.1
Hydrogen content (wt. %)	12.0	13.8
Oxygen content (wt. %)	10.1	<1

2.2 Engine Tests

To understand the performance of the WCO and diesel fuels in a real engine, engine tests were performed using the Robin DY23-2D direct injection single cylinder engine. With the aid of a tachometer, at full load, a constant engine speed of 1300rpm was maintained by the engine in testing WCO here in referred to as B100 (100% biodiesel) and its blends with diesel namely B20 (20% biodiesel, 80% diesel) B40 (40% biodiesel, 60% diesel), B60 (60% biodiesel, 40% diesel) alongside conventional diesel fuel (B7). At 1300rpm, constant engine full load of 3.73 Nm was maintained for all the fuels injected with slight variations in the mass flow rate (change in fuel density). For the full load the quantity of fuel consumed is 10ml in 61 secs. Figure 2 presents the schematic diagram of the engine set up with data acquisition system for testing the fuels.
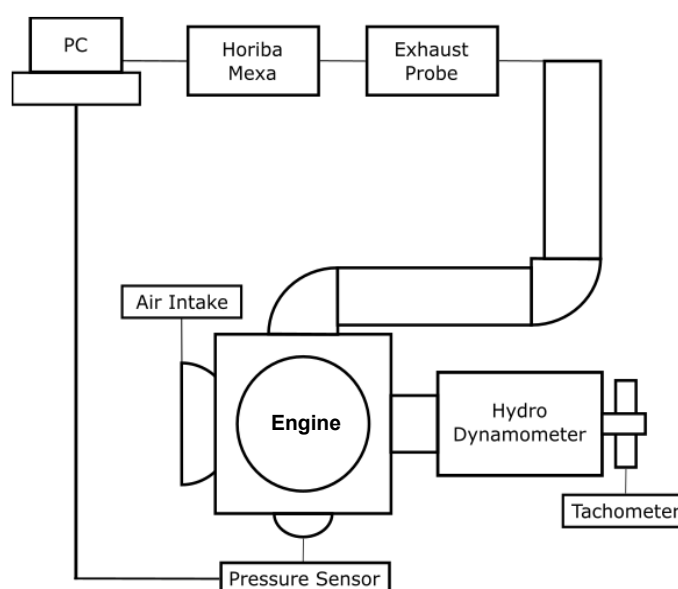
Fig. 2. Engine test set up with instrumentation

A hydro-turbomachinery dynamometer connected to the shaft was used to apply load unto the engine. Engine load via the dynamometer was controlled using the inlet valve which monitors the amount of water supplied to the system. A fixed injection pressure at 191.23 bar and fixed injection start timing of 23 BTDC (Before Top Dead Centre) could be obtained in the engine test bench. Furthermore, intake valve close and exhaust valve opening timings were maintained at 126 and 126 CA (crank angle) respectively. The Kistler Piezo transducer (6124A) was used to obtain the engine in cylinder pressure data. A LabVIEW programme was designed to control the engine set-up and acquire the in-cylinder pressure and crank angle data. The in-cylinder pressure data were used to obtain the rate of heat release data using an empirical model. Exhaust measurements of CO, CO_2, HC and NO_x were obtained using the HORIBA MEXA-584L emission analyser. Table 3 presents information about the single cylinder engine used for testing the fuels.

Table 3. Description of engine set up

Engine model	Robin DY23-2D Diesel
Type	single-cylinder, direct injection, air- cooled
Bore*Stroke	70 mm *60 mm
Piston displacement	230 cc
Compression ratio	21
Output	4.8 Hp @3600 rpm
Injection start (fixed)	23 BTDC
Injection pressure (fixed)	191.23 bar
Number of injector holes	4
Injector hole diameter	0.22 mm
Fuel pump model	ZEXEL PFRIMD55/2NP1

3. Results and Discussion

3.1 Non-evaporating spray characteristics

The line-of-sight spray morphology with gas entrainment velocities of the WCO and diesel fuels obtained through the LIF-PIV experiments are presented in Fig. 3. The images were obtained as a result of the elastic scattering of the laser beam by the spray droplets. For clarity, an enlarged form of the spray with air entrainment velocity field for diesel is presented alongside
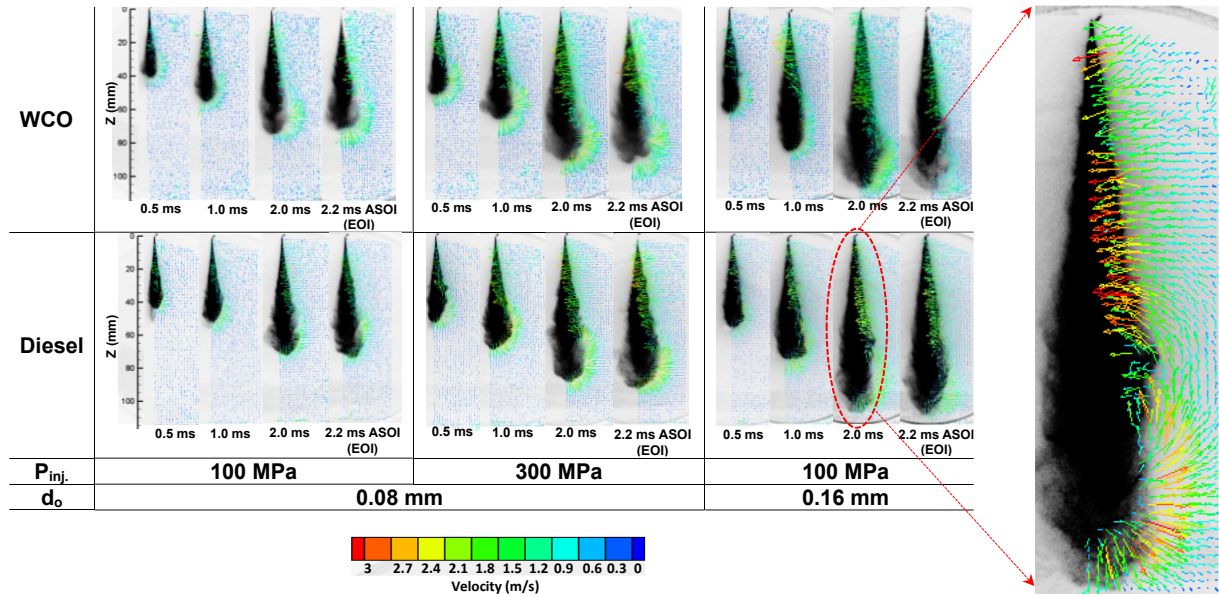

Fig. 3. Temporal variations in spray geometry and velocity distributions of ambient gas around spray

It could be observed as the spray propagates downward; the surrounding gas moved along creating an entrainment effect towards the upstream part of the spray.
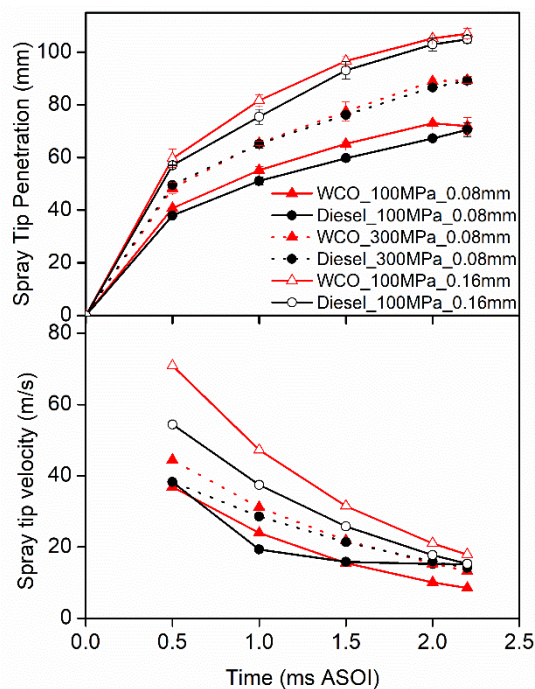
Fig. 4. Temporal variations in spray penetration and spray tip velocity

For both fuels, at 0.08mm, the sprays penetrate further downstream as injection pressure increased to 300 MPa. Furthermore, at an injection pressure of 100 MPa, the sprays penetrate further downstream as nozzle increased to 0.16mm. Further analyses on the line-of-sight images presented in Fig. 3 led to the temporal variation in spray tip penetrations and velocities in Fig. 4. As earlier discussed, for the 0.08mm nozzle, the increase in spray tip penetration as injection pressure increased to 300 MPa is due to increase in injection flow velocity. As a result of momentum increase, at the 100MPa, increase of the nozzle diameter from 0.08mm to 0.16mm led to increase in the spray tip penetration for both fuels. It could also be observed that the spray tip penetration at 100MPa with the 0.16mm nozzle is longer than that at 300 MPa with 0.08mm nozzle. Irrespective of fuel injection conditions as time proceeds WCO biodiesel tends to produce longer spray tip penetration compared to diesel. The WCO biodiesel viscosity and density which is about one and a half times of diesel could have played a major role in the atomization process thereby leading to longer spray penetration. For WCO, at an injection pressure of 100MPa and nozzle size of 0.08mm, the spray tip penetration decreased slightly at 2.2ms after the start of injection (ASOI) which corresponds to the end of injection (EOI). The reason for this needs further investigation. The spray tip velocity which was derived by finding the first derivative of the spray tip penetration is also presented in Fig. 4. It could be observed that the spray tip velocity decreased with time after the start of injection (ASOI). Considering the effect of injection conditions and fuel types, the spray tip velocity followed similar trend as the spray penetration. Furthermore, the spray tip velocity is higher than the surrounding gas velocity (about 3m/s maximum).
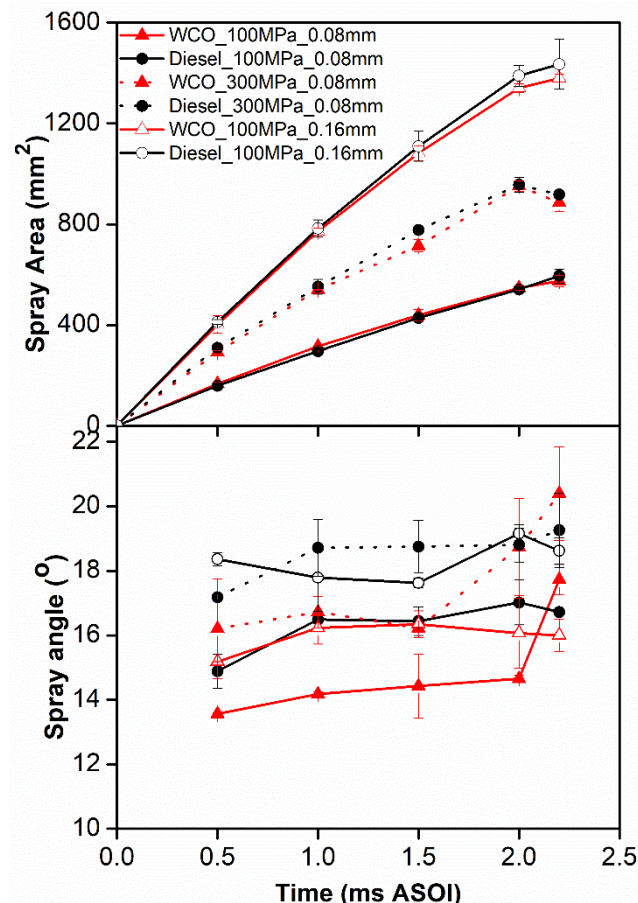

Fig. 5. Temporal variations in spray area and spray angle

The spray surface area for both fuels is presented in Fig. 5. For the 0.08mm nozzle, it could be observed as injection pressure increased to 300MPa, the spray surface area increased. Furthermore, by increasing the nozzle diameter to 0.16mm, the spray surface increased at 100MPa. At 100 MPa, the spray surface area by the 0.16mm nozzle is larger compared to that of 0.08mm at 300MPa. For both fuels there was no significant difference in the spray surface area at 100 MPa with the 0.08mm nozzle. However, as the injection pressure increased to 300MPa at 0.08mm and nozzle size increased to 0.16mm at 100MPa, the spray surface area of diesel fuel tends to be larger than WCO especially at the latter part of the spray development. On the other, the level of spray dispersion in the quiescent ambient condition characterized by the spray angle is also presented in Fig. 5. The spray angle was defined

based on the method described in previous work [13] by drawing lines touching the spray periphery tangentially. A horizontal line is drawn across the periphery lines utilising 60% of the spray tip penetration forming a triangle. Through this, the spray angle can be calculated using trigonometry. It can be observed that for the 0.08mm nozzle the spray angle increased for both fuels as injection pressure increased to 300MPa. Furthermore, at 100MPa as the nozzle increased to 0.16mm, the spray angle increased for diesel fuel whereas for WCO it was the opposite. This shows that the effect of nozzle size on spray angle is inconclusive taking into consideration fuel types and further investigation is required to understand the reasons behind this. It can be deduced that injection pressure had a significant impact on spray dispersion. As a result of higher fuel viscosity and density, at all injection conditions, WCO sprays tend to disperse less by producing smaller spray angles. As a result of the larger spray angle, the wider dispersion of diesel spray could have contributed to the larger surface area when injection pressure increased to 300MPa at 0.08mm nozzle and nozzle size increased to 0.16mm at 100MPa injection pressure.

3.2 Spray Entrainment Characteristics (Total entrained Gas, lateral and tip gas entrained)

The total entrained gas in the WCO and Diesel sprays was analysed using the entrainment velocity data presented alongside the spray images in Fig. 3. In calculating the total mass flow of the entrained gas, the schematic diagram in Fig. 6 earlier described in previous works by the authors [16] provides detailed information on the gas entrainment mechanisms in fuel sprays.
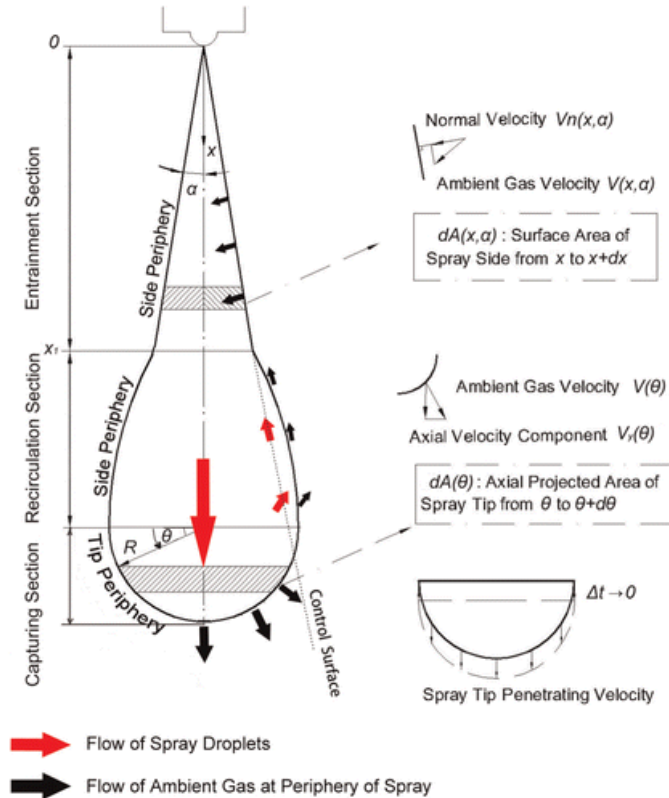
Fig. 6. Definition of velocity components and sections around spray periphery

In the schematic diagram, three sections namely entrainment, recirculation and capturing can be identified. The side periphery of the spray is associated with the entrainment and recirculation sections while the tip periphery of the spray is associated with the capturing section. From the schematic diagram, it could be noted that the recirculated gas constitutes the gas entrained at the spray periphery close to the injector.

From Fig. 6, the total mass flow rate of the gas entrained, $\dot{m}_{a_{entrained}}$ via the spray periphery can be defined as,

$$\dot{m}_{a_{entrained}} = \int_0^{X_1} \rho_a . V_n(x, \alpha). dA(x, \alpha) \tag{1}$$

At a point of the spray tip hemispherical (tip periphery) with radius, R measured from the centre at an angle θ , as the spray propagates, some quantity of surrounding gas is captured while some are pushed further downstream. Hence the total mass flow rate for the pushed gas, $\dot{m}_{a_{tip,pushing}}$ can be defined as,

$$\dot{m}_{a_{tip,pushing}} = \int_0^{\theta_1} \rho_a . V_y(\theta). dA(\theta) \tag{2}$$

For the entire spray tip hemispherical (tip periphery) region with radius R, the gas entrained during spray penetration, $\dot{m}_{a_{entire\ hemisphere}}$ is defined as,

$$\dot{m}_{a_{entire\ hemisphere}} = \pi R^2 \rho_a . V_{entire\ hemisphere} \tag{3}$$

From equations (2) and (3), the total gas captured at the spray tip, $\dot{m}_{a_{captured}}$ can be defined as,

$$\dot{m}_{a_{captured}} = \dot{m}_{a_{entire\ hemisphere}} - \dot{m}_{a_{tip,pushing}} \tag{4}$$

Therefore, the total mass flow rate of the gas entrained by the spray can be calculated as,

$$\dot{m}_{a_{total}} = \dot{m}_{a_{entrained}} + \dot{m}_{a_{captured}} \tag{5}$$

With equation (5) the temporal variation of the total gas entrained by the spray is presented in Fig. 7.

In Fig. 7, as the spray propagates, the total mass flow rate of the gas entrained increased with time and decline towards the end of injection especially at 100MPa with 0.16mm and 300MPa with 0.08mm. As a result of larger spray area, the total mass flow rate of the gas entrained is higher for the 100MPa with 0.16mm followed by 300MPa with 0.08mm. As a result of superior atomization processes, at all injection conditions, the total mass flow rate for diesel fuel is higher compared to WCO. Further analyses show that out of the total mass flow rate entrained, the percentage of gas entrained laterally increased as time proceeds while the percentage of gas entrained via the spray tip decreased. The implication of the decrease in the percentage of entrained gas via the spray tip could explain the existence of gas recirculation region as the spray propagates. The recirculated gas contributes to the gas entrained on the lateral side of the spray.
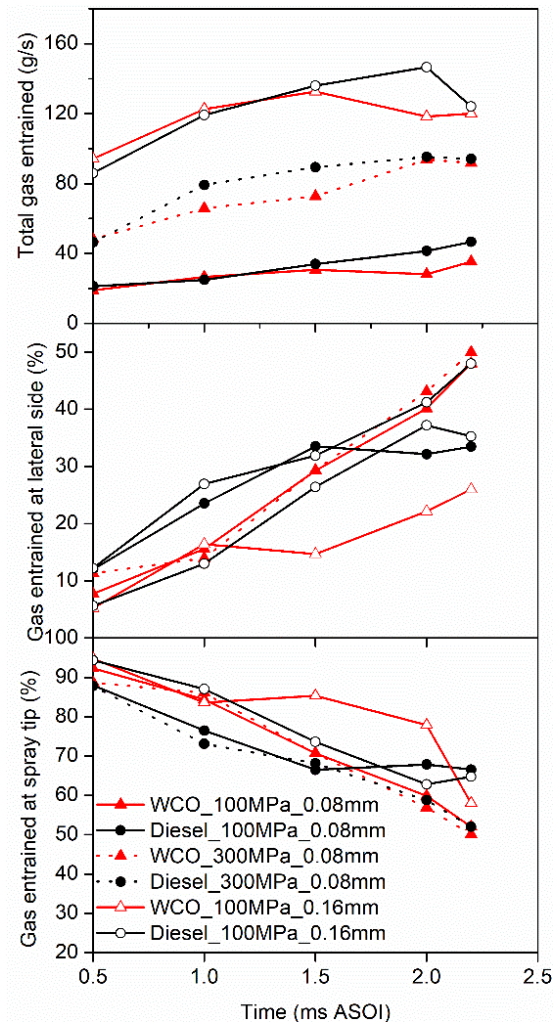
Fig. 7. Temporal variation of total gas entrained with percentage entrained at the spray lateral side and tip

To investigate the effectiveness of the fuel type and injection conditions on gas entrainment, the total mass flow rate of gas entrained in Fig 7. was normalized with the fuel mass flow rate.
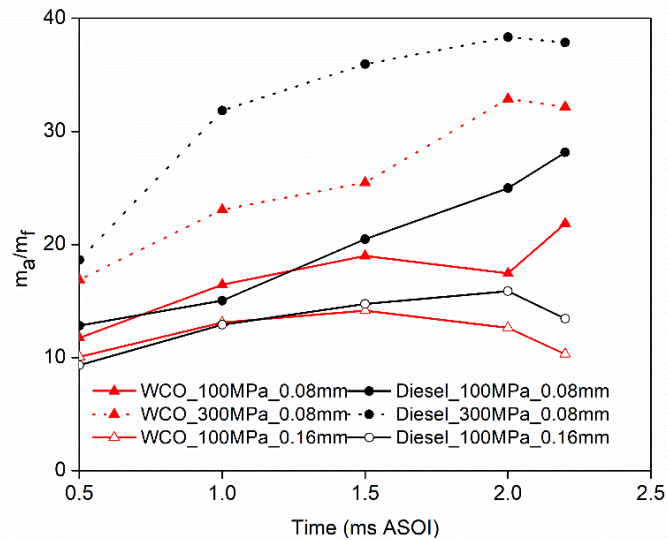

Fig. 8. Ratio of total mass flow rate of gas entrained to mass flow rate of fuel

It can be observed in Fig. 8, that the normalized gas mass flow rate increased with time while the spray propagates. Furthermore, for both fuels, the combined effect of the 300MPa injection pressure with 0.08 mm played a vital role in gas entrainment. As observed earlier the normalized total gas mass flow rate for diesel is higher compared to WCO.

3.3 Evaporating Spray

Under the evaporating conditions, the liquid length of the vaporized sprays is presented in Fig. 9. It could be observed in Fig. 9 that after an initial liquid spray development period, the tip of the liquid
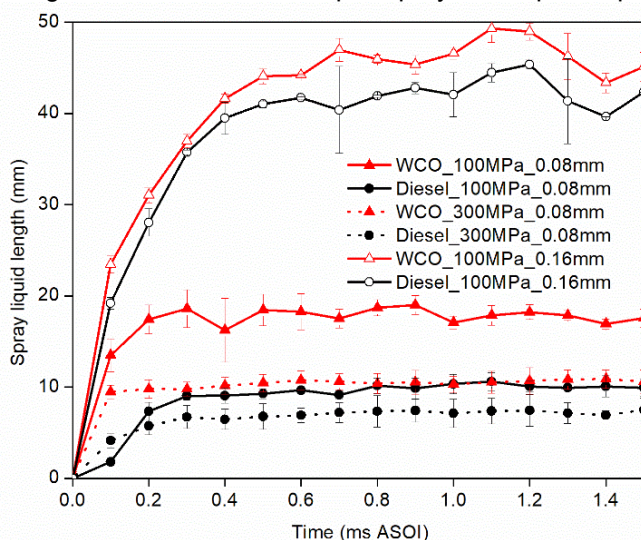
Fig. 9. Temporal variation of spray liquid length of evaporating sprays

phase fuel region reached a steady condition and fluctuated about a mean axial location due to turbulence. Furthermore, the impact of gas entrainment at the 300MPa injection pressure with 0.08 mm nozzle size can be identified on the vaporization processes causing shorter liquid lengths in both sprays. At all injection conditions, both WCO produced a longer liquid length compared to diesel. The reason for this can be attributed to inferior atomization by WCO, which limited the rate of evaporation as a smaller quantity of air was entrained in the spray. In addition, the higher boiling point property of WCO with low volatility could have initiated a longer liquid phase length. This phenomenon has been observed in previous works on liquid-phase penetration length [17-18].

3.4 Combustion Characteristics (OH- Ignition delay and LOL and Two Colour- KL factor)

The OH chemiluminescence and two colour pyrometry line of sight images of the combustion characteristics of WCO biodiesel are presented in Fig. 10. In Fig. 10 (a), autoignition spots with high temperatures can be identified. Furthermore, the auto-ignition spots have been observed in previous work [1] to be formed the fuel-air rich mixture location. As a result of enhancement in mixing which further accelerated the rate of reaction, it can be observed that increase in injection pressure led to shorter ignition delay (inset of Fig. 10 (a)) for both fuels. Furthermore, ignition delay timings for WCO biodiesel were shorter at all injection pressures. Cetane number and fuel oxygen content have been observed to have an influence on the reactivity of fuels [1]. Therefore, the shorter ignition delay by WCO could be attributed to its higher cetane number and fuel oxygen content. After autoignition, during the fuel injection period, the flame size increased and became quasi- steady at a location as presented in Fig. 10 (b). The distance from the injector tip to the quasi-steady location (represented by horizontal red lines) of the lifted flame is referred to as the flame lift-off length. Upstream of the lifted flame, the air entrained played a vital role in soot formation processes in a diesel engine. The region downstream of the flame lift-off is defined by a non-premixed zone characterized by OH radical species. As injection pressure increased, the spray velocity increased thus making the flame structure to be pushed further pushed downstream as it stabilized. At 100MPa, the difference in the flame lift-off length of WCO and diesel is not significant. However, at the 200 and 300 MPa, the flame lift-off length tends to be shorter
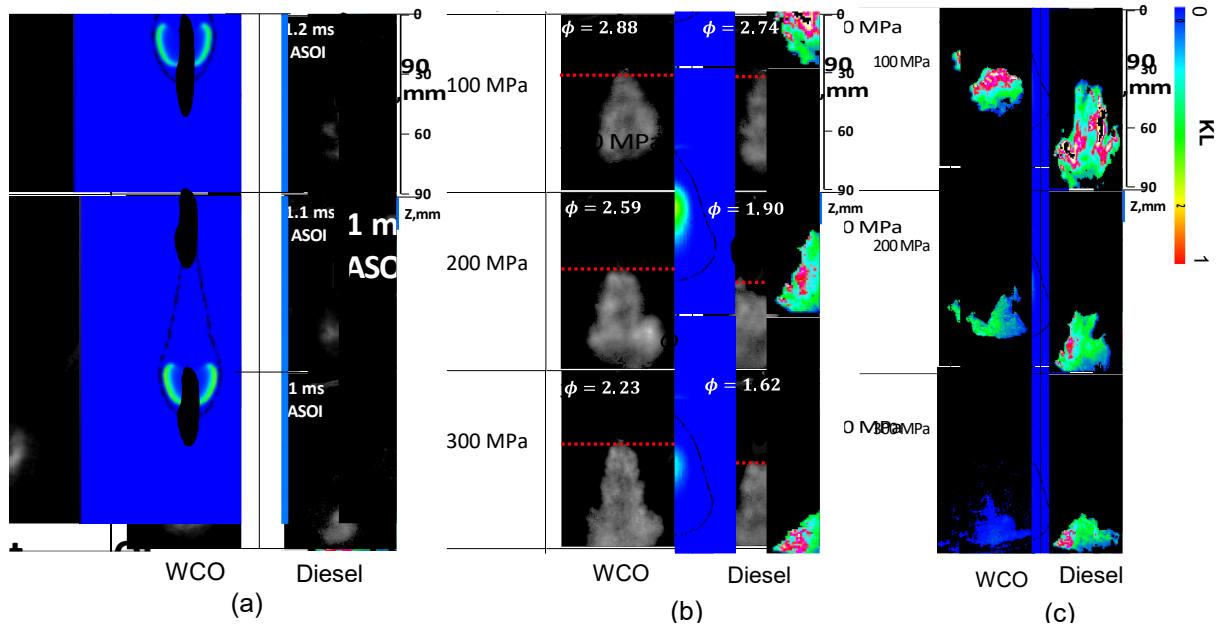
Fig. 10. Variations of (a) ignition delay, (b) lifted flames during injection event (1.4 ms ASOI) and (c) soot formation (0.25 ms AEOI) with injection pressure

compared to diesel. The presence of a cool flame (at low temperature) upstream of has been observed to play a vital role in the formation of a stabilized high temperature lifted flame. The cool flame is usually characterized by the formation of the formaldehyde (CH_2O) species [1]. The presence of the cool flame is an indication that ignition processes at low temperature are continuously occurring within the reacting spray as fuel and air mix upstream of the lifted flame. As hot air is entrained upstream during the fuel injection period, it mixes with the cool flame thus leading to a high-temperature ignition flame. The downstream high-temperature flame propagates upward joining the new flame to form a quasi-stable flame. The transition from the cool flame to high temperature lifted flame has been reported to be influenced strongly by the fuel type [19]. Therefore, the shorter flame lift-off length observed in WCO could be attributed to the closer location of the CH_2O species to the injector. In addition, as a result of higher fuel density yielding a lower injection velocity (obtained by Bernoulli's equation) and higher viscosity (lower discharge coefficient), WCO flame lift off length is shorter than diesel. These observations have been reported in previous works by [20].

In quantifying the amount of air entrained upstream of the lifted flame in (Fig. 10 (b)), the model by Naber and Siebers (21) presented in equation (6) was used.

$$\phi = \frac{2(A/F)_{st}}{\sqrt{1 + 16\left(\frac{L_o}{x^+}\right)^2} - 1} \tag{6}$$

Where ϕ is an expression for the cross-sectional local equivalence ratio, at any axial location L_o (autoignition location and flame lift of length) in a combusting fuel jet. The ϕ values provide information about the quantity of air entrained in forming reacting mixtures. The term, x^+ is a characteristics length scale for the fuel jet while $(A/F)_{st}$ is the stoichiometric air fuel ratio by mass which can be obtained by using the carbon, hydrogen and oxygen contents as obtained in Table 2. For WCO and diesel, $(A/F)_{st}$ have values of 12.61 and 14 respectively. Detailed explanation of x^+ can be found in previous work [13]. As presented in Fig. 10 (b) (see inset), it could be observed that the local equivalence ratio decreased as injection pressure increased up to 300MPa. This further led to more air entrained upstream while the flame reaction zone was further pushed downstream. As observed earlier in the LIF-PIV experiments, more air was entrained upstream of the flame because of the enhancement in mixture formation during flame propagation. At all injection pressures, due to poor atomization, WCO lifted flame were shorter with less air entrained upstream which further led to higher equivalence ratio.
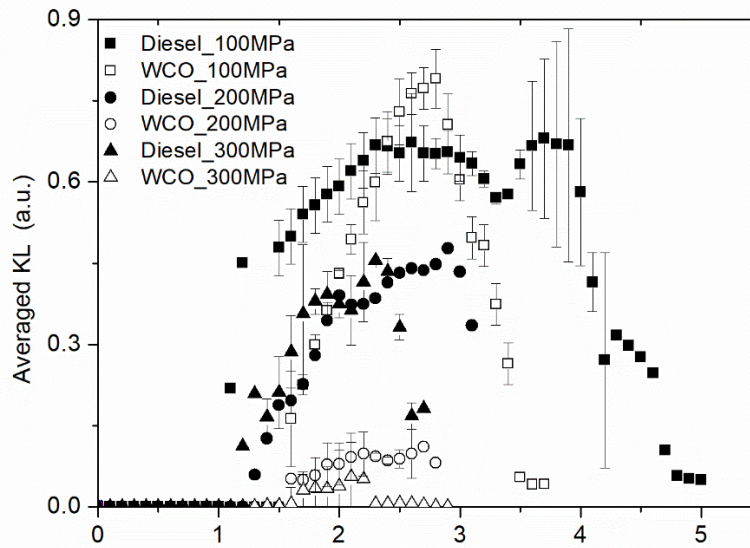
**Fig. 11.**   Temporal variations of predicted soot formed with injection pressure

In gaining detailed understanding on the soot characteristics of the fuels, the KL images obtained from the two-colour pyrometry experiments are presented in Fig. 10 (c). The soot KL factor is expressed in soot number per cm^2. It can be observed in Fig. 10, that as injection pressure increased from 100 to 300 MPa, both soot quantity and area decreased. With WCO equivalence ratios higher (refer to Fig. 10 (b)), the intensity of the KL contours was lower compared to diesel especially at the 200 and 300 MPa injection pressures. This implies that WCO soot formation does not depend on the quantity of air entrained of the lifted flame. In addition, works by [22] has showed that equivalence ratio is not a valid metric to define the relationship of oxygenated fuel with an oxidizer in terms of its mixture stoichiometry. Therefore, the use of oxygen ratio, Ω,defined in equation (7) has been proposed by [22] to deal with these ambiguities.

$$\Omega = \frac{n_O}{2n_C + \frac{1}{2}n_H} \tag{7}$$

Where n_O, n_C and n_H are the number of oxygen, carbon and hydrogen atoms respectively in the stoichiometry chemical reactions taking into consideration the elemental composition of both fuels in Table 2. Equation 7 is valid if the product of the stoichiometry reaction is considered saturated i.e. saturated stoichiometry products (SSP). Carbon dioxide, water, and molecular nitrogen are typical examples of SSPs in combustion reactions. With equation 7, the oxygen ratio of WCO is 1.6% while diesel fuel has a value of zero since it has no oxygen in its atom. Compared to diesel, the higher oxygen ratio promoted soot oxidation in WCO despite its higher local equivalence ratio which is dependent on the entrained air. Fig. 11 presents the temporal variation of the soot quantity formed by WCO and diesel fuels. Soot quantity increased from the beginning of the combustion event towards the end of injection period. However, after the end of fuel injection, it decreased due to the enhancement in oxidation processes. As a result of enhancement in air entrainment, increase in injection pressure led to the decrease in soot quantity. WCO displayed early soot formation and produced more soot especially at 100 MPa compared to diesel after the end of injection (AEOI). However, at a later period (about 0.75 ms AEOI), at all injection pressures, the net soot formed by WCO declined faster compared to diesel. Since WCO entrained less air compared to diesel, the reduction in net soot could be attributed significantly to the chemical bounded fuel oxygen. Hellier et al. [23] reported that the oxygen content of a fuel has the tendency to play vital role in soot oxidation. As earlier presented in Table 3, oxygen content in WCO is 11.1% as against diesel which is less than 1% or negligible. Therefore, as injection pressure increased, the oxygen atom in WCO could have enhanced soot oxidation during the combustion events.

3.5 Engine test measurements

In Fig. 12, the in-cylinder pressure data for WCO biodiesel (B100) and its blends (B20, B40 and B60) obtained through the Kistler transducer are presented alongside conventional diesel (B7 i.e., 7% of biodiesel). The in-cylinder data was obtained from 200 engine cycle mean data.
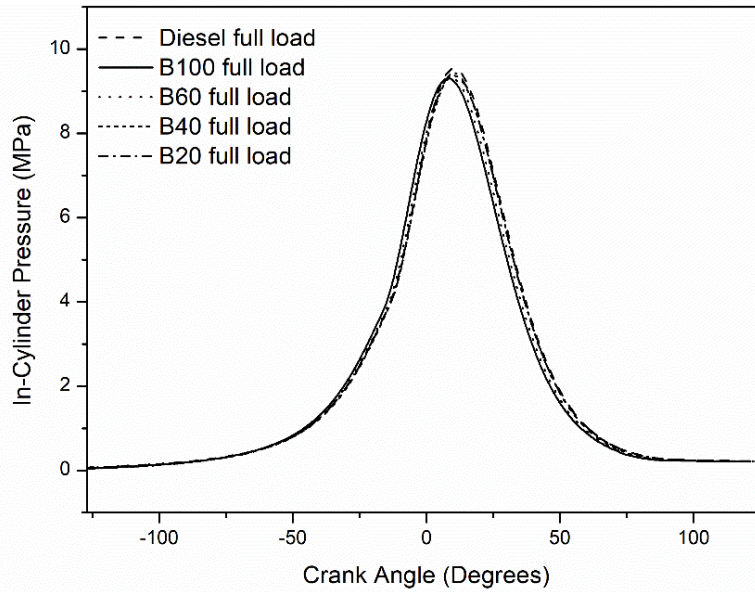
Fig. 12.   Variation of engine in-cylinder pressure with crank angle

After the maximum in-cylinder pressure during motoring (around 5.7 to 5.8 MPa), it can be observed that the in-cylinder pressure for B100 increased more towards the top dead centre (TDC i.e., 0° crank angle). However, after the TDC, B7 produced the highest peak pressure. The in-cylinder pressure in Fig. 11 can be used to evaluate the rate at which chemical energy is released during the combustion event. This is referred to as the apparent heat release rate (HRR). The HRR is calculated using the empirical model by [22] as presented in equation (8).

$$HRR = \frac{\gamma}{\gamma - 1} P \frac{dV}{d\theta} + \frac{1}{\gamma - 1} V \frac{dP}{d\theta} \qquad (8)$$

Where θ is the crank angle and γ is the specific heat ratio assumed to be constant at 1.33, V is the cylinder volume, P is the in-cylinder pressure, γ is the polytropic index with a value of 1.33. As presented in Fig. 13, it could be observed that the HRR increased from the start of fuel injection and reach the peak after the TDC. B7 produced the highest peak HRR compared to WCO and its blends. As presented in Table 2, the higher peak HRR by B7 could be attributed to the fuel higher energy content.
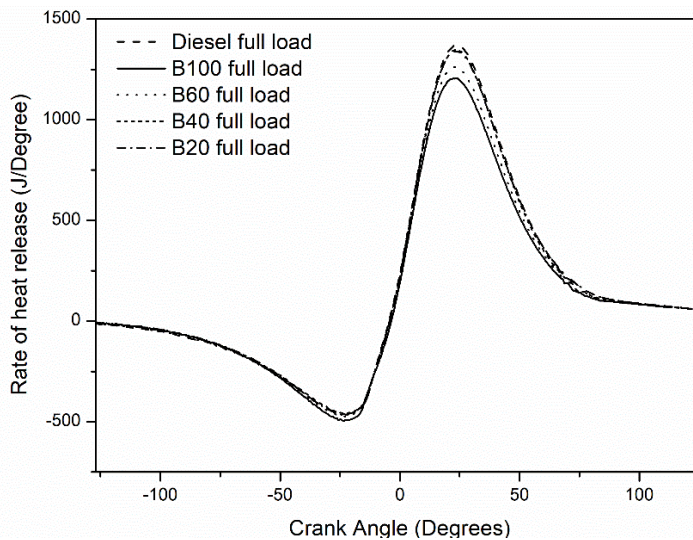
Fig. 13.   Variation of heat release rate (HRR) with crank angle

The shortcoming of equation (8) in analysing the HRR is that it lacks the heat transfer model.   Therefore, a CFD analyses was performed to obtain the apparent HRR (AHRR) taken into consideration the convection/diffusion heat transfer model. Fig. 14, presents the AHRR from the CFD analyses
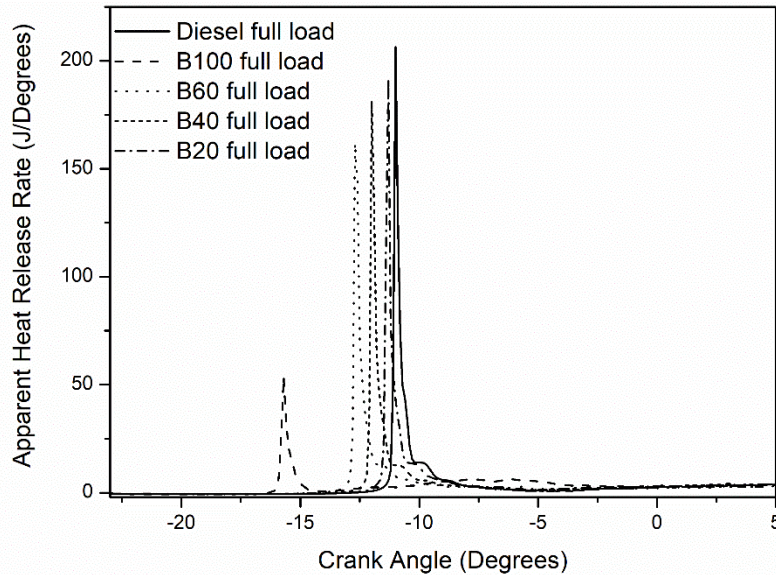
Fig. 14. Simulation of apparent heat release rate (AHRR) with the heat transfer model

As presented in Fig. 14, peak AHRR decreased as the quantity of biodiesel increase and diesel decrease in the blend. Furthermore, there is an early rise of heat release as the quantity of biodiesel increase in the blend. This implies that increase of biodiesel enhanced faster reactivity of the fuel. As obtained earlier in Fig. 13, diesel has the highest peak AHRR.

Ignition delay was determined using the method described in [24-25]. In Fig. 15, ignition delay was obtained by finding the difference between crank angle of the start of injection (23° BTDC) and the maximum first derivative in-cylinder pressure, $\left(dP_{incyl.}/d\theta\right)_{max}$.
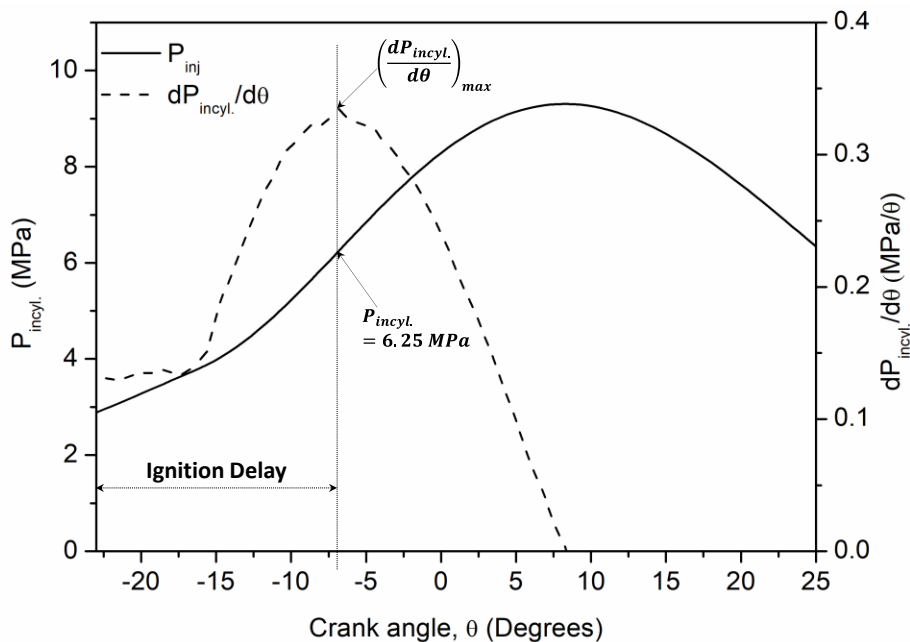
Fig. 15. Definition of ignition delay using B100 In-cylinder pressure data

The value of $\left(dP_{incyl.}/d\theta\right)_{max}$ corresponds to an in-cylinder pressure of 6.25 MPa, which is more than the maximum motoring pressure. By using the method in Fig 15., it can be observed in Fig. 16, that ignition delay was shorter for B100 compared to B7. Furthermore, ignition delay decreased as the

quantity of biodiesel increased in the blends. As observed in previous works [26] the reduction in ignition delays can be attributed to the higher cetane number of WCO biodiesel.
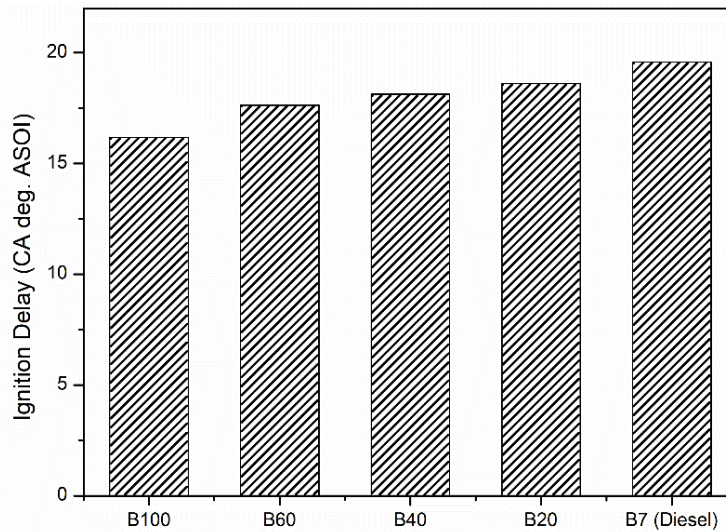
Fig. 16.   Ignition delay of WCO biodiesel, with blends and conventional diesel

Furthermore, the CO and CO_2 emission species measured by using the Horiba emission analyzer at the exhaust is presented in Fig. 17.
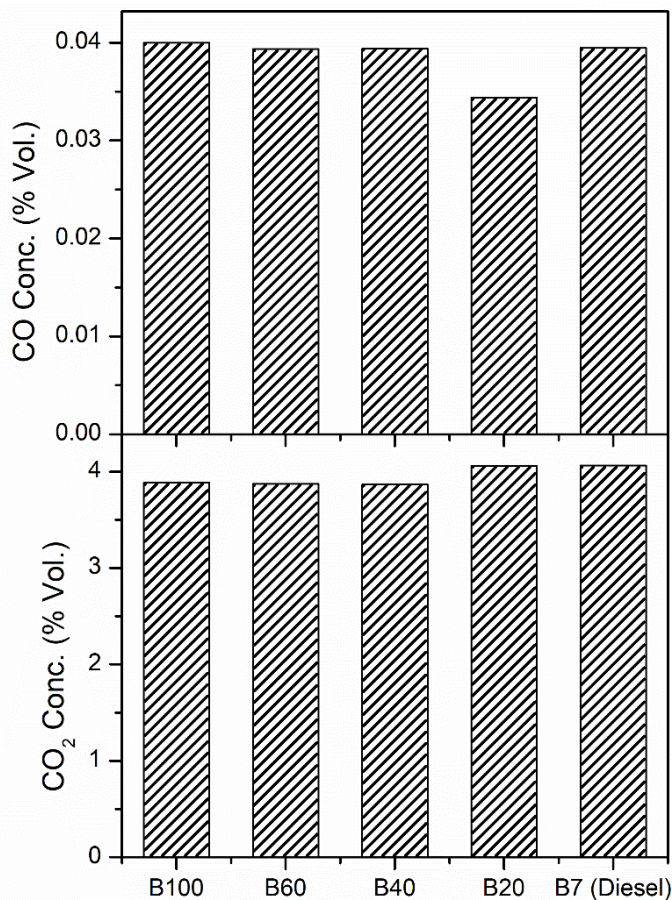
Fig. 17.   CO and CO_2 exhaust emission for WCO, WCO blends and conventional diesel

Except for B20, there is no significant difference for the concentration of CO. The reason for this needs further observation.   Furthermore, there is a slight increase in CO_2 as the quantity of the biodiesel

decreases in the blend. As observed in [27] the slight decrease in CO_2 in WCO biodiesel and its blends could be due to higher oxygen and lower carbon content.

In order to account for the fuel's chemical energy released in the engine, the combustion efficiency, η_C is defined in equation (9) and analysed using the CO and CO_2 concentrations as defined.

$$\eta_C = \frac{\tilde{x}_{CO_2}CO_2}{\tilde{x}_{CO_2}CO_2 + \tilde{x}_{CO}CO} \tag{9}$$

Where $\tilde{x}_{CO_2}$ and $\tilde{x}_{CO}$ are the mole fractions (% by volume) of CO2 and CO respectively.

Furthermore, the thermal efficiency, η_T which indicates the extent to which workdone by the engine is converted to heat output is calculated as follows;

$$\eta_T = 1 + \frac{1}{\gamma} \left[\frac{1}{\left(\frac{r_c^\gamma}{r_e}\right) - r_c^{\gamma-1}} - \frac{1}{r_e^{\gamma-1} - \left(\frac{r_e^\gamma}{r_c}\right)} \right] \tag{10}$$

Where r_e and r_c are the expansion and compression ratio respectively.
Figure 18 presents the variations of η_C and η_T for the fuels;
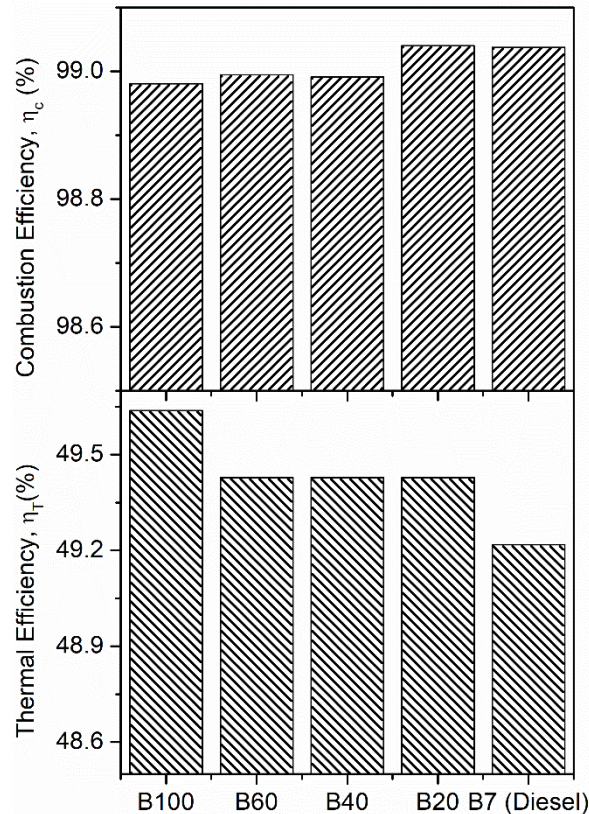
Fig. 18. Combustion and Thermal Efficiencies for WCO, WCO blends and conventional diesel

As presented in Fig. 18, increase in WCO in blends led to decrease in combustion efficiency. The decrease could be as a result of inferior atomization of WCO since it has higher density and viscosity compared to diesel. This observation has been reported by [28]. On the other hand, there was no significant difference in thermal efficiency for B20, B40 and B60. However, as WCO increase in the blends, thermal efficiency increased. This could be as a result of the enhanced combustion due to the fuel borne oxygen content of WCO which is significant compared to diesel.
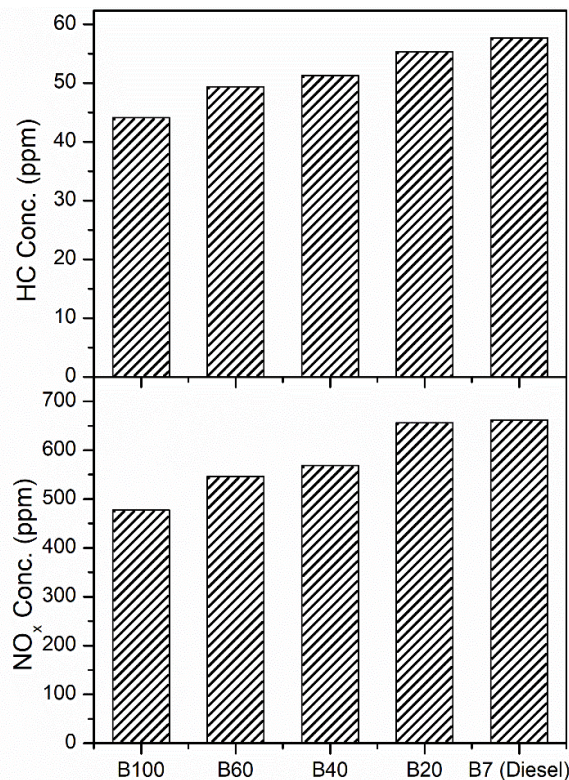
Fig. 19. HC and NOx exhaust emission for WCO, WCO blends and conventional diesel

In addition to Fig. 19, the NO_x and HC emission characteristics of the fuels are presented in Fig. 16. Compared to B7, it can be observed that both HC and NO_x emission decreased as the quantity of biodiesel increased. As reported in [27] due to the shorter ignition delay of WCO, the level of mixture over leaning is reduced thereby promoting faster premixed combustion durations which further led to the reduction of HC emission as the quantity of WCO increased in the blends. On the other hand, as the quantity of WCO biodiesel increased the quantity of NO_x emission reduced. As observed in [29], the reduction in NO_x could be due to the lower energy content of WCO biodiesel. Furthermore, it was observed in [23] that longer ignition delay has the tendency of leading to higher quantity of NO_x production. Therefore, since increase in WCO biodiesel quantity led to decrease in ignition delay, the quantity of NO_x is reduced.

4. Conclusion

Fundamental experiments using optical diagnostics such as the LIF-PIV, shadowgraphy and chemiluminescence techniques with high pressure rig have used to characterize WCO biodiesel spray combustion processes under diesel engine conditions. Furthermore, tests using a single cylinder engine were done to complement fundamental experiments. Under non-evaporating conditions, it was observed that due to higher viscosity, WCO biodiesel produced longer spray penetration, spray velocity and shorter spray angle. Furthermore, due to the inferior atomization of WCO biodiesel, the quantity of gas entrained was lower. Under evaporating conditions, WCO biodiesel longer liquid length due to less quantity of gas entrained and higher distillation temperature. The combined effect of ultra-high injection pressure of 300 MPa with smaller nozzle hole diameter of 0.08mm was observed to enhance gas entrainment processes. Due to higher cetane number WCO biodiesel produced shorter ignition delay. With less air entrained upstream of the lifted flame, it was observed that the oxygen atoms in WCO biodiesel molecule played a crucial role in soot formation. From the engine experiments, due to lower heating value, the peak in-cylinder pressure decreased as the quantity of biodiesel increased in the blends. It was also observed that as the quantity of biodiesel increased, ignition delay and peak heat release rate decreased. Emission measurements at the exhaust showed that for all fuels, there was no significant change in CO and CO_2 species. However, hydrocarbon and NO_x were observed to reduce

drastically as the quantity of biodiesel increased in the blends. It was observed that the shorter ignition delay of the WCO biodiesel played a crucial role in the HC and NO_x.

References

[1] O.A. Kuti, S.M. Sarathy, K. Nishida, Spray combustion simulation study of waste cooking oil biodiesel and diesel under direct injection diesel engine conditions. Fuel 267 (2020) 117240.

[2] The Role of Biofuels Beyond 2020 Commissioned by BP Executive summary 2013:1–30. Element Energy Limited 20 Station Road Cambridge CB1 2JD.

[3] Automotive fuels - Diesel - Requirements and test methods 2009. http://www.envirochem.hu/www.envirochem.hu/documents/EN_590_2009_hhV05.pdf.

[4] O.A. Kuti, W. Zhang, K. Nishida, X. Wang, Z. Huang, Effect of injection pressure on Ignition, flame development and soot formation processes of biodiesel fuel spray. SAE Int. J. Fuels and Lub. 3 (2010) 1057- 1070.

[5] C. Jin, M. Yao, H. Liu, C.F. Lee, J. Ji, Progress in the production and application of n-butanol as a biofuel Renew Sustain Energy Rev, 15 (2011) 4080-4106.

[6] A. Hull, I. Golubkov, B. Kronberg, J. van Stam, Alternative Fuel for a Standard Diesel Engine Int J Engine Res, 7 (2006) 51-63.

[7] A.N. Ozsezen, M. Canakci, C. Sayin, Effects of biodiesel from used frying palm oil on the performance, injection, and combustion characteristics of an indirect injection diesel engine Energy Fuels 22 (2008) 1297-1305.

[8] M. Lapuerta, J. Rodríguez-Fernandez, J.R. Agudelo, Diesel particulate emissions from used cooking oil biodiesel. Bioresour Technol, 99 (2008) 731-740.

[9] K. Muralidharan, D. Vasudevan, Performance, emission and combustion characteristics of a variable compression ratio engine using methyl esters of waste cooking oil and diesel blends Appl Energy 88 (2011) 3959-3968.

[10] J. Hwang, Y. Jung, C. Bae, Spray and combustion of waste cooking oil biodiesel in a compression-ignition engine. Int J Engine Res, 16 (2015) 664-679

[11] J. Hwang, C. Bae, T. Gupta, Application of waste cooking oil (WCO) biodiesel in a compression ignition engine. Fuel 176 (2016) 20-31.

[12] W. Zhong, P. Tamilselvan, Q. Wang, Z. He, H. Feng, X. Yu, Experimental study of spray characteristics of diesel/hydrogenated catalytic biodiesel blended fuels under inert and reacting conditions. Energy 153 (2018) 349-358.

[13] O.A. Kuti, K. Nishida, J.Y. Zhu, Experimental studies on spray and gas entrainment characteristics of biodiesel fuel: Implications of gas entrained and fuel oxygen content on soot formation. Energy 57 (2013) 434-442.

[14] J.Y. Zhu, C. Shan, K. Nishida, W. Long, D. Dong, Simultaneous PIV/LIF-PIV measurements and numerical simulation of liquid flow and ambient gas flow for transient diesel spray. Fuel 309 (2022) 122211.

[15] O.A. Kuti, J.Y. Zhu, K. Nishida, X.G. Wang, Z.H. Huang, Characterization of spray and combustion processes of biodiesel fuel injected by diesel engine common rail system. Fuel 104 (2013) 838 846.

[16] J.Y. Zhu, O.A. Kuti, K. Nishida, An investigation of the effects of fuel injection pressure, ambient gas density and nozzle hole diameter on surrounding gas flow of a single diesel spray by the laser

induced fluorescence–particle image velocimetry technique. Int J Engine Res, 14 (6) 630-645.

[17] T. Fang, Y.-C. Lin, T.M. Fong, C.-F. Lee, Biodiesel combustion in an optical HSDI diesel engine under low load premixed combustion conditions. Fuel 88 (2009) 2154-2162.

[18] D. Siebers, Liquid-phase fuel penetration in diesel sprays. SAE Paper 980809, 1998.

[19] L.M. Pickett, D. Siebers, C. Idicheria, Relationship between ignition processes and the lift-off length of diesel fuel jets. SAE Paper 2005-01-3843, 2005.

[20] D. Siebers, B. Higgins, Flame lift-off on dierect injection diesel sprays under quiescent conditions. SAE Paper 2001-01-0530, 2001.

[21] J. Naber, D. Siebers, Effects of gas density and vaporization on penetration and dispersion of diesel sprays. SAE Paper 960034, 1996.

[22] C.J Mueller, The quantification of mixture stoichiometry when fuel molecules contain oxidizer ele ments or oxidizer molecules contain fuel molecules. SAE Paper 2005-01-3705, 2005.

[23] P. Hellier, M. Talibi, A. Eveleigh, N Ladommatos, An overview of the effects of fuel molecular structure on the combustion and emissions characteristics of compression ignition engines. Proc IMechE Part D: J Automobile Engineering 2018, 232(1) 90 –105.

[24] J.B. Heywood, Internal Combustion Engines Fundamentals. edn. McGraw-Hill., 1988.

[25] N.A. Nieto, A.A.M Oliveira, E. Bazzo, An ignition delay correlation for compression ignition engines fueled with straight soybean oil and diesel oil blends. Fuel 257 (2019) 116050.

[26] A. Blazevic, D. Bibic, I. Filipovic, Influence of determining the period of ignition delay on the heat release characteristics of diesel engines fueled with diesel and biodiesel. International congress motor vehicles and motors 2018.

[27] O. Sogbesan, C.P. Garner, M.H. Davy, The effects of increasing FAME biodiesel content on combustion characteristics and HC emissions in high-EGR low temperature combustion. Fuel 302 (2021) 121055.

[28] P. Thaiyasult, K. Painthong, B. Milton, Combustion efficiency and performance of RSO biodiesel as alternative fuel in a single cylinder CI engine. Energy Exploration and Exploitation. 30 (2012) 153–166.

[29] Y.D. Wang, T. Al-Shemmeri, P. Eames, J. McMullan, N. Hewitt, Y. Huang, S. Rezvani, An experimental investigation of the performance and gaseous exhaust emissions of a diesel engine using blends of a vegetable oil. Appl. Thermal Eng. 26 (2006) 1684–1691.

Session S1.3 H$_2$ Fundamental Studies

A Fundamental Investigation of Premixed Hydrogen Oxy-Combustion in Carbon Dioxide

N. Nasim[1], B. Nawaz[1], S. K. Das[1], A. SubLaban[1], J. H. Mack[1]

[1] Department of Mechanical Engineering, University of Massachusetts Lowell, 1 University Avenue,

Lowell, MA, USA.

E-mail: John_Mack@uml.edu
Telephone: +(1) 978 934 5766

Abstract. Hydrogen (H_2) is increasingly viewed as an attractive carbon-free fuel due to its potential compatibility with the existing transportation and conversion infrastructure. However, one of the major challenges facing large-scale deployment is the fundamentally different combustion properties it has in comparison to commonplace hydrocarbon fuels such as natural gas. For example, the laminar burning velocity (LBV) of a combustible mixture has a direct impact on how it can be used in internal combustion engine or gas turbines; the LBV of hydrogen is over 7 times greater than that of natural gas when combusted in air. Carbon dioxide (CO_2) can be used as a working fluid, as opposed to nitrogen (in air), to reduce the flame speed of hydrogen combustion. A mixture of hydrogen, oxygen, and carbon dioxide as a working fluid can provide LBVs comparable to natural gas in air, which potentially enables existing conversion architectures. Furthermore, by replacing nitrogen (N_2) with CO_2 in the mixture, NO_x emissions are avoided and opportunities for carbon sequestration or closed-cycle processes are possible. This study experimentally explores fundamental premixed oxy-combustion properties of H_2/CO_2 mixtures in a constant volume combustion chamber (CVCC) across a range of initial pressures (1, 1.5 and 2 bar) and equivalence ratios (0.4, 0.6, 0.8, 1). The spherically expanding flames are examined to determine the flame speed, LBV, and lower flammability limits (LFL) with respect to different CO_2 concentrations (40%, 60%, 65%). Furthermore, it was identified that the flame speed of the 65% CO_2 case at an equivalence ratio of 1 and initial pressure of 1 bar matches the closest with methane-air stoichiometric combustion.

Nomenclature

LBV	Laminar burning velocity
CVCC	Constant volume combustion chamber
LFL	Lean flammability limit
P_i	Initial pressure
MIE	Minimum ignition energy

1. Introduction

The transportation sector requires approximately 5.6×10^{20} J of energy per year, primarily dependent on fossil fuels by consuming around 11 billion liters of fuel every day to power approximately 380 million commercial vehicles and 1.2 billion passenger cars worldwide [1-4]. Light-duty vehicles, especially gasoline-fueled passenger cars, supply 44% of global transport energy demand and gasoline-based spark-ignition engines power around 80% of the total passenger cars worldwide [5,6].

With the increasing energy demand and decarbonization technology transition, it is imperative to reduce the usage of fossil fuels by utilizing cleaner alternative fuels that can leverage the existing internal combustion engines and gas turbines to ensure efficient combustion with low anthropogenic carbon emission. Hydrogen is one of the cleanest fuels with lower minimum ignition energy (0.017 mJ) [7], lower volumetric energy density [8], higher diffusivity [9], and a wider flammability range (4–75 vol%) [10] in comparison to traditional alternative fuels. These intrinsic properties of hydrogen result in a highly energetic rapid/instantaneous burning and propagation velocity, which is ten times higher than methane [11] and poses challenges to a potential drop-in replacement strategy. One method to address the rapid combustion is to add inert gases that suppress the rapid combustion event. Depending on the dilutant

type and dilutant ratio, a different predominant effect is observed during the combustion process [12-14]. One of the critical metrics to quantify this difference is the laminar burning velocity (LBV), a key parameter in premixed combustion measured as the normal component of flame velocity relative to unburned gas. It contributes to understanding the mixture diffusivity, reactivity, and exothermicity [15-17]. Numerous experimental efforts demonstrated the effect of inert gas addition such as argon, helium, nitrogen, carbon di-oxide and water vapor on hydrogen premixed combustion [18, 13, 19]. Duan and Liu [20] investigated premixed laminar flame of a H_2-air mixture with diluted N_2+H_2O and concluded a 64.3% decrease in flame propagation velocity with a dilution ratio from 10-40% at an equivalence ratio of 1, an initial pressure of 0.1 MPa and an initial temperature of 393K. Morovatiyan et al. [21] utilized argon as a working fluid in a $H_2/O_2/N_2$ premixed flames for 0.2–0.6 bar initial pressure, 298 K initial temperature and a broad range of equivalence ratio (0.2–3.0) and concluded that with the increasing argon content in the mixture, the flame speed and burning velocity increased while extending the lean flammability limit. Wang et al [22] examined the flame characteristics under sub-atmospheric pressure and room temperature with a wide range of equivalence ratios of H_2/air pre-mixtures diluted with Ar, N_2, and CO_2. Their experiments indicated that maximum pressure rises, and deflagration index are primarily dependent on dilutant type, and fraction while CO_2 was mentioned as a most effective inert gas for decreasing the speed associated with flame front expansion followed by the N_2 and Argon. Zhang et al. [18] conducted a computational study in terms of the efficacy of combustion suppression for N_2, He, Ar, and CO_2 and indicated Ar < N_2 < He < CO_2 in terms of effectiveness. When CO_2 is mixed with H_2 for ignition, [23] additional energy is required to raise the mixture temperature compared to nitrogen due to the higher specific heat capacity [24]. Li. et al. [25] investigated laminar combustion characteristics of $N_2/$ H_2/air and $CO_2/$ H_2/air and summarized that CO_2 has a more substantial dilution effect than N_2 in reducing LBV owing to both chemical effect and thermal effect. Katsumi et al. [26] studied the effects of CO_2 and water vapor mixture on hydrogen/air premixed flames and concluded that the addition of CO_2 or H_2O advances the unstable motion of hydrogen flames, and the reason was explained by the increment of diffusive-thermal behaviors of the flames. One standard method to intake CO_2 or H_2O vapor into the engine cylinder is utilizing the exhaust gas recirculation [27,28]; however, different CO_2 reformer methodology is still under research which can be implemented and incorporated into the future mobile transportation system [29].

Considering all the above, using CO_2 as the working fluid has the potential to balance the high LBV and make the use of H_2 more compatible with existing systems. Furthermore, replacing nitrogen eliminates the potential NOx emissions and may be used with carbon sequestration and closed-loop cycles. This experimental work investigated premixed hydrogen oxy-combustion with CO_2 as a working fluid, varying equivalence ratios ranging from 0.6 to 1.0 under different initial pressure conditions. The experiments were carried out in an optically accessible constant volume combustion chamber and a z-type schlieren technique was utilized to capture the flame morphology and a dynamic pressure sensor to measure chamber pressure.

2. Methodology

Flame speed, laminar burning velocity (LBV), and the lower flammability limits (LFL) are calculated for hydrogen gas combustion under a matrix of experimental conditions of varying the percentage of CO_2 in the mixture (CO_2%), initial pressure (1.0 bar, 1.5 bar, 2.0 bar), and equivalence ratio (1.0, 0.8, 0.6). Figure 1 shows the experimental setup, including the constant volume combustion chamber (CVCC), gas tanks, pressure transducers, and Schlieren imaging used to acquire data for the analysis.

The stainless-steel CVCC has an internal diameter of 140 mm and a volume of 1.93 L. Two 127 mm thick quartz viewing windows are supported by flanges. Proper sealing of the chamber is required for filling the chamber with the gas mixtures, ensuring constant volume during combustion, and for sufficient vacuuming after combustion; therefore, a high temperature O-ring is planted between the quartz windows and flanges. In order to generate a spark ignition, two electrodes are inserted from symmetrically opposite sides of the chamber, leaving a 1.36 mm gap where the spark occurs. The spherically expanding flame is observed using the optically accessible CVCC and a Z-type Schlieren imaging setup. The optical system uses a halogen light source (FSI-1060-250, 250 watt) that passes through a pinhole, two condensing lenses, the CVCC itself, a knife edge, two concave mirrors (internal diameter of 152.4 nm, focal length of 1524 nm), and a complementary metal oxide semiconductor (CMOS) Edgertronic SC2+ camera. Figure 1 shows the route of light path starting at the halogen source and ending at the high-speed camera. Table 1 includes all the characteristics of the optical system in use.
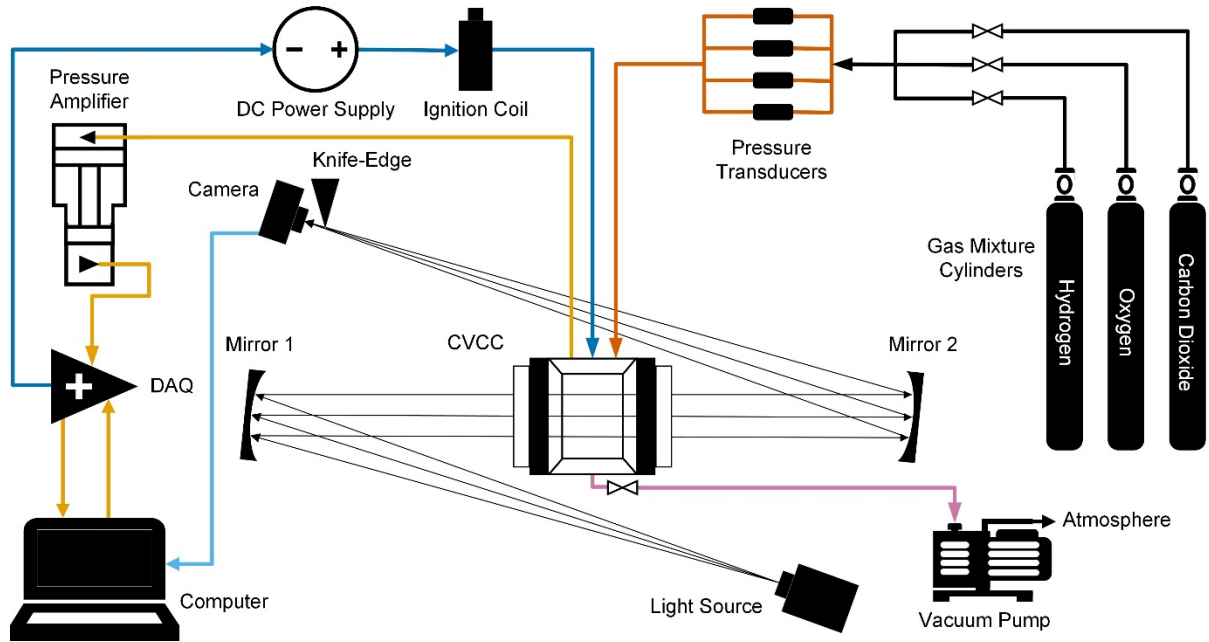
Figure 1: Schematic diagram of the experimental setup

Table 1. Optical System Configuration

Camera type	Complementary metal oxide semiconductor (CMOS)
Field of view	14 cm
Frame rate	8000 fps
Exposure	1/8500 seconds
Spatial resolution	4 mm/pixel

The start of a trial begins with vacuuming the CVCC and gas supply lines to <300 millitorrs to ensure the absence of undesired gases. The hydrogen gas, oxygen, and carbon dioxide are added to the chamber in ascending order of partial pressures. The gas supply lines are vacuumed in between the addition of each gas. Once all gases are loaded into the chamber, the mixture is allowed to mix for 3 minutes before spark. The spark is then triggered, and the data acquisition system records the image of the flame propagation, pressure, and time data. Each experimental condition, found within the experimental matrix, is repeated three times to guarantee repeatability and a >95% confidence level.

2.1 Flame Speed and Laminar Burning Velocity (LBV)

The images recorded using the Schlieren setup are digitally processed for flame speed calculations. Equation 1 is used:

$$S_b = \frac{dr_f}{dt} \tag{1}$$

where dr_f is the change of flame radius (cm) and dt is the change in time (s). The flame radii of interest are analyzed within upper and lower limits; the lower limit is set to 14 mm, or about 10x the distance of the 1.36 mm electrode gap, and the upper limit is set to 40 mm which is the maximum distance the flame can travel before making physical contact to the chamber walls. The laminar burning velocity is measured through two different methods. The first method uses the Schlieren images. This method is based on an experimental approach to calculate the flame speeds from Schlieren imaging. The images are converted into greyscale and then binarized to detect the edge of the expanding flame. Image processing and edge detection was performed with the image processing toolbox in MATLAB. The equivalent diameter of the propagating flame was calculated for each frame assuming the captured

region to be a complete circle. After identifying the region where the flame was expanding in a quasi-steady state, the instantaneous flame speed and stretch rate were calculated within that range for two consecutive images from the sequence. The flame stretch rate is defined as the time rate of the change of the flame surface area normalized by the area itself [30], as shown in Equation 2.

$$K = \frac{1}{A}\frac{dA}{dt} = \frac{2}{r_f}\frac{dr_f}{dt} = 2\frac{S_b}{r_f} \qquad (2)$$

The unstretched flame speed was then measured by applying a linear fit to the stretch rate versus flame speed curve. The laminar burning velocity of the gas mixture was determined by multiplying the average unstretched flame speed with the expansion factor, i.e., density ratio of the burned and unburned gases which was determined by the free flame function in CANTERA for each of the mixture configurations tested. Hence, each experiment yielded a single value of laminar burning velocity and burned gas Markstein length.

The second method in which the LBV is calculated shows its correlation with the unburned gas temperature using a thermodynamic multi-shell model that relies on the experimental pressure data obtained during the flame propagation. Considering conservation of mass and energy, and employing ideal gas laws, the multi-shell model divides the chamber into different shells: the burned and unburned gas shells, which are divided by a negligibly thick flame front, and a third shell located between the wall of the chamber and the unburned gas shell. Further details regarding the fundamentals of the Metghalchi and Keck multi-shell model are expanded on in past literature [31] and more thorough mathematical details of converting pressure data to LBV are outlined in previous works [32].

2.3 Lower Flammability Limit (LFL)

The LFL of the hydrogen gas mixtures is determined by a trial-and-error approach that gradually alters conditions until the mixture does not ignite. For example, at a constant initial pressure, CO_2% was gradually increased in increments of 1% until the hydrogen gas ceases to ignite. In all experiments, the distance between the electrodes was always kept constant.

3. Result and Discussion

3.1 Flame morphology

Figure 2 and 3 illustrate the Schlieren images of spherically expanding flames inside the CVCC for H_2-O_2-CO_2 combustion at different initial pressures (1 bar and 2 bar, respectively) and fractions of CO_2 (40%, 60%, 65%) at stoichiometric conditions. These images give a qualitative validation to the assumption that increasing the CO_2 concentration in the mixture allows for the reduction of the flame speed for hydrogen oxy-combustion. From Figure 2, it can be seen that the spherically propagating flame takes only 3 ms to reach a radial value of 4.6 cm from the onset of ignition. The time to reach a similar radial value increases to 13.63 ms and 29.88 ms for the cases where CO_2 concentration was increased to be 60% and 65% respectively. Figure 4 exhibits a comparison of the flame speed between the 65% CO_2 case and methane-air stoichiometric combustion. It shows that the flame speed of hydrogen has become slower than that of methane-air combustion which took 18.63 ms to reach a radial value of 4.6 cm inside the CVCC.

Figure 3 shows another interesting in trend that, at 40% CO_2 conditions, the flame front propagates faster as the initial pressure is increased from standard pressure to an elevated pressure (2 bar). A similar trend was observed for hydrogen-air combustions by Ijima and Takeno [33]. However, as the percentage of CO_2 was increased above 40%, this trend changed and the flame speed started to decrease with increasing initial pressures. At this stage, the hydrogen oxy-combustion started showing characteristics similar to that of natural gas combustion, where the flame speed decreases with increasing initial pressures [32]. This can be attributed to the high thermal heat capacity of CO_2 compared to N_2 (~35 times greater), where the working fluid acts like a heat sink and decreases the net reaction rate, thereby reducing the flame speed. Increasing the CO_2 concentration of the mixture lowers the mixture's ability to overcome the activation energy for several reactions relevant to ignition [34]. Upon increasing the concentration of CO_2, the flame speed is lower than that of methane-air stoichiometric combustion.
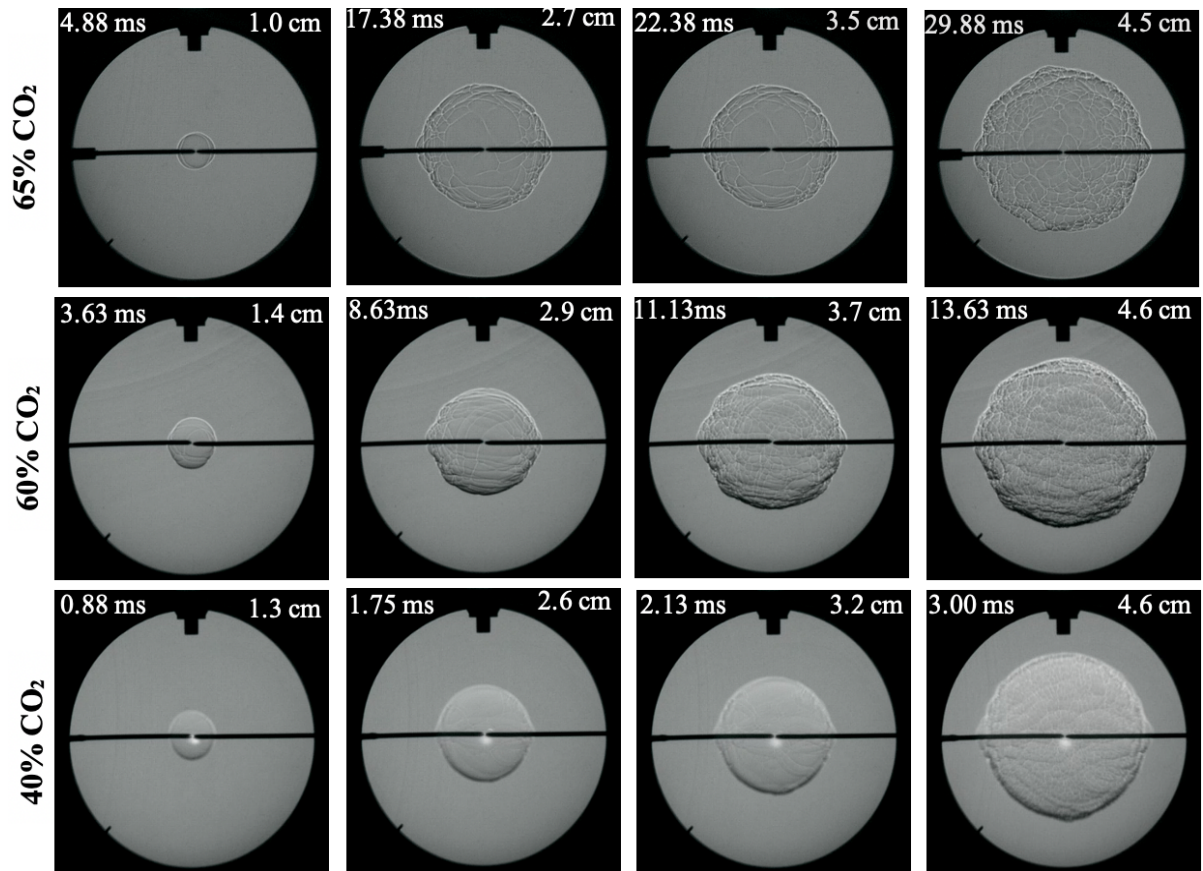
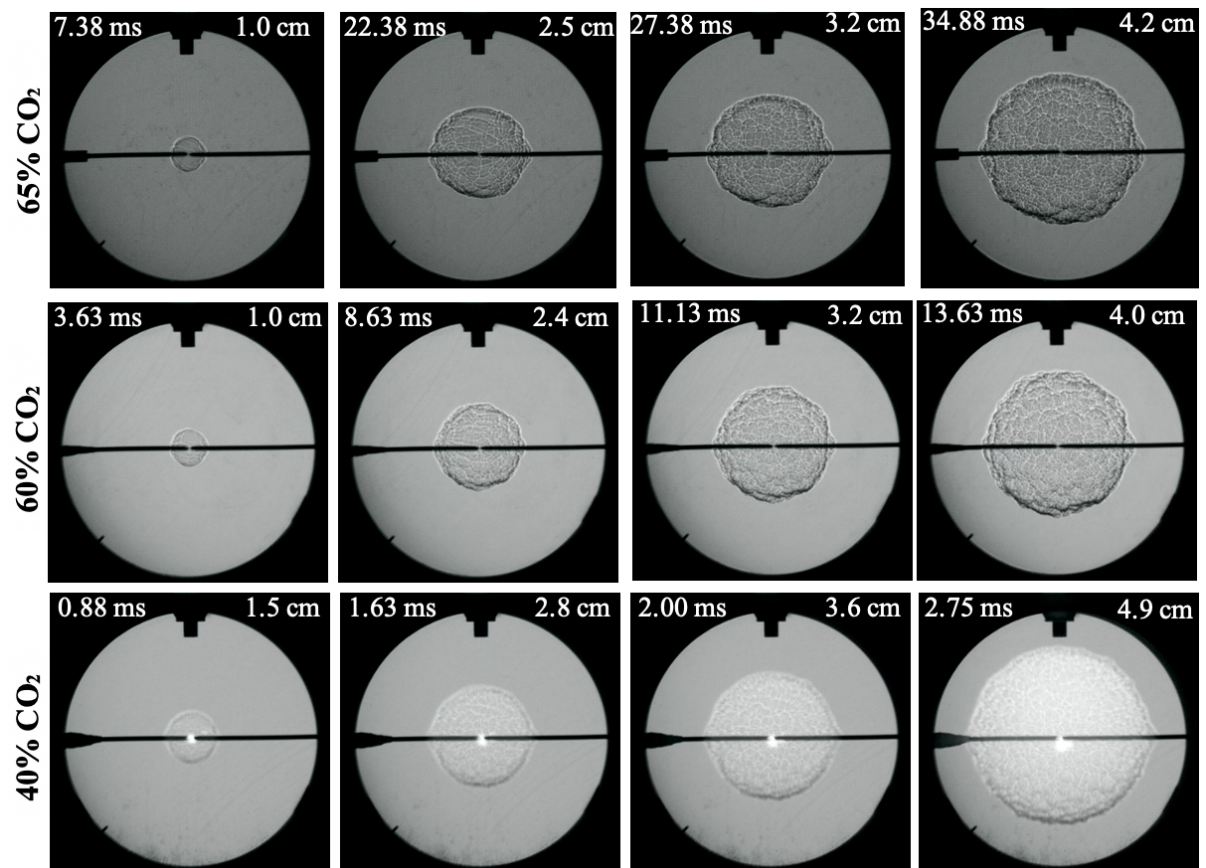**Figure 2:** Schlieren images of H_2-O_2-CO_2 flame fronts at $\varphi = 1$ and $P_i = 1$ bar.

Figure 3: Schlieren images of H_2-O_2-CO_2 flame fronts at $\varphi = 1$ and $P_i = 2$ bar.

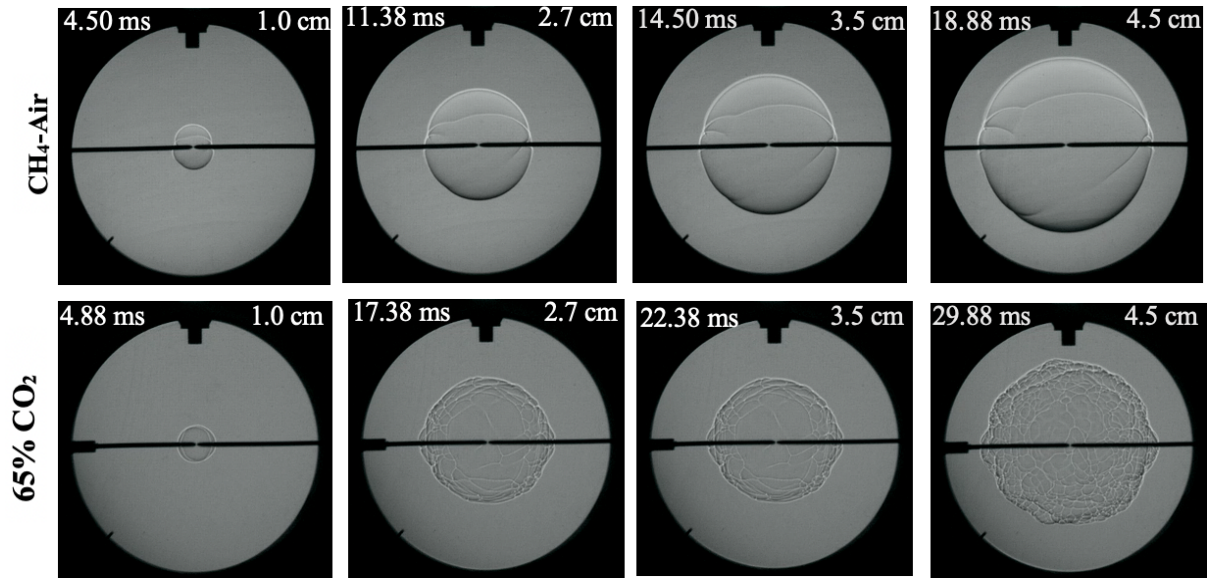**Figure 4:** Schlieren images of H_2-O_2-65% CO_2 and CH_4-O_2-N_2 flame fronts at $\varphi = 1$ and $P_i = 1$ bar.

3.2 Flame speed and laminar burning velocity from Schlieren imaging method

Figure 5 shows the flame speed versus stretch rate curve for stoichiometric hydrogen oxy-combustion at different CO_2 concentrations (40%, 60%, 65%). The same line generated from the schlieren images for stoichiometric methane-air combustion falling between the H_2-O_2-60%CO_2 and H_2-O_2-65%CO_2 lines prove that reduced flame speed of hydrogen oxy-combustion was achieved by gradually increasing the concentration of CO_2 in the mixture.
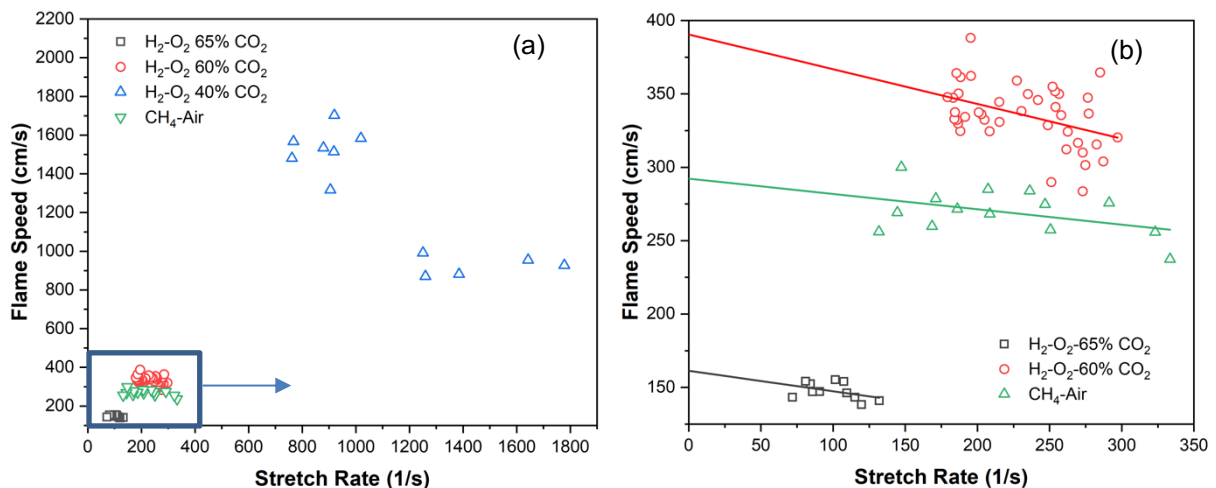

Figure 5: (a) Flame speed vs stretch rate curve for premixed H_2-O_2-65%CO_2, H_2-O_2-60%CO_2, H_2-O_2-40%CO_2 and methane-air combustion at $\varphi = 1$ and $P_i = 1$ bar and (b) linear fit applied to measure the unstretched flame speed.

The unstretched flame speed was calculated by extrapolating these fitted lines for different equivalence ratios at initial pressures of 1 and 2 bar. The average unstretched flame speed was utilized to calculate the laminar burning velocity for these conditions which is presented in Figure 6. It is evident from this plot that regardless of the initial pressure and CO_2 concentration, the LBV showed a reducing

trend from stoichiometric to the flame lean conditions. Both 60% and 65% CO_2 cases exhibited an inverse relation of LBV with initial pressure of the gaseous mixture. This trend was also observed in methane-air combustion at different equivalence ratios.
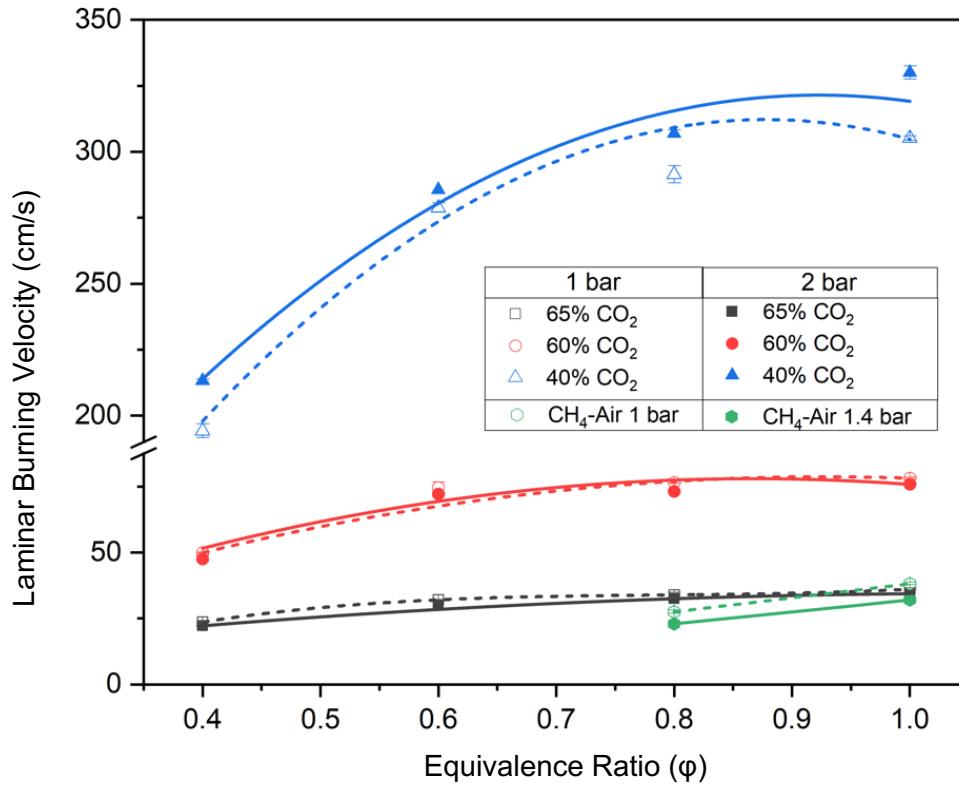
Figure 6: LBV of hydrogen oxy-combustion with CO_2 as the working fluid at different concentrations and equivalence ratios.

An opposite trend was observed for the LBV of H_2-O_2-40% CO_2 combustion where the LBV tends to rise with the increasing initial pressure. This trend matches with the observations made by Ijima and Takeno [33] for hydrogen-air combustion, which indicates that as the CO_2 percentage in the mixture starts to decrease, the data set begins to replicate the conditions seen in standard hydrogen combustion. From the Schlieren images shown in Figures 2 and 3, it is quite evident that at higher pressures, instabilities start to appear quite early in the flame development for H_2-O_2-40%CO_2 combustion. Since these self-accelerating cellular structures, commonly characterized by the Darrieus-Landau instability [35], [36], become more dominant at higher pressures, the flame propagates at a much faster rate.

The sources of error in this method can be classified into two categories: error in mixture preparation and error in data analysis. The first one can be attributed to the purity of the gases used and the accuracy of the pressure transducers in determining the partial pressures of the reactant gasses while filling up the chamber. Since all the gases used in this study had the purity level of 99.999% and the pressure transducer in use had an uncertainty level of ≤ ± 0.3%, this type of error was deemed extremely small and were not presented in Figure 6. The error from data analysis is the compilation of the errors made during the flame radius calculations. These were mitigated by repeating each experiment three times and then applying a linear fit to the flame speed vs stretch rate curve. This error is listed in the Y-axis direction of Figure 6 for each of the cases tested.

3.3 Laminar burning velocity from timed pressure data

Figure 7 shows a positive correlation between the measured laminar burning velocity, S_u from the timed pressure data and the unburned gas temperatures of all the conditions of premixed H_2-O_2-

CO_2 combustion experiments. By means of extrapolation, the LBV at 298K can be calculated which can be compared with the measured LBV from the schlieren images.

The LBV has a steeper climb with increasing unburned gas temperatures for cases with 60% CO_2 compared to the 65% cases. Just like the LBV measurements from the schlieren images, the 65% data matches the closest with the stoichiometric methane-air combustion observed by Baghirzade et. al. [32]. It is also interesting to note that the measured LBV from the Schlieren images (Figure 6) turned out to be almost identical with the extrapolated LBV from the pressure rise method at 298K for 65% cases, whereas the values for 60% cases were slightly lower.
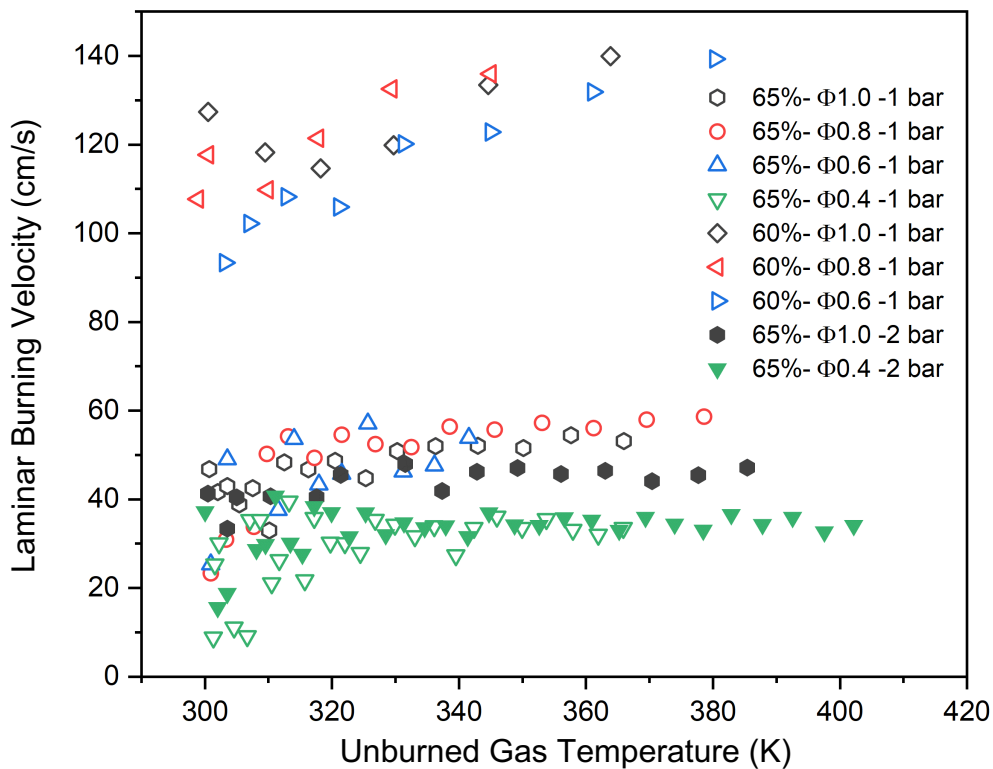
Figure 7: Effect of unburned gas temperature on the laminar burning velocity, S_u, of premixed H_2-O_2-CO_2 combustion experiments

The error in the velocity measurements can be attributed to multiple factors: calibration of the pressure transducers and data analysis errors. Numerical modelling shows that a 1% error in pressure measurements will result in a 1% error in the burning velocity measurements since the fractional pressure rise is not quite proportional to the burned mass fraction [37]. This effect is more dominant in the cases where the CO_2 concentration in lower (60%, 40%), resulting in the measured LBV values from two methods not being identical in the presented 60% CO_2 cases.

3.4 LFL and H_2-O_2-CO_2 concentrations

The LFL of each of the mixture configuration was obtained in accordance with the procedure mentioned in Section 2.3. Table 2 exhibits the maximum allowed percentage of CO_2 as a function of equivalence ratio and initial pressure of the mixture.

Table 2. Maximum Percentage of CO_2 at which ignition occurred for each oxy-combustion equivalence ratio

	Initial Pressure, P_i (bar)		
φ	1	1.5	2
1	76%	76%	75%
0.8	80%	80%	79%
0.6	82%	82%	82%

The equivalence ratio in Table 2 is that of oxy-combustion, i.e., the ratio of stoichiometric H_2-O_2 to the mixture's H_2-O_2 molar ratio, with the working fluid (CO_2) varied separately as a percentage of the total mixture. Varying the two independently leads to an interesting observation, wherein decreasing the equivalence ratio at a fixed pressure allows for more CO_2 in the mixture before the LFL is reached. For example, with φ = 1 at an initial pressure of 1 bar, the mixture can be up to 76% of CO_2 before it stops igniting. However, with the same pressure, when the equivalence ratio was decreased to 0.8 and 0.6, the maximum amount of CO_2 which results in ignition was 80% and 82% respectively. This means that more CO_2 can be added to the mixture, despite the fuel being more diluted. There are several factors that could be contributing to this phenomenon. The minimum ignition energy (MIE) is affected by the mixture's properties if all other factors pertaining to the energy source are kept constant. The properties that are relevant to this current case (where only the fraction of the working fluid is changing) include the initial values of the mixture's density (ρ), specific heat at constant pressure (c_p), thermal diffusivity (α), and the associated laminar-flame propagation velocity [38]. C_p and thermal conductivity (k) are greater for H_2 compared to O_2 and CO_2. While both properties have the opposite effect on the thermal diffusivity, the higher density of O_2 and CO_2 means that hydrogen ultimately has a much higher thermal diffusivity. Therefore, as the ratio of hydrogen in the mixture decreases, the effective thermal diffusivity of the mixture becomes low enough to significantly reduce the MIE and allow for the addition of more of the working fluid (CO_2). However, the interplay between these factors could be more complicated and warrants a more detailed investigation. It is also worth noting that the flame at such extremely lean equivalence ratios with higher CO_2 percentages experience a noticeably increased buoyancy as well.

4. Conclusions

The effect of using CO_2 as a working fluid for hydrogen oxy-combustion at different initial pressures and equivalence ratios in an optically accessible CVCC was studied in terms of the flame structure, stretched and unstretched flame speed, laminar burning velocity, and lean flammability limit. The different observations from all the tested cases can be summarized by the following,

- The highest flame speed and laminar burning velocity was achieved at stoichiometric conditions for all the tested cases (different CO_2 concentrations and initial pressures). The flame speed decreased gradually as the mixture got leaner.
- Increasing the concentration of CO_2 in the mixture lowers the flame speed. After comparing the varying CO_2 concentrated cases, it was shown that the flame speed of the methane-air stoichiometric combustion falls between the unstretched flame speed range for mixtures containing 60% and 65% CO_2.
- At 40% CO_2 concentration, the flame front propagated faster as the initial pressure was increased. The opposite trend was observed for 60% and 65% CO_2, which resembles CH_4-air combustion.
- A positive correlation was seen between the laminar burning velocity and the unburned gas temperature irrespective of equivalence ratio and initial mixture pressure. Furthermore, decreasing the CO_2 percentage in the gaseous mixture resulted in the LBV vs unburned gas temperature curve exhibiting a steeper rise.
- A leaner H_2-O_2 mixture allows for CO_2 in the total mixture, albeit with increased buoyancy.

The inclusion of carbon dioxide as a working fluid in hydrogen oxy-combustion provides the opportunity to achieve flames with LBVs that are appropriate for practical combustion applications. It also eliminates the production of NOx emissions and enables carbon separation or closed-cycle processes. It also opens up opportunities for future studies to pinpoint the mixture configuration where the relation between the LBV and initial mixture pressure inverts. Additional studies will be conducted to determine the parameters that enable the extension of LFL for H_2-O_2-CO_2 combustion as the mixture gets leaner.

References

[1]   S. K. Ribeiro, M. J. Figueroa, F. Creutzig, C. Dubeux, J. Hupe, S. Kobayashi, L. A. d. M. Grettas, T. Thrasher, S. Webb and J. Zou, "Chapter 9 - Energy End-Use: Transport," in *Global Energy Assessment - Towards a Sustaiable Future*, Cambridge University Press, 2012, pp. 575 - 648.

[2]   S. M. Sarathy, A. Farooq and G. T.Kalghatgi, "Recent progress in gasoline surrogate fuels," *Progress in Energy and Combustion Science,* vol. 65, no. March, pp. 67-108, 2018.

[3]   G. Kalghatgi, H. Levinsky and M. Colket, "Future transportation fuels," *Progress in Energy and Combustion Science,* vol. 69, no. November, pp. 103-105, 2018.

[4]   G. Kalghatgi, "Is it really the end of internal combustion engines and petroleum in transport?," *Applied Energy,* vol. 225, no. September, pp. 965 - 974, 2018.

[5]   OPEC Secretariat, "World Oil Outlook 2045," OPEC, Vienna, 2021.

[6]   A. Hula, A. Maguire, A. Bunker, T. Rojeck and S. Harrison, "The 2021 Automotive Trends Report," US Environmental Protection Agency (EPA), 2021.

[7]   A. Kumamoto, H. Iseki, R. Ono and T. Oda, "Measurement of minimum ignition energy in hydrogen-oxygen-nitrogen premixed gas by spark discharge," *Journal of Physics: Conference Series,* vol. 301, no. June, p. 012039, 2011.

[8]   L. V. Hoecke, L. Laffineur, R. Campe, P. Perreault, S. W. Verbruggen and S. Lenaerts, "Challenges in the use of hydrogen for maritime applications," *Energy and Environmental Science,* vol. 14, no. 2, pp. 815-843, 2021.

[9]   J. Lee, J. Kim, J. Park and O. C. Kwon, "Studies on properties of laminar premixed hydrogen-added ammonia/air flames for hydrogen production," *International Journal of Hydrogen Energy,* vol. 35, no. 3, pp. 1054-1064, 2010.

[10]   H. Dagdougui, R. Sacile, C. Bersani and A. Ouammi, "Hydrogen Logistics: Safety and Risks Issues," in *Hydrogen Infrastructure for Energy Applications: Production, Storage, Distribution and Safety*, Academic Press (Elsevier), 2018, pp. 127-131.

[11]   V. D. Sarli and A. D. Benedetto, "Effects of non-equidiffusion on unsteady propagation of hydrogen-enriched methane/air premixed flames," *International Journal of Hydrogen Energy,* vol. 38, no. 18, pp. 7510-7518, 2013.

[12]   L. Qiao, Y.Gu, W. J. A. Dahm, E. S. Oran and G. M. Faeth, "A study of the effects of diluents on near-limit H2–air flames in microgravity at normal and reduced pressures," *Combustion and Flame,* vol. 151, no. 1-2, pp. 196-208, 2007.

[13]   L. Qiao, C. H. Kim and G.M.Faeth, "Suppression effects of diluents on laminar premixed hydrogen/oxygen/nitrogen flames," *Combustion and Flame,* vol. 143, no. 1-2, pp. 79-96, 2005.

[14]   H. Wei, Z. Xu, L. Zhou, J. Zhao and J. Yu, "Effect of hydrogen-air mixture diluted with argon/nitrogen/carbon dioxide on combustion processes in confined space," *International Journal of Hydrogen Energy,* vol. 43, no. 31, pp. 14798-14805, 2018.

[15]   N. F. Munajat, C. Erlich, R. Fakhrai and T. H.Fransson, "Influence of water vapour and tar compound on laminar flame speed of gasified biomass gas," *Applied Energy,* vol. 98, pp. 114-121, 2012.

[16]   E. Monteiroa, A. Rouboa, M. Bellenoue, B. Boust and J. Sotton, "Multi-zone modeling and simulation of syngas combustion under laminar conditions," *Applied Energy,* vol. 114, pp. 724-734, 2014.

[17]   J.Natarajan, T. Lieuwen and J. Seitzman, "Laminar flame speeds of H2/CO mixtures: Effect of CO2 dilution, preheat temperature, and pressure," *Combustion and Flame,* vol. 151, no. 1-2, pp. 104-119, 2007.

[18]   W. Zhang, Z. Chen and W. Kong, "Effects of diluents on the ignition of premixed H2/air mixtures," *Combustion and Flame,* vol. 159, no. 1, pp. 151-160, 2012.

[19]   Y. Li, M. Bi, L. Huang, Q. Liu, B. Li, D. Ma and W. Gao, "Hydrogen cloud explosion evaluation under inert gas atmosphere," *Fuel Processing Technology,* vol. 180, pp. 96-104, 2018.

[20]   J. Duan and F. Liu, "Laminar combustion characteristics and mechanism of hydrogen/air mixture diluted with N2 + H2O," *International Journal of Hydrogen Energy,* vol. 42, no. 7, pp. 4501-4507, 2017.

[21]   M. Morovatiyan, M. Shahsavan, J. Aguilar and J. H. Mack, "Effect of Argon Concentration on Laminar Burning Velocity and Flame Speed of Hydrogen Mixtures in a Constant Volume Combustion Chamber," *Journal of Energy Resources Technology,* vol. 143, no. 3, p. 032301, 2021.

[22]   L.-Q. Wang, H.-H. Ma and Z.-W. Shen, "Explosion characteristics of hydrogen-air mixtures diluted with inert gases at sub-atmospheric pressures," *International Journal of Hydrogen Energy,* vol. 44, no. 40, pp. 22527-22536, 2019.

[23]   W. Feng, L. Shibo, H. Yizhuo and J. Huiqiao, "The chemical effect of CO2 on the methane laminar flame speed in O2/CO2 atmosphere," *IOP Conference Series: Earth and Environmental Science,* vol. 186, p. 012050, 2018.

[24]   A. Ueda, K. Nisida, Y. Matsumura, T. Ichikawa, Y. Nakashimada, T. Endo and W. Kim, "Effects of hydrogen and carbon dioxide on the laminar burning velocities of methane–air mixtures," *Journal of the Energy Institute,* vol. 99, pp. 178-185, 2021.

[25]   H.-M. Li, G.-X. Li, Z.-Y. Sun, Z.-H. Zhou, Y. Li and Y. Yuan, "Fundamental combustion characteristics of lean and stoichiometric hydrogen laminar premixed flames diluted with nitrogen or carbon dioxide.," *Journal of Engineering for Gas Turbines and Power,* vol. 138, no. 11, 2016.

[26]   T. Katsumi , Y. Yoshida, R. Nakagawa, S. Yazawa, M. Kumada, D. Sato, T. T. Aung, N. Chaumeix and S. Kadowaki, "The effects of addition of carbon dioxide and water vapor on the dynamic behavior of spherically expanding hydrogen/air premixed flames," *Journal of Thermal Science and Technology,* 2021.

[27]   N. Ladommatos , S. Abdelhalim, H. Zhao and J. Hu, "The Dillution, Chemical, and ThermEffects of Exhaust Gas Recirculation on Diesel Engine Emissions Parts 2: Effect of Carbon Dioxide," in *Society of Automotive Engineers*, Warrendale, PA, 1996.

[28]   N. Ladommatos , S. Abdelhalim, H. Zhao and J. Hu, "The Dillution, Chemical, and Thermal Effects of Exhaust Gas Recirculation on Diesel Engine Emissions Parts 4: Effects of Carbon Dioxide and Water Vapor," in *Society of Automotive Engineers*, Warrendale, PA, 1997.

[29]   H. Gossler , S. Drost , S. Porras, R. Schießl, U. Maas and O. Deutschmann, "The internal combustion engine as a CO2 reformer," *Combustion and Flame,* vol. 207, pp. 186-195, 2019.

[30]   D. Bradley, P. H. Gaskell and X. J. Gu, "Burning Velocities, Markstein Lengths, and Flame Quenching for Spherical Methane-Air Flames: A Computational Study," *Combustion and Flame,* vol. 104, pp. 176-198, 1996.

[31]   M. Metghalchi and J. C. Keck, "Burning velocities of mixtures of air with methanol, isooctane, and indolene at high pressure and temperature," *Combustion and Flame ,* vol. 48, p. 191–210, 1982.

[32]   M. Baghirzade, M. N. Nasim, B. Nawaz, J. Aguilar, M. Shahsavan, M. Morovatiyan and J. H. Mack, "Analysis of Premixed Laminar Combustion of Methane With Noble Gases as a Working Fluid," in *ASME 2021 Internal Combustion Engine Division Fall Technical Conference*, 2021.

[33]   T. Iijima and T. Takeno, "Effects of temperature and pressure on burning velocity," *Combustion and Flame,* vol. 65, no. 1, pp. 35-43, 1986.

[34]   W. Feng, L. Shibo, H. Yizhuo and J. Huiqiao, "The chemical effect of CO2 on the methane laminar flame speed in O2/CO2 atmosphere," *IOP Conference Series: Earth and Environmental Science,* vol. 186, no. 2, 2018.

[35]   W. Kim, Y. Sato, T. Johzaki, T. Endo, D. Shimokuri and A. Miyoshi, "Experimental study on self-acceleration in expanding spherical hydrogen-air flames," *International Journal of Hydrogen Energy,* vol. 43, no. 27, pp. 12556-12564, 2018.

[36]   C. Bauwens, J. Bergthorson and S. Dorofeev, "Experimental investigation of spherical-flame acceleration in lean hydrogen-air mixtures," *International Journal of Hydrogen Energy,* vol. 42, no. 11, pp. 7691-7697, 2017.

[37]   N. Hinton, R. Stone and R. Cracknell, "Laminar burning velocity measurements in constant volume vessels– Reconciliation of flame front imaging and pressure rise methods," *Fuel,* pp. 446-457, 2018.

[38]   V. Kurdyumov, J. Blasco, A. Sánchez and A. Liñán, "On the calculation of the minimum ignition energy," *Combustion and Flame,* vol. 136, no. 3, pp. 394-397, 2004.

THIESEL 2022 Conference on Thermo- and Fluid Dynamics of Clean Propulsion Powerplants

Experimental Investigation of Hydrogen Combustion in a Single Cylinder PFI Engine

L. Buzzi[1], V. Biasin[1], A. Galante[1], D. Gessaroli[1], F. Pesce[1], D. Tartarini[1], A. Vassallo[1], S. Scalabrini[2], N. Sacco[2], R. Rossi[2]

[1] PUNCH Torino SpA, Torino, Italy.

E-mail: davide.gessaroli@punchtorino.com
Telephone: +39 334 6402595

[2] PUNCH Hydrocells Srl, Torino, Italy.

E-mail: riccardo.rossi@punchhydrocells.com
Telephone: +39 331 6652188

Abstract. The simultaneous reduction of Green-House Gases (GHG) and criteria pollutants is the main target of current Internal Combustion Engines (ICE) development.

Hydrogen (H_2) fuelling is one of the best options available in both regards, as it does not emit tailpipe CO_2 as well as significantly abates all criteria pollutants already at engine-out level. However, optimizing hydrogen combustion in order to exploit the fuel proprieties at best is a challenging task due to the very particular properties of the fuel.

In fact, H_2 combustion in ICE promotes a very clean, fast and complete combustion process, with extremely low HC, CO and PM engine-out emissions stemming only from lubricant oil. The usage of lean-boosted and EGR-diluted combustion strategies can significantly contribute to raise the brake thermal efficiency and lower the NOx emission to extremely low levels.

To this end, the Authors tested a 0,5ℓ single cylinder engine featuring an optimized PFI layout and dedicated piston bowl profile for a retrofitted Diesel operating as H_2 monofuel, in SI mode.

In this paper, the authors discuss the effect of the main engine parameters, extensively investigated by means of Design of Experiments (DoE) techniques, as well as the effect of dilution and EGR to promote clean and efficient hydrogen combustion, in order to recommend the most effective practices.

Notation (optional)

AFR   *Air-Fuel Ratio*
BMEP   *Brake Mean effective Pressure*
CA   *Crank Angle*
CFD   *Computational Fluid Dynamics*
CNG   *Compressed Natural Gas*
CoV-IMEP   *Coefficient of Variation of IMEP (100 consecutive cycles)*
CR   *Compression Ratio*
DoE   *Design of Experiments*
EGR   *Exhaust Gas Recirculation*
EVC, EVO   *Exhaust Valve Closing, Exhaust Valve Opening*
FMEP   *Friction Mean Effective Pressure*
GHG   *Green-House Gases*
HRR   *Heat Release Rate*
ICE   *Internal Combustion Engine*
IEA   *International Energy Agency*
IMEP   *Indicated Mean Effective Pressure*
ISFC   *Indicated Specific Fuel Consumption*
IS-NOx *Indicated Specific NOx Emissions (engine-out)*
IVC, IVO   *Intake Valve Closing, Intake Valve Opening*
LP-DI   *Low-pressure, Direct Injection*

LEL   Low Emission Level
MCE   Multi-Cylinder Engine
MFB50 50% of Mass Fraction Burned
OEM   Original Equipment Manufacturer
PFI   Port Fuel Injection
PFP   Peak Firing Pressure
RAFR   Relative Air-to-Fuel Ratio
SA   Spark Advance
SOI   Start of Injection
SCE   Single-Cylinder Engine
TDC   Top Dead Centre
TJI   Turbulent Jet Ignition
TRL   Technology Readiness Level
WOT   Wide-open Throttle

1. Introduction

As it is well known, the mass popularity of vehicles for people and goods transportation fitted with Internal Combustion Engines began in the early 20th century. ICE development and manufacturing processes were established and perfected over the years: the application of this technology have come to cover so many fields with the result that today billions of people enjoy every day affordable and convenient transport and goods delivery thanks to it, while millions of people are working in the ICE industry, either directly with Original Equipment Manufacturers (OEMs) or within Suppliers, Academia, Operations, Maintenance & Servicing,…

However, this has also caused growing concerns about the negative effects that fossil-fuel based transport has on human health and environment, both due to local criteria pollutants emitted in urban dense areas, as well as to global Greenhouse Gases Emission (GHG) - primarily in the form of CO_2. In fact, according to a 2018 study by the International Energy Agency (IEA), more than a quarter of global CO_2 emissions were caused by the transport sector alone, and in turn 75% of transport emissions were caused by road traffic ([1]).

In this context, by using Hydrogen (H_2) as fuel for ICE, it's possible to keep efficiency and convenience of internal combustion engines – including their wide industrial footprint and servicing network, skilled workforce, – while practically eliminating criteria pollutants and reducing GHG emissions to very low levels by using „blue" and „green" H_2 (**Figure 1**).
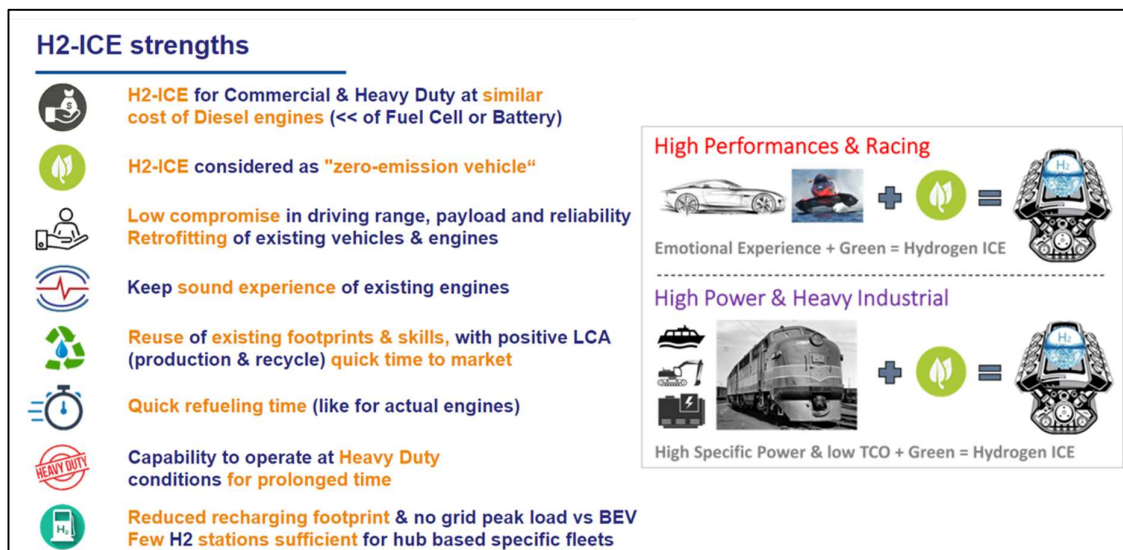

Fig. 1. H_2-ICE strengths

The use of hydrogen fuel in ICE is a proven technology. In fact, various automobile manufacturers (e.g. BMW, MAN, Ford, Mazda) have continuously researched the potential of hydrogen combustion

until the last decade, with good outcomes in terms of compatibility and safety of operation. However, due to various technical limitations, development had concentrated on combustion control via fully stoichiometric operation and therefore largely ignored the potential of efficiency.

In the very last years, however, a new wave of attention has been given to H₂-fuelled ICEs that can rival in efficiency with Hydrogen Fuel Cells, thanks to a complete overhaul of the combustion process. This is exemplified in the **Figure 2**, reprinted from [2]. The figure shows, as function of Air-to-Fuel Ratio (AFR), the qualitative trends for engine BMEP, engine-out NOx and Thermal Efficiency. As can be seen, stoichiometric operation for H₂-ICEs is not preferable as knock onset at high load occurs at lower BMEPs, while thermal efficiency and NOx emissions are unfavourable due to high in-cylinder temperatures. If combustion is instead controlled at high relative AFRs (RAFR 2.0 – 2.5), a sweet-spot of performance, efficiency and NOx emissions can be simultaneously achieved. Of course, with the benefits above-described, also challenges come, especially in terms of combustion stability control (slow burn, misfire) and engine-out NOx during transients.

However, as pros do exceed cons, this is the region targeted by the new combustion concepts described in [3-8], which will be examined in this paper and assessed via testing on a single-cylinder engine (SCE) purposely built. The SCE object of the present paper, in particular, features a homogenous port-fuel injection (PFI) combustion system and dedicated piston bowl profile for a retrofitted Diesel operating as spark-ignited H₂ monofuel that has been designed by PUNCH following extensive simulation activities described in [9, 10].
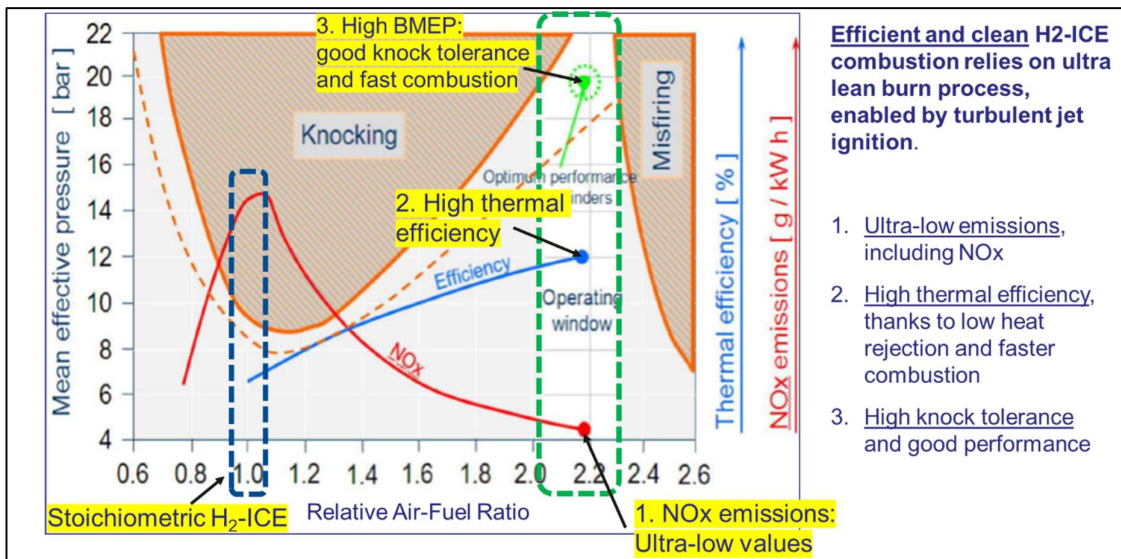
Fig. 2. Schematic for the combustion concept of traditional stoichiometric-operated SI H2 ICE vs new generation, ultra-lean burn concept [2]

While Diesel engine may not represent the ideal hardware for a homogeneous-charge, spark-ignited flame propagation concept – indeed a pent-roof cylinder head with tumbling intake ports would be much more suitable than a flat desk, swirling system typical for Diesel engines – there is emerging consensus in the Academia and Industry that Diesel base engine may actually be the donor for the first H₂-ICE commercial applications [4, 11, 12].

The reasons for this choice reside in the durability and reliability of the base engine, which can resist high in-cylinder peak firing pressures (PFP) typical of the highly-boosted lean combustion strategy described above, as well as are better suited against the fuel embrittlement and infiltration to engine materials thanks to the rugged heavy-duty mission of this engine type [13]. In addition, the operating speeds well match commercial applications already on the market, and finally the lean aftertreatment system for NOx reduction is already present to address the residual engine-out emissions from H₂-ICE and enable compliance to the most stringent standards in the world.

Such benefits overcome the drawbacks related essentially to the combustion concept not well suited for homogenous spark-ignited flame-propagation, even if developments are ongoing to minimize them, by applying – among other techniques – stratified low-pressure direction injection (LP-DI) and Turbulent Jet Ignition (TJI), a pre-chamber assisted ignition concept capable to ignite very lean mixtures and promote fast combustion process.

In this paper, the Authors focus on the first step in this ideal 'journey' to a highly-optimized H$_2$ system, by testing the spark-ignited homogeneous PFI version which builds on proven commercial-grade technology which is derived from CNG engines essentially by optimizing the piston, the spark plug and the injector for hydrogen operation, including materials' compatibility [13]. The Authors discuss the effect of the main engine parameters, extensively investigated by means of DoE techniques, in order to recommend the most effective combustion regimes and the relevant control strategies.

2. Test Unit

The test unit in focus for the study is a 0.5 ℓ/cyl single-cylinder engine (SCE) that has been manufactured and assembled in-house by PUNCH and it is based, among others, on the thermodynamics and CFD studies previously discussed in [9, 10]. The SCE main features are reported in the **Table 1**.

Table 1. Main single-cylinder engine characteristics

| Part	Value
Bore	83.0 mm
Stroke	90.4 mm
Unit Displacement	0.5 ℓ
CR	12.0
Piston Type	Hemi-spherical bowl, shallow
Intake Ports	Swirling, low turbulence
Spark-plug	Cold-type, low protrusion
Fuel System	PFI with rail, 6-8bar$_{REL}$ feed pressure
Injector type	Solenoid, 'peak & hold', 2.2g/s static flow @ 8bar Delta Pressure
Valve phasing	IVO =356 CA, IVC =592 CA; EVO =115 CA, EVC =392 CA

The power unit, i.e. the upper part of the SCE including the cylinder head, intake manifold and piston, has been specifically designed in order to be representative of a Diesel engine retrofit with hydrogen Port Fuel Injection (H$_2$-PFI), in order to prove the potential of this commercial-grade technology (TRL = 7-8) in terms of performance, emissions and specific fuel consumption. The choice of a Diesel base engine, as described in the Introduction, is consciously done because of the expected success of this type of retrofit that - while from combustion and thermodynamics standpoint is not ideal – has significant appeal in terms of supporting lean combustion thanks to its robust design featuring high PFP and turbocharger with VGT, as well as reliability thanks to the sturdy design of parts and components that provide a good compatibility with hydrogen [13].

Figure 3, left shows an axonometric view of the SCE power unit, with - in partial transparency – the camshafts and cam-carrier construction, as well as the pipe of the spark plug and its coil. In foreground, on the left side of the cylinder head, is visible the PFI injector close to the intake valves, fed by a top-mounted hydrogen rail. It is important to highlight that the intake manifold, the fuel rail, the cylinder head itself, as well as its cover, have been all designed and manufactured using additive manufacturing technology, which provides an ideal framework for a quick and agile prototyping able to adapt to the fast-moving environment of new hydrogen ICE concepts. On the right-hand side of **Figure 3** a detail of the aluminum piston with hemi-spherical bowl is reported, highlighting the strength of the Diesel-derived piston blank concept, as well as the relative simplicity of the homogenous combustion bowl concept featuring 12.0 CR.
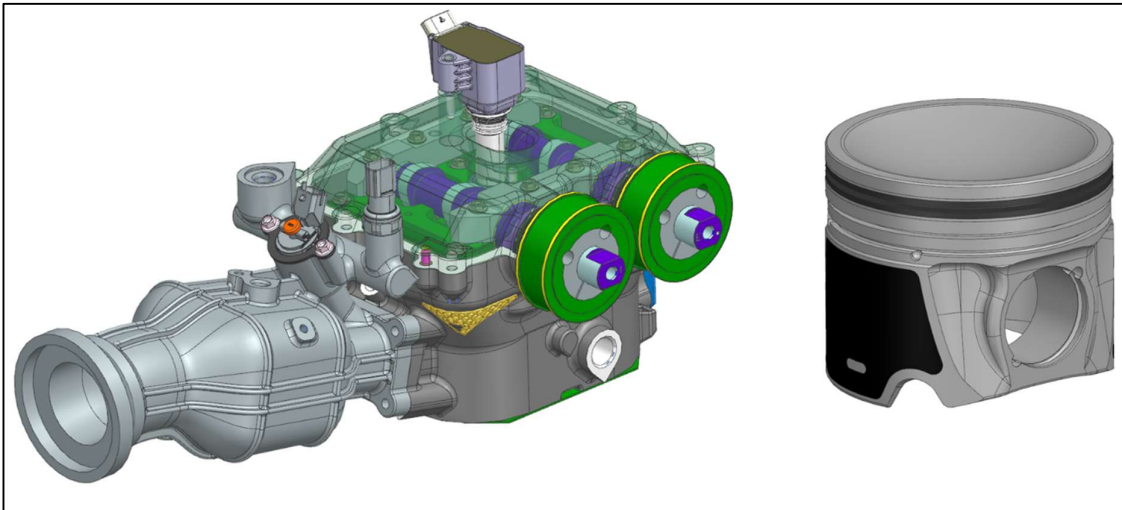
Fig. 3. Axonometric view of single-cylinder engine head (left) and piston bowl (right)

Finally, in **Figure 4** is reported a rendering of the overall single-cylinder assembly, together with some pictures of actual physical components and parts highlighting the additive manufacturing details. It is interesting to note that, as usual for single-cylinder engines, the feeding of combustion air and the evacuation of burnt gases is managed by an external test cell system instead of a standard turbocharger: in the rendering this is apparent by the two pressurized vessels placed on the sides of the engine, to provide two controlled environments for homogenizing pressure and temperature upstream and downstream of the combustion process, and critical to measure boundary condition with great accuracy.
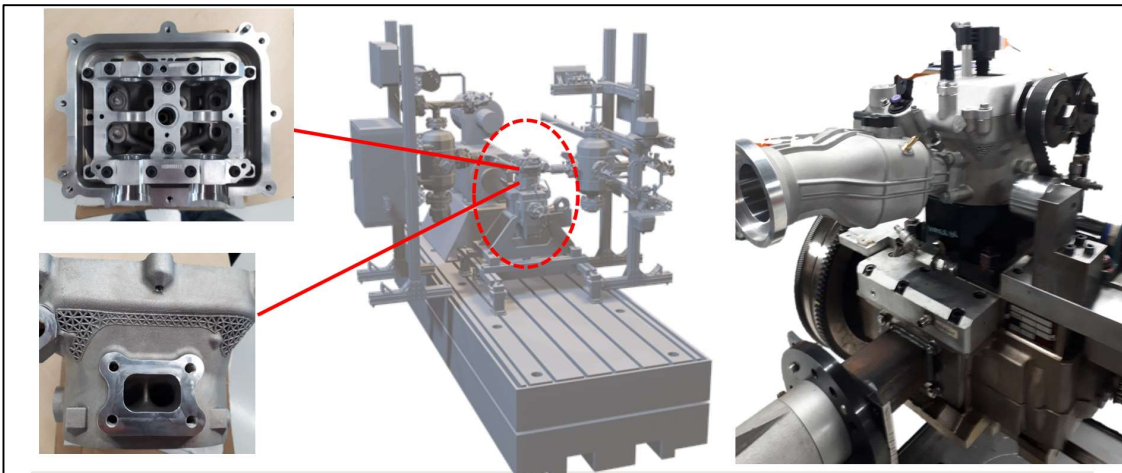
Fig. 4. Overall single-cylinder engine assembly with pictures and details of actual physical components

3. Experimental setup

3.1 SCE test cell layout, instrumentation, and automation

As described in the previous 'Test unit' section, the SCE has some peculiar characteristics with respect to a standards multi-cylinder engine. This is reflected in a different test cell configuration.
The focus aspects are:
- H_2 delivery system and its related safety.
- Automation to reproduce the multicylinder auxiliary systems and their functionality.
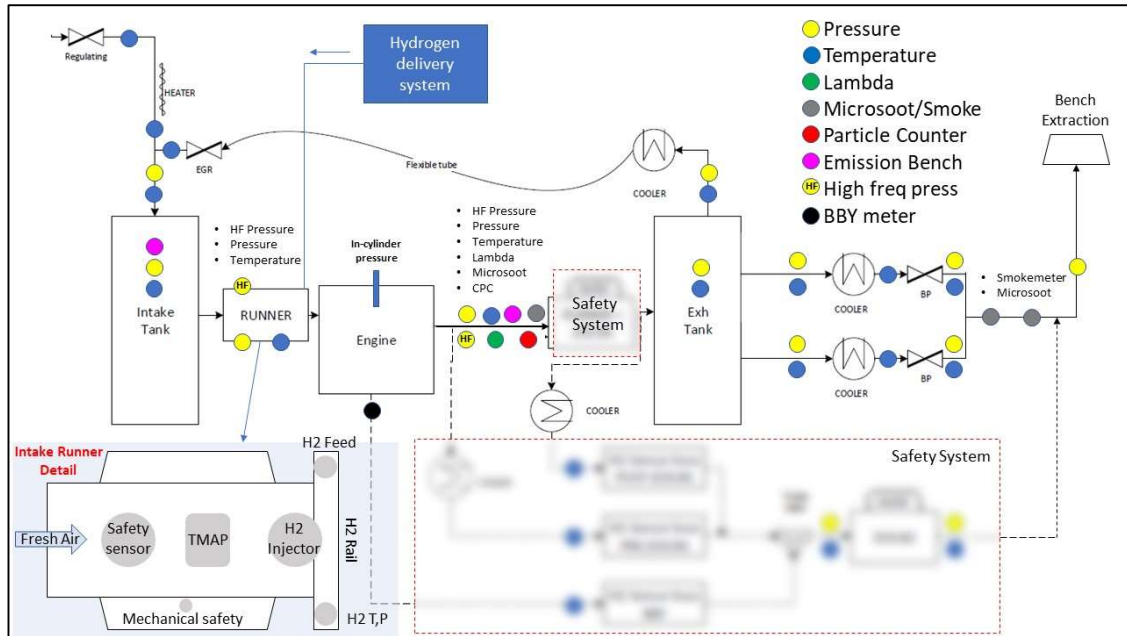- Instrumentation's layout.

3.2 SCE test cell layout

In **Figure 5** the overall test cell layout and the whole instrumentation used during the investigations is reported in form of a schematic representation.

The main system of the test cell, as well as the most peculiar one from the point of view of the novelty and safety, is the hydrogen fuel delivery and management. This system can regulate the pressure of hydrogen in the range of 0 – 60 bar (suitable for both PFI and LP-DI injection systems), measure the real-time fuel consumption thanks to a Coriolis mass flow meter and it is at the center of each safety countermeasure (including emergency shut-off).

As standard, the SCE does not feature a turbocharger, therefore in terms of test cell automation an important part is the intake combustion air and exhaust gases flow control, to replicate whatever compressor / turbine matching may be of interest, and to parameterize the boosting and back-pressure to the relevant values for exploring hydrogen combustion properties in a wide range. In particular, the intake system can deliver compressed air up to 5 bar abs with a controlled temperature via dedicated heater. As anticipated, the intake manifold is preceded by an intake tank of about 50ℓ capacity to dampen the pressure waves and promote stable flow, as well as to measure input parameters with high quality.

In a similar way, the exhaust part features the same structure, with an anti-explosion 50ℓ exhaust tank and a set of water-cooled flow control valves to set the backpressure of the engine to the desired value. The EGR routing completes the air/boosting system and is composed by a connecting tube between the exhaust and intake tanks, fitted with a flow control valve and a water-cooled radiator to appropriately set the mass flow and temperature of the EGR gas. The radiator itself is appropriately sized to mimic both low-pressure and high-pressure EGR systems, thanks to the closed-loop control of the intake vessel temperature based on enthalpy matching between intake air and EGR gas. It is important to notice in this regard that, due to significant water vapor quantity recirculated by the EGR system (each kg of hydrogen burned generates $\sim$ 8.9kg of water), the system uses a moisture condensation model to limit the amount of EGR recirculated and/or the mixture temperature to avoid excessive condensation which would not be acceptable also in view of a real engine application (particularly relevant in case of low-pressure EGR systems).

Fig. 5. Test cell layout and details of instrumentation

3.3 Safety

As it is well known, hydrogen features a high potential in terms of combustion characteristics (in terms of flammability range and flame speed), but the drawback of such favorable engine-related properties is its dangerous reactiveness with oxygen in the storage and testing environments. Safety is therefore at

the center of hydrogen research, with the goal to make this technology acceptable to the wide public and robustly demonstrate its suitability for a sustainable society to come. For the present investigation, this objective has worked on different sides, encompassing the storage facility, the hydrogen delivery system, the test cell itself, the engine and finally the exhaust gases collection system. In each of these environments, safety has been implemented in specific and customized ways by considering the hazards of the environment conditions like temperature, H_2 concentration and possible ignition spots.

For the test cell environment, the main systems are: H_2 sensors detector installed in the entire volume of the cell with the scope to detect possible leakages of H_2 from delivery system, and the second an extractor hood on the engine to suck-up H_2 coming from the engine. The onboard engine safety and then the exhaust gases collection safety are other key areas to be considered in the countermeasure safety system. On this side, different subsystems, as showed as safety box in Figure 5, have been implemented. Their aim is to avoid cumulating the hydrogen in the exhaust line and especially in the exhaust tank where the condition of auto-ignition temperature could be present.

The target of maximum allowed hydrogen concentration is set following a LEL limit for the hydrogen (4%). One of the countermeasures implemented is the detection of the misfire. The misfire over a certain limit cause H_2 slip in the exhaust. The strategy consists in two different detections and a dedicated countermeasure. The detections are based on indicating pressure analysis and the exhaust gas analysis. Crossing data to generate an alarm starting actions in parallel:

- Stop the H_2 delivery
- Injection – Ignition stop by ECU
- Decrease the heater setpoint
- Increase the air mass flow
- Close EGR Valve
- Open exhaust valve

The aim is to dilute as much as possible the exhaust and, in the meantime, decrease the overall temperature reducing autoignition condition.

3.4 Test bench and instrumentation characteristics

Table 2. Main test bench and instrumentation characteristics

Part	Charateristic
Dyno	Horiba Dynas Low Inertia
	Max torque: 480Nm Max Power: 250kW Max RPM: 10000 rpm
Emission bench	Emission Bench AVL Dual Stream
	CLD for NO/NO$_x$ 0-1000 ppm FID for THC 0-2000 ppm PMD for O$_2$ 0- 20%Vol NDIR for CO 0 – 1000 ppm NDIR for CO$_2$ 0- 20%Vol Sampling system: 191° Heated ceramic filter and PTFE probe. Sample Flow around 12 l/ min
FTIR	FTIR AVL i60 Emission system single stream
	NO 0 -1000 ppm NO$_2$ 0-1000 ppm N$_2$O 0-1000 ppm H$_2$O 0- 25 % Vol Sampling system: 191° Heated ceramic filter and PTFE probe. Sample Flow around 10 l/ min
Microsoot	AVL Microsoot sensor 483
	Real time particulate soot measurement 0 – 1000 mg/m^3 Sample flow 2 l/min
Particle counter	AVL particle counter advanced 489
	Real time particulate number measurement Heated sample probe, Sample flow 5 l/min

4. Experimental results

The experimental campaign to characterize the combustion of the developed H$_2$-ICE and optimize its calibration has been carried-out on several operating points at both part load and full load. For the sake of brevity, in this paper the results achieved at two interesting operating conditions will be described, notably the 2000 rpm, 6 bar BMEP part load point and the 2000 rpm – WOT full load point (rated torque).

Before diving more into the details of the two above conditions, it is important to remark that the data measured on the whole engine map have been used for a comparison with the analytical model developed and discussed in [9, 10], in order to improve the accuracy of the digital twin of the SCE and enable more virtual development for future PUNCH H$_2$-ICEs applications.

4.1 Correlation of Experimental Data with Analysis

The possibility to improve 1D- and 3D-CFD models is of great relevance for the virtualization of engine development, and in case of H$_2$-ICE the scarcity of experimental data makes any opportunity particularly valuable.

Therefore, the Authors took advantage of the experimental campaign performed on the SCE to feed-back the measurements into the analytical model and in this way to close the loop between the SCE itself and its 1D-CFD digital twin. For reference, the 1D-CFD model described in [9, 10] has been developed in GT-Power environment with customized predictive 'SI-Turb' and 'Knock' sub-models tuned on purposely-run 3D-CFD Converge simulations, in order to capture the hydrogen turbulent flame speed at high dilution levels (high RAFR and EGR rates) and the knock-limited performance at high peak firing pressures and temperatures.

It proved to be rather accurate and after some tuning of the charge-exchange loop and further refinement of the turbulent combustion sub-routines, was capable to correctly capture the main sensitivities to engine operating conditions and control parameters, such as Start-of-Injection (SOI), Spark Advance (SA), Relative Air-to-Fuel Ratio (RAFR) and EGR rate.

Figure 6 represents a high-level summary of the results achieved, by comparing a set of engine operating conditions (represented on the X-axis by the Case setup number) experimentally measured ('Exp', dashed black line) with their simulated twins ('Sim', solid red lines) in terms of RAFR, Air Mass Flow Rate, ISFC and Net IMEP. As will be the case for a few following graphs, the absolute values of the axes are not reported as they are 'sensitive PUNCH information'; however, absolute deltas of the axes gridlines are provided in order to let the Reader understand the sensitivity of the developed trends or the quality of the matching between simulations and experiments as in this specific case.

As can be noticed, the expanded Y-scales put in light some differences particularly in RAFR and ISFC patterns at high mass flow rates, but, overall, the trend is correctly captured underlying a fundamental robustness and accuracy of the modelling.
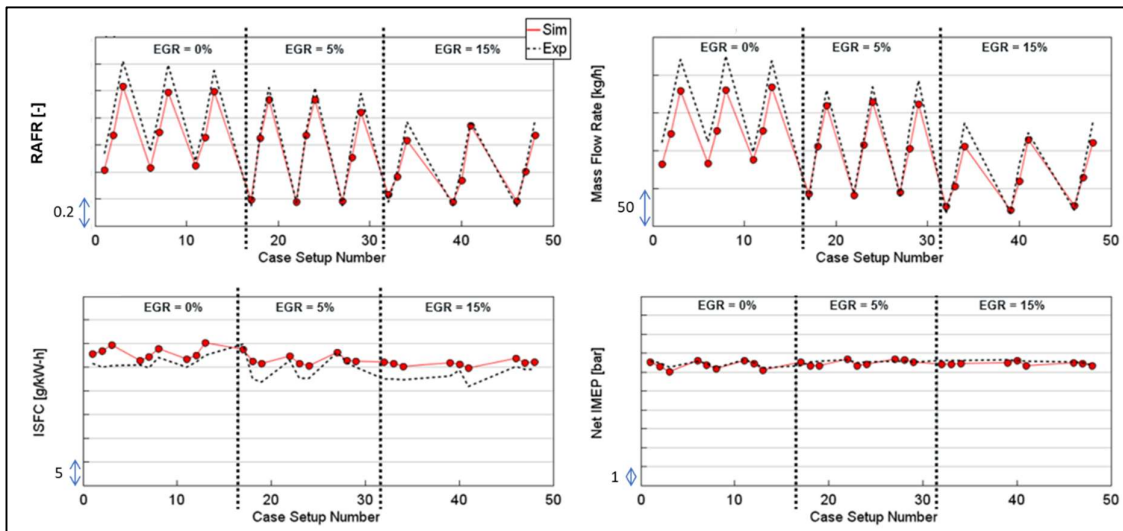
Fig. 6. Correlation between 1D-CFD model output (Sim, red solid lines) and experimental results (Exp, black dashed lines) for a RAFR and EGR rate variation (EGR levels indicated on the plots)

Figure 7, as indicated by the caption, reports correlation of CA-based indicating parameters (in-cylinder pressure and HRR) between 1D-CFD model output ('Sim', red curves) and experimental results ('Exp', black curves) for a sub-set of Figure 6 operating conditions at different speeds and loads, as indicated on the diagrams. As anticipated, the quality of the cycle-resolved quantities of Figure 6 is well evident in the accuracy of the CA-based in-cylinder pressure and HRR curves: these latter are particularly sensitive to the reliability of the modelling and exhibit predictive capability to capture dilution effects.
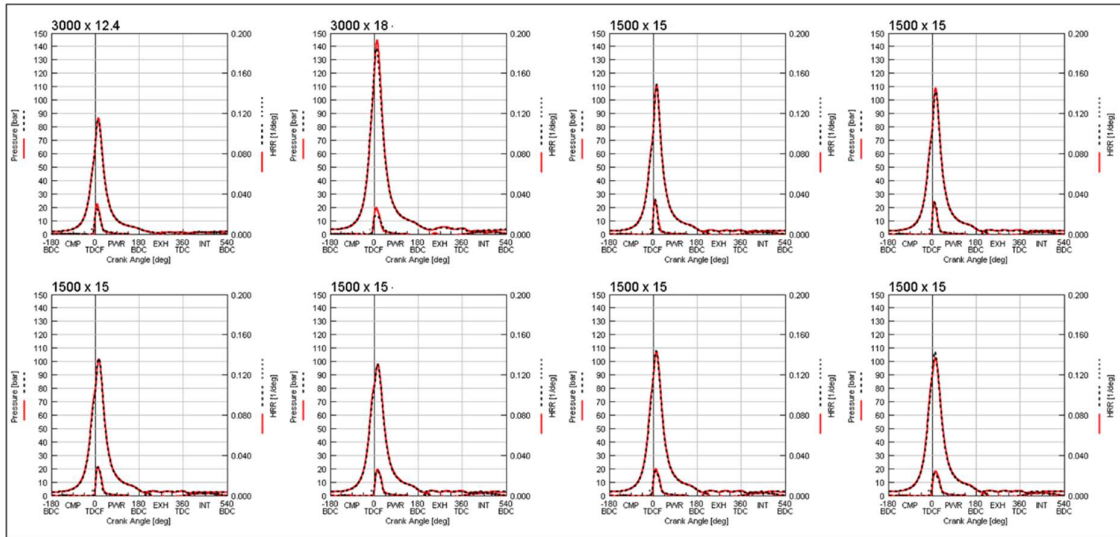
Fig. 7. Correlation of CA-based indicating parameters (in-cylinder pressure and HRR) between 1D-CFD model output (Sim, red curves) and experimental results (Exp, black curves) for a set of operating conditions at different speeds (rpm) and loads (bar of BMEP), as indicated on the diagrams

4.2 Part Load: 2000 rpm x 6 bar BMEP

The point considered for part load is 2000 rpm, 6 bar BMEP which falls in the middle of the engine operating map, and as such can be considered an 'average' condition. In addition, the engine at this load features some initial boosting requirement and can be operated unthrottled thanks to the wide hydrogen flammability limit; on the other side, the combustion stability can still be a challenge due the mix of air and EGR dilution. Because of these reasons, it can be considered a rather interesting condition to examine more in details.

Before deep-diving into the results, let's consider that being an SCE application, the BMEP level cannot be measured directly as typical on MCE applications, but it is rather an output of IMEP indicated measurement coupled with a friction and accessory model (FMEP), as described in [14] for a similar SCE application. It goes without saying that in this case the friction and accessory model has been updated and parameterized according to the specific contents of the MCE H_2 reference application, which lacks for example the high-pressure Diesel pump, and therefore features a lower friction level.

The ranges used for building the DoE variation list, which primarily explored the effect of EGR rate, RAFR and MFB50 on combustion behavior (including engine-out emissions, efficiency and exhaust temperature) have been quite ample in order to fully capture the effects of the above quantities; in particular: ~16% EGR, ~1.1 RAFR and ~17 CA MFB50 variations have been considered. Each single test of the variation list was run with a specific combination of the variable main thermodynamics parameters: Manifold Absolute Pressure, EGR rate, Start of Injection and Spark Timing, according to pre-determined values to cover the relevant ranges and adjusting Fuel Injected Quantity to keep Net IMEP constant (corresponding to BMEP of 6bar). In addition, Spark Timing advance was limited to knock-free combustion to avoid NVH issues and engine damages.

Figure 8 reports the main results of the DoE investigation in graphical form, through the output clouds generated starting from the variation list above-described. About 5700 points – extrapolated by means of Kriging methodology – have been identified and are represented by the blue points; among them, those exhibiting the best trade-off between ISFC and IS-NOx are indicated by orange dots, whereas the best overall operating area (low ISFC & low NOx) is identified by the green dots. It is interesting to observe that a calibration featuring medium-high levels of EGR, high RAFR (high boost)

and advanced combustion phasing (MFB50 ~8CA deg ATDC) represents, as reported in the literature, the best combination of parameters [6, 14].
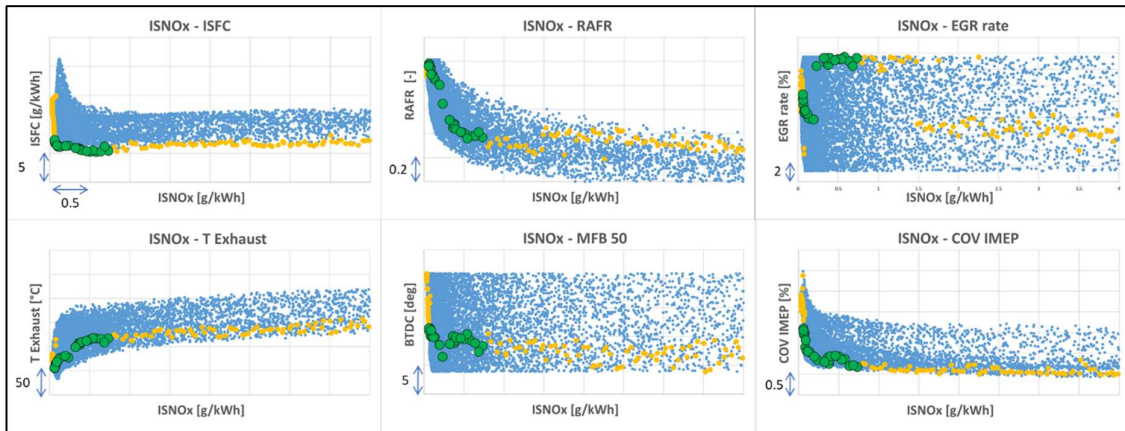
Fig. 8. DoE output clouds for the 2000 rpm – 6 bar BMEP operating condition for several output parameters (blue points) – ISFC vs IS-NOx leading-edge is represented by orange points, whereas the green dots define the optimal calibration region

This optimized calibration setting provides also a quite good combustion stability, as measured through the CoV-IMEP: the green area is close to the leading edge of lower CoV-IMEP, and this happens thanks to the completeness of the hydrogen flame propagation process, notwithstanding a certain cycle-to-cycle variation in the pressure diagrams as apparent from **Figure 9** for the same engine operating point 2000 rpm – 6 bar BMEP. The high degree of combustion completeness has been recognized as a peculiar behavior of optimized lean hydrogen combustion (RAFR ~2.0÷2.5), which exhibits fast flame propagation (up to 6 times faster than gasoline or CNG stoichiometric mixtures), higher tolerance to in-cylinder inhomogeneities (which allow to burn effectively locally richer/leaner pockets) and a minimal quenching distance. The combination of these features contribute to a consistent IMEP delivery (as apparent from the cumulative MFB curves with minimal changes in end-of-combustion value in Figure 9) despite a variability in pressure cycles similar to gasoline or CNG applications. In completing the comments related to Figure 9, it is worth mentioning that the curves illustrate 100 consecutive cycles, with blue lines representing in-cylinder pressure, green lines instantaneous HRR and purple curves the cumulative MFB. The solid thick lines indicate the average cycles, whereas the colored area limited by solid thin lines the upper and lower envelopes.
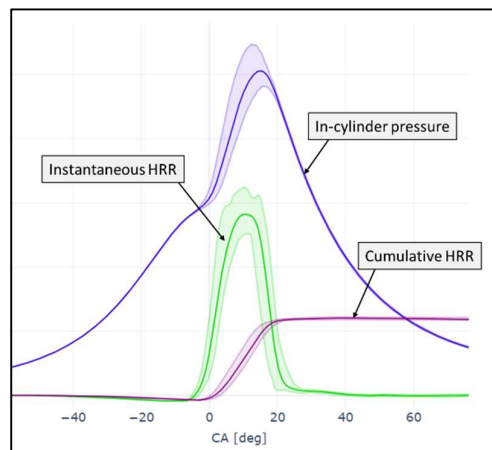
Fig. 9. Cycle-to-cycle variability of in-cylinder pressure (blue), instantaneous HRR (green) and cumulative MFB (purple) for 100 consecutive cycles at 2000 rpm – 6 bar BMEP with optimized calibration

Figure 10 is a simplified illustration of the flame propagation process characteristic of the investigated combustion system. While qualitative, the position of the piston vs the spherical flame front for different crank angles is meaningful and shows the main parameters governing the shape of the HRR

recorded for this operating condition, in particular the reason behind the HRR peaking when the flame front reaches the piston top, then keeping roughly flat for a few crank-angle degrees due to the constancy of the total flame front area (as flame moves laterally after reaching piston top and while piston uncovers additional combustion chamber height in its descent from TDC), as well as the rapid flame extinction following the eventual approaching of the liner walls. It is especially helpful in explaining how even small variations in the isotropy of the flame propagation, and hence a deviation for the ideal spherical flame front, can determine a different position in the HRR peak(s), as well as in their relative magnitude, while still providing a consistent cumulative HRR at the end of the process, which is the reason behind the low CoV-IMEP.
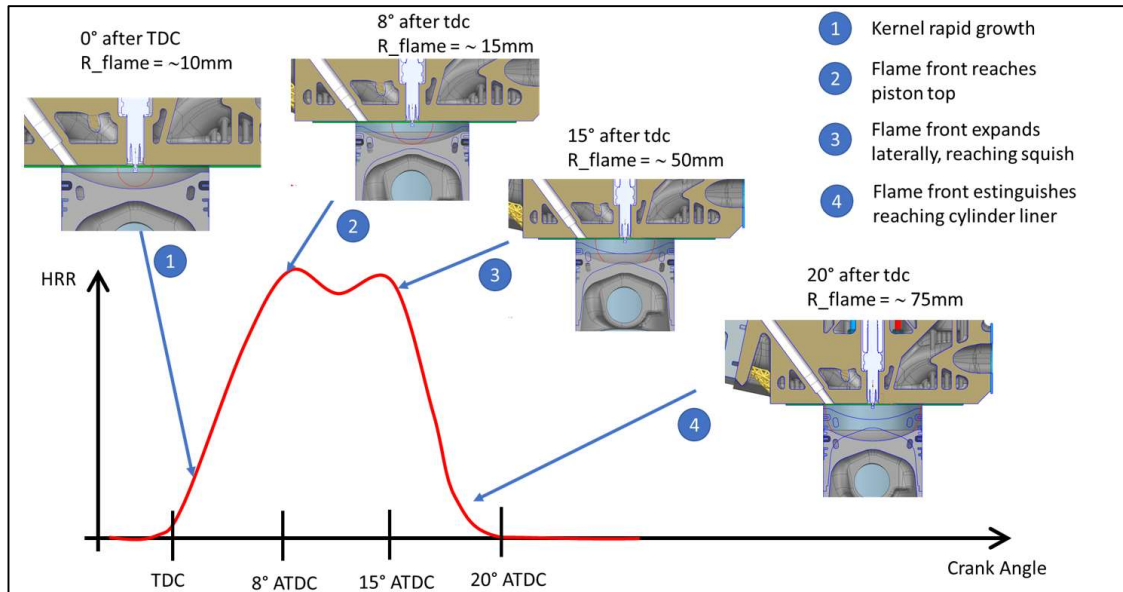

Fig. 10. Sketch of the HRR behavior with illustration of the corresponding flame-propagation phases

Figure 11 focuses on the ANalysis Of VAriation (ANOVA) for the 2000 rpm – 6 bar BMEP operating point, and analyzes the trends and relative contributions of MFB50, EGR and RAFR input variables to IS-NOx (left), ISFC (center) and CoV IMEP (right). The Y-axes easily show not only the sensitivity of the output quantity to each input quantity, but also the trend that the output quantity has for the range investigated of the input variables. The left chart for example highlights that MFB50 optimum range is – as expected – in the low MFB50 range, where the sensitivity of ISFC to MFB50 is also tiny, whereas rapidly deteriorates as MFB50 overcomes a critical threshold and expansion efficiency is rapidly decaying. On the contrary, low RAFR and EGR rates impact negatively ISFC (high wall heat losses), as happens in the case of RAFR also for too high values (longer combustion duration and incomplete hydrogen oxidation). This is especially interesting and witnesses the power of this techniques, as can quantitatively capture the effects described in the literature.
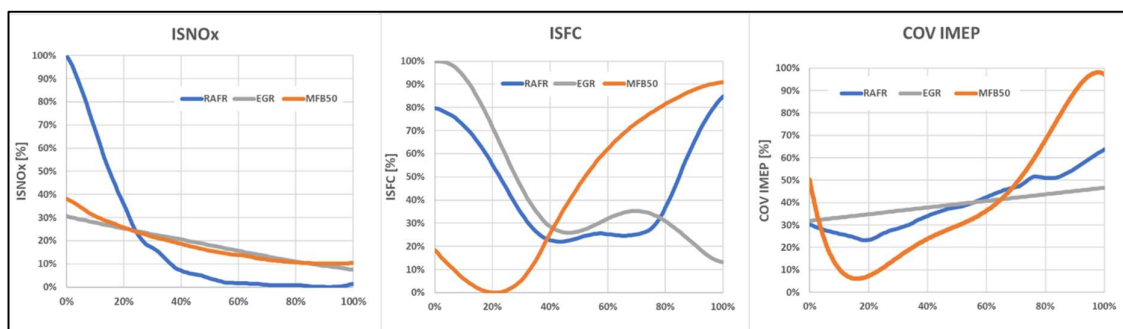

Fig. 11. ANOVA outputs for IS-NOx (left), ISFC (center) and CoV IMEP (right)

### 4.3 Full Load: 2000 rpm WOT (Rated Torque)

Let's now analyze the rated torque point, i.e. 2000 rpm - WOT. This point is very interesting as is one of the most critical regions for H_2-ICE, where the desire of high torque density and low BSFC challenges the knock resistance of the fuel under lean conditions.

Figure 12 reports the results of the ANOVA analysis for 2000 rpm, full-load (rated torque) conditions: the four dominating parameters in order of contribution to the final quantity are reported for ISFC, IS-NOx, IMEP and Exhaust Temperature. It is interesting to observe that, as typical for hydrogen combustion, the RAFR is dominating most of them through the lean-out of the charge and reduction of combustion temperature (which, in turn, reduces NOx production and heat losses), with MFB50 taking the second spot overall.
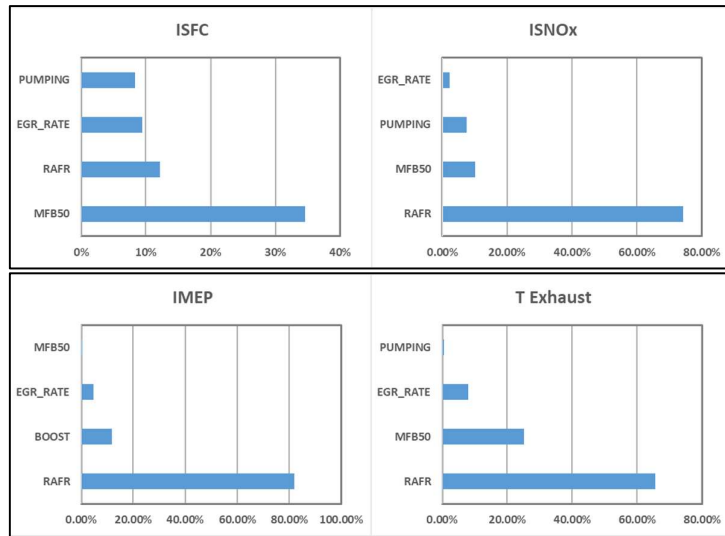
Fig. 12. ANOVA output contributions for (clockwise): ISFC, IS-NOx, Exhaust Temperature and IMEP

Figure 13 reports – similarly to what Figure 8 did for Part Load operating point – the output of the DoE investigation in graphical form, through the output clouds generated starting from the specific variation list for this operating point. Among the cloud points, those exhibiting the best trade-off between IMEP and IS-NOx are indicated by orange dots (leading edge performance curve), whereas the best overall operating area is again identified by the green dots. In this case, as represented in the top left diagram, it is interesting to observe that there is a clear relationship between the attainable performance level and the corresponding engine-out NOx emissions, in other words ultra-low emissions H_2-PFI ICEs need somewhat to compromise their power output [6].
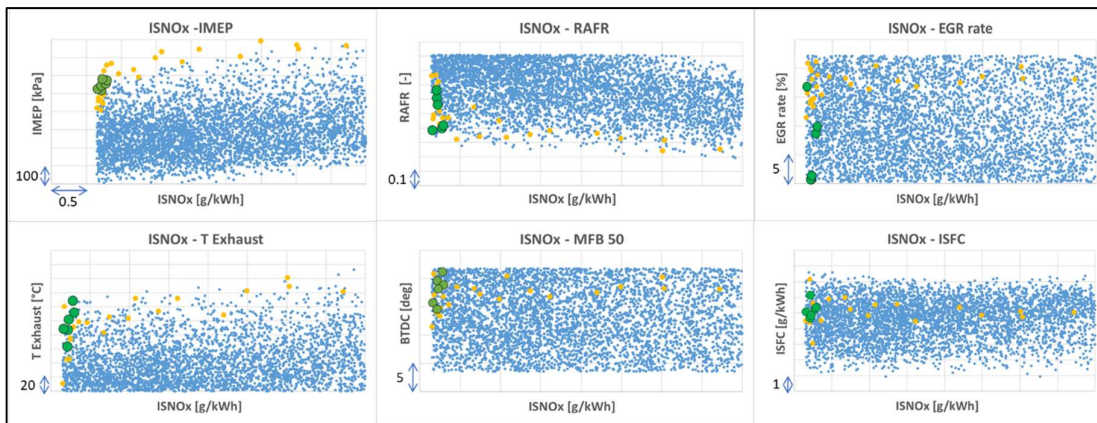

Fig. 13. DoE output clouds for the 2000 rpm – WOT operating condition for several output parameters (blue points) – IMEP vs IS-NOx leading-edge is represented by orange points, whereas the green dots define the optimal calibration region

4.4 EGR effect

As a final focus of this brief article on hydrogen combustion, let's now analyze the EGR effect on hydrogen combustion at the Part Load, without pretending to be exhaustive but with the objective to cast some light on its effect on H_2-PFI homogenous combustion compared to Diesel Combustion. In fact, the effect of EGR – which for H_2-ICEs is essentially composed by recirculated, air-diluted water vapor – on hydrogen combustion and its relative benefit versus an equivalent fresh air dilution in controlling knock and NOx production is still a debated topic, not entirely comprehended and accepted in literature [6].

Figure 14 reports the results of two sweep variations of MFB50 (left) and EGR rate (right) on IS-NOx vs RAFR on 2000 rpm – 6 bar BMEP engine operating point, as indicated by the legends. As the X- and Y- scales are the same for both figures, it is possible to capture the relative magnitude of both parameters: the effect of MFB50 appears to be slightly larger than the EGR one for a similarly practical variation in the controlling parameter (SA timing or EGR rate) and seems to hint that EGR rate is not as effective for H_2 combustion as it is for Diesel one.
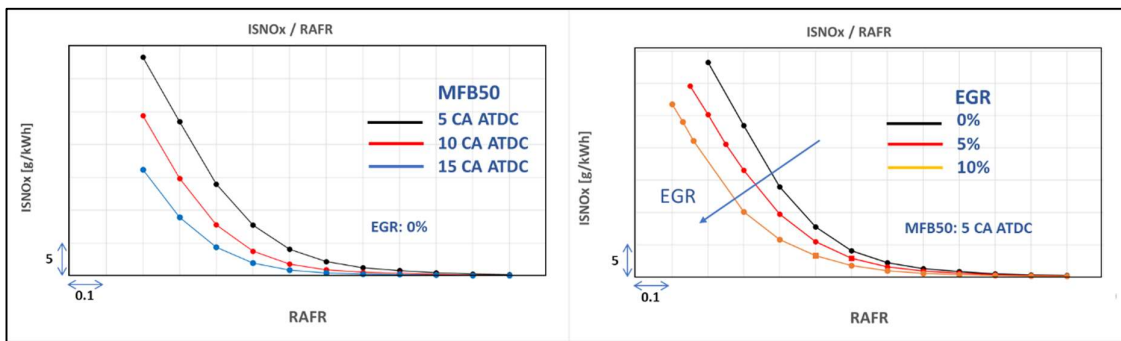
Fig. 14. Effects of MFB50 and EGR rate on IS-NOx emissions vs RAFR, at 2000 rpm – 6 bar BMEP

In order to prove or disprove the above observation, and to quantitatively capture the effect of air vs EGR dilution, the Authors calculated a "diluted RAFR" parameter that is defined as RAFR':
$RAFR' = \frac{\frac{M_{AIR}+M_{EGR}}{M_{FUEL}}}{\alpha_{st}}$, where: M_{AIR} is the air mass flow, M_{EGR} is the EGR mass flow, M_{FUEL} is the fuel mass flow and α_{st} is the stoichiometric air-to-fuel ratio. Differently from the conventional definition of RAFR, the newly introduced RAFR' defines, rather than the stoichiometry of the combustion, the overall dilution of the fuel (and hence of the combustion products) either by fresh air or by recirculated exhaust gases.

Figure 15 re-plots the EGR sweep variation of Figure 14 (right) at 2000 rpm – 6 bar BMEP engine operating point, using RAFR' as X-axis (EGR rates are indicated in the legend). It is quite interesting to observe that the three curves (representing three different levels of EGR) tend to collapse, and two RAFR' regions appear, indicated by a blue and orange shadow. The orange shadow, characteristic of very lean mixtures, does not exhibit any difference at all in the IS-NOx emission due to the three different EGR levels (including no EGR), indicating that EGR and fresh air have the same effect on nitrogen oxides formation. The blue shadow, characteristic of less lean mixtures, is instead showing a scatter among the three NOx curves corresponding to the different EGR levels: at same dilution level, the presence of EGR is more efficient in reducing the NOx formation. In the Authors' opinion, this may be due to the effect of the higher heat capacity of water vapor vs fresh air, an effect that is increasing as RAFR' is reduced thanks to the higher water concentration in the recirculated exhaust gases.
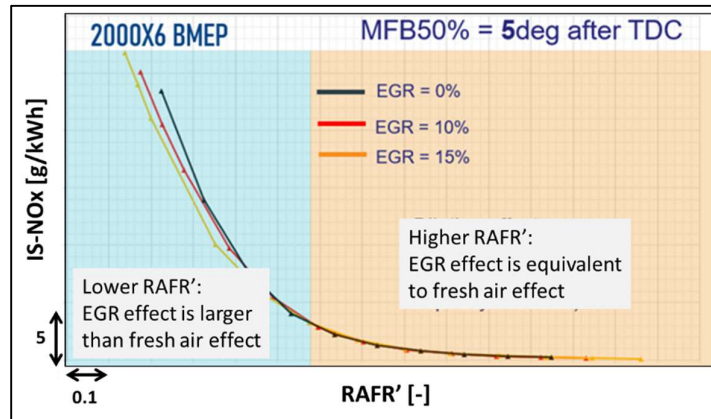
Fig. 15. Effects of EGR rate on IS-NOx emissions vs RAFR' for three EGR rates, at 2000 rpm – 6 bar BMEP

Figure 16, for the same engine operating conditions 2000 rpm – 6 bar BMEP, performs a comparison between H_2-PFI and Diesel combustion, overlapping the corresponding IS-NOx curves for three EGR levels: 0%, 5%, 10% (in case of Diesel combustion, only a 12% value was available as the highest EGR rate, therefore the comparison should be taken with a little approximation). It is striking the quite different shape of the curves: in fact, Diesel experimental points corresponding to the same EGR level do not highlight any appreciable sensitivity to RAFR' (even for the lower RAFR' region), and in addition – at same RAFR' – the sensitivity of NOx formation to EGR is quite larger for the Diesel combustion vs the H_2-PFI one (especially for the higher RAFR' region). Concluding the comments related to Figure 16, it's worth noting that in the actual RAFR' optimal range of operation for hydrogen the IS-NOx values for the gaseous fuel are much lower than the diesel ones and according to literature [4].
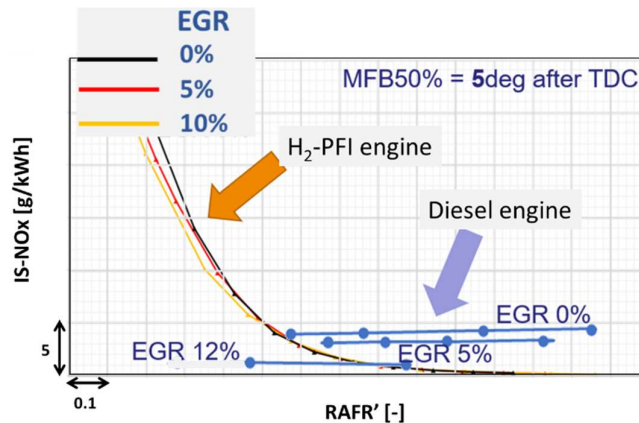

Fig. 16. Effects of EGR rate on IS-NOx emissions vs RAFR' for three EGR rates, at 2000 rpm – 6 bar BMEP. Comparison between H_2-PFI and Diesel combustion

In order to reconcile and explain such apparently inconsistent behavior, the Authors prepared a qualitative sketch of the two different combustion regimes, comparing the specific Diesel and H_2-PFI areas of operation in terms of actual RAFR and flame temperature under which NOx formation mostly happens for the two combustion regimes, as reported in **Figure 17 (left)**. The first thing to consider is that Diesel combustion mostly happens in a highly-inhomogeneous, mixing-controlled charge, with fuel oxidizing under slightly lean conditions at the boundary between the fuel vapor plume and the surrounding air/EGR. In this thin region, the gas temperature is the highest reached, before the surrounding air brings excess oxygen to dilute the burnt gases and rapidly drops their temperature: the NOx formation, which is exponential with local temperature, and proportional to local oxygen concentration (according to the Zeldovich mechanism), is the result of this combustion kinetics. In case of H_2-PFI, instead, the flame propagates from the initial kernel generated by the spark plug through a roughly spherical front and progressively involves the homogeneous pre-mixed charge of hydrogen and air/EGR in the chamber. The local temperature at the flame front, and its oxygen concentration, therefore, tend to be very

close to the chamber average (excluding local small inhomogeneities), and as a consequence of the lean burn combustion, quite lower than the Diesel one. Due to this, the NOx production of H_2-PFI engine in the optimal regime highlighted by the orange shadow in Figure 15 is low and also the sensitivity to EGR is smaller. In fact, the EGR gas reduces - through its higher heat capacity and dilution – local flame temperature, thus impacting the NOx formation with a magnitude that depends – via the exponential Zeldovich mechanisms – on the baseline flame temperature. As **Figure 17 (right)** exemplifies qualitatively, this effect is much stronger in case of the inhomogeneous Diesel combustion happening locally in near- stoichiometric conditions, rather than the homogenous H_2-PFI one which is locally as lean as the charge average.
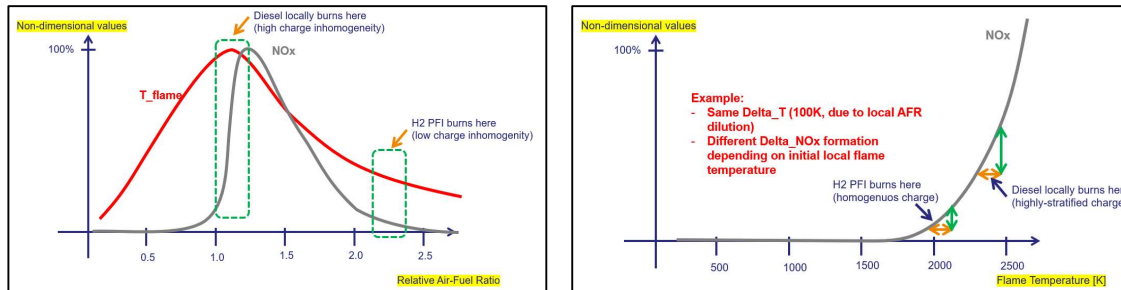
Fig. 17. Qualitative sketch of the RAFR and Flame Temperature effect of NOx production, comparing the different Diesel and H_2-PFI areas of operation

Conclusions

In the present paper, the Authors tested a 0,5ℓ single cylinder H_2-fuelled engine featuring an optimized PFI layout and a dedicated piston bowl coupled to a retrofitted Diesel engine operated as H_2 monofuel, in SI mode.

The effects of the main engine parameters, extensively investigated by means of DOE techniques at one Part Load and one Full Load point, as well as the effect of dilution and EGR to promote clean and efficient hydrogen combustion, have been discussed in order to recommend the most effective practices.

For the Part Load point (2000 rpm, 6bar BMEP), it is interesting to observe that a calibration featuring medium level EGR, high RAFR (high boost) and advanced combustion phasing (MFB50 ~8CA deg ATDC) represents, as reported in the literature, the best combination of parameters. This optimized calibration setting provides also a quite good combustion stability, notwithstanding a certain cycle-to-cycle variation in the cylinder pressure, thanks to a very high degree of combustion completeness which leads to a consistent IMEP delivery. The ANOVA analysis highlights that MFB50 optimum range is – as expected – in the low MFB50 range, where the sensitivity of ISFC to MFB50 is also tiny, whereas rapidly deteriorates as MFB50 overcomes a critical threshold and expansion efficiency is rapidly decaying. On the contrary, low RAFR and EGR rates impact negatively ISFC (high wall heat losses), as happens in the case of RAFR also for too high values (longer combustion duration and incomplete hydrogen oxidation).

For the Full Load point (2000rpm, rated torque), results of the ANOVA analysis show that, as typical for hydrogen combustion, the RAFR is dominating most of output parameters through the lean-out of the charge and reduction of combustion temperature (which, in turn, reduces NOx production and heat losses), with MFB50 taking the second spot overall. Looking at the DoE output clouds, it is interesting to observe that there is a clear relationship between the attainable performance level and the corresponding engine-out NOx emissions: in other words ultra-low emissions H_2-PFI ICEs need somewhat to compromise their power output.

Finally, the EGR effect on hydrogen combustion at the Part Load point (2000 rpm, 6bar BMEP) has been discussed, without pretending to be exhaustive but with the objective to cast some light on its effect on H_2-PFI homogenous combustion compared to Diesel Combustion. At very lean mixtures, EGR and fresh air have the same effect on nitrogen oxides formation for H_2-PFI combustion; for less lean mixtures, the presence of EGR is more efficient in reducing the NOx formation than fresh air dilution. In the Authors' opinion, this may be due to the effect of the higher heat capacity of water vapor vs fresh air, an effect that is increasing as RAFR' is reduced thanks to the higher water concentration in the recirculated exhaust gases. It is also interesting to observe that Diesel combustion does not exhibit any

appreciable difference between dilution due to EGR or fresh air, but – for the same overall dilution level – the sensitivity of NOx formation to EGR is quite larger for the Diesel combustion vs the H_2-PFI.

Bibliography

[1]   Korn, T., "The Most Efficient Way for CO_2 Reduction: the New Generation of Hydrogen Internal Combustion Engines", 41th International Vienna Motoren Symposium 2020, Vienna

[2]   Beatrice, C., "Technology review for SI ICE based powertrains with 50% brake thermal efficiency", presented at „Does the internal combustion engine have a future?" International Workshop on Jan 21st, 2020 - Politecnico di Torino Energy Center

[3]   Matthias, N., Wallner, T., and Scarcelli, R., "A Hydrogen Direct Injection Engine Concept that Exceeds U.S. DOE Light-Duty Efficiency Targets," *SAE Int. J. Engines* 5(3):838-849, 2012, https://doi.org/10.4271/2012-01-0653.

[4]   Yamane, K., "Hydrogen Fuelled ICE, Successfully Overcoming Challenges through High Pressure Direct Injection Techonologies: 40 Year of Japanese Hydrogen ICE Research and Development", SAE Paper 2018-01-1145

[5]   Klepatz, K., Rottengruber, H., Zeilinga, S., Koch, D. et al., "Loss Analysis of a Direct-Injection Hydrogen Combustion Engine," SAE Technical Paper 2018-01-1686, 2018, https://doi.org/10.4271/2018-01-1686.

[6]   Koch, D. T., Sousa, A., and Bertram, D., "H_2-Engine Operation with EGR Achieving High Power and High Efficiency Emission-Free Combustion", SAE Paper 2019-01-2178

[7]   Pauer, T., Weller, H., Schünemann, E., Eichlseder, H., Grabner, P., and Schaffer, K., "H_2 ICE for Future Passenger Cars and Light Commercial Vehicles", 41th International Vienna Motoren Symposium 2020, Vienna

[8]   R. Rezaei, C. Hayduk, M. Sens, A. Fandakov and C. Bertram, "Hydrogen Combustion, a puzzle piece of future sustainable transportation", SIA Powertrain 2020, Paris

[9]   Golisano, R. et al., "PUNCH Hydrogen Internal Combustion Engine & KERS: an Appealing Value-Proposition for Green Power Pack", 42nd International Vienna Motoren Symposium, 2021

[10]   Vassallo, A. et al., "Ultra-lean Combustion System Optimization for H2-fuelled ICEs via Synergistic Application of 1D- and 3D-CFD", SIA International Conference and Exhibition on Powertrain & Power Electronics, Paris, 2021.

[11]   Sens, M., Danzer, C., von Essen, C., Brauer, M., Wascheck, R., Seebode, J., Kratzsch, M., „Hydrogen Powertrains in Competition to Fossil Fuel based Internal Combustion Engines and Battery Electric Powertrains", 42nd International Vienna Motoren Symposium, 2021

[12]   Verhelst, Sebastian & Wallner, Thomas. (2009). Hydrogen-Fueled internal combustion engines. Progress in Energy and Combustion Science. 35. 490-527. 10.1016/j.pecs.2009.08.001.

[13]   Azeem, N., Beatrice, C., Vassallo, A., Pesce, F. et al., "Review and Assessment of the Material's Compatibility of Rubbers and Elastomers in Hydrogen Internal Combustion Engines," SAE Technical Paper 2022-01-0331, 2022.

[14]   Di Blasio, G., Vassallo, A., Pesce, F., Beatrice, C. et al., "The Key Role of Advanced, Flexible Fuel Injection Systems to Match the Future CO2 Targets in an Ultra-Light Mid-Size Diesel Engine," SAE Int. J. Engines 12(2):129-144, 2019, https://doi.org/10.4271/03-12-02-0010.

Session S1.4 H$_2$ – ICE Emissions

Examining Trade-offs between NOx Emissions and Hydrogen Slip for Hydrogen Combustion Engines

P. Atkins[1], N. Fox[1], A. Saroop[2], J. Hughes[2], N. Coles[2], T. Downes[2], A. Thurston[3]

[1]Advanced Engineering Centre, University of Brighton, Brighton, BN2 4AT, UK.

E-mail: p.a.atkins@brighton.ac.uk
Telephone: +44(0)1273 642307

[2]Ricardo UK Ltd, Ricardo Shoreham Technical Centre, Shoreham by Sea, BN43 5FG, UK

E-mail: john.hughes@ricardo.com
Telephone: +44(0)1273 794094

[3] HORIBA UK, Kyoto Close, Moulton Park, Northampton, NN3 6FL, UK

E-mail: andy.thurston@HORIBA.com
Telephone: +44 (0)1604 5425752

Abstract. Hydrogen combustion engines could provide a timely, robust and cost effective way to decarbonise hard to electrify transport applications like heavy duty trucks. However, near zero harmful emissions and vehicle range, and therefore high engine efficiency, are key to market and legislative acceptance. This paper will present the results of new experimental work undertaken in a collaboration between Ricardo and University of Brighton to examine hydrogen combustion in a single cylinder engine representative of Euro VI heavy duty hardware with medium pressure hydrogen direct injection. Test work has been carried out to investigate the performance of measures to reduce NOx (EGR and lean combustion) to understand more deeply trade-offs between NOx emissions and efficiency. Research to date has shown that lean conditions can result in near zero NOx emissions and measurement of hydrogen slip at these conditions is needed to understand whether hydrogen slip is increased. In this work, hydrogen exhaust emissions are measured using a newly developed analyser from HORIBA which uses mass spectrometer technology to measure concentrations of hydrogen up to 5% in exhaust gas. Hydrogen emissions data measured using this analyser shows that hydrogen slip increases with air fuel ratio and EGR rate, with a clear trade-off between NOx emissions and slip. Indicated efficiency over the test conditions investigated was relatively constant, deteriorating as high EGR rates led to less stable combustion.

1. Introduction

Decarbonisation of transport is an important part of the route to reducing the impact of climate change, with transport accounting for around of quarter of greenhouse gas emissions in the UK. Recent work from IPCC has demonstrated that rapid reductions in GHG emissions are needed to limit warming to 1.5^{o}C, with GHG emissions reductions of 45% needed by 2030 [1]. Vehicle electrification, combined with deep decarbonisation of the electricity supply, is seen as a popular solution for light duty vehicles. However, for larger vehicles like heavy duty trucks and off highway machinery, this technology is challenging due to high power and energy requirements which lead to large battery size and long charging times, significantly increasing cost of ownership. Hydrogen is recognised as an alternative to electrification for these applications due to its increased energy density compared to Li-ion batteries and faster refuelling, combined with zero CO_2 emissions at point of use. Where hydrogen is produced using renewable electricity, very low well to wheel carbon emissions can also result. PEM fuel cell passenger cars have been in low volume production for a number of years, although high cost and low penetration of hydrogen refuelling infrastructure have limited their uptake. PEM fuel cell systems are in development and trial for a range of heavy-duty vehicles where more predictable routes and back to base refuelling reduce the required infrastructure investment. However, the power output and durability requirements for these systems mean that they are not expected to be cost effective until after 2030. Hydrogen engines can provide an alternative powertrain, based on a modification of the existing

diesel or LNG technology. This approach gives the advantage of a technology with an existing manufacturing base and relatively low cost which could encourage a fast roll out to meet the urgent need for deep cuts in GHG emissions.

Alongside priorities for GHG emissions reductions, it is also vital to ensure that air quality emissions from transport are reduced, including NOx and particulate emissions. Hydrogen engines (H2 ICE) in theory will have greatly reduced particulate emissions compared to hydrocarbon based fuels, however levels of NOx can be significant. For commercial applications, low cost of ownership is key to industry acceptance of propulsion technology, so lowest possible fuel costs, driven by H2 ICE efficiency are also important. Recent work has also shown that although the Global Warming Potential (GWP) of hydrogen itself is zero, its effect on other reactions in the atmosphere, particularly those involving methane and ozone, means that its indirect GWP is between 6 and 16 [2]. This means that slip from the engine must be minimised, alongside measures to eliminate fugitive emissions from the distribution and refuelling infrastructure. Key development priorities for hydrogen ICE are therefore near zero tailpipe NOx emissions, minimal hydrogen slip and high efficiency alongside performance to meet market sector needs for power output and driveability.

Approaches to NOx reduction for H2 ICE have been explored by a range of researchers including lean air fuel ratios, water injection and changes to compression ratio, with good coverage in review papers such as [3]. For example, in [4] variation in air fuel ratio, alongside exhaust gas recirculation (EGR) was used to control NOx in a converted production gasoline engine. In this case, the boosting system limited the degree of enleanment that was possible at higher loads, and the authors concluded that lean air fuel ratios were a suitable strategy to reduced NOx at lower loads, although stoichiometric operation with EGR was preferable at higher loads. In [5] the authors compared the effectiveness of water injection and EGR for NOx reduction and reducing the incidence of backfire (combustion in the intake manifold). The authors conclude that both strategies were effective, although the benefits of water injection were greater with NOx reduction of 97% compared to 57% with EGR. In [6] the authors consider the effect of compression ratio on knock and performance. The research shows the combined effects of compression ratio and air fuel ratio, with higher compression ratios amplifying the effect of air fuel ratio on knock. Both EGR and lean air fuel ratios are expected to affect hydrogen emissions in the exhaust, however there are very few studies which include the use of analysers to quantify these emissions. Studies by the research group at the Research Center for High Efficiency Hydrogen Engine and Engine Tribology, Tokyo City University [7, 8, 9] have investigated the use of a plume combustion concept, with high pressure (>100bar) direct injection hydrogen, showing potential for very low NOx emissions and high efficiency, although high injection pressures could limit vehicle range due to reduced differential pressure between the engine hydrogen supply and hydrogen storage tank pressure. In [10] the authors examine NOx emissions with EGR rates up to 40% for a port fuel injected engine and in [11] the effect of lean air fuel ratios (1<lambda<2.2) and spark advance timing on emissions and performance are investigated, where results show reductions in NOx with leaner air fuel ratios and rising hydrogen emissions for 2>lambda >2.2.

Ricardo and University of Brighton have been conducting single cylinder hydrogen engine test work in the University of Brighton's laboratories to examine the performance and emissions of H2ICE. The work examines the performance of a single cylinder engine representative of a heavy duty truck engine, and moderate fuel injection pressures (35 bar). This paper presents results showing the effectiveness of EGR (0-45%) and lean combustion (up to lambda 3) for NOx reduction, combined with hydrogen emissions measurement using a new prototype analyser from HORIBA to understand the trade-off between NOx, hydrogen emissions and efficiency for these approaches.

2. Experimental Setup

2.1 Engine configuration

Test work was carried out on a Ricardo Proteus single cylinder research engine at University of Brighton representative of a Euro VI heavy duty diesel engine, which has been converted to direct injection hydrogen operation as detailed in Table 1.

Table 1. Proteus Engine Configuration

Component	Diesel Proteus	Hydrogen Proteus Conversion
Piston and bottom end	Volvo D13 12.8L diesel, 131mm bore, 158mm stroke	D13 piston machined to give a plain bowl shape and reduced compression ratio
Cylinder Head	Scania DC13 diesel unit head	Scania OC13 CNG unit head modified for direct injection
Ignition system	None	Custom spark ignition system using AEM smart coil
Injection System	Delphi DI common rail system variable (300-2000 bar) injection pressure	Borg Warner prototype H2 injector (35 bar injection pressure)
Throttle	None	Throttle located pre-intake manifold.
Compression ratio	16.17:1	12.62:1

Combustion air supply is controlled via a compressor and critical flow nozzles to minimize the effect of pulsations. Fuel injection, spark timing, throttle position and EGR valve position are controlled via an in-house National Instruments module. A water based cooling system is used to regulate the temperature of recirculated exhaust gas in the EGR system. Hydrogen fuel pressure is controlled using hand operated regulators, with injection quantity controlled by varying injector opening time. A photograph of the test cell installation is shown in Figure 1.
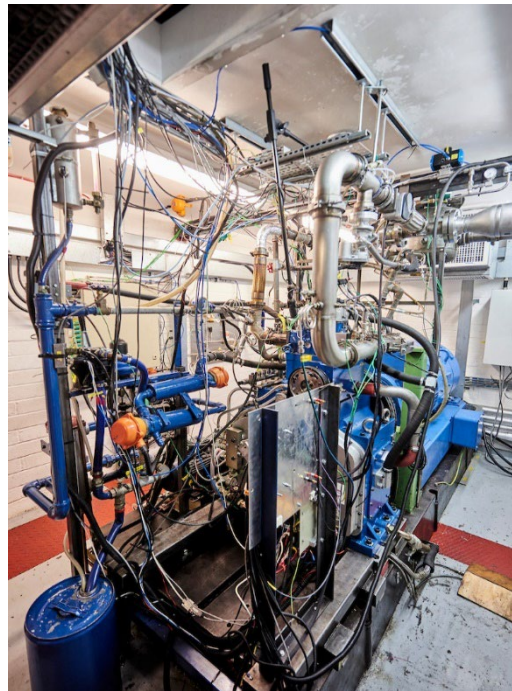
Figure 1: University of Brighton single cylinder hydrogen engine test cell

2.2 Instrumentation

Test bed control and low speed data acquisition were carried out using a HORIBA STARS Lite, with high speed logging carried out using an A&D Phoenix Combustion Analysis system (CAS). Instrumentation is summarised in the Table 2.

Table 2. Instrumentation Summary

Logging Type	Instrumentation Detail
High speed logging	Intake and exhaust manifold and in-cylinder dynamic pressure measurements using Kistler 6025 pressure transducers Spark and fuel injection timing using current clamps
Low speed logging	Engine and test cell system temperatures and remaining pressures Fuel mass flow rate using a Bronkhorst F-113AC mass flow meter Air mass flow via a T Mass sensor and critical flow nozzles Injection and spark timing, throttle and EGR valve position data from National instruments control system Calculated AFR, lambda and EGR rate
Emissions	Two HORIBA MEXA 7000 exhaust gas analysers monitoring intake and exhaust composition measuring- Oxygen (intake and exhaust) Carbon Dioxide (exhaust) Carbon Monoxide (exhaust) Unburnt Hydrocarbons (HC, exhaust) Oxides of Nitrogen (NOx, exhaust)) Exhaust hydrogen concentration using HORIBA HyEVO prototype analyser (see details below)

The HORIBA HyEVO prototype, shown in Figure 2, is a gas analysis system for the measurement of exhaust hydrogen emissions from internal combustion engines and hydrogen fuel cell systems. The gas sampling path into the analyser unit is heated, enabling the direct measurement of exhaust gases from internal combustion engines. The analyser measures hydrogen content of the exhaust as a percentage of the exhaust gas flow.

Figure 2: HORIBA HyEVO prototype hydrogen exhaust analyser

Specifications and system performance for the unit are shown in Tables 3 and 4 below

Table 3. HORIBA HyEVO prototype System Specification

HORIBA HyEVO prototype specification	
Measurement Targets	Internal Combustion Engine (ICE) exhaust, Fuel Cell (FC) exhaust
Measurement Principal	Sectoral Mass Spectrometry
Sample line flow rate	3.5 +/- 0.5 L/min
Sample line Inlet Pressure	-5 kPa to +200 kPa (Gauge pressure)
Data update in-	0.2 secs

terval	
Sample line Inlet Temperature	Below 200 °C (At Sample Probe)
Installation Conditions	In-house use Temperature 5～35 °C Humidity: relative humidity 80% or less Altitude: Below 1000 m sea level

Table 4. HORIBA HyEVO prototype performance

HORIBA HyEVO prototype performance	
Noise	Zero: ≦ 0.5%FS Span: ≦ 0.5%FS
Scale Accuracy	< ±1%FS
Repeatability	Zero: ≦ 1%FS Span: ≦ 1%FS
Interference Effects	Zero: < ±1%FS
Coexistence Effects	Span: < ±2%FS
Calibration gas line response time	t10-90 < 1.0 s
Sample line response time	t10-90 < 2.0 s
Drift	Zero: < ±1%FS/8 hours Span: < ±1%FS/8 hours
Warm-up time	Approx. 3 hours after start-up
Sample line pressure fluctuations effect	< ±1%FS

2.3 Test Programme

The test programme covers a range of operating conditions representative of the expected torque speed map. For clarity, this paper presents results from a limited number of conditions (900 rpm and 1400 rpm, 9 bar GIMEP). Testing was carried out at a lambda of 2, 2.5 and 3, with EGR rate varying between 0 and 45%.

For each test point, the following test process was used to ensure repeatability:
- Adjust hydrogen fuelling rate to supply correct GIMEP

- Adjust air flow to give required air fuel ratio

- Select ignition timing for a target 50% Mass Fraction Burnt (MFB) of 8°ATDC, and avoid adverse combustion events such as preignition or knock

The effectiveness of NOx control with EGR is affected by reductions in intake air oxygen content and changes in specific heat capacity of combustion air. In the case of hydrogen combustion, changes in specific heat capacity are affected by water vapour content so implementation of cooled EGR should avoid condensation in the EGR system. Therefore, to maintain the humidity of recirculated exhaust gas, the EGR system cooling rate was regulated to maintain the temperature of exhaust gas at the cooler outlets at around 70°C. The EGR rate calculated from measured intake and exhaust oxygen content as shown in equation (1), where $O2air$ is oxygen concentration in ambient air (assumed to be 20.96%), and $O2intake$ and $O2exhaust$ are oxygen concentrations at the intake and exhaust measured simultaneously using the two HORIBA Mexa analysers [12].

$$EGR\ rate\ (\%) = \frac{O2air - O2intake}{O2air - O2exhaust}\ (1)$$

Note that Air Fuel Ratio (AFR) calculated for test conditions with EGR is effectively 'metered AFR' based on fuel flow rate and combustion air mass flow rate measured at the test cell air intake, so will differ slightly from trapped AFR due to exhaust gas dilution. Other test bed conditions were controlled as follows: oil temperature 75°C; coolant temperature 90°C; intake port entry temperature 50°C.

Repeatability of test results is illustrated in Table 5 below showing the variation of a range of test parameters at nominally the same test condition (1400 rpm, 9 bar IMEP, 35% EGR). The table shows the arithmetic difference between measured or calculated parameters for the two test conditions.

**Table 5**. Test to test variation of key measured parameters

Test parameter	Test to test variation
IMEP	0.01 bar
EGR rate	1.2%
Spark timing	0.00
MFB10-90	0.06°
MFB50	0.77°
Peak cylinder pressure	4.33 bar
NOx	8 ppm
H2 slip	0.01%

3. Results

This section presents test results at 900 rpm and 1400 rpm, 9 bar GIMEP for EGR rates between 0 and 45% and air fuel ratios of lambda 2, 2.5 and 3. Data focuses initially on combustion properties, before presenting indicated efficiency, NOx and hydrogen emissions.
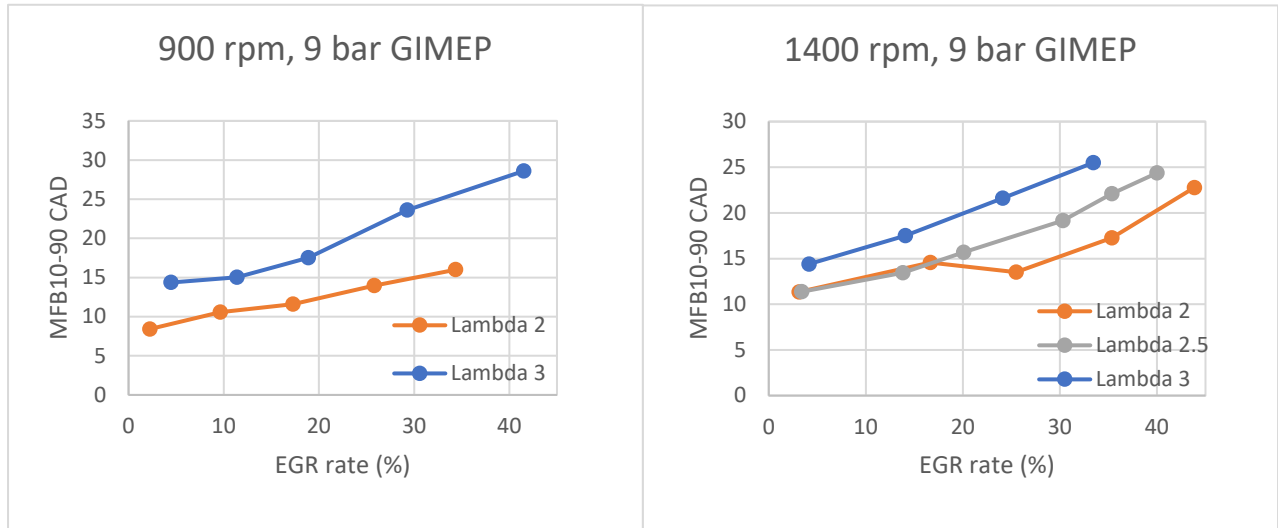
3.1 Combustion

For each test condition, spark timing was adjusted to give 50% MFB at 8°ATDC or retarded to control abnormal combustion. Figure 3 shows the spark timings for each condition. The figure shows that as combustion duration is increased by the increasing dilution of EGR or increasing air fuel ratio, the spark timing to maintain 50% MFB angle (in general) is advanced. At lambda 2 conditions, the richer mixture means that there is greater propensity to preignition/knock, and at lower EGR rates spark timing is retarded to reduce this (for example at 900 rpm 10% EGR or at 1400 rpm lambda 2 and 2.5, 10% EGR). This change in spark timing has a detrimental effect on efficiency, as shown in Section 3.2.
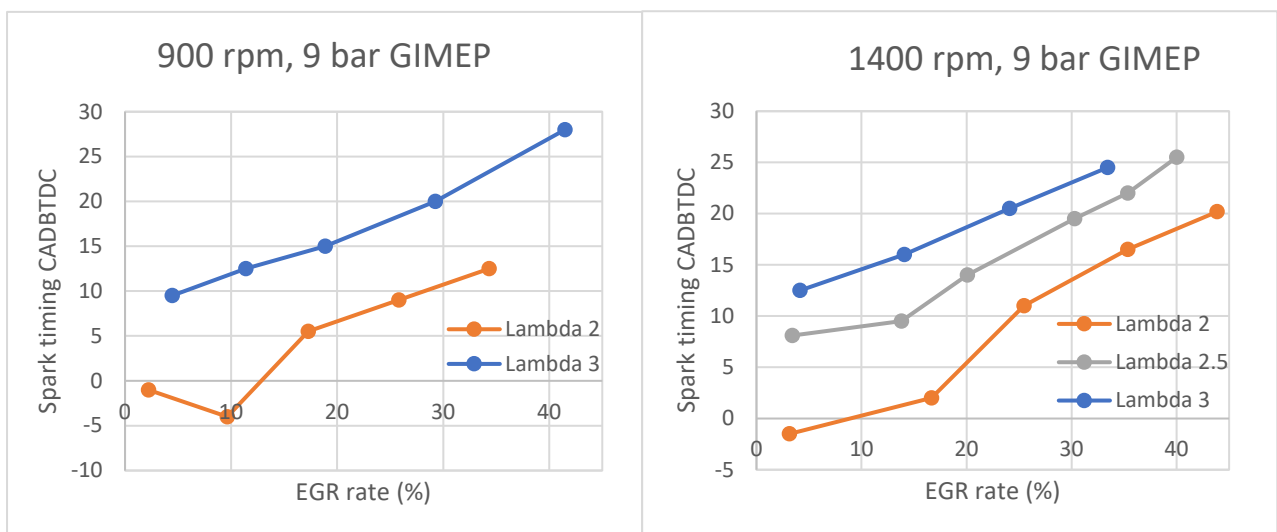

Fig. 3. Spark timing vs EGR rate

Figure 4 shows combustion duration, as calculated from 10% (MFB10) and 90% (MFB90) mass fraction burned angles. Data shows that the general trend is that as EGR rate and lambda increase, increasing dilution of the hydrogen air mixture, combustion duration increases. This trend is modified for 1400 rpm, lambda 2 condition due to changes in spark timing to control preignition/knock at this condition.


Fig. 4. Combustion duration calculated from MFB10 and MFB90 burn angles vs EGR rate

Figure 5 shows 50% Mass Fraction Burned angle (MFB50) vs EGR rate for all test conditions. The data shows that the target 50% MFB angle of 8°ATDC was maintained for the majority of test conditions. Deviations from this MFB50 angle are seen where spark timing was adjusted to avoid preignition/knock, or combustion was relatively unstable, for example at 900 rpm, lambda 2, 10% EGR and at 1400 rpm lambda 2 above 30% EGR.
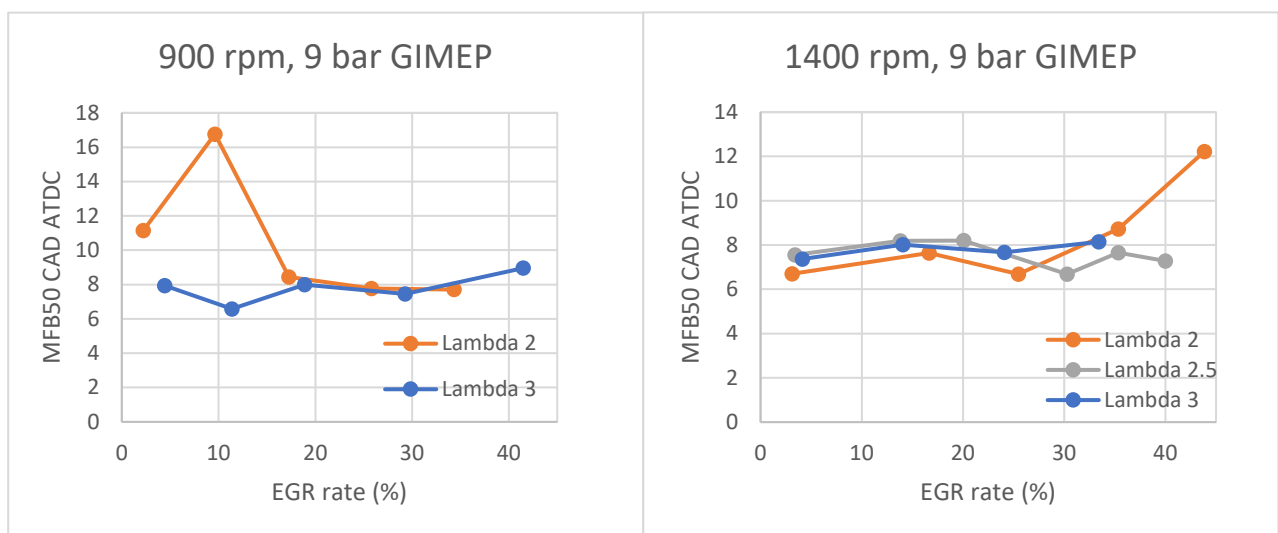

Fig. 5. 50% mass fraction burned angle vs EGR rate

Figures 6 and 7 show combustion stability as indicated by the Lowest Normalised Value (LNV) and Covariance (COV) of IMEP. It is generally recognised that for production engines, COV of IMEP up to 3% and LNV above 90% are acceptable. COV data in Figure 6 shows that at 1400 rpm, COV remains at around 2% for all the air fuel ratios tested up to 30% EGR. At 900 rpm, for lambda 2 conditions, COV at 10% EGR is higher where preignition/knock was found to affect combustion, but otherwise remains below 2%. For lambda 3 conditions at 900 rpm, COV increases for EGR rates above 20%.
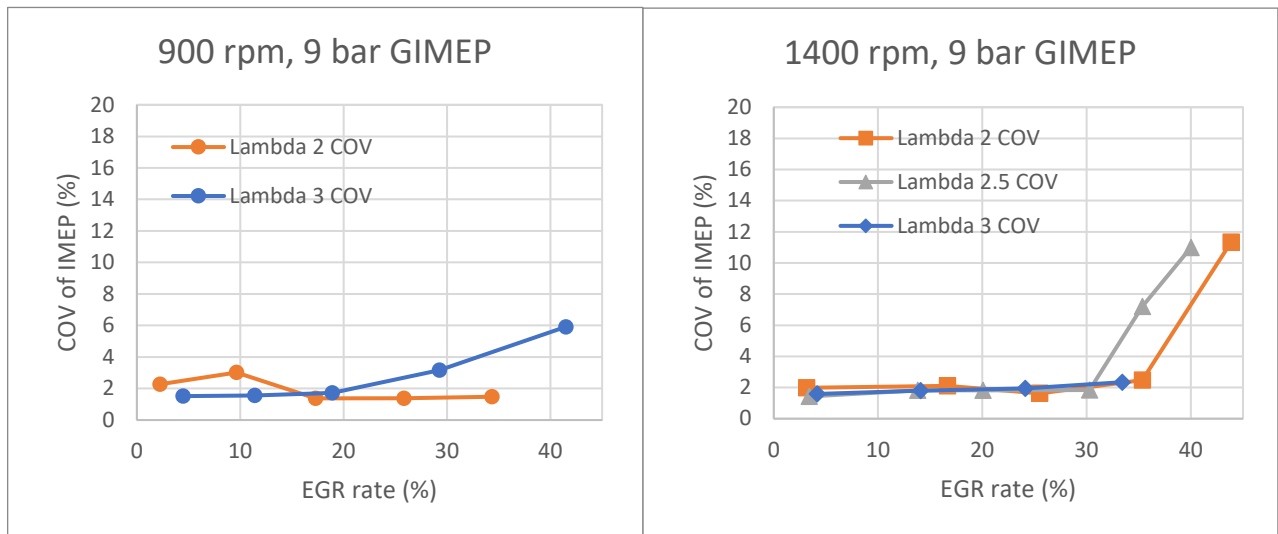
Fig. 6. Combustion stability, COV of IMEP vs EGR rate

Figure 7 shows LNV demonstrating clearly the relatively less stable combustion at Lambda 2 that was experienced during testing at low EGR rates due to preignition/knock. Areas of stable combustion, with LNV above 90%, were indicated at 900 rpm between 18% and 30% EGR and 16% - 25% at 1400 rpm for this air fuel ratio. At higher air fuel ratios, stability is affected by dilution, with LNV reducing and COV increasing as EGR rates increase.
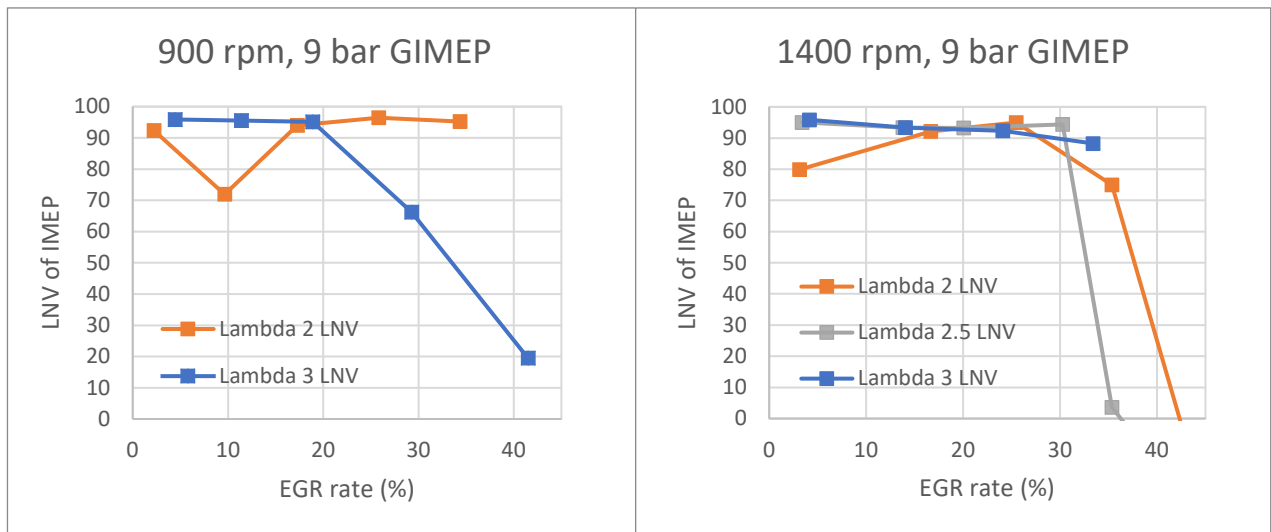
Fig. 7. Combustion stability, COV and LNV of IMEP vs EGR rate

3.2 Indicated efficiency

Figure 8 shows indicated efficiency vs EGR rate. A range of factors affect indicated efficiency including changes to spark and combustion timing and EGR and hydrogen slip. It can be seen from Figure 8 that at lambda 2, efficiency is reduced at lower EGR rates, where spark timing has been adjusted to avoid preignition/knocking conditions. At other air fuel ratios due to the fixed 50% MFB target used in this testing, efficiency remains at a similar level until combustion stability deteriorates, eg at 900 rpm lambda 3 above 20% EGR and at 1400 rpm, lambda 2 above 25% EGR.
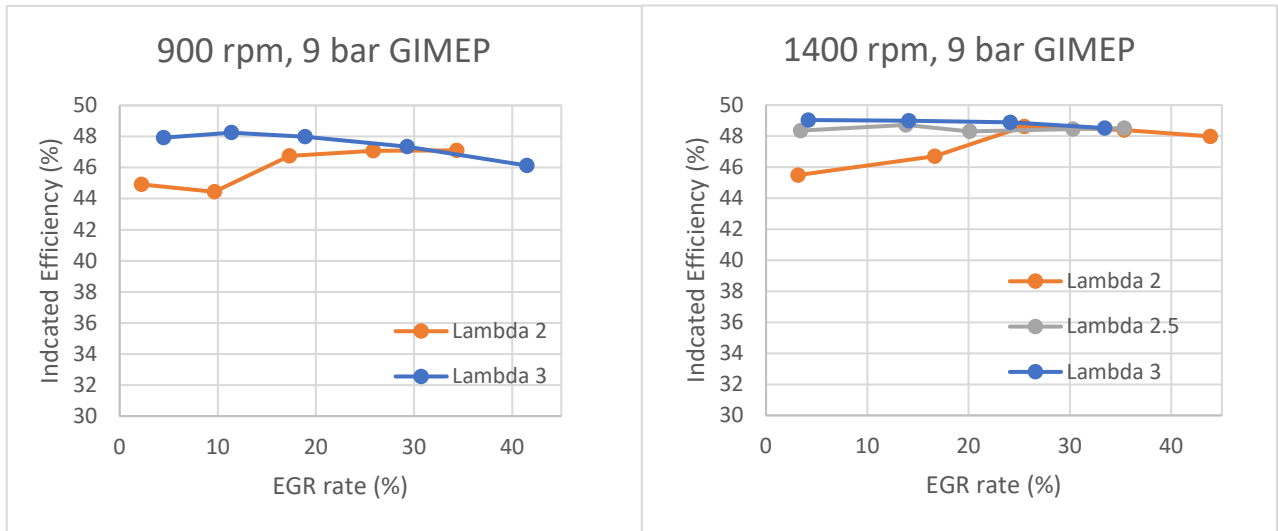

Fig. 8. Indicated efficiency vs EGR rate

3.3 NOx Emissions

Measured NOx emissions results show that dilution of the charge by either excess air or exhaust gas can reduce NOx to very low, single digit ppm emissions. Figure 9 shows that for this un-optimised single cylinder conversion from diesel to hydrogen fuelling, NOx levels at lambda 2 for near zero EGR are high at 3500 ppm and 2000 ppm for 900 rpm and 1400 rpm respectively. At the same EGR rate, increasing the air fuel ratio to lambda 2.5 and 3 reduces NOx significantly – at 900 rpm to 30 ppm for lambda 3, and at 1400 rpm to 430 ppm and 47 ppm for lambda value of 2.5 and 3 respectively. Increasing the EGR rate then further reduces NOx for all air fuel ratios. At 900 rpm, NOx reduces with increasing EGR rate. At 1400 rpm, NOx reduces to a minima and then increases in regions of abnormal combustion with increasing EGR rate. Further investigation is needed to develop understanding of changes in NOx emissions under these conditions. For Lambda 2, this minima is around 35% EGR where combustion stability is deteriorating, as demonstrated by the LNV value of 75%. For Lambda 2.5, NOx emissions of ~10ppm are measured for between 20% and 30% EGR where combustion is stable. Combined with NOx aftertreatment with an estimated 80% NOx reduction efficiency, NOx levels of <1 ppm could therefore be achieved.
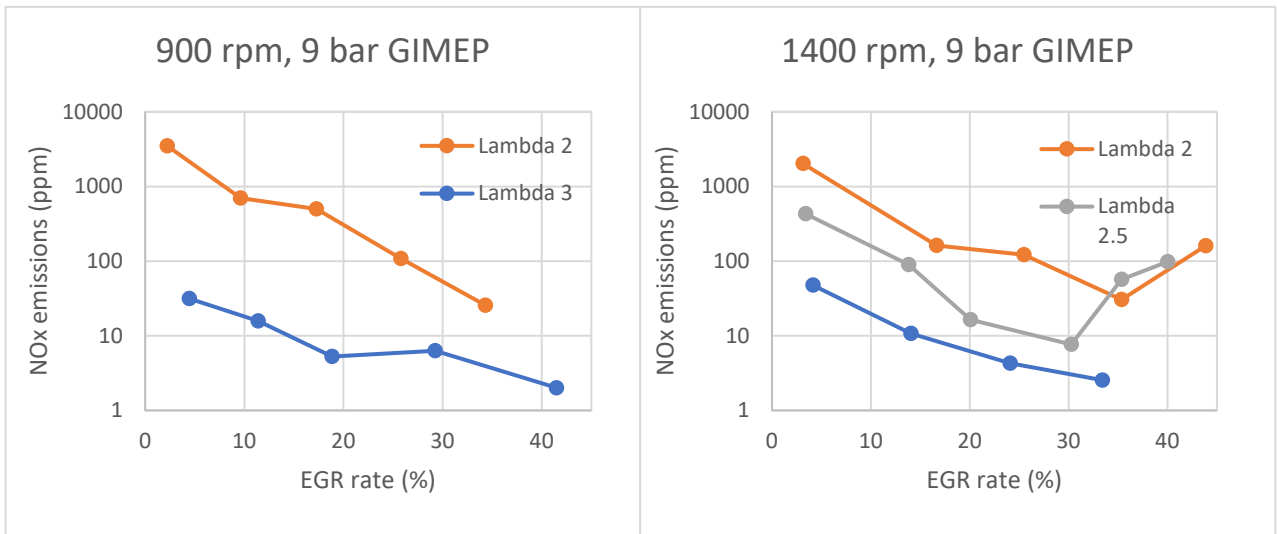
Fig. 9. NOx emissions vs EGR rate

3.4 Hydrogen slip

Emissions for 900 rpm and 1400 rpm are shown in Figure 10. The results show that at near zero levels of EGR, hydrogen emissions levels increase for higher for air fuel ratios. Further dilution with exhaust gas at higher EGR rates, increases hydrogen emissions levels. Comparison of results at 900rpm and 1400rpm shows that hydrogen slip is greater at lower speed conditions with the effect more pronounced at lambda 3. Cylinder head temperature, measured using thermocouples embedded in the cylinder head near the injector, in Figure 11 shows that wall temperatures were lower at lower engine speeds. This is likely to be due to different rates of heat rejection from the cylinder head via the coolant at different speeds. The lower cylinder wall temperature may increase the level of unburnt hydrogen at the walls, worsening hydrogen slip at lower speed conditions.
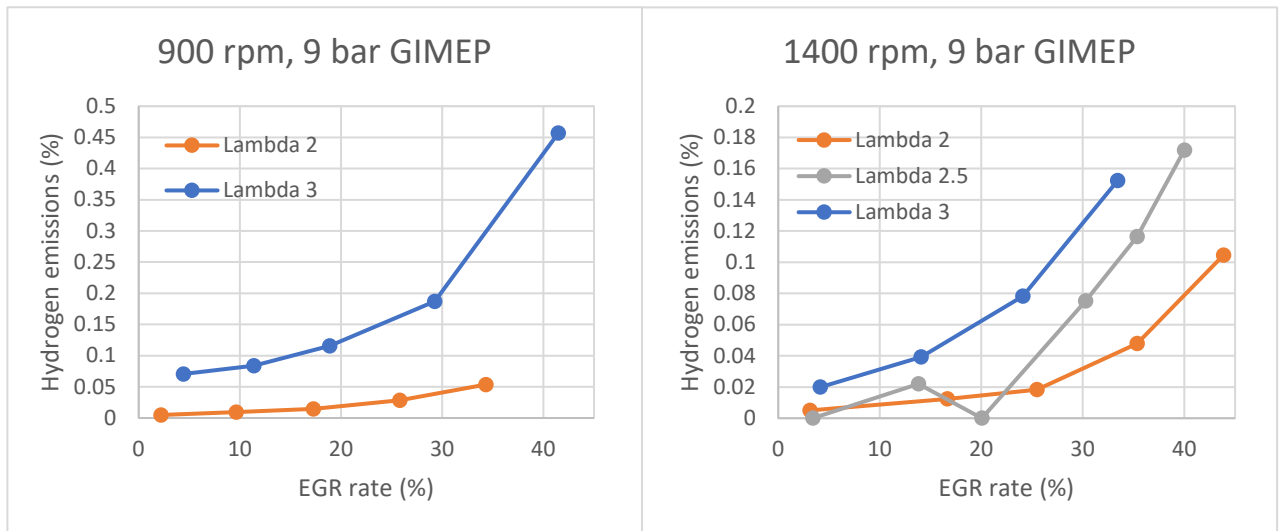

Fig. 10. Hydrogen emissions levels vs EGR rate, as recorded by the HORIBA HyEVO prototype analyser

Hydrogen emissions can be affected by incomplete combustion in the combustion chamber, and also hydrogen which remains in crevice volumes within the cylinder after combustion. At higher air fuel ratios, the hydrogen volume in the crevice volumes would be expected to reduce due to higher dilution, so the dominant effect seems to be biased towards reduced combustion efficiency due to unburnt end gas boundary layer at combustion chamber walls.
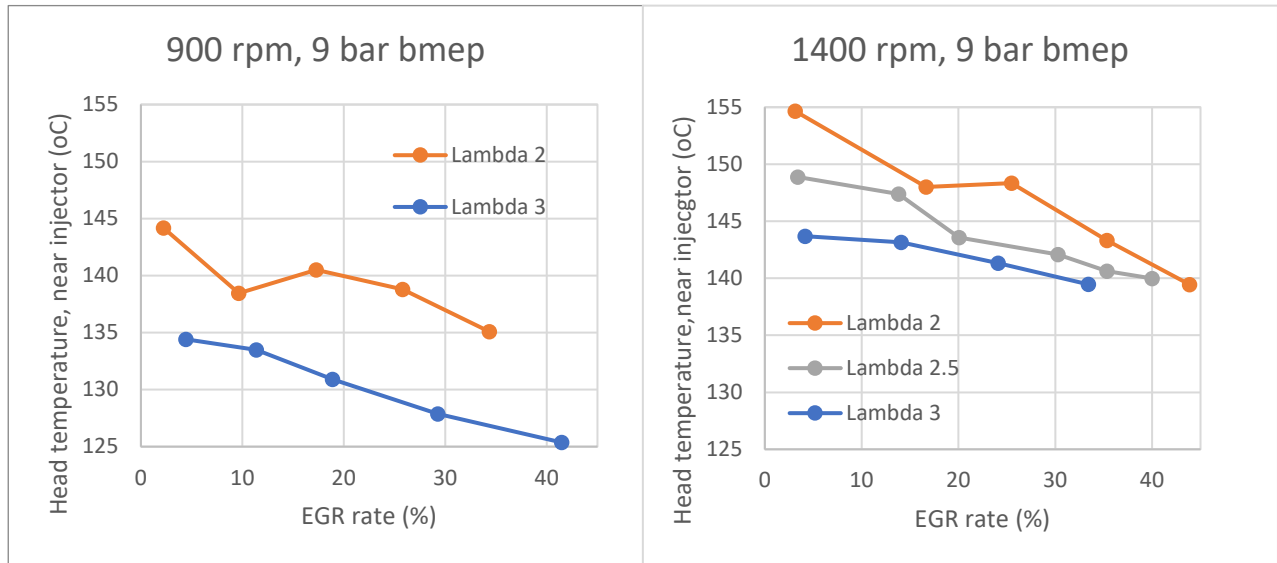
Fig. 11. Cylinder head temperature, near injector

3.5 Trade-off between NOx emissions, hydrogen slip and efficiency

   Figures 12, 13a and 13b show the trade-off between NOx emissions and hydrogen slip at 900 rpm and 1400 rpm. At 900 rpm Figure 12 shows that at Lambda 2, NOx emissions reduce with increasing EGR levels, while H2 emissions rise steadily to a relatively low level. At lambda 3, hydrogen slip climbs steadily until 30% EGR after which it increases at a faster rate. NOx levels reach their lowest level above around 15% EGR, which means that low levels of NOx can be achieved without rapid increases in hydrogen slip. At 1400 rpm, Figure 13a shows that behaviour at lambda 3 is similar to 900 rpm. At lambda 2, and 2.5 combustion stability was lower at EGR rates above 30% due to misfire, causing higher NOx emissions and hydrogen slip. For lambda 2, minimum NOx emissions were measured at 35% EGR where the rate of increase of hydrogen slip is increasing. At Lambda 2.5, Figure 13b shows that minimum NOx emissions were measured at between 20% and 30% EGR, before hydrogen slip increases rapidly.
   Indicated efficiency has a relatively flat profile with varying EGR rate and air fuel ratio where combustion is stable and doesn't show any trade-offs with either hydrogen slip or NOx for the conditions tested.
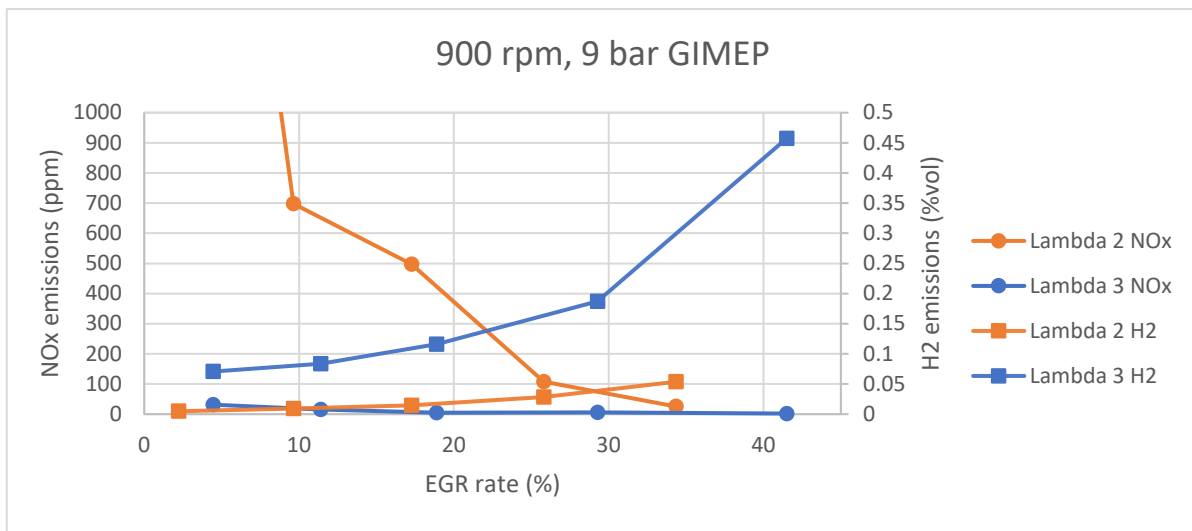

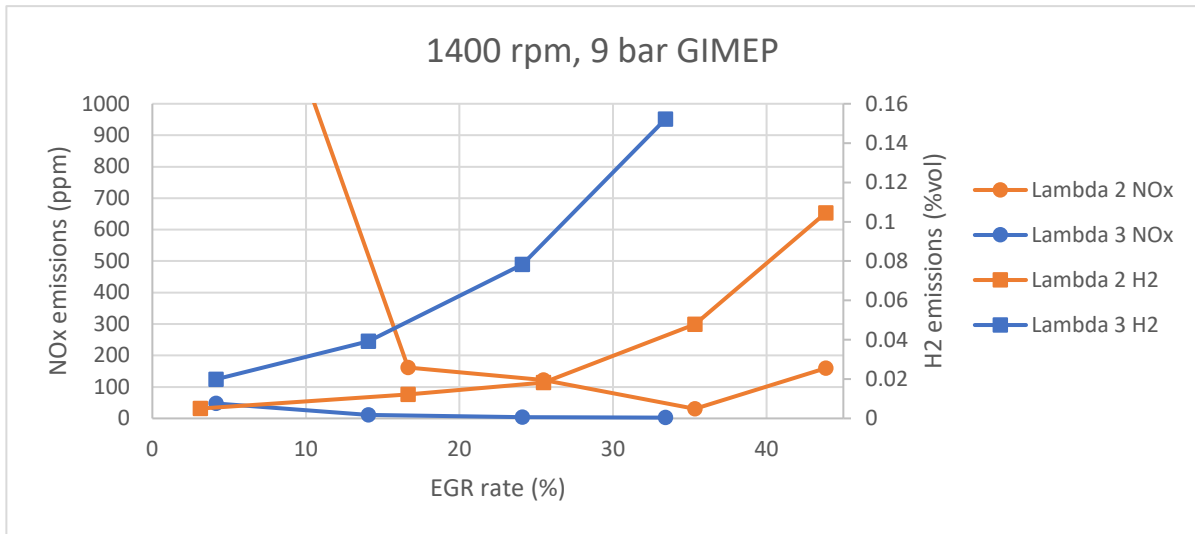**Fig. 12.** Trade-off between NOx emissions and hydrogen slip at 900 rpm

Fig. 13a. Trade-off between NOx emissions and hydrogen slip at 1400 rpm, lambda 2 and 3
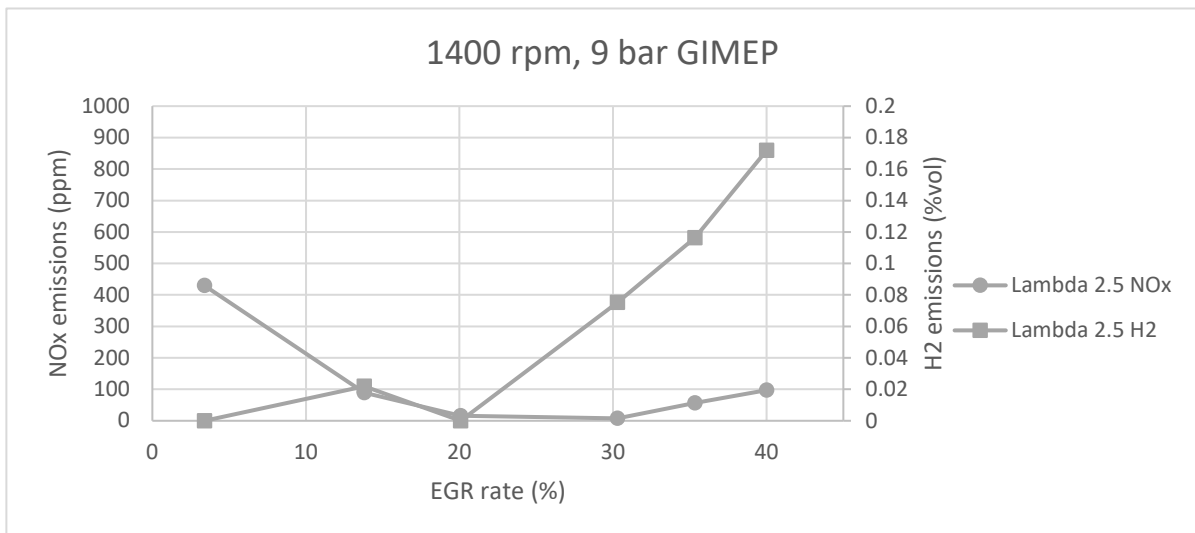

Fig. 13b. Trade-off between NOx emissions and hydrogen slip at 1400 rpm, lambda 2.5

4. Conclusions

This paper has presented results from a direct injection single cylinder hydrogen research engine, investigating the effect of lean combustion and EGR on NOx emissions, hydrogen slip and indicated efficiency. Results show that:

- For this engine configuration, at lambda 2 and lower AFRs, preignition/knocking has a significant impact on operation. At low levels of EGR, optimisation of spark timing is required to minimise this phenomenon. The propensity to knock reduces with increasing EGR and air fuel ratio

- Due to the fixed 50% Mass Fraction Burned target used in this work for ignition timing, indicated thermal efficiency is relatively constant across the EGR rates and air fuel ratios tested, except for where combustion stability is reduced. In these areas, efficiency is reduced

- Lean combustion and cooled EGR give potential for very low engine out NOx emissions, with levels <10 ppm measured

- The use of EGR and lean combustion increases levels of hydrogen slip. The level of hydrogen slip increases with EGR rate, where the rate of increase appears to grow steeply at higher EGR rates and the point where the slope of the graph changes depends on the air fuel ratio. This means that there is a region where there is a more favourable trade-off between reducing NOx emissions and increasing hydrogen slip, which varies with air fuel ratio. For example, at 1400 rpm, lambda 2.5 minimum NOx emissions are measured between 20% and 30% EGR before hydrogen slip increases rapidly

Acknowledgements

References

[1] IPCC, Special Report: Global warming of 1.5°C, Global Warming of 1.5 °C — (ipcc.ch), (accessed 26.4.22)

[2] Nicola Warwick, Paul Griffiths, James Keeble, Alexander Archibald, John Pyle, Keith Shine, Atmospheric implications of increased hydrogen use, April 2022, Atmospheric implications of increased hydrogen use (publishing.service.gov.uk) (accessed 22.4.22)

[3] Ho Lung Yip, Aleš Srna, Anthony Chun Yin Yuen, Sanghoon Kook, Robert A. Taylor, Guan Heng Yeoh, Paul R. Medwell and Qing Nian Chan, A Review of Hydrogen Direct Injection for Internal Combustion Engines: Towards Carbon-Free Combustion, Appl. Sci. 2019, 9(22)

[4] Marcus Fischer, Stefan Sterlepper, Stefan Pischinger, Jörg Seibel, Ulrich Kramer, Thomas Lorenz, Operation principles for hydrogen spark ignited direct injection engines for passenger car applications, International Journal of Hydrogen Energy, Volume 47, Issue 8, 2022

[5] Vipin Dhyani, K.A. Subramanian, Control of backfire and NOx emission reduction in a hydrogen fueled multi-cylinder spark ignition engine using cooled EGR and water injection strategies, International Journal of Hydrogen Energy, Volume 44, Issue 12, 2019

[6] Yong Li, Wenzhi Gao, Pan Zhang, Zhen Fu, Xingda Cao, Influence of the equivalence ratio on the knock and performance of a hydrogen direct injection internal combustion engine under different compression ratios, International Journal of Hydrogen Energy, Volume 46, Issue 21, 2021

[7] Kaname Naganuma, Toru Honda, Kimitaka Yamane, Yasuo Takagi, Atsuhiro Kawamura, Tadanori Yanai and Yoshio Sato, Efficiency and Emissions-Optimized Operating Strategy of a High-pressure Direct Injection Hydrogen Engine for Heavy-duty Trucks, SAE 2009-01-2683

14   P. Atkins, N. Fox, A. Saroop, J. Hughes, N. Coles, T. Downes, A. Thurston

[8] Yasuo Takagi, Hiroki Mori, Yuji Mihara, Nobuyuki Kawahara, Eiji Tomita, Improvement of thermal efficiency and reduction of NOx emissions by burning a controlled jet plume in high-pressure direct-injection hydrogen engines, International Journal of Hydrogen Energy, Volume 42, Issue 41, 2017

[9] Masakuni Oikawa, Yoshihisa Kojiya, Ryota Sato, Keisuke Goma, Yasuo Takagi, Yuji Mihara, Effect of supercharging on improving thermal efficiency and modifying combustion characteristics in lean-burn direct-injection near-zero-emission hydrogen engines, International Journal of Hydrogen Energy, Volume 47, Issue 2, 2022

[10] G.M. Kosmadakis, C.D. Rakopoulos, J. Demuynck, M. De Paepe, S. Verhelst, CFD modeling and experimental study of combustion and nitric oxide emissions in hydrogen-fueled spark-ignition engine operating in a very wide range of EGR rates, International Journal of Hydrogen Energy, Volume 37, Issue 14, 2012

[11] Jeongwoo Lee, Cheolwoong Park, Jongwon Bae, Yongrae Kim, Young Choi, Byeungjun Lim, Effect of different excess air ratio values and spark advance timing on combustion and emission characteristics of hydrogen-fueled spark ignition engine, International Journal of Hydrogen Energy, Volume 44, Issue 45, 2019

[12] SS. Verhelst, J. Vancoillie, K. Naganuma, M. De Paepe, J. Dierickx, Y. Huyghebaert, T. Wallner, Setting a best practice for determining the EGR rate in hydrogen internal combustion engines, International Journal of Hydrogen Energy, Volume 38, Issue 5, 2013

Emission Behavior and Aftertreatment of Stationary and Transient Operated Hydrogen Engines

S. Roiser, P. Christoforetti, E. Schutting, H. Eichlseder

Institute of Thermodynamics and Sustainable Propulsion Systems, Technical University of Graz, Austria

E-mail: roiser@ivt.tugraz.at

Telephone: +(43) 316 873 30036

Abstract

As society moves toward climate neutrality, hydrogen fueled internal combustion engines (H_2 ICEs) should be considered as a prime technology. These engines are valued for their robustness, superior lifetimes, manufacturing techniques and characteristics, which are already known from diesel or gasoline engines. Since an H_2 ICE is run on hydrogen (H_2), carbon-based emissions are only released on a very low level from the lube oil. Nitrogen oxides (NO_x) emissions are de facto the only gaseous pollutant that must be processed by the exhaust aftertreatment system (EAS) of such engines.

This paper provides an overview of the raw exhaust gas emission behavior of a two-liter four-cylinder passenger car engine that is run solely on hydrogen. As already mentioned, the main challenge faced by the EAS is to reduce NO_x. Thus, the inspected EAS includes a selective catalytic reduction (SCR) catalyst with ammonia (NH_3) as a reductant. The species of NO_x was reduced under stationary operation conditions at all of the considered engine load points at an efficiency of at least 98%.

Strategies that could be applied to conduct a load change of an H_2 ICE were experimentally investigated. To perform a load change under high performance conditions, H_2 ICEs needed to be run on a richer air-fuel mixture than under stationary operation conditions in order to provide enough exhaust enthalpy for the turbocharger. If a richer air-fuel mixture was used, higher NO_x emissions were detected, indicating that an EAS is essential for H_2 ICEs.

A WLTC and two RDE cycles were investigated to determine their raw and tailpipe exhaust gas emissions. By applying a simple AdBlue dosing strategy, the raw NO_x exhaust gas emissions from the WLTC could be reduced from 79.9 mg/km to as low as 7.3 mg/km. Carbon-based and secondary emissions such as NH_3 and N_2O were measured at levels well below 5 mg/km.

1. Introduction

In order to achieve future climate targets, alternative fuels must increasingly be used in internal combustion engines. Among others, hydrogen might be able to be used as one of these fuels to achieve the targets. When burning hydrogen in an engine, there may rise emissions. These pollutants must be reduced by suitable methods to guarantee not only low-CO_2 levels but also low-emission engine operation.

Hydrogen internal combustion engines (H_2 ICEs) have shown promising results in terms of both their thermal efficiency and emission behavior in heavy-duty and light-duty vehicle applications [1] [2] [3]. For mobility purposes, battery electric propulsion can also be seen as a sustainable solution. Currently, the major drawbacks of battery electric propulsion as compared to H_2 ICEs are the low energy densities and long charging times [4]. Hydrogen refueling time, on the other hand, can be compared to that of the known diesel or gasoline vehicles.

Hydrogen can be converted either in an ICE or in fuel cells. Both options have some advantages but also present major challenges. The ICE is well known for its sturdy robustness and long lifetime. In addition, H_2 ICE manufacturing can be easily ramped up, since this is not significantly different to the production of diesel or gasoline engines. When comparing efficiencies of H_2 ICEs and fuel cells, the latter displays an advantage regarding the idle and partial load, but the ICE performs with equal efficiency in high-load applications. Fuel cells are free of pollutant emissions, but their thermal management presents challenges. Fuel cells can remove only small quantities of heat by the exhaust enthalpy, resulting in a large amount of heat, that has to be dissipated via the radiators [4].

Since an open-minded attitude should be taken toward propulsion technology, H_2 ICEs should also be taken into account as a prime technology that can help society move toward climate neutrality, targeted by the EU until 2050 [5]. To support the development of H_2 ICEs, some key issues such as minimizing exhaust gas emissions have to be covered. This challenge will be addressed in this paper.

2. Objective

This paper provides the reader with an overview of the emission behavior of a lean-burn H_2 ICE with and without various catalysts for passenger car applications. Existing catalysts that are already used in diesel and gasoline vehicles were characterized under stationary and transient operation conditions. The catalysts were applied in a net-oxidizing environment, and no rich combustion was considered.

All experiments were conducted on a test bed with a four-cylinder engine, which was adapted to run on hydrogen fuel. The stationary conversion efficiencies of various catalysts were tested at engine speeds of 1000 to 4000 rpm and a brake mean effective pressure (BMEP) ranging from zero to 20 bars. In order to reduce nitrogen oxides (NO_x), an ammonia (NH_3) selective catalytic reduction (SCR) catalyst was evaluated. To minimize unburned hydrogen (H_2), carbon monoxide (CO) and hydrocarbons (HC), an oxidation catalyst (OC) was tested.

Analysis why exhaust aftertreatment of H_2 ICEs is needed and how NO_x is formed in stationary and transient operation was conducted. In addition, measures to perform fast load changes and reduce NO_x emissions during transient operations were investigated.

One main goal of the study was to evaluate the raw exhaust gas emission behavior of a transient operated H_2 ICE during different driving cycles and to reduce the recorded pollutants to a near-zero level. The goal was to achieve low tailpipe emissions with a low investment in effort.

The application of a particulates filter (PF) was not considered in this work. The authors are aware that a PF may be necessary when lube oil is burned, even if this quantity occurs at a close-to-zero level.

3. Research

The research was conducted experimentally on an engine test bed. Therefore, a gasoline engine was adapted to run on hydrogen fuel. An exhaust aftertreatment system (EAS) with a flexible catalyst arrangement was used to quickly enable different catalyst configurations. Details are described in the following section.
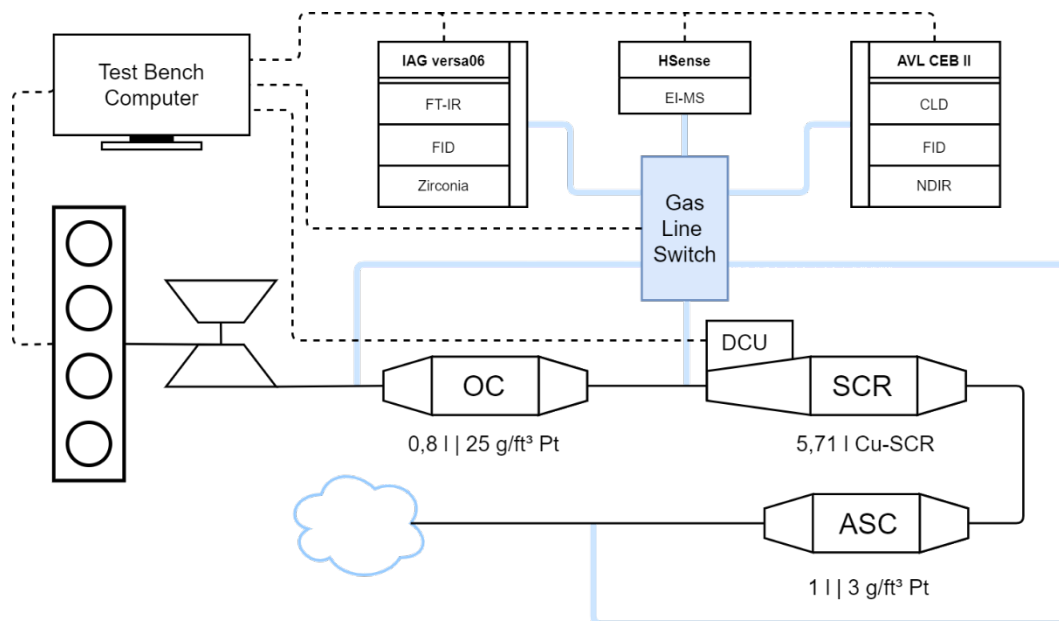
3.1.   Experimental setup

To carry out the research, an in-line, straight, four-cylinder, spark-ignited gasoline engine with two liters of displacement was adapted to run on hydrogen fuel. Gaseous hydrogen was injected directly into the engine, whereby it is possible to change the fuel pressure from 5 to 12 MPa, depending on the engine load. The engine was operated under lean conditions with turbocharging, making it possible to run most load points at an air-fuel equivalence ratio (lambda) greater than 2.0. Further details about the engine are provided in [1].

The exhaust aftertreatment system was constructed in a modular manner. This made it possible to change each substrate easily to another one or to switch components out. The examined configuration, as shown in **Fig. 1**, includes:

- Oxidation catalyst (OC) with a volume of 0.8 liters and 25 g/ft³ platinum loading
- Selective catalytic reduction catalyst with a volume of 5.71 liters on a Cu-SSZ-13 basis
- Ammonia slip catalyst (ASC) with a volume of 1 liter and 3 g/ft³ platinum loading

All catalysts, which were initially designed for diesel or gasoline applications, were provided by Umicore AG & Co KG. The catalyst volumes were sized on the basis of experience gained during previous diesel EAS development studies.

Fig. 1 Experimental setup

Upstream and downstream of each catalyst, the temperature and pressure are measured. Exhaust gas was analyzed by various systems, including an FT-IR spectrometer, a hydrogen mass spectrometer and a combustion emission bench. Each device could be used to analyze the exhaust gas via a gas line switched to different positions. Automotive lambda sensors and NO_x sensors were used to support the exhaust gas analysis.

Data from the exhaust gas analyzers, engine parameters as well as information gathered by the sensors were collected centrally on the test bench computer. The data was processed using software on this computer and then sent back to the engine or stored for post-processing.

3.2.   Differences in raw emission behavior between diesel and hydrogen-fueled internal combustion engines

In this section, a comparison of the emission behavior of diesel and hydrogen internal combustion engines is made. The comparison to diesel engines is made because its exhaust aftertreatment occurs in a net oxidizing environment, as it is designated in the EAS of H_2 ICEs. First, the biggest difference is the fuel itself. Hydrogen contains no carbon. Thus, CO and HC emissions are negligible in H_2 ICEs. Diesel engines, on the other hand, emit both CO and HC in significant concentrations, as can be seen in **Fig. 2**. These emissions from diesel engines can arise either from the fuel itself or from the lube oil [6] . In H_2 ICEs, CO and HC originate only from lube oil [7] [4] [8].

CO_2 emissions are not shown in this figure. In the exhaust gas of diesel engines, the CO_2 concentration is approximately 80000 ppm, depending on the engine and load point [9]. In H_2 ICEs, measurements have shown that only a few ppm CO_2 are released from the engine by burning lubricant, whereby most of the CO_2 emitted originates from the ambient air.

When comparing the NO_x emissions, two main differences are observed. In H_2 ICEs, the NO_x emission magnitude is higher and, at a higher lambda value, the NO_x emission drop down to zero, while diesel engines always release a certain level of NO_x emissions. The hot burning flame of hydrogen can mainly explain the high magnitude in NO_x emissions observed [10]. Overall, NO_x emissions are the main exhaust pollutant from H_2 ICEs.
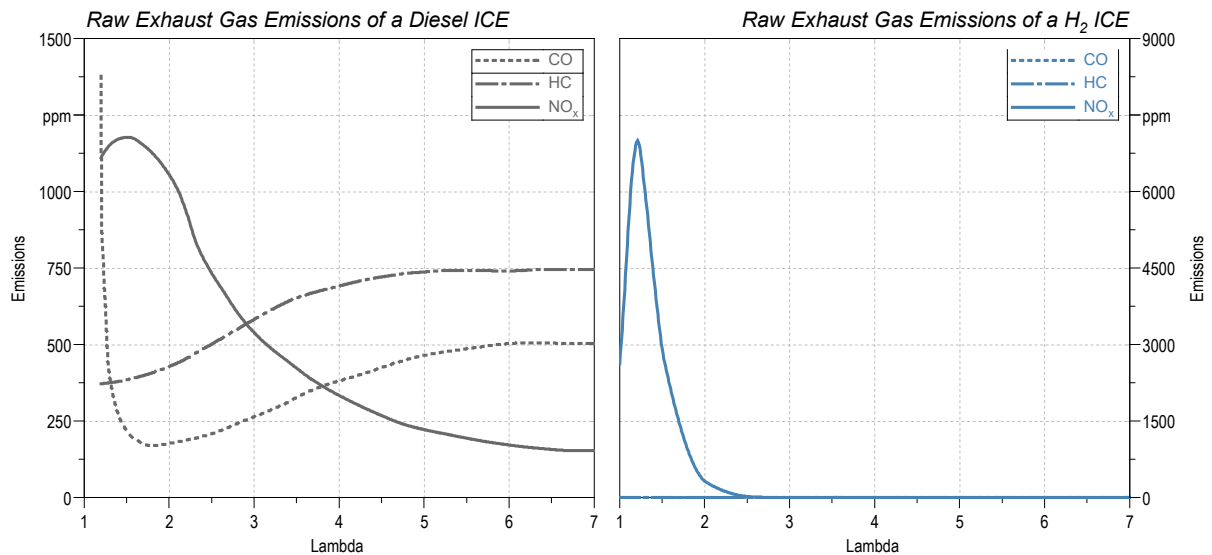

Fig. 2 Raw exhaust gas emission behavior of diesel and hydrogen internal combustion engines [6]

3.3.   Catalysts to reduce raw emissions in H_2 ICEs under steady-state operation

To gain more insight into the emission behavior of H_2 ICEs and to evaluate the efficiencies of different catalysts, numerous measurements were conducted at the Institute of Thermodynamics and Sustainable Propulsion Systems (ITNA). Using the two-liter engine, described in section 3.1, emissions were measured up- and downstream of different catalysts.

As described in section 3.2, the main exhaust gas emissions from H_2 ICEs are NO_x. **Fig. 3** shows that NO_x emissions upstream of the SCR catalyst can rise to a maximum of about 10 g/kWh in the stationary application mode with this specific engine. The maximum appears to be the upper limit of the BMEP, due to the boost limit of the turbocharger. Below 12 bar BMEP, minor raw exhaust gas emissions are observed. The effect of turbocharger boosting on NO_x emission behavior is discussed in detail in section 3.4.

Downstream of the SCR catalyst, NO_x emissions drop to a maximum of 0.14 g/kWh in the stationary application mode, resulting in a catalyst efficiency of at least 98%. The SCR catalyst in this study uses ammonia as a reductant. The downstream emissions were measured at 10 ppm NH_3 slip to maximize the NO_x conversion rates and to limit the NH_3 emissions, since these will be restricted by the planned exhaust gas emission standard [11].
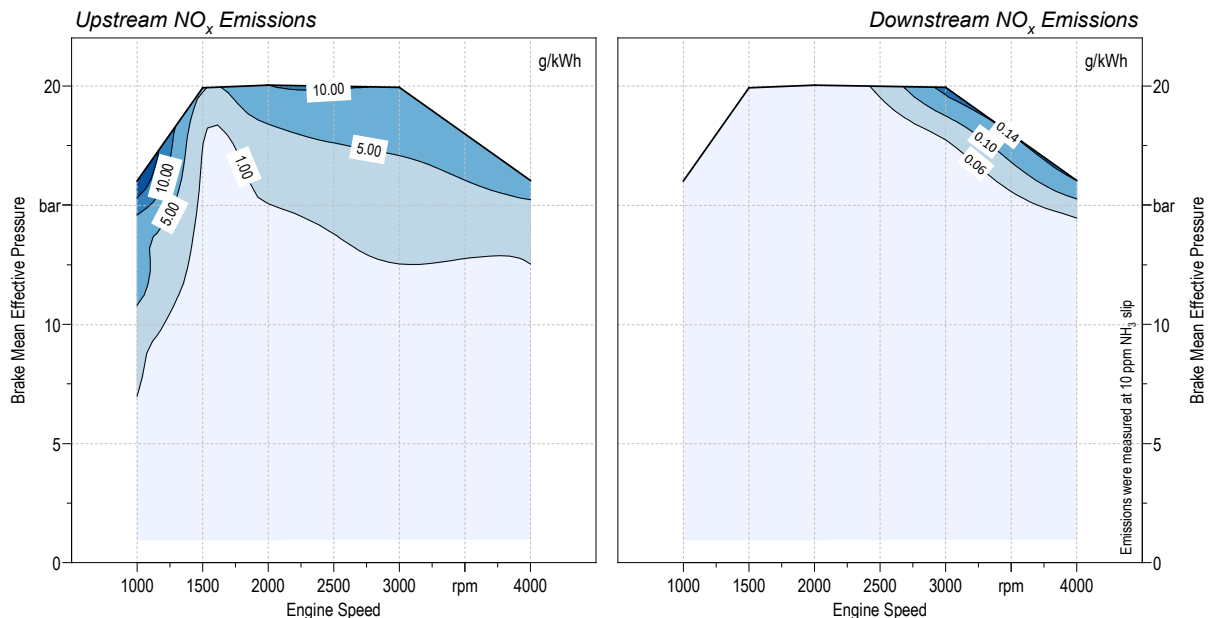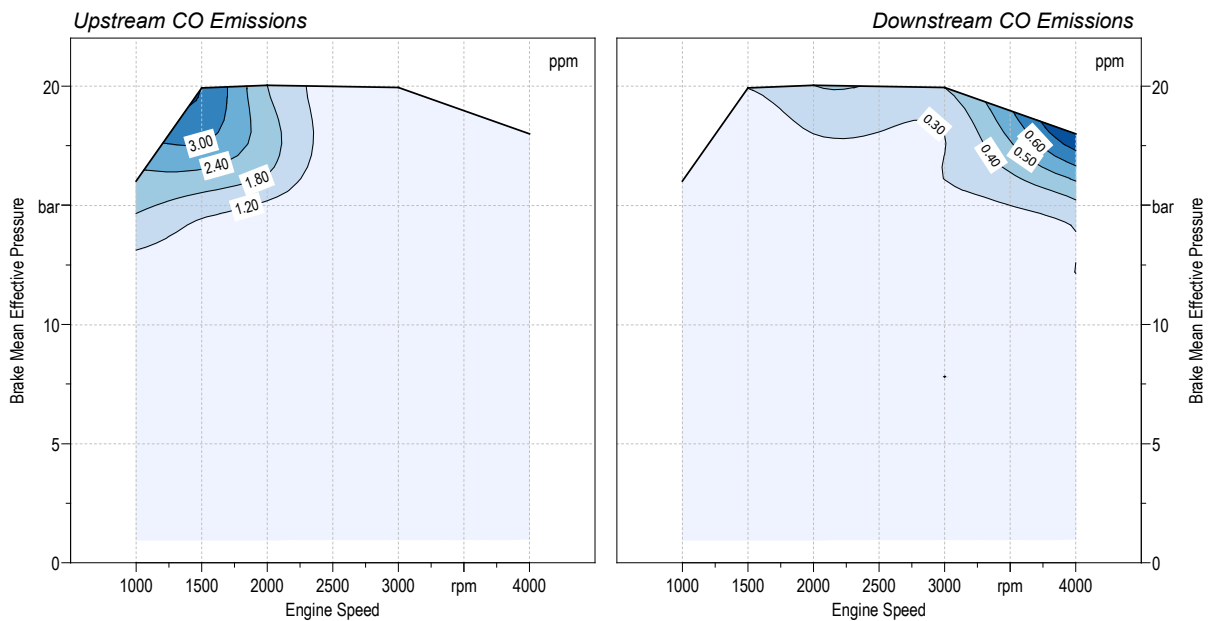

Fig. 3 NO_x exhaust gas emissions up- and downstream of a SCR catalyst

Unburned hydrogen was detected in the exhaust gases of H_2 ICEs due to the incomplete combustion of the air-fuel mixture. The hydrogen is oxidized by an OC, as described in section 3.1. **Fig. 4** shows the up- and downstream hydrogen emissions detected and reveals that the unburned hydrogen is oxidized to a near-zero level in stationary application mode. Research conducted at the ITNA has shown that hydrogen is generally relatively easy to oxidize. More information about hydrogen oxidation with different OCs can be found in [12].
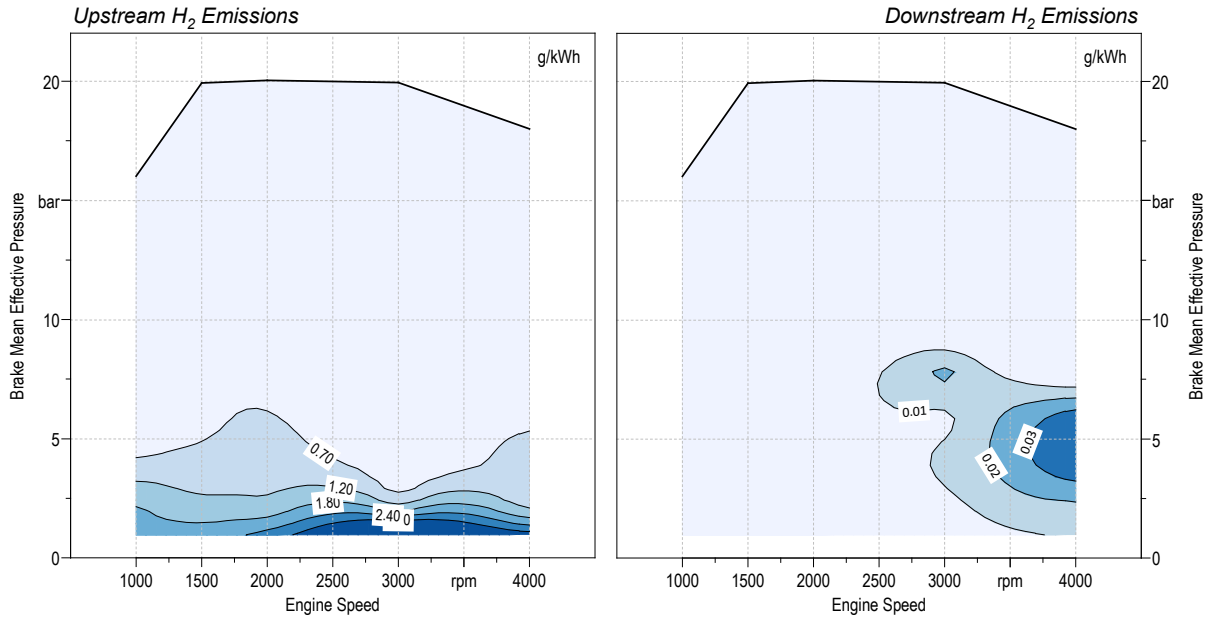
Fig. 4 H_2 exhaust gas emissions up- and downstream of an OC

Although no carbon is present in the fuel used in H_2 ICEs, carbon-based emissions can be detected in the exhaust gas. In **Fig. 5**, CO emissions are shown up- and downstream the OC. CO levels within a single-digit ppm range were measured upstream the catalyst; thus, these levels are near the lower detection limit of the gas analyzer. Although the detection limit of the analyzer was reached, the single-digit ppm emission could be measured at an even lower level after the OC, indicating that oxidation of CO took place in the catalyst.

Fig. 5 CO exhaust gas emissions up- and downstream of an OC

The HC emission behavior is similar to that of CO. Although the emissions are higher, HC species are oxidized in the OC to a single-digit ppm range troughout the whole engine map. In **Fig. 6**, the maximum HC emission levels measured on basis of carbon (ppmC) are at 1500 rpm at full load. As previously mentioned, these carbon-based pollutants are caused by lube oil and only occur on a low level.
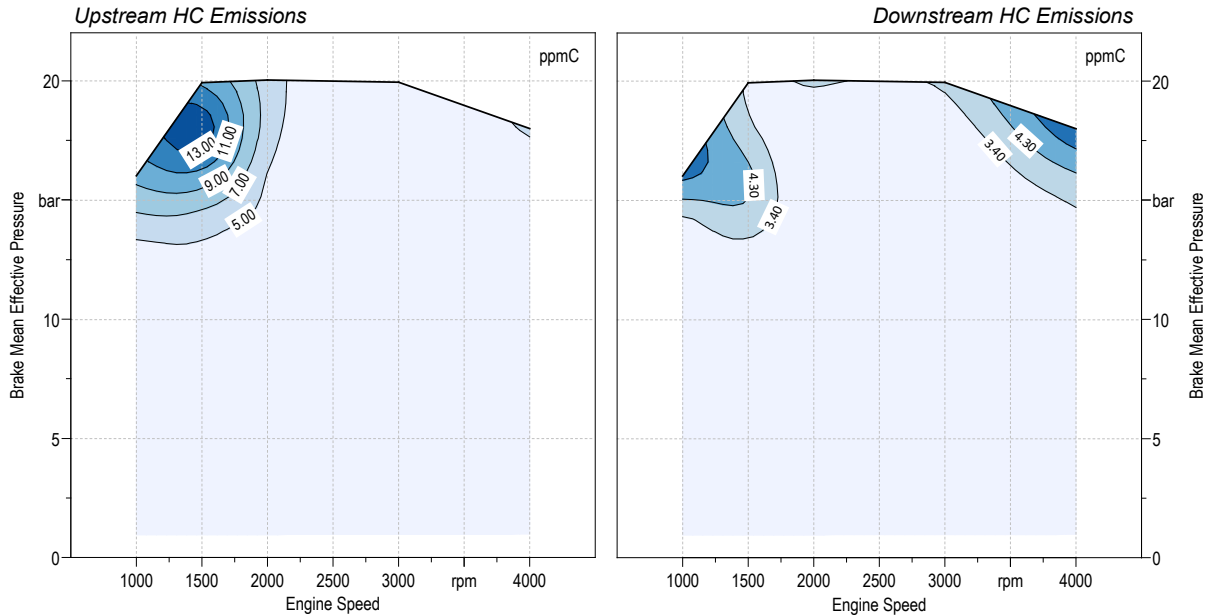
Fig. 6 HC exhaust gas emissions up- and downstream of an OC

To provide a complete overview of emissions from H_2 ICEs, CO_2 should also be mentioned. As discribed in section 3.2, most of the CO_2 measured in the exhaust gas, can be traced back to the intake air. Measurements at the ITNA have shown that the CO_2 amount of ambient air at the test bench facilities varies from 420 to 440 ppm. **Fig. 7** shows that only a small amount of CO_2 is added in the combustion process. CO_2 is also formed in the OC, indicating that oxidation of CO and HC occur in the catalyst.
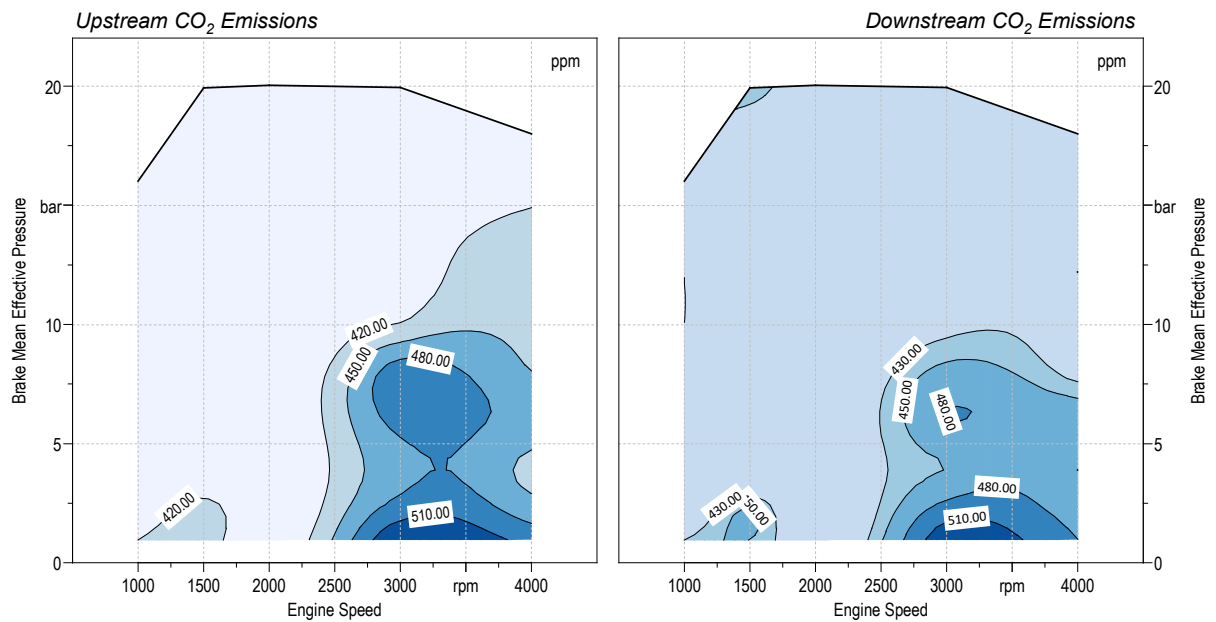
Fig. 7 CO_2 exhaust gas emissions up- and downstream of an OC

3.4.   Why exhaust aftertreatment is needed in H$_2$ ICEs

Generally, only NOx serves as a raw exhaust pollutant, as discussed in section 3.2. Thus, it cannot be neglected. In **Fig. 3**, the raw NO$_x$ exhaust gases are shown and, depending on the engine speed, raw emissions are nearly zero, i.e. below 12 bar BMEP. The reason for these low NO$_x$ emissions can be found by examining the correlation between NO$_x$ and lambda, shown in **Fig. 2**. If the engine operates in an area, where the turbocharger can supply enough air, lambda will be high, and NO$_x$ emissions will be low. If the engine operates at higher loads, the air supplied by the turbocharger will be limited, because its operation limit is reached. Less air results in a lower lambda and, thus, sharply rising NO$_x$ emissions.

In **Fig. 8**, the boost pressure and NO$_x$ exhaust gas emissions at an engine speed of 2000 rpm are shown. Up until roughly 14 bar BMEP, the NO$_x$ emissions are low due to the fact that the boost pressure gradually increases with the rising load. Above 14 bar BMEP, the boost pressure limit is reached and, as previously described, the NO$_x$ emissions increase sharply due to decreasing lambda.

The results, shown in **Fig. 8**, were obtained with a standard diesel turbocharger, which was not adapted for the specific H$_2$ ICE application. The boosting behavior can be improved by using a turbocharger that is specifically adapted to fit the particular application. In addition, an electric compressor for low loads and a larger turbocharger for high loads can be an option to improve NO$_x$ emission behavior.
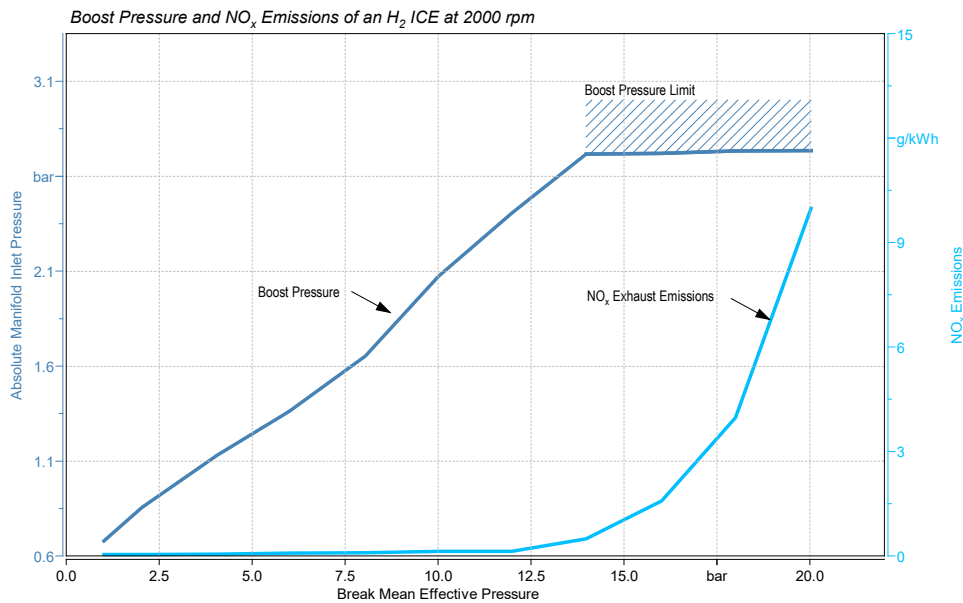
Fig. 8 Boost pressure and NO$_x$ emissions at an engine speed of 2000 rpm

NO$_x$ is not only formed at high BMEPs, but also when rapid load changes occur [3]. Thus, when operating an H$_2$ ICE, a special focus must be placed on load change strategies. In general, to achieve low NO$_x$ emissions, the load points of H$_2$ ICEs are operated in a highly lean manner. Operating under lean conditions means that the exhaust gas lacks the enthalpy to provide a quick turbocharger response when changing loads.

To overcome this lack of exhaust enthalpy, it is possible to briefly shift to richer engine operation while executing the load change and switch back to highly lean operation again when the desired load point has been reached. In **Fig. 9**, the exhaust gas lambda of a load change from 1500/2 (engine speed/ BMEP) to 2000/14 is featured. This figure shows that the load point 1500/2 is operated at a lambda of about 2.9, and the desired load point is operated at a lambda of 2.4. Three different load change strategies are illustrated in **Fig. 9**. The load change strategy with a minimum lambda of 1.5 is the quickest, but also results in the most NO_x emissions. On the other hand, the load change with a minimum lambda of 2.2 clearly takes the longest. **Fig. 9** also shows the NO_x emissions produced during the load change. This clearly shows that load changes with a low lambda have highest emissions, whereas high-lambda -strategies emit the lowest.
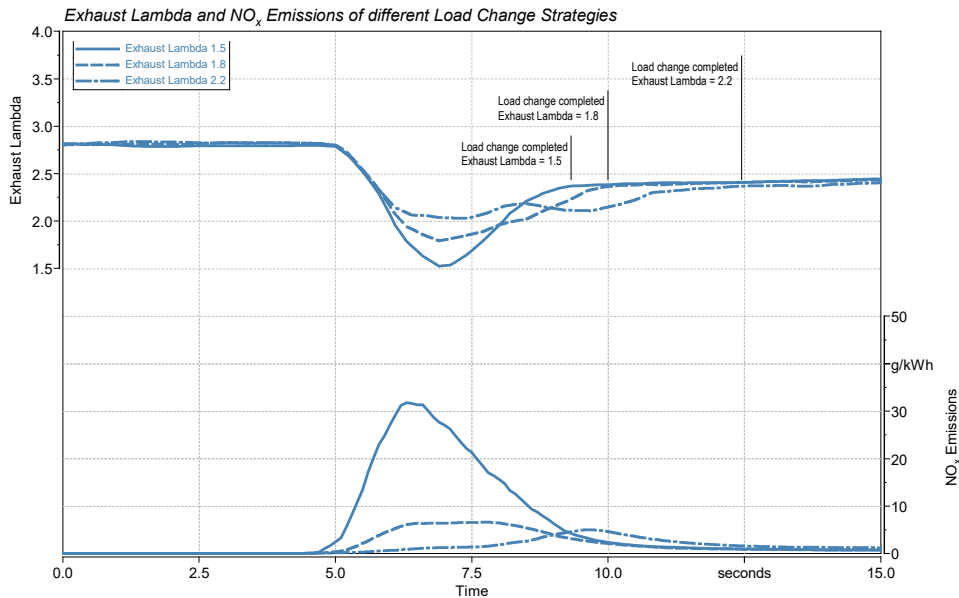

Fig. 9 Exhaust gas lambda and NO_x emissions for different load change strategies

To switch from one load point to another can be done under different conditions. **Fig. 10** shows the correlation between the response time and the NO_x emissions. If the load change is executed under highly lean conditions, the response time is high, but NO_x emissions are low. If the load change is executed under lambda values which go down to 1.5, the response time is low, but the NO_x emissions are quite high. A similar "response time – NO_x emission – trade off" was also reported in [3].
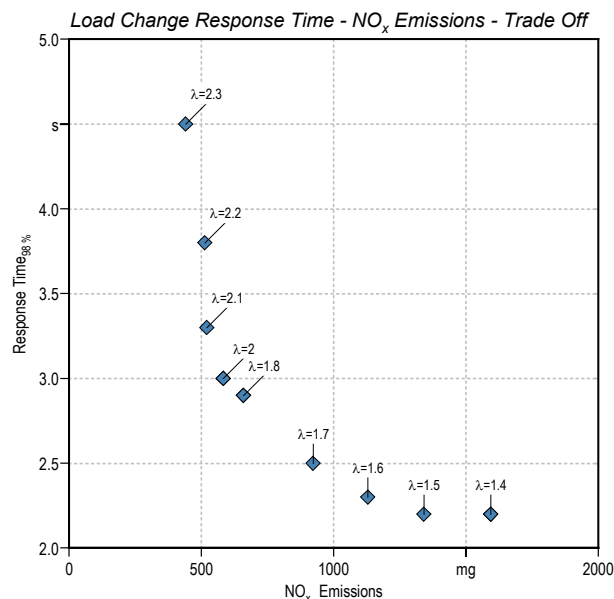
Fig. 10 Response time and NO_x emissions when a load change from 1500/2 to 2000/14 occurs

To perform the load change at low lambda in order to obtain a fast response time, on the one hand, and to limit the NO_x emissions upon execution, on the other hand, it was found that the ignition timing had a major effect. **Fig. 11** shows the impact of the late ignition timing on the load change behavior. Ignition timing is set late by up to 14 degree crank angle, whereas the lag is only applied during the load change. Late ignition timing significantly reduces the NO_x emissions, produced during the load changes, regardless of the lambda value. The late ignition timing has a greater influence on the low-lambda than on the high-lambda load changes regarding the NO_x emissions. When high-lambda load changes occur, not only are the NO_x emissions reduced but also a decrease in response time is achieved. When low-lambda load changes occur, the reduction in response time is minor, since the load change was conducted with a ramp-up time of two seconds.
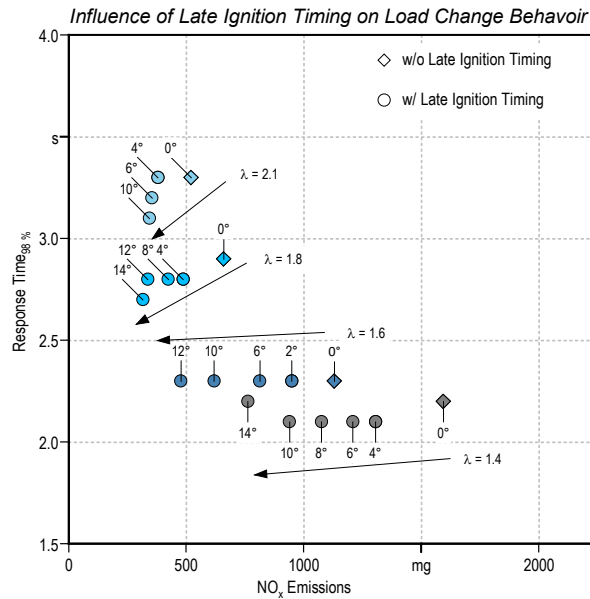
Fig. 11 Influence of late ignition timing on load change behavior from 1500/2 to 2000/14

3.5.   Raw exhaust gas emissions of different driving cycles

In order to evaluate the emission behavior under transient operation conditions, three different driving cycles were assessed. A special focus is directed toward the "Worldwide Harmonized Light Vehicles Test Cycle" (WLTC). To consider real driving emission (RDE) legislation, a low load cycle ("Transport for London" (TfL)) and an aggressive RDE cycle were also measured, whereby only the key parameters are shown here.

The velocity profile, average positive torque and maximum torque of each cycle are shown in **Fig. 12**. Based on the velocity profile, the torque and engine speed were calculated using PHEM, which is a simulation tool for longitudinal vehicle dynamics available from TU Graz. The simulation was carried out for a C-segment vehicle with a mass of 1675 kg, seven gear automatic transmission and start-stop functionality.

With a total duration of 2312 seconds, the TfL cycle represents the longest one in the portfolio. This cycle's average positive torque equals 14.7 Nm, whereas it reaches a maximum of 177 Nm. At the other extreme, the shortest cycle is the aggressive RDE with a duration of 882 seconds. This cycle has an average positive torque demand of 58.7 Nm and reaches up to 317 Nm. In between is the WLTC with a duration of 1800 seconds, an average positive torque of 41.5 Nm and a maximum of 297 Nm.
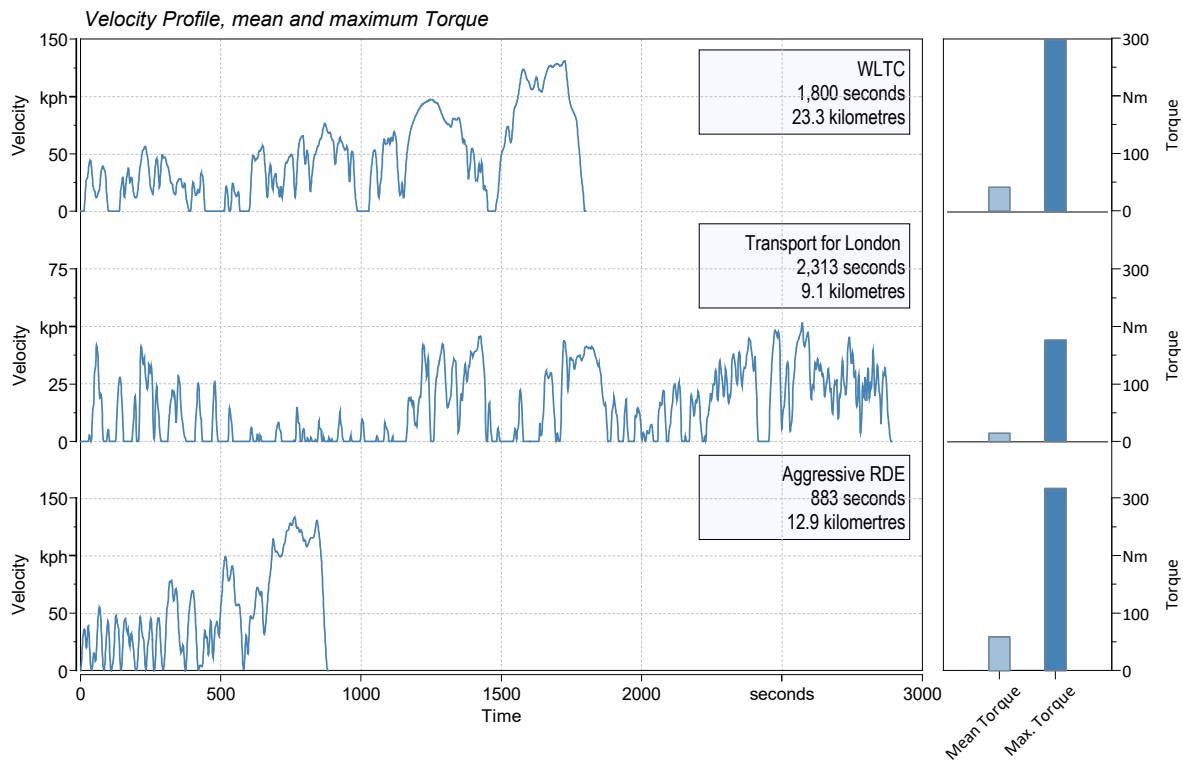
Fig. 12 Velocity profile, mean and maximum torque of the different driving cycles

To obtain comparable results, the engine and exhaust aftertreatment system were conditioned before each cycle in the same manner. Both systems were cooled to a starting temperature of 25 °C. The engine coolant was conditioned with a heat exchanger to reach the defined temperature. The coolant chills the engine and the lubricant oil. To rapidly cool the system, fans blow air onto the oil pan and engine block to force convection. The exhaust aftertreatment system is cooled with a special method called RCD+ (Rapid Cool-Down Plus) with which dry air flows through the exhaust to avoid any water deposition on the SCR catalyst. Detailed descriptions of the RCD+ method can be found in [13] and [14]. The cycles were performed at 23 °C ambient temperature and without external heating or cooling of the coolant. By conditioning the system in the described manner, it was possible to start each cycle with the same initial parameters as a "cold" cycle. To more clearly depict the devices used to cool the engine, the exhaust aftertreatment catalysts, fans and the inlets for the dry air for RCD+ are shown in **Fig. 13**.
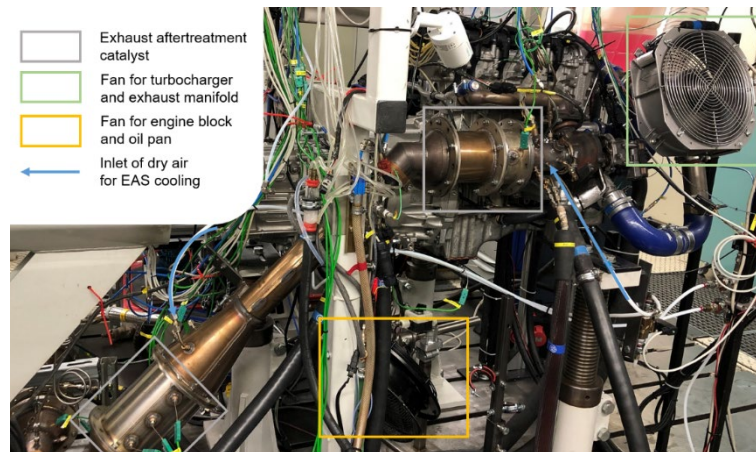
Fig. 13 Exhaust aftertreatment catalysts, fans and inlet of the dry air for RCD$^+$

In order to avoid going beyond the scope of this paper, a special focus is placed on the WLTC, and only key figures are shown for the TfL and aggressive RDE cycle. Beginning with raw exhaust gas emissions, the previously discussed species are shown in **Fig. 14**. As expected, the NO_x raw exhaust gas emissions at a level of 41.95 mg/km are lowest for the low load TfL cycle and the highest for the aggressive RDE cycle (204.08 mg/km). In the WLTC, with a mean torque between that of the TfL and aggressive RDE, the NO_x raw emissions rise to 79.92 mg/km.

To have a better understanding of the NO_x raw emission levels, a comparison to diesel engines is drawn. Measurements taken at the ITNA, but also those reported in [15], show that diesel engines emit around two times the amount of NO_x raw emissions as H_2 ICEs in test cycles. In [15], the measurements were conducted with a C-segment car with a four-cylinder 1.5-liter engine.

CO and HC are also shown in **Fig. 14**. Since hydrogen is a non-carbon-based fuel, CO, HC and only occur as a result of burning lubricant oil and only in very small amounts. The CO_2 emission values shown in **Fig. 14** exclude the ambient air concentration, which is assumed to be at about 420 ppm. Due to the burning of lubricant, CO_2 emissions are released, but on a low level, compared to diesel engines, where this species is about a thousand times higher in the raw exhaust gas. Other exhaust gas emissions such as NH_3 or nitrous oxide (N_2O) are not considered in raw exhaust gases, because measurements have shown that these emissions can not be detected in lean-operated H_2 ICEs. These secondary emissions are addressed in section 3.6.
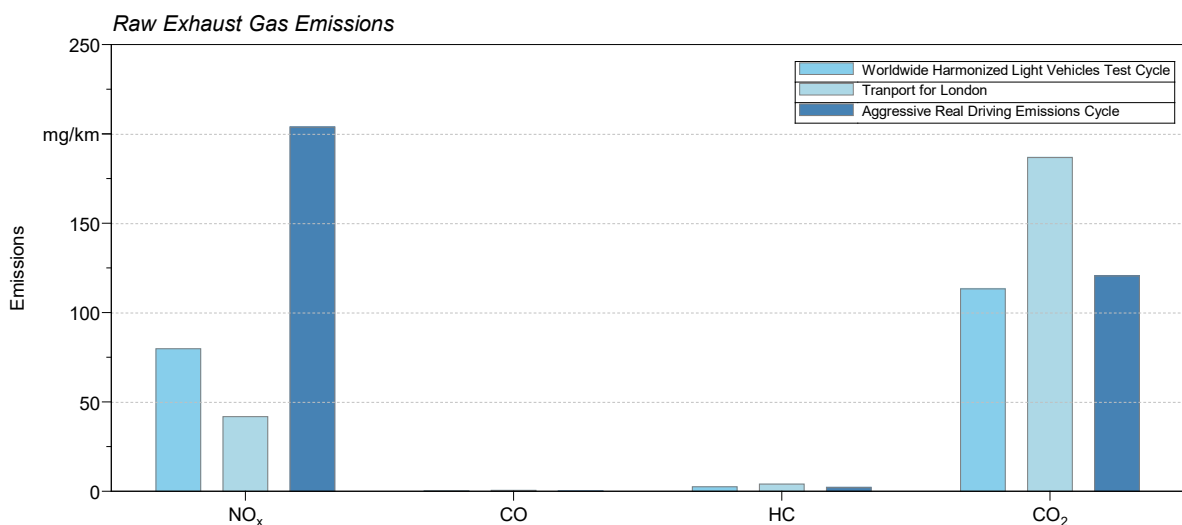
Fig. 14 Raw exhaust gas emissions for the different driving cycles

Fig. 15 provides a deeper insight into NO_x raw exhaust gas emission behavior. The picture displays the positive torque over the cycle time in the upper graph. In the lower graph, NO_x raw exhaust gas emissions in the accumulated mode are shown. NO_x emissions clearly only arise during the load change to a high torque. When the load stays below a certain torque, the NO_x raw emissions are nearly zero. This also undermines the assumption posed in section 3.4, namely, that NO_x emissions are only formed in H_2 ICEs when load changes occur or the engine is operated at high loads, where the boost pressure is insufficient.
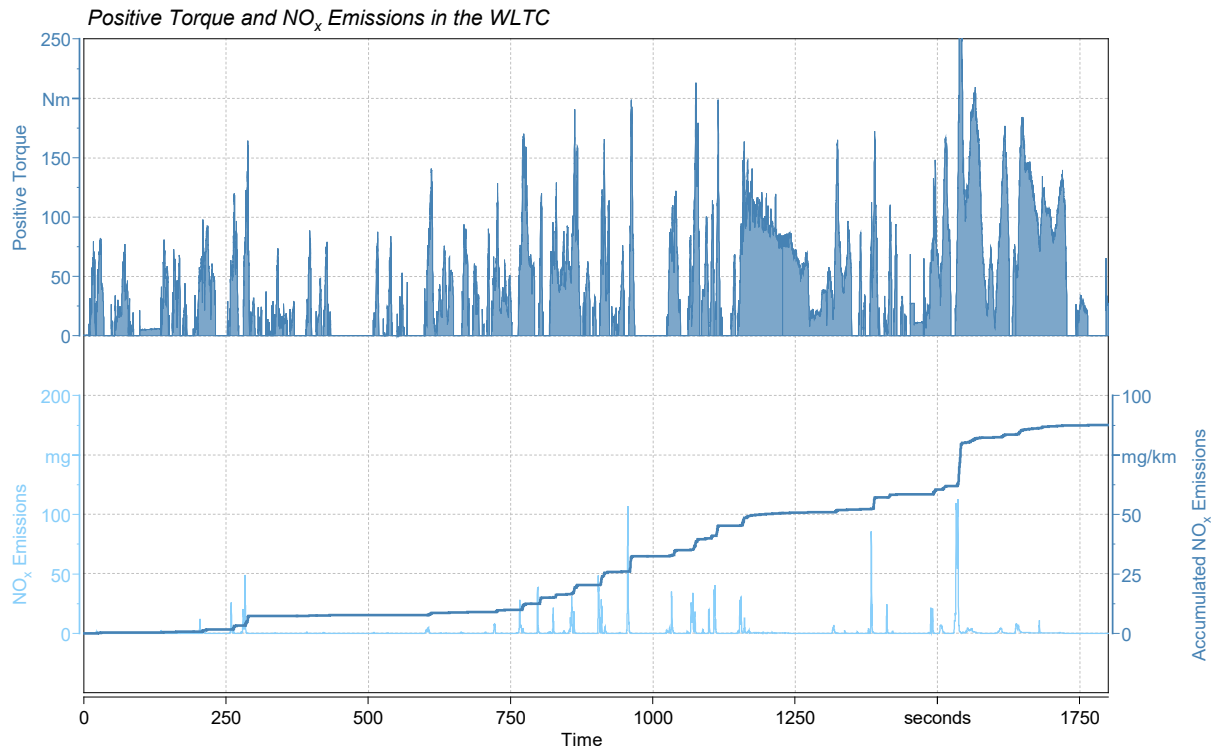
Fig. 15 Positive torque, NO_x raw emissions and accumulated NO_x emissions

3.6.   Tailpipe exhaust gas emissions of hydrogen internal combustion engines

In this section, the tailpipe emissions from the already known driving cycles are described. The starting condition of the engine and the EAS are similar to those described in section 3.5, but with one major difference. To get approach real-world values for NO_x, N_2O and NH_3 emissions, the SCR catalyst was pre-conditioned regarding the NH_3 loading. The SCR catalyst was emptied at 300 °C so that no NH_3 loading remained and then loaded until one-third of its NH_3 storage capacity was reached. From that point on, the engine was turned off and conditioned with the RCD[+] method in order to start the cycle in a "cold" state. The AdBlue® dosing strategy applied is simple. First, dosing is only enabled when the temperature upstream the SCR catalyst reaches a value greater than 180 °C. Second, AdBlue® is only dosed when NO_x emissions are detected with an ammonia-to-NO_x ratio of 1.2.

Nevertheless, the initial results achieved by applying this simple dosing strategy are quite remarkable. **Fig. 16** shows that it was possible to cut the NO_x emissions of the WLTC to 7.3 mg/km. With an exhaust aftertreatment configuration consisting of an OC and NH_3-SCR, a deNO_x system efficiency of 90.1% could be achieved. Other researchers have described the promising deNOx system efficiencies of hydrogen internal combustion engines. [16] reported a deNO_x system efficiency of about 60%, which was achieved with a cold World Harmonized Transient Cycle (WHTC) and an EAS consisting of an diesel oxidation catalyst (DOC) and NH_3 - SCR catalyst. [2] even reported of a 98% deNO_x system efficiency in a hot WHTC cycle with an SCR-only EAS. In addition, the CO, non-methane hydrocarbons (NMOG) and secondary emissions such as NH_3 and N_2O could be held well below 5 mg/km.

Using the Transport for London cycle, the NO_x emissions remained quite high, although AdBlue® dosing was activated. The main reason for this is the low load, which led to a temperature that did not exceed 180 °C upstream the SCR catalyst throughout most of the cycle and, thus, did not activate the AdBlue® dosing.

The aggressive RDE cycle resulted in the highest NO_x tailpipe emissions, although its deNO_x system efficiency amounts to 77.2% as compared to the TfL cycle with roughly 56.4%. Both deNO_x system efficiencies were achieved with an EAS consisting of an OC and NH_3-SCR. The RDE cycle quickly enables dosing due to the high power demand, which results in a rapid EAS heat-up. Nevertheless, the SCR system cannot reduce all of the NO_x emissions. When using both the TfL and aggressive RDE cycles, the CO, NMOG, NH_3 and N_2O levels remain well below 5 mg/km.
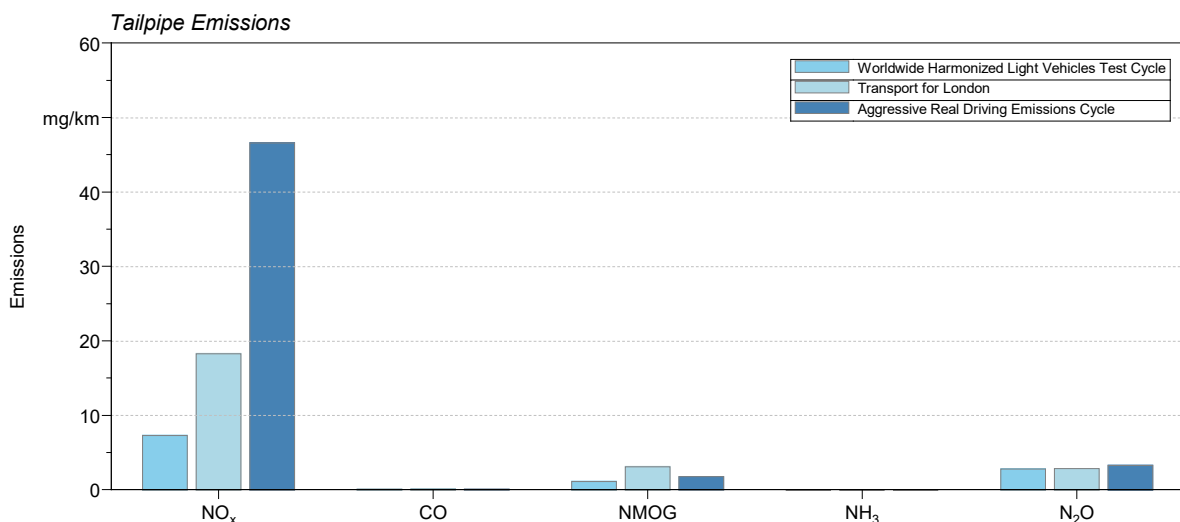
Fig. 16 Tailpipe emissions for different driving cycles

To gain a better understanding of the tailpipe emission behavior, the WLTC was investigated in detail. **Fig. 17** shows the raw and tailpipe NO_x emissions. As previously mentioned, it was possible to achieve a significant reduction in the NO_x emissions. At the beginning of the cycle, both of the accumulated NO_x emission curves are equal. At about 800 seconds, the SCR light-off point is reached and NO_x conversion starts. The raw and tailpipe emission curves clearly differ from that point and on. Although the tailpipe emission curve flattens out, NO_x breakthroughs are detectable when certain load changes occur.

Fig. 16 shows that no NH_3 can be detected throughout the cycle. That means that the SCR catalyst is not filled with NH_3 at any point. One major improvement that could be made in $deNO_x$ system efficiency could be to apply a more aggressive dosing strategy, i.e. to raise the initial NH_3 storage level. A sophisticated NH_3 loading model is expected to also raise the $deNO_x$ system efficiency. Dosing starts quite late, which can be explained by the fact that no heating measures were applied. Changing the ignition timing or the heating modes, such as using electric heaters in the EAS, have been effective tools in diesel exhaust aftertreatment [17]. Those tools are also expected to also work with H_2 ICEs.
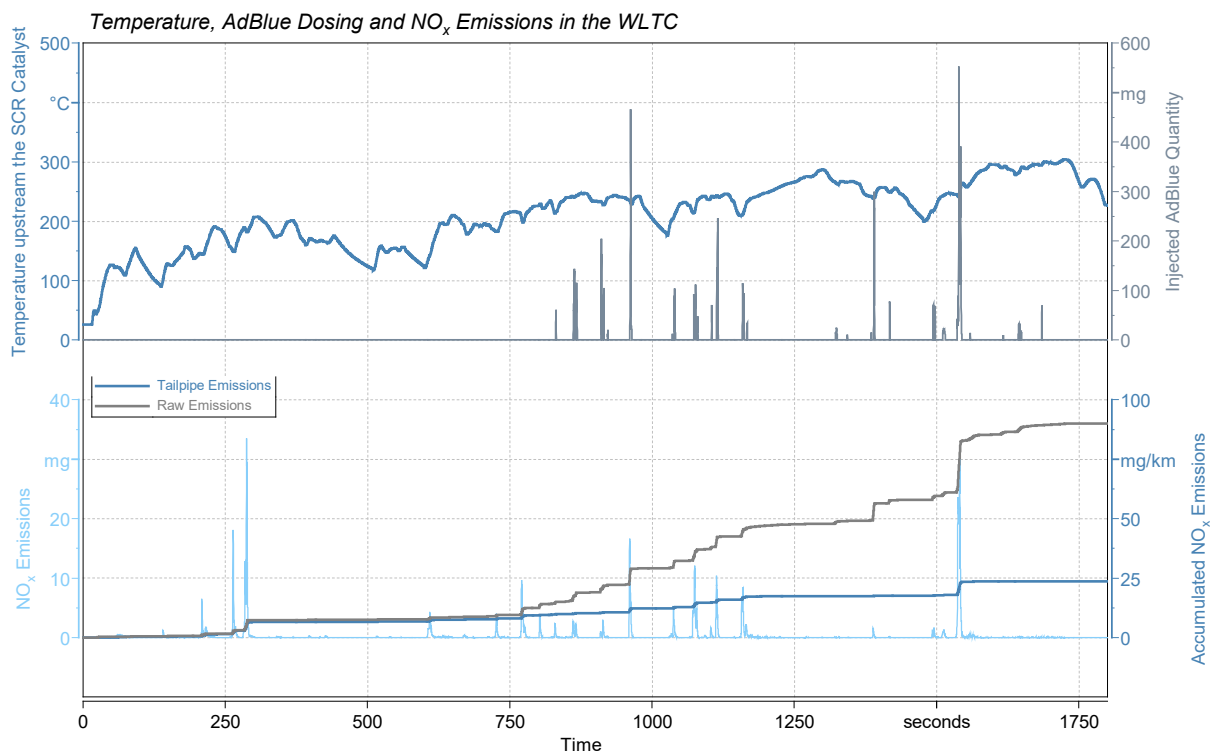
Fig. 17 Temperature upstream the SCR catalyst, AdBlue® dosing, raw and tailpipe NO_x emissions in the WLTC

Conclusions and Outlook

To summarize the knowledge gained through these experiments, it is important to review the engine operation modes available to H_2 ICEs. Under stationary operation conditions, the inspected H_2 ICE emits NO_x gases on a low level, but these can rapidly rise if the lambda becomes low. This case may occur when engines operate at full load where the boost pressure limit is reached. Under transient engine operation conditions, the turbocharger needs a high exhaust enthalpy to perform load changes with a sufficient response time and NO_x emissions can be quite high. Thus, exhaust aftertreatment will be required to comply with the upcoming exhaust gas emission legislations.

The results show that the raw emissions from the observed H_2 ICE with an EAS consisting of OC and NH_3-SCR can be reduced to a near-zero level in the stationary application mode. Very low levels of CO and HC emissions were detected in the raw exhaust gas. Unburnt hydrogen can be easily oxidized by an OC with only minor platinum loading and well-known NH_3-SCR catalysts can successfully reduce NO_x emissions.

However, the raw exhaust gas emission levels from the examined H_2 ICEs in driving cycles are lower than those form comparable diesel engines. In addition, only NO_x emissions needed to be reduced, meaning that the CO, HC and CO_2 emissions can be neglected. These low raw exhaust gas emissions can be further reduced by using an NH_3-SCR to improve the deNOx system efficiencies from 50 up to over 90%, depending on the driving cycle. No measures considering thermal management or sophisticated dosing strategies were applied.

The steps that can be taken to lower tailpipe emissions will be carried out by applying several strategies that enable a rapid heat-up during cold start. Shifting the light-off of the SCR catalyst to an early point in the driving cycles has been shown to be crucial to minimize NO_x emissions in earlier diesel projects. As already mentioned, applying an AdBlue® dosing strategy, which has its own NH_3 storage model, enables the SCR catalyst to be operated at maximum performance. An EAS without an OC could result in a fast SCR catalyst light-off, since it can be positioned directly after the turbocharger. Further experiments will show if hydrogen will have a negative effect on the SCR under transient operation conditions.

Acknowledgements

References

[1] D. Seboldt, M. Mansbart, P. Grabner, H. Eichlseder: 'Wasserstoffmotoren für zukünftige Pkw und leichte Nutzfahrzeuge', in : 'MTZ 02/2021', pp. 46–51

[2] A. Sommermann, F. Ginrichsen, T. Mlischewski, D. Hyna, C. Karl, J. Schmitt, M. McMackin, H. Beck: 'MAN H45 hydrogen engine: a robust and highly efficient technology for CO2-neutral mobility', in : 'Symposium „Sustainable Mobility, Transport and Power Generation"', pp. 162–177

[3] B. Nork, A. Qriqra, R. Kleuser: 'Deutz Hydrogen-ICE - a simulation of the entire system', in : 'Symposium „Sustainable Mobility, Transport and Power Generation"', pp. 150–161

[4] M. Klell, H. Eichlseder, A. Trattner: 'Wasserstoff in der Fahrzeugtechnik' (Springer Fachmedien Wiesbaden, Wiesbaden, 2018)

[5] European Comission: 'Communication from the Commission to the European Parliament, the European Council, the Council, the European Economic and Scial Committee, the Committee of the Regions and the European Investment Bank' (Brussels, 2018)

[6] R. Pischinger, M. Klell, T. Sams: 'Thermodynamik der Verbrennungskraftmaschine' (Springer Vienna, Vienna, 2009)

[7] S. Sterlepper, M. Fischer, J. Claßen, V. Huth, S. Pischinger: 'Concepts for Hydrogen Internal Combustion Engines and Their Implications on the Exhaust Gas Aftertreatment System', *Energies*, 2021, **14**, (23)

[8] S. Zbigniew: 'A Comprehensive Overview of Hydrogen-Fueled Internal Combustion Engines: Achievements and Future Challenges', *Energies*, 2021, **14**, (20), p. 6504

[9] G. P. Merker, R. Teichmann: 'Grundlagen Verbrennungsmotoren: Funktionsweise, Simulation, Messtechnik' (Springer Fachmedien Wiesbaden GmbH, Wiesbaden, 2014, 7th edn.)

[10] L. Alastair: 'Optimising air quality co-benefits in a hydrogen economy: a case for hydrogen-specific standards for NO x emissions', *Environ. Sci.: Atmos.*, 2021, **1**, (5), pp. 201–207

[11] Z. Samaras, S. Hausberger, D. Mellios: 'Preliminary findings on possible Euro 7 emission limits for LD and HD vehicles' (27. 10. 2020)

[12] E. Schutting, S. Roiser, H. Eichlseder, S. Lux, S. Kleiber: 'Hydrogen Engine Exhaust Aftertreatment' (Wien, 2022)

[13] G. Kühberger, H.W.: 'Patent A 50650'. A 50650

[14] E. Schutting: 'Method for Accelerated EAS Cold Start Cycle Measurements: FFG Success Story', 2021 (2021)

[15] J. Demuyncka, C. Favrea, D. Bosteelsa, A. Kuhrtb, J.Spittab, F. Bunarb: 'Ultra-low on-road NOx emissions of a 48 V mild-hybrid diesel with LNT and dual-SCR', 2019 (2019)

[16] V. Huth, L. Virnich, A. Pfortje, S. Prischinger, S. Sterlepper: 'The Hydrogen Combustion Engine as Zero Impact Emission Powertrain Concept', in : 'Aachen Colloquium Sustainable Mobility 2021', pp. 1113–1130

[17] C. W. Kim, M. Paratore, E. Gonze, S. Solbrig, S. Smith: 'Electrically Heated Catalysts for Cold-Start Emissions in Diesel Aftertreatment'. SAE 2012 World Congress & Exhibition, APR. 24, 2012

THIESEL 2022 Conference on Thermo- and Fluid Dynamics of Clean Propulsion Powerplants

Hydrogen Internal Combustion Engine: Viable Technology for Carbon Neutral Mobility

Y. H. Chi[1], B. S. Shin[1], S. Hoffmann[2], J. Ullrich[2], P. Adomeit[3], J. Fryjan[3], R. Drevet[4]

[1]Hyundai Motor Company. 150, Hyundai Yeonguso-ro, Namyang-eup, Hwaseong-si, Gyeonggi-do, 18280, Korea

E-mail: yohan@hyundai.com
Telephone: +82 10 3173 8197

[2]Hyundai Motor Europe Technical Center GmbH. Hyundai Platz, 65428 Ruesselsheim, Germany

E-mail: shoffmann@hyundai-europe.com
Telephone: +49 6142 7899 781

[3]FEV Europe GmbH. Neuenhofstrasse 181, D-15072, Aachen, Germany

E-mail: adomeit@fev.com
Telephone: +49 160 7463 602

[4]BorgWarner France SAS. 9 boulevard de l'Industrie 41042 Blois Cedex, France

E-mail: rdrevet@borgwarner.com
Telephone: +33 2 54 55 57 65

Abstract.

Increasing concern on global warming and climatic catastrophe as a result of rising atmospheric CO_2 is leading more stringent greenhouse gas regulations. In 2021 European Commission has proposed, as part of 'European Green Deal', highly ambitious target to reduce fleet averaged CO_2 emission from new passenger cars registered in 2025 and 2030 by 15 and 55 % (formerly 37.5 %) respectively from 2021. Technology portfolio should be considered for robust compliance of regulations in viable and timely manner. And it will include increased share of electrification toward Battery and Fuel Cell EV's along with certain penetration of low and neutral CO_2 energy carriers.

Hydrogen (H_2) is an attractive energy carrier for internal combustion engine to achieve CO_2 neutral mobility because it is carbon free and has advantageous properties of much wider flammability limit and higher burning velocity than conventional fossil fuels enabling high efficiency and low emission. Expanding hydrogen refueling infrastructure in important markets is providing favorable environment and synergic effect with fuel cell by sharing hydrogen dedicated parts is another advantage. Possibility to use already existing robust engine system as a basis for conversion to H_2 Internal Combustion Engine with moderate effort is another benefit.

Main objective of this research is to evaluate efficiency, emission and performance potentials of H_2 ICE based on existing 4 cylinder 1.6 liter T-GDI engine and modified to install H_2 dedicated parts, such as injectors, rail and boosting system. It is developed as dedicated engine for hybrid electric vehicle (HEV) to realize highest system efficiency with hardware matching and calibration focused on medium load between BMEP 9 to 13 bar and below 3000 rpm for enhanced efficiency and minimized NOx.

Extensive design front loading is made to optimized injector configuration, valve timing and hydrogen injection strategies to secure volumetric efficiency for homogeneous lean combustion and mixture uniformity crucial for efficiency and NOx emission. Significant potentials in efficiency, NOx emission at hybrid main area along with comparable specific torque and power with base T-GDI engine validated in this study clearly indicates that H_2 ICE can be an important bridging and complementary technology to BEV and FCEV during the transition phase to full electrification.

1. Introduction

Over the last few decades, climate change has become one of the clear and imminent threat to sustainability and stringent greenhouse gas regulations have been introduced focused on mobility sector. To comply with these regulations, global automotive OEMs' are focusing on expanding their battery electric vehicle (BEV) line-up and enhancing degree of electrification through shifting from simple start-stop and mild hybrid to full, plug-in hybrids and BEV. BEV can be an ultimate solution to realize CO_2 neutral mobility, still there are issues on the cleanness of electricity and availability of charging infrastructure. Hence, internal combustion engine (ICE) based technology using low or neutral CO_2 fuels should also be considered to comply with the regulations in viable way.

Hydrogen (H_2) has long been considered as attractive fuel for internal combustion engine due to its unique properties. Various H_2 combustion and engine concepts have been developed and some of them were introduced to small scale series production [1-3]. Still there was no H_2 ICE application in large volume due to limited H_2 infrastructure and not enough readiness of technologies. But H_2 infrastructure is expanding in important markets, such as Europe, Korea and Japan, driven by announcement and subsidy by government [4]. And key technologies have been developed to overcome the hurdles faced in early stage of H_2 ICE development, that include high pressure H_2 on-board storage with 700 bar system pressure, turbocharger, H_2 direct injection and aftertreatment systems to handle NOx emission.

Currently H_2 ICE is being developed by lots of OEMs' and suppliers as 'Zero CO_2' powertrain technology to comply with upcoming greenhouse gas regulations using currently available and well established internal combustion engine line-up and production facility [5-8]. And main objective of this research is to validate overall potential and technology readiness level (TRL) of H_2 ICE.

2. Target engine and development concept

2.1 Engine specification

Series production 1.6 litre spark ignited engine with direct injection system and wastegate turbocharger is modified to operate with hydrogen. Main technical features and specifications of this engine is summarized in Fig. 1. The engine is equipped with Continuously Variable Valve Duration (CVVD) for intake valve that is capable of varying valve duration combined with Continuously Variable Valve Timing (CVVT) for both intake and exhaust valves allowing high control flexibility in valve timing and duration for improved fuel economy, low end torque and catalyst heating performance.

Engine Type	-	In-Line 4 Cylinder
Displacement Volume	cc	1,598
Bore X Stroke	mm	75.6 X 89.0
Valve Train	-	Intake CVVD / In.–Ex. CVVT
Power	kW (PS)	132 (180)
Torque	Nm (kgm)	265 (27.0)
Compression Ratio	-	10.5
Boosting System	-	Wastegate Turbocharger
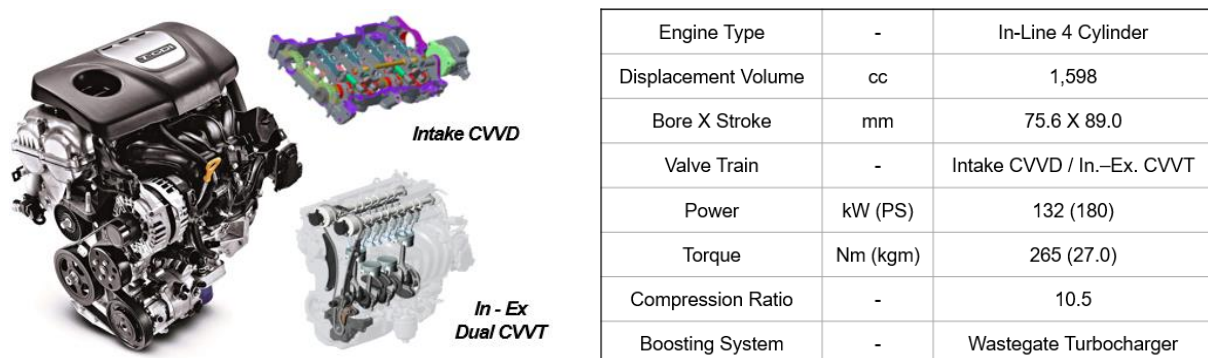
Fig. 1. Main features and specification of 1.6 litre turbo GDI engine

2.2 Hybrid dedicated powertrain

1.6 litre H_2 ICE will be developed as hybrid dedicated powertrain for medium class SUVs' where CO_2 reduction is highly challenging and highest system efficiency with extremely low emission can be achieved by implementing H_2 ICE as powertrain for hybrid system. From engine speed and torque traces measured from various test cycles shown in Fig. 2, main test points are selected to be focused on. 12 representative points ranging 1200 to 2600 rpm and 80 to 160 Nm are selected where control parameters are optimized to validate thermal efficiency and emission potential.
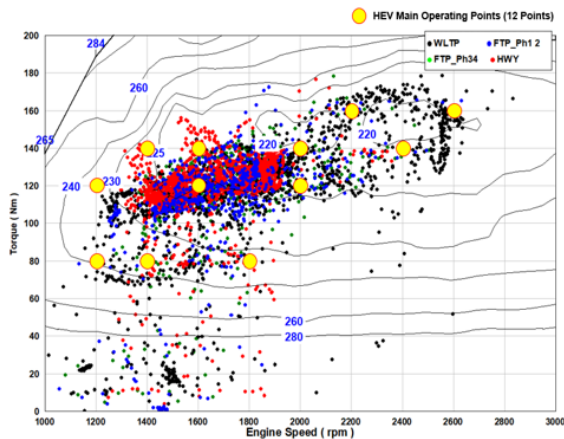
Fig. 2. Selection of 12 main test points, engine speed and torque traces of medium SUV

3. Conversion to Hydrogen Internal Combustion Engine

3.1 Hydrogen injection system

CHG 6.2 hydrogen injector provided by BorgWarner is introduced to prototype engine. This injector is driven by solenoid actuator with 35 bar maximum operating pressure. It has outwardly opening nozzle to achieve high flow rate required for low density hydrogen injection. Another advantage of outwardly opening nozzle is that self-sealing by cylinder pressure is possible. Injector tip diameter is 7.5 mm that is same as gasoline injector, which enables easy conversion from gasoline to hydrogen engine.

Oil lubrication is required for this injector. Lubricant is precisely measured and fed to hydrogen supply line as shown in Fig. 3.
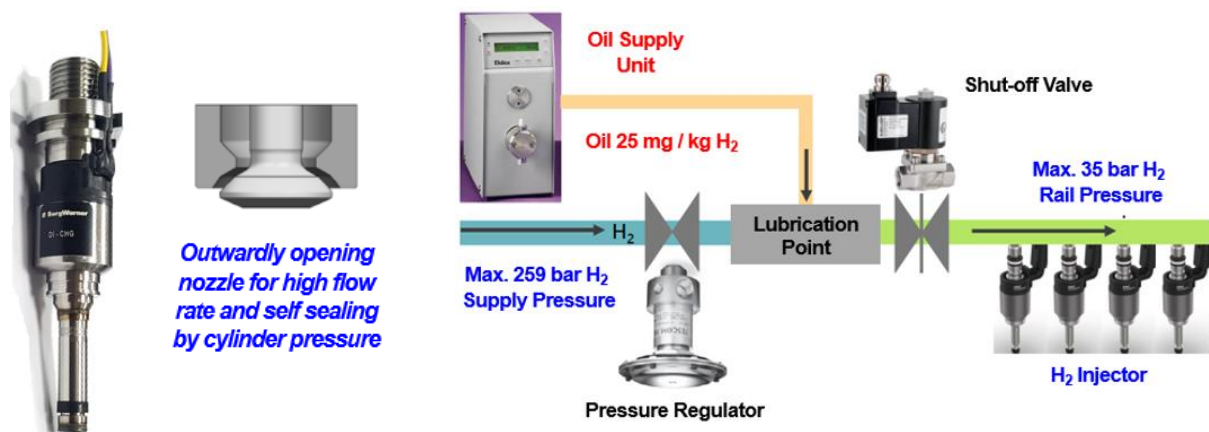
Fig. 3. BorgWarner CHG 6.2 hydrogen injector, layout for Hydrogen supply and injector lubrication

3.2 Boosting system

Main objective of hydrogen engine control is to realize highly lean combustion throughout entire operating range for enhanced thermal efficiency with extremely low NOx emission and achieve high full load performance potential without abnormal combustion, such as pre-ignition and knocking.

It is well accepted that near zero NOx emission is possible with relative air-fuel ratio (λ) over 2.5 (Fig. 4) and target λ is defined according to engine operating range [9]. For engine speed and load frequently visited during normal vehicle operation, including 12 test points, target is to achieve $\lambda > 2.5$ focused on high efficiency and low Nox emission. For high load, including full load, target is to achieve λ higher than 1.7 to prevent abnormal combustion.
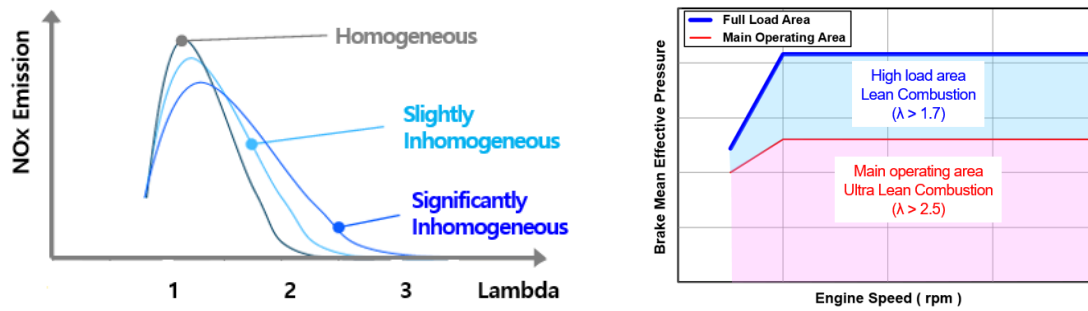
Fig. 4. NOx emission with λ and target according to operating range

Elaborated boosting system matching is crucial to address this high air mass flow requirement. Table 1 lists the turbochargers and their specification tested in current research. Boosting system matching starts with validation of wastegate turbocharger already introduced in series production and it is followed by testing with variable geometry turbochargers (VGT) tuned considering full load performance. Test results indicate that it's not possible to provide required air mass flow both for main operating and high load areas with single-stage boosting system. As will be explained in following chapter, two-stage boosting system combining 48 V driven electric supercharger and VGT is used for development.

Table 1. Specification of turbochargers

		Production WGT	VGT #1	VGT #2
Compressor	Wheel Dia.	43 mm	46 mm	52 mm
	Trim	80	56	62
Turbine	Wheel Dia.	37 mm	42.2 mm	43.9 mm
	Trim	86	79	83

4. Design front loading

Extensive design front loading is performed through visualization of hydrogen jet and CFD simulation to optimize the injector position and injection strategy for improved mixture uniformity.

4.1 Jet visualization by high speed Schlieren Photography

As shown in Fig. 4, not only relative air-fuel ratio but mixture uniformity has substantial impact on NOx emission as well. For improved mixture uniformity, higher hydrogen jet penetration is beneficial for better spatial distribution of hydrogen and providing momentum for air and fuel mixing. Hydrogen injector used in this research has outwardly opening nozzle and it is observed that injector recess has big impact on jet penetration and resulting mixture uniformity.

Penetration and shape of jet are optically investigated by high speed Schlieren photography using helium as surrogate for hydrogen. Visualization is done with varying injector recess for both plain chamber and combustion chamber resembling insert. Definition of injector recess and shape of insert are shown in Fig. 5.

Fig. 6 shows Schlieren images of hydrogen jet taken at 1.5 ms after start of injection in plain chamber with 0, 4 and 7 mm recess. 35 bar injection pressure and 2 bar ambient pressure is applied. Schlieren images indicate that jet penetration is highest with 4 mm recess. With 0 mm recess, jet collapses at the exit of nozzle and penetration reduces due to Coanda effect. With 7 mm recess, compared with 4 mm recess, penetration also reduces due to increased shear loss in injector hole. And higher recess also leads to increased volume of locally rich mixture inside injector hole.

Similar effect is observed with insert resembling combustion chamber shape (Fig. 7). With 0 mm recess, jet is deflected to combustion chamber roof side due to Coanda effect, leading to rich mixture near spark plug and reduced penetration. Meanwhile, much increased penetration and not deformed jet is formed with 3 and 4 mm recess. Based on these observation, 3 mm injector recess is selected and applied to prototype engine.
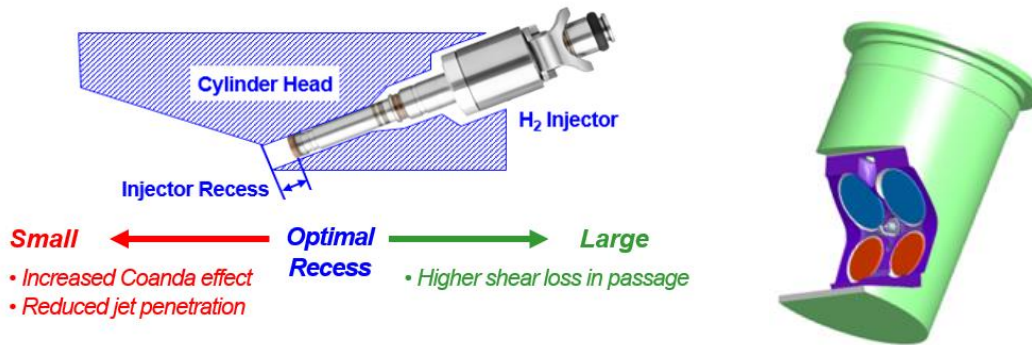
Fig. 5. Injector recess, insert resembling combustion chamber shape
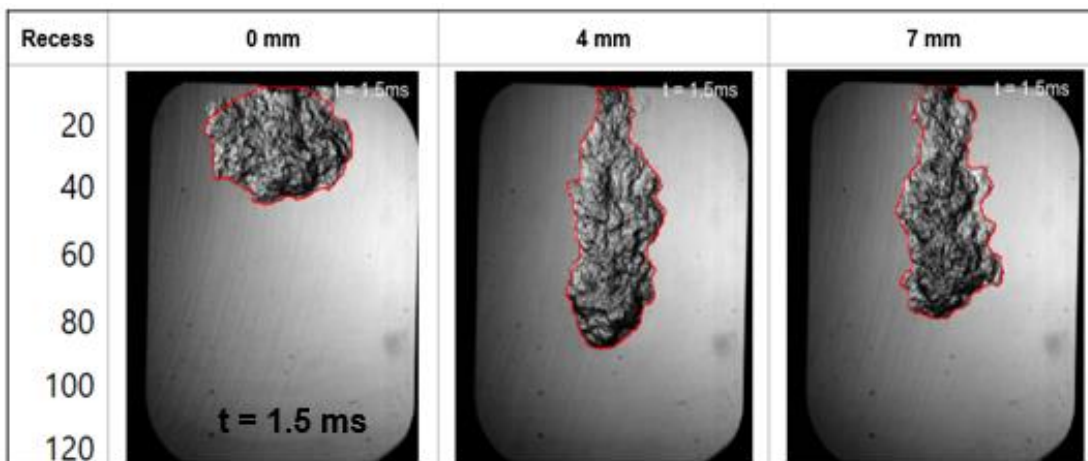
Fig. 6. Schlieren image of jet in plain chamber (35 bar injection pressure, 2 bar ambient pressure)
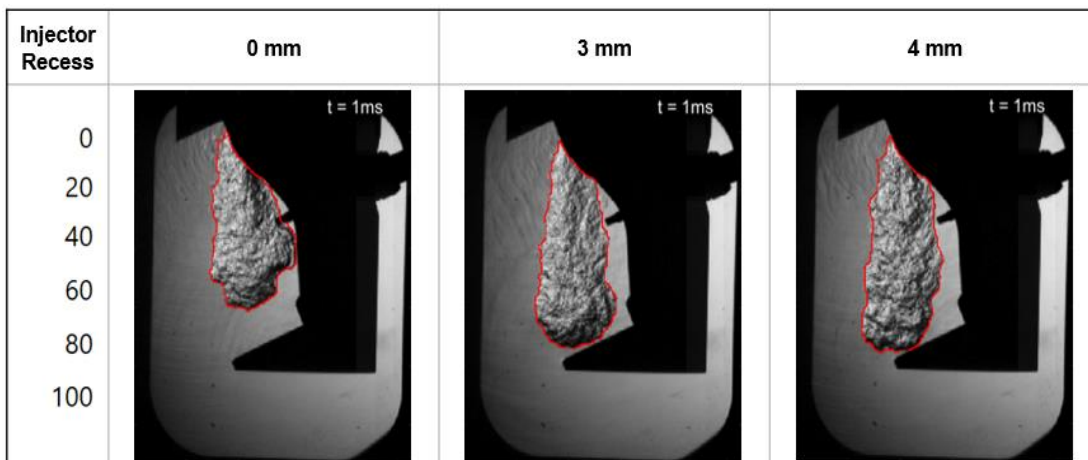
Fig. 7. Schlieren image of jet with combustion chamber resembling insert (35 bar injection pressure, 2 bar ambient pressure)

4.2 CFD simulation

CFD simulation is performed to confirm the impact of injector recess on jet development and pre-optimize hydrogen injection timing. The CFD study is carried out using commercial software package CONVERGE CFD in version 3.0 utilizing two-equation Re-Normalization Group (RNG) k-eps turbulence model. The computational domain inside the cylinder is set up with a cubic base grid size of $\Delta_{Cylinder}$ = 1 mm, a one level refinement is carried out dynamically, depending on the subgrid-gradient of velocity, temperature as well as hydrogen species. Pre-defined refinement is set on all combustion chamber walls (Δ_{Wall} = 0.5 mm) as well as in the vicinity of hydrogen jet during injection with Δ_{min} = 0.125 mm as a compromise between computational runtime and resolution of geometry details. An explicit scheme is utilized with unity velocity CFL number, leading to time-step sizes in the order of 1e-8 s during injection. Fig. 8 shows the details of computational grid used for CFD simulation.

Fig. 9 is the simulation results indicating the effect of injector recess on jet development and penetration. It is clear that without recess (0 mm recess) jet collapses immediately after it exits nozzle leading to reduced penetration. While with 3 mm recess jet is guided by wall of injector hole to generate highly concentrated and penetrating jet.

Hydrogen Injection timing is pre-optimized through CFD simulation. As shown in Fig. 10, adequately retarded injection timing leads to improved thermal efficiency and mixture uniformity eventually leading to lower NOx emission. Compared with earlier hydrogen injection (560 deg. ATDC$_f$: 160 deg. before firing TDC), retarded injection (620 deg. ATDC$_f$: 100 deg. before firing TDC) leads to lower compression work confirmed by lower cylinder pressure during compression stroke and considerably higher secondary tumble ratio. Higher tumble ratio is a results of shorter distance between injector and piston with retarded injection timing and increased secondary tumble leads to reduction of locally rich area below λ 2.0 that is critical for NOx emission as shown in λ histogram at firing TDC in Fig.11.

(a)   (b)
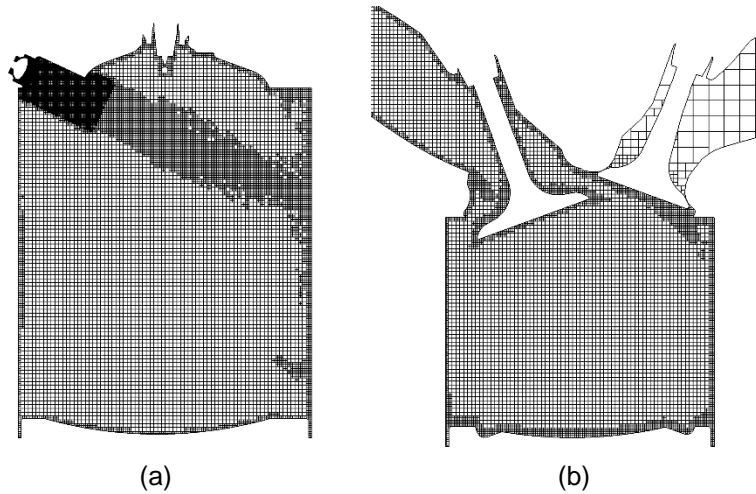
Fig. 8. (a) Computational grid in central plane at 570 °CA, (b) in intake valve plane at 450 °CA
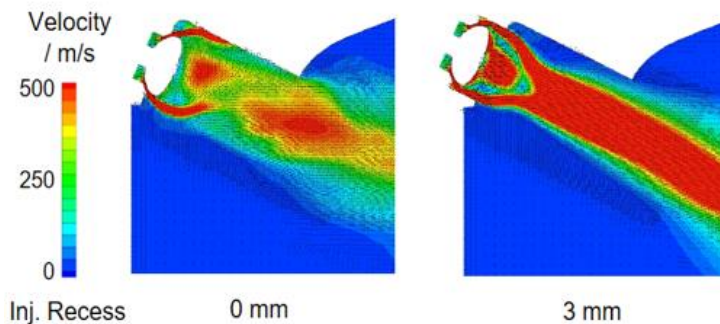
Fig. 9. Hydrogen jet shape with injector recess (CFD simulation)
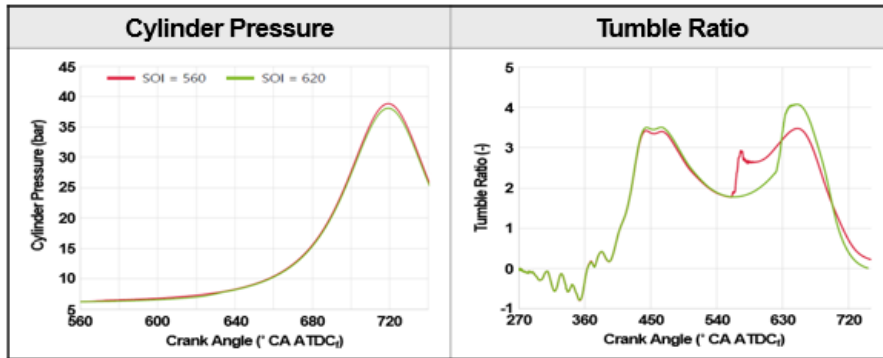
Fig. 10. Effect of hydrogen injection timing on cylinder pressure and tumble ratio
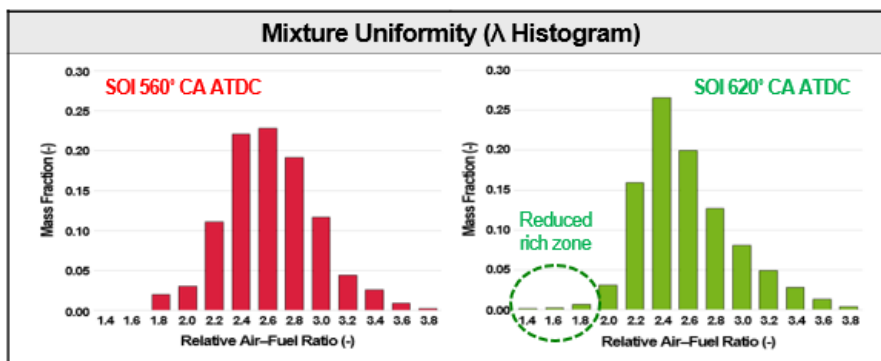
Fig. 11. Effect of hydrogen injection timing on mixture homogeneity (λ histogram at firing TDC)

5. Main results

5.1 Turbocharger matching

To address the requirement of far higher air mass flow than gasoline turbocharged engine to realize lean combustion crucial for high thermal efficiency and extremely low NOx emission, turbocharger matching is performed. Fig. 12 and 13 plot relevant parameters measured from BMEP sweep test at 2000 rpm both for baseline wastegate turbocharger already introduced to mass production engine (Fig. 12) and large VGT tuned considering full load performance (Fig. 13).

For WGT, it is not possible to increase BMEP above 12.5 bar even with fully closed wastegate valve because λ already reduces down to 1.67 and it leads to excessively high NOx emission and pressure rise rate due to rich combustion. It indicates that base WGT is too small to provide air required for lean combustion especially at high load area.
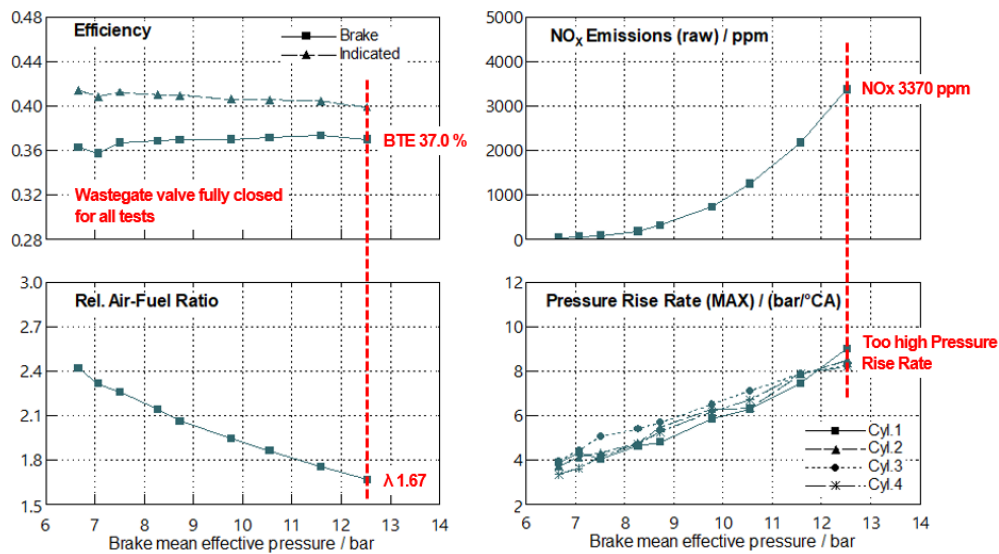
Fig. 12. BMEP sweep at 2000 rpm with base wastegate turbocharger

Fig. 13 shows BMEP sweep test results with VGT #2 in Table 1 that is tuned focused on enhancing full load performance. Although VGT #2 has higher potential at high speed and load area, it is obvious from the comparison with WGT that boosting performance and resulting relative air-fuel ratio is worse than WGT at medium load area.
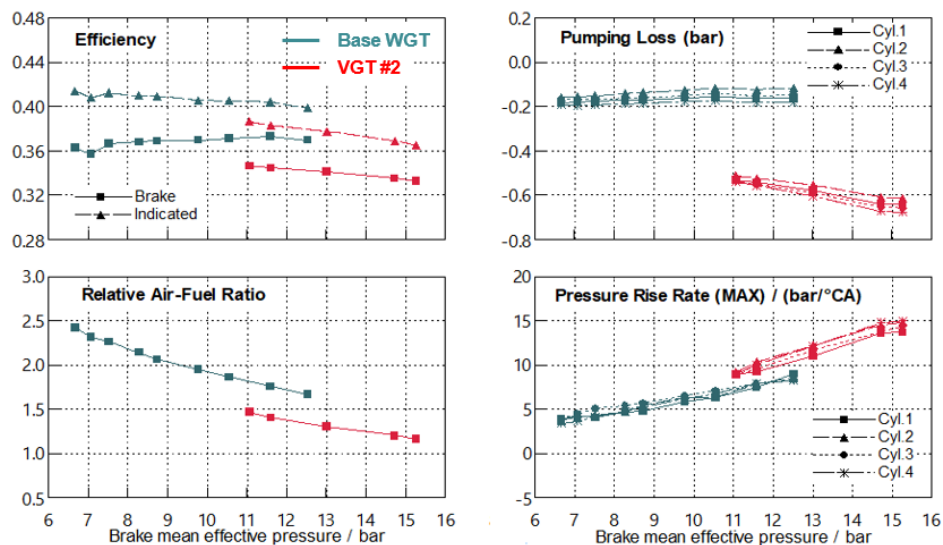
Fig. 13. Comparison of BMEP sweep at 2000 rpm between base WGT vs MGT 1752V VGT

Above test results indicate that single stage boosting system, regardless of WGT or VGT, cannot comply with wide air mass flow requirement for both medium load main operating area and full load. 2-stage boosting system combining 48 V driven electric supercharger and VGT is introduced for simultaneous achievement of high thermal efficiency and low NOx emission at main operating area and high performance at full load area. As shown in Fig. 14 electric supercharger is located upstream of turbocharger and charge air cooler is located downstream of turbocharger.

In this research, two VGTs' (Table 1) with different compressor and turbine wheel size are combined with 48 V driven electric supercharger for validation. Test results indicate that combination of 48 V electric supercharger and VGT #1 (smaller) has better overall potential than VGT #2 (bigger). Hereinafter, all test results are measured with electric supercharger and VGT #1.

Item	Spec.	Note
Voltage (V)	36 ~ 54	
Limit Peak Power (kW)	6.2	Instant use for hyper Boosting (48 V – 130 A)
Max. Power (kW)	5	Limited by temperature
Max. Speed (rpm)	72,000	
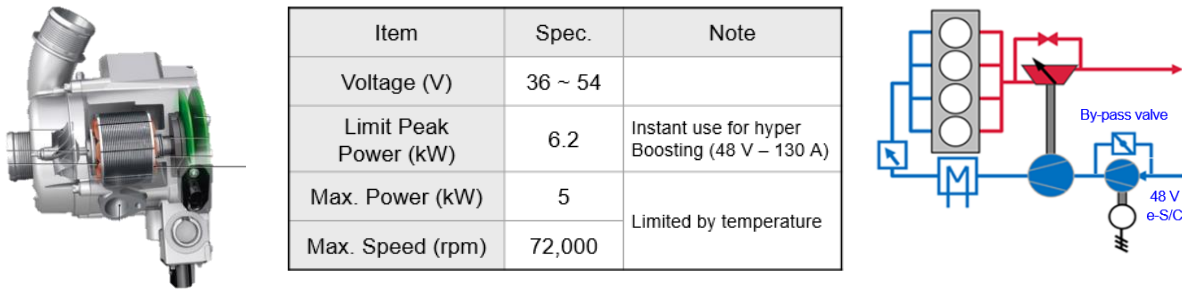
Fig. 14. 48 V driven electric supercharger, specification and layout of 2-stage boosting system

5.2 Test results at HEV main area (12 points)

By combining 48 V driven electric supercharger and VGT #1, relative air-fuel ratio ranging from 2.6 to 3.2 is achieved throughout hybrid main operating area that is higher than target of λ 2.5 (Fig. 15). With combustion of highly lean mixture, maximum brake thermal efficiency of 40.7 % is achieved at 2000 rpm and 140 Nm (11 bar BMEP) with compression ratio of 10.5 that is same as baseline 1.6 litre turbocharged engine. Although the impact on engine out NOx and abnormal combustion, such as knock and pre-ignition, should be verified, increasing compression ratio will suggest further potential in brake thermal efficiency.
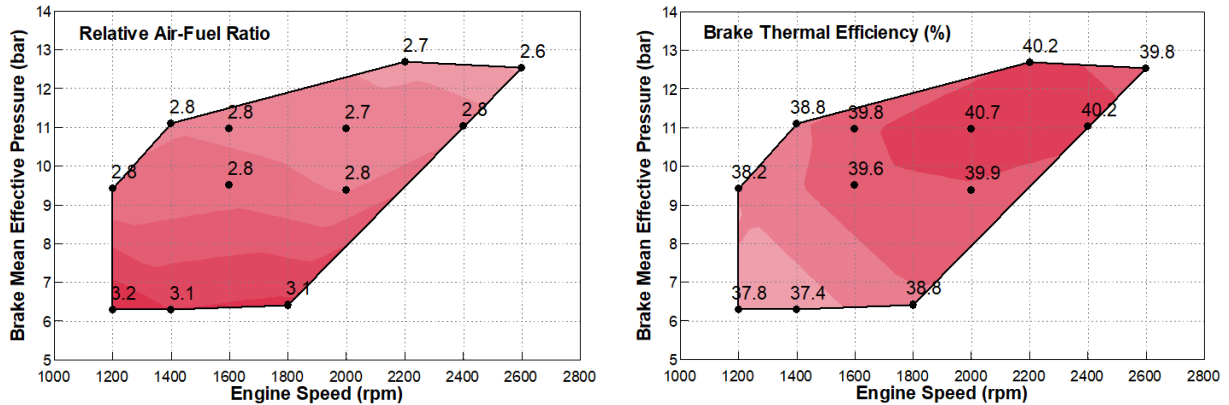
Fig. 15. Relative air-fuel ratio (left) and brake thermal efficiency (right)

Due to highly lean combustion, extremely low NOx emission is possible at hybrid main operating area. Engine out NOx emission is only 3 to 4 ppm at 80 Nm (6.3 bar BMEP) and generally below 10 ppm up to 140 Nm (11 bar BMEP) except low speed high load area and maximum 15 ppm NOx is measured at 2600 rpm, 160 Nm (Fig. 16). Engine out specific NOx lower than 0.2 g/kW-h is measured throughout entire hybrid main area.
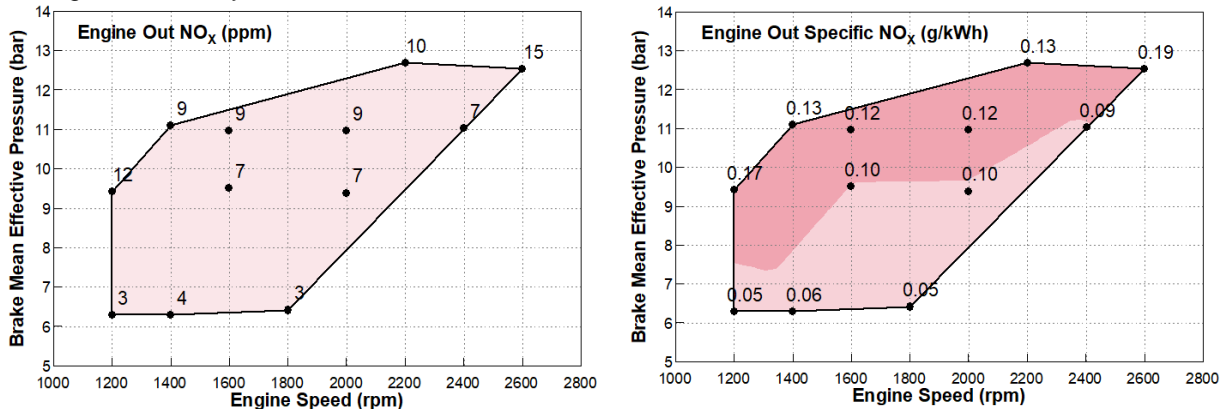
Fig. 16. Engine out NOx in ppm (left) and specific NOx in g/kW-h (right)

Since hydrogen is carbon free fuel, only detectable level of HC and CO emission below 1 ppm caused by burning of lubrication oil is measured in the entire operating area and this extremely low emission will contribute in handling engine out emission especially even during cold condition. (Fig. 17)
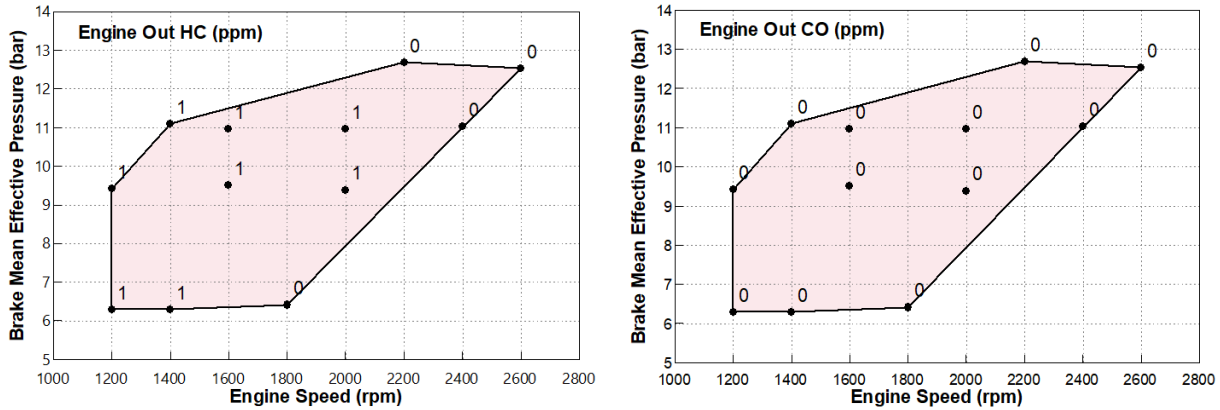
Fig. 17. Engine out HC (left) and CO (right) emission

Fig. 18 shows the coefficient of variation (COV) of indicated mean effective pressure (IMEP) that is an important indicator for combustion stability. $IMEP_{COV}$ is lower than 2 % in entire map indicating that stable combustion is possible even with highly lean mixture.

Another concern of hydrogen internal combustion engine is too high pressure rise rate due to high burning speed of hydrogen that will result in unacceptable combustion noise. But maximum pressure rise rate (PRR, $dP/d\theta_{max}$) is below 3.5 bar/$°$CA at entire map. It is comparable to normal spark ignited engine and comparable acoustic characteristics is expected.
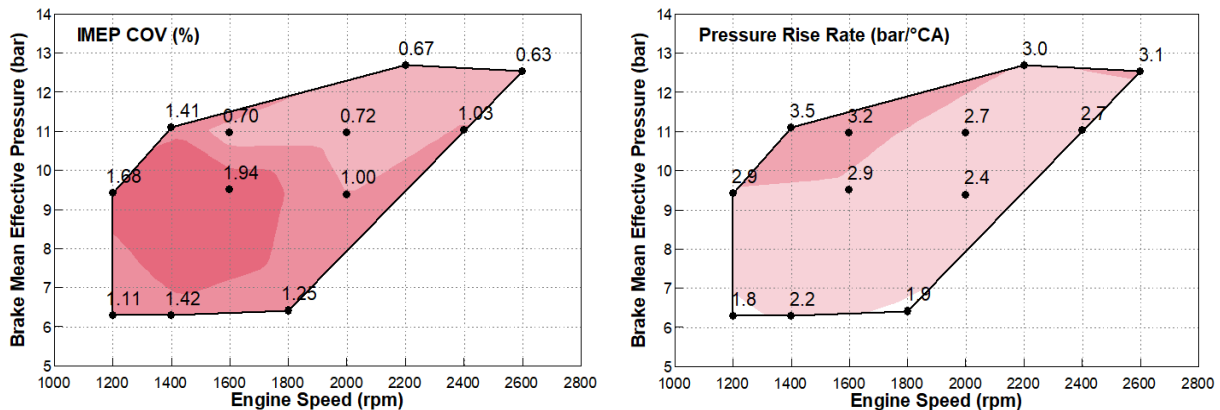
Fig. 18. IMEP COV (left) and maximum pressure rise rate (right)

5. 3 Full load performance

Fig. 19 shows comparison of full load performance between hydrogen internal combustion engine and baseline 1.6 litre gasoline turbocharged engine along with relative air-fuel ratio of H_2 ICE. Up to 3000 rpm, same full load performance as gasoline T-GDI engine can be reached, while at 4000 rpm about 20 Nm torque loss occurred due to pre-ignition. Relative air-fuel ratio drops below 1.6 at 4000 rpm and pre-ignition is seemingly caused by rich combustion. Third VGT with increased compressor wheel diameter will be validated as next step to increase boosting performance at high speed and high load operating condition.
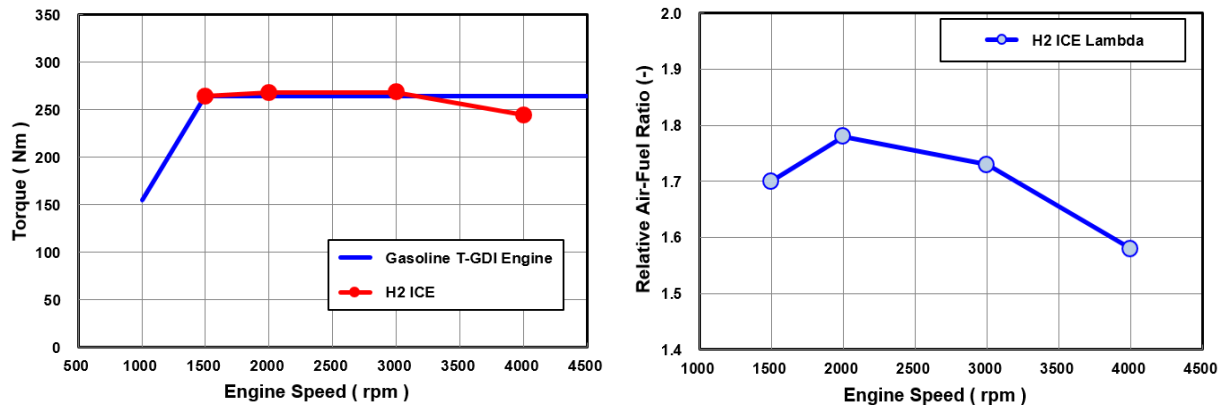
Fig. 19. Comparison of full load performance (left) and relative air-fuel ratio of H_2 ICE at full load

Conclusion

Series production 1.6 litre spark ignited engine is modified to operate with hydrogen as fuel by implementing hydrogen injector with outwardly opening nozzle and modified boosting system.

Injector recess and hydrogen injection timing is pre-optimized by high speed Schlieren photography of hydrogen jet and CFD simulation. With 0 mm recess, Schlieren images indicate that penetration reduces due to Coanda effect and locally rich mixture near spark plug can be formed. Meanwhile, highly concentrated and penetrating jet is achieved with 3 ~ 4 mm recess. Based on this observation 3 mm injector recess is applied to prototype engine. It is observed from CFD simulation that adequately retarded hydrogen injection timing leads to reduced compression work that is confirmed by lower cylinder pressure during compression stroke and far enhanced secondary tumble that eventually contribute in reducing locally rich mixture.

It is verified that single-stage boosting system, regardless of WGT or VGT, cannot cover wide air mass flow requirement for both main operating and full load areas. 2-stage boosting system combining 48 V driven electric supercharger and variable geometry turbocharger is implemented.

12 important test points, ranging 80 ~ 160 Nm (6.3 ~ 12.6 bar BMEP) and 1200 ~ 2600 rpm, are selected based on engine speed and torque traces for various test modes of medium SUV. At these test points, relative air-fuel ratio of 2.6 to 3.2 with 40.7 % maximum brake thermal efficiency at 2000 rpm and 140 Nm achieved. NOx emission lower than 15 ppm and 0.2 g/kW-h is possible throughout entire range. Only traceable level of HC and CO emission below 1 ppm is confirmed and it will contribute in reducing cost of aftertreatment system. IMEP COV is below 2 % at entire range indicating stable combustion and maximum pressure rise rate is below 3.5 bar/ ° CA that is comparable to normal spark ignited engine and comparable acoustic characteristics is expected.

Up to 3000 rpm, same full load performance as base 1.6 litre turbocharged engine is achieved. But at 4000 rpm, full load torque is reduced by about 20 Nm due to onset of pre-ignition. Pre-ignition is suspected to be caused by rich combustion with λ lower than 1.6. VGT with bigger compressor wheel than current one will be validated as next step.

Thermal efficiency and emission potential confirmed at hybrid main area and comparable full load performance with base gasoline turbocharged engine clearly indicates that H_2 ICE can be an important bridging and complementary technology to BEV and FCEV during the transition phase to full electrification.

Reference

1. Tang, X. et al, "Ford P2000 Hydrogen Engine Dynamometer Development", SAE 2002-01-0242
2. Boyer, B. et al, "Challenges in Developing Hydrogen Direct Injection Technology for Internal Combustion Engines", SAE 2008-01-2379
3. Waller, T. et al, "Fuel Economy and Emissions Evaluation of BMW Hydrogen 7 Mono-Fuel Demonstration Vehicles", International Journal of Hydrogen Engines, 2008

4. European Hydrogen Backbone grows to meet REPowerEU's 2030 hydrogen targets and develops 28,000 km in 2030 and 53,000 km in 2040, now covering 28 European countries - Gas for Climate 2050

5. Toyota Developing Hydrogen Engine Technologies Through Motorsports | Corporate | Global Newsroom | Toyota Motor Corporation Official Global Website

6. Korn, T. "The Most Efficient Way for CO_2 Reduction: The New Generation of Hydrogen Internal Combustion Engines", 2020 Vienna Motor Symposium

7. Pauer, T. "H2 ICE for Future Passenger Cars and Light Commercial Vehicles", 2020 Vienna Motor Symposium

8. Dreisbach, R. et al, "The Heavy-Duty Hydrogen Engine and its Realization until 2025", 2021 Vienna Motor Symposium

9. Gabin, D. et al, "Hydrogen Conversion of Existing Powertrain", 18th Symposium Sustainable Mobility, Transport and Power Generation, 2021

Session S2.1 Thermal Management

Computational Investigation on Radiation Induced Li-Ion Battery Thermal Runaway

Liwen Zhang[1], Yi Chen[2], Haiwen Ge[3], Peng Zhao[1*]

[1]Department of Mechanical, Aerospace & Biomedical Engineering, UT Space Institute, University of Tennessee, Knoxville, TN 37388, United States

[2]A123 Systems, Novi, Michigan 48377, USA

[3]Department of Mechanical Engineering, Texas Tech University, Lubbock, TX 79409, USA

*Correspondence E-mail: pzhao12@utk.edu
Telephone: +(1) 931-393-7261

Abstract. With the global trend of electrification and the fast expansion of electrical vehicle market, research and development of Li-ion battery as main energy storage medium has attracted extensive interest. One of the key issues that need to be resolved is thermal runaway and its propagation, where side reactions can occur when the battery is exposed to heat and other abuse conditions. Thermal runaway reactions are largely exothermic and can lead to subsequent fire and explosions when thermal runaway propagates to adjacent cells. In the current work, we focus on the effect of radiation on thermal runaway, which is especially relevant when a battery is exposed to adjacent heat and fire sources. To validate the numerical simulation, calculated radiation heat flux is compared with analytical solutions of radiation heat flux based on view factor expressions obtained in simple 2D cylinder-to-cylinder geometries. Very good agreement has justified the validity of the radiation calculation. Furthermore, radiation induced thermal runaway is evaluated between two cylindrical 18650 batteries. It has shown that depending on the temperature of the triggering cell, thermal runaway can either be triggered in the region close to the cell surface or internal domain within the cell, with different roles of the pre-runaway chemistry. Integrated radiation heat flux is calculated under a wide range of triggering temperatures, showing different limits under low and high temperature conditions. By analyzing the pre-runaway chemical heat release, it is further seen that radiation plays a dominant role under higher temperature conditions, while its significance gradually decreases under lower temperature conditions. Results from this work evaluate the role of radiation in thermal runaway propagation and provide useful insights into the thermal runaway control.

1. Introduction

With the global tendency of decarbonisation and electrification in energy, Li-ion battery (LIB) has attracted extensive research interest, and it has become one of the most promising technologies for future energy storage [1]. Indeed, LIBs can provide a very high energy conversion efficiency between chemical and electrical energies. If the electricity comes from clean and renewable energy resources, LIB technology with sufficiently long cycle life will not further increase the carbon footprint to electricity generation and utilization. Meanwhile, LIBs can be seamlessly integrated with the existing infrastructure in the energy sector and on-going efforts of decarbonisation, for example, the electricity grid, centralized carbon capture and sequestration, the growing capabilities of advanced manufacturing, battery regeneration and material recycling, etc. LIBs play a central role in the synergetic integration of these technologies toward decarbonisation.

However, there are still substantial challenges associated with LIB research and development. First of all, although the current LIBs have reached an energy density of approximately 250 Wh/kg, which is nevertheless only equivalent to 2% of that of gasoline or diesel. The relatively low energy density issue constraints the usage of LIBs in heavy duty applications and stimulates research efforts in higher energy density LIBs. Second, LIBs are subject to relatively short cycle life from internal degradation and irreversible changes. This aggravates the cost and emissions of LIBs on the life cycle basis. Last but not the least, the operation of LIBs is sensitive to temperature. Thermal runaway and subsequent fires can be triggered when LIBs are exposed to abused conditions such as overheating, internal short circuit, collision and nail penetration, placing direct threat to lives and properties.

Thermal runaway of LIBs has attracted extensive research interest in the past decade. These research efforts primarily include the characterization of the thermal stability of battery materials [2-3], cell and pack level thermal runaway testing under abused testing conditions [4-5], development of thermal kinetic models of thermal runaway [6-7], optimized cooling system design to mitigate thermal runaway and its propagation [8-9], modelling and simulation of thermal runaway using detailed and re-duced-order models [10-11], venting gas generation and subsequent fires [12-14]. Fundamentally, a charged LIB carries "fuel" and "oxidizer" internally, which is potentially flammable and explosive. Fig. 1 shows the thermal runaway mechanism using a typical LIB with $LiCoO_2$ cathode, electrolyte of eth-ylene carbonate ($C_3H_4O_3$) and Lithium hexafluorophosphate ($LiPF_6$), and a graphite anode. The solid-electrolyte-interphase layer is thermally unstable and can decompose when it is subject to high tem-perature conditions. The lithium in the anode will then directly contact with the electrolyte and form lith-ium carbonate and ethylene. In addition, the cathode and electrolyte can directly react through the ox-ygen generated from cathode decomposition. Finally, the electrolyte material carbonate and salt can decompose under elevated temperatures. These reactions are largely exothermic and are accompa-nied with the formation of gases such as ethylene and oxygen.
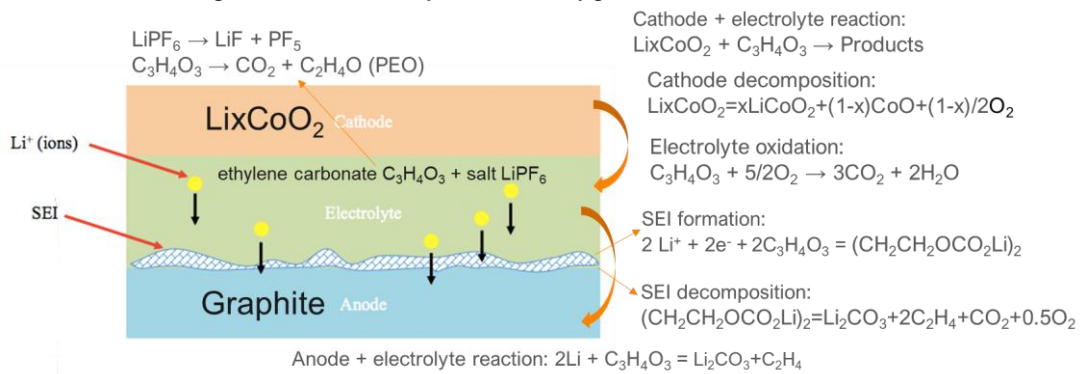
Fig. 1. Configuration and thermal runaway reactions for a typical LCO LIB

The current research aims to understand one of the most common thermal runaway triggering mechanisms when a LIB is exposed to heat and fire sources. It is expected that under such condi-tions, thermal radiation plays a critical role to increase the battery temperature and further activate the thermal runaway reactions [15-18]. However, due to the strong nonlinearity of radiation and its cou-pling with thermal runaway chemistry, the fundamental of radiation induced thermal runaway is still not fully understood. Mishra and Jain [19] have computationally investigated the role of radiation in ther-mal runaway propagation among a cylindrical pack. Their results have shown that neglecting radiation leads to a prediction of onset in the trigger cell but an erroneous prediction of no thermal runaway propagation. In addition, thermal radiation is frequently combined with the effects of conduction and convection in thermal runaway triggering, leading to great ambiguities to isolate its role. In the follow-ing, we have computationally investigated limiting condition when thermal runaway is triggered by ra-diative heat transfer between two adjacent cylindrical cells. It is seen that although radiation occurs in the surface, not all the thermal runaway is triggered in the surface region. Depending on the time scale of thermal runaway, role of radiation in thermal runaway triggering can vary.

2. Methodology

In this study, a 2D model is developed in COMSOL Multiphysics 5.5, where the heat transfer module is used to implement surface-to-surface radiation. The problem of radiation induced thermal runaway be-tween cylindrical cells is simplified as a 2D radiation heat transfer problem between two equal cylin-ders and the schematic of the simulation geometry is shown in Figure 2.
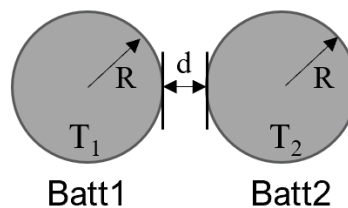
Fig. 2. Schematic of simulation geometry of two equal cylinders with radius R and separation *d*

To eliminate the influence of flow and convective heat transfer, heat convection at the interface is ignored, and only thermal radiation at the surface of cell is considered. Within the battery, heat conduction in the axial and azimuthal directions as well as thermal runaway chemical heat release are considered:

$$\rho c_p \frac{\partial T}{\partial t} = \frac{1}{r}\frac{\partial}{\partial r}\left(kr\frac{\partial T}{\partial r}\right) + \frac{1}{r^2}\frac{\partial}{\partial \theta}\left(k\frac{\partial T}{\partial \theta}\right) + Q$$

where $t, r, \theta, \rho, c_p, T, k$ and Q are time, radial coordinate, azimuthal coordinate, cell density, heat capacity, thermal conductivity, and heat generation within the cell, respectively. The values of some thermal physical properties are provided in Table 1. For simplicity, we assume the same thermal conductivity value in the radial and azimuthal directions. The heat generation Q comes from four semi-global thermal runaway chemical reactions. These exothermic reactions include the solid-electrolyte-interface decomposition reaction, the anode-electrolyte reaction, the cathode-electrolyte reaction, and the electrolyte decomposition. The rates of these reactions depend on the battery material properties, thermal chemical parameters, and the battery temperature. The reaction model, frequency factor, and activation energy that describe the kinetics between the electrolyte and electrode materials have been previously obtained by fitting the experimental measurements from accelerating rate calorimetry (ARC) and differential scanning calorimetry (DSC) tests [6]. The chemical reaction rates and heat generation in a single cell jellyroll domain are shown in Table 2, with the parameters the same as adopted in our previous work [20,21]. This model has been validated over literature reported oven test, with satisfactory performance.

Table 1. Model parameters in the thermal radiation model

Parameter (unit)	Value
Cell radius, $R(mm)$	9
Cell density, $\rho(kg/m^3)$	2060
Heat capacity, $c_p(J/kg \cdot K)$	1000
Thermal conductivity, $k(W/m \cdot K)$	0.8

Table 2. Heat generation from side chemical reactions equations of thermal abuse model

Reaction term	Equations	
SEI decomposition	$\frac{dc_{sei}}{dt} = -A_{sei}exp\left[-\frac{E_{a,sei}}{RT}\right]c_{sei}^{m_{sei}}$	$Q_{sei} = -H_{sei}W_c\frac{dc_{sei}}{dt}$
Anode-electrolyte reaction	$\frac{dc_{ne}}{dt} = -A_{ne}exp\left[-\frac{t_{sei}}{t_{sei0}}\right]c_{ne}^{m_{ne,n}}exp\left[-\frac{E_{a,ne}}{RT}\right]$	$Q_{ne} = -H_{ne}W_c\frac{dc_{ne}}{dt}$
	$\frac{dt_{sei}}{dt} = A_{ne}exp\left[-\frac{t_{sei}}{t_{sei0}}\right]c_{ne}^{m_{ne,n}}exp\left[-\frac{E_{a,ne}}{RT}\right]$	
Cathode-electrolyte reaction	$\frac{d\alpha}{dt} = A_{pe}\alpha^{m_{pe,p1}}(1-\alpha)^{m_{pe,p2}}exp\left[-\frac{E_{a,pe}}{RT}\right]$	$Q_{pe} = -H_{pe}W_p\frac{d\alpha}{dt}$
Electrolyte decomposition	$\frac{dc_e}{dt} = -A_eexp\left[-\frac{E_{a,e}}{RT}\right]c_e^{m_e}$	$Q_e = -H_eW_e\frac{dc_e}{dt}$
Overall heat generation	$Q = Q_{sei} + Q_{ne} + Q_{pe} + Q_e$	

At the surface, thermal radiation is considered, and the schematic diagram of thermal radiation as shown in Figure 3. The radiation heat flux emitted from Batt 1 is the irradiation *G*:

$$G = \varepsilon\sigma(T_1^4 - T_{amb}^4)$$

For Batt 2, we can define the radiosity *J*, the radiation heat flux leaving its surface:

$$J = \varepsilon\sigma T_2^4 + (1-\varepsilon)F_{12}G$$

where *J* is the radiosity, which is the sum of diffusively reflected and emitted radiation from Batt 2. Consequently, the net radiation heat flux on Batt 2 can be evaluated:

$$q = F_{12}G - J$$

In these equations, ε is the emissivity, σ is the Stefan-Boltzmann constant, T_1 is the temperature of Batt1, T_2 is the temperature of Batt2, T_{amb} is ambient temperature, and F_{12} is view factor.
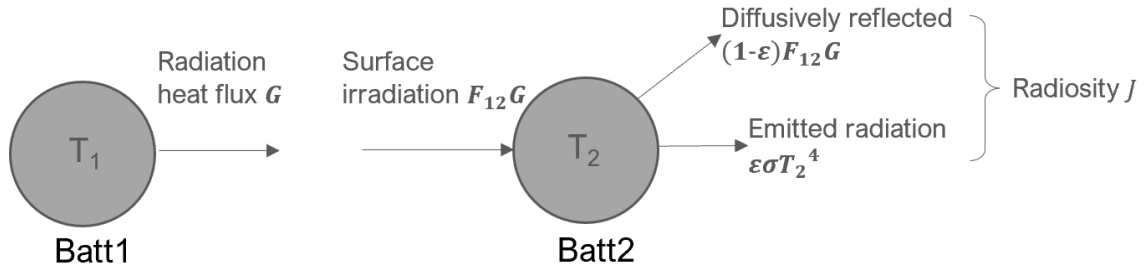
Fig. 3. Schematic of thermal radiation between two equal external cylindrical cells

In order to validate the thermal radiation modeling, a quasi-steady state radiative heat transfer problem between two equal cylinders of radius (R = 9 mm) is considered. With given separation distance and cylinder temperatures, we can numerically simulate the radiation heat flux received by Batt 2 among the total radiation emitted from Batt 1, that is, GF_{12}. Meanwhile, in classical heat transfer theory, the radiation heat flux between two cylinders is analytically available with known view factor, which can be used to validate the simulation results. The view factor between two equal cylinders is given by:

$$F_{12} = \frac{\sqrt{(\frac{2R+d}{R})^2 - 4} - \frac{2R+d}{R} + 2\arcsin(\frac{2R}{2R+d})}{2\pi}$$

As shown in Figures 4(a) and (b), the numerical radiation heat flux is compared with the analytical theory between two equal blackbody cylinders (i) with fixed temperature but varying distance, and (ii) with fixed distance but varying temperature of the Batt 1. The results suggest that as the distance of two cells increases, the radiation heat flux decreases. Also, as the temperature of Batt1 increases, the radiation heat flux received by Batt 2 increases. The numerical calculation of the radiation heat flux achieves excellent agreement with analytical results, further substantiating the adopted simulation tool.
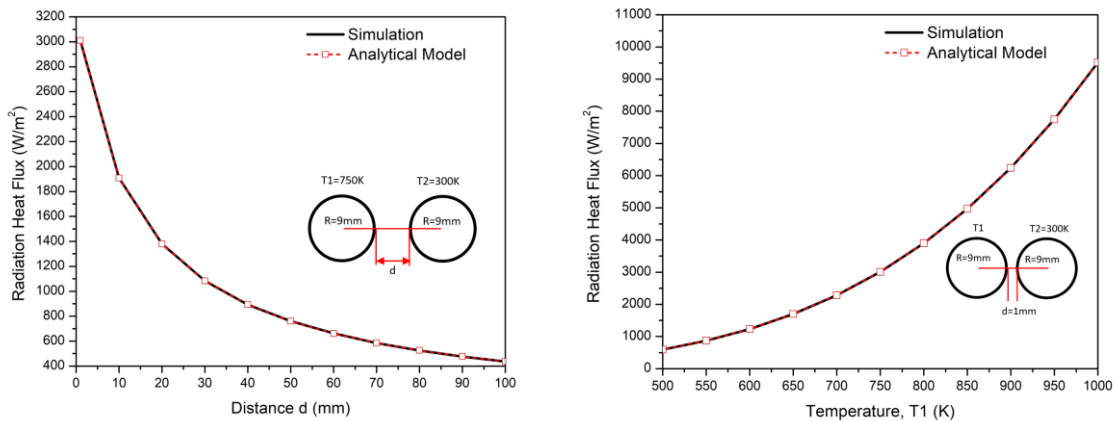
Fig. 4. Validation of simulation results against analytical model for surface-to-surface radiation modeling: (a) Radiation heat flux vs. Distance d of two cells (b) Radiation heat flux vs. Temperature T1 of Batt1

In the thermal runaway simulation, we fix the temperature T1 of Batt 1 and the ambient temperature (293 K) in each case. The initial temperature of Batt 2 is given as 293 K. The evolution of T2 is numerically solved by accounting for radiation, conduction, and thermal runaway chemical heat release. The surface-to-surface radiation is simulated using the Hemicube method in the heat transfer module. A time-dependent solver of MUMPS (Multifrontal Massively Parallel Sparse) was used to solve for the thermal energy conservation equation. Backward Differentiation Formula (BDF) method is used for time stepping. The relative tolerance for the solution is 1E-3.

3. Results and discussion
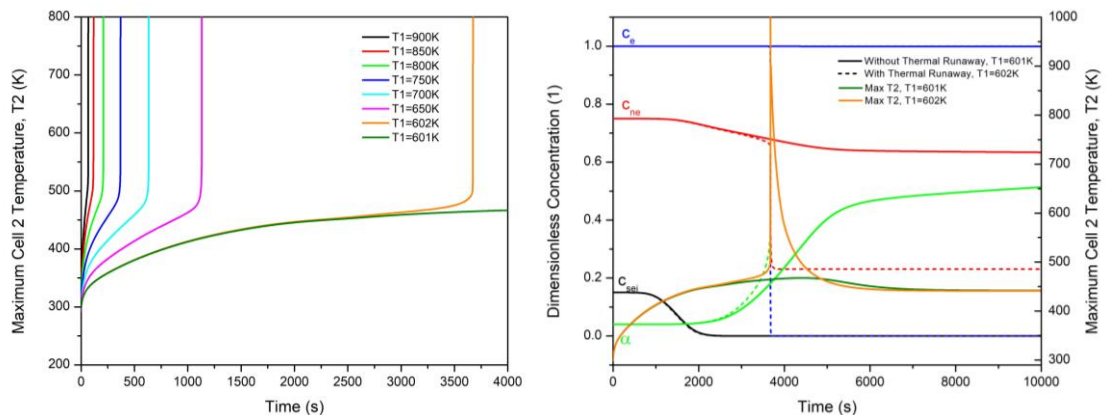
Fig. 5. (a) Maximum temperature of Batt 2 versus time for different T1 (b) Comparison of evolution of average dimensionless concentration and temperature close to the threshold thermal runaway temperature 602 K

Figures 5(a) shows the evolution of maximum temperature of Batt 2 with different temperature of Batt 1, T1. The results have shown that for all the T1 above 601 K, thermal runaway occurs in Batt 2, as indicated by the sharp increase in T2. For all these cases, the higher the T1, the earlier thermal runaway can be triggered in Batt 1, as expected. When T1 is increased to 900K, the thermal runaway delay time is reduced to around 1 min. For T1 below 602 K, it is seen in Fig. 5(b) that thermal runaway cannot be triggered in Batt 2, even with the much longer time scale of 10000 s, and the maximum temperature of Batt 2 eventually reduces to around 450 K where a quasi-thermal equilibrium is reached due to the balance between the net radiation heat flux and chemical heat generation. It should be also noted that the dimensionless SEI concentration is completely consumed around 2000s both T1 = 602 and 601 K, much earlier than the complete consumptions of other species, which occur at the instant of thermal runaway. The results suggest that the four chemical reactions might occur at different stages of thermal runaway, and their occurrence can be decoupled depending on the thermal runaway time scale.
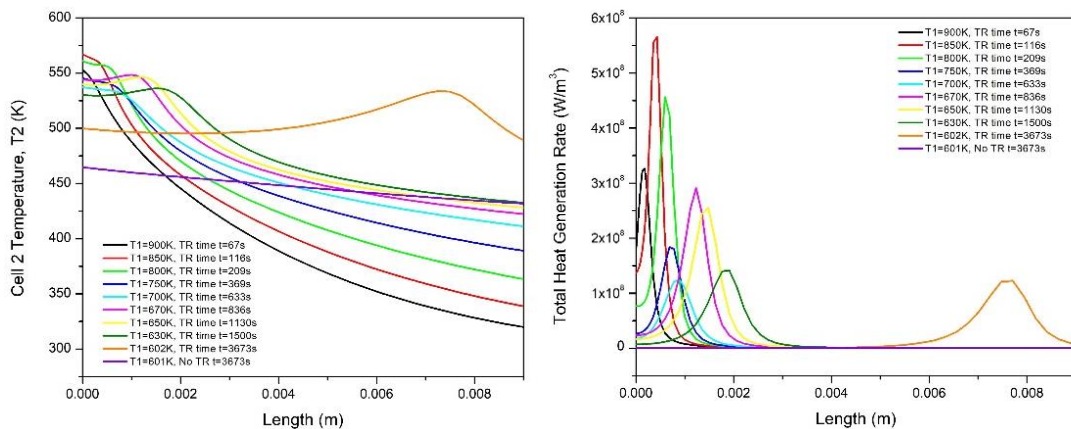
Fig. 6. (a) Profile of T2 along the center radial line of Batt 2 when thermal runaway is triggered by different T1 (b) Profile of total heat generation rate along the center radial line of Batt 2 aligning with the centers of Batt1 and 2, when thermal runaway is triggered by different T1

By defining the onset of thermal runaway as the instant with maximum temperature rise rate, Figure 6 (a) and (b) show the temperature and net heat generation rate distribution along the centre radial direction of Batt 2 at the onset of thermal runaway. It can be seen that the maximum temperature and peak heat release occurs in the vicinity of the surface of Batt 2, for high triggering temperature T1. Given that thermal runway for high T1 occurs very fast, so for these cases, it is expected that radiation plays the sole dominant role for the temperature increase during thermal runaway. As T1 gradually reduces, the location corresponding to the maximum temperature and peak heat release gradually moves to the internal region of the battery, indicating increasing effect from heat conduction

and the heat generation from the chemical reactions during the much longer thermal runaway. For the threshold case with T1 = 602 K, the peak heat release occurs very closely to the centre of Batt 2.
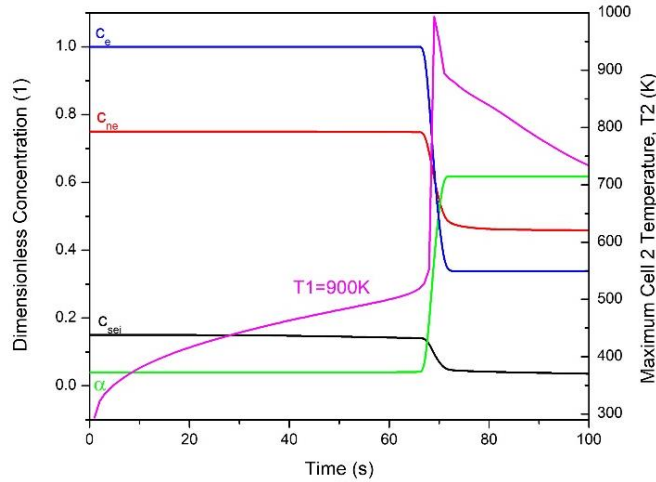
Fig. 7. Evolution of average dimensionless concentration and temperature with thermal runaway triggering temperature T1 = 900 K

To show the different thermal chemical processes for thermal runaway triggered by high and low temperature radiation, Fig. 7 shows the evolution of dimensionless concentration and temperature in Batt 2 for a relatively high triggering temperature T1 = 900K. Compared to the low triggering temperature case with T1 = 602 K shown in Fig. 5 (b), the thermal runaway is triggered must quicker. More interestingly, the mean dimensionless concentrations in the high temperature 900K scenario do not exhibit obvious change before thermal runaway is triggered. The reactions are not separated in either spatial or time domain, they tend to be activated simultaneously in the vicinity of the battery surface due to the fast radiative heating.

In summary, the results so far demonstrate that radiation induced thermal runaway exhibits intrinsic differences under low and high triggering temperatures: when T1 is high, the thermal runaway is triggered very fast in the vicinity of the battery surface, and the thermal runaway reactions occurs simultaneously in spatial and time, radiation plays a solely dominant and direct role; whereas for low T1, the thermal runaway is triggered much slowly in the internal region of the battery, and the thermal runaway reactions can separate in spatial and time domains due to the depletion of certain species, in this case the significance of radiation is less dominant and indirect.
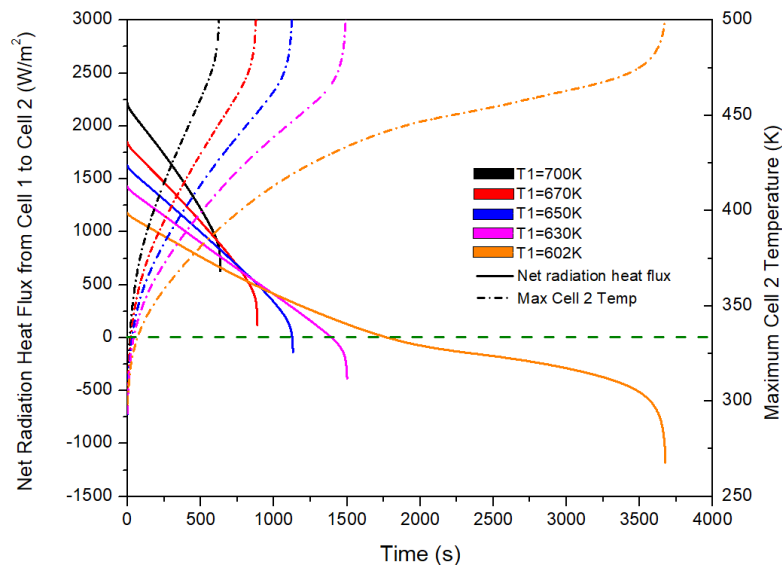
Fig. 8. Evolution of net radiation heat flux q during thermal runaway with different T1

It should be noted that although Batt 2 receives radiation heat flux from Batt 1, it meanwhile emits radiation to the ambient. So at a certain state, the net radiation heat flux can become zero, even before thermal runaway occurs. In this scenario, the net radiation heat flux on Batt 2 can actually be-

come negative when thermal runaway occurs, counteracting with thermal runaway. Fig. 8 shows the evolution net radiation heat flux q over the surface of Batt 2. It can be seen that for cases with T1 = 602 K, q transitions to negative much earlier than the onset of thermal runaway – the instant with maximum temperature rise rate. Hence it means radiation facilitates thermal runaway in the early stage before net radiation flux vanishes, and it mitigates thermal runaway in the later stage when net radiation flux becomes negative. With elevated temperature – when T1 reaches close to 650 K, the cross over state of q occurs very close to the onset of thermal runaway, indicating the constant promotion effects of radiation during thermal runaway at higher triggering temperatures.
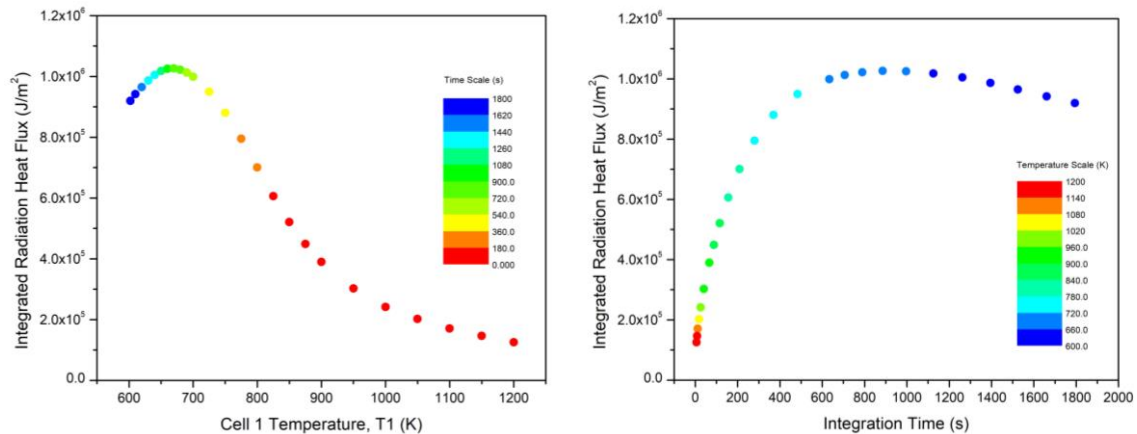
Fig. 9. (a) Time integrated net radiation heat flux at different triggering temperature, color indicates the time with zero net radiation flux (b) Time integrated net radiation heat flux versus integration time, color indicates thermal runaway triggering temperature

To identify the role of radiative heat transfer at different triggering temperatures, a time integrated radiative heat flux is calculated by integrating the net radiation flux q over the surface of Batt 2 from the initial condition to the instant of when the net radiation heat flux in Batt 2 vanishes. This gives a basis to evaluate the maximum facilitation effect of radiation on the triggering of thermal runaway. Interestingly, the time-integrated radiative heat flux so defined exhibits a non-monotonic dependence on temperature, which is quite counter-intuitive as shown in Fig. 9. On the high temperature branch, the integrated radiative heat flux does decrease with the increase of the triggering temperature, as expected. However, the peak integrated radiative heat flux does not occur at the lowest temperature as one might expect, instead, it occurs at some intermediate temperature around 700 K. One possible explanation of such a non-monotonic trend is to consider the time duration for the integral: higher triggering temperature T1 leads to higher radiative heat flux, which nevertheless leads to a much shorter time scale to cancel out net radiation flux q; lower triggering temperature T1 leads to lower radiative heat flux, which however elongates the time scale to cancel out net radiation. This nevertheless only partially explains the role of radiation with varying triggering temperature, in that the heat release from the exothermic thermal runaway reactions will also facilitate the temperature increment. With longer thermal runaway delay time at low temperatures, it allows longer residence time for the chemical reaction progress and heat release to accumulate internally within the battery.
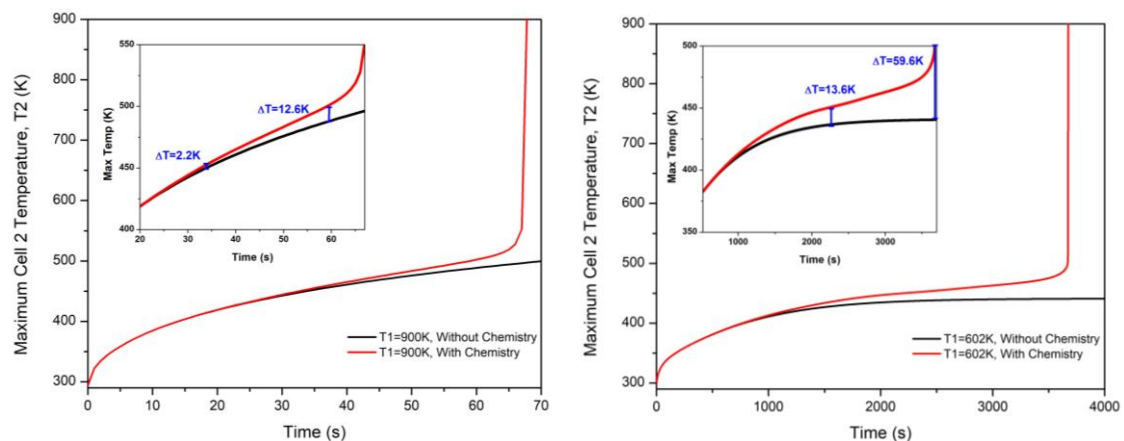
Fig. 10. (a) Time integrated net radiation heat flux at different triggering temperature, color indicates the time with zero net radiation flux (b) Time integrated net radiation heat flux versus integration time, color indicates thermal runaway triggering temperature

To isolate the effect of chemical heat release before thermal runaway, Fig. 10 compares the maximum temperature evolution of Batt 2 with and without the chemical heat source term. The results without chemical heat release represent the contribution solely from radiation, while the difference between the cases with and without chemistry can effectively isolate the contribution from chemical heat release. We can define an exothermal temperature as the onset temperature of thermal runaway, for example 450 K or 500 K, and evaluate the temperature differences at these selected reference points. Fig. 10 (a) shows the temperature evolution with and without chemistry in high triggering temperature case $T1 = 900$ K. At reference onset temperature $T_{ref} = 450$ K, the temperature difference ΔT between the cases with and without chemistry is around 2.2 K, indicating the role of pre-runaway chemistry. Considering the total temperature rise at the reference $T_{ref} - T_{ini} = 450 - 293 = 157$K includes the combined effects of radiation and pre-runaway chemistry, the contribution of chemistry can therefore be reasonably isolated. Similarly, in the lower triggering temperature case as in Fig. 10 (b), the contribution of pre-runaway chemistry increases the battery temperature by 13.6 K, much higher compared to the higher triggering temperature case in Fig. 10 (a).

The ratio of temperature rise from pre-runaway chemistry to the total temperature rise is evaluated at different triggering temperatures. It is shown in Fig. 11 that at high triggering temperatures, the contribution of pre-runaway chemistry is very small, below 1% for thermal runaway onset reference temperature 450 K, and below 5% for onset reference temperature 500 K. This indicates the sole dominant role of radiation for high temperature radiation induced thermal runaway. While for the low triggering temperature conditions, the contribution of pre-runaway chemistry increases to around 10% for reference temperature 450 K and nearly 30% for onset reference temperature 500 K. The effect from pre-runaway chemistry becomes comparable to the radiation and hence cannot be neglected.
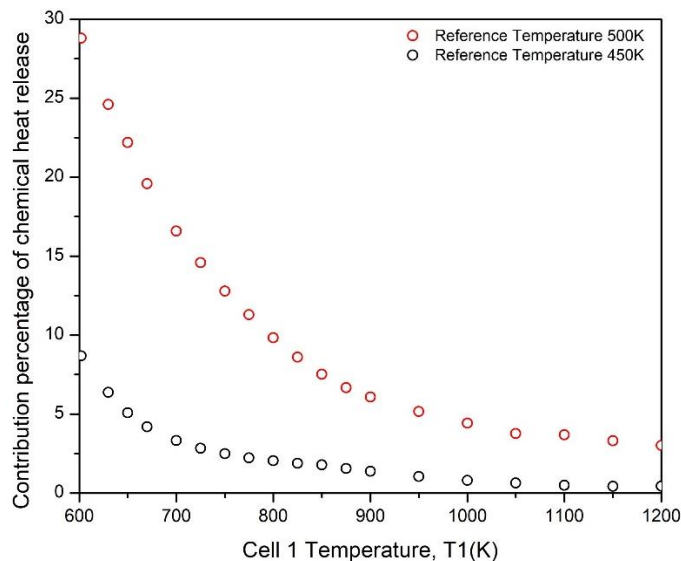
Fig. 11. The contribution of chemical heat release during radiation induced thermal runaway with different T1

4. Conclusion

From carefully conducted and validated numerical simulation, the role of radiation and pre-runaway chemistry in radiation induced battery thermal runaway is identified in the current study. The results have shown that a threshold temperature exists in radiation induced thermal runaway, below which thermal runaway cannot be triggered. When temperature is above the threshold temperature, the higher the triggering temperature, the shorter the thermal runaway delay time.

We have found that radiation induced thermal runaway exhibit intrinsic differences under low and high triggering temperatures: for high triggering temperatures, the thermal runaway is triggered very fast in the vicinity of the battery surface, and the thermal runaway reactions occurs simultaneously in spatial and time, radiation plays a solely dominant and direct role; whereas for low triggering temperature, the thermal runaway is triggered much slowly in the internal region of the battery, and the

thermal runaway reactions can separate in spatial and time domains due to the depletion of certain species.

By investigating the evolution of the net radiation flux during thermal runaway, we have found that the net radiation heat flux has a cross-over instant beyond which the net radiation heat flux becomes negative. Therefore, radiation can either facilitate or mitigate thermal runaway. For high temperature conditions, the cross-over state is very close to the instant of thermal runaway, as such radiation constantly facilities thermal runaway; while for low temperature conditions, the cross-over state can be far ahead of the instant of thermal runaway, therefore radiation facilitates thermal runaway in the earlier stage and mitigates thermal runaway in the later stage.

The time-integrated radiation heat flux exhibits a non-monotonic dependence on the triggering temperature. The underlying reasons can be twofold: for one thing, the delay time of thermal runaway is substantially longer for low temperature conditions, albeit with a lower radiation heat flux; for another, the pre-runaway chemistry plays an increasingly significant role in increasing the battery temperature under lower triggering temperature conditions, which must be considered for radiation induced thermal runaway.

Acknowledgement

References

[1] National Blueprint for Lithium batteries, (2021) 2021-2030, US Department of Energy, DOE/EE-2348.

[2] D. Ren, X. Liu, X. Feng, L. Lu, M. Ouyang, J. Li, X. He, Model-based thermal runaway prediction of lithium-ion batteries from kinetics analysis of cell components, Appl. Energy, 228 (2018), pp. 633-644

[3] J. Gong, Q. Wang, J. Sun, Thermal analysis of nickel cobalt lithium manganese with varying nickel content used for lithium-ion batteries, Thermochim. Acta 655 (2017) 176–180

[4] B. Lei, W. Zhao, C. Ziebert, N. Uhlmann, M. Rohde, H. J. Seifert, Experimental Analysis of Thermal Runaway in 18650 Cylindrical Li-Ion Cells Using an Accelerating Rate Calorimeter, Batteries 3 (2017) 14

[5] C. Zhao, T. Wang, Z. Huang, J. Wu, H. Zhou, M. Ma, J. Xu, Z. Wang, H. Li, J. Sun, Q. Wang, Experimental study on thermal runaway of fully charged and overcharged lithium-ion batteries under adiabatic and side-heating test, J. Energy Storage 38 (2021) 102519

[6] T.D. Hatchard, D.D. MacNeil, A. Basu, J.R. Dahn, Thermal model of cylindrical and prismatic lithium-ion cells, J Electrochem Soc 148 (2001) A755-A761

[7] Y. Wang, D. Ren, X. Feng, L. Wang, M. Ouyang, Thermal kinetics comparison of delithiated LiNMC cathodes, J. Power Sources 514 (2021) 230582.

[8] J. Xu, C. Lan, Y. Qiao, Y. Ma, Prevent thermal runaway of lithium-ion batteries with minichannel cooling, Appl Therm Eng, 110 (2017) 883-890.

[9] G. Offer, Y. Patel, A. Hales, L. Diaz, M. Marzook, Cool metric for lithium-ion batteries could spur progress, Nature 582 (2020) 485-487.

[10] P. Zhao, A. Garcia, T. Burton, Initiation and propagation of curved reaction front in solids: Insights into solid combustion and battery thermal runaway, Combust. Flame 238 (2022) 111951

[11] D. Ren, X. Feng, L. Lu, M. Ouyang, S. Zheng, J. Li, et al. An electrochemical-thermal coupled overcharge-to-thermal-runaway model for lithium ion battery, J Power Sources, 364 (2017), pp. 328-340

[12] Z. Jia, P. Qin, Z. Li, Z. Wei, K. Jin, L. Jiang, Q. Wang, Analysis of gas release during the process of thermal runaway of lithium-ion batteries with three different cathode materials, J. Energy Storage 50 (2022) 104302.

[13] D. Mishra, K. Shah, A. Jain, Investigation of the impact of flow of vented gas on propagation of thermal runaway in a Li-ion battery pack, J. Electrochem. Soc. 168 (2021) 060555.

[14] Q. Wang, P. Huang, P. Ping, Y. Du, K. Li, and J. Sun, Combustion behavior of lithium iron phosphate battery induced by external heat radiation, Journal of Loss Prevention in the Process Industries 49 (2017) 961-969.

[15] T.D. Hatchard, D.D. MacNeil, D.A. Stevens, L. Christensen, and J. R. Dahn, Importance of heat transfer by radiation in li-ion batteries during thermal abuse, Electrochemical and Solid-State Letters 3, no. 7 (2000), 305.

10   L. Zhang, Y. Chen, H. Ge, P. Zhao

[16] J. Fang, J. Cai, and X. He, Experimental study on the vertical thermal runaway propagation in cylindrical Lithium-ion batteries: Effects of spacing and state of charge, Appl Therm Eng, 197 (2021) 117399.

[17] Z. Tang, A. Song, S. Wang, J. Cheng, and C. Tao, Numerical Analysis of Heat Transfer Mechanism of Thermal Runaway Propagation for Cylindrical Lithium-ion Cells in Battery Module, Energies 13, no. 4 (2020) 1010.

[18] W. Yan, Z. Wang, and S.Chen, Quantitative analysis on the heat transfer modes in the process of thermal runaway propagation in lithium-ion battery pack under confined and semi-confined space, International Journal of Heat and Mass Transfer 176 (2021) 121483.

[19] D. Mishra, A. Jain, Multi-mode heat transfer simulations of the onset and propagation of thermal runaway in a pack of cylindrical Li-ion cells, J. Electrochem. Soc. 168 (2021) 020504.

[20] L. Zhang, P. Zhao, M. Xu, X. Wang, Computational identification of the safety regime of Li-ion battery thermal runaway, Applied Energy 261 (2020) 114440.

[21] P. Zhao, L. Liu, L. Zhang, Y. Chen, Mitigating battery thermal runaway through mild combustion, Chem. Engr. J. Adv. 9 (2022) 100208.

Battery System Lumped Thermal Model for Efficient Temperature Prediction

Hyunjun Jang, Byungsoo Park, Taewoo Kang, JaeShin Lee, WooSung Kim

150, Hyundaiyeonguso-ro, Namyang-eup, Hwaseong-si, Gyeonggi-do, Korea

E-mail: hjjang@hyundai.com
Telephone: +(82) 31 368 7268

Abstract. Lithium-ion battery is most often used in xEV. Its degradation is basically affected by the level of temperature. Thus, it is an crucial factor considered in order to analyze the heat generation characteristic in the battery system control. In particular, energy density of the battery and the performance needed in electric vehicle rapidly increase in response to the demand of extending available driving distance through short-time charging. Internal heat generation density of the battery system also increases as a result, which causes the temperature increase of the PE(Power Electric) system. The main objective of this research is to create thermal model by focusing on the critical variables which affects battery system temperature. Battery system lumped thermal model focuses on cooling-related factors and cell heat generation which are major elements of temperature estimation. It is a simple model using a few variables, but it can estimate the battery system temperature with high accuracy.

1. Introduction

Recently, automobile companies develop products based on eco-friendly energy to cope with global environmental regulations and the exponential growth of the xEV markets. [1] In addition, the demand and the importance of high voltage battery increases. This is mainly because battery system can determine more than 40% of the price and core performance of xEV.[2]

Since a large-capacity lithium ion battery most frequently used in an eco-friendly vehicle depends on a state of health (SOH) and system safety according to a temperature management capability, a temperature analysis for a heat generation characteristic should be considered in designing and controlling a battery system.[3] The system internal temperature caused by the battery's own heating can reach 50℃ or higher depending on the outside environment.[3] For continuous use under high load conditions, such as fast charging, or severe driving, thermal management performance has a fatal effect on the battery life and system availability.

In particular, the energy density of battery system increases and the performance of xEV improves fast in response to the demand for the continuous improvement of the drivable distance when charging in a short time. As a result, the heating density inside the battery system increases, which also increases the temperature of the PE system. [4]

In order to control the temperature to maintain optimal performance based on heat-related information of the battery system of an electric vehicle, the temperature should be efficiently managed and controlled with Battery Thermal Management System (BTMS).[5] Predicting the battery temperature in advance is essential for the efficient management of the battery system. Previous studies conducted temperature estimation by interpreting the physical properties of materials in a battery cell unit based on physical formulas[6] [7] [8] However, at the system level, there is a limitation to implement it due to the large error and high complexity caused by the thermal characteristics of various electronic components.[9]

Therefore, this paper aims to develop a model through a several test in a battery system unit that may perform temperature prediction faster and more efficiently than previous complex models based on a lumped parameter model. This model is developed through the Thermal RC model based on thermal capacity and thermal resistance to predict the heating value and internal temperature distribution of a battery.

The heating characteristics of the battery are closely related to the remaining capacity and the changes in electrochemical characteristics. And experiments through actual vehicles to identify heating properties need enormous time and cost. To solve these problems, concentrated variables representing the thermal characteristics of the battery system were used in the experiments, resulting in the model with lower complexity but higher accuracy. The temperature estimation of the model proposed in this paper is analyzed according to the cooling water temperature of the water-cooled cooling battery system, EWP(Electric Water Pump) LPM(Liter Per Minute) and the ambient air temperature.

In the paper, the parameters of the suggested thermal model and the degree of heat generation are estimated by a Constant Current test on a battery system basis. A high accuracy temperature estimation model is constructed by placing a heat correction coefficient in order to reflect the various heat generation characteristics by SOC(State Of Charge) and current load. To verify the temperature estimation accuracy of the proposed thermal model, the battery system temperature was measured with a temperature sensor according to an irregular current sequence and the temperature estimated model was verified as RMSE(Root Mean Square Error), MAE(Mean Absolute Error), and maximum error.

2. Battery Cell Electrical Model

Battery system is the most important element in PE components that require thermal management, and battery cells have complex structures connected through various electrical components. Therefore, accurate modelof the operation and heat generation of the battery cell and the smallest unit of the battery system are required for accurate temperature distribution estimation.

The electrochemical characteristics of the battery cells are designed as an equivalent circuit model using electrical components, and the response characteristics of the battery cell by the current load are analyzed through this model. In this study, a commonly used 2-RC equivalent circuit model is utilized to analyze the terminal voltage by current load for calculating the heat generation amounts to ensure the performance and reliability of the model.

2.1 Equivalent Circuit Model

The 2-RC equivalent circuit model in Fig. 1 consists of internal resistance (R_i), parallel polarization resistance (R_{pa}, R_{pb}), and capacitors (C_{pa}, C_{pb}) to reflect both no-load and load characteristics of the battery. Internal resistance refers to an Instantaneous electrochemical reaction and a contact resistance, and two parallel-connected resistance refers to voltage drop(V_{pa}, V_{pb}) due to polarization caused by an electrochemical reaction with a time delay. Two capacitors connected in parallel reflect the transient state characteristics due to the polarization. It means that they are effective resistances, activating and concentrating polarization.

HPPC(Hybrid Pulse Power Characterization) experiments extracts battery equivalent circuit model parameters [10] [11] [12], with which the model estimate OCV(Open Circuit Voltage) ,a major factor to calculate the battery cell heat generation with terminal voltage(V_t) and current(I) sensing data.
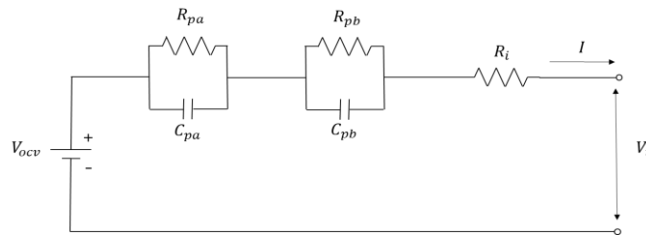
Fig. 1. Battery Cell Equivalent Circuit Model

2.2 Battery Cell Heat Generation Calculation

A polarized voltage by a current load is calculated by battery cell equivalent circuit model; the voltages for respective RC-parallel circuits are shown in the equations (1),(2). The equations can calculate the OCV of the battery cells. (3).

$$V_{pa}(t) = I * R_{pa} - I * R_{pa} * e^{\frac{-t}{R_{pa}C_{pa}}} \tag{1}$$

$$V_{pb}(t) = I * R_{pb} - I * R_{pb} * e^{\frac{-t}{R_{pb}C_{pb}}} \tag{2}$$

$$V_{ocv}(t) = V_t(t) + I * R_i + V_{pa}(t) + V_{pb}(t) \tag{3}$$

The internal heat generation of the battery cell($\dot{Q}_{cell}$) shows the amount of electrical loss generated during the power transmission process, as shown in equation (4).

$$\dot{Q}_{cell} = |(V_{ocv} - V_t)| * I \tag{4}$$

3. Battery System Lumped Thermal Model

To estimate battery system temperature, It needs various variables like resistance of various electrical components such as PRA(Power Relay Assembly), bus bars, structural characteristics of battery system, coolant temperature, and flow rate. In order to accurately estimate battery system temperature in the environment that takes into account various variables, experiments are conducted in BSA(Battery System Assembly) units to extract thermal parameters in Lumped Thermal Model. A factor highly correlated with the temperature of the battery system is extracted by correlation analysis based on the experimental data. The selected factor is called the concentrated variable; the thermal model is shown as Fig. 2 based on the concentrated variable.
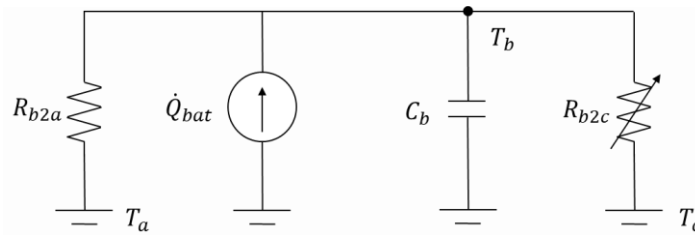
Fig. 2. Battery System Lumped Thermal Model

3.1 State Equation for Temperature Estimation

$\dot{Q}_{bat}$ indicates heat generation in the battery system, T_a is ambient air temperature, T_b is battery system average temperature and T_c is coolant temperature. C_b is the heat capacity of the battery system. A simple but accurate temperature estimation can be performed by representing various structural characteristic values of the battery system with a capacitor. R_{b2a} is the relationship between the battery system and the ambient air temperature. R_{b2c} is the relationship between the battery system and the coolant. The coolant flow rate is set to different variable resistance for each LPM because it greatly affects the temperature change of the battery system. Equation (5) refers to a state equation that estimates the temperature of the battery system through the proposed lumped thermal model.

$$\frac{dT_b}{dt} = \frac{\dot{Q}_{bat}}{C_b} - \frac{T_b - T_a}{R_{b2a}C_b} - \frac{T_b - T_c}{R_{b2c}C_b} \tag{5}$$

3.2 Battery System Heat Generation Calculation

To calculate the sophisticated battery system heat generation, an expression composed of a thermal correction factors (α, β, γ) are added to represent not only the cell's own heat generation but also the current load, SOC and the direct and indirect effects of electrical components in the battery system. The correction factor α represents the heat generation's correct value caused by various electrical components in the battery system. Battery cell have different resistance and heat generation values depending on the SOC. Correction factor β is applied to reflect this part in detail. Correction factor γ is applied to balance changes in battery system heat generation that can be caused by α and β. By applying the value of the thermal correction factor, the battery system temperature can be estimated with high accuracy in various complex situations.

$$\dot{Q}_{bat} = |(V_{ocv} - V_t) * I * (\alpha * I + \beta * SOC + \gamma)| \tag{6}$$

3.3 Model Parameter Estimation

Battery system-based experiments are conducted under various conditions to secure data for thermal parameter estimation. A gradient descent method is applied and this method is repeatedly performed with the temperature measured in the experiment to optimize the thermal parameters. Fig. 3 shows a parameter estimation flow chart.
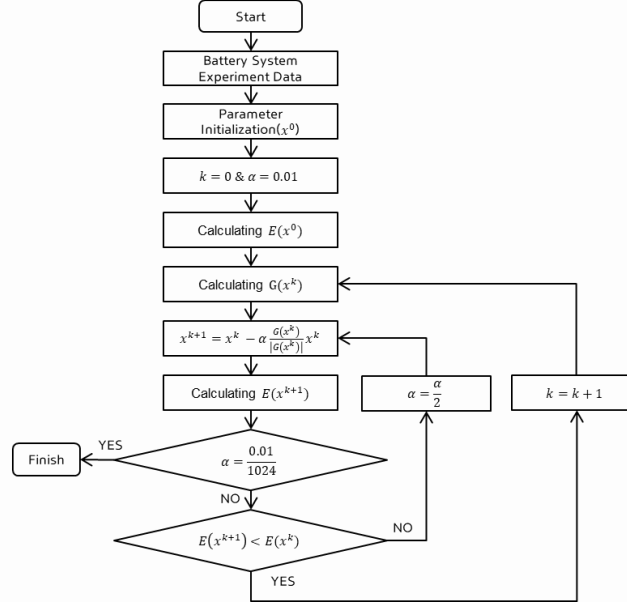
Fig. 3. Parameter Optimization Flow Chart

Equations (7)-(11) refer to a gradient descent algorithm process. k is the number of iterations of the algorithm, M is the total number of experiments used for optimization, and N is the total time of each experiment. It is optimized based on the parameter initial value x^0 and the optimization determination reference value α. The loss function for gradient descent is defined as the expected value of the difference between the estimated temperature of the model and the actual measured temperature for each experiment. If equation (10) is satisfied for each x_k, increase α. By repeating the above process, it is optimized completely when α reaches the target condition. In this study, the target condition is set to 10.

$$x^k = [x_1, x_2, x_3, x_4, x_5, x_6] = [R_{b2c}^k, R_{b2a}^k, C_b^k, \alpha^k, \beta^k, \gamma^k] \tag{7}$$

$$E(x^k) = \frac{1}{M}\sum_{m=1}^{M}[\frac{1}{N}\sum_{n=1}^{N}\{\hat{T}_{sys}^k(t_n) - T_{sys}(t)\}] \tag{8}$$

$$G(x^k) = diag(\frac{dE(x^k)}{dx_1}, \frac{dE(x^k)}{dx_2}, \frac{dE(x^k)}{dx_3}, \frac{dE(x^k)}{dx_4}, \frac{dE(x^k)}{dx_5}, \frac{dE(x^k)}{dx_6}) \tag{9}$$

$$E(x^k) > E(x^{k+1}) \tag{10}$$

$$\frac{G(x^k)}{|G(x^k)|} = diag(\frac{G(x^k)_{11}}{|G(x^k)_{11}|}, \frac{G(x^k)_{22}}{|G(x^k)_{22}|}, \frac{G(x^k)_{33}}{|G(x^k)_{33}|}, \frac{G(x^k)_{44}}{|G(x^k)_{44}|}, \frac{G(x^k)_{55}}{|G(x^k)_{55}|}, \frac{G(x^k)_{66}}{|G(x^k)_{66}|}) \tag{11}$$

4. Experiments

The experimental environment is shown in Fig. 4. ARBIN RBT is used to experiment with the battery system and the voltage range is up to 500V. Cells are lithium manganese nickel($LiNiMiCoO_2$) chemicals. It is a 400 voltage battery system and the chiller was used for coolant control.

Battery pack was soaked at the chamber temperature for more than 12 hours and the initial temperature and the chamber temperature were the same. Constant current experiments were conducted from 0.1C-rate to 1.5C-rate based on the battery system and the temperature data were secured by changing the ambient temperature and coolant LPM. The lumped thermal model parameter was estimated through the above experiments.

To verify the accuracy of the temperature estimation of the lumped thermal model, experiments were conducted under harsh conditions that continually change current and cooling conditions. In order

to confirm the situation similar to the actual vehicle, the CP(Constant Power) charging, step current charging and charge/discharge mixing profiles were selected as representative load profiles.
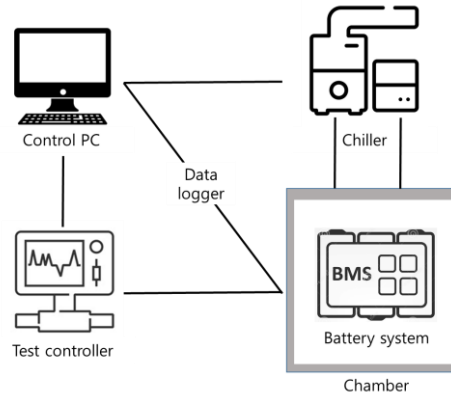
Fig. 4. Schematic of Experiment Environment

The coolant temperature is 293.15K. Constant current experiments are conducted to estimate the parameters of the lumped thermal model and are shown in Table 1. In the case of the experimental results of LPM and ambient temperature conditions, the temperature estimation and actual temperature of the lumped thermal model are shown in Fig. 5. The lumped thermal model parameters and thermal correction factors estimated through the above process is shown in Table 2. Each variable in the lumped thermal model has the same value depending on the state of the battery system and R_{b2c} is a variable that varies with coolant LPM.

Table 1. Temperature Estimation Performance under Constant Current Profile(15LPM)

LPM	Ambient Temperature[K]	C-rate	RMSE	MAX Error
15	303.15	0.1	0.3366	1.4460
		0.25	0.4452	1.0118
		0.5	0.5203	0.9410
		1	0.2540	0.4122
		1.25	0.3749	0.8268
		1.5	0.3624	0.6989
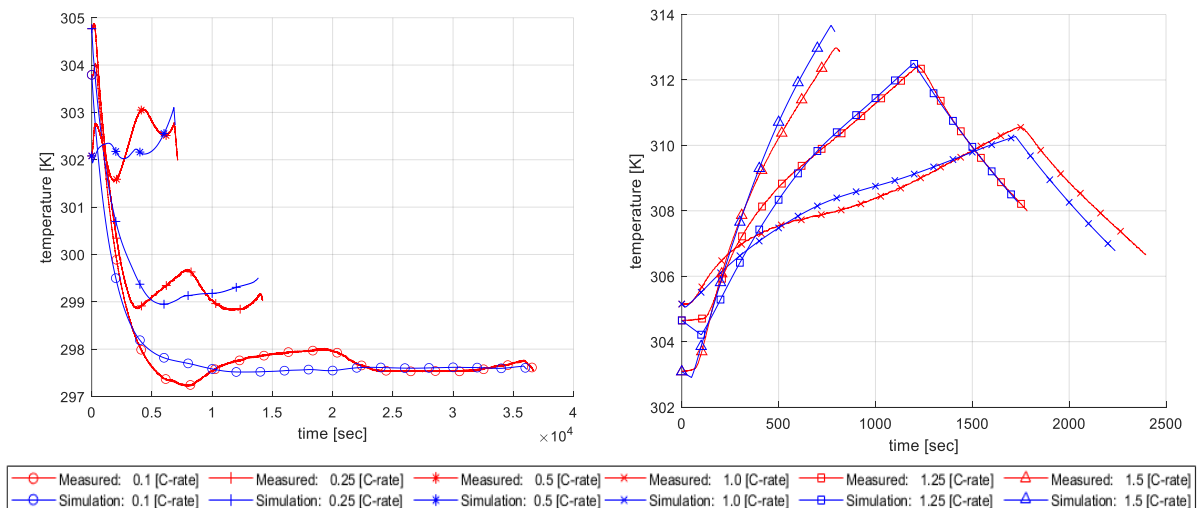
Fig. 5. Measured and Estimated Temperature in Constant Current Profile

Table 2. Parameters and Heat Correction Factors

LPM	R_{b2c}	R_{b2a}	C_b	α	β	γ
15	0.1514	0.3011	16468	9.7331e-06	1.3973e-04	-0.9412

5. Model Performance

The lumped thermal model completed through the constant current experiment is verified under for three load profiles used in actual vehicles.

First, the temperature estimation performance is verified when the current is continuously changed. Check the temperature estimation accuracy in the load profile as shown in Fig. 6. The coolant flow rate is 25LPM and the ambient temperature is 304.5K and 315.7K. The verification results are shown in Fig. 7 and Table 3.
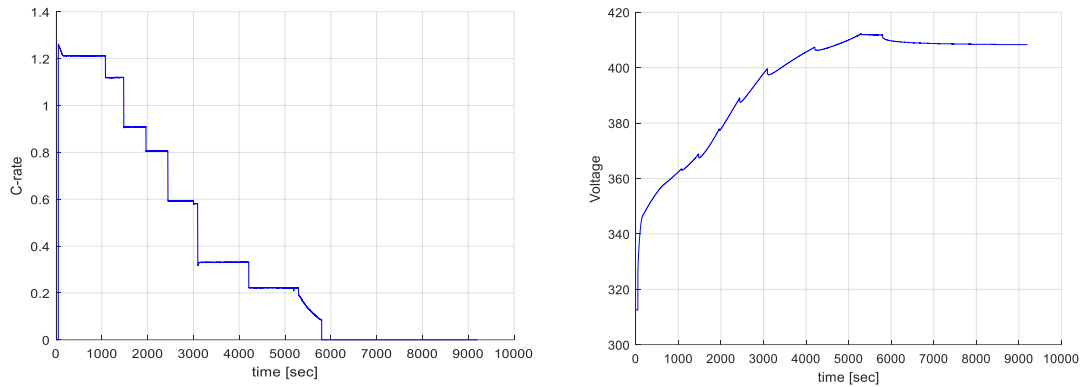
Fig. 6. Step Current Charging Profile

Measured: Step Charge   Simulation: Step Charge
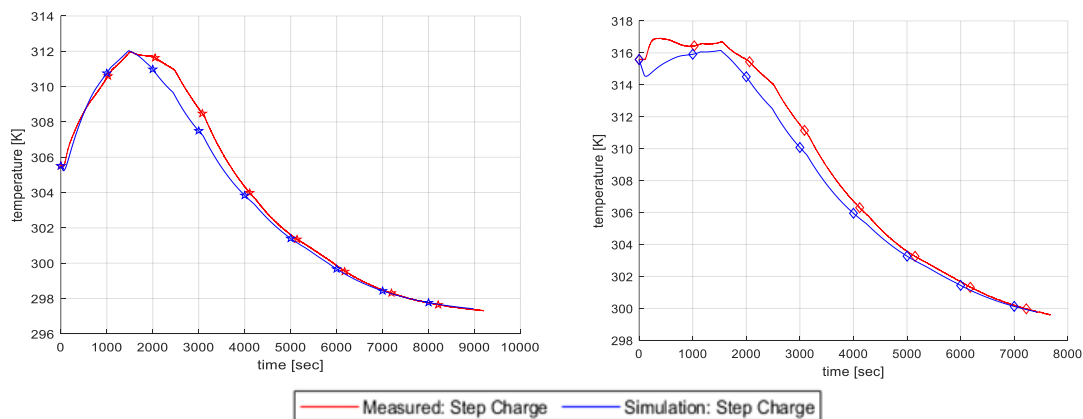
Fig. 7. Model performance at Fixed Coolant LPM (Left:305.4K, Right:315.7K)

This model was verified even under harsh conditions that continuously change current and LPM at the same time. In the load profile as shown in Fig. 6, the experiment was conducted by repeatedly changing 15LPM/25LPM every 600 seconds. The results are shown in Fig. 8 and Table 3.

Measured: Step Charge   Simulation: Step Charge
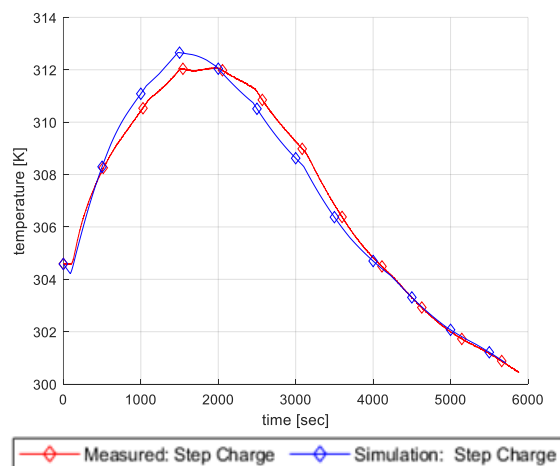
Fig. 8. Model performance at Changing Coolant LPM(15/25LPM)

Table 3. Temperature Estimation Performance under Variable Charging Current Profile

LPM	Ambient Temperature[K]	RMSE	MAX Error
25	305.4	0.4225	1.2105
25	315.7	0.7159	2.0136
15/25	304.6	0.3632	0.6534

Secondly, the temperature estimation performance is verified for the CP charging profile as shown in Fig. 9. The coolant flow rate is 15LPM and the ambient temperature is 313.15K. The verification result is shown in Fig. 10 and Table 4.
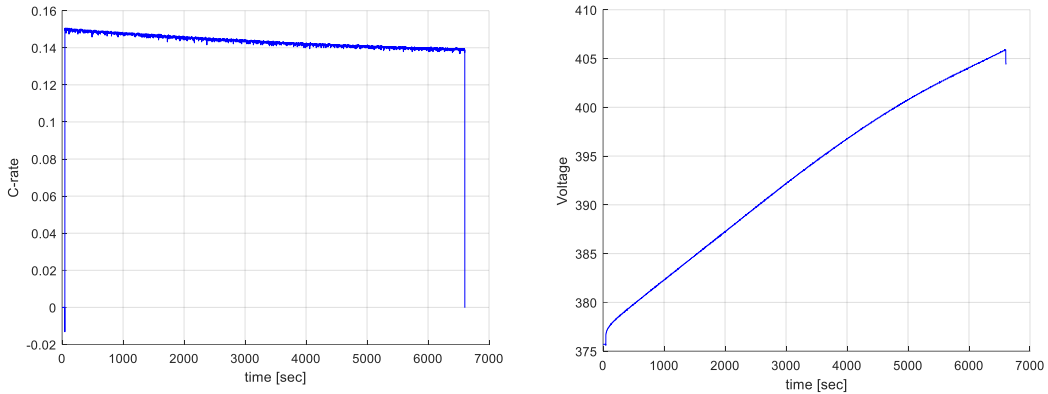
Fig. 9. Constant Power Charging Profile
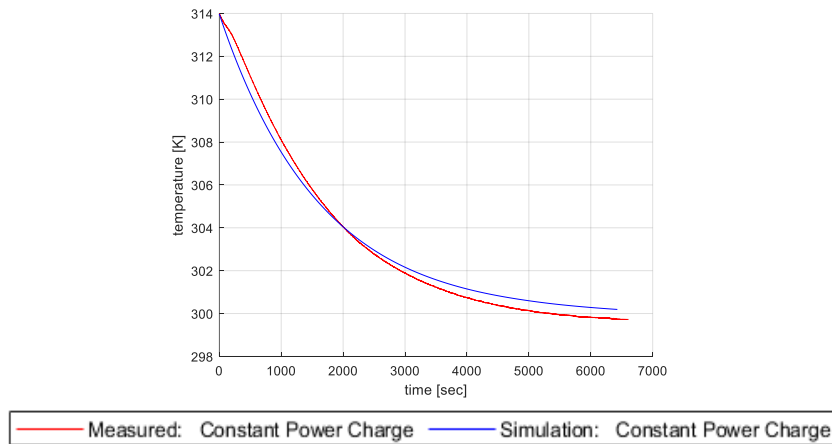
Fig. 10. Model performance at Constant Power Charging Profile

Third, the temperature estimation performance is verified for the charge/discharge mixing profile as shown in Fig. 11. The coolant flow rate is 15LPM and the ambient temperature is 305.65K. the verification results are shown in Fig. 12 and Table 4.
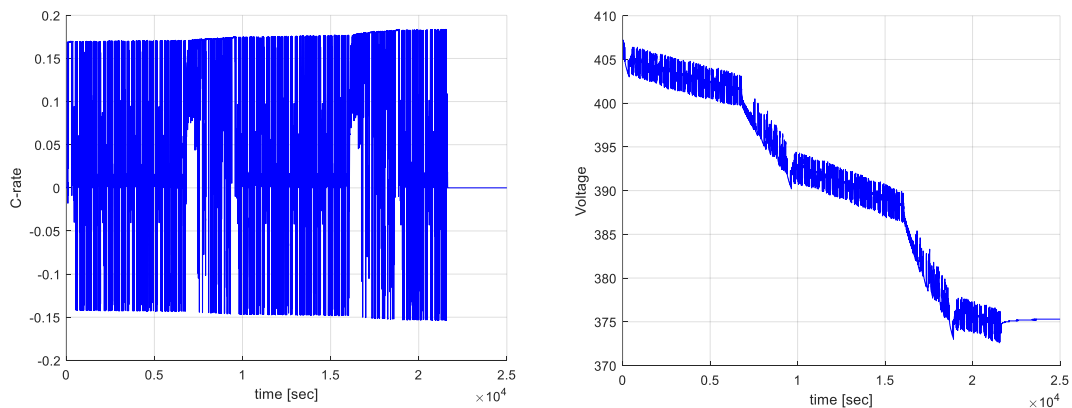
Fig. 11. Charge/Discharge Mixing Profile
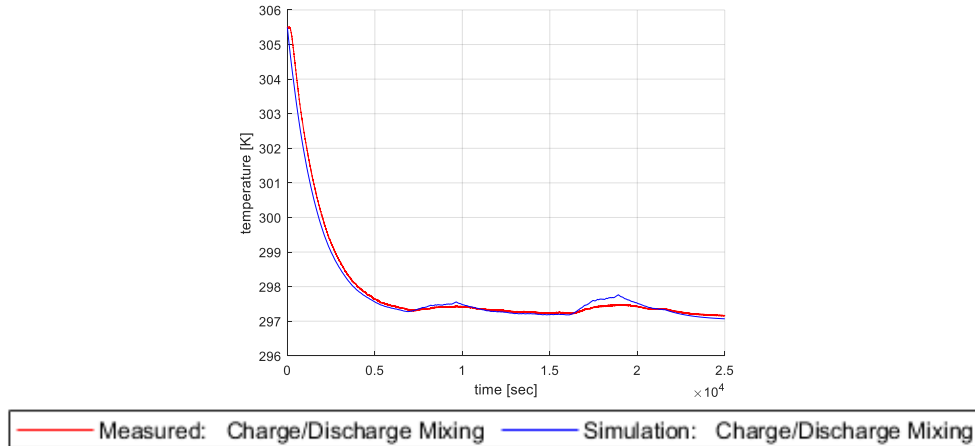
Fig. 12. Model performance at Charge/Discharge Mixing Profile

Table 4. Temperature Estimation Performance under CP and Discharging Profile.

Test	LPM	Ambient Temperature	RMSE	MAX Error
Constant Power	15	313.15	0.4554	0.7784
Charge/Discharge	15	305.65	0.1347	0.8986

Conclusions

In the paper, the study shows the lumped thermal model without complex equations through several simple experiments. The model has RMSE 0.4K to 0.7K for a step charging current profile and high accuracy. In the case of the experiment that simultaneously changes the current and coolant LPM, the performance was verified with RMSE 0.3632K and the maximum error 0.66K. In addition, the CP charging profile that may occur when charging through AC-DC converter in an actual vehicle and the charge/discharge mixing profile that occurs during driving were verified. As a result, constant power profile is RMSE 0.4554K, Maximum Error 0.7784K, charge/discharge mixing profile RMSE 0.1347K, and Maximum Error 0.8986K. In conclusion, the lumped thermal model proposed in this paper is a simple but a highly accurate model.

In the study, a concentrated variable-based temperature estimation model was designed to efficiently estimate the temperature of the battery system. A high-precision temperature estimation model is designed by analyzing the major factors affecting battery system temperature by dividing them into numbers in various cases by simple experiments and extracting thermal parameters by numerical analysis optimization techniques.

The methods proposed in this paper include not only electrical models for battery cells, but also a variety of design factors such as electrical component resistances of battery system, coolant temperature, and flow rate. A battery system temperature can be easily estimated without electrochemical analysis of battery cells and complex processes of physical property values and physical analysis bases for various components in the battery system. Prior researches has a limitation that if the chemical changes in the battery cell, the thermal model must be re-modeled from the battery cell. However, since the lumped thermal model proposed in the paper models battery system itself, so it is not sensitive to changes in battery cell chemical elements and it is easy to implement. Even considering BMS specifications for mass-production vehicles, it is fast and simple enough to apply.

The expected work is to design a robust battery management system (BMS) logic that increases the stability and reliability of battery systems by flexibly controlling temperature changes expected during driving or charging a vehicle. That is, by predicting the temperature of the battery system, the battery power and available energy may be flexibly controlled to alleviate the battery degradation problem. The proposed model can be used for battery safety diagnosis. It is possible to infer that there may be an abnormal heat source when a sensor measures a temperature that exceeds a threshold value relative to a model estimated value in a specific current sequence.

References

1. IEA, Global EV Outlook 2019, International Energy Agency, Paris, 2019.

2. ICCT, Update on electric vehicle costs in the united states through 2030, International Council on Clean Transportation, 2019.

3. Q.Xie, J.Kim, Y.Wang, D.Shin, N.Chang, and M. Pedram, "Dynamic thermal management in mobile devices considering the thermal coupling between battery and application processor," in Proc. Of ICCAD, pp.242-247, Nov. 2013,

4. A. Pesaran, A. Vlahinos, and S. Burch, "Thermal performance of EV and HEV battery modules and packs, "in Proc. Of the 14th International Electric Vehicle Symposium, 1997.

5. A. Pesaran, "Battery Thermal Management in EVs and HEVs : Issues and Solutions, "in Adv. Automotive Battery Conf., February 2001.

6. R. Rizk, H. Louahlia, H. Gualous, P.Schaetzel, "Experimental analysis and transient thermal modeling of a high capacity prismatic lithium-ion battery," in Int .Commun. Heat Mass Trasft., vol. 94, pp.115-125, May 2018.

7. N. Damay, C. Forgez, M. -P. Bichat, and G. Friedrich, "Thermal modeling of large prismatic LiFePO4/graphite battery .Coupled thermal and heat generation models for characterization and simulation," Journal of Power Sources, vol. 286, no. Supplement C, pp.37-45, Jun. 2015

8. D Shin, S. W. Chung, E. Chung and N. Chang, "Energy-Optimal Dynamic Thermal Management : Computation and Cooling Power Co-Optimization," in IEEE Transactions on Industrial Informatics, vol.6, no. 3n 99. 340-351, Aug.2010.

9. Byung-Soo. Park, "Lumped-parameter model for battery thermal management system in EV and energy optimization" Korea Advanced Institute of Science and Technology;2021.

10. L. Zhang, H. Peng, Z. Ning, Z. Mu, and C. Sun, "Comparative Research on RC Equivalent Circuit Models for Lithium-Ion Batteries of Electric Vehicles," Applied Sciences, vol.7, Sept. 2017.

11. S. Jiang, "A Parameter Identification Method for a Battery Equivalent Circuit Model," SAE International, April 2011.

12. M. Hossain, S. Saha, M. E. Haque, M. T. Arif and A. Oo, "A Parameter Extraction Method for the Thevenin Equivalent Circuit Model of Lithium-ion Batteries," 2019 IEEE Industry Applications Society Annual Meeting, 2019, pp. 1-7, doi: 10.1109/IAS.2019.8912326.

THIESEL 2022 Conference on Thermo- and Fluid Dynamics of Clean Propulsion Powerplants

Energy Consumption of Mobile Air-Conditioning Systems in Electrified Vehicles under Different Ambient Temperatures

S. Gil-Sayas[1], G. Di Pierro[2], A. Tansini[2], S. Serra[2], D. Currò[3], A. Broatch[1], G. Fontaras[2*]

[1]CMT – Motores Térmicos. Universitat Politècnica de València. Camino de Vera s/n, E-46022 Valencia, Spain.

E-mail: abroatch@mot.upv.es
Telephone: +(34) 963 877 650

[2]Joint Research Centre, European Commission. Ispra, Italy

*Correspondence: georgios.fontaras@ec.europa.eu

[3]Piksel s.r.l. Milano, Italy

Abstract. In 2019, passenger car CO_2 emissions peaked at 3.2 billion metric tons globally. Despite efforts to curb vehicle CO_2 emissions and the ambitious targets adopted for greenhouse gas mitigation in the European Union (EU), emissions from road vehicles increased steadily over the past decade. Electrified vehicles have gained significant market share in the last years and are an essential technical option to reduce CO_2 emissions. Range anxiety and insufficient charging infrastructure limit electrified vehicles' customer acceptance and market attractiveness. The use of auxiliary systems under certain circumstances may reduce vehicle range. In this regard, energy management improvements lead to better vehicle range results. As well-considered in numerous studies, the most consuming auxiliary system is the vehicle's heating, ventilation, and air-conditioning (HVAC) system, also known as Mobile Air-Conditioning (MAC) . The present work explores the influence of different parameters on the energy consumption of the MAC system in plug-in hybrid vehicles (PHEV) and battery electric vehicles (BEV). For this purpose, one PHEV and one BEV were tested in laboratory conditions at different cell temperatures of -7ºC (19.4ºF), 22ºC (71.6ºF) and 35ºC (95ºF), over the Worldwide Harmonised Light vehicle Test Cycle (WLTC). Laboratory tests with the same conditions were repeated with MAC on and off for each temperature. For the reference 23ºC (73.4ºF) condition, additional factors affecting energy consumption were analysed, such as the impact of depleting/sustaining modes on the MAC performance in PHEV, or the effect of warm and cold start in PHEV and BEV. Results suggest that the electric energy required to heat the cabin at low temperature (-7º) could be 4 to 10 times higher than the energy needed to cool down the cabin in hot conditions (35ºC). Compared to the vehicle energy required at the wheels during a WLTC, the MAC impact at -7ºC ranges from 35% to 45% while at 35ºC goes from 15% to 18%.

1. Introduction

In 2019, CO_2 emissions from passenger cars led to 3.2 billion metric tons globally. During the past decade, emissions from road vehicles have increased steadily [1], [2] regardless of the efforts to curb vehicle CO_2 emissions with the ambitious targets adopted for Greenhouse Gas (GHG) mitigation in the European Union (EU). Also in 2019, road transport represented the highest share of the whole transport emissions, with 72% of all domestic and international transport GHG emissions [3]. The transport sector accounts for about one-fourth of the European Union's GHG emissions. In these circumstances, the European Commission (EC) has published a "Roadmap to a Single European Transportation Area" [4], listing different objectives to be achieved in the following decades, such as the reduction of CO_2 emissions in 55% compared to the levels of 1990 by 2030. The European Parliament has approved the plan to reach zero-emissions road mobility by 2035 [5]. More in detail, the European Union (EU) has set stricter CO_2 emissions targets for the next years, demanding, for newly registered passenger cars, a 15% and a 37.5% reduction in 2025 and 2030, respectively, concerning the 2021 levels [6]–[8].

Consequently, the newly introduced regulations have required vehicles to achieve higher fuel economy. This is pushing manufacturers to improve not only the powertrain efficiency [9], but also working

on other components and systems in the vehicle [10]. Powertrain electrification has been seen as a key solution in fleet decarbonisation with the development of Hybrid Electric Vehicles (HEVs), Plug-in Hybrid Electric Vehicles (PHEVs) and Battery Electric Vehicles (BEVs) [11]–[13]. Electrified vehicles have gained significant market share in the last years and are an essential technical option to reduce CO_2 emissions [14]. However, powertrain electrification comes with a higher level of complexity due to the cohabitation of more power sources and numerous components [15], [16]. For example, using auxiliary systems under certain circumstances may reduce vehicle range, e.g., the mobile air conditioner (MAC), one of the largest power consumers [17]. Differently from conventional ICE vehicles, in which the A/C compressor is driven as an engine accessory and wasted heat can be recovered for cabin conditioning, the energy consumption from the heating, venting, and conditioning (HVAC) system significantly influences the fuel economy and the driving range of BEVs and PHEVs [18].

Especially in very low-temperature conditions, BEVs are seriously affected by using high-voltage positive thermal coefficient (HV-PTC) resistive heaters to heat the cabin and the powertrain fluids [19]. Moreover, the BEV electric range can be reduced by up to 10–15% in warm ambient conditions and up to 60% in low-temperature situations according to literature [20], [21]. This is why increasing MAC efficiency has become a priority for automotive manufacturers to improve overall fuel economy [22] and manufacturers have made significant progress in many parts of the MAC system [23]. The European Commission is invenstigating the possibility of including MAC in the ECO-innovations scheme according to Regulation 2019/631/EU [24].

The present article focuses on evaluating the influence of various parameters on the energy consumption of the MAC system in a C-segment plug-in hybrid vehicle (PHEV) and an SUV battery electric vehicle (BEV). In this regard, these two vehicles were tested in a dedicated laboratory with different conditions of cell temperatures, ranging from -7ºC (19.4ºF) to 22ºC (71.6ºF) and 35ºC (95ºF), over the Worldwide Harmonized Light-duty Test Cycle (WLTC). The same laboratory test conditions were repeated with MAC on and off to perform a sensibility analysis. Moreover, additional factors were considered, such as the influence of the impact of driving in depleting/sustaining mode for the PHEV, the result of warm and cold start, and the investigation of the electric heater's performance. Unfortunately, numerous studies available in the scientific community are investigating the impact of HVAC in conventional ICE vehicles, and the same methodology is hard to apply to PHEVs and BEVs [26], [27]. As a further step, this work aims at building a testing procedure that can be set as a solid basis for the development of a standardised test procedure for the assessment of the energy consumption and CO_2 emissions related to the deployment of the MAC system in electrified vehicles.

This paper is organised into three sections. The specifications of the two vehicles are defined in Section 2, along with the instrumentation implemented on-board and the test protocol followed in the laboratory. In Section 3, the breakdown of the testing campaign is outlined and discussed. Finally, Section 4 provides the work conclusions and a discussion about future work.

2. Methodology

2.1 Test Vehicles

The vehicles under investigation are two new cars in the European market: a Euro 6 Gasoline Plug-in Electric Vehicle and a Battery Electric Vehicle. The PHEV is a 5-seat C-segment car. The powertrain features a 1.4-litre direct-injection gasoline engine and a six-speed Dual-Clutch Transmission (6-DCT). The P2 electric motor (EM) is coaxially placed before the transmission and linked to the ICE by a mechanical clutch. The BEV is a 5-seat D-segment SUV, a 4WD BEV capable of driving 400 km on a single charge. The powertrain features two Permanent Magnet (PM) synchronous electric motors, one per axle. The vehicle fits a single-speed automatic transmission. The main specifications of the two vehicles are listed in Table 1.

Regarding the object of this study, both vehicles are equipped with an HVAC system used to control the fan speed and the cabin temperature. As for the PHEV, the HVAC system consists of a conventional heater/blower unit, supplemented by an HV electric A/C compressor and an electric heater, also referred to as Positive Temperature Coefficient (PTC) heater. In this layout, the compressor and heater draw their electric power directly from the high voltage system of the car. The outlet temperature is continuously adjusted by mixing hot and cold air. As far as the BEV is concerned, the HVAC system consists

of an HV electric A/C compressor and an electric PTC heater; in this case, the entire system draws energy from the main HV traction battery.

Regardless of the powertrain specifications and configuration, the HV systems can be simplified considering that the energy stored in the main HV traction battery is either used for propelling the vehicle by the EM(s), to power the MAC components like heater (PTC) and cooler (A/C compressor), to feed the LV system of the vehicle through the DC/DC converter or to feed the rest of HV loads (hereafter named HV others, not related to any of the previous consumers). To this extent, the power balance equation enables to calculate of the quantities not measured as follows:

$$P_{HV\ Battery} = P_{Motor(s)} + P_{MAC} + P_{DC/DC} + P_{HV} others \qquad (1)$$

Table 1. *Vehicles specification*

	PHEV	BEV
Segment	C	D-seg SUV
Curb Weight	1590 kg	2138 kg
Configuration	Front-Wheel Drive (FWD)	Four-Wheel Drive (4WD)
ICE	1.4l Turbo Gasoline	-
Power/Torque	110 kW / 250 Nm	-
EM Type	PM Synchronous motor	2x PM Synchronous motor
Max Power / Max Torque	80 kW / 350 Nm	198 kW / 580 Nm
Gearbox	6-DCT	Automatic
Final Drive (FD)	-	Single-speed 9.05
Battery Type	Lithium-ion NCM	Lithium-ion
Rated Voltage	350V	350V
Capacity	13 kWh / 37Ah	75.7 kWh / 216 Ah

2.2 Vehicle Instrumentation

These vehicles were tested on a four-wheel-drive (4WD) chassis-dynamometer, made of two axes of 300 kW each, with a maximum speed of 260 km/h and acceleration of ±10 m/s^2. The facility is the Vehicle Emission LAboratory (VELA) of the European Commission Joint Research Centre (EC-JRC) in Ispra, Italy. It has a climatic chamber suitable for testing all kinds of Electric Vehicles (EVs) and HEVs from -30 °C to +50 °C under controlled humidity, providing access to numerous types of scientific instrumentation. In this regard, measurements such as vehicle speed, forces from the dyno, ambient pressure, temperature and humidity, GHG emissions, and On-Board Diagnostics (OBD) data can be recorded during testing. The OBD is a standardised way to connect to the vehicle's self-diagnostics system and communicate with the vehicle's control units [28]. The laboratory is equipped with a data logger for the real-time acquisition of signals from the measurement devices available. A precision power analyser is used for the electrical components during this test campaign.

This work adopted three solutions: extended Parameter IDs (PIDs) OBD logging, Controller Area Network (CAN) data logging and actual electrical and thermal measurements using current clamps, voltage probes and thermocouples that are all connected to the power analyser. Collecting all the necessary instantaneous measurements is a key step to characterise the powertrain operation, reconstructing the energy flow, and analysing the impact of the MAC system on the overall energy consumption, assuming that the MAC power is the sum of the individual powers of the heater and the cooler.

Integrating different types of measurements allowed the authors to acquire variables that would be impossible to measure with conventional measurement techniques. Moreover, it gave better context to the measured data, creating redundancy for validating physically measured signals when affected by measurement issues. In this context, the measurement chain could acquire several signals at an appropriate sampling frequency (10Hz).

As previously mentioned, this activity counts on the acquisition of the main electrical and thermal quantities. In this regard, the schematic of the vehicles under investigation and the electrical instrumentation are depicted in Figure 1 and Figure 2; for the sake of brevity, only the relevant components to this analysis are shown. Regarding the acquired data, a general overview of the time series recorded during the experiments is presented in Table 2 In general, the energy consumption analysis relies on the electrical quantities such as current and voltage for the:

- HV Battery
- Electric Machine (EM)
- DC/DC converter from High-Voltage to Low-Voltage
- HVAC system

Regarding the PHEV instrumentation, data were recorded from different channels such as the OBD and a power analyser, using zero-flux current clamps and voltage probes. The P2 propulsion EM current was measured with a dedicated clamp. On the LV side, the DC/DC converter current was recorded and constant conversion efficiency of 92.5% [29] was assumed to calculate the electric load on the HV side. The voltage and current of the HV battery were both measured and read via the OBD channel, together with the overall current going to the MAC components. In this case, the A/C compressor current (cooler) was also recorded but only used as a flag signal to validate its activation/deactivation status.

As for the EV, data were collected also from the OBD and a power analyser with zero-flux current clamps and voltage probes. The front and rear propulsion EMs current were measured using two clamps. The LV side of the DC/DC converter was also physically measured, and a constant efficiency of 92.5% was used to calculate the electric load on the HV side. The voltage and current of the HV battery were both measured and read via the OBD channel, as well as the A/C compressor current. For this vehicle, it was not possible to instrument the heater due to time and technical restrictions, but a work-around was used, and its power consumption was calculated by subtraction from the power balance in Equation 1.

Moreover, on the OBD communication channel, it was possible for both vehicles to record vehicle speed, ambient temperature, battery State of Charge (SoC) and battery temperature.

Table 2. Time-series recorded from the experiments

	PHEV	EV
Battery voltage and current	◍	◍
SoC	◍	◍
Motor voltage and current	◍	◍
Motor torque and speed	◍	◍
ICE torque and speed	◍	
Heater voltage and current	◍	
Cooler voltage and current	◍	◍
DC/DC voltage and current	◍	◍
Ambient temperature	◍	◍
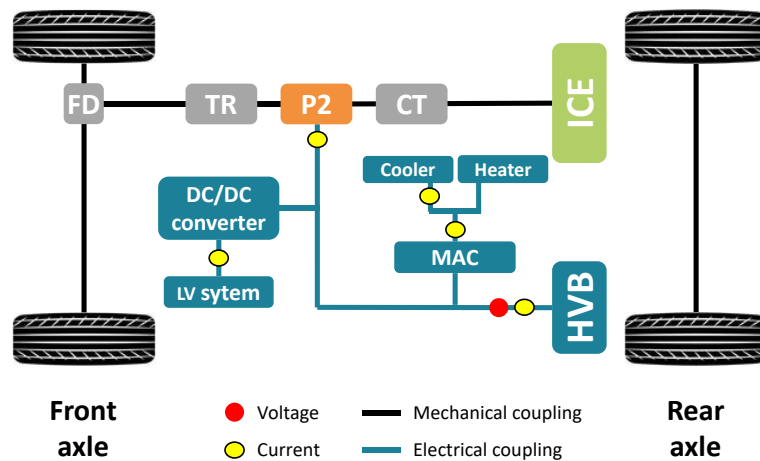
Figure 1. PHEV - Powertrain layout with instrumentation details
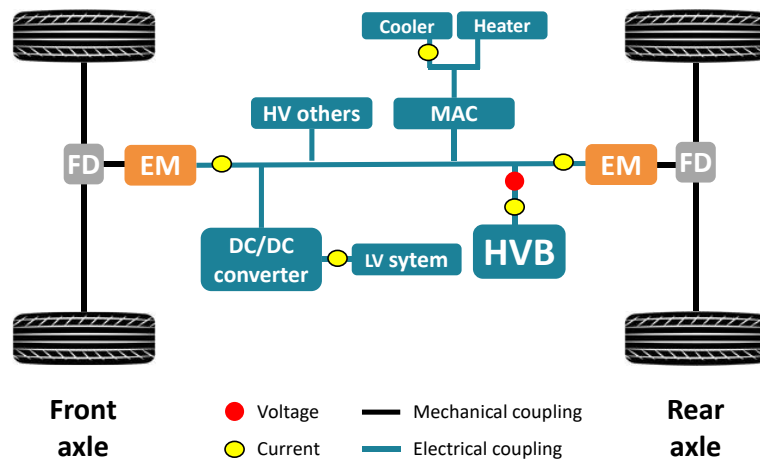
Figure 2. BEV - Powertrain layout with instrumentation details

All the data gathered during the testing campaign can be stored in the power analyser or recorded in real-time by the laboratory software. As far as the cabin thermal acquisition is concerned, the authors followed some of the specifications described in the European MAC draft test procedure [30] in placing the thermal sensors around the vehicle cabin as illustrated by the dots in Figure 3; via the laboratory logger system, temperature data were synchronised to all the other signals. As depicted in the scheme below (Figure 3), thermocouple number 1 is placed close to the front blower on the passenger side; number 2 is positioned on top of the ceiling between the front seats, and numbers 3 and 4 are on the back of the front-seat headrests, while number 5 and 6 are placed respectively on the ceiling in the back and in between the back seats at passenger level.

2.3 Test Procedure

The impact of the MAC system on two different vehicles was evaluated by chassis-dyno testing. In this regard, the Road Load (RLs) coefficient was determined according to the Worldwide Harmonized Light-duty Test Procedure (WLTP) regulations [31], [32]: Table 3 reports the adopted values. The WLTC for LDVs [33] was adopted as a reference cycle to determine the energy and fuel consumption of the HVAC system. It is characterised by four phases: low, medium, high and extra-high speed. These phases represent urban traffic, mixed conditions and highway conditions, respectively.

Later, the vehicles were tested at three different laboratory temperatures: −7 °C, 23 °C and 35 °C. Such temperatures were chosen because 23 °C is the reference temperature adopted for the Type 1 test for Light-Duty Vehicles (LDVs) type approval in Europe; −7 °C is the temperature chosen during the cold temperature procedure in different regions of the world, such as the EU, USA, China and Korea

[34]–[37], while 35 °C was chosen as it represents an extremely high ambient temperature according to the SAE Recommended Practice outlined in the SAE International Standard J1634 [38].

Even though low-temperature emission type-approval testing in EU (Type 6 test) is carried out without heating, the vehicles' performance was also analysed with the cabin air-conditioning system turned on and set at 22 °C. Likewise, vehicle testing at 35 °C was also performed with the air conditioning in cooling mode and set at 22 °C. All types of tests were performed with and without the usage of the HVAC system of the vehicle. When on, the A/C was set to automatic mode at a temperature of 22 °C, enabling the automatic control of the blower fan speed. For the BEV and the PHEV in Charge Depleting (CD) mode, at one given cell temperature, the high-voltage battery energy used from a cycle with MAC off was subtracted from the energy used during a cycle with MAC on. For the PHEV in Charge Sustaining (CS) mode, the fuel consumption was used instead of HV battery energy. The fuel consumed was transformed into electric consumption by considering the gasoline density (i.e., 743 g/l) and the efficiency of the gasoline turbo engine, the Willans' factor, (0.28 l/kWh) [39], as in Equation (2). The difference between energies from both cycles (with MAC on and MAC off) represents the impact of the MAC system in those conditions.

$$Electric\ consumption\ from\ fuel\ kW = \frac{Fuel\ consumption\ \frac{g}{s} * 3600\ \frac{s}{h}}{743\ \frac{g}{l} * 0.28\ \frac{l}{kWh}} \qquad (2)$$

Table 4 illustrates the details of the testing campaign performed on the two vehicles. For the PHEV, it was important to evaluate the MAC impact both in charge sustaining and charge depleting mode, while the BEV can only perform in pure electric mode. Hence, for each of the three cell temperatures mentioned before, a full day of testing was dedicated as described in the table. Due to the higher number of combinations for the PHEV, the first day was always carried out with MAC off and the second day with MAC on, before moving to the next temperature level. To completely understand the MAC consumption, cold-start tests were also carried out by monitoring the ICE/EM coolant temperature. In cold start tests, the coolant temperatures of the ICE and EM are very close to the laboratory cell temperature. Warm start tests were performed right after other tests; hence the coolant temperature of the ICE was around 87 °C. In the BEV tests, the authors considered warm start when the test was performed after another test, since the temperature of the electric machine was not monitored. The "forced cooling" time was introduced to speed up the cool-down of the powertrain fluids before starting a cold driving cycle. At the end of the day, the HV traction battery was recharged using electrical energy from the main grid.
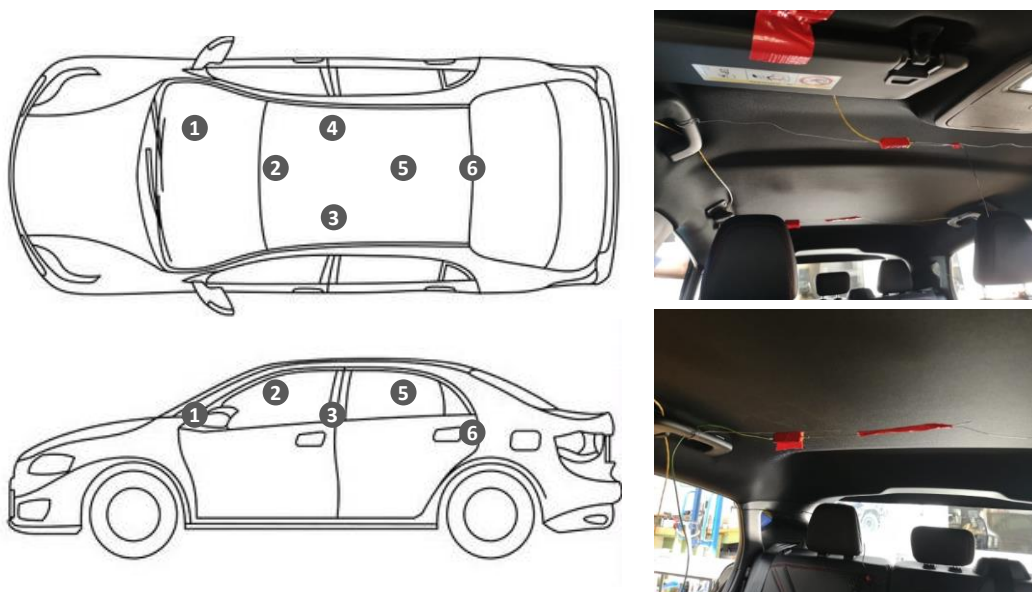
Figure 3. Cabin temperature sensor location: schematics (left) and examples (right)

Table 3. *Vehicle Road Loads and Test Mass for WLTC*

	PHEV	**BEV**
Test Mass [kg]	1698	2269
F0 [N]	115.5	196.2
F1 [N/(km/h)]	0.106	0.638
F2 [N/(km/h)^2]	0.03217	0.0378

Table 4. *Laboratory driving test schedule for PHEV and BEV at laboratory temperatures −7°C, 23°C and 35°C*

PHEV		BEV
MAC off	**MAC on**	**MAC on/off**
WLTC CD cold start	**WLTC CD cold start**	**WLTC MAC ON cold start**
WLTC CD warm start	**WLTC CD warm start**	
WLTC CS warm start	**WLTC CS warm start**	Forced Cooling
Forced Cooling	Forced Cooling	
WLTC CS cold start	**WLTC CS cold start**	**WLTC MAC OFF cold start**
WLTC CS warm start	**WLTC CS warm start**	**WLTC MAC ON warm start**
		WLTC MAC OFF warm start
Overnight HV battery charging	Overnight HV battery charging	Overnight HV battery charging

3. Results and Discussion

3.1. MAC energy demand

In this section, the energy impact of the MAC system is evaluated as a difference between the MAC ON and MAC OFF cases. Hence, for each vehicle and laboratory temperature, the points plotted in the following figures 4 - 6 represent the delta energy consumption measured while turning either on or off the conditioning system. The MAC energy demand during WLTC for the tested BEV is plotted in Figure 4, both in cold start (blue line) and warm start (red line) conditions. Comparing the two extreme points, the energy gap required for cabin heating at -7ºC is much higher than the energy for cooling the cabin at 35ºC, resulting in about six times higher energy demand in warm start and 4 times more in cold start. To this extent, the energy consumption decreases when the difference between the cabin set-point (i.e. 22ºC) and the cell temperature decreases. The energy demand at a cold start is higher than warm start conditions of about 0.2 and 0.3 kWh at -7ºC and 35ºC, respectively. As expected, the energy required by the MAC under ambient temperature operation at 23ºC is almost negligible, the small consumption seen is due to various 12V auxiliary loads.

Similarly, the PHEV in charge depleting (CD) mode presents a similar V-shape tendency as expected, since the PHEV with fully charged battery can complete the WLTC cycle without turning on the internal combustion engine, thus driving in full electric mode. As depicted in Figure 5, there is no concrete difference in 35ºC testing between warm and cold start conditions; while the energy demand between the cold and warm start at -7ºC is higher (about 0.9 kWh). Also, in this case, the energy required by the MAC at -7ºC is higher when compared to 35ºC, consuming about 5 times more in warm start and 10 times more in cold start. Due to time and laboratory issues, it was not possible to test this vehicle at 23ºC cell temperature, but the authors have decided to assume zero consumption for the MAC system (hence 0 Wh) for a visual analysis of the trend. The assumption is based on the fact that there is no delta between the external lab temperature and the cabin target temperature. It should be noted that the heat load introduced by the driver and measurement is assumed to the same over all test conditions and hence is not expected to affect the difference.

Figure 6 shows the energy gap required at different temperatures regarding the PHEV operation in CS mode. Additionally, in this situation, the vehicle was tested at 7ºC and 28ºC and there is some substantial difference that can be highlighted. Generally, also in this case, it can be seen that the energy consumption decreases when the difference between the cabin set-point (i.e. 23ºC) and the cell temperature decreases. The energy required at 35ºC is slightly lower than in the previous cases, for both in the cold and warm start. Considering that in CS mode the ICE is fully operative along with the HV battery, the thermal energy wasted by the engine can be used to heat the cabin, thus avoiding the usage of the PTC that draws electric current from the battery. When comparing CD and CS modes, the difference in cold start conditions is very small, while in warm start conditions the vehicle consumes around 0.4 kWh more in CD mode. As mentioned in the Methodology, the energy consumption is calculated considering both the electric and the fuel contribution; the latter was converted into energy considering the low heating value, as per Equation (2).
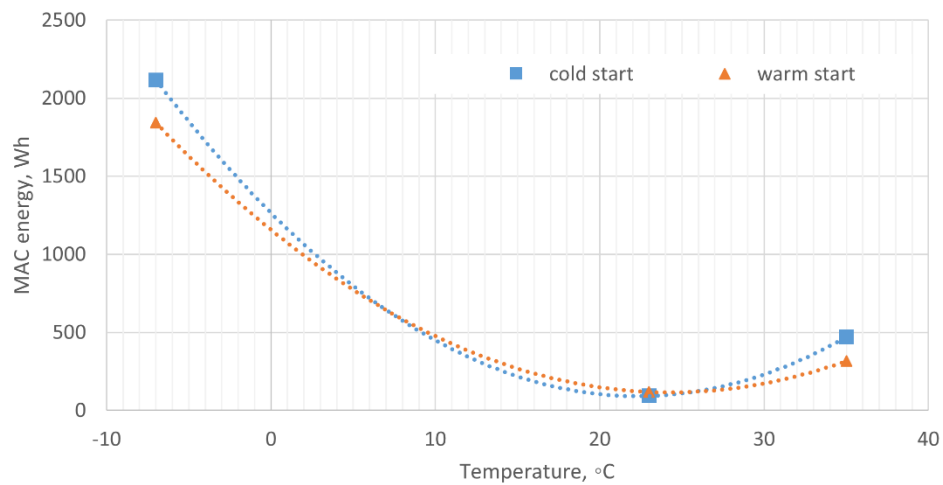
Figure 4. Difference in MAC energy demand for the BEV at different cell temperatures, cold start (blue) and warm start (red)
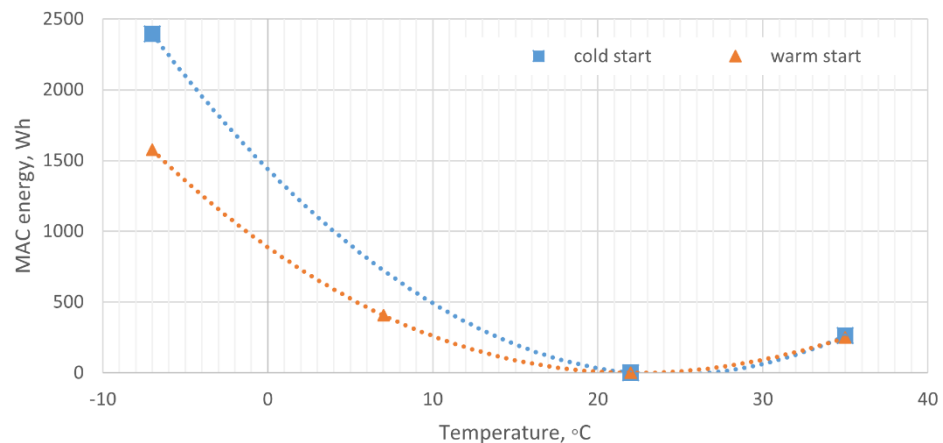
Figure 5. Difference in MAC energy demand of the PHEV in CD mode at different cell temperatures, cold start (blue) and warm start (red)
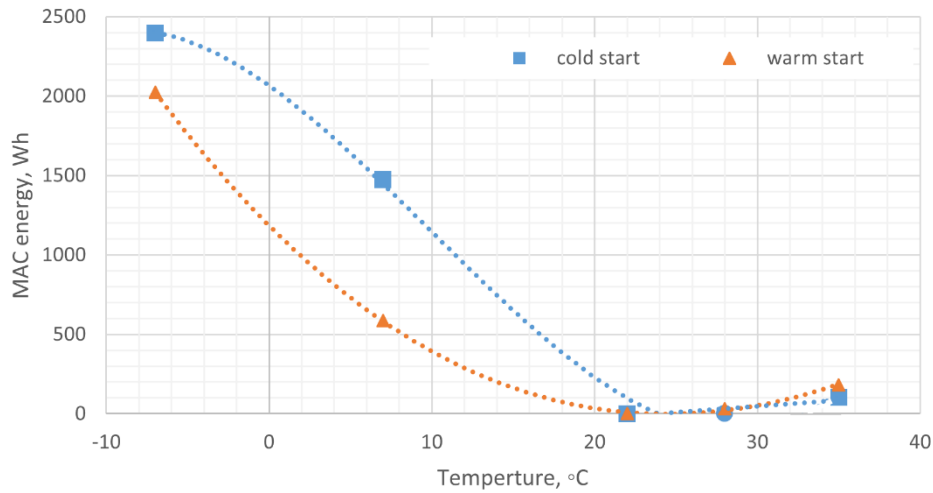
***Figure 6**. Difference in MAC energy demand of the PHEV in CS mode at different cell temperatures, cold start (blue) and warm start (red)*

3.2. Energy share of MAC systems

In this section, the impact of the electrical energy consumed by the MAC is shown as a percentage of the traction energy required by the vehicle to drive a WLTC cycle. The cycle energy is calculated according to the formulas in Regulation 1151, Sub-Annex 7, Paragraph 5 [40]. Figure 7 and Figure 8 depict the PHEV behaviour in warm start conditions, in CS and CD modes, respectively. Figure 9 and Figure 10 illustrate the energy share for the BEV in warm start and cold start conditions respectively.

The energy share in the PHEV in CS mode (Figure 7) includes a wider range of cell temperatures to understand the tendency of the energy share with the ambient conditions. As already explained, a "V-shape" trend can be seen again. The highest impact of MAC (i.e., 35%) is seen at the lowest temperatures (-7ºC), while at mild temperatures the MAC energy share ranges from 5% to 0%, and at higher temperature (35ºC) the MAC energy share is about 15%.
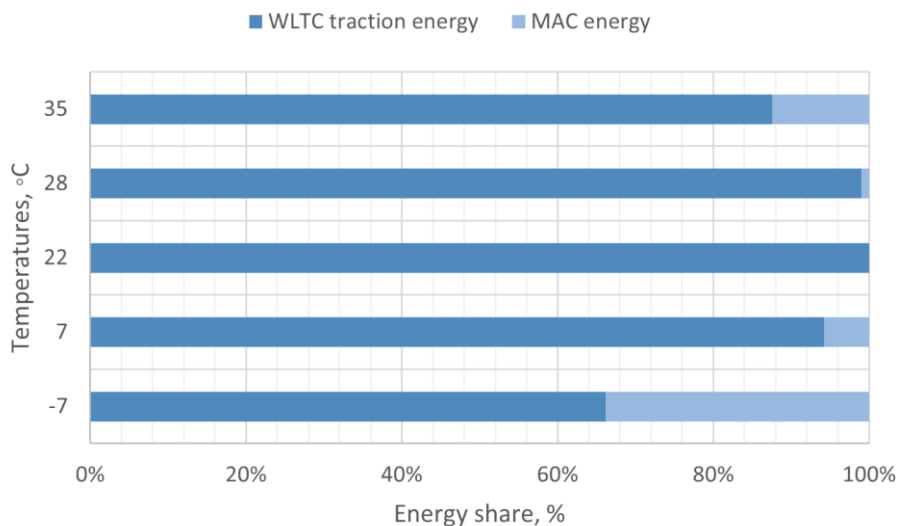
***Figure 7**: Energy share for the PHEV, CS mode, warm start.*

The energy shares for the PHEV are different if CS and CD modes are compared, as seen in Figure 7 and Figure 8. The main difference between the two modes is the MAC energy share at -7 ºC: MAC represents 55% of the cycle energy in charge depleting mode, meaning that the operation of the ICE provides almost 25% of the heating energy. The MAC share at 35 ºC is very similar in both CS and CD

modes. At +7 ⁰C, the MAC accounts for about 12% of the cycle energy, which is approximately double the value in CS mode.
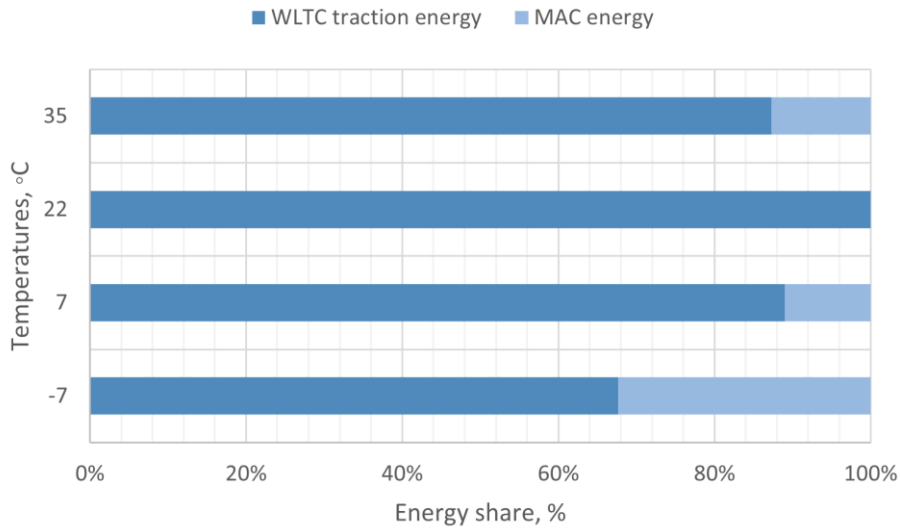
Figure 8: *Energy share for the PHEV, CD mode, warm start.*

As a further step, the energy share for the PHEV in CD mode in warm start conditions (Figure 8) can be compared to the MAC energy share in warm conditions for the BEV (Figure 9). Under the same conditions, the BEV's MAC energy share at 35ºC (about 25%) is found to be higher than the one for the PHEV in CD (about 15%). Although the energy share differs of 10% between the two powertrains, the absolute energy consumption (as reported in Figure 4 and Figure 5) shows similar values (i.e., around 250 and 300 Wh), being the cycle energy the only relevant different in the calculation of the ratios. At -7ºC, the MAC consumption is about 35% of the cycle energy. The MAC required less energy at mild temperatures to power 12V consumers since the A/C compressor and heating were off.
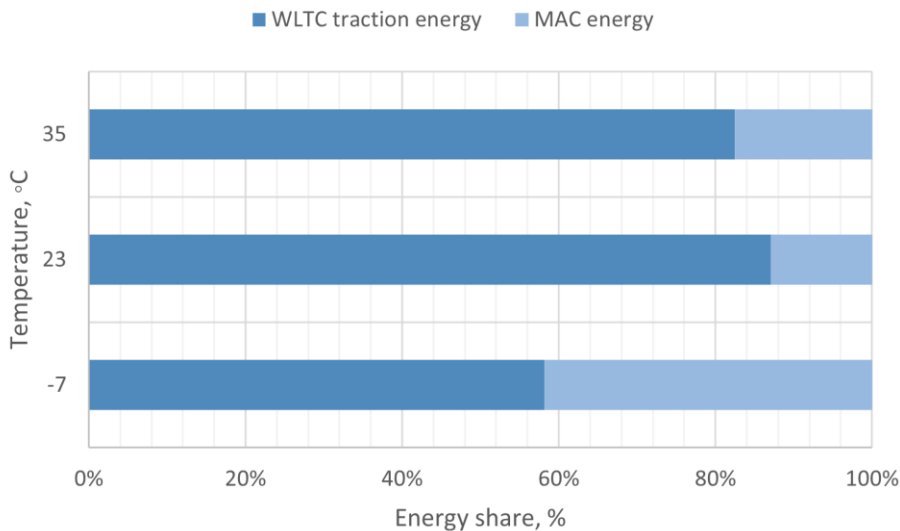
Figure 9: *Energy share for the BEV, warm start.*

The analysis of the BEV can be extended to compare warm (Figure 9) and cold start (Figure 10). At higher temperature (35ºC), the MAC energy share is very similar in both cold and warm start, around a 16%. On the other hand, MAC at -7ºC uses around 40% of the cycle energy in warm start and 45% of the cycle energy at cold start conditions.
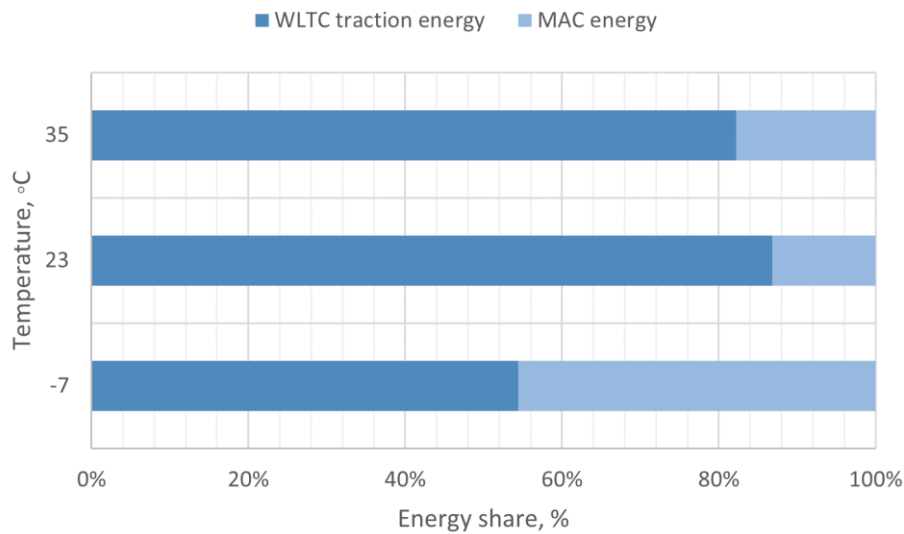
Figure 10: Energy share for the BEV, cold start.

3.3 Cabin temperatures and A/C compressor power

As explained in the methodology section, six k-type thermocouples were installed in the cabin of each car, covering the locations highlighted in Figure 3. In the following pictures, from Figure 11 to Figure 14, the temperature measurements over a WLTC cycle inside the cabin are shown, for both the BEV and the PHEV, at 35ºC and -7ºC cell temperature. Since there is no significant difference between CD and CS mode in the PHEV, only the CD mode results are shown in this analysis. In all figures, only the cold start case is plotted since the investigation of the cabin temperature is not really affected by the initial temperature of the powertrain when working in electric mode. Moreover, thermocouples measurements with MAC off are displayed on the top, while with MAC on at the bottom.

The BEV shows a higher difference between the air-outlet temperature (TC1) and the rest of the cabin, if compared to the PHEV. In the latter, all the temperatures are very similar, meaning that the distribution of air in the cabin is more uniform. This is mainly due to the fact that the TC1 in the BEV was misplaced and it was too close to the air blower, thus sensing the cold-air coming from the A/C system before being mixed with the air in the cabin.

As for the BEV, it can be seen that when the MAC is turned on, the temperature target is reached faster than the PHEV. This is true for both cabin heating and cooling: from the bottom part of Figure 11 and Figure 12. it can be highlighted that the BEV achieves the target cabin temperature of 22ºC in 300s and 500s respectively. On the other side, the target temperature for the PHEV is reached in 500s and 800s respectively (Figure 13 and Figure 14). Furthermore, at 35ºC cell temperature in MAC off condition, the cabin temperature does not change significantly, while at -7ºC cell temperature in MAC off condition, the inside temperature shows a slight increase due to the fact the powertrain operation comes with a waste of thermal energy that is transferred to the vehicle cabin. With this being said, the main purpose of the temperature analysis is to have a valuable set of data that can later be used to calibrate and validate the vehicle MAC model.

Additionally, the power consumed by the A/C compressor during a WLTC in both BEV and PHEV was investigated. As a matter of fact, the power trace shows a peak at the beginning of the cycle to take care of bigger temperature gradient. Afterwards, it starts lowering and it gets stable for the rest of the cycle. The BEV's compressor (Figure 15) has a higher peak of 3.5 kW of consumption in the very beginning, a second smaller peak of 2.5 kWh around the second 250, while after fluctuates around 1.8 kW. The PHEV's compressor (Figure 16) shows a series of peaks in the beginning of the cycle (up to 3 kW) and goes down considerably at the second 700 approximately, when it drops and stabilises around 0.5 kW. In some point around 1300s, the compressor has a peak of higher consumption (1 kW) linked to the extra-power needed to meet the target temperature.

As expected, the power consumed by the compressor is dependent on the cell temperatures. The analysis of the energy demanded by the compressor of the BEV can be seen in Figure 17, considering the tests at cold and warm start. At cold temperatures (-7ºC), the compressor is not working, and the cabin is heated by the electric heater. As the cell temperature increases, the energy required by the compressor increases accordingly, showing a linear dependency. This will help to predict future case studies of A/C compressor consumption at different temperature.
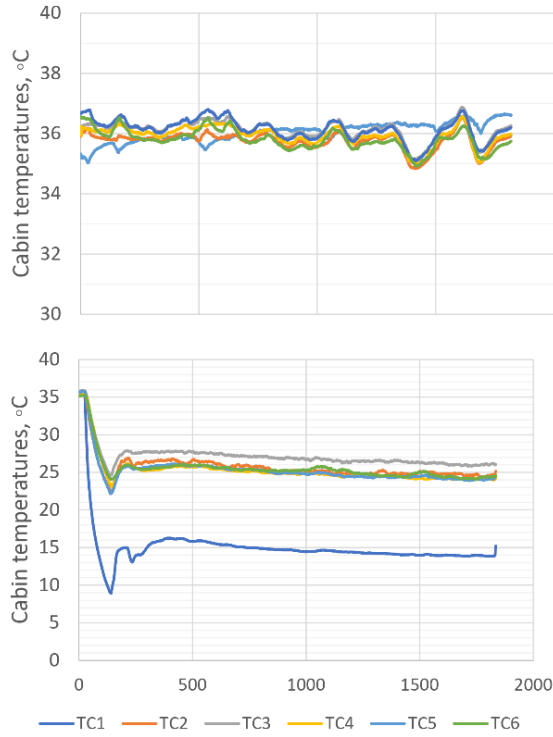
Figure 11: *BEV cabin thermocouples (TC) at 35ºC cell temperature: MAC off (top) and MAC on (bottom)*
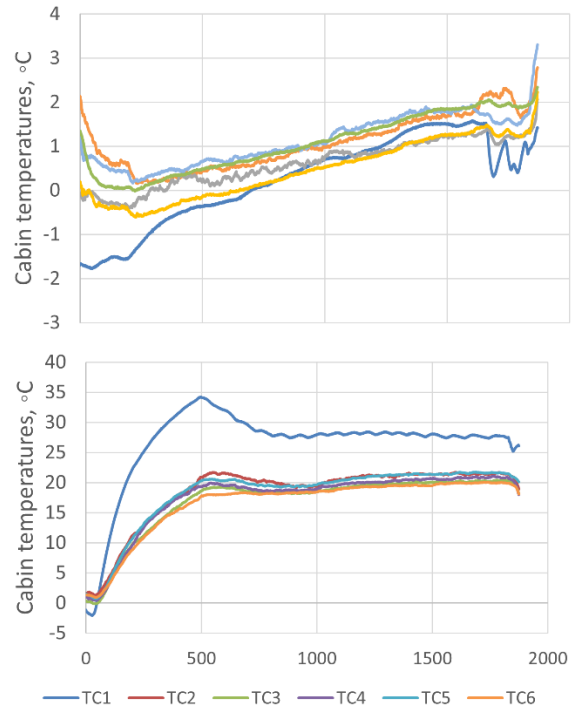
Figure 12: *BEV cabin thermocouples (TC) at -7ºC cell temperature: MAC off (top) and MAC on (bottom)*
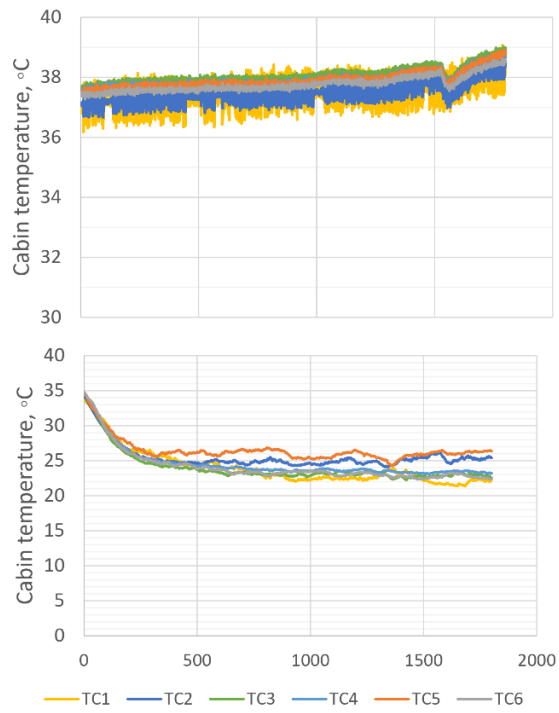
Figure 13. PHEV cabin thermocouples (TC) at 35ºC cell temperature: MAC off (top) and MAC on (bottom)
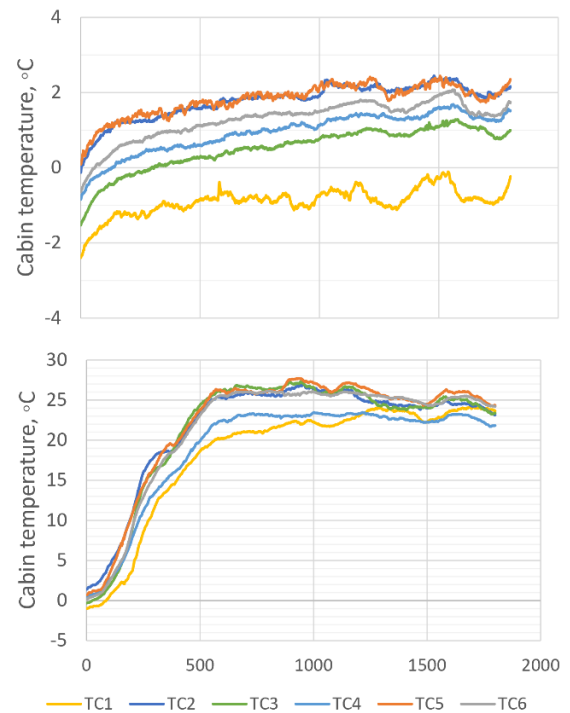
Figure 14. PHEV cabin thermocouples (TC) at -7ºC cell temperature: MAC off (top) and MAC on (bottom)
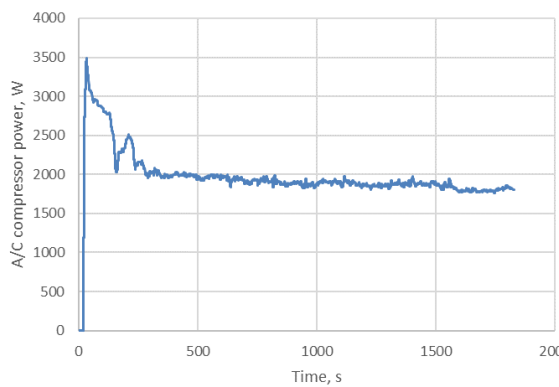
Figure 15: A/C compressor power in the BEV. Cold start. 35CºC. MAC on.
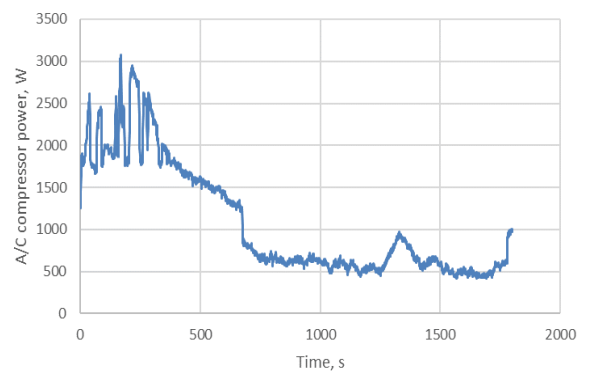
Figure 16: A/C compressor power in PHEV. CD mode, cold start. 35ºC. MAC on.
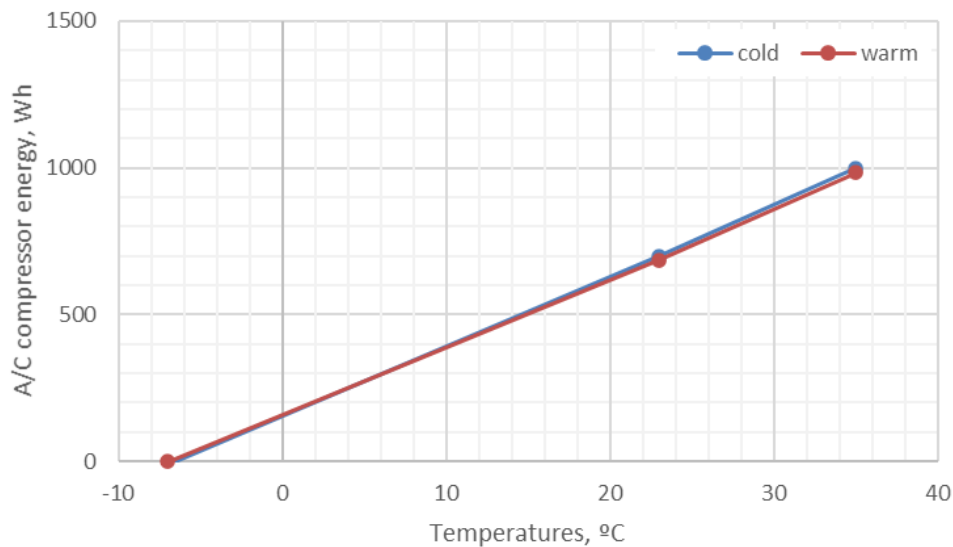
Figure 17: A/C compressor energy in the BEV. Cold and warm start. MAC on.

4. Conclusions

This paper analyses the impact of different parameters in the energy consumption of the MAC system in a gasoline PHEV and BEV, both equipped with a PTC heater and a HV A/C compressor for cooling the passenger cabin. In this regard, tests on the two-case study were performed in controlled laboratory conditions at different cell temperatures of -7ºC (19.4ºF), 22ºC (71.6ºF) and 35ºC (95ºF), over the WLTC standard driving cycle. Laboratory tests with the same conditions were repeated with MAC on and off for each temperature. For the reference 23ºC (73.4ºF) condition, additional factors affecting energy consumption were analysed.

As for the BEV, the MAC energy demand at -7ºC is higher than the energy at 35ºC. Moreover, the energy demand at cold start is higher than at warm start conditions, mainly at -7 ºC. It was found that the highest energy demand of MAC appears at -7ºC for the BEV when there is a cold start (45% of the cycle energy). The BEV with a warm start leads to a MAC energy share of around 40%.The PHEV in charge depleting mode, the MAC uses around 30% of the cycle energy, similar to the charge sustaining mode. With hot cell temperature (35ºC), BEV's MAC uses around 18% of the cycle energy with a cold start and warm start. Both higher than the MAC share in the PHEV in CD and CS mode (around 15%). At mild temperatures, the BEV's MAC energy is very low as expected. Finally, it was noticed that the compressor energy increases linearly with the cell temperature.

As follow-up activities, the research group is continuously working on different vehicles to enlarge the quantity and the type of data available. This work intends to build a testing procedure that can be applied to various vehicles and that can be used as a start point for the development of a standardised test procedure for the assessment of the energy consumption and CO_2 emissions related to the deployment of the MAC system in electrified vehicles. Moreover, the study team is working on an internally developed HVAC model and a cabin thermal model. Hence, this experimental activity constitutes a valuable asset to calibrate and validate the mentioned model. The virtual environment would ideally be used in the future to complement or substitute real vehicle testing, which is time and resource-consuming. The MAC impact on the vehicle's energy during real driving is an important aspect to examine, as the consumption of MAC systems will differ from laboratory conditions. The suitability of the methodology described in this paper in real-driving conditions is under investigation.

References

[1] 'CO2 emissions from cars: facts and figures (infographics) | News | European Parliament', Mar. 22, 2019. https://www.europarl.europa.eu/news/en/headlines/society/20190313STO31218/co2-emissions-from-cars-facts-and-figures-infographics (accessed May 02, 2022).

[2] 'Global CO2 emissions from passenger cars 2020', *Statista*. https://www.statista.com/statistics/1107970/carbon-dioxide-emissions-passenger-transport/ (accessed May 03, 2022).

[3] 'Greenhouse gas emissions from transport in Europe'. https://www.eea.europa.eu/ims/greenhouse-gas-emissions-from-transport (accessed May 02, 2022).

[4] European Commission, 'Roadmap to a Single European Transport Area—Towards a Competitive and Resource Efficient Transport System', May 2011. [Online]. Available: https://eur-lex.europa.eu/legal-content/EN/TXT/PDF/?uri=CELEX:52011DC0144&from=EN

[5] Text adopted by Parliament, '2021/0197(COD) - 08/06/2022 - CO2 emission standards for cars and vans'. https://oeil.secure.europarl.europa.eu/oeil/popups/summary.do?id=1706841&t=e&l=en (accessed Jul. 04, 2022).

[6] P. Mock, 'The role of standards in reducing CO2 emissions of passenger cars in the EU', p. 10.

[7] 'CO$_2$ emission performance standards for cars and vans'. https://ec.europa.eu/clima/eu-action/transport-emissions/road-transport-reducing-co2-emissions-vehicles/co2-emission-performance-standards-cars-and-vans_en (accessed May 02, 2022).

[8] 'Reducing carbon emissions: EU targets and measures | News | European Parliament', Aug. 03, 2018. https://www.europarl.europa.eu/news/en/headlines/society/20180305STO99003/reducing-carbon-emissions-eu-targets-and-measures (accessed May 02, 2022).

[9] A. Joshi, 'Review of Vehicle Engine Efficiency and Emissions', *SAE Int. J. Adv. & Curr. Prac. in Mobility*, vol. 1, no. 2, Art. no. 2019-01–0314, Apr. 2019, doi: 10.4271/2019-01-0314.

[10] C. Li, E. Brewer, L. Pham, and H. Jung, 'Reducing Mobile Air Conditioner (MAC) Power Consumption Using Active Cabin-Air-Recirculation in A Plug-In Hybrid Electric Vehicle (PHEV)', *World Electric Vehicle Journal*, vol. 9, no. 4, Art. no. 4, Dec. 2018, doi: 10.3390/wevj9040051.

[11] ICCT, 'European vehicle market statistics 2020/2021', p. 57, 2021.

[12] B. Mebarki, B. Draoui, B. Allaou, L. Rahmani, and E. Benachour, 'Impact of the Air-Conditioning System on the Power Consumption of an Electric Vehicle Powered by Lithium-Ion Battery', *Modelling and Simulation in Engineering*, vol. 2013, pp. 1–6, 2013, doi: 10.1155/2013/935784.

[13] 'Experimental investigation on the dynamic performance of a hybrid PEM fuel cell/battery system for lightweight electric vehicle application'.

[14] 'Trends and developments in electric vehicle markets – Global EV Outlook 2021 – Analysis', *IEA*. https://www.iea.org/reports/global-ev-outlook-2021/trends-and-developments-in-electric-vehicle-markets (accessed Feb. 17, 2022).

[15] F. Millo, L. Rolando, L. Pulvirenti, and G. Di Pierro, 'A Methodology for the Reverse Engineering of the Energy Management Strategy of a Plug-In Hybrid Electric Vehicle for Virtual Test Rig Development', *SAE Int. J. Elec. Veh.*, vol. 11, no. 1, pp. 14-11-01–0009, Sep. 2021, doi: 10.4271/14-11-01-0009.

[16] G. DiPierro, E. Galvagno, G. Mari, F. Millo, M. Velardocchia, and A. Perazzo, 'A Reverse-Engineering Method for Powertrain Parameters Characterization Applied to a P2 Plug-In Hybrid Electric Vehicle with Automatic Transmission', *SAE Int. J. Adv. & Curr. Prac. in Mobility*, vol. 3, no. 1, pp. 715–730, Jun. 2020, doi: 10.4271/2020-37-0021.

[17] B. Song, J. Kwon, and Y. Kim, 'Air Conditioning System Sizing for Pure Electric Vehicle', *World Electric Vehicle Journal*, vol. 7, no. 3, Art. no. 3, Sep. 2015, doi: 10.3390/wevj7030407.

[18] G. L. Patrone *et al.*, 'Assessing the Energy Consumption and Driving Range of the QUIET Project Demonstrator Vehicle', *Energies*, vol. 15, no. 4, Art. no. 4, Jan. 2022, doi: 10.3390/en15041290.

[19] M. H. Park and S. C. Kim, 'Heating Performance Characteristics of High-Voltage PTC Heater for an Electric Vehicle', *Energies*, vol. 10, no. 10, Art. no. 10, Oct. 2017, doi: 10.3390/en10101494.

[20] E. Paffumi, M. Otura, M. Centurelli, R. Casellas, A. Brenner, and S. Jahn, 'Energy Consumption, Driving Range and Cabin Temperature Performances at Different Ambient Conditions in Support to the Design of a User-Centric Efficient Electric Vehicle: the QUIET Project', p. 18.

[21] M. De Gennaro *et al.*, 'Experimental Test Campaign on a Battery Electric Vehicle: Laboratory Test Results (Part 1)', *JRC Publications Repository*, Apr. 21, 2015. https://publications.jrc.ec.europa.eu/repository/handle/JRC92283 (accessed May 03, 2022).

[22] R. Suarez-Bertoa *et al.*, 'Effect of Low Ambient Temperature on Emissions and Electric Range of Plug-In Hybrid Electric Vehicles', *ACS Omega*, vol. 4, no. 2, pp. 3159–3168, Feb. 2019, doi: 10.1021/acsomega.8b02459.

[23] Q. Zhang, Y. Meng, C. Greiner, C. Soto, W. Schwartz, and M. Jennings, 'Air Conditioning System Performance and Vehicle Fuel Economy Trade-Offs for a Hybrid Electric Vehicle', SAE International, Warrendale, PA, SAE Technical Paper 2017-01–0171, Mar. 2017. doi: 10.4271/2017-01-0171.

[24] EC, *Regulation (EU) 2019/631 of the European Parliament and of the Council of 17 April 2019 setting CO2 emission performance standards for new passenger cars and for new light commercial vehicles, and repealing Regulations (EC) No 443/2009 and (EU) No 510/2011 (recast)*.

[25] R. Smith, 'Regulation (EC) No 883/2004 of the European Parliament and of the Council of 29 April 2004', in *Core EU Legislation*, London: Macmillan Education UK, 2015, pp. 288–318. doi: 10.1007/978-1-137-54482-7_27.

[26] M. K. Shete, 'Influence of Automotive Air Conditioning load on Fuel Economy of IC Engine Vehicles', vol. 6, no. 8, p. 6, 2015.

[27] R. Monforte, F. Lovuolo, M. Rostagno, R. Seccardini, and T. Matton, 'New MAC Technologies: Fuel Efficiency Effect in Real Driving of the Air Intake Flap Management', Apr. 2015, pp. 2015-01–1609. doi: 10.4271/2015-01-1609.

[28] Wikipedia, 'On-board diagnostics'. [Online]. Available: https://en.wikipedia.org/wiki/On-board_diagnostics

[29] C. Thiel *et al.*, 'Impact of climatic conditions on prospects for integrated photovoltaics in electric vehicles', *Renewable and Sustainable Energy Reviews*, vol. 158, p. 112109, Apr. 2022, doi: 10.1016/j.rser.2022.112109.

[30] I. Directorate-General for Internal Market *et al.*, *MAC performance test procedure: co-ordination of the pilot test phase and follow up towards the drafting of the regulatory text: final report*. LU: Publications Office of the European Union, 2014. Accessed: Apr. 28, 2022. [Online]. Available: https://data.europa.eu/doi/10.2873/820839

[31] United Nations, *Addendum 15 : Global technical regulation No . 15 - Worldwide harmonized Light vehicles Test Procedure*, vol. ECE/TRANS/. 2014, pp. 1–234.

[32] UNECE, *Regulation No. 101 Uniform provisions concerning the approval of passenger cars powered by an internal combustion engine only, or powered by a hybrid electric power train with regard to the measurement of the emission of carbon dioxide and fuel consumptio*. 2013.

[33] 'Commission Regulation (EU) 2017/ of 1 June 2017 supplementing Regulation (EC) No 715/2007 of the European Parliament and of the Council on type-approval of motor vehicles with respect to emissions from light passenger and commercial vehicles (Euro 5 and Euro 6) and on access to vehicle repair and maintenance information, amending Directive 2007/46/EC of the European Parliament and of the Council, Commission Regulation (EC) No 692/2008 and Commission Regulation (EU) No 1230/2012 and repealing Commission Regulation (EC) No 692/2008', p. 643.

[34] Commernet, 2011, 'Subpart H—Cold Temperature Test Procedures, Part 1066 - VEHICLE-TESTING PROCEDURES, SUBCHAPTER U — AIR POLLUTION CONTROLS, CHAPTER I — ENVIRONMENTAL PROTECTION AGENCY, Title 40 - Protection of Environment, Code of Federal Regulations', *CODE OF FEDERAL REGULATIONS & FEDERAL REGISTER*. http://federal.elaws.us/cfr/title40.part1066.subparth (accessed May 05, 2022).

[35] 'South Korea fuel economy and greenhouse gas standards for new LDVs 2016-2020', *International Council on Clean Transportation*. https://theicct.org/publication/south-korea-fuel-economy-and-greenhouse-gas-standards-for-new-ldvs-2016-2020/ (accessed May 05, 2022).

[36] European Commission, *Regulation (EU) 2019/631 of the European Parliament and of the Council of 17 April 2019 setting CO2 emission performance standards for new passenger cars and for new light commercial vehicles, and repealing Regulations (EC) No 443/2009 and (EU) No 510/2011*, vol. 111. 2019. Accessed: May 05, 2022. [Online]. Available: http://data.europa.eu/eli/reg/2019/631/oj/eng

[37] The Standardization Administration of the People's Republic of China, 'Standard english version, China National Standards'. https://www.gbstandards.org/GB_standard_english.asp?code= (accessed May 05, 2022).

[38] SAE International, 'J1634_202104: Battery Electric Vehicle Energy Consumption and Range Test Procedure - SAE International'. https://www.sae.org/standards/content/j1634_202104 (accessed May 05, 2022).

[39] EC, *Technical Guidelines for the preparation of applications for the approval of innovative technologies pursuant to Regulation (EC) No 443/2009 and Regulation (EU) No 510/2011 - Revision: July 2018*. 2018. Accessed: Mar. 20, 2019. [Online]. Available: http://europa.eu/!ch88vv

[40] European Commission, *Commission Regulation (EU) 2017/1151 supplementing Regulation (EC) No 715/2007 of the European Parliament and of the Council on type-approval of motor vehicles with respect to emissions from light passenger and commercial vehicles (Euro 5 and Euro 6) and on*

access to vehicle repair and maintenance information, amending Directive 2007/46/EC of the European Parliament and of the Council, Commission Regulation (EC) No 692/2008 and Commission Regulation (EU) No 1230/2012 and repealing Commission Regulation (EC) No 692/2008 (Text with EEA relevance), vol. 175. 2017. Accessed: Jun. 09, 2020. [Online]. Available: http://data.europa.eu/eli/reg/2017/1151/oj/eng

Session S2.2 Fuel Injection and Sprays

Characterization of End of Injection Events for a High-Pressure Gasoline Direct Injection System in a Constant Volume Chamber

V. Chakrapani[1], J.E. Stolzman[1], E.S. Simoes[2], M. Medina[2], M. Wooldridge[1]

[1]University of Michigan. Ann Arbor, Michigan, USA

E-mail: cvarun@umich.edu, stolzmaj@umich.edu, mswool@umich.edu
Telephone: +1 (734) 764-2694

[2]California State University. Los Angeles, California, USA

E-mail: mmedin114@calstatela.edu, ejunior@calstatela.edu
Telephone: +1 (323) 343-4490

Abstract

High fuel injection pressures (e.g., > 100 bar) are an important method for improving combustion efficiency and engine performance of gasoline direct injection (GDI) engines; however, engine-out emissions remain a challenge at some operating conditions. Recent studies have shown that fuel injector tip wetting is a source of unburned hydrocarbons and particulate emissions in GDI engines. The objective of the current work was to experimentally characterize end-of-injection (EOI) phenomena like fuel injector dribbling and injector tip-wetting of gasoline at injection pressures of 600, 900 and 1500 bar. The experiments were conducted at non-reactive and non-flash boiling conditions using a constant-volume spray chamber. High-speed, diffuse, backlit shadowgraph imaging was used to optically examine EOI events for three chamber pressures (1, 5 and 20 bar) at each fuel injection pressure. A research grade fuel injector configured with two nozzle diameters was used to study orifice size effects. Relatively large, low-momentum droplets and ligaments were formed after EOI (aEOI), and tip-wetting was consistently observed for the smaller diameter nozzle. Image processing methods were used to quantify fuel dribble and fuel films formed on the injector tip as a function of the test conditions. The number and mean projected area of the droplets at EOI increased with higher chamber pressure for all fuel injection pressures. When fuel films were formed, the projected area of the films were not sensitive to chamber pressure, injection pressure or fuel temperature. Nozzle geometry played the largest role in reducing tip wetting and fuel dribbling at the EOI at the conditions studied.

Notation

aEOI	After end of injection
aSOI	After start of injection
CVSC	Constant volume spray chamber
GDI	Gasoline direct injection
HC	Hydrocarbon
PN	Particulate number

1. Introduction

High fuel injection pressures improve fuel atomization and combustion performance in gasoline direct injection engines (GDI) [1]. However, engine-out particulate emissions are a concern for GDI engines at some operating conditions, particularly at cold-start conditions [2]. Multiple studies have confirmed fuel dribbling and tip wetting that occurs at the end of fuel injection are major sources of particulate emissions as well as unburned hydrocarbons in GDI engines [3-5]. Incomplete combustion of the fuel film formed on the surface of the injector tip leads to particulate emissions and injector deposits. Deposits exacerbate particulate emissions by absorbing fuel, which can become an additional source of particulate emissions [6]. Internal and external deposits (i.e., fouling) can also alter the geometry of fuel injectors, changing the

fuel spray characteristics [5]. Fouling can also increase hydrocarbon (HC) emissions by 30% and particulates by a factor of five compared with clean injectors [6]. Deposits on the injector needle can also lead to potential misfire and eventual injection failure due to seizure [7]. Since modern GDI fuel injectors often encompass design features such as smaller orifices and more complex geometries, the injectors can be more susceptible to detrimental effects of injector deposits. Additionally, modern GDI engines operate at much higher fuel injection pressures, e.g., with fuel injection pressures over 500 bar, and use more injection events of shorter duration per cycle. Thus, more end-of-injection (EOI) events are occurring per cycle at higher fuel injection pressures and over a larger range of in-cylinder conditions.

The mechanisms leading to fuel dribbling, tip wetting, and the formation of fuel films on fuel injector tips are complex (see Sykes et al [7] for more information). Also, there are few experimental data that quantify the characteristics of fuel dribbling and tip wetting to guide and inform fuel-injector design and to develop and validate associated theory. **Table 1** provides a summary of the recent experimental studies of EOI events using high-pressure fuel injection. Using either instrumented GDI engines or constant volume spray chambers (CVSCs), important observations have been documented in these prior works. However, challenges in generalizing the trends include differences in fuels used (from simple surrogates like n-heptane to complex "real" fuels like pump-grade gasoline); differences in fuel injector internal geometries, and differences in experimental platforms (from production engines to spray chambers). The consensus that has emerged from the literature is that higher fuel injection pressure and smaller injector nozzle counterbore may lower tip wetting and potentially reduce particulate number (PN) emissions from GDI engines. Conversely, flash-boiling conditions can increase tip wetting, and thus increase PN emissions. Notably, none of the previous works considered EOI events at fuel injection pressures above 400 bar. The current work addresses this knowledge gap with the objective of quantifying the effects of high fuel injection pressure (>400 bar) on EOI events for gasoline at conditions not previously investigated. The technical approach used a CVSC and high-speed imaging to capture key phenomena, including EOI spray features (such as fuel injector dribbling of droplets and ligaments) and fuel films formed on the nozzle tip. Furthermore, the effects of two nozzle diameters were investigated. The results are discussed in the context of trends to minimize EOI sources of emissions from GDI fuel injectors.

2. Experimental Setup and Methodology

2.1. Setup

The same experimental methods applied in Medina et al. [8] to study bulk gasoline spray features were used in the current work to study EOI spray characteristics. The approach is briefly summarized here. Diffuse backlit shadowgraph imaging was used to record the spray EOI behavior in a constant volume chamber equipped with optical access and instrumentation ports as shown in **Fig. 1**. A high-speed camera (Vision Research Phantom 7.11 12-bit CMOS array) with a 90 mm lens (Elicar) was used at a frame rate of 13,600 fps and 10 μs exposure time. The camera resolution was set to 800 x 352 pixels resulting in an image resolution of 41.5 pixels per mm. High-purity nitrogen (PurityPlus Gases, purity rating 99.999%) was used to pressurize the chamber and a pressure gauge (Supco-DPG1000) was used to monitor chamber pressure with an uncertainty of ± 0.2 bar. A K-type thermocouple was used to monitor the chamber temperature which was 298 K ± 3 K.

Table 2 summarizes the experimental conditions studied. Gasoline fuel was pressurized with a diesel fuel pump and supplied via a common rail. The range of injection pressures used in this study was 600 to 1500 bar with an uncertainty of ± 10 bar. Reference grade gasoline (HF0072, Haltermann Solutions) was blended with 350 ppm by vol. fuel lubricity additive (Infineum R655) to increase compatibility between gasoline fuel and the diesel pump. The fuel properties are provided in **Table S1** of the Supplemental Material. The injection duration for each event was set to 1 ms and 13 injection events were recorded for each test condition. Note that for a fixed injection duration, the mass of fuel injected increased with higher injection pressure. The time between injection events was approximately three minutes. The chamber was not purged of fuel vapor between injection events. The potential impact of not purging the chamber was investigated and found to be negligible (discussed further in the Results section 3.1). The temperature of the fuel was monitored using a K-type thermocouple connected to the return line of the fuel from the injector. The fuel temperature was not controlled and increased slightly with fuel injector use.

Table 1. Summary of recent studies of gasoline EOI tip-wetting phenomena

Reference	Fuel Type/Fuel Temperature	Experimental Setup/ Chamber Pressure [bar]	Injection Pressure [bar]	Geometry Description	Key Study Outcomes
Current work	Reference grade gasoline/ < 65°C	CVSC/1, 5, 20	600, 900, 1500	Diesel injector with two straight hole nozzles. See Table 4 for more details.	See text for details.
Leick et al. [10]	Gasoline/ surrogate/ 23 °C, 90 °C	GDI Engine/ CVSC/ 0.40, 0.70, 1.05	50, 200	GDI injector with relatively small and large counterbore diameters	• Flash-boiling (i.e., ↑ fuel temperature and ↓ chamber pressure) ↑ tip wetting • ↑ injection pressure ↓ tip wetting and ↓ particulate emissions • Injector geometry had negligible impact on tip wetting
Backes et al. [11]	Commercial grade gasoline/ 20 °C, 60 °C, 80 °C, 100 °C	CVSC/ 0.40, 0.50, 1.00, 1.50	150, 250, 350	Three GDI injector counterbore designs: (1) Conventional counterbore dia. (2) Conical divergent counterbore (3) 35% larger counterbore dia. than (1)	• Flash-boiling ↑ tip wetting • Injection pressure had no significant effect on tip wetting • ↑ counterbore diameter ↑ tip wetting
Huang et al. [12]	n-heptane	CVSC/ 1.00	40, 100, 200	Various GDI injectors with increasing counterbore diameter (0.25 – 0.55 mm with 0.05/step)	• ↑ injection pressure ↓ tip wetting • ↑ counterbore diameter ↑ tip wetting for counterbore dia. < 0.40 mm • ↑ counterbore diameter ↓ tip wetting for counterbore dia. > 0.40 mm
Huang et al. [6]	n-heptane/ 30 °C, 55 °C, 80 °C	CVSC/ 0.10, 0.50, 1.00	40, 100, 200	Standard GDI injector with 6 holes with same diameter hole and counterbore	• Flash-boiling ↑ tip wetting • ↑ injection pressure slightly ↓ tip wetting
Dageforde et al. [13]	Gasoline/ 25 °C – 120 °C	GDI Engine/ CVSC/ 0.20 – 5.00	50 – 400	GDI injector with relatively small and large counterbores	• ↓ counterbore diameter ↓ tip wetting • ↓ counterbore diameter ↓ PN emissions in engine study • ↑ injection pressure ↓ PN emissions
Peterson et al. [3]	Pump-grade gasoline	GDI Engine	50, 200	-	• ↑ injection pressure ↓ soot
Medina et al. [4]	Reference-grade gasoline	GDI Engine	100, 200, 300	Various GDI injectors with different hole lengths	• ↑ injector nozzle hole length ↓ PN emissions

The fuel temperature was below 65°C for all experiments. The effects of the drift in fuel temperature were considered in the results and analysis.

It should be noted that previous work by Medina et al. [9] used the same injector geometry and experimental conditions as the current work and found the injector to be operating within the cavitating regime as determined by momentum coefficient measurements. However, the spray images within this study did not exhibit features attributable to cavitation and the authors believe this will not have an effect on the EOI results and analyses.

Flash-boiling occurs when the chamber pressure is lower than the fluid saturation pressure. The saturation pressure of the reference grade gasoline used in the current work was estimated as 0.6 bar based on the saturation pressure data experimentally determined for gasoline by Araneo et al. [14]. With a saturation pressure of 0.6 bar, all experiments in the study were under non-flash boiling conditions.

Table 2. Summary of experimental conditions
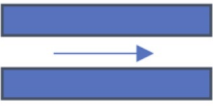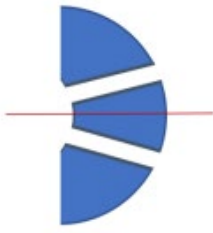
Parameter	Value
Fuel type	Reference grade gasoline
Chamber gas	Nitrogen
Fuel injection pressure [bar]	600, 900, 1500
Chamber temperature [°C]	25
Chamber pressure, [bar]	1, 5, 20
Fuel temperature [°C]	31 - 64.5
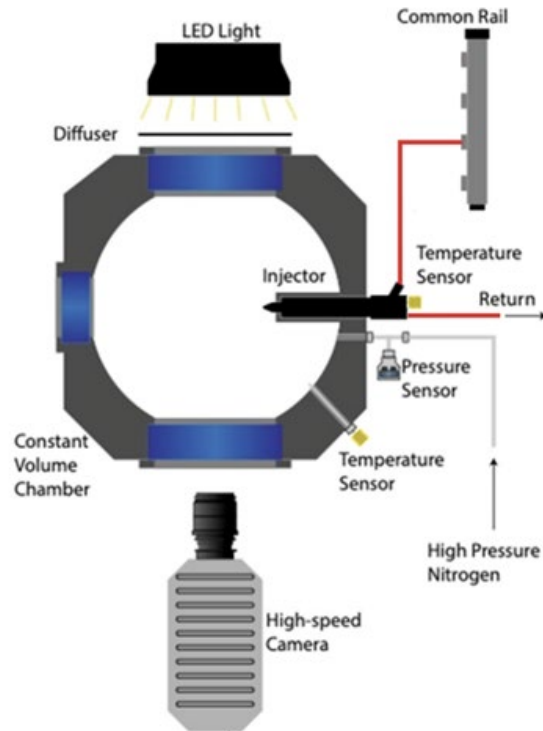
Fig. 1. Top view of the experimental setup

The fuel injector was a research design (Injector B in the study by Medina et al. [8,9]) and consisted of a commercial diesel-type injector body with a custom nozzle tip with two holes located 15° above and below the horizontal plane. An advantage of using a diesel injector is the ability to inject gasoline at pressures not investigated previously. The nozzle holes were oriented on the same vertical plane with 30° of separation as shown in **Table 3**. Both nozzles had the same length with straight nozzle passages and no inlet rounding; however, the top hole had a diameter 57.8% of the diameter of the lower hole. Thus, the length over diameter ratio of the nozzles differed by a factor of 1.73. The nozzle passages contained no pre-hole or counterbore features which are a common cause of tip-wetting due to fuel impingement in gasoline injectors (as described in Section 1).

Table 3. Nozzle characteristics of the research fuel injector used in the study.

Orifice designation	Nozzle outlet diameter [µm]	Nozzle flow passage	Orientation of nozzles in the fuel injector tip
Top - hole 1	110		
Bottom - hole 2	190		

2.2. Image Processing

Image processing was used to quantify key EOI characteristics, including the projected area of the fuel film and the number of droplets during fuel dribbling at the EOI. First, the nozzle surface was identified from images without the sprays present. The focal points of the sprays were identified as the orifice coordinates. This allows for the separation of data between orifices (hole 1 versus hole 2). The start of injection and end of injection in the videos were identified based on changes in the pixel intensity in the region near the exit of the nozzle orifices. Each image was converted to grayscale then to binary scale by applying an intensity threshold. The characteristics of the droplets and ligaments and the fuel films were analyzed separately. The binary images were used to determine the total projected area of the fuel film on the injector tip, defined as the projected area of tip-wetting, using custom image analysis processing via MATLAB.

Droplets and ligaments were characterized using ImageJ software [15-17] to quantify the projected area and number of droplets. The following steps were applied to the images after aEOI. The unprocessed data were imported into ImageJ, converted into grayscale and binarized using an intensity threshold. The Image J algorithm (*Analyze Particles*) was then used to calculate the projected area and the number of droplets and ligaments.

Figure 2 shows typical time histories of unprocessed and processed imaging data. The boundary of the injector tip is highlighted for reference in the images, and the earliest image shows excellent uniformity to the background intensity throughout the imaging region. From left to right, the panels show the progression of the spray from before the start of injection (SOI), immediately after SOI (aSOI), and after the EOI. The SOI is set as t = 0 s and is defined as the first frame where liquid is identified as leaving a nozzle orifice. The images after the EOI (i.e., times > 1 ms) show droplets and ligaments are still being ejected from the nozzle orifice well after the injection duration has ended. The second-to-last image in the sequence shows a ligament over 1 mm in length that is still connected to the top nozzle orifice and the presence of a fuel film on the tip of the upper hole is clearly visible. After more time, the last image in the sequence (t = 2.78 ms aSOI) shows the ligament breaks into smaller components and the fuel film has changed in size and location. While the presence of the fuel films and ligaments are clear in the images, the data represent two-dimensional projections of three-dimensional phenomena. The images are not isolated to one planar

cross-section, and consequently, the image analysis yields projected areas of the films, ligaments, and droplets.

In many cases, low momentum ligaments are still connected to the injector nozzle tip for times up to 1.5 ms after EOI (aEOI). The film analysis cannot distinguish between ligaments attached to the nozzle tip and fuel films. Consequently, to ensure only film data are compared (and not convolved with ligament data), the projected area is reported for times after 2.5 ms aSOI. The threshold value for detection of tip wetting was selected by first analyzing images where minimal tip-wetting was observed using a range of threshold settings. The final threshold value was selected to ensure data processing did not omit detection of tip wetting (i.e., false negatives). The uncertainty due to varying the threshold level was identified as less than 12%.
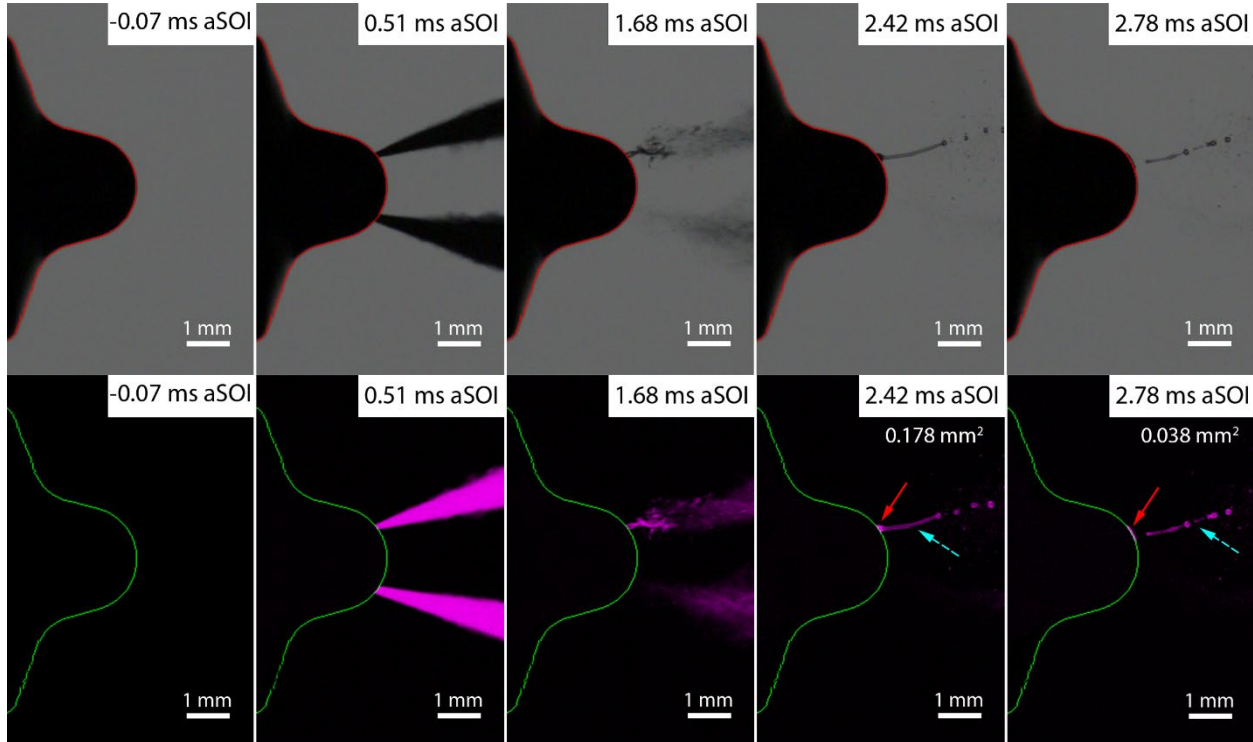
Fig. 2. Imaging sequence from a typical injection event for 1500 bar injection pressure and 20 bar chamber pressure. The top row presents the gray-scale data, and the corresponding processed images are shown in the bottom row. Tip wetting is observed at approximately 2.42 ms after SOI and is highlighted by the solid red arrow. Low momentum droplets and ligaments, highlighted by the dashed cyan arrow, are observed at the same time as the formation of the fuel film

3. Results and Discussion

3.1. Tip wetting

Figure 3 shows the measured projected tip wetting area as a function of time for hole 1 for each of the thirteen injection trials at two operating conditions. It should be noted that trials without tip wetting were excluded from the figure. **Figure 3** only includes projected area above 0 mm². The larger nozzle hole (#2) rarely exhibited tip-wetting or late large droplets. The SOI and EOI events are labeled in the figure. The data presented in **Figure 3** are from the experiments with the lowest injection and chamber pressures and the highest injection and chamber pressures. For both sets of pressure conditions, a slight decrease in projected area is observed with time, and if films are formed, the films persist for long times (>25 ms). Note that the films ultimately evaporate, as no films are observed at the start of the next injection cycle. No trends

with injection trial number are observed, and films are formed with injection events early in the sequence and later. The trends observed in the tip-wetting data were consistent for all injection and chamber pressures. Data from the other conditions are provided in the Supplemental Material.
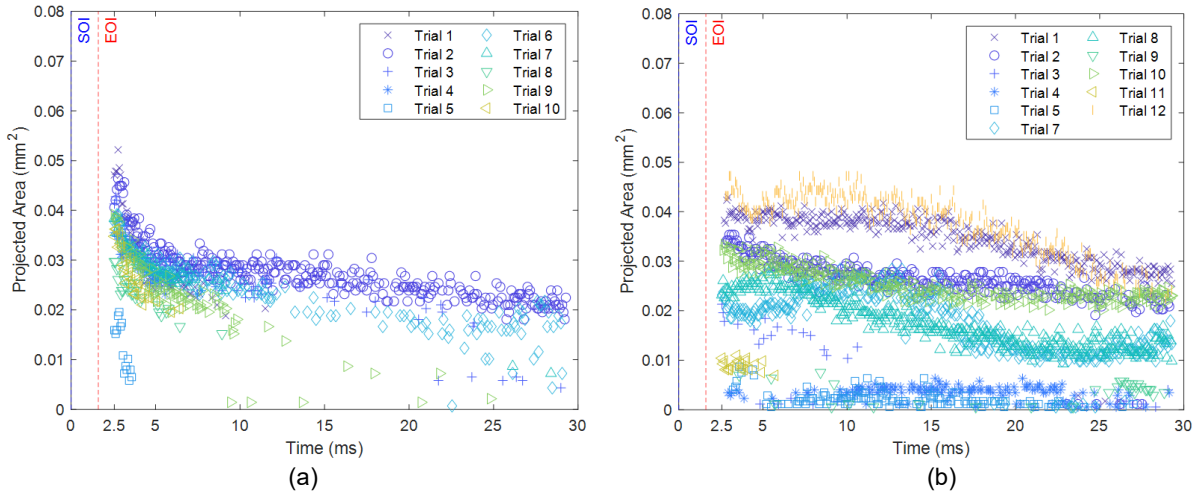
Fig. 3. Fuel film results for hole 1 for (a) 600 bar injection pressure and 1 bar chamber pressure and (b) 1500 bar injection pressure and 20 bar chamber pressure. The film projected area was documented for times > 2.5 ms aSOI. For clarity, trials are not reported when tip wetting was not observed

The decrease in tip-wetting area with time could be due to fuel evaporation or fuel dispersion and spreading over the injector tip. It is interesting to note the lower pressure conditions showed a more rapid decrease in projected area between 2.5 to 5 ms compared with the higher-pressure condition (additional results are provided in the Supplemental Material). The change in the slope of the film area indicates potential shift in the tip-wetting or drying phenomena at the different test conditions.

Closer inspection of the imaging results indicated there were two distinct modes of tip wetting. In a majority of the cases, when tip-wetting occurred it was associated with the presence of ligaments and slow-moving droplets, as seen in **Fig. 2**. **Figure 4** shows a similar example from a lower injection pressure of 600 bar. In the image sequence, a ligament of liquid-phase fuel is physically connected to the surface of the fuel injector tip. The images indicate the momentum of the fuel ligaments are often insufficient to overcome the surface tension forces required to separate the fuel from the surface of the injector tip. The image sequence shown in **Fig. 4** includes the corresponding time history of the projected area of the fuel film. For times before the ligament separates from the injector tip (before 2.5 ms aSOI), the projected area is relatively large (>0.1 mm^2). This overcounting of the projected area is an artifact of the image processing and should be ignored. After the ligament separates, the film persists on the injector tip for ~5 ms before evaporating or dispersing below the detectable limit of the imaging system. The characteristics of this tip-wetting mode are consistent with ligament "retraction" described by Sykes et al. [7].

Figure 5 shows the second mode of tip wetting that was observed. For some conditions, a small volume of fuel exited the nozzle after the EOI and without the presence of any fuel ligaments. The occurrence of this mode of tip wetting was infrequent and did not correlate with fuel injection or chamber pressure. The projected area indicates the film appears on the surface of the fuel injector tip, experiences some changes, and then reaches an almost steady projected area for over 10 ms. The characteristics of this tip-wetting mode are consistent with an 'overspill' event as described by Sykes et al. [7].

As previously mentioned, the mechanisms behind ligament dynamics and overspill aEOI are complex (see Sykes et al. [7] for more information) and the fundamental development of the mechanisms is beyond the scope of this paper. For the current study, ligaments appear to be a common occurrence with a tip-wetting event; however, tip-wetting also occurs when there are no ligaments present in the frames aEOI. The latter event is caused by fuel overspill (leakage) and may be the main source of tip-wetting.
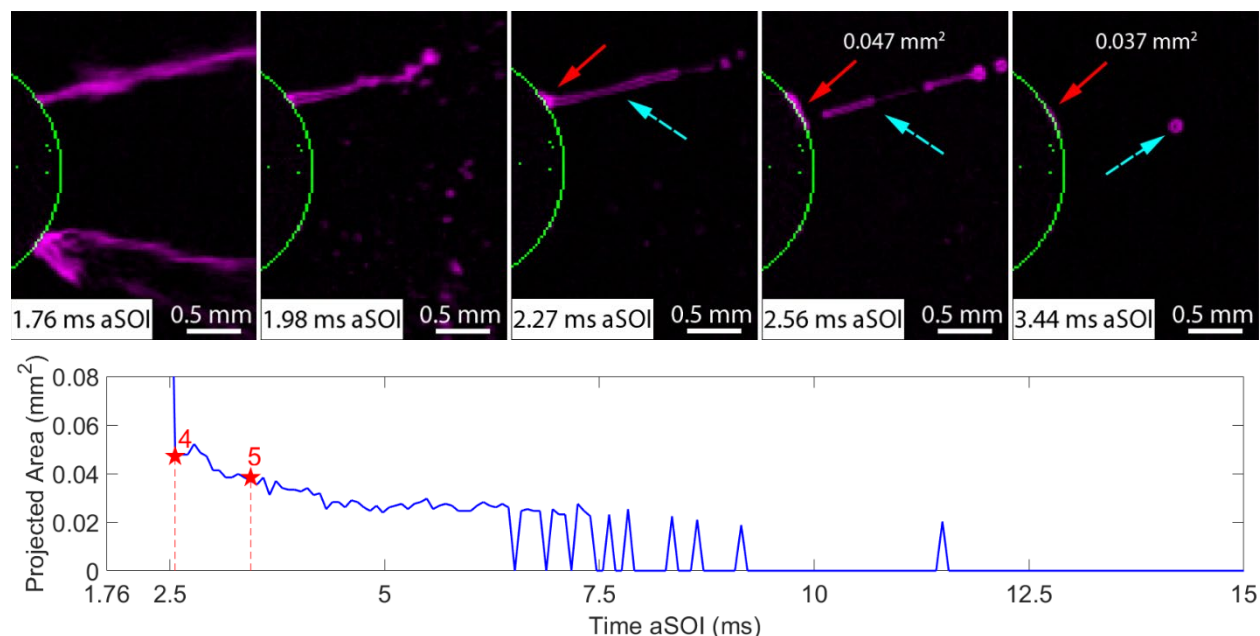
Fig. 4. Imaging sequence (top panel) from typical 600 bar injection pressure and 1 bar chamber pressure experiment and corresponding tip wetting area (bottom panel). The fuel film on the injector tip is highlighted by the red solid arrows and the ligament and slow-moving droplets are highlighted by the dashed cyan arrows. The red numbers in the lower panel correspond to the frame numbers in the image sequence
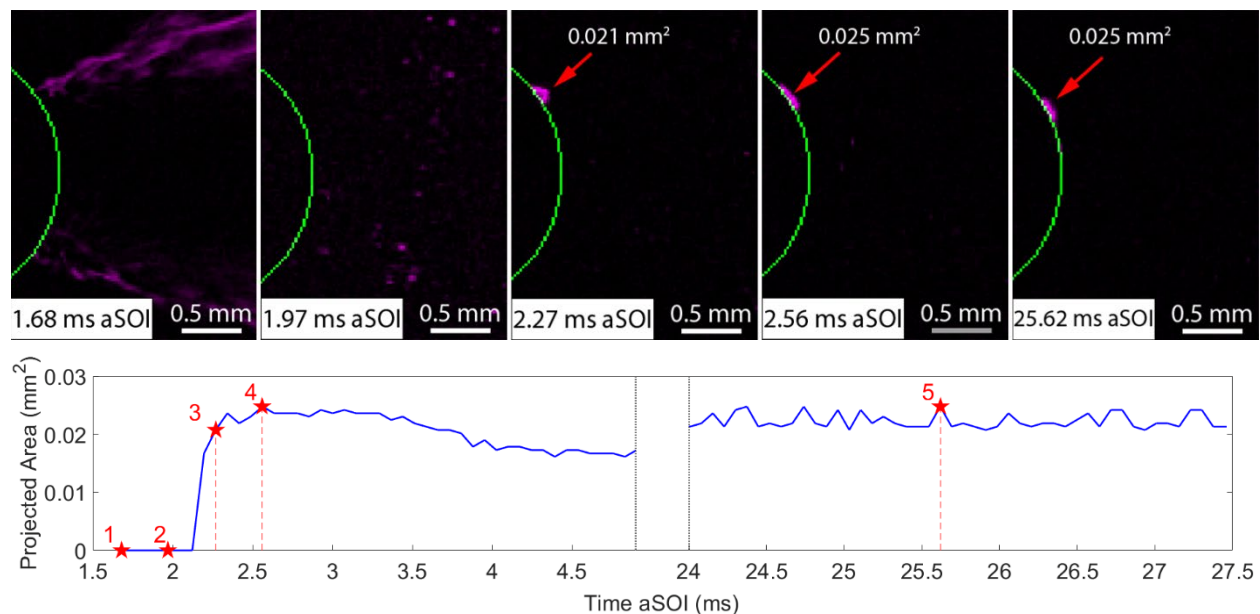
Fig. 5. Frames 1-5 show the sequence of binarized images illustrating the overspill mode of tip wetting (red solid arrow) observed during a trial at 1500 bar injection pressure and 5 bar chamber pressure. The area of the tip wetting corresponding to the frame is shown in the bottom row. The ligament and slow-moving droplets are highlighted by the dashed cyan arrows. EOI was observed at 1.68 ms aSOI for this trial

Statistics of the projected areas of the fuel films for both nozzle holes are presented in **Fig. 6**. The box and whiskers plots show the statistical results of the projected area data (366 data points) for each trial from 2.5 to 30 ms aSOI. To the best of the authors' knowledge, the tip wetting data illustrated in Fig. 6 are the first transient data capturing cycle-to-cycle variability of tip wetting at these conditions. It is very likely that this variability arises from the stochastic nature of the turbulent sprays and the ligament dynamics involved during separation from the nozzle tip after end of injection. The red solid bar within each box

represents the median of the trial, and the bottom and top edges of the box indicate the 25th and 75th percentiles, respectively. Points highlighted in red lying outside the box are outliers, meaning they lie more than 1.5 times the interquartile range away from the bottom or top of the box. The whiskers represent the remaining data that lie outside the 75th and 25th percentile, that are not considered as outliers. The dashed reference line across the plot represents the average of median values reported for the given operating condition. For all conditions studied, fuel films were observed for a minimum of 10 out of 13 trials for the smaller nozzle (hole 1). For hole 2, the nozzle with the larger diameter, none of the trials or operating conditions resulted in significant tip wetting. The results show the strong role injector internal geometry can play on tip wetting. **Figure 6** also includes the average of the medians for all trials where tip wetting was detected. No clear trend is observed between trials, indicating accumulation of fuel vapor in the CVSC did not affect the dominant tip-wetting and tip-drying mechanisms. The data also show the films exhibited generally more consistent behavior at the lower injection and chamber pressure. Data from the other conditions are provided in the supplemental material.

(a)   (b)
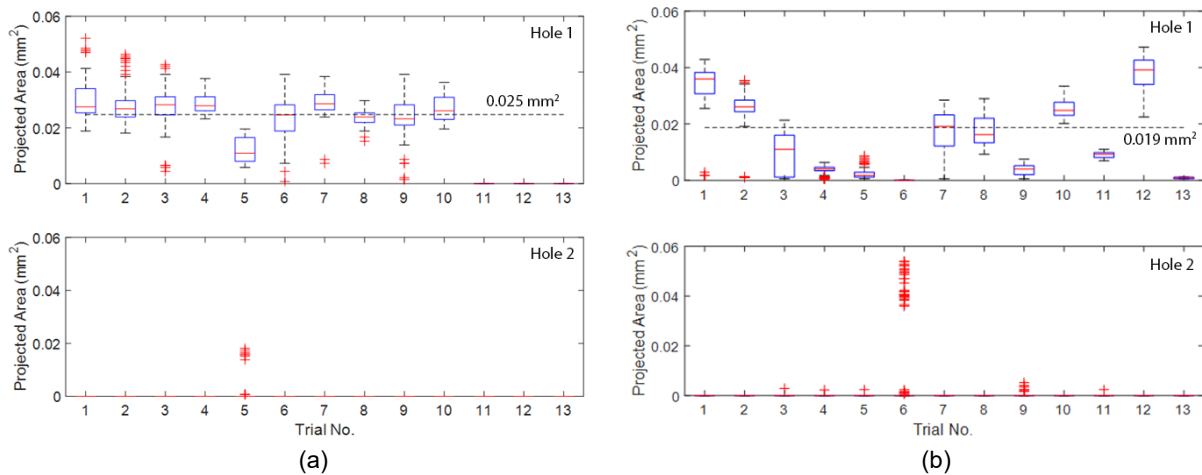
Fig. 6. Comparison of tip wetting results for (a) 600 bar injection pressure and 1 bar chamber pressure and (b) 1500 bar injection pressure and 20 bar chamber pressure. The top plot represents hole 1 data, and the bottom plot represents hole 2 data.
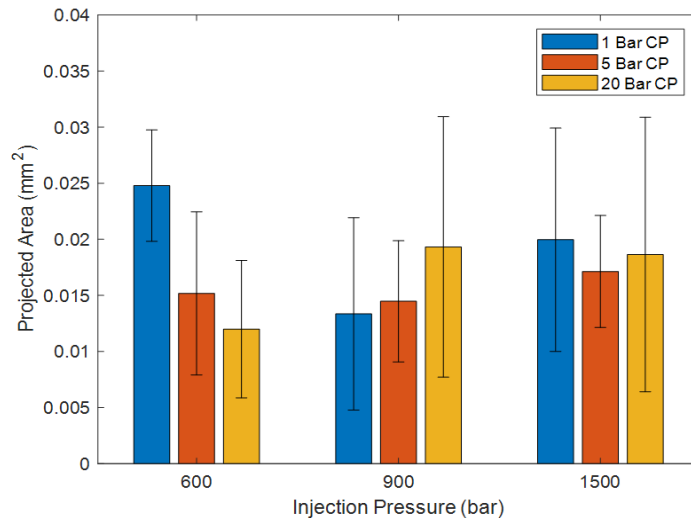
Fig. 7. Average projected area of the fuel films as a function of test conditions for hole 1. The error bars represent the standard deviation of the data for the 13 trials at each condition. CP = chamber pressure.

The average median values of the time history data are compared in **Fig. 7** where the error bars represent one standard deviation from the mean. At 600 bar injection pressure, the data show an inverse relationship between chamber pressure and projected tip wetting area. However, the inverse trend is not

observed at the higher injection pressures. Similarly, no trend is observed between injection pressure and projected area at fixed chamber pressures. The results are consistent with Backes et al. [11] who used counterbore geometry injectors and reported negligible effects of injection pressure on tip wetting in CVSC studies of gasoline at injection pressures of 150, 250 and 350 bar. Importantly Huang et al. [6 & 12] reported decreased tip wetting at similar fuel injection pressures as [11]; however, the studies by Huang et al. [6 & 12] used n-heptane. While the density of n-heptane is within 10% of that of gasoline, the Reid vapor pressure of gasoline (see Table S1 of the supplemental material) is an order of magnitude higher than that of n-heptane (which is 0.06 bar at 298 K [18]). Additionally, the viscosity of gasoline is approximately 30% higher than that of n-heptane (0.41 mPa-s [19]). These parameters will impact ligament formation; the effectiveness of shear forces and viscous tension on droplet breakup; and vaporization rates and thereby tip-drying mechanisms. Comparison of the differences in the trends with fuel injection pressure indicates the effects of fuel properties are critical for understanding tip-wetting phenomena.

1.1. Fuel dribbling

The effects of operating conditions on droplet and ligament formation were also quantified for both holes of the fuel injector. For simplicity, ligaments are included in the term droplets and the number of droplets are reported as the droplet count. **Figure 8** compares the results for droplet projected area and droplet count for the three chamber pressures studied with 600 bar fuel injection pressure, and **Fig. 9** shows the results for 1500 bar fuel injection pressure. The data show strong correlation between increasing chamber pressure and increasing projected area of droplets and droplet count; however, no trends are obvious with injection pressure. The data from the 900 bar fuel injection pressure show the same trends and are provided in the supplemental material for reference.

Although not shown here, the smaller nozzle hole (hole 1) produced more low-momentum droplets and ligaments at the EOI compared with hole 2. While a smaller orifice diameter is favorable for finer atomization and smaller spray plume angle, the current work indicates smaller fuel injector holes have higher potential for forming fuel films (as shown in Section 3.1) and more and larger low-momentum droplets and ligaments that are potential sources of increased particulate emissions in a GDI engine.
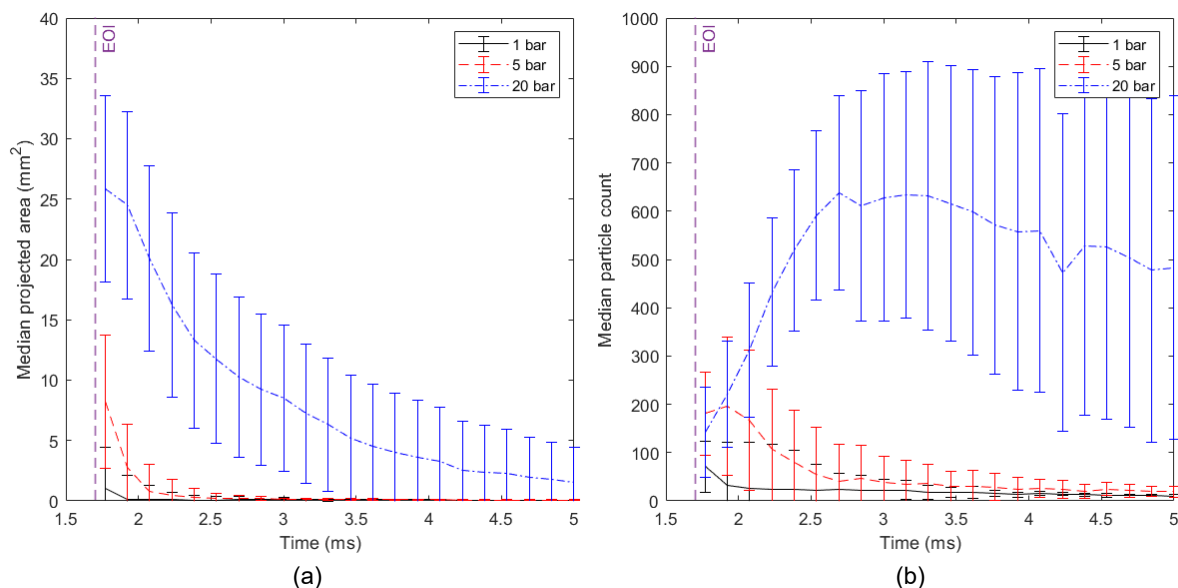
Fig. 8. Effects of chamber pressure on (a) median droplet projected area and (b) median droplet count for 600 bar injection pressure. The results include data from both injector holes. The error bars represent the standard deviation of the data.

(a)   (b)
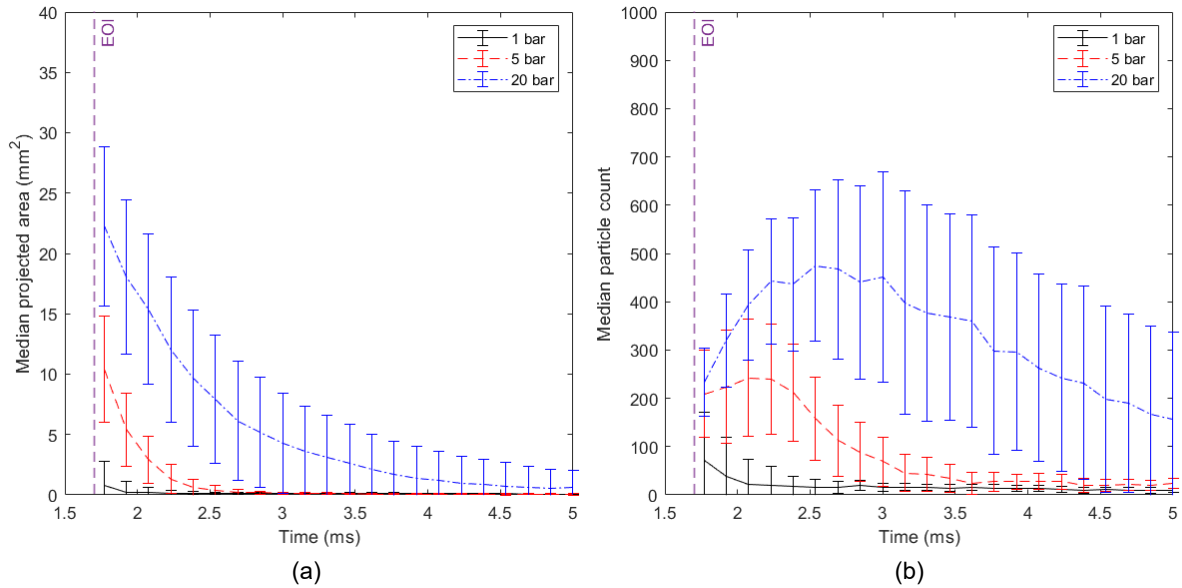
Fig. 9 Effects of chamber pressure on (a) median droplet projected area and (b) median droplet count for 1500 bar injection pressure. The results include data from both injector holes. The error bars represent the standard deviation of the data.

3.3 Effects of Fuel Temperature

(a)   (b)
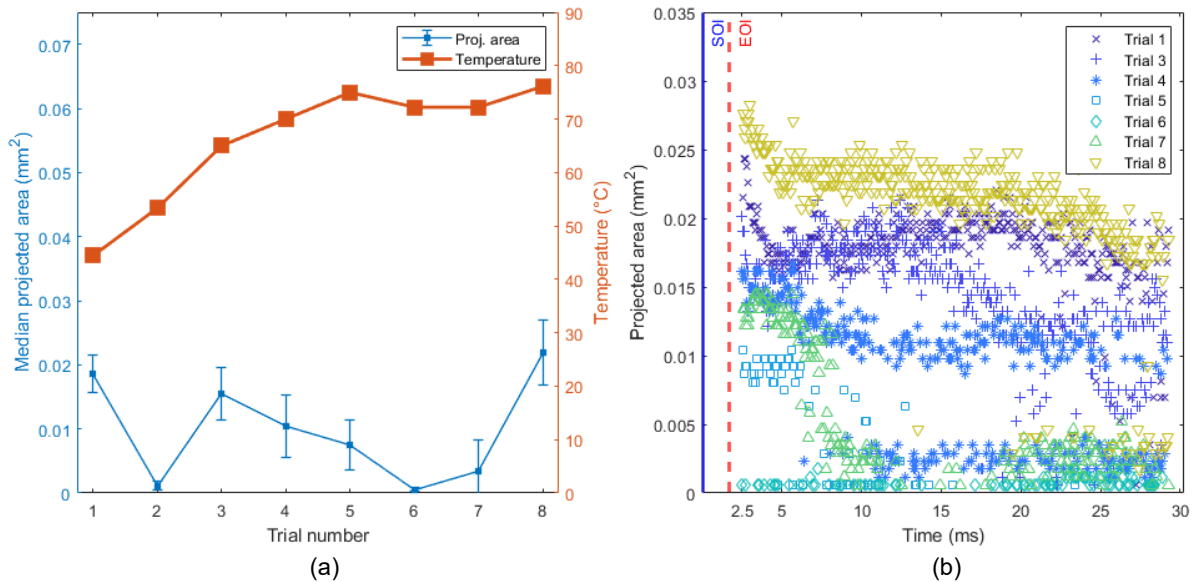
Fig. 10. Effects of fuel temperature on the (a) projected area of tip wetting and (b) and time history of the projected area of tip wetting for fuel injection pressure of 1500 bar and chamber pressure of 5 bar. The median projected areas were calculated for each trial from 2.5 ms to 30 ms. The error bars are the standard deviation of the time-history data. For clarity, trial 2 is not reported since tip wetting was not observed.

The previous trials on tip-wetting (Section 3.1) presented results from experiments where the fuel temperature was regulated to be below 65 °C. To understand the effects of fuel temperature on tip wetting at non-flash boiling conditions, eight trials were conducted with longer time intervals between injection events to allow the fuel to warm passively throughout the experiments. **Figure 10** shows the temperature of the fuel as measured in the fuel return line (see **Fig. 1**) without fuel temperature control. The fuel temperature increased from ~45 °C to ~75 °C over the course of the eight tests conducted. **Figure 10** also presents the average projected area of the fuel films and the time-histories of the project area of the fuel

films for 1500 bar injection pressure and 5 bar chamber pressure. The data show no correlation between the fuel films and the temperature of fuel; either in the rate of film removal/dispersion or the size of the films formed. While the temperature of the fuel increased during the trials, the fuel did not transition to flash boiling due to the high chamber pressure.

2. Conclusions

The high-speed imaging data presented here are the first to capture end-of-injection dribbling effects and injector tip-wetting of gasoline at fuel injection pressures above 500 bar. The experiments spanned a broad range of fuel injection and chamber pressures, and the use of a research nozzle allowed the investigation of the effects of two orifice sizes. The high fidelity of the imaging allowed qualitative and quantitative analyses of the tip wetting phenomenon. The following conclusions are outcomes of the analyses.

1) Fuel films were observed to form preferentially at the exit of the smaller orifice for all conditions tested. The larger orifice exhibited little to no formation of fuel films. Due to the absence of a counterbore (commonly found in gasoline injectors) in the nozzle design, spray plume impingement is not considered as a source of tip wetting.
2) For conditions where fuel films were observed, two categories of tip-wetting phenomena were identified. In the majority of the cases, a fuel ligament was connected to the surface of the nozzle and over time the ligament separated from the tip leaving a remnant of the fuel on the surface on the injector. For the remaining cases, no ligaments were present, and the film appeared to "leak" from the interior volume of the injector onto the tip surface.
3) Both nozzle orifices produced larger droplets and ligaments (relative to the smaller droplets produced by the main spray) with low momentum at the end of injection for all conditions studied.
4) The size of the fuel films (characterized by the projected areas) produced by the smaller nozzle orifice were negligible functions of injection pressure, chamber pressure and fuel temperature. The films persisted for significant periods of time (often over 20 ms) at the ambient temperatures used in the spray chamber. The lack of sensitivity of tip-wetting to fuel injection pressure is contrary to the trends reported in the literature for lower fuel injection pressures.
5) The amount of fuel dribbling (characterized by the projected area of the droplets and ligaments at EOI and the number of droplets and ligaments) increased with higher chamber pressure for all injection pressures.

For the injector design and range of operating conditions considered in the study, injector geometry played a more prominent role in tip wetting compared with injection and chamber pressure and fuel temperature. Flash boiling was not expected at the conditions studied and was not observed for any experiments. While gasoline sprays would experience higher temperatures and turbulence different than the conditions studied, the larger droplets and structures observed here at the end of injection will take more time to evaporate and mix with air and could be a source of HC and particulate emissions in GDI engines. Additionally, the consistency and persistence of the fuel films observed indicate tip wetting can be difficult to mitigate without careful and intentional design of the injector nozzle.

Acknowledgements

References

[1] Yamaguchi, A., Koopmans, L., Helmantel, A., Dillner, J., & Dahlander, P. (2022). Spray Behaviors and Gasoline Direct Injection Engine Performance Using Ultrahigh Injection Pressures up to 1500 Bar. SAE International Journal of Engines, 167-183.

[2] Badshah, H., Kittelson, D., & Northrop, W. (2016). Particle Emissions from Light-Duty Vehicles during Cold-Cold Start. SAE International Journal of Engines, 1775-1785.

[3] Peterson K and Grover R. Application of optical diagnostics and simulation to fuel injector tip wetting and soot production. In:*11th international symposium on combustion diagnostics*, Kurhaus of Baden-Baden, 1–2 July 2014, pp. 78–85. Mainz: AVL Deutschland.

[4] Medina, M., Alzahrani, F., Fatouraie, M., Wooldridge, M., & Sick, V. (2020). Mechanisms of fuel injector tip wetting and tip drying based on experimental measurements of engine-out particulate emissions from gasoline direct-injection engines. *International Journal of Engine Research*, 1–19. https://doi.org/10.1177/1468087420916052

[5] Henkel, S., Hardalupas, Y., Taylor, A., Conifer, C., Cracknell, R., Goh, T. K., Reinicke, P. B., Sens, M., & Rieß, M. (2017). Injector Fouling and Its Impact on Engine Emissions and Spray Characteristics in Gasoline Direct Injection Engines. *SAE International Journal of Fuels and Lubricants*, *10*(2). https://doi.org/10.4271/2017-01-0808

[6] Huang, W., Gong, H., Moon, S., Wang, J., Murayama, K., Taniguchi, H., Arima, T., Arioka, A., & Sasaki, Y. (2021). Nozzle Tip Wetting in GDI Injector at Flash-boiling Conditions. *International Journal of Heat and Mass Transfer*, *169*, 120935. https://doi.org/10.1016/j.ijheatmasstransfer.2021.120935

[7] Sykes, D., Stetsyuk, V., Turner, J., de Sercey, G., Gold, M., Pearson, R., & Crua, C. (2022). A phenomenological model for near-nozzle fluid processes: Identification and qualitative characterisations. *Fuel*, *310*, 122208. https://doi.org/10.1016/j.fuel.2021.122208

[8] Medina, M. (2020). *Experimental studies of high-pressure gasoline fuel sprays for advanced internal combustion engines*. [Doctoral dissertation, University of Michigan, Ann Arbor].

[9] Medina, M., Bautista, A., Wooldridge, M., & Payri, R. (2021). The effects of injector geometry and operating conditions on spray mass, momentum and development using high-pressure gasoline. Fuel. https://doi.org/10.1016/j.fuel.2021.120468

[10] Leick, P., Bork, B., & Geiler, J. (2018). Experimental characterization of tip wetting in gasoline DI injectors. ICLASS Conference (pp. 1-9). Chicago: ICLASS.

[11] Backes, F., Blochum, S., Hartl, M., & Wachtmeister, G. (2020). Experimental analysis of gasoline direct injector tip wetting. *SAE International Journal of Engines*, 77-91. doi:10.4271/03-13-01-0006

[12] Huang, W., Moon, S., & Wang, J. (2020). Nozzle tip wetting in gasoline direct injection injector and its link with nozzle internal flow. *International Journal of Engine Research*, 340-351. DOI: 10.1177/1468087419869774

[13] Dageforde, H., Kiefer, A., Samenfink, W., Wiese, W., & Kufferath, A. (2015). Requirements for spray and tip design of a multi-hole injector for DISI engines. *ICLASS Conference* (pp. 1-8). Tainan: ICLASS.

[14] Araneo, L., & Donde', R. (2017). Flash boiling in a multihole G-DI injector - Effects of the fuel distillation curve. *Fuel*, 500-510.

[15] Rasband, W.S., ImageJ, U. S. National Institutes of Health, Bethesda, Maryland, USA, https://imagej.nih.gov/ij/, 1997-2018;

[16] Schneider, C.A., Rasband, W.S., Eliceiri, K.W. "NIH Image to ImageJ: 25 years of image analysis". *Nature Methods 9*, 671-675, 2012;

[17] Abramoff, M.D., Magalhaes, P.J., Ram, S.J. "Image Processing with ImageJ". *Biophotonics International*, volume 11, issue 7, pp. 36-42, 2004

[18] Carruth, G. F., & Kobayashi, R. (1973). Vapor Pressure of Normal Paraffins Ethane Through n-Decane from Their Triple Points to About 10 Mm Hg. *Journal of Chemical and Engineering Data*, 115-126.

[19] Sagdeev, D. I., & Fomina, M. G. (2013). Experimental study of the density and viscosity of n-Heptane at Temperatures from 298 K to 470 K and Pressure up to 245 MPa. *International Journal of Thermophysics*, 1-33.

Supplemental Material

Table S1. Summary of fuel properties

Property	Test Method	Value
Fuel type	-	Reference grade gasoline (HF0072, Haltermann Solutions)
Specific gravity 289 K	ASTM D4052	0.742
Reid vapor pressure 310 K [kPa]	ASTM D5191	61.0
Research octane number (RON)	ASTM D2699	91.8
Motor octane number (MON)	ASTM D2700	84.0
Heat of combustion [MJ/kg]	ASTM D240	43.03
H/C ratio [Mole basis]	Gage-calculated	1.87
Distillation, IBP [K]	ASTM D86	305.15
Distillation, 10% [K]	ASTM D86	326.15
Distillation, 50% [K]	ASTM D86	369.15
Distillation, 90% [K]	ASTM D86	425.15
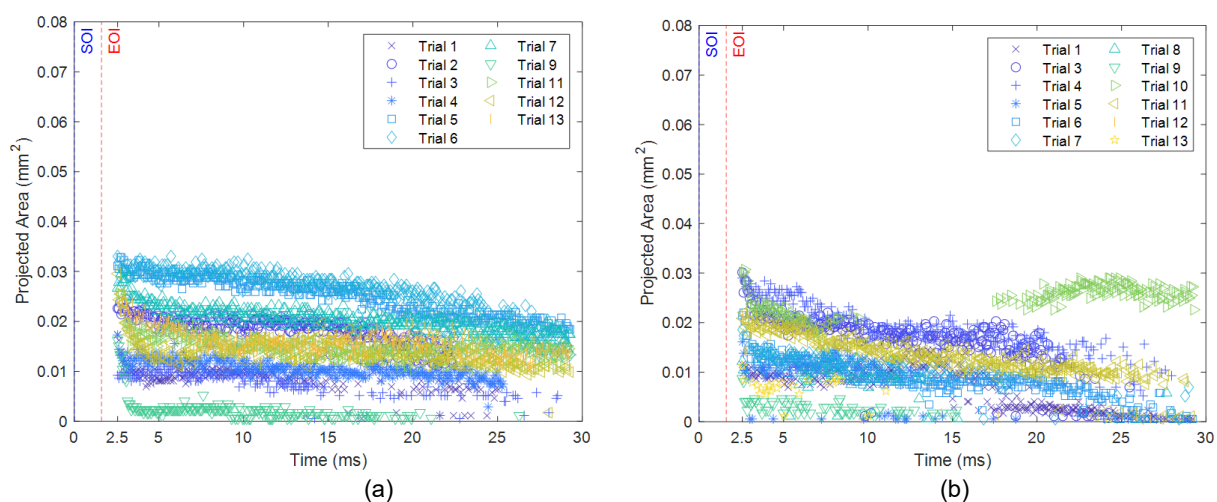
Fig. S1. Fuel film results for hole 1 for (a) 600 bar injection pressure and 5 bar chamber pressure and (b) 600 bar injection pressure and 20 bar chamber pressure. The film projected area was documented for times > 2.5 ms aSOI.
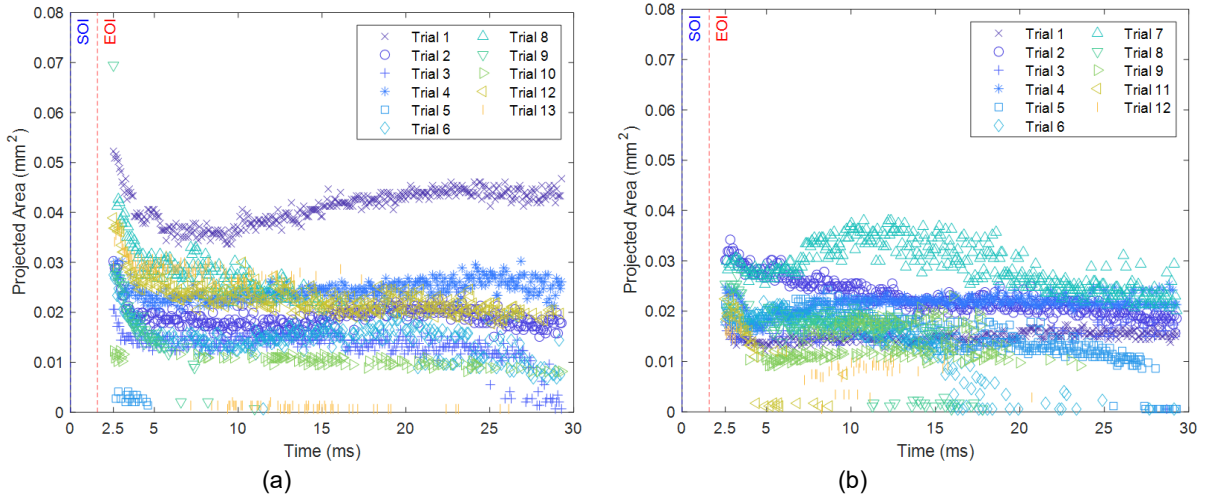
Fig. S2. Fuel film results for hole 1 for (a) 1500 bar injection pressure and 1 bar chamber pressure and (b) 1500 bar injection pressure and 5 bar chamber pressure. The film projected area was documented for times > 2.5 ms aSOI.
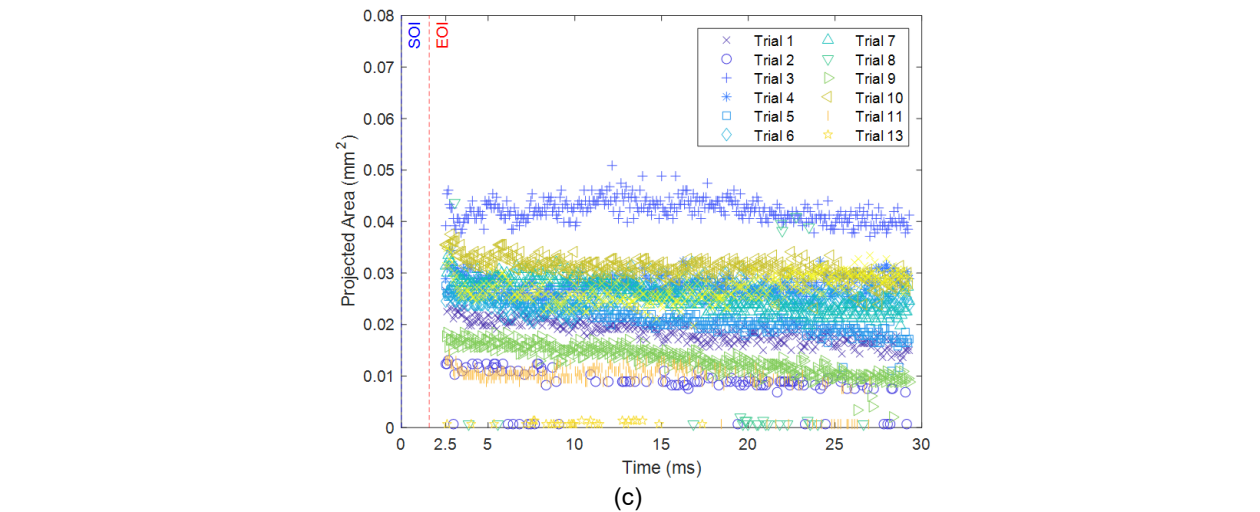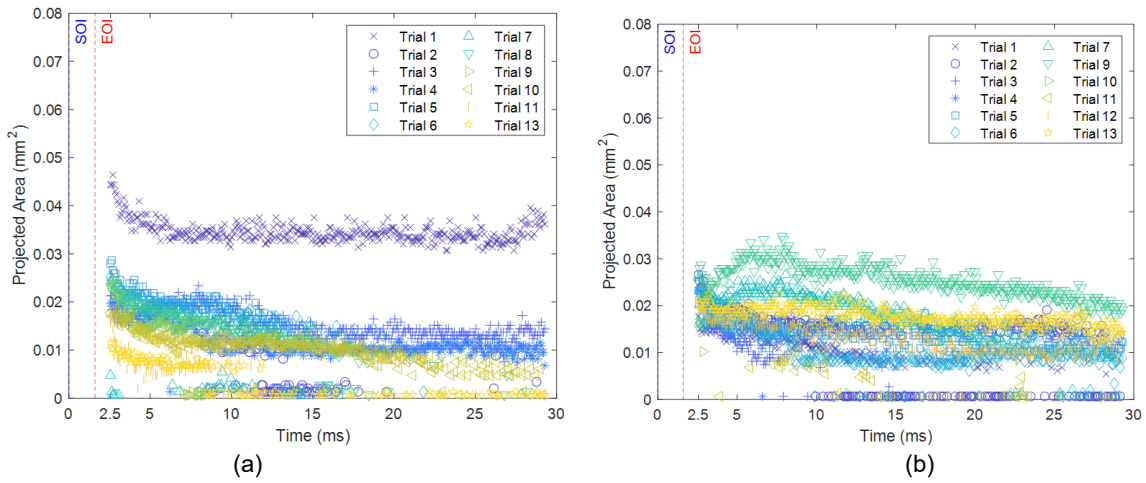
Fig. S3. Fuel film results for hole 1 for (a) 900 bar injection pressure and 1 bar chamber pressure and (b) 900 bar injection pressure and 5 bar chamber pressure and (c) 900 bar injection pressure and 20 bar chamber pressure. The film projected area was documented for times > 2.5 ms aSOI.
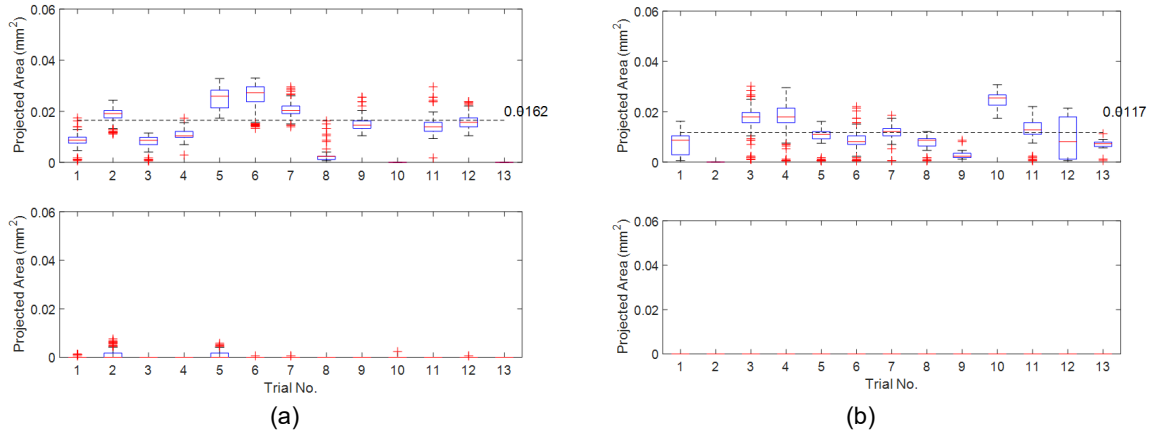
Fig. S4. Comparison of tip wetting results for (a) 600 bar injection pressure and 5 bar chamber pressure and (b) 600 bar injection pressure and 20 bar chamber pressure. The top plot represents hole 1 data and the bottom plot represents hole 2 data.
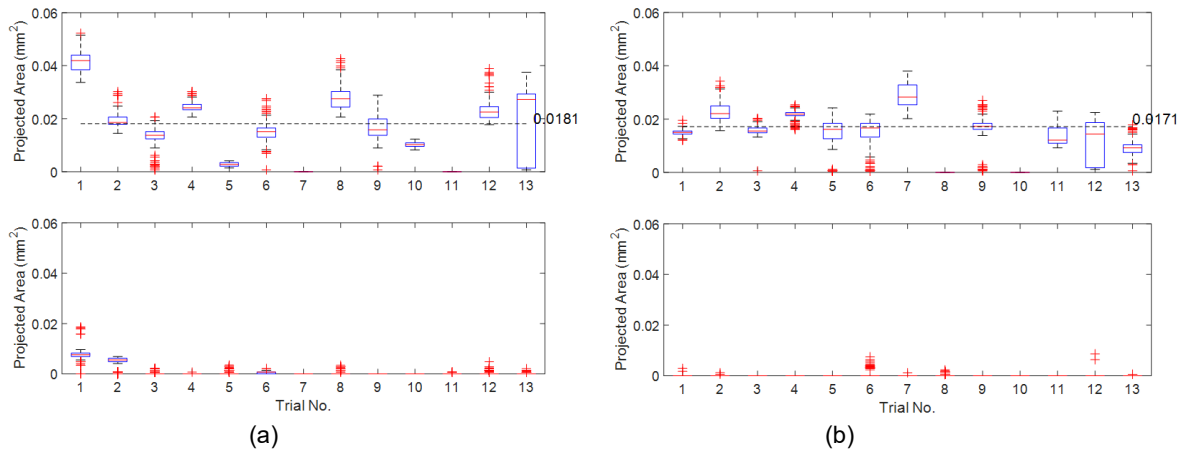
Fig. S5. Comparison of tip wetting results for (a) 1500 bar injection pressure and 1 bar chamber pressure and (b) 1500 bar injection pressure and 5 bar chamber pressure. The top plot represents hole 1 data and the bottom plot represents hole 2 data.
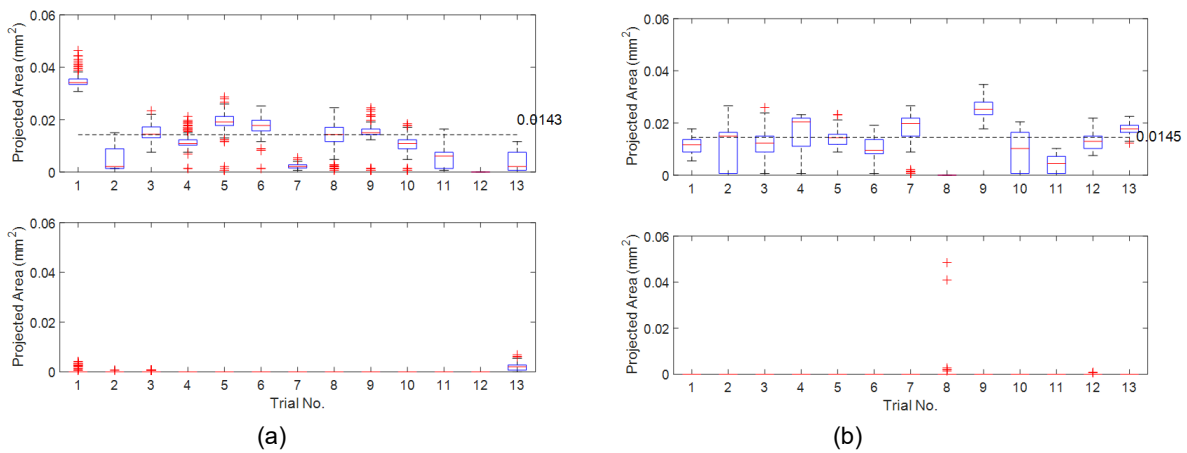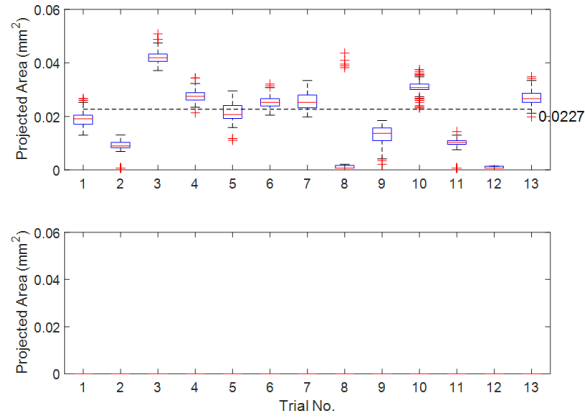
(c)

Fig. S6. Comparison of tip wetting results for (a) 900 bar injection pressure and 1 bar chamber pressure and (b) 900 bar injection pressure and 5 bar chamber pressure and (c) 900 bar injection pressure and 20 bar chamber pressure. The top plot represents hole 1 data and the bottom plot represents hole 2 data.
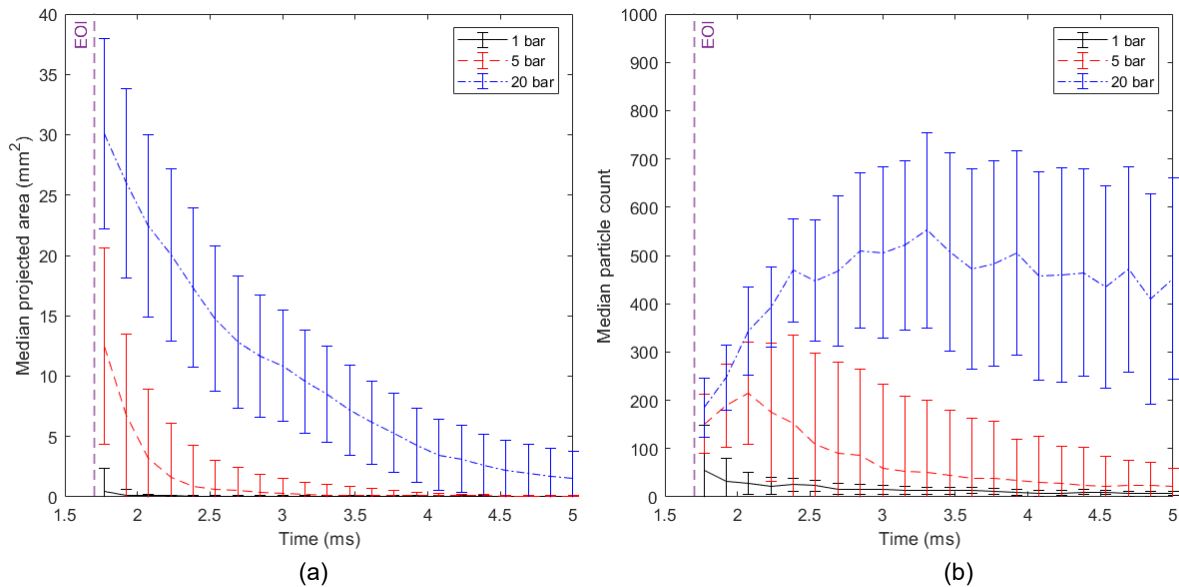
(a)   (b)

Fig. S7. Effects of chamber pressure on (a) median droplet projected area and (b) median droplet count for 900 bar injection pressure. The results include data from both injector holes. The error bars represent the standard deviation of the data
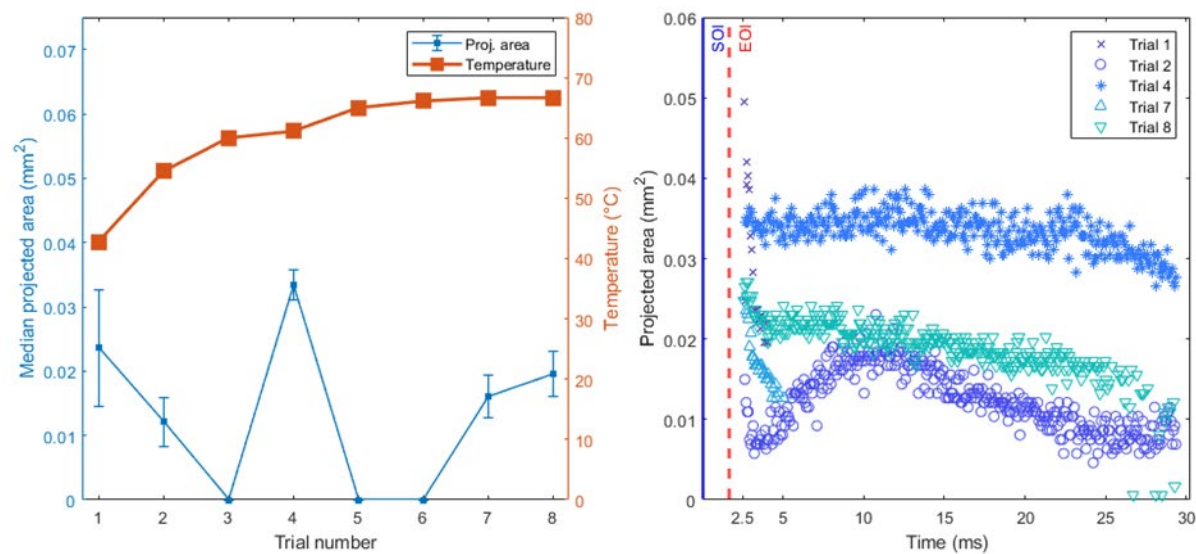
Fig. S8. Effects of fuel temperature on the (a) projected area of tip wetting and (b) and time history of the projected area of tip wetting for fuel injection pressure of 600 bar and chamber pressure of 5 bar. The median projected areas were calculated for each trial from 2.5 ms to 30 ms. The error bars are the standard deviation of the time-history data. For clarity, trials 3,5 and 6 are not reported since tip wetting was not observed.

THIESEL 2022 Conference on Thermo- and Fluid Dynamics of Clean Propulsion Powerplants

Measurement of Needle and Armature Dynamics in a Gasoline Direct Injector by High-Speed Neutron Imaging

L. Wissink[1], T.J. Toops[1], D.A. Splitter[1], E.J. Nafziger[1], C.E.A. Finney[1], H.Z. Bilheux[2], Y. Zhang[2]

[1]Oak Ridge National Laboratory, Energy Science and Technology Directorate, Oak Ridge, TN 37830

[2]Oak Ridge National Laboratory, Neutron Sciences Directorate, Oak Ridge, TN 37830

E-mail: wissinkml@ornl.gov

Abstract. In modern spark ignition engines, precise delivery of fuel with gasoline direct injection has become increasingly important in the effort to meet ever stricter efficiency and emissions regulations. Use of multiple small close-coupled injections has become more common in attempt to precisely control fuel distribution in the cylinder, but these strategies are hindered by nonlinear injection effects due to operation in the ballistic region of the solenoid-operated valve and due to armature bounce at the end of injection. Understanding the internal dynamics of the injector is crucial to minimizing and controlling non-linearity and shot-to-shot variation, but the experimental techniques available to date are capable only of tracking the position of either the top of the needle (via laser sensors or by monitoring current and voltage in the solenoid coil) or the bottom of the needle (via transparent nozzles or high-speed x-ray imaging). A complete picture of the axial and radial motion of valve needle has until now remained elusive. In this work, we present high-speed ensemble neutron transmission imaging of an entire 8-hole gasoline direct injector operating at 200 bar, allowing for both visualization and quantification of the actuation dynamics including lift and wobble of the valve ball, oscillation and bending of the valve needle, lift, rocking, and bounce of the armature, compression of the springs, and radial swelling of the solenoid during energization. Because neutrons offer high penetration through the metal injector while also being sensitive to the ^{1}H nuclei in fuel molecules, it is also possible to simultaneously see the fluid dynamics of the injection process, including filling of the sac volume, emanation of the spray through the nozzle holes and into the downstream gas, and the formation and evolution of fuel films on the tip of the injector and the walls of the spray container.

Notation

CT   *computed tomography*
DOE   *Department of Energy*
EOE   *end of energization*
GDI   *Gasoline direct injection*
HFIR   *High Flux Isotope Reactor*
MCP   *microchannel plate*
ORNL   *Oak Ridge National Laboratory*
PM   *particulate matter*
SOE   *start of energization*

1. Introduction

Over the last decade, spark ignition engines have undergone a shift toward downsizing, turbocharging, and gasoline direct injection (GDI) in order to meet increasingly stringent fuel economy regulations [1]. GDI offers multiple benefits including charge cooling and the ability to tailor the delivery of the fuel into the cylinder to optimize the combustion process. However, high spray penetration with GDI can lead to wall films which cause high levels of particulate matter (PM), especially during cold start [2].

    One method to reduce PM formation is to split the fuel delivery into multiple smaller injections, which reduces the spray penetration and formation of wall films [3]. However, this leads to additional

challenges. The use of multiple injections requires a smaller minimum injection quantity, while the trend towards downsizing and turbocharging requires a larger maximum injection quantity to meet the higher load per cylinder. It is also generally desirable to place the multiple injections as close together as possible to achieve a homogenous fuel–air mixture before combustion. These requirements can lead to operation in the nonlinear range of the injector due to short injections which end before the needle is fully open and due to close-coupled injections which occur in the ballistic region of the solenoid-operated valve.
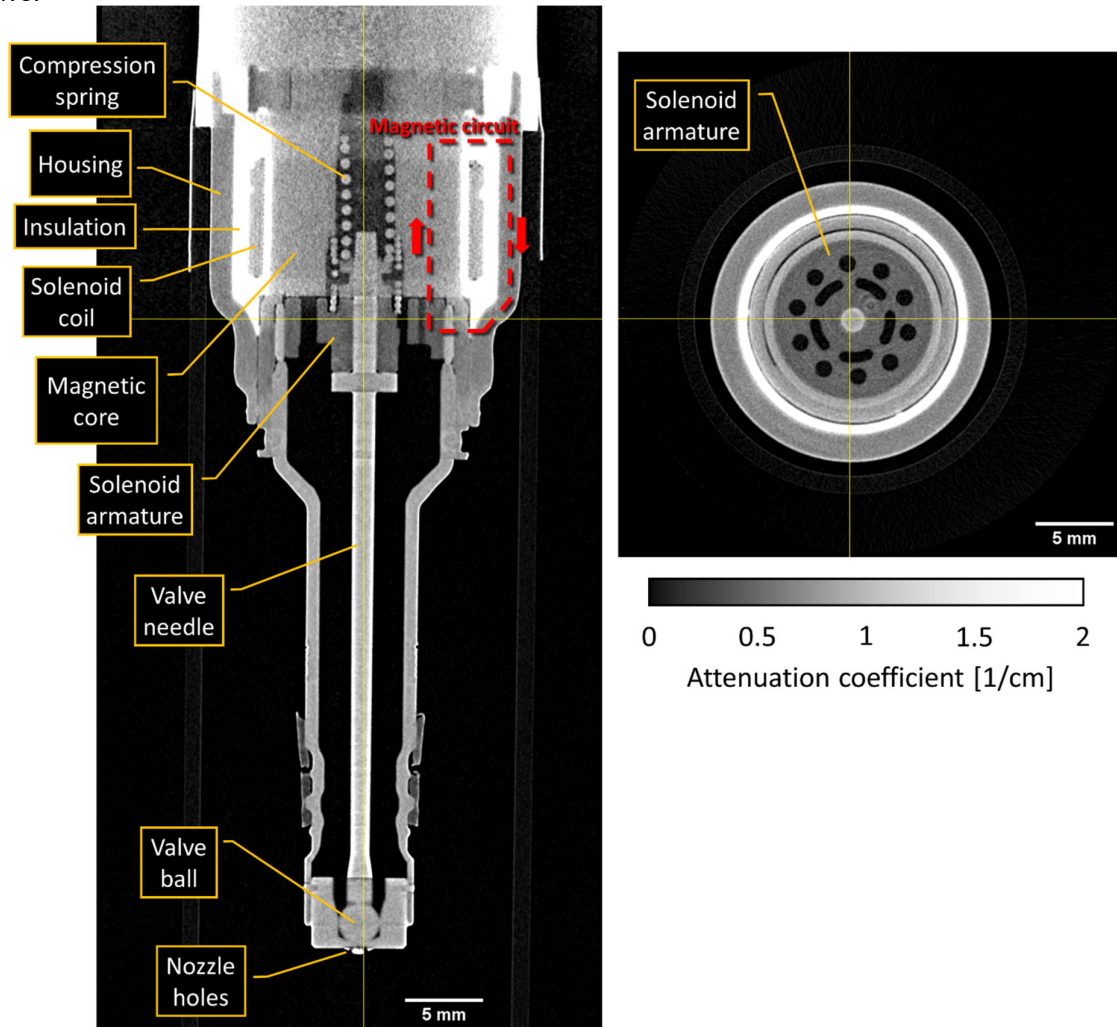
Figure 1. Sagittal and transverse cut planes from neutron CT reconstruction of a gasoline direct injector show internal components and geometry

Cut planes from a neutron computed tomography (CT) reconstruction of an 8-hole gasoline direct injector [4], shown in **Figure 1**, illustrate its internal features and construction. Fuel flow is controlled by a valve ball, which is compressed against the valve seat by a spring when closed. To open the injector, current is passed through the solenoid coil, generating a magnetic field which creates vertical force on the armature, causing the entire valve needle assembly to lift. If the solenoid armature is still in motion from the closing of a previous injection when a subsequent injection begins, significant nonlinearity in total fuel quantity may be observed as dwell time between injections is modified. Additionally, the armature may bounce upon closing, resulting in unintended fuel delivery.

Several methods have been developed to reduce nonlinearity and/or armature bounce, including optimization of the electromagnetic geometry [5], armature mass reduction [6], non-rigid coupling of the armature to the needle [7], and modulation of the current waveform [7, 8]. Measurement of motions of the internal components is critical to understanding and improving injectors. The most common measurement of interest is the axial motion, or lift, of the armature and/or valve needle. Armature lift can be measured by using the solenoid itself as a sensor by analysis of the voltage and current waveforms [9]. Needle lift at the top of the needle has been measured by laser Doppler vibrometry [10], and lift and

wobble (radial motion) of the check ball have been observed via optically transparent nozzles [11, 12] and x-ray imaging [13, 14]. However, it is not possible to make an entire injector optically transparent due to the high fuel pressure, and the thick metal cross section of the solenoid makes x-ray imaging challenging. A full accounting of the internal dynamics of injectors has not yet been achieved.

Unlike photons, which interact primarily with the electrons in matter, neutrons interact primarily with atomic nuclei, and therefore have high penetration through most materials including many metals. Neutron interactions are isotope-specific, and ^1H has a particularly high incoherent scattering cross section, which means that neutrons are sensitive to any hydrogenous material, including hydrocarbon fuel. This makes neutron imaging an ideal tool for studying the fluid and mechanical dynamics inside fuel injectors, as neutrons can easily penetrate the metal injector while having high contrast to the liquid fuel inside. In recent work, we demonstrated that high-speed neutron imaging could resolve oscillatory motions of an injector needle on the order of 5 μm at 5 μs time scale [15]. However, the field of view in that effort was restricted to only the very end of the needle near the valve ball. In this work, we extend the field of view to cover the entire injector, offering a complete picture of the internal mechanical dynamics while simultaneously imaging the internal and external fluid dynamics.

2. Experimental setup

2.1 Neutron imaging

High-speed neutron imaging was performed at the CG-1D cold neutron imaging beamline [16] at the High Flux Isotope Reactor (HFIR), a Department of Energy user facility operated by the Oak Ridge National Laboratory (ORNL). A ^{10}B-doped microchannel plate (MCP) detector with 2 × 2 Timepix readout was used. The MCP detector has 512 × 512 pixels with 2.8 × 2.8 cm field of view, a physical pixel size of 55 μm, and 1 μs timing capability [17]. The instrument has an adjustable aperture, which was set to 16 mm, and a fixed aperture-to-detector distance of 6.59 m, resulting in an L/D ratio of 412.

One of the biggest challenges with neutron imaging of dynamic processes is the relatively low flux of neutrons. Single-shot measurements of dynamics inside injectors, which occur at μs to ms timescales, are not possible with existing neutron sources. However, high temporal resolution can still be achieved by making cyclic ensemble measurements. In this case, we operated the injector in synchronization with the MCP detector at an injection frequency of 50 Hz to make ensembles consisting of ~5–6×10^6 injection events for each movie. As described in previous work [15], ensemble image sequences were acquired in a series of shutters with time bin sizes ranging from 5.12 μs to 20.48 μs. The raw data, which is in the form of neutron counts per pixel per time bin, were overlap corrected [18], re-binned to 20.48 μs (equivalent to 48,828 frames/s), and normalized to count rate to account for the variation in number of successfully acquired shutters. The resulting image sequences were further processed with a 10 kHz, zero-phase, second-order Butterworth lowpass filter in the temporal domain.

2.2 Spray rig

An 8-hole gasoline direct injector was mounted in a spray rig developed specifically for neutron imaging, pictured in **Figure 2**. The inlet of the injector was connected to a heated fuel rail via a high-pressure rotary union, and a rotation mount with a custom adapter allowed the injector to be rotated precisely to any desired angle. The outlet of the injector was fitted into a thin-walled aluminum tube, which is highly transparent to neutrons. The aluminum tube was connected to a stainless steel tee fitting which was continuously purged with nitrogen gas at a fixed rate provided by a mass flow controller. A pilot-operated backpressure valve located downstream of the tee controlled the pressure of the environment inside the aluminum tube.

The spray rig was mounted on a 3-axis positioning stage at the CG-1D instrument. The stage allowed the injector to be positioned directly in front of the MCP detector and allowed for translation of the injector to different positions, at it is too large to fit entirely within the field of view of the detector. Boron impregnated rubber was used to shield all parts of the spray rig except for the injector itself, which was open to air in order to provide an unobstructed view for the neutron beam, as shown in **Figure 2C**. All connections to the spray rig, including fuel supply, sweep gas supply, exhaust vacuum line, and electrical signals were made with flexible hoses and wiring in order to allow unimpeded movement of the spray rig on the positioning stage.

A diagram of the gas flow path is shown in **Figure 3**. The majority of the equipment for the experiment was located outside of the instrument radiation shielding, denoted as "cage" in **Figure 3**, to minimize

neutron activation. The nitrogen sweep gas was provided by cryogenic cylinders located outside of the building on a gas manifold to enable seamless switching between cylinders. After passing through the mass flow controller, the nitrogen passed through a flexible heated hose before entering the spray rig, which allowed for control of the gas temperature downstream of the injector. All components downstream of the mixing tee, including the backpressure regulator and the exhaust vacuum line, were heated to prevent condensation of fuel in the exhaust flow path, which passed out of the instrument and into a fuel recovery system. This system used a cold trap operated at −45 °C to condense the fuel out of the exhaust. The recovered fuel was then returned to the fuel system, which operated in a closed loop to minimize fuel quantity in the building.
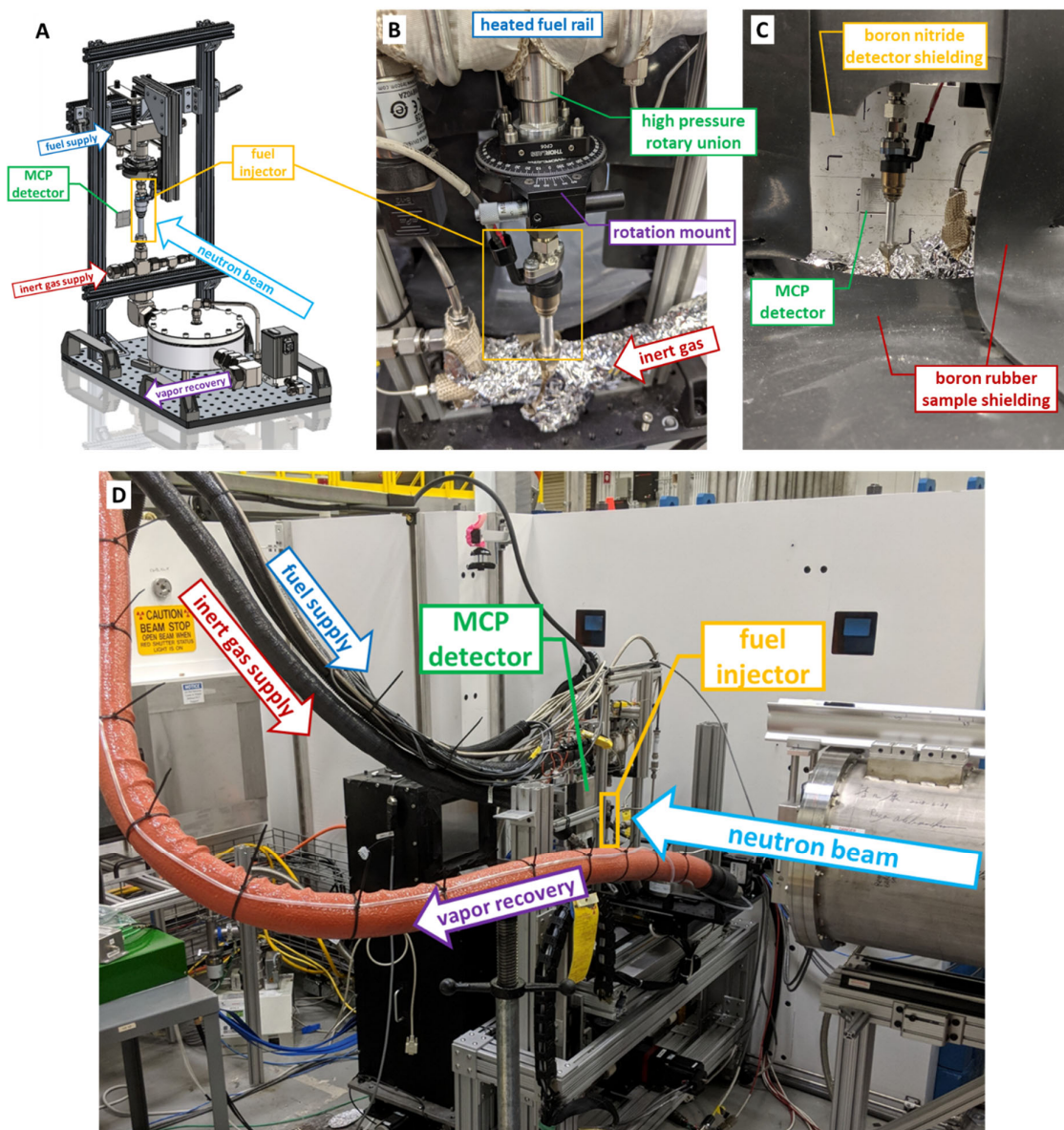
Figure 2. Experimental setup. **A:** Model of the injector spray rig. **B:** View of spray rig from behind. **C:** View of spray rig from front (approximate neutron perspective). **D:** Spray rig installed at CG-1D on 3-axis positioning stage

2.3 Operating conditions

The injector was operated at 50 Hz with a single injection per cycle and a commanded duration of 680 μs per injection. The fuel was iso-octane (C_8H_{18}, 2,2,4-trimethylpentane) and was supplied at 200 bar and 90 °C. The nitrogen sweep gas was supplied at 60 °C, and pressure downstream of the injector

was maintained at 100 kPa to emulate conditions of injection early in the compression stroke of a GDI engine.
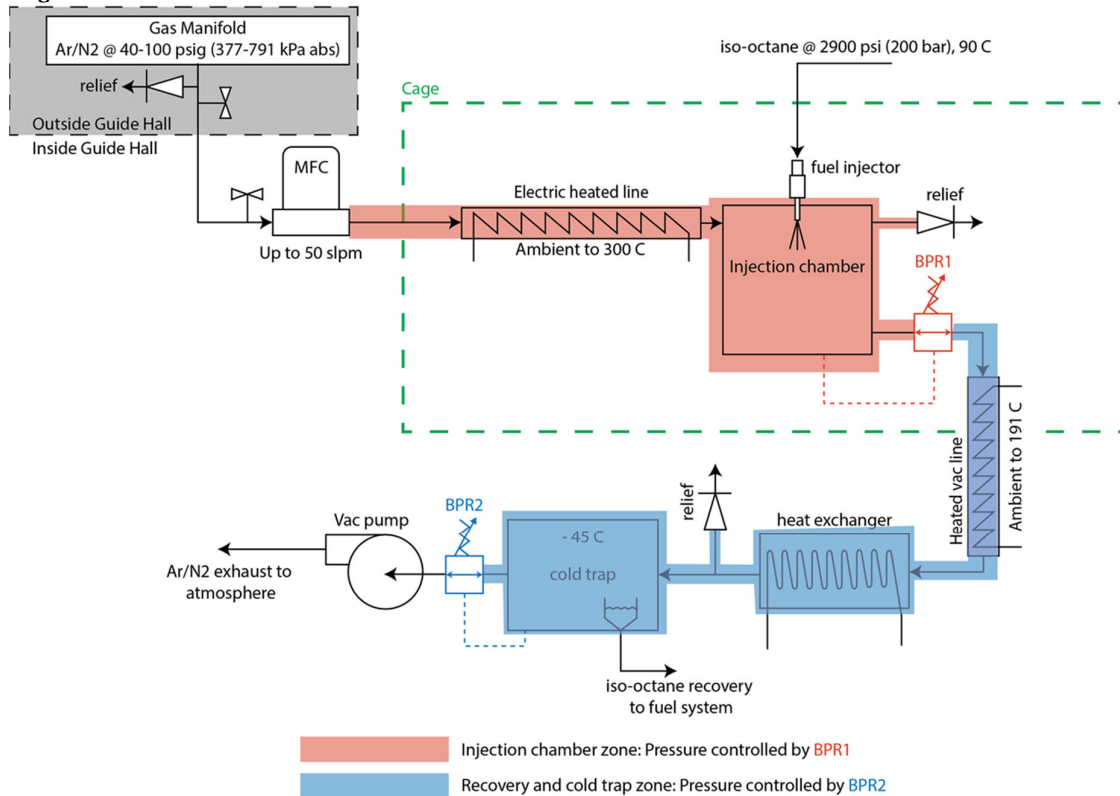
Figure 3. Spray rig gas flow path and fuel recovery diagram

3. Methodology

Neutron imaging is a form of transmission radiography. As a neutron beam passes through a sample, it is attenuated according to the Beer–Lambert law:

$$T = \frac{I}{I_0} = e^{-\Sigma d} \tag{1}$$

Here I_0 is the incident intensity, I is the transmitted intensity, Σ is the macroscopic attenuation coefficient, and d is the path length. For a sample comprised of multiple materials or phases (A, B, C, …),

$$T = \frac{I}{I_0} = e^{-(\Sigma_A d_A + \Sigma_B d_B + \Sigma_C d_C + \cdots)} \tag{2}$$

where each phase may have a different attenuation coefficient and path length. An example of a neutron transmission image for the fuel injector used in this study is shown in **Figure 4**. As shown in **Figure 4A**, the field of view of the MCP detector does not cover the entire injector; therefore the injector was translated to three different positions, and the resulting images were stitched together to produce the linear-scaled transmission image in **Figure 4B** and the log-scaled transmission image in **Figure 4C**. Because the injector was filled with fuel, which strongly attenuates neutrons, the inside of the injector appears almost black in the linear-scaled image. However, due to the high contrast between fuel and steel, the internal components become visible when presented in log scale.

For the stitched transmission image in **Figure 4**, each of the three positions was normalized against an "open beam" (I_0) image in which no sample is present. All images were acquired with 60 s exposure time. In principle, this same normalization approach could be used in high-speed imaging. However, much of the dynamic behavior inside the injector occurs at length scales below the 55 μm pixel size of the MCP detector and will not be readily apparent in a transmission image. To overcome this, we instead normalize our high-speed image sequence against a frame or set of frames from the same sequence.
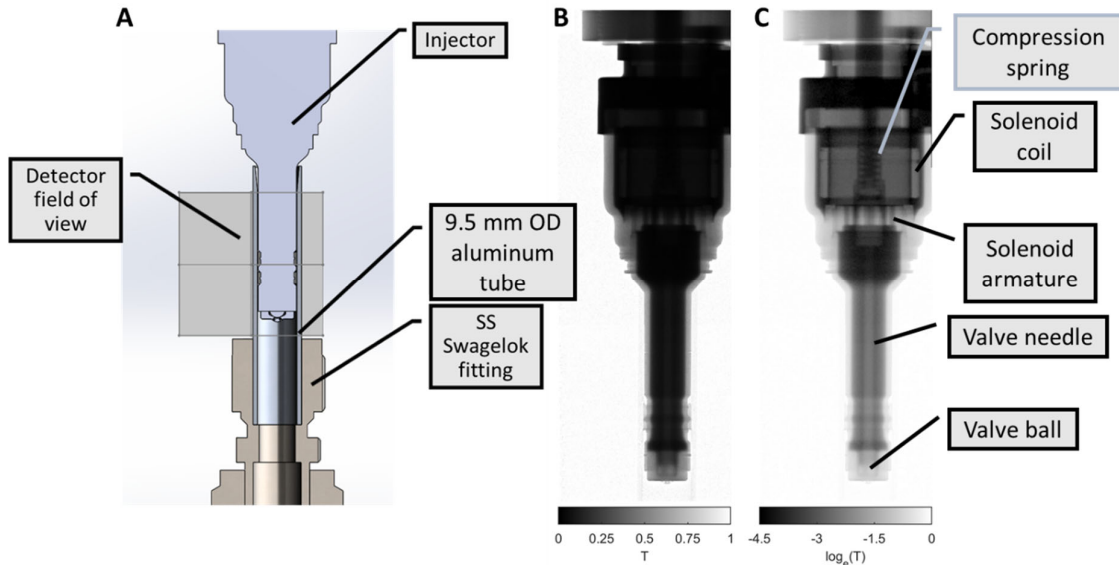
Figure 4. A: Detector field of view compared to injector model. **B:** Linear-scaled transmission image of stitched radiographs. **C:** Log-scaled transmission image reveals internal features of injector

As described in our previous work [15], this results in an image

$$\frac{I(t)}{I_{\text{ref}}} = e^{-\left[\Sigma_A\left(d_A(t) - d_{A,\text{ref}}\right) + \Sigma_B\left(d_B(t) - d_{B,\text{ref}}\right) + \Sigma_C\left(d_C(t) - d_{C,\text{ref}}\right) + \cdots\right]} \qquad (3)$$

which essentially represents how the path lengths through each phase have changed in the dynamic image $I(t)$ compared to the reference image I_{ref}, weighted by the attenuation coefficient of each phase. This can be simplified by assuming that there are only two moving phases. For our injector, these may be the armature (phase A) and the fuel around the armature (phase B). If we assume that the housing of the injector (phase C) is static, then the distance that a given neutron must travel through the housing and the air around the housing will be the same in both the dynamic and reference images, so all the path length difference terms other than A and B will drop out in Equation (3). This assumption also means that the total length through A and B is conserved:

$$d_{A,\text{ref}} + d_{B,\text{ref}} = d_A(t) + d_B(t) \qquad (4)$$

By substituting Equation (4) into Equation (3) and taking the natural logarithm, we obtain

$$\log_e\left(\frac{T(t)}{T_{\text{ref}}}\right) = (\Sigma_B - \Sigma_A)\left(d_A(t) - d_{A,\text{ref}}\right) \qquad (5)$$

This image is a map of how the path length through phase A changed, scaled by the attenuation coefficient difference between the phases A and B. This image can then be analyzed according to the approach described in our previous work [15], in which the geometry and attenuation coefficients of the internal components of the injector are extracted from a neutron CT scan and are then used to create a model of how the path length seen by each pixel on the detector would change if the geometry were displaced by a given amount. This model can then be fit to the log-normalized image described in Equation (5) to estimate the displacement that best fits the data.

The geometry of the solenoid armature and the valve ball were modelled based on the CT scan of the injector shown in **Figure 1**. Two-dimensional path length models were developed for each following the approach described in our previous work [15]. The models are illustrated in **Figure 5**, with the armature displaced horizontally by 0.25 px and vertically by 0.5 px, and the valve ball displaced horizontally by 0.1 px and vertically by 0.5 px. The distance maps of the reference and displaced geometry are visually indistinguishable, but in the distance difference map, the displacement is readily apparent. Note that the distance difference $d(t) - d_{\text{ref}}$ is an order of magnitude larger for the armature than the valve ball due to the steep gradient in path length at the edges of the armature. For simplicity, the internal holes in the armature shown in **Figure 1** have been ignored, with the armature modeled as a solid body. This is addressed by fitting only the edges of the armature to the data.
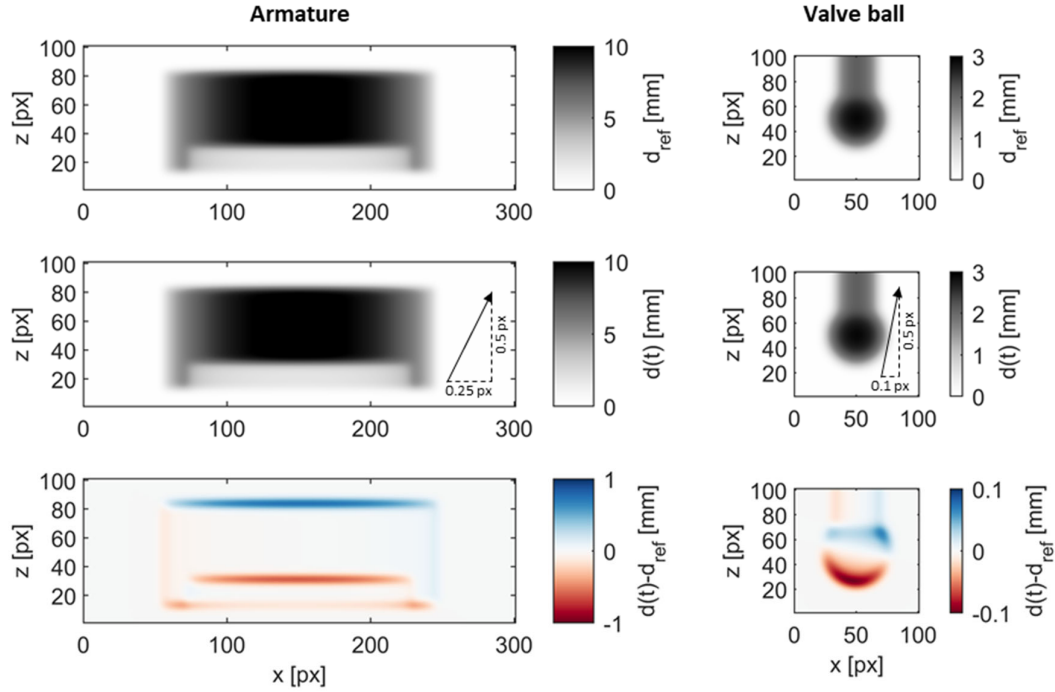
Figure 5. Path length models for solenoid armature and valve ball

Attenuation coefficients were extracted from the neutron CT scan and are shown in **Table 1**. The values measured within the solid components (Σ_A) are effectively constant, whereas the values for the fuel surrounding the components (Σ_B) will vary with path length due to beam hardening, as discussed in our previous work [15]. There it was shown that selecting a representative value of Σ_B based on the average path length produces good results, but there is uncertainty in the fit due to uncertainty in the absolute value of Σ_B, which is affected not only by beam hardening by also by incoherent scattering, which will vary with sample-to-detector distance. Here we have included upper and lower bounds on Σ_B based on the path length range in each component to provide an estimate of the uncertainty in the fit.

Table 1. Attenuation coefficients used in model. Upper and lower bounds for fuel attenuation coefficient due to beam hardening shown in parentheses

Component	Solid: Σ_A [cm^{-1}]	Fuel: Σ_B [cm^{-1}]	$\Sigma_B - \Sigma_A$ [cm^{-1}]
Solenoid armature	0.6	4.1 (3.71, 4.49)	3.50 (3.11, 3.89)
Valve ball	1.0	4.24 (3.99, 4.49)	3.24 (2.99, 3.49)

4. Results and discussion

Selected images from the high-speed image sequence are shown in **Figure 6**. The injector was imaged in two positions to cover the region of interest. The upper position, which includes the solenoid, was formed as the ensemble of 6.38×10⁶ injection events, while the lower region, which includes the valve ball and spray, was formed as the ensemble of 4.89×10⁶ injection events. The two regions overlap by ~3 mm and were not stitched together in the images shown. The sequence is displayed using two normalization approaches, both of which use a reference image generated by taking the median of the 10 images immediately preceding start of energization (SOE). The first normalization, shown in a sequential black and white colormap, is formed by subtracting 95% of the reference image I_{ref} from the time series image $I(t)$, and is purely qualitative in that it allows for visualization of the changes in intensity while preserving a faint image of the injector. The second normalization, shown in a diverging red, white, and blue colormap, is the log-ratio described in Equation (5) and was used to perform the model fits of the solenoid armature and valve ball displacement.
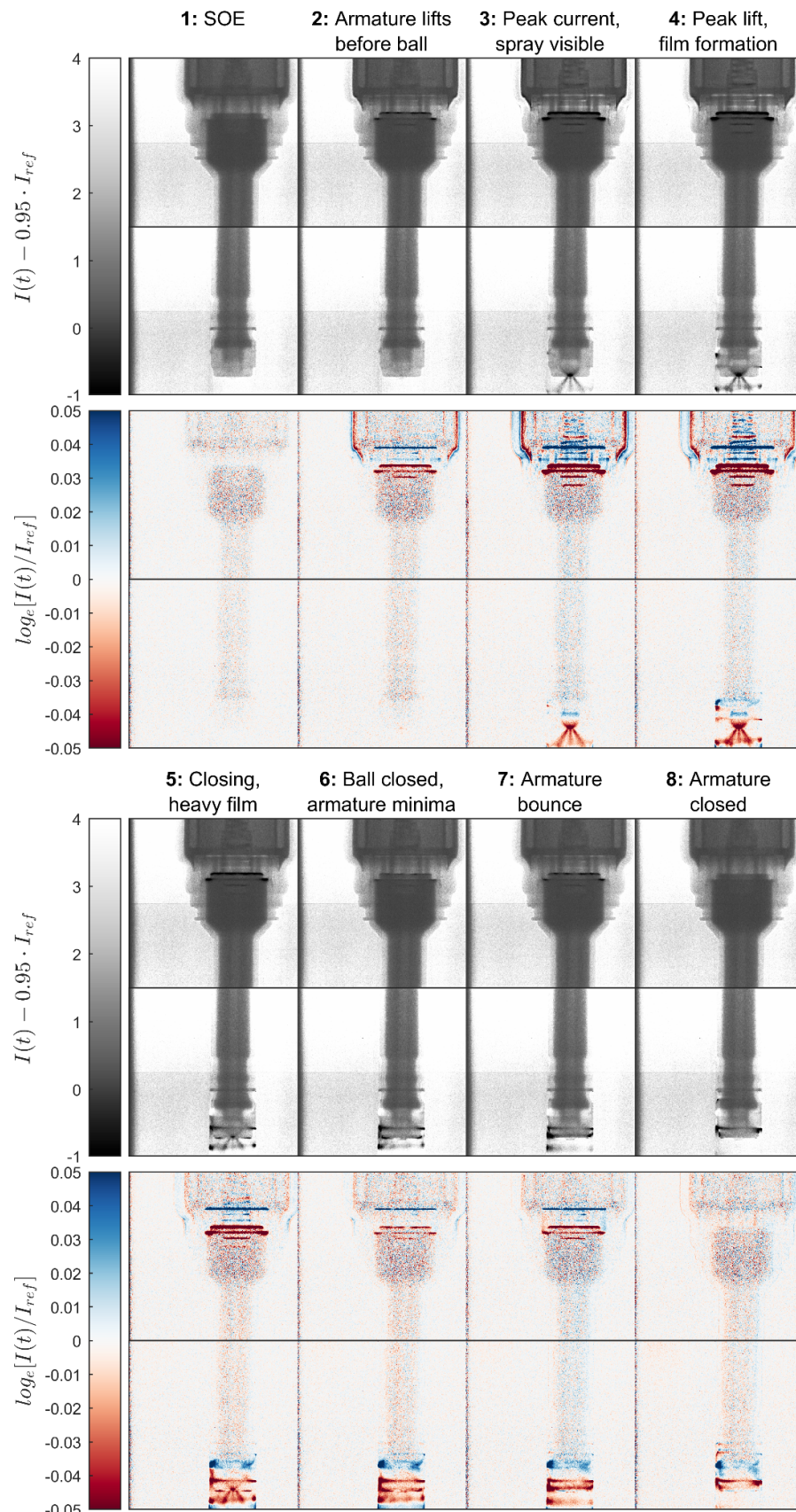
Figure 6. Normalized high-speed neutron images of gasoline direct injector dynamics
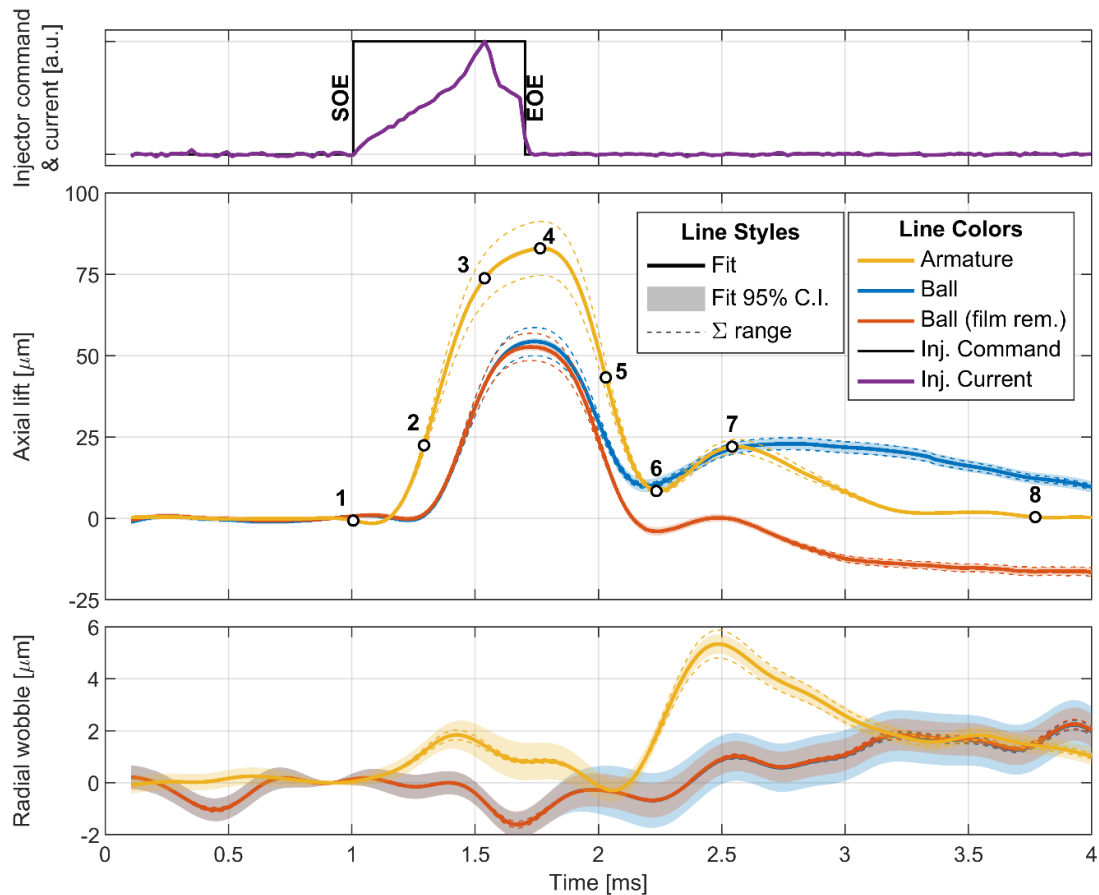
Figure 7. Results of solenoid armature and valve ball displacement model fitting

The injector energization command and current profile, and the fits of axial lift and radial wobble of the solenoid armature and valve ball are shown in **Figure 7** with annotations corresponding to the selected images shown in **Figure 6**. The shaded region behind each curve corresponds to the 95% confidence interval associated with the displacement model fit, while the dashed lines correspond to the range due to uncertainty in the attenuation coefficients. There are several results of note:

Image 1 (1.00 ms): At SOE, the log-ratio image is flat, indicating no change relative to the reference image. However, note the presence of increased noise within the injector, where the total neutron count rates are lower due to their passage through the strongly attenuating fuel.

Image 2 (1.29 ms): The armature lifts 22 μm before any motion is observed in the valve ball. This is presumed to be due to the long valve needle, which can deflect slightly to store compressive energy much like a spring. Variations are also observed in the housing around the solenoid.

Image 3 (1.54 ms): At peak injector current, the armature lift is 74 μm, while the valve ball lift is 41 μm. The fuel spray plumes can be seen emanating from the nozzle holes, and the motion of the compression spring above the armature is also visible. The variations in the solenoid and housing are now stronger and will be discussed subsequently.

Image 4 (1.76 ms): Peak lift occurs just after end of energization (EOE), with armature lift reaching 83 μm and valve ball lift reaching 52 to 55 μm. The spray plumes can be seen impinging on the inner surface of the aluminum tube, and fuel film is developing around the tip of the injector, as indicated by the horizontal red bands in the log-ratio image.

Image 5 (2.03 ms): Both the armature and valve ball are closing, and heavy film development can be seen around the injector tip. The location of impingement on the aluminum tube has also climbed up due to a low-pressure recirculation zone behind the spray. The blue horizontal band above the valve ball indicates that a fuel film which was present in the reference image has been pulled down to the location indicated by the red horizontal band centered on the valve ball. The presence of this film

interferes with the valve ball displacement model, and an additional fit is shown in **Figure 7** by the red curve in which the film has been (partially) removed from the images, as described in the next section.

Image 6 (2.23 ms): The valve ball is now completely closed, and no spray is seen. However, the armature does not close, but reaches a minimum lift of 8 μm.

Image 7 (2.54 ms): The armature bounces back up to 22 μm and shifts to the right by 5 μm. The valve ball fit performed on the image with fuel film indicates a lift of 21 μm, but no spray is visible in the image, and this is believed to be a spurious result. The valve ball fit performed on the image with the fuel film removed indicates ~0 μm lift. Heavy bands of fuel film are seen both around the injector tip and the inner circumference of the aluminum tube.

Image 8 (3.77 ms): The armature settles rather slowly, requiring 1.54 ms to fully close after reaching its initial minimum in Image 6. The fuel films continue to slowly dissipate beyond this point.

While not readily apparent in these still images, the valve needle can also be seen to oscillate during injection when the image sequence is played as a movie.

Examples of the solenoid armature and valve ball fits are shown in **Figure 8**. Because the internal features of the armature were not modeled, the center of the armature was ignored in the fit, which used only the sides and the bottom edge to compute displacement. Similarly, the sac volume below the valve ball involves three phases (valve ball, fuel, nitrogen) and was cropped out of the images used in the valve ball displacement fits. As shown in **Figure 8**, the armature fit to image 7 and the ball fit to image 3 both do an excellent job of matching the data, leaving little if any structure in the residual. However, once fuel films begin to develop around the outside of the injector tip, they interfere with the valve ball fit, as seen in the fit of image 5. This was accounted for by developing a model which assumes that a horizontally symmetric film of constant radius exists in the image, and then fitting the radius and film thickness to the data one line at a time, as shown for image 5 in **Figure 8**. This approach does remove much of the film from the image, but there are artifacts in the residual image due to the asymmetry of the film. As shown in **Figure 7**, this approach does remove the positive bias in the valve ball lift beyond 2 ms but ends up resulting in a negative bias beyond 2.5 ms. The presence of the film and the associated higher noise in that region of the image is likely also the reason for the slowly increasing fitted value of ball radial wobble beyond 2 ms. The best approach to deal with the fuel film would be to seal the end of the injector in the tube so that film cannot develop around the injector, but that was beyond the scope of this work.

The variations observed in the solenoid during energization in **Figure 6** merit further discussion. Neutrons have a magnetic moment and will undergo precession at the Larmor frequency when passing through a magnetic field. This property can be used to enable imaging and tomography of magnetic fields by spin-polarizing the neutron beam [19, 20]. However, because neutrons do not have charge, their trajectory is not altered by passing through a magnetic field, and because we are using unpolarized neutrons, there should be no change in total neutron count rate due to interaction with the magnetic fields in the energized solenoid.

When the coil is energized, a magnetic field develops around the coil, which passes through the magnetic core, the external housing, and the armature [7], as illustrated in **Figure 1**. This field creates both axial and radial forces within the coil, which tend to compress the coil in the axial direction and expand the coil in the radial direction [21]. Additionally, the electrical resistance of the coil leads to Joule heating which in turn causes thermal expansion of the coil [22]. Cyclic compressive stresses and high temperature can lead to degradation of the insulation between the coil wires, which is the leading cause of solenoid failure. The normalized images 2, 3, and 4 of **Figure 6** show the entire coil, magnetic core, and housing expanding radially outward. Though not pursued in this work, quantitative analysis of this expansion could be a valuable tool for validation of finite element models investigating solenoid lifetime and reliability.
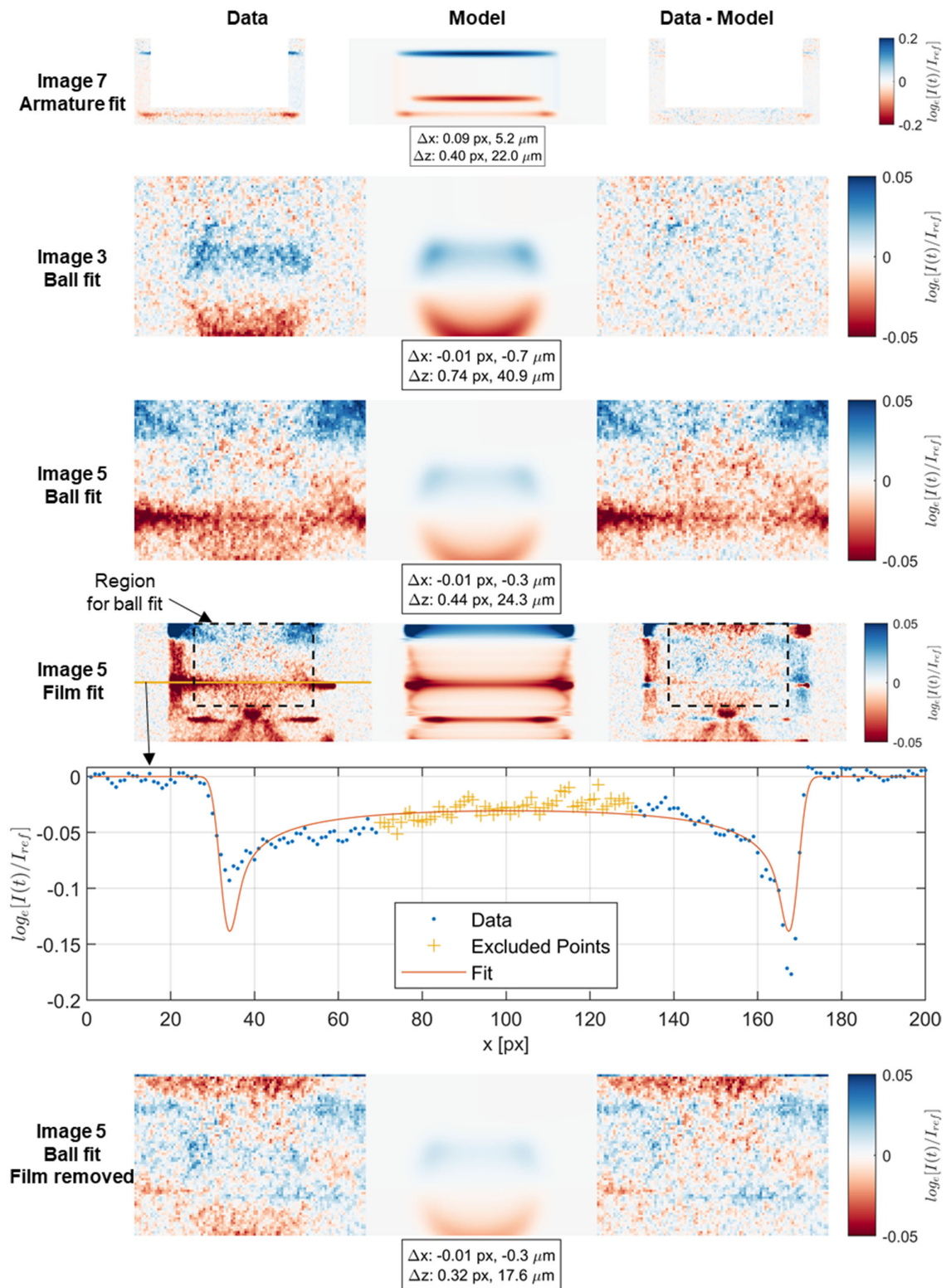
Figure 8. Example fits for the solenoid armature and valve ball displacement models and wall film model

5. Conclusions

We have demonstrated that high-speed neutron imaging can enable visualization of the internal mechanical dynamics of an entire gasoline direct injector, and our recently developed attenuation model allows for the quantification of motions of components such as the solenoid armature and valve ball at subpixel scales of the order of 1 µm in both axial and radial directions. It is also possible to see dynamics such as the swelling of the solenoid during energization, the development of the fuel spray both inside and outside the injector, fuel impingement on internal surfaces, and the development and transport of fuel films, all through solid metal components. Future prospects for this approach may include validation of electromagnetic and hydromechanical models of solenoid actuators and visualization of hydrogenous sprays and films inside dense metallic objects such as internal combustion engines, oil-lubricated compressors, multi-phase heat exchangers, and many other applications [23].

Acknowledgements

References

1.   *The 2021 EPA Automotive Trends Report: Greenhouse Gas Emissions, Fuel Economy, and Technology since 1975.* 2021 [cited 2022 May]; Available from: https://www.epa.gov/automotive-trends.

2.   Myung, C.L. and S. Park, *Exhaust nanoparticle emissions from internal combustion engines: A review.* International Journal of Automotive Technology, 2011. **13**(1): p. 9. DOI: https://doi.org/10.1007/s12239-012-0002-y.

3.   Raza, M., et al., *A Review of Particulate Number (PN) Emissions from Gasoline Direct Injection (GDI) Engines and Their Control Techniques.* Energies, 2018. **11**(6): p. 1417. DOI: https://doi.org/10.3390/en11061417.

4.   Duke, D.J., et al., *High-resolution x-ray and neutron computed tomography of an engine combustion network spray G gasoline injector.* SAE International Journal of Fuels and Lubricants, 2017. **10**(2): p. 328-343. DOI: https://doi.org/10.4271/2017-01-0824.

5.   Shin, Y., et al., *Shape optimization to minimize the response time of direct-acting solenoid valve.* Journal of magnetics, 2015. **20**(2): p. 193-200. DOI: https://doi.org/10.4283/JMAG.2015.20.2.193.

6.   Passarini, L. and P. Nakajima, *Development of a high-speed solenoid valve: an investigation of the importance of the armature mass on the dynamic response.* Journal of the Brazilian Society of Mechanical Sciences and Engineering, 2003. **25**(4): p. 329-335. DOI: https://doi.org/10.1590/S1678-58782003000400003.

7.   Kusakabe, R., et al., *Injection Quantity Range Enhancement by Using Current Waveform Control Technique for DI Gasoline Injector.* SAE International Journal of Engines, 2014. **7**(2): p. 560-567. DOI: https://doi.org/10.4271/2014-01-1211.

8.   Skiba, S. and J. Melbert, *Dosing Performance of Piezo Injectors and Sensorless Closed-Loop Controlled Solenoid Injectors for Gasoline Direct Injection.* SAE International Journal of Engines, 2012. **5**(2): p. 330-335. DOI: https://doi.org/10.4271/2012-01-0394.

9.   Koch, A., H. Glasmachers, and J. Melbert, *Sensorless Movement Control of Solenoid Fuel Injectors.* 2006, SAE International. DOI: https://doi.org/10.4271/2006-01-0407.

10.   Cavicchi, A. and L. Postrioti, *Simultaneous needle lift and injection rate measurement for GDI fuel injectors by laser Doppler vibrometry and Zeuch method.* Fuel, 2021. **285**: p. 119021. DOI: https://doi.org/10.1016/j.fuel.2020.119021.

11.   Mamaikin, D., et al. *High speed shadowgraphy of transparent nozzles as an evaluation tool for in-nozzle cavitation behavior of GDI injectors.* in *Ilass Europe. 28th european conference on Liquid Atomization*

and Spray Systems. 2017. Editorial Universitat Politècnica de València. DOI: http://dx.doi.org/10.4995/ILASS2017.2017.4639.

12. Mamaikin, D., et al., *Experimental investigation of flow field and string cavitation inside a transparent real-size GDI nozzle.* Experiments in Fluids, 2020. **61**(7): p. 154. DOI: https://doi.org/10.1007/s00348-020-02982-y.

13. Baldwin, E.T., et al., *String flash-boiling in gasoline direct injection simulations with transient needle motion.* International Journal of Multiphase Flow, 2016. **87**: p. 90-101. DOI: https://doi.org/10.1016/j.ijmultiphaseflow.2016.09.004.

14. Pratama, R.H., et al., *Hydraulic flip in a gasoline direct injection injector and its effect on injected spray.* Fuel, 2022. **310**: p. 122303. DOI: https://doi.org/10.1016/j.fuel.2021.122303.

15. Wissink, M.L., et al., *Quantification of Sub-Pixel Dynamics in High-Speed Neutron Imaging.* Journal of Imaging, 2022. **8**(7): p. 201. DOI: https://doi.org/10.3390/jimaging8070201.

16. Santodonato, L., et al., *The CG-1D Neutron Imaging Beamline at the Oak Ridge National Laboratory High Flux Isotope Reactor.* Physics Procedia, 2015. **69**: p. 104-108. DOI: https://doi.org/10.1016/j.phpro.2015.07.015.

17. Tremsin, A.S., et al., *Detection efficiency, spatial and timing resolution of thermal and cold neutron counting MCP detectors.* Nuclear Instruments and Methods in Physics Research Section A: Accelerators, Spectrometers, Detectors and Associated Equipment, 2009. **604**(1): p. 140-143. DOI: https://doi.org/10.1016/j.nima.2009.01.041.

18. Tremsin, A.S., et al., *Optimization of Timepix count rate capabilities for the applications with a periodic input signal.* Journal of Instrumentation, 2014. **9**(05): p. C05026. DOI: http://dx.doi.org/10.1088/1748-0221/9/05/C05026.

19. Kardjilov, N., et al., *Imaging with Polarized Neutrons.* Journal of Imaging, 2018. **4**(1): p. 23. DOI: https://doi.org/10.3390/jimaging4010023.

20. Hilger, A., et al., *Tensorial neutron tomography of three-dimensional magnetic vector fields in bulk materials.* Nature Communications, 2018. **9**(1): p. 4023. DOI: https://doi.org/10.1038/s41467-018-06593-4.

21. Hao, S. and B. Li, *Calculating the magnetic force of solenoid inductor wound by rectangular cross-section wire.* IET Electric Power Applications, 2021. **15**(9): p. 1154-1160. DOI: https://doi.org/10.1049/elp2.12085.

22. Angadi, S.V., et al., *Reliability and life study of hydraulic solenoid valve. Part 1: A multi-physics finite element model.* Engineering Failure Analysis, 2009. **16**(3): p. 874-887. DOI: https://doi.org/10.1016/j.engfailanal.2008.08.011.

23. Craster, R.V. and O.K. Matar, *Dynamics and stability of thin liquid films.* Reviews of Modern Physics, 2009. **81**(3): p. 1131-1198. DOI: https://doi.org/10.1103/RevModPhys.81.1131.

Investigation on Effect of Nozzle Diameter and Inclusion Angle to Combustion and Emissions under High Compression Ratio Heavy-Duty Diesel Engine

K. Cung[1], C. Bitsis[1], E. Smith[1], T. Briggs[1]

[1]Southwest Research Insitute, San Antonio, Texas, USA.

E-mail: khanh.cung@swri.org
Telephone: +(1) 210 522 3934

Abstract. Flame-wall interaction plays a crucial role in diesel combustion, especially in heavy-duty engine platforms. In this study, a single-cylinder engine (SCE) experiment was carried out to evaluate different injector configurations' combustion and emissions performance. The flow rate of the injectors varied from stock up to 25% higher flow by increasing nozzle diameter. Spray targeting was changed by varying inclusion angles of 145 to 155 degrees. Combustion profiles and emissions were analyzed and discussed. It was found that thermal efficiency and NOx emissions can be improved with higher flow. Higher inclusion angle was also more effective in controlling emissions of incomplete combustion products. In the end, challenges associated with spray development and flame-wall interaction for heavy-duty engine platforms are discussed to consider potential improvement in the future design of advanced compression-ignition engines.

Notation

CFD	*Computational fluid dynamics.*
CR	*Compression ratio.*
LL	*Liquid length.*
LOL	*Lift-off length.*
gITE	*Gross indicated thermal efficiency.*
ICE	*Internal combustion engine*
ROI	*Rate of injection.*
SCE	*Single-cylinder Engine.*

1. Introduction

Internal combustion engines (ICE) have been critical in the transportation sector. Recently, ICE is under increasing scrutiny for efficiency and greenhouse gas emissions (GHG). Alternatively, battery electric vehicles (BEV) are strongly viewed as a solution to GHG reduction, especially, if they use renewable energy. However, challenges associated with BEV include long charging time, infrastructure, mining, and weather [1]. Hybrid vehicle (HEV) is being seen as a practical solution to combine features of both ICE and BEV. HEV allows ICE vehicles to operate more efficiently by recovering energy that would be wasted via electric motors. For example, energy during vehicle braking can be stored and reused to both improve efficiency and reduce CO_2 emissions. It is evident that the internal combustion engines are still an important part of the overall transportation system to reduce CO_2 emissions. Therefore, improving ICE is one of the utmost important tasks.

Among ICE platforms, the compression-ignition (CI) engine has been known as a more efficient engine than spark-ignited (SI) due to its utilization of high compression ratio (CR), no throttling loss, and high resistance to knock [2]. Higher CR can fundamentally improve the thermodynamic efficiency of the combustion [3]. For example, 22:1 CR system has been evaluated in a heavy-duty diesel engine with a significant improvement in thermal efficiency [4]. However, a higher CR system typically results in a more confined combustion chamber or piston geometry. This could greatly affect the spray/flame development and spray-piston interaction. Beside piston geometry, the injector and its nozzle configuration

also play a crucial role in characterizing the spray/flame development. **Fig. 1** shows a picture of a heavy-duty diesel injector with a zoomed-in picture from CT scan of the nozzle tip.

Diesel combustion has been long studied for CI engine application. The initial conceptual mechanism of a diesel flame [5] through visualization of in-cylinder combustion provides a great understanding of the evolution of flame development. As liquid diesel fuel is introduced into the combustion chamber, ambient gas at high temperature evaporates the liquid fuel and initiates some low-temperature reactions. The empirical liquid length (LL) proposed by Payri et al. [6] is given as the following equation:

$$LL = \frac{60256 D_0^{1.08}}{\rho_a^{0.51} T_{gas}^{1.7} \Delta P^{0.015}} \qquad \text{Equation 1}$$

with D_o, ρ_a, T_{gas}, and ΔP are nozzle diameter, ambient density, ambient temperature, and injection pressure drop across the nozzle, respectively.

One of the first models was developed by Hiroyasu & Arai [7], in which spray penetration is calculated by the injection, nozzle geometry, fuel density, and the ambient condition. The following equations can depict the model:

$$S = 0.39 \left(\frac{2(P_{inj} - P_g)}{\rho_f} \right)^{0.5} t \text{ as } 0 \le t \le t_b \qquad \text{Equation 2}$$

$$S = 2.95 \left(\frac{P_{inj} - P_g}{\rho_f} \right)^{0.25} (D_0 t)^{0.5} \text{as } t > t_b \qquad \text{Equation 3}$$

$$t_b = 28.65 \frac{\rho_f D_0}{\left(\rho_g (P_{inj} - P_g) \right)^{0.5}} \qquad \text{Equation 4}$$

with "**S**" spray penetration, "**P_{inj}**" injection pressure (Pa), "**P_g**" ambient pressure (Pa), "**ρ_f**" fuel density, "**ρ_g**" ambient gas density, "**D_0**" as nozzle diameter (μm), "**t**" as time after start of injection (ms), "**t_b**" break-up time.

As the fuel jet enters hot ambient gas, vaporized fuel-air mixture reaches autoignition at a certain time after the start of injection which is also known as ignition delay (ID). Pickett et al. [8] represented Arrhenius type of correlation for ignition delay based on a constant-volume combustion vessel experiment in the following

$$\tau \propto \rho^a f_{st}^b \exp \left(\frac{E_a}{\bar{R}T} \right) \qquad \text{Equation 5}$$

with ρ, f_{st}, Ea, $\bar{R}T$ are ambient density, stoichiometric mixture fraction, global activation energy, gas constant, and ambient temperature. Here, a and b constants are usually negative. Hence, it is understood that ignition delay becomes shorter with higher ambient density, higher mixture fraction, and/or higher ambient temperature. As fuel is kept being injected after autoignition, diffusion flame starts with rising flame temperature as spray penetrates downstream. Diffusion flame has been reported from experimental observation of Dec et al. [5] in which the flame extends upstream to a certain location, namely, lift-off length (LOL). The magnitude of the lift-off length provides important information of the spatial spray extent in which fuel is mixed with air before high-temperature reaction of fuel-air mixture occurs. Lift-off length is obtained experimentally using OH* chemiluminescence imaging via 310 nm bandpass filter [8, 9]. Here, OH* is a key excited-state species that indicates high-temperature region of the flame. An empirical equation to calculate flame lift-off (**H**) basing on an experimental study under effect of various ambient conditions, and spray momentum for diesel was developed [8, 10]:

$$H = C T_a^{-3.74} \rho_a^{-0.85} d^{0.34} U^1 Z_{st}^{-1} \qquad \text{Equation 6}$$

with "C" as a constant (5.64×10^8 for n-heptane [11]), "T_a" as ambient temperature, as "ρ_a" ambient density, "d" as nozzle, "U" as injection velocity, and "Z_{st}" is stoichiometric mixture fraction, $Z_{st} = \left(\frac{F}{F+A} \right)_{st}$. It shows that a longer lift-off length is achieved with lower ambient temperature, lower ambient density,

larger nozzle diameter, high injection pressure, and/or lower mixture fraction. Numerous studies have demonstrated this [8, 12-17].

Salvador et al.[18] shows the effect of inclusion angle (90, 140, and 150 degrees) on hydraulic performance of a multihole diesel injector nozzle by analyzing rate-of-injection (ROI) measurements. They found no significant difference in the opening and closing phases of the ROI profiles by different inclusion angles. However, the flow rate at steady-state phase (top flow) was lower at higher inclusion angle which was explained by stronger change in flow direction in the case of higher inclusion angle. At higher Reynolds number (increased rail pressure), the empirically developed discharge coefficient increased more quickly with smaller inclusion angle. Payri et al. [19] later carried out spray experiment of the same nozzle sets to investigate the effect of inclusion angle on spray development. With a higher mass flow rate, a smaller inclusion angle resulted in faster spray penetration. The effect was also more obvious at increased injection pressure.

Given the results and analysis of some of the above studies, it can be understood that nozzle diameter affects significantly to most spray and flame characteristics such as liquid length (LL), spray penetration (S), and lift-off length (LOL). The inclusion angle is believed to have more impact on steady-state flow. A smaller inclusion angle would result in a higher flow rate, hence faster spray penetration. In this study, a single-cylinder engine (SCE) experiment was carried out to investigate the effect of nozzle diameter (or flow rate) and inclusion angle on the performance of a heavy-duty diesel injector.
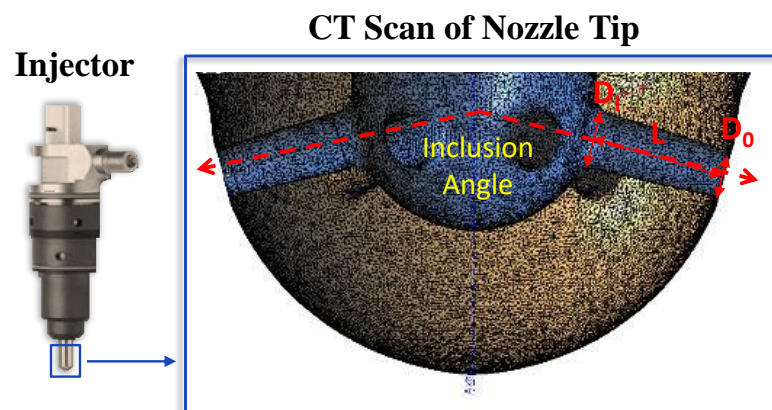
Fig. 1. Example of injector nozzle from CT-scanned imaging

2. Experimental Setup

The experiment was performed using a single-cylinder research engine (SCE) designed by Southwest Research Institute (SwRI). It is a modular design so that it can be adapted to match a given production multi-cylinder engine. For this study, it was configured to match a 2017 Volvo D13 engine by using a segment of the production cylinder head, production liner, and connecting rod, and a crankshaft made with the same crank throw. **Fig. 2** shows a picture of the SCE. **Table 1** provides a summary of engine hardware. **Table 2** provides information on properties of the tested fuel, which is a typical ultra-low sulfur diesel (USLD) fuel.

The cylinder head was similar to the stock hardware of the 2017 Volvo D13 (peak power of 500 hp, peak torque of 1750 ft-lb) with two intake valves and two exhaust valves, and a centrally mounted injector. The peak firing pressure was limited to 250 bar. The Wave piston (see **Fig. 3**) was tested with a 6-hole injector. The Wave piston is similar to the stock piston on the Volvo D13 engine but was redesigned for higher efficiency by increased CR. This system was developed and optimized for diesel combustion within the CHEDE consortium [20]. This combustion system is referred to as "Wave 22" throughout the paper's discussion.
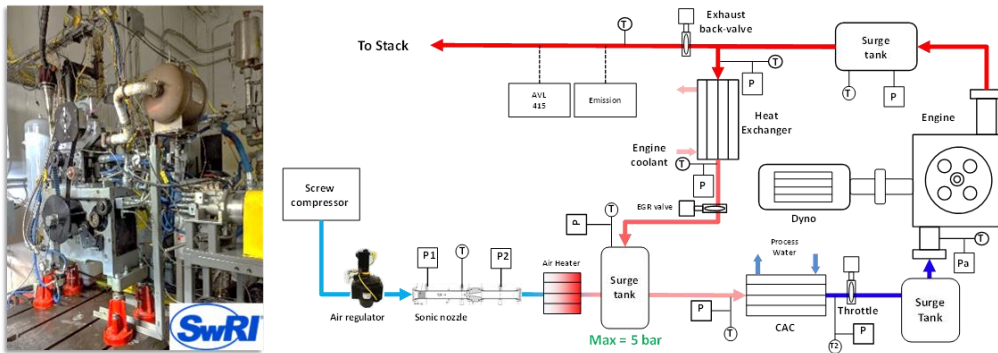
Fig. 2. Single-cylinder research engine (left) and test cell layout (right)

Table 1. Engine & Hardware Configurations

Engine Type	Single-Cylinder Engine 4-Valve Compression Ignition
Displacement	13 liters
Bore x Stroke	131 mm x 158 mm
Compression Ratio	22:1 (SwRI design)
Piston & Injector	Wave (6-hole with nozzle diameter 248 μm) Stepped-lip (12-hole with nozzle diameter of 175 μm)
Swirl ratio	Quiescent (~0)
Fuel System	Delphi DFI5.1 2700 bar
Air System	Screw Compressor
Engine Control	NI cRIO based ECU

Fig. 3. High compression ratio (CR = 22:1) wave piston

Table 2 General properties of tested fuels

Property	Method	Diesel
Density @ 15°C, g/ml	D4052	0.8217
LHV (net), MJ/kg	D240	43.068
Cetane Number	D613	54.3
H/C Ratio	D5291	1.922

3. Experimental Setup

Fuel flow is measured with high precision Coriolis mass flow meter. Intake pressure was measured with an absolute pressure transducer. Other pressure transducers and thermocouples are indicated in the schematic to measure pressure and temperature, respectively, around the engine inlet, outlet, and EGR cooler. Cylinder pressure was measured using a Kistler 6045A pressure transducer with a 5010 Charge

Amplifier. The cylinder pressure profile was processed using SwRI-developed high-speed combustion analysis. An average of 200 cycles was used for combustion analysis. Raw engine-out gaseous emissions were measured using a Horiba emissions bench. Smoke emission was measured by an AVL 415S smoke meter. Indicated efficiency is reported in this study.

Fig. 4 explains the overall calculations for SCE analysis. In this study, the efficiency breakdown includes gITE (gross indicated thermal efficiency), EXH (exhaust energy), HT (heat transfer), and CL (combustion loss). All of them are based on total fuel energy (100%). Indicated emissions are ISNO$_X$ (indicated specific NO$_X$ emissions), ISPM (indicated specific particulate matters), ISCO (indicated specific carbon monoxide emissions), and ISHC (indicated specific hydrocarbons emissions).

$$Fuel\ energy = \dot{Q}_{fuel} = \dot{m}_{fuel}\,h_{fuel} = \dot{m}_{fuel}\,LHV$$

$$Brake\ (FE\%) = \frac{\dot{W}_{brake}}{\dot{Q}_{fuel}}$$

$$Friction\ (FE\%) = \frac{\dot{W}_{friction}}{\dot{Q}_{fuel}} = \frac{\dot{W}_{ind,net} - \dot{W}_{brake}}{\dot{Q}_{fuel}}$$

$$Pumping\ (FE\%) = \frac{\dot{W}_{pumping}}{\dot{Q}_{fuel}} = \frac{\dot{W}_{ind,gross} - \dot{W}_{ind,net}}{\dot{Q}_{fuel}}$$

$$Gross\ (FE\%)$$

$$Comb\ Loss\ (FE\%) = \frac{\dot{Q}_{CL}}{\dot{Q}_{fuel}}$$

$$Exhaust\ (FE\%) = \frac{\dot{Q}_{exh} - \dot{Q}_{Int} - \dot{W}_{pumping}}{\dot{Q}_{fuel}} = \frac{\dot{m}_{exh}h_{exh} - \dot{m}_{int}h_{int} - \dot{W}_{pumping}}{\dot{Q}_{fuel}}$$

$$Heat\ Transfer\ (FE\%) = 100 - (brake + exhaust + friction + pumping + comb\ loss)$$
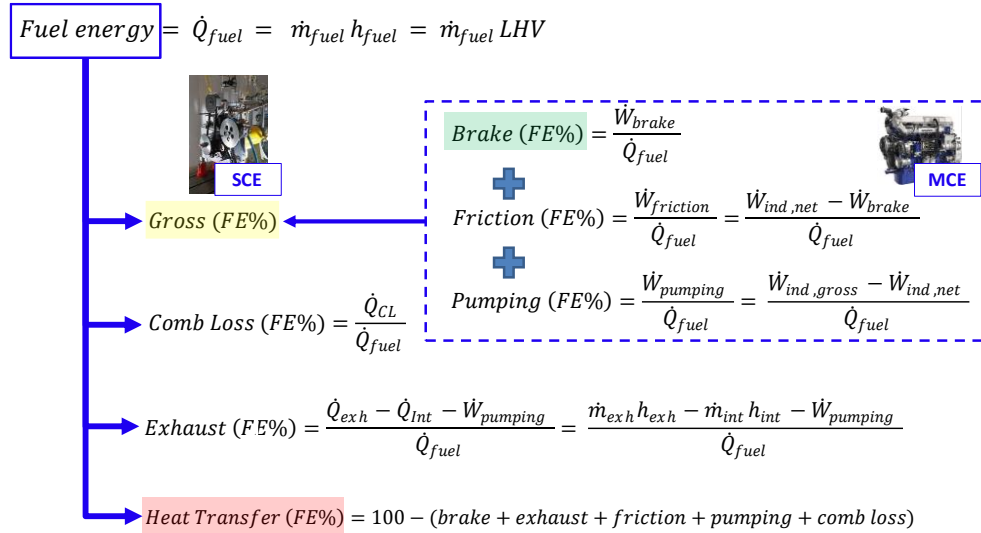
Fig. 4. Energy breakdown analysis for SCE experiment

4. Experimental Setup

Table 3 summarizes the test condition of the SCE experiment. The operating condition is also known as "A75": A speed of 1200 rpm, 75% maximum load. This is commonly known for heavy-duty engines tested under European stationary cycle (ESC) [21]. The boundary condition includes a moderate EGR level of 18% to control NO$_X$ emissions. The rail pressure was 1600 bar. Single injection strategy was used. While multiple injection strategy has been known to improve combustion and emissions, this study does not include further optimization of injection strategy.

Table 3 Summary of test conditions

Parameter	Value or Description	Unit
Piston + Injector	Wave 22 + 6-hole Injector	-
Speed	1200	RPM
gIMEP	19	bar
EGR	18	%
Rail Pressure	1600	bar
Injection Strategy	Single Injection (Diesel)	-

Combustion performance of Wave 22 piston was evaluated with high flow rate (larger nozzle diameter) injectors. The tested high flow injectors with different flow rates and inclusion angles are summarized in **Fig. 5**.
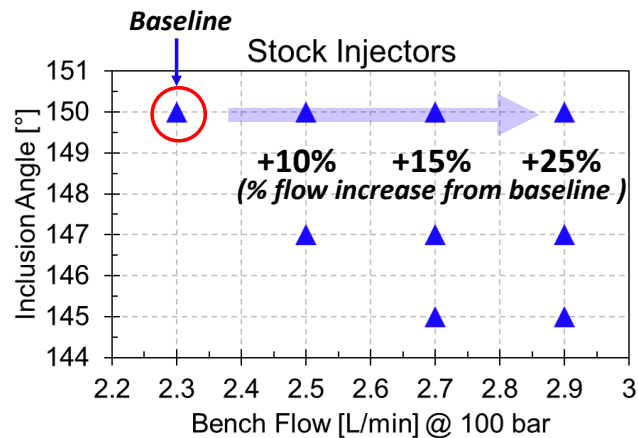
Fig. 5. Tested injectors of different inclusion angle and bench flow rate

The flow increase was based on a target flow rate (L/min), typically measured at rail pressure of 100 bar. However, the results from engine testing note the flow increase based on the actual fuel flow measurement by the flow meter at the test cell. For example, the total fuel (mg) per unit of energizing duration (1 ms) was higher for the high flow injectors. The percentage increase will be used for the following analysis and plots. A general demonstration of the injection rate profile between baseline and high flow injectors is shown in **Fig. *6***.
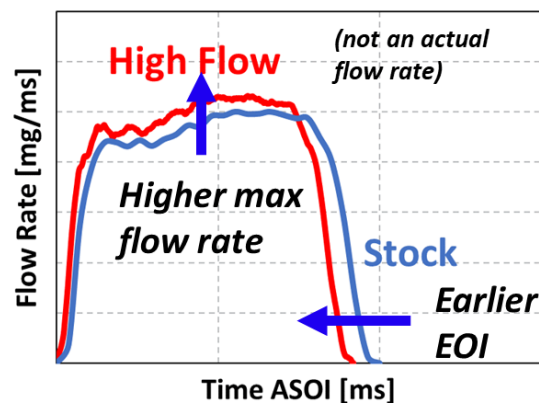
Fig. 6. Comparison of examples of ROI profiles between high flow nozzle and baseline nozzle

It shows that the higher flow injector (red curve) delivers a higher peak flow rate and requires a shorter injection duration than the baseline injector (blue curve). This implies a faster fueling rate and earlier end of injection, both of which potentially contribute to a shorter combustion duration overall. Higher thermal efficiency can be expected for shorter combustion durations since more work is performed with a more reduction in heat transfer penalty during expansion. Of course, high flow injector is associated with larger nozzle diameter which can affect fuel atomization, hence combustion performance. However, it is believed that the current combustion system (Wave) has strong spray-piston interaction that most of "mixing" event occurs by spray-piston interaction rather than by the introduction of the fuel near the nozzle. Some related reference work can be found in Ref [22]. However, further work are needed to confirm the current hypothesis.

5. Results and Discussion

5.1. Combustion Characteristics of Wave piston

The wave-like piston was developed and introduced by Volvo. Eismark et al. [23] described the effect of bowl shape of the Wave piston on diesel flame combustion. The wave piston generally features a wave bump geometry that was designed to optimize a wall-flow-guided combustion system. Each spray jet is injected in between these bumps. In the following discussion, we refer to bump as "separator", and the region between each bump as "pocket". Upon interacting with the piston, the flame is guided by

piston geometry to recirculate radially toward bowl central regions, also known as radial mixing zone (RMZ). **Fig. 8** shows a visual description of RMZ region by the change in higher CR and higher injector flow, which both would potentially result in stronger RMZ.
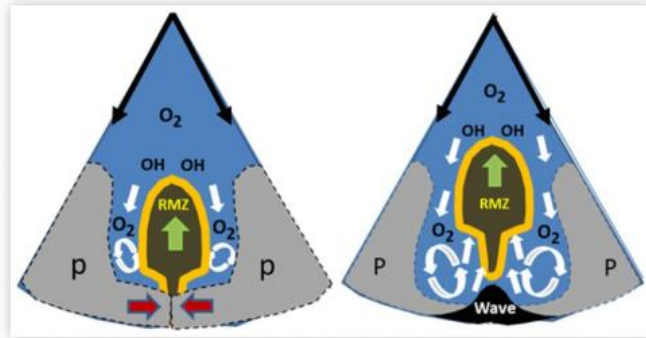
Fig. 7. Radial mixing zone (RMZ) between conventional (left) and wave piston (right)
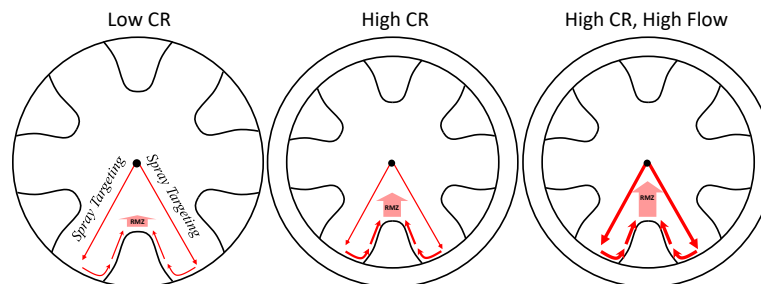
Fig. 8. Flame recirculation in wave systems (from left to right): low CR with stock nozzle flow; high CR with stock nozzle flow; high CR with high nozzle flow

5.2. Effect of Nozzle Diameter

The effect of nozzle diameter or higher flow nozzle is being discussed first. **Fig. 9** and **Fig. 10** show several information of combustion and emissions performance for different nozzle flow rates of the same inclusion angle (150 degrees). Heat release rate (HRR) profiles show a higher peak of HRR with a higher nozzle flow rate as expected with more instantaneous fuel delivered. The combustion duration, MFB10-90, was not necessarily decreased as expected for higher nozzle flow (shorter injection duration). This is possibly due to the balance between shortened injection duration and poor atomization from a large nozzle orifice that would result in relatively similar combustion duration.
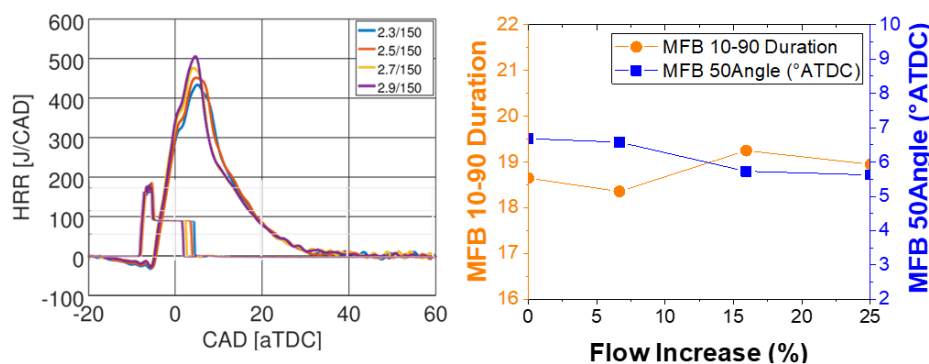
Fig. 9. Combustion profiles comparison by different injector flow rate at same inclusion angle of 150 degrees

Gross indicated thermal efficiency (gITE) is increased significantly by increased flow rate. This is contributed by more combustion occurs near TDC, which could possibly lower heat transfer loss due to smaller total surface area of the combustion chamber . However, it must be acknowledged that the combustion phasing or MFB50 was advanced due to a higher flow rate. Therefore, the efficiency gain

might have been overstated in **Fig. *10***. Combustion loss was relatively similar as the flow rate increased. This can be understood as the following. As mentioned above, a higher flow nozzle or large nozzle diameter would result in poor fuel atomization but increase spray momentum. Poor atomization or poor mixing with a larger nozzle could result in higher smoke emissions, as seen here by the higher value of filter smoke number (FSN). The latter effect can lead to a stronger turbulence energy of the charge that would further promote the oxidation of unburned hydrocarbon and CO. Finally, NO_X emissions are slightly lower with increased flow rate, even with a more advanced combustion phasing. One possible explanation for lower NO_X emissions can be drawn from the stronger RMZ flame in the nozzle of higher flow rates. This provides an in-cylinder dilution effect during the mixing-controlled combustion of the jet. Another explanation could come from a more fuel-rich (much higher than stoichiometric) combustion introduced by the high flow injector. So even peak of HRR is higher, peak flame temperature could occurs at richer condition where NO_X emission might be lower (see plot of soot-NOx regions in Ref [24]). Further analysis, including computational fluid dynamics (CFD) simulations, can provide more insights into the in-cylinder process that would affect NO_X emissions and others.
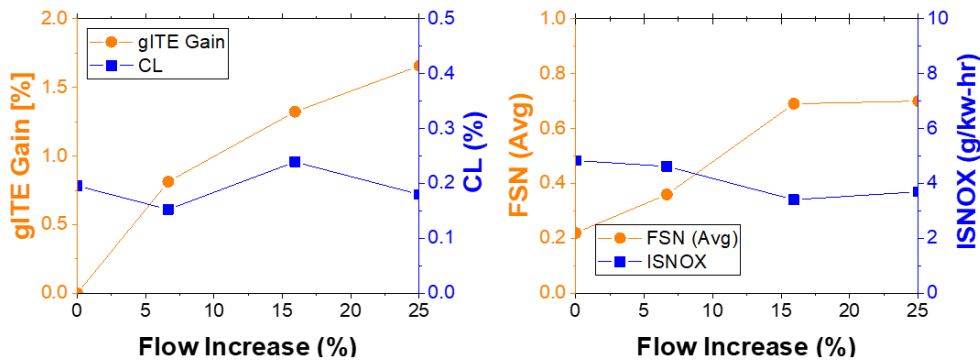
Fig. 10. Efficiency (gITE gain as absolute values from baseline) and emissions performance by different injector flow rate at same inclusion angle of 150 degrees

5.3. Effect of Inclusion Angle

At a fixed flow rate of 2.9 l/min, the effect of inclusion angle on combustion and emissions performance is shown in **Fig. *11*** and **Fig. *12***, respectively. The baseline injector was also added to the plots for comparison to the initial stock injector configuration. HRR profiles show a relatively similar combustion profile between different inclusion angles of the same flow rate of 2.9 l/min. The peak of HRR is slightly higher with an inclusion angle of 145 degrees than other 2.9 l/min nozzles. This agrees with the previous study [18] described earlier in the introduction with a higher flow rate for a smaller inclusion angle. The combustion duration decreased as the inclusion angle increased with an inclusion angle of 150 degrees, resulting in shorter MFB10-90. The shorter combustion duration also supports the trend in higher gITE with a nozzle of higher inclusion angle.

FSN and combustion loss trends indicate a mixing problem associated with smaller inclusion angles. This can be explained as the following. **Fig. *13*** shows the different incident angles between spray targeting and piston if the inclusion angle changes. With an inclusion angle smaller than 150 degrees, the spray-piston interaction became less favorable for jet-to-jet mixing downstream by the re-circulation flame or flame development that would generally lead to poor oxidation of unburned fuel hydrocarbons. Meanwhile, there is no significant difference in NOx emissions by different inclusion angles.
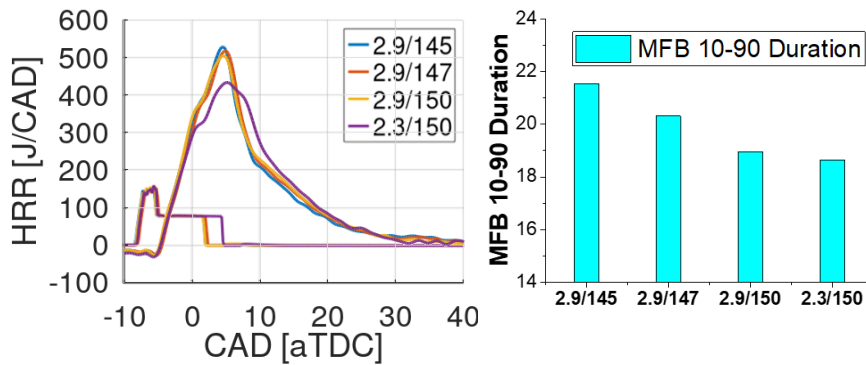
Fig. 11. Combustion profiles comparison of different injector configurations: inclusion angle sweep vs. baseline injector
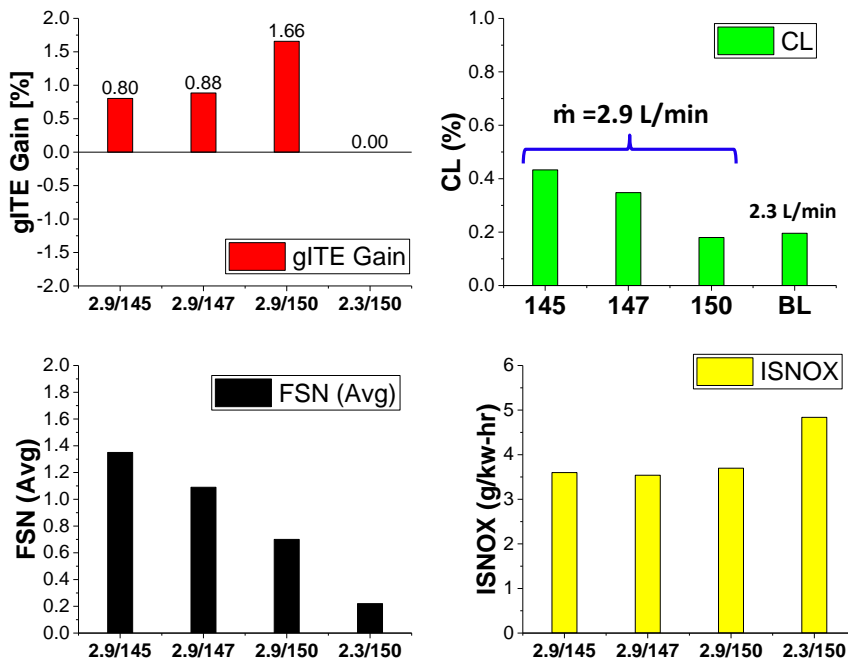
Fig. 12. Efficiency (gITE gain as absolute values from baseline) and emissions performance comparison of different injector configurations: inclusion angle sweep vs. baseline injector
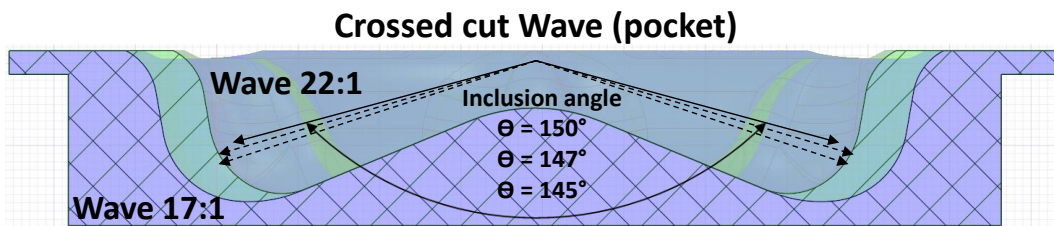
Fig. 13. Spray targeting with different inclusion angle

5.4. Overall performance

Fig. *14* summarizes the overall performance of various nozzles of different inclusion angles and flow rates. A more considerable gITE gain was achieved with higher fuel flow injectors. It also showed that injectors with wider inclusion angles performed better. An injector of 25% flow increase and a 150°

inclusion angle showed the largest gITE gain. The NO$_X$ emissions were reduced as flow increased but did not show a significant effect from the inclusion angle. As the flow increased, a narrower inclusion angle showed the worst MFB10-90, FSN, and combustion loss performance. An ~8 bar increase in PCP was observed from the baseline injector to the highest flow injector. Overall the injector with a 25% flow increase and 150° inclusion angle provided the best performance in terms of gITE and NOX, with a modest penalty in FSN (increased by ~0.5) and PCP (increased by ~8 bar). While the gITE map showed a 1.7% pt. increase, later discussion will indicate a more realistic gITE% pt. (absolute) gain to be expected.
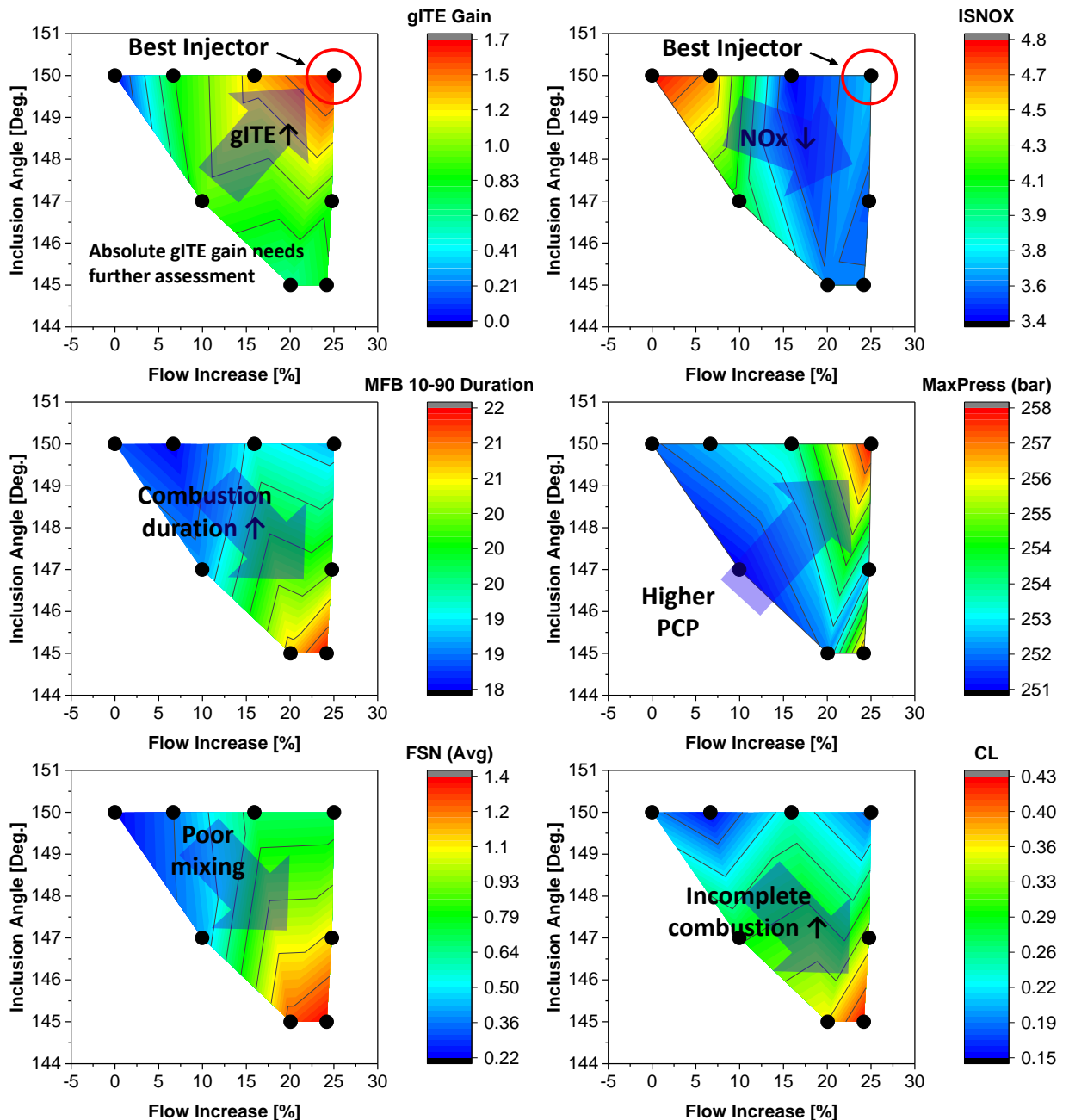
Fig. 14. Efficiency (gITE gain as absolute values from baseline) and emissions performance comparison of different injector configurations: inclusion angle sweep vs. baseline injector

5.5. Empirical Model

Realizing the sensitivity of gITE to both EGR and MFB50, a linear regression model was used to extract a more realistic gITE change to be expected under the influence of only a flow increase and inclusion angle change. In other words, the operating conditions of MFB50 and EGR were fixed in the regression model to yield gITE as a function of only (ideal) flow increase and inclusion angle. Results in **Fig. 15**

showed a similar trend of increasing gITE with a flow increase, while a narrower inclusion angle reduced gITE. There was a 0.4% pt. gITE increase as flow increased up to ~25% as shown in **Fig. 16** for increasing flow rate at fixed inclusion angle. Results from a multi-cylinder engine (MCE) testing with similar engine configuration also showed an approximately 0.1% pt. gITE gain with a flow increased to ~10%. Although the MCE testing was performed with a injector of narrower inclusion angle of 147°, the result further support empirical model of increased flow on gITE gain.
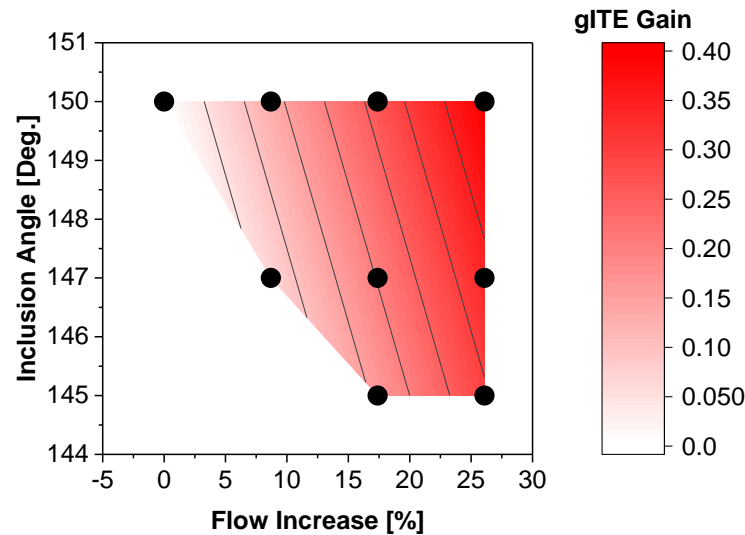
Fig. 15. Empirical model for gITE gain by using different injector configurations: inclusion angle and flow rate
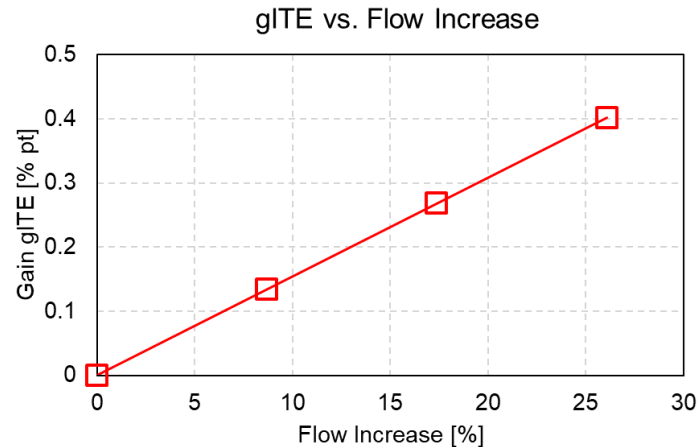
Fig. 16. Empirical model for gITE gain (absolute values from baseline) by using different injector configurations at increasing flow rate (fixed inclusion angle of 150°)

A similar linear regression approach was used to predict emissions trends as flow and inclusion angles are varied. The result is shown in **Fig. 17**. Lower NO_X and higher FSN emissions are seen at higher flow increases. There is a stronger inclusion angle effect than flow increase on combustion loss. The effect of the inclusion angle on NO_X and FSN emissions are less significant.
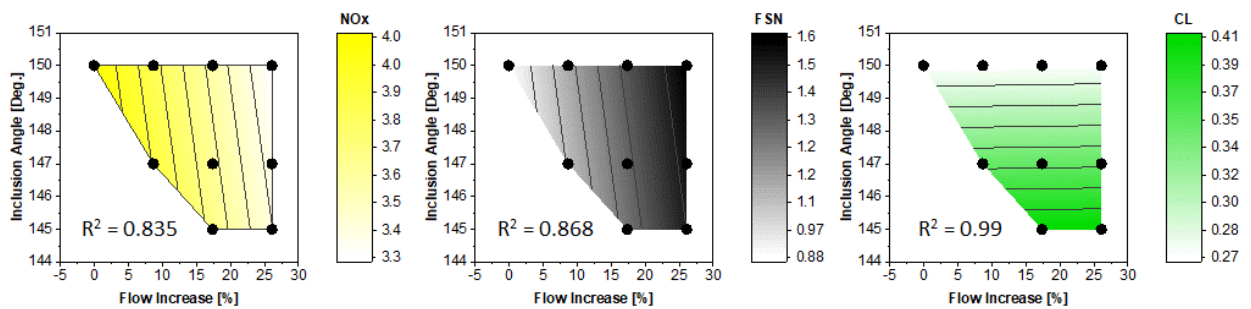
Fig. 17. Empirical model for emissions by using different injector configurations at flow rate

6. Conclusions

In the current paper, injectors of different flow rates and inclusion angles were investigated experimentally using a single-cylinder engine (SCE) facility. Testing was performed at condition of 1200RPM, 19 bar gIMEP, and 18% EGR. The combustion system was designed to have a high compression ratio of 22:1. The combustion system follow closely with a wave-like piston design. The injection pressure was fixed at 1600 bar. The injection timing was also fixed. Some findings are summarized below:

- Higher flow rate or wider inclusion angle results in better gross indicated thermal efficiency (gITE) in the Wave combustion system. This was achieved by stronger spray momentum and shorten injection duration (by higher flow rate); as well as favorable incident angle of spray and piston with nozzle configuration of wider inclusion angle.

- Specifically, at fixed inclusion angle, high flow nozzle delivers a larger amount of fuel injected instantaneously that result in more combustion occurring simultaneously near TDC, therefore reduce heat transfer loss. The nozzle with 150 degrees inclusion angle and 2.9 l/min flow rate shows the highest gITE gain compared to the baseline injector configuration.

- Combustion duration is relatively similar to the change of nozzle flow rate. This is because of the balance between fuel atomization (poorer with higher flow) and spray momentum (stronger with higher flow). However, combustion duration tends to increase with smaller inclusion angle, which also results in higher combustion loss, and slightly lower gITE.

- Empirical correlation analysis shows that high flow injector application can achieve improved thermal efficiency and lower NO_x. However, soot emissions can still be a challenge due to poor fuel atomization. Wider inclusion angle tends to improve combustion and emissions as compared to narrower inclusion angle.

Future work will look into energy and emissions breakdown analysis from engine data to further explain efficiency gain. Additionally, computational fluid dynamics (CFD) simulation is needed to understand the in-cylinder phenomenon and confirm some of the hypothesis mentioned above on the current test results.

Acknowledgment

Reference

1.   Senecal, K. and F. Leach, Racing Toward Zero: The Untold Story of Driving Green. 2021.
2.   Ciatti, S.A., Compression Ignition Engines – Revolutionary Technology That has Civilized Frontiers all Over the Globe from the Industrial Revolution into the Twenty-First Century. *Frontiers in Mechanical Engineering*, 2015. **1**.
3.   Heywood, J.B., Internal combustion engine fundamentals. Vol. 930. 2018: *Mcgraw-hill New York.*
4.   Cung, K., et al., Demonstration of High Compression Ratio Combustion Systems for Heavy-Duty Diesel Engine with Improved Efficiency and Lower Emissions. 2022, *SAE International.*

5.   Dec, J.E., A Conceptual Model of DI Diesel Combustion Based on Laser-Sheet Imaging*. 1997, SAE Technical Paper.
6.   Payri, R., et al., Study of liquid and vapor phase behavior on Diesel sprays for heavy duty engine nozzles. *Applied Thermal Engineering*, 2016. **107**: p. 365-378.
7.   Hiroyasu, H. and M. Arai, Structures of fuel sprays in diesel engines. 1990, *SAE Technical Paper*.
8.   Pickett, L.M., D.L. Siebers, and C.A. Idicheria, Relationship between ignition processes and the lift-off length of diesel fuel jets. 2005, *SAE technical paper*.
9.   Dec, J.E. and C. Espey, Chemiluminescence Imaging of Autoignition in a DI Diesel Engine. 1998, *SAE International*.
10.   Siebers, D. and B. Higgins, Flame Lift-Off on Direct-Injection Diesel Sprays Under Quiescent Conditions. 2001, *SAE International*.
11.   Idicheria, C.A. and L.M. Pickett, Soot formation in diesel combustion under high-EGR conditions. 2005, *SAE Technical Paper*.
12.   Khanh Cung, A.Z., Seong-Young Lee. Ignition and Formaldehyde Formation in Dimethyl Ether Spray Combustion: Experiment and Chemical Modeling, *9th U.S. National Combustion Meeting*, Cincinnati, Ohio, USA. 2015.
13.   Payri, R., et al., Diesel ignition delay and lift-off length through different methodologies using a multi-hole injector. *Applied Energy*, 2016. **162**: p. 541-550.
14.   Benajes, J., et al., Experimental characterization of diesel ignition and lift-off length using a single-hole ECN injector. *Applied Thermal Engineering*, 2013. **58**(1–2): p. 554-563.
15.   Pei, Y., et al., Engine Combustion Network (ECN): Global sensitivity analysis of Spray A for different combustion vessels. *Combustion and Flame*, 2015. **162**(6): p. 2337-2347.
16.   Pei, Y., et al., Modelling n-dodecane spray and combustion with the transported probability density function method. *Combustion and Flame*, 2015. **162**(5): p. 2006-2019.
17.   Payri, R., et al., Experimental and numerical study of lift-off length and ignition delay of a two-component diesel surrogate. *Fuel*, 2015. **158**: p. 957-967.
18.   Salvador, F.J., et al., Experimental investigation of the effect of orifices inclination angle in multihole diesel injector nozzles. Part 1 – Hydraulic performance. *Fuel*, 2018. **213**: p. 207-214.
19.   Payri, R., et al., Experimental investigation of the effect of orifices inclination angle in multihole diesel injector nozzles. Part 2 – Spray characteristics. *Fuel*, 2018. **213**: p. 215-221.
20.   Li, F., et al., Optical investigation on impacts of ambient pressure on macroscopic spray characteristics of ducted fuel injection under non-vaporizing conditions. *Fuel*, 2020. **268**: p. 117192.
21.   DieselNet.
22.   Cung, K., et al., Gasoline Compression Ignition (GCI) Combustion of Pump-grade Gasoline Fuel under High Compression Ratio Diesel Engine. *Transportation Engineering*, 2021: p. 100066.
23.   Eismark, J., et al., Role of Piston Bowl Shape to Enhance Late-Cycle Soot Oxidation in Low-Swirl Diesel Combustion. 2019, *SAE International*.
24.   Pickett, L.M., et al., Evaluation of the equivalence ratio-temperature region of diesel soot precursor formation using a two-stage Lagrangian model. *International Journal of Engine Research*, 2006. **7**(5): p. 349-370.

Parametric Evaluation of Ducted Fuel Injection in an Optically Accessible Mixing-Controlled Compression-Ignition Engine with Two- and Four-Duct Assemblies

B.F. Yraguen[1], A.M. Steinberg[1], C.W. Nilsen[2], D.E. Biles[2], C.J. Mueller[2]

[1]Georgia Institute of Technology. USA

E-mail: byraguen3@gatech.edu
Telephone: +(1) 404 894 2000

[2]Sandia National Laboratories. USA

E-mail: cjmuell@sandia.gov
Telephone: +(1) 925 294 2223

Abstract. Ducted fuel injection (DFI) is a strategy to improve fuel/charge-gas mixing in direct-injection compression-ignition engines. DFI involves injecting fuel along the axis of a small tube in the combustion chamber, which promotes the formation of locally leaner mixtures in the autoignition zone relative to conventional diesel combustion. Previous work has demonstrated that DFI is effective at curtailing engine-out soot emissions across a wide range of operating conditions. This study extends previous investigations, presenting engine-out emissions and efficiency trends between ducted two-orifice and ducted four-orifice injector tip configurations. For each configuration, parameters investigated include injection pressure, injection duration, intake manifold pressure, intake manifold temperature, start of combustion timing, and intake-oxygen mole fraction. For both configurations and across all parameters, DFI reduced engine-out soot emissions compared to conventional diesel combustion, with little effect on other emissions and engine efficiency. Emissions trends for both configurations were qualitatively the same across the parameters investigated. The four-duct configuration had higher thermal efficiency and indicated-specific engine-out nitrogen oxide emissions but lower indicated-specific engine-out hydrocarbon and carbon monoxide emissions than the two-duct assembly. Both configurations achieved indicated-specific engine-out emissions for both soot and nitrogen oxides that comply with current on- and off-road heavy-duty regulations in the United States without exhaust-gas aftertreatment at an intake-oxygen mole fraction of 12%. High-speed in-cylinder imaging of natural soot luminosity shows that some conditions include a second soot-production phase late in the cycle. The probability of these late-cycle events is sensitive to both the number of ducted sprays and the operating conditions.

Notation

AHRR	Apparent heat release rate.
ATDC	After top-dead center.
CAD	Crank angle degree.
CDC	Conventional diesel combustion.
CFA	Certification fuel batch A.
CFB	Certification fuel batch B.
DFI	Ducted fuel injection.
DOI	Duration of injection.
EGR	Exhaust gas recirculation.
EOC	End of combustion $\equiv$ MFB95.
EOI	End of injection.
EOPMB	End of pre-mixed burn.
IMAP	Intake manifold absolute pressure.
$IMEP_g$	Indicated mean effective pressure (gross).
LLFC	Leaner lifted-flame combustion.
LOL	Lift-off length.

NL   *Natural luminosity.*
MFB80 *Crank angle at which 80% of the total integrated heat release has occurred.*
MFB95 *Crank angle at which 95% of the total integrated heat release has occurred ≡ EOC.*
$P_{inj.}$ *Injection Pressure.*
SCORE *Sandia compression-ignition optical research engine.*
SINL   *Spatially integrated natural luminosity.*
SOC   *Start of combustion.*
TDC   *Top dead center.*
TKE   *Turbulent kinetic energy.*

1. Introduction

This paper reports emissions and efficiency trends for ducted fuel injection (DFI) in two- and four-duct configurations over a wide parameter space of mixing-controlled compression-ignition (i.e., diesel) engine operating conditions. DFI aims to reduce diesel emissions by facilitating the development of diesel engines that do not produce soot. DFI does this by achieving lower spray-flame equivalence ratios than conventional diesel combustion (CDC), particularly lower peak values in the center of the spray, thereby achieving leaner lifted-flame combustion (LLFC, i.e., diesel combustion that does not produce soot) [2-4]. DFI was introduced by Mueller et al. [5]. It has demonstrated the ability to achieve LLFC, thereby avoiding the typical soot-NO$_x$ tradeoff that occurs in diesel combustion (e.g., with exhaust gas recirculation, EGR) [6].

In DFI, each fuel spray is injected along the axis of a cylindrical duct. Both air and fuel are entrained into the duct and mix along its length, similar to a Bunsen burner. This longer mixing length prior to ignition improves the diesel spray's potential to achieve LLFC. Based on early successes, multiple research groups have begun to investigate DFI both experimentally [1, 5, 7-21] and computationally [8, 19, 22-27].

A number of studies have investigated the impact of duct geometry on DFI combustion in pressure vessels [1, 8-13, 18, 26] and engines [14-17, 19, 20, 28]. Figure 1 shows important geometric parameters in DFI, including the duct inlet and exit shape, the duct inner diameter (D), the duct length (L), and the gap distance between the injector orifice and the duct inlet (G). Gehmlich et al. [1] compared different inlet and exit geometries, finding that the best geometry (among those tested) was an inlet with a rounded inner surface and an exit with a tapered outer surface (compared to chamfered inlets or no exit taper); this so-called "delta" ge-

Figure 1. Key geometric parameters for DFI. Duct diameter (D), duct length (L), and gap distance (G). The geometry shown, with a curved inlet and tapered exit is the delta geometry [1].

ometry is shown in Fig. 1. In general, authors have found that ducts with smaller inner diameters ($D \approx 2$ mm) perform better than those with larger inner diameters ($D \approx 4$ mm), provided the spray diameter does not exceed that of the duct at the inlet [8-10, 12].

Some authors have found that longer ducts ($L \cong 14$ mm) lead to greater spray dispersion [11] and were better at mitigating soot luminosity [18], whereas Gehmlich et al. [1] found that there were minimal effects of duct length for $L > 8$ mm under certain conditions. When studied in an engine, Nilsen et al. [15] found that increased length generally decreases soot emissions, but an optimum duct length exists for some duct diameters, beyond which soot begins to increase. Svensson et al. [18] studied the effects of gap distance and concluded that a shorter gap distance produced less soot luminosity. Nevertheless, other authors found that larger gap distances increased the spray velocity (increased tip penetration relative to a free spray), which also would be expected to reduce soot [10, 26]. When comparing gap distances in an engine, Nilsen et al. [14] found that a longer axial gap distance consistently showed superior performance up to the maximum tested value of $G = 3$ mm.

Other parameters that impact DFI performance are ambient pressure, injection pressure, and ambient temperature. Li et al. [9, 10, 12] studied these parameters under non-reacting conditions, finding

that the spray penetration difference between a free spray and DFI becomes larger with larger injection pressure. They also found that increasing ambient pressure increases the penetration advantage DFI has over a free spray. That is, increasing the ambient pressure still decreases penetration, but at a lower rate for a ducted spray than a free spray [9]. Under reacting conditions in a combustion vessel, Gehmlich et al. [1] and Fitzgerald et al. [8] found that increasing temperature decreased the lift-off length (LOL), with combustion even starting at the duct exit at some conditions, yet DFI soot reduction was maintained relative to CDC.

Modelling work has been conducted to investigate DFI's soot reduction. Some studies have found that there is limited effect on air entrainment into the spray upstream of the duct [19], yet others have found that DFI significantly increases entrainment upstream of the duct [13, 24]. This increase in potential entrainment is attributed to a low-pressure region at the entrance of the duct that drives flow into the duct [24, 26]. Segatori [26] showed that the low-pressure region might be up to 10 bar below ambient pressures and that the annular region between the spray and the duct inner wall corresponds to the minimum pressure zone. Thus, the duct diameter and gap distance play a role in optimizing the increased entrainment into the duct.

In general, modelling results show that the mixing section of the duct is important in reducing the centerline equivalence ratio and creating a more homogeneous equivalence ratio profile [19, 24]. Nilsen et al. [24] concluded that this improved mixing is appreciable even in shorter ducts ($L = 8$ mm), and thus shorter ducts might optimize the balance between lowering the centerline equivalence ratio and maximizing post-duct entrainment.

Liu et al. [22] concluded that DFI promotes a larger low-temperature heat release region and smaller high-temperature heat release region, the combination of which suppresses soot formation. They found that ducted sprays had a longer liquid-length than free-sprays due to lower initial temperatures within the duct. These lower initial temperatures led to lower mixture reactivity and longer ignition delay but had little effect on LOL. This result correlates with the de-coupling of ignition delay and LOL trends seen in experimental work [1, 8].

The modelling work by Segatori [26] also provided some insight into the experimental results of Li et al. [9, 10, 12], which showed the existence of a mushroom shaped spray head and recirculation region after the duct exit in some cases. Segatori showed that the existence of a separated wall boundary layer inside the duct raises the turbulent kinetic energy (TKE) of the spray. Then, due to the local positive pressure gradients at the sharp-edged duct exit, a large high-intensity recirculation area forms and further increases the TKE of the spray by an order of magnitude. There is a high diffusion of TKE in this region that enhances mixing.

Nilsen et al. [14] were the first to successfully deploy DFI in an engine. The study, conducted in an optical engine, found that soot could be significantly reduced while other regulated emissions, such as NO_x, hydrocarbons (HC), and CO were relatively unchanged from CDC. Nilsen et al. [16, 17] conducted two follow-up studies in the optical engine to compare DFI and CDC over a wide range of operating conditions, including idle and a high-load condition up to 10 bar gross indicated mean effective pressure ($IMEP_g$). Similar to their previous studies, they found that DFI reduced engine-out soot at all the conditions tested and broke the soot-NO_x tradeoff that occurs with EGR, allowing for simultaneously low soot and NO_x emissions. One interesting, previously unobserved phenomenon was the existence of late-cycle spatially integrated natural luminosity (SINL) flare-ups that are indicative of soot production. They attributed these flare-ups to spray-spray interactions and/or entrainment of product gases upstream of the established LOL [2], which likely decrease entrainment and increase soot production [16, 29]. Wilmer et al. [20] examined soot particle mass and number density from an optical heavy-duty single cylinder research engine for both CDC and DFI conditions at one operating condition using a 4-orifice/4-duct set up. They confirmed that DFI can significantly reduce engine-out soot and showed that DFI both reduces the total number of soot particles as well as their average size.

Other authors have deployed DFI in engines with varying levels of success. For example, Tanno et al. [19] found that DFI reduced engine-out soot by up to 52%, while Svensson et al. [28] found that DFI consistently produced more soot than CDC at full-load conditions. Indeed, the results of Svensson et al. contrast with others in the literature in several ways. They discussed physical mechanisms that might be the cause of these differences, e.g., re-entrainment upstream of the LOL or increased spray-to-spray interactions due to faster DFI sprays compared to non-ducted sprays.

These contrasting results demonstrate a need to better understand how to successfully deploy DFI in an engine at a wide range of operating conditions. The present work aims to address this need by assessing the efficiency and engine-out emissions trends for two different ducted configurations, namely a 2-orifice/2-duct and a 4-orifice/4-duct setup, over a wide parameter space. In addition to the exhaust emissions, high-speed natural luminosity (NL) images are used to explore the dynamics of the in-cylinder combustion processes. It is noted that the 4-duct configuration has some prior analysis by

Nilsen et al. [16]. The current work addresses the 2-duct configuration and the trends associated with increasing engine load by increasing the number of spray/duct pairs.

2. Experimental Facility

The parameter sweeps conducted for this study started at the baseline condition and changed only one variable at a time (to the extent this is possible). The engine speed was held constant at 1200 rpm for all testing. Slightly different parameter sweeps were conducted for the 2-orifice/2-duct and 4-orifice/4-duct configurations; the baseline and swept conditions for both configurations are given in Table 1. A total of six parameters were explored, namely duration of injection (DOI), injection pressure (P_{inj}), intake manifold absolute pressure (IMAP), intake manifold temperature (IMT), start of combustion timing (SOC), and intake charge-gas oxygen mole fraction (i.e., dilution). The slight differences in baseline and swept parameters between configurations were guided by the results from the 2-duct study, which occurred first.

It is noted that the tested IMAP and IMT conditions were chosen to account for differences in peak cylinder pressures between the test engine (see below) and modern diesel engines with higher compression ratios. The test engine has a compression ratio of 12.5, while modern diesel engines commonly have compression ratios of 16 or higher. Therefore, IMAP and IMT conditions in this study were chosen to better match peak cylinder pressures and temperatures, respectively, in modern engines. The IMAPs across both sweeps are 1.5, 2.0, 2.5, and 3.0 bar, which would correspond to IMAPs of 1.02 1.36, 1.70, and 2.04 bar, respectively, in a 16.5 compression ratio engine. The IMTs tested were 50 °C, 70 °C, and 90 °C, which are equivalent to 17 °C, 35 °C, and 53 °C, respectively, in a 16.5 compression ratio engine.

Table 1. Experimental test matrix with baseline conditions in bold.

Ducts	2D2L12G3δ	4D2L12G3δ
Injector Tip Configuration	2 × 0.110 mm × 140°	4 × 0.110 mm × 140°
Fuel*	CFA	CFB
Duration of Injection	1500, 2500, **3500**, 4500 μs	1500, 2500, **3500**, 4500 μs
Total mass of fuel injected per cycle**	11.7, 20.1, **28.5**, 36.8 mg	27.6, 47.2, **66.8**, 85.7 mg
Injection Pressure	60, 120, **180**, 240 MPa	80, **180**, 240 MPa
Total mass of fuel injected per cycle**	16.3, 23.5, **28.5**, 31.0 mg	44.4, **66.8**, 76.4 mg
Intake Manifold Absolute Pressure	1.50, **2.0**, 2.5 bar	2.0, **2.5**, 3.0 bar
Intake Manifold Temperature	50, 70, **90** °C	50, 70, **90** °C
Start of Combustion Timing	-10.0, -5.0, **0.0**, +5.0 CAD ATDC	-5.0, **0.0**, +5.0 CAD ATDC
O₂ mole fraction (Dilution)	12, 14, **16**, 18, 21 mol% O₂	12, 14, **16**, 18, 21 mol% O₂

*The fuel used for each parameter sweep has the same nominal fuel properties. The different naming convention for the two batches of fuel used represents Certification Fuel Batch A (CFA) and B (CFB), respectively. SOC is measured in crank angle degrees (CAD) after top dead center (ATDC).

**The total injected fuel mass/cycle is constant for all parameter sweeps except for DOI and P_{inj}. For all other parameters the injected mass is that of the baseline condition (shown in bold).
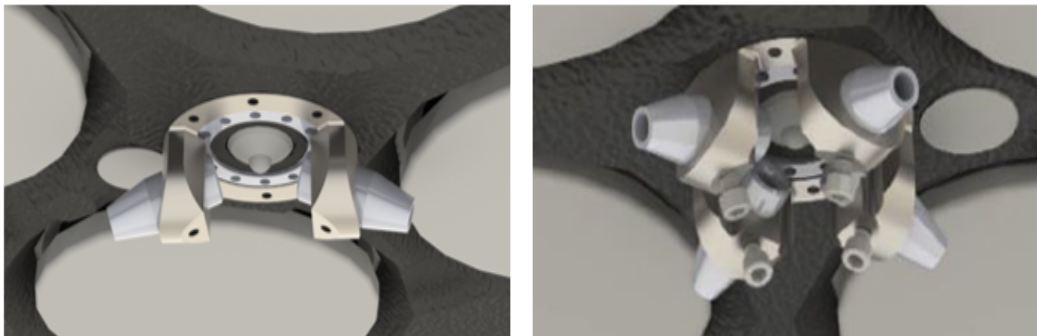
Figure 2. 2- and 4-duct mounting assemblies.

Figure 2 shows the different orifice/duct configurations. Each configuration used a $D = 2$ mm, $L = 12$ mm, $G = 3$ mm duct with the aforementioned "delta" geometry, designated D2L12G3δ. Alignment is a critical component for successful DFI operation [1]. As such, the ducts are mounted in the engine using a custom fixture that provides enough degrees of freedom to allow accurate alignment of each duct with its corresponding spray (see [14, 16]).

The different orifice/duct configurations were installed in the optical engine (Fig. 3), which has a 1.7-L displacement and operates using a four-stroke cycle. The piston has a bowl with a flat fused-silica window that allows for imaging of the cylinder, both for duct alignment and combustion measurements. The engine, its basic instrumentation, and operation are described in detail in [30]. Data from at least three replicate engine runs consisting of 180 fired cycles each were acquired and used to make the scalar and timeseries plots shown herein. The fuel used for this study was a No. 2 S15 diesel certification fuel containing ~30 wt% aromatics. The fuel injector is a common-rail solenoid-actuated injector with an orifice diameter of 0.110 mm and an umbrella angle of 140 deg, which is mounted at the top of the engine in the center of the cylinder head.

3. Diagnostics

Optical, in-cylinder, and exhaust measurements were made at each test condition. Imaging data was collected for the first seven fired cycles in each run. NL images were acquired using a high-speed camera (Photron SA-Z) equipped with a commercial camera lens (Nikon NIKKOR 105-mm, f/2.8 lens). A broadband mirror directed light from the combustion chamber to-

Figure 3. Schematic of the optical engine. The camera used in this study for collection of natural luminosity is a Photron SA-Z.

ward the camera, where a 600 nm short wave pass filter and a 3 mm thick heat-absorbing filter (Schott KG3) suppressed infrared and red-light contributions. Image acquisition was triggered at 5 CAD before the planned SOC and continued for 50 CAD at a frequency of one image every .5 CAD (14.4 kHz). At this repetition rate, the camera had an active sensor resolution 640×640 pixels. The exposure duration and lens aperture settings were varied depending on the conditions to take advantage of as much camera dynamic range as possible.

The collected NL signal is emitted primarily by soot; the high-speed NL images provide spatio-temporal characterization of the soot luminosity in the cylinder. To compare the in-cylinder soot more quantitatively between cases, the calibrated SINL time sequence for each test condition was calculated as

$$\text{SINL(CAD)} = \frac{f_s^2}{t_{exp}\text{SINL}_{max}} \sum_{i=1}^{m} \sum_{j=1}^{n} \text{NL}(i, j, \text{CAD}), \qquad (1)$$

where i and j are the pixel indices on the camera sensor, t_{exp} is the exposure time, SINL_{max} is a fixed normalization constant, and f_s is the lens f-stop. This calibration has previously been shown to accurately account for differences in exposure and aperture, allowing comparison between data acquired with different camera/lens settings [2]. The scalar value used to compare SINL condition-to-condition is ΣSINL, which is the time integral over the entire combustion event of the time-dependent SINL signal.

While, NL, SINL, and ΣSINL are good indicators of the amount of hot soot within the combustion chamber for a given condition, they do not always correlate with quantitative soot values measured in the exhaust because the magnitude of the NL signal is typically a complicated function of the concentration, temperature, and properties of the soot particles inside the combustion chamber [31, 32]. Additionally, NL images are integrated along the camera line-of-sight, such that light from the far side of the combustion chamber must travel through the soot formed in regions of the chamber closer to the camera
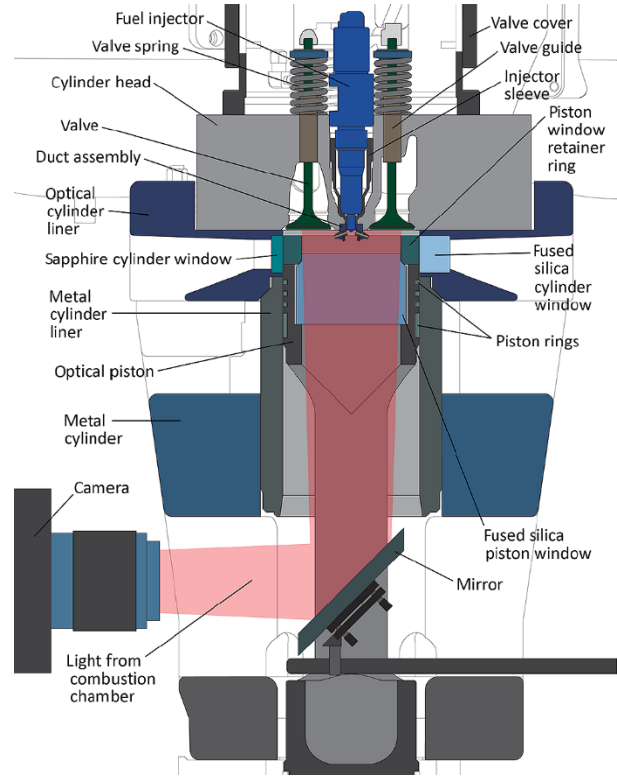
lens. Hence, some signal can be absorbed and therefore not captured in NL images. Nevertheless, NL, SINL, and ΣSINL are useful for deducing qualitative sooting behavior for some conditions.

In-cylinder pressure measurements and exhaust gas measurements also characterized DFI performance. In-cylinder pressure measurements provided in-cylinder temperature, combustion noise, combustion timing, and apparent heat release rate (AHRR). Pressure data was recorded by a water-cooled pressure transducer (AVL QC34C) at 0.1 CAD increments (72 kHz). The exhaust was monitored using a set of gas analyzers. NO_x was measured using chemiluminescence detection (CAI 600HCLD); O_2, CO, CO_2 were measured using non-dispersive infrared analysis (CAI 602-P NDIR); HCs were measured using flame ionization detection (CAI 600 HFID); and soot was measured using a smoke meter (AVL 415S).

4. Results and Discussion

The engine performance is quantified by the indicated-specific emissions (mass of emissions per unit indicated work) and fuel-conversion efficiency,

$$\eta_f = \frac{W}{m_f * \text{LHV}_f},$$

(2)

where W, m_f, and LHV_f are the indicated work output, mass of fuel injected, and fuel lower heating value, respectively. The indicated work output is taken as the integral of pressure versus volume over the compression and expansion strokes (i.e., from 180 CAD before TDC to 180 CAD after TDC). All emissions discussed within this paper will be on an indicated-specific basis unless otherwise noted. Furthermore, we quantify engine load by $\text{IMEP}_g = W/V_{disp}$, where V_{disp} is the displacement volume. Figure 4 shows the engine load for each condition. The load has a greater sensitivity to DOI and P_{inj} for the 4-duct configuration compared to the 2-duct configuration. Sensitivity is defined as the change in dependent variable divided by the change in independent variable. This definition will be used here and throughout when discussing trends as functions of parameters swept.

4.1 DOI Sweep

DOI is an important parameter to study because engine manufacturers use it to control engine load. In this study, DOI was swept from 1500 to 4500 µs, corresponding to a load range of 0.7-3.5 bar IMEP_g for the 2-duct configuration and 2.4-8.7 bar IMEP_g for the 4-duct configuration.

Figure 5 shows the emissions and η_f for the DOI sweeps in the 2- and 4- duct configurations. For both configurations, specific NO_x emissions decrease with increasing DOI, with the largest decrease occurring between DOI = 1500 and 2500 µs. It is typical for absolute NO_x emissions to increase with higher engine load (i.e., increasing DOI). Indeed, this is the case for the current results, but engine load increases more quickly with DOI than absolute NO_x, resulting in decreasing indicated-specific NO_x emissions with DOI.

Specific NO_x emissions are higher for the 4-duct configuration than

Figure 4. Measured IMEP_g across all parameters swept for both the 2-and 4-duct configurations. The variability of engine load between runs is on the order of 0.001-0.01 bar and therefore cannot been seen in this figure

the 2-duct configuration at all DOIs except for 1500 µs. The discrepancy at 1500 µs DOI is due to the indicated-specific nature of the data shown. For most conditions tested in this study, increasing the number of ducted sprays from two to four increases the load by a factor of approximately 2.5; however, the load is increased by a factor of about 3.5 for the 1500 µs condition in the 4-duct configuration. Hence, for this condition, it is the higher engine load in the 4-duct configuration that leads to the lower specific NO_x emissions.

Figure 5. Emissions data for DOI sweeps with the 2- and 4-duct configurations. The color variation seen in the legend indicates the DOI condition for both configurations. Note that the numbers annotated at the top of each group indicates the extent of the y-axis for that group.
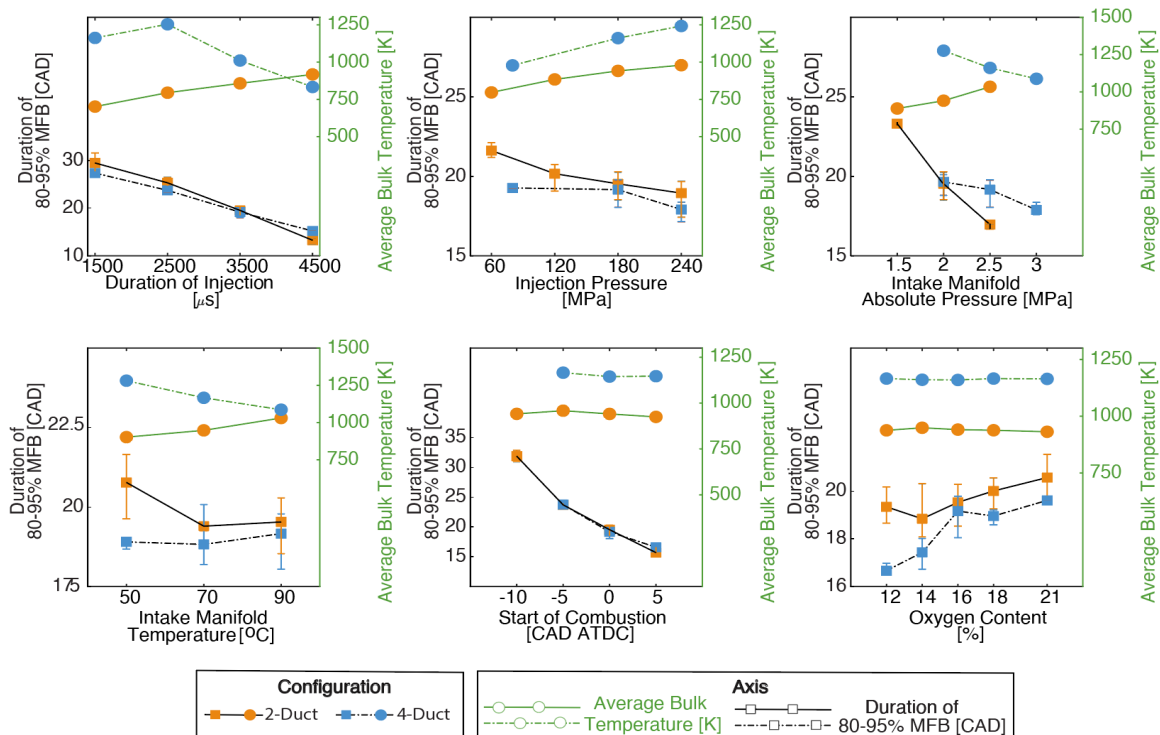
Figure 6. The duration of combustion in CAD between MFB80 and MFB95 and the average bulk temperature during that period for all parameters swept.

Specific HC and CO emissions are lower for the 4-duct configuration than the 2-duct configuration. For the 2-duct configuration, specific HC and CO emissions have a minimum at the 3500 μs DOI condition. However, specific HC and CO continuously decrease with increasing DOI for the 4-duct configuration.

Mass Fraction Burned (MFB) and bulk temperature are useful when comparing configurations. First, the 2-duct's bulk temperatures are lower than the 4-duct's, leading to lower NO_x, but higher HC and CO. Lower in-cylinder temperatures lead to a larger portion of combustion occurring later in the cycle for the 2-duct configuration relative to the 4-duct configuration. Figure 6 shows the duration of late-cycle combustion: from 80% to 95% of total MFB. MFB95 defines the end of combustion (EOC). The 2-
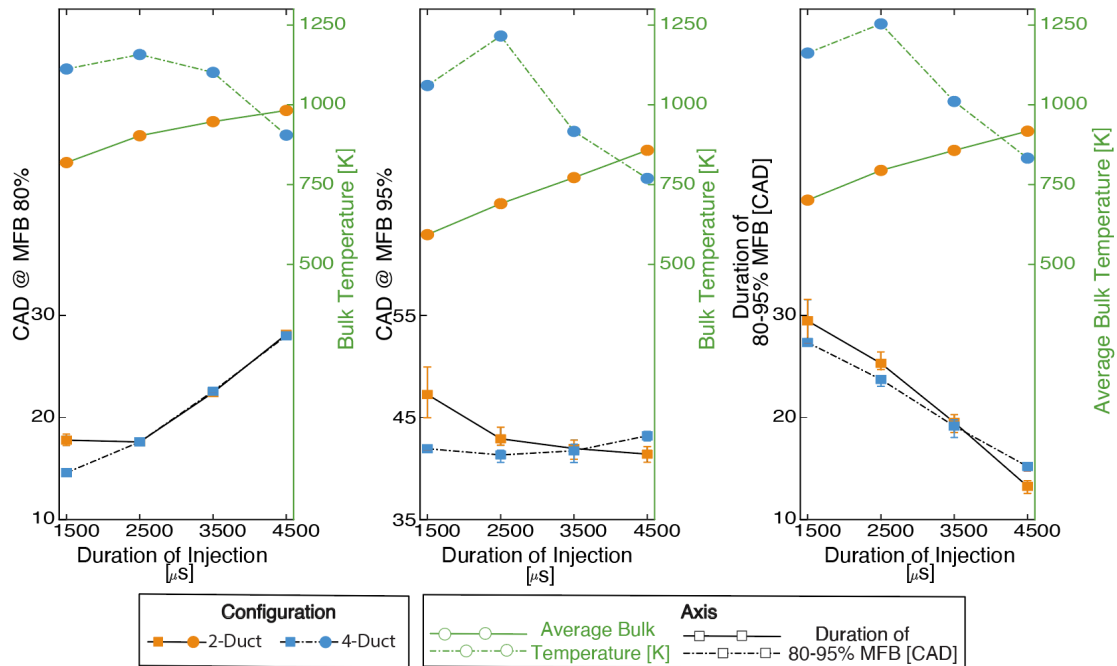
Figure 7. CAD and Bulk Temperature at MFB80 (left) and MFB95(center). The duration of combustion in CAD between MFB80 and MFB95 and the average bulk temperature during that period (right). All sub-figures are for the DOI sweep

duct configuration experiences longer late-cycle combustion for all but three conditions. Additionally, the average bulk temperature during this period is lower for the 2-duct configuration. A longer duration of late-cycle combustion at lower temperatures suggests less-complete oxidation and explains the increased HC and CO emissions for the 2-duct configuration. The degraded combustion efficiency and later combustion phasing with the 2-duct configuration also help explain why the load with the 4-duct configuration is more than twice as high as the load with the 2-duct configuration, all other parameters being equal.

MFB80 and MFB95 further explain HC and CO trends. Figure 7 shows that, for all but the 1500 µs condition, MFB80 is similar for the 2- and 4-duct configurations. However, MFB95 differs between the two configurations, which might cause different HC and CO emissions. The EOC trends are opposite between the configurations: the 2-duct configuration EOC occurs earlier with increasing DOI, while the 4-duct configuration EOC occurs later with increasing DOI. This suggests that combustion is ending prematurely in the 2-duct configuration relative to that of the 4-duct configuration, giving a HC and CO emissions spike. This effect shown in Fig. 5 is exacerbated given the emissions' indicated-specific nature and relatively low engine-load sensitivity for DOI changes with the 2-duct configuration.

All 2-duct DOIs experienced soot below the smoke meter's sensitivity threshold. On the other hand, the 4-duct configuration gave measurable soot at both the shortest (1500 µs) and longest (4500 µs) DOIs. The ΣSINL and time-resolved SINL data shed additional light on the soot trends, e.g., why the 4-duct soot increases at 4500 µs DOI. Section 4.7 discusses the SINL results.

The η_f increases with DOI for both configurations and was consistently higher for the 4-duct configuration, which is in line with its higher load and consistent with observations from other studies [16].

4.2 Fuel Injection Pressure Sweep

Injection pressure also influences engine-out emissions and load; hence, it is important to understand trends associated with injection pressure for DFI. For this sweep, the load range was 1.2-2.9 bar IMEP$_g$ and 4.2-7.9 bar IMEP$_g$ for the 2- and 4-duct configurations, respectively. Figure 8 shows the emissions and η_f.
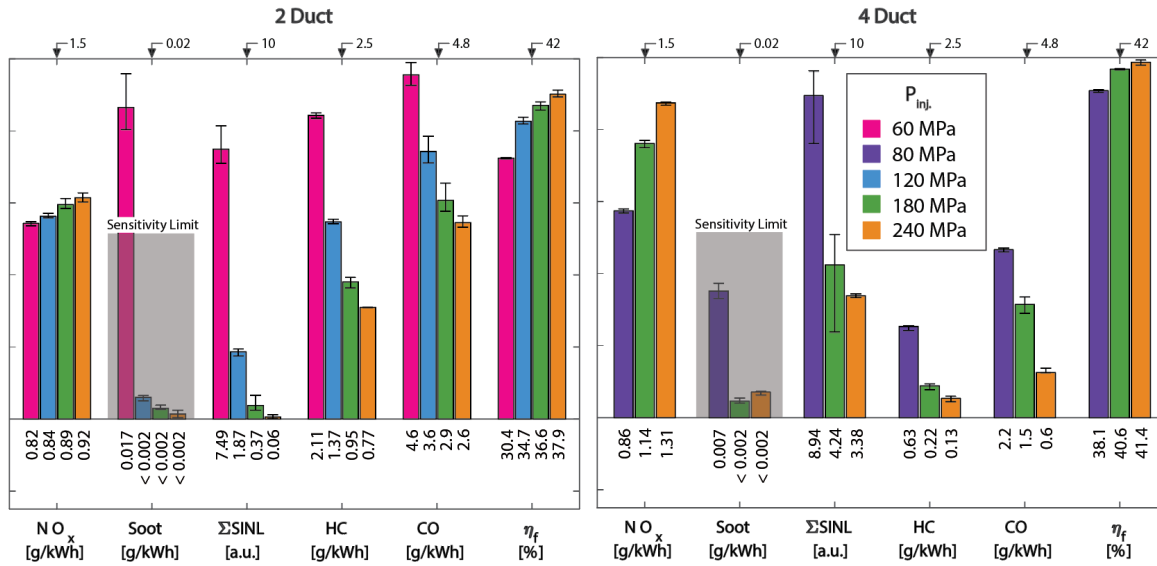
Figure 8. Emissions data for injection pressure sweeps with the 2- and 4-duct configurations. The color variation seen in the legend indicates the injection pressure condition for both configurations. Note that the numbers annotated at the top of each group indicates the extent of the y-axis for that group.

For both the 2- and 4-duct configurations, specific NO_x emissions increase with injection pressure. As for the preceding sweep, it is typical for absolute NO_x emissions to increase with increasing load (e.g., higher loads correlate with higher temperatures and increased NO_x formation). Nevertheless, for the current sweep, the increased $IMEP_g$ with injection pressure does not offset the absolute increase in NO_x emissions with increased injection pressure. Additionally, specific NO_x emissions are higher for the 4-duct configuration than the 2-duct configuration. This result is consistent with that seen in the DOI sweep and expected due to the increased number of spray-flames and higher in-cylinder temperatures in the 4-duct configuration.

As with the DOI sweep, specific HC and CO emissions are lower for the 4-duct configuration than the 2-duct configuration. This is likely due to the lower temperatures and longer duration of late-cycle combustion in the 2-duct case as shown in Fig 6. Furthermore, the specific HC and CO emissions decrease with increasing injection pressure for both configurations.

For all injection pressures tested other than the lowest-pressure condition for the 2-duct configuration (60 MPa), the measured soot values were lower than the sensitivity threshold of the smoke meter. Therefore, quantitative sooting trends beyond this condition cannot be observed. The ΣSINL values show that the natural luminosity signal from soot decreases as injection pressure increases.

The fuel-conversion efficiency increased with increasing injection pressure for both the 2- and 4-duct configuration, with the 4-duct configuration having higher efficiency. This agrees with the trend of higher η_f with higher engine load observed in the DOI sweep.

4.3 IMAP Sweep

IMAP is used to adjust the amount of charge-gas in the engine cylinder. In this study, the IMAP conditions varied between the two DFI configurations. For the 2-duct configuration, IMAPs of 1.5, 2.0, and 2.5 bar were tested, with the baseline condition set to 2.0 bar. For the 4-duct configuration, IMAPs of 2.0, 2.5, and 3.0 bar were tested, with the baseline condition adjusted to 2.5 bar. The baseline condition was altered between the 2- and 4-duct configurations due to the fact that the 1.5 bar condition is not representative of realistic IMAP conditions in a 16.5 compression ratio engine. Note that, while engine load is not strongly impacted by IMAP, opposite trends were seen between the 2- and 4-duct configurations. For the 2-duct configuration $IMEP_g$ was 2.8, 2.6, and 2.5 bar for IMAPs of 1.5, 2.0, and 2.5 bar respectively. For the 4-duct configuration, $IMEP_g$ was 6.7, 6.8, and 6.8 bar at IMAPs of 2.0, 2.5, and 3.0 bar, respectively.

The emissions and η_f results for this sweep are shown in Fig. 9. Specific NO_x emissions are higher for the 4-duct configuration than the 2-duct configuration in all comparable conditions. As with the previous sweeps, this result is expected due to the increased number of spray-flames and higher in-cylinder temperatures in the 4-duct configuration. Specific NO_x emissions decrease with increasing
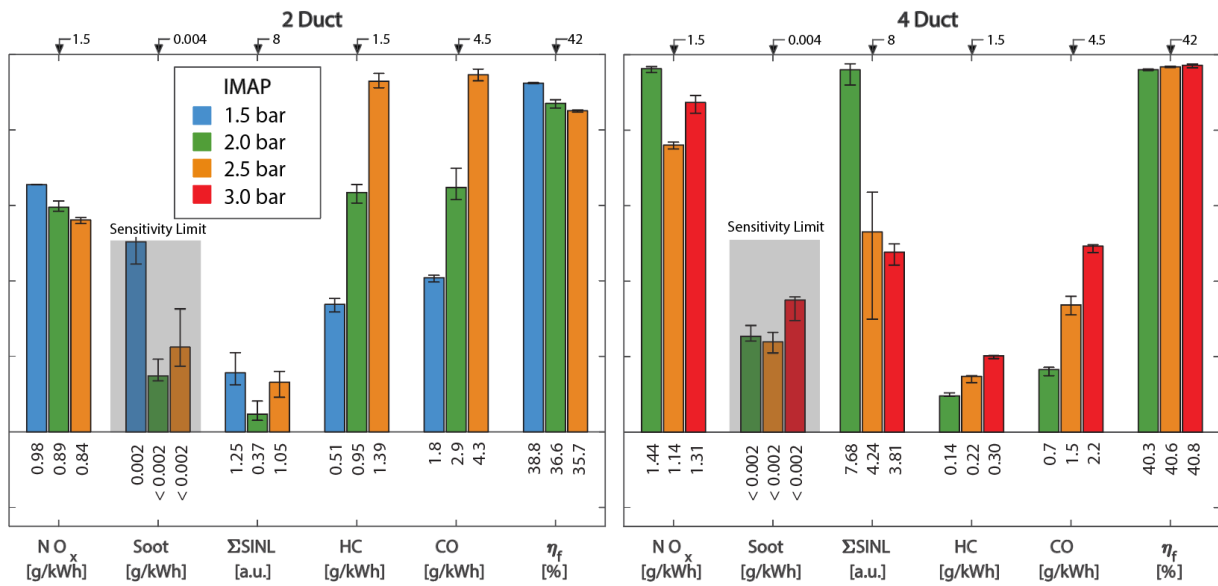
Figure 9. Emissions data for the IMAP sweeps with the 2- and 4-duct configurations. The color variation seen in the legend indicates the IMAP condition for both configurations. Note that the numbers annotated at the top of each group indicates the extent of the y-axis for that group.

IMAP for the 2-duct configuration, but the 4-duct case shows a non-monotonic trend. This difference in specific emissions trends can be partially explained by the levelling-off in engine load between the 2.5 and 3.0 bar IMAP conditions in the 4-duct configuration. This stagnation in engine load should indicate that the change in indicated-specific NO_x shown is due predominately to a change in absolute NO_x. Absolute NO_x results for the 4-duct IMAP sweep are 81.5, 52.5, and 49.1 ppm for 2.0, 2.5, and 3.0 bar respectively. The difference then is the result of the way indicated-specific NO_x is calculated. The conversion from the measured emissions in ppm to grams accounts for the mass flow rate of the exhaust. At higher boost levels (3 bar IMAP), the mass flow rate through the engine is higher. Ultimately this leads to an increase in indicated specific NO_x at this condition even though absolute NO_x continues to decrease with increasing IMAP.

Specific HC and CO emissions increase with increasing IMAP for both configurations. As seen in previous sweeps, HC and CO emissions are lower for the 4-duct configuration than the 2-duct configuration due to temperature differences during the combustion process. Typically lower temperatures lead to a longer duration of late-cycle combustion in the 2-duct configuration, but as seen in the DOI sweep, they can also lead to a premature EOC (MFB95). Similarly, this is seen in the 2.5-bar IMAP condition (see Fig. 10) where the 2-duct configuration exhibited earlier EOC and a shorter duration of late-cycle combustion yet larger indicated-specific HC and CO emissions relative to those of the 4-duct configuration.

Soot emissions were at or below the sensitivity limit for all conditions tested in both duct configurations. Only at the lowest IMAP condition did soot reach a value of 0.002 g/kWh. This would indicate that for DFI, lower IMAP increases soot emissions, which is opposite of the trend in CDC [16]. The 1.5 bar IMAP is not particularly representative of realistic engine conditions. This fact, coupled with the observation that it had the highest soot emissions in the 2-duct study, led to the elimination of this condition in the 4-duct study. The ΣSINL values for the 2-duct configuration show a minimum at the 2.0-bar IMAP condition. This is not the case for the 4-duct configuration, for which the ΣSINL signal continuously decreases as IMAP is increased.

For the 2-duct configuration, η_f decreases with increasing IMAP. Conversely, η_f slightly increases with increasing IMAP for the 4-duct configuration. These trends follow $IMEP_g$ load trends in Fig. 4, wherein the load decreases with IMAP for the 2-duct case and is nearly constant with IMAP in the 4-duct case. Both the efficiency and load are higher for the 4-duct configuration than the 2-duct configuration at all IMAP conditions tested.

4.4 IMT Sweep

The intake temperature sweep simulates conditions such as cold-start and low ambient temperatures. While IMT is not typically used as a control parameter in commercial engines, it affects realistic
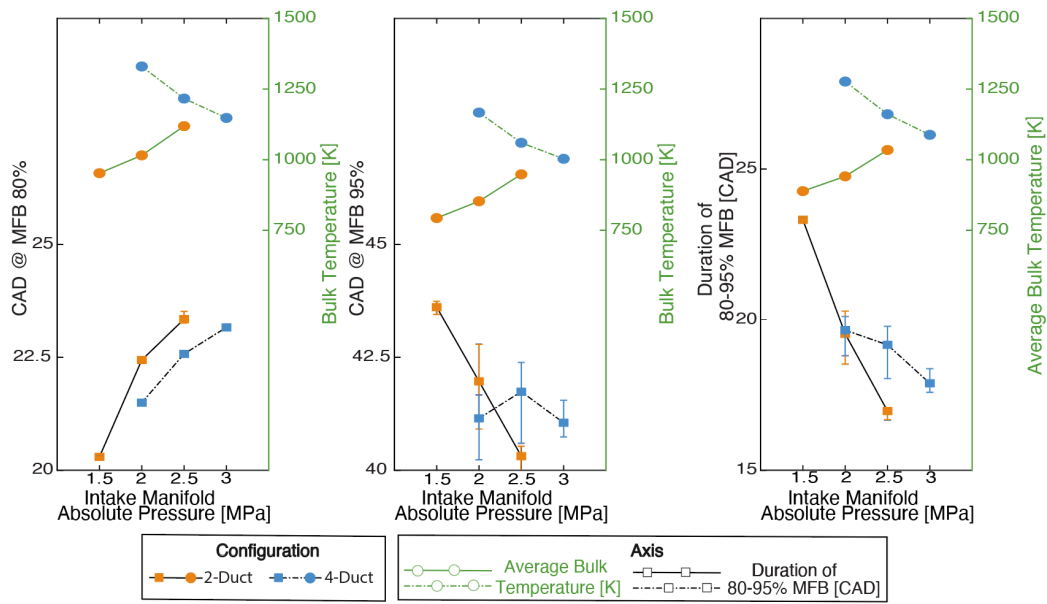
Figure 10. CAD and Bulk Temperature at MFB80 (left) and MFB95 (center). The duration of combustion in CAD between MFB80 and MFB95 and the average bulk temperature during that period (right). All sub-figures are for the IMAP sweep
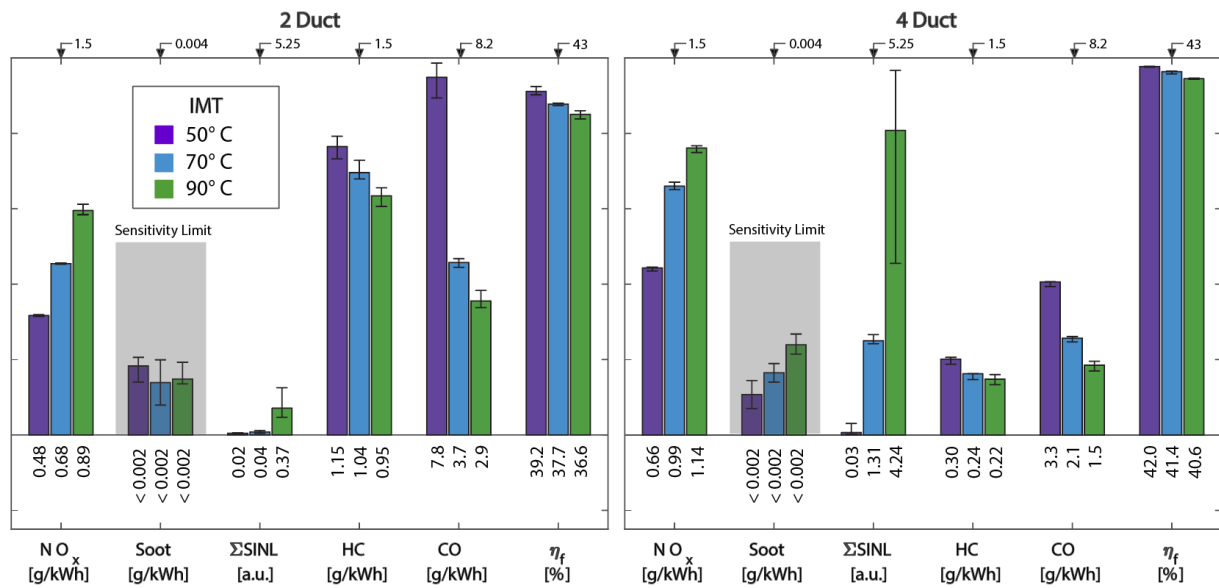

Figure 11. Emissions data for the IMT sweep with the 2- and 4-duct configurations. The color variation seen in the legend indicates the IMT condition for both configurations. Note that the numbers annotated at the top of each group indicates the extent of the y-axis for that group.

engine operation and must be understood. The range of IMT values tested was set by considering conditions that are likely to be encountered in actual applications (~15 – 55 °C for a 16.5:1 compression-ratio engine), limitations of the air- and water-heater systems, and the operating temperature range of the gapless compression ring of the optical engine. The results of this sweep are shown in Fig. 11.

For both configurations, specific NO_x emissions increase with increasing IMT as expected based on higher in-cylinder temperatures during and after combustion. As in the previous sweeps, specific NO_x emissions are higher for the 4-duct configuration than the 2-duct configuration for all IMT conditions. Specific HC and CO emissions decrease with increasing IMT for both configurations. Like the previous sweeps, specific HC and CO emissions are lower for the 4-duct configuration than the 2-duct configuration, as expected based on lower temperatures and longer late-cycle combustion durations for the 2-duct configuration. This is particularly the case at the lowest IMT condition. It can be seen in Fig. 6 that

the 2-duct configuration had a significantly longer duration of late-cycle combustion at lower temperatures compared to that of the 4-duct configuration at the 50 °C condition. This contributes to in a spike in specific CO emissions for the 2-duct configuration.

For all IMTs tested in both the 2- and 4-duct configurations, the measured soot values were lower than the sensitivity threshold of the smoke meter. The ΣSINL values show that the natural luminosity signal from soot increases with IMT. While the ΣSINL signal is very low at the lower temperatures, there is a sizeable increase in ΣSINL for both the 2- and 4-duct configurations at the highest IMT tested. This effect is at least partially due to the temperature dependence of NL signal. The IMT condition could significantly impact soot temperatures, and therefore the ΣSINL values for different IMT conditions should not be compared against each other directly.

The η_f is decreased for both configurations with increasing IMT. Between the 2- and 4-duct configurations, the IMT has a slightly larger effect on η_f for the 2-duct configuration. Like the previous sweeps shown, η_f is higher for the 4-duct configuration than the 2-duct configuration at all IMTs tested.

4.5 SOC Sweep

SOC is important because it can be adjusted by changing the start of injection timing to affect engine-out emissions and efficiency from cycle to cycle. The results of this sweep are shown in Fig. 12. For the 2-duct SOC sweep, NO_x emissions decrease with increasing SOC ATDC, as expected. While the 4-duct sweep did not test SOC of -10 CAD ATDC (see discussion below), the general trend is the same for the 4-duct configuration between -5 and +5 CAD ATDC. As observed in previous sweeps, specific NO_x emissions are higher for the 4-duct configuration than the 2-duct configuration.

As seen in the preceding sweeps, specific HC and CO emissions are lower for the 4-duct configuration than the 2-duct configuration due to relatively lower temperatures in the 2-duct configuration compared to the 4-duct configuration. Specific HC and CO emissions increase with retarded SOC timing for both configurations. Retarding SOC timing leads to significantly lower peak temperatures. For example, peak bulk temperatures decrease by almost 100 K from SOC of -5 to +5 CAD ATDC in the 4-duct configuration. This leads to lower oxidation rates and therefore increased HC and CO emissions. It also leads to greater portions of the combustion process occurring later in the expansion stroke. This can be seen in Fig. 13, which shows that the time when 80% MFB is reached increases by approximately 5 CAD for every 5 CAD increase in SOC timing. Even so, the duration of 80-95% MFB decreases with increasing SOC, indicating that more un-oxidized HC and CO are left at EOC as SOC increases.

Across the SOC sweep for both configurations, the measured soot values were at or below the sensitivity threshold of the smoke meter. The ΣSINL values show that the natural luminosity signal from
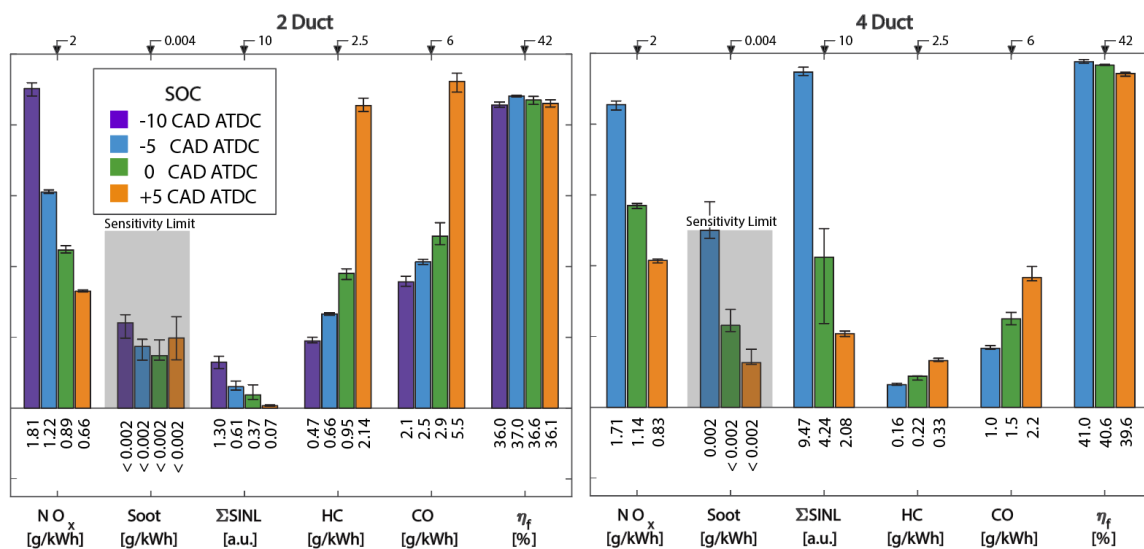
Figure 12. Emissions data for SOC sweeps with the 2- and 4-duct configurations. The color variation seen in the legend indicates SOC condition for both configurations. Note that the numbers annotated at the top of each group indicates the extent of the y-axis for that group.

soot decreases with retarded SOC timing.
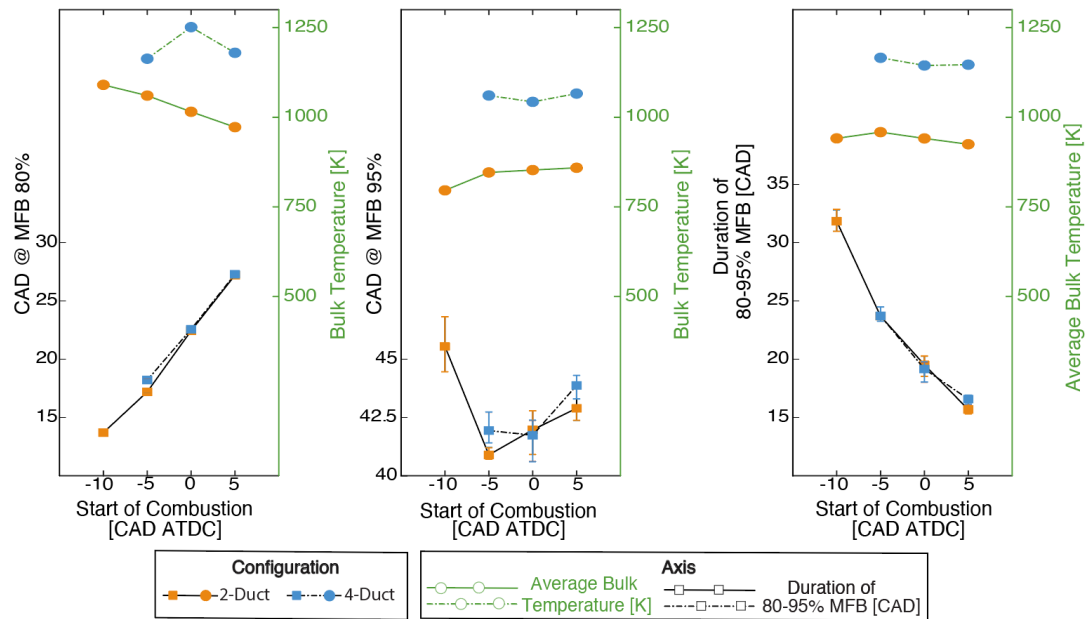
Figure 13. CAD and Bulk Temperature at MFB80 (left) and MFB95(center). The duration of combustion in CAD between MFB80 and MFB95 and the average bulk temperature during that period (right). All sub-figures are for SOC sweep.

The η_f generally decreased as a function of retarded SOC timing for both configurations. The exception to this trend is seen only in the 2-duct configuration between the earliest two SOC timings (-10 and -5 CAD ATDC). Since the 2-duct study showed the highest specific NO_x, highest $\Sigma SINL$, lowest η_f, and highest cylinder-pressure rise-rates at the earliest timing, it was determined that timings significantly earlier than -5 CAD ATDC would not be desired. Hence, the -10 CAD ATDC timing was not included in the 4-duct parameter sweep. As seen in the other parameter sweeps, η_f is higher for the 4-duct configuration than the 2-duct configuration.

4.6 Dilution Sweep

Dilution (i.e., EGR) is a common strategy for mitigating NO_x emissions. Increased dilution decreases in-cylinder temperatures and oxygen mole fractions (XO_2), which curtail the formation of NO by the thermal (or Zeldovich) mechanism. Unfortunately, for CDC, this decrease in NO_x typically comes with a significant increase in soot. In this parameter sweep, XO_2 was swept from 21 to 12% for both configurations. Previous work has shown that, for DFI, soot emissions do not significantly increase with dilution [14, 16].

The emissions and η_f data for this sweep can be seen in Fig. 14. For both configurations, specific NO_x emissions decrease with increasing dilution (i.e., decreasing XO_2), as expected. The sensitivity of engine load to dilution is comparable between the two configurations. As with the previous sweeps, specific NO_x emissions are higher for the 4-duct configuration than the 2-duct configuration.

Specific HC and CO emissions increase with increasing dilution for both configurations. This effect is in-line with expected results, as limiting oxygen content would naturally lead to incomplete oxidation. Like the other parameter sweeps, the specific HC and CO emissions are lower for the 4-duct configuration than the 2-duct configuration. Again, this is due to the relatively lower temperatures and longer duration of late-cycle combustion for the 2-duct configuration (see Fig. 6).

For all conditions tested in this sweep and for both configurations, the measured soot values were below the sensitivity threshold of the smoke meter. Typically with CDC, as oxygen content is decreased, the soot emissions would drastically increase, yet this was not the case for either the 2- or 4-duct configurations. As with the IMT sweep, the $\Sigma SINL$ results at different XO_2 should not be compared directly, because the combustion-chamber temperature varies greatly with changes in XO_2, and the NL signal is a strong function of soot temperature as well as soot volume fraction.

The η_f increased with dilution for both configurations. The 2-duct η_f was slightly more sensitive to changes in XO_2 than the 4-duct configuration. With increasing dilution, the efficiency increased a total of 1.8% for the 2-duct configuration, while for the 4-duct it increased by 1.1%. Like the other trends, the
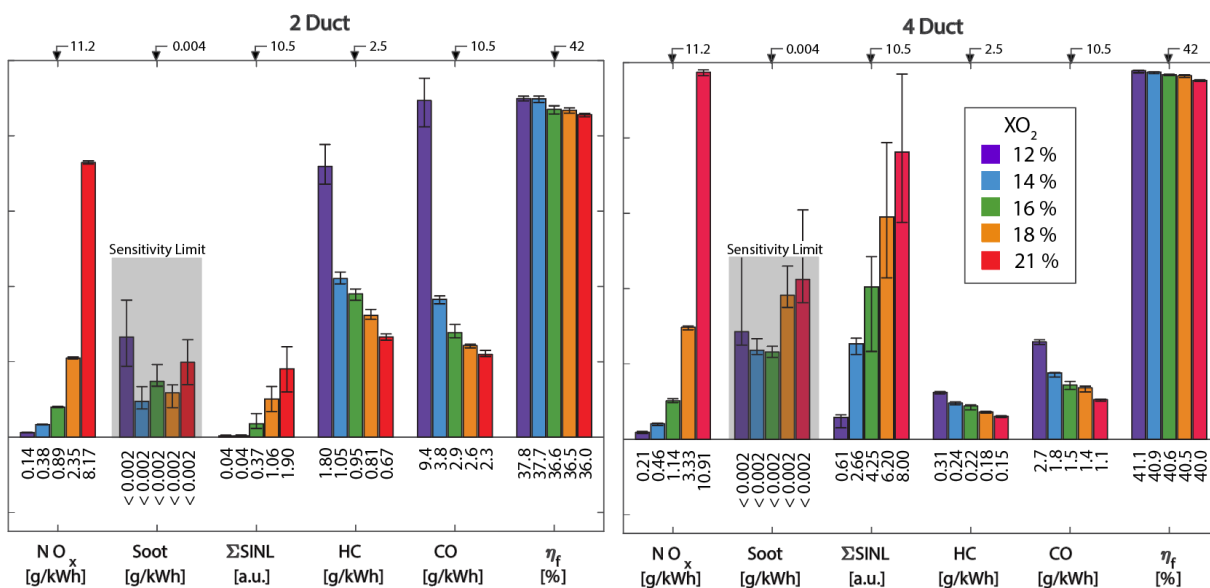
Figure 14. Emissions data for the dilution sweeps with the 2- and 4-duct configurations. The color variation seen in the legend indicates the dilution condition for both configurations. Note that the numbers annotated at the top of each group indicates the extent of the y-axis for that group.

efficiency is nominally higher for the 4-duct configuration than the 2-duct configuration at all conditions tested.

4.7 SINL – Late-Cycle Flare-up Behavior

As previously described, the engine-out soot emissions were low across all conditions studied. The DOI sweep with the 4-duct configuration was the only sweep having at least two conditions with soot emissions above the smoke-meter sensitivity limit. In this sweep, soot emissions were elevated for both the lowest and highest DOIs. This trend can be explained from SINL data. Indeed, SINL data across all conditions show interesting flame and soot dynamics.

    A sample of time resolved SINL data from seven cycles in one run of the 2-duct baseline case is shown in Fig. 15. A typical SINL curve will begin to grow in intensity near the end of the pre-mixed burn/beginning of the steady-state phase of the combustion process. Then, at some point, it will peak and slowly taper off. However, some cycles show a second intensity peak occurring toward the end of the cycle, which we term a "late-cycle flare-up".

Nilsen et al. [16] first noted the existence of late-cycle flare-ups for DFI and attributed their existence to flame-to-flame interactions and/or entrainment of hot product gases upstream of the established LOL, as discussed in [2]. In the present study, such late-cycle flare-ups occurred intermittently across most conditions studied, with the amplitude and probability of a flare-up changing with conditions. Furthermore, the amplitude of the flare-ups varied cycle-to-cycle at the same conditions, and NL images showed that the particular injector(s)/duct(s) at which the flare-ups occurred also varied cycle-to-cycle. Hence, flare-ups are not attributed to systematic geometric or operational parameters.

    Figures 16 and 17 show the ensemble-averaged SINL data from all sweeps and configurations. Even though the flare-ups are intermittent, they can appear in the SINL signal
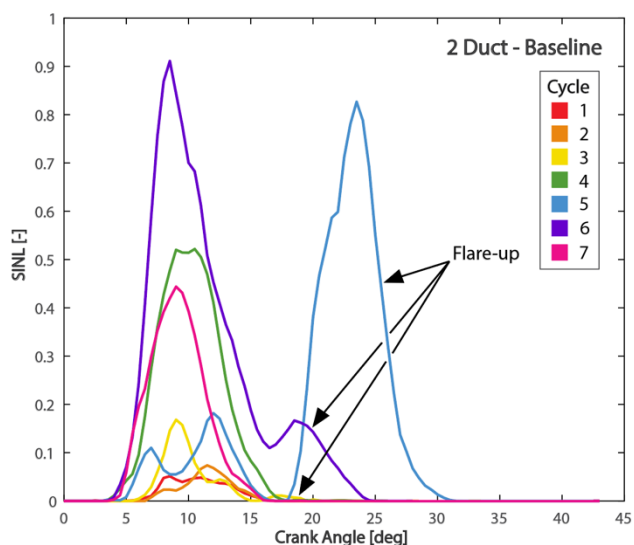
Figure 15. Cycle-to-cycle variation in SINL behavior for one run at the 2-duct baseline condition.

when averaged across all cycles in a given engine run. Indeed, at some conditions (e.g., 4-duct 4500 μs DOI, 2.0 bar IMAP, and 240 MPa P_{inj}), the peak intensity of the late-cycle flare-up signal is similar to or greater than the initial peak intensity, indicating that the flare-up can be a significant contributor to the total engine-out soot, particularly because the flare-up occurs late in the cycle when bulk temperatures are lower and there is less time to completely oxidize the soot before the exhaust valves open.

The late-cycle flare-up generally was more pronounced in the 4-duct configuration than the 2-duct configuration; e.g., see the 2.0 bar condition in the IMAP sweep in Fig. 16. For both configurations, late-cycle flare-ups tended to begin at approximately 17 CAD. However, the mean flare-up SINL intensity in the 2-duct configuration was much lower than that of the initial peak, whereas the flare-up intensity in the 4-duct configuration was sometimes larger than the initial peak. Examination of individual cycles across all conditions shows that these greater average intensities are a function of both greater frequency of a flare-up occurring and/or greater intensity in the individual flare-up events.

Increasing DOI increased the prevalence of late-cycle flare-ups for both configurations. Flare-ups were first seen at 3500 μs DOI and became more prevalent at 4500 μs. In the IMAP sweep, flare-ups decrease with increasing IMAP. Indeed, for the lowest IMAP in the 2-duct configuration (1.5 bar), the late-cycle flare-up dominates the SINL signal, and essentially no SINL is detected during the initial phases of combustion. As IMAP is increased, the prevalence of flare-ups decreased, and they occurred slightly later in the cycle. Increasing the injection pressure also increased the likelihood of flare-ups. Increasing the duct configuration from two to four decreased the injection pressure limit for which flare-ups occurred. For the 2-duct configuration, flare-ups were observed at injection pressures of 180 MPa or higher, but they were seen at all injection pressures for the 4-duct configuration.

As shown in Fig. 17, for the dilution sweep, SINL signals at 12% XO_2 were too low to reliably assess whether flare-ups occurred, but flare-ups were observed for all other dilution levels. This could mean that the oxygen concentration does not impact the prevalence of the flare-up behavior. While SINL signals for the 2-duct IMT sweep appear to show flare-ups for all conditions, further examination of NL images indicated that flare ups only occurred for 70 °C and 90 °C IMT. Instead, for 50 °C IMT in the 2-duct case, NL images showed flames anchored around the intake valves. Late-cycle flare-ups were seen in the 4-duct configuration at this 50 °C IMT condition (and the other IMT conditions), though the signal intensity was quite weak. These observations demonstrate the importance of cross-referencing SINL signals with the flame configuration from the images, not relying on the integrated signals alone. For the SOC sweep, the 2-duct SINL data do not clearly show two identifiable peaks. Thus, detailed image analysis that can differentiate between the flame characteristics of the main sooting portion of the burn and flare-up behavior is needed. This is not the case for the 4-duct configuration, for which flare-ups became more prevalent as SOC timing is retarded (there were no flare-ups at -5 deg ATDC).

While the 4-duct configuration did exhibit more late-cycle flare-ups than the 2-duct configuration, there is evidence that this is not due to direct spray-spray interactions, i.e., it is not due to proximity coupling. If flare-ups were due to proximity coupling, one would expect a longer delay between the initial flame and flare-up for the 2-duct configuration. Direct comparison of the flare-up timing between the 2-duct and 4-duct configurations is difficult due to the different baseline conditions; exact conditions overlap only for the 2 bar case in the IMAP sweep. However, Fig. 16 indicates that the timing of the late-cycle flare-up is the same between the configurations at this condition. Preliminary examination of the flare-up behavior in NL images indicates the flare-ups generally do not initiate or develop in regions of spray-spray interaction. More detailed analysis of the dynamics of these late-cycle flare-ups will be the subject of future work.

5. Conclusions

Based on the results of this study and observations summarized in the previous sections, the following conclusions can be drawn:

- Indicated-specific NO_x emissions and fuel-conversion efficiency are typically increased as the number of ducted sprays is increased from two to four. Additionally, NO_x emissions tend to be more sensitive to adjustments in the parameter space for the 4-duct configuration than the 2-duct configuration.
- HC and CO emissions are typically decreased as the number of ducted sprays is increased from two to four. This is because lower temperatures in the 2-duct configuration lead to a greater fraction of fuel oxidation taking place later in the cycle or not at all.
- Late-cycle flare-ups observed in SINL signals might cause higher engine-out soot emissions.
- The onset of late-cycle flare-ups occurs at similar crank angles and operating conditions for both the 2- and 4-duct configurations, but the 4-duct cases increase late-cycle flare-ups.
- Late-cycle flare-ups are largely a function of engine operating conditions. In particular, longer DOIs, lower IMAPs, and higher P_{inj} tend to favor the flare-up behavior.
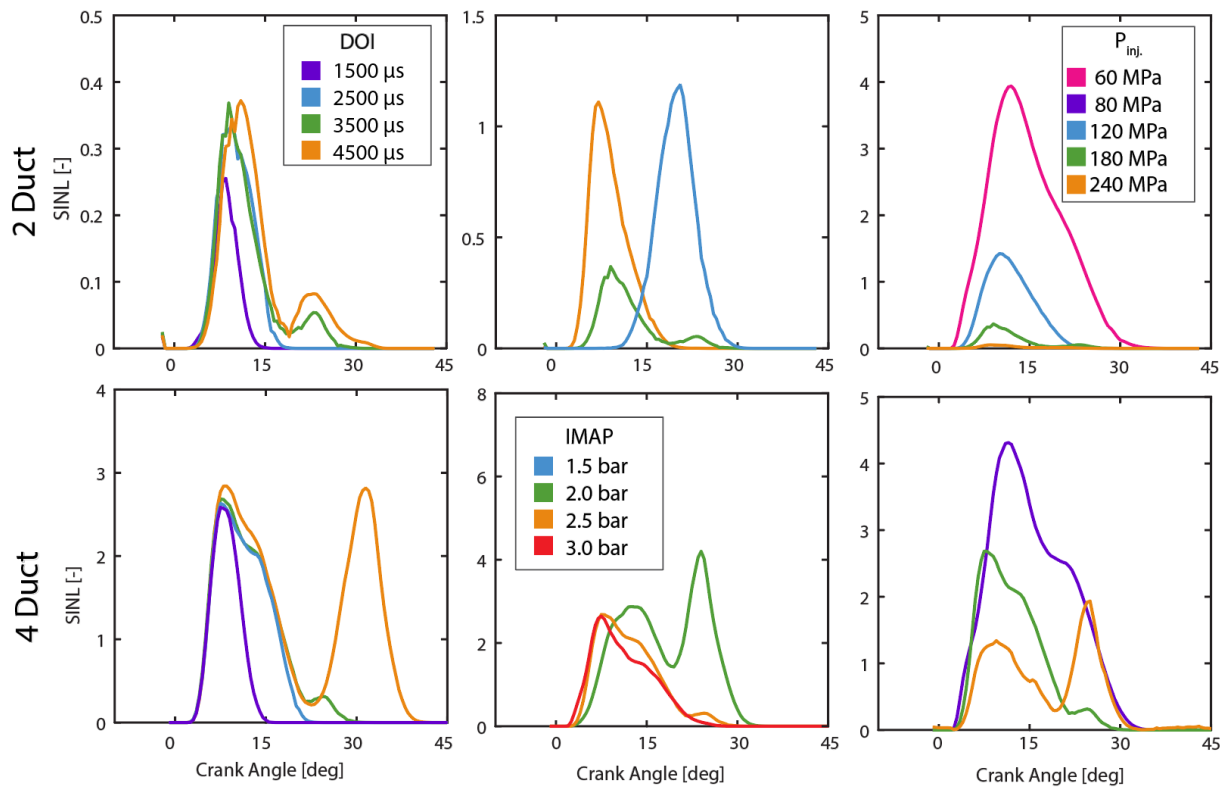
Figure 16. Time-resolved SINL data averaged over all recorded injections from the DOI, IMAP, and Injection Pressure sweeps. Data are shown as examples of how the conditions tested in the parameter sweep can impact the existence and intensity of the late-cycle flare-up.
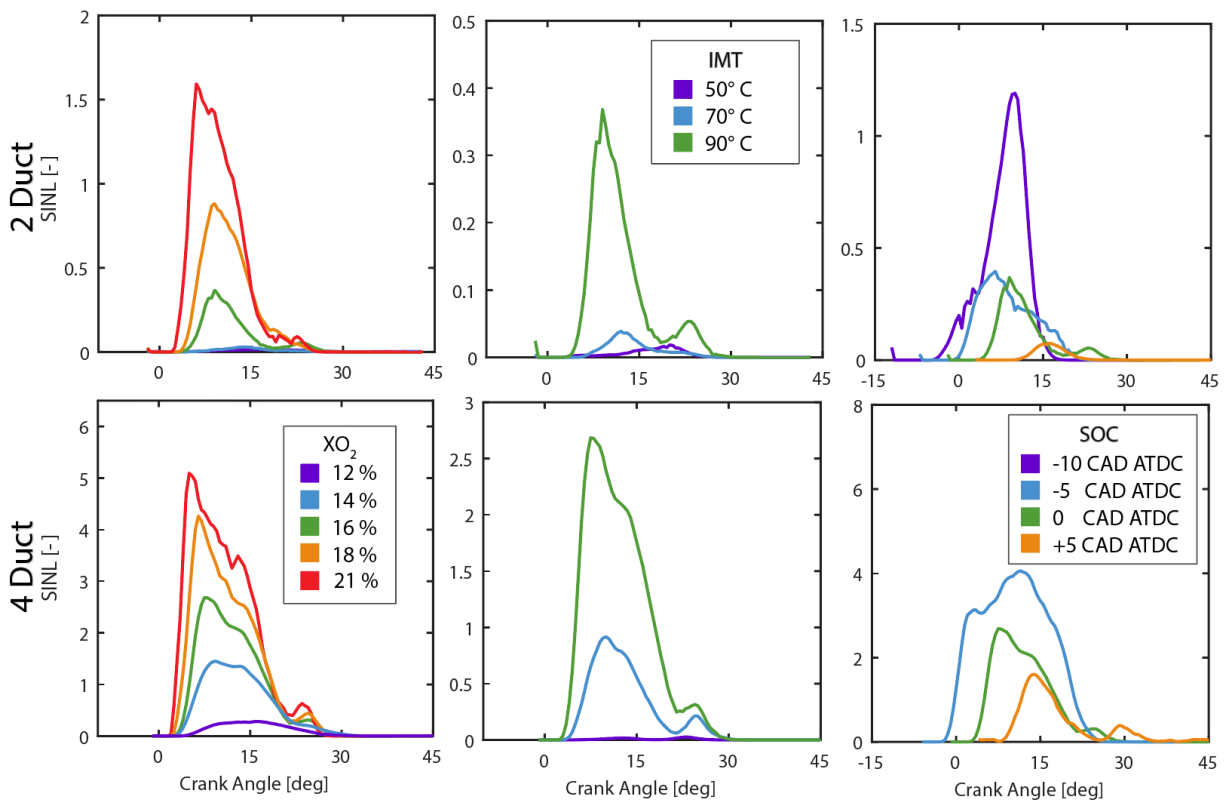
Figure 17. Time-resolved SINL data averaged over all recorded injections from the Dilution, IMT, and SOC sweeps. Data are shown as an example of how the conditions tested in the parameter sweep can impact the existence and intensity of the late-cycle flare-up.

6. Future Work

It will be valuable to understand the frequency, timing, and spatial characteristics of the late-cycle flare-ups as a function of engine operating conditions. Detailed image analysis is needed to determine the frequency and spatial characteristics of the late-cycle flare-up behavior. Identifying which sprays exhibit flare-ups and commonalities in the spatial evolutions of flare-ups can be of benefit. Thus, future work will aim to answer these questions using detailed image analysis to better characterize the flare-up behavior. This type of analysis could help improve DFI by eliminating flare-ups.

7. Acknowledgements

8. References

[1]   R. Gehmlich, C. Mueller, D. Ruth, C. Nilsen, S. Skeen, and J. Manin, "Using ducted fuel injection to attenuate or prevent soot formation in mixing-controlled combustion strategies for engine applications," *Applied energy,* vol. 226, pp. 1169-1186, 2018.

[2]   C. J. Polonowski, C. J. Mueller, C. R. Gehrke, T. Bazyn, G. C. Martin, and P. M. Lillo, "An experimental investigation of low-soot and soot-free combustion strategies in a heavy-duty, single-cylinder, direct-injection, optical diesel engine," *SAE International Journal of Fuels and Lubricants,* vol. 5, no. 1, pp. 51-77, 2012.

[3]   L. M. Pickett and D. L. Siebers, "Non-sooting, low flame temperature mixing-controlled DI diesel combustion," *SAE transactions,* pp. 614-630, 2004.

[4]   J. Manin, S. Skeen, L. Pickett, E. Kurtz, and J. E. Anderson, "Effects of oxygenated fuels on combustion and soot formation/oxidation processes," *SAE International Journal of Fuels and Lubricants,* vol. 7, no. 3, pp. 704-717, 2014.

[5]   C. J. Mueller, C. W. Nilsen, D. J. Ruth, R. K. Gehmlich, L. M. Pickett, and S. A. Skeen, "Ducted fuel injection: A new approach for lowering soot emissions from direct-injection engines," *Applied energy,* vol. 204, pp. 206-220, 2017.

[6]   M. Okubo and T. Kuwahara, in *New Technologies for Emission Control in Marine Diesel Engines*. Cambridge, MA: Elsevier, 2019, ch. 3. Principles and Design of Emission Control Systems, pp. 54-142.

[7]   R. Fitzgerald, K. Svensson, and G. Martin, "Mixture Fraction Measurements of Diesel Sprays with Ducted Fuel Injection," in *International Conference on Liquid Atomization and Sprays*, 2021, vol. 1, no. 1.

[8]   R. Fitzgerald, K. Svensson, G. Martin, Y. Qi, and C. Koci, "Early investigation of ducted fuel injection for reducing soot in mixing-controlled diesel flames," *SAE International Journal of Engines,* vol. 11, no. 6, pp. 817-834, 2018.

[9]   F. Li, C.-f. Lee, Z. Wang, and G. Lu, "Optical investigation on impacts of ambient pressure on macroscopic spray charachteristics of ducted fuel injection under non-vaporizing conditions," *Fuel,* vol. 268, 1/22/2020 2020.

[10]   F. Li, C.-f. Lee, Z. Wang, Y. Pei, and G. Lu, "Impacts of duct inner diameter and standoff distance on macroscopic spray charachteristics of ducted fuel injection under non-vaporizing conditions," *International Journal of Engine Research,* pp. 1-12, 2/25/2020 2020, doi: 10.1177//1468087420914714.

[11]   F. Li, C.-f. Lee, Z. Wang, H. Wu, and G. Lu, "Schlieren investigation on impacts of duct size on macroscopic spray charachteristics of ducted fuel injection," *Applied Thermal Engineering,* vol. 176, 5/3/2020 2020.

[12]   F. Li, C.-f. Lee, H. Wu, Z. Wang, and F. Liu, "An optical investigation on spray macroscopic characteristics of ducted fuel injection," *Experimental Thermal and Fluid Science,* vol. 109, p. 109918, 2019.

[13]   F. Millo *et al.*, "Ducted Fuel Injection: Experimental and numerical investigation on fuel spray characteristics, air/fuel mixing and soot mitigation potential," *Fuel,* 2021 2021.

[14]   C. W. Nilsen, D. E. Biles, and C. J. Mueller, "Using Ducted Fuel Injection to Attenuate Soot Formation in a Mixing-Controlled Compression Ignition Engine," *SAE International Journal of Engines (Online),* vol. 12, no. SAND-2019-1518J; SAND-2018-12942J, 2019.

[15]   C. W. Nilsen, D. E. Biles, B. M. Wilmer, and C. J. Mueller, "Investigating the effects of duct length and diameter and fuel-injector orifice diameter in a compression-ignition engine equipped with ducted fuel injection.," *Applications in Energy and Combustion Science,* 2021.

[16]   C. W. Nilsen, D. E. Biles, B. F. Yraguen, and C. J. Mueller, "Ducted Fuel Injection versus Conventional Diesel Combustion: An Operating-Parameter Sensitivity Study Conducted in an Optical Engine with a Four-Orifice Fuel Injector," *SAE International Journal of Engines,* vol. 13, no. 3, 2020.

[17]   C. W. Nilsen, D. E. Biles, B. F. Yraguen, and C. J. Mueller, "Ducted Fuel Injection vs. Conventional Diesel Combustion: Extending the Load Range in an Optical Engine with a Four-Orifice Fuel Injector," *SAE International Journal of Engines,* vol. 14, no. 1, 2020.

[18]   K. I. Svensson and G. C. Martin, "Ducted Fuel Injection: Effects of Stand-Off Distance and Duct Length on Soot Reduction," *SAE International Journal of Advances and Current Practices in Mobility,* vol. 1, no. 2019-01-0545, pp. 1074-1083, 2019.

[19]   S. Tanno, J. Kawakami, K. Kitano, and T. Hashizume, "Investigation of a novel leaner fuel spray formation for reducing soot in diffusive diesel combustion-Homogenizing equivalence ratio distribution in the lift-off region," SAE Technical Paper, 0148-7191, 2019.

[20]   B. M. Wilmer, C. W. Nilsen, D. E. Biles, C. J. Mueller, and W. F. Northrop, "Solid particulate mass and number from ducted fuel injection in an optically accessible diesel engine in skip-fired operation," *International Journal of Engine Research,* 03/12/2021 2021.

[21]   Y. Zhang, Z. Wang, C.-f. Lee, F. Li, and H. Wu, "Analysis of mechanism of ducted fuel injection under non-vaporizing conditions," *Fuel,* vol. 305, no. 121496, 2021.

[22]   X. Liu, B. Mohan, and H. G. Im, "Numerical Investigation of the Free and Ducted Fuel Injection under Compression Ignition Conditions," *Energy and Fuels,* vol. 34, 10/21/2020 2020.

[23]   F. Millo *et al.*, "Ducted fuel injection: A numerical soot-targeted duct geometry optimization," *SAE International Journal of Engines,* vol. 15, no. 03-15-02-0014, 2021.

[24]   C. W. Nilsen, B. F. Yraguen, C. J. Mueller, C. Genzale, and J.-P. Delplanque, "Ducted Fuel Injection vs. Free-Spray Injection: A study of Mixing and Entrainment Effects Using Numerical Modelling," *SAE International Journal of Engines,* vol. 13, no. 5, 2020.

[25]   J. C. Ong, M. Zhang, M. S. Jensen, and J. H. Walther, "Large eddy simulation of soot formation in a ducted fuel injection configuration," *Fuel,* vol. 313, p. 122735, 2022.

[26]   C. Segatori, "Ducted Fuel Injeciton: a Computational Fluid Dynamics analysis of soot formation mitigation mechanisms," Masters, Politencnico Di Torino, 2020.

[27]   R. Şener, "Ducted fuel injection: Numerical study of soot formation and oxidation using detailed soot modeling approach in a compression ignition engine at different loads," *Journal of the Brazilian Society of Mechanical Sciences and Engineering,* vol. 44, no. 1, pp. 1-16, 2022.

[28]   K. Svensson, C. Kim, P. Seller, G. Martin, and C. Koci, "Performance and Emission Results from a Heavy-Duty Diesel Engine with Ducted Fuel Injection," presented at the SAE World Congress, Detroit, MI, 4/6/2021, 2021.

[29]   G. Nyrenstedt, K. Watanabe, K. Enya, H. Shi, N. Uchida, and B. Johansson, "Thermal efficiency comparison of different injector constellations in a CI engine," 2019.

[30]   C. J. Mueller, C. W. Nilsen, D. E. Biles, and B. F. Yraguen, "Effects of fuel oxygenation and ducted fuel injection on the performance of a mixing-controlled compression-ignition optical engine with a two-orifice fuel injector," *Applications in Energy and Combustion Science,* vol. 6, p. 100024, 2021.

[31]   C. J. Mueller and G. C. Martin, "Effects of oxygenated compounds on combustion and soot evolution in a DI diesel engine: broadband natural luminosity imaging," *SAE Transactions,* pp. 518-537, 2002.

[32]   C. J. Mueller, A. L. Boehman, and G. C. Martin, "An experimental investigation of the origin of increased NOx emissions when fueling a heavy-duty compression-ignition engine with soy biodiesel," *SAE International Journal of Fuels and Lubricants,* vol. 2, no. 1, pp. 789-816, 2009.

THIESEL 2022 Conference on Thermo- and Fluid Dynamics of Clean Propulsion Powerplants

Computational Analysis of Ducted Fuel Injection at High-Pressure Transcritical Conditions using Large-Eddy Simulations

J. Guo, W. T. Chung, M. Ihme[*]

Department of Mechanical Engineering, Stanford University. Stanford, CA, 94305, USA.

*Corresponding author: mihme@stanford.edu
Telephone: +(1) 650 815 5892

Abstract.   Ducted fuel injection (DFI) is a proposed fuel injection concept for achieving substantial reductions in emissions. In this concept, the fuel is injected through a coannular duct, resulting in increased fuel-air mixing and minimized formation of soot and other unwanted combustion products. So far, DFI has largely been studied experimentally and computationally using Reynolds-averaged Navier Stokes (RANS) with single-point models. By complementing these investigations, large-eddy simulations with the diffuse-interface method are performed to examine the physical mechanisms and combustion processes of DFI, specifically focusing on the mixing process and the effect of combustion and pollutant emissions. To this end, finite-rate chemistry simulations are performed of DFI configurations at the same injection conditions of the Engine Combustion Network (ECN) Spray A configurations at transcritical conditions (n-dodecane fuel, 60 bar pressure and 900 Kelvin temperature chamber conditions). A two-equation soot model is employed for the qualitative analysis of soot emission. Direct comparisons of averaged and instantaneous flow field results with Spray A configuration are performed to assess the effect of DFI on the first- and second-stage ignition and soot formation. The results demonstrate the ability of a diffuse-interface method in capturing key engine metrics for transcritical fuel injection. The findings also highlight the turbulent mixing and chemistry behaviors that are present, especially in the region after the jet leaves the duct.

1. Introduction

Diesel engines offer higher efficiency than spark ignition engines and are widely used as heavy-duty engines in the transportation sector (Chambers and Schmitt 2015). However, diesel engines are prone to generating harmful emissions such as soot and nitrogen oxides (NO_x). As such, numerous strategies have been investigated to mitigate the formation of these harmful substances (O'Connor and Musculus 2013, Upatnieks *et al.* 2005). One proposed solution for decreasing soot formation, as well as increasing engine efficiency, involves the employment of the so-called ducted fuel injection (DFI), as first proposed experimentally by Mueller *et al.* (2017). In this DFI setup, a liquid fuel is injected as a spray at high-pressure conditions through a coannular duct. The ducted confinement modifies the dynamics and structure of the fuel spray and reduces the soot produced when compared to a standard non-ducted free spray.

Mixing is a key behavior to explain the physics of DFI (Mueller et al. 2017). The presence of the duct walls confines the liquid fuel spray, which increases the axial component of spray velocity and also limits overmixing at the radial periphery. The solid duct walls themselves also increase mixing, both hydrodynamically and thermally. The inner wall of the duct enforces a no-slip boundary condition on the fluid, resulting in steeper velocity gradients than found in an unconfined free spray. The associated increase in the shear rate increases the turbulence and scalar mixing. Furthermore, variation in temperature between the duct and the interior fluid increases the thermal mixing.

A number of studies in literature have discussed the resultant effect of mixing on the velocity, temperature, and chemistry fields of the spray (Fitzgerald *et al.* 2018, Liu *et al.* 2020, Zhang *et al.* 2021a, Ong *et al.* 2022). These studies broadly agree that the DFI spray – when compared with an unconfined free spray – is faster and cooler at the duct exit; as the spray continues downstream of the duct, these features bring about increased fuel-air mixing. With this increased mixing comes a longer ignition delay time and larger lift-off length, bringing about more complete combustion and decreased soot production. However, a lack of consensus and understanding is present for certain aspects of the physics present. Fitzgerald *et al.* (2018) concluded that mixing enhancement happens only downstream of the duct exit and not within the

duct, thus leading to a richer fuel-air mixture at the duct exit. Other studies (Liu *et al.* 2020, Ong *et al.* 2022) disagree and present results that show a leaner mixture at the duct exit. Additionally, the interaction between turbulence and the mixing are not fully understood and have not been investigated comprehensively. Such analysis requires scale-resolving turbulent calculations, and so performing such computations is a major objective of this work.

In addition to mixing, another important and related physical behavior for DFI is the entrainment of charge gas into the fuel spray, which has been investigated by a number of different studies. Investigation by Nilsen *et al.* (2020) and Zhang *et al.* (2021a) have shown enhanced levels of entrainment compared to an unconfined free spray, which is attributed to the higher axial velocities and associated lower pressure within the duct interior. The low-pressure region within the duct then draws in fluid at the inlet to drive the increased entrainment; the phenomenon has been termed as a "jet-pump" effect. In contrast, numerical studies by Ong *et al.* (2022) have found no evidence of enhanced inlet entrainment, and correspondingly no evidence of a region of significantly decreased pressure in the duct interior.

In the duct interior itself, the duct wall is also hypothesized to provide a secondary effect of limiting the entrainment of combustion products into the spray. This "shielding" helps prevent shortening of the lift-off length, which is beneficial given that a shortened lift-off length was associated with increased soot formation (Mueller *et al.* 2017, Polonowski *et al.* 2012). At the outlet region between the duct and the lift-off length, increased entrainment is also hypothesized due to the longer lift-off length and longer ignition delay time observed for DFI.

Since the initial conception of the concept, DFI has been studied both experimentally and computationally; for further discussion and overview we refer the reader to Ong *et al.* (2022) and Gehmlich *et al.* (2018). Experimental DFI studies by Gehmlich *et al.* (2018) and Nilsen *et al.* (2019) found significant soot reduction for a wide range of duct design parameters. Results showed that DFI was robust to parameters including duct length, axial gap between injector and duct inlet, ambient oxidizer mole fraction, and amount of dilution. DFI also has the potential to be employed together with other pollutant-mitigating strategies. If designed in conjunction with exhaust-gas recirculation, the technology can then be used a means of decreasing NOₓ emissions (Mueller et al. 2017, Gehmlich *et al.* 2018, Nilsen *et al.* 2019).

For the purposes of comparing with and complementing experimental findings, computational studies of DFI have been carried out, especially in recent years. RANS studies at inert (non-evaporating and non-reacting) conditions have been performed by Zhang *et al.* (2021a) and Nilsen *et al.* (2020), as previously mentioned in our discussion of the physics. From these studies, the available information on averaged-flow quantities provided introductory insight into the mixing and entrainment. RANS DFI studies at reacting conditions have also been performed (Millo *et al.* 2021, Fitzgerald *et al.* 2018, Liu *et al.* 2020) to gain insight into the interaction between the hydrodynamics and the reacting chemistry. Results from these studies complement experimental findings; the presence of the duct increases the ignition delay time and flame lift-off length, leading to increased mixing at the duct exit and resulting in attenuated soot.

Findings from these previous experiments and RANS studies have led to foundational understanding of the DFI physics. It is recognized, however, the need for higher-fidelity scale-resolving simulations to more accurately capture the transient evolution of the physical processes present in spray combustion (Zhang *et al.* 2021b). For this purpose, large-eddy simulations (LES) can provide detailed insights into the differences between DFI and unconfined free sprays. Ong *et al.* (2022) performed LES incorporating a Lagrangian particle method to examine the effects of heat transfer from the duct in a DFI configuration. Good agreement with experimental data has been reported with the use of such Eulerian-Lagrangian framework methods. However, these methods mentioned in these previous studies model the spray as a multiphase flow, which necessitates the selection of parameters for modelling breakup and evaporation and thus leads to parameter dependencies.

An alternative simulation method that can be employed in high-pressure flows, such as those encountered in diesel engines, is the diffuse-interface method. Under trans- and supercritical conditions, the transitions between liquidous and gaseous phases are no longer distinguishable. This absence of a physical interface makes it attractive to thermodynamically represent the flow as a single phase using a real-fluid equation-of-state. This diffuse-interface method for fluids at supercritical pressures (Ma *et al.* 2017) has been demonstrated on LES studies (Ihme *et al.* 2019, Chung *et al.* 2020) for Engine Combustion Network (ECN) diesel configurations (Engine Combustion Network).

The objective of this study is to perform LES computations to investigate DFI for n-dodecane injection at realistic engine-like thermodynamic conditions. We specifically look to complement the existing understanding of DFI by providing insight from scale-resolving LES computations into the fluid and chemical

behavior, including key differences from an unconfined free spray. We consider both inert and reacting chemistry setups. Our calculations involve a compressible Navier-Stokes formulation with realistic thermodynamic considerations to represent accurately the thermodynamic behavior of fluids at supercritical states. In Section 2, the mathematical model and computational configuration are presented. Afterwards in Section 3, the results and their associated analyses are presented. Finally, conclusions are presented in Section 4.

2. Methods and Computational Setup

2.1 Governing Equations

In the present study, we solve the large-eddy simulation (LES) conservation equations for Favre-filtered mass, momentum, total energy, and chemical species:

$$\partial_t \overline{\rho} + \nabla \cdot (\overline{\rho}\widetilde{\boldsymbol{u}}) = 0 \tag{1a}$$

$$\partial_t (\overline{\rho}\widetilde{\boldsymbol{u}}) + \nabla \cdot (\overline{\rho}\widetilde{\boldsymbol{u}}\widetilde{\boldsymbol{u}}) = -\nabla \cdot (\overline{p}\boldsymbol{I}) + \nabla \cdot (\overline{\boldsymbol{\tau_v}} + \overline{\boldsymbol{\tau_{SGS}}}) \tag{1b}$$

$$\partial_t (\overline{\rho}\widetilde{e}_t) + \nabla \cdot [\widetilde{\boldsymbol{u}}(\overline{\rho}\widetilde{e}_t + \overline{p})] = \nabla \cdot [(\overline{\boldsymbol{\tau_v}} + \overline{\boldsymbol{\tau_{SGS}}}) \cdot \widetilde{\boldsymbol{u}}] - \nabla \cdot (\overline{\boldsymbol{q_v}} + \overline{\boldsymbol{q_{SGS}}}) \tag{1c}$$

$$\partial_t (\overline{\rho}\widetilde{Y}_k) + \nabla \cdot (\overline{\rho}\widetilde{\boldsymbol{u}}\widetilde{Y}_k) = -\nabla \cdot (\overline{\boldsymbol{J}_{k,v}} + \overline{\boldsymbol{J}_{k,SGS}}) + \ddot{\omega}_k \tag{1d}$$

where ρ is the density, $\boldsymbol{u}$ is the velocity vector, p is the pressure, e_t is the specific total energy, $\boldsymbol{\tau}$ is the stress tensor, and $\boldsymbol{q}$ is the heat flux. Y_k, $\boldsymbol{J}_k$ and $\dot{\omega}_k$ are the mass fraction, diffusion flux, and chemical source term for species k, respectively. The overline denotes traditional LES filtering, and the tilde overbar denotes Favre-filtering; for a quantity ϕ, $\widetilde{\phi} = \overline{\rho\phi}/\overline{\rho}$. For $\boldsymbol{\tau}$ and $\boldsymbol{q}$, Chung's method with high-pressure correction (Chung *et al.* 1988) is used to evaluate the dynamic viscosity μ and the thermal conductivity λ. For binary diffusion coefficients, Takahashi's high-pressure correction (Takahashi 1975) is employed. The subscript v is used for viscous quantities, and the subscript SGS denotes subgrid-scale turbulent quantities. We employ the Peng-Robinson (PR) equation of state (Peng and Robinson 1976)

$$p = \frac{\rho R T}{1 - b\rho} - \frac{\rho^2 a}{1 + 2a\rho - b^2\rho^2}, \tag{2}$$

to close the governing equations. R is the mixture-specific gas constant, and the coefficients a and b depend on mixture composition and on temperature (Poling *et al.* 2001). The PR EoS has been shown to perform well in describing fluid thermodynamics at transcritical conditions (Miller *et al.* 2001, Congiunti and Bruno 2003, Hickey *et al.* 2013) Details of evaluating necessary thermodynamic quantities for mixtures are provided in Ma *et al.* (2015).

The reaction chemistry in this numerical study is modelled using a reduced 33-species chemical mechanism (Ma *et al.* 2019), and 21 additional species have been identified as suitably modelled using a quasi-steady-state assumption. The soot dynamics of the system are modelled using the Hiroyasu-Nagle-Strickland-Constable (Hiroyasu-NSC) model, which has been used in previous diesel injection studies (Hao *et al.* 2021, Moiz *et al.* 2016) as well as specifically in DFI studies (Liu *et al.* 2020, Fitzgerald *et al.* 2018). As originally formulated by Patterson *et al.* (1994), the model consists of a first-order ordinary differential equation (ODE):

$$\frac{dm_s}{dt} = \frac{dm_{sf}}{dt} - \frac{dm_{sc}}{dt} \tag{3a}$$

where m_s is the (net) soot mass, m_{sf} is the mass of formed soot, and m_{sc} is the mass of oxidized soot. All masses as specified here are given per volume. m_{sf} and m_{sc} are each given as

$$\frac{dm_{sf}}{dt} = A_f m_{fv} \left(\frac{p}{p_{ref}}\right)^{0.5} \exp\left(-\frac{E_{sf}}{RT}\right) \tag{3b}$$

$$\frac{dm_{sc}}{dt} = \frac{6m_s}{\rho_s D_s} M_C \dot{R}_{NSC}.$$ (3c)

p_{ref} is given a value of 1 bar. Parameters and the definitions that are used in the model are specified in Patterson *et al.* (1994). In our study, the fuel vapor mass m_{fv} is estimated as

$$m_{fv} = \rho \beta Z_B$$ (4)

where $\beta = (\rho_{ub} - \rho_l)/(\rho_{ox} - \rho_l)$ is an approximate vapor fraction, following the procedure introduced by Traxinger *et al.* (2019). ρ_l is the liquid fuel density, ρ_{ox} is the oxidizer density, and ρ_{ub} is the unburned mixture density calculated from interpolating on the inert mixing profile of Bilger mixture fraction Z_B versus ρ, following Bilger's definition for Z_B (Bilger 1979).

2.2 Numerical Solver

The numerical simulations are computed using a compressible unstructured finite-volume solver. A sensor-based hybrid scheme (Khalighi *et al.* 2011) is used to discretize the convective fluxes, with an added entropy-stable flux correction technique developed by Ma *et al.* (2017). A second-order Strang-splitting scheme (Strang 1968) is used to separate the convection, diffusion, and reaction operators. The chemical source terms are time-integrated using a semi-implicit fourth-order Rosenbrock-Krylov (ROK4E) scheme (Wu *et al.* 2019, Tranquili and Sandu 2014), which has linear cost with respect to the number of species. All other operators are integrated using a strong stability-preserving third-order Runge-Kutta (SSP-RK3) scheme (Gottlieb *et al.* 2001). The Vreman SGS model (Vreman 2004) is used to model the sub-grid turbulent stresses. A dynamic thickened-flame model (Colin *et al.* 2000) is utilized, with maximum thickening factor set to a value of 4.

2.3 Computational setup

The thermodynamic conditions of the numerical studies we perform follow those of the ECN (Engine Combustion Network) Spray A n-dodecane spray. Our study focuses primarily on the reacting conditions, but inert conditions are also considered for validation and to study the hydrodynamics. For inert and reacting settings, the ambient pressure $p_\infty = 6.00\, MPa,$ the duct temperature $T_{duct} = 461\, K$, and the injection pressure $p_{\mathrm{rail}} = 150.0\, MPa$. The inert cases have ambient temperature $T_\infty = 900\, K$ and ambient oxygen mole fraction of 0.0%, while the reacting conditions have $T_\infty = 1000\, K$ and ambient oxygen mole fraction of 21.0%.

The results and discussion by Ong *et al.* (2022) spotlight the importance of the DFI results (specifically the ignition delay time and the flame lift-off length) on the so-called "dwell period.". The dwell period is defined as the time period before the initial spark ignition and the fuel injection in an experiment. To approximate the dwelled temperature field, the initial temperature of the fluid phase within the duct, for our LES simulations, is prescribed the solution to the steady-state heat equation. For the boundary conditions of this steady-state heat equation, the temperature at the inner diameter of the duct is set to be $T = T_{duct}$, and the temperature at the two lateral faces of the cylinder (at x = 2 mm and at x = 16 mm) are set to be the ambient temperature $T = T_\infty$. Subject to these boundary conditions, the temperature field then evolves to reach the steady-state solution, which we use as the starting point of the LES simulations.

Our present study uses the D3L14G2 duct configuration, following the specification and naming convention proposed by Mueller *et al.* (2017). This setup involves a duct with inner diameter of 3 mm, wall thickness of 1 mm, cylinder axial length L of 14 mm, and an offset (or "stand-off distance") G of 2 mm of the duct inlet from the fuel injector location. A 45° × 0.5 mm chamfer is applied to the inner diameter at the inlet and outlet of the duct.
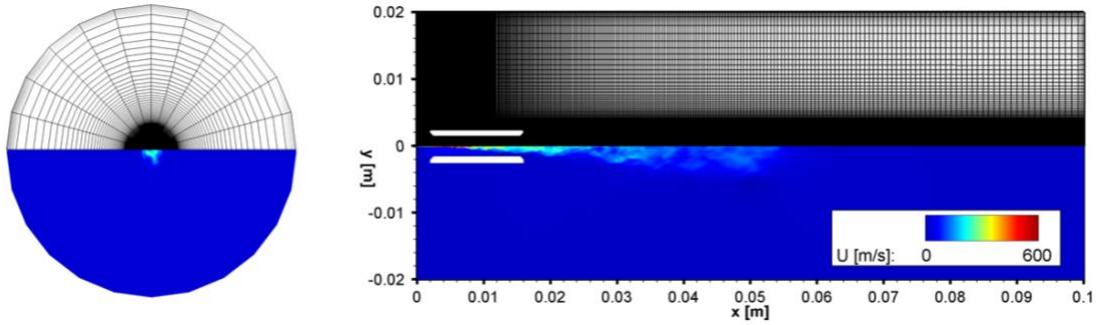
Fig. 1. Radial (left) and axial (right) view of mesh used, along with velocity magnitude profiles. The duct is visible in the axial view. The mesh consists of 2.20 million grid points. Minimum cell size is 8 μm.

The computational domain is a three-dimensional cylinder, discretized by a structured mesh with 2.20 million hexahedral elements. The domain dimensions are 40 mm in diameter and 100 mm in axial length. The mesh is adapted from the one used in Chung *et al.* (2020), with the duct geometry added in as an additional element. A minimum grid spacing of 8 μm in the spray core is used in order to resolve the ignition kernels. The domain and mesh are shown in Fig 1. The injector geometry is not included in the simulations; instead, inlet boundary conditions to match nozzle conditions as prescribed by ECN (Lillo *et al.* 2012) are assigned. The inlet fuel mass flux is determined with a time-dependent rate of injection, as provided by the CMT virtual injection rate generator (Wehrfritz *et al.* 2016).

The solution is advanced with a unity CFL number for time-stepping, resulting in a typical time step of 5×10^{-9} seconds.

3. Results

Fig. 2 compares the penetration lengths of the inert simulations for both the DFI case and the free spray case, with standard conditions of $p_\infty = 6.00\ MPa$ and $T_\infty = 900K$ as specified by ECN (Engine Combustion Network). Spray A computation case is data as presented in Chung *et al.* 2020; experimental data is from Lillo *et al.* (2012) and Westlye *et al.* (2016), using Schlieren imaging for vapor penetration length and Mie scattering for the liquid penetration length. The vapor penetration length is defined as the furthest axial position where the mixture fraction Z_B exceeds 0.01, and the liquid penetration length uses a value of $Z_B =$ 0.6.
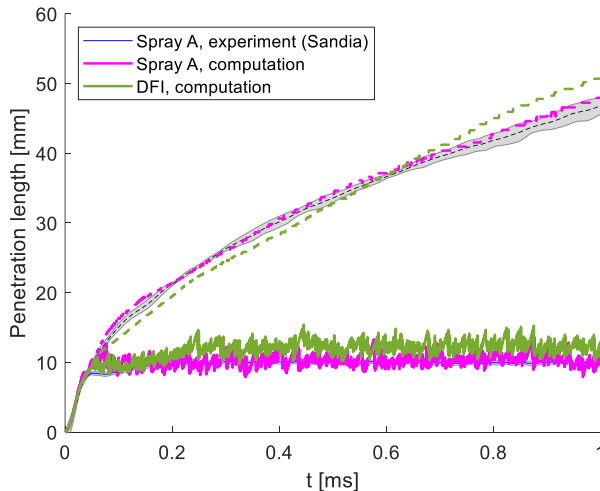
Fig. 2. Comparison of liquid (solid line) and vapor (dashed line) penetration lengths for the inert DFI case. Experimental comparisons for the free spray are also provided
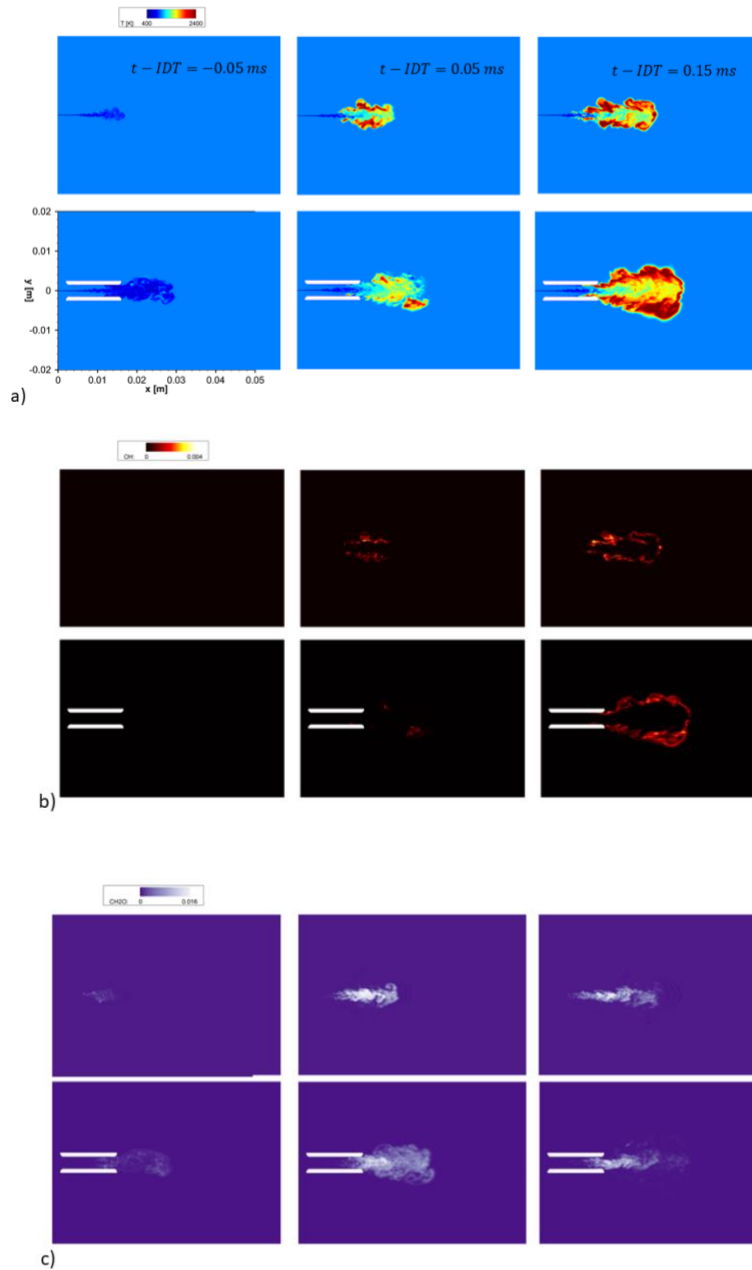
Fig. 3. Contours of a) transient temperature, b) Y_{OH}, and c) Y_{CH_2O} contours for the DFI case (bottom) and the free spray case (top) at various times offset by the ignition delay time (IDT), $t - IDT$; from left to right , $t - IDT$ = -0.05 ms, 0.05 ms, 0.5 ms
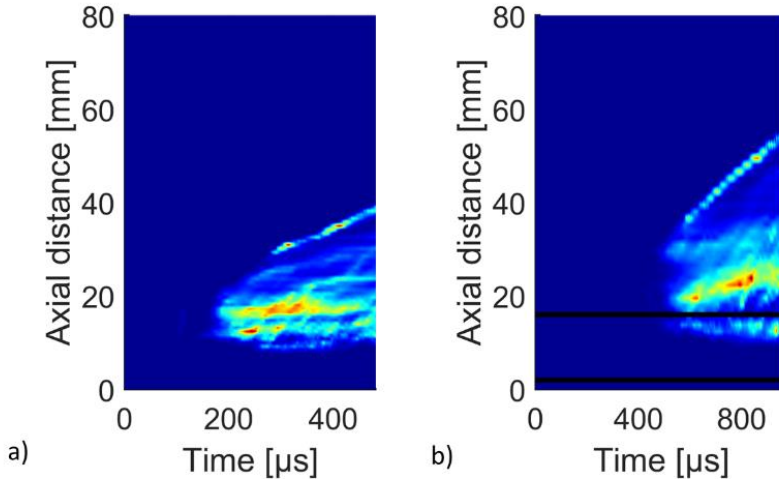
Fig. 4. Planar-integrated intensity OH intensity $I_{xt,OH}$ plots for a) the free spray case and b) the DFI case. The contour colorbar is scaled such that red corresponds to maximum intensity, and dark blue corresponds to minimum intensity. The duct inlet (at x = 2 mm) and outlet (at x = 16 mm) locations are provided in the DFI case as black lines

The vapor penetration length for the DFI case does not show significant deviation from that of free spray computations or experiments; this observation is consistent with findings by Ong *et al.* (2022) and Li *et al.* (2021). Ong *et al.* (2022) also observed significant increase in the DFI liquid penetration length (an increase in excess of ~50%, with a peak value occurring at around 0.4 seconds) that then decreases down to the free spray value at later times. In our current study, we note that the liquid penetration length is larger in the DFI case by ~25%. As noted by Ong *et al.* (2022), this enlargement in the DFI case can be explained by the presence of cooler, higher-density fluid inside the duct that results from the dwell period. This region of low temperature fluid attenuates the vaporization of the liquid fuel as the spray passes through the duct, thus contributing to the observed increase in liquid penetration length. From these observations, with respect to the inert mixing of species, the DFI and free spray cases exhibit similarity in behavior, but also display differences that arise from the presence of the duct.

To illustrate the differences in the dynamic evolution of the spray for the DFI and free spray cases, Fig. 3 shows contour plots at a centerline plane of temperature and of mass fractions of intermediate species: OH mass fraction contours as an indication of high temperature chemistry, and CH_2O mass fraction contours as an indication of low temperature chemistry. Snapshots are given at various times offset the ignition delay time (IDT). From the temperature fields, the effects of DFI in modifying the structure of the spray and flame, including in lengthening the flame lift-off length position with respect to the injector location, are visible. Starting from the first time snapshot just before ignition at $t - IDT = 0.05$ ms, formation of CH_2O is observable in the core region in both cases, although in the DFI case the contour values downstream of the duct exit are more diffuse in volume and less concentrated in magnitude, indicating the presence of increased mixing. In the free spray at later times, an increased presence of OH coincides with the consumption of CH_2O near the spray periphery as noted in Chung *et al.* (2020). For the DFI, the consumption of CH_2O at the spray edges is more pronounced compared to the free spray case, despite there still being an increase of OH at later times for both cases.

Table 1. Reported flame lift-off length values from literature and from current investigation, with $p_\infty = 6.00 \; MPa$ and $T_\infty = 1000K$

Case	DFI lift-off length (mm)	Free Spray lift-off length (mm)
Gehmlich *et al.* 2018	14.73	8.41
Mueller *et al.* 2017	16.68	10.00
Current investigation	12.26	8.15

To provide insight into the ignition behavior and to examine the lift-off length, Fig. 4 plots planar-integrated intensity plots of OH; the intensity $I_{xt,OH}$ (Maes *et al.* 2016) is given as

$$I_{xt,OH}(x,t) = \int \tilde{Y}_{OH}(x,y,t)dy \qquad (5)$$
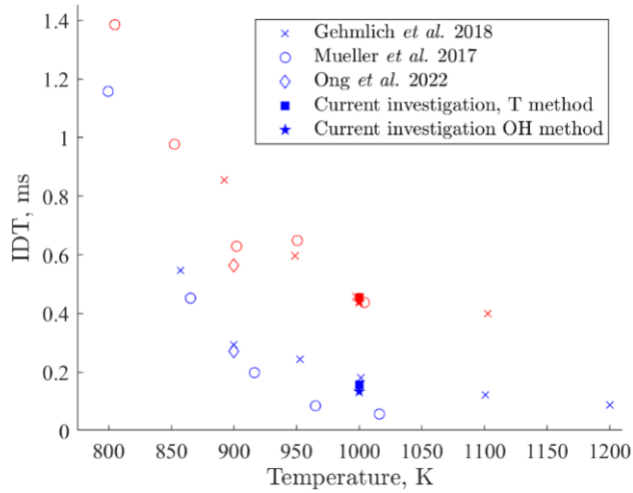
Fig. 5. Computed values of ignition delay time, for the DFI case (red) and the free spray case(blue). Values from literature are given as comparison Note that the data by Mueller *et al.* (2017) has been corrected by a reported hydraulic delay of 0.32 ms.
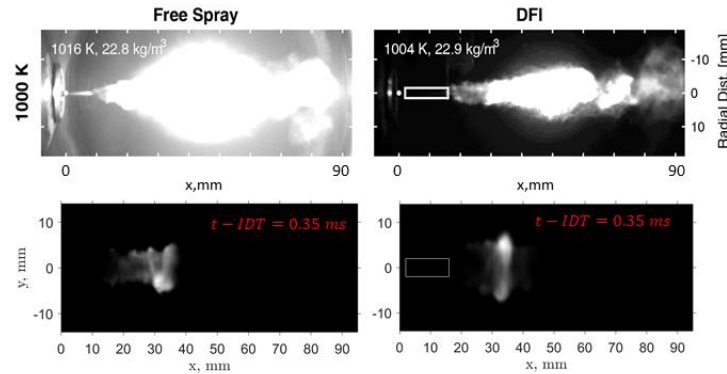
Fig. 6. (Top) Natural luminosity (NL) image frames for free spray and for DFI from Mueller *et al.* (2017), taken at time 3.03 ms after the start of injection. (Bottom) Contours of line-of-sight integrated soot mass of our current investigation for time 0.35 ms after the ignition delay time. Contours are normalized to be black at 0 and white at the maximum value of soot in the domain. For the DFI cases, the duct is shown as a rectangular box

From Fig. 4, the delayed ignition delay time for the DFI case is clearly visible. Regions of high OH (which corresponds to high-temperature chemistry) occur further downstream for the DFI case as well, as also seen in visualizations of the temperature and species contours in Fig. 3. The flame lift-off length is qualitatively visualized by the region of the luminous zone closest to the ignition point in Fig. 5. In Table 1, the lift-off lengths for both experimental measurements and for our results are listed. Following

recommendation by ECN (Engine Combustion Network) and by Ong *et al.* (2022), the lift-off length is defined as the minimal axial distance from the injection location to the point where 2% of the maximal OH mass fraction is found.

For both the DFI and the free spray cases, the lift-off length is underpredicted with respect to experimental values; the amount of deviation from experimental values is comparable to that of Ong *et al.* (2022) and is within the range of typical experimental uncertainty (Skeen *et al.* 2016). However, the DFI's effect in increasing the lift-off length by ~50% with respect to the free spray case value is captured, consistent with the percentage increase found in the experimental values at the same condition.

Fig. 5 compares the ignition delay time predictions for both the DFI and free spray cases with experimental results by Mueller *et al.* (2017) and Gehmlich *et al.* (2018). The results of two different methodologies for calculating the ignition delay time are presented. The T method is used by Ong *et al.* (2022) and defines the ignition delay time the time at which the rate of change of the maximum temperature in the domain is the largest. The OH method instead determines the time at which 14% of the maximum OH mass fraction is reached; this method has been found to be in good agreement with experimental measurements based on a 50% OH* chemiluminescence (Pei *et al.* 2015). For our cases, both methods yield similar results, with <14% and <4% discrepancy for the free spray case and for the DFI case, respectively. Both methods also produce quantitative agreement with experimental results.

Fig. 6 shows comparisons of spatial images (NL for experimental data by Mueller *et al.* (2017), and contours of integrated line-of-sight soot mass for our current investigation). Regions of bright (white) NL signal represent the presence of hot soot in the domain. We see that contours of line-of-sight integrated soot mass are qualitatively similar to the corresponding NL experimental images, with the onset region of maximum soot for the DFI pushed to be further from the injection site than the free spray. Given that the total mass of soot and of C_2H_2 have not reached their peak values, each case would need to be run further

a)   b)
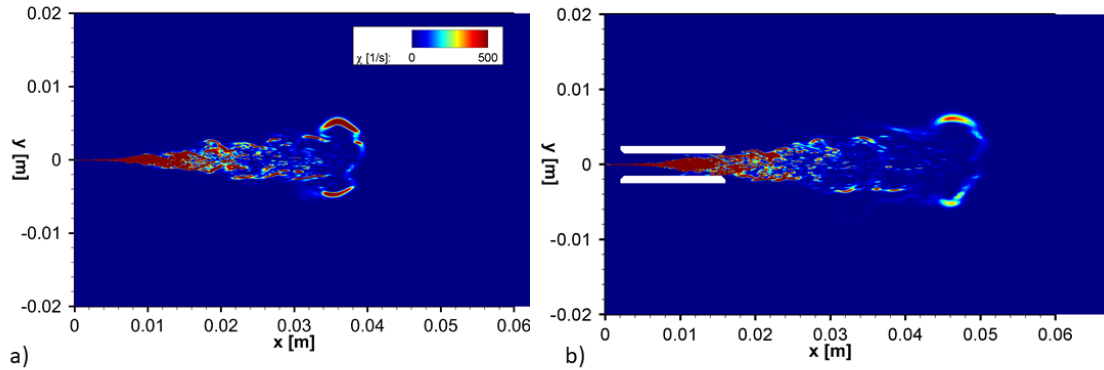
in time to yield more conclusive observations about the soot attenuation of DFI for the simulated cases.

Fig. 7. Plots of the turbulent scalar dissipation rate χ_t, for the (a) free spray case and (b) the DFI case. Contours for both cases are plotted at times of $t - IDT = 0.4$

Fig. 7 shows the turbulent scalar dissipation rate χ_t, which provides an indication of the rate of molecular scalar mixing (Pitsch and Steiner 2000) and thus insight as to the measure of the maximum rate for the chemical reaction for non-premixed turbulent combustion. χ_t is defined as (Girimaji and Zhou 1996)

$$\chi_t = 2D_t \left(\nabla \widetilde{Z_B} \right)^2 \tag{6}$$

where the laminar diffusivity has been neglected and $D_t = \nu_{SGS}/Sc_t$, where ν_{SGS} is the subgrid-scale kinematic viscosity and Sc_t is the turbulent Schmidt number (for which a value of 0.4 is assumed). The contours of χ_t exhibit a number of similarities, specifically in structure and radial extent. The DFI case

exhibits significant magnitude of χ_t further downstream than the free spray; χ_t thus acts as a signature of the enhanced turbulent mixing for DFI within the duct and after the spray leaves the exit. On the other hand, distributions of χ_t do not show significant differences near the duct inlet or within the duct. The localized enhanced mixing is thus evident from the turbulent dynamics.

As discussed in Introduction, the jet-pump effect refers to the region of low-pressure created inside the duct that has important consequences on the jet entrainment and fluid being drawn in at the duct inlet. For our cases, we find that there is indeed a region of instantaneous pressure that is significantly lower than the initial ambient pressure, with certain local regions reaching a pressure value of 25% less than the initial ambient value. However, this feature is not limited to the DFI case, as the free spray exhibits an even larger spatial extent of region of low pressure. The feature thus appears to be a result of the spray dynamics. Our results also suggest that a pressure decrease mechanism within the duct is present and may play a significant role in explaining entrainment dynamics at the duct inlet. This finding is contrary to the conclusions discussed by Ong *et al.* (2022), whose results showed no region of significant decrease in pressure.

4. Conclusions

In the current investigation, LES computations are performed for transcritical n-dodecane spray injection with auto-ignition, in order to investigate DFI as a concept to achieve increased combustion efficiency and soot attenuation. A diffuse-interface method is used with a finite-volume compressible fluid solver with multi-species finite-rate chemistry capability and real fluid thermodynamic and transport property considerations. Differences in behavior between the DFI and free spray cases are highlighted. For both, the ignition delay time and flame lift-off length show relative agreement with past studies. Results of soot show preliminary qualitative agreement with experimental images, but confidence in the soot attenuation requires further computation and study. A study of the turbulent scalar dissipation shows the enhanced turbulent mixing after the jet leaves the duct, with little difference in the regions within duct or before the jet enters the duct. The region inside the duct additionally exhibits a region of low pressure (which has been a point of disagreement in the literature), but this feature is present irrespective of the presence of the duct. The results of the study serve as evidence that diffuse-interface methods can be used to capture diesel spray behavior under varying conditions and geometries.

5. References

1. Chambers, M., & Schmitt, Rolf (2015). Diesel-powered Passenger Cars and Light Trucks. Bureau of Transportation Statistics, https://www.bts.gov/archive/publications/bts_fact_sheets/oct_2015/entire
2. O'Connor, J., & Musculus, M. (2013). Post injections for soot reduction in diesel engines: a review of current understanding. SAE International Journal of Engines, 6(1), 400-421, https://doi.org/10.4271/2013-01-0917.
3. Upatnieks, A., Mueller, C. J., & Martin, G. C. (2005). The influence of charge-gas dilution and temperature on DI diesel combustion processes using a short-ignition-delay, oxygenated fuel. SAE transactions, 773-785, https://doi.org/10.4271/2005-01-2088.
4. Mueller, C. J., Nilsen, C. W., Ruth, D. J., Gehmlich, R. K., Pickett, L. M., & Skeen, S. A. (2017). Ducted fuel injection: A new approach for lowering soot emissions from direct-injection engines. Applied energy, 204, 206-220.
5. Fitzgerald, R., Svensson, K., Martin, G., Qi, Y., & Koci, C. (2018). Early investigation of ducted fuel injection for reducing soot in mixing-controlled diesel flames. SAE International Journal of Engines, 11(6), 817-834, https://doi.org/10.4271/2018-01-0238.
6. Liu, X., Mohan, B., & Im, H. G. (2020). Numerical investigation of the free and ducted fuel injections under compression ignition conditions. Energy & Fuels, 34(11), 14832-14842.
7. Zhang, Y., Wang, Z., Lee, C. F., Li, F., & Wu, H. (2021). Analysis of mechanism of ducted fuel injection under non-vaporizing condition. Fuel, 305, 121496.

8. Ong, J. C., Zhang, M., Jensen, M. S., & Walther, J. H. (2022). Large eddy simulation of soot formation in a ducted fuel injection configuration. Fuel, 313, 122735.
9. Nilsen, C. W., Biles, D. E., Yraguen, B. F., & Mueller, C. J. (2020). Ducted Fuel Injection versus Conventional Diesel Combustion. SAE International Journal of Engines, 13(3), 345-362, https://doi.org/10.4271/2019-01-0545.
10. Polonowski, Christopher J., et al. "An experimental investigation of low-soot and soot-free combustion strategies in a heavy-duty, single-cylinder, direct-injection, optical diesel engine." SAE International Journal of Fuels and Lubricants 5.1 (2012): 51-77, https://doi.org/10.4271/2011-01-1812.
11. Gehmlich, R. K., Mueller, C. J., Ruth, D. J., Nilsen, C. W., Skeen, S. A., & Manin, J. (2018). Using ducted fuel injection to attenuate or prevent soot formation in mixing-controlled combustion strategies for engine applications. Applied energy, 226, 1169-1186.
12. Nilsen, C. W., Biles, D. E., & Mueller, C. J. (2019). Using ducted fuel injection to attenuate soot formation in a mixing-controlled compression ignition engine. SAE International Journal of Engines, 12(3), 309-322, https://doi.org/10.4271/03-12-03-0021.
13. Millo, F., Piano, A., Paradisi, B. P., Postrioti, L., Pieracci, L., Bianco, A., ... & Vassallo, A. (2021). Ducted fuel injection: Experimental and numerical investigation on fuel spray characteristics, air/fuel mixing and soot mitigation potential. Fuel, 289, 119835.
14. Zhang, M., Ong, J. C., Pang, K. M., Bai, X. S., & Walther, J. H. (2021). An investigation on early evolution of soot in n-dodecane spray combustion using large eddy simulation. Fuel, 293, 120072.
15. Ma, P. C., Lv, Y., & Ihme, M. (2017). An entropy-stable hybrid scheme for simulations of transcritical real-fluid flows. Journal of Computational Physics, 340, 330-357.
16. Ihme, M., Ma, P. C., & Bravo, L. (2019). Large eddy simulations of diesel-fuel injection and auto-ignition at transcritical conditions. International Journal of Engine Research, 20(1), 58-68.
17. Chung, W. T., Ma, P. C., & Ihme, M. (2020). Examination of diesel spray combustion in supercritical ambient fluid using large-eddy simulations. International Journal of Engine Research, 21(1), 122-133.
18. Engine Combustion Network, Sandia National Laboratory, https://ecn.sandia.gov/
19. Chung, T. H., Ajlan, M., Lee, L. L., & Starling, K. E. (1988). Generalized multiparameter correlation for nonpolar and polar fluid transport properties. Industrial & engineering chemistry research, 27(4), 671-679.
20. Takahashi, S. (1975). Preparation of a generalized chart for the diffusion coefficients of gases at high pressures. Journal of Chemical Engineering of Japan, 7(6), 417-420.
21. Peng, D. Y., & Robinson, D. B. (1976). A new two-constant equation of state. Industrial & Engineering Chemistry Fundamentals, 15(1), 59-64.
22. Poling, B. E., Prausnitz, J. M., & O'Connell, J. P. (2001). Properties of gases and liquids. McGraw-Hill Education.
23. Miller, R. S., Harstad, K. G., & Bellan, J. (2001). Direct numerical simulations of supercritical fluid mixing layers applied to heptane–nitrogen. Journal of Fluid Mechanics, 436, 1-39.
24. Congiunti, A., & Bruno, C. (2003, January). Supercritical combustion properties. In 41st Aerospace Sciences Meeting and Exhibit (p. 478).
25. Hickey, J. P., Ma, P. C., Ihme, M., & Thakur, S. S. (2013). Large eddy simulation of shear coaxial rocket injector: Real fluid effects. In 49th AIAA/ASME/SAE/ASEE Joint Propulsion Conference (p. 4071).
26. Ma, P. C., Bravo, L., & Ihme, M. (2015). Supercritical and transcritical real-fluid mixing in diesel engine applications. ARMY RESEARCH LAB ABERDEEN PROVING GROUND MD VEHICLE TECHNOLOGY DIRECTORATE.
27. Ma, P. C., Wu, H., Jaravel, T., Bravo, L., & Ihme, M. (2019). Large-eddy simulations of transcritical injection and auto-ignition using diffuse-interface method and finite-rate chemistry. Proceedings of the Combustion Institute, 37(3), 3303-3310.

28. Hao, C., Lu, Z., Feng, Y., Bai, H., Wen, M., & Wang, T. (2021). Optimization of fuel/air mixing and combustion process in a heavy-duty diesel engine using fuel split device. Applied Thermal Engineering, 186, 116458.

29. Moiz, A. A., Ameen, M. M., Lee, S. Y., & Som, S. (2016). Study of soot production for double injections of n-dodecane in CI engine-like conditions. Combustion and Flame, 173, 123-131.

30. Patterson, M. A., Kong, S. C., Hampson, G. J., & Reitz, R. D. (1994). Modeling the effects of fuel injection characteristics on diesel engine soot and NOx emissions. SAE transactions, 836-852, https://doi.org/10.4271/940523.

31. Traxinger, C., Zips, J., & Pfitzner, M. (2019). Single-phase instability in non-premixed flames under liquid rocket engine relevant conditions. Journal of Propulsion and Power, 35(4), 675-689.

32. Bilger, R. W. (1979). Turbulent jet diffusion flames. In Energy and Combustion Science (pp. 109-131). Pergamon.

33. Khalighi, Y., Ham, F., Nichols, J., Lele, S., & Moin, P. (2011). Unstructured large eddy simulation for prediction of noise issued from turbulent jets in various configurations. In 17th AIAA/CEAS Aeroacoustics Conference (32nd AIAA Aeroacoustics Conference) (p. 2886).

34. Strang, G. (1968). On the construction and comparison of difference schemes. SIAM journal on numerical analysis, 5(3), 506-517.

35. Wu, H., Ma, P. C., & Ihme, M. (2019). Efficient time-stepping techniques for simulating turbulent reactive flows with stiff chemistry. Computer Physics Communications, 243, 81-96.

36. Tranquilli, P., & Sandu, A. (2014). Rosenbrock--Krylov Methods for Large Systems of Differential Equations. SIAM Journal on Scientific Computing, 36(3), A1313-A1338.

37. Gottlieb, S., Shu, C. W., & Tadmor, E. (2001). Strong stability-preserving high-order time discretization methods. SIAM review, 43(1), 89-112.

38. Vreman, A. W. (2004). An eddy-viscosity subgrid-scale model for turbulent shear flow: Algebraic theory and applications. Physics of fluids, 16(10), 3670-3681.

39. Colin, O., Ducros, F., Veynante, D., & Poinsot, T. (2000). A thickened flame model for large eddy simulations of turbulent premixed combustion. Physics of fluids, 12(7), 1843-1863.

40. Lillo, P. M., Pickett, L. M., Persson, H., Andersson, O., & Kook, S. (2012). Diesel spray ignition detection and spatial/temporal correction. SAE International Journal of Engines, 5(3), 1330-1346, https://doi.org/10.4271/2012-01-1239.

41. Wehrfritz, A., Kaario, O., Vuorinen, V., & Somers, B. (2016). Large eddy simulation of n-dodecane spray flames using flamelet generated manifolds. Combustion and Flame, 167, 113-131.

42. Westlye, F. R., Battistoni, M., Skeen, S. A., Manin, J., Pickett, L. M., & Ivarsson, A. (2016). Penetration and combustion characterization of cavitating and non-cavitating fuel injectors under diesel engine conditions (No. 2016-01-0860). SAE Technical Paper, https://doi.org/10.4271/2016-01-0860.

43. Li, F., Lee, C. F., Wang, Z., Pei, Y., & Lu, G. (2021). Impacts of duct inner diameter and standoff distance on macroscopic spray characteristics of ducted fuel injection under non-vaporizing conditions. International Journal of Engine Research, 22(5), 1702-1713.

44. Maes, N., Meijer, M., Dam, N., Somers, B., Toda, H. B., Bruneaux, G., ... & Manin, J. (2016). Characterization of Spray A flame structure for parametric variations in ECN constant-volume vessels using chemiluminescence and laser-induced fluorescence. Combustion and Flame, 174, 138-151.

45. Skeen, S. A., Manin, J., Pickett, L. M., Cenker, E., Bruneaux, G., Kondo, K., ... & Hawkes, E. (2016). A progress review on soot experiments and modeling in the engine combustion network (ECN). SAE International Journal of Engines, 9(2), 883-898, https://doi.org/10.4271/2016-01-0734.

46. Pei, Y., Som, S., Pomraning, E., Senecal, P. K., Skeen, S. A., Manin, J., & Pickett, L. M. (2015). Large eddy simulation of a reacting spray flame with multiple realizations under compression ignition engine conditions. Combustion and Flame, 162(12), 4442-4455.

47. Pitsch, H., & Steiner, H. (2000). Scalar mixing and dissipation rate in large-eddy simulations of non-premixed turbulent combustion. Proceedings of the Combustion Institute, 28(1), 41-49.
48. Girimaji, S. S., & Zhou, Y. (1996). Analysis and modeling of subgrid scalar mixing using numerical data. Physics of Fluids, 8(5), 1224-1236.

Session S2.3 Advances towards ICE Emission Reduction

THIESEL 2022 Conference on Thermo- and Fluid Dynamics of Clean Propulsion Powerplants

Experimental Validation of Laminar Flame Model for CH4/Diesel Dual Fuel Engine applied to H2/Diesel Combustion

R. De Robbio*[1], E. Mancaruso[1], B.M. Vaglieco[1], S. Artham[2], J. Martin[2]

[1]STEMS – CNR. Viale G. Marconi 4, 80125, Naples, Italy.

E-mail: roberta.derobbio@stems.cnr.it; ezio.mancaruso@stems.cnr.it; biancamaria.vaglieco@stems.cnr.it

[2]CMT – Motores Térmicos. Universitat Politècnica de València. Camino de Vera s/n, E-46022 Valencia,

Spain.
E-mail: susar1@upv.edu.es; jaimardi@mot.upv.es

Abstract.
Despite of having high thermal efficiency and wide range of operation, compression ignition (CI) engines have high exhaust emissions of particulate matter (PM) and nitrogen oxides (NOx) which are harmful for the environment. In order to keep up with the latest stringent regulations on emissions, CI engines have been pushed to work with different fuels. In particular, the usage of gaseous fuels along with diesel fuel in dual fuel mode demonstrated to be a valid solution, especially for large bore applications. Indeed, a large part of the diesel liquid fuel is substituted with alternative gaseous fuels that is injected into the intake manifold to form a premixed charge with air, which significantly reduces PM and, in many cases, NOx. Even though, methane has been the mostly used gaseous fuel for dual fuel CI engine, the necessity to reduce CO_2 emissions as well, has led hydrogen to be one of the most promising alternatives. Because of its faster burning velocity and wide range of air to fuel ratios, a different model for its combustion must be used for predictive purposes. In current work, a dual-fuel combustion model has been implemented in GT-Power with the aim of simulating and investigating the characteristics of hydrogen-diesel combustion. Initially, a dual fuel model with methane was used and experimentally validated. A laminar flame speed model was built and incorporated in the software with the approaches of Heywood and Gülder studies. Design of experiments and design optimizer were used to find the optimal values of the combustion model parameters matching in-cylinder pressure curves. Once the model was validated with methane, the same methodology has been adapted to use hydrogen instead. Two new correlations are built and implemented in the code starting from literature experimental measurements. The simulated results of hydrogen-diesel combustion allow to foresee a burn rate consistent with methane-diesel ones.

Notation

BMEP	*Brake mean effective pressure.*
BTE	*Brake thermal efficiency.*
CI	*Compression ignition.*
DF	*Dual fuel.*
ECU	*Electronic control unit.*
HC	*Unburned hydrocarbons.*
NOx	*Nitrogen oxides.*
NG	*Natural gas.*
PM	*Particulate matter.*
RCCI	*Reactivity controlled compression ignition.*
RoHR	*Rate of heat release.*
RP	*Premixed ratio.*

1. Introduction

Compression ignition (CI) engines cover from large marine to small car applications. Despite of having high thermal efficiency and wide range of operation, it is well-know that CI engines have high exhaust emissions of particulate matter (PM) and nitrogen oxides (NOx). Since they have significant effects on human health and are harmful for the environment, several efforts have been made to improve

the emissions, preserving the performance of modern diesel engines. In order to keep up with the latest stringent regulations on emissions [1] [2], the implementation of alternative solutions is necessary. Some of such alternative solutions, such as the usage of after treatment systems, are not cost efficient and decreases global efficiency because of the higher pumping work required [3].

On the contrary, other solutions have been proposed and concern the way of combustion and cleaner fuels that power the engine. In particular, the combustion of gaseous fuels, usually natural gas (NG) or methane, has demonstrated to be effective in the resolution of the previous mentioned issues when is initiated by pilot injection of diesel fuel in dual fuel (DF) configuration. Indeed, the literature review of Lijiang and Peng [4] collects several scientific papers that analyzed DF combustion, emissions, and performance characteristics for different NG/air mass ratios. They illustrated that dual fuel mode has a lower pressure ratio and a longer ignition delay with respect to diesel mode. More significantly, DF introduces a trade-off between NOx and PM emissions, and unburned hydrocarbons (HC) and carbon monoxide (CO). In fact, NOx and PM substantially decrease while the HC and CO increase with a consequent negative effect on engine power and brake thermal efficiency (BTE).

The authors of the present work have studied dual fuel (methane-diesel) combustion both experimentally [5], [6], [7], [8], and numerically [9], [10], [11]. In particular, the experimental activity was carried out on an optically accessible single cylinder diesel engine. Innovative spectroscopic and infrared visualization have been obtained with intensified and fast cameras, respectively, able to investigate different emission wavelengths, and therefore, to follow the evolution of fundamental species in the long chain of reactions. Then, experimental results have been utilized for the validation of the CFD calculations that three-dimensional codes can be useful tools to deepen the knowledge of the in-cylinder phenomena. However, the main issue of the dual fuel modelling is the description of the combustion development characterized by a propagation of a flame in the premixed charge and the flame is started by diesel ignition. Other researchers proposed different methodologies to address this matter. A reliable model is presented in [12] where Amirante et al. analyze the flame propagation of different fuels based on the works of Heywood [13] , Metghalchi [14] and Gülder [15] [16]. This model has been used in the 3D codes and validated in [11]. Nevertheless, the implementation of such model in a 0D/1D code can be decisive for a faster evaluation and optimization of a dual fuel engine performances. This methodology was used by Millo et al. [17] for the simulation of a large bore diesel engine supplied with natural gas, since marine applications seem the most suited for the implementation of dual fuel technology. They developed a phenomenological fast running 0D/1D combustion model, only for natural gas, in GT-Power validated against experimental data.

Particular attention must be paid to low load conditions, since they can be significantly critical for dual fuel combustion; in [18] an in-house 1D code is used to evaluate the influence of the main injection parameters on the efficiency and emissions. It is demonstrated that with respect to single pilot injection, double injection strategies lead to an enhancement of efficiency; increasing the rail pressure promotes a more prominent premixed combustion phase leading to a smoother combustion development; adjusting injection parameters together with methane percentage, it is possible to obtain an improvement of efficiency up to 3.5%.

Even though methane is the mostly used gaseous fuel with a wide availability across the globe that ensures economical prices, for dual fuel CI engine, hydrogen is one of the most promising alternative fuels, because of its faster burning velocity, wide range of air to fuel ratios and rapid combustion [19], [20]. Therefore, with the use of hydrogen as gaseous fuel more significant drop in CO_2 emissions can be obtained, and the engine can be operated at very lean equivalence ratios as well. Many researchers proposed the addition of hydrogen to diesel in the CI engines as a method to improve the performance as it increases the H/C ratio of the entire fuel and reduce the combustion duration due to the high flame speed of hydrogen in comparison to other fuels.

Miyamoto et al. [21] experimentally investigated the performance and emission characteristics of a diesel engine with small volume percentages of hydrogen added to the intake air at late diesel-fuel injection timings. They focused on the reduction of NOx and PM emissions but keeping an acceptable level of in-cylinder pressure rise to avoid excessive noise. They demonstrated that an appropriate late diesel timing in combination with H_2 addition can lead to low temperature combustion with a decrease of nitrogen oxides emissions without enhancing smoke in the exhaust. In [22] Ghazal simulated the combustion of different hydrogen-diesel blends for different engine speed and different air to fuel ratios. Results demonstrated that small amounts of H_2 reduce the diesel ignition lag and the pressure rise rate providing softer run conditions and improving the durability of the engine. In general, the engine power is improved, and CO emissions are reduced with respect to the base diesel engine. Ultimately, the comprehensive review in [23] summarized the results of different works in literature reporting that the utilization of hydrogen in dual fuel engines, reduces unburned hydrocarbons, carbon monoxide and smoke to near zero level and significantly decreases greenhouse emissions (CO_2 and methane). On

the contrary, the high adiabatic flame temperature of H_2 generates high localized in-cylinder temperatures, leading to increasing emissions of NOx. Moreover, an enhancement of hydrogen substitution advances the start of combustion, and if a critical value is achieved the autoignition of the premixed H_2-air charge could occur and lead to an abnormal combustion (knocking). In the review, solutions to these problems, such as low temperature strategies or water injections are proposed. Also, for dual fuel hydrogen-diesel engine GT-Power can be used. Indeed, Ghazal [24] numerically investigated the performances and emissions of reactivity controlled compression ignition (RCCI) engine in DF mode combined with port water injection. Results demonstrated that engine speed and injection timing affect the efficiency and emissions; in particular, advancing the injection could lead to high in-cylinder temperature, pressure rising rate and NOx emissions, on the contrary the CO emissions are reduced but at the expense of a lower BTE.

In the current work, a dual-fuel combustion model is built in GT-Power, with the aim of simulating and investigating the characteristics of hydrogen-diesel combustion. Initially, a dual fuel engine model with methane was built and validated. The previously cited approaches of Heywood [13] and Gülder [15] [16] are used and incorporated in the software, to model laminar flame speed. The optimal values of combustion constants are found through design of experiments and design optimizer in order to match in-cylinder pressure curves. The validation of diesel-methane cases is obtained with the aid of an experimental campaign on an optically accessible single cylinder research engine. Experimental tests are characterized by different load levels, 2 and 5 bar of brake mean effective pressure (BMEP), and different engine speeds, 1500 and 2000 rpm. Dual fuel methane-diesel results represent the starting point to foresee a burn rate for hydrogen-diesel combustion consistent with the previous ones, obtained by adapting the same methodology. However, for hydrogen simulations, not only the correlation must be implemented in the software, but it must be built starting from laminar flame speed empirical measurements found in the literature [25] [26]. The numerical cases are based on an experimental campaign forecasted on the same engine supplied with hydrogen instead of methane. Since the main issue regards the correct determination of laminar flame speed in extremely lean conditions, two new correlations are presented in different ranges of equivalence ratio.

2. Engine set-up

The research activity has been carried out on an optically accessible single cylinder diesel engine supplied with methane in the intake manifold. The engine, specifically designed for the optical access, is equipped with the original common rail injection system of the four-cylinder engine. The characteristics are listed in Table 1. The timing of the injection of direct injected diesel fuel can be arbitrarily controlled via a fully flexible Electronic Control Unit (ECU). The gaseous fuel is port fuel injected into the intake manifold. Gaseous fuel injection is managed by a delay unit synchronized with the engine shaft encoder. The features of the injection systems for the two fuels are reported in Table 2.

Table 1. Engine specifications

Engine type	4-stroke, single cylinder
Stroke [mm]	92
Bore [mm]	85
Cylinder volume displacement [cm³]	522
Combustion bowl volume [cm³]	19.7
Compression ratio	16.5:1
Exhaust Valve Opening (EVO)	116°ATDC
Exhaust Valve Closing (EVC)	340°BTDC
Intake Valve Opening (IVO)	344°ATDC
Intake Valve Closing (IVC)	132°BTDC

Table 2. Injection system specifications

Diesel injection system	Common rail
Number of holes	7
Cone angle of fuel jet axis [deg]	148
Hole diameter [mm]	0.141
Methane injection system	PFI
Number of holes	1
Maximum injection pressure [bar]	5

For a better comprehension, in Figure 1 the scheme of the whole system is displayed. It is important to highlight that to make the engine optically accessible, a sapphire window was placed in the bottom part of the combustion bowl, which now presents a flat shape. However, the modification was made without altering the original bowl volume (Table 1).
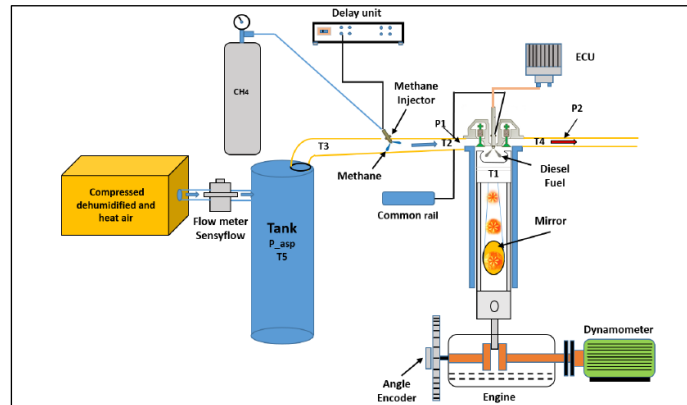
Fig. 1. Experimental set-up scheme

The different signals were measured via a multichannel acquisition system. The diesel injector current of the solenoid was detected by means of a Hall-effect sensor. A piezoelectric pressure transducer, set in the glow plug seat of the engine head, was used for the acquisition of the in-cylinder pressure both in motored and fired conditions. All the current signals were digitalized and recorded at 0.2° crank angle increments. For each test point, the in-cylinder pressure cycle taken as reference is a calculated average from 200 consecutive combustion cycles through the AVL-Indicom software. Also, the same software used the averaged pressure for the calculation of the heat release rate via the energy balance equation [13].

The experimental tests, used for the validation of the model are characterized by two load levels, 2 and 5 bar BMEP and two different engine speeds, 1500 and 2000 rpm. The operating conditions for the four cases are listed in Table 3. For each case, the original double (pilot and main) injection timing is maintained with respect to the full diesel case. However, in DF mode the main injection has been reduced until it has same duration as pilot one, so to inject the same amount of liquid fuel. The amount of methane is added with the aim to achieve the same BMEP as the corresponding full diesel case.

Table 3. Engine operating conditions

Case	#1	#2	#3	#4
Engine Speed [rpm]	1500	1500	2000	2000
BMEP [bar]	2	5	2	5
SOI pilot	16°BTDC	11.6°BTDC	21.2°BTDC	18.6°BTDC
SOI main	6°BTDC	0.3°ATDC	8°BTDC	2.4°BTDC
Dwell interval [deg]	10	11.9	13.2	16.2
Duration pilot and main [deg]	2.6	2.4	3.4	3.1
Diesel mass injected pilot + main [mg/cycle]	1.42	1.64	1.43	1.66
Methane mass [mg/cycle]	7.579	11.191	7.554	10.148
Rail pressure [bar]	615	867	700	891
Pressure inlet [bar]	1.5	1.7	1.5	1.7
Temperature inlet [°C]	44	46	50	51
Air mass [mg/cycle]	750.9	802.4	679.3	741.2
Methane/air equivalence ratio	0.174	0.240	0.192	0.236
Methane RP [%]	86.1	88.8	86.0	87.6
Hydrogen mass [mg/cycle]	2.457	4.331	2.305	3.904
Hydrogen/air equivalence ratio	0.117	0.189	0.120	0.183
Hydrogen RP [%]	82.8	88.0	81.8	86.7

In addition, Table 3 reports the premixed ratio (RP), that is the ratio of energy input from methane expressed as follows:

$$RP = \frac{\left(m_p LHV_p\right)}{\left(m_p LHV_p + m_d LHV_d\right)} \times 100$$

Where m_p and m_d are the mass flow rate of premixed fuel (methane) and directly injected fuel (diesel), respectively, LHV_p and LHV_d their lower heating values. All the cases are then characterized by an extremely low equivalence ratio and RP values higher than the 80%. Although a major replacement and reduction of liquid fuel has been accomplished, still a small amount of diesel fuel must be injected to ignite the premixed charge.

Following the same approach, a research activity is forecasted using hydrogen. The four cases are expected to be performed on the same engine supplied with hydrogen instead of methane in order to reach the same BMEP. The values of the mass injected are reported in the Table 3 as well. Moreover, the equivalence ratio and the RP are expected to be lower than methane ones. However, the premixed ratios are still higher than 82%.

The in-cylinder pressures measured for the four cases are displayed in Figure 3. It is possible to see that the main differences are given by the load level. Engine speed has a minor influence on combustion. However, it is important to recall that the injection timing is varied with the operating condition.
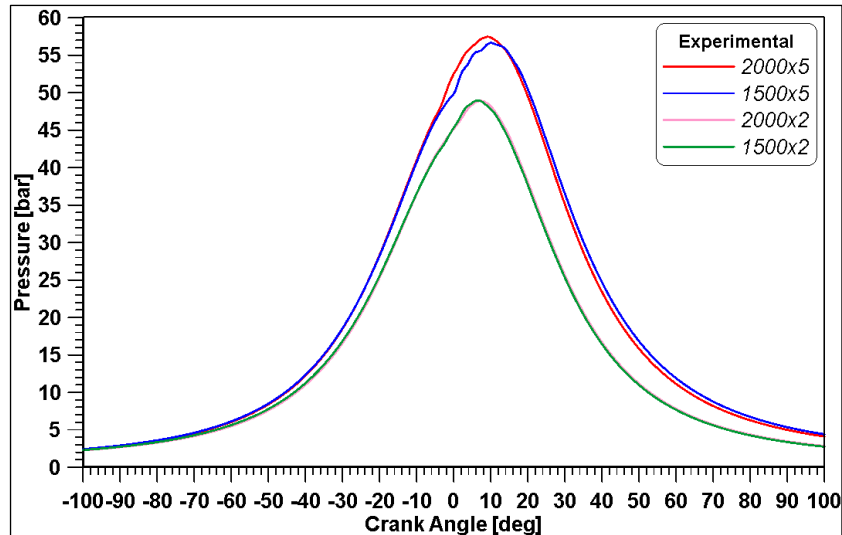
Fig. 2. Experimental in-cylinder pressure curves

3. Model set-up
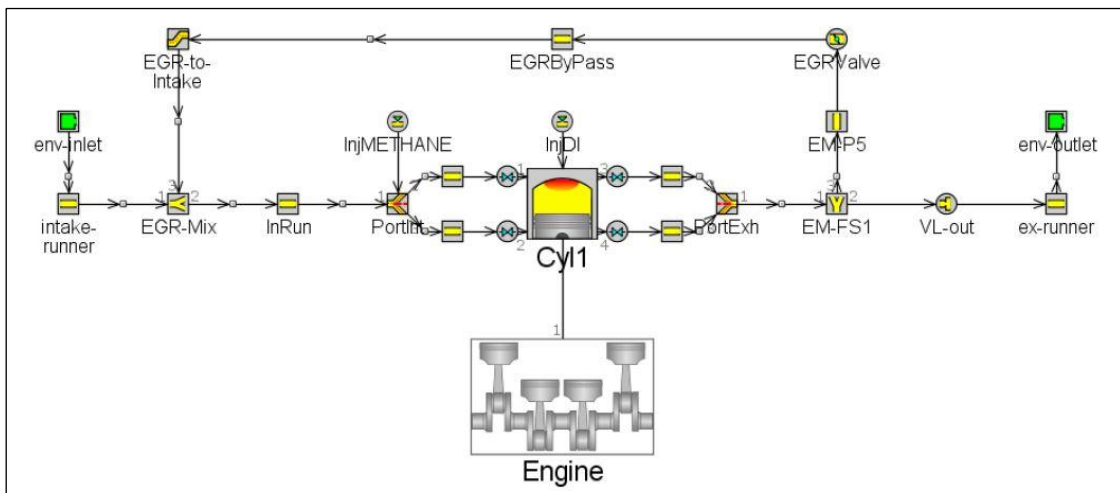
Fig. 3. GT-Power model of the compression ignition single cylinder diesel engine in dual fuel mode

The engine was modelled in the engine simulation software, according to the specifications from engine test bench, as shown in the Figure 3. As it can be seen, the model has two injectors, one at the intake port, where methane or hydrogen fuel is injected and a second one in the engine cylinder head, where diesel is injected into the cylinder to initiate combustion. The engine model was updated with all the intake and exhaust conditions, initial pressures and temperatures at various locations, fuel mass flow rate for hydrogen, start of injection and injected fuel mass for diesel, according to the experimental results of dual fuel methane-diesel engine, for various operating points as shown in Table 3. After initial calibration, the interest was shifted to the combustion model, where a new laminar flame model was built and incorporated in the set-up for methane-diesel dual fuel model.

In the software, a specific model is provided for dual fuel combustion named "EngCylComb-DualFuel". It consists of two models, "DIPulse" and "SITurb", usually used for conventional diesel combustion and flame propagation in spark ignition engines, respectively.

3.1 DI Pulse

This combustion model predicts the combustion rate for direct-injection diesel engines with single and multi-pulse injection events. It tracks the evaporation, mixing with surrounding gas and burning of the fuel jet. The DIPulse model benefits from faster runtime while maintaining or exceeding the predictive accuracy seen by other predictive models. It requires an accurate injection profile to achieve good results.

The DIPulse model includes several submodels which simulate the relevant physical processes taking place during injection and combustion. There are four attributes in the 'DIPulse' template which should be used for calibration.

3.1.1 Entrainment

As the spray penetrates, it slows down as the surrounding unburned and burned gases are entrained into the pulse. The intermixing of pulses occurs through entrainment. The entrainment rate can be modified by the entrainment rate multiplier (C_{ent}).

3.1.2 Ignition

The fuel mixture in each pulse undergoes an ignition delay modelled with an Arrhenius expression which can be modified by the ignition delay multiplier (C_{ign}).

$$\tau_{ign} = C_{ign}\, \rho^{-1.5} \exp\left(\frac{3500}{T}\right) [O_2]^{-0.5}$$

Where, τ_{ign} is ignition delay, T is pulse temperature, ρ pulse gas density and $[O_2]$ is oxygen concentration.

3.1.3 Premixed Combustion

When the pulse ignites, the mixture present at that time is set aside for premixed combustion. The rate of this combustion is assumed to be kinetically limited and can be modified by the premixed combustion rate multiplier (C_{pm}).

$$\frac{dm_{pm}}{dt} = C_{pm} m_{pm} \mathrm{k}\left(\mathrm{t} - t_{ign}\right)^2 f([O_2])$$

Where, t_{ign} is the time at ignition, m_{pm} is premixed mass, k is turbulent kinetic energy and t is the time.

3.1.4 Diffusion Combustion

After the pulse ignites, the remaining unmixed fuel and entrained gas in the pulse continue to mix and burn in a primarily diffusion-limited phase. The rate of this combustion can be modified by the diffusion combustion rate multiplier (C_{df}).

$$\frac{d\mathrm{m}}{dt} = C_{df}\mathrm{m}\, \frac{\sqrt{k}}{\sqrt[s]{V_{cyl}}}\, f([O_2])$$

3.2 SI Turb

This model predicts the burn rate for homogeneous charge, spark-ignition engines. This prediction considers the cylinder's geometry, spark locations and timing, air motion, and fuel properties. There are four important attributes in the 'EngCylCombSITurb' template which should be used for calibration.

3.2.1 Laminar Flame Speed

The laminar flame speed is calculated by an equation, except for the hydrogen and methane options which use different proprietary equations to quantify the flame speed [13]. Detailed explanation of laminar flame speed model is given in further sections.

3.2.2 Entrainment and Burn-up

The unburned mixture of fuel and air is entrained into the flame front through the flame area at a rate proportional to the sum of the turbulent and laminar flame speeds as shown in formula (1). The burn rate is proportional to the amount of unburned mixture behind the flame front, $(M_e - M_b)$, divided by a time constant, τ, as shown in formula (2). This model requires that in-cylinder flow is described by an 'EngCylFlow' reference object so the turbulent intensity and length scale will be provided. The effects of turbulent intensity and length scale can be modified using the turbulent flame speed multiplier (C_{TFS}) and Taylor length scale multiplier (C_{TLS}). Additionally, the flame kernel growth multiplier (C_{FKG}) can be used to adjust the initial growth rate of the flame kernel. All the related equations are shown in the formulas (3), (4) and (5).

$$\frac{dM_e}{dt} = \rho_u A_e (S_T + S_L) \tag{1}$$

$$\frac{dM_b}{dt} = \frac{M_e - M_b}{\tau} \tag{2}$$

Here, turbulent flame speed S_T can be calculated with the help of C_{TFS} and C_{FKG} as shown below

$$S_T = C_{TFS}\, u'\left(1 - \frac{1}{1 + C_{FKG}(\frac{R_f}{L_i})^2}\right) \tag{3}$$

$$\tau = \frac{\lambda}{S_L} \tag{4}$$

$$\lambda = \frac{C_{TLS} L_i}{\sqrt{Re_t}} \tag{5}$$

3.3 Calibration and optimization

In the current work, C_{ign} C_{ent} C_{df} C_{pm} C_{TFS} C_{FKG} and C_{TLS} have been calibrated. The aim of calibration is to find the optimal set of constants that will provide the best possible match to various operating points. The calibration was performed using design of experiments (DOE) and design optimizer in GT power. Initially, the operating point with low speed and low load (1500 rpm engine speed and 2 bar BMEP) was considered and DOE was performed for the individual constants. Once a set of values were obtained for the combustion constants, they were used for the other operating points to test the consistency. After further tuning, a pre-final set of values for the combustion constants was obtained for all the operating points. In order to be precise with the required targets, design optimizer was used and a final set of values for all the combustion constants are obtained. It is seen that C_{ent} C_{df} C_{FKG} and C_{pm} have low influence on the peak pressures and their lower limits (ranging from 0.05 to 1) give good results. C_{TFS} and C_{TLS} have high influence and the values range from 1.3 to 1.6.

The ignition delay multiplier, C_{ign} has high influence on combustion and has a strong dependence on speed and load. Hence it was decided to use a table with a 14x38 matrix, for the C_{ign}, instead of giving a constant value for all the operating points. The table was created using the values obtained through design optimizer. This table consists of the values of the constants for various operating points, with engine speed starting from 1200 until 2500 rpm, along with a load starting from 0.3 until 4 bars. This table interpolates the required constant according to the operating point. The values of the parameters after the optimization are reported in Table 4.

Table 4. Values of the constants

C_{ign}	-
C_{ent}	2.70
C_{df}	1.40
C_{pm}	0.07
C_{TFS}	3
C_{FKG}	3
C_{TLS}	0.5

4. Laminar Flame Speed model

As already stated in the introduction section, the aim of this work is to model dual fuel combustion through a model of flame propagation. The main issue is that in GT-Power a specific flame model for methane and hydrogen is not present.

In general, the laminar flame speed is calculated proportionally to the laminar flame speed in standard conditions, i.e. T_{ref} = 298 K and p_{ref} = 1.03 kPa. In order to account for the different temperature and pressure condition the dependency is expressed via the power law formula (6) [14]:

$$S_L = S_{L,0} \left(\frac{T_u}{T_{ref}}\right)^\alpha \left(\frac{p}{p_{ref}}\right)^\beta \tag{6}$$

$$\alpha = 2.18 - 0.8(\phi - 1) \tag{7}$$

$$\beta = -0.16 - 0.22(\phi - 1) \tag{8}$$

From equations (6) it is observed that the laminar flame speed depends on the temperature of the unburned charge (T_u) and pressure (p) via two constants, α and β, which are a function of the equivalence ratio φ, eq. (7) and (8).

The laminar flame speed in standard condition $S_{L,0}$ is an intrinsic property of the mixture. The software makes use only of the standard correlation (eq. 8) by Metghalchi [14] expressed as follows:

$$S_{L,0} = B_m + B_\phi(\phi - \phi_m)^2 \tag{9}$$

Therefore, reference laminar flame speed and the equivalence ratio are linked via a second order polynomial equation. Nevertheless, such correlation assumes negative values below an equivalence ratio of 0.6, as it is possible to observe from Figure 4 (red dotted line).
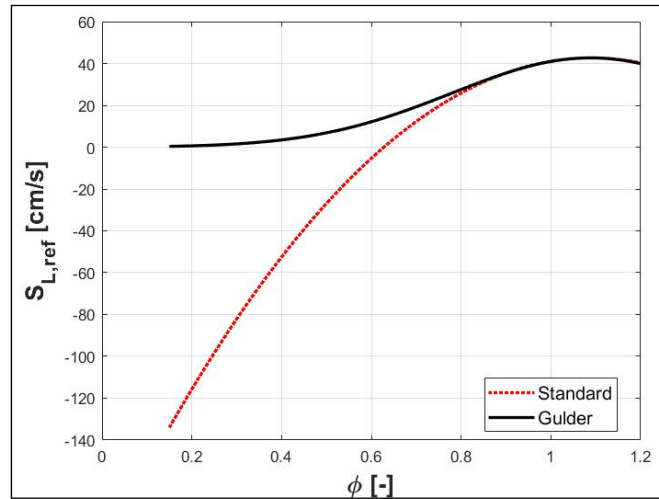
Fig. 4. Reference laminar flame speed vs equivalence ratio for standard [14] and Gülder [16] correlations

Generally, gaseous fuels burn in lean conditions, like in the engine under investigation. As already pointed out in Table 3 the equivalence ratio of air-methane mixture ranges between 0.17 and 0.24, far below 0.6 where the laminar flame speed is passing the zero value. Therefore, under such circumstances the software would provide a negative flame speed and this is not acceptable. For this reason, Gülder proposed an exponential correlation (eq. 10), still illustrated in Figure 4 (black continuous line) that never assumes negative values. The values for the different constants are listed in Table 4.

$$S_{L,0}(\phi) = \omega\phi^\eta exp(-\xi(\phi - \sigma)^2) \tag{10}$$

Table 4. Coefficients of methane [16]

ω [cm/s]	η	ξ	σ
42.2	0.15	5.18	1.075

This correlation can be provided to the software by setting the B_ϕ term equal to 0 so to nullify the second term of the polynomial and by providing to the B_m a matrix, created in Matlab, with the Gülder laminar flame speed values in function of the equivalence ratio.

For hydrogen, the same approach was used. However, the correlations found in literature refers to different conditions than the standard ones. Moreover, particular attention must be paid to the estimation of the laminar flame speed for low equivalence ratio, which in the simulations with hydrogen is even lower than methane's one (Table 3). To overcome this problem, a new correlation must be elaborated. To this scope the values listed by Taylor [25] and Marinov et al. [26], are used as starting point, respectively black circles and red squares displayed in Figure 5.
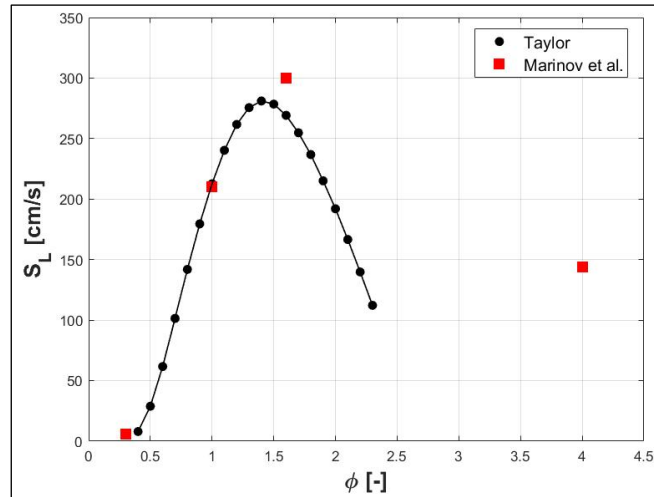
Fig. 5. Hydrogen reference laminar flame speed vs equivalence ratio from Taylor [25] and Marinov et al. [26]

The necessity to use values proposed by Marinov et al. is due to the impossibility to find an exponential correlation that approximates the Taylor curve for the complete range of air/gaseous fuel ratio. Indeed, an exponential correlation seems the right choice link flame speed and equivalence ratio with the aim to avoid negative flame speeds for lean conditions. For these reasons, a first 4th order polynomial is built to follow the trend proposed in [25] (red dotted line in Figure 6) for $\phi > 0.5$ and a second exponential correlation valid for $\phi < 0.5$ is added by integrating the values proposed in [26] (black continuous line in Figure 6). Therefore, two new correlations (eq. 11 and 12) are proposed to describe the laminar flame speed trend with particular attention to the extremely low conditions.

$$S_{L,0}(\phi) = 62.02\phi^4 - 417.85\phi^3 + 728.9\phi^2 - 163.1\phi \qquad \phi = 0.5 \div 2 \qquad (11)$$

$$S_{L,0}(\phi) = 217exp\{-[(\phi - 093)/0.3572]^2\} \qquad \phi = 0 \div 0.5 \qquad (12)$$
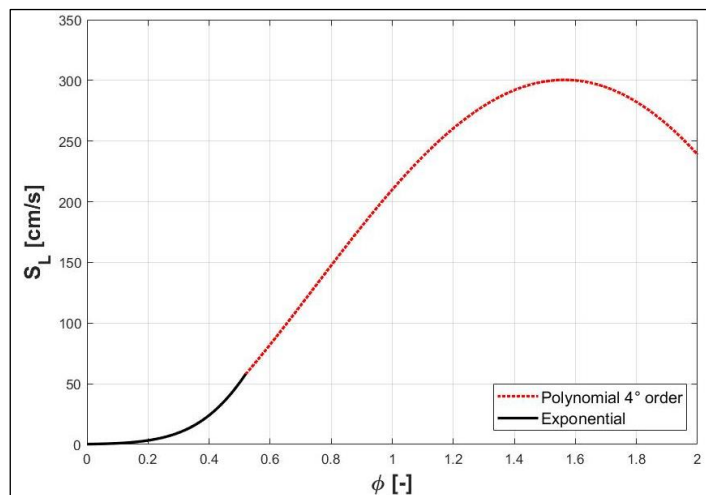
Fig. 6. Hydrogen reference laminar flame speed vs equivalence ratio curve

5. Results

In this section, at first, the validation of dual fuel diesel-methane numerical calculations is presented; then the hydrogen cases are performed using the new presented correlations with the aim to foresee the engine behaviour when supplied with this different gaseous fuel. In particular, the comparison of pressures is necessary to check if the model is capable to provide a good prediction of the original engine performances, while the apparent rate of heat release (RoHR) is a fundamental result to demonstrate that the combustion development is correctly described by the model.

5.1 Diesel-methane model validation

From the comparison of experimental and numerical pressure curves in Figures 7-10 (a) it is possible to observe that the laminar flame model is capable to describe dual fuel combustion. Indeed, among all the cases, only the 1500x5 case shows light differences between the measurements and the calculations. As already illustrated, all the cases have been calibrated to obtain the same air and methane masses, and the correct equivalence ratio as the experimental tests carried out at the bench, considering the blow-by as well. The calibration seems adequate since compression curves perfectly match in each case. Also, with the only exception of the 1500x5 case, the table constants allow to correctly detect the start of diesel fuel ignition, as demonstrated by the fair correspondence of pressure rises. Moreover, the good agreement of the expansion phases evidences the validity of the flame propagation model. This consideration can be confirmed in the 1500x5 case as well, that, although it shows an anticipated start of combustion, the expansion trend follows the experimental one.

Both experimental and numerical apparent rates of heat release, displayed in Figures 7-10 (b), are postprocessed and calculated via the first law of thermodynamic, the energy equation, starting from the pressure curve:

$$\frac{dQ}{dt} = \frac{\gamma}{\gamma - 1} p \frac{dV}{dt} + \frac{1}{\gamma - 1} V \frac{dp}{dt}$$

(13)

Even though simple, equation (13) allows to catch the main details of the development and the different phases of combustion, identifying the role of diesel and methane. From Figures 7-10 (b) it is also possible to observe that an acceptable accordance of overall combustion is achieved, the start of combustion, the maximum intensity, and the duration of the whole process match in all four cases. Again, the 1500x5 case presents some deviations, but it is likely that they are due to the higher noise of the experimental acquisition.
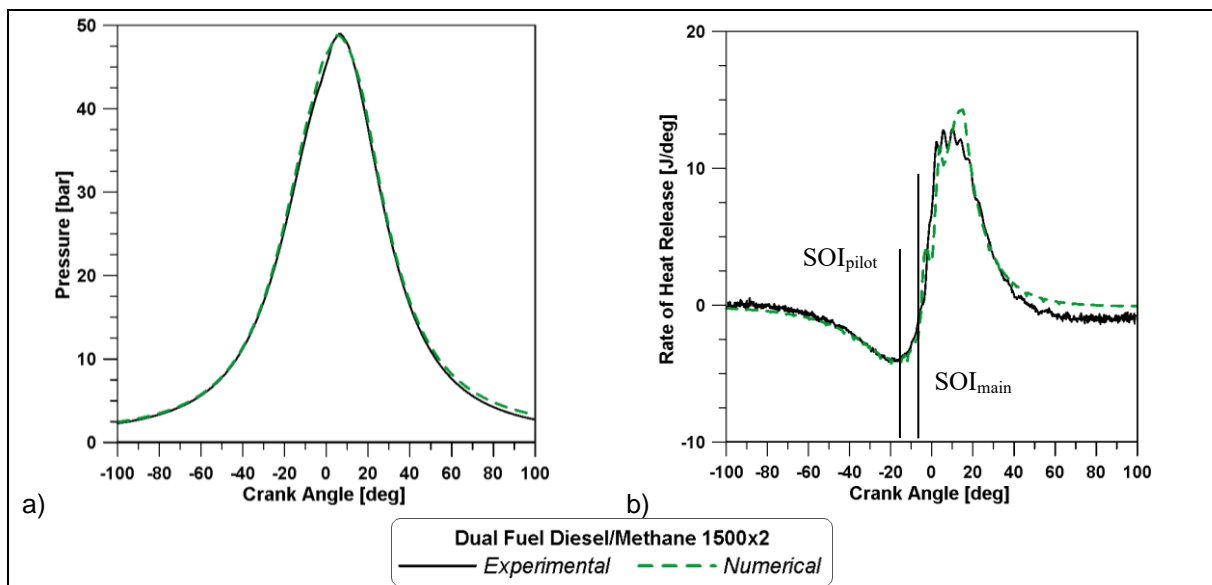
Fig. 7. Experimental and simulated in-cylinder pressures (a) and RoHR (b) for the diesel-methane 1500x2 case
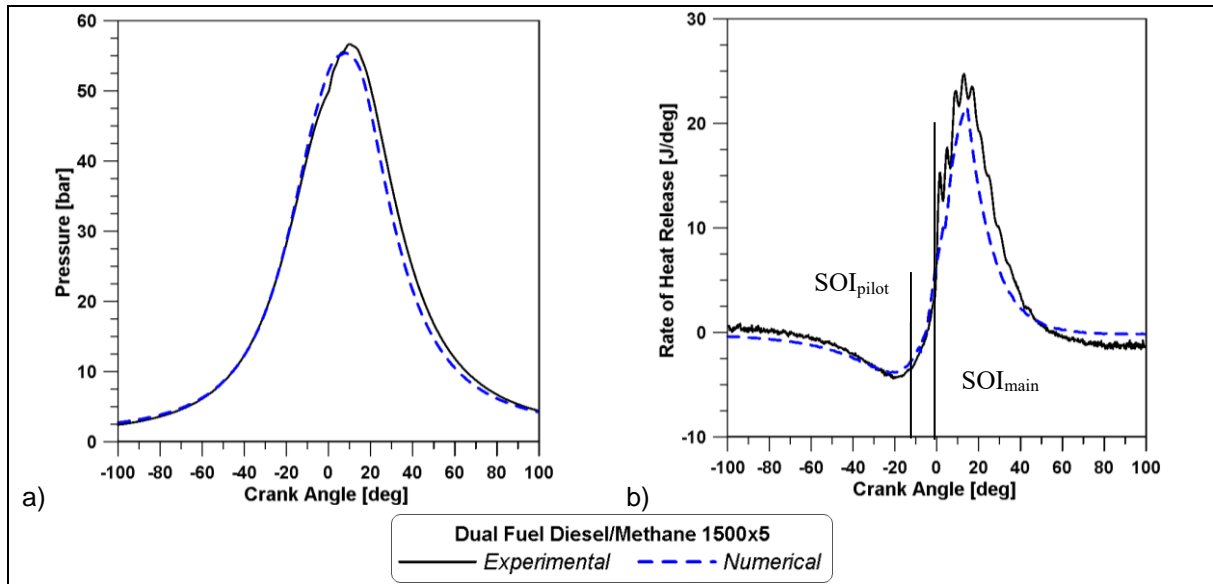
Fig. 8. Experimental and simulated in-cylinder pressures (a) and RoHR (b) for the diesel-methane 1500x5 case
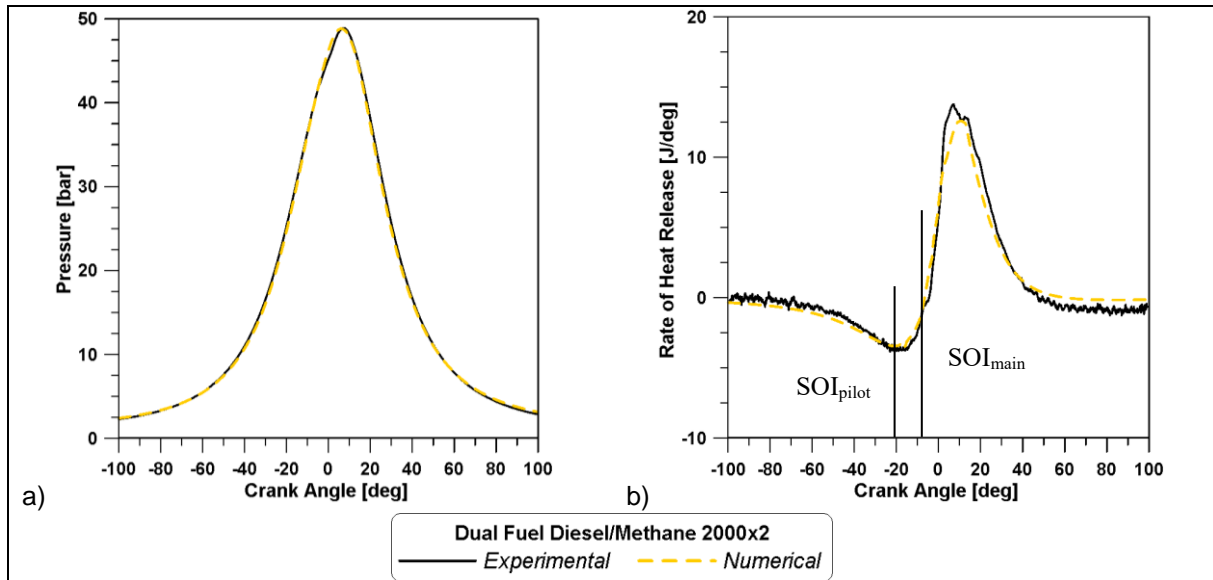
Fig. 9. Experimental and simulated in-cylinder pressures (a) and RoHR (b) for the diesel-methane 2000x2 case
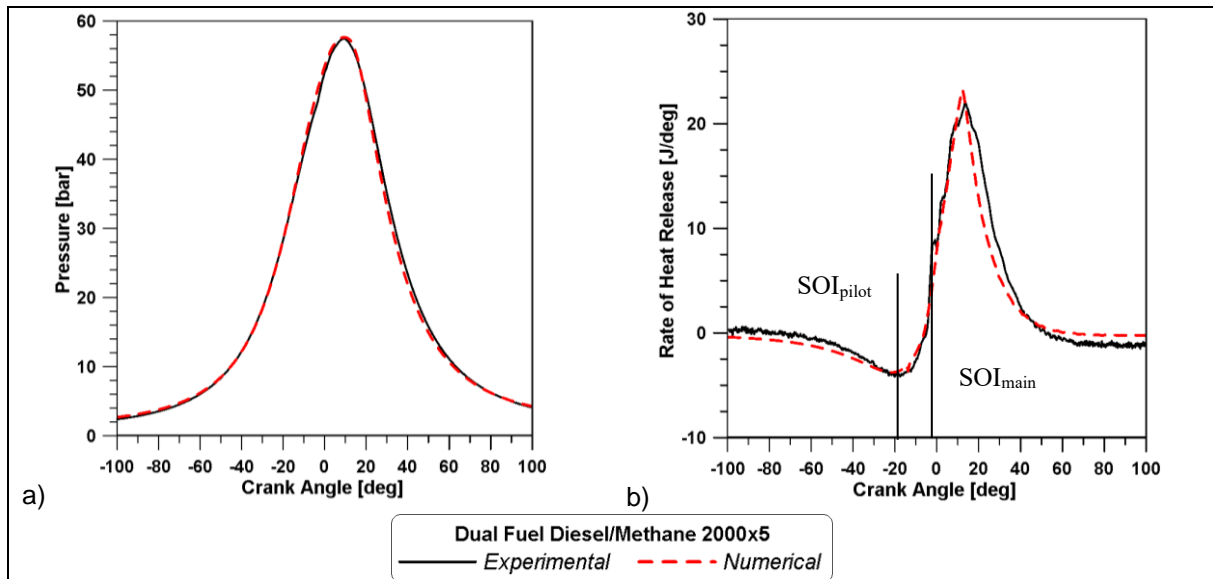
Fig. 10. Experimental and simulated in-cylinder pressures (a) and RoHR (b) for the diesel-methane 2000x5 case

The rates of heat release reveal that combustion can be divided in different parts. Firstly, heat is transferred to the cylinder walls due to the high temperature achieved by the mixture at the end of the compression phase; on the other hand, the vaporization of the injected liquid fuel produces a significant heat subtraction, as observed by the negative values of the RoHR during this phase. Secondly the low temperature reactions are activated and the RoHR starts to increase and assumes a positive value. Then three bumps can be identified: the first two combustion events after the pilot and main injections are mainly due to the diesel combustion, while the third, and largest event, is mainly due to the combustion flame through air-methane premixed mixture. Although more evident in the low engine speed cases (Figures 7(b) and 8(b)), this effect can be seen in both experimental and simulated results, thus illustrating the good model performance. Moreover, the aim to catch the general timing can be considered accomplished. Indeed, it is noted that the major contribution to combustion activation and consequently to the rising slopes of RoHR is associated with the main injection ignition. In all four cases, during this phase the two curves present a satisfying timing agreement and matching slope during the rising phase. The same consideration can be made regarding the peak related to the flame propagation. Even though the model tends to underestimate the RoHR during the compression and overestimate the RoHR during the last part of the expansion, this must be mainly attributed to the uncertainties in the heat transfer calculation during the simulation, and thus it is not due to the combustion model performance.

5.2 Diesel-hydrogen predictions

The numerical results previously illustrated are shown in Figures 11-14 together with simulations relative to the forecasted cases using hydrogen instead of methane. The operating conditions have been already mentioned in Table 3. Figures 11-14 (a) demonstrate that in all cases the use of hydrogen causes a significant enhancement of the peak pressure. A likely explanation is the well-known higher flame speed of hydrogen, that not only leads to a general fast consumption of fuel but to an anticipated increased pressure rise right after the start of pilot ignition.

All the above assumptions are confirmed by the apparent rates of heat release in Figures 11-14 (b). Differently from methane cases, where gaseous combustion was activated by the main injection ignition and three bump could be observed, the high reactivity and fast combustion of hydrogen lead to a massive oxidation process started right after diesel pilot ignition. In each case the experimental and numerical rising slopes of RoHR do not match anymore but a steeper increase is observed when hydrogen is involved. The fast consumption of gaseous fuel accelerates the whole process: a single peak of enhanced intensity is produced reducing the gaseous combustion duration. As consequence of the faster consumption of hydrogen, in all cases the expansion phase is below the corresponding one with methane.
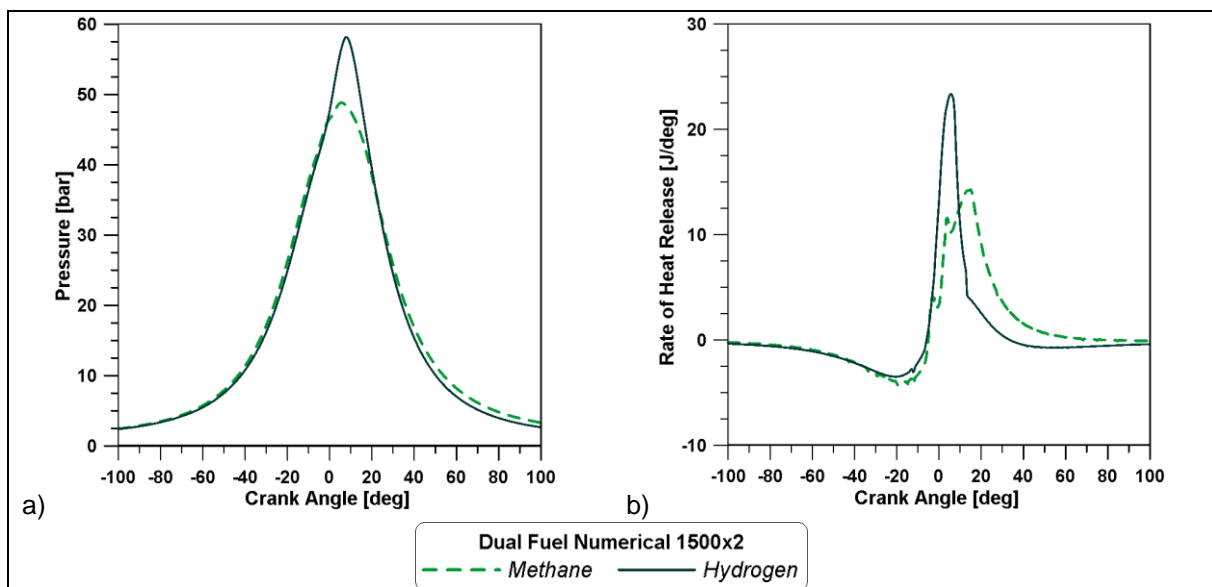
Fig. 11. In-cylinder pressure (a) and Rate of heat release (b) for the DF 1500x2 numerical cases
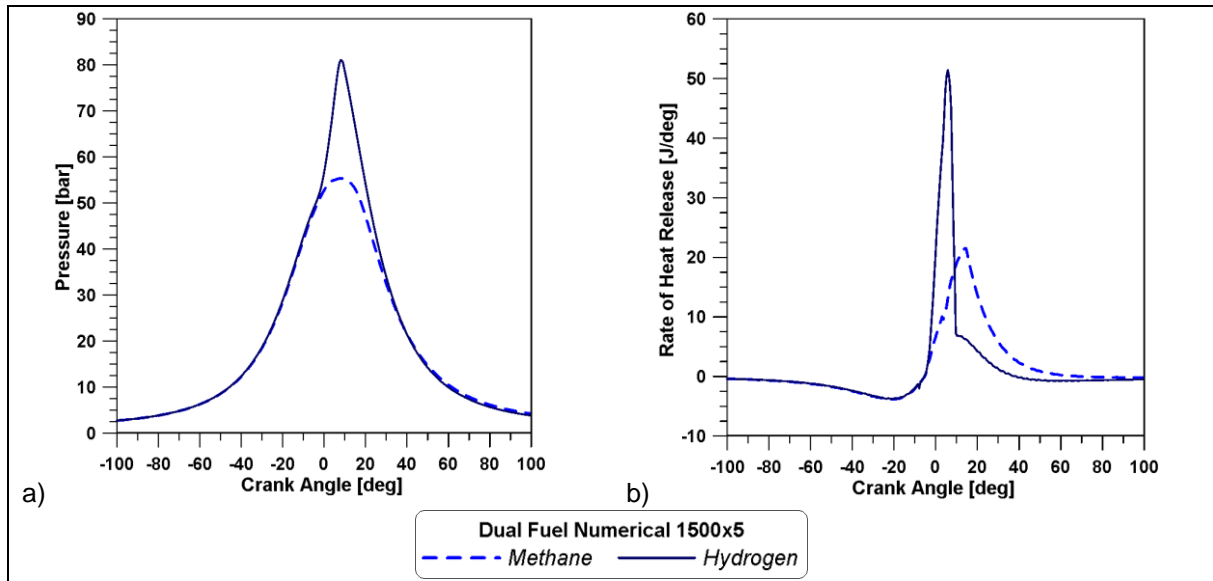
Fig. 12. In-cylinder pressure (a) and Rate of heat release (b) for the DF 1500x5 numerical cases
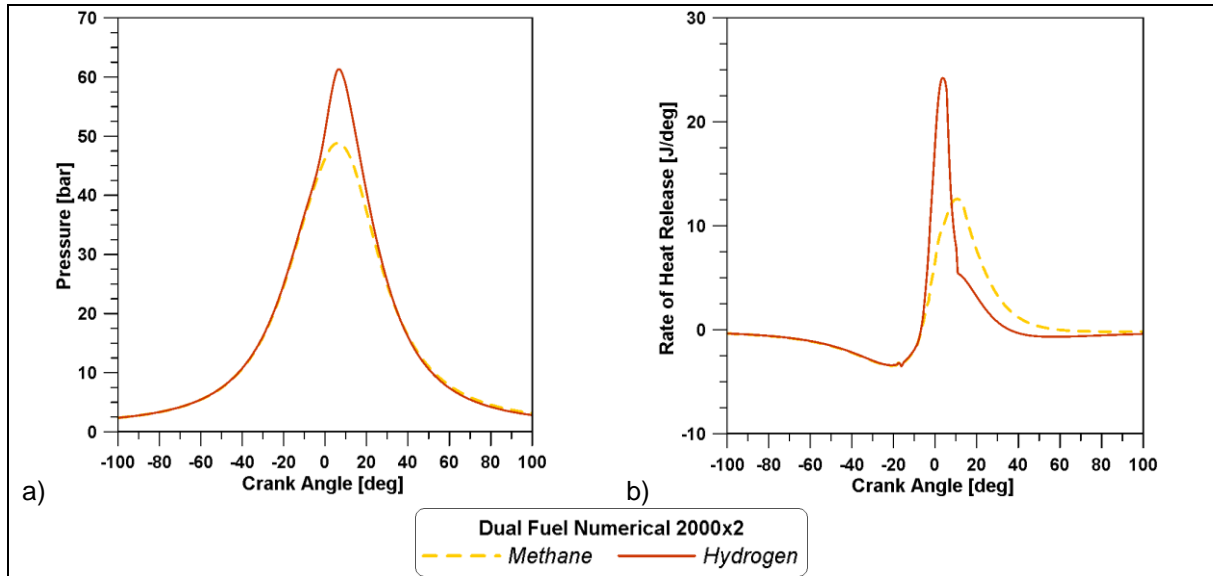
Fig. 13. In-cylinder pressure (a) and Rate of heat release (b) for the DF 2000x2 numerical cases
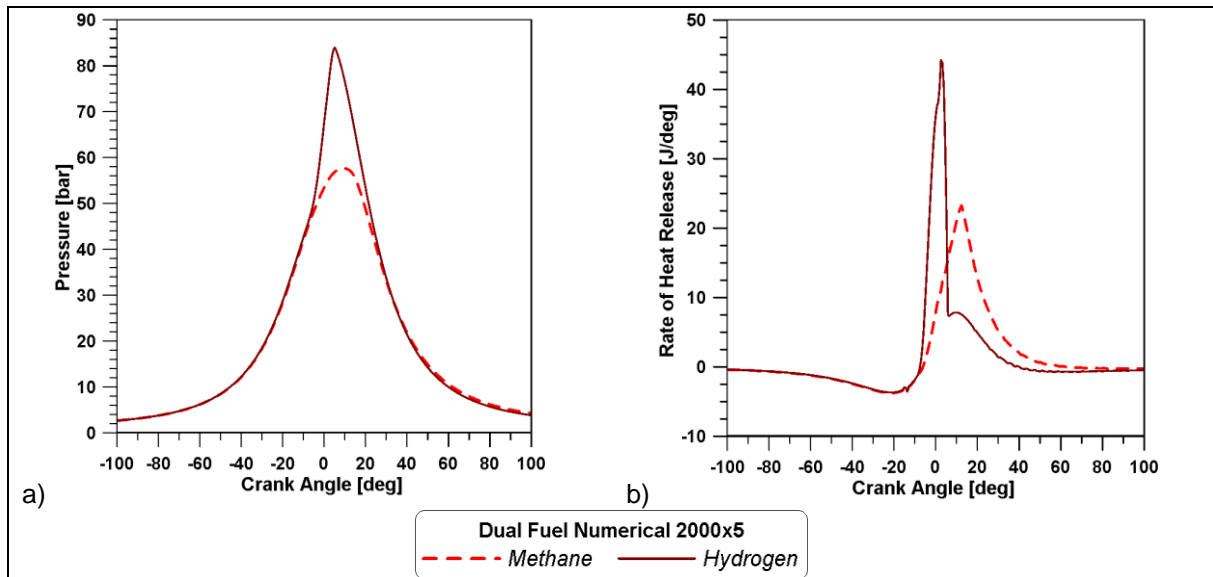
Fig. 14. In-cylinder pressure (a) and Rate of heat release (b) for the DF 2000x5 numerical cases

Conclusions

In the present work, a dual-fuel combustion model was built in GT-Power, with the aim to validate a methodology for the simulation of diesel-methane combustion and to use the same methodology for the prediction of hydrogen-diesel combustion characteristics.

Initially, the model of the dual fuel engine with methane was built and the laminar flame speed model by Gülder for air-methane mixture was incorporated in the software. The validation was obtained through design of experiments and design optimizer in order to match in-cylinder pressure curves measured during an experimental campaign on an optical accessible single cylinder research engine. Experimental tests are characterized by different load levels, 2 and 5 bar of BMEP, and different engine speeds, 1500 and 2000 rpm.

Results demonstrated that the model is capable of reproducing the pressure trends for different loads and speeds. In addition, although the rates of heat release displayed significant differences in terms of intensity, the overall combustion timing showed an acceptable accordance with the measurements' elaborations.

For the simulations with hydrogen two new correlations were built and implemented in the 0D code, one of them specifically accounts for the extremely lean conditions of dual fuel engines operating conditions. Also, the numerical cases are based on an experimental campaign forecasted on the same engine supplied with hydrogen instead of methane at the same BMEP.

The model foresaw a substantial enhancement of pressure levels with the use of hydrogen. They were mainly caused by a strong enhancement of pressure rise rate due to the higher burn velocity, typical of this gaseous fuel. This consideration is also confirmed by rates of heat release, that evidenced how combustion developed in a shorter crank angle interval with respect to the diesel-methane corresponding cases. Therefore, it can be affirmed that this innovative flame model provides results consistent with the characteristics observed on hydrogen combustion.

Funding

References

[1]   *REGULATION (EC) No 595/2009 OF THE EUROPEAN PARLIAMENT AND OF THE COUNCIL,* 18 June 2009.

[2]   *REGULATION (EU) 2019/631 OF THE EUROPEAN PARLIAMENT AND OF THE COUNCIL,* 17 April 2019.

[3]   J. Hu, J. Liao, Y. Hu, J. Lei, M. Zhang, J. Zhong, F. Yan and Z. Cai, "Experimental investigation on emission characteristics of non-road diesel engine equipped with integrated DOC + CDPF + SCR aftertreatment," *Fuel,* vol. 305, no. 121586, 2021, https://doi.org/10.1016/j.fuel.2021.121586.

[4]   W. Lijiang and G. Peng, "A review on natural gas/diesel dual fuel combustion, emissions and performance," *Fuel Processing Technology,* no. 142, p. 264–278, 2016, http://dx.doi.org/10.1016/j.fuproc.2015.09.018.

[5]   E. Mancaruso and B. M. Vaglieco, "Spectroscopic measurements of premixed combustion in diesel engine," *Fuel,* vol. 90, p. 511–520, 2011, doi:10.1016/j.fuel.2010.09.052.

[6]   A. Magno, E. Mancaruso and B. M. Vaglieco, "Combustion Analysis of Dual Fuel Operation in Single Cylinder Research Engine Fuelled with Methane and Diesel," in *SAE Technical Paper 2015-24-2461*, 2015, https://doi.org/10.4271/2015-24-2461.

[7]   S. Di Iorio, A. Magno, E. Mancaruso and B. M. Vaglieco, "Diesel/Methane Dual Fuel Strategy to Improve Environmental Performance of Energy Power Systems," *International Journal of Heat and Technology,* vol. 34, no. 2, pp. S581-S588, 2016, doi: https://doi.org/10.18280/ijht.34S254.

[8]   E. Mancaruso, M. Todino and B. M. Vaglieco, "Study on dual fuel combustion in an optical research engine by infrared diagnostics varying methane quantity and engine speed," *Applied*

Thermal Engineering, vol. 178, no. https://doi.org/10.1016/j.applthermaleng.2020.115623, 2020, https://doi.org/10.1016/j.applthermaleng.2020.115623.

[9]   E. Mancaruso, L. Sequino, B. M. Vaglieco, M. C. Cameretti, R. De Robbio and R. Tuccillo, "CFD Analysis of the Combustion Process in Dual-Fuel Diesel Engine," in *SAE Technical Paper 2018-01-0257*, 2018, doi:10.4271/2018-01-0257.

[10]   R. De Robbio, M. C. Cameretti, E. Mancaruso, R. Tuccillo and B. M. Vaglieco, "CFD Study and Experimental Validation of a Dual Fuel Engine: Effect of Engine Speed," *Energies,* vol. 14, no. 4307, 2021, https://doi.org/10.3390/en14144307.

[11]   R. De Robbio, M. C. Cameretti, E. Mancaruso, R. Tuccillo and B. M. Vaglieco, "Combined CFD - Experimental Analysis of the In-Cylinder Combustion Phenomena in a Dual Fuel Optical Compression Ignition Engine," in *SAE Technical Paper 2021-24-0012*, 2021, doi:10.4271/2021-24-0012.

[12]   R. Amirante, E. Distaso, P. Tamburrano and R. D. Reitz, "Laminar flame speed correlations for methane, ethane, propane and their mixtures, and natural gas and gasoline for spark-ignition engine simulations," *International Journal of Engine Research,* vol. 18, no. 9, p. 951–970, 2017, doi: 10.1177/1468087417720018.

[13]   J. B. Heywood, Internal Combustion Engine Fundamentals., 1988.

[14]   M. Metghalchi, "Burning Velocities of Mixtures of Air with Methanol, Isooctane, and Indolene at High Pressure and Temperature," *Combustion and Flame,* vol. 48, pp. 191-210, 1982.

[15]   Ö. Gülder, "Turbulent Premixed Flame Propagation Models for Different Combus-tion Regimes," in *Syposium on Combustion*, 1990.

[16]   Ö. Gülder, "Correlations of Laminar Combustion Data for Alternative S.I. Engine Fuels," in *SAE Technical Paper 841000, doi:https://doi.org/10.4271/841000*, 1984.

[17]   F. Millo, F. Accurso, A. Piano, G. Caputo, A. Cafari and J. Hyvonen, "Experimental and numerical investigation of the ignition process in a large bore dual fuel engine," *Fuel,* vol. 290, no. 120073, 2021, https://doi.org/10.1016/j.fuel.2020.120073.

[18]   J. Monsalve-Serrano, G. Belgiorno, G. Di Blasio and M. Guzmán-Mendoza, "1D Simulation and Experimental Analysis on the Effects of the Injection Parameters in Methane–Diesel Dual-Fuel Combustion," *Energies,* vol. 13, no. 3734, 2020, doi:10.3390/en13143734.

[19]   C. White, R. Steeper and A. Lutz, "The hydrogen-fueled internal combustion engine: a technical review," *International Journal of Hydrogen Energy,* vol. 31, pp. 1292-1305, 2006, doi:10.1016/j.ijhydene.2005.12.001.

[20]   S. Ravi and E. L. Petersen, "Laminar flame speed correlations for pure-hydrogen and high-hydrogen content syngas blends with various diluents," *International Journal of Hydrogen Energy,* vol. 37, pp. 19177-19189, 2012, http://dx.doi.org/10.1016/j.ijhydene.2012.09.086.

[21]   T. Miyamoto, H. Hasegawa, M. Mikami, N. Kojima, H. Kabashima and Y. Urata, "Effect of hydrogen addition to intake gas on combustion and exhaust emission characteristics of a diesel engine," *International Journal of Hydrogen Energy,* vol. 36, pp. 13138-13149, 2011, doi:10.1016/j.ijhydene.2011.06.144.

[22]   O. Ghazal, "Performance and combustion characteristic of CI engine fueled with hydrogen enriched diesel," *International Journal of Hydrogen Energy,* vol. 38, pp. 15469-15476, 2013, http://dx.doi.org/10.1016/j.ijhydene.2013.09.037.

[23]   V. Chintala and K. Subramanian, "A comprehensive review on utilization of hydrogen in a compression ignition engine under dual fuel mode," *Renewable and Sustainable Energy Reviews,* vol. 70, p. 472–491, 2017, http://dx.doi.org/10.1016/j.rser.2016.11.247.

[24]   O. Ghazal, "Combustion analysis of hydrogen-diesel dual fuel engine with water injection technique," *Case Studies in Thermal Engineering,* vol. 13, no. 100380, 2019, https://doi.org/10.1016/j.csite.2018.100380.

[25]   S. Taylor, "Burning Velocity and the Influence of Flame Stretch," PhD Thesis, University of Leeds, 1991.

[26]   N. Marinov, C. Westbrook and W. Pitz, "Detailed and Global Chemical Kinetics Model for Hydrogen," in *8th International Symposium on Transport Properties*, San Fancisco, CA, 1995.

THIESEL 2022 Conference on Thermo- and Fluid Dynamics of Clean Propulsion Powerplants

The Impact of Diesel-hythane Dual-Fuel Combustion on Engine Performance and Emissions in a Heavy-Duty Engine at Low-Load Condition

K. Longo, X. Wang, H. Zhao

Centre for Advanced Powertrain and Fuels. Brunel University London. Kingston Lane, Uxbridge, Middlesex, UB8 3PH, UK.

E-mail: kevin.longo@brunel.ac.uk
xinyan.wang@brunel.ac.uk
hua.zhao@brunel.ac.uk

Abstract. Heavy-duty diesel vehicles are currently a significant part of the transportation sector, as well as one of the major sources of carbon dioxide (CO_2) emissions. International commitments to reduce greenhouse gas (GHG) emissions, particularly CO_2 and methane (CH_4) highlight the need to diversify towards cleaner and more sustainable fuels. Hythane, a 20% hydrogen and 80% methane mixture, can be a potential solution to this problem in the near future. This research was focused on an experimental evaluation of partially replacing diesel with hythane fuel in a single cylinder 2.0 litres heavy-duty diesel engine operating in the diesel-gas dual fuel combustion mode. The study investigated different gas substitution fractions (0%, 40% and 80%) of hythane provided by port fuel injections at 0.6 MPa indicated mean effective pressure (IMEP) and a fixed engine speed of 1200 rpm. Various engine controls strategies, such as diesel injection timing optimisation, low intake air pressure and exhaust gas recirculation (EGR) addition were employed in order to optimise the dual-fuel combustion mode. The results indicated that by using hythane energy fraction (HEF) of 80% combined with 125 KPa intake air boost and 25% EGR dilution, CO_2 emissions could be decreased by up to 23%, while soot was maintained below Euro VI limit and NOx level was held below the Euro VI regulation limit of 8.5 g/kWh assuming a NOx conversion efficiency of 95% in a SCR system. Nevertheless, net thermal efficiency was compromised by around 6%, while carbon monoxide (CO), unburned hydrocarbon (HC) and methane slip levels were considerably higher, compared to the diesel-only baseline. The use of a pre-injection prior to the diesel main injection was essential to control the heat release and pressure rise rates under such conditions.

1. Introduction

Transportation energy demands account for approximately 20% of global energy consumption and are anticipated to rise by 25% between 2019 and 2050. This is due to an expected increase in the number of vehicles, in particular heavy-duty (HD) vehicles as a result of economic growth [1].

According to the Intergovernmental Panel on Climate Change (IPCC) [2], the combustion of fossil fuels is a major contributor to the global warming by releasing substantial concentration of greenhouse gases (GHG), such as carbon dioxide (CO_2) into the atmosphere. In 2017, HD vehicles were responsible for about 6% of the CO_2 emissions in European Union (EU) [3]. Therefore, this increasing concern about CO_2 has prompted the implementation of new regulations to limit the CO_2 generation in the transportation sector.

Currently, the criterion for the evaluation of internal combustion (IC) engines is their tailpipe emissions [4]. Thereby, a conventional diesel combustion (CDC) engines will thus no longer be able to meet the upcoming strict emission regulations, requiring the employment of new technologies and alternative low and zero carbon fuels. At present, the most intensive research is being conducted on two possibilities. The first is an attempt to completely eliminate the use of fossil fuels in IC engines, while the second is to burn more efficiently with particular attention to exhaust emissions. The latter has been the most common approach in recent years and has contributed to the substantial reduction in pollutant emissions.

Co-combustion of fuels with different properties, often known as dual-fuel (DF) combustion, are capable of reducing both the pollutant and CO_2 emissions when a low carbon fuel is used [5]. In particular, diesel-natural gas dual-fuel compression ignition (CI) combustion has been demonstrated as an effective solution for HD applications thanks to their simplicity of adaptation to existing IC engines [6]. Compressed natural gas or bio-gas can be fed through a port fuel injection (PFI) system in a dual-fuel CI engine to provide a lean and homogeneous distribution of the low reactivity fuel in the combustion chamber, resulting in multiple ignition spots [7]. When compared to a diesel-only operation, this method

allows for reduced local fuel-air equivalence ratios and combustion temperatures, resulting in lower soot and nitrogen oxides (NOx) formation [8]. Another reason for the simultaneous decrease in soot and NOx suggested by Iorio et al. [9] was this combustion mode has a low flame temperature due to a higher ratio of heat capacity of CH_4.

According to Stettler et al. [10], when compared to diesel-only vehicles, lean-burn CNG dual-fuel vehicles reduced CO_2 emissions by up to 9%. This conclusion was obtained after studying the energy consumption, greenhouse gas emissions, and pollutants produced by five aftermarket dual-fuel engine configurations in two vehicle platforms.

In fact, both the diesel injection timing and the properties of low reactivity fuel have a significant impact on DF combustion operation, affecting both engine performance and exhaust emissions [11, 12]. With increasing diesel injection advance, NOx increased while carbon monoxide (CO) and soot emissions were reduced [11]. Moreover, Pedrozo et al. [13] concluded that the combination of reactivity-controlled compression ignition (RCCI) and late intake valve closing (LIVC) can reduce methane slip and also NOx emissions up to 80%.

Though, due to the properties of methane (CH_4), diesel-gas dual-fuel combustion has some drawbacks, such as slower flame propagation, which results in longer combustion duration and, as a result, lower efficiency [14]. Also, this combustion mode is frequently accompanied by unburned CH_4 emission, also known as methane slip [13]. CH_4 is a GHG with 28 times higher global warming potential (GWP) than CO_2 emission over a 100-year lifetime [15].

When produced from renewable sources, hydrogen, on the other hand, has no carbon and is a clean and environmentally friendly fuel [16]. Nonetheless, when hydrogen is burned on its own, it is associated with a number of undesirable effects, such as engine knocking, pre-ignition, and backfire. By that, the usage of hydrogen blended with methane, commonly known as hythane, has the potential to mitigate the problems associated with sperate CH_4 and hydrogen combustion [14]. The higher reactivity of the hydrogen improves combustion stability, resulting in lower unburned CH_4 [17]. Graham et al. [18] indicated that hythane can provide a 10%-20% decrease in GHG levels, namely CO_2 emissions at the tailpipe when compared with diesel. However, this reduction is only relevant when the hydrogen is produced from renewable sources.

Because of the higher flame temperature of hydrogen, NOx concentration increases with hydrogen addition for a given air-fuel ratio, whereas CO and HC levels decrease [19, 20]. Nevertheless, Talibi et al. [14] has noted a different trend by investigating the effect of hythane enrichment with diesel pilot injection in a conventional CI engine. It was found that CO and HC were significantly higher while employing diesel-hythane dual-fuel (DHDF) mode. Furthermore, a considerable reduction of PM emissions was achieved compared to CDC. Tutak et al. [21] tested various compositions of hydrogen and CNG in a diesel engine and concluded that the addition of hydrogen accelerated combustion, shortening the duration of the combustion event. Additionally, it was also found that higher hydrogen and CNG fractions resulted in an increase in peak pressure and temperature as well as higher NOx emissions.

The use of EGR has been proven as an effective method to extend DF operation. This is associated with a reduction in combustion temperature as a result of the increased specific heat capacity and dilution level of the in-cylinder charge [22, 23]. This delays the ignition time of the premixed fuel and hence allows to decrease the levels of PRR and NOx emissions during dual-fuel operation [24]. Moreover, flame stability improves in the presence of EGR at various air-fuel ratios [25, 26]. Nonetheless, Qian et al. [27] conducted a study on a hydrogen-enriched diesel combustion and determined that increasing EGR levels reduced thermal efficiency at all load engine settings. On the other hand, as the combustion temperature reduces as the air-fuel ratio increases, combining hydrogen addition with higher air-fuel ratios, i.e. greater intake air pressures, can lead to a decrease in NOx emissions. [20, 28].

In general, hythane with hydrogen concentrations ranging from 0% to 20% by volume can be run in IC engines without significant modification to engine hardware [29]. The majority of previous works have been mainly focused on the impact of hythane composition mixture on the combustion process and NOx concentration, with very limited research and discussion on the potential of high hythane energy fraction (HEF) on carbon emission reduction, such as CO_2 and CH_4. Therefore, the current study, which was conducted on a single-cylinder heavy-duty diesel engine with port fuel injected hythane at an engine load of 0.6 MPa indicated mean effective pressure (IMEP), aims to explore the engine performance as well as the CO_2 reduction potential by using a HEF of up to 80%. Advanced engine and combustion control strategies, such as late diesel injection, intake air pressure and EGR dilution were explored to identify the optimum strategies for minimum GHG emissions of CO_2 and CH_4 without harming net thermal efficiency and NOx emissions. The optimised DHDF results were then compared to the conventional diesel only and a baseline diesel-hythane dual fuel operations.

2. Experimental setup

2.1 Engine setup and specifications

A schematic diagram of the single cylinder compression ignition engine experimental setup is illustrated in Fig. 1. An eddy current dynamometer was used to absorb the power produced by the engine. An external compressor supplied fresh intake air to the engine, which was controlled by a closed-loop system for boost pressure. The intake manifold pressure was precisely controlled by a throttle valve positioned upstream of a surge tank. A thermal mass flow metre was used to measure the air mass flow rate ($\dot{m}_{air}$). A water-cooled heat exchanger was used to regulate the temperature of the boosted air. To mitigate pressure oscillations, another surge tank was installed in the exhaust manifold. The required exhaust manifold pressure was set using an electrically controlled backpressure valve placed downstream of the exhaust surge tank.
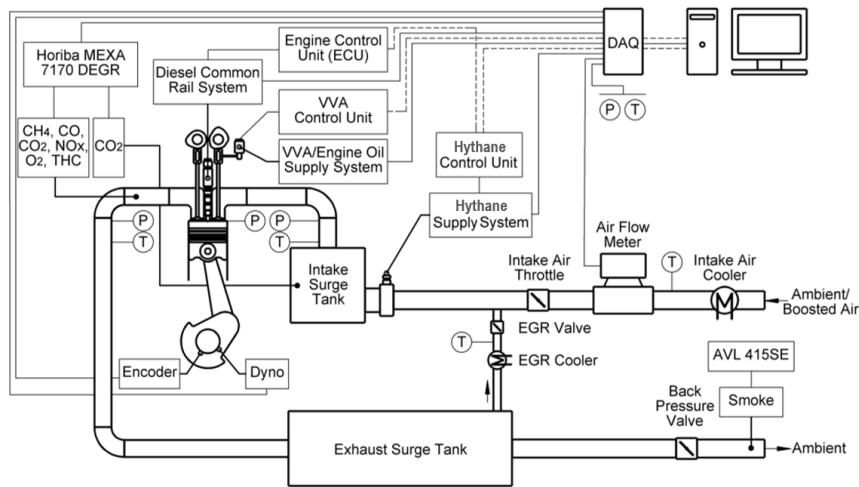
Fig. 1: Schematic diagram of the dual-fuel engine experimental setup.

Table 1 shows the HD engine hardware specifications. A 4-valve swirl-oriented cylinder head and a stepped-lip piston bowl design constituted the combustion system. Separate electric motors controlled the coolant and oil pumps. Throughout the experiments, the engine coolant and oil temperatures were set to 80°C, and the oil pressure was kept at 400 kPa.

Table 1: Single cylinder HD engine specifications.

Parameter	Value
Bore/stroke	129/155 mm
Connecting rod length	256 mm
Displaced volume	2026 cm^3
Clearance volume	128 cm^3
Geometric compression ratio	16.8
Maximum in-cylinder pressure	18 MPa
Piston type	Stepped-lip bowl
Diesel injection system	Bosch common rail, injection pressure of 30-220 MPa, 8 holes, 150° spray
Hythane port fuel injection system	G-Volution controller and two Clean Air Power injectors SP-010, injection pressure of 800kPa

Furthermore, the engine also included a prototype hydraulic lost-motion variable valve actuation (VVA) system on the intake camshaft. This allows for the intake valve closing (IVC) to be adjusted, enabling for a decrease in the effective compression ratio (ECR). This reduces compression pressures and temperatures, as well as the mass trapped in the cylinder at a given boost pressure.

However, in order to simplify the experimental investigation, intake valve timings were kept constant at baseline values throughout the experiments, with its intake valve opening (IVO) at -330 ± 1 crank angle degrees (CAD) and IVC at -187 ± 1 CAD.

2.2 Fuel supply and proprieties

In this study, hythane gas was employed as the premixed fuel of the dual-fuel combustion and it is composed of 80% methane and 20% hydrogen gas mixture (molar).

Hythane gas was stored in a rack of six interconnected 20 MPa bottles outside of the engine test cell. Specially developed hoses for the conveyance of CNG have been used, as they are constructed of a conductive nylon core designed to dissipate static build-up. From there, Hythane was fed into a pair of pneumatically controlled safety valves, a high-pressure filter and a high-pressure regulator that dropped the gas pressure to 1 MPa. The pressure regulator was kept constant by the hot engine coolant to counteract the reduction in temperature experienced by the gas during expansion.

After flowing through the high-pressure regulator, hythane was fed into the test cell into an Endress + Hauser Promass 80A Corilis flow meter. After this mass flow meter, a low-pressure filter, a purge/pressure regulator that adjusted the final hythane pressure to 0.8 MPa, and an emergency shut-off valve were connected, before a flex hose connected the gas stream to the injector block. The injector block, designed for NG application, was installed upstream of the intake surge tank to facilitate the mixing of the fuel gas with the intake air. An injector driver controls the pulse width of the gas injectors and allowed the engine to run at different HEF by altering the hythane mass flow rate ($\dot{m}_{hythane}$).

The high-pressure common rail diesel injection system, which can provide up to three injections per cycle, was controlled by a dedicated engine control unit (ECU). The diesel mass flow rate ($\dot{m}_{diesel}$) was determined using two Endress + Hauser Promass 83A Corilis flow meters by measuring the total fuel supplied to and from the diesel high-pressure pump and injector.

During the dual-fuel operation, the bulk fuel mass of port fuel injected hythane was ignited by direct injected diesel. Table 2 lists the key properties of the diesel and hythane utilised in this experiment.

Table 2: Fuel proprieties of diesel and hythane.

Property	Unit	Diesel	Hythane
General proprieties			
Lower heating value (LHV)	MJ/kg	42.9	63.8
Stoichiometric air-fuel ratio (AFR)	-	14.5	20.6
Gas density	kg/m^3	-	0.4589
Cetane number	-	> 45	< 5
Liquid density (101.325 kPa, 20°C)	kg/dm^3	0.827	-
Gas composition (mole fraction)			
Methane (CH_4)	%	-	80.0
Hydrogen (H_2)	%	-	20.0
Fuel contents (mass fraction)			
Carbon (%C$_{fuel}$)	%	86.6	72.6
Hydrogen (%H$_{fuel}$)	%	13.2	27.4
Oxygen (%O$_{fuel}$)	%	0.2	-
Calculated carbon intensity			
Assuming the complete conversion of hydrocarbon fuel into CO_2	%CO_2/MJ	73.9	52.1
Maximum theoretical CO_2 reduction considering a constant brake efficiency	%	-	29.5
Estimated CO_2 reduction with a HEF = 80%	%	-	23.6

An important parameter for the dual-fuel operation is the hythane energy fraction (HEF), which is given by the ratio of the energy content of the hythane injected to the total fuel energy supplied to the engine. As shown in Table 2, using a HEF of 80% can minimise exhaust CO_2 emissions by approximately 24% when hydrocarbon fuel is completely converted into CO_2.

$$HEF = \frac{\dot{m}_{hythane} LHV_{hythane}}{\dot{m}_{hythane} LHV_{HCNG} + \dot{m}_{diesel} LHV_{diesel}} \tag{1}$$

where: $\dot{m}_{diesel}$ and $\dot{m}_{hythane}$ the mass flow rate of diesel and hythane, respectively; LHV$_{diesel}$ and LHV$_{hythane}$ the lower heating value of diesel and hythane, respectively.

2.3 Exhaust emissions measurements and analysis

An AVL 415SE smoke metre was used to measure the smoke number downstream of the exhaust back pressure valve. The measurement was taken in filter smoke number (FSN). Other exhaust emissions, such as CO_2, CO, CH_4, HC, and NOx, were monitored using a heated line on a Horiba MEXA-7170 DEGR emission analyser located in the exhaust pipe before the exhaust back pressure valve. The concentration of these gaseous emissions in the exhaust stream was measured in parts per million (ppm). All the exhaust gas components were then converted to net indicated specific gas emissions in g/kWh, according to Regulation No. 49 of UN/ECE [30]. The following is an example of the CO_2 conversion calculation:

$$ISCO_2 = \frac{\dot{m}_{CO_2}}{P_{ind}} = \frac{u_{CO_2}\,[CO_2]\,\dot{m}_{exh}}{P_{ind}} \tag{2}$$

where: u_{CO_2} the raw exhaust gas constant; $[CO_2]$ the concentration of CO_2 in ppm; $\dot{m}_{exh}$ the total exhaust mass flow rate; P_{ind} the engine net indicated power calculated from the measured IMEP

The aforementioned regulation also required that NOx and CO emissions be converted to a wet basis by using a raw exhaust gas correction factor that is dependent on the in-cylinder fuel mixture composition. In addition, the measurement of the HC was performed on a wet basis by a heated flame ionisation detector (FID), while CO and CO_2 were measured through a non-dispersive infrared absorption (NDIR). A chemiluminescence detector (CLD) was used to quantify NOx emissions. In this study, the EGR rate was defined as the ratio of the measured CO_2 concentration in the intake surge tank to the CO_2 concentration in the exhaust manifold.

2.4 Data acquisition and analysis

Two National Instruments data acquisition (DAQ) cards linked to a computer were used to acquire the signals from the measurement devices. The crank angle resolution data was sent to a USB-6251 high-speed DAQ card, which was synchronised with an optical encoder with 0.25 CAD resolution. The low-frequency engine operation conditions were recorded using a USB-6210 low-speed DAQ card. An in-house designed DAQ software and combustion analyser displayed this data in real time.

Temperatures and pressures at relevant points were measured using K-type thermocouples and pressure gauges, respectively. Intake and exhaust manifold pressures were measured by two Kistler 4049A water-cooled piezoresistive absolute pressure sensors coupled to Kistler 4622A amplifiers. The in-cylinder pressure was measured by a Kistler 6125C piezoelectric pressure sensor coupled with an AVL FI Piezo charge amplifier.

The crank angle-based in-cylinder pressure traces were averaged over 200 consecutives cycles for each operating point and used to calculate the IMEP. It was also used to obtain the apparent net heat release rate (HRR), following Heywood's equation [31]

$$HRR = \frac{dQ}{d\theta} = \frac{\gamma}{\gamma - 1} p \frac{dV}{d\theta} + \frac{1}{\gamma - 1} V \frac{dp}{d\theta} \tag{3}$$

where: p the in-cylinder pressure; V the in-cylinder volume; γ the ratio of specific heats; θ the CAD.

Due to the fact that the absolute value of the heat released is less essential in this study than the bulk shape of the curve to crank angle, a constant γ of 1.33 was assumed throughout the engine cycle.

The mass fraction burned (MFB) was estimated by the ratio of the integral of the HRR to the maximum cumulative heat release. Combustion phasing was determined by the crank angle of 50% (CA50) MFB. Combustion duration was represented by the period between the crank angles of 10% (CA10) and 90% (CA90) cumulative heat release.

The ignition delay was defined as the period between the start of diesel main injection (SOI_2) into the combustion chamber and the start of combustion (SOC), which was set to 2% MFB. The average in-cylinder pressure and resulting HRR were smoothed using a Savitzky-Golay filter, after the combustion characteristics and ignition delay were estimated.

The pressure rise rate (PRR) was calculated as the average of the maximum pressure variations over 200 cycles of in-cylinder pressure versus crank angle. The coefficient of variation of IMEP (COV_IMEP) was determined using the set of IMEP values from the 200 sampled cycles of the test engine.

$$COV_{IMEP} = \frac{\sigma_{IMEP}}{\overline{IMEP}} \times 100\% \qquad (4)$$

where: σ_{IMEP} the standard deviation of IMEP; $\overline{IMEP}$ the mean of IMEP.

The mean in-cylinder gas temperature at any crank angle position was computed using the ideal gas law [31].

The electric current signal sent from the ECU to the diesel injector solenoid was measured using a current probe. The signal was corrected by adding the energising time delay that had previously been measured in a constant volume chamber. The resulting diesel injector current signal allowed the diesel injections be determined.

The net thermal efficiency was classified as the ratio of work done to the rate of fuel energy supplied to the engine, as shown below:

$$Net\ thermal\ efficiency = \frac{3.6P_{ind}}{\dot{m}_{hythane}LHV_{hythane} + \dot{m}_{diesel}LHV_{diesel}} \qquad (5)$$

where: P_{ind} the engine net indicated power calculated from the measured IMEP.

Combustion efficiency calculations were based on the emissions products not fully oxidised during the combustion process except soot as:

$$Combustion\ efficiency = 1 - \frac{P_{ind}}{1000} \times \left[\frac{ISCO\ LHV_{CO} + ISHC\ LHV_{hythane}}{\dot{m}_{hythane}LHV_{hythane} + \dot{m}_{diesel}LHV_{diesel}}\right] \qquad (6)$$

where: LHV_{CO} is equivalent to 10.1 MJ/kg [31].

Combustion losses associated with HC emissions were thought to be caused entirely by unburned hythane fuel. This is a conservative approach since the $LHV_{hythane}$ is higher than the LHV_{diesel}.

At last, the λ (air-fuel ratio) was determined as follows:

$$\lambda = \frac{\dot{m}_{air}}{\dot{m}_{hythane} + \dot{m}_{diesel}}$$

3. Test methodology

The experimental testing was carried out under steady-state at an engine load of 0.6 MPa IMEP and a constant engine speed of 1200 rpm. That load is equivalent to 25% of the full engine load, which represents a high residency area in a typical HD vehicle drive cycle, such as WHSC. Fig. 2 depicts the location of this test point on an estimated speed and load map.
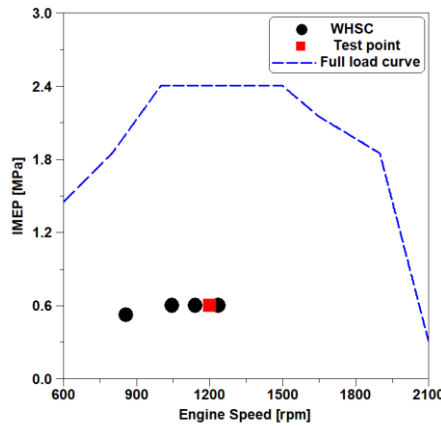
Fig. 2: The selected test point over the experimental HD engine speed-load map.

Table 3 summarises the engine test conditions for the CDC, baseline DHDF and optimised DHDF operation modes. The first part of the experiments comprised a comparison on engine emissions and performance between the two aforementioned combustion modes by varying the HEF. This comparison was carried out using a constant baseline late diesel injection. Both COV$_{IMEP}$ and PRR were used to define the HEF limit, which was approximately 80%, resulting in an overall combustion mixture of 20%

diesel, 64% methane, and 16% hydrogen. Also, the intake and exhaust air pressure set-points from a Euro V compliant multi-cylinder HD diesel engine were used in order to provide a sensible starting point.

Other experiments were carried out to obtain the engine calibration for optimised DHDF combustion mode. This optimisation included the sweep of several engine control parameters, namely diesel injections timing, intake air pressure (P_{int}), and EGR rate. As a result, an optimal point was reached that achieved with the best trade-off between the GHG emissions (CO_2 and CH_4) and the net thermal efficiency whilst keeping the engine-out NOx of less than 8.5 g/kWh. This NOx level was necessary in order to achieve a Euro VI emissions compliance with a NOx conversion of approximately 95% in the selective catalyst reduction (SCR) system.

Throughout the experiments, exhaust pressures were adjusted to provide a constant pressure differential of 10 kPa above the intake air pressure to achieve a fair comparison with equivalent pumping work and to realise the required EGR rate. Intake air temperature was maintained constant at 35°C during all the experiments by using an air-to-water cooler and intake air heater. A diesel pre-injection (SOI_1) with an estimated volume of 3 mm^3 and a constant delay time of 1.1ms (7.92 CAD at 1200 rpm) before SOI_2 was employed to reduce the levels of PRR. Moreover, the diesel main injection timings were optimised to achieve the highest net thermal efficiency in DHDF combustion mode. However, it is worth noting that during this optimisation, the hythane supply was maintained constant while the diesel was automatically adjusted by the ECU in order to achieve the same IMEP, resulting in a slightly HEF variation (around 4%). The limits of the highest average in-cylinder pressure (P_{max}) and the maximum PRR were set to 18 MPa and 2.0 MPa/CAD, respectively. Finally, the COV_IMEP of 3% limit was used to determine stable engine operation.

Table 3: Engine testing conditions.

Parameter	Unit	CDC	Baseline DHDF	Optimised DHDF
Engine load (IMEP)	MPa	0.6	0.6	0.6
Engine speed	rpm	1200	1200	1200
Diesel injection strategy	-	Pre- and main injection	Pre- and main injection	Pre- and main injection
Diesel SOI_2	CAD ATDC	-5	-5	Sweep
Diesel injection pressure	MPa	100	100	100
Intake air pressure (P_{int})	kPa	125	125	Sweep
Exhaust air pressure	kPa	135	135	Sweep
Intake air temperature	°C	35 ± 1	35 ± 1	35 ± 1
ECR	-	16.8	16.8	16.8
HEF	%	0	Sweep	~80
EGR	%	0	0	Sweep

Regarding the control of GHG and pollutant emissions from DF combustion engines, Regulation No. 49 of the United Nations Economic Commission for Europe (UN/ECE) [30] enhances the Euro VI emissions standards for on-road HD vehicles by establishing five different types of dual-fuel engines. For the sake of clarity, this study will focus on the evaluation of Type 2B heavy-duty dual-fuel (HDDF) engines. These operate in the hot section of the World Harmonised Transient Driving Cycle (WHTC), with an average gas energy fraction (GEF_WHTC) ranging from 10% to 90%, while still enabling for diesel-only engine operation.

The Euro VI emissions standards for Type 2B HDDF engines are shown in Table 4 for both the stationary (WHSC) and transient (WHTC) test cycles. It is worth noting that, with the exception of the HEF experiment, all optimised DHDF experiments used the highest HEF with the goal of maximising hythane utilisation, which contributed to achieve a GEF_WHTC of more than 68%.

Table 4: Euro VI emissions limits for Type 2B heavy-duty dual-fuel engines

Emission	Unit	WHSC	WHTC (GEF%_WHTC > 68%)
Nitrogen oxides (NOx)	g/kWh	0.40	0.46
Carbon monoxide (CO)	g/kWh	1.50	4.00
Particulate matter (PM)	g/kWh	0.01	0.01
Total unburned hydrocarbon (HC)	g/kWh	0.13	-
Methane (CH_4)	g/kWh	-	0.50

4. Results and discussion

4.1 The impact of HEF

In this study, a baseline diesel main injection at -5 CAD ATDC (after top dead centre) with a small diesel pre-injection to attenuate COV_{IMEP} and PRR were employed for different HEF, varying from 0% (diesel-only) to a maximum value of 80%. Because of the exponential growth of PRR, which caused strong knocking, unstable combustion (high COV_{IMEP}) was observed for HEF higher than 80%. Additionally, this experiment was performed without EGR and with a constant intake air pressure of 125 kPa.

Table 5 shows the engine performance, combustion characteristics and indicated specific exhaust emissions whereas Fig. 3 depicts the in-cylinder pressure, mean in-cylinder gas temperature, HRR and MFB traces, for CDC and DHDF operations. As seen in Table 5, increasing the HEF resulted in a 15% reduction in CO_2 emissions for a HEF of 80%. This was expected of the addition of hydrogen into the combustion, because the low reactivity port injected fuel has a lower carbon composition than diesel, as shown in Table 2. Nonetheless, methane slip rose dramatically as HEF increased. This was mainly attributed to the two following reasons. First, hythane is mainly composed by methane, resulting in increased unburned CH_4 levels in the exhaust pipe from the crevices. Second, the inclusion of hythane resulted in a longer ignition delay, in other words, a later SOC, due to the fact that the premixed charge has a lower cetane number comparing to CDC. This aspect, combined with the slower flame propagation speed of methane that results in a longer combustion duration (CA10-CA90) [6], and a lower and longer HRR peak (Fig. 3), resulting in an increase in unburned CH_4 and HC, and as a consequence, a reduction of combustion efficiency [14]. The slower combustion rate can be seen in the MFB trace, which is also shown in Fig. 3, with a clear delay of CA50. This lower combustion efficiency had a direct impact on the loss in net thermal efficiency of roughly 20% at 80% HEF.

The increase in CO generated by the addition of hythane, on the other hand, can be explained by the longer mixing time, as SOC-SOI_2 is longer. The probable reason is the lower availability of oxygen (lower λ as shown in Table 5). One possible solution could be the introduction of higher boost pressure, which it would lead to higher λ.

Moreover, a minor increase in NOx was seen with increasing HEF percentage. This is explained in part by the presence of hydrogen, which has a higher flame temperature, resulting in a larger peak in-cylinder gas temperature, as shown in Fig. 3. As the result, DHDF produced higher exhaust temperature. Specifically, the DHDF operation with 80% HEF yielded a higher exhaust gas temperature (EGT) by about 32°C higher than that measured for CDC. This level of temperature is more favourable for the methane oxidation catalyst (MOC) used in DF engines, since the device typically requires an EGT of more than 400°C for high CH_4 conversion efficiency, and hence a reduction in methane slip [32, 33]. Furthermore, at the maximum HEF, soot emissions were slightly reduced, as shown in Table 5. This is likely because diesel fuel contributed for only 20% of total energy supplied to the engine, resulting in lower local fuel-air equivalence ratios [8].

Table 5: The impact of HEF on low engine load operation.

Parameter	Unit	HEF = 0%	HEF = ~40%	HEF = ~80%
SOI_2	CAD ATDC	-5	-5	-5
COV_{IMEP}	%	2.07	2.37	2.54
PRR	MPa/CAD	0.55	0.56	0.44
P_{max}	MPa	7.54	7.38	6.85
EGT	°C	359	385	391
SOC-SOI_2	CAD	6.4	6.8	7.2
SOC	CAD ATDC	0.9	1.3	1.7
CA50	CAD ATDC	9.1	9.2	11.4
CA10-CA90	CAD	21.1	24.6	25.2
λ	-	2.60	2.22	1.99
Net Thermal Efficiency	%	44.2	38.9	35.2
Combustion Efficiency	%	99.5	95.5	93.1
$ISCO_2$	g/kWh	665.7	621.5	565.6
ISNOx	g/kWh	7.7	8.6	8.9
ISsoot	g/kWh	0.0169	0.0193	0.0152
ISCO	g/kWh	1.2	7.7	9.0
ISHC	g/kWh	0.7	7.0	11.2
$ISCH_4$	g/kWh	0.7	7.6	12.0

In terms of the combustion process, Fig. 3 indicates that increasing the HEF resulted in a decrease in the in-cylinder pressure. This can be explained by the slower propagation speed of methane [6], the major compound in the mixture.

However, it was observed in Fig. 3 that the peak of HRR in DHDF was earlier than that in CDC. And on this event, the addition of hydrogen can possibly increase the reactivity of the fuel mixture, leading to earlier peak of the heat release rate. In addition, it can be seen that there was a small heat release of the pre-injected diesel (SOI_1) before SOI_2, which was visible only in the DF combustion mode. This can be further explained by the increased reactivity of the fuel mixture by adding hydrogen.

Fig. 3: In-cylinder pressure, mean in-cylinder gas temperature, HHR and MFB for low engine load operation with various HEF.

4.2 The effect of diesel main injection (SOI_2)

In this study, diesel injection timing was investigated in order to analyse its influence on exhaust emissions and engine performance with 80% HEF. Diesel pre- and main injections were used in a DHDF engine. The experiment was performed without EGR and with a constant intake air pressure of 125 kPa.

Fig. 4, Fig. 5 and Fig. 6 show indicated specific exhaust emissions, engine performance and combustion characteristics for different HEF respectively, while the in-cylinder pressure, mean in-cylinder gas temperature, HRR and MFB traces of 3 different SOI_2 at approximately 80% HEF were depicted in Fig. 7.

Although CO_2 emissions decreased with more advanced SOI 2, which can be explained in part by a shorter combustion period near top dead centre (TDC), the main reason was the lower diesel consumption. This smaller $ISFC_{diesel}$, as seen in Fig. 4, can be explained by the ECU's automatic diesel amount adjustment to maintain IMEP constant, since the hythane supply was held constant during the diesel injection sweep, resulting in a slight HEF variation. This increase in diesel amount at late injection timings, on the other hand, contributed to higher combustion efficiency by enhancing the combustion process. Besides, more advanced timings improved the homogeneity of the in-cylinder charge, leading in lower CO and soot levels [11]. By using more advanced SOI_2, both pressure and temperature were significantly increased as shown in Fig. 7, which increased NOx emissions but also improved reduced unburned fuel (HC and CH_4) at the end of combustion, and hence improving combustion efficiency.

Delaying the diesel injection, on the other hand, retarded the combustion phasing, resulting in a longer CA10-CA90. As a result, both the net thermal efficiency and the in-cylinder pressure decreased. However, it is noted that the peak thermal efficiency was obtained at intermediate injection timing, due to optimised combustion phasing as indicated by the values of CA50. As a conclusion, more advanced SOI_2 demonstrated lower carbon emissions and higher engine performance, being -11 CAD ATDC the best timing to optimal trade-off between net thermal efficiency and carbon emissions. It allowed for a reduction in CO_2 of 44.6 g/kWh, corresponding to an 8% drop, and a reduction in CH_4 of 0.3 g/kWh, equivalent to a 3% reduction. The net thermal efficiency was also increased by roughly 1%. Likewise, at this SOI_2 timing, soot emissions were reduced by about 55%, maintaining them below Euro VI limits. Despite this, EGT dropped as SOI_2 advanced, moving away from the optimal temperature of the MOC in order to achieve high CH_4 conversion efficiency.

Fig. 4: Effect of diesel SOI_2 on net indicated specific exhaust emissions for low engine load DHDF operation.

Fig. 5: Effect of diesel SOI_2 on engine performance for low engine load DHDF operation.

Fig. 6: Effect of diesel SOI_2 on combustion characteristics for low engine load DHDF operation.
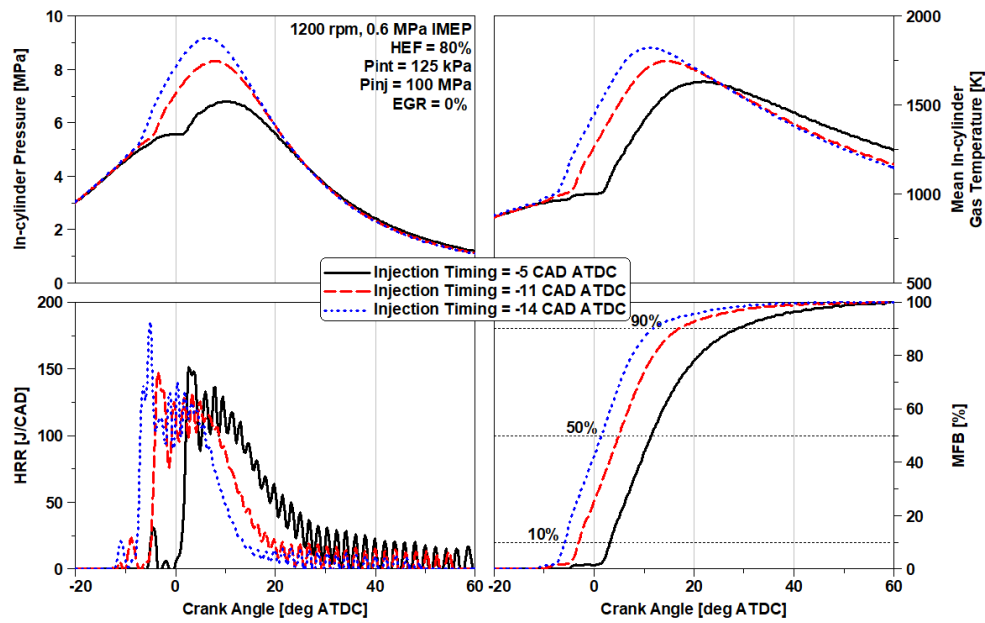
Fig. 7: In-cylinder pressure, mean in-cylinder gas temperature, HHR and MFB for low engine load DHDF operation with various diesel SOI_2 at 80% HEF.

4.3 The effect of intake air pressure

Following the studies of DHDF with different injection timings, intake air pressure was swept for 3 different pressures at 80% HEF: 125 kPa, 135 kPa and 145 kPa. EGR was not used in this experiment and diesel injection timing was kept constant at -11 CAD ATDC, which corresponded to the optimised timing achieved in the previous experiment.

The combustion characteristics, performance and exhaust emissions results for the intake pressure sweep are summarised in Table 6, whereas Fig. 8 depicts the in-cylinder pressure, mean in-cylinder gas temperature, HRR and MFB traces of this experiment.

Table 6: The effect of P_{int} on low engine load DHDF operation.

Parameter	Unit	P_{int} = 125 kPa	P_{int} = 135 kPa	P_{int} = 145 kPa
HEF	%	80	80	80
SOI_2	CAD ATDC	-11	-11	-11
COV_{IMEP}	%	2.33	3.12	2.35
PRR	MPa/CAD	0.73	0.78	0.62
P_{max}	MPa	8.39	8.80	9.10
EGT	°C	363	341	326
SOC-SOI_2	CAD	6.5	6.3	6.1
SOC	CAD ATDC	-5.0	-5.2	-5.4
CA50	CAD ATDC	4.8	4.8	5.0
CA10-CA90	CAD	19.2	20.6	21.4
λ	-	2.04	2.23	2.35
Net Thermal Efficiency	%	36.2	35.3	34.6
Combustion Efficiency	%	93.3	91.9	91.1
$ISFC_{diesel}$	g/kWh	52.5	54.6	57.8
$ISFC_{hythane}$	g/kWh	127.5	127.9	128.8
$ISCO_2$	g/kWh	516.9	519.1	530.4
ISNOx	g/kWh	14.9	14.6	14.4
ISsoot	g/kWh	0.0071	0.0118	0.0086
ISCO	g/kWh	5.9	7.4	9.0
ISHC	g/kWh	11.0	13.5	15.1
$ISCH_4$	g/kWh	11.3	14.0	15.6

Higher intake air pressures allowed for more air dilution of the charge in the combustion chamber, resulting in a leaner and lower reactivity mixture (higher λ). This, however, resulted in poor ignition and more incomplete combustion, leading to a longer CA10-CA90 and thus more unburned fuel (HC and CH_4). This resulted in a drop in combustion efficiency as well as a 1.6% loss in net thermal efficiency for the highest P_{int}, as shown in Table 6. Albeit the decreased amount of burned fuel led in a slightly decrease in CO_2 ppm, $ISCO_2$ increased when P_{int} was increased due to lower thermal efficiency. On the other hand, CO also suffered an increase with higher P_{int}. One possible reason is that incomplete combustion (longer CA10-CA90) generates more CO because CO does not have enough time to oxidise and form CO_2 [34]. However, the higher air dilution of the charge for higher intake air pressures increased the heat capacity ratio, allowing the peak in-cylinder gas temperature to be reduced, as shown in Fig. 8, resulting in lower NOx formation [20, 28].

Additionally, the longer combustion process is believed to be responsible for the $ISFC_{diesel}$ increase of around 4% and 10% for P_{int} of 135 kPa and 145 kPa, respectively. It is noted that the intake pressure of 125 kPa provided the best compromise between performance and carbon emissions.
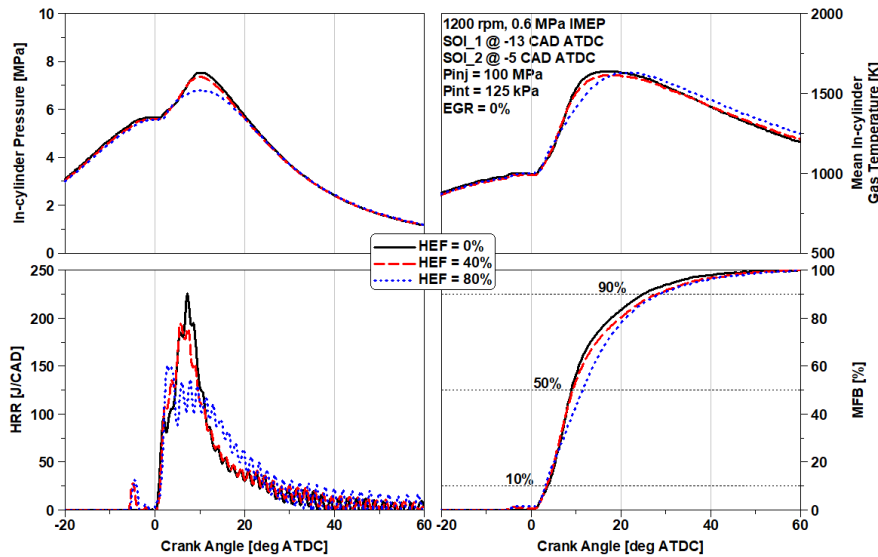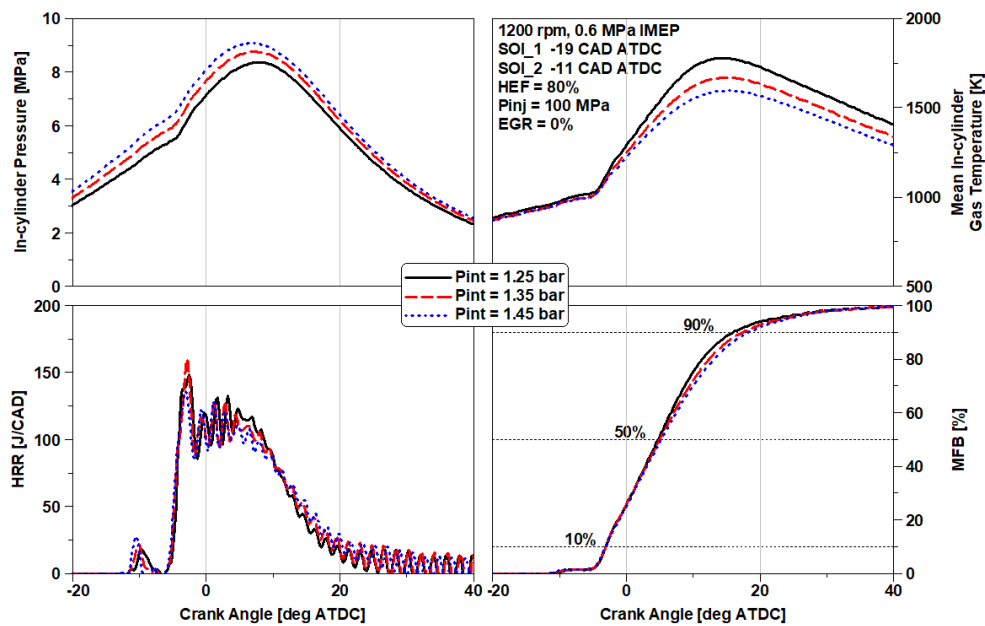

Fig. 8: In-cylinder pressure, mean in-cylinder gas temperature, HHR and MFB for low engine load DHDF operation with various P_{int}.
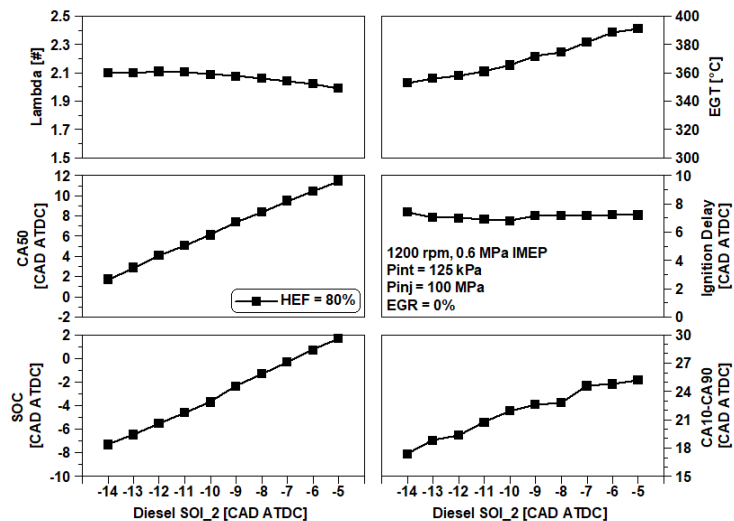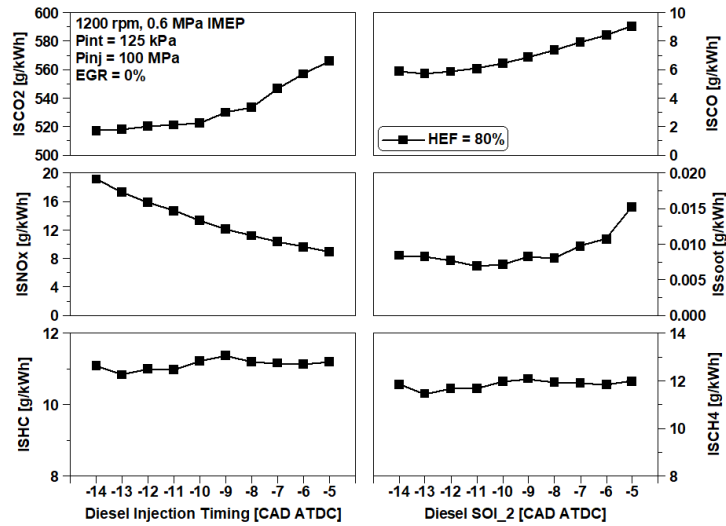
4.4 The effect of EGR

The last approach used in this study to optimise DHDF for the highest HEF operation was the sweep of EGR rate up to 30%, as shown in Table 7. SOI_2 and P_{int} were kept constant at -11 CAD ATDC and 125 kPa, respectively, which corresponded to the optimised values achieved in the previous experiments. The combustion characteristics, performance and exhaust emissions results for EGR rate sweep are summarised in Table 7, while Fig. 9 depicts the in-cylinder pressure, mean in-cylinder gas temperature, HRR and MFB traces of this experiment.

The increase in EGR rate produced lower oxygen concentration and higher heat capacity in the in-cylinder charge, resulting in a slightly longer ignition delay. The longer ignition delay, on the other hand, resulted in a more homogeneous in-cylinder charge, resulting in a higher first HRR peak, as shown in Fig. 9. In addition, the utilisation of EGR extended the combustion duration. As a result, CA50 was delayed, indicating that there was room to optimise SOI_2 for more advanced timing when EGR was employed [35].

Regarding the CO_2 emissions, a small decrease was observed with the increase in EGR dilution, thanks to the higher thermal efficiency and lower ISFC of both diesel and hythane. The NOx emissions were dramatically reduced from 14.9 to 3.1 g/kWh with 30% EGR while the soot emissions were slightly increased due to the reduction in the in-cylinder air-fuel ratio. The increased in-cylinder temperature, as shown in Fig. 9, contributed to a little reduction in CO and HC emissions as well as methane slip, resulting in higher combustion efficiency. As the result, the net thermal efficiency was higher with EGR addition than without EGR. However, at 30% EGR rate, a reverse effect was found, resulting in an increase

in CO, HC, and CH_4, while soot emissions exceeded the Euro VI limit. This can be due to a lack of oxygen, resulting in poor combustion and more unburned fuel.

As a conclusion, it can be stated with a degree of confidence that EGR of 25% provided the best trade-off between exhaust emissions and efficiency.

Table 7: The effect of EGR on low engine load DHDF operation.

Parameter	Unit	EGR = 0%	EGR = 10%	EGR = 20%	EGR = 25 %	EGR = 30%
HEF	%	80	80	80	80	80
SOI_2	CAD ATDC	-11	-11	-11	-11	-11
COV_{IMEP}	%	1.76	1.52	1.61	1.56	1.76
PRR	MPa/CAD	0.75	0.70	0.62	0.58	0.61
P_{max}	MPa	8.61	8.46	8.44	8.35	8.32
EGT	°C	361	363	367	368	369
SOC-SOI_2	CAD	6.4	6.5	7.2	7.4	7.5
SOC	CAD ATDC	-5.1	-5.0	-4.3	-4.1	-4.0
CA50	CAD ATDC	4.5	4.8	5.1	5.3	5.4
CA10-CA90	CAD	19.1	19.2	19.3	19.6	19.7
λ	-	2.16	1.90	1.74	1.66	1.58
Net Thermal Efficiency	%	36.3	36.8	37.3	37.6	37.7
Combustion Efficiency	%	93.3	94.1	94.2	94.5	94.3
$ISFC_{diesel}$	g/kWh	50.7	47.6	45.0	43.8	43.8
$ISFC_{hythane}$	g/kWh	121.2	121.1	121.0	120.4	120.1
$ISCO_2$	g/kWh	517.1	518.4	513.9	513.1	513.8
ISNOx	g/kWh	14.9	10.4	6.4	4.3	3.1
ISsoot	g/kWh	0.0071	0.0081	0.0093	0.0098	0.0128
ISCO	g/kWh	6.0	5.6	4.9	4.8	4.9
ISHC	g/kWh	10.5	9.5	8.8	8.2	8.4
$ISCH_4$	g/kWh	10.9	9.9	9.0	8.4	8.6
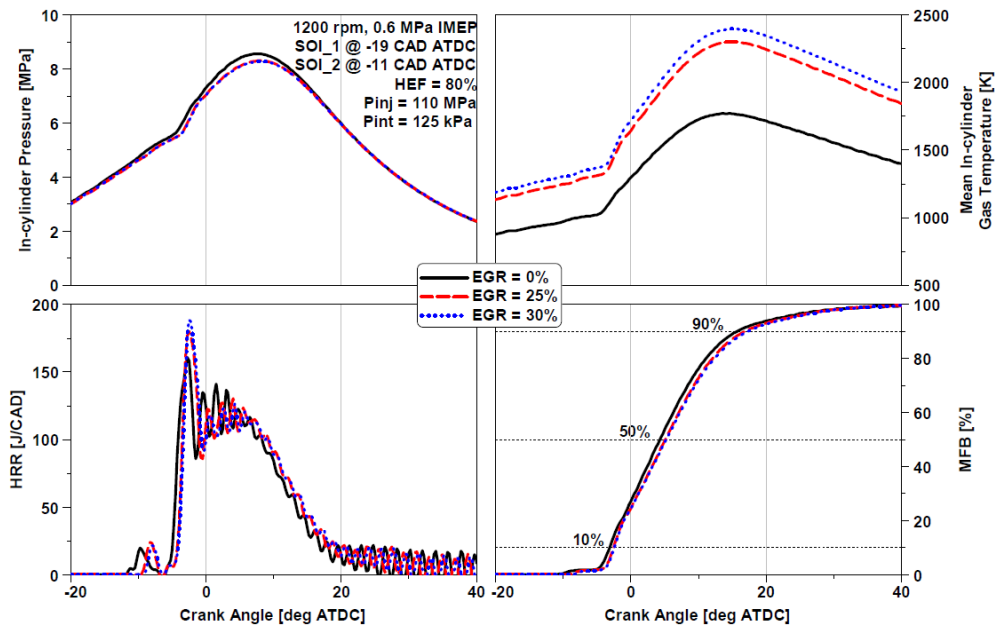
Fig. 9: In-cylinder pressure, mean in-cylinder gas temperature, HHR and MFB for low engine load DHDF operation with various EGR.
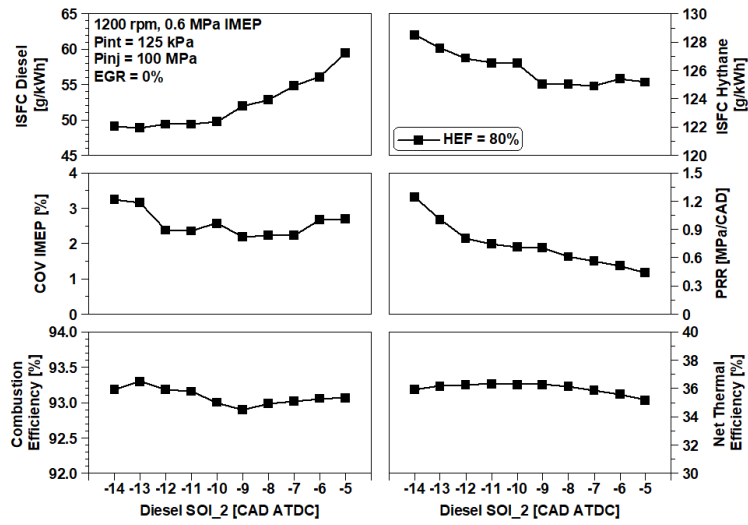
4.5 Comparison of different engine combustion modes

This section compares the three different combustion modes employed in this study to demonstrate the impact of baseline DHDF and optimised DHDF on engine performance and exhaust emissions at low engine load. Table 8 shows that direct 80% HEF with a baseline DHDF lowered CO_2 emissions by

15% and reduced combustion efficiency by another 6%. The addition of hythane, on the other hand, reduced net thermal efficiency while elevating methane slip, CO, and HC. Despite this, optimising DHDF combustion using advanced engine control strategies, such as low booster pressure, diesel injection optimisation, and EGR dilution might mitigate the aforementioned negative effects.

In summary, with the optimisation of DHDF, the CO_2 was reduced by 23% when compared to CDC, which is consistent with the estimated CO_2 reduction provided in Table 2, while NOx emission and soot emissions were reduced by 44% and 42%, respectively. However, both thermal efficiency and combustion efficiency were lower than the baseline CDC, and CO, HC and CH_4 emissions were higher, which would require appropriate aftertreatment system to meet the regulated emission standard.

Table 8: Comparison of engine efficiencies and emission for three combustion modes

Parameter	Unit	CDC	Baseline DHDF		Optimised DHDF	
Net Thermal Efficiency	%	44.2	35.2	(-9%)	37.6	(-6%)
Combustion Efficiency	%	99.5	93.1	(-6%)	94.5	(-5%)
$ISCO_2$	g/kWh	665.7	565.6	(-15%)	513.1	(-23%)
ISNOx	g/kWh	7.7	8.9	(+16%)	4.3	(-44%)
ISsoot	g/kWh	0.0169	0.0152	(-10%)	0.0098	(-42%)
ISCO	g/kWh	1.2	9.0	(+650%)	4.8	(+300%)
ISHC	g/kWh	0.7	11.2	(+1500%)	8.2	(+1071%)
$ISCH_4$	g/kWh	0.7	12.0	(+1614%)	8.4	(+1100%)

Conclusions

In this study, engine experiments were conducted in order to investigate the impact of hythane energy fraction (HEF) on engine performance and exhaust emissions of diesel-hythane dual-fuel combustion, as well as its potential benefit compared to a conventional diesel combustion (CDC). Testing was carried out with port fuel injection of hythane, containing 20% hydrogen and 80% methane molar basis, on a heavy-duty engine operating at an engine load of 0.6 MPa IMEP and a constant speed of 1200 rpm. The HEF was held at 80% ± 2% while dual-fuel combustion mode was optimised for the best trade-off between the lowest CO_2/CH_4 and the highest net thermal efficiency possible, whilst keeping the NOx emission low. Engine control strategies, such as intake air boosting, diesel injection strategy and EGR addition were explored to identify and achieve an optimised diesel-hythane dual-fuel (DHDF) combustion operation. The main findings can be summarised as follows:

1. The DHDF combustion mode using 80% hythane energy fraction demonstrated a direct impact on CO_2 emissions by 15% when compared to the CDC under the same combustion operating conditions. This was due to the 14% lower carbon composition of hythane than conventional diesel, which was influenced by the mixture's hydrogen content. However, this was accompanied with a 9% drop in the net thermal efficiency as well as an increase in CO and unburned HC and CH_4. Soot emissions, on the other hand, were lowered by around 10% to remain within the Euro VI standard due to lower local fuel-air equivalence ratios caused by a reduction in diesel percentage in the in-cylinder mixture.
2. More advanced diesel injection timings indicated a considerable reduction in CO_2 emissions as well as lower CO and soot levels due to a shorter combustion duration around TDC, which improved in-cylinder mixture reactivity by promoting the fast burning rate of hydrogen. SOI_2 at -11 CAD ATDC provided the best balance of net thermal efficiency and carbon emissions. As a result, CO_2 emissions were decreased by 44.6 g/kWh, reflecting an 8% drop, and a reduction in methane slip of 0.3 g/kWh, equivalent to a 3% reduction.
3. The increase of intake air pressure led to lower reactivity of the in-cylinder charge, causing poor ignition and incomplete combustion, resulting in slightly higher CO and CO_2 levels and a substantial increase of unburned HC and methane slip (from 11.3 to 15.6 g/kWh). Consequently, both combustion and net thermal efficiencies fell by about 2.2% and 1.6%, respectively.
4. The introduction of 25% EGR significantly controlled the NOx emissions from 14.9 to 4.3 g/kWh due to a reduction in λ. This NOx level was well below the Euro VI regulation limit of 8.5 g/kWh used to estimate a NOx conversion efficiency of 95% in a SCR system. Also, this EGR dilution percentage allowed a little CO_2 reduction (about 0.8%) due to improved combustion efficiency and thermal efficiency.

5. The optimised DHDF operation for HEF of 80% with a combination of diesel injection optimisation, lower intake air pressure, and EGR addition, resulted in a CO_2 reduction of 23% compared to CDC, though net thermal efficiency was reduced by around 6%.

Overall, this experimental study provides a better understanding of the impact of high HEF on performance and all engine-out emissions of a diesel-hythane dual-fuel combustion at low engine load. Nonetheless, it is worth mentioning that, as demonstrated in this study, hythane has the potential to contribute to a reasonable CO_2 reduction in the transportation sector if clean energy is employed to produce the hydrogen content of hythane.

Furthermore, different engine speeds and loads will be investigated in the future in order to verify the potential impact of hythane at different engine operating conditions, while RCCI mode and LIVC may also be investigated to lower exhaust emissions.

Acknowledgements

References

[1]   Exxon Mobil Corporation, "2021 Outlook for Energy: Enery supply," Texas, 2021.

[2]   Intergovernmental Panel on Climate Change (IPCC), "IPCC Press Release - Climate change widespread, rapid and intensifying," 2021.

[3]   European Commission, "Climate Action - Reducing CO_2 emissions from heavy-duty vehicles," [Online]. Available: https://ec.europa.eu/clima/eu-action/transport-emissions/road-transport-reducing-co2-emissions-vehicles/reducing-co2-emissions-heavy-duty-vehicles_en. [Accessed 21 December 2021].

[4]   S. Szwaja, E. Szwaja, S. Rao, M. Szwaja, K. Grab-Rogalinski, J. D. Naber and M. Pyrc, "Influence of exhaust residuals on combustion phases, exhaust toxic emission and fuel consumption from a natural gas fueled spark-ignition engine," *Energy Conversion and Management,* vol. 165, pp. 440-446, 2018.

[5]   G. Szabados, A. Bereczky, T. Ajtai and Z. Bozoki, "Evaluation analysis of particulate relevant emission of a diesel engine running on fossil diesel and different biofuels," vol. 161Energy, pp. 1139-1153, 2018.

[6]   T. Sandalcı, Ö. Işın, S. Galata, Y. Karagöz and İ. Güler, "Effect of hythane enrichment on performance, emission and combustion characteristics of an ci engine," *International Journal of Hydrogen Energy,* vol. 44, no. 5, pp. 3208-3220, January 2018.

[7]   S. L. Kokjohn, R. M. Hanson, D. A. Splitter and R. D. Reitz, "Fuel reactivity controlled compression ignition (RCCI): a pathway to controlled high-efficiency clean combustion," *Internation Journal of Engine Research,* vol. 12, no. 3, pp. 209-226, 2010.

[8]   V. B. Pedrozo, I. May, W. Guan and H. Zhao, "High efficiency ethanol-diesel dual-fuel combustion: A comparison against conventional diesel combustion from low to full engine load," *Fuel,* pp. 440-451, 2018.

[9]   S. D. Iorio, A. Magno, E. Mancaruso and B. M. Vaglieco, "Analysis of the effects of diesel/methane dual fuel combustion on nitrogen oxides and particle formation through optical investigation in a real engine," *Fuel Processing Technology,* vol. 159, pp. 200-210, 2017.

[10]   M. E. J. Stettler, W. J. B. Midgley, J. J. Swanson, D. Cebon and A. M. Boies, "Greenhouse Gas and Noxious Emissions from Dual Fuel Diesel and Natural Gas Heavy Goods Vehicles," *Environmental Science and Technology,* vol. 50, no. 4, pp. 2018-2026, 2016.

[11]   R. G. Papagiannakis, S. R. Krishnan, D. C. Rakopoulos, K. K. Srinivasan and C. D. Rakopoulos, "A combined experimental and theoretical study of diesel fuel injection timing and gaseous fuel/diesel mass ratio effects on the performance and emissions of natural gas-diesel HDDI engine operating at various loads," *Fuel,* vol. 202, pp. 675-687, 2017.

[12]   A. García, J. Monsalve-Serrano, D. Villalta and R. Sari, "Fuel sensitivity effects on dual-mode dual-fuel combustion operation for different octane numbers," *Energy conversion and management,* vol. 201, no. 10, 2019.

[13]   V. B. Pedrozo, X. Wang, W. Guan and H. Zhao, "The effects of natural gas composition on conventional dual-fuel and reactivity-controlled compression ignition combustion in a heavy-duty diesel engine," *International Journal of Engine Research,* vol. 23, no. 3, pp. 397-415, 2021.

[14]   M. Talibi, R. Balachandran and N. Ladommatos, "Influence of combusting methane-hydrogen mixtures on compression–ignition engine exhaust emissions and in-cylinder gas composition," *International Journal of Hydrogen Energy,* vol. 42, no. 4, pp. 2381-2396, 2017.

[15]   Intergovernmental Panel on Climate Change (IPCC), "IPCC, 2014: Climate Change 2014: Synthesis Report. Contribution of Working Groups I, II and III to the Fifth Assessment Report of the Intergovernmental Panel on Climate Change [Core Writing Team, R.K. Pachauri and L.A. Meyer (eds.)]," Geneva, 2014.

[16]   P. K. Bose and D. Maju, "An experimental investigation on engine performance and emissions of a single cylinder diesel engine using hydrogen as inducted fuel and diesel as injected fuel with exhaust gas recirculation," *International Journal of Hydrogen Energy,* vol. 34, no. 11, pp. 4847-4854, 2009.

[17]   G. P. McTaggart-Cowan, S. R. Munshi, S. N. Rogak, P. G. Hill and W. K. Bushe, "Hydrogen-Methane Blend Fuelling of a Heavy-Duty, Direct-Injection Engine," ASME Internation Mechanical Engineering Congress and Exposition, Washington, 2007.

[18]   L. Graham, G. Rideout, D. Rosenblatt and J. Hendren, "Greenhouse gas emissions from heavy-duty vehicles," *Atmospheric Environment,* vol. 42, no. 19, pp. 4665-4681, 2008.

[19]   R. Sierens and E. Rosseel, "Variable Composition Hydrogen/Natural Gas Mixtures for Increased Engine Efficiency and Decreased Emissions," *ASME Journal of Engineering for Gas Turbines and Power,* vol. 122, pp. 135-140, 2000.

[20]   K. Collier, N. Mulligan, N. Shin and S. Brandon, "Emission Results from the New Development of A Dedicated Hydrogen-Enriched Natural Gas Heavy Duty Engine," SAE Technical Paper 2005-01-0235, 2005.

[21]   W. Tutak, A. Jamrozik and K. Grab-Rogaliński, "Effect of natural gas enrichment with hydrogen on combustion process and emission characteristic of a dual fuel diesel engine," *International Journal of Hydrogen Energy,* vol. 45, no. 15, pp. 9088-9097, 2020.

[22]   U. Asad and M. Zheng, "Exhaust gas recirculation for advanced diesel combustion cycles," *Applied Energy,* 2014.

[23]   N. Ladommatos, S. Abdelhalim, H. Zhao and Z. Hu, "The Dilution, Chemical, and Thermal Effects of Exhaust Gas Recirculation on Diesel Engine Emissions - Part 4: Effects of Carbon Dioxide and Water Vapour," SAE Technical Paper 971660, 1997.

[24]   R. Hanson, A. Ickes and T. Wallner, "Comparison of RCCI Operation with and without EGR over the Full Operating Map of a Heavy-Duty Diesel Engine," SAE Technical Paper 2016-01-0794, 2016.

[25]   J. F. Larsen and J. S. Wallace, "Comparison of Emissions and Efficiency of a Turbocharged Lean-Burn Natural Gas and Hythane-Fueled Engine," *ASME Journal of Engineering for Gas Turbines and Power,* vol. 119, pp. 218-226, January 1997.

[26]   S. Allenby, W.-C. Chang, A. Megaritis and M. L. Wyszynski, "Hydrogen enrichment: A way to maintain combustion stability in a natural gas fuelled engine with exhaust gas recirculation, the potential of fuel reforming," *Proceeding of the Institution of Mechanical Engineering, Part D: Journal of Automobile Engineering,* vol. 215, no. 3, pp. 405-418, 2001.

[27]   Y. J. Qian, C. J. Zuo, J. Tan and H. M. Xu, "Effect of intake hydrogen addition on performance and emission characteristics of a diesel engine with exhaust gas recirculation," *Proceeding of the Institution of Mechanical Engineers, Part C: Journal of Mechanical Engineering Science,* vol. 225, no. 8, pp. 1919-1925, June 2011.

[28]   S. r. Munshi, C. Nedelcu, J. Harris, T. Edwards, J. Williams, F. Lynch, M. Frailey, G. Dixon, S. Wayne and R. Nine, "Hydrogen Blended Natural Gas Operation of a Heavy Duty Turbocharged Lean Burn Spark Ignition Engine," SAE Technical Paper 2004-01-2956, 2004.

[29]   J. R. Anstrom and K. Collier, "Blended hydrogen-natural gas-fueled internal combustion engines and fueling infrastructure," in *Compendium of Hydrogen Energy*, Woodhead Publishing Series, 2016, pp. 219-232.

[30]   Economic Commission for Europe of the United Nations (UN/ECE), "Regulation No 49 - Uniform provisions concerning the measures to be taken against the emission of gaseous and particulate pollutants from compression-ignition engines and positive-ignition engines for use in vehicles," Official Journal of the European Union, 2013.

[31]   J. B. Heywood, Internal Combustion Engine Fundamentals, Second ed., McGraw-Hill Education, 2018.

[32]   I. Smith, J. Chiu, G. Bartley, E. Jimenez, T. Briggs and C. Sharp, "Achieving Fast Catalyst Light-Off from a Heavy-Duty Stoichiometric Natural Gas Engine Capable of 0.02 g/bhp-hr NO X Emissions," SAE Technical Paper 2018-01-1136, 2018.

[33]   D. J. Worth, M. E. J. Stettler, P. Dickinson, K. Hegarty and A. M. Boies, "Characterization and Evaluation of Methane Oxidation Catalysts for Dual-Fuel Diesel and Natural Gas Engines," *Emiss. Control Sci. Technol,* vol. 2, pp. 204-214, 2016.

[34]   V. Rapp, N. Killingsworth, P. Therkelsen and R. Evans, "Lean-Burn Internal Combustion Engines," in *Lean Combustion: Technology and Control*, Second ed., D. Dunn-Rankin and P. Therkelsen, Eds., Academic Press, 2016, pp. 111-146.

[35]   W. Guan, X. Wang, H. Zhao and H. Liu, "Exploring the high load potential of diesel–methanol dual-fuel operation with Miller cycle, exhaust gas recirculation, and intake air cooling on a heavy-duty diesel engine," *International Journal of Engine Research,* vol. 22, no. 7, pp. 2318-2336, 2020.

[36]   C. G. Bauer and T. W. Forest, "Effect of hydrogen addition on the performance of methane-fueled vehicles. Par I: effect on S.I. engine performance," *Internation Journal of Hydrogen Energy,* pp. 55-70, January 2001.

Appendix

Test cell measurement devices

Variable	Manufacturer	Device	Measurement range	Linearity/Accuracy
Speed	Froude Hofmann	AG 150 dynamometer	0-8000 rpm	±1 rpm
Torque	Froude Hofmann	AG 150 dynamometer	0-500 Nm	±0.25% of FS
Clock Signal	Encoder Technology	EB58	0-25000 rpm	0.25 CAD
Diesel flow rate (supply)	Endress+Hauser	Proline Promass 83A02	0-20 kg/h	±0.10% of reading
Diesel flow rate (return)	Endress+Hauser	Proline Promass 83A01	0-100 kg/h	±0.10% of reading
Hythane flow rate	Endress+Hauser	Proline Promass 80A02	0-20 kg/h	±0.15% of reading
Intake air mass flow rate	Endress+Hauser	Proline T-mass 65F	0-910 kg/h	±1.5% of reading
In-cylinder pressure	Kistler	Piezoelectric pressure sensor Type 6125C	0-30 MPa	≤ ±0.4% of FS
Intake and exhaust pressures	Kistler	Piezoresistive pressure sensor Type 4049A	0-1 MPa	≤ ±0.5% of FS
Oil pressure	GE	Pressure transducer UNIK 5000	0-1 MPa	< ±0.2% of FS
Temperature	RS	Thermocouple K Type	233-1473 K	≤ ±2.5 K
Fuel injector current signal	LEM	Current probe PR30	0-20 A	±2 mA
Smoke number	AVL	415SE	0-10 FSN	-
CO	Horiba	MEXA-7170-DEGR (Non-Dispersive Infrared Detector)	0-12 vol%	≤ ±1.0% of FS or ±2.0% of readings
CO2	Horiba	MEXA-7170-DEGR (Non-Dispersive Infrared Detector)	0-20 vol%	≤ ±1.0% of FS or ±2.0% of readings
HC	Horiba	MEXA-7170-DEGR (Heated Flame Ionization Detector)	0-500 ppm or 0-50k ppm	≤ ±1.0% of FS or ±2.0% of readings
CH4	Horiba	MEXA-7170-DEGR (Non-Methane Cutter + Heated Flame Ionization Detector)	0-0.25k ppm or 0-25k ppm	≤ ±1.0% of FS or ±2.0% of readings
NO/NOx	Horiba	MEXA-7170-DEGR (Heated Chemiluminescence Detector)	0-500 ppm or 0-10k ppm	≤ ±1.0% of FS or ±2.0% of readings
EGR	Horiba	MEXA-7170-DEGR (Non-Dispersive Infrared Detector)	0-20 vol%	≤ ±1.0% of FS or ±2.0% of readings

THIESEL 2022 Conference on Thermo- and Fluid Dynamics of Clean Propulsion Powerplants

Innovative Diesel Piston Geometries for Soot Emissions Reduction and Cleaner Combustion: an Optical Investigation

J. V. Pastor[1], C. Micó[1], F. Lewiski[1], F. J. Tejada[1], A. Vassallo[2], F. C. Pesce[2]*, G. Belgiorno[2]

[1]CMT – Motores Térmicos, Universitat Politècnica de València, Camino de Vera s/n, 46022

E-mail: carmirec@mot.upv.es
Telephone: +34 96 6528425

[2]PUNCH Torino S.p.A, Corso Castelfidardo, 36, 10129, Torino, TO, Italy

E-mail: francesco_concetto.pesce@punchtorino.com
Telephone: +39 334 6878173

Abstract. The upcoming strict regulations regarding transport pollutant emission made the automotive industry to look for innovative solutions. Electrification has shown to be very promising for light-duty vehicles. However, in medium and heavy-duty applications, this is still a big challenge and in the short- and medium-term internal combustion engines (especially compression ignition engines) will still play an important role. In this context, new hardware designs have shown great potential to reduce pollutant emissions and comply with current and future regulations. Some engine manufacturers are working on the development of new piston designs. Within this framework, the authors investigate a geometry based on the inclusions of radial lips evenly distributed inside the bowl. It has demonstrated potential for reducing soot formation and improving soot oxidation inside the combustion chamber. For this reason, the present works addresses the impact of using two different radial lip geometries on soot formation and combustion behaviour in a medium-duty optical single cylinder compression ignition engine. High-speed OH* chemiluminescence imaging and 2-Colour pyrometry were applied simultaneously, in combination with a thermodynamic analysis of the in-cylinder pressure signal.

Notation

ICE	*Internal combustion engine.*
CI	*Compression ignition.*
OH*	*Excited state hydroxyl radical.*
2C	*2-Color pyrometry.*
CS1	*Combustion system 1.*
CS2	*Combustion system 2.*
CAD	*Crank angle degree.*
aHRR	*Apparent heat release rate.*
BMEP	*Break mean effective pressure.*
Pinj	*Injection pressure.*
SOE	*Start of energizing.*
% O₂	*oxygen concentration.*
EGR	*Exhaust gas recirculation.*
FWHM	*Full width half maximum.*
KL	*Soot optical thickness.*
aTDC	*after top dead center.*

1. Introduction

The harmful impact of pollutants produced by internal combustion engines (ICE) in road transport applications motivates the constant improvement of regulations that limit allowable emissions in order to mitigate their effect on the environment and public health. Therefore, it becomes necessary to look for alternatives to reduce these emissions and ensure the future and sustainability of the road transport industry.

In this scenario, the electric motor has emerged as a potential alternative to the ICE mainly for avoiding or drastically reducing the fossil fuel consumption replacing them with electricity produced by renewable and sustainable sources [1]. However, this solution presents some drawbacks that hinder their expansion such as the battery capacity, the full decarbonization of the electricity production system or the cost of electricity [2]. For this reason, new proposals based on ICE technology can play a major role on the pursue of pollutant emission reduction and regulatory compliance. A path that has been followed during the last decade is the development of new combustion strategies, such as the Reactivity Controlled Compression Ignition combustion (RCCI) or Partially Premixed Combustion (PPC) concepts [3–6]. However, they still present several challenges related with combustion control and stability, as well as certain pollutant formation (unburned hydrocarbons or carbon monoxide). All of this needs to be solved before its implementation in commercial applications. Another proposal that has shown potential in the last years is the use of alternative fuels such as biofuels or e-fuels [7]. Different studies can be found in the literature where noticeable results were reported in this regard [6,8,9]. Nevertheless, the different properties of these new fuels compared to the conventional ones limit their application with the current ICE technology.

Another way to address the pollutant emission reduction, which has provided great advances in the past, is the design of new hardware concepts directly involved with the combustion process. One example is the development of new piston geometries as they could have a high influence on the air/fuel mixture formation, which is directly related with the oxidation processes (and soot formation) inside the cylinder. In light and medium-duty compression ignition (CI) engines the re-entrant bowl design is typically used (Fig. 1). The purpose of this geometry is to re-direct the spray (and the flame) towards the bowl center after it impinges the wall. This promotes the consumption of oxygen that is available at this region during the late stages of combustion and increase the late soot oxidation [10]. An evolution of the re-entrant bowl design was achieved by the inclusion of a stepped lip at the upper part of the bowl (Fig. 1), in contrast to the characterisical protruding lip of more conventional re-entrant bowl designs. This feature splits the sprays, driving part of the fuel towards the squish region to improve oxygen usage there. This concept has been implemented by different research groups [11,12]. They reported significant reductions in soot emissions, as well as a shorter combustion that lead to thermal efficiency improvements and fuel consumption reductions [12–14].

One of the most innovative proposals that has been presented in the last year is the introduction of protrusions or radial lips at the periphery of a re-entrant bowl. The idea was first presented by Volvo Group for heavy-duty engines. Up to 80% of soot emission reductions as well as efficiency improvements [10,15] were reported. Going one step further, Pastor et al. [16] and Millo et al. [17] evaluated the combination of this new concept with the introduction of a stepped lip at the top of the bowl (Fig. 1) for light-duty vehicles, with higher swirl ratios. The results confirmed the improvement of mixture formation that led to in-cylinder soot reduction.
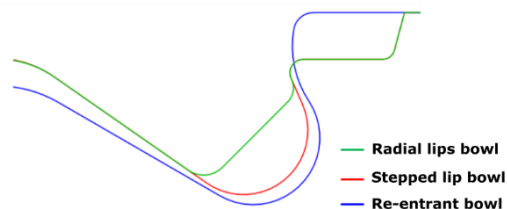
Fig. 1. Sketch of different bowl designs. Image reproduced from [18]
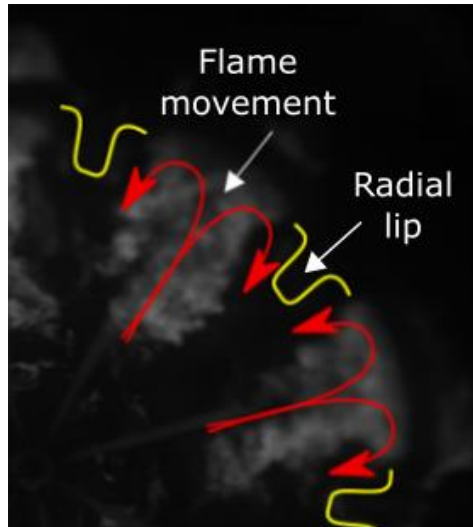
Fig. 2. Flame movement caused by the use of radial lips

The working principle of the radial lips is based on avoiding the tangential spread of the sprays (and flames) when they reach the periphery of the bowl while improving the re-direction effect towards the piston center. In this way, the in-cylinder oxygen consumption is improved while the formation of rich fuel regions is avoided as the flame-to-flame interactions are reduced (Fig. 2) [17–19]. Therefore, the design of the bowl as well as the radial lips would play a major role on the effectiveness of this new piston concept.

Considering all the above mentioned, the objective of this study is to analyse the effect of both bowl and radial lips geometry on the effectiveness of these new piston concepts to improve oxidation and reduce soot formation. To achieve this, a medium-duty optically accessible compression ignition single cylinder engine was used and two different quartz realistic piston designs were evaluated. Both of them combine the use of a stepped lip with radial lips. However, the second one presents more pronounced radial lips with less steep bowl pip. Simultaneous high-speed excited state hydroxyl radical (OH*) chemiluminescence imaging and 2-Colour pyrometry (2C) were used to analyse the behaviour of both geometries under several engine operating conditions, including different engine loads and in-cylinder oxygen concentrations among others. The results confirm the significance of the radial lips geometry on the effectiveness of this concept. The use of more pronounced lips improves the re-circulation effect and reduce flame-to-flame interaction while promoting the use of in-cylinder oxygen. However, its impact over soot formation is more noticeable when the need of oxygen is higher, i.e., low oxygen concentration scenarios, higher loads or during the main injection combustion event.

2. Methodology

2.1. Optical Engine

The study was performed in a single cylinder optical engine (Fig. 3), which is based on a medium-duty CI engine platform. It is an overhead valve design, with valves located in the cylinder head (2 for exhaust and 2 for intake) but the camshaft is in the engine block. Therefore, to reproduce the same pushrod mechanism in the optical engine, an additional box was installed between the block and the cylinder head. It was design to contain the camshaft while keeping the same distance to the valves as the original engine. The main drawback of this configuration is that any optical access to the combustion chamber from its side is blocked, so access is only available through the piston bottom by means of a Bowditch-type piston extension design. A conventional high-pressure pump (Bosch CP3) and a common rail were used to deliver the fuel to a standard solenoid injector with 8-hole nozzle. The main characteristics of the engine are summarized in Table 1.

Table 1. Optical engine characteristics

Engine type	4-stroke, compression ignition
Number of cylinders [-]	1
Number of valves [-]	4
Stroke [mm]	99
Bore [mm]	103
Displacement [cm^3]	825
Connecting Rod length [mm]	1636.3
Effective compression ratio	13.3
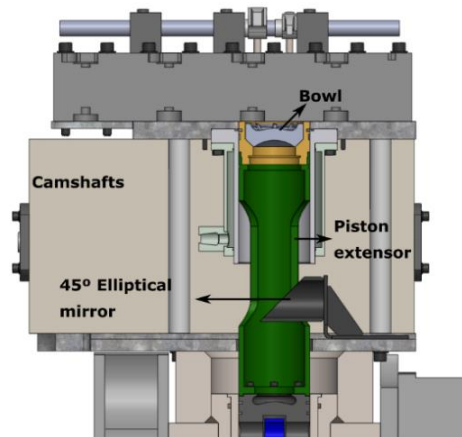
Fig. 3. Sketch of the optical engine

Two different bowl designs were used in this study, which are shown in Fig. 4. From now on, they will be referred as combustion system 1 (CS1) and combustion system 2 (CS2). Both of them present a hybrid geometry, combining a stepped lip and radial lips. However, CS2 presents more pronounced radial lips while the bowl pip has been smoothed. This variation of the geometry in comparison with CS1 was proposed looking for a balance between increasing the influence of the bowl over the air/fuel mixture process while not penalizing other aspects like thermal efficiency [17,19]. In addition, it was decided to build CS2 asymmetrical, without radial lips in one side. The aim was to be able to isolate the effect of the re-designed radial lips from other additional modifications included in CS2 by comparing both halves of the piston. For this reason, data from each side has been analysed separately. The red shadowed areas in Fig. 4 indicate the region of the bowl considered for the side with radial lips (CS2-Lips) and without lips (CS2-NoLips). Finally, it is worth mentioning that the lack of optical access from the side of the engine allowed to utilize a piston design where the rings were located closer to its top, reaching a higher compression ratio than other similar optical engines.

The engine was motored by an electric dynamometer. A screw compressor provided the intake air at the required pressure while a valve located at the exhaust pipe was used to simulate a backpressure of 0.2 bar over the intake one. Additionally, the required intake temperature was achieved by an air heater located just before the intake port. Instantaneous intake and exhaust pressure were measured with a piezoresistive transducer (Kistler-4049A5). The in-cylinder pressure was obtained by a piezoelectric transducer (Kistler-6124A), which was processed to obtain the apparent heat release rate (aHRR) by applying a standard first-law thermodynamic analysis [20]. An oscilloscope (Yokogawa DL708E) was used for recording all the engine signals and the acquisition was synchronized with a crankshaft encoder with 0.5° crank angle degree (CAD) resolution. The engine was operated under skip-fire mode to minimize thermal stress and window fouling while avoiding any effect caused by thermal transients. Therefore, injection and combustion took place only one cycle every 20 motored cycles.
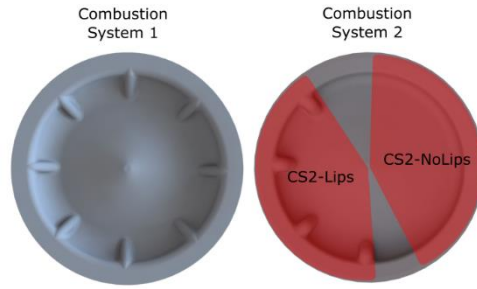
Fig. 4. Combustion systems designs.

2.2. Operating conditions

In this study, the influence of different operating conditions over the piston performance were evaluated. Two different engine loads were tested corresponding to 2 and 6 bar brake mean effective pressure (BMEP) respectively. The combination of operating conditions defined for each of them was chosen to be representative of a realistic configurations of the type of engine on which the optical one is based. Additionally, for each baseline engine load conditions (Table 2), injection pressure (Pinj) was varied ± 100 bar, start of energizing (SOE) of the nozzle was increased 4° and 8° and oxygen concentration (% O_2) was reduced to 18% and 15% to simulate exhaust gas recirculation (EGR). To avoid the influence of cycle-to-cycle variability on the analysis, 10 combustion cycles were registered per operating condition and data was averaged.

A realistic injection strategy was used for both engine loads including two pilot injections, one main injection and one post injection. The dwell time between consecutive pulses and the duration of each pulse was defined for each engine load (Fig. 5).

Table 2. Baseline operating conditions for the two engine loads

BMEP (bar)	Engine Speed (rpm)	Intake pressure (bar)	Exhaust pressure (bar)	Intake Temp. (°C)	Pinj (bar)	SOE (°aTDC)	% O_2 (%)
2	1200	1.04	1.24	102	731	-20.4	21
6	1400	1.34	1.54	55	1182	-33.7	21
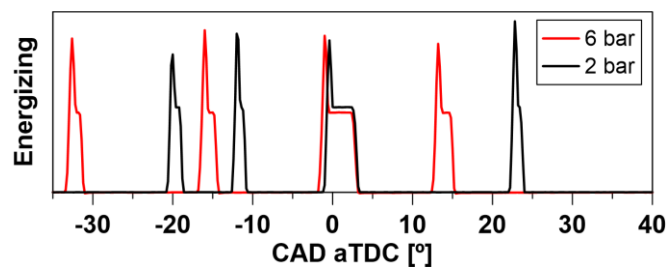
Fig. 5. Injection strategy for each engine load
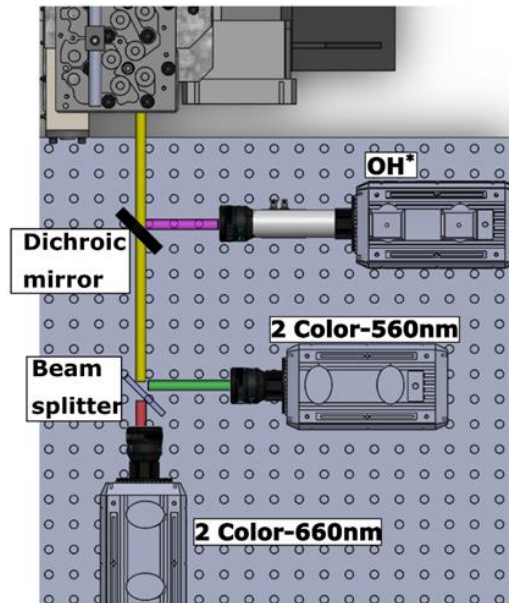
Fig. 6. Optical setup

2.3. Optical Techniques

High-speed OH* chemiluminescence imaging and 2-color pyrometry were applied simultaneously in order to analyse the soot formation and the oxidation process during combustion. The optical setup is shown in Fig. 6. It was designed so flame radiation went through the quartz piston and was reflected by the 45° elliptical mirror (see Fig. 3) towards a dichroic mirror (DMSP805L). This element transmitted visible radiation and reflected only a small portion of the ultraviolet spectrum, around 310 nm. This made this element suitable for reflecting the OH* chemiluminescence towards a high-speed intensified camera. The visible light that went through the dichroic mirror reached a beam splitter that reflected 50% of the incident light and transmitted the other 50%. This allowed to split the radiation into the two high-speed cameras used for the application of the 2C technique. The three high-speed cameras were triggered simultaneously so that image-by-image comparison between them could be made.

2.3.1. High-speed OH* chemiluminescence imaging

The OH* chemiluminescence is considered as a good tracer of high-temperature oxidation reactions in hydrocarbon diffusion combustion [21,22]. For this reason, high-speed OH* chemiluminescence imaging was used in this work to trace the oxidation reactions within the piston bowl. However, it is important to remark that the signal obtained was line-of-sight integrated, which limits the spatial resolution of the results. A high-speed Photron SA5 (CMOS) was used, coupled (1:1 relay optics) to a Hamamatsu C10880-03F high-speed intensifier. The photocathode is a multialkali (S-20), providing sensitivity from ultraviolet to near infrared (185-900 nm). Additionally, a ultraviolet-Nikor Rayfact 105 mm f4.5 was used as the system lens. A narrowband bandpass filter centered at 310 nm and 10 nm full width half maximum (FWHM) was placed in front of the lens to reject other radiation than the OH* peak emission. The exposure time of the high-speed camera also defined the gating time of the intensifier, which was set to 39.75 µs. Its gain was adjusted to maximize the dynamic range under each engine load. The acquisition speed was 25000 fps and the resolution was 4.4 pixels/mm.

2.3.2. 2-color pyrometry

The 2C methodology is based on registering thermal radiation from soot at two different wavelengths to calculate temperature and optical thickness. By applying the Plank's law to define the intensity of radiation of a black body at a certain temperature and specific wavelength, the concept of emissivity (ε_λ) of a non-black body and the concept of apparent temperature [23], the emissivity of a radiation source (hot soot particles) can be defined by (1).

$$\varepsilon_\lambda = \frac{e^{\left(C_2/\lambda T\right)}-1}{e^{\left(C_2/\lambda T_a\right)}-1} \qquad (1)$$

Where C_2 is the second Planck's constant ($C_2 = 1{,}4388 \cdot 10^{-2}$ mK), T is the temperature of the radiation source and T_a is the apparent temperature (or brightness temperature). In practice, the emissivity of soot particles can be estimated using the empirical correlation developed by Hottel and Broughton [24] as represented in (2).

$$\varepsilon_\lambda = 1 - e^{-\left(KL/\lambda^\alpha\right)} \qquad (2)$$

Where K is an absorption coefficient that is proportional to the number density of soot particles and L is the geometric thickness of the flame along the optical axis of the detection system. The parameter α depends on the physical and optical properties of soot and in the visible range α = 1.39 can be used for most fuels [23]. Due to the complex geometry of flames in engine combustion chambers, it is difficult to calculate the flame geometric thickness. Therefore, both K and L are usually evaluated as a single parameter representing the optical thickness of the soot cloud (KL). Combining (1) and (2), an expression for KL can be derived that is represented in (3).

$$KL = -\lambda^\alpha ln\left[1 - \left(\frac{e^{\left(C_2/\lambda T\right)}-1}{e^{\left(C_2/\lambda T_a\right)}-1}\right)\right] \qquad (3)$$

Assuming that the KL parameter does not vary with the change of the wavelength (as long as it belongs to the visible range), (3) can be applied for the two measured wavelengths λ_1 and λ_2 to obtain the temperature (T) of the hot soot particles, as in (4). Once T is calculated, the corresponding KL value can be obtained from (3).

$$\left[1 - \left(\frac{e^{\left(C_2/\lambda_1 T\right)}-1}{e^{\left(C_2/\lambda_1 T_{a1}\right)}-1}\right)\right]^{\lambda_1^{\alpha_1}} = \left[1 - \left(\frac{e^{\left(C_2/\lambda_2 T\right)}-1}{e^{\left(C_2/\lambda_2 T_{a2}\right)}-1}\right)\right]^{\lambda_2^{\alpha_2}} \qquad (4)$$

Two high-speed Photron NOVA S9 cameras (CMOS) were used to register the thermal radiation of soot particles at two specific wavelengths. For both cameras, a 100 mm f2 Karl-Zeiss Makroplanar camera lens was used together with a narrowband bandpass filter centered at 560 (λ_1) and 660 nm (λ_2) respectively with 10 nm FWHM. The exposure time of each camera was adjusted to the intensity of radiation of each wavelength, being higher for the 560 nm channel. As reference, for low load operating conditions the exposure times were set to 5 and 0.5 μs for 560 and 660 nm respectively.

To ensure the maximum accuracy on the application of the 2C algorithm, time and spatial matching between the signal of both wavelengths must be ensured. The first is achieved by synchronizing acquisition of both cameras. The second is achieved by applying a pre-processing routine that transform one of the channels using the other as reference. For this purpose, a transformation matrix needs to be calculated including translation, rotation and scaling. A scale invariant algorithm [25] is applied to obtain a list of feature points from the images of both wavelengths. Then, the matching between features of both lists is calculated and used to obtain the spatial transformation matrix. Finally, the transformation matrix is applied to one of the channels and the spatial matching is obtained. The results of the pre-processing routine can be seen in Fig. 7. The composition of both wavelengths (red and green signals) is shown before (left) and after (right) the pre-processing routine. A good pixel-by-pixel matching leads to yellow pixels.
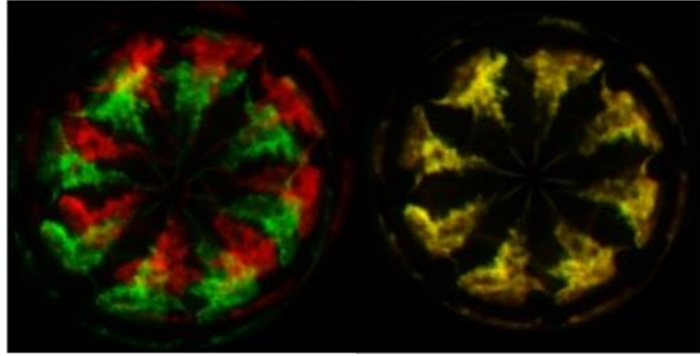
Fig. 7. Image composition (yellow) from the signal of both cameras, where 560 nm is represented in green and 660 nm is represented in red. Left: composition before pre-processing. Right: composition after pre-processing

3. Results

As stated previously, CS2 geometry was proposed to increase the influence of radial lips over in-cylinder flow dynamics. This can be analysed based on the flame movement inside of each combustion system. In Fig. 8, a sequence of KL and OH* chemiluminescence distribution is shown for CS1 and CS2 at 2 bar BMEP and baseline operating conditions. At 6.1° aTDC, the flame reaches the bowl wall and starts spreading tangentially guided by the periphery of the bowl. At this instant, where the injection event is still occurring, no significant differences are observed among the three geometries (CS1, CS2-Lips and CS2-NoLips) in terms of KL distribution. When looking at OH* chemiluminescence, it is possible to see no differences between the three geometries either. Most of the oxidation reactions are located upstream the bowl periphery (even separated several millimeters). Once the flame front reaches the radial lips, differences start to appear. At 10.1° aTDC the radial lips (CS1 and CS2-Lips) stop the tangential spreading movement and redirect the flame towards the bowl center. This is not observed for the CS2-NoLips side, which keeps the flame concentrated at the periphery of the bowl. The flame-to-flame collision is stronger for this geometry, forming more soot than the CS1 and CS2-Lips, as the higher KL indicate. The OH* chemiluminescence signal also shows that most of the oxidation reactions in this side are taking place close to the bowl periphery. In contrast, for the geometries with the radial lips, the oxidation reactions spread towards the bowl center. Besides that, some small differences between both radial lip designs can also be highlighted at this instant. The CS2-Lips (more pronounced) conduct the flame closer to the bowl center than the CS1, which can improve the use of in-cylinder oxygen. This statement is supported also by OH* radiation, which shows larger clouds closer the center for the CS2-Lips in comparison with CS1. Going forward on the combustion process, at 20.2° aTDC, during the late oxidation phase, CS1 and CS2-Lips are much more similar. Both geometries show very low KL and OH* chemiluminescence levels, which indicates that combustion has almost finished. However, for the CS2-NoLips, still relatively intense OH* radiation is visible showing that oxidation reactions are still taking place. This confirms that the radial lips can also accelerate the reaction.

The combustion process described in the previous paragraph is represented in Fig. 9 in terms of aHRR (a) and the evolution of average KL (b) for both combustion systems. On the one hand, it is possible to see that both designs provide very similar aHRR although a slightly higher peak is reached by CS2. On the other hand, the KL evolution shows a lower soot formation by the radial lips geometries in comparison with CS2-NoLips as it was observed previously. However, it is also possible to see that CS2-Lips provides lower KL even than CS1. This indicates that the more intense re-entrant movement achieved by the more pronounced radial lip profile can improve the effectiveness of this concept on soot reduction.
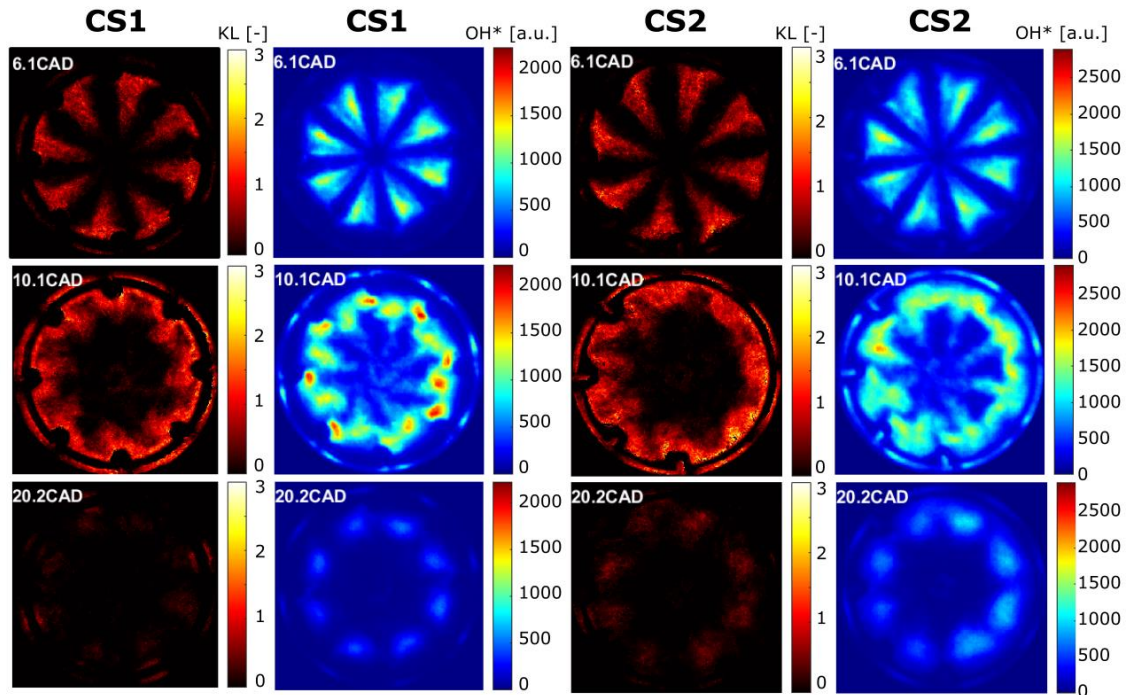
Fig. 8. KL and OH* chemiluminescence for CS1 and CS2 at 2 bar BMEP and baseline conditions
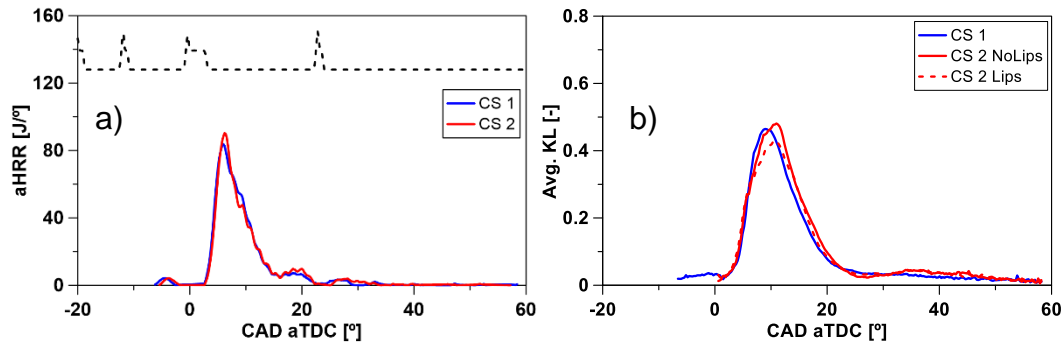
Fig. 9. HRR (a) for CS1 and CS2 and average KL evolution (b) for CS1, CS2-Lips and CS2-NoLips at 2 bar BMEP and baseline conditions. The dashed line on top of the HRR represents the injection strategy for reference.

3.1. Effect of radial lips geometry at different operating conditions

The previous description was based on a single operating point. Therefore, it is interesting to extend the analysis to different experimental conditions. Therefore, a sweep of operating conditions was performed as described in previous sections. Fig. 10 shown the aHRR (a) and average KL evolution (b) when SOE is increased, delaying injection by 4° and 8°. In this way, the late oxidation stages will take place later in the cycle with lower in-cylinder pressure and temperature. The aHRR curves confirm that the pistons are operating under the same in-cylinder conditions and a similar BMEP is achieved despite the modifications. As SOE is increased, the combustion of the main injection event is delayed. Until 4° increase, the aHRR is very similar to the one of the baseline case. However, when the injection is delayed by 8° a more intense peak is achieved which suggest a more premixed combustion. This can be related with the fact the main injection event starts later during the expansion stroke (lower pressure and temperature), leading to a longer ignition delay. For the three cases, differences in terms of average KL are observed between CS1 and CS2-Lips. For the first one, a slight increase is observed for 4°, while a slight decrease is achieved at 8°. In contrast, for the CS2-Lips a higher increase is observed in the first case but also a larger decrease is achieved when moving to 8°. These results show that CS2-Lips is more effective in reducing the soot formation when combustion conditions are worsened but more mixing time is allowed.
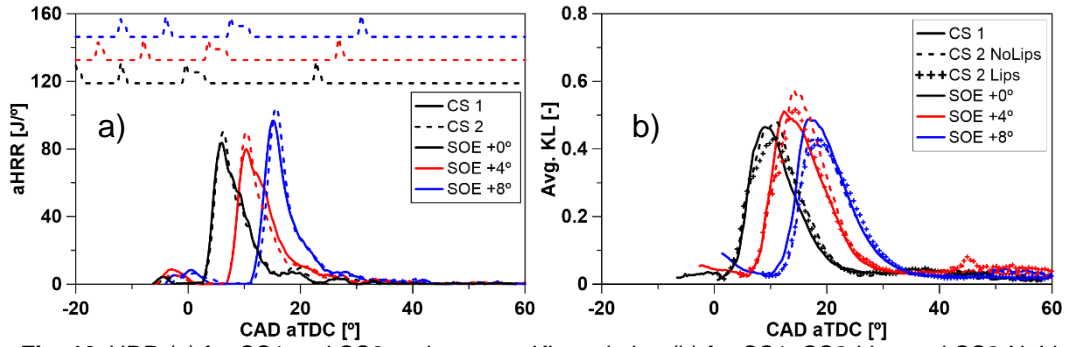
Fig. 10. HRR (a) for CS1 and CS2 and average KL evolution (b) for CS1, CS2-Lips and CS2-NoLips at 2 bar BMEP and different SOE configurations. The dashed line on top of the HRR represents the injection strategy for reference.
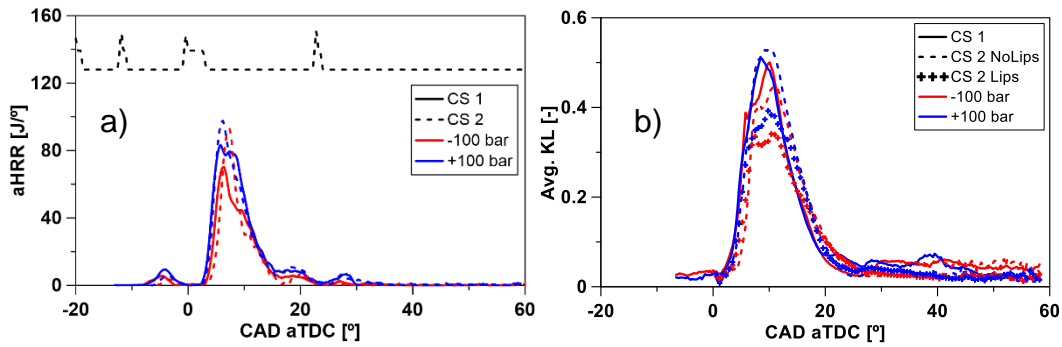
Fig. 11. HRR (a) for CS1 and CS2 and average KL evolution (b) for CS1, CS2-Lips and CS2-NoLips at 2 bar BMEP and different Pinj. The dashed line on top of the HRR represents the injection strategy for reference.

The performance of the different geometries at different injection pressures is shown in Fig. 11. When the pressure is increased by 100 bar, even if the atomization process improves, more fuel is injected into the cylinder. In this case, both combustion systems have a similar aHRR. However, again less KL values were obtained for CS2-Lips compared to CS1. The difference is even larger when the injection pressure is reduced by 100 bar from the nominal one. However, in this case, a slight delay is observed in the aHRR which could lead to a better air/fuel mixture and a consequent reduction of soot formation in addition to the influence of the CS2-Lips geometry.

Under EGR conditions, combustion systems are forced to work under low oxygen concentrations. Therefore, the benefits of redirecting flames towards the center part of the bowl could be affected. In Fig. 12, aHRR (a) and average KL evolution (b) for 18% and 15% O_2 concentration are shown, simulating different EGR rates. At 15% O_2, the aHRR curves indicate that combustion starts much later than the baseline case for both combustion systems. When looking at the evolution of average KL for this case, a big reduction is observed for both CS1 and CS2 which difficult the analysis. This behaviour can be related to a much more premixed combustion due to the longer ignition delay. It is in agreement with the higher peak of the aHRR. In contrast, at 18% O_2, the benefits of CS2-Lips are more visible. A more intense peak of CS2 aHRR compared to CS1 could suggest a more premixed combustion. However, no delay is observed for this condition between both geometries. Thus, all the differences observed for this operating condition can be related with the radial lip geometry. First, a faster oxidation process is taking place for CS2 as the higher aHRR peak indicates. In addition, it is possible to see that CS2-Lips is able to keep KL values even when decreasing from 21% to 18% O_2, while this is not observed for CS1.
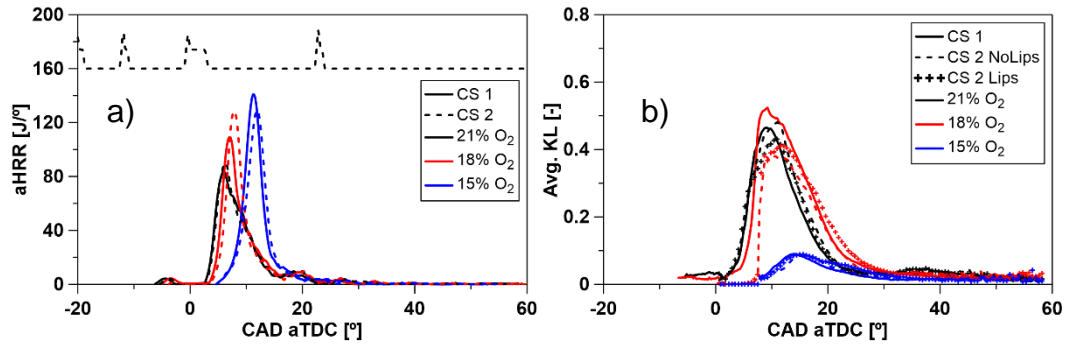
Fig. 12. HRR (a) for CS1 and CS2 and average KL evolution (b) for CS1, CS2-Lips and CS2-NoLips at 2 bar BMEP and different oxygen concentrations. The dashed line on top of the HRR represents the injection strategy for reference.

3.2. Effect of radial lips geometry at different engine loads

The results presented previously suggested that the differences between CS1 and CS2-Lips became more relevant under more sooting operating conditions. For this reason, their performance at a higher engine load (6 bar BMEP) has been investigated. The injection strategy in this case used a higher injection pressure and longer energizing pulses, which resulted in much more fuel injected and potentially more soot formed. In Fig. 13, the aHRR (a) and average KL evolution (b) is shown for CS1 and CS2 at 6 bar BMEP and baseline operating conditions. In this case, it is possible to see that pilot and post injection gain much more relevance in the combustion process as both aHRR peaks are visible in comparison with the low load cases. Regarding soot formation, it is possible to see that during the main injection combustion event (from 0° to 15°aTDC) the CS2-Lips forms less soot than CS1 as it was observed with the lower engine load. However, during the post injection combustion event (from 15° to 30° aTDC), both geometries show similar KL values. This change in the behaviour could be related to the fact that the pilot injections are so short that the fuel has not enough momentum to exploit the benefits of this geometry.
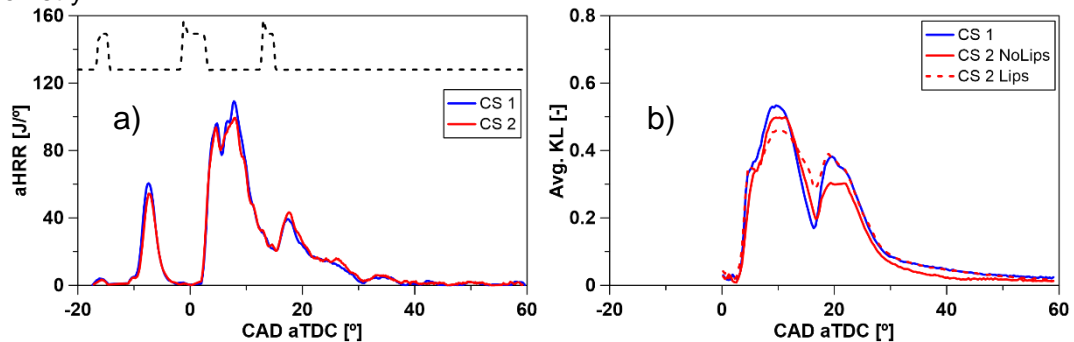
Fig. 13. HRR (a) for CS1 and CS2 and average KL evolution (b) for CS1, CS2-Lips and CS2-NoLips at 6 bar BMEP at baseline operating conditions. The dashed line on top of the HRR represents the injection strategy for reference.
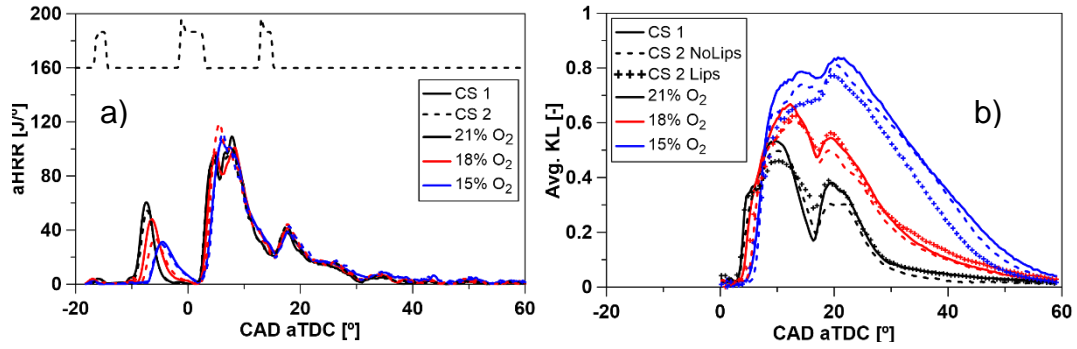
Fig. 14. HRR (a) for CS1 and CS2 and average KL evolution (b) for CS1, CS2-Lips and CS2-NoLips at 6 bar BMEP and different oxygen concentrations. The dashed line on top of the HRR represents the injection strategy for reference.

The more fuel injected due to an increase of the engine load together with a decrease of oxygen concentration when using EGR could be a critical point of high soot formation. For this reason, the performance of CS1 and CS2 was evaluated at 6 bar BMEP and different % O_2. Fig. 14 shows the aHRR (a) and average KL evolution (b) for both combustion systems at 18% and 15% O_2. For the first case, it is possible to see that the ignition of the pilot injection is delayed. However, the energy released is enough to compensate for the oxygen reduction and the main injection combustion event starts at the same time as the baseline case. In terms of soot, it is possible to see an increase of the KL value for the three geometries. The relative behaviour between CS1 and CS2-Lips is still the same as reported for 21% O_2. At lower oxygen concentrations (higher EGR rate), the differences are more noticeable. An increase of soot is observed for both combustion systems. However, when comparing CS1 and CS2-Lips, the second one shows much lower KL values during the whole combustion event, including the main and the post injection. These results show that the radial lip design of CS2 is effective, even under low oxygen concentration, mitigating the in-cylinder soot production when compared to CS1. This is in agreement with previous results and confirms that the benefits of this new radial lips profile in CS2 are more noticeable under high soot conditions.

4. Conclusions

A comparison between two novel bowl designs from the point of view of combustion and soot formation has been presented. They are based on the combination of a stepped lip and radial lips to promote the oxygen usage at the squish region and the center of the piston. The work was carried out in an optical medium-duty compression ignition single cylinder engine. Different operating conditions (Pinj, SOE, % O_2) and engine loads were evaluated. The following conclusions can be drawn from the analysis:

- The more pronounced profile of the CS2-radial lip drives the flames closer to the bowl center than the CS1 design. This reduces soot formation but also accelerates the oxidation process.
- At lower engine loads, a reduction of the in-cylinder soot formation was observed in CS2-Lips when compared with CS1. It was a common behaviour, observed at all the operating conditions evaluated, which confirms that the radial lips of CS2 are more effective on reducing soot formation. This is coherent with the higher flame re-directing effect that was also reported.
- At higher engine load, the effect of the CS2-Lips is more noticeable specially under unfavorable operating conditions as low oxygen concentration.

5. References

[1]   Ağbulut Ü, Bakir H. The Investigation on Economic and Ecological Impacts of Tendency to Electric Vehicles Instead of Internal Combustion Engines n.d.

[2]   Lešnik L, Kegl B, Torres-Jiménez E, Cruz-Peragón F. DSC used to follow the evolution of W/O emulsions versus time on ground and in space in the ISS (International Space

Station) n.d. https://doi.org/10.2516/ogst/2020051.

[3]   García A, Monsalve-Serrano J, Rückert Roso V, Santos Martins ME. Evaluating the emissions and performance of two dual-mode RCCI combustion strategies under the World Harmonized Vehicle Cycle (WHVC). Energy Convers Manag 2017;149:263–74. https://doi.org/10.1016/j.enconman.2017.07.034.

[4]   Benajes J, García A, Monsalve-Serrano J, Lago Sari R. Fuel consumption and engine-out emissions estimations of a light-duty engine running in dual-mode RCCI/CDC with different fuels and driving cycles. Energy 2018;157:19–30. https://doi.org/10.1016/j.energy.2018.05.144.

[5]   Benajes J, García A, Monsalve-Serrano J, Boronat V. Dual-Fuel Combustion for Future Clean and Efficient Compression Ignition Engines. Appl Sci 2017;7:1–16. https://doi.org/10.3390/APP7010036.

[6]   Benajes J, García A, Monsalve-Serrano J, Balloul I, Pradel G. Evaluating the reactivity controlled compression ignition operating range limits in a high-compression ratio medium-duty diesel engine fueled with biodiesel and ethanol. Int J Engine Res 2017;18:66–80. https://doi.org/10.1177/1468087416678500.

[7]   Runge P, Sölch C, Albert J, Wasserscheid P, Zöttl G, Grimm V. Economic comparison of different electric fuels for energy scenarios in 2035. Appl Energy 2019;233–234:1078–93. https://doi.org/10.1016/j.apenergy.2018.10.023.

[8]   Pastor J V., Garcia-Oliver JM, Micó C, Tejada FJ. Combustion Behaviour of Blends of Synthetic Fuels in an Optical Single Cylinder Engine. SAE Tech Pap Ser 2021;1. https://doi.org/10.4271/2021-24-0038.

[9]   Pastor J V., García A, Micó C, Lewiski F. Simultaneous high-speed spectroscopy and 2-color pyrometry analysis in an optical compression ignition engine fueled with OMEX-diesel blends. Combust Flame 2021;230. https://doi.org/10.1016/j.combustflame.2021.111437.

[10]   Eismark J, Andersson M, Christensen M, Karlsson A, Denbratt I. Role of Piston Bowl Shape to Enhance Late-Cycle Soot Oxidation in Low-Swirl Diesel Combustion. SAE Int J Engines 2019;12:03-12-03–0017. https://doi.org/10.4271/03-12-03-0017.

[11]   Neely GD, Sasaki S, Sono H. Investigation of alternative combustion crossing stoichiometric air fuel ratio for clean diesels. SAE Tech Pap 2007. https://doi.org/10.4271/2007-01-1840.

[12]   Smith A. Ricardo low emissions combustion technology helps JCB create the off-highway industry ' s cleanest engine. Ricardo Press Release 2010:4–6.

[13]   Busch S, Zha K, Kurtz E, Warey A, Peterson R. Experimental and Numerical Studies of Bowl Geometry Impacts on Thermal Efficiency in a Light-Duty Diesel Engine, 2018. https://doi.org/10.4271/2018-01-0228.

[14]   Dahlstrom J, Andersson O, Tuner M, Persson H. Experimental Comparison of Heat Losses in Stepped-Bowl and Re-Entrant Combustion Chambers in a Light Duty Diesel Engine. SAE Tech Pap 2016. https://doi.org/10.4271/2016-01-0732.

[15]   Eismark J, Christensen M, Andersson M, Karlsson A, Denbratt I. Role of fuel properties and piston shape in influencing soot oxidation in heavy-duty low swirl diesel engine combustion. Fuel 2019;254:115568. https://doi.org/10.1016/j.fuel.2019.05.151.

[16]   Pastor J V., García A, Micó C, Lewiski F. Soot reduction for cleaner Compression Ignition Engines through innovative bowl templates. Int J Engine Res 2021;22:2477–91. https://doi.org/10.1177/1468087420951324.

[17]   Millo F, Piano A, Roggio S, Bianco A, Pesce FC, Vassallo AL. Numerical Assessment of Additive Manufacturing-Enabled Innovative Piston Bowl Design for a Light-Duty Diesel Engine Achieving Ultra-Low Engine-Out Soot Emissions. SAE Int J Engines 2021;15.

https://doi.org/10.4271/03-15-03-0022.

[18]   Pastor J V., García A, Micó C, Lewiski F, Vassallo A, Pesce FC. Effect of a novel piston geometry on the combustion process of a light-duty compression ignition engine: An optical analysis. Energy 2021;221:119764. https://doi.org/10.1016/J.ENERGY.2021.119764.

[19]   Blasio G Di, Ianniello R, Beatrice C, Pesce FC, Vassallo A, Belgiorno G, et al. Experimental Investigation on an Innovative Additive Manufacturing- Enabled Diesel Piston Design to improve Engine-out Emissions and Thermal Efficiency beyond Euro6 2020:1–19.

[20]   Heywood JB. Internal Combustion Engine Fundamentals. Intern Combust Engine Fundam Second Ed 2018:64–5.

[21]   Dec JE, Coy EB. OH radical imaging in a di diesel engine and the structure of the early diffusion flame. SAE Tech Pap 1996. https://doi.org/10.4271/960831.

[22]   Higgins B, Siebers D. Measurement of the flame lift-off location on di diesel sprays using OH chemiluminescence. SAE Tech. Pap., 2001. https://doi.org/10.4271/2001-01-0918.

[23]   Zhao H, Ladommatos N. Optical diagnostics for soot and temperature measurement in diesel engines. Prog Energy Combust Sci 1998;24:221–55. https://doi.org/10.1016/S0360-1285(97)00033-6.

[24]   Hottel HC, Broughton FP. Determination of True Temperature and Total Radiation from Luminous Gas Flames. Ind Eng Chem Anal Ed 1932;4:166–75. https://doi.org/10.1021/ac50078a004.

[25]   Lowe DG. Distinctive Image Features from Scale-Invariant Keypoints. Int J Comput Vis 2004;60:91–110. https://doi.org/10.1023/B:VISI.0000029664.99615.94.

Session S2.4 New Concepts for Ultraefficient and Clean ICEs

THIESEL 2022 Conference on Thermo- and Fluid Dynamics of Clean Propulsion Powerplants

Developing an Accelerated Procedure for Assessing the Injector Fouling Abatement of Different Fuel Additives

G. Brinklow[1], J.M. Herreros[1], S. Zeraati Rezaei[1], A. Tsolakis[1], F. Oliva [2]

[1]The University of Birmingham. Edgbaston, Birmingham, B15 2TT, United Kingdom.
E-mail: g.brinklow@bham.ac.uk, j.herreros@bham.ac.uk, s.zeraatirezaei@bham.ac.uk
a.tsolakis@bham.ac.uk
Telephone: +(44) 0121 414 3344

[2] Repsol Technology Lab. Móstoles, Madrid, 28935, España.
E-mail: fermin.oliva@repsol.com

Abstract

The design of fuel formulations including effective deposit control additives (DCAs) is key to prevent issues in modern engines, which can lead to increased emissions, fuel consumption and even engine failure. Test procedures, such as the CEC F-98-08 method DW10 cycle, are developed to evaluate the injector nozzle fouling propensity of fuels and DCAs performance. Whilst this can be effective, it requires a long duration (32 to 64 hours) and reliance on the addition of zinc to the test fuel. The aim of this work is twofold, first to develop a new accelerated (shorter) injector deposit test procedure without the addition of zinc and then to demonstrate its effectiveness to assess DCAs.

New test procedures were designed and investigated to understand the effects of engine operating conditions, frequency of transition between conditions, and the operating cycles within the procedure on the injector deposits formation/loss rate. The new accelerated injector deposit test procedure was de-veloped through investigating engine operating points, frequencies and cycle format. The effect of each proposed procedure was evaluated in a modern multi-cylinder diesel engine in terms of performance and emissions, as well as using an injector flow test rig to compare the fuel flow rate through the injectors at a constant pressure before and after the procedure. The final test procedure was selected based on the level of flow loss through the injector and featured two main stages. The first stage included alter-nating between a high power and low power engine operating point for an hour, whilst the second stage includes a constant high speed idle engine operating point for 4 hours. These two stages are repeated 4 times to give a total time of 20 hours, achieving an injector flow rate loss of 11% using the baseline fuel, whilst a DW10 cycle (60 hours) adapted without zinc addition and using the diesel engine in this study achieved under 4%.

The new test procedure was utilised for fuel design and to evaluate the impact of the DCAs in fuel formulation. Fuel Additive A and Additive B reduced the injector flow losses to 9 % and 7 %, compared to the 11% obtained with the baseline fuel, as well as engine fuel consumption by 0.88 % and 2.56 %, respectively. This illustrated that different additives can be evaluated by injector flow loss and fuel consumption benefit using this procedure.

Notation

CO   *Carbon Monoxide*
DCA   *Deposit Control Additive*
ECU   *Engine Control Unit*
EDID   *External Direct Injector Deposits*
EGR   *Exhaust Gas Recirculation*
EU   *European Union*
FAME   *Fatty Acid Methyl Ester*
IDID   *Internal Direct Injector Deposits*
OEM   *Original Equipment Manufacturer*
PIBSI *Polyisobutylene succinimide*
ULSD   *Ultra Low Sulphur Diesel*

1. Introduction

As vehicle emission regulations have become stricter over recent years, fuel injection equipment has developed further in order to meet these demands. The delivery of diesel fuel into the combustion chamber has been enhanced to provide improved spray quality [1]. This is in order to improve the fuel and air

mixing process to minimise soot, CO and unburnt hydrocarbon emissions. However, since this has mostly been achieved through the design of injectors with reduced tolerances, it has increased the susceptibility of diesel injectors to the formation of deposits [2][3]. These deposits are classified as either external direct injector deposits (EDID) or internal direct injector deposits (IDID). The former of these form on external surfaces of the injector and can partially or completely cover the nozzle holes. Whilst the latter of these form around the needle, control valves or armature group [4].

A build-up of injector deposits can cause serious problems for the operation of an engine, even having the potential for complete engine failure. If external diesel injector deposits (EDID) form, they have the ability to alter the spray pattern of the fuel. Modern injector nozzles have been precision engineered in order to optimise the spray pattern. As a result, any alteration caused by injector deposits will deteriorate the spray pattern hindering the air and fuel mixture quality. Furthermore, the formation of deposits will reduce the hydraulic diameter of the nozzle and therefore limit the fuel flow. This will have a negative impact on engine performance, fuel economy and emissions [5]. On the other hand, internal diesel injector deposits (IDID) can be detrimental to injector control since these can cause sticking of the moving parts such as the needle. In this case, issues can include incorrect fuel metering – over or under fuelling depending on whether the injector is sticking whilst opening or closing [4]. Furthermore, if the fuelling is varying from cylinder to cylinder or cycle to cycle, this can cause unstable engine running and is most noticeable at idle [4]. If internal injector deposits develop further, they can reach the point where it is no longer possible for the injector to open and therefore cause complete engine failure due to lack of fuelling.

Over the last decade, the number of engine failures related to injector deposits has increased [6], this is related to the injectors themselves and fuel quality. As previously alluded to, the push for cleaner and more efficient diesel engines has led to reduced tolerances within the injectors. Therefore, modern injectors are much more sensitive to the build-up of injector deposits, increasing the number of engine failures or malfunctions related to these deposits [7]. To compound this problem, modern efficient nozzles feature honed entry and tapered nozzle holes to limit cavitation. Cavitation within the injector can help clean deposits so limiting this will lead to increased deposit formation [8]. Furthermore, in modern diesel fuel injection systems the pressures and temperatures witnessed are considerably higher [8]. Increased pressures and temperatures within the injector will lead to increased deposit formation due to fuel degradation at these harsh conditions. However, the increased injection pressures may also have a secondary phenomenon of washing away deposits before they have been able to stabilise on the surface. This is a complicated relationship since these two phenomena of deposit formation and washing away are both influenced by load. Further causes of the recent problems encountered regarding injector deposits has been the shift to alternative fuels which can increase the risk of deposit formation if the quality of the alternative fuels does not achieve the required standard [9]. This has included addition of biofuel to conventional diesel fuel in order to alleviate pressures on oil reserves and improve sustainability in transport since biodiesel is classed as renewable and more environmentally benign [10][11]. Currently, within the EU there is an allowance for 7 % biodiesel addition in the form of Fatty Acid Methyl Esters (FAME) to diesel fuel [12]. However, the addition of FAME also is known to reduce the stability of the fuel and therefore favour the formation of injector deposits. In addition to biodiesel being used to substitute diesel it can also be added as a lubricity improver for ultra-low sulphur diesel (ULSD) [13]. Secondly, Fuels can become contaminated with metallic components during processing or distribution. In the case that these are alkali metals these can form deposits through reacting with any acidic components within the fuel [14]. The most common of these metals has been reported to be sodium [4]. This can be introduced into the processing of the fuel during the addition of sodium nitrile as a corrosion inhibitor or through careless or incorrect storage and handling [4]. Another factor identified has been the addition of polyisobutylene succinimide (PIBSI) as a detergent/deposit control additive (DCA) [15]. Conventional PIBSI compounds with a molecular weight of approximately 1000 work effectively as DCAs. However, the manufacture and processing of these DCAs is vitally important to their success. Over recent years, it has emerged that the low molecular weight PIBSI (approximately 600 [15]) can increase deposit formation rate [16]. These lower weight PIBSI compounds are often formed as a by-product of conventional PIBSI production and can enter the supply chain and contaminate conventional PIBSI formulations. It should be made clear that industry standard higher molecular weight PIBSI compounds (molecular weight of approximately 1000) have not been reported to assist in the formation of deposits, it is the trace amounts of lower molecular weight PIBSI compounds (approximately 600) that have been linked to deposit formation [16].

Usually, formation of injector deposits to problematic levels in vehicles occur over thousands of kilometres. In order to investigate the performance of different DCAs it is desirable to have a test procedure that will achieve a sufficient level of injector fouling within a shorter period. At present, the DW10 test is the industry standard for evaluating fuel and additive effects on injector deposit formation [17].

The aim of this work was to improve upon the current industry standard test procedure to investigate the fouling propensities of different fuels and additives - the current European test procedure CEC F-98-08 [18][19]. The need to improve upon this cycle stems from the procedure's requirement to dose the test fuel with zinc. If a cycle could be developed to produce injector fouling without the need to dope the fuel with zinc it will reduce test complexity and provide conditions more applicable to conventional engine operation running on conventional fuel. Furthermore, the full DW10 test procedure needs 60-hours to complete, or 32-hours for keep clean evaluation and 64-hours for clean-up evaluation. This is costly in terms of fuel consumption and engine wear but also development time. An improved and realistic test procedure will aid in the testing and development of new DCAs. The development of DCAs is vital in reducing the emissions from modern diesel engines in order to help meet the increasingly stringent emission regulations.

2. Materials and Methodology

2.1 Engine test cell and fuels

Experiments were conducted using a 4-cylinder, turbocharged, Euro 6 diesel engine. The engine featured a common rail direct injection fuelling system typical of modern diesel engines. The details of the engine are provided in **Table 1**. The engine was instrumented enabling the measurement of all the main injection parameters during experiments. This included injection pressure, duration and timing. The fuel consumption was measured using a Pierburg PLU 401_116H and a Mettler Toledo gravimetric balance and soot emissions were measured with a Horiba 1230 PM analyser.

Table 1. Engine specification

Engine specifications	
Displacement	1969 cm^3
Configuration	Inline 4-cylinders
Cylinder Bore	82 mm
Piston Stroke	93.2 mm
Valves	16 (4 per cylinder)
Air Charging	Bi-turbo
Max Engine Power	133 kW @ 4250 rpm
Max Torque	400 Nm @ 1750-2500 rpm
Environmental Classification	Euro 6
Year	2015

The diesel fuel used in this investigation was produced in house ensuring that it contained 10 % v/v of fatty acid methyl ester (FAME), grade A for summer quality according to UNE EN 14214. This was chosen since it could be representative of the future diesel fuel available at fuel stations, and it has a slightly higher FAME content of current fuel market (up to 7% v/v of FAME). The motivation of adjusting the FAME content to 10 % v/v is because the presence of FAME has been reported to increase injector fouling rates. Then, looking for severe fuel that provides a realistic fouling process. The properties of the fuel are shown in **Table 2**.

Table 2. Selected diesel fuel properties

Properties	Diesel	FAME (100 %)
Density (@15 °C)	832.5 kg/m^3	879.1 kg/m^3
Viscosity (@40 °C)	2.801 cSt	4.407 cSt
CFPP	-7 °C	5 °C
Cloud point	-5 °C	9 °C
Lower Heating Value	39.78 MJ/kg	-----
Carbon Content (m/m)	85.30 %	-----
Hydrogen Content (m/m)	13.40 %	-----
Nitrogen Content (m/m)	0.17 %	-----
Sulphur Content (m/m)	<0.1 %	-----

2.2 Injector test flow bench

Whilst the engine control settings were used to infer the development of injector deposits during the cycle, further analysis of the individual injectors was carried out after each engine test. This was done using a Bosch EPS 200 injector test flow bench. This was used to measure the fuel flow rates through the injectors using a specific test oil adhering to ISO 4113. The fuel flow rates through the injectors were then compared before and after each experiment in order to quantify the reduction in flow rate through the injector. The EPS 200 allowed for injection pulse durations between 0.1 ms – 20 ms over a 2 minute test period whilst measuring the flow rate. All 4 injectors were tested using the EPS 200 after each engine test. Each individual injector was tested 3 times to provide a total of 12 flow rate results per engine test (4 injectors x 3 tests per injector = 12 flow rate results). The average of these 12 flow rates were used to compare the performance of the different test cycles with the confidence intervals on each plot showing the 95 % confidence level for each result.

Once an engine test had been completed, the fouled injectors were then tested as per the process discussed above before being cleaned. The injectors were cleaned using an injector cleaning solution in an ultrasonic bath. After the injectors had been cleaned, the flow rate test was completed again in order to check that the injectors have been sufficiently cleaned ready for the next test. **Fig. 1** shows the flow rates for injector group 1 at three different injection test pressures before any injector fouling and then after an injector fouling test and subsequent cleaning. The difference between the flow rates before the engine test and then after the engine test and cleaning was less than 1 % for all of the injection pressures. This validates the cleaning process as suitable for this test methodology.
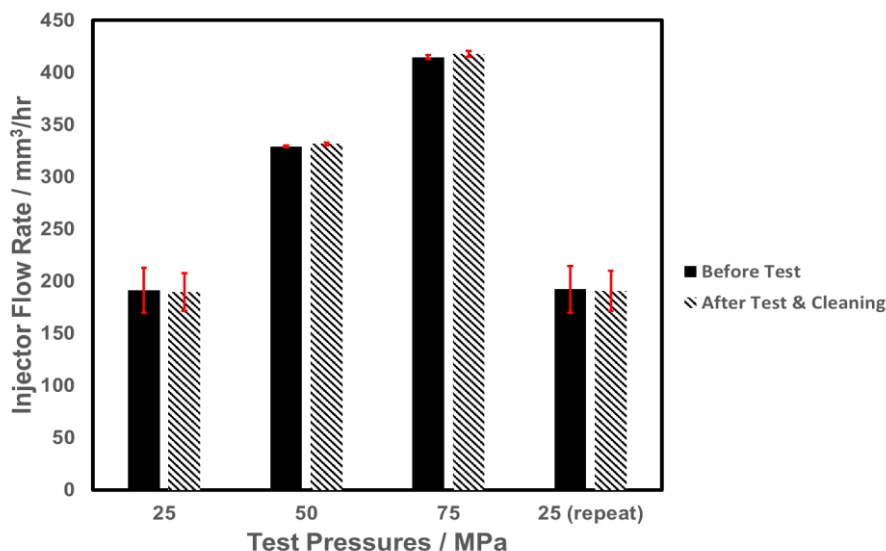
Fig. 1. Fuel flow rate comparison (using the EPS 200) between the same group of injectors before the engine test and after the engine test and subsequent cleaning

2.3 Methodology to develop the accelerated injector fouling procedure

A baseline test of the DW10 engine cycle conditions was competed with a modern engine in order to provide comparisons for the levels of injector deposits. Contrary to the standard DW10 cycle, no zinc was added to the fuel to accelerate deposit formation. Instead of zinc, 10 % v/v of FAME was blended with diesel to promote injector fouling in a way closer to the current fuel market composition. Current diesel fuel available on the market contains up to 7 % v/v of FAME. However, 10 % v/v was selected for this work to help accelerate deposit formation whilst still forming deposits in a realistic manner. Two DW10 cycles were completed, the first one followed the DW10 cycle, whilst the second cycle was completed with the engine operating at the same engine speed but at half of the DW10 load. The DW10 and DW10 half load cycles are shown in **Fig. 2**. The hour long test cycle was repeated 8 times in order to achieve an total engine on time of 8 hours between each 4 hour engine off soaking period.
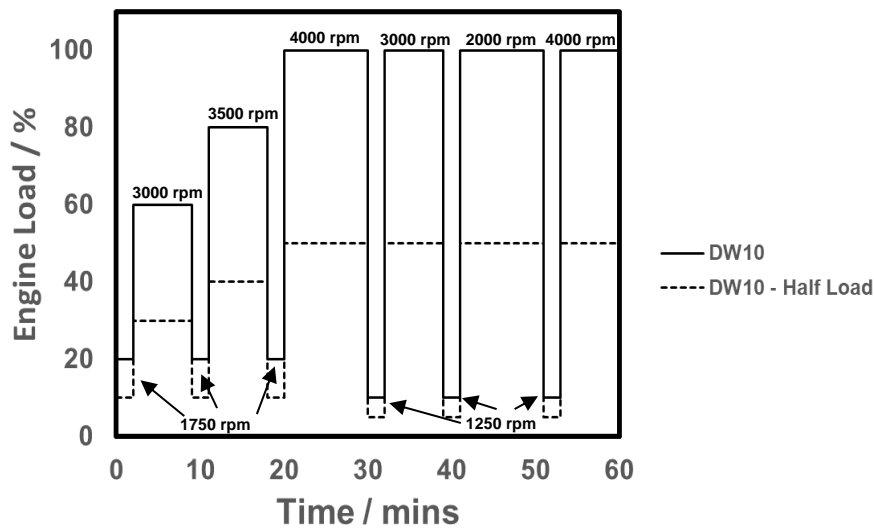
Fig. 2. DW10 and DW10 half load test profiles. Each hour long cycle is repeated 8 times. Note that the speed for the DW10 half load cycle and DW10 cycle were maintained at the same values

The engine was operated using the original OEM ECU maps. In order to develop a new accelerated injector fouling cycle, the engine needed to be mapped to understand which operating points would be favourable to increase injector-fouling rates. The engine was mapped from 50 Nm and 1000 rpm up to 250 Nm and 4000 rpm at the points shown in **Fig. 3** The main parameters of interest were fuel return temperature, EGR rate, injection timing, duration and pressure, soot emissions and fuel consumption. Based on the literature it was decided to target points with high fuel return temperature since this would give an indication of the fuel temperature within the injector. Higher fuel temperatures have been reported to accelerate oxidation and decomposition of the fuel within the injector and assist with the formation of IDID [8][20]. Furthermore, operating points with high EGR rates were also targeted due to the increased amount of soot within the combustion chamber that will assist in the formation of EDID [21].
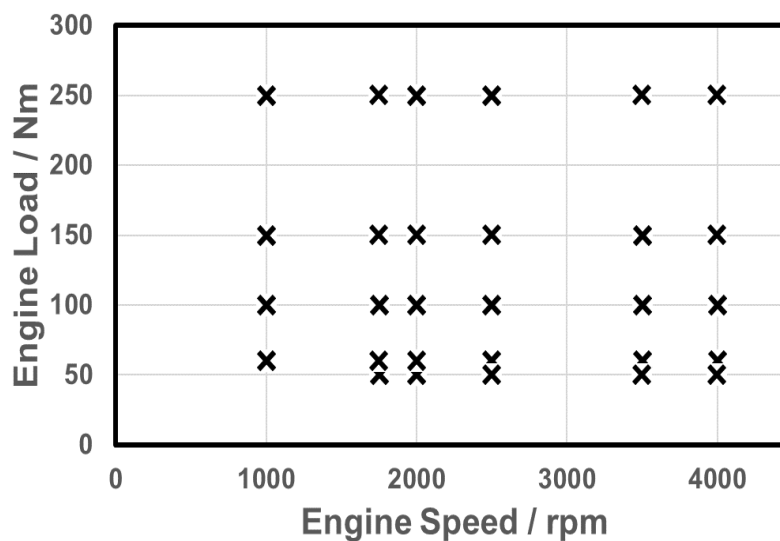
Fig. 3. Engine points mapped

Once the engine had been mapped, two operating points were selected composing the first phase/sequence of the accelerated injector fouling procedure. The two-point format was selected in order to help increase the formation rate of both EDID and IDID. A high engine power operating point was selected in order to increase the temperature in the injector to a level where degradation of the fuel began to occur. Pairing this operating point with a lower engine power operating point where the injection pressure

and fuel flow rate are lower would then give time for any injector deposit to stabilise without being washed away by the high flow rate and injection pressure. In addition to this, it was desirable to have a higher EGR flow rate at the lower engine power point to assist with the formation of EDID due to the increased levels of soot in the combustion chamber. Parameters were changed such as the engine loads and speeds of the high and low power operating points, phase/sequence duration, operating point frequency and general test format were also investigated with the aim to increase the injector fouling rate. In addition to the first two operating points phase/sequence an additional operating point was included that was at high speed and low load. This was selected to aid with the formation of external deposits. High engine speeds reduce the cycle time and therefore reduce the time available for complete combustion leading to increased soot and unburnt hydrocarbons in the combustion chamber. Additional soot and hydrocarbon species will increase the formation of EDIDs. The different parameters investigated alongside any reasoning are shown in **Table 3**.

Table 3. Test parameters studied

Variable	Investigation	Reasoning
Total cycle duration	Testing 1, 2 and 4 cycle repeats	Target the lowest number of cycle repeats whilst still achieving injector fouling rates. Compromise between time and injector fouling
High engine power operating point	Testing how different high power points affect injector deposit formation	The high power point was identified as key for increasing injector temperature and causing fuel degradation in the injector
Cycle frequency	Testing reduced time at each point but an increased frequency of switching between the high and low power points	Increasing the amount of high injector temperature events while maintaining low levels of injection pressure and flow rate to degrade the fuel was targeted by increasing the test cycle frequency.
Ratio of time spent at high power and low power	Identify if there was an advantage to increasing high power point duration relative to the low power point	Identify whether high power or low power points had a greater effect on the fouling rate
High speed idle	Addition of a point where combustion is poor – high speed, low load	Poorer combustion will lead to increased HC species and soot in the engine combustion chamber which could assist in the formation of deposits on the injector

The cycle would follow a similar format to that of the DW10 whereby the cycle would include an 8-hour engine on period followed by a 4-hour engine off soak period that would allow for any deposits formed to stabilise. Once the cycle had been developed, the base fuel was changed to include different additive packages. These additives were then assessed to understand their effect on the injector fouling rate.

3. Results and Discussion

3.1 tDW10 and half load tDW10 injector fouling cycle

A translated DW10 cycle to the diesel engine used in this study (henceforth referred to as tDW10 cycle) and a second tDW10 cycle with the operating point loads halved were ran in order to provide a baseline for the test cycles that would follow. These tDW10 tests followed the full DW10 cycle which consisted of 32 hours of engine operation and 12 hours of engine off time (four 8-hour engine cycles with a 4-hour engine off soaking period between them). The flow rate loss of the injectors after completing the full tDW10 cycle was 3.81 %. This contrasts to the 8.41 % flow rate loss achieved by the half

load tDW10 cycle. The comparison for both the tDW10 cycle and tDW10 half load cycles are shown in **Fig. 4**.
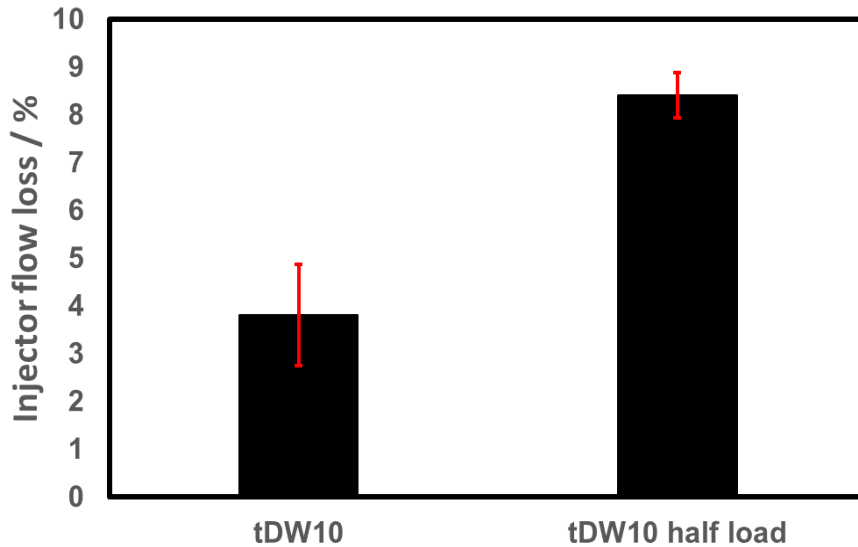
Fig. 4. Injector flow rate loss after cycle completion relative to before the cycle comparison for both the tDW10 cycle and half load tDW10 cycle

These results suggest that in the tDW10 half load cycle for the diesel engine used in this work is over twice as effective as the base tDW10 cycle when considering the rate of injector flow loss. One suggestion for this result is the effect of zinc addition to the fuel. Since no zinc was added for these tests, it could be that zinc addition catalysed the fuel degradation and therefore assists the formation of injector deposits at high load as the formation of deposits actuated by the zinc appears to require higher temperatures and pressures. Without the zinc addition in this work, the formation phenomena at high load could be reduced which would shift the balance towards the phenomena of any deposits that have formed being washed away by the higher injection pressures witnessed at higher loads. Furthermore, the DW10 engine test is very specific concerning engine set up and fuel. Therefore, the different characteristics of the combustion (e.g. injector pressure, boost pressure, in-cylinder flow motion, air-fuel mixture, etc.) or injectors used with each different engine could change the fouling tendencies at each engine operating point. The increased injection pressure within the full load tDW10 cycle will increase the temperature in the injector and therefore increase the formation of IDID [22]. However, this work suggests that higher loads and therefore higher injection pressures reduce the injector flow rate loss, when zinc it is not added. It has been suggested by the authors that the increased pressure can lead to deposits that have not yet stabilised being washed away. Further study of the formation of deposits at different injection pressures and temperatures is required to understand the trade-of between deposits formation and wash-up phenomenon.

3.2 Effect of total test duration

A shorter and simplified first sequence/phase was proposed only featuring one low power and one high power point. One complete cycle featured an 8-hour engine on period followed by a 4-hour soaking period. During the engine on period, the engine cycled between a high engine power and low engine power point. These were 4000 rpm / 120 Nm and 1750 rpm / 60 Nm respectively. The high power point was selected for its high injector temperature, whilst the low power point was selected for its higher EGR rate and lower injection pressure and fuel flow rate. The engine was held at each point for 15 minutes. The newly designed cycle reported an average injector flow loss of 4.24 % which is a relative percentage increase of 11 % compared to the original tDW10 cycle despite being 32 hours shorter in duration. The flow loss for the proposed cycle was half that of the tDW10 half load cycle. This was also effective since the proposed cycle duration was 12 hours compared to 44 hours.

Continuing on from the initial test cycle, the cycle duration was investigated. This involved repeating the cycle once, twice and four times in order to understand what benefit there would be to increasing the cycle duration in terms of injector flow loss. The total flow loss through the injector is shown in **Fig. 5**.
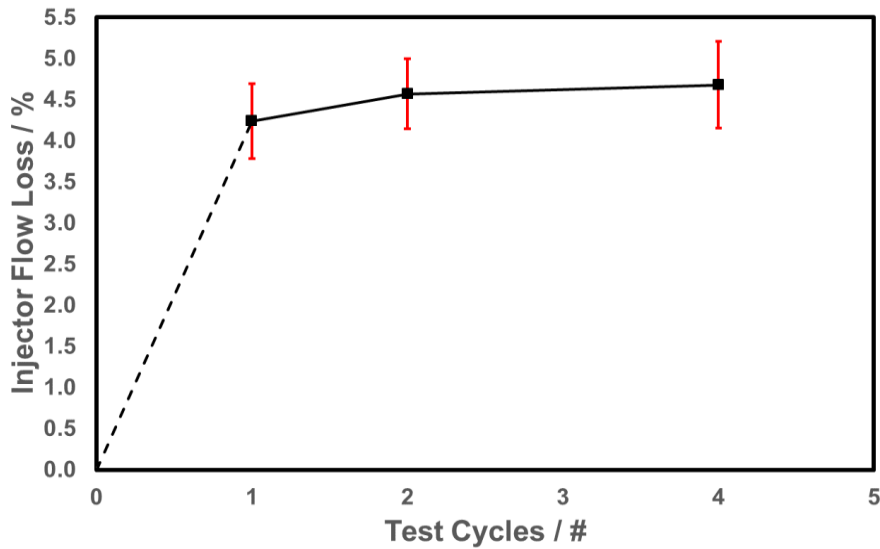
Fig. 5. Effect of the number of cycle repeats on injector flow loss. Each test cycle contained 8 hours of engine operation and 4 hours of engine off soaking time

The results indicate that the majority of the injector fouling occurs during the first test cycle. Therefore, the relationship between the number of test cycle repetitions and the injector flow rate loss is not linear. After completion of one cycle the flow loss measured was 4.24 %. This further increased to 4.57 % after completion of a second cycle which represents a relative percentage increase of 7.78 % compared to the first test cycle. However, extending the test to four cycles only saw a total flow rate loss of 4.68 % which only represents a relative percentage increase of 2.41 % for double the test time. It was found that additional cycles after the second produced little further flow loss; two were deemed optimum. This provided a total cycle duration of 24 hours.

3.3 Effect of different high engine power point

The effect of different engine operating conditions on the injector flow rate loss was studied. The high engine power point is of interest as this will influence the temperature of the injector and the fuel within the injector and therefore the rate of IDID formation. The increase in injector temperature can be achieved through either increases in the engine speed or engine load. Three different engine points were selected with a similar power value but different levels of engine speed and load. These are shown in **Table 4**.

Table 4. High engine power points tested

Engine Speed / rpm	Engine Load (Nm)	Engine Power (kW)	Injection Pressure (bar)	Fuel Return Temperature (ºC)
2000	250	52.36	1240	58.9
4000	120	50.27	870	72.1
4250	120	53.41	890	70.1

The different high engine power points were selected in order to understand whether or not engine speed or engine load had the greater effect on fuel injector deposit formation. An additional high-speed point was also selected at 4250 rpm. This was selected as it is the maximum rated speed for the engine. The cycle format for this investigation was two repetitions of the 8-hour engine on cycle followed by the 4-hour engine off soak after each 8-hour period (8 + 4 + 8 + 4 = 24).
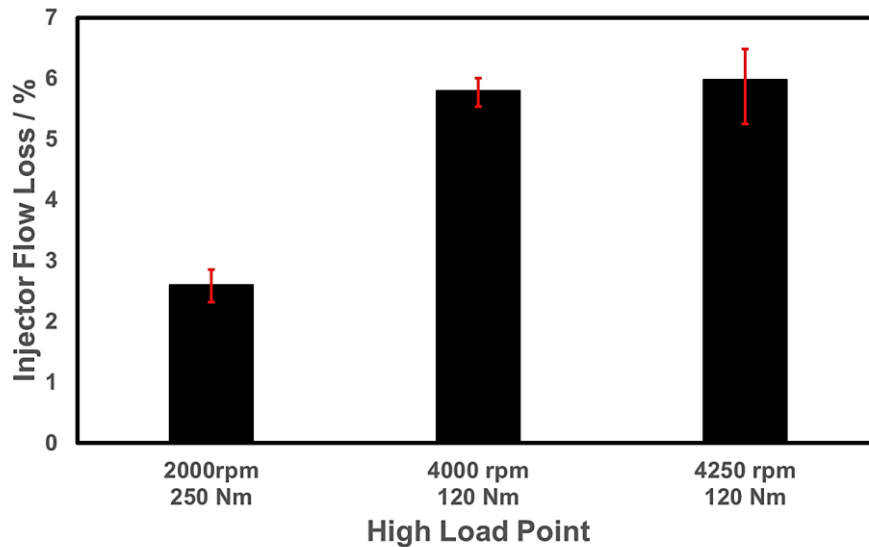
Fig. 6. Effect of high engine power operating point on injector flow loss

The results of the high engine power point investigation shown in **Fig. 6** suggest that there is increased injector deposit formation at higher engine speeds as opposed to higher engine loads. This could be a result of the higher injection pressure used for the higher loads. For approximately the same amount of power, the injection pressure was more than 300 bar less for the higher speed conditions when compared to the higher load cases. Additionally, there will be an increased number of injection events at the higher speed conditions over a given time period due to the increased number of cycles per time period. It has been reported that during the injection event, the release of high pressure fuel can result in a sharp increase in fuel temperature resulting from the high fluid shear [22]. Increasing the number of injection events over a given time period will increase the amount of these temperature spikes which will facilitate the formation of IDID. Furthermore, the temperature of the fuel in the injector return line (used to estimate the injector temperature) was higher for the higher speed conditions suggesting higher speeds are more suited to the reductions in injector flow rate targeted by this testing. Also, increasing the number of injections at high engine speeds, the fuel amount passing through the fuel system at critical conditions is higher for the same testing time. Then, a way to accelerate the injector fouling is to include a high speed engine point with high fuel temperature in the testing procedure. The recommendation from these results is that lower load but higher speed conditions are optimal for the formation of injector deposits. This also supports the result where the half load conditions of the tDW10 produced an increased injector fouling rate when compared to the full load tDW10 cycle.

3.4 Effect of operating point duration

The durations that the engine spent at the high power and low power operating points during the cycle were investigated. This was done in order to understand how these impacted the fouling rates of the injectors. The total cycle time was maintained whilst the duration at each operating point was adjusted to vary the number of repeats of each operating point per cycle. The high power and low power operating points were maintained the same – 4250 rpm / 120 Nm and 1600 rpm / 50 Nm respectively. The first comparison was to reduce the time at each point by 5 minutes in order to complete more test cycles but keep the ratio of high power point and low power point relatively similar. The comparison of the flow rate loss for different frequencies is shown in **Fig. 7**.
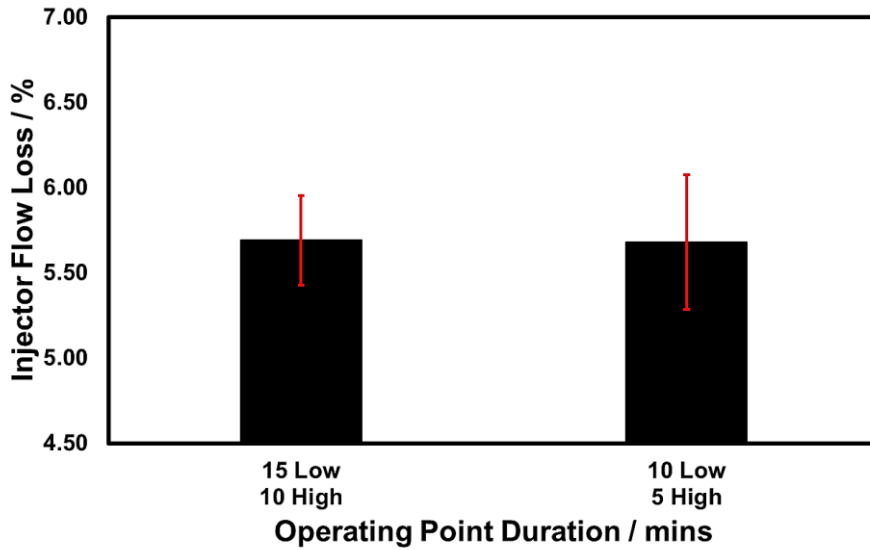
Fig. 7. Flow rate loss for the high frequency (10 min low / 5 min high) and low frequency (15 low / 10 high) tests

From **Fig. 7** it is apparent that there is no statistically significant difference between the higher and lower frequencies. The fuel return temperature from the injector was still able to reach a stable high temperature in order to help accelerate IDID for both the lower frequency and higher frequency tests. This result suggested that 5 minutes was a sufficient amount of time to reach temperatures where IDID could form. An additional investigation was completed by changing the ratio of time between the high power and low power point. This involved a comparison between a cycle that operated at the high power and low power point for 10 minutes each, and a cycle where the low power point was maintained for 25 minutes and the high power point maintained for 5 minutes. Both of these tests had the same total cycle duration, but the equal duration test (10 mins / 10 mins) completed more individual cycles as it took 20 minutes to complete each individual cycle as opposed to 30 minutes. The flow rate loss for the equal duration test and the extended low power point duration test are shown in **Fig. 8**.
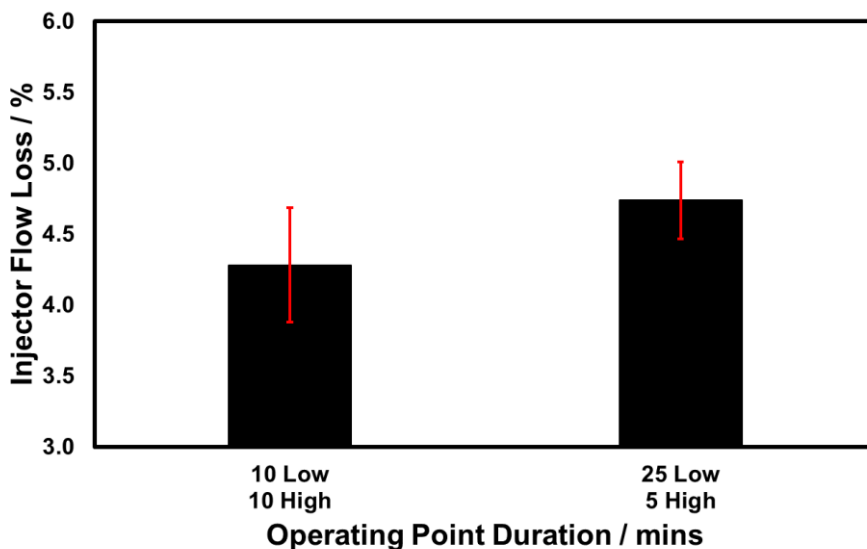
Fig. 8. Flow rate loss for the increased duration at the low power point (25 min low / 5 min high) and equal duration point (10 min low / 10 min high)

By spending a reduced amount of time at the high power point, the injector flow rate loss was increased. This could be a result of the reduced time at higher injection pressures and fuel flow rates that could risk washing away newly formed deposits. Spending longer at a lower injection pressure could provide more time for the deposits that formed during the higher temperature and pressure condition to stabilise.

3.5 Inclusion of high speed idle

Since the lower loads had been more successful in generating injector deposits, an additional test was carried out looking at the effect of low load and high speed which will henceforth be referred to as high speed idle. These conditions are representative of high speed engine decelerations. These are often witnessed during vehicle acceleration events when changing gear as the engine speed has increased up the speed range and the load needs to be disconnected from the engine in order to change gear. This is typical of urban driving where there are multiple vehicle accelerations interrupted by gear changes where the engine load is reduced. Five different high speed idle points were mapped first in order to measure soot emissions and select the optimum point to increase injector deposit formation. These are all shown in **Table 5**.

Table 5. High speed idle point mapping

Engine Speed rpm	Engine Load (Nm)	Engine Power (kW)	Number of Injections (#)	Soot Emissions (mg/m^3)
4000	60	25.13	3	
4250	15	6.68	2	3.08
4500	15	7.07	2	3.97
4750	15	7.46	2	5.77
5000	15	7.85	2	6.97

Comparing the results for the high speed idle mapping, there was a reduction in the number of injection events when the engine speed increased from 4000 rpm to 4250 rpm. This is most likely due to the constraint enforced by the engine speed and the reduced time to complete each cycle. It was also evident that as the engine speed increased so too did the soot emissions. The soot emissions increased due to the reduced combustion efficiency at higher engine speeds. This additional soot formation will enhance the formation of EDID. As the maximum rated speed for the engine was 4250 rpm it was decided that the test should not exceed that speed. 4250 rpm still produced a high level of soot emissions and had the reduced number of injections and therefore behaved similarly to the other high speed points.

A high speed idle point of 4250 rpm and 15 Nm was added to the cycle format and the total time cycling between the high and low power conditions was reduced. This new format contained two hours of cycling between the high power and low power conditions. This was then followed by 12 hours at the high speed idle point. This contrasted to the baseline format which featured the 12-hour cycle between the high power and the low power point with the 8-hour engine off soaking period. The comparison between the two cycles is shown in **Fig. 9**.
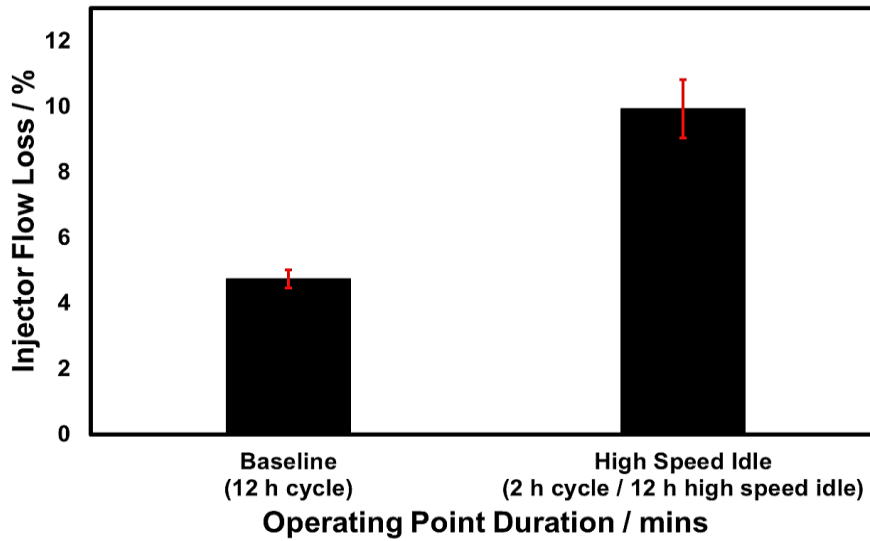
Fig. 9. Flow rate loss comparison between the baseline cycle and the cycle featuring the high speed idle

It can be seen in **Fig. 9** that the addition of a high speed idle point into the cycle increased the flow rate loss by 109 % relative to the cycle without a high speed idle point. This is most likely due to increased formation of EDID. The cycle featuring the high speed idle did not feature any engine off soaking time. This replacement of the engine soaking period with a high speed idle provided a much increased fuel flow rate loss.

3.6 Accelerated injector fouling cycle

Based upon the investigations completed and results obtained in the previous sections, a final accelerated injector fouling cycle was selected. The format of the cycle is shown in **Fig. 10** with the justification for each part of the cycle shown in **Table 6**.
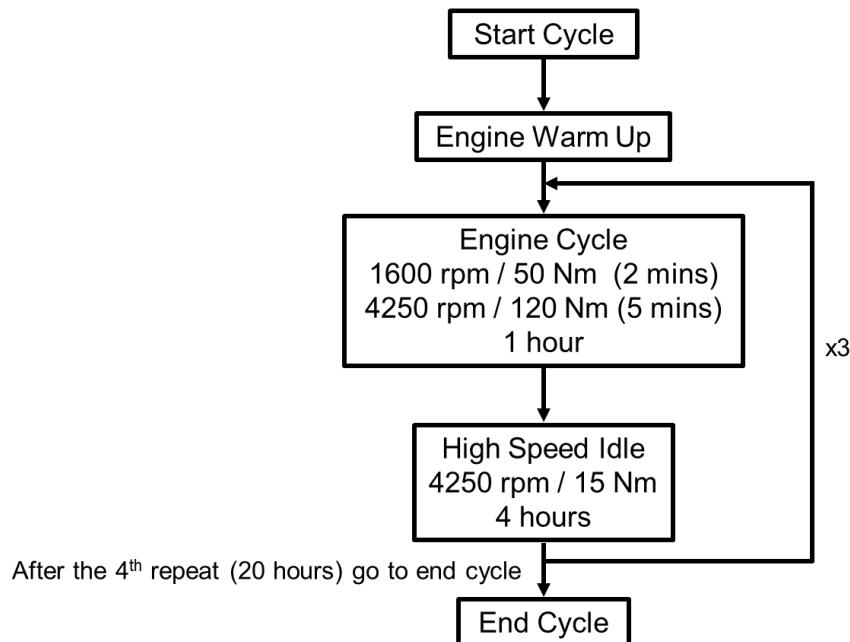
Fig. 10. *Proposed accelerated injector fouling cycle. Please note the engine cycle containing the high power and low power point lasted for 1 hour. 8 cycles were completed with the 9th cycle completing 2 minutes at low power but then 2 minutes at high power*

The cycle consists of two fundamental sequences/phases repeated four times. The first sequence/phase of engine cycling between the high and low power points has been designed to aid in the formation of IDID. This is because cycling between the high and low engine power points encourages conditions in the injector where the temperature is high, but the flow rate and injection pressures are low. The optimum conditions occur immediately after the end of the high engine power point when the engine switches to the low power point. This is because some heat has been retained by the injector, but the pressures and flow rate are low as the condition has just changed to the low power point. On the other hand, the second sequence/phase of the cycle features the high speed idle was chosen for its apparent ability to form EDID. This high speed idle can encourage poor combustion and therefore a surplus of soot and hydrocarbons with a high boiling point that will aid in EDID formation.

Table 6. Justification of *accelerated injector fouling cycle*

Factor	Justification
20-hour cycle duration	There is little increase in injector fouling after 20 hours
4250 rpm / 120 Nm High power point	Higher speed and lower load increased injector fouling
1600 rpm / 50 Nm Low power point	This point was selected based on higher soot emissions and EGR rates.
Cycle frequency	The 5-minute at high power was selected to avoid long durations at high load. A 2-minute low load time was selected to keep the injector temperature high for longer during the cycle.
High speed idle	A high speed idle point increased injector fouling.

These results have been visibly observed when removing the injectors after the cycle was completed. Whilst it was not possible to observe IDID visually without damaging the injector, it could be seen that there was a substantial amount of EDID formed during the cycle. **Fig. 11** shows the amount of deposits formed on the injector tip during the cycle when compared to the injector tip before the cycle.

Fig. 11. Injector tip before cycle (left cycle) and after cycle (right side)

3.7 Accelerated injector fouling cycle validation and additive testing

After the new cycle was defined, it was then validated with the use of different DCAs. This was done in order to observe if there were any difference in injector performance when using different additives. This would also prove the cycle was fit for purpose as it would be able to distinguish between different additives. There were two different additives tested. These were the currently available additives used in the standard diesel fuel and used in the premium diesel fuel. The injector flow losses are plotted in **Fig. 12**.
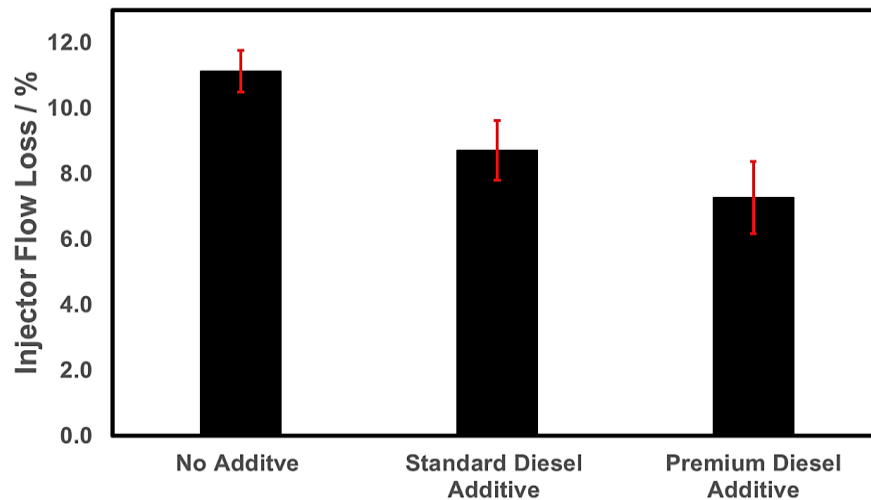
Fig. 12. Test cycle validation with different additives

The baseline test cycle without any additives resulted in an injector flow rate reduction of approximately 11 %. The flow rate losses for the additives of standard and premium diesel were 8.72 % and 7.27 % respectively. This shows that the cycle is able to distinguish between a fuel without an additive and a fuel with an additive. Furthermore, the cycle was also able to detect a difference in the flow loss between the different additives. This shows the cycle is able to compare the performance of different additives.

In addition to the injector flow loss results, it was also possible to see the evolution of the fuel consumption throughout the cycle. With the addition of DCAs to the test fuel, differences in the total fuel consumption during the tests were observed. The total fuel used during the cycle was compared for each of the tests with the results shown in **Table 7**. There was very little difference in the injection pressures and injection pulse durations over the cycle. This meant that the better way to assess the performance was the accumulated fuel consumption that was able to capture the differences over the whole cycle. It was most likely due to the high injection pressures typical of modern diesel engine that small changes in the injection pulse duration yield a sufficient change in the fuel delivered to the cylinder.

Table 7. Fuel consumption comparisons between the baseline and different fuel additives with the fuel saving relative to the baseline over the 20-hour cycle

Fuel	Fuel Usage (l)	Fuel Saving (%)
No additive diesel	142.7	-
Standard diesel	141.4	0.91
Premium diesel	139.0	2.59

During the cycle, fuel consumption will increase as injector deposits begin to form and therefore affect the spray characteristics and fuelling. This will have a detrimental effect on the engine performance meaning that more fuel will need to be injected per engine cycle to achieve the torque demanded by the cycle. This explains the difference in fuel usage during the cycle since additives will reduce the formation of deposits that will hinder performance.

4 Conclusions

The aim of this study was to develop an engine cycle test method with the function of being able to differentiate between the performances of different diesel DCAs in the shortest possible time without the addition of zinc to the test fuel. This is an important and current topic due to the need to develop DCAs in order to minimise the effects of diesel injector deposits. This will continue to be a focus as emission regulations become tighter and meeting these will require the optimisation of all powertrain systems including the fuel delivery system. The newly developed engine cycle consistently reaches injector flow loss rates greater than 10 % using the base fuel. This is higher than the 4 % injector flow reduction achieved by the original tDW10 cycle tested for this work. Furthermore, the higher levels of injector

fouling achieved with the newly developed cycle was achieved in 20-hours as opposed to the 60-hours required to complete the tDW10 cycle.

The cycle was also shown to be able to distinguish between the different DCAs with both injector flow rate reduction and total fuel consumption during the cycle. The DCA packages of standard and premium diesel were able to demonstrate a tangible improvement in fuel consumption and injector flow. The injector flow loss was reduced by a relative percentage of 21.65 % and 33.18 % respectively for the standard and premium DCA packages. The fuel consumption during the cycle was reduced by 0.91 % and 2.59 % respectively. Since the fuel consumption and injector flow losses are directionally in agreement, it could be concluded that the cycle shows high promise to evaluate different DCAs.

The newly developed cycle could be used in its current format. However, there are additional studies that could be completed to investigate the effects of additives on already fouled injectors. At present, the only tests completed have been the 'keep clean' tests where the additive was used from the start of the test with a clean set of injectors. Additional tests could include the use of a 'clean up' test where the additive is added to the fuel part way through the test cycle. This would give the indication of DCA performance when clearing deposits that have already formed. This injector deposit testing technique can also be used to complete further studies using renewable fuels to investigate their deposit forming proclivity and the performance of different DCAs in renewable fuels.

References

[1]   S. Kang, W. Cho, C. Bae, and Y. Kim, "Influence of the Injector Geometry at 250 MPa Injection in a Light-Duty Diesel Engine," *SAE Tech. Pap.*, vol. 2017-March, no. March, 2017.

[2]   Z. Stepien, "A study of factors influencing the formation of harmful deposits in the diesel engine injectors," *Maint. Reliab.*, vol. 19, no. 3, pp. 331–337, 2017.

[3]   S. Kumagai, A. Takahashi, H. Nagato, and R. J. Stradling, "Development of an Injector Deposit Formation Test Method for a Medium-Duty Diesel Engine," *SAE Tech. Pap.*, vol. 2015-Septe, no. September, pp. 1–6, 2015.

[4]   G. Ngoi, R. Barbour, D. Arters, J. Ray, and A. Stevens, "A study of the internal diesel injector deposit phenomenon," *Annu. Fuels Lubes Asia Conf. Exhib.*, p. 15, 2011.

[5]   J. Barker, P. Richard, C. Snape, and W. Meredith, "Diesel injector deposits - An issue that has evolved with engine technology," *SAE Tech. Pap.*, 2011.

[6]   J. Galante-Fox and J. Bennett, *Diesel injector internal deposits in high pressure common rail diesel engines*. Woodhead Publishing Limited, 2012.

[7]   A. Birgel *et al.*, "Deposit formation in the holes of diesel injector nozzles: A critical review," *SAE Tech. Pap.*, no. 2008-01–2383, 2008.

[8]   A. T. Hoang and A. T. Le, "A review on deposit formation in the injector of diesel engines running on biodiesel," *Energy Sources, Part A Recover. Util. Environ. Eff.*, vol. 41, no. 5, pp. 584–599, 2019.

[9]   M. A. Fortunato, F. Lenglet, A. Ben Amara, and L. Starck, "Are Internal Diesel Injector Deposits (IDID) Mainly Linked to Biofuel Chemical Composition or/and Engine Operation Condition?," *SAE Tech. Pap. Ser.*, no. 2019-01–0061, 2019.

[10]   M. Canakci and H. Sanli, "Biodiesel production from various feedstocks and their effects on the fuel properties," *J. Ind. Microbiol. Biotechnol.*, vol. 35, no. 5, pp. 431–441, 2008.

[11]   D. N. Tziourtzioumis and A. M. Stamatelos, "Diesel-injection equipment parts deterioration after prolonged use of biodiesel," *Energies*, vol. 12, 2019.

[12]   T. H. E. E. Parliament and P. Union, "European Parliament Directive 2009/30/EC," *Off. J. Eur. Union*, no. April, p. L140/88-L140/113, 2009.

[13]   M. A. Hazrat, M. G. Rasul, and M. M. K. Khan, "Lubricity Improvement of the Ultra-low Sulfur Diesel Fuel with the Biodiesel," *Energy Procedia*, vol. 75, pp. 111–117, 2015.

[14]   C. Trobaugh, C. Burbrink, Y. Zha, S. Whitacre, C. Corsi, and N. Blizard, "Internal Diesel Injector Deposits: Theory and Investigations into Organic and Inorganic Based Deposits," *SAE Int. J. Fuels Lubr.*, vol. 6, no. 3, pp. 772–784, 2013.

[15]   J. Reid and J. Barker, "Understanding polyisobutylene succinimides (PIBSI) and internal diesel injector deposits," *SAE Tech. Pap.*, vol. 11, 2013.

[16]   J. Barker, J. Reid, C. Snape, D. Scurr, and W. Meredith, "Spectroscopic Studies of Internal Injector Deposits (IDID) Resulting from the Use of Non-Commercial Low Molecular Weight Polyisobutylenesuccinimide (PIBSI)," *SAE Int. J. Fuels Lubr.*, vol. 7, no. 3, pp. 762–770, 2014.

[17]   R. Williams, A. Smith, and I. Buttery, "Formation and Removal of Injector Nozzle Deposits in Modern Diesel Cars," *SAE Int. J. Fuels Lubr.*, vol. 6, no. 1, pp. 230–240, 2013.

[18]   R. Barbour, R. Quigley, D. Browne, and A. Panesar, "A Comparison of Peugeot DW10

Dynamometer and Vehicle Engine Performance," *8th Int. Colloq. Fuels Conv. Futur. Energy Automob.*, no. March, 2011.

[19]   Z. Stepien and W. Krasodomski, "Effect of trace zinc amounts introduced in various chemical structures in diesel fuel on coke deposits of fuel injectors of a CI engine," *Int. J. Engine Res.*, 2018.

[20]   Z. Stępień, "The reasons and adverse effect of internal diesel injector deposits formation," *Combust. Engines*, vol. 156, no. 1, pp. 20–29, 2014.

[21]   D. Agarwal, S. K. Singh, and A. K. Agarwal, "Effect of Exhaust Gas Recirculation (EGR) on performance, emissions, deposits and durability of a constant speed compression ignition engine," *Appl. Energy*, vol. 88, no. 8, pp. 2900–2907, 2011.

[22]   P. Lacey, S. Gail, J. M. Kientz, G. Benoist, P. Downes, and C. Daveau, "Fuel Quality and Diesel Injector Deposits," *SAE Int. J. Fuels Lubr.*, vol. 5, no. 3, pp. 1187–1198, 2012.

THIESEL 2022 Conference on Thermo- and Fluid Dynamics of Clean Propulsion Powerplants

A Three-Stage Arrhenius Approach with a Coupled 0D-Model to Predict Ignition Delays in a Premixed Charge Compression Ignition (PCCI) Diesel Engine

M. Wahl[1], M. Bargende[1], A. Casal Kulzer[1], H.-J. Berner[2], S. Schneider[3]

[1]IFS – Institut für Fahrzeugtechnik Stuttgart. University of Stuttgart, Pfaffenwaldring 12, 70569 Stuttgart, Germany

E-mail: {Marvin.Wahl,Michael.Bargende,Andre.Kulzer}@ifs.uni-stuttgart.de
Telephone: +(49) 711 685 61778 (M. Wahl)

[2]FKFS - Forschungsinstitut für Kraftfahrwesen und Fahrzeugmotoren Stuttgart, Pfaffenwaldring 12, 70569 Stuttgart, Germany

E-mail: Hans-Juergen.Berner@fkfs.de
Telephone: +(49) 711 685 65714

[3]MAHLE International GmbH, Pragstr. 26 - 46, 70376 Stuttgart, Germany

E-mail: Simon.Schneider@mahle.com
Telephone: +(49) 711 501 20887

Abstract. To comply with global exhaust emission regulations for CO_2 and pollutants in diesel internal combustion engines, ways of reducing raw engine-out emissions have been the focus of numerous research projects in recent years. Homogeneous charge compression ignition (HCCI) is one approach to simultaneously decrease both soot and NO_x pollutants by reaching a homogeneous mixture of fuel and air before the start of combustion. Therefore, homogeneous charge compression ignition (HCCI) is one possibility to reduce both soot and NO_x significantly. However, diesel fuel injection around bottom dead center or in the early compression stroke to reach a homogeneous mixture without significant wall impingement was never qualified for serial use. Premixed charge compression ignition (PCCI) is a way to counteract the well-known soot and NO_x trade-off with a state-of-the-art direct injector, while combustion phasing can be controlled by the main injection. That qualifies PCCI for serial use, but engine load and engine speed are still limited for highly premixed injection strategies. Due to combustion phasing with multiple injections, engine load and speed range can be extended theoretically compared to HCCI-mode.

In this project, a Mercedes-Benz single-cylinder engine was used for investigations. The test bench configuration, the thermodynamic analysis to infer constraints for the 0D-model and the developed model to predict ignition delays for PCCI are presented. For the experimental investigations, intake temperature, intake pressure, piston cooling, cooling water temperature, high-pressure exhaust gas recirculation, exhaust pressure, inlet swirl (swirl flap), fuel pressure and injection strategy were varied to provide a diverse data set for the model development. Ignition delays for multiple injections were determined based on the calculated heat release rate. It has to be considered that a low and a high-temperature heat release also exists for PCCI-mode. Therefore, up to four ignition delays can be detected.

In this work, the measurements at the single-cylinder test bench were performed and a model to predict ignition delays for PCCI mode was developed. The combined model to predict ignition delays, the parameter setting and the comparison of different variations (as EGR rate, injection strategies, engine load and speed) will be published.

Notation

CARB	*California Air Resources Board*
CA	*Crank Angle*
CAbTDC	*Crank Angle before Top Dead Center*
CAaTDC	*Crank Angle after Top Dead Center*

CF	Cool Flame
EGR	Exhaust Gas Recirculation
EOI	End of Injection
EPA	Environmental Protection Agency
HCCI	Homogeneous Charge Compression Ignition
HTHR	High Temperature Heat Release
ID	Ignition Delay
ISFC	Indicated Specific Fuel Consumption
LTHR	Low Temperature Heat Release
PCCI	Premixed Charge Compression Ignition
ROHR	Rate of Heat Release
SMD	Sauter Mean Diameter
SOI	Start of Injection
SOB	Start of Burning
TDC	Top Dead Center
WLTC	Worldwide Harmonized Light Vehicles Test Cycle

1   Introduction

Diesel engines, from small to large size, are still necessary to power our daily life in many fields all over the globe. From small size engines for local water pumping, as an independent emergency generator up to heavy-duty diesel engines for transportation - these are just a few examples where diesel engines are in use aside from individual public transportation. While maximizing engine power output is one goal of the development process, cost reduction and lowering the (raw) exhaust pipe emissions are on the other side of the development triangle. Nowadays, diesel engines are equipped very differently in the case of hardware components and exhaust aftertreatment. Whereas a 4-stroke process with 130 bar injection pressure can be sufficient in small size engine types, a 2-stroke process combined with over 2000 bar injection pressure is typical in large engines. The legislation of exhaust pipe emissions, costs, and the use case (for example: stationary/not stationary, size, output power, noise, etc.) are drivers of the development process. Worldwide, different limitations for exhaust pipe emissions are valid. While Euro 6d is valid for legislation of passenger cars and commercial vehicles up to 3,500 kg in Europe, the emissions legislation is different in North America. In California, the autonomous emissions legislation is developed and monitored by the independent authority CARB (California Air Resources Board). It has to be mentioned that twelve other states use CARB emission laws, although EPA (Environmental Protection Agency) publishes the regulations for federal emissions legislation in the USA. Additionally, heavy-duty on-road, nonroad vehicles, locomotives, marine engines, domestic marine engines, stationary engines, two or 3-wheel vehicles, low-speed trucks, generator sets and many more are independently regulated in many different legislations in different regions all over the world.

Diesel engines for passenger cars and light commercial vehicles have to be tested and certificated in different test procedures - for which the test cycle WLTC was introduced in some regions to reduce the global test variety. The next milestone in Europe will be Euro 7. Initial information indicates that additional (compared to Euro 6d) exhaust gas components will be restricted. To reach this emission limit, the exhaust aftertreatment has to be combined with a highly efficient engine with low raw emissions for high load in an expanded temperature window for a cold start.

In this paper, a state-of-the-art single-cylinder 4-stroke engine from Mercedes-Benz was used at the test bench. The base 6-cylinder engine was used in passenger cars as in the transportation sector of Mercedes-Benz (Sprinter and Viano). Furthermore, Chrysler and Jeep used this engine to power the 300C and the Grand Cherokee.

1.1   Injection Pattern for Premixed Diesel Combustion

To reach high engine efficiency combined with low raw emissions and noise, the highly dynamic variation of the injection strategy from cycle to cycle is essential. In case of a common rail combined with a solenoid valve or piezo injector, more than seven injections per cycle are feasible. This system also leads to shifting the start of injection (SOI) into the expansion phase to increase exhaust gas temperature or early compression stroke. A late injection offers the opportunity to increase the exhaust temperature to heat up the exhaust aftertreatment system, whereas an early injection has the advantage of reaching a premixed mixture before combustion to reduce noise and the pressure increase gradient.

As known from literature and preliminary projects with homogeneous charge compression ignition (HCCI), the cetane number, compression ratio, inlet temperature and exhaust gas recirculation (EGR) rate play a dominant role in the ignition delay. While for conventional diesel, the pre-injection is injected up to around 20 °CAbTDC (crank angle before top dead center), in HCCI, the injection is advanced up to the open inlet valve (around 180 °CAbTDC). In case of port fuel injection (open inlet valve), the fuel has to be atomized before injection to neither form unusual wall wetting by penetration depth nor to inject diesel droplets with a large Sauter mean diameter (SMD). A way between those two is a very early injection in the compression stroke with the serial injector. Counteracting these are limitations of wall wetting and the amount of injected fuel, which is described in section *2.2*.

DCCS	HPLI	HCCI	HCLI	PCCI
Dilution Controlled Combustion System	Highly Premixed Late Injection	Homogeneous Charge Compression Ignition	Homogeneous Charge Late Injection	Premixed charge compression ignition
– Injection timing as conv. Diesel – EGR rate > 80% – Lowest local flame temperature compared to the other strategies	– Injection after TDC – Wide range of air-fuel equivalence ratio – EGR rate ~ 40% – EOI before SOB to lower soot emissions	– Early injection (PFI) for homogeneous conditions – SOB depends on in-cylinder conditions – High EGR rate, air-fuel equivalence ratio ~1	– As HPLI, injection timing before TDC for homogeneous conditions	– Several early injections (or PFI) for partially premixed conditions. Main injection near TDC to control combustion phasing
High HC-Emissions and low indicated efficiency	Efficiency, HC- and CO-Emissions comparable to conv. Diesel	Small range of RPM and IMEP	Efficiency as conv. Diesel engine HC- and CO-emissions as state-of-the-art Otto-engines	Similar or slightly increased HC- and CO-emissions (to conventional Diesel)

Figure 1 Comparison of Injection Strategies Aside of Conventional Diesel [1]

For homogeneous and premixed diesel combustion, various strategies have been developed in recent years. As presented in *Figure 1*, the main focus is the injection timing and the rate of recirculated exhaust gas, where the combination of both leads to different mapping conditions due to changing ignition delay. The conventional diesel has four phases from SOI to the end of the expansion, starting with the ignition delay, premixed combustion, mixing controlled combustion and late combustion phase. The soot formation mainly occurs in local fuel-rich areas, and nitrogen oxide has its main formation mechanism in local fuel-lean or stoichiometric areas with high temperatures. These main formation areas for soot and NO_x are typically present for short ignition delays since the fuel is not mixed reasonably well with the air in the combustion chamber.

As it is described in the middle of *Figure 1*, the injection strategy of HCCI relies on a comparably high homogeneity of the mixture at the start of burning (SOB). Therefore, fuel is only injected very early (in the open inlet valve as port fuel injection or the early compression stroke). On the other hand, highly premixed late injection (HPLI) has an injection strategy with SOI after top dead center (TDC). In combination with a high EGR rate of around 40 %, the combustion is defined to start after the end of injection (EOI). This counteracts the problem of the soot formation process in fuel-rich areas mentioned above.

For the examinations in this paper, a PCCI injection strategy was used. This approach of premixing follows that the first injections (one or multiple) are set to the early compression stroke. The ignition delay is expected to support the mixture homogenization due to of elapsed time. Then, the main injection around TDC is used for combustion phasing and further pressure forming. This main injection has the disadvantage of a pre-heated combustion chamber for the first injection's heat release. This leads to shorter ignition delay and may cause higher soot and NO_x emissions. Summing up, the advantages and disadvantages of HCCI and conventional diesel combustion are merged in the PCCI application. In conclusion, it has to be mentioned that improvements in PCCI are not to be dismissed in the case of hybridization of the propulsion system.

1.2   Theoretical Improvements of PCCI over Conventional Diesel Configuration

First of all, the serial setup concerning hardware such as injector, rail, pump, cylinder head and piston can be used for PCCI mode. This is, compared to HCCI, an advantage for investigations regarding serial use.
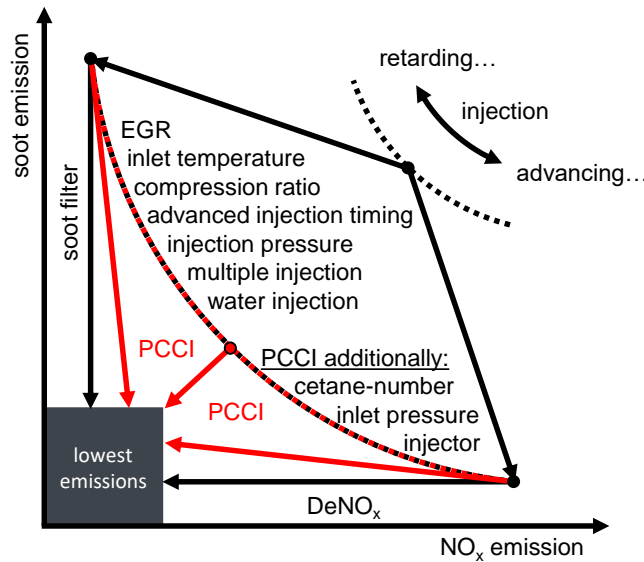
Figure 2 Soot and NOx Trade-off in Diesel Engines

In *Figure 2*, the soot to nitrogen oxide trade-off for conventional diesel engines is illustrated. Either soot or NO_x can be reduced drastically by adapting the injection pattern and the given parameters. However, a soot filter or $DeNO_x$ System has to be used theoretically to reduce both at once. As shown with red arrows, PCCI configuration can reduce the soot and NO_x emissions to a minimum in a limited load and engine speed range. However, known from literature and own investigations, this PCCI mode leads to increased carbon monoxide (CO) and hydrocarbons (HC) emissions. The availability of oxygen in the exhaust pipe reduces these emissions by a catalytic converter. In any case, the light-off temperature of this catalytic converter has to be exceeded, although exhaust gas temperature is relatively low for premixed combustion. Therefore, a heated catalytic converter could be used.

To reach this lowest emission point, a combination of the described parameters in the PCCI Mode can be used for application. The EGR rate and compression ratio mainly contribute to lower soot and NO_x emissions, but indicated specific fuel consumption (ISFC) slightly increases due to wall wetting and thermodynamic reasons (combustion phasing).

1.3   Ignition Delay Modelling

The ignition delay models in the literature are mainly separated into 'empirical' and 'detailed chemistry mechanisms'. For empirical models, experiments at the test bench are used to fit the 0D approach. For detailed chemical mechanism models, fundamentals of chemical reductions are applied to predict the in-cylinder conditions. Furthermore, hybrid ignition delay models were developed to combine the advantages of both [1].

For the empirical models, different methods are used to reach a fast calculation and comparable good predictability. In literature, an Arrhenius approach is common [2, 3, 4] and described as:

$$k = A \cdot \exp\left[-\frac{E_A}{RT}\right] \tag{1}$$

where A and b are variables for model parameterization, T is the (actual) process temperature, E_A the activation energy and R is the universal gas constant.

The first ignition delay models - based on the Arrhenius equation - were presented by Wolfer (1938), Bauer (1939) and Elliot (1949) [5, 6, 7]. Wolfer and Bauer integrated a pressure-dependent term to adapt the Arrhenius equation to experimental investigations. Later, the equation was extended to adapt for recirculated exhaust gases, mean piston speed, fuel to air mixture and additional parameters affecting the ignition delay.

The main focus of the experimental investigations published in the literature lies on HCCI or similar to HCCI (single injection event) conditions. Due to a single injection event, the ignition delay can be directly linked to a parameter variation (for example, inlet temperature, inlet pressure or EGR rate variation). However, for PCCI configuration with multiple injections, the ID of LTHR and HTHR also varies due to interference of the injection timing, injection duration and the introduced turbulence. Therefore, a 3-Arrhenius approach combined with a termination criterion is applicable. These three stages depend on the analysis of ignition behavior for n-heptane with detailed chemistry [8], where the first term is valid for the LTHR and the second and third term extend the Arrhenius approach to be used for HTHR ignition delay calculation.

In this work, already published ignition delay models were compared and extended to fit for the variations of inlet temperature, inlet pressure, injection strategy (timing, pressure, and duration), engine speed, engine load and EGR rate. The model is depicted in section 3.1.

2   Single Cylinder Test Bench

The single-cylinder test bench is based on a Mercedes-Benz OM642 diesel engine. As shown in *Table 1*, a close to series hardware with a single-cylinder crankcase and a full engine cylinder head is used for the investigations. The injection signal is measured by a clamp meter. This analog signal is converted to a digital signal by a Schmitt trigger. The measurement resolution for high-frequency signals (as clamp meter and in-cylinder pressure) is 1 °CA (Crank Angle).

Table 1 Engine and Test Bench Parameters

Test Bench	Single Cylinder Only
High Pressure Sensor	Kistler 6041A
Exhaust Gas Measurement	Horiba 7170 DEGR
Fuel Type	Diesel
Fuel Density	829.1 kg/m^3
Fuel Cetane Number	51.9
Net Calorific Value	42.99 MJ/kg
Engine Type	Mercedes-Benz OM642
Displacement Volume	498 mm^3
Stroke	92 mm
Bore	83 mm
Stroke/Rod (s/r) Ratio	0.27
Connecting Rod length	168 mm
Compression Ratio (geo.)	15.34:1
Number of Valves	4 (one inlet port with swirl flap)
Swirl Flap	Open
Injection System	CRI3-20
Nozzle Number	8 holes
Spray Angle	157°
Orifice Diameter	0.126 mm
Fuel Pressure	40 to 140 MPa

2.1   Test Bench Configuration

The schematic airflow for the test bench in *Figure 3* starts on the right side of the illustration. The air can be compressed externally up to 3 bars relative. Downstream, two intake air coolers are mounted. The conditioning of these water-to-air intercoolers is external. Intake air temperatures down to 12 °C (no EGR rate) are feasible but not realistic for the PCCI configuration. An intake plenum with a water jacket is installed for premixing of air and the recirculated exhaust gas. Further downstream, a mixing apparatus is installed in the inlet pipe for additional mixing. The full engine cylinder head is mounted with the associated air intake plenum. Temperature and pressure (dynamic and static) measurement equipment as a sampling point to detect the proportion of CO_2 in the intake plenum is inserted near the inlet valves. The integrated swirl flap has not been used yet.

As major characteristic for PCCI, the inert gas in the combustion chamber influences the ignition delay and rate of heat release (ROHR) relevant. Furthermore, this influences the combustion process and the

raw emissions of the engine. A calculation of the 3-Stage Arrhenius, as described in section *3*, requires the knowledge of the summed up internal and external inert gas. The external portion is calculated with the measured CO_2 in the inlet, exhaust, and background (portion of carbon dioxide in the environment out of literature). Dynamic pressure sensors in the inlet and exhaust port are necessary to calculate the residual (internal recirculated exhaust) gas. In combination with the known valve lift curve and the flow coefficients, a charge change calculation can be implemented and is required for further calculations. The addition of external and internal recirculated exhaust gas at "inlet valve closes" position is sufficient for the Arrhenius approach. The investigations show that the external recirculated exhaust gas portion is mainly responsible for the summed-up EGR rate, even with a negative valve overlap.

The EGR Line is equipped with a heat exchanger (cooler), an EGR Valve and a condensate drain. For the heat exchanger, the cooling temperature is regulated to 90 °C. As a result, the precipitating condensate is negligible for thermodynamic aspects. To control the EGR valve position, a pulse wide-modulated signal of 150 Hz is set once. For the static measuring, no regulator is used for consistent results.

An AVL Smoke Meter is installed downstream of the exhaust flap due to a maximum allowed relative pressure for the surge line of 750 mbar. Additionally, ambient pressure and temperature in the test bench area and humidity of the fresh inlet air is measured.
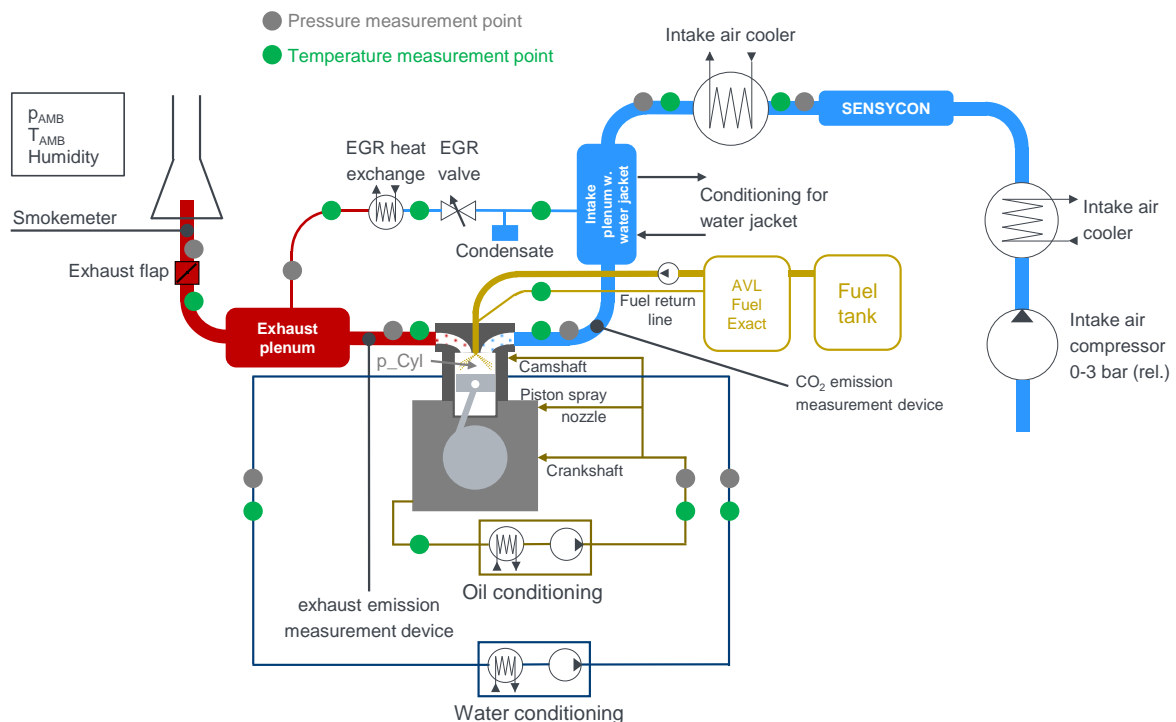
Figure 3 Schematic Single Cylinder Test Bench Configuration (adapted from **[9]**)

2.2   Thermodynamic Analysis and Results

Since the cycle-to-cycle variation is low compared to a spark ignition engine, an average of measured cycles is still useful to examine differences in the combustion for variations (e.g. injection timing or EGR rate). Therefore, the average of 199 cycles leads to one static point. The calculation of the ROHR and the gas exchange analysis is accomplished with TIGER from EnginOS GmbH. As a result of the gas exchange calculation, the rate of stoichiometric internal recirculated gas and the total mass in the combustion chamber at "inlet valve closes" is available.

As a first visualization, *Figure 4* shows an injection strategy with one (late) pre-injection and one main injection after TDC. On the left side of the figure, only one averaged static measuring point is shown. On the right side, a shift of the pre-injection in 2 °CA steps between the different injections is plotted. The first measuring of the variation is at 5 bar indicated mean pressure with a pre-injection at 20 °CAbTDC. The following measurements are at approximately 5 bars because the injected fuel mass is held constant, and the indicated pressure varies with changing combustion phasing. This leads to a variation in the indicated mean pressure over variation. Further measurement parameters are: λ = 2.2,

T_2 = 42 °C, p_2 = 0.964 bar, MFB50 = 10 °CAaTDC, n = 1500 min^{-1}, EGR = 0 %. To inject the same fuel mass for all pilot injections in the variation, the injection duration was compensated to achieve the same mass-flow measured by AVL Fuel Exact.

This variation has high NO$_x$ raw emission compared to the same variation with 20 % EGR. Also, a variation with 30 % EGR is performed, where NO$_x$ raw emission is below 80 ppm. For the PCCI configuration, this late pre-injection variation is not common but due to the low EGR rate and short ignition delay a benefit for HC and CO emission. To reach the advantage of PCCI and nearly no NO$_x$ (below 10 ppm) and soot, the pre-injection was shifted earlier and separated in up to three single injections. This showed the best results at the test bench and is described in the following section.

Figure 4 should illustrate the multi-stage ignition of the pre-injected diesel fuel. Where after the first injection the low heat release (LTHR) starts. This LTHR - also known as cool flame (CF) in literature - terminates at 166 °CA (left figure) and the negative temperature coefficient (NTC) area forms out [10] (the definition of LTHR and HTHR can be seen in Figure 6). The NTC area is due to missing chemical reactions in this temperature (approximately 800 - 1000 K) and pressure region [11]. This NTC is followed by the high temperature heat release (HTHR) starting at around 170 °CA. For the methodology of the Arrhenius approach, it is relevant that the start of combustion (for LTHR and HTHR) is defined accurately. As first criteria, the zero crossing of the ROHR is assumed. If no zero crossing for the heat release of the LTHR or HTHR is available as it is for most plots of the HTHR of the right plot in *Figure 4* the SOC has to be defined by the gradient as it is described in section 3.1.
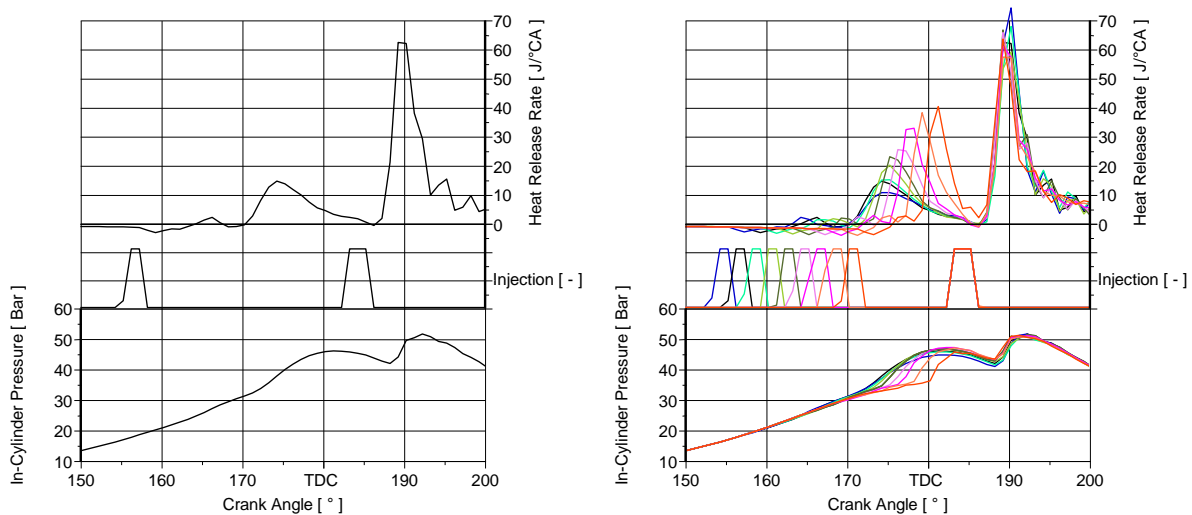
Figure 4 Pre-Injection Variation (right) with In-Cylinder Pressure, Injection Peak and Heat Release Rate
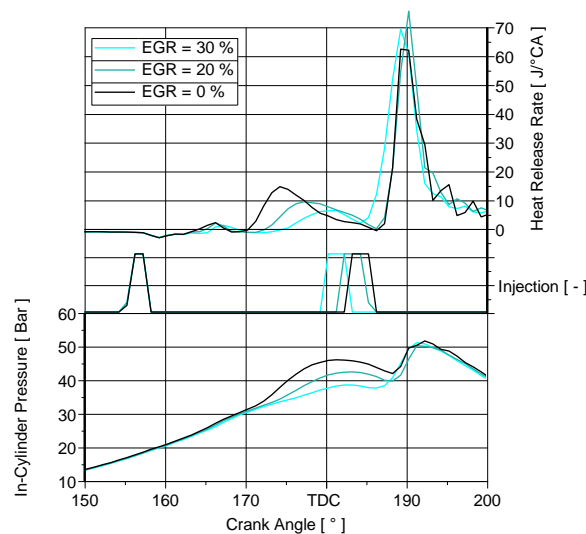
Figure 5 EGR Variation from 0 – 30 %

Complementary, an EGR variation is shown in *Figure 5*. For the measuring with zero external exhaust gas recirculation illustrated in *Figure 4*, additional measurements were performed. In this figure, the

(late) pre-injection for the 20 and 30 % EGR measurement is with the same timing for SOI and injection duration. Obviously, lambda decreases with a higher EGR rate due to the same totally injected fuel, inlet temperature and inlet pressure. The main injection is advanced to reach a 50 % mass fraction burn location (MFB50) of 10 °CAaTDC for all measurements. For the zero crossing of the LTC and HTC, a longer ignition delay is detected for increasing EGR rate. For the main injection, an empirical explanation of the SOC is challenging due to the high impact of in-cylinder conditions such as temperature, pressure and ongoing chemical processes that accelerate chemical processes. This can be seen in the ignition delay of the main injection comparing 0 and 20 % EGR rate where the SOI of the main injection of the 20 % EGR point is earlier than the SOI of the 0 % EGR point. For both, the first ROHR can be detected at 186 °CA and the following ROHR is comparable in increase. It can be concluded from this that the reactivity from SOI to SOC is slower for increased EGR rate. Following this first chemical reactions, the burning process seems to be similar in a time-based matter.

3   3-Stage Arrhenius Approach to Predict Ignition Delay (SOC) for the Premixed Combustion (LTHR and HTHR)

As described in the previous sections, with this experimental set-up different variations concerning load, engine speed, inlet temperature, inlet pressure, EGR rate and fuel pressure were recorded. For the following Arrhenius approach explained in section 3.2, 88 measurements were used to fit the model's parameters. For the ignition delay model of the high temperature combustion, 71 measuring points were valid. The difference from 88 to 71 is because not every injection pattern has a low and high temperature heat release. As a definition, the combustion has to start before the main injection is set. If the main injection is set before the HTHR started, no HTHR (of the pre-injection) is available. So, 17 measurements had this special case that an LTC started but the main injection was set before the HTC could start out of chemical reasons. In case of high EGR rates, the mass mean temperature and local-lean conditions could lead to an absent HTHR.

3.1   Parameters to Concern for Model Set-Up

For the ignition delay model, the start of calculation and the start of combustion from both LTHR and HTHR have to be determined. As shown in *Figure 6*, calculation start is established at the SOI of the first pre-injection. The elapsed time from calculation start to the first heat release - marked with "1" in red - is defined as ID (LTHR). Mainly, this low temperature combustion is characterized with a zero-crossing in the ROHR due to the fact that pre-injected fuel evaporates before start of burning (SOB). If not so, proceed with the same strategy as described in the following section for the ID (HTHR).

The ID (HTHR) - as in *Figure 6* marked with "2" - is detected as follows. Either a zero-crossing of the ROHR is available, whereby the crossing towards the maximum HTHR is the SOC, or a tangent method is used. This tangent method is works with the first derivation of the ROHR. The maximum of this derivation of the ROHR is the upper point. The lower point has to be calculated: This is done by finding the minimum before the maximum (or the zero-crossing of the derivative - which is the same), calculate the distance between these two points and add 20 % of the total distance to the minimum. An interconnection between these two points and the extrapolated zero-crossing is defined as the SOC of the HTC.

Furthermore, it has to be said that in this paper only the chemical ignition delay was considered for the pre-injections. But for the main injection the physical ignition delay is particularly essential for low EGR points and is not described in this paper.

n = 2000 min^{-1}
$p_{m,i}$ = 5 Bar
T_2 = 45 °C
T_3 = 396 °C
p_2 = 0.955 Bar
p_3 = 1.000 Bar
MFB50 = 17 °CAaTDC
EGR = 30 %
λ = 1.55
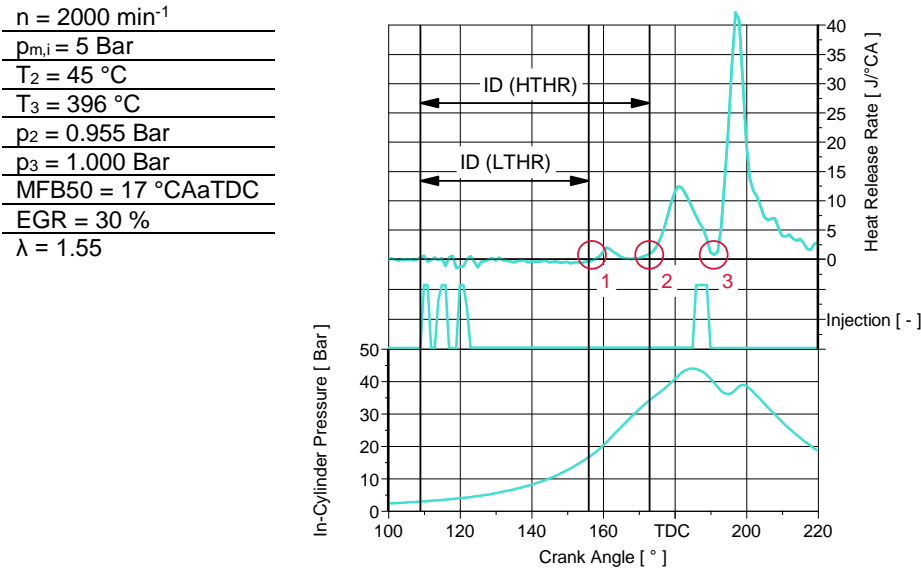
Figure 6 Early Pre-Injections and Late Main Injection to Describe the Ignition Delay of the Premixed and Main Combustion

The start of the heat release of the main injected fuel is marked with "3" in Figure 6. However, a distinction must be made here. The ignition delay of the main injection is more dependent on the in-cylinder conditions as it is for the pre-injected fuel. Also, the physical ignition delay is more significant as for the pre-injections. The percentage time scale for physical ignition delay against chemical ID is comparable high for the main injection due to higher pressure and mass mean temperature at SOI as or the pre-injections (which decreases the time scale for the chemical ignition delay drastically). The primary and secondary spray breakup is mainly responsible the physical ignition delay.

This means that the knowledge about the actual conditions of the EGR rate, the actual pressure and mass mean temperature, local and global lambda, homogenization, and residual fuel at SOI (main injection) are necessary. For a 0D-model, these parameters have to be estimated with an empirical approach. Due to the complexity, no predictable model could be found yet.

3.2   Model Methodology and Description

The Arrhenius equation was developed by Svante Arrhenius as a single stage approach to describe the temperature dependency of a systems reactivity (chemical kinetics). This approach was further used for empirical models to quantitatively describe complex interconnections with a zero-dimensional model. To describe the reactivity of a system with changing boundary conditions (in-cylinder conditions), the Arrhenius model was adapted.

As *equation (2)* shows, the equation was modified to take the in-cylinder pressure, the in-cylinder temperature, lambda (after the injection - if three pre-injections were set, the global air-fuel mixture after the third injection is used), and the EGR rate into account. For "i", three parameter sets are available if LTHR and HTHR should be calculated. Each parameter set is independent and "1" is only used for LTHR, "2" and "3" are used for HTHR.

A parameter set for LTHR ("1") has to be validated. The ignition integral of *equation (3)* is therefore used with *equation (2)* and i = 1. For "j", each time step starting with SOI is calculated. In this case, the time step was 1 °CA. For *equation (3)* the termination criteria is one. Furthermore, for the first calculation repetition the ignition integral could reach one, but this would not be valid. If the ignition integral reaches one in this first calculation step, meaning that at SOI of the pre-injection the ignition would occur instantly, the parameter set would not be valid. It is defined that the ignition integral (which means the ignition delay) has to be at "°CA SOI + 1 °CA".

Also, the parameter set has to be valid for all measurements. For this, a parameter set has to be found where all 88 ignition delays can be theoretically calculated.

$$\tau_{ID,i} = A_i \cdot \left[\frac{p_j}{p_{ref}}\right]^{\text{ß}_i} \cdot T_j^{b_i} \cdot \exp\left[\frac{T_{A,i}}{T_j}\right] \cdot \lambda^{y_1} \cdot \exp\left[\frac{EGR \cdot c_i}{T_j}\right] \qquad (2)$$

$$\int\limits_{\tau_{SOI}}^{\tau_{SOC}} \frac{1}{\tau_{ID}} dt = 1 \tag{3}$$

3.3   Combined Model to Predict Ignition Delay of LTHR and HTHR

A hyperparameter optimization - also known as parameter sweep - was used to fit the model seen in equation *(4)* (with *(2)* in *(3)*). Therefore, "ID,2" and "ID,3" were set to zero. The first calculation results in a parameter setting for the LTHR. As second step, these parameters are fixed. A parameter setting for the HTHR has to be found. Therefore, the ignition integral has to be calculated using the complete term of equation *(4)* which was developed by Weisser and published in 2001 [8]. This leads to a dataset with twelve parameters where every measurement has to be calculated with the "new" parameter set. As a result, 18 parameters are used to calculate both the LTHR and HTHR.

$$\frac{1}{\tau_{ID}} = \frac{1}{\tau_{ID,1} + \tau_{ID,2}} + \frac{1}{\tau_{ID,3}} \tag{4}$$

Firstly, every parameter set gets fully calculated with all measurements. The crank angle - where the ignition integral reaches one – is relevant. A comparison of this calculated "SOI" and the engine test bench measurement leads to a calculated-measured derivation. The sum off all derivations has to be small – while every new parameter set has to be compared with the "best parameter set". Furthermore, a weighting is embedded. For each derivation of measurement to calculation over 2 °CA a multiplier by two was used. For derivations over 3 °CA a multiplier of four was used and so on. The "best parameter set" consequently has less runaways but the overall accuracy is not as good as it could be. Also, the coefficient of determination could be calculated and used as evaluation criteria. As summary, it is more important to find a way to capable evaluate all measurements than to find the best-looking result.

The coefficient of determination of approximately 0.92 for the LTHR seems to be good for this optimization task. It has to be considered that start of calculation is always at SOI (of the pre-injection). As seen in *Figure 7*, measured and calculated ignition (crank angle dependency) starts at 155 °CA earliest. The latest ignition start of the LTHR is at 176 °CA. As in *Figure 4*, *Figure 5* and *Figure 6* seen, TDC is at 180 °CA. This means that this parameter setting can handle a wide variation of SOI with different ignition delays depending on the in-cylinder conditions.
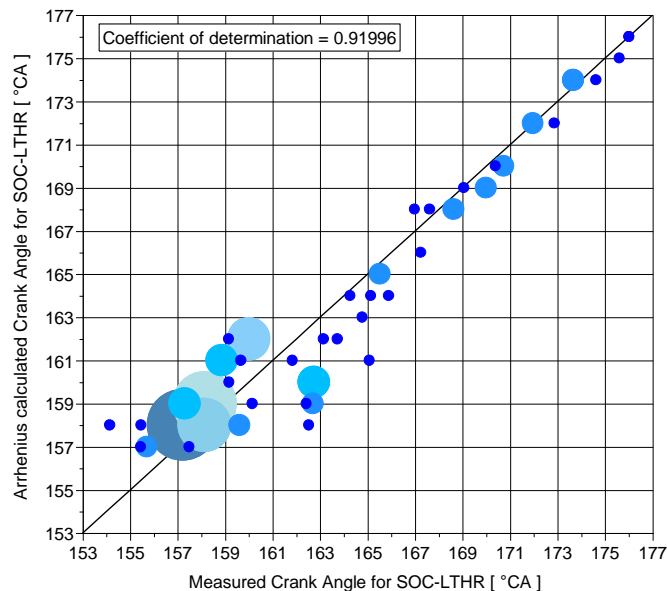
Figure 7 Calculated Over Measured Start of Low Temperature Heat Release (88 measurements)
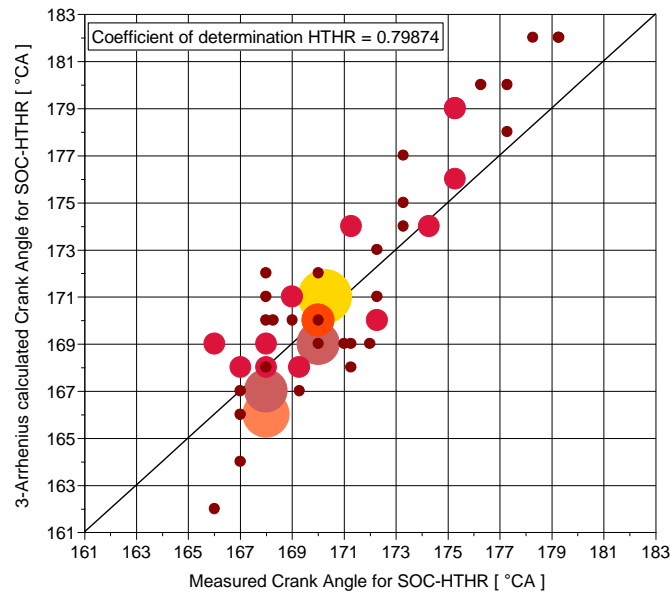
Figure 8 Calculated Over Measured Start of High Temperature Heat Release (71 measurements)

The plots in *Figure 7* and *Figure 8* show the results of the pre-described one and 3-stage Arrhenius approach. Each small dot (blue and red) illustrates one point. As bigger the dot (and lighter the color) the more points were calculated at this position. On the abscissa, the calculated values are plotted. While on the ordinate, the engine measured crank angle is plotted. Furthermore, the bisector line (black) demonstrates the optimum where the calculated ignition delay and the measured ignition delay are exactly at the same position.

To further explain the coefficient of determination of the HTHR, it has to be mentioned that also for the HTHR the calculation start of the ignition integral is at SOI (pre-injection). May better results could be reached by finding a better solution for the calculation start. As a possibility, the start of LTC could be used. However, the in-cylinder conditions are complex and the variations at the test bench can be expanded regarding different effects on the conditions.

To summarize, the introduced single-stage and 3-Arrhenius approach with ignition integral is sufficient to calculate the start of low and high temperature heat release of a partially premixed diesel combustion. As a next step, all measured points will be included to find a valid parameter set. Also, an optimization tool will be integrated, and the weighting of deviations has to be defined to get a good result overall.

4   Outlook

Figure 9 Diesel Spray (Video Sequence) of a 2-Hole Injector (left) and the Binary File (right)

Additionally, high speed camera recordings of a 2-hole injector are available. For this, six of the 8-holes of the serial injector are welded to achieve an optimized spray form for the video capture. The pressure in the spray chamber, as illustrated in *Figure 9*, is 10 bars. The air temperature in the chamber is similar to ambient air temperature (23 °C). Due to this, the density in the chamber is not comparable with 10 bars in the combustion chamber (at higher temperature). The correlation of density in the spray chamber and the engine are connected and integrated in an elementary visualization as seen in *Figure 10*.

The two illustrations (bottom and top) show the combustion chamber (black) as used for the investigations. In white, the piston is displayed. Grey shows the simplified form of the spray of the binary file (right) in *Figure 10*. The measurements were performed with a variation in rail pressure and in air

pressure. The spray tip velocity was evaluated and integrated in the model of *Figure 10*. Furthermore, the spray angle and spread can be varied in the code as seen in the top and bottom of the figure. The SOI and the injection duration can be set independently. As result, the wall wetting could be calculated for the ignition delay model. While this approach is not detailed, it has to be validated and matched for different injection patterns. But measurements with different combustion chamber surface temperatures (mainly piston temperature) have shown that the evaporation of diesel fuel and the following ignition delay are mainly affected.

Figure 10 Injection Characteristics with Computational Transfer. 156° Spray Angle (top) and 120° (bottom)

Integration of this knowledge for wall and piston wetting in the ignition delay model could give an additional opportunity to optimize the results. Mainly for injection patterns where the spray impinges the piston crown, the quantity of applied fuel could improve the ignition delay model.

Further measurements could be performed with an optimized injector (angle), lower load (improvements for PCCI) or a port fuel injection strategy for better premixing. The range of variations could be expanded, but for example EGR rate, inlet temperature, injection timing, fuel pressure, inlet pressure and piston cooling variations were performed. A fuel variation concerning cetane-number could also be advantage for higher load points. The lower cetane-number would lead to longer ignition delays. Due to ignition delay and therefore optimized combustion phasing more fuel could be pre-injected. This could lead to higher load with very low soot and NOx emissions [12].

In addition, an improved algorithm can be used to enhance performance in means of speed and accuracy. For example, the Rprop+ algorithm described in [13] could be used to find a local minimum. Therefore, the hyperparameter optimization would be used to find the "global minimum" approximately - the Rprop+ algorithm is applied to find the absolute minimum next to this point.

Conclusions

In this paper, the single-cylinder test bench at IFS University of Stuttgart was introduced. As a next step, the partially premixed diesel combustion was presented with variations in pre-injection and EGR rate. A definition of the model set-up is done and the performed test bench measurements are pre-defined by thermodynamic aspects. Furthermore, the adjusted 3-stage Arrhenius approach with the ignition integral is defined and explained in detail. One optimized parameter setting for the parameters of the approach was used to calculate the low temperature heat release of 88 measurements and the high temperature heat release of 71 measurements. As a resume, it can be summarized that the developed Arrhenius approach is valid for a wide range of measurements as soon as an optimization tool for parameter setting is instrumented. In a next step, the algorithm to calculate the best variables for the test bench set up and the engine parameters will be developed as described in section 4.

5   References

[1]   M. Halstead, L. Kirsch und C. Quinn, „The autoignition of hydrocarbon fuels at high temperatures and pressures—Fitting of a mathematical model," *Combustion and Flame,* pp. 45-60, 1977.

[2]   C. B. C. B. K. e. a. Barba, „Empirisches Modell zur Vorausberechnung des Brennverlaufes bei Common-Rail-Dieselmotoren.," *MTZ Motortechnische Zeitschrift,* Nr. 60-4, pp. 262-270, 1999.

[3]   G. P. Merker und C. Schwarz, „Reaktionskinetik," in *Grundlagen Verbrennungsmotoren*, Vieweg+Teubner, 2009, pp. 167-188.

[4]   K. J. Laidler, *The development of the Arrhenius equation,* Journal of Chemical Education, 1984 61(6), 494.

[5]   H. Wolfer, „Der Zündverzug im Dieselmotor," *VDI-Forschungsheft 392: Zündverzug und Klopfen im Motor,* 1938.

[6]   S. G. Bauer, „Ignition Lag in Compression Ignition Engines," *Engineering Vol. 148,* pp. 368-369, 1939.

[7]   M. Elliott, „COMBUSTION OF DIESEL FUEL," *SAE Technical Papers,* Nr. ISSN: 0148-7191, 1949.

[8]   G. A. Weisser, Modelling of Combustion and Nitric Oxide Formation for Medium-Speed DI Diesel Engines: A Comparative Evaluation of Zero- and Three-Dimensional Approaches (Dissertation), Zurich: ResearchGate, 2001.

[9]   M. Wahl, S. Schneider and M. Bargende, "An Empirical Based Model to Predict Ignition Delays in Partially Premixed Compression Ignition Mode," *22. Internationales Stuttgarter Symposium,* vol. 1, pp. 615-628, (2022).

[10]   S. A. Beck, BESCHREIBUNG DES ZÜNDVERZUGES VON DIESELÄHNLICHEN KRAFTSTOFFEN IM HCCI – BETRIEB, Stuttgart, Dissertation, (2012).

[11]   D. Rether, Modell zur Vorhersage der Brennrate bei homogener und teilhomogener Dieselverbrennung, Stuttgart, Dissertation, (2012).

[12]   Y. Takeda, N. Keiichi und N. Keiichi, Emission Characteristics of Premixed Lean Diesel Combustion with Extremely Early Staged Fuel Injection, SAE Technical Paper 961163, (1996).

[13]   C. Igel und M. Hüsken, „Empirical evaluation of the improved Rprop learning algorithms," *Neurocomputing,* Nr. 50, pp. 105-123, January 2003.

THIESEL 2022 Conference on Thermo- and Fluid Dynamics of Clean Propulsion Powerplants

CFD Modeling of Ducted Fuel Injection Compression-Ignition Combustion

T. Lucchini, L. Sforza, Q. Zhou, G. D'Errico, D. Severgnini, A. Onorati

Department of Energy. Politecnico di Milano. Via Lambruschini 4, 20156 Milano, Italy

E-mail: tommaso.lucchini@polimi.it
Telephone: +(39)0223998636
Fax: +(39)0223998050

Abstract. Internal combustion engines need to be further improved to reduce pollutant and greenhouse gas emission levels for the so-called *hard-to-abate* sectors, where replacement of conventional technologies and fuels seems to be very complex even in a long term horizon. In particular, ducted fuel injection (DFI) technology has the potential to reduce soot emissions in compression-ignition (CI) engines, since it increases the air-fuel mixing rate and the lift-off length. However, the design of CI engines with DFI technology requires predictive numerical models to correctly describe the fuel-air mixing and the combustion process, accounting for the effects of piston bowl and duct geometry under a wide range of operating conditions.
Purpose of this work is the assessment of a CFD methodology for the simulation of DFI combustion. RANS turbulence modeling was used in combination with the Lagrangian approach to describe the spray evolution. Combustion was modeled using tabulated kinetics and taking interaction between turbulence and chemistry into account. Experimental validation was carried out by simulating constant-volume vessel and engine experiments at different operating conditions. Computed results were compared with experimental data of ignition delay, flame lift-off, cylinder pressure, heat-release rate and soot emissions. The consistency between results from 2D and 3D meshes was also discussed, as well as differences on the DFI combustion process between constant-volume conditions and engine configurations.

1. Introduction

Over the last decades significant efforts have been spent to reduce the toxic emissions of compression-ignition (CI) engines. Innovative low-temperature combustion modes were proposed to simultaneously reduce engine-out NO_x and particulate matter emissions [1]. At the same time, the efficiency of the dedicated after-treatment systems (ATS) was continuously improved [2]. However, because of the applications where CI engines are still required, attention must be focused mainly on full-load conditions. Here, multiple injections and advanced combustion modes cannot be exploited, due to the complexity in achieving stable operation without knock or misfire.
Among the different investigated solutions to reduce the soot formation during the combustion process [3–5], ducted fuel injection (DFI) appears to be one of the most promising. The concept of DFI technology is illustrated in Fig. 1: the injected fuel passes through a small cylindrical pipe (with diameter D and length L) which is placed at a predefined *standoff* distance from the nozzle (G). Longer lift-off lengths (H) compared to a free-spray (FJ), combined with an increased turbulence mixing inside the duct, have the potential to reduce the formation of soot, carbon monoxide and hydrocarbon emissions. Additional benefits for the reduction of particles emissions can be provided by the cooling effect that the charge drawn in the duct experiences when it skims the cylinder walls and the surface of the duct itself. Increased vapor penetration is expected to shorten the combustion duration and to compensate the longer ignition delay, with no need of an injection pressure variation and in absence of relevant losses in terms of engine performance and efficiency.
DFI technology was initially presented in [6] and assessed on constant-volume vessel experiments under reacting and non-reacting conditions [7–9] to identify, with the support of optical measurements, its potentials in terms of soot emission reduction. Results were then confirmed in [10,11], where the effects of ambient conditions (density and oxygen concentration), real Diesel fuel properties, duct shape and

size were evaluated. First applications in optically accessible engine prototypes [12–14] confirmed the early findings: compared to conventional Diesel combustion, DFI produces always lower HC emissions and at least one order or magnitude lower soot levels. Of course, many challenges still need to be well addressed. Hence, parallel experimental-numerical activities are required to exploit the fundamental of the governing physical and chemical processes, with the purpose to optimize the DFI injector and the combustion chamber configuration.
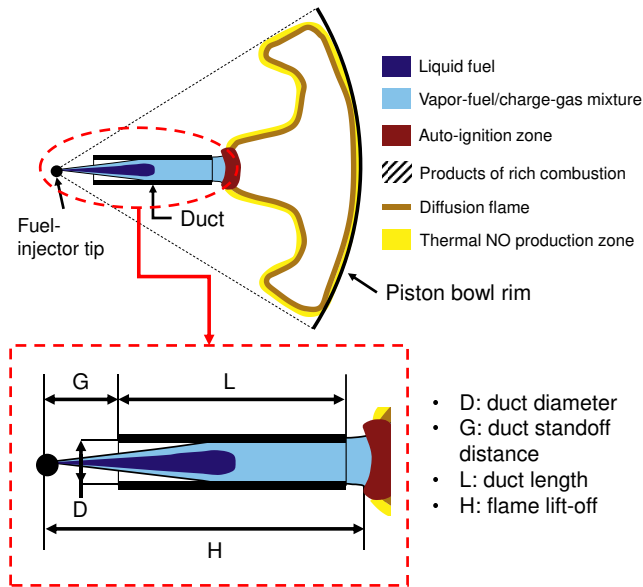
Figure 1: DFI concept applied to a single fuel spray inside the combustion chamber of a compression-ignition, direct-injection engine. The inset defines the fundamental geometric parameters that are used to characterize DFI configurations [6].

On the modelling side, the definition of the mesh requirements is one of the primary tasks. This is necessary to correctly capture the duct inflow process in presence of separation, the air-fuel mixing with boundary layer development inside the duct, and the large velocity gradients at the duct exit. Then, the identification of a suitable combustion model is needed, in order to properly reproduce the flame structure, including the influence of the ducted injection on the lift-off.

In this work, CFD simulations of the DFI combustion process were performed using the Lib-ICE, which is a code based on the OpenFOAM technology and developed by the authors. Lib-ICE was extensively validated for the simulation of the compression ignition combustion process, both at constant-volume conditions and in engine configurations [15–18]. Focus is given on the consistency of the methodology between 2D and 3D meshes, as well as between simulations in constant-volume vessels and in engine conditions. As matter of fact, these issues, mostly of a numerical nature, must be well addressed to ensure that the CFD tool can be widely used to deepen the understanding of the occurring phenomena. This is crucial for the optimization of the injector-engine configurations, to step up from a prototype to a real engine technology.

Experimental data from constant-volume vessel and engine applications [10] were here numerically investigated with both FJ and DFI. Computed and measured data were compared considering the main combustion indicators and the soot mass evolution. Simulation results show the capability of the proposed approach to predict increased flame lift-off lengths and reduced soot emissions, demonstrating the consistency of the methodology in reproducing the main observed trends on both types of experiments.

2. Computational Model

In the present work, the tabulated presumed PDF combustion model (TPPDF), implemented by the authors in the Lib-ICE code, is employed to simulate the combustion process occurring with the DFI

technology. Reaction rates and chemical composition are stored in lookup tables to accurately describe the oxidation of complex fuels including the formation of soot precursors. This enables to use a large number of species and reactions with low CPU effort since in the CFD domain a limited number of equations is solved. The progress variable C summarizes the status of fuel oxidation.

2.1. Tabulated presumed PDF combustion model (TPPDF)

In this approach, applied by [19, 20] to simulate CI engines, the turbulence-chemistry interaction is incorporated in the computation of the progress variable source term, assuming a probability density function for both the progress variable and the mixture fraction:

$$\dot{C}_{TPPDF} = \int_0^1 \int_0^1 \dot{C}\left(P, T_u, Z, c\right) p\left(Z, \widetilde{Z''^2}\right) p\left(c, \widetilde{c''^2}\right) dcdZ \tag{1}$$

Here, P is the pressure, T_u the unburned mixture temperature, Z the mixture fraction and $\widetilde{Z''^2}$ its variance, c the normalized progress variable and $\widetilde{c''^2}$ its variance, while $p\left(x, \widetilde{x''^2}\right)$ is the probability density function of the generic magnitude x. Since this work is mainly focused on diffusion combustion, a δ-PDF distribution was assumed for $p\left(c, \widetilde{c''^2}\right)$ while a β-PDF function was used for $p\left(Z, \widetilde{Z''^2}\right)$. This requires to additionally solve the mixture fraction variance $\widetilde{Z''^2}$ equation:

$$\frac{\partial \rho \widetilde{Z''^2}}{\partial t} + \nabla(\rho \mathbf{U} \widetilde{Z''^2}) - \nabla\left(\mu_t \nabla \widetilde{Z''^2}\right) = 2\frac{\mu_t}{Sc_t}|\nabla Z|^2 - \rho \chi \tag{2}$$

in which ρ is the mixture density, $\mathbf{U}$ the flow velocity, while μ_t and Sc_t are the turbulent dynamic viscosity and Schmidt number, respectively. The sink term appearing in Eq. 2 is the average scalar dissipation rate χ, which is function of the turbulent time scale and mixture fraction variance:

$$\chi = C_\chi \frac{\varepsilon}{k} \widetilde{Z''^2} \tag{3}$$

being k the turbulent kinetic energy and ε its dissipation rate, while C_χ is a model constant of order unity, assumed equal to 2. To conveniently apply this model to engine simulations without introducing significant computational overheads, a table, built up with the homogeneous reactor assumption, is processed to include the effects of turbulence chemistry interaction as shown in Fig. 2. In particular, first, the user specifies ranges of mixture fraction and progress variable segregation factors (S_Z and S_c, respectively), defined as the ratio between variance and maximum variance values:

$$S_Z = \frac{\widetilde{Z''^2}}{Z(1-Z)} \tag{4}$$

$$S_c = \frac{\widetilde{c''^2}}{c(1-c)} \tag{5}$$

Then, for any value of Z, S_Z, c and S_c it is possible to compute variances and the coefficients for the probability density function distributions. Finally, integration is performed for any tabulated quantity f_{HR} and a table, including the effects of mixture fraction and progress variable fluctuations, is available for the presumed PDF combustion model:

$$f_{seg} = \int_0^1 \int_0^1 f_{HR}\left(p, T_u, Z, c\right) p\left(Z, \widetilde{Z''^2}\right) p\left(c, \widetilde{c''^2}\right) dcdZ \tag{6}$$

Compared to other widely used combustion models for non-premixed combustion, the TPPDF model does not consider any sub-grid diffusion in the mixture fraction space, while other approaches does either through a suitable mixing model [21] or by means of the scalar dissipation rate term. Turbulence-chemistry interaction with the presumed PDF combustion model is expected to reduce the maximum flame temperatures and to increase the thickness of the flame compared to the well-mixed model.

For further details related to the application of tabulated kinetics to CI combustion simulations, the reader is referred to [22] describing the generation of the homogeneous reactor table, the validity of the TPPDF approach and a detailed comparison between tabulated kinetics and direct chemistry integration for both constant-volume and engine simulations.
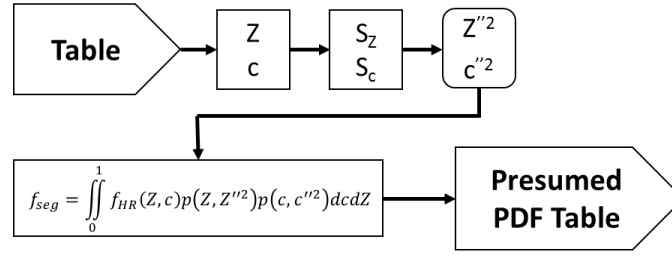
Figure 2: Generation of the chemistry table used for the tabulated presumed PDF combustion model (TPPDF).

2.2. Soot emissions

The semi-empirical model proposed in [23] is employed to predict soot. Transport equations are solved for both the soot particle number density N_p and the volume fraction f_v, with source terms (ω_{N_p} and ω_{f_v}, respectively) related to inception ($\dot{\omega}_{inc}$), coagulation ($\dot{\omega}_{coag}$), surface growth ($\dot{\omega}_{grow}$) and oxidation ($\dot{\omega}_{oxi,O_2}$ and $\dot{\omega}_{oxi,OH}$) processes:

$$\dot{\omega}_{N_p} = \dot{\omega}_{inc} - \dot{\omega}_{coag} \tag{7}$$

$$\dot{\omega}_{f_v} = \dot{\omega}_{inc} + \dot{\omega}_{grow} - \dot{\omega}_{oxi,O_2} - \dot{\omega}_{oxi,OH} \tag{8}$$

Inception and surface growth source terms depend linearly on the concentration of the soot precursor, which here is considered to be acetylene, consistently with previous works on Diesel combustion [24]. From experimental observations, the reactivity of the soot particles decreases in time. In this work, this aspect was accounted for by assuming the soot surface growth rate proportional to the square root of the specific surface area, S_{soot}, to guarantee consistency with the original study from Lindstedt [23]. Coagulation of soot particles is modeled using the normal square dependence, while soot oxidation is considered controlled by O_2 and OH concentrations [23].

3. Validation and Results

3.1. Constant Volume Combustion Vessel

In the present study, simulations were performed to replicate experiments carried out in an optically accessible constant-volume vessel and single-cylinder engine. For what regards the former, among the different tested geometries in [10], the so called δ configuration was investigated in this work: it has a fillet radius at the inlet and a taper at the outlet. The specific simulated duct configuration is called D2L16G1.4δ, in which the duct is placed at a 1.4 mm standoff distance from the nozzle and it has a 2 mm diameter and 16 mm length. The nearly cubical chamber is approximately 1.24 L in volume, and each side can be equipped with a window for optical access. To test the DFI technology, the vessel was equipped with a single-hole nozzle of 90 μm diameter and n-dodecane was used as fuel. Such injector configuration was selected because it has been widely investigated in the context of the Engine Combustion Network (ECN) [25]. Experiments were done at different ambient conditions for both FJ and DFI configurations and two simultaneous high-speed optical diagnostics were used to investigate the combustion event. The first, by detection and imaging of natural luminosity to identify the hot-soot regions [26]. The second, by imaging of chemiluminescence from electronically excited hydroxyl (OH*) radicals, which indicates where high-temperature reactions are occurring.

The six different simulated conditions are listed in Tab. 1, corresponding to three nominal ambient temperatures (850, 900 and 1000 K) and two different oxygen concentration (21 and 15 [% vol]) at constant density (22.8 kg/m^3).

The geometry of the vessel, including eventually the presence of the duct, is axi-symmetric. Therefore, a 2D mesh can be used without loss of details and having the possibility to adopt both a local refinement near the walls and an adequate reduced mesh size where higher gradients are expected. This approach has already been adopted in a previous study [27], in which a detailed analysis of the effects of the mesh size and turbulence model was carried out, including the simulation of non-reacting conditions. In this

work, the same optimal 2D mesh has been adopted, where both FJ and DFI grids preserve the same structure: an average 0.2 mm mesh size near the axis of the jet and a boundary layer consisting in 6 computational cells with a 10 μm thickness. Since real engines cannot be discretized by 2D meshes, in this study also a 3D mesh was built, so as to verify the consistency of the computed results from the 2D to the 3D mesh. Fig. 3(a) shows the adopted 2D computational mesh for the FJ and DFI cases, while the equivalent cut planes of the 3D meshes are shown in Fig. 3(b), in which local refinements around the jet were adopted to have in the 3D case a mesh size similar to the 2D mesh cell. Further details about the mesh size and near-wall resolution are provided in Tab. 2. Here, it is possible to observe how the mesh resolution increases by one order of magnitude in the 3D configuration and, to keep an acceptable mesh size, the number of layers above the duct wall was reduced from 6 to 1. The $k - \varepsilon$ model with standard high-Reynolds wall-functions was used for turbulence, in which the C_1 constant was increased to 1.5 to properly match the FJ vapor penetration. Initial vessel ambient temperature and pressure values were taken from [25] together with the injected fuel mass flow rate profile. Vessel wall and duct temperatures were set to 500 K, such value was found to reproduce correctly, in FJ condition, the vessel pressure reduction after the preburn phase.

Table 1: Simulated operating conditions for FJ and DFI combustion.

	O_2 [% vol]	T_{amb} [K]	ρ [kg/m^3]	Configuration
1	21	850	22.8	DFI/FJ
2	21	900	22.8	DFI/FJ
3	21	1000	22.8	DFI/FJ
4	15	850	22.8	DFI/FJ
5	15	900	22.8	DFI/FJ
6	15	1000	22.8	DFI/FJ

(a) 2D mesh   **(b) 3D mesh**

DFI   FJ   DFI   FJ
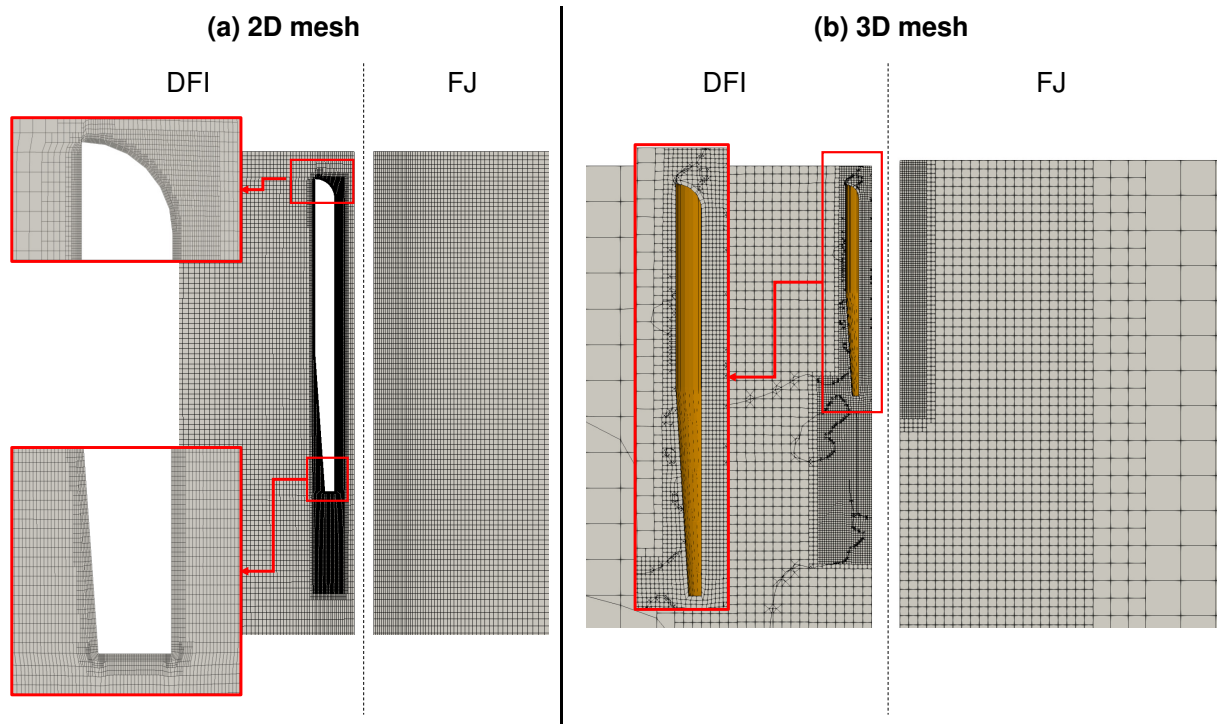
Figure 3: 2D axi-symmetric (a) and 3D (b) computational grids used for the simulation of FJ and DFI simulations.

Instantaneous heat release rate as well as combustion indicators (such as the ignition delay and the flame lift-off) were considered both to evaluate the capability of the proposed approach in predicting the main features of DFI combustion and to verify the consistency of the results between 2D and 3D meshes. A mechanism with 257-species and 1521-chemical reactions [28] was used to describe the

oxidation of n-dodecane and to generate the TFPV table, whose resolution is reported in Tab. 3. Here it is possible to verify that all the expected thermodynamic conditions in the simulation were included.

Table 2: Mesh details for the constant volume combustion vessel simulations.

	FJ	DFI
2D mesh cells	20'000	40'000
3D mesh cells	400'000	600'000
Duct wall layers 2D mesh	-	6
Duct wall layers 3D mesh	-	1
Minimum mesh size [mm]	0.1	0.1

Table 3: Chemistry table discretization used for the constant-vessel combustion simulations.

Unburned Temperature [K]	750, 800, 850, 900, 950, 1000
Pressure [bar]	30, 50, 70
Equivalence ratio	0-1.6 (step 0.05) 1.6-2 (step 0.1) 2-5 (step 0.25) 5-8 (step 0.5)
Mixture fraction segregation	0, 0.001, 0.005, 0.01, 0.05, 0.1, 1
Normalized progress variable c	0-1 s-shape profile (200 points)

Fig. 4 shows the instantaneous heat release rate (HRR) for the Case 1 (O_2 = 21%, T = 850 K, ρ = 22.8 kg/m^3, see Tab. 1) for the FJ and DFI configurations computed with both the 2D and 3D meshes. Fig. 4(a) illustrates that simulations correctly describe the main features of DFI combustion: ignition delay increase and reduced combustion duration [10]. In particular, as shown by Fig. 4(b), details of the HRR in the first 2 ms after the start of injection (SOI) remark the ability of the model to predict an increase in both the ignition delay and the premixed-burn spike moving from FJ to DFI because of the modification on the initial fuel-air mixing obtained with the introduction of the fuel duct [10, 27].
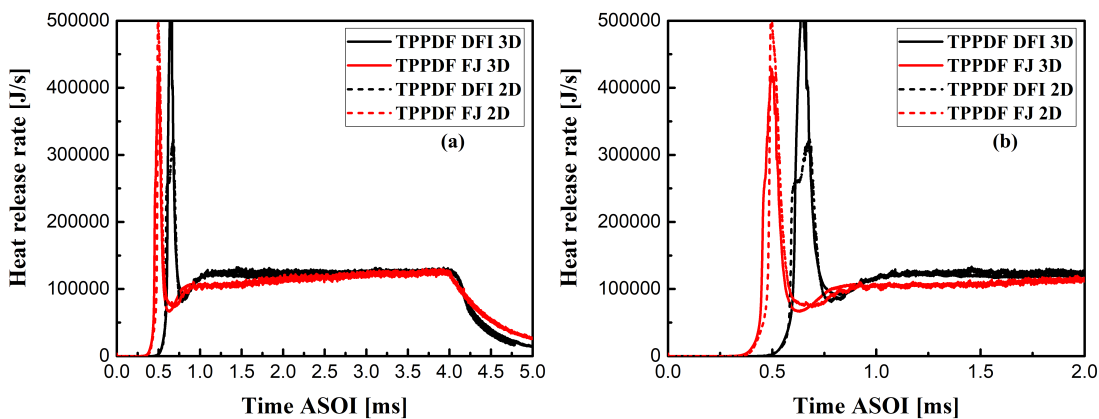
Figure 4: (a) DFI and FJ heat release profiles computed by the 3D and 2D meshes ; (b) detail of the previous figure in the 0-2 ms interval.

As explained before, the 2D approach is valid by virtue of the geometric characteristics of the case studied, but it is important to verify that the proposed methodology remains valid with the 3D mesh whose structure is no more axi-symmetrical like the fuel jet. For this reason, 3D mesh simulation results could be affected by numerical diffusivity.

Fig. 5 shows the results of the ignition delay and flame lift-off trends for both applied numerical approaches (2D and 3D), compared with each other and with the experimental data. Only minor differences can be observed between 2D and 3D results, leading to the conclusion that consistent mesh size have been used and the methodology can be applied to 3D cases as it will be required by real engine configuration.
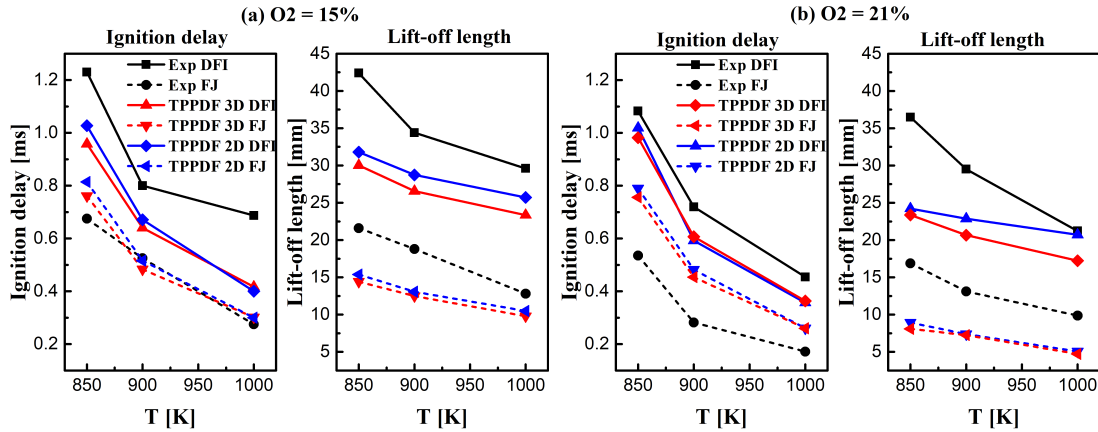
Figure 5: Measured and computed ignition delay and lift-off length for FJ and DFI at different conditions: (a) ambient oxygen concentration 15%; (b) ambient oxygen concentration 21%.

Simulation results correctly reproduce the trends of ignition delay and flame lift-off reduction with temperature increase, but there are discrepancies between computed and experimental results. In particular:

- For the O_2 = 15% the FJ ignition delay is estimated correctly, while the DFI values are underestimated 0.2 - 0.3 ms. The FJ flame lift-off length is underestimated by 5 mm (T = 850 K), while a rather good agreement was achieved at T = 1000 K. The DFI flame lift-off length underestimation ranges from 10 mm (T = 850 K) to 2 mm (T = 1000 K).

- For the O_2 = 21% the FJ ignition delay is overestimated by about 0.1 - 0.2 ms while DFI values are rather well predicted. The flame lift-off is always underestimated, with maximum differences found at 850 K of about 5 mm (FJ) and 15 mm (DFI).

Such differences are expected to affect the prediction of soot emissions and effects of DFI technology on its potential reduction. The kinetic mechanism seems to be capable to reproduce the 15% O_2 FJ configuration which was extensively studied in literature and in the context of the Engine Combustion Network. Probably the mechanism requires some modifications to match the ignition delay for the O_2 = 21% configuration. The underestimation of the flame lift-off is probably related to the adopted combustion model which does not account for the local mixing effects on the flame stabilization process. The underestimation of the DFI results needs further investigations including the effects of fuel-evaporation and sub-grid mixing on the reaction rate which will be addressed in future works.

Figs. 6(a)-(b) confirm the results achieved in terms of combustion indicators for the Case 1. In particular, Fig. 6(a) compares the distributions of soot and temperature computed with the 2D and 3D meshes for the DFI case. It is possible to see that the stabilization point of the flame is very similar for both tested grids. Slight differences can be observed in the soot distribution. A possible reason for this is mainly related to the slightly lower lift-off length predicted by the 3D mesh, as reported in Fig. 5(b). The differences between FJ and DFI combustion for the Case 1 are shown in Fig. 6(b). DFI flame stabilizes away from the duct and at a longer distance from the injector compared to FJ. This is the reason for a different distribution of soot which is more stretched and located near the injector axis for the DFI case. The evolution of the computed soot mass for the DFI and FJ configurations is reported in Fig. 7(a)-(b) for 15% and 21% ambient oxygen concentration, respectively. Simulations show that DFI has the potential to reduce the soot emissions despite the computed amount of such abatement is lower than what was experimentally found in [10], where DFI steady state soot mass was one order of magnitude lower than FJ. Possible reasons for such discrepancy are related to two different aspects:
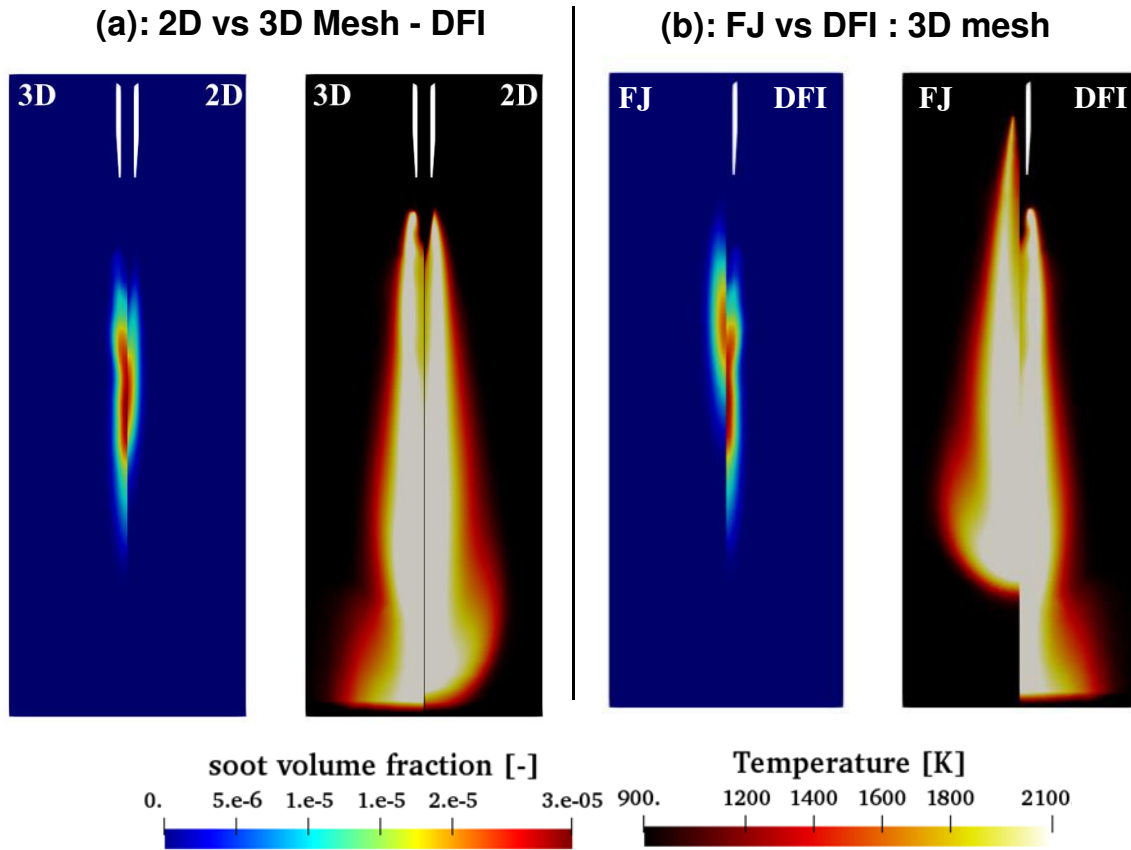
Figure 6: (a): comparison between temperature and soot volume fraction distributions computed by the 2D and 3D meshes; (b) comparison between temperature and soot volume fraction distributions computed for the FJ and DFI configurations. Operating condition: Case 1 (O_2 = 21%, T = 850 K, ρ = 22.8 kg/m^3, see Tab. 1)
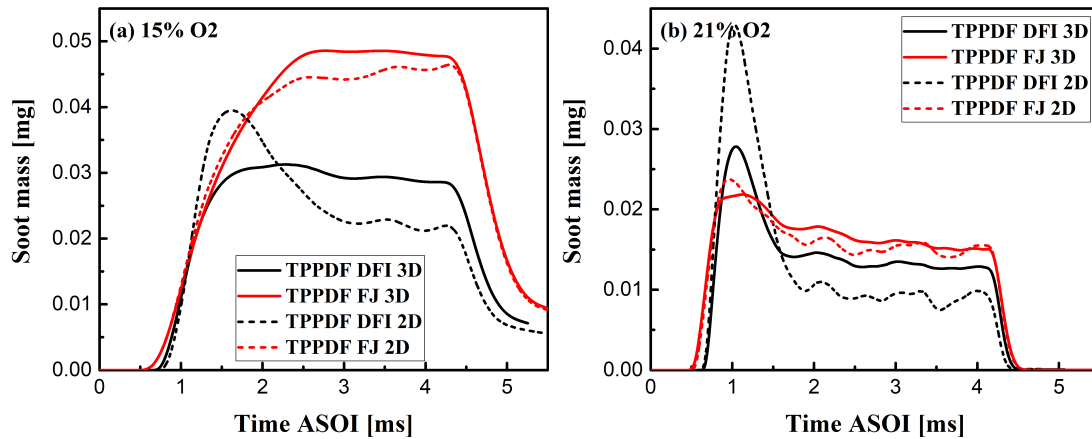
Figure 7: Comparison between the soot mass computed from 2D and 3D meshes for both FJ and DFI configurations: (a) ambient oxygen concentration 15%; (b) ambient oxygen concentration 21%.

1. Lift-off underestimation for both the DFI and FJ configurations: the fuel burns at richer equivalence ratio and this increases the amount of soot which is formed;

2. Soot model tuning constants: they were calibrated in a previous work [18] where simulations were performed with a different mechanism and combustion model. Probably increasing the oxidation rate coefficients will produce a reduction which is more similar to what was found in experiments. The choice of not changing the soot model constants is related to the discrepancy found between

computed and experimental data of ignition delay and lift-off length illustrated in Fig. 5. With such differences, we do not expect any capability of a set of calibrated soot model constants to produce a proper agreement with experimental data considering variation of ambient temperature and use of DFI technology.

While lift-off length and soot mass values seem to be almost independent on the computational mesh structure in the FJ configuration, numerical diffusivity reduces slightly the distance at which the flame stabilizes in the 3D mesh. The consequence of this is relevant for the 21% O_2 concentration, where it is possible to see that the computed DFI reduction of soot emissions is very low.

To better predict the flame lift-off length and soot emissions, the potential of flamelet progress variable combustion models will be assessed in future works to see if the inclusion of the scalar dissipation rate on reaction rate will provide some improvements [29].

3.2. Single Cylinder Engine

Constant-volume vessel results show the capability of the proposed methodology to describe the effects of DFI on the flame structure and potential for soot reduction. However, the application of DFI in engines poses further design and modeling challenges. The most important is related to the enhanced flame-wall interaction, because of the increased fuel vapor penetration. Experimental data available from a single-cylinder optical engine were used in this work for a preliminary validation. The experimental setup and the optical techniques employed to investigate the combustion process are accurately described in [13, 30], where tests were performed at different loads and speeds confirming the potential of DFI technology. The engine has a transparent piston with a cylindrical bowl and its main geometry data are reported in Tab. 4.

Table 4: Main geometry data of the simulated single-cylinder engine.

Bore	125 mm
Stroke	140 mm
Compression ratio	11.8
Number of injector holes	4
Injector diameter	170 μm
Duct properties	D3L12G3
Injector opening angle	140°
Fuel	Diesel
Swirl ratio	0.5

Table 5: Details of the simulated operating condition.

Speed	1200 rpm
GMEP	10 bar
Injected fuel mass	97 mg
SOI	7 CAD BTDC
Injector duration	17.5 CAD
Injection pressure	1800 bar
Intake O_2 concentration	15%

A four-hole injector was mounted with the possibility to evaluate different duct configurations. In this work, a mid-load operating condition was selected to compare FJ and DFI engine combustion. The tested duct, named D3L12G3, has a 3 mm diameter, 12 mm length and is placed at a 3 mm stand-off distance from the injector nozzle. Details of the simulated operating condition are provided in Tab. 5. The injection pressure is 1800 bar and the fuel starts to be injected near the top dead center (TDC). The intake oxygen volume fraction is about 15% by volume to reproduce a 25% EGR rate which is particularly demanding for the control of soot emissions. N-heptane (nC_7H_{16}) was assumed to be representative for the kinetics of the Diesel fuel, whose liquid properties were taken from [31]. The lookup table was

generated considering larger pressure (1-150 bar) and unburned temperature (400 - 1200 K) ranges compared to those used in constant-volume vessel simulations and presented in Tab. 3. The mechanism has 167 species and 1500 reactions and it has been extensively validated in [32].

Fig. 8 illustrates the details of the computational grid used to perform engine simulations with FJ and DFI configurations. A 45° sector of the combustion chamber was considered with a total number of 60 cells in the tangential direction. A spray-oriented layout was adopted, to better describe the air-fuel mixing process and limit the effects of the numerical diffusion. The layer addition/removal technique handles the grid motion [33] ensuring an optimum cells size for the whole simulation. The FJ mesh has a total number of 200'000 cells at TDC, while a larger number of cells was necessary for the DFI configuration. The mesh size adopted in engine simulations is similar to the one used for the constant-volume vessel configuration. Local refinements were placed inside the duct and at its outlet, to better describe the air-fuel mixing and stabilization processes. The refinement box placed at the duct outlet has a 10 mm length, 5 mm thickness and height. The mesh size in that region is 0.1 mm, similar to the size used in the constant-volume vessel 3D mesh. Simulations start at IVC with cylinder pressure derived from experimental data and temperature computed from the measured air mass flow rate. In-cylinder flow was initialized according to the measured swirl ratio and assuming a wheel-flow profile. Wall temperatures were taken from [34] where a similar optical engine was studied. Availability of experimental injected mass flow rate for different injection pressures and energizing times allowed to provide to the simulation the correct amount of diesel fuel mass considering also the correct start of injection timing.
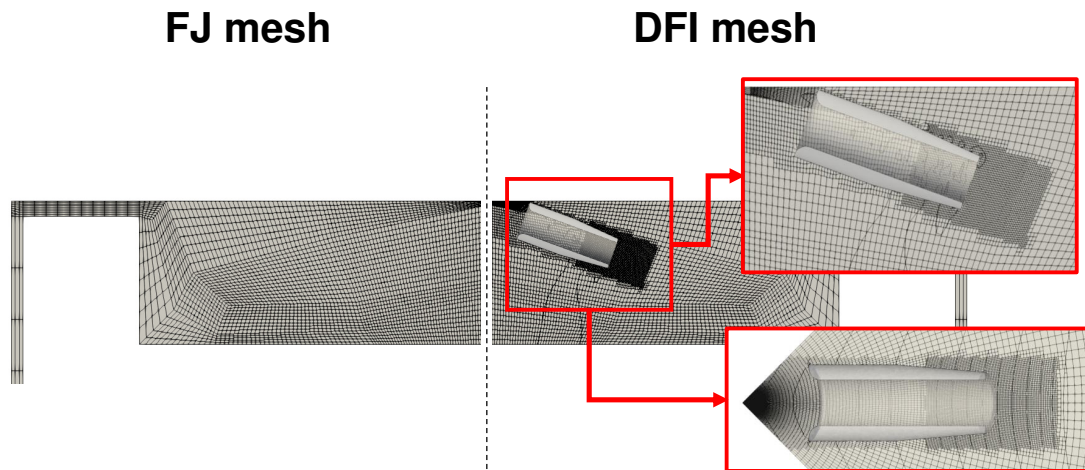
Figure 8: Details of the computational mesh used in engine simulations.

Fig. 9 reports the computed evolution of the spray and the temperature fields for the FJ and DFI configuration during the combustion process in the simulated engine. Fuel starts to be injected 7 CAD before top dead center (BTDC) and auto-ignition is reached 3 CAD BTDC for the FJ configuration. DFI ignition is about 1 CAD later and this confirms what was observed in the vessel experiments. After ignition, the computed FJ flame stabilizes almost at the location where the steady-state liquid penetration was found. At the end of injection, which is about 10 CAD ATDC, combustion recession happens and then oxidation is completed near the piston bowl. DFI engine combustion is substantially different. First, increased vapor penetration promotes a strong flame-wall interaction right immediately after the ignition. Then, for most of the injection process, the flame stabilizes at a certain distance from the duct exit and this is expected to reduce the formation of soot. After the end of injection, we can see that in the 11-12 CAD interval combustion recession promotes a fast oxidation of the mixture left inside the duct. During the burnout phase, the flame seems to be more confined near the center of the piston bowl and this could be related to the combination of duct, piston bowl design and charge swirl motion.

Figs. 10(a)-(b) display a numerical-experimental comparison of the cylinder pressure and HRR traces for both FJ and DFI configurations. The agreement between computed and measured data is rather good, mainly in the model capability to predict both the ignition delay time and the DFI increased amount of HRR after auto-ignition. DFI peak pressure increase compared to FJ is correctly estimated by simulations. In the second part of the injection process, the HRR is underestimated due to a strong interaction between the flame and the piston bowl walls. This aspect increases the predicted combustion duration

and it is related to the chosen turbulence model: the use of $k - \omega$-SST will improve such prediction as illustrated by the authors in previous works [18, 35].
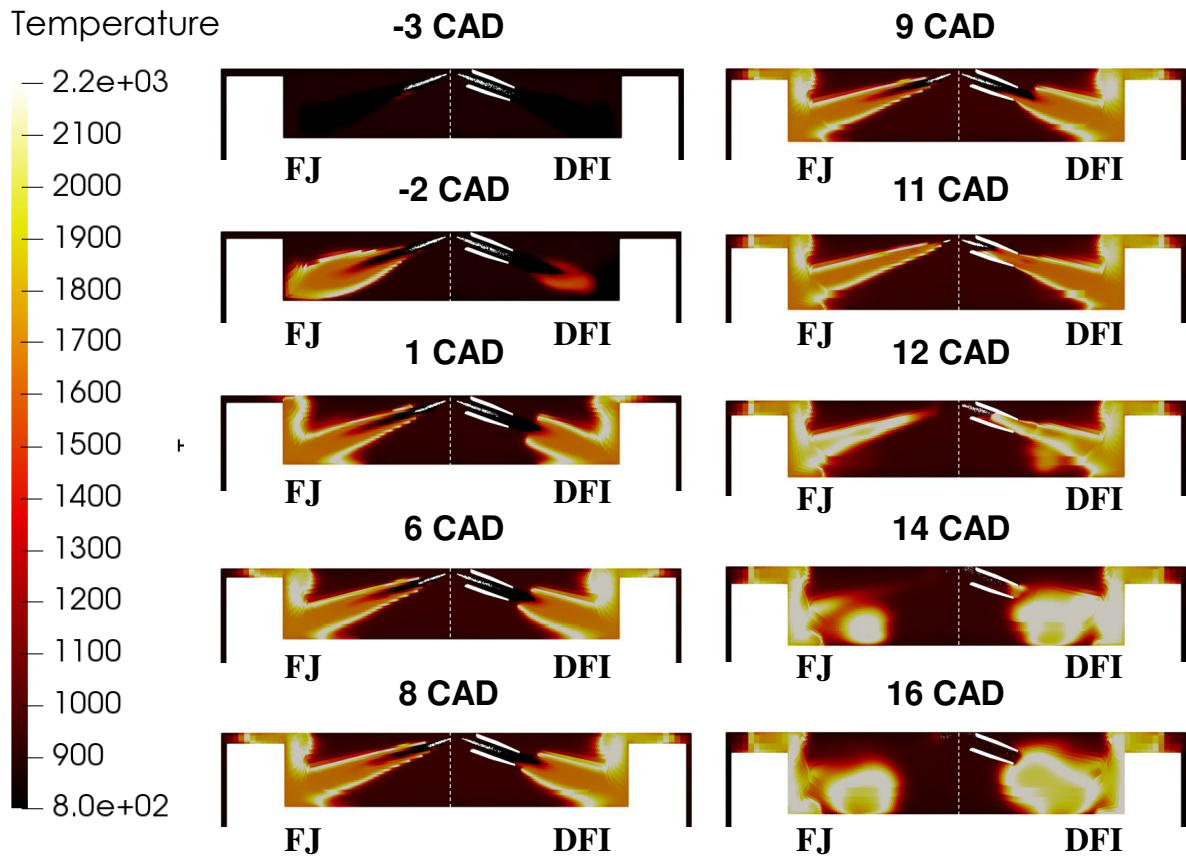
Figure 9: Computed evolution of spray and in-cylinder temperature field during the combustion process for the DFI and FJ configurations.
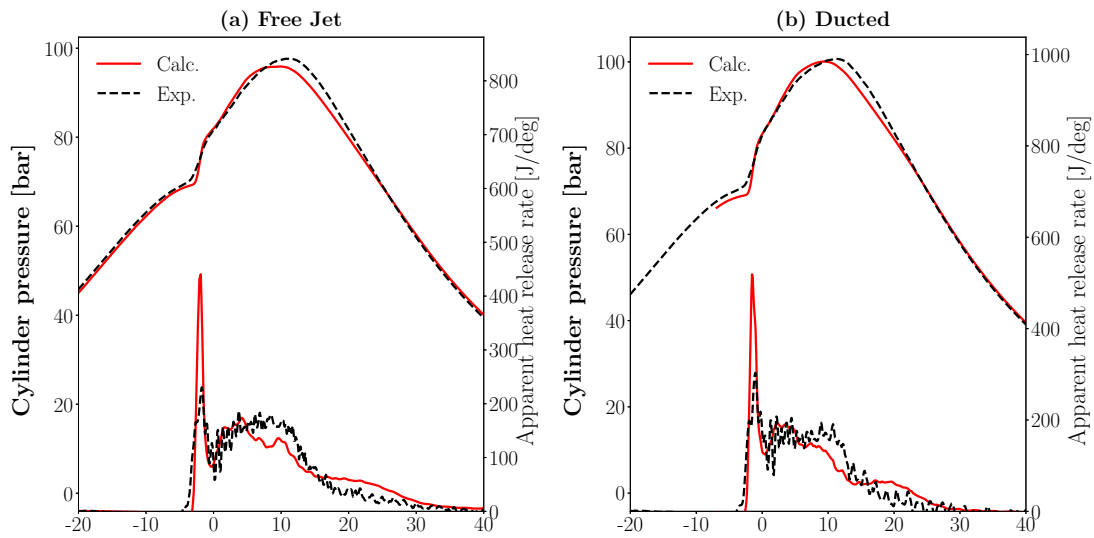
Figure 10: Comparison between computed and experimental cylinder pressure and HRR profiles for the FJ (a) and DFI (a) configurations in the single-cylinder engine.

CFD simulations allow a detailed visualization of the combustion process, which could be described by

means of the mixture, temperature and soot distributions. This is useful to properly select a suitable spray targeting, identifying the best design of the piston bowl. To understand the potential of DFI for the reduction of soot emissions in CI engines, Figs. 11-12 report the evolution of soot volume fraction (f_v) and mixture fraction (Z) on two orthogonal planes, both including the spray axis. To better understand how the mixing and combustion affect soot formation, the same figures also report the contours of both stoichiometric mixture fraction (white contour) and normalized progress variable $c = 0.5$ (red contour). Three different instants, representative of the combustion process, were selected:

- 2 CAD ATDC: middle of the injection process;

- 10 CAD ATDC: end of injection;

- 20 CAD ATDC: burnout phase.

At 2 CAD, Figs. 11-12 show that the DFI flame stabilizes at a longer distance from the nozzle compared to FJ, at lower equivalence ratio values. This explains the reason why soot formation starts closer to the piston bowl in the DFI configuration. DFI and FJ simulations predict similar peak values of soot volume fraction f_v because in both the cases the mixture fraction distribution near the piston bowl is still rich and promotes the formation of soot. This is the reason why at 10 CAD ATDC, when injection is almost finished, computed DFI and FJ f_v distributions look very similar. However, Fig. 11 clearly shows a relevant DFI reduction of f_v compared to FJ at 20 CAD. The reason for this can be found in Fig. 12, where also the direction of the swirl flow is reported. DFI reduced momentum diffusion increases the mixing between air and fuel and the potential for soot oxidation, better exploiting the available swirl at the end of combustion. It should be noticed that soot volume fraction results are still affected by a non-optimized model constants tuning and further investigations are still required for a better quantification of its distribution inside the combustion chamber.

Figs. 13(a)-(b) illustrate the evolution of the average in-cylinder turbulent kinetic energy k and the air entrainment rate. Reduced momentum diffusion seems to be the main reason why in Fig. 13(a) k is higher for DFI, enhancing the fuel-air mixing and promoting the soot oxidation also during the expansion stroke after the end of injection. While in [27] a DFI increase of the air entrainment rate was observed in constant-volume vessel simulations, Fig. 13(b) shows that such quantity is higher for DFI only before the instant in which jet-wall interaction happens. Increased air entrainment for DFI is the reason why a higher premixed HRR peak was found in Fig. 10. This demonstrates the importance of accounting for the jet-wall interaction when performing the design of the piston-bowl, to fully exploit the potential of DFI technology.
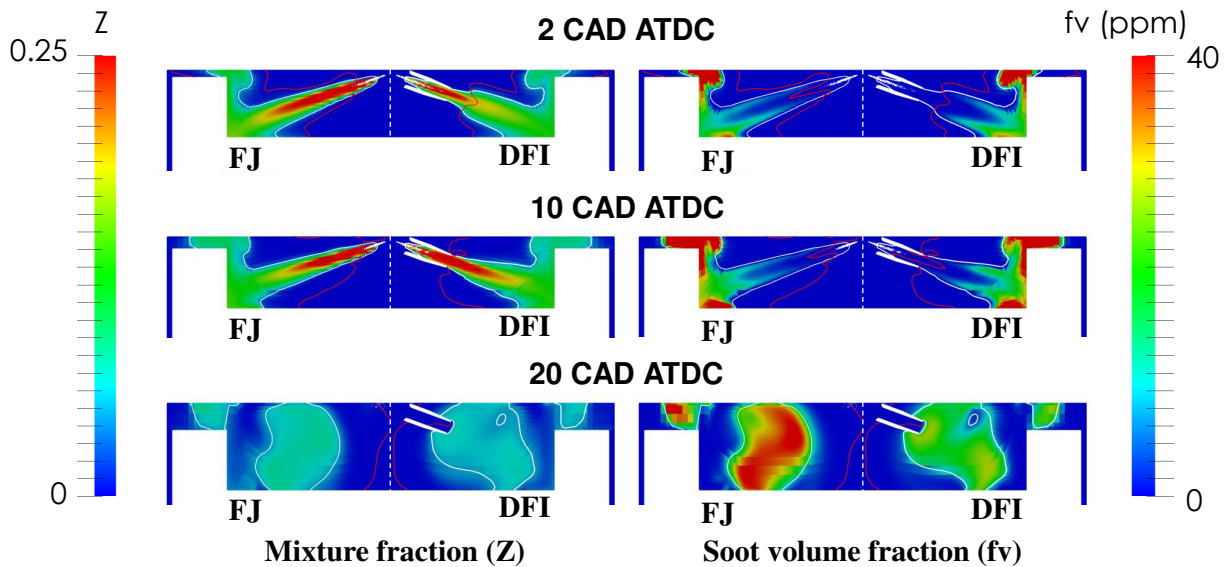
Figure 11: Computed evolution of the mixture fraction distribution Z and soot volume fraction f_v in a cut plane passing through the spray and cylinder axis. White contour: stoichiometric mixture fraction; red contour: normalized progress variable $c = 0.5$.
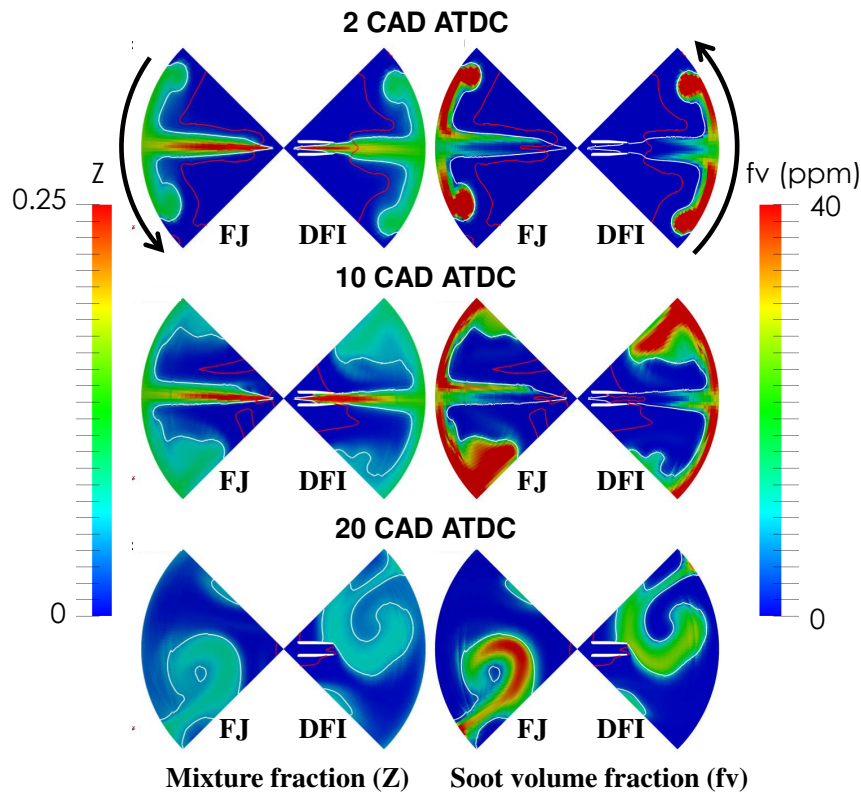
Figure 12: Computed evolution of the mixture fraction distribution Z and soot volume fraction f_v in a cut plane passing through the spray axis and orthogonal to that of Fig. 11. White contour: stoichiometric mixture fraction; red contour: normalized progress variable $c = 0.5$; black arrows: direction of the swirl flow.
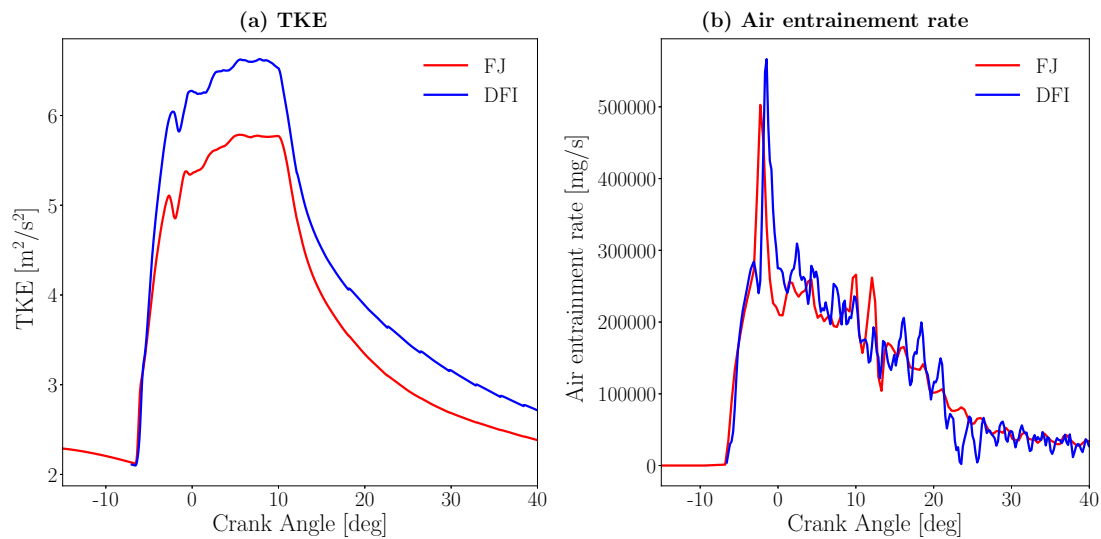
Figure 13: (a) computed evolution of average in-cylinder turbulent kinetic energy for DFI and FJ configurations; (b) computed evolution of the air entrainment rate for DFI and FJ configurations.

Finally, Fig. 14 reports the evolution of the computed soot mass. It is possible to see that, thanks to the better mixing and increased lift-off length, DFI produces:

• A reduced amount of the peak soot mass;

• A $\sim 60\%$ reduction of the soot mass at EVO, which is close to the $\sim 80\%$ value which was found

in experiments.

An improvement in terms of soot emission results is expected after a combined investigation of the influence of model tuning coefficients and turbulence model.
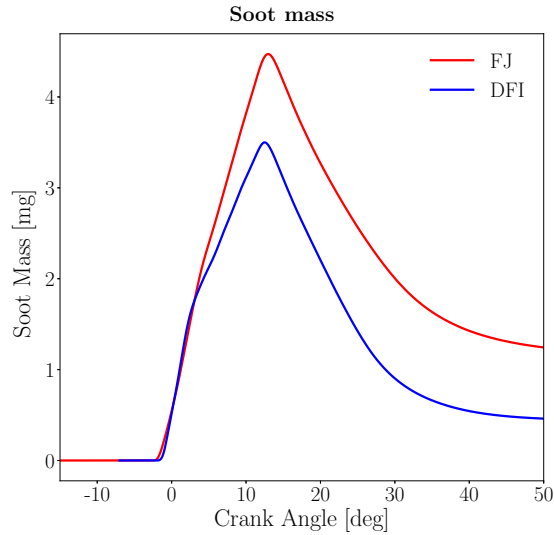
Figure 14: Computed evolution of in-cylinder soot mass for the DFI and FJ configuration in the single-cylinder engine.

4. Conclusions

Purpose of this paper is a CFD investigation of the ducted fuel injection (DFI) combustion process on both constant-volume vessel and engine experiments. The proposed methodology is based on the RANS approach, while a combustion model based on tabulated kinetics and turbulence-chemistry interaction is chosen. Results of the investigations can be summarized as follows:

- The proposed set of models can properly describe the main features of DFI combustion both at constant volume and in engine simulations: increase of the lift-off length, reduction of soot mass, increased peak of HRR and cylinder pressure.

- Despite a slightly increased numerical diffusivity and a corresponding reduction of the computed lift-off, the results of the 3D mesh are in agreement with those achieved for a 2D axi-symmetric one. This makes possible to employ a spray-oriented sector mesh configuration for the simulation of the DFI process in CI engines.

- Mixing at the duct outlet is responsible for the flame stabilization process. Improving the combustion model by including the effects of the local scalar dissipation rate is expected to provide a better agreement with experimental data in terms of computed flame lift-off and, consequently, DFI potential to reduce soot emissions.

- The comparison between constant-volume vessel and single-cylinder engine results allowed to better understand the mechanisms leading to soot reduction in both the configurations. Combustion chamber geometry limits the advantages of an increased DFI lift-off length but, at the same time, the higher amount of generated turbulence resulting from reduced momentum diffusion enhances the mixing and the potential for oxidation of soot.

- DFI engine combustion is strongly affected by flame-wall interaction. This aspect requires attention on the turbulence modeling side and near-wall mesh resolution since the family of $k - \varepsilon$ models is not completely able to correctly describe the features of flow in presence of strong curvatures.

- A better tuning of the semi-empirical soot model is necessary for an improved quantification of the DFI soot reduction potential and selection of suitable duct and piston bowl configurations.

5. Acknowledgments

References

[1] John E. Dec. Advanced compression-ignition engines - understanding the in-cylinder processes. *Proceedings of the Combustion Institute*, 32 II:2727 – 2742, 2009.

[2] Timothy Johnson and Ameya Joshi. Review of vehicle engine efficiency and emissions. *SAE Technical Papers*, 2017-March, 2017.

[3] Christopher J. Polonowski, Charles J. Mueller, Christopher R. Gehrke, Tim Bazyn, Glen C. Martin, and Peter M. Lillo. An experimental investigation of low-soot and soot-free combustion strategies in a heavy-duty, single-cylinder, direct-injection, optical diesel engine. *SAE International Journal of Fuels and Lubricants*, 5(1), 2011.

[4] Clément Chartier, Ulf Aronsson, Oivind Andersson, Rolf Egnell, Robert Collin, Hans Seyfried, Mattias Richter, and Marcus Aldén. Analysis of smokeless spray combustion in a heavy-duty diesel engine by combined simultaneous optical diagnostics. In *SAE World Congress And Exhibition*. SAE International, apr 2009.

[5] Ryan K. Gehmlich, Cosmin E. Dumitrescu, Yefu Wang, and Charles J. Mueller. Leaner lifted-flame combustion enabled by the use of an oxygenated fuel in an optical ci engine. *SAE International Journal of Engines*, 9(3):1526–1543, 2016.

[6] C.J. Mueller, C.W. Nilsen, D.J. Ruth, R.K. Gehmlich, L.M. Pickett, and S.A. Skeen. Ducted fuel injection: A new approach for lowering soot emissions from direct-injection engines. *Applied Energy*, 204:206–220, 2017.

[7] M. Meijer, B. Somers, J. Johnson, J. Naber, S.-Y. Lee, L. M. Malbec, G. Bruneaux, L. M. Pickett, M. Bardi, R. Payri, and T. Bazyn. Engine combustion network (ecn): Characterization and comparison of boundary conditions for different combustion vessels. *Atomization and Sprays*, 22(9):777–806, 2012.

[8] J. Manin, L. Pickett, and S. Skeen. Two-Color Diffused Back-Illumination Imaging as a Diagnostic for Time-Resolved Soot Measurements in Reacting Sprays. *SAE International Journal of Engines*, 6(1):1908–1921, 2013.

[9] F. Millo, A. Piano, B. Peiretti Paradisi, L. Postrioti, L. Pieracci, A. Bianco, F.C. Pesce, and A. Vassallo. Ducted fuel injection: Experimental and numerical investigation on fuel spray characteristics, air/fuel mixing and soot mitigation potential. *Fuel*, 289, 2021.

[10] R.K. Gehmlich, C.J. Mueller, D.J. Ruth, C.W. Nilsen, S.A. Skeen, and J. Manin. Using ducted fuel injection to attenuate or prevent soot formation in mixing-controlled combustion strategies for engine applications. *Applied Energy*, 226:1169–1186, 2018.

[11] K. Svensson, C. Kim, P. Seiler, G. Martin, and C. Koci. Performance and emission results from a heavy-duty diesel engine with ducted fuel injection. *SAE Technical Papers*, 2021.

[12] B.M. Wilmer, C.W. Nilsen, D.E. Biles, C.J. Mueller, and W.F. Northrop. Solid particulate mass and number from ducted fuel injection in an optically accessible diesel engine in skip-fired operation. *International Journal of Engine Research*, 2021.

[13] C.W. Nilsen, D.E. Biles, B.F. Yraguen, and C.J. Mueller. Ducted fuel injection vs. conventional diesel combustion: Extending the load range in an optical engine with a four-orifice fuel injector. *SAE International Journal of Engines*, 14(1), 2020.

[14] C.W. Nilsen, D.E. Biles, and C.J. Mueller. Using ducted fuel injection to attenuate soot formation in a mixing-controlled compression ignition engine. *SAE International Journal of Engines*, 12, 2019.

[15] Q. Zhou, T. Lucchini, G. D'Errico, G. Hardy, and X. Lu. Modeling heavy-duty diesel engines using tabulated kinetics in a wide range of operating conditions. *International Journal of Engine Research*, 22(4):1116–1132, 2021.

[16] A. Pati, D. Paredi, C. Welch, M. Schmidt, C. Geschwindner, B. Böhm, T. Lucchini, G. D'Errico, and C. Hasse. Numerical and experimental investigations of the early injection process of spray g in a constant volume chamber and an optically accessible disi engine. *International Journal of Engine Research*, 2021.

[17] T. Lucchini, A. Della Torre, G. D'Errico, and A. Onorati. Modeling advanced combustion modes in compression ignition engines with tabulated kinetics. *Applied Energy*, 247:537–548, 2019.

[18] Q. Zhou, T. Lucchini, G. D'Errico, N. Maes, B. Somers, and X.-C. Lu. Computational modeling of diesel spray combustion with multiple injections. *SAE Technical Papers*, 2020-April, 2020.

[19] M.J. Wankhede, F.A. Tap, P. Schapotschnikow, and W.J.S. Ramaekers. Numerical study of unsteady flow-field and flame dynamics in a gas turbine model combustor. *Proceedings of the ASME Turbo Expo*, 4A, 2014.

[20] R. Aglave, U. Riedel, and J. Warnatz. Turbulence-Chemistry Interactions in CFD Modelling of Diesel Engines. *Combustion Theory and Modelling*, 12(2):pp. 305–328, 2008.

[21] A. Krisman, J.C.K. Tang, E. R. Hawkes, D. O. Lignell, and J. H. Chen. A {DNS} evaluation of mixing models for transported {PDF} modelling of turbulent nonpremixed flames. *Combustion and Flame*, 161(8):2085 – 2106, 2014.

[22] T. Lucchini, G. D'Errico, A. Onorati, A. Frassoldati, A. Stagni, and G. Hardy. Modeling non-premixed combustion using tabulated kinetics and different flame structure assumptions. *SAE International Journal of Engines*, 10(2):593–607, 2017.

[23] K.M. Leung, R.P. Lindstedt, and W.P. Jones. A simplified reaction mechanism for soot formation in nonpremixed flames. *Combustion and Flame.*, 87:289–305, 1991.

[24] M. Bolla, D. Farrace, Y. M. Wright, K. Boulouchos, and E. Mastorakos. Influence of turbulence-chemistry interaction for n-heptane spray combustion under diesel engine conditions with emphasis on soot formation and oxidation. *Combustion Theory and Modelling*, 18(2):330–360, 2014.

[25] SANDIA Engine Combustion Network Database. http://www.ca.sandia.gov/ecn, 2021.

[26] Charles J. Mueller and Glen C. Martin. Effects of oxygenated compounds on combustion and soot evolution in a di diesel engine:broadband natural luminosity imaging. In *Spring Fuels And Lubricants Meeting And Exhibition*. SAE International, 2002.

[27] Tommaso Lucchini, Qiyan Zhou, Gianluca D'Errico, and Davide Severgnini. Modeling fuel-air mixing, combustion and soot formation with ducted fuel injection using tabulated kinetics. Number 2022, 2022.

[28] K. Narayanaswamy, P. Pepiot, and H. Pitsch. A chemical mechanism for low to high temperature oxidation of n-dodecane as a component of transportation fuel surrogates. *Combustion and Flame*, 161(4):866–884, 2014.

[29] B. Naud, R. Novella, J.M. Pastor, and J.F. Winklinger. Rans modelling of a lifted h2/n2 flame using an unsteady flamelet progress variable approach with presumed pdf. *Combustion and Flame*, 162(4):893–906, 2015.

[30] C.W. Nilsen, D.E. Biles, B.F. Yraguen, and C.J. Mueller. Ducted fuel injection versus conventional diesel combustion: An operating-parameter sensitivity study conducted in an optical engine with a four-orifice fuel injector. *SAE International Journal of Engines*, 13(3):345–362, 2020.

[31] Sergei S. Sazhin. Advanced models of fuel droplet heating and evaporation. *Progress in Energy and Combustion Science*, 32(2):162 – 214, 2006.

[32] Marco Mehl, William J. Pitz, Charles K. Westbrook, and Henry J. Curran. Kinetic modeling of gasoline surrogate components and mixtures under engine conditions. *Proceedings of the Combustion Institute*, 33(1):193 – 200, 2011.

[33] T. Lucchini, A. Della Torre, G. D'Errico, G. Montenegro, M. Fiocco, and A. Maghbouli. Automatic Mesh Generation for CFD Simulations of Direct-Injection Engines. *SAE Paper*, 2015-01-0376, 2015.

[34] S. Singh, R. D. Reitz, and M. P. B. Musculus. Comparison of the Characteristic Time (CTC), Representative Interactive Flamelet (RIF), and Direct Integration with Detailed Chemistry Combustion Models against Optical Diagnostic Data for Multi-Mode Combustion in a Heavy-Duty DI Diesel Engine. *SAE Paper*, 2006-01-0055, 2006.

[35] Noud Maes, Nico Dam, Bart Somers, Tommaso Lucchini, Gianluca D'Errico, and Gilles Hardy. Heavy-duty diesel engine spray combustion processes: Experiments and numerical simulations. *SAE Technical Papers*, 2018-September, 2018.

Session S3.1 Advanced Powertrain

THIESEL 2022 Conference on Thermo- and Fluid Dynamics of Clean Propulsion Powerplants

Understanding the Fuel Consumption of Plug-In Hybrid Electric Vehicles: a Real-World Case Study

M.A. Ktistakis[1], A. Tansini[2], A. Laverde[3], D. Komnos[1], J. Suarez[2], G. Fontaras[2]

[1] FINCONS SPA Group[2], Vimercate 20871, Italy

[2] European Commission's Joint Research Centre (JRC), Ispra 21027, Italy

[3] Polytechnic University of Valencia, VRAIN, Valencia 46022, Spain

E-mail: alessandro.tansini@ec.europa.eu
Telephone: +(39 0332786462)

Abstract

Road transport is currently one of the largest sources of CO_2 emissions, with light-duty vehicles having the lion's share. Plug-in Hybrid Electric Vehicles (PHEVs) are associated with low official Fuel Consumption (FC) values (consequently, CO_2 emissions) and are expected to contribute significantly to climate change mitigation. However, there is evidence that the FC gap between official and real-world measurements of PHEVs is large. This study examines a PHEV driven by seven drivers, in 2021 and 2022, for almost 6,000 km. The collected data are used to quantify and analyse FC and its intrinsic variability. Regression models are utilised to evaluate the importance of each factor by partitioning their contribution to the FC's variability. Results showed that most of the FC variability (90%) could be explained by the factors examined in this campaign. The highest contributors were found to be the trips' electrically driven share and the battery's initial state of charge. The presented analysis can be used to set up a more detailed and refined prediction model, which could assist in closely monitoring and understanding the FC gap and the underlying factors generating it. Furthermore, the study highlights the importance of understanding PHEVs' real-world (RW) usage and charging frequency.

Notation

CD   Charge Depleting
CS   Charge Sustaining
EAER   Equivalent All-Electric Range
EDS   Electric drive share
EU   European Union
FC   Fuel Consumption
GhG   Greenhouse Gas
ICE   Internal Combustion Engine
LDV   Light Duty Vehicles
OBD   On-Board Diagnostics
PHEV   Plug-in Hybrid Electric Vehicle
RDE   Real Driving Emissions
RW   Real World
SOC   State of Charge
TA   Type Approval
UDS   Unified Diagnostics Services
WLTP   World Harmonized Light vehicles Test Procedure

1. Introduction

European Union (EU) has adopted a union-wide law [1] that sets a minimum reduction target of 55% by 2030 for the Greenhouse Gas (GhG) emissions. In Europe, the transport sector is responsible for approximately a quarter of the GhG emissions, the majority of which originates from Light-Duty Vehicles (LDV). The need to reduce these emissions has motivated different initiatives from policymakers toward

---

[1] The views expressed in this paper are purely those of the authors and shall not be interpreted as an official position of the European Commission under any circumstance

[2] The work was carried out for/at the European Commission's Joint Research Centre of Ispra

the electrification of the vehicle fleet, setting stringent targets for the average LDV EU fleet CO_2 emissions.

Plug-in Hybrid Electric Vehicles (PHEV) stand as a readily available bridging solution towards the complete decarbonisation of the transport sector due to their potential to partially operate in a zero-tailpipe CO_2 emissions mode. These vehicles combine an Internal Combustion Engine (ICE) with an electric motor [2]. During the last two years, a significant sales increase contributed to the considerable reduction of the official CO_2 emissions, approaching the 95 g/km target for the 2020/2021 EU car fleet [3,4]. Regarding the vehicle's operation, PHEVs can work using electric energy stored in the high-voltage battery, which is called Charge Depleting (CD) mode or using the ICE and consume fuel in the so-called Charge Sustaining (CS) mode. Although the CD mode should in principle take a significant share of the distance driven in the lifetime and return zero emissions at the tailpipe, when the battery State of Charge (SOC) is low the CS mode is necessarily activated. Furthermore, fuel-consuming modes might be required under other unfavourable circumstances as extreme temperatures or transient high-power demand phases [5,6]. Consequently, the benefit of reducing Fuel Consumption (FC) is directly related to the amount of driven distance that the vehicles drive in purely (or mostly) electric mode, referred to as Electric Drive Share (EDS) in this study.

The effectiveness of the fuel and CO_2 emissions reduction measures depends on how reliable the Type Approval (TA) emission values (on which the CO_2 emissions targets are based) prove to be. The discrepancies between the Real-World (RW) and TA emissions and fuel consumption are a well-known problem that has been identified in the past as the FC Gap [7–9]. During the last years, accumulated evidence indicates that the CO_2 emission figures of PHEVs provided in TA might be significantly lower than the RW values, which would negatively affect the emissions reduction actually obtained under RW conditions [10]. Several studies [11,12] have recently quantified these discrepancies as a more than 200% deviation. The reason behind the higher FC gap in PHEVs is two-fold: on the RW side, there is a manifold of intrinsically variable factors with a direct impact on the vehicle's performance and the driveable distance on a full battery charge. For instance, variable on-road driving conditions (weather, traffic), the use of electric auxiliaries and the driving mode selected by the driver [13] can negatively affect the electric energy consumption. At the same time, long trip distances, high-speed ranges and variable charging habits might imply a different share of CS driving. These factors result in large variabilities among different users and even among different trips from the same driver, with considerably higher variances than conventional passenger cars [12].

FC in RW conditions depends on different factors, which can be split into three main groups described by Fontaras et al. [8] and Pavlovic et al. [14]: driver-related factors, environmental and traffic factors and vehicle factors. Vehicle factors are composed of the vehicle characteristics (mass, engine rated power etc.) and have been studied in the past for a fleet of vehicles [15–17]. This study uses data from seven volunteers that drove the same vehicle to quantify the intrinsic FC gap and its variability on a single-vehicle basis. By examining one vehicle driven by different users, the variabilities that arise from vehicle characteristics have been removed, and the variabilities of the driver-related factors and traffic and environmental factors have been isolated and studied. In the past a similar study was performed for an Internal Combustion Engine vehicle [14]. In this study, a PHEV is investigated and additional PHEV-specific parameters, that were not relevant for an ICE, such as the EDS and the initial SOC, are examined.

2. Material and methods

2.1 Real-driving campaign

An ad-hoc novel experimental campaign was carried out to gather data under RW conditions and assess how the driving, the charging practices the traffic and the environmental conditions influence the FC. The experimental driving campaign was carried out with a PHEV representative of the European market (see Table A1 in Appendix for the vehicle's technical specifications). Among the initial volunteers, seven that were expected to drive in a mix of urban (speed below 60 km/h), rural (speed between 60 and 90 km/h) and motorway (speed above 90 km/h) driving conditions, were selected and each of them was provided the car for about three weeks. Most of the trips took place in the surroundings of the Joint Research Centre site in Ispra, Varese (Italy). The drivers were asked to keep the same driving behaviour as in their everyday life, and the refuelling and recharging costs were at the user's expense. The driving campaign was designed for an entire year (2021-2022), capturing all seasons' weather conditions. A series of laboratory tests following the EU TA procedure [18] and Real Driving Emission tests (RDE)

[19–22] compliant on-road tests were also carried out better to ascertain the vehicle's performance in standard conditions.

To assess the performance of the PHEV regarding the fuel economy and the driving variables, a tailored data-logging system was prepared and installed. Data collection relied on the availability of signals from the vehicle On-Board Diagnostics (OBD) for standardised parameters and Unified Diagnostics Services (UDS) for vehicle-specific parameters. Around 50 instantaneous parameters were logged from the OBD/UDS and stored with a sampling frequency of approximately 1 Hz. This extensive dataset captured the operating conditions encountered in RW driving, quantifying the fuel and battery electric energy consumption and the key affecting parameters: environmental and vehicle conditions, trip characteristics, and driving style. Because of technical issues with the newly developed data logging system, altitude data was not available at the moment the analysis was carried out; anyhow, this important piece of information is going to be taken in consideration in follow-up studies on this topic.

The final dataset used in this analysis was obtained by processing the raw time series dataset, identifying the individual trips and removing corrupted and inaccurate records. The final cleaned dataset consists of 389 trips, with a total mileage of 5,887 km and 125 driving hours. The seven drivers used the vehicle between 32 and 80 times, providing a solid statistical basis for the assessment of the individual factors impacting the FC. The obtained urban, rural and motorway distance-shares on the total mileage were 36.6%, 18.6% and 44.8%, respectively. Specific values per driver, as well as a measure of the trips' dynamics (VA [95]) that provides better level of context to the results, can be found in Table A2 of the Appendix. Overall, the urban distance-share was found to be within the RDE boundaries of the specific phase (29% - 44%), whereas rural was substantially lower (23% - 44%) and motorway conditions only marginally higher (23% - 44%) [19–22]. The selection of parameters analysed in this research, was based on availability and previous studies examining the impact of different factors on the FC [12,14]. The goal was to include and examine important driver-related and traffic and environmental factors. Special attention was given to PHEV-specific parameters that were expected to have a large impact on the FC, such as the EDS and the initial SOC.

2.2 Multiple regression analysis

Multiple regression models were utilised to quantify the importance of the factors examined in this study to the FC (L/100km). There are many possible ways to define importance, in this paper, dispersion importance metrics were used, as they answer the main questions posed at the beginning of the study. Dispersion importance defines the amount of the response variable's (FC) variability explained by the regression model that is attributable to each explanatory factor. In this study, the game-based metric introduced by Lindeman, Merenda and Gold [23] was used to assess the dispersion importance. This metric decomposes the variability of the RW FC (the R-squared coefficient - R^2), to the explanatory variables' contributions.

3. Results and discussions

3.1 Overall fuel consumption analysis

As a starting point, the distribution of the trips' RW FC, normalised to each driver's distance (L/100km) is presented in Figure 1. The distributions differ substantially, depending on each user's driving habits and charging practice. A descriptive way to characterise the driving patterns is through the EDS. Drivers 1 and 7 show a similar highly efficient FC pattern, with most of the trips at very low or zero FC. They also present the highest EDS among all the drivers (85% and 87%, respectively). As a result, they are the only two cases that have an average FC value even lower than the official WLTP (World Harmonized Light vehicles Test Procedure) value of 0.9 L/100 km.

In contrast, driver 4 has the lowest EDS (20%), and consequently, the average FC is the highest one (5.1 L/100 km), with most of his trips around 6.5L/100km. This figure is comparable to what would be expected from a conventional gasoline ICE vehicle of similar characteristics. As intermediate cases, drivers 3 and 5 FC values show a bimodal distribution. These drivers incorporate many trips on CD mode, with zero FC, and trips with high FC, resulting in overall FC averages of 4.5 and 5 L/100km, respectively. Leaving aside the exceptional performance of drivers 1 and 7, the average FC among drivers is in the range of 3.4-5.1 L/100km.

Another critical aspect of Figure 1 is the intra-driver FC variability. Drivers 1 and 7 also exhibit the smallest variability in FC, with standard deviations of 1.6 and 0.9 L/ 100km, respectively. The FC standard deviations of the other drivers are consistently ranging from 3.6 to 4.0 L/100km. Additional information can be gathered from the median of each distribution, which minimises the contribution from outliers. All the drivers, except drivers 2 and 4, have a median FC of 0 L/100km, meaning that at least half of the trips were driven in pure electric mode.
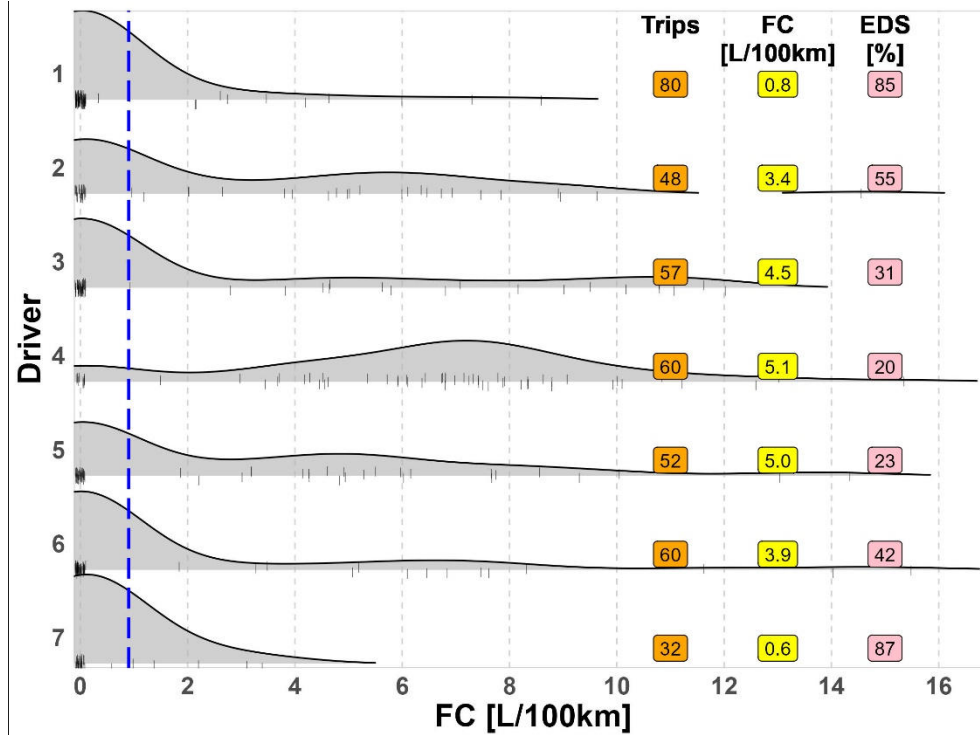
Fig. 1. FC per driver. Labels depict the total trip characteristics per driver; blue dashed line: type approval FC (0.9 L/100km)

Table 1. Number of charging events per day and driver. Bold: most frequent number of charges per driver

Charge events / day	Driver 1	Driver 2	Driver 3	Driver 4	Driver 5	Driver 6	Driver 7
0	2	**12**	7	**20**	**9**	6	0
1	**10**	8	**11**	7	6	5	7
2	6	0	0	0	3	**7**	**8**
3	2	0	0	0	0	1	0
Days with full-SOC at first trip	80%	5%	50%	14%	5%	36%	67%
Days with depleted-SOC at last trip	19%	15%	33%	81%	41%	28%	31%

Table 1 displays the number of charging events per day and driver, both full-charging and partial-charging are considered. Only two out of the seven drivers (driver 1 and 3) showed more tendency to charge the battery once a day. Three other drivers (2, 4 and 5) opted not to charge the battery most days, while drivers 6 and 7 frequently charged multiple times per day. Contrary to a fundamental assumption present in EU Regulation 2017/1151, the charges applied were only partial on many days. Only driver 1 (with an 80% occurrence) and in a lower extent driver 7 (almost 70% of the trips) are close to the full-charge-per-day assumption. As expected, these two are also the drivers with lower RW FC than the TA FC. For the rest of the drivers, the days starting with a fully-charged battery oscillate between the very poor 5% of driver 2 and driver 5 and the mediocre rate of driver 3 (50 %). Concerning the times that the battery was completely depleted at the end of the day, driver 4 is clearly above the rest of the users. Combined with the very low rate of fully-charged battery at the beginning of the day, this inefficient

charging habit is at the root of the high FC (similar to an ICE-type vehicle with similar technical characteristics) that this driver exhibits.

In view of the previous findings, one can reasonably expect that the FC has a clear dependency on the trip's mileage and initial SOC. In Figure 2 the relationship between these factors is depicted. The impact of the initial SOC on the FC is clear, trips starting with low or empty battery (initial SOC lower than 25%) take place almost entirely in CS mode, reaching a FC up to 15 L/100km for very short trips (less than 2 km) due to the vehicle working on cold conditions, possibly in combination with battery charging events. On the other hand, trips starting with a SOC above 50% exploit CD operation, yielding a significantly reduced FC. However, these favourable battery conditions do not grant, by themselves, a low FC value in a single trip perspective. For driven distances above the EAER (Equivalent All-Electric Range), the FC increases rapidly, stabilising at a constant value of 6 L/100km (in the same order of an ICE vehicle) for trips longer than 120km. With a fully charged battery, the electric range ensures that the vehicle is driven at least for a range of 50-60 km even under RW driving conditions (usually unfavourable in comparison to the laboratory conditions where the EAER is calculated). As the initial SOC decreases, the probability of driver on CD mode decreases and we find more frequently pure CS trips.

To supplement this analysis and get a better understanding of the FC's dependency on the trip mileage and initial SOC, a 16-parameters fitting surface has been used; it combines an exponential expression for the dependency on the initial SOC and an arctangent-type function to describe the distance dependency. This last function ensures the correct asymptotic behaviour both at large distances (where the contribution from CS is dominant) and in the short distances, where the vehicle mostly operates in CD with zero or nearly-zero FC. The proposed surface perfectly adapts to the set of points elaborated from the anonymised trips and can therefore be considered vehicle-specific and driver-independent.
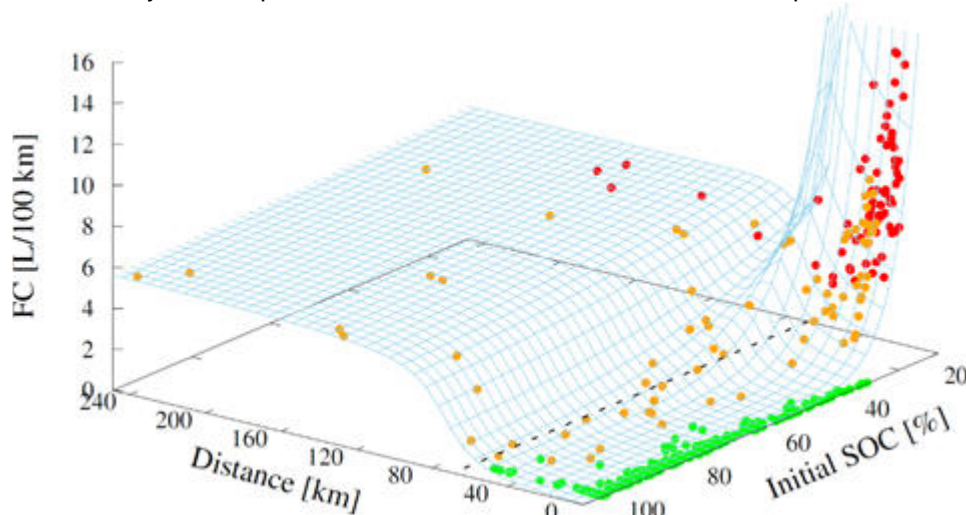
Fig. 2. FC in relation to trip mileage and initial SOC. Black dashed line: electric range (70km); trips driven only in CD mode (green); trips driven only in CS mode (red); trips driven in both modes (orange)

3.2 Contribution to FC variability

Multiple regression analysis was employed to understand and quantify the importance of the different factors (explanatory variables) examined in this study to the FC in L/100km (response variable). Three models were used, the first utilised all driver-related, environmental and traffic factors examined in this research, the second model employed all factors except the average engine speed. This was done because of two reasons: 1. the very high correlation between the FC, the EDS and the average engine speed (84-92%). Therefore, this model enabled the examination of the importance of the other factors impacting the FC, without considering one of these two highly inter-correlated explanatory variables (average engine speed - EDS). 2. for PHEVs the average engine speed is an indicator of traffic conditions, the driving style and the charging behaviour. Hence, the second model made possible to further isolate the pure driver-related factors and examine their explanatory power. In the third model, both the average engine speed and the EDS were excluded, this way the explanatory power of the rest of the parameters could be examined without taking into consideration the two largest contributors (according to model 1). In addition, it allowed to assess whether the contribution of the EDS and the average engine speed can be split between more elementary factors.

Model 1: $FC = \beta_0 + \beta_1 EDS + \beta_2 EngSpeed + \beta_3 SOC_{init} + \beta_4 Speed + \beta_5 Mileage + \beta_6 Cruise + \beta_7 Duration + \beta_8 Stop + \beta_9 VA\ [95] + \beta_{10} AmbTemp + \sum_{j=11}^{17} \beta_j\ Driver$

Model 2: $FC = \beta_0 + \beta_1 EDS + \beta_2 SOC_{init} + \beta_3 Speed + \beta_4 Mileage + \beta_5 Cruise + \beta_6 Duration + \beta_7 Stop + \beta_8 VA\ [95] + \beta_9 AmbTemp + \sum_{j=10}^{16} \beta_j\ Driver$

Model 3: $FC = \beta_0 + \beta_1 SOC_{init} + \beta_2 Speed + \beta_3 Mileage + \beta_4 Cruise + \beta_5 Duration + \beta_6 Stop + \beta_7 VA\ [95] + \beta_8 AmbTemp + \sum_{j=9}^{15} \beta_j\ Driver$

Where EDS: electric drive share; $EngSpeed$: average engine speed; SOC_{init}: initial state of charge; $Speed$: average vehicle speed; $Mileage$: trip distance; $Cruise$: cruise percentage; $Duration$: trip duration; $Stop$: stop percentage; $VA\ [95]$: 95th percentile of the product of vehicle speed and acceleration; $AmbTemp$: average ambient temperature; $Driver$: driver factor.

The R-squared (R^2) of model 1 (all factors) is 89.6%, which means that almost 90% of the trips' FC variability is explained by the factors examined in this research. When not considering the average engine speed (model 2), there was a very small drop on the model's effectiveness ($R^2 = 88.5\%$). The same holds true for the adjusted R-squared coefficient (model 1: Adjusted R-squared=89.2%, model 2: 88.0%), which means that the actual contribution of the average engine speed to the FC is not as large as model 1 indicates (Figure 3). Excluding also the EDS (model 3) the explanatory power reduced significantly ($R^2 = 59.5\%$), which attests to the great importance of the EDS to the FC.

In Figure 3 the importance of each factor composing the models is depicted. According to model 1, the two highest contributors to the FC's variability are the EDS and the average engine speed, followed by the initial SOC and the driver factor. The EDS explains 34.2% of the variability and the average engine speed 28.2%, summing up to 62.4%. The impact of the initial SOC (15.9%) and the driver factor (6.3%) are relatively high, while the other seven factors have minimal contributions (combined 5.0%). In the model without the average engine speed (model 2), the impact of the variables highly correlated to the average engine speed increased. However, the order of importance, of the factors with high contributions (EDS, initial SOC and driver) remained the same. In this case, the EDS explained more than half of the trips' FC total variability (53.8%). The Initial SOC and driver contributed another 22.6% and 8.3% respectively, while the individual impact of the rest of the factors was below 1.0%. When excluding also the EDS (model 3), a large portion of the EDS contribution is attributed to the initial SOC, since this contribution increases from 22.6% in model 2 to 42.1% in model 3 (Figure 3). The impact of the driver factor is also increased by 4.5%, while the cumulative impact of the rest of the factors remained below 5%. This further highlights the significant difference between ICE vehicles, where those non-PHEV-specific variables play a much more important role [14], and PHEVs, in which case the FC is mostly attributable to the EDS and charging behaviour.

To summarise, model 1 results show the high correlation and importance of the EDS and the average engine speed with respect to the FC (L/100km). Concerning the EDS, this is in line with the analysis presented in the previous section (overall fuel consumption analysis). Regarding the average engine speed, model 1 assigns a large contribution to the average engine speed, however the causal effect between the average engine speed is doubtful. For non-PHEVs the average engine speed indicates the traffic congestion, the driving style and the urban-rural-motorway mix; therefore, it affects significantly the FC [14]. In PHEVs, though, it also captures the information of which trips were driven with zero FC, resulting in a significantly higher contribution and a large correlation with other factors, such as the EDS. To address this, model 2 was employed, and it was found that the contribution of the average engine speed was overestimated and its inclusion to the model was almost redundant. Model 3 was finally used in order to examine whether it was possible to decompose the EDS's contribution to more fundamental factors. It was found that it is not possible to achieve this with satisfactory results, using the variables examined in this study, as this causes a significant drop (almost 30%) in the model's explanatory power.
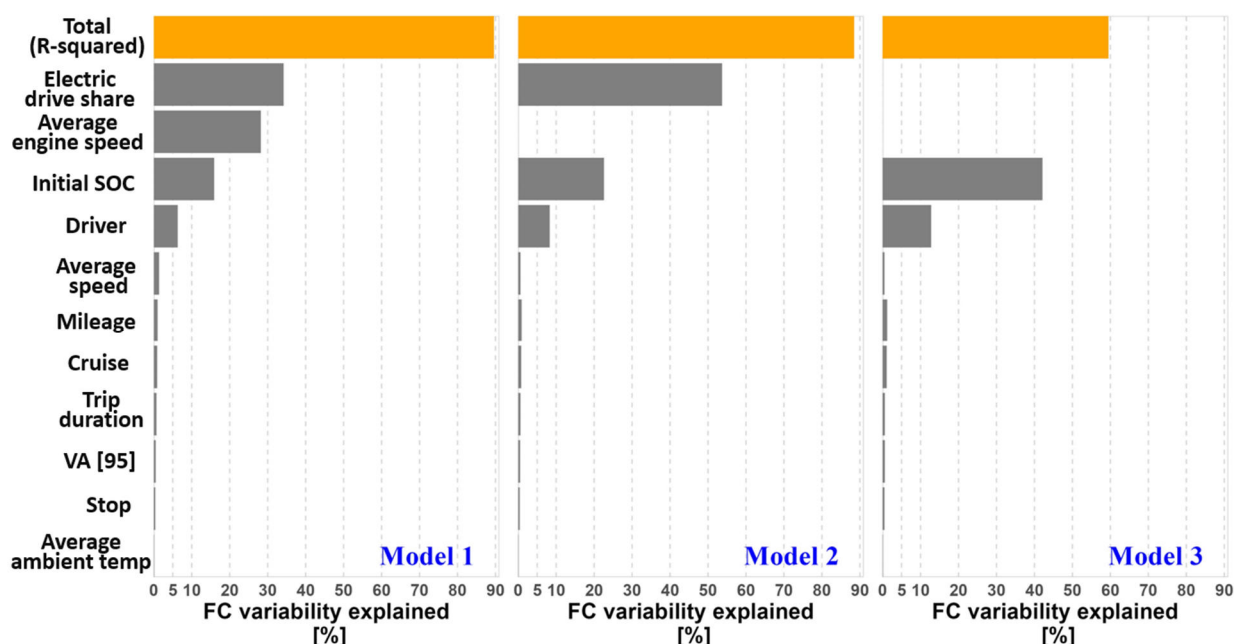
Fig. 3. FC variability explained by the models and each factor. Model 1: all factors; Model 2: excluding average engine speed; Model 3: excluding average engine speed and electric drive share

Conclusions

This paper presented the preliminary results of an ongoing experimental campaign that investigates on the RW FC performance of PHEVs. The data measured under RW conditions from seven different drivers were used to understand which are the main factors influencing the RW FC and how they contribute to the gap between RW FC measurements and official TA values. Significant differences were found between the drivers, confirming the intrinsic high variability of FC in PHEVs. Strong correlations were identified between the FC, the EDS and the average engine speed. However, in a second formulation of the regression model, the latter proved to be not as impactful as estimated by the first formulation, since the R^2 only drops from 89.6% to 88.5% when the average engine speed is removed. The initial SOC and implicitly the charging frequency were also critical in explaining the FC variability.

   The regression analysis confirmed the importance of the driver's behaviour in a larger perspective covering beyond the driving part, and encompassing also the charging frequency, the charging depth and the vehicle usage. These factors explain 85% of the total variability of the RW FC. A third regression model was examined, excluding also the EDS, and it was found that in this case the explanatory power of the model reduced to 59.5%. Consequently, it can be inferred that the impact of traffic and environmental factors to the RW FC is minimal for PHEVs, whereas the driver-related factors largely dominate. This study further highlights, adding to the findings from other studies, the importance of charging frequency and usage characteristics in determining the FC of PHEVs. In addition, it presents an approach to the modelling of the RW FC that could be used to predict the FC obtained under different usages, therefore helping to solve the intrinsic complexity of PHEVs FC. The continuation of the activity presented in this study will enable to better characterise the TA to RW FC gap from PHEVs, by incorporating additional variables such as the road grade. Once a larger sample of drivers will be covered and the main assumptions regarding the expected lifetime driven distance in CD mode can be verified, the activity presented in this study might finally be able to return a piece of evidence towards how fit the TA procedure is with respect to representing the RW performance of PHEVs.

Acknowledgments

References

[1]   Regulation (EU) 2021/1119 of the European Parliament and of the Council of 30 June 2021 establishing the framework for achieving climate neutrality and amending Regulations (EC) No 401/2009 and (EU) 2018/1999 ('European Climate Law'). 2021.

[2]   Rizzoni G, Guzzella L, Baumann BM. Unified modeling of hybrid electric vehicle drivetrains. IEEE/ASME Transactions on Mechatronics 1999;4:246–57. https://doi.org/10.1109/3516.789683.

[3]   ACEA. Fuel types of new cars: battery electric 7.5%, hybrid 19.3%, petrol 41.8% market share in Q2 2021 2021.

[4]   Zheng J, Sun X, Jia L, Zhou Y. Electric passenger vehicles sales and carbon dioxide emission reduction potential in China's leading markets. Journal of Cleaner Production 2020;243:118607. https://doi.org/10.1016/j.jclepro.2019.118607.

[5]   Tran D-D, Vafaeipour M, El Baghdadi M, Barrero R, Van Mierlo J, Hegazy O. Thorough state-of-the-art analysis of electric and hybrid vehicle powertrains: Topologies and integrated energy management strategies. Renewable and Sustainable Energy Reviews 2020;119:109596. https://doi.org/10.1016/j.rser.2019.109596.

[6]   Cubito C, Rolando L, Millo F, Ciuffo B, Serra S, Trentadue G, et al. Energy Management Analysis under Different Operating Modes for a Euro-6 Plug-in Hybrid Passenger Car, 2017, p. 2017-01–1160. https://doi.org/10.4271/2017-01-1160.

[7]   Weiss M. Analyzing on-road Emissions of Light-duty Vehicles with Portable Emission Measurement Systems (PEMS). 2011.

[8]   Fontaras G, Zacharof N-G, Ciuffo B. Fuel consumption and CO_2 emissions from passenger cars in Europe – Laboratory versus real-world emissions. Progress in Energy and Combustion Science 2017;60:97–131. https://doi.org/10.1016/j.pecs.2016.12.004.

[9]   Pavlovic J, Ciuffo B, Fontaras G, Valverde V, Marotta A. How much difference in type-approval CO2 emissions from passenger cars in Europe can be expected from changing to the new test procedure (NEDC vs. WLTP)? Transportation Research Part A: Policy and Practice 2018;111:136–47. https://doi.org/10.1016/j.tra.2018.02.002.

[10]   Ramírez Sanchez PP, Ndiaye AB, Martín-Cejas RR. Plug-In Hybrid Electric Vehicles (PHEVS): A possible perverse effect generated by Environmental Policies. International Journal of Transport Development and Integration 2019;3:259–70. https://doi.org/10.2495/TDI-V3-N3-259-270.

[11]   Transport & Environment. A new Dieselgate in the making. 2020.

[12]   Plötz P, Moll C, Bieker G, Mock P. From lab-to-road: real-world fuel consumption and CO_2 emissions of plug-in hybrid electric vehicles. Environ Res Lett 2021;16:054078. https://doi.org/10.1088/1748-9326/abef8c.

[13]   Ehrenberger SI, Konrad M, Philipps F. Pollutant emissions analysis of three plug-in hybrid electric vehicles using different modes of operation and driving conditions. Atmospheric Environment 2020;234:117612. https://doi.org/10.1016/j.atmosenv.2020.117612.

[14]   Pavlovic J, Fontaras G, Ktistakis M, Anagnostopoulos K, Komnos D, Ciuffo B, et al. Understanding the origins and variability of the fuel consumption gap: lessons learned from laboratory tests and a real-driving campaign. Environmental Sciences Europe 2020;32. https://doi.org/10.1186/s12302-020-00338-1.

[15]   Tsiakmakis S, Fontaras G, Ciuffo B, Samaras Z. A simulation-based methodology for quantifying European passenger car fleet CO_2 emissions. Applied Energy 2017;199:447–65. https://doi.org/10.1016/j.apenergy.2017.04.045.

[16]   Zacharof N-G, Fontaras G. Review of in use factors affecting the fuel consumption and CO2 emissions of passenger cars. 2016.

Understanding the Fuel Consumption of Plug-In Hybrid Electric Vehicles: a Real-World Case Study 9

[17]   Ktistakis MA, Pavlovic J, Fontaras G. Developing an optimal sampling design to monitor the vehicle fuel consumption gap. Science of The Total Environment 2022;832:154943. https://doi.org/10.1016/j.scitotenv.2022.154943.

[18]   COMMISSION REGULATION (EU) 2017/1151 of 1 June 2017 supplementing Regulation (EC) No 715/2007 of the European Parliament and of the Council on type-approval of motor vehicles with respect to emissions from light passenger and commercial vehicles (Euro 5 and Euro 6) and on access to vehicle repair and maintenance information, amending Directive 2007/46/EC of the European Parliament and of the Council, Commission Regulation (EC) No 692/2008 and Commission Regulation (EU) No 1230/2012 and repealing Commission Regulation (EC) No 692/2008. 2017.

[19]   Commission Regulation (EU) 2016/427. 2016.

[20]   Commission Regulation (EU) 2016/646. 2016.

[21]   Commission Regulation (EU) 2017/1154. 2017.

[22]   Commission Regulation (EU) 2018/1832. 2018.

[23]   Lindeman RH, Merenda PF, Gold RZ. Introduction to Bivariate and Multivariate Analysis. Scott, Foresman; 1980.

Appendix

Table A1. Vehicle technical specifications

Vehicle type	C-Segment, 5 seats
Powertrain	Gasoline PHEV
WLTP test mass [kg]	1,698
Engine displacement [cm]	1,395
Engine power [kw]	110
Electric motor power [kw]	80
Combined power [kw]	150
Equivalent all electric range [km]	70
WLTP fuel consumption [l/100km]	0.9

Table A2. Trip characteristics for each driver

Driver	Trips	Total distance (km)	Urban share (%)	Rural share (%)	Motorway share (%)	Urban VA [95] (m^2/s^3)	Rural VA [95] (m^2/s^3)	Motorway VA [95] (m^2/s^3)
1	80	598	69.3%	27.1%	3.6%	22.5	30.7	48.9
2	48	497	50.8%	29.5%	19.7%	25.9	37.7	36.9
3	57	685	39.1%	9.0%	52.0%	18.5	35.9	34.6
4	60	1,224	38.2%	22.1%	39.7%	25.0	40.1	49.7
5	52	1,181	24.2%	9.8%	66.0%	23.4	41.5	41.5
6	60	653	38.1%	14.1%	47.8%	20.3	37.9	35.7
7	32	1,050	58.8%	35.5%	5.7%	19.2	19.6	25.4
Total	389	5,887	36.6%	18.6%	44.8%	22.8	35.8	37.7

Development of Hybrid Electric Vehicles in the Context of Life Cycle Assessment

P. Weber, O. Toedter, T. Koch, T. Weyhing

IFKM – Institute of Internal Combustion Engines. Karlsruhe Institute of Technology (KIT). Rintheimer Querallee 2, 76131 Karlsruhe, Germany.

E-mail: philipp.weber@kit.edu
Telephone: +(49) 721 608 48551

Abstract. Apart from the tank-to-wheel approach, which is currently used for passenger car homologation, the importance of emissions in other life cycle phases is more and more acknowledged. This includes the production and disposal of the vehicle as well as the upstream emissions of the energy carriers. In order to evaluate the eco-friendliness of passenger cars, life cycle assessment (LCA) gained large popularity over the last few years.

Within this work, an overview of different life cycle-based methods is given, including methodological background such as the ISO 14040/44 standards and combined technical LCA (TLCA) approaches. Hereby, a research gap regarding the TLCA of HEVs could be identified, with related publications lacking detail in LCA modelling.

On this basis, the authors present a toolchain consisting of a vehicle co-simulation platform and a full LCA tool. The proposed environment allows for a large variety of influencing factors, such as powertrain configuration, operating strategy, driver behavior as well as the materials and manufacturing processes involved in the vehicle production. Exemplarily, a conventional gasoline-fueled vehicle is compared to a mild hybrid and full hybrid electric vehicle in a cradle-to-grave context.

In the considered use cases, fuel savings of up to 8.5 % can be achieved by full hybridization in a real driving scenario. When tested in a WLTC, the considered full hybrid only achieves a fuel consumption reduction of 5 %. In both cases, an even larger savings potential is hampered by the additional mass introduced through an increased hybridization degree. Moreover, the additional environmental impact caused by hybrid components cannot always be compensated through improved fuel consumption. Particularly in case of impact categories other than the global warming potential, such as mineral resource scarcity potential, hybridization can result in increased environmental burdens. This work provides a methodology to assess such interactions between technical features and environmental impact.

Abbreviations

BEV	Battery electric vehicle
CO_{2eq}	CO_2 equivalent
CPP	Common parameter platform
EEA	European Environment Agency
EM	Electric machine
EU	European Union
FHEV	Full hybrid electric vehicle
GHG	Greenhouse gas
GREET	Greenhouse gases, Regulated Emissions, and Energy use in Technologies
GWP	Global warming potential
HEV	Hybrid electric vehicle
ICE(V)	Internal combustion engine (vehicle)
ILCD	International Reference Life Cycle Data System
LCA	Life cycle assessment
LCI	Life cycle inventory
LCIA	Life cycle impact assessment
MHEV	Mild hybrid electric vehicles
PC	Passenger car
PHEV	Plug-in hybrid electric vehicle
SOC	State of charge
TLCA	Technical LCA
TTW	Tank-to-Wheel
WTW	Well-to-Wheel

1. Introduction

In recent years, the European Union (EU) has further intensified its climate protection efforts. As shown in Figure 1, total greenhouse gas (GHG) emissions in the EU27 could be decreased by 31.9 % between 1990 and 2020, when considering all contributing sectors, which is denoted as "total". The difference between total CO_2 and greenhouse gas (GHG) emissions, which amounts to 20.2 % in 2020, underlines the importance of properly specifying the regarded emission species and metrics, which will be discussed in more detail in section 2. In contrast to the overall positive trend, the road transport sector CO_2 emissions increased by 11.9 % over the considered time period, and even by 28.6 % from 1990 to 2019 before the pandemic. In the year 2020, passenger cars (PC) contributed 59.5 % of CO_2 emissions within road transport, highlighting the strong impact of individual mobility and the need for CO_2 reduction.
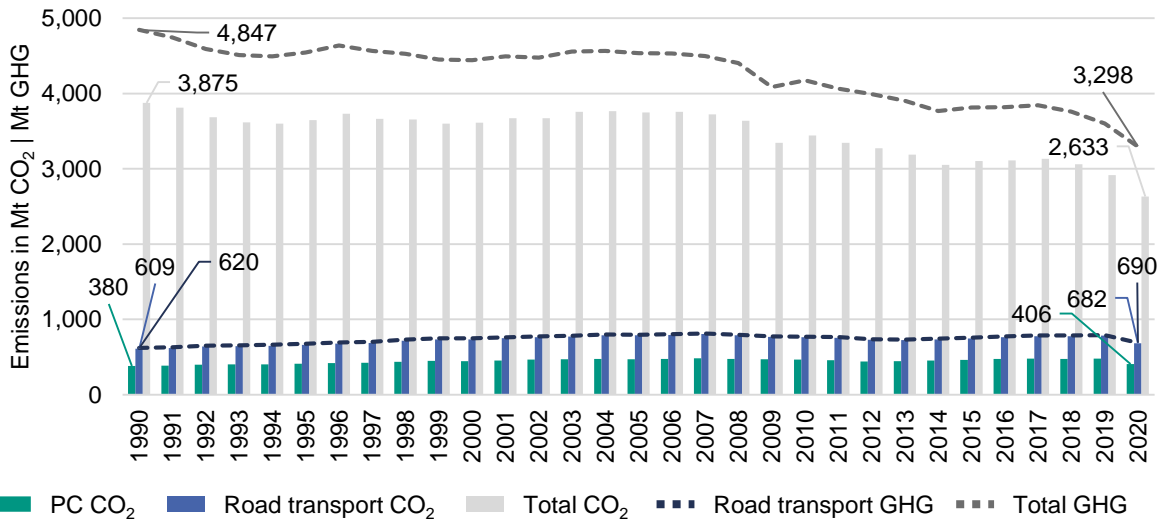
Figure 1. Development of CO_2 and GHG emissions in the EU27 from 1990 to 2020 based on data from the European Environment Agency (EEA) with a focus on road transport and passenger cars [1]

In 2019, the most recent PC CO_2 emission regulation (Regulation (EU) 2019/631) was enforced, including a further reduction by 37.5 % in 2030 based on an EU-wide PC fleet average emission of 95 g CO_2/km in 2021 [2]. At the end of 2019, the European Commission announced a new roadmap called the European Green Deal, which aims at enabling a sustainable EU economy. Regarding climate protection policy, more ambitious targets were formulated, such as the reduction of overall GHG emissions by up to 55 % in 2030 compared to 1990 levels [3].

In 2021, the pathway towards the Green Deal GHG reduction goal was defined more precisely in the "Fit for 55" package of measures. It involves sector-specific targets, such as a tightening of the PC CO_2 reduction target for 2030 from 37.5 % towards 55 % and a reduction to 0 g CO_2/km in 2035. The development of fleet emission targets and annual historic values is displayed in Figure 2.
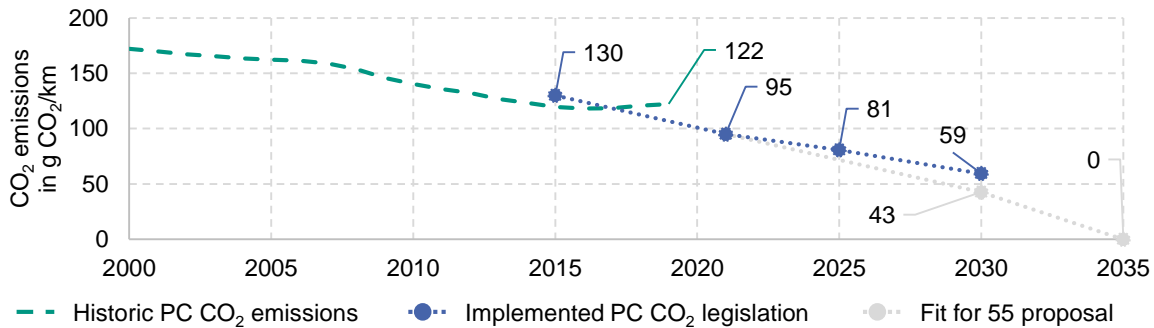
Figure 2. Development of fleet emissions and CO_2 emission targets in the EU, based on EEA data [4]

Although the renewed CO_2 reduction objectives have not yet been implemented, the legislative trends in the EU increasingly urge vehicle manufacturers to decrease the CO_2 emissions of newly registered cars. As CO_2 emissions are determined according to a tank-to-wheel (TTW) approach, only local emissions are included. Thus, a value of 0 g CO_2/km is attributed to battery and fuel cell electric vehicles.

Moreover, this procedure also favors plug-in hybrid electric vehicles (PHEVs), as it accounts for the purely electrically driven range with zero emissions as well [2].

Owing to these boundary conditions, the automotive industry focuses more and more on electrification, i.e., through hybridization and particularly towards purely electric vehicles. Exemplarily, the Volkswagen Group states in its most recent sustainability report that it targets an ambitious electric vehicles' sales share of at least 60 % by 2030 in the EU [5]. Such a portfolio shift helps manufacturers to comply with their fleet targets.

However, the current diversity in powertrain configurations cannot be compared fairly through the current TTW methodology only, as the upstream part of driving energy carriers as well as vehicle production and end-of-life are neglected. In order to evaluate the entire vehicle life, the methodology of life cycle assessment (LCA) has grown significantly in popularity. Hill, Amaral et al. 2020 [6] published an LCA study, which also includes a vast literature review. As a result, 228 vehicle-related LCA publications could be identified, which highlights the importance of LCA for this application [6]. This is further emphasized by the fact that paragraph (50) in current CO_2 emission regulation recognizes the importance of considering vehicle life cycle emissions [2, p. 9].

In the area of life cycle assessment, a large variety of approaches can be found. Apart from purely environmental considerations, this includes extensions towards sustainability. Another research field deals with the combination of LCA with vehicle development methodologies. This work follows such an approach by the example of hybrid electric vehicles (HEVs), which cannot be charged externally.

To this end, methodological background information is provided in section 2, including a brief overview of existing approaches in literature. Subsequently, the development environment proposed for this work is presented in section 3. This entails the toolchain, assumptions for LCA and vehicle simulation as well as use cases. In section 4, the results of the simulations are shown, followed by a discussion of methodological observations. Finally, section 5 concludes this paper with a summary and outlook.

2. Methodological background and state of the art

In the following, an overview of requirements and methods regarding vehicle development and life cycle-based evaluation is given, including the involved metrics.

2.1 Established requirements and tools in vehicle development

In the past, vehicle and powertrain developers have focused on the optimization of certain technical properties. These criteria include fuel consumption, pollutant emissions and driving comfort as well as cost-efficient solutions. This requires suitable tools and development methodologies.

In Anselma, Belingardi 2019 [7], an overview of past, current and future design tools in HEV powertrain design is provided. Apart from a temporal classification of HEV development activities into three eras, the authors identify limitations of existing design methodologies. These can be classified according to modelling approach, driving requirements, control strategy, design space and design disciplines. Some of these categories will be further discussed in the sections 3 and 4 with respect to the toolchain described in this work. Research challenges in HEV development are partly attributed to the lack of flexibility of existing automotive industry standards, such as the V model [7]. This approach will be further elaborated in the following paragraph.

Originally stemming from software development, the V model was incorporated into the VDI 2206 standard, which in its first edition from 2004 [8], provides a design methodology for mechatronic systems. Since its release, the standard has resulted in various applications in vehicle and powertrain development, as mentioned by Anselma, Belingardi 2019 [7]. According to the V model, the procedure entails the transformation of requirements into a system design, which is subsequently subdivided into subsystems and subfunctions, representing the left side of the V. At component level, domain-specific design ensues. Then, on the right side of the V, components, subsystems, etc. are subsequently integrated and validated, leading to the final product or an intermediate maturity level. In addition to the features and limitations mentioned by Anselma, Belingardi 2019 [7], the standard also mentions software- and hardware-in-the-loop solutions, which accompany the development process from virtual to physical components, ideally enabling a seamless integration of software and hardware [8]. Consequently, the renewed version of the VDI 2206 standard from 2021 further accounts for this virtualization trend, by adding "cyber-physical systems" to its name [9].

In general, the mentioned methodologies are aimed at yielding measurable and verifiable results, which can then be compared to legislative targets as well as customer needs, such as fuel consumption in liters of fuel per 100 km or a certain CO_2 and pollutant emission in grams per kilometer. However, the objectives traditionally refer mostly to "isolated" quantities during the usage phase of a vehicle. In this context, life cycle assessment can provide a broader view.

2.2 Life cycle assessment

As opposed to the current tank-to-wheel approach in passenger car energy demand and emission measurement, life cycle assessment (LCA) accounts for the environmental impact of the entire vehicle life cycle, including the energy carrier upstream emissions as well as for the production and disposal of the vehicle. There are several methods revolving around the life cycle of products. This work is oriented towards the LCA methodology standardized in ISO 14040 and 14044 [10, 11], which results in certain methodological implications, see section 2.3 and 3.2.

In Figure 3, the LCA framework is displayed according to ISO 14044. Four main phases can be identified. In the goal and scope definition phase (1), the boundary conditions of the LCA study are determined. Afterwards, the life cycle inventory (LCI) analysis (2) is performed, which mainly includes data acquisition and calculation. As a result, the practitioner receives a list of emissions, materials, products, etc., which are generated during the product life. In the following life cycle impact assessment (LCIA) phase (3)[1], the environmental impact is calculated based on the LCI results and an impact assessment method, which in turn includes impact categories. The most commonly used category, the global warming potential (GWP), summarizes all GHG emissions according to their individual impact in a certain period of time. Exemplarily, the GWP100 evaluates the GWP over 100 years, expressed in CO_2 equivalent emissions (CO_{2eq}). Finally, the results are subjected to an interpretation (4), which involves several checks, e.g., for completeness and sensitivity. As a result, conclusions, limitations and recommendations are drawn [10, 11].
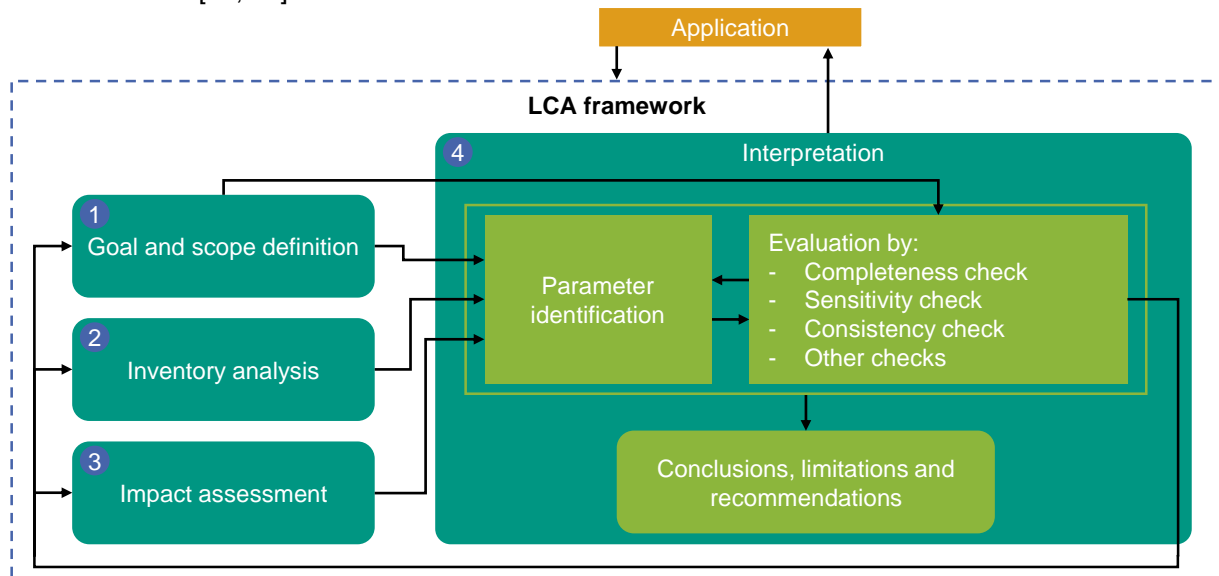
Figure 3. Life cycle assessment framework, including the four phases of LCA, remodeled after ISO 14044 [11]

LCA implies an iterative approach, which is indicated in Figure 3 via several arrows. Exemplarily, this applies if initially formulated goals (phase 1) cannot be met due to insufficient data availability (phase 2). Moreover, it has to be noted, that LCA studies require a great extent of transparency, as the chosen assumptions can heavily influence the results. Partly, this challenge can be covered with the aforementioned sensitivity check. In the context of publications, at least in research journals, LCA papers are usually provided with extensive supplementary material. This includes all assumptions, LCIA results as well as preferably LCI data. The latter information, however, can sometimes not be published for reasons of data protection.

In contrast to the "isolated" target values stated in the previous section 2.1, LCA is directed towards entire environmental categories. As indicated in the CO_2 and GHG figure in section 1, this aspect urges authors and readers to bring to mind the difference between CO_2, GHG and CO_{2eq} emissions.

Moreover, LCA introduces further metrics, for instance to evaluate water depletion, natural land transformation or human toxicity potential.

According to the standards, the normalization, grouping and weighting of several impact category results is considered optional. This is mainly due to the possible oversimplification in comparisons of different product types. If the products exhibit large differences, e.g., in case of battery electric vehicles (BEVs) and conventional cars, a critical review is required [10, 11].

---

[1] So-called LCI studies exclude the LCIA phase, which is why the terms LCI study, LCA study and the LCI phase need to be differentiated carefully.

Despite the explanations and guidelines included in the mentioned ISO standards, LCA remains a challenging methodology, particularly with regard to consistency and robustness as well as comparability between studies. For this reason, several initiatives deal with the improvement of LCA. Hereby, the International Reference Life Cycle Data System (ILCD) Handbook, including its guideline document, can be named [12]. It aims at the mentioned aspects in the context of "Sustainable Consumption and Production" policies, but does not provide specific guidance.

At this point, further guidelines are positioned, for instance the recommendations developed within the project eLCAr, short for "E-Mobility Life Cycle Assessment Recommendations". Hereby, the focus is laid on LCA of BEVs as well as serial plug-in hybrid electric vehicles [13]. Despite initially not intended for the use with other forms of HEVs, the proposed development environment (section 3) refers to certain elements introduced in the eLCAr guideline. These include that the systematic subdivision of vehicles into glider and powertrain is further detailed. Hereby, the powertrain is split up into the subsystems ICE, transmission, electric machine/motor, battery, power electronics and charger. In case of HEVs without plug-in functionality, the charger subsystem is not present. Still, the similar, more consistent setup might help in comparison with BEVs and serial PHEVs. Another concept utilized in the eLCAr guideline is the common parameter platform (CPP). This term mainly refers to the parameters, that are required for vehicle modeling. In case of technical LCA investigations, this might not only imply the powertrain characteristics, such as power or gearbox type, but also vehicle dimensions and aerodynamic parameters.

2.3 Related evaluation methods

As implied at the beginning of this section and in the previous subsection, there are several further approaches in the context of vehicle development and life cycle-based evaluation.

For specific environmental categories, additional standards have been developed, such as ISO 14067 for the carbon footprint of products [14], or water footprint in ISO 14046 [15]. Similar to the ILCD Handbook and the eLCAr guidelines mentioned in the section before, both standards expand the existing LCA standards.

In the aforementioned, updated VDI 2206:2021-11 standard [9], life cycle assessment is listed as a main feature for organizations in the development of mechatronic and cyber-physical systems. This further underlines the increased importance of LCA. In this case, LCA represents the only subcategory of sustainability, while ecology and economy are ascribed to "social acceptance". Other definitions of the term sustainability include all three mentioned aspects. Following this concept, Klöpffer, Grahl 2014 [16] describe life cycle sustainability assessment (LCSA) as the sum of LCA, life cycle costing (LCC) and social LCA. As the term life cycle assessment does not explicitly include a reference to environment, some authors also refer to it as environmental LCA (ELCA), such as in Reuter 2016 [17].

In the context of environmentally aware design and development, several publications can be identified. In Abele et al. 2005 [18], the authors describe the results of the Collaborative Research Center 392 project called "Design for Environment – Methods and Tools". Hereby, a product development methodology was generated, which considers both technical, economic and environmental aspects. This way, designers, developers and engineers are enabled to evaluate the eco-friendliness of products before the production start. Similar elements can be found in the ISO/TR 14062 technical report on the integration of environmental aspects in design and development [19]. In Broch et al. 2015 [20], an example of the integration of LCA into company-specific processes can be found. Hereby, LCA is used as a life cycle management tool to identify ecological hotspots. Within this approach, also called life cycle engineering, improvements can be derived, evaluated and transformed into innovations. The authors employ one commonly used example for possibly shifted environmental burdens between production and usage phase, the effect of lightweight measures on the vehicle life cycle emissions. In the related dissertation, Broch 2017 [21] further elaborates, how LCA can be integrated into vehicle development.

The previous paragraph served to give a short overview of company-wide implementations of LCA, which cover a broad area. In comparison, this work aims at a more specific topic, which is the combination of powertrain engineering and LCA. The next section provides insight into such approaches.

2.4 Combination of powertrain engineering and environmental assessments

This section provides a short literature review about publications, which have a closer look at the interaction of life cycle metrics with technical details. This can also be denoted as technical LCA, or TLCA, a term that was used by Ryding in 1994 [22]. In a previous publication, the authors provided literature on the subjects sustainability and LCA in the automotive industry, common LCA applications, as well as application-specific usage, see Toedter, Weber et al. 2021 [23].

In order to facilitate the understanding and comparison of the approaches researched for this publication, a brief insight into existing LCA databases and software is given. In Wang, Tang 2022 [24], the authors review the state of the art of life cycle-based environmental efficiency evaluations.

Hereby, the authors focus on new energy vehicles, denoted "ideal vehicles approaching zero pollution and zero emissions…" [24, p. 1]. Based on a research of LCA-related publications available in Web of Science, the authors identified and categorized 282 studies. The GREET model ranks at the top of the software/database list with 62 appearances. GREET, short for "Greenhouse gases, Regulated Emissions, and Energy use in Technologies", is developed by the Argonne National Laboratory. Used in 52 publications, the LCA database ecoinvent reaches the second place. The extensive ecoinvent database is also used in this work, as well as the open source LCA software openLCA, which was used in 5 publications considered in [24]. It has to be noted that 100 publications apparently do not include information on the employed LCA tool. Moreover, the authors also investigated the choice of "evaluation scales", a term which is not further defined, and seemingly mixes up methodologies, tools and impact assessment methods. To our knowledge, the top-ranked "ISO 14040/ISO14044" refers to the standards, while the following "Recipe", "CML" and "IPCC" actually represent impact assessment methods, that include different impact categories. The largest proportion of publications does not include detailed information on "evaluation scales", which shows a similar lack of information as in the software selection category.

Within a literature review conducted for this work, several publications could be identified, which combine a powertrain simulation with LCA, see Table 1.

Table 1. Overview of TLCA literature regarding LCA restrictions, application towards HEVs and modeling approach

Publication	Impact assessment method / category (environmental / cost & social) metric (if not full LCA)	Inclusion of ICE HEVs	Modeling tools / approaches	
			Technical	Environmental
Ahmadi et al. 2017 [25]	GHG, cost	No	"In-house tool" / driving resistances	"In-house tool"
Bauer et al. 2015 [26]	IPCC (GWP 100a), ReCiPe (PMFP, HTP, POFP, TAP)	HEV-g, HEV-d, HEV-cng	ADVISOR / propulsion + auxiliary loads in driving cycles	ecoinvent
Benajes et al. 2020 [27]	CO$_2$, GHG-100, (CO, NO$_x$, soot) TTW	(MHEV, FHEV, PHEV)-dual-fuel	GT-SUITE / detailed powertrain modeling	GREET
Bouter et al. 2020 [28]	ILCD 2011 (CC, OD, PM, IR-HH, POF, Ac, Eu-terr./aq., RD)	MHEV-g, HEV-g, PHEV-g	Existing values for different cycles	ecoinvent, SimaPro
Cox et al. 2020 [29]	IPCC (CC, GWP 100a), ReCiPe (CED, HTP, MDP, PMFP, POFP), TCO	HEV-g, PHEV-g	Python / Monte Carlo for statistical relevance	ecoinvent
Del Pero et al. 2018 [30]	ILCD 2011 (CC, PMP, HT, POFP, AP, RDP)	No	AMESim / driving cycles	GaBi
Frambach et al. 2022 [31]	GHG	HEV-g, PHEV-g	MATLAB / operation strategy: DP, ECMS, RDE profiles	Weight-based approach [32, 6]
García et al. 2020 [33]	CO$_2$, GWP-100, (CO, NO$_x$, soot) TTW	HEV (dual fuel with ethanol, H$_2$, diesel)	GT-SUITE / detailed powertrain modeling	GREET
Meywerk et al. 2018 [34]	CO$_2$	No	Not specified / mainly efficiency factor-based	No LCA tool, but various sources for CO$_2$
Orbaiz et al. 2018 [35]	CO$_{2eq}$, TCO	HEV-d (bus)	AUTONOMIE / driving cycles	GREET
Raykin et al. 2012 [36]	(Total energy, fossil energy, GHG) WTW	HEV-g, PHEV-g	TTW efficiency models for Greater Toronto Area	GREET
Schwarz 2018-2019 [37–39]	GWP100, eutrophication, acidification, summer smog, cost, social aspects	HEV-d/g/cng	MATLAB/Simulink / lap time-optimized race cars	GaBi
Syré et al. 2020 [40]	ReCiPe (GWP100, AP, EP, POFP, PMFP, MDP)	No	MATSim Open Berlin Scenario	ecoinvent
Ternel et al. 2021 [41]	IPCC (GWP 100a)	HEV-g, PHEV-g	AMESim / WLTP + NEDC	ecoinvent, SimaPro
Toedter et al. 2020-2021 [42, 43]	ILCD 2.0 (GWP100)	No	CarMaker / map-based simulation	ecoinvent, openLCA

The publications listed in Table 1 are evaluated regarding the used impact assessment methods (including the chosen metrics), the employed technical and environmental tools and approaches, and whether HEVs with internal combustion engines are assessed.

The GREET model represents the most widely used tool for environmental assessment in this overview, which matches the observations of the previously discussed meta study. Owing to the prevalence of GREET, several aspects are further elaborated. Regarding system boundaries, Wang, Tang 2022 state that GREET was specifically used for tank-to-wheel investigations, a statement which seemingly indicates that vehicle production and disposal are neglected [24, p. 11]. On the contrary, the ANL homepage reports that GREET considers the entire life cycle [44]. Considering TLCA publications, we identified four publications, which employed the GREET model [36, 35, 27, 33]. Only one publication, by Raykin et al. 2012 [36], does not include vehicle production and disposal. In another publication by Ternel et al. 2021 [41], the authors specifically decided against using GREET, as it mainly includes US data, which did not meet the explicitly formulated scope of modeling passenger cars in France [41, p. 4]. In Table 1, the "Impact assessment method…" column illustrates that GREET publications (highlighted in green) mainly focus on life cycle CO_{2eq} emissions as well as tank-to-wheel pollutant emissions. Compared to publications using the widespread ecoinvent database, this leaves out further environmental impact categories, such as ozone depletion (OD) and particulate matter (PM).

With regard to technical modeling, several similarities and differences can be identified. Usually, vehicle simulations include at least a model for driving resistances, in order to estimate the required amount of mechanical energy. Hereby, both commercial as well as "in-house" tools are used. Methodically, the publications can be differentiated in terms of technical level of detail, both in relation to categorization of powertrain technology and modeling depth. Considering the first aspect, some publications merely generally state that HEVs are regarded, while other publications exactly specify technical details, such as hybridization degree, topology and operating modes. Secondly, some publications use map-based models as opposed to more sophisticated powertrain models. Both aspects are covered in detail by [27, 31, 33]. The methodology presented in this work aims at a similar approach, which will be further explained in the following section.

3. Proposed development environment

In the last subsection, the challenges of TLCA have been indicated, including several approaches in literature. In this context, the authors identify the need for a development environment, which satisfies certain requirements:

- LCA:
  - o Technical description of vehicle on a system, but also subsystem and component level
  - o Extended LCA metrics, which do not only consider GHG emissions, but also further impact categories
- Vehicle/powertrain energy demand simulation:
  - o Capability to evaluate influencing factors, such as vehicle mass, driving pattern, etc.
  - o Flexibility towards more detailed powertrain models

In this work, the authors extend an approach presented in two previous publications [42, 23] towards hybrid electric vehicles. In the next subsections, an overview of the toolchain is given and the assumptions for this work are displayed, including the considered use cases.

3.1 Toolchain overview

The toolchain used for this work involves a vehicle/powertrain simulation tool as well as an LCA software and an LCA background database. At the moment, pre- and postprocessing is still mostly conducted manually. Apart from the analysis of results, this mainly involves data collection, which is further described in 3.2.2.

3.1.1 Vehicle/powertrain simulation

For vehicle and powertrain simulation, the software **CarMaker 10.2.1** by IPG Automotive is used. The tool was chosen, as it includes a multitude of submodels regarding vehicle dynamics, driver behavior, environment, powertrain, suspension, tires, etc. Existing basic, mostly map-based models can be parameterized rapidly and investigated in various test scenarios.

Moreover, existing models can be replaced by more detailed implementations in commonly used tools, such as GT-SUITE, MATLAB/Simulink, etc. As the software is also available for test beds, it can also be used to transfer office simulations towards hardware-in-the-loop test benches (see section 2.1).

This includes proprietary, as well as standardized interfaces, such as the Functional Mock-Up Interface[2] or the Distributed Co-Simulation Protocol[3].

Within the scope of this work, the most basic approach was chosen, i.e., the selection of several powertrain topologies supplied by CarMaker, including a rule-based operating strategy, which relies on boundary conditions, such as the battery state of charge (SOC). Fuel consumption was considered by a mere fuel consumption map, which is based on engine measurements at IFKM. Through a graphical user interface, additional loads, i.e. masses of hybrid components, such as a HV battery, can be positioned. This helps to rapidly realize different powertrains, while keeping glider mass constant.

3.1.2 Life cycle assessment

For life cycle assessment, the authors employ the aforementioned **ecoinvent v3.7.1** database in conjunction with the open source LCA tool **openLCA 1.11.0**. In the used ecoinvent background database, extensive information is included regarding energy sources, such as technology- and country-specific electricity and fuel production pathways, common materials and production techniques as well as some end products, e.g., the so-called vehicle glider.

Hereby, a mass-based bottom-up modeling approach is followed. Components are modeled by means of information about mass, material composition and ideally manufacturing processes. These components are then grouped to form subsystems, which finally result in the entire powertrain. With each integration step, a resulting mass is calculated[4]. On the basis of the curb weight and the powertrain mass, the mass of the remaining vehicle components, summarized as "glider", is determined. Through the combination of flows and processes in openLCA, the authors achieve a certain modularity. One specific flow, e.g., "transmission", can be provided by different processes, e.g., "manual transmission" and "dual-clutch transmission". Further information regarding the LCA modeling process, the authors of this work employ, can be found in [45].

3.2 Assumptions

The results of LCA studies are heavily influenced by the involved assumptions, which therefore need to be documented accurately. This mainly affects the first two phases of LCA, goal and scope definition (1) and life cycle inventory (2), which are further detailed in the following subsections.

3.2.1 Goal and scope definition

This section provides definitions of goal and scope according to ISO 14040/14044, see Table 2 and Table 3.

The goal definition (Table 2) mainly repeats some of the aspects mentioned before. The TLCA shown in this work specifically addresses engineers, which might be interested in the incorporation of LCA elements into their development activities. Although three different subtypes of powertrains are compared, this work mainly serves to illustrate the capability of this methodology and does not provide information for decision making.

Table 2. Goal definition of the LCA involved in this work

Intended application	Evaluation of differently hybridized vehicles with regard to their life cycle impact in various driving cycles
Reasons for carrying out the study	Combined technical and environmental assessment of hybridization in a TLCA
Intended audience	Developers in vehicle and powertrain engineering
Use in comparative assertions disclosed to the public	Mostly for illustration purposes of the methodology

In Table 3, the elements of the defined scope are listed. This includes the considered vehicle and powertrain configurations. The results are scaled to the functional unit of one vehicle kilometer[5].

---

[2] https://fmi-standard.org/

[3] https://dcp-standard.org/

[4] One example of this integration process would be: throttle actuator > air system > internal combustion engine > powertrain.

[5] In LCA studies dealing the transport of passengers, the environmental impact can be referenced both to a vehicle kilometer and a passenger kilometer. The latter metric is used, if different transport means, such as PC and buses, are compared with each other. This is not the case in this study.

In this case, two hybridization degrees, mild and full hybridization, are considered. Despite their increasing popularity, BEV and PHEV are not considered in this work, as they involve a great number of additional assumptions, which might overload this paper. Particularly, this refers to the electric driving energy. Moreover, homologation and actual use cases might differ greatly, e.g., in case of PHEVs.

The system boundary includes both vehicle production and usage including energy carrier provision. The third LCA phase, LCIA, is conducted with the ReCiPe midpoint (H) impact assessment method, which provides several impact categories, including the global warming potential over 100 years, GWP100.

Based on manufacturer bills of materials, the vehicle powertrains are modeled down to component level. Some information on the electric part of the hybrid powertrains was gathered from publications on battery electric vehicles. In default of more recent data, the glider was modeled through an existing ecoinvent dataset, which is based on the fourth generation VW Golf [46]. Further information on the technical details of the vehicles, including LCI data sources are provided in the next section.

Table 3. Scope definition of the LCA involved in this work

Product systems	ICEV-g MT, MHEV-g P1-MT, FHEV-g P2-DCT, no vehicles with plug-in charging capability (BEV, PHEV)
Functions of the product systems	Transportation of passengers
Functional unit	Vehicle kilometer
System boundary	All life cycle phases, including vehicle production raw materials and source of energy carriers, end of life of glider and internal combustion engine
Allocation procedures	According to ecoinvent database
Impact assessment method and categories	ReCiPe 2016 Midpoint (H) [47]: GWP100, SOP, etc.
Data requirements	Contemporary vehicle technology, including bills of materials from manufacturers
Assumptions	Consideration of FHEV technology without an exact corresponding vehicle model in the market, see section 3.2.2
Limitations	ecoinvent data set for glider, electric powertrain LCA data, partly dating back a few years, stemming from a BEV
Initial data quality requirements	Mass-based description of powertrain components
Type of review	Conference paper submission review, but no critical review according to ISO 14040/14044
Type and format of the study report	Conference paper, followed by a presentation

3.2.2 Life cycle inventory and further technical information

As mentioned in section 2.2, concepts of the eLCAr project [13] were utilized, such as the common parameter platform (CPP). In Table 4, the CPP for the vehicles considered in this study is displayed.

Table 4. Common parameter platform of the considered vehicles (abbreviations see[6])

Powertrain configuration	ICEV-g MT	MHEV-g P1-MT	FHEV-g P2-DCT
Reference vehicle	Ford Focus		
Curb weight in kg	1,330	1,349	1,421
Vehicle dimensions in mm	4,382 / 1,825 / 1,425; 2,700; 1,572; 1553; 769 (vehicle length / width / height; wheel base; track width; rear overhang)		
Tire parameters	205 / 60 / 16		
Drag coefficient	0.273		
Cross section in m^2	2.226		
ICE power in kW	92		
Gearbox	6-speed MT		7-speed DCT
EM power in kW (technology, voltage)	2 (starter motor, 12 V)	11.5 (BISG, PMSM, 48 V)	30 [48, 49] (Gearbox-integrated, PMSM, 400 V)
HV battery capacity in kWh (technology)	-	0.384 (Li-ion, NMC111 [50])	2 (Li-ion, NMC111 [50])
Power electronics	-	ecoinvent	[51, 52]
Tank volume in l	52		

---

[6] BISG = Belt integrated starter generator, PMSM = permanent-magnet synchronous motor

Three different gasoline-powered vehicles are considered: a conventional vehicle with manual transmission (ICEV-g MT), a P1 mild hybrid with manual transmission (MHEV-g P1-MT) and a P2 full hybrid electric vehicle with a dual clutch transmission (FHEV-g P2-DCT).

The small (MHEV) and the large (FHEV) battery are assumed to have the same component proportions, i.e., the share of cells, battery management system, packaging, etc. remains constant. Thus, the battery capacity linearly affects the mass of the entire battery and its components.

The first two models are based on existing Ford Focus passenger cars, while the data for the FHEV was approximated through several assumptions, which are shortly described in the following.

For the modeled vehicles, the same glider mass was assumed. In order to estimate the FHEV mass, additional masses for the DCT and the electric powertrain need to be estimated, see Table 5.

Table 5. Additional assumptions for FHEV modeling

Component	Assumption	Mass in kg
Dual-clutch transmission	Based on curb weight difference of Ford Focus MHEV-g models with manual and dual-clutch transmission	38
Battery	2 kWh, energy density according to [50]	19
Electric machine	30 kW, based on scalable LCI [48, 49]	17.6
Power electronics	Matching EM power, based on scalable LCI [51, 52]	8.4
Cables	Based on in-house data for PHEV vehicles	7.5

Owing to the different hybridization degrees and powertrain topologies, the vehicles provide diverse operation modes, which affect the overall powertrain operation strategy, see Table 6.

Table 6. Overview of operation modes of the considered vehicles

Powertrain configuration	ICEV-g MT	MHEV-g P1-MT	FHEV-g P2-DCT
ICE			
Start/Stop			
Recuperation, load point shift, boosting, coasting			
Electric driving			

To obtain application-specific fuel consumption values, the vehicles are operated according to several test cycles, including WLTC, NEDC, NYCC, as well as an RDE track around Karlsruhe.

4. Results and discussion

In the following, the results of the TLCA simulations are shown. Hereby, several aspects are discussed, starting with a brief comparison of the fuel consumption calculations. Subsequently, these results are used as an input for LCA evaluation.

In Figure 4, the results of the vehicle simulation conducted with CarMaker are shown. On the left side, the fuel consumption of the three vehicles is plotted according to the NEDC, NYCC, RDE and WLTC test cycles. The conventional vehicle exhibits the largest fuel consumption, regardless of the testing scenario. The strongest hybridization (FHEV-g) shows the best fuel economy potential despite its increased curb weight. However, it has to be noted that the strikingly low NYCC result does not include electric energy, which was additionally used in this particular case. This might be explained by the short duration and low-speed profile of the NYCC cycle, which favors electric driving. In this case, the battery was depleted by 10 % starting from 70 %.

In the other cycles, both HEVs maintained their target SOC. In order to quantify the effect of SOC, both HEVs were operated in a WLTC at different starting and target SOC values, which can be found on the right side in Figure 4. Both in charge-sustaining mode ($SOC_{start} = SOC_{end} = 70 \%$) as well as in charge-depleting mode ($SOC_{start} = 90 \%$, $SOC_{end} = 30 \%$), full hybridization is favorable.

It should be noted that Figure 4 represents intermediate results, which are based on a first approach that employs built-in CarMaker submodels. Hereby, simplified map-based components and rule-based control algorithms are utilized, which require further optimization and tuning in the future. As the emphasis of this work is set particularly on methodology development, we still consider the simulation as valuable, because it allows to differentiate between different use cases, whose boundary conditions can be modified. Other approaches, which are based on fuel consumption measurement values only, cannot provide the same flexibility. Further improvements will involve more detailed submodels, which allow the consideration of more technical features.
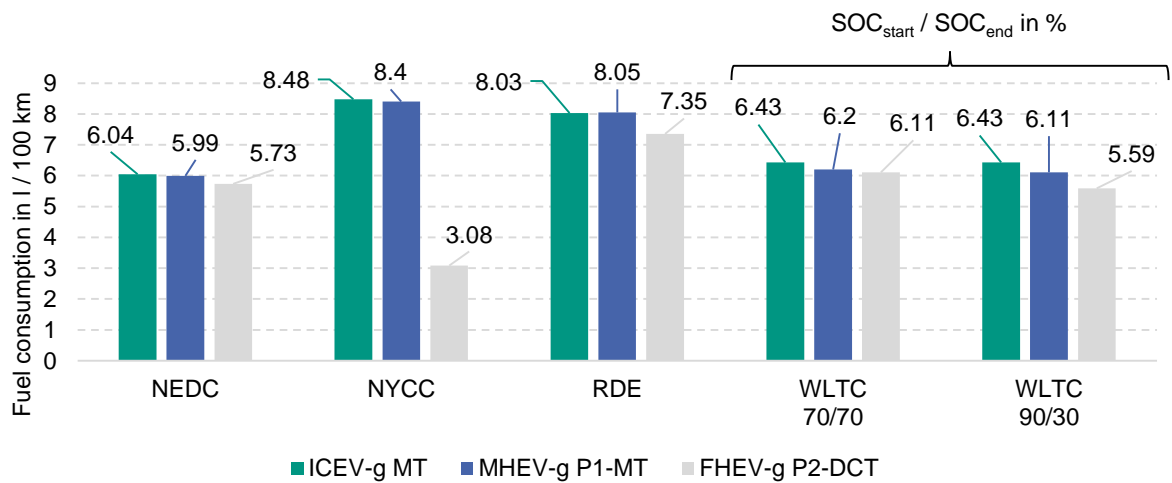
Figure 4. Fuel consumption in different driving cycles, including SOC sensitivity in WLTC

Figure 5 provides a first glimpse into the impact of hybridization on the interrelation of production and use phase. It can be seen, that the vehicles start with different production burdens, which increase with the hybridization degree. As in the considered WLTC and RDE use cases, fuel consumption improves with further electrification, the lines eventually intersect. Owing to the little differences in fuel consumption in the WLTC 70/70 test case, the MHEV still remains the best powertrain option at 200,000 km by a slight margin. If the vehicles are operated according to an RDE scenario, the additional fuel savings potential of full hybridization overcompensates the production burden of FHEVs compared to ICEVs and MHEVs. Consequently, FHEVs represent the most CO_{2eq}-efficient solution in this case. Generally, this shows the importance of the driving pattern assumptions.
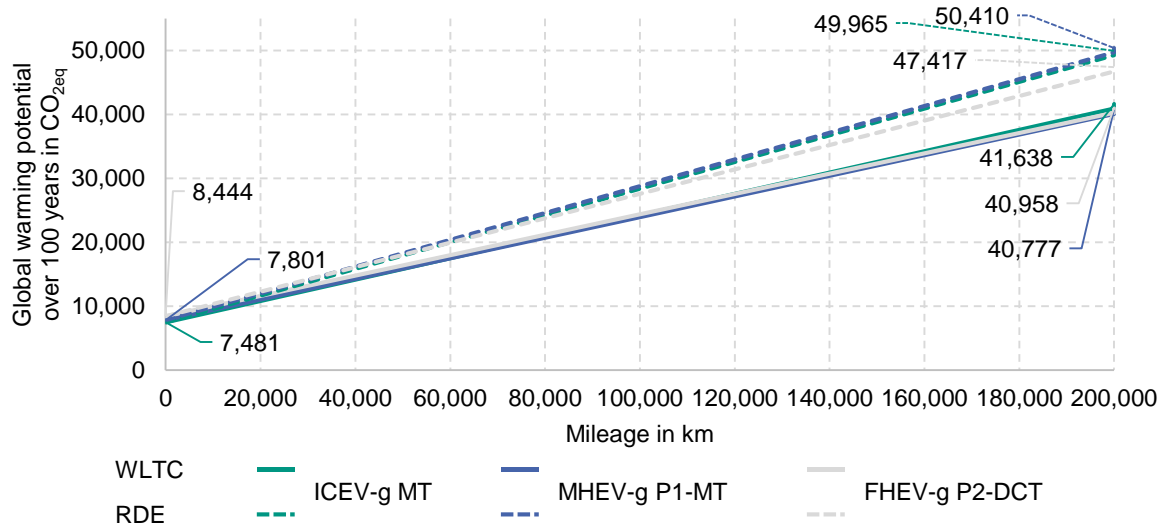
Figure 5. Development of global warming potential of the considered vehicles over mileage in a WLTC (solid lines) and an RDE (dashed lines) driving scenario

To further elaborate the effects of hybridization in an LCA context, the following results consider the WLTC 70/70 conditions. As the WLTC serves as a testing cycle in the EU, this provides a certain representativeness and reproducibility.

In Figure 6, the GWP100 results are plotted for the entire vehicle life over 200,000 km. On the left axis, the absolute values of GWP100 are displayed. Firstly, the results are divided into production, usage and disposal.

Typically for vehicles powered by ICEs with fossil fuels, the usage phase dominates the life cycle, while disposal is almost negligible. Secondly, the results are further split up into subcategories, i.e., glider and powertrain for the production phase. Owing to the large mass difference, the glider contributes the majority of production emissions. The usage phase is subdivided into fuel production and conversion into locally emitted CO_2, maintenance and pollutants. This aspect is dominated by indirect CO_{2eq} (WTT) and direct CO_2 (TTW) emissions caused by the fuel production and combustion.

Maintenance and particularly pollutants (via the GHG CH₄) only make little contribution. In line with the functional unit defined before, the results are also referred to the mileage, which yields the CO_{2eq} emissions per kilometer.

Hereby, the usage part attains values of up to 167 g CO_2/km. Compared to the mentioned emission targets, this seems relatively high. However, one has to consider that in contrast to legislation, the displayed metric additionally includes WTT fuel emissions, maintenance and the effect of pollutants.
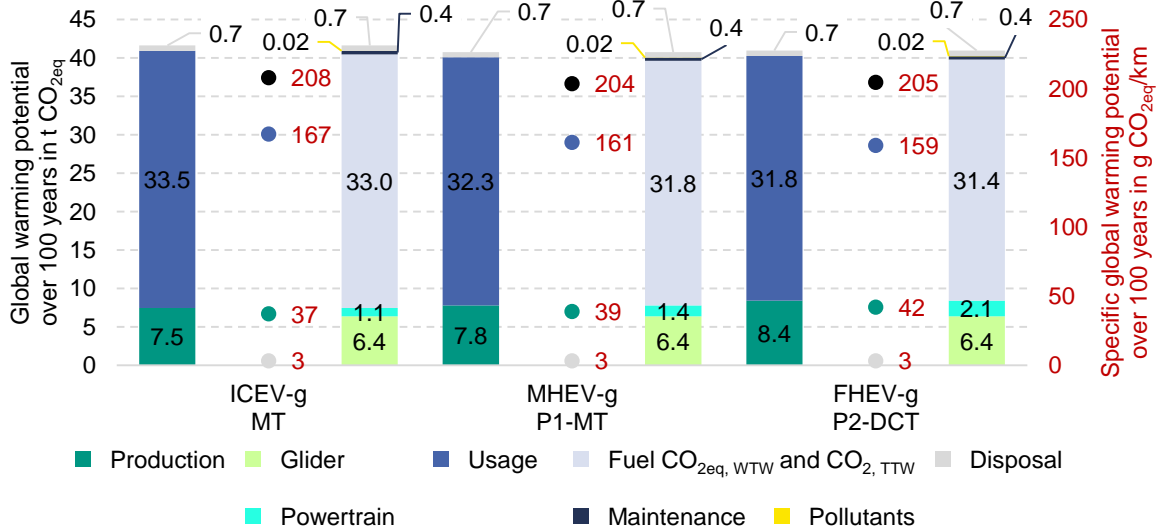
Figure 6. GWP100 of the considered vehicles, divided into categories and results referred to the functional unit (vehicle kilometer) at 200,000 km driven in WLTC

In Figure 7, the production effect of electrifying a conventional vehicle is further detailed. Starting with an overview of the GWP100 of the ICEV-g powertrain on the left side, the other two bars show the emissions that are involved by adding HEV components. Particularly in case of the strongest hybridization, the FHEV-g P2-DCT vehicle, the added GHG burden ranges in the same magnitude as the GWP100 of the conventional powertrain. About half of this impact can be attributed to the battery, but also the electric machine, which both operate at 400 V.
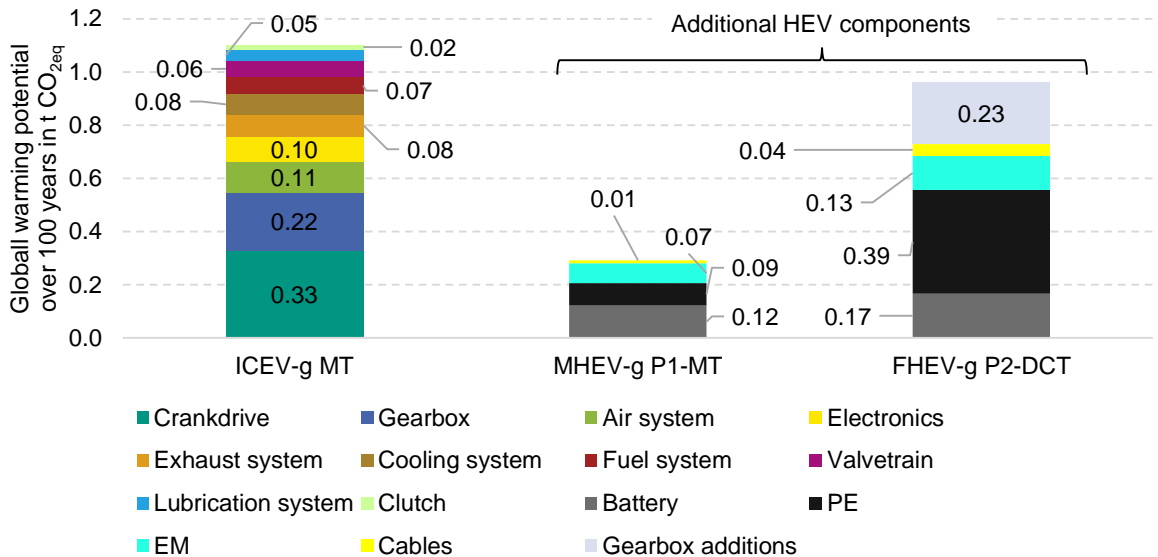
Figure 7. GWP100 results for the conventional powertrain and the additional HEV components

Finally, the assessment within this work is concluded with further life cycle impact categories, see Figure 8. In order to facilitate an overview, a compact normalized depiction has been chosen. To this end, the HEV results were put in reference to the ICEV-g model results. The chart shows only slight differences in some of the categories, including GWP100. Still, other categories deviate around 20 % up to 30 %.

Exemplarily, mineral resource scarcity, which is abbreviated as SOP, is significantly larger in case of the FHEV-g. This can be partly explained by the utilization of rare earth minerals, such as neodymium and dysprosium, in the electric machine. Due to the working principle of the machine, the elements are used as permanent magnets. This shows that despite possible benefits regarding GHG emissions, technology shifts can also imply certain downsides.
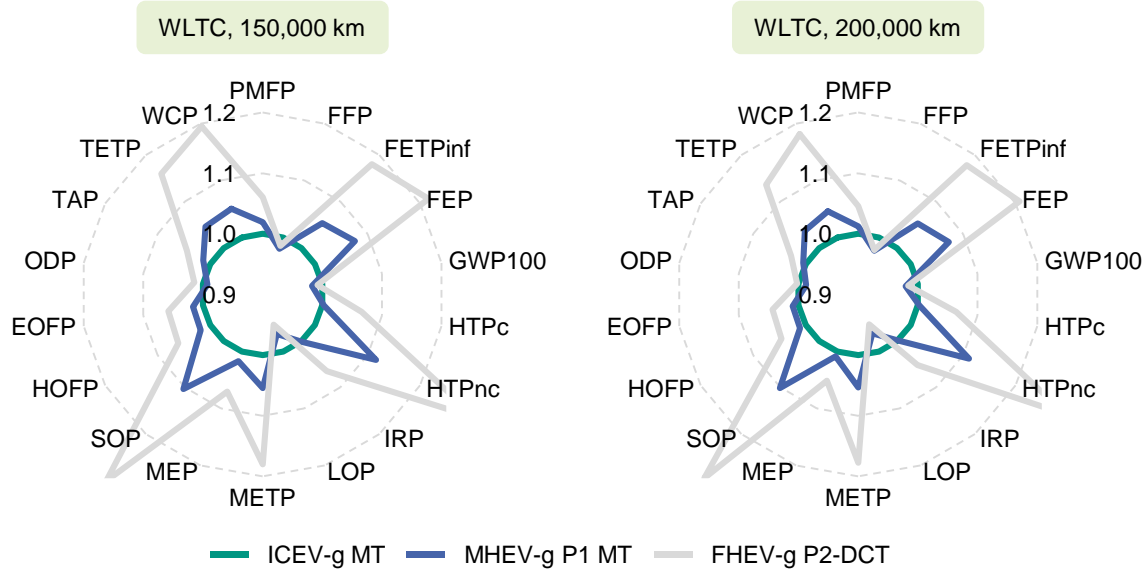
Figure 8. Results for all impact categories included in the ReCiPe 2016 (H) midpoint method, assuming WLTC operation for 150,000 km and 200,000 km, normalized to the respective ICEV-g MT results for improved overview; Abbreviations (P = potential): PMFP = fine particulate matter, FFP = fossil resource scarcity, FETPinf = freshwater ecotoxicity, FEP = freshwater eutrophication, GWP100 = global warming, HTPc = human carcinogenic toxicity, HTPnc = human non-carcinogenic toxicity, IRP = ionizing radiation, LOP = land use, METP = marine ecotoxicity, MEP = marine eutrophication, SOP = mineral resource scarcity, HOFP = ozone formation (human health), EOFP = ozone formation (terrestrial ecosystems), ODP = stratospheric ozone depletion, TAP = terrestrial acidification, TETP = terrestrial ecotoxicity, WCP = water consumption

5. Conclusions

5.1 Summary

Within this work, the need for life cycle-based, technical evaluations of vehicles was discussed. In this context, an overview of relevant publications was given. This includes both standardized methodologies, such as the ISO 14040/14044 LCA standards, as well as resulting advanced guidelines and approaches. Hereby, the term technical LCA (TLCA) was addressed in a literature review. As a result, the prevalence of the tool GREET could be identified. While the GREET model considers the full life cycle regarding CO_2, GHG-100 and several pollutant emissions, it does not provide further impact categories, known from common LCA tools. The authors considered this aspect as a research gap in TLCA.

For this reason, a development environment was presented, which aims at describing vehicles realistically both in an LCA and a vehicle dynamics software. By the example of hybridization, the capability of the introduced toolchain was showcased. Based on detailed LCA powertrain models and a map-based powertrain modeling approach, the interaction of vehicle production and technical properties during operation could be demonstrated. Apart from a conventional vehicle (ICEV), a mild and full hybrid electric vehicle were considered, all equipped with a gasoline engine. Hereby, several aspects were elaborated, such as the influence of the SOC on fuel consumption, the vehicle emissions over a certain mileage, the individual impact of added hybridization components as well as a holistic view on all available environmental impact categories.

The vehicle dynamics simulations showed a significant influence of driving patterns on fuel consumption. Exemplarily, the considered full hybridization yields 5 % and 8.5 % in fuel savings compared to the conventional vehicle in a WLTC and an RDE scenario, respectively. In the following, these consumption values were used as an input for the usage phase of the vehicle life cycle. Over a mileage of 200,000 km, the seemingly low relative difference between WLTC and RDE yields two outcomes: in case of the WLTC, the FHEV only ranks second in GWP100. Hereby, the additional production CO_{2eq} emissions could not be compensated in the usage phase in comparison with the less hybridized MHEV-g. When other use cases are applied, this trend might change. When the RDE scenario is considered, the FHEV

achieves the best global warming potential over its lifetime, due to the improved fuel savings potential in that application.

After highlighting the effect of use case on overall life cycle CO_{2eq} emissions, including resulting "break-even points", the three life cycle phases (production, usage, disposal) were further elaborated. In case of the ICEV, the usage phase contributes about 80 % to the overall CO2eq emissions of 41 t CO_{2eq}. Both HEVs report slightly lower total emissions as well as reduced percentages of the use phase of about 79 % (MHEV) and 77 % (FHEV). Within the ICEV usage phase, fuel production and combustion contribute the largest share by far, while maintenance and pollutants only account for 1.2 % and 0.05 % of the CO_{2eq} emissions, respectively. This trend also applies for the MHEV and FHEV. As a conclusion, this underlines the enormous GHG reduction potential of renewable fuels.

This work also covered the composition of vehicle production in more detail. Hereby, the production of the conventional powertrain contributes only 14.7 % to the overall vehicle, with the rest being ascribed to the glider. This highlights the importance of considering the correct vehicle segment, as it not only affects the powertrain, but also the glider mass to a large extent. With the constant glider mass along all three vehicles, both hybridizations result in an increased powertrain mass share, i.e., 17.9 % and 24.7 % for MHEV and FHEV. In terms of GHG emissions, the full hybridization causes about twice the amount of CO_{2eq} compared to the conventional powertrain.

Lastly, the effect of hybridization on other environmental impacts was discussed shortly by means of spider graphs, based on a WLTC operation over 150,000 km and 200,000 km. Hereby, 18 impact categories were displayed. Despite advantages regarding GWP100, both MHEV and FHEV might cause additional environmental damages compared to the ICEV. Exemplarily, the mineral resource scarcity (SOP) indicator increases about 30 % in case of the FHEV, which can be attributed to the utilization of rare earth minerals.

At least with regard to the calculations performed in this work, the strongest hybridization does not necessarily result in the lowest CO_{2eq} emissions. Apart from the use case, this can be explained by the relatively low fuel savings potential achieved in this work. Other publications, such as the mentioned paper by Frambach et al. 2022 [31], reports a higher fuel economy for 48 V HEVs of up to 23 %. However, it has to be noted that the cited publication also includes a rather large real-driving use case database. Moreover, the authors performed numerous dimensioning variations in order to find an optimized hybrid system, including the implementation of several energy management strategies. By contrast, the vehicle models used for this work, are built mainly on the basis of existing vehicles and rather simple subsystem models. Still, this work allows for a holistic assessment of individual technical features up to entire hybridization concepts. To conclude, the simulation showed the large variety of influencing factors, which need to be considered, when conducting an LCA in conjunction with powertrain simulations.

5.2 Outlook

Owing to the flexibility of the toolchain, further improvements will be implemented in the future, particularly regarding the fuel consumption potential mentioned in the last paragraph. In this context, the use of renewable fuels will also be considered.

In general, it remains a challenge to model realistic behavior and guarantee a certain comparability at the same time, including data availability and validity. In the context of this work, this implies the update of data, such as battery technology, which continuously improved over the last years. Moreover, a further subdivision of the glider might be of interest. Firstly, this refers to the implementation of more current data. Secondly, this might be methodically useful, as some components, such as the wheels, are considered more thoroughly in the vehicle dynamics simulation.

Further development might include an increased level of detail and variety, both in LCA models and vehicle dynamics. This might imply additional nuances in hybridization. To this end, the integration of more sophisticated control models or physically motivated models might be helpful.

Apart from optimized HEV models, the toolchain should also be extended towards further powertrain technologies, such as PHEVs and BEVs. These powertrain types become increasingly important and can also help decrease the environmental impact, if optimized over the entire life cycle.

Finally, the presented toolchain can be enhanced towards increased automation, as the involved tools offer application interfaces, for instance in Python. Hereby, large parameter studies can be realized more easily.

6. References

[1]   EUROPEAN ENVIRONMENT AGENCY (EEA). National emissions reported to the UNFCCC and to the EU
       Greenhouse Gas Monitoring Mechanism. 31 May 2022, 12:00 [viewed 22 June 2022]. Available from:
       https://www.eea.europa.eu/data-and-maps/data/national-emissions-reported-to-the-unfccc-and-to-the-eu-
       greenhouse-gas-monitoring-mechanism-18.

[2]   EUROPEAN UNION. *Regulation (EU) 2019/631 of the European Parliament and of the Council of 17 April
       2019 setting CO2 emission performance standards for new passenger cars and for new light commercial
       vehicles, and repealing Regulations (EC) No 443/2009 and (EU) No 510/2011. Regulation (EU) 2019/631,*
       2019.

[3]   EUROPEAN COMMISSION. Communication from the Commission to the European Parliament, the Euro-
       pean Council, the Council, the European Economic and Social Committee and the Committee of the Re-
       gions. The European Green Deal. 11 December 2019, 12:00 [viewed 7 January 2020]. Available from:
       https://eur-lex.europa.eu/resource.html?uri=cellar:b828d165-1c22-11ea-8c1f-
       01aa75ed71a1.0002.02/DOC_1&format=PDF.

[4]   EUROPEAN ENVIRONMENT AGENCY (EEA). *CO2 performance of new passenger cars in Europe* [online].
       18 November 2021, 12:00 [viewed 22 April 2022]. Available from: https://www.eea.europa.eu/ims/co2-perfor-
       mance-of-new-passenger.

[5]   VOLKSWAGEN AG. Sustainability Report 2021. 2022 [viewed 22 April 2022]. Available from:
       https://www.volkswagenag.com/presence/nachhaltigkeit/documents/sustainability-report/2021/Nonfinan-
       cial_Report_2021_e.pdf.

[6]   HILL, Nikolas, Sofia AMARAL, Samantha MORGAN-PRICE, Tom NOKES, Judith BATES, Hinrich HELMS,
       Horst FEHRENBACH, Kirsten BIEMANN, Nabil ABDALLA, Julius JÖHRENS, Eloise COTTON, Lizzie
       GERMAN, Anisha HARRIS, Sebastien HAYE, Chris SIM, and Ausilio BAUEN. Determining the environmen-
       tal impacts of conventional and alternatively fuelled vehicles through LCA. Final report. 2020. Available from:
       https://op.europa.eu/de/publication-detail/-/publication/1f494180-bc0e-11ea-811c-01aa75ed71a1. Available
       from: 10.2834/91418.

[7]   ANSELMA, Pier Giuseppe, and Giovanni BELINGARDI. Next Generation HEV Powertrain Design Tools:
       Roadmap and Challenges. *SAE Technical Paper Series:* SAE International400 Commonwealth Drive, War-
       rendale, PA, United States, 2019.

[8]   Verein Deutscher Ingenieure e. V. (VDI e. V.). 2206:2004-06, *Design methodology for mechatronic systems.*
       Düsseldorf: Beuth.

[9]   Verein Deutscher Ingenieure e. V. (VDI e. V.). 2206:2021-11, *Development of mechatronic and cyber-physi-
       cal systems.* Düsseldorf: Beuth.

[10]   International Organization for Standardization (ISO). 14040:2009-11, *ISO 14040.* Berlin: Beuth.

[11]   International Organization for Standardization (ISO). 14044:2006-10, *ISO 14044.* Berlin: Beuth.

[12]   EUROPEAN COMMISSION AND JRC. International Reference Life Cycle Data System (ILCD) Handbook.
       General guide for Life Cycle Assessment - Detailed guidance, (First edition March 2010). 2010. Available
       from: 10.2788/38479.

[13]   DEL DUCE, Andrea, Patricia EGEDE, Gerlind ÖHLSCHLÄGER, Tina DETTMER, Hans-Jörg ALTHAUS,
       Thomas BÜTLER, and Eva SZCZECHOWICZ. eLCAr: Guidelines for the LCA of electric vehicles. 2013
       [viewed 21 November 2019]. Available from: http://www.elcar-project.eu/fileadmin/dokumente/Guideline_ver-
       sions/eLCAr_guidelines.pdf. Available from: 10.13140/RG.2.1.2782.8244.

[14]   Deutsches Institut für Normung e. V. (DIN). 14067:2019-02, *Greenhouse gases – Carbon footprint of prod-
       ucts – Requirements and guidelines for quantification* [viewed 3 September 2020]. Available from:
       https://perinorm-s.redi-bw.de/perinorm/fulltext.ashx?fulltex-
       tid=ff9d8a955ac247108ff322b9729975a6&userid=1a37bae9-63b1-4cef-8afa-a5709d199868.

[15]   Deutsches Institut für Normung e. V. (DIN). 14046:2016-07, *Environmental management – Water footprint –
       Principles, requirements and guidelines.*

[16]   KLÖPFFER, Walter and Birgit GRAHL. *Life Cycle Assessment (LCA). A guide to best practice.* Weinheim:
       Wiley-VCHVerlag GmbH & Co. KGaA, 2014. 978-3-527-32986-1.

[17]   REUTER, Benjamin. Assessment of sustainability issues for the selection of materials and technologies dur-
       ing product design: a case study of lithium-ion batteries for electric vehicles [online]. *International Journal on
       Interactive Design and Manufacturing (IJIDeM).* 2016, **10**(3), 217-227. Available from: 10.1007/s12008-016-
       0329-0.

[18]   ABELE, Eberhard, Reiner ANDERL, and Herbert BIRKHOFER, eds. *Environmentally-Friendly Product De-
       velopment Methods and tools.* London: Springer Verlag, 2005. 978-185-23390-3-6.

[19] Deutsches Institut für Normung e. V. (DIN). 14062:2022, *DIN-Fachbericht ISO/TR 14062:* Beuth.

[20] BROCH, Florian, Jens WARSEN, and Stephan KRINKE. Implementing Life Cycle Engineering in Automotive Development as a Helpful Management Tool to Support Design for Environment. In: Guido Sonnemann and Manuele Margni, eds. *Life Cycle Management.* Dordrecht: Springer Netherlands, 2015, pp. 319-329.

[21] BROCH, Florian. *Integration von ökologischen Lebenswegbewertungen in Fahrzeugentwicklungsprozesse.* Wiesbaden: Springer Fachmedien Wiesbaden, 2017. 978-3-658-18217-5.

[22] RYDING, Sven-Olof, ed. *Environmental management handbook. The holistic approach, from problems to strategies.* Unrev. paperback ed. Amsterdam: IOS Press, 1994. 90-5199-171-1.

[23] TOEDTER, Olaf, Philipp WEBER, and Thomas KOCH. LCA – additional requirement for engineers. In: Johannes Liebl, Christian Beidl, and Wolfgang Maus, eds. *Internationaler Motorenkongress 2021.* Wiesbaden, Heidelberg: Springer Vieweg, 2021, pp. 123-139.

[24] WANG, Nenming, and Guwen TANG. A Review on Environmental Efficiency Evaluation of New Energy Vehicles Using Life Cycle Analysis [online]. *Sustainability.* 2022, **14**(6), 3371. Available from: 10.3390/su14063371.

[25] AHMADI, Pouria, and Erik KJEANG. Realistic simulation of fuel economy and life cycle metrics for hydrogen fuel cell vehicles [online]. *International Journal of Energy Research.* 2017, **41**(5), 714-727. Available from: 10.1002/er.3672.

[26] BAUER, Christian, Johannes HOFER, Hans-Jörg ALTHAUS, Andrea DEL DUCE, and Andrew SIMONS. The environmental performance of current and future passenger vehicles: Life cycle assessment based on a novel scenario analysis framework [online]. *Applied Energy.* 2015, **157**, 871-883. Available from: 10.1016/j.apenergy.2015.01.019.

[27] BENAJES, Jesús, Antonio GARCÍA, Javier MONSALVE-SERRANO, and Santiago MARTÍNEZ-BOGGIO. Emissions reduction from passenger cars with RCCI plug-in hybrid electric vehicle technology [online]. *Applied Thermal Engineering.* 2020, **164**, 114430. Available from: 10.1016/j.applthermaleng.2019.114430.

[28] BOUTER, Anne, Emmanuel HACHE, Cyprien TERNEL, and Sandra BEAUCHET. Comparative environmental life cycle assessment of several powertrain types for cars and buses in France for two driving cycles: "worldwide harmonized light vehicle test procedure" cycle and urban cycle [online]. *The International Journal of Life Cycle Assessment.* 2020, **25**(8), 1545-1565. Available from: 10.1007/s11367-020-01756-2.

[29] COX, Brian, Christian BAUER, Angelica MENDOZA BELTRAN, Detlef P. VAN VUUREN, and Christopher L. MUTEL. Life cycle environmental and cost comparison of current and future passenger cars under different energy scenarios [online]. *Applied Energy.* 2020, **269**, 115021. Available from: 10.1016/j.apenergy.2020.115021.

[30] DEL PERO, Francesco, Massimo DELOGU, and Marco PIERINI. Life Cycle Assessment in the automotive sector: a comparative case study of Internal Combustion Engine (ICE) and electric car [online]. *Procedia Structural Integrity.* 2018, **12**, 521-537. Available from: 10.1016/j.prostr.2018.11.066.

[31] FRAMBACH, Tobias, Ralf KLEISCH, Ralf LIEDTKE, Jochen SCHWARZER, and Egbert FIGGEMEIER. Environmental Impact Assessment and Classification of 48 V Plug-in Hybrids with Real-Driving Use Case Simulations [online]. *Energies.* 2022, **15**(7), 2403. Available from: 10.3390/en15072403.

[32] BIEKER, Georg. A global comparison of the life-cycle greenhouse gas emissions of combustion engine and electric passenger cars [online]. *communications.* 2021, **49**(30), 847129-102. Available from: https://theicct.org/sites/default/files/publications/Global-LCA-passenger-cars-jul2021_0.pdf.

[33] GARCÍA, Antonio, Javier MONSALVE-SERRANO, Santiago MARTÍNEZ-BOGGIO, Vinícius RÜCKERT ROSO, and Nathália DUARTE SOUZA ALVARENGA SANTOS. Potential of bio-ethanol in different advanced combustion modes for hybrid passenger vehicles [online]. *Renewable Energy.* 2020, **150**, 58-77. Available from: 10.1016/j.renene.2019.12.102.

[34] MEYWERK, Martin, and Tobias HELLBERG. Greenhouse Gas Life Cycle Comparison of Internal Combustion and Battery Electric Vehicles [online]. *MTZ worldwide.* 2018, **79**(1), 58-63. Available from: 10.1007/s38313-017-0145-3.

[35] ORBAIZ, Pedro, Nicolás VAN DIJK, Santiago COSENTINO, Nicolas OXENFORD, Mauro CARIGNANO, and Norberto Marcelo NIGRO. A Technical, Environmental and Financial Analysis of Hybrid Buses Used for Public Transport. *SAE Technical Paper Series:* SAE International400 Commonwealth Drive, Warrendale, PA, United States, 2018.

[36] RAYKIN, Leon, Heather L. MACLEAN, and Matthew J. ROORDA. Implications of driving patterns on well-to-wheel performance of plug-in hybrid electric vehicles [online]. *Environmental science & technology.* 2012, **46**(11), 6363-6370. Available from: 10.1021/es203981a.

[37] SCHWARZ, Lea. *Methodische Untersuchung und ganzheitliche Potentialbewertung zukünftiger Antriebssysteme zur CO2-Neutralität im Rennsport.* Dissertation. Wiesbaden: Springer Fachmedien Wiesbaden, 2019. 978-3-658-28084-0.

[38] SCHWARZ, Lea, Michael BARGENDE, Stefan DREYER, Ulrich BARETZKY, Wolfgang KOTAUSCHEK, and Florian BACH. Sustainable drive concepts for future Motorsports. In: Michael Bargende, Hans-Christian Reuss, Andreas Wagner, and Jochen Wiedemann, eds. *19. Internationales Stuttgarter Symposium,* 2019, pp. 60-78.

[39] SCHWARZ, Lea, Michael BARGENDE, Stefan DREYER, Wolfgang KOTAUSCHEK, and Florian BACH. The holistic life cycle assessment caught between development targets, usage profiles and methodology. In: Johannes Liebl, Christian Beidl, and Wolfgang Maus, eds. *Internationaler Motorenkongress 2018,* 2018, pp. 395-420.

[40] SYRÉ, Anne Magdalene, Florian HEINING, and Dietmar GÖHLICH. Method for a Multi-Vehicle, Simulation-Based Life Cycle Assessment and Application to Berlin's Motorized Individual Transport [online]. *Sustainability.* 2020, **12**(18), 7302. Available from: 10.3390/su12187302.

[41] TERNEL, Cyprien, Anne BOUTER, and Joris MELGAR. Life cycle assessment of mid-range passenger cars powered by liquid and gaseous biofuels: Comparison with greenhouse gas emissions of electric vehicles and forecast to 2030 [online]. *Transportation Research Part D: Transport and Environment.* 2021, **97**, 102897. Available from: 10.1016/j.trd.2021.102897.

[42] TOEDTER, Olaf, Philipp WEBER, Lukas HEINZ, Thomas KOCH, and Jens BUCHGEISTER. Life Cycle Analysis - Base for Decision or Object for Discussion? *SIA POWERTRAIN & ENERGY,* 2020.

[43] TOEDTER, Olaf, Philipp WEBER, and Thomas KOCH. LCA – additional requirement for engineers. *8. Internationaler Motorenkongress,* 2021.

[44] ARGONNE NATIONAL LABORATORY. *GREET Model* [online] [viewed 25 April 2022]. Available from: https://greet.es.anl.gov/.

[45] ANDRESH, Manuel, Andreas PATYK, Martina HAASE, Olaf TOEDTER, and Philipp WEBER. Ökobilanzen im Projekt reFuels – Kraftstoffe neu denken. 2021. Available from: 10.5445/IR/1000141494.

[46] SCHWEIMER, Georg W. and Marcel LEVIN. Sachbilanz des Golf A4. 2000.

[47] HUIJBREGTS, M.A.J., Z.J.N. STEINMANN, and P.M.F. ELSHOUT. ReCiPe 2016. A harmonized life cycle impact assessment method at midpoint and endpoint level. Report I: Characterization. 2016.

[48] NORDELÖF, Anders, Emma GRUNDITZ, Anne-Marie TILLMAN, Torbjörn THIRINGER, and Mikael ALATALO. A scalable life cycle inventory of an electrical automotive traction machine—Part I: design and composition [online]. *The International Journal of Life Cycle Assessment.* 2018, **23**(1), 55-69. Available from: 10.1007/s11367-017-1308-9.

[49] NORDELÖF, Anders, and Anne-Marie TILLMAN. A scalable life cycle inventory of an electrical automotive traction machine—Part II: manufacturing processes [online]. *The International Journal of Life Cycle Assessment.* 2018, **23**(2), 295-313. Available from: 10.1007/s11367-017-1309-8.

[50] ELLINGSEN, Linda Ager-Wick, Guillaume MAJEAU-BETTEZ, Bhawna SINGH, Akhilesh Kumar SRIVASTAVA, Lars Ole VALØEN, and Anders Hammer STRØMMAN. Life Cycle Assessment of a Lithium-Ion Battery Vehicle Pack [online]. *Journal of Industrial Ecology.* 2013, **18**(1), 113-124. Available from: 10.1111/jiec.12072.

[51] NORDELÖF, Anders, Mikael ALATALO, and Maria Ljunggren SÖDERMAN. A scalable life cycle inventory of an automotive power electronic inverter unit—part I: design and composition [online]. *The International Journal of Life Cycle Assessment.* 2019, **24**(1), 78-92. Available from: 10.1007/s11367-018-1503-3.

[52] NORDELÖF, Anders. A scalable life cycle inventory of an automotive power electronic inverter unit—part II: manufacturing processes [online]. *The International Journal of Life Cycle Assessment.* 2019, **24**(4), 694-711. Available from: 10.1007/s11367-018-1491-3.

THIESEL 2022 Conference on Thermo and Fluid Dynamics of Clean Propulsion Powerplants

HORIBA Intelligent Lab – Digitalisation of Propulsion System Development for Emissions Compliance

P. Roberts, K. Tabata, L. Bates, A. Headley, S. Whelan

HORIBA MIRA Ltd, Watling Street, Nuneaton, CV10 0TU, United Kingdom

Email: phil.roberts@horiba-mira.com

Telephone: +(44) 7711 193737

Abstract

Vehicle propulsion systems are becoming increasingly complex and diverse whilst regulations associated with emissions, battery longevity, and efficiency are becoming increasingly stringent and cover a broader range of real-world operating conditions. Due to this, it is extremely challenging for vehicle manufacturers to gain full confidence in a vehicle's compliance across the entire range of regulated conditions and potential use cases with physical testing alone.

To reduce the requirement for prototypes, overseas seasonal and altitude testing, a frontloading vehicle and powertrain development programme has been established. This utilises road, chassis dynamometer, Engine-in-the-Loop (EiL) and digital twin virtual toolset methodologies. The current report describes the application of a powertrain and vehicle digital twin toolset for assessing propulsion system performance and compliance across various regulatory and real-world driving scenarios.

Propulsion system performance and emissions were predicted using fully validated dynamic empirical models obtained through a high-fidelity transient characterisation of a contemporary turbocharged diesel engine across the regulatory operating space of altitude and temperature described in European Real Driving Emissions (RDE) testing regulations. These models were coupled with IPG CarMaker software enabling prediction of performance and emissions attributes across controlled, reproducible virtual test driving of both stochastic real-road and targeted edge-case scenarios for a light-duty passenger vehicle. The described methodology allows for a physical testing reduction of >70% for a single vehicle programme, increasing significantly if the propulsion system is shared across multiple vehicle platforms.

1. Introduction

The effort to prevent climate change has accelerated substantially in recent years with harsher policies enforced with the goal of lowering criterion pollutants throughout the world. The proliferation of increasingly stringent laws in the transportation sector has prompted Original Equipment Manufacturers (OEMs) to vary their propulsion systems, with nearly all manufacturers now producing some level of electrified powertrain. However, large numbers of prototype vehicles and overseas climatic test trips are required to ensure compliance with ever-broadening emissions regulations and increases to in-service conformity limits, making these technologically advanced powertrains extremely expensive to develop in terms of both cost and time.

The impending implementation of Euro 7 emissions rules across Europe in the coming decade, as well as the phase-out of specific propulsion systems in some regions, will force OEMs to innovate even more to avoid large fines for non-compliance. The evolution of current electrified internal combustion engine powertrains or Battery Electric Vehicles (BEV) will take a significant amount of time and money; as a result, OEMs and Tier 1 suppliers will need to heavily frontload vehicle and powertrain development to the concept stage of a programme using digital twinning of vehicles, powertrains, routes, drivers, and other stochastic instances that may occur during real-world driving.

HORIBA has developed a vehicle and powertrain frontloading technique known as HORIBA Intelligent Lab, using a suite of methodologies to combat the greater scrutiny that will inevitably accompany future emissions regulations. This methodology has been extensively described in [1-4] when it was originally referred to as RDE+, and includes platforms for road to chassis, road to engine, and virtual vehicle engineering. The creation of a powertrain digital twinning approach, paired with real-world driving scenarios delivered using a virtual scenario development toolkit, is documented in the current work. This has enabled the faster-than-real-time prediction of powertrain performance and emissions for hundreds of real-world driving situations without the need for significant engine testing, prototype vehicles, or international climatic test trips.

The powertrain digital twin was created using a combination of dynamic Design of Experiments (DOE), environmental emulation hardware, Engine-in-the-Loop (EiL), and virtual driving toolsets. Fully validated dynamic empirical performance and emissions models for several attributes were created by dynamically 'mapping' the powertrain over its entire operating range (engine speed and accelerator pedal position) over a wide range of environmental conditions – in this case the moderate and extended Real Driving Emissions (RDE) boundary conditions of temperature and altitude. These models were then coupled with IPG CarMaker virtual vehicle and driving scenario software to predict engine performance and emissions faster than real-time over a variety of fully validated RDE routes, driving styles, traffic densities, altitudes, and temperatures.

Dynamic DOEs have recently been used in the research of [5-9] to anticipate the transient behaviour of numerous systems using both physics-based and empirical modelling techniques. All these sources have investigated using dynamic modelling to enhance engine and/or aftertreatment performance in isolation. In the current study, dynamic powertrain performance and emissions models were created and combined with real-world driving scenarios to identify how non-typical, but fully compliant, driving behaviour may result in unfavourable emissions and regulation non-compliance. As a result, the focus of this research is on the impacts of real-world situations on powertrain performance and emissions, rather than on the implications of calibration or hardware modifications.

The investigation was made feasible with the use of a cutting-edge EiL system, a virtual driving simulation toolset inclusive of virtualised vehicles, drivers, routes, and stochastic driving instances, and the environmental emulation hardware. By utilising the environmental emulation hardware, the effects of altitude and temperature on engine performance and emissions are represented within the empirical models. This technique therefore allows for rapid prediction of powertrain performance and emissions for real-world driving situations using any combination of the moderate and extended RDE boundary conditions.

The detection of 'hotspots' – so-called unfavourable operating circumstances resulting in non-compliance with the current Euro 6d criteria – was made possible by resolving RDE cycle performance and emissions at faster than real-time. This ensures OEMs and Tier 1 suppliers can have confidence that vehicle and engine emissions will conform to localised laws well before prototype and certification testing is necessary. While the current project has focused on predicting performance and emissions from a light-duty C-segment vehicle with a modern light-duty diesel powertrain, this methodology is directly compatible with electrified powertrains and BEVs, as well as other propulsion technologies such as hydrogen internal combustion engines and Fuel Cell Electric Vehicles (FCEV). The methodology detailed in this paper can be easily adopted to optimise electrical energy or gas consumption under real-world driving scenarios without the need for extensive physical testing.

The current article details the methodology used to generate powertrain digital twin and how it was coupled with a plethora of fully compliant (in terms of cycle dynamics, distance share, stop time etc) RDE scenarios produced with IPG CarMaker to predict powertrain performance and emissions. Potential hotspots with the current vehicle and engine are presented, along with a measure of the methodology's success in decreasing the physical testing periods necessary to ensure compliance with Euro 6d emissions regulations.

2. Methodology

2.1. Dynamic Design of Experiments and Design Space

For all parts of the dynamic DOEs, including design, modelling, and prediction, the Ricardo Efficient Calibration Global DOE Toolkit (ηCal) was used. More information about this toolbox may be found in [10], however it is not explored in depth in this paper.

The dynamic design inputs were the accelerator pedal position, engine speed, altitude (which is ultimately pressure delivered to the engine), and temperature; the latter two were delivered to the engine airbox using the environmental emulation hardware. The engine speed range included idle to engine run-out speed, while the accelerator pedal position range was adjusted from zero to full travel. These two parameters were varied across their full ranges to ensure that the effects of driving style on vehicle and powertrain performance and emissions were captured within the training data, where drivers can exercise the powertrain across varying speed/load ranges based on their preferred driving style. Covering the whole accelerator pedal position and engine speed ranges and constructing performance and emissions models that encapsulate these factors has the added benefit of being transferable across multiple virtual car platforms that share a common powertrain. With OEMs attempting to minimise development timeframes and costs, the ability to test powertrain performance across numerous vehicle configurations without using prototype cars is clearly beneficial.

It would have been ideal to dynamically control pressure and temperature across the entire extended RDE boundary conditions (-7°C to 35°C and 0m to 1300m) with a single dynamic design. However, due to the slower transient response of the environmental emulation hardware, this was practically impossible to achieve, since this would have involved 90+ hours of continuous engine operation. Consequently, the moderate and extended RDE boundary conditions were divided into 15 distinct sections (**Figure 1**), with altitude, temperature, accelerator pedal position and engine speed dynamically varied within each explicit section. Accordingly, there was one set of training data and therefore one set of models per section. It was possible however to combine training datasets to generate models covering a wider range of environmental conditions if required. This was outside the scope of the current research, however.

The slowest responding system was the environmental emulation hardware which ultimately controlled the length of each dynamic design; 6 hours per dynamic DOE. Accelerator pedal position and engine speed design inputs were tuned to obtain rates of pedal position actuation and engine speed change that were like those encountered during real-world driving. This meant that the models generated were representative of dynamic conditions seen during real-world driving. **Figure 2** shows a snapshot sample of the dynamic profiles for the four design inputs for Section 1.
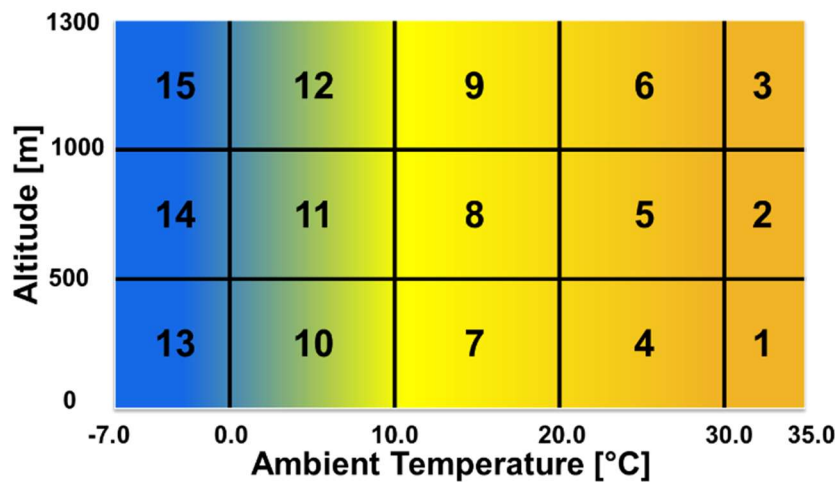
Figure 1. Explicit sections of the moderate and extended RDE boundary conditions for dynamic mapping of the test engine
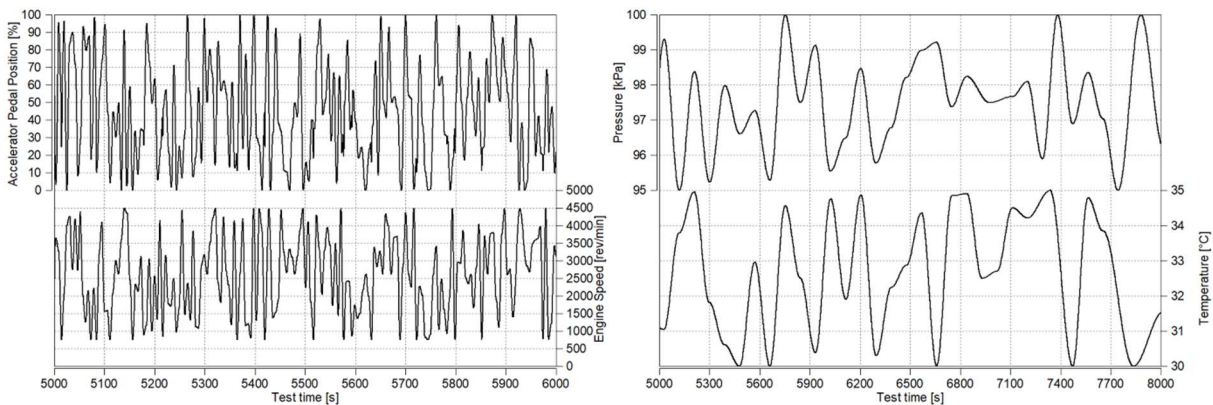
Figure 2. Dynamic design of accelerator pedal position and engine speed for Section 1

2.2. Engine Specification and Engine-in-the-Loop

The engine used was a light-duty modern turbocharged direct injection diesel engine which was installed in a testcell at the HORIBA MIRA in the UK (**Figure 3**) with the engine's specifications listed in **Table 1**. The engine had no aftertreatment, so engine backpressure was emulated using an orifice plate mounted downstream of the emissions monitoring apparatus.

The EiL is shown diagrammatically in **Figure 4**. Engine speed and accelerator pedal position from the dynamic DOE design was 'pushed' to the relevant test automation system controllers. Setpoints for altitude and temperature were provided to the environmental emulation hardware via the test automation system; this is

covered in more depth in the next section. Fuel mass flow was measured using a HORIBA FQ3100 positive displacement fuel meter (accurate to 0.5% of the observed value) with air mass flow measured with an ABB FMT700-p thermal mass flow metre (accurate to 0.6% of the measured value). Exhaust mass flow was calculated using these measurements. It was subsequently used to calculate emissions mass flow and cycle emissions according to the current Euro 6d requirements [12]. Engine out emissions were measured using a single-line HORIBA MEXA ONE with a measurement accuracy ranging from 0.2% to 2.0% of the observed value, depending on the measurement range. Tailpipe PN was not measured during this research, since the engine did not have a Diesel Particulate Filter (DPF). ATI Vision was used to capture measurements from the vehicle and engine's ECU, which were synchronised with the test automation system. All measurements were recorded at 10Hz.

Table 1. Test engine specification

Maximum Power	kW	96 @3500rpm
Maximum Torque	Nm	385 @1500-2000rpm
Displaced volume	cc	1995
Bore x Stroke	mm	84.0 x 90.0
Compression Ratio	ratio	16.5
Number of Cylinders	#	4
Valves per Cylinder	#	4
Air Handling	-	Variable geometry turbocharger + EGR
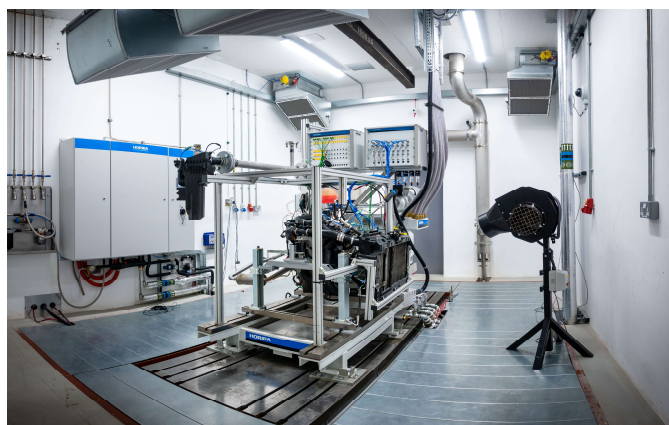
Figure 3. Development engine installation
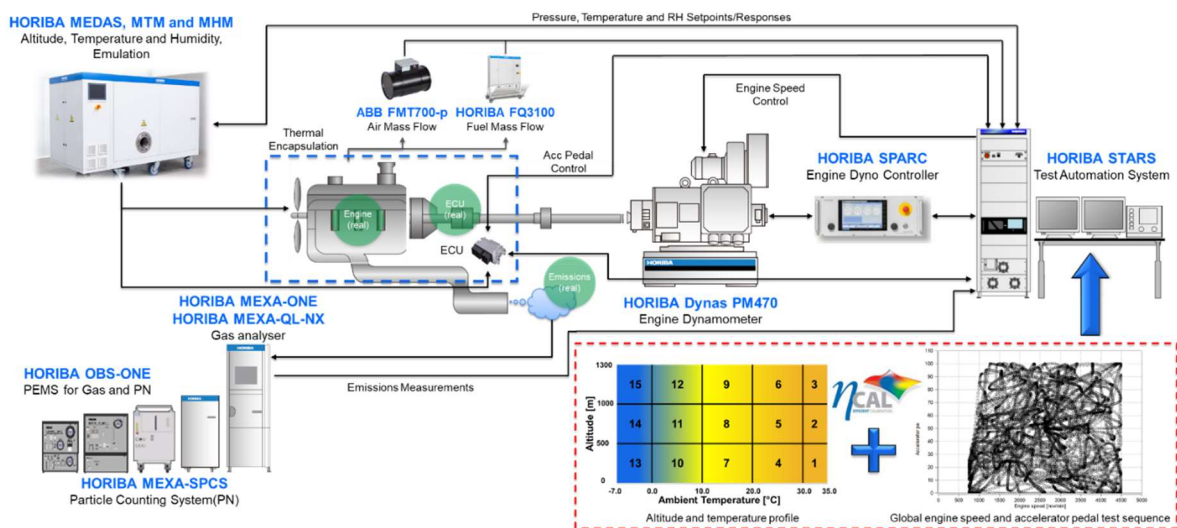
Figure 4. Schematic of the EiL setup used for creating the dynamic digital twin

2.3. Environmental Emulation Hardware

A HORIBA Multi-function Efficient Dynamic Altitude Simulation (MEDAS) system with a MEDAS Temperature Module (MTM) and MEDAS Humidity Module (MHM) was used to simulate altitude and temperature. Combustion air was conditioned to the correct pressure (ultimately altitude), temperature, and relative humidity and supplied to the engine intake with the exhaust system connected to achieve equilibrium. For the sake of brevity, MEDAS will be used to refer to all elements of the system's pressure, temperature, and relative humidity components from now on. The MEDAS is described in full in [11], and precise transient control of the system is reported in [4].

Engine changes were made to ensure correct behaviour for if it were physically tested at high altitude. This meant connecting the intake and exhaust systems and the crankcase breather to MEDAS; essentially any part of the engine that was open to atmosphere. Ordinarily, the engine's ECU would also be referenced to ensure corrections were applied to engine operating variables to account for altitude. However, the ECU was not referenced in this case therefore allowing for the 'true' effects of altitude and temperature on powertrain performance and emissions to be measured.

The MEDAS dynamically controlled the relative humidity to maintain absolute humidity at 2.5g/kg independent of altitude or temperature. Dynamic pressure, temperature, and relative humidity were maintained to within 1kPa, 1°C, and 10% of their respective dynamic design setpoints.
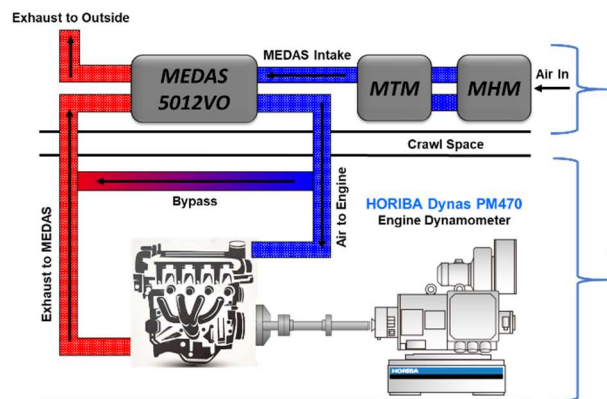

Figure 5. Schematic of the MEDAS connections to the engine

2.4. Dynamic Model Generation and Validation

The Ricardo Efficient Calibration Toolbox (ηCal) used dynamic training data acquired from the engine for each of the 15 sections to build models of several engine attributes; for clarity, the model inputs were accelerator pedal position, engine speed, pressure (altitude) and temperature with these listed alongside the models created using the training data in **Table 2**. The models were built using the Stochastic Process Model (SPM) modelling function within the toolbox. This is a Nonlinear Autoregressive Exogenous (NARX) model that can learn to anticipate time series responses. It can represent extremely nonlinear systems with high dimensionality, making it well-suited to powertrain applications. The training data was additionally subjected to an extra logarithmic transformation function, which increased model quality.

The R^2 correlation coefficient obtained in the ηCal toolkit was first used to assess model accuracy which was further quantified by comparing measured and predicted engine data. Several transient engine tests were conducted with the engine with the physical data recorded – these are known as validation tests. Engine speed, accelerator pedal position, altitude, and temperature from these engine tests were used with the models created to predict performance and emissions attributes for the same test. A good correlation of measured and predicted engine performance and emissions was obtained over various environmental boundaries and driving styles. In cases where model quality was poorer than expected, extra training data was collected, hence boosting the predictive power of the models. The validation methodology process flow is depicted in **Figure 6**.

Examples of measured vs. predicted responses of engine out emissions and engine performance measures are shown in **Figure 7**, **Figure 8** and **Figure 9**. This data is from Section 1 of the moderate and extended RDE boundary conditions with similar levels of correlation achieved for all other sections. CO_2 mass flow, NOx mass flow, and fuel and air consumption predictions were all in excellent agreement with the measured engine data. Conversely, engine out CO and THC emissions (**Figure 9**), were more challenging to predict. This was mainly caused by trying to generate a model to fit close-to-zero data with periodic excursions of high engine out CO and

THC. This issue will be solved in a later generation of modelling toolset that is currently under development. This advanced modelling toolset will also be required for accurate prediction of PN, since this criteria emission is similar in production to CO and THC.

Table 2. Models generated from training data

Model Inputs	Models Generated	
Accelerator pedal position	Engine out CO mass flow	Air mass flow
Engine speed	Engine out CO_2 mass flow	Fuel mass flow
Intake air pressure (altitude)	Engine out O2 mass flow	Exhaust mass flow
Intake air temperature	Engine out NOx mass flow	Compressor out temperature
	Engine out THC mass flow	Turbine in temperature
	Engine brake torque	EGR rate
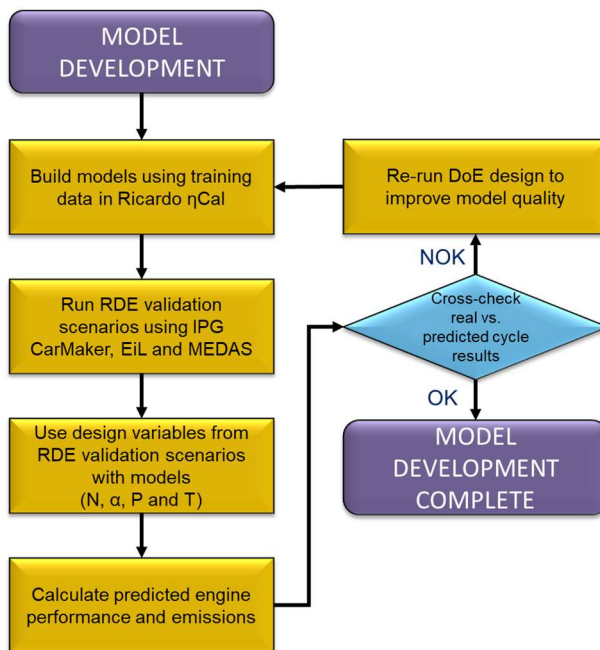
Figure 6. Model development and validation process flow
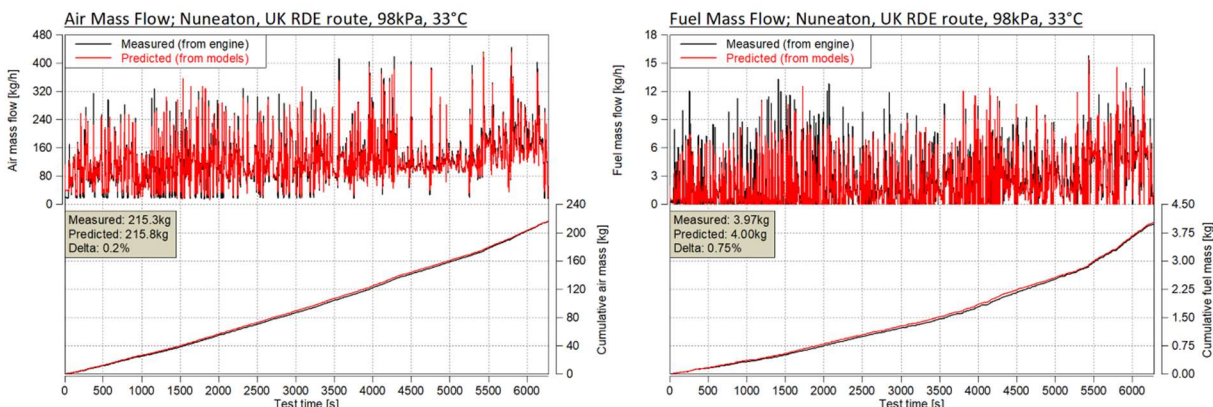
Figure 7. Measured vs. predicted responses for air mass flow and fuel mass flow, Section 1 models
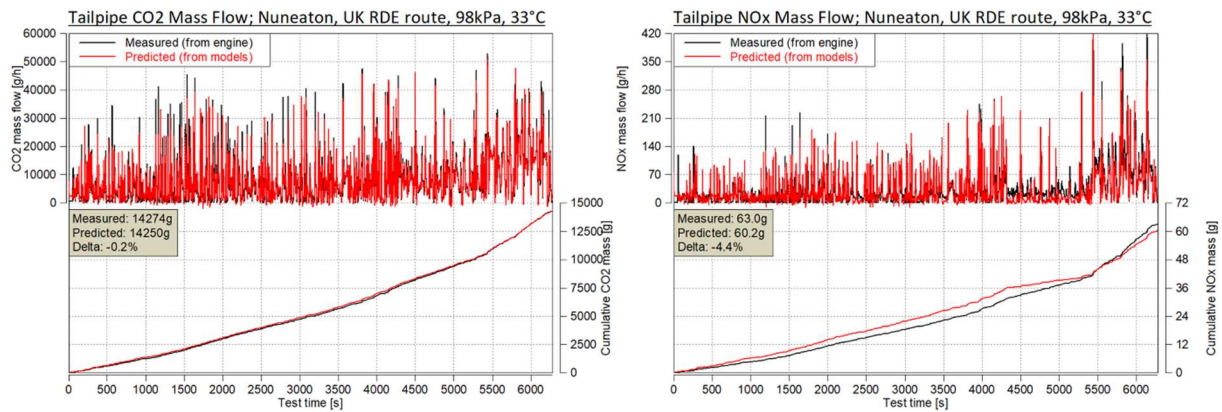
Figure 8. Measured vs. predicted responses for engine out CO_2 and NOx, Section 1 models
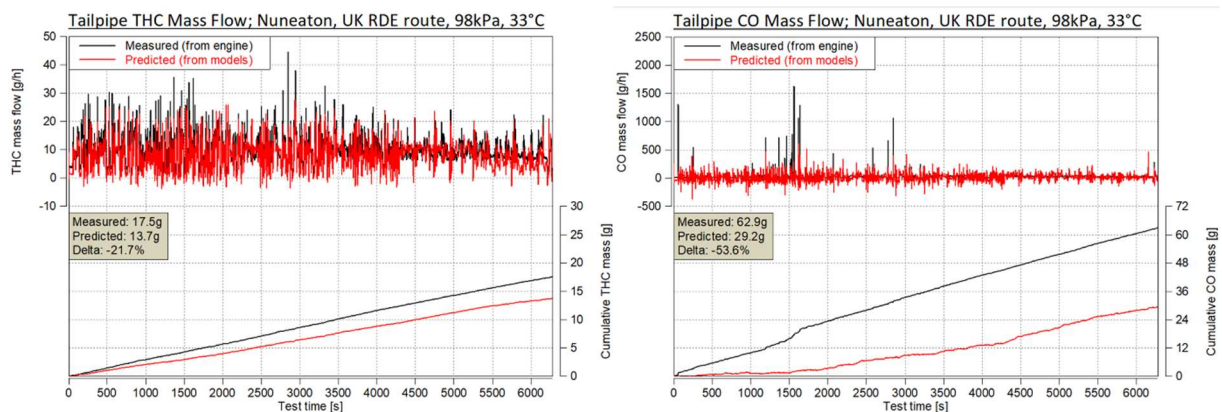

Figure 9. Measured vs. predicted responses for tailpipe THC and CO mass flow, Section 1 models

2.5. CarMaker for Real-world Scenario Generation

IPG CarMaker was used generate real-world driving scenarios. These scenarios were then coupled with the empirical models from each section to predict performance and emissions for these scenarios. Only the four most extreme environmental sections and associate models are discussed here for brevity. **Table 3** summarises the characteristics of the environmental corner sections, whereas **Table 4** details the IPG CarMaker real-world driving scenarios that were generated. All scenarios generated fulfilled all Euro 6d RDE trip criteria with route, driving style and traffic density altered accordingly.

Engine performance and emissions of 51 scenarios per section (a total of 204) were predicted. This took approximately 15 hours computational runtime to achieve (excluding model training as this had already been completed). For comparison, 204 physical RDE cycles would take roughly 306 hours to complete assuming back-to-back testing. The Euro 6d RDE regulation parameter va_pos[95] as a percentage of its limit was used to parameterise the virtual driver within IPG CarMaker with higher va_pos[95] values indicating more aggressive driving (driver parameterisation techniques are discussed in detail in [4]). To provide realism to the scenarios, traffic density was varied from none to heavy and was introduced on the virtual roads using the IPG CarMaker RDX Generator programme. Each route was populated with distinctive velocity makers serving as virtual 'speed limits'; the virtual driver then accelerated, decelerated, or came to a complete stop when indicated. The position of the traffic was determined using a phenomenological traffic algorithm based on a real-world driving database that is unique to IPG Automotive software [13].

A virtual C-segment car model was used within IPG CarMaker. It was parameterised using known vehicle features such as true coastdown coefficients, vehicle mass, gear ratios, final drive ratios, and tyre size. Some crucial metrics such as frontal area and drag coefficient were calculated since they were unknown. These unknown parameters do not detract from the results obtained however, since the same reference vehicle was used throughout the study.

An additional prediction of performance and emissions for a WLTP was included in the results that served as a reference value for comparison with all other predicted performance and emissions from the 204 scenarios.

This utilised the light-duty WLTP vehicle velocity profile integrated with IPG CarMaker where the subsequent accelerator pedal position and engine speed profiles were used with the models created in Section 4. Environmental conditions in this case were 23°C and 100kPa and were used to reflect the laboratory conditions necessary for WLTP testing.

Table 3. Environmental conditions for the models used with IPG CarMaker real-world scenarios

		Section 1	Section 3	Section 13	Section 15
Altitude	m	0	1300	0	1300
Pressure	kPa	100	87	100	87
Temperature	°C	35	-7	35	-7

Table 4. Details of the scenario characteristics utilised with the models created for Sections 1, 3, 13 and 15

Section and Environment	Section 1 – 0m, 100kPa, 35°C Section 3 – 1300m, 87kPa, 35°C Section 13 – 0m, 100kPa, -7°C Section 15 – 1300m, 87kPa, -7°C															
RDE Route	Innsbruck, Austria (88.0km)				Nuneaton, UK (85.0km)				Vera, Spain (74.8km)				Stuttgart, Germany (83.7km)				WLTP (22.4km 100kPa, 23°C)
Traffic Density	None	Light	Moderate	Heavy	None	Light	Moderate	Heavy	None	Light	Moderate	Heavy	None	Light	Moderate	Heavy	None
Driving Style vapos[95] [m²s³]					60	60	60	60					60				68
	70	70	70	70	70	70	70	70	70	70			70	70	70	70	
	80	80	80	80	80	80	80	80	80	80	80	80	80	80	80	80	
	90	90	90	90	90	90	90	90	90	90	90	90	90	90	90	90	

3. Results

3.1. Introduction to Results

Described in the current section are the predictions of engine performance and emissions for the scenarios detailed in **Table 4**. While every attempt was made to quantify why such trends occur, it was not possible to provide detailed answers without a thorough understanding of the powertrain calibration strategy which was unavailable at the time. These findings should therefore be taken in the perspective of emphasising the shortcomings of the WLTP as well as adopting a single RDE cycle for certification testing.

The WLTP is conducted in favourable laboratory settings and is used as a tool for ensuring compliance and comparing vehicle to vehicle emissions under controlled conditions. The supplementary RDE certification cycle is supposed to inform regulators and consumers about how the vehicle will perform under real-world driving conditions. However, it is entirely possible that the 'true' impacts of real-world driving on performance and emissions are not accounted for completely during this on-road test, as a result of favourable routes, driving styles and other stochastics instances that might occur. In this respect, OEMs and Tier 1 Suppliers can use the digital twin methodology described here to screen real-world driving scenarios in less than real-time and stress-test their vehicles to ensure not only compliance with localised regulations, but also that they are not vulnerable to damaging investigations by third parties, such as the Volkswagen "Dieselgate" scandal of the recent past.
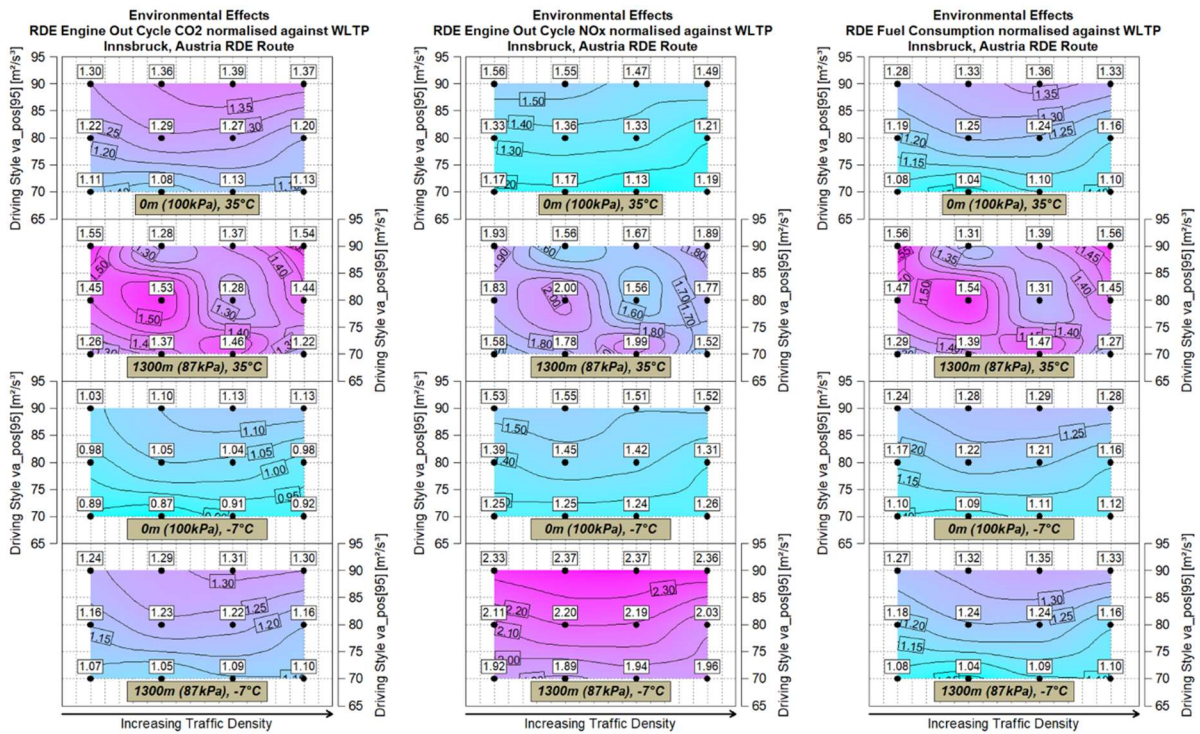
3.2. Effects of Environment on Performance and Emissions

Contour plots of engine out CO_2, engine out NOx, and fuel consumption for variations in driving style and traffic density for four distinct environmental conditions for Innsbruck, Austria virtual RDE route are shown in **Figure 10**. The corresponding WLTP value predicted using the models produced in Section 4 (95-100kPa, 0-500m, 20-30°C) was used to normalise all data. Depending on the type of driving, traffic density, and environmental conditions of the RDE cycle, engine out CO_2 can be up to 55% higher or 13% lower than the WLTP result for this particular RDE route. Engine out CO_2 is normally highest around 1300m and 35°C, owing to the reduced intake

charge density and the requirement for the engine to run below optimum efficiency to produce the same performance as at sea level and mild temperatures. The lowest altitude and coldest temperature create the least CO_2, with cycle results in some circumstances being lower than the WLTP. The thermodynamic benefits of the cooler and denser intake charge are obvious in this scenario. However, this benefit must be balanced against colder aftertreatment temperatures and hence longer aftertreatment light-off durations, which are unavoidable during cold starts.

Depending on the mix of driving scenario and climate, engine out NOx and fuel consumption were up to 137% and 54% higher, respectively, than the reference WLTP value; no scenarios produced cycle engine out NOx and fuel consumption values lower than the WLTP reference. Without prior knowledge of engine calibration parameters such as EGR rate, injection quantities and injection timing, quantifying engine out NOx trends is very challenging. Nevertheless, engine out NOx emissions tend to be highest at higher altitudes and colder temperatures, owing to the engine's need to function sub-optimally in order to provide equivalent performance compared to more favourable environmental circumstances.

For all climatic situations, engine out CO_2, NOx, and fuel consumption were typically greater for more aggressive driving; this aligns well with the results reported in [4]. The impacts of traffic density are more difficult to isolate, with high traffic density frequently resulting in the lowest engine exhaust emissions; this might be due to excessive stop-start circumstances. Excessive stop-start however, must be balanced with aftertreatment efficiency, which will be impacted by the lower exhaust gas temperatures produced when the engine is idling or stopped.

Figure 10. Normalised cycle engine out CO_2, NOx and fuel consumption for various driving styles and traffic densities across different environmental conditions for the Innsbruck, Austria virtual RDE route

3.3. Effects of RDE Route on Performance and Emissions

Contour plots of engine out CO_2, NOx, and fuel consumption for changes in driving style and traffic density for four different routes at sea level (100kPa intake pressure) and 35°C are shown in **Figure 11**. These results have been normalised against the predicted WLTP value. All virtual routes utilised met the RDE trip criteria standards. Unfortunately, it was not possible to simulate the same number of scenarios per route as some combinations of traffic density and driving style resulted in non-compliance with RDE trip criteria standards.

Across all routes, engine out CO_2, NOx, and fuel consumption varied by 7%, 12%, and 7%, respectively. As a result of these findings, one might deduce that certain routes are more favourable than others, providing evidence to suggest compliance testing should be conducted over several routes and test locations to ensure real-world driving has been completely accounted for. Unfortunately, it is difficult to define the specific reasons

why driving one route produces more favourable results than another without delving into the finer points of each route. However, the urban, rural, and highway distance shares, traffic signals, speed restrictions, gradients, and even roundabouts are likely to contribute to route-to-route variance for identical driving behaviour, traffic density and environment. This type of data analysis allows OEMs and Tier 1 suppliers to identify favourable testing locations for certification testing. Whilst this viewpoint is not in the 'spirit' of ensuring complete compliance during all real-world driving scenarios, the frontloading exercise presented here provides evidence for enforcing stricter emissions regulations that will force vehicle manufacturers to stress-test their products across a wider range of real-world scenarios.
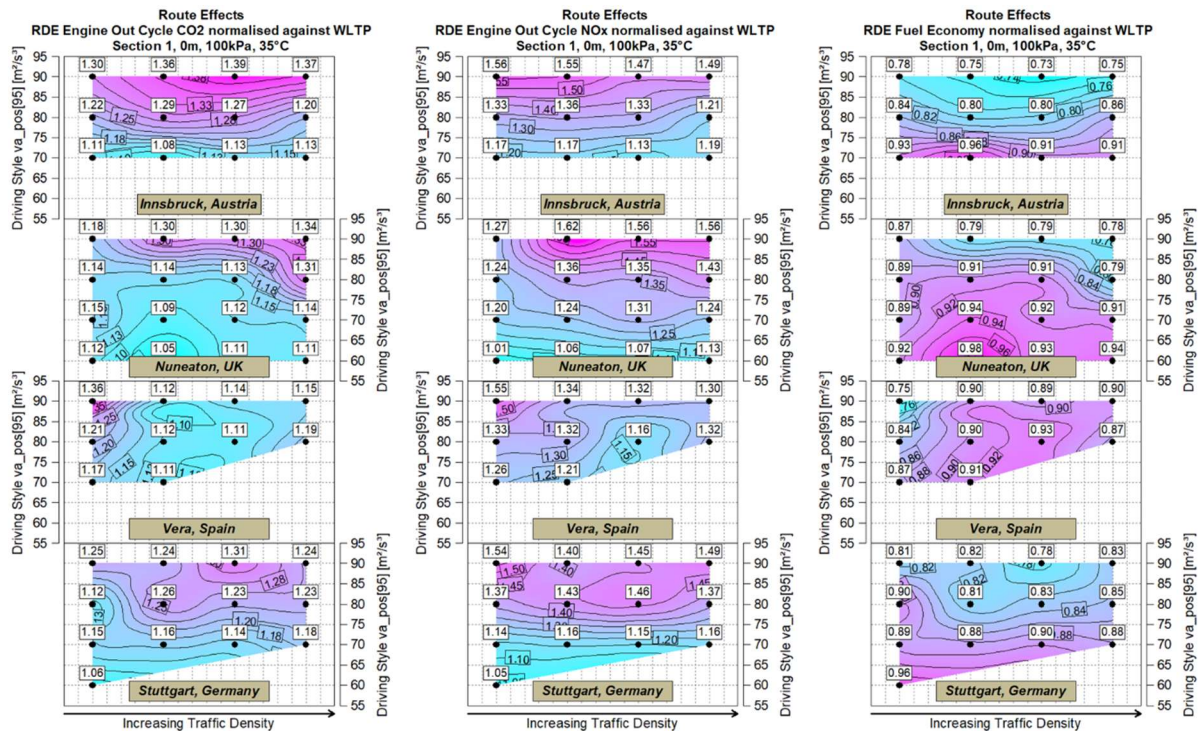
Figure 11. Normalised cycle engine out CO_2, NOx and fuel consumption for various driving styles and traffic densities across different RDE routes at 0m, 100kPa, 35°C

3.4. Overall Results

Figure 12 shows histograms of predicted engine out CO_2, NOx, and fuel consumption for all RDE cycles for various environmental conditions, routes, traffic densities, and driving styles. The predicted WLTP value (displayed as 1 in each figure) was used to normalise the RDE cycle results. The magnitude of the problem that OEMs and Tier 1 suppliers face in trying to ensure compliance with current and, in the near future, more stringent emissions regulations is highlighted in these figures. Almost all RDE cycles result in higher emissions and fuel consumption than the WLTP result; with some RDE scenarios producing engine out NOx emissions that are twice as high as the WLTP value. In other cases, CO_2 and fuel consumption are 50-60% higher than the WLTP. These results are unsurprising and ultimately provide evidence that the WLTP is unsuitable for certification purposes. Furthermore, the large scatter in cycle emissions across 204 RDE cycles suggests a single witness test should not be used for certification as it is not necessarily representative of real-world driving.

RDE cycle results for criteria pollutant emissions have been predicted here using the digital twin methodology. However, it is likely that prediction of BEV attributes across a wide range of real-world driving scenarios will produce similarly alarming results when compared to the laboratory i.e. large deviations in real-world electric range depending on driving scenario. However, since the BEV charging infrastructure found in most developed countries is immature at present, not achieving the certified BEV range during real-world driving is arguably more problematic for consumers compared to an equivalent ICE vehicle, since liquid fuel refueling infrastructure is mature. Furthermore, since fuel consumption and electric-only range are important factors to consider when purchasing a vehicle for personal or commercial use, providing consumers with certification figures that do not reflect real-world usage is problematic.
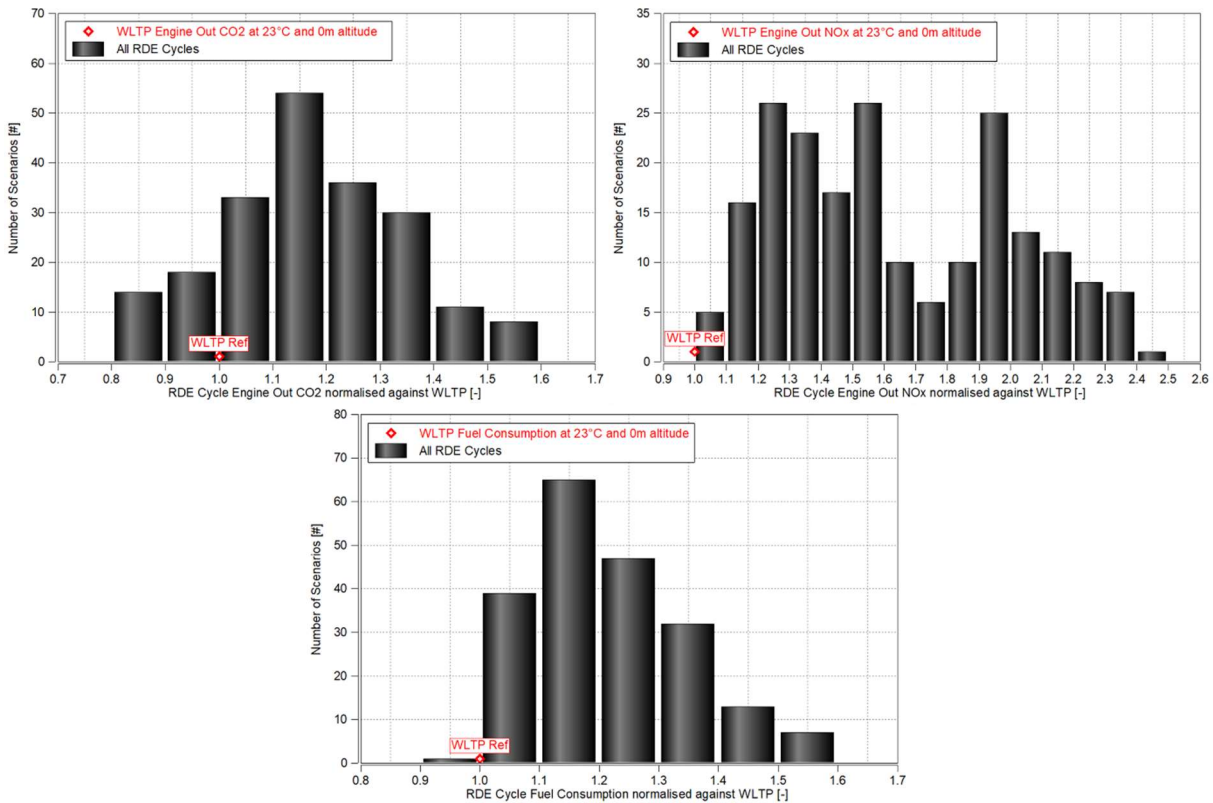
Figure 12. Histogram of RDE engine out CO_2, NOx and fuel consumption normalised against the WLTP result

3.5. Identification of Estimated Tailpipe NOx Hotspots

The importance of predicting performance and emissions for RDE scenarios that fulfil all regulation criteria will allow OEMs and Tier 1 suppliers to focus development and calibration activities on scenarios and 'hotspots' that could result in non-compliance before prototype vehicle testing and certification.

The engine under test did not have aftertreatment, therefore only engine out emissions was collected. Tailpipe NOx emissions were however estimated using Selective Catalytic Reduction (SCR) conversion efficiency vs. exhaust gas temperature data from a twin SCR system used on a contemporary light-duty diesel engine vehicle similar to the one used in this study [14]; this depicted schematically in **Figure 13**. The goal of estimating tailpipe NOx was to highlight how the dynamic digital twin methodology could be used to identify unfavourable vehicle or engine operation or real-world scenarios that would result in non-compliance with Euro 6d emissions regulations. Predicted turbine-in temperatures from each RDE scenario were used to calculate turbine-out and thus exhaust gas temperature into the close-coupled SCR. The NOx mass flow after conversion from the close-coupled upstream SCR was calculated using this temperature, the NOx conversion rate data shown in **Figure 13** (black line) and the predicted engine out NOx. For the sake of simplicity, exhaust gas temperature was conserved between the upstream and downstream SCRs. In reality, this could increase or decrease depending on the exothermic or endothermic characteristics of the SCR, the NO/NO_2 balance, and the system's underbody location. The temperature from the close-coupled SCR into the underfloor SCR was then used in conjunction with the NOx conversion efficiency data shown in **Figure 13** (red line) and the calculated NOx mass flow from the close-coupled SCR to calculate instantaneous tailpipe NOx.

The red line in **Figure 14** represents the normalised WLTP Euro6d limit value for tailpipe NOx (80mg/km for a diesel engine). The blue line represents the RDE Euro 6d limit – 80mg/km multiplied by the NOx conformity factor of 1.43. All tailpipe NOx values calculated according to the methodology above have been normalised against the WLTP value. Approximately 92% of the 204 RDE scenarios produced tailpipe NOx emissions above the Euro 6d RDE cycle limit (blue line). As a result, these findings highlight the importance of favourable certification testing conditions to achieve a compliant test result for this particular vehicle and powertrain combination. If the SCR efficiency were increased by 10% or 25% from the baseline, the percentage of non-compliant cycles reduces to 82% and 57% respectively – broadening the range of real-world scenarios that can be accommodated during witness testing.

While it is acknowledged that these predictions are not finite – all models contain some inaccuracies and assumptions – this methodology can be used to rapidly quantify and directionally identify potentially problematic areas of the RDE boundary conditions, powertrain hardware or software, or vehicle operation. Furthermore, the wide range of completely compliant RDE scenarios (from a trip dynamic perspective) and the resulting tailpipe NOx emissions highlight the inadequacies of adopting a single RDE cycle for compliance from a legislative standpoint. This is because, in addition to the favourable laboratory result, all real-world stochastic instances that influence pollutant creation cannot be covered by a single certification test.
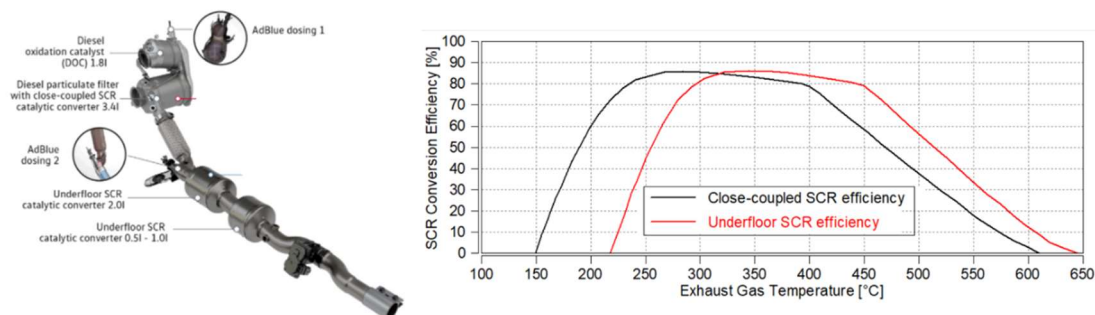

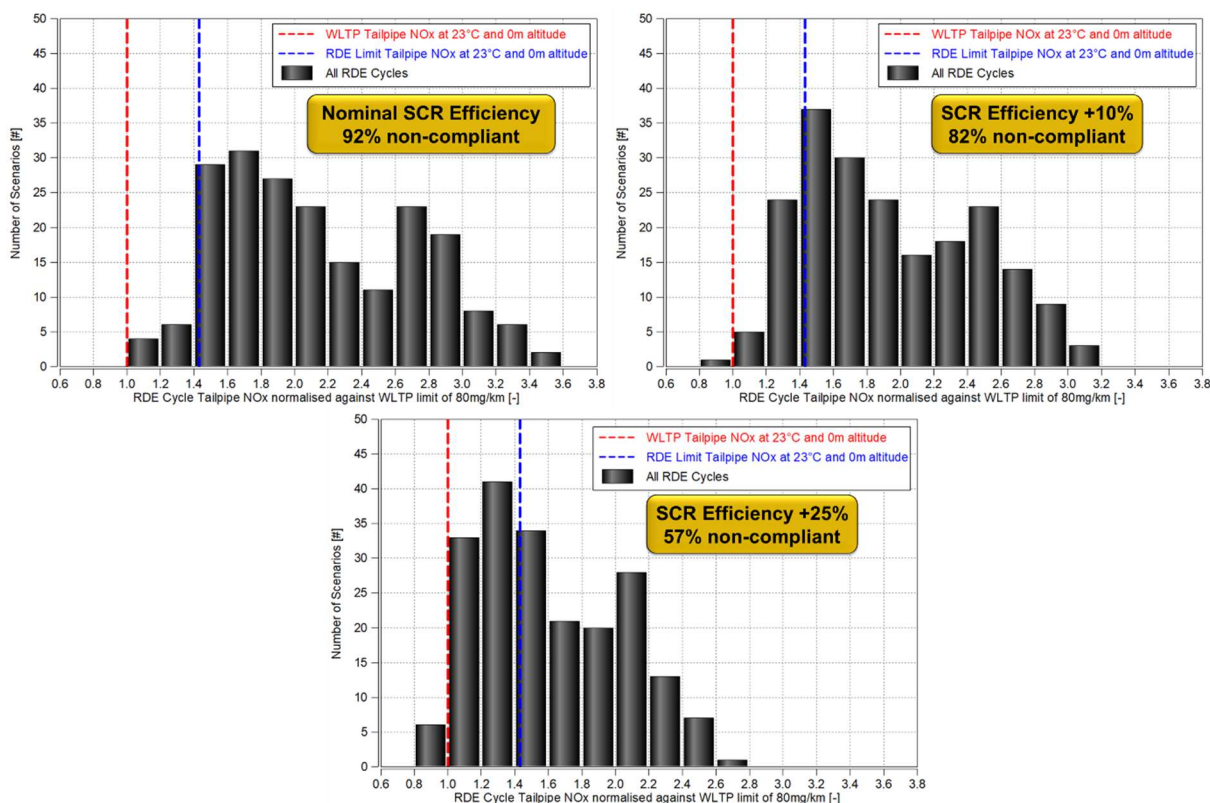**Figure 13.** Volkswagen twin-SCR dosing system for Euro 6d compliance [14]

Figure 14. Normalised RDE cycle tailpipe NOx for each scenario; nominal SCR efficiency calculated according to [**Figure 13**], +10% and +25% increases in SCR efficiency

Figure 15 shows an example of estimated tailpipe NOx for a variety of RDE cycles with varying driver dynamics and traffic densities, normalised against the WLTP Euro 6d tailpipe NOx limit discussed earlier. The RDE Euro 6d tailpipe NOx limit is highlighted as the blue line (1.43). The Nuneaton, UK RDE route and the models used in Section 1 (0-500m and 30-35°C) were used to create this dataset. Several scenarios result in tailpipe NOx emissions exceeding the RDE limit, restricting certification testing to a narrow window of driving styles and traffic densities – the latter of which is almost always uncontrollable due to its stochastic nature.

To expand the compliance region, the OEM could i.) improve aftertreatment efficiency to reduce criteria pollution, ii.) improve engine efficiency through software or hardware changes, or iii.) distil the problematic cycles into localised residencies that allow for detailed investigation. The cycle with the highest traffic density and most aggressive driving (normalised value of 1.60), as shown in **Figure 15**, has been distilled into tailpipe

NOx and time residencies as a percentage of the cycle result and is shown in **Figure 16**. Due to the heavy traffic and the driver accelerating up to the speed limit as quickly as possible as soon as the traffic subsides, the engine spends a significant amount of time around idle and mid speeds; low-mid speed and low-mid load ranges of the engine calibration should be focused on, and efficiencies improved upon. Furthermore, by combining residences from different scenarios, common problematic areas of the operating map can be identified, and remedies to improve efficiency can be deployed earlier in the development programme if necessary.
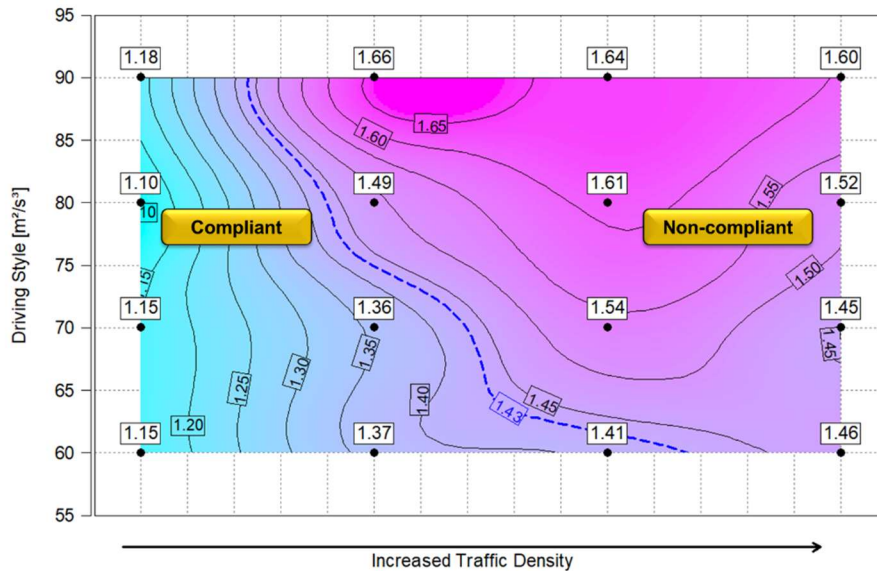
Figure 15. Normalised cycle tailpipe NOx for the Nuneaton, UK RDE route, various driving styles and traffic densities at 0m altitude (100kPa) and 35°C
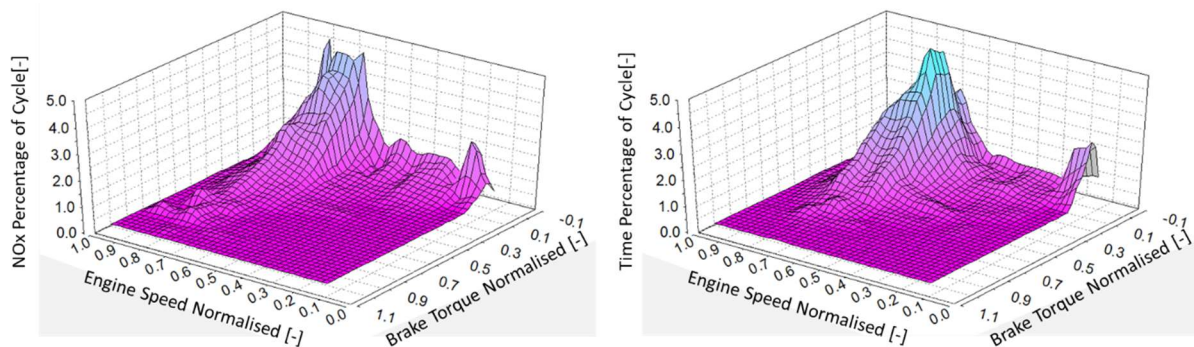
Figure 16. Localised residency of normalised engine speed and torque vs. NOx percentage of the cycle and time percentage of the cycle for the highest traffic density and most aggressive driving scenario represented in **Figure 15**

3.6. Methodology Effectiveness

It took approximately 5.6 days to dynamically map the engine across the entire moderate and extended RDE boundary conditions, running two 8-hour shifts per day. The creation of the models, validation cycles, simulation/prediction took an additional 1.9, 5.6, and 0.5 days respectively for a total of 13.6 days. By comparison, it would take 45 days to complete the same number of tests using physical vehicles, assuming back-to-back and right-first-time testing; this represents a 70% reduction in test time when using the digital twin approach (**Figure 17**).

The powertrain models developed can be used with any virtual vehicles that share a common powertrain. Therefore, only the simulation/prediction part of the methodology must be completed for additional vehicles (0.5 days per vehicle). Physical testing, on the other hand, is proportional to the number of vehicle variants, even for common powertrains. Therefore, predicting powertrain performance and emissions for a hypothetical group of ten vehicles saves 96% of the time required to test an equivalent number of physical vehicles. **Figure 17** shows the time savings for a single vehicle and the extreme example of ten vehicles, respectively.
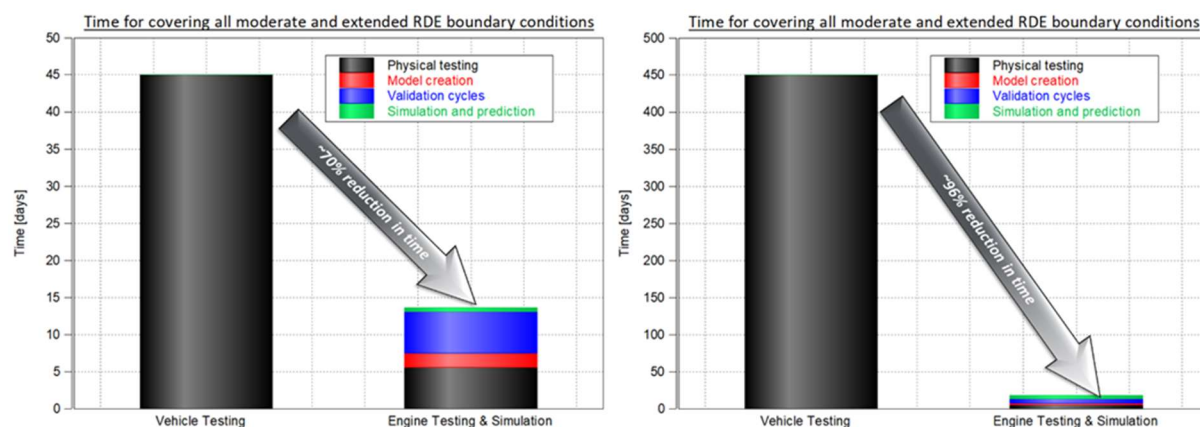
Figure 17. Digital twin methodology effectiveness for a single vehicle and multiple vehicles adopting a common powertrain

4. Conclusions

A digital twin of a modern turbocharged light-duty diesel engine has been developed using dynamic DOEs to generate empirical performance and emissions models. When the digital twin models were coupled with IPG CarMaker, engine out performance and emissions were predicted for hundreds of real-world driving scenarios.

This allowed for the rapid identification of unfavourable real-world scenarios, as well as powertrain performance and emissions 'hotspots' without the need for costly prototype vehicles or climatic test trips. OEMs will be able to choose specific real-world driving scenarios to meet legislative requirements. However, these results highlight the drawbacks of using a laboratory-based certification protocol in conjunction with a single RDE cycle for certification.

When using the digital twin methodology, physical testing times for covering the moderate and extended RDE boundary conditions across a variety of real-world driving scenarios can be reduced by up to 70% for a single vehicle. If different vehicles utilise a common powertrain, this reduction can be increased further.

Finally, this methodology can be readily applied to determine real-world efficiency use cases for electrified powertrains and battery electric vehicles.

5. References

1   Roberts, P.J., Mumby, R., Mason, A., Redford-Knight, L., and Kaur, P., "RDE Plus – The Development of a Road, Rig and Engine-in-the-Loop Methodology for Real Driving Emissions Compliance," SAE Technical Paper 2019-01-0756, 2019, DOI:10.4271/2019-01-0756.

2   Roberts, P.J., Mason, A., Whelan, S., Tabata, K., Kondo, Y., Kumagai, T., Mumby, R., and Bates, L., "RDE Plus – A Road to Rig Development Methodology for Whole Vehicle RDE Compliance: Overview," SAE Technical Paper 2020-01-0376, 2020, DOI:10.4271/2020-01-0376.

3   Mason, A., Roberts, P.J., Whelan, S., Kondo, Y and Breton, L., "RDE Plus – A Road to Rig Development Methodology for Whole Vehicle RDE Compliance: Road to Chassis Perspective," SAE Technical Paper 2020-01-0378, 2020, DOI:10.4271/2020-01-0378.

4   Roberts, P.J., Mason, A., Tabata, K., and Whelan, S., "RDE Plus – A Road to Rig Development Methodology for Whole Vehicle RDE Compliance: Engine-in-the-Loop and Virtual Tools," SAE Technical Paper 2020-01-2183, DOI:10.4271/2020-01-2183.

5   Gutjahr, T., Kruse, T., and Huber, T., "Advanced Modelling and Optimization for Virtual Calibration of Internal Combustion Engines," NDIA Ground Vehicles Systems Engineering and Technology Symposium, 2017.

6   Shishido, T., He, J., Kaihatsu, M., Haukap, C., Dreher, T., and Hegmann, M., "Dynamic Modelling for Gasoline Direct Injection Engines," Keihin Technical Review, Volume 6, 2017.

7   Le Corre, S.D., Mason, B., Steffen, T., Winward, E., Yang, Z., Childs, T., Cary, M., and Lygoe, R., "Application of Multi-Objective Optimization Techniques for Improved Emission and Fuel Economy over Transient Manoeuvers," SAE Technical paper 2019-01-1177, 2019, DOI:10.4271/2019-01-1177.

8   Tulpule, P, Rezaeian, A., Karumanchi, A., and Midlam-Mohler, S., "Model Based Design (MBD) and Hardware In The Loop (HIL) Validation: Curriculum Development," American Control Conference, 2017, DOI:10.23919/ACC.2017.7963788.

9   Xiaohang, F., Papaioannou, N., Leach, F., and Davy, M.H., "On the application of artificial neural networks for the prediction of NOx emissions from a high-speed direct injection diesel engine," International Journal of Engine Research, Volume 22, Issue 6, Pages 1808-1824, 2021, DOI:10.1177/1468087420929768.

10   Azmin, F.M., Mortimer, P., and Seabrook, J., "Accurate Cycle Predictions and Calibration Optimization Using a Two-Stage Global Dynamic Model," SAE Technical Paper 2017-01-0583, 2017, DOI:10.4271/2017-01-0583.

11   Broatch, A., Bermúdez, V., Serrano, J.R., Tabet-Aleixandre, R., Gómez, J., and Bender, S., "Analysis of passenger car turbocharged diesel engines performance when tested at altitude and of the altitude simulator device used," ASME Journal of Engineering for Gas Turbines and Power, August 2019, 141(8), DOI:10.1115/1.4043395.

12   European Commission, "Commission Regulation (EU) 2017/1154 of 7 June 2017 amending Regulation (EU) 2017/1151 supplementing Regulation (EC) No 715/2007 of the European Parliament and of the Council on type-approval of motor vehicles with respect to emissions from light passenger and commercial vehicle (Euro 5 and Euro 6) and on access to vehicle repair and maintenance information, amending Directive 2007/46/EC of the European Parliament and of the Council, Commission Regulation (EC) No 692/2008 and Commission Regulation (EC) No 1230/2012 and repealing Regulation (EC) No 692/2008 and Directive 2007/46/EC of the European Parliament and of the Council as regards real-driving emissions light passenger and commercial vehicle (Euro 6)," Official Journal of the European Union, 2017.

13   Zulehner, W., "IPG RDX Test Generator," Documentation Version 8.1, 2019.

14   Helbing, C., Kohne, M., Kassel, T., Wietholt, B., Krause, A., Lohre, L., Gerhardt, N., and Eiglmeier, C., "Volkswagen's TDI-Engines for Euro 6d – Clean Efficiency for Modern Mobility," 41st International Vienna Motor Symposium, April 2020.

15   Bhandarkar, T., Satish, N., Sridhar, S., Sivakumar, R., and Ghosh, S., "Earthquake trend prediction using long short-term memory RNN," International Journal of Electrical & Computer Engineering, 9(2), Pages 1304-1312, DOI: 10.11591/ijece.v9i2.pp1304-1312.

16   https://circabc.europa.eu/d/d/workspace/SpacesStore/83a09cc8-7f8f-4ca6-9764-0b77da57d4cc/AGVES-2021-04-08-LDV_Exhaust.pdf, Accessed 12/110/2021.

Session S3.2 Advances for Ultraefficient ICEs

Optical Imaging for Understanding of Thermal Barrier Coated Piston Engine Performance

Chad Koci[1], Kenth Svensson[1], Glen Martin[1], Charlie Kim[1], Patrick Seiler[1], Felipe Caliari[2], John Saputo[2], Sanjay Sampath[2]

[1]Caterpillar Inc. – Technical Center, 14009 N Old Galena Road, Chillicothe, IL 61523, USA

E-mail: koci_chad@cat.com
Telephone: +(1) 309 675 6747

[2]Center for Thermal Spray Research, Stony Brook University – Stony Brook, NY 11794, USA

E-mail: felipe.caliari@stonybrook.edu
Telephone: +(1) 631 632 9512

Abstract. Thermal barrier coatings (TBC) applied to pistons have been a recently renewed research topic in the field of internal combustion engines. Single cylinder testing of a conventional C15™ Tier 4 final production steel piston and a TBC coated piston showed that the Yttrium stabilized Zirconia (YSZ) TBC did not significantly alter engine performance, with the TBC piston having slower combustion rates and higher criteria emissions. For deeper understanding, research continued by studying 3D-piston sections optically in a constant pressure vessel using photodiodes, four high-speed cameras (natural luminosity, CH*, and OH*), and visualization of the flame from two orthogonal directions. Particle Imaging Velocimetry (PIV) algorithms were adapted to perform Combustion Imaging Velocimetry (CIV) to aid in quantification of the observed visual combustion flow field differences. The optical work showed that the TBC piston flame development is slower, spatially different, with lower mixing energy for the TBC variant. Geometric profiles of engine pistons and optical vessel 3D-piston sections were measured using a Coordinate Measurement Machine (CMM), and surface roughness was measured with a stylus surface profilometer. CMM results showed that the TBC piston bowl had reasonable macroscopic accuracy, but the rim had a larger radius with less re-entrancy. A discussion of the results and analyses in relation to future TBC effort and direction concludes the work.

1. Introduction

Thermal barrier coatings (TBC) for internal combustion engines have been a topic of interest for many decades, with work dating back to the 1970's. The motivation for this was clearly reduced fuel consumption and potentially higher engine power density, enabled by the ability to achieve higher working temperatures while adhering to the same substrate temperature limits. A renewed interest was spurred by the work of Kosaka et al. [1] from Toyota Motor Company and a burst of research continued for the coming decade. The TBC review paper by Uchida et al. [2] provides an excellent overview of the TBC efforts to circa 2020 and ends with key steps surrounding measurements of detailed TBC surface temperature, spatial variation understanding, physical property measurements including the impact of deposits, and performing measurements without intrusive disturbance to the temperature field – all of these are challenging endeavours.

The primary assumption of the modern TBC efforts focuses on the idea of a rapidly changing surface temperature to reduce the temperature difference and reduce convective heat flux between the in-cylinder gases and the combustion chamber surfaces. This is attempted through alteration of the combustion chamber surface with a TBC which has low thermal effusivity $e = \sqrt{kC_p\rho}$ (where k is thermal conductivity, C_p is specific heat and density is ρ). Significant development of the initial TBC concepts utilizing a silica-reinforced porous anodized aluminum "SiRPA" showed promising results in reducing heat transfer and increasing engine efficiency at moderate loads [3]. This work also highlighted the detrimental impact of the elevated coating surface roughness on heat transfer, combustion, and flame development through imaging of spray impingement on a flat surface in a rapid compression machine. Kawaguchi et al. [4] furthered the importance and understanding of the detrimental roughness impact

and found that only coating the top of the piston crown, where there is much reduced spray-wall inter-action, produced superior efficiency results. The authors also extended this to the importance of a TBC for cold-start benefits in reduced NOx and fuel consumption attributed to lower heat transfer and there-fore lower fuelling required to idle the engine under minimal or idle loads. These results have significant relevance to engines with aluminum pistons but have a disconnect with heavy-duty engines utilizing steel alloys, typically used for temperature limit and strength improvements.

Research on a heavy-duty steel piston coated with a YSZ thermal sprayed TBC by Binder et al. [5] provided data on surface temperature using a 10 Hz phosphor lifetime thermometry technique with a 2-9 μm phosphor coating thickness. The work concluded that the maximum surface temperature variations between the steel and TBC piston were similar. Heat flux was reduced for the TBC piston due an elevated mean surface temperature; however, the resulting heat release was slower for the TBC piston and the net efficiency was reduced from the steel baseline. Limitations on the 10 Hz diagnostic forced an ensemble averaging and fitting approach to the temperature data. Recent diagnostic developments from Witkowski and Rothamer [6] may be a way to extend these types of surface temperature experi-ments to the kHz regime for high-precision individual cycle resolution, and spatial surface temperature mapping. Additionally, the assumption of the non-intrusiveness of ~1-10 μm thick phosphor coatings may need re-examining for measurements on steel/metal surfaces since the effusivity of these phos-phors are similar to TBC coatings, and therefore may be only well matched for TBC surfaces.

Andrie et al. [7] used newly developed non-thermal spray coatings, with very low effusivity, in a premixed SI engine application and found successes with +1% absolute brake efficiency improvements. This very different combustion application, from a diesel mixing-controlled system with strong spray-wall interac-tion, indicates promise for the temperature swing concept to be realized with significant impact. A coun-ter point to this is the finding that a permeable porous TBC used in a pre-mixed SI application by An-druskiewicz et al. [8] brought alternate combustion and efficiency loss pathways, highlighting significant problems with porosity and pre-mixed fuel. Additional recent SI application TBC research showed that increased wall temperature reduced the flame quenching distance and actually increased heat flux Ha-zhizume et al. [9], only very thin (<0.1mm) coatings with low conductivity and specific heat do not suffer from excessive charge heating, and only small efficiency benefit ranges (0.1-0.3%) were identified with a minor impact of TBC surface roughness on heat transfer and combustion Broatch et al. [10, 11].

Other TBC piston relevant works include those of Gingrich et al. [12], where only smoothed thermal sprayed TBC pistons showed efficiency benefits, and Somhorst et al. [13] where a robust statistical testing and analysis found no efficiency benefits with detriments attributed to increased TBC surface roughness. On the topic of TBC durability, Koustakis et al. [14] developed a TBC elastic strain energy mechanics model for coating delamination prediction following prior work on an analytical solution to unsteady heat conduction in TBC applications [15]. A recent work from Kawaharazuka et al. [16] showed high promise by utilizing an alternate approach to create a rapidly changing piston surface temperature without detrimental increases in roughness. A highly polished stainless steel piston bowl was produced with a YSZ TBC on the under-crown cooling gallery. This novel heat insulation increased efficiency by ~1% (56.1 to 56.8% ITE) at an extremely high cylinder pressure and already very efficient operating point. The authors additionally point out the importance of the outstanding convective insula-tion properties of soot layers, which develop on combustion chamber surfaces, and the high radiative absorption of soot which may allow a rapid and large surface temperature swing. The authors noted increased efficiency the longer the engine was run, with further soot layer accumulation.

The many renewed attempts at TBC application to a mixing controlled diesel combustion system have been challenged by many aspects. Unclear surface temperature and heat transfer phenomena, fluid dynamic and boundary layer changes imposed by surface roughness changes, slowed combustion rates, unclear impacts of exposed porosity, and the precise role of soot deposits in heat transfer are the major aspects of interest. For improved TBC performance and industry adoption, the following are some suggested areas of needed focus:

- Overcoming surface roughness increases from TBC materials and application methods
- Understanding combustion system intrusiveness of the TBC application
- Validating the coating durability
- Quantifying the role of soot deposits, exposed porosity, and temporal evolution
- Measuring 3D spatial impacts on local heat transfer

- Improving the coating process accuracy and cost for complex diesel piston geometries

This work attempts to add some insight into the changes TBC surfaces impose on a heavy duty mixing controlled combustion system using single cylinder engine testing and a 3D piston combustion vessel optical diagnostic.

2. Experimental Setup

For the TBC efforts within this experimental setup the thermal properties of the coating layers were measured using a commercially available (DXF 900, TA Instruments, New Castle, DE, USA) standardized thermal flash method (ref ASTM E1461) along with Archimedes principle and a precision mass balance. Thermal diffusivity and specific heat were simultaneously measured using the former technique and used along with density measured through the latter to calculate thermal conductivity, taken as the product of the three directly measured variables.

The coatings used were derivatives of TBCs used in gas turbines. A NiCrAl based "bond-coat" alloy (443NS, Oerlikon-Metco, Westbury, NY, USA) was applied directly to the component to increase adhesion of the ceramic TBC, grade the transition of thermal and mechanical properties, and aid in oxidation resistance. Afterwards an insulating Yttria-Stabilized Zirconia "top-coat" layer (SG204, Saint-Gobain Coating Solutions, Worcester, MA, USA) toughened with the inclusion of 5% volume of the metallic bond-coat phase was applied. Table 1 lists the nominal material properties relevant to the coating and piston efforts, while
Table 2 lists average piston combustion bowl surface roughness as measured by a 1D stylus surface profilometer and are averages of measurements over two different azimuthal locations for each bowl radial location. A clear increase for the TBC pistons can be seen and is in the range from 2-5 µm Ra, which is rougher than the steel pistons but in the same range as other reported piston TBC attempts [12,13].

Table 1. Material and nominal properties at 300K reference temperature

Layer	Material	Thickness mm	Conductivity W/m-k	Density kg/m^3	Vol. Heat Capacity kJ/m^3-K	Thermal Effusivity W-s$^{0.5}$/m^2-K
Bond Coating	NiCrAl	0.100	4.85	7120	2814	3694
TBC Topcoat	95/5% YSZ/NiCrAl	0.225	0.91	5299	1864	1299
Steel	4140	N/A	43.4	7850	3423	12187
Stainless Steel	304	N/A	16.2	8000	4000	8050

Table 2. Piston Surface Roughness, Ra

Component	Material	Center µm	Bowl µm	Chamfer µm	Crown µm
SS Optical-Piston	Stainless Steel	1.2	1.1	0.8	0.6
Steel Piston	Steel	1.7	1.3	1.0	1.2
TBC Optical-Piston	Polished TBC Topcoat	2.1	2.2	4.6	3.1
TBC Piston	Polished TBC Topcoat	2.2	5.3	3.4	4.8

2.1 TBC Application Process

A direct current (DC) argon-hydrogen air plasma spray (APS) process (F4MB, Oerlikon-Metco, Westbury, NY, USA) configured with a 6 mm nozzle and a 90° 1.8 mm injector was used to fabricate all coatings described in this work. Before deposition, all surfaces were degreased and grit blasted at 80 psi from a 125 mm distance using 24 mesh alumina grit. Primary and secondary gas flow rates were held at 45 and 6 NLMP with a current setpoint of 550 A operating at 57 V. Carrier gas flow rates were set between 2.5 and 4 NLMP for the bond and top-coat layers and were optimized on a per-run basis to ensure consistent deposition between components.

Coatings on both optical-piston sections and C15™ Tier 4 piston crowns were produced by traversing the spray torch along the component centerline normal to the crown geometry while rotating the component. To ensure microstructural uniformity and aid in the control of thickness buildup the surface velocity was kept uniform as the torch moved towards the component center. This was

accomplished through trial and error by varying both the rotational speed of the component and the torches traverse speed. To aid in rapid toolpath development mock component geometries were produced that could be easily attached to the crown of a production piston. These mock geometry components could then quickly be destructively tested to confirm the coating uniformity. This process is shown schematically in Fig. 1. The same optimized toolpath was then used to deposit coatings on the optical-piston sections by fixturing them in a manned identical to the production pistons.
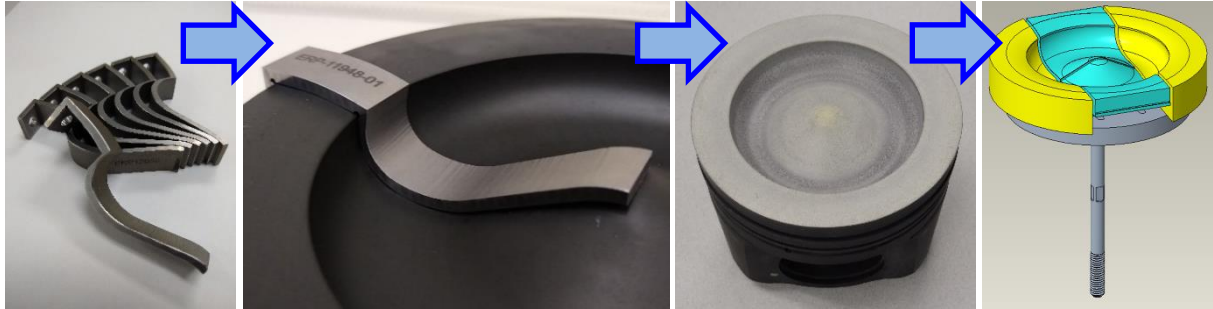

Fig. 1. TBC application process utilizing profile strips for spray setup and ease analysis

2.2 Single Cylinder Test Engine

The experimental methodology for the present work centered on Single Cylinder Test Engine (SCTE) experiments. A heavy-duty diesel SCTE platform was used based on a Cat® C15™ (15 L) production engine, but with a modified cylinder head, valvetrain, and fuel injection system. The geometric specification for the engine is listed in Table 3 with a nominal displacement of 2.5 L/cylinder.

Table 3. Single Cylinder Test Engine Nominal Specifications

	SCTE
Displaced volume	2.53 L
Bore	137.19 mm
Stroke	171.45 mm
Connecting Rod	270.76 mm
Compression Ratio (nominal)	16.9:1
Piston Bowl Shape	Conventional Open
Valves	4-valve
Swirl Level	< 1 Swirl Number
Valve Train	DOHC
Fuel Injector	Common Rail: 7-hole/ 258 µm / 130° SA / 4.9 kg/min

The engine was coupled to a General Electric DC Motoring Dynamometer. Torque was measured at the end of a 21" arm using an Artech 90515 load cell. A central low speed data acquisition system was used to interface between all instrumentation in the single cylinder laboratory and recorded temperature, pressure, flow, and emissions measurements at 1 Hz. An AVL Indicom high speed data acquisition system provided crank angle resolved cylinder pressure, intake manifold pressure, exhaust manifold pressure, and engine speed. The encoder resolution was 0.1 crank angle degrees (CAD). Cylinder pressure was measured with a Kistler 6125C piezoelectric transducer connected to an AVL Micro IFEM charge amplifier that used a 100 kHz low pass digital filter and cyclic drift compensation. Kistler 4045a piezoresistive transducers were used to measure intake and exhaust manifold pressures. 200 consecutive cycles of high speed data were recorded at each data point.

A schematic of the single-cylinder engine laboratory is shown in Fig. 2. The engine air handling system allows for complete control of the intake pressure, intake temperature, and exhaust pressure. A Horiba MEXA 7100 DEGR was used to measure gaseous emissions including NO, NO_2, CO, total hydrocarbons (THC), O_2, intake CO_2 and exhaust CO_2. Particulate emissions were measured with an AVL 415S smoke meter.
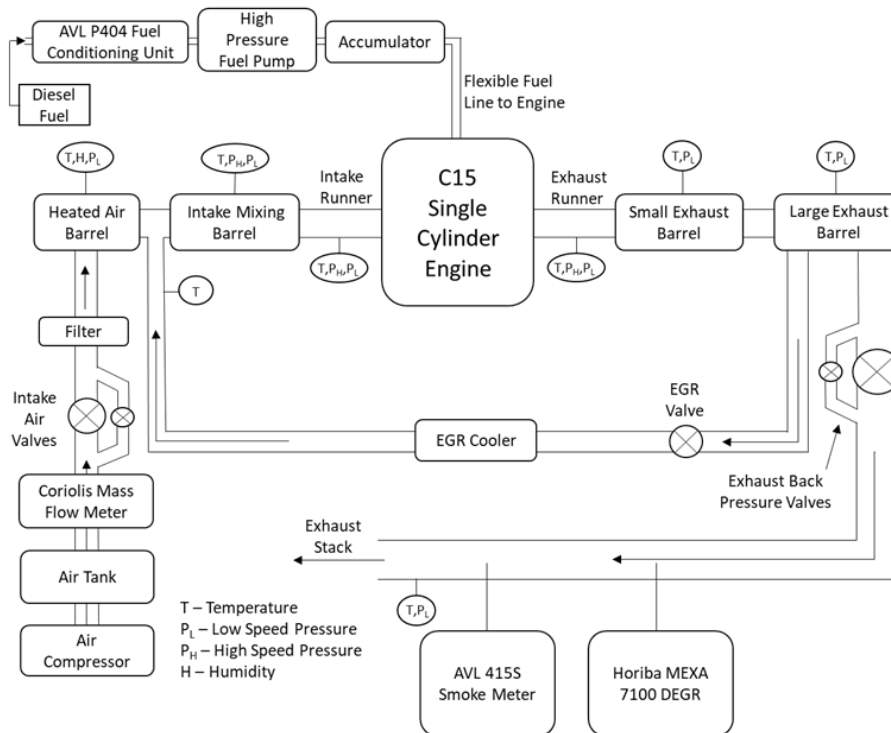
Fig. 2. Schematic of Single Cylinder Engine Laboratory

The experimental pistons were measured using a coordinate measuring machine for specific interest in the resulting bowl profile shape. Fig. 3 overlays the profiles between the optical TBC, single cylinder test engine TBC, and production steel piston in the left of the figure. The right inset plot compares the optical steel and TBC profiles to the target production piston. The macroscopic bowl profile shape is good, while there is notable deviation at the corner with the TBC variants having less reentrancy and more rounding. The challenge of thermal spray TBC bowl accuracy was noted by Binder et al. [5], and the present work looks to be improved despite the remaining inaccuracies. The impact of this deviation on combustion and emissions performance will be discussed in the results sections.
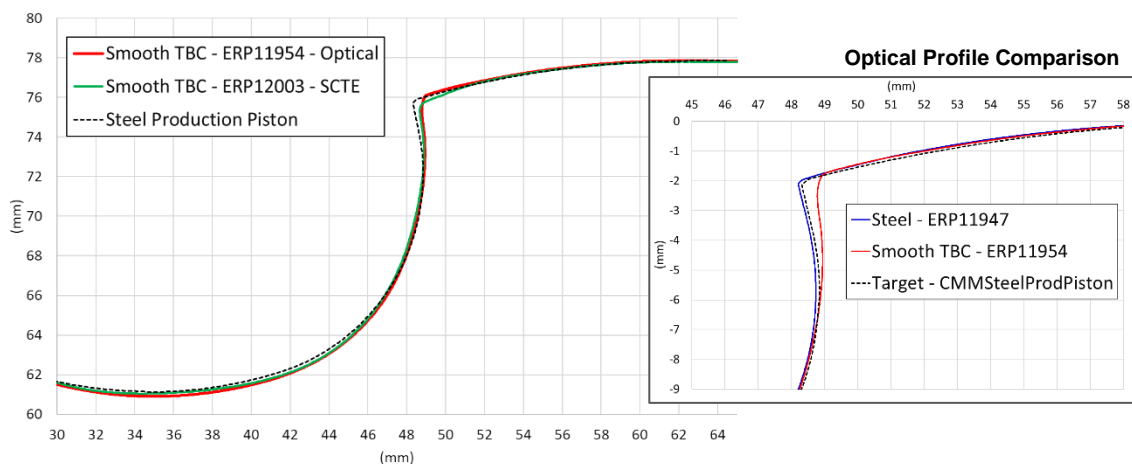

Fig. 3. Coordinate Measuring Machine piston bowl profile comparison plots showing the steel and TBC differences between the SCTE and the optical vessel

2.3 High Temperature Pressure Vessel

Designed to enable repeated observation of fuel sprays, the High Temperature Pressure Vessel (HTPV) employed in this work can reach steady pressures of 150 bar and temperatures of 1100 K

uniformly across the inner core of the test section [17]. 3D piston sections were mounted in the HTPV to enable study of the combusting fuel jet interaction with both production-similar and TBC coated surfaces. This setup shown in Fig. 4, enabled orienting the fuel-jet relative to the piston bowl to match the 130° included angle utilized in engine testing [18]. Utilizing an on-axis single-orifice injector tip required holding the piston section base with a 25° angled block. The overall 3D piston section optical setup includes a flat fused-silica window to represent a simplified cylinder-head surface. The stainless plate that holds the window also simulates the crevice volume above the top piston ring, see Fig. 5. The 3D piston section was sized to represent geometry equivalent to a C15 engine fitted with a 6-hole injector tip. Two linear adjustments allow for sliding the 3D piston section away from the injector tip while simultaneously maintaining the injector to cylinder head offset. This allows for setting the equivalent crank-angle positioning of the 3D piston section. For the current study the 3D section is offset by 2 mm to simulate a 10 CAD BTDC/ATDC position.
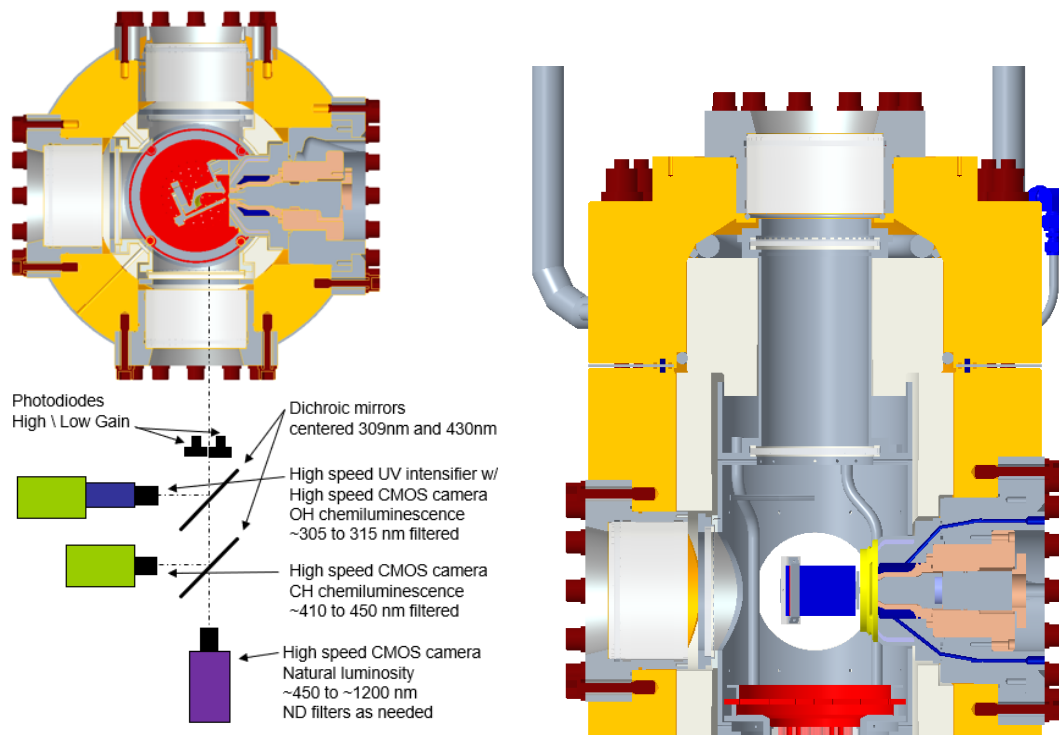
Fig. 4. High Temperature Pressure Vessel experimental and optical setup
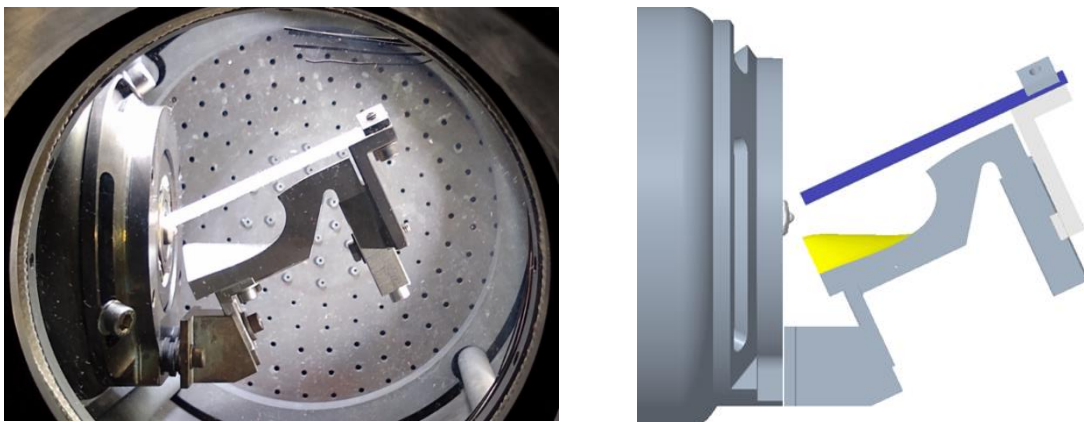
Fig. 5. Physical 3D-Piston Setup

Four high-speed cameras and two photo diodes allowed for observation of the combustion during the interaction of the fuel-jet with the 3D piston section and glass cylinder head. One camera with a CH* (430 nm ±20 nm) filter provided a profile view, and the other three cameras (NL, CH*, OH*) provided a top view of the piston bowl through the transparent cylinder head as shown in Fig. 4.

The HTPV was operated with an ambient pressure of 120 bar for all testing, corresponding approximately to cylinder pressure at start of combustion (SOC) for the engine testing. The ambient flow was 40 m^3/h with 18% O_2 concentration. Testing of the 3D piston sections was accomplished by varying ambient temperature, injection pressure, and injection duration as shown in Table 4 below. The final bowl profile for the TBC coated piston differs slightly from the production bowl profile targets as shown in Fig. 3. Detailed analysis is focused on the 975 K, 200 MPa, and 840 µs condition targeting a hydraulic injection duration of 1900 µs.

A single-orifice on-axis fuel injector was used in the HTPV. The orifice diameter was 239 µm which was the closest single-orifice available to the engine injector orifice diameter. Because of it having a single-orifice fuel injector tip, the rate shape was very square with little front-end ramp.

Table 4. Summary of HTPV test conditions.

Temperature (K)	Injection pressure (MPa)	Injection duration (µs)
875	100	410 - 1050
875	200	340 - 840
975	100	410 - 1050
975	200	340 - 840

2.4 Engine Operating Conditions

In an effort to evaluate the benefits of TBC piston over standard steel piston, high load settings at various engine speeds were selected as shown in Table 5 below.

Table 5. Engine Test Conditions

Engine Speed	rpm	2100	2100	1800	1800	1425	1425
EGR	%	18	0	20	0	14	14
Fueling	g/min	317	317	231	231	265	209
Rail Pressure	MPa	250	160	180-220	140-180	160	180-220
Torque	N-m	361-427	356-416	297-373	315-375	486-532	387-434
Inj Duration	° (deg)	19.9	25.8	15.2-17.4	17.3-20.2	21.3	13.8-15.5
Intake Temp	°C	66	50	59	50	53	63
Intake Pres	kPa-a	362	333	334	298	411	287
Exhaust Pres	kPa-a	419	433	389	349	468	310

These test settings are representative of typical EGR levels in various engine applications and existing state of art turbochargers on heavy duty diesel engines. At each test condition, the full range of engine operation was realized by changing injection timings to achieve peak cylinder pressure and to stay within the end of injection limit at constant fueling.

Data point 2 in Table 6 below has been used in the detailed analysis of steel and TBC pistons.

Table 6. Test Data – Steel vs. TBC Piston

Data Point		2	2	2
Piston		Steel	Steel (Repeat)	TBC
Engine Speed	rpm	1800	1800	1800
EGR	%	20	20	20
Fueling	g/min	231	231	231
Rail Pressure	MPa	220	220	220
Torque	N-m	353	355	347
Start of Injection	° crank angle (ATDC)	-1.85	-1.7	-1.71
End of Injection	° crank angle (ATDC)	13.38	13.58	13.56
Injection Duration	° crank angle	15.23	15.28	15.28
Intake Runner Temperature	°C	59	59	59
Intake Runner Pressure	kPa-a	334	334	334
Exhaust Runner Pressure	kPa-a	389	389	389

3. Results and Analysis

3.1 Single Cylinder Test Engine

A detailed view of the in-cylinder combustion processes is shown in Fig. 6 for the second SOI timing point at an 1800 rpm 1900 kPa IMEPn mode. The steel piston and TBC piston cases are shown with a repeat of the steel piston. The lower pressure of the TBC case is attributed to a slightly lower measured geometric compression ratio of 16.77 vs. 16.98 and a slightly lower pressure at IVC for the same nominal IMAP boundary condition. Ideally the compression pressure would be better matched, but the authors do not believe this variance impacts the result trends significantly. Evidence toward this is the repeat steel piston case which has good peak heat release rate consistency despite cylinder pressure variance originating from simply rebuilding the engine and remeasuring.

Differences in heat release rates can be seen with the TBC piston having lower peak rates in the apparent heat release rate (AHRR) plot and a slower 50-90% burn in the cumulative AHRR plot. A slower fuel-air mixing system can be inferred from these immediate heat release observations, but some further analysis rigor can help with detailed and fair comparisons. A useful parameter which consolidates the impact of the heat release rate, duration, shape and phasing in the cycle is the Heat Release Rate Efficiency in (Eqn. 1) and is similar to other calculations of degree of constant volume combustion [19] or effective expansion ratio 20].

$$Heat\ Release\ Rate\ Efficiency = \frac{\int_{soc}^{eoc} \frac{dQ}{d\theta} \eta_{otto(\theta)}\, d\theta}{\int_{soc}^{eoc} \frac{dQ}{d\theta} d\theta} \qquad \text{(Eqn. 1)}$$

This utilizes a simple Otto cycle efficiency calculation of the instantaneous expansion ratio (V_{max} / $V(\theta)$) in (Eqn. 2),

$$\eta_{otto(\theta)} = 1 - \frac{1}{\left(\frac{V_{max}}{V(\theta)}\right)^{\gamma-1}} \qquad \text{(Eqn. 2)}$$

where γ is the ratio of specific heats computed from the heat release analysis. Integration of the heat release dQ/dθ weighted Otto cycle efficiency, over the combustion duration from SOC to end of combustion (EOC), provides a single metric to compare and contrast engine cycles with heat release, compression ratio, and expansion ratio variation. This heat release rate efficiency will be used for comparisons in the following figures.

The difference between the fuel input energy and the cumulative AHRR, at the end of the closed cycle, in Fig. 6 is shown and is one way to define the in-cylinder heat transfer. Between the three cases there are differences in this heat transfer metric, but it is small and susceptible to the quality of the cylinder pressure measurement. Further plots in Fig. 7 and Fig. 8 compare larger data sets and differences.

Fig. 7 shows the emissions and engine performance comparisons for the timing sweep which includes point #2 from Table 6 and Fig. 6. The TBC piston has a slightly shifted-left NOx/ISFC response, which is expected due to the slower heat release rates, and it produces the highest particulate. CO emissions go generally with the particulate emissions while hydrocarbon emissions are very low for all cases. The volumetric efficiency of the TBC piston is the lowest and indicates a charge air heating phenomena classic to the historical TBC efforts in diesel engines. The tighter collapse of the ISFCn plotted against heat release rate efficiency, compared to when it is plotted against CA50, shows the usefulness of this method for normalization – clearly no efficiency benefit is observed for the TBC piston.

The final two plots in Fig. 7 attempt to describe the differences in heat transfer with the in-cylinder heat transfer metric previously described, and a direct measurement of oil heat rejection through oil flow and oil temperature increase. The TBC piston in-cylinder heat transfer goes between the two steel piston data sets with a flatter trend with SOI/CA50. However, the TBC piston oil heat rejection matches the steel piston repeat data set very closely. The lower steel piston oil heat rejection, relative the repeat steel piston, was a result of a misaligned piston cooling oil jet and the discovery of produced the need for the repeated steel piston data. This provides a useful discussion point in that if this magnitude of oil heat rejection reduction from a cooling system modification could not produce measurable efficiency differences, similar reductions in heat transfer from a TBC likely would also not produce measurable efficiency differences. The caveat here being that the actual surface temperature change or "swing" from the TBC should be larger than that imposed by a simple cooling change, and theoretically (by 0D

and 3D models) should be able to reduce heat transfer more effectively. A lack of sufficient experimental TBC surface temperature understanding confounds this issue. A final point is that only adding thermal resistance to one of the multiple in-cylinder heat transfer paths/surfaces (i.e., just the piston) may be insufficient to significantly reduce or change the total heat transfer, as the heat may find other less resistive paths.
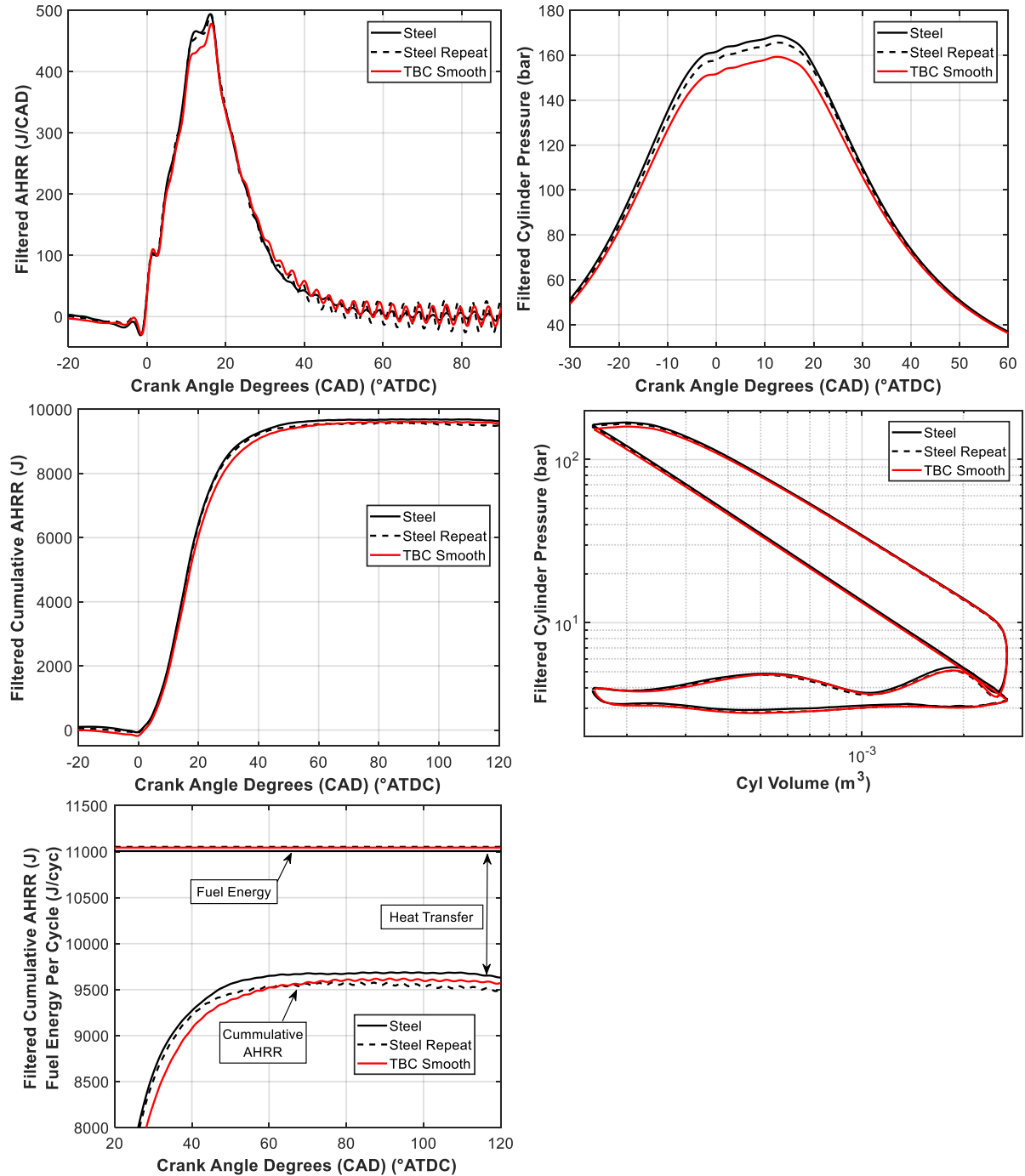
Fig. 6. SOI Point #2 from Table 6, 1800 rpm, 231 g/min fueling (nominally 1900 kPa IMEPn), 24.5 AFR, 20% EGR, 220 MPa rail pressure high-speed data
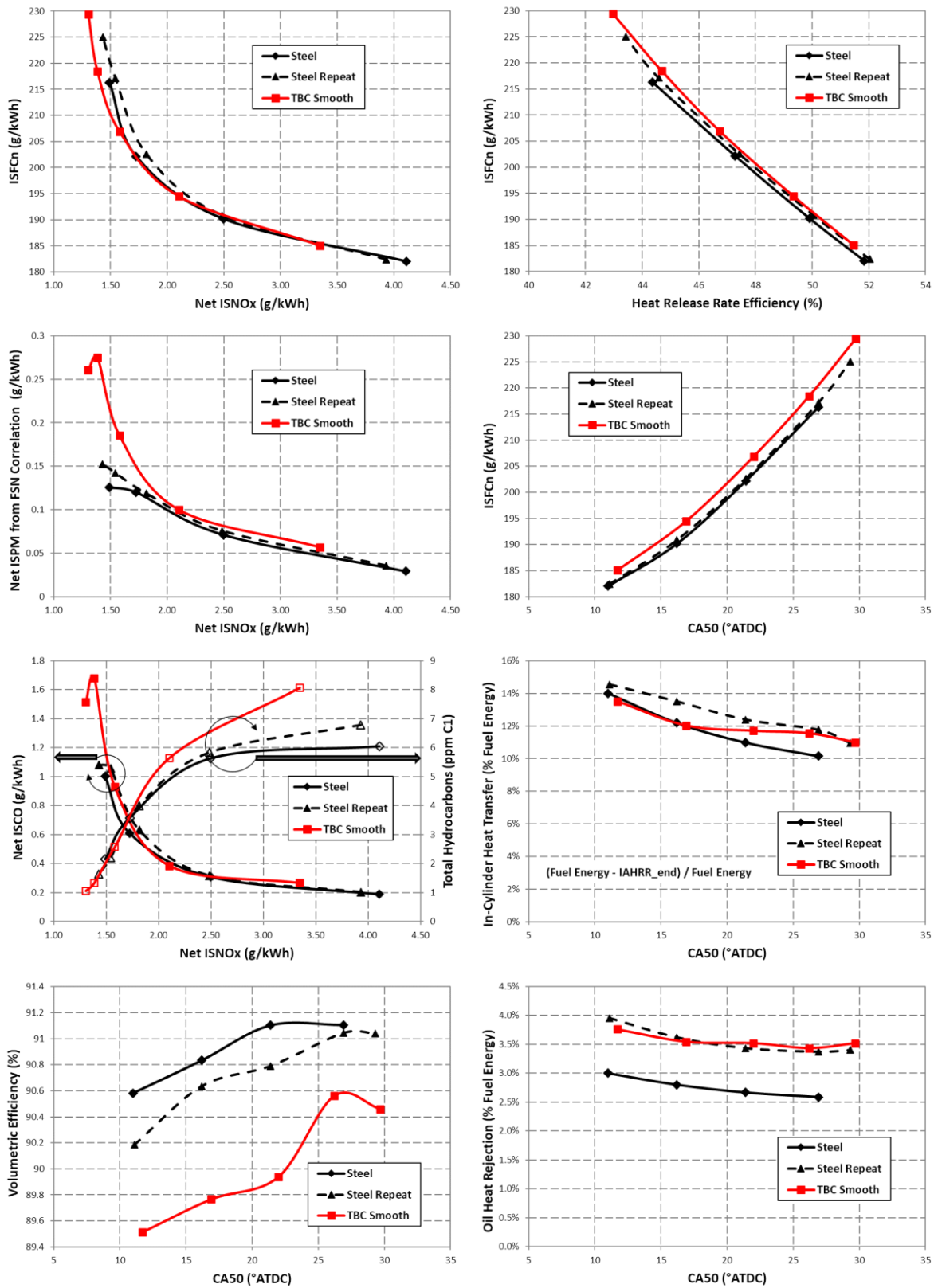
Fig. 7. 1800 rpm, 231 g/min fueling (nominally 1600-2000 kPa BMEP), 24.5 AFR, 20% EGR, 220 MPa rail pressure, timing sweep low-speed data

The data plotted in Fig. 8 attempts to provide a macroscope view of the general efficiency and heat loss trends from the present single cylinder engine experimental campaign. All the comparable data between the steel (repeat) piston and TBC piston are overplotted and show very similar trends and scatter. The in-cylinder heat transfer plot agrees with the data for oil and total heat rejection, and these are not shown

for brevity. Fig. 8 solidifies the conclusion that there was no obvious fuel consumption or heat transfer differences confidently observed and motivated the need toward further fundamental investigation into combustion system differences imposed by the addition of the TBC piston surface. It should be noted that there are a small number of points, similar to Fig. 6 and Fig. 7, where a possible heat transfer reduction could be argued, but the overwhelming trend is one of similar heat transfer for a given heat release efficiency. Toward this fundamental understanding, the following sections will discuss the optical efforts in the high temperature pressure vessel.
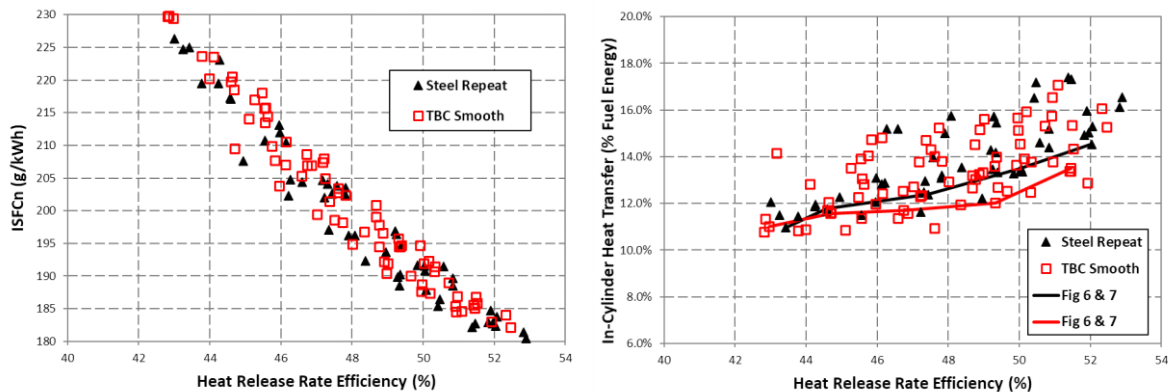
Fig. 8. All comparable operating points (1425-2100 rpm and 1500-2800 kPa IMEPn) showing no obvious fuel consumption (ISFCn) or macroscopic heat transfer difference between the steel and TBC pistons in the SCTE.

3.1 High Temperature Pressure Vessel

Fig. 9 shows an alignment image from the TCH* camera where the single-orifice fuel injector tip is on the left and the 3D piston section is rotated such that the fuel jet mimics a 130 deg included angle. The 3D piston section is located 2 mm below the TDC position, which is the 10 CAD BTDC/ATDC position to represent a 20 CAD time window. A fused silica window, seen above the 3D piston section, represents the cylinder head positioned correctly relative to the fuel jet.
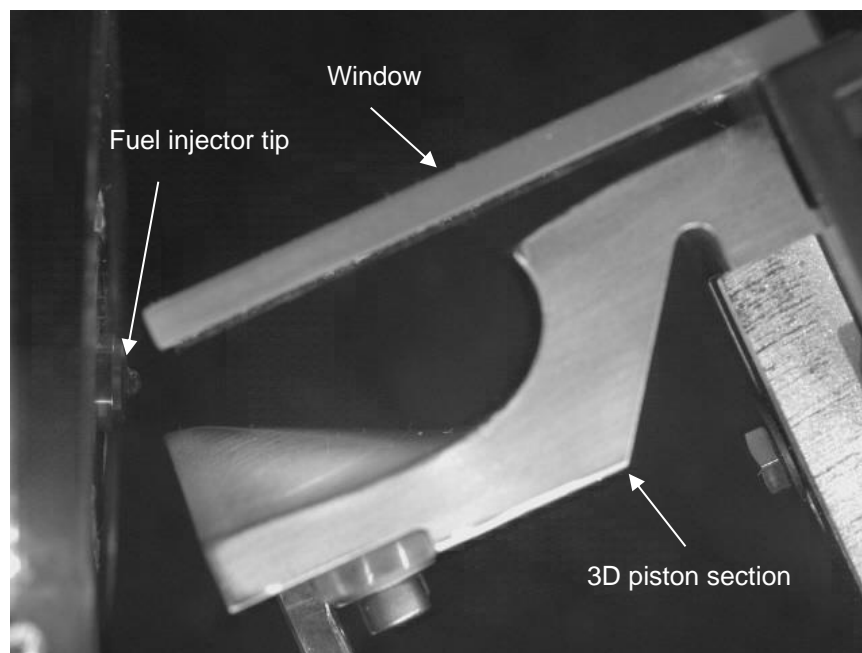
**Fig. 9.** TCH* camera view of 3D piston section installed in HTPV

Fig. 10 shows the image in Fig. 9 after it has been masked and false-colored according to light intensity. The mask generated from the alignment image is then applied to all images taken with that hardware setup. The masking reduces CIV processing time, improves the CIV results, and it makes it easier to view the CIV results.
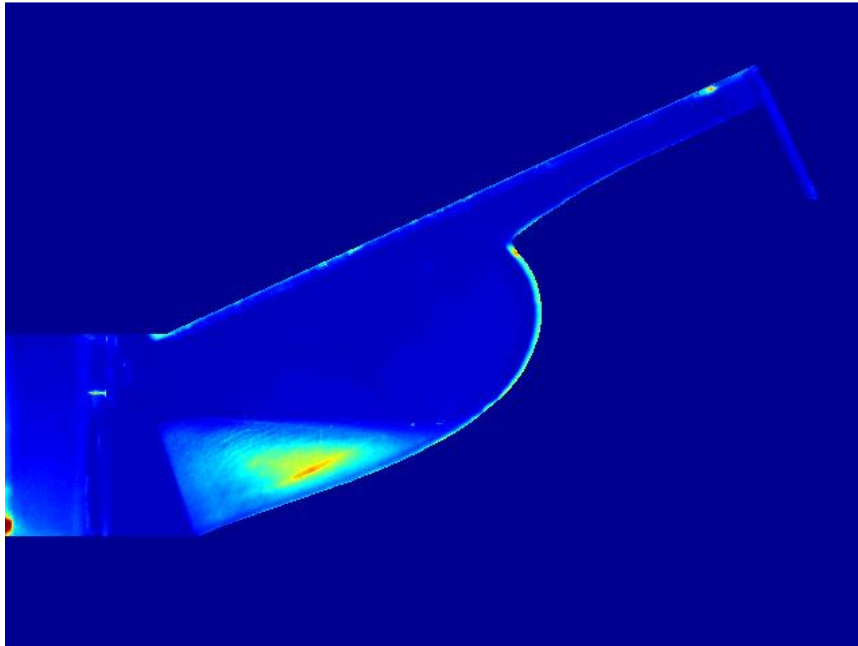
Fig. 10. False-colored TCH* camera view with mask applied for CIV processing

Fig. 11 shows a sequence of averaged raw images from the TCH* camera where the ambient temperature is 975 K, the injection pressure is 200 MPa, and the commanded injection duration is 840 μs. The false-color scaling is the same for all images and each image shows an average of four injections. The left column shows the metal piston, and the right column shows the smooth TBC piston. The columns are time aligned where the inserted text shows the time after start of injector current. The first time is when the flame front has come out of the piston bowl, has filled the squish region, and is starting to move back toward the injector along the cylinder head. The second time is when the flame is moving along the head toward the injector, and it is also starting to escape the volume between the piston and the window indicating that it is the time of jet-jet interaction. The third time is when the flame front is very near the lift-off length, and it can be clearly seen that the flame in the metal piston has moved closer to the injector. This is due to the more rounded piston bowl lip that the smooth piston has. The fourth time is at end of injection. The flame in the metal piston bowl exhibits a brighter flame consistently, which may be another indication of faster mixing.
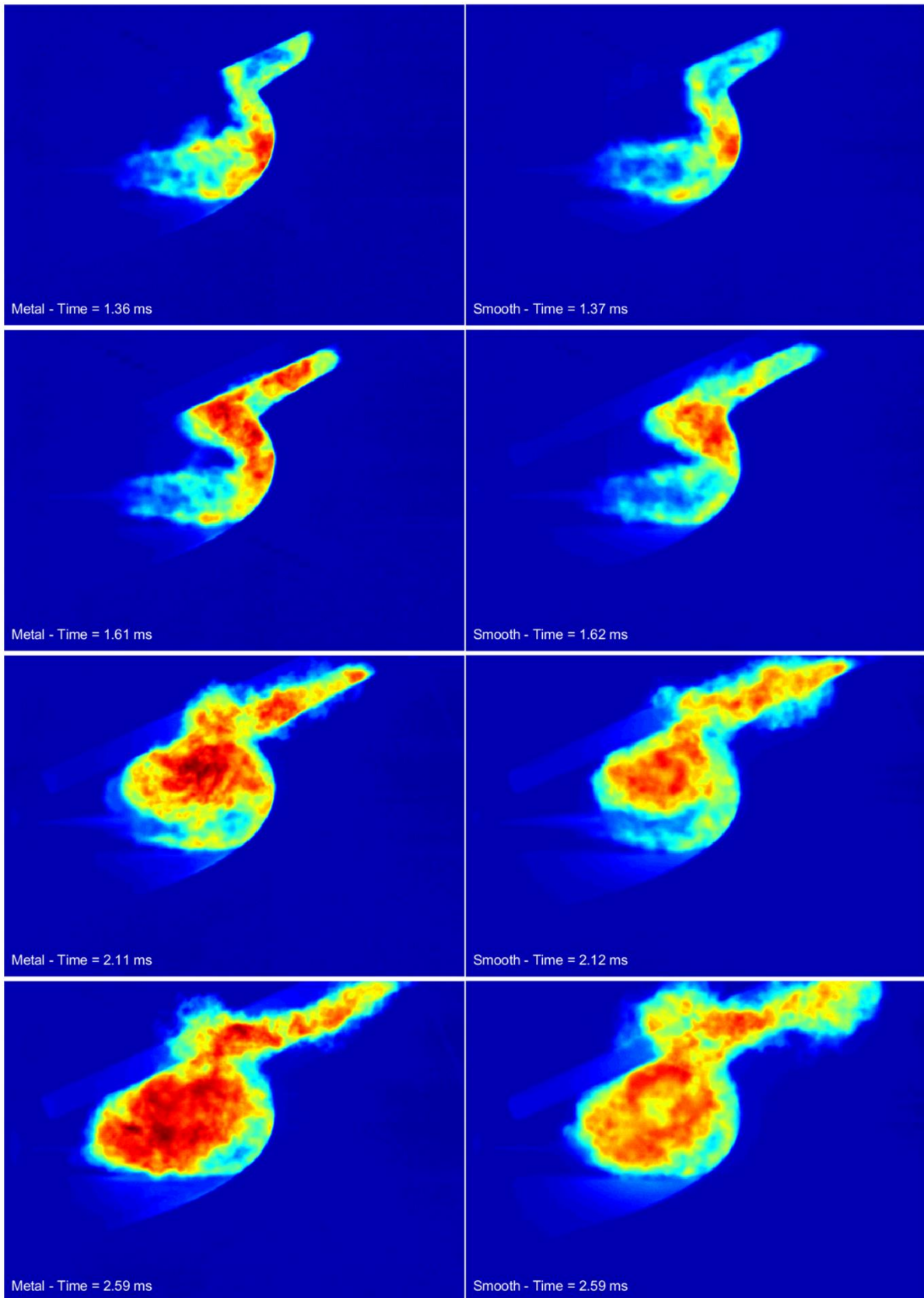
Fig. 11. Comparison of flame propagation for the metal (left) and smooth TBC (right) piston bowl sections at 4 times. Each image is an average of 4 shots. 975 K, 200 MPa, 840 µs.

3.3 CIV image processing

Particle Imaging Velocimetry techniques were used to process the combustion images even though no seed particles were used. The assumption was that the sooty, bright flame envelope would have distinctive spots that would move from one image to the next and that the PIV code could track those, hence Combustion Imaging Velocimetry (CIV). The groundwork for CIV in optical engines was laid with Dembinski et al. [21-22] and expanded and proliferated by others such as Zha and Busch et al. [23-24] It should be noted that under these conditions, using a 239 μm orifice, the flame is optically thick. This means that the camera images the first surface closest to the camera, and therefore the CIV processing is based on the edge of the flame. The freely available MATLAB code PIVlab was used [25].

The raw high speed TCH* movies were pre-processed in MATLAB before being imported into PIVlab. The pre-processing consisted of applying a mask, a sharpening filter, and then the intensity was stretched from the movie minimum to the movie maximum intensity values. The sharpening and the intensity stretching was done to maximize contrast. Finally, it was saved in the MPEG4 format which could be imported into PIVlab.

Fig. 12 show plots of the mean correlation coefficients and the mean of correlation coefficients greater than 0.5 as a function of time for the metal and smooth piston bowl sections. The plots are a good representation for other operating points. This suggests that there is good confidence in the velocity results from the CIV image processing. The regularly appearing outliers (every 0.5 ms) are artifacts of the processing and should be ignored.
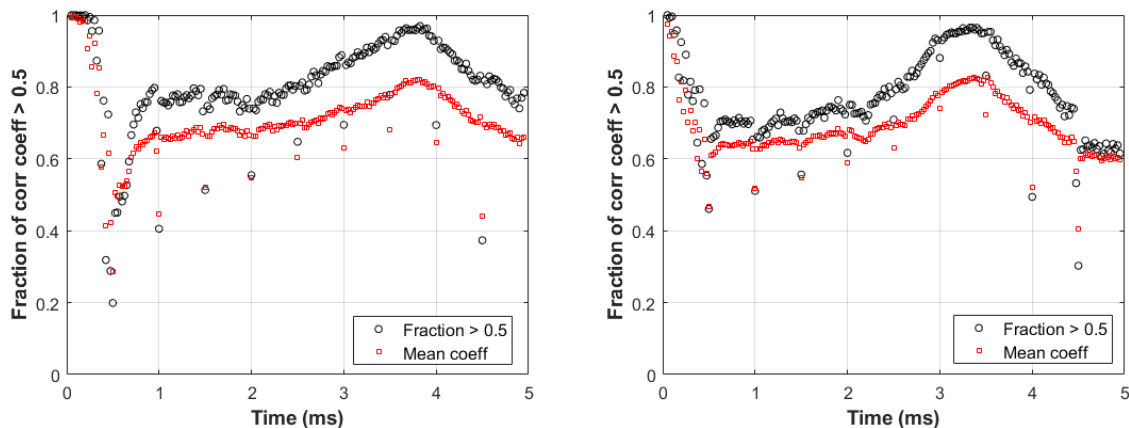
Fig. 12. Correlation coefficients for the metal (left) and smooth TBC (right) piston bowls at 975 K, 200 MPa, 840 us. In general representative for all cases.

Fig. 13 shows a calculated velocity field from CIV image processing at time 2.1 ms at 975 K, 200 MPa, 840 μs. The velocity field is calculated from shot 1 and is superimposed on a false-colored image from shot 1. When displaying the velocity field, a moving average in time was also applied to smooth it out and make it look more consistent. There is a very clear vortex and a clockwise rotation. Peak velocities reach about 60 m/s for the 200 MPa injection pressure. The vortex forms when the flame front reaches the cylinder head and lasts until the flame is burned out.

Pastor et al. [26] proposed a numerical method using the curl of the velocity field to locate the center of the vortex. This method was applied to the CIV velocity field in the hope of tracking the vortex center in time but did unfortunately not yield a good result for this data.
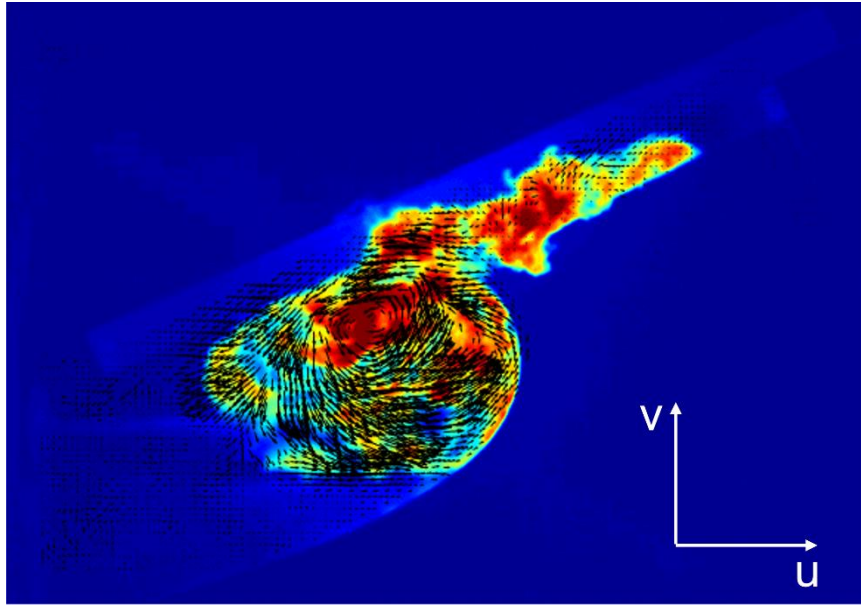
Fig. 13. Velocity field superimposed on false-colored TCH* image of individual shot at 975 K, 200 MPa, 840 µs. Metal piston at 2.1 ms after start of injector current.

While the flame clearly expands along the piston bowl in the azimuthal direction (in and out of the image), most of the momentum is in the direction of the spray. Therefore, it is assumed that the majority of the momentum is illustrated by the two-dimensional velocity field shown in Fig. 13. From this idea the apparent chamber mixing energy in the velocity field can be calculated as shown below in Eqn. 3.

$$Apparent\ chamber\ mixing\ energy = \sum \frac{1}{2}(u^2 + v^2)$$
(Eqn. 3)

Fig. 14 shows the calculated apparent chamber mixing energy and its u and v components for the metal and smooth piston sections as a function of time. The apparent chamber mixing energy is only calculated inside the masked area. The u component is clearly larger which makes sense since that is the direction of the fuel jet. It is also clear that the metal piston exhibits a greater mixing energy, mostly due to the faster penetration in the u direction as the v components are very similar. This is numerical evidence of the brighter flame which was visually seen in Fig. 11.
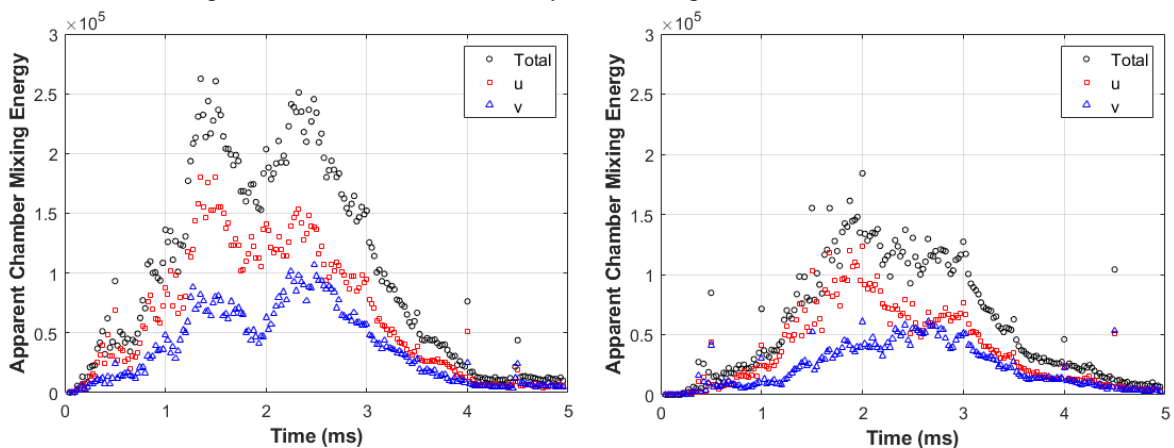
Fig. 14. Apparent chamber mixing energy for the Metal (left) and Smooth (right) piston bowl sections at 975 K, 200 MPa, and 840 µs.

Fig. 15 and Fig. 16 show side by side comparisons between metal and smooth for the lower injection pressure of 100 MPa, and a shorter duration of 355 µs. Note that the scales are the same for all 6 plots. One variable at a time is varied from the focus case of 975 K, 200 MPa, and 840 µs. The comments for Fig. 15 generally are true for Fig. 15 and Fig. 16. Note that the lower injection pressure of 100 MPa shown in Fig. 16 also shows a lower apparent chamber mixing energy.
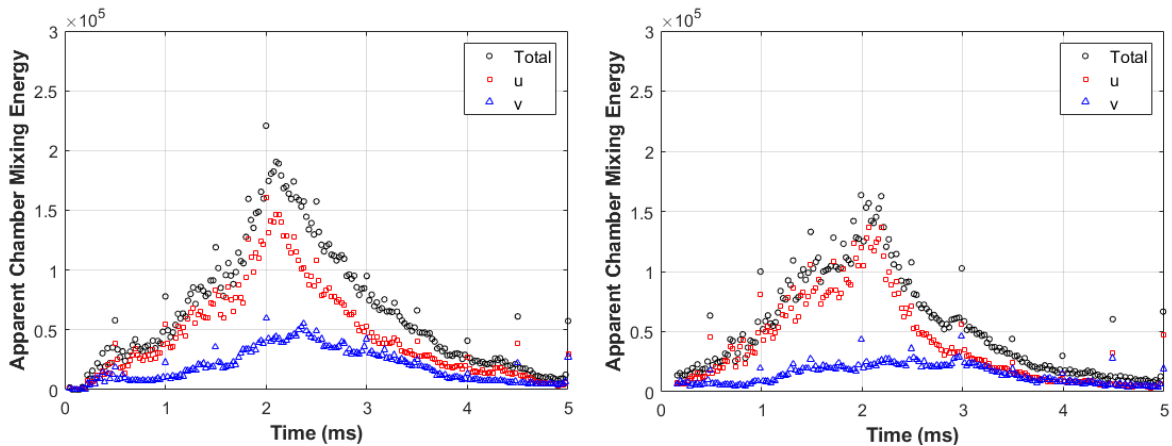
Fig. 15. Apparent chamber mixing energy for the Metal (left) and Smooth (right) piston bowl sections at 975 K, 100 MPa, and 1050 µs.
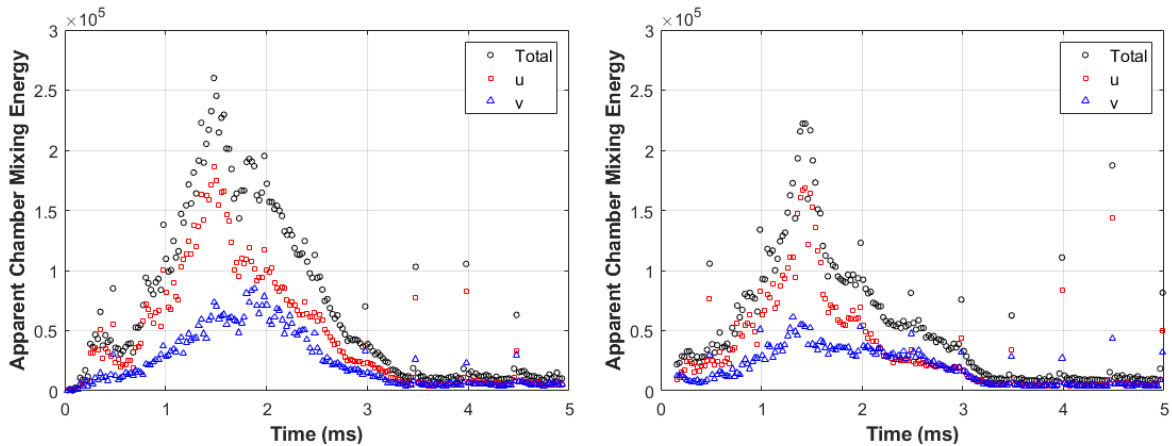

Fig. 16. Apparent chamber mixing energy for the Metal (left) and Smooth (right) piston bowl sections at 975 K, 200 MPa, and 355 µs.

Conclusions

In the present effort to measure and understand the impact of adding a TBC to a diesel engine piston the following conclusions were found. These were obtained using single cylinder engine testing and optical imaging diagnostics in a continuous flow high temperature pressure vessel.

- High-load engine performance, combustion and emissions measurements between a steel and a smoothed TBC (YSZ-type coating) piston showed the TBC piston had slower heat release rates, elevated PM and CO at retarded timings, and similar single digit ppm hydrocarbons. Comparing performance based on net ISNOx and Heat Release Rate Efficiency indicated that the smoothed TBC piston behaved like a slower mixing system with a naturally lower NOx response.
- No reduction in in-cylinder heat transfer or engine/piston oil heat rejection could confidently be measured at times with normalized heat release performance. Repeat measurements of the steel piston indicate the variability of the physical SCTE hardware and measurement system is significant, in the same range as the desired TBC heat transfer benefits and adds difficulty for comparisons between low repetition testing campaigns.
- The piston bowl corner feature, radius, and fine geometry are known to be critical to the mixing-controlled combustion system performance. The TBC coating process was not able to achieve the precise corner and reentrancy geometry and is the primary aspect attributed to the deteriorated system fuel-air mixing.

- The 3D-piston section test concept for optical vessels was found to be very useful for understanding flame development in the combustion chamber, albeit with limitations. It is also believed to have produced useful data for future simulation validation efforts.
- The rounded piston bowl rim for the smooth TBC case slows the flame development and reduces the mixing energy, as seen in the HTPV results, and explains the slow heat release rate in the engine case. The mechanism for reduced fuel-air mixing was found to be the rounder bowl corner and reduced corner reentrancy which produced weaker mixing vortices with lower momentum.
- The concept of apparent chamber mixing energy was introduced through CIV methods. It was found to capture the effect of the rounded bowl edge sufficiently, and it also captured impact of injection pressure.
- The 3D-piston section test concept, with analyses such as CIV, can give an experimental understanding of the combustion and flame development changes to a mixing-controlled combustion system due to perturbations such as a TBC surface. The importance of understanding the combine system impact should be highlighted, as the system is highly refined and there are interactions which can offset and hide the desired outcome or result.

After reviewing the present work and discussing with team members, the following steps are proposed to further the research and development on both the 3D-piston diagnostic and TBC for engine efficiency.

- Employ the 3D-piston section test concept to other combustion system topics and questions of interest.
- Simulate the HTPV results with CFD to determine the magnitude of importance for the different surface roughness – and use this data for CFD simulation validation.
- Produce steel variants of the pistons matching the as-produced TBC bowl shapes so further testing can eliminate the differences in bowl geometry.
- Gain fundamental surface temperature and heat flux data to understand what the true impact of the TBC is on heat transfer and the near-wall temperature gradient.

Acknowledgements

References

1. Kosaka, H., Wakisaka, Y., Nomura, Y., Hotta, Y. et al., "Concept of "Temperature Swing Heat Insulation" in Combustion Chamber Walls, and Appropriate Thermo-Physical Properties for Heat Insulation Coat," SAE Int. J. Engines 6(1):142-149, 2013, https://doi.org/10.4271/2013-01-0274.
2. Uchida, Noboru. "A Review of Thermal Barrier Coatings for Improvement in Thermal Efficiency of Both Gasoline and Diesel Reciprocating Engines." International Journal of Engine Research 23, no. 1 (January 2022): 3–19. https://doi.org/10.1177/1468087420978016
3. Wakisaka, Y., Inayoshi, M., Fukui, K., Kosaka, H. et al., "Reduction of Heat Loss and Improvement of Thermal Efficiency by Application of "Temperature Swing" Insulation to Direct-Injection Diesel Engines," SAE Int. J. Engines 9(3):1449-1459, 2016, https://doi.org/10.4271/2016-01-0661.
4. Kawaguchi, A., Wakisaka, Y., Nishikawa, N., Hidemasa Kosakaet, H., et al. "Thermo-Swing Insulation to Reduce Heat Loss from the Combustion Chamber Wall of a Diesel Engine" International Journal of Engine Research 20, no. 7, September 2019: 805–16. https://doi.org/10.1177/1468087419852013.

5. Binder, C., Abou Nada, F., Richter, M., Cronhjort, A. et al., "Heat Loss Analysis of a Steel Piston and a YSZ Coated Piston in a Heavy-Duty Diesel Engine Using Phosphor Thermometry Measurements," SAE Int. J. Engines 10(4):1954-1968, 2017, https://doi.org/10.4271/2017-01-1046.

6. Witkowski, D., Rothamer, D.A., "Precise surface temperature measurements from 400 to 1200 K using the Pr:YAG phosphor," Appl. Phys. B 127, 171 (2021). https://doi.org/10.1007/s00340-021-07723-5

7. Andrie, M., Kokjohn, S., Paliwal, S., Kamo, L. et al., "Low Heat Capacitance Thermal Barrier Coatings for Internal Combustion Engines," SAE Technical Paper 2019-01-0228, 2019, https://doi.org/10.4271/2019-01-0228.

8. Andruskiewicz, P., Najt, P., Durrett, R., and Payri, R., "Assessing the Capability of Conventional In-Cylinder Insulation Materials in Achieving Temperature Swing Engine Performance Benefits" International Journal of Engine Research 19, no. 6, August 2018: 599–612. https://doi.org/10.1177/1468087417729254.

9. Hazhizume, T., Tanno, S., Mori, S., Yoshihara, Y. "Study of the Heat Transfer in the Spark-ignited Engines for Reducing Heat Loss," JSAE Transaction 53(1):107-113, 2022. https://www.jst-age.jst.go.jp/article/jsaeronbun/53/1/53_20224041/_pdf

10. Broatch, A., Olmeda, P., Margot, X., Gomez-Soriano, J. "Numerical simulations for evaluating the impact of advanced insulation coatings on H2 additivated gasoline lean combustion in a turbocharged spark-ignited engine," Applied Thermal Engineering 148 (2019): 674-683. https://doi.org/10.1016/j.applthermaleng.2018.11.106.

11. Broatch A., Olmeda P., Margot X., Gomez-Soriano, J. "A one-dimensional modeling study on the effect of advanced insulation coatings on internal combustion engine efficiency," International Journal of Engine Research 22(7):2390-2404, 2021, doi:10.1177/1468087420921584

12. Gingrich, E., Tess, M., Korivi, V., Schihl, P., et al. "The Impact of Piston Thermal Barrier Coating Roughness on High-Load Diesel Operation." International Journal of Engine Research, December 2019, https://doi.org/10.1177/1468087419893487.

13. Somhorst, J., Oevermann, M., Bovo, M., and Denbratt, I., "Evaluation of Thermal Barrier Coatings and Surface Roughness in a Single-Cylinder Light-Duty Diesel Engine" International Journal of Engine Research, October 2019, https://doi.org/10.1177/1468087419875837.

14. Koutsakis, G., Saputo, J., Gingrich, E., Tess, M. et al., "Delamination Failure on High-Output Diesel Engine Thermal Barrier Coatings," SAE Technical Paper 2022-01-0440, 2022.

15. Koutsakis, G., and Ghandhi, J.B. "Analytical solution of unsteady heat conduction in multilayer internal combustion engine walls," Applied Thermal Engineering 213 (2022): 118681. https://doi.org/10.1016/j.applthermaleng.2022.118681.

16. Kawaharazuka, F., Uchida, N., and Osada, H., "A Novel Piston Insulation Technique to Simultaneously Improve Both Heat Loss and Thermal Efficiency for Diesel Engines," SAE Int. J. Adv. & Curr. Prac. in Mobility 3(5):2173-2181, 2021, https://doi.org/10.4271/2021-01-0453.

17. Svensson, K. and Martin, G., "Ducted Fuel Injection: Effects of Stand-Off Distance and Duct Length on Soot Reduction," SAE Int. J. Adv. & Curr. Prac. in Mobility 1(3):1074-1083, 2019, https://doi.org/10.4271/2019-01-0545.

18. Svensson, K. and Martin, G., "Improved Method for Studying MCCI Flame Interactions with an Engine Combustion Chamber," SAE Technical Paper 2021-01-0507, 2021, doi:10.4271/2021-01-0507.

19. Shudo, T, S Nabetani, and Y Nakajima., "Analysis of the Degree of Constant Volume and Cooling Loss in a Spark Ignition Engine Fuelled with Hydrogen," International Journal of Engine Research 2(1): 81–92, 2001, https://doi.org/10.1243/1468087011545361.

20. Stanton, D., "Systematic Development of Highly Efficient and Clean Engines to Meet Future Commercial Vehicle Greenhouse Gas Regulations," SAE Int. J. Engines 6(3):1395-1480, 2013, https://doi.org/10.4271/2013-01-2421.

21. Dembinski, H., Angstrom, H., and Razzaq, H., "In-Cylinder Flow Pattern Evaluated with Combustion Image Velocimetry, CIV, and CFD Calculations during Combustion and Post-Oxidation in a HD Diesel Engine," SAE Technical Paper 2013-24-0064, 2013, https://doi.org/10.4271/2013-24-0064.

22. Dembinski, H.W.R., "The Effects of Injection Pressure and Swirl on In-Cylinder Flow Pattern and Combustion in a Compression-Ignition Engine," International Journal of Engine Research 15(4):444-459, 2014, doi:10.1177/1468087413491262.

23. Zha, K., Busch, S., Warey, A., Peterson, R. et al., "A Study of Piston Geometry Effects on Late-Stage Combustion in a Light-Duty Optical Diesel Engine Using Combustion Image Velocimetry," SAE Int. J. Engines 11(6):783-804, 2018, https://doi.org/10.4271/2018-01-0230.

24. Busch, S., Park, C., Warey, A., Peterson, R. et al., "A Study of the Impact of Pilot-Main Dwell on Late-Cycle Flow in the Piston Bowl of a Light Duty Optical Diesel Engine," 12th International Symposium on Combustion Diagnostics, May 10-1, Baden-Baden, Germany, 2016. https://www.osti.gov/servlets/purl/1367016

25. Thielicke, William, and René Sonntag. "Particle Image Velocimetry for MATLAB: Accuracy and Enhanced Algorithms in PIVlab." Journal of Open Research Software, vol. 9, Ubiquity Press, Ltd., 2021, doi:10.5334/jors.334.

26. Pastor, J.V., Garcia-Oliver, J.M., and Pachano, L. "Evaluation of Vortex Center Location Algorithms for Particle Image Velocimetry Data in an Optical Light-Duty Compression Ignition Engine," SAE Technical Paper 2018-01-0209, 2018.

A Novel Combustion Control to Achieve Higher Thermal Efficiency for a Heavy-Duty Diesel Engine with High Compression Ratio

N. Uchida[1], K. Watanabe[2]

[1]New ACE Institute Co., Ltd. 2530 Karima, Tsukuba-shi, Ibaraki Pref. 305-0822, Japan.

E-mail: n_uchida@nace.jp
Telephone: +(81) 29 856 1801

[2]Denso Corporation. 1-1 Showa-cho, Kariya-shi, Aichi Pref. 448-8661Japan.

E-mail: kazumasa.watanabe.j7g@jp.denso.com
Telephone: +(81) 566 57 4442

Abstract. For further increase in thermal efficiency of a heavy-duty diesel engine, improvement of heat energy utilization must be essential. As of the measures, we have been investigating into the optimum heat release rate (HRR) profile to maximize the thermal efficiency with a higher compression ratio. In our previous study with a multiple-injector system, it concluded that Sabathe- or Seiliger-like thermodynamic cycle could be the optimum. Furthermore, there are still more rooms for increasing in compression ratio. However, higher compression ratio for diesel combustion could result in higher cooling & mechanical losses and/or an inactive diffusion combustion by the deteriorated mixture formation even with its higher potential for the ideal thermal efficiency. Furthermore, the mechanical constraint for the peak cylinder pressure will limit not only the maximum compression ratio but the degrees of constant volume combustion (η_{gl}). This study firstly investigated a novel thermodynamic cycle (HRR profile) to achieve the higher thermal efficiency under the high compression ratio. Although isochoric cycle is the ideally optimal, spontaneous heat release at top dead centre (TDC) only increases internal energy of the working gas, which does not increase indicated work but rather increases heat loss until the piston starts to move downward. Therefore, the new thermodynamic cycle is based on isobaric combustion around TDC to suppress heat loss in minimum, and is followed by, when the in-cylinder volume change rate is increased by the piston movement, the significant increase in HRR until the maximum cylinder pressure reaches to the limit to maximize the indicated work. We called this revised HRR profile as 'High-heels' from its shape. Then, to practically achieve the High-heels HRR and to confirm our hypothesis experimentally, a variable-rate-shaping fuel injection system and a new combustion chamber piston were prototyped. Even though the achieved thermal efficiency has not reached to the target, the experimental results indicated the potential for further brake thermal efficiency (BTE) improvement.

Notation

AHRR	*Apparent Heat Release Rate (in engine experiments) J/deg.*
BTE	*Brake Thermal Efficiency %.*
dP/dθ	*In-cylinder pressure change rate MPa/deg.*
HRR	*Heat Release Rate J/deg.*
ITE	*Indicated Thermal Efficiency %.*
PFP	*Peak Firing Pressure MPa.*
SR	*Swirl Rario.*
TDC	*Top Dead Centre.*
TKE	*Turbulen Kinetic Energy m^2/s^2*
V.I.R.	*Variable Injection Rate shaping system.*
η_{gl}	*Degree of constant volume combustion.*
λ	*Excess air ratio (Lambda).*
τ_{turb}	*Turbulent time scale µs.*

1. Introduction

To achieve higher BTE for internal combustion engines, cooling loss reduction is essential to increase heat energy in the cylinder for converting indicated work combined with increased cycle efficiency, energy conversion efficiency from practical available heat in the cylinder to indicated work [1].

Thermal barrier coating intends to physically reduce heat loss, whereas it is not so easy for state-of-the-art diesel engines which utilizes a high fuel injection pressure equipment to reduce wall heat loss in higher temperature and pressure conditions. Thermal efficiency optimum HRR profile has been generally thought as that based on isochoric combustion from theory. However, Burger [2] concluded that wall heat and leakage losses have predominated in comparison with theoretical thermal efficiency improvement by utilizing a modified spark ignition gasoline engine to realize isochoric combustion with a piston resting time around TDC. For diesel combustion, we have reported in the past study [3] that significantly increase in HRR and peak firing pressure (PFP) around TDC by shortened combustion period with overlapped injection durations of multiple injectors resulted in increased cooling loss and deteriorated BTE. On the contrary, it was experimentally revealed that the modified combustion control by suppressing initial HRR and enhancing later HRR has a potential to effectively reduce both cooling loss and PFP with maintaining BTE [4]. Although a simple isobaric combustion could also have the same effects by suppressing working gas temperature increase, theoretical thermal efficiency is significantly reduced even it is not combined with over expansion stroke (to realize Atkinson or Brayton cycle with very high expansion ratio) [5]. Furthermore, longer combustion period by isobaric combustion may increase in friction loss by a higher piston thrust force in the expansion stroke [6]. Namely, neither isochoric combustion nor isobaric combustion will be the best for BTE, and practical HRR optimization strategy should be investigated from both cycle efficiency and total energy losses viewpoints.

The main technology to increase thermal efficiency is not to increase η_{gl} but to utilize a piston with higher compression (expansion) ratio. As a result, a higher in-cylinder volume change rate is achieved in the expansion stroke, which can suppress the working gas temperature and convert the fuel energy more into indicated work effectively than gas internal energy. This study firstly generalizes the idea of suppressing initial HRR into a novel HRR profile to reduce cooling losses with increased thermal efficiency. Then, the development and experimental confirmation of a new combustion system, including variable -rate-shaping fuel injection system, for achieving the designed HRR is described.

2. Novel HRR profile concept

2.1 Concept Objectives

As in the past study [4], reduced initial HRR near TDC and increased later HRR was effective to reduce both PFP and cooling loss without any deterioration of BTE (see Figure 1). This HRR profile modulation is not the same with the retarded injection timing because of higher HRR in the latest part of combustion period. It is also noticeable that even though the maximum in-cylinder temperature was almost the same, in-cylinder average temperature around TDC was reduced and the duration of high temperature were shortened by the reduction of initial HRR.
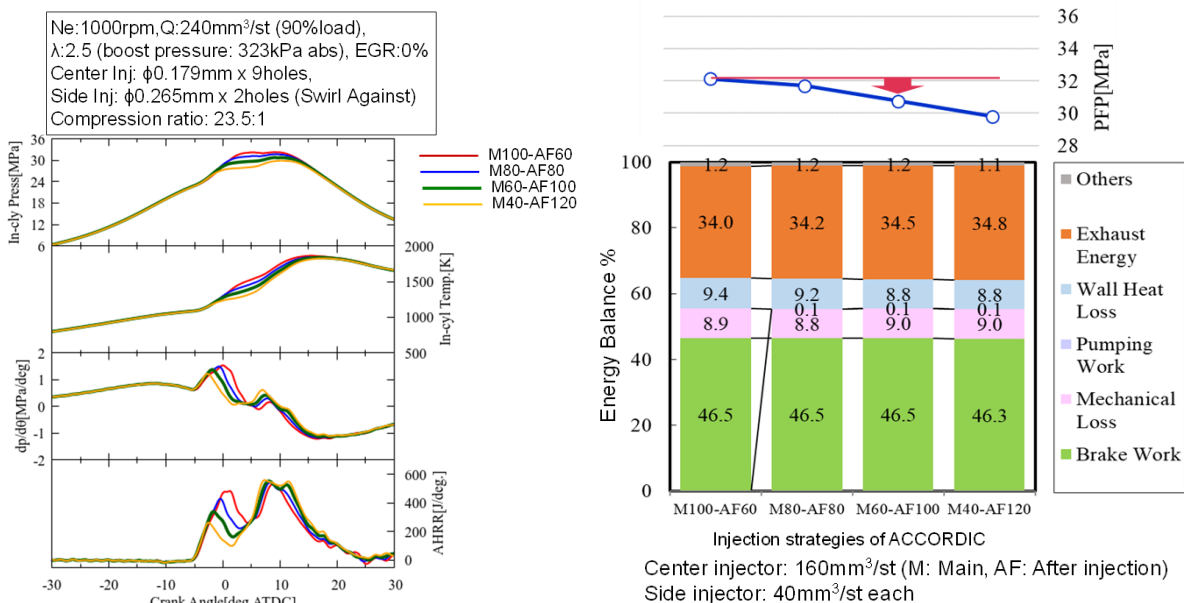

Fig. 1. HRR profile modulation by changing injection strategy of three injectors [4]

Since in-cylinder volume change rate close to TDC is very little, heat release just after TDC is only converted to the increase in internal energy of working gas, resulting in the increase in cooling loss and the decrease in indicated work especially with higher compression ratios. On the other hand, further increased HRR in retarded timing will increase indicated work and concurrently suppress the increase in gas temperature by increased volume change rate. That is the major cause why the experimental BTE was not deteriorated with retarded centroid of HRR (although theoretical thermal efficiency could be decreased).

From the experimental confirmation, it is desirable that initial HRR is much reduced to modify only to keep constant pressure combustion during the piston almost stands still just after TDC by delta shape profile. Or, if the in-cylinder pressure is reduced less than that at TDC like traditional retarded fuel injection timing, extra-heat is consumed only for pressure recovery to the pressure at TDC along with the increase in volume change rate resulting in the deterioration of specific fuel consumption. Even though the combustion is started with isobaric combustion, its duration must be kept in minimum for further improvement in ITE. Therefore, HRR is then faster increased along the increase in volume change rate until PFP reaches to the limit. Rapid HRR under increased volume change rate also has a merit to minimize the duration of high gas temperature. The theoretical thermal efficiency, i.e. regardless of energy losses, with the new thermodynamic cycle of modified HRR profile could be less than Sabathe cycle as shown in Figure 2 (showing narrower area in pressure-volume diagram), whereas BTE will have a potential to increase by the reduction of other energy losses in comparison with the conventional thermodynamic cycle.
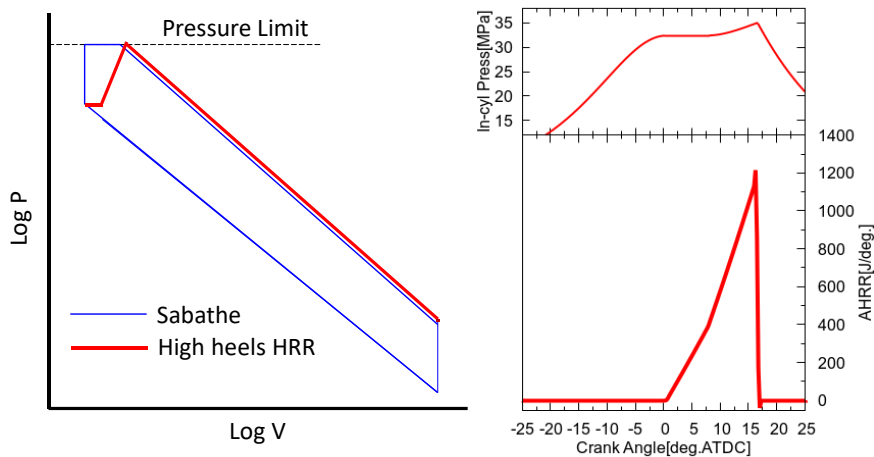

Fig. 2. Conceptual drawing of novel thermodynamic cycle

Furthermore, the remaining room of in-cylinder pressure up to the limit at TDC could be utilized for the integration of other thermal efficiency improvement technologies. As shown in the right figure in Figure 2, HRR profile of the new concept is compounded from two delta shape with different inclination. We call this concept as 'High-heels' from its typical shape in lieu of well-known 'Boots'.

The determination of combustion phasing for this new HRR profile is important. Too retard peak HRR achieves less ITE by the reduction of effective expansion ratio with worse friction loss, whereas too early peak HRR cannot reduce cooling loss even with the deteriorated mixture formation. Figure 3 simply compares the centroid of High-heels HRR effect on ITE under constant PFP: 35MPa between zero-dimensional engine model calculation without heat loss sub-model and engine experiments. It is obvious that cooling loss is reduced by the retarded centroid of HRR by the suppression of gas temperature. Engine specifications are later listed in Table 1. The zero-dimensional engine model was intended to investigate the degree of ITE deterioration without considering instantaneous cooling loss and/or other energy loss variation. The initial HRR profile is determined to fulfill isobaric combustion. The later part of HRR was to adjust the peak and raising timing (end timing is the same) simultaneously to maintain the total heat energy for retarded centroid of HRR. In the experiments, precise High-heels-like HRR was not achieved, but delta-shape-like HRR was emulated with multiple injections of the baseline common rail system. As shown in this figure, calculated ITE without considering heat loss gradually decreases with the delayed centroid of HRR. Red circle plot is the point where the calculated ITE is diverged from the red dash-dot straight line. Calculated in-cylinder pressure and HRR profile at this point was shown in the right-hand figure of Figure 2. On the other hand, ITE in the engine experiments was not change or slightly increased even though the PFP for delayed centroid of HRR was significantly reduced by

lower maximum AHRR (longer combustion period). That is, the proposed thermodynamic cycle with High-heels HRR has ideally less potential in thermal efficiency improvement, but practically much potential than other cycles. And, there are still more rooms for ITE improvement in the experiment, if maximum HRR is increased more with the centroid of HRR around 11 deg.ATDC (Crank angle deg. After TDC) for this engine specifications.
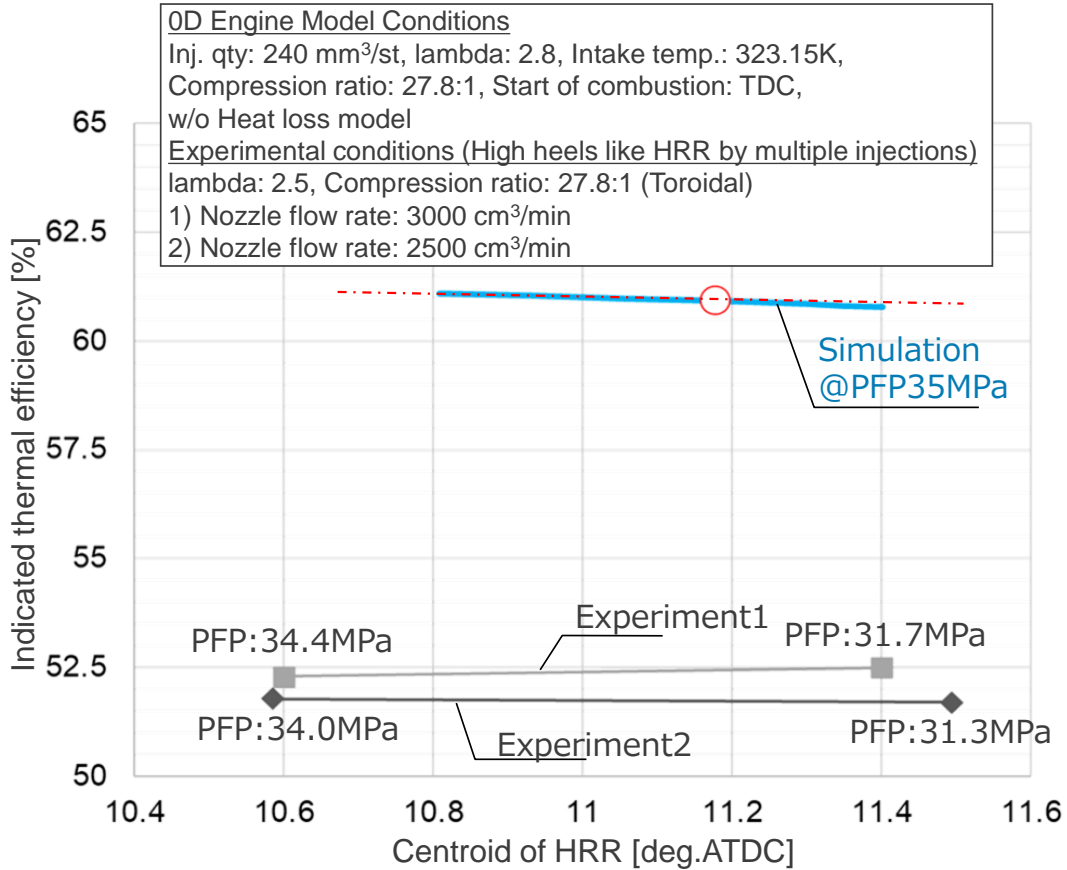

Fig. 3. Comparison of indicated thermal efficiency for varied centroid of (A)HRR timings under numerical and experimental conditions

2.2 Implementation measures

Most diesel engines are equipped high pressure common-rail injection system, which have less degree of freedom in injection rate shaping except for a rectangular injection rate. Therefore, multiple injection control is exclusively utilized for HRR profile modulation. However, the system requires dwell time inevitably between injection events resulting in the longer injection duration and worse mixture formation in the non-steady periods. If the injection rate shape is continuously modified within a seamless single injection, e.g. similar to the objective HRR profile, there will be a potential to further improvement in the thermal efficiency. For such a new requirement, Aizawa et al. proposed a new injection rate shaping equipment [7] even though their target injection rate shaping was exactly opposite from ours; their focus has been on better mixture formation by inverse-delta shape, whereas High-heels-like injection rate shaping aims the achievement of the optimum HRR profile. The similar injection rate shaping with High-heels, however, could deteriorate initial mixture formation because of almost zero momentum of the fuel spray. Therefore, initial injection rate slant is more gradual than that of current common-rail system, but convex to maintain least initial momentum of the spray as shown in Figure 4. Furthermore, in-cylinder pressure increase in the later expansion stroke requires extremely high injection rate (also see Figure 4, comparison with the 'conventional' injection rate) and HRR against high in-cylinder volume change rate. On one side, the flow rate (coefficient) of nozzle orifice should be increased on the diffusion combustion basis. On the other side, significant mixture formation improvement especially in the late combustion phase should be essential. It is very difficult only with higher injection pressure (higher momentum of spray), since turbulent kinetic energy of the injected spray is almost decayed just before

mixing enhancement. A new combustion chamber design intending to increase turbulent kinetic energy (TKE) and air utilization is also investigated later in this study aiming to improve maximum HRR in the end of combustion period.
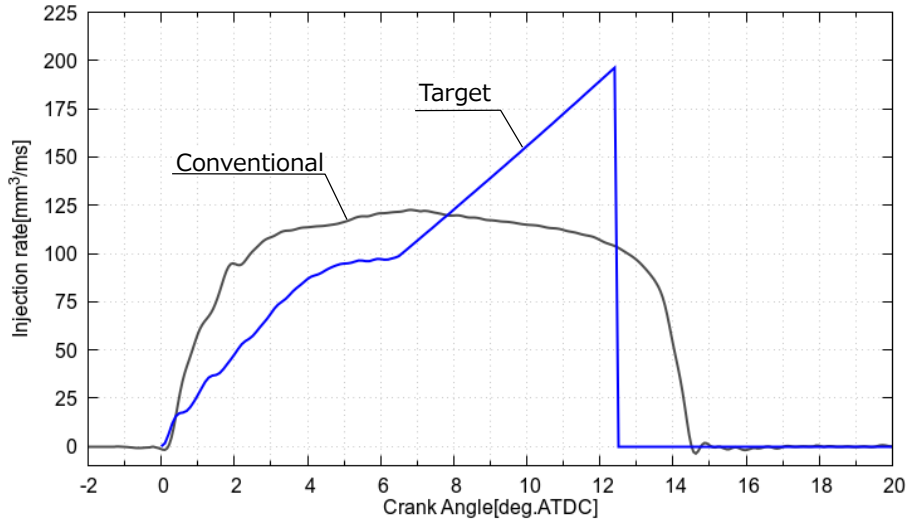

Fig. 4. Designed injection rate profile (Target) to achieve High-heels-like HRR

3. Engine specifications and schematics of experimental system

3.1 Engine and fuel specifications

A single cylinder four-stroke direct-injection diesel engine with displacement volume of 2147 cm^3 was utilized for engine experiments. Detailed specifications of the engine and test fuel are listed in Table 1. The engine was specially designed to have a tolerance up to 35 MPa of peak firing pressure.

Table 1. Engines specifications

Engine	Specification
Engine type	Single cylinder 4 stroke DI diesel
Cylinder bore x Stroke	Φ135 mm×150 mm
Engine displacement	2147 cm^3
Connecting rod length	370.46 mm
Piston material	Forged steel (Mahle Monotherm)
Top clearance	0.85 mm
Compression ratio	27.8:1
Piston cavity type	Toroidal: α, New open toroidal types: β, γ, δ
Valve system	Camless hydraulic VVA (Sturman Industries DHVVA)
Fuel injection equipment	Common rail system (Denso G4S modified, engine driven)
Maximum fuel injection pressure	300 MPa
Nozzle orifice	Φ0.179 mm×9-150°(base), Φ0.223 x 8-156°(open toroidal)
Nozzle flow rate	1750, 2500 cm^3/min. @10 MPa
Intake swirl ratio	1.4, 2.8
Peak firing pressure limit	35 MPa
Fuel	Diesel fuel JIS #2 (Japanese market fuel) Sulfur content: 7 ppm (mass) Cetane number: 56.8, Density: 0.8271 g/cm^3

The compression ratio is significantly higher than that of current products or any short-term research targets, since this study intends to find a long-term BTE-optimum compression ratio with the combination of higher expansion ratio and reduced energy losses by applying new technologies except for any waste heat recovery systems.

The test engine simulates turbocharged and after-cooled heavy-duty diesel engines by an externally driven supercharger and exhaust throttling. A hydraulic variable valve actuation system and an electronically controlled high-pressure common rail injection system which enable a maximum injection pressure of 300 MPa were also equipped.

A variable-rate-shaping fuel injection system based on a conventional common rail injection system is equipped with a sort of external pressure intensifier as shown in Figure 5. The pressure of the rail directly connected with fuel injector is controlled in lower pressure than that of two rails upstream pressure switching valves before starting injection. The turn-on timing of the four pressure switching valves is independently controlled to modulate injection rate by intensifying injection pressure with the upstream rails pressure.

In this study, gross indicated thermal efficiency, integral of in-cylinder pressure during compression and expansion strokes, was principally utilized for numerical and experimental examination focusing only on the combustion characteristics variation and eliminating uncertainty of the friction model and/or increased auxilialy mechanical losses with the devices of the single cylinder engine.
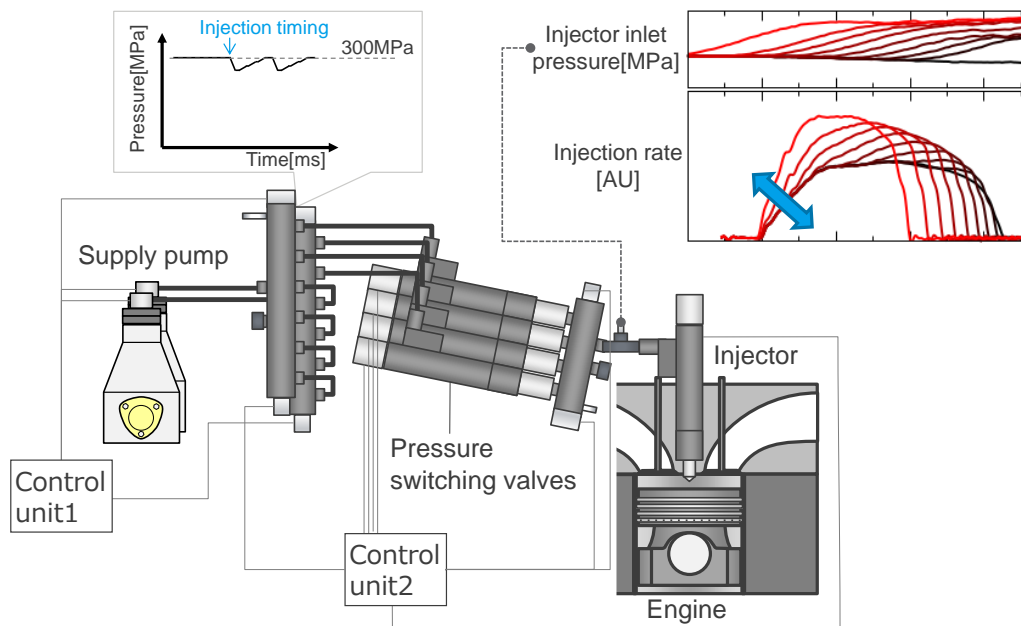

Fig. 5. Schematic of variable-rate-shaping fuel injection system

3.2 Schematics of experimental system

Figure 6 shows a schematic of the experimental apparatus. Intake boost pressure, exhaust back pressure, intake manifold temperature and EGR rate (EGR was not added as the parameter in this study) are widely controlled independently at any engine operating points. Intake boost pressure of up to 500 kPa (abs.) is possible with an externally driven supercharger. Both intake boost pressure and exhaust back pressure were made equal throughout the tests so that the external work done by the supercharging system could be ignored. The effect of variations in actual turbocharger efficiency and EGR cooler efficiency on the engine performance and emission characteristics with boost pressure and EGR rate conditions were also excluded.

3.3 Measuring instruments

Instantaneous in-cylinder pressure was measured by a water cooled piezo-type pressure transducer (Kistler Type6043AU20SP), and then the apparent HRR (AHRR) was analyzed with measured pressure data by utilizing a combustion characteristics analyzer (ONO-SOKKI DS3000 series). Other pressures in the manifolds were measured by piezoresistive pressure sensors (Kistler 4075A). Fuel consumption was measured by AVL 735S+753C. Air flow rate was measured by a Karman vortex flow meter (OVAL VXW040GA). Instantaneous fuel injection rate was measured by a Zeuch type measurement system (Moehwald HDA) with engine driven fuel supply pump and the experiment-ready fuel piping,

i.e. pressure source, pressure losses and pressure control are the same as those for the engine experiments, except for the pipe connected with the fuel injector.
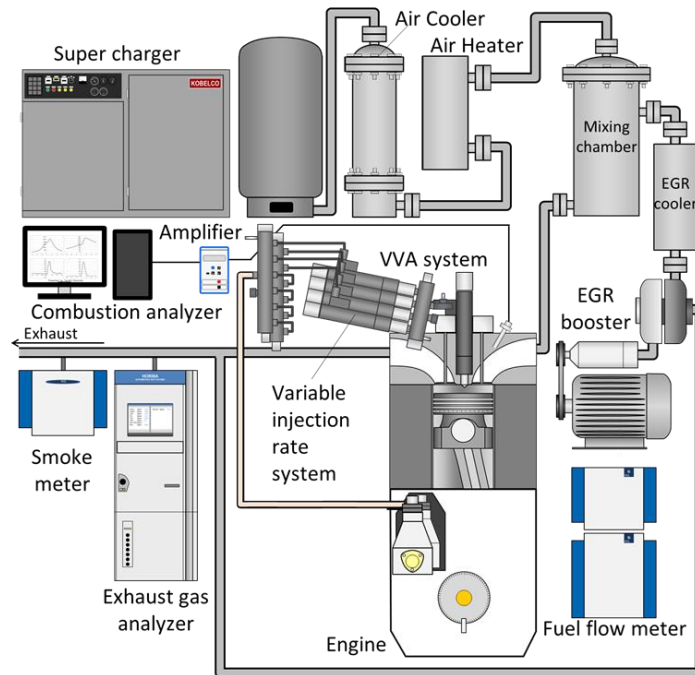
Fig. 6. Schematic of engine test system

4. Effect of injection rate modulation

4.1 Variable injection rate achievement

Figure 7 compares the achieved various injection rate shapes with a rectangular shape by utilizing the conventional common rail system. The initial upstream and downstream rail pressures were set at 300 and 100 MPa respectively. For No.1 and 2 of injection rates, the pressure switching valves were opened 11.2 and 6.3 deg. prior to the injection start. Other injection rates were achieved with 2 deg. delayed opening timing of pressure switching valves to each of previous condition.
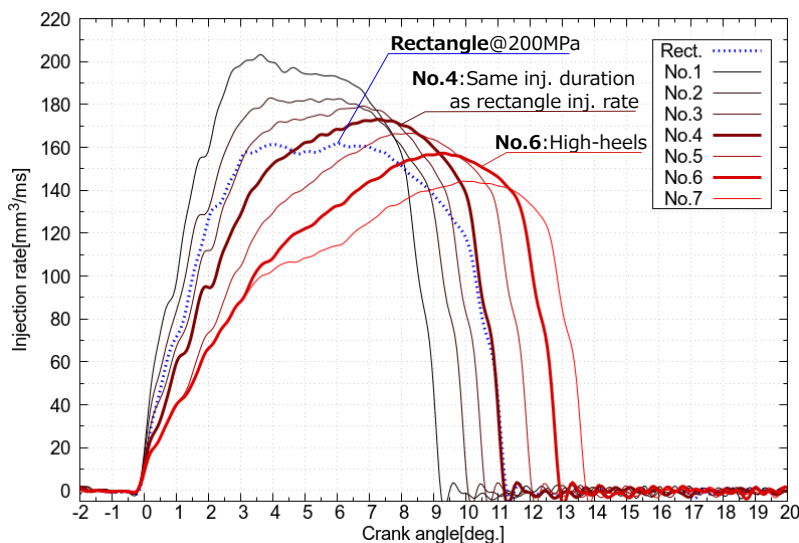
Fig. 7. Comparison of various fuel injection rates with a typical 'rectangular' shape

In later discussions, combustion characteristics for two typical injection rates are compared with the baseline rectangular shape. No.6 is the closest shape to the target injection rate as shown in Figure 4, even though the maximum injection rate runs short by the system constraint. Peak injection rate of No.4 is earlier and higher than that of No.6, whilst injection duration is the same as the baseline.

4.2 Experimental results

Table 2 shows the experimental conditions with the toroidal type combustion chamber. To maintain the initial isobaric combustion, injection timing was adjusted to fulfil in-cylinder pressure change rate (dP/dθ) at TDC of 0 MPa/deg. and above.

Table 2. Engine test conditions for different injection rate shapes

Item	Condition	
Engine speed	1006 rpm	
Injection quantity	240 mm³/st	
Injection timing	dP/dθ ≤ 0 MPa/deg. @ TDC	
EGR rate	0 %	
Excess air ratio λ	2.0	Max. (up to PFP=35 MPa)
(Intake boost pressure)	252 kPa abs.	Adjusted
Intake air temperature	323.15 K	

For the constant excess air ratio of 2.0, AHRR was gradually decayed and elongated possibly along with the reduced initial inclination of injection rate as shown in Figure 8. There could also be an effect of maximum injection rate, which is not so high than expectation by the system constraints. On the other hand, PFP was significantly reduced by the initial injection rate modulation. Therefore, to shorten combustion duration by enhancing late part of combustion for 'High-heels' injection rates, each intake boost pressure was then tried to adjust up to reaching maximum PFP. Figure 9 shows the comparison of combustion characteristics under fixed PFP for each injection rate shapes. As can be seen in the figure, maximum AHRR was increased for the injection rate shaping conditions, while that for rectangular shape was not changed, since PFP was high enough even with excess air ratio of 2.0.
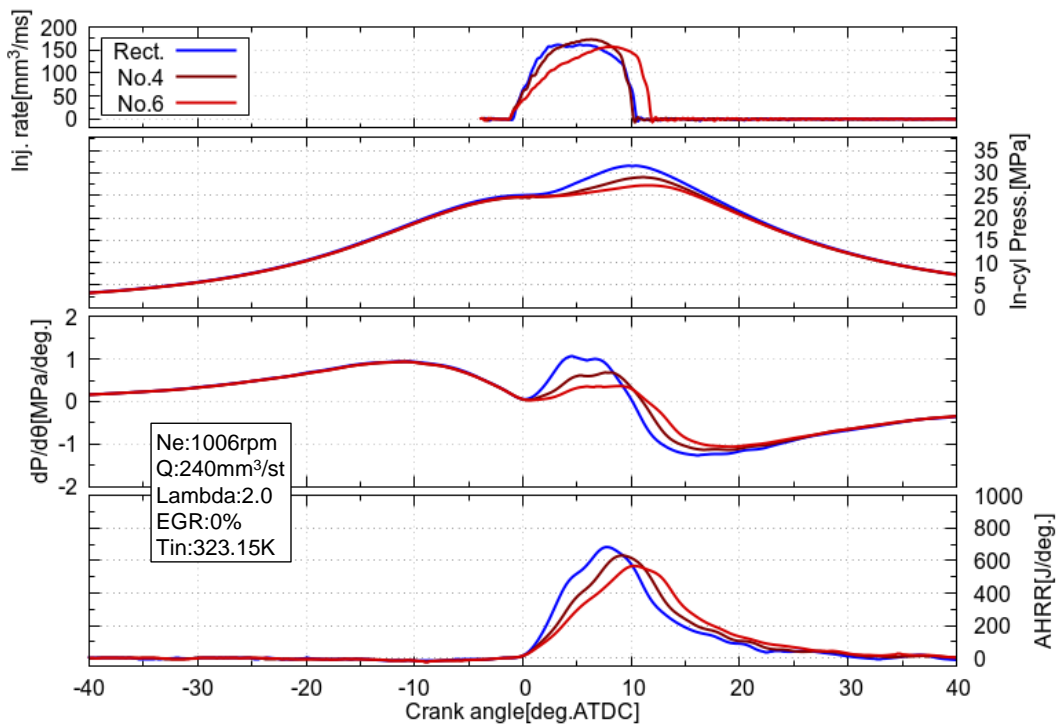
Fig. 8. Combustion Characteristics @excess air ratio: 2.0
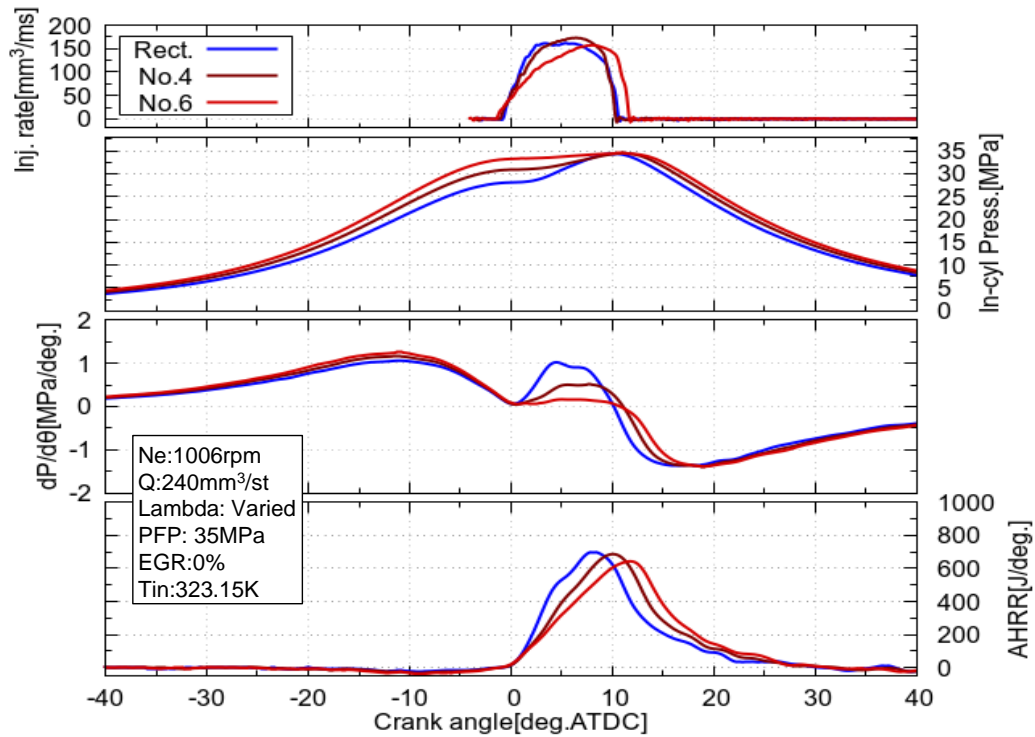
Fig. 9. Combustion Characteristics @PFP: 35 MPa

Figure 10 compares indicated thermal efficiency, exhaust loss and heat loss (detailed analysis method was described in the reference [8]) for various injection rate shapes under fixed excess air ratio and fixed PFP conditions. Heat loss was reduced by retarding the centroid of AHRR as intended. Therefore, the suppressed peak AHRR under the fixed excess air ratio condition could not be caused by the increase in cooling loss, but by the deterioration of mixture formation in the late combustion phase. The result also indicates 'High- heels HRR' oriented injection rate shape has a potential to achieve higher thermal efficiency than the rectangular injection rate even though HRR of the late combustion did not reach to our intension. To improve HRR in the late combustion with higher compression ratio, a novel combustion chamber is proposed in the next chapter.
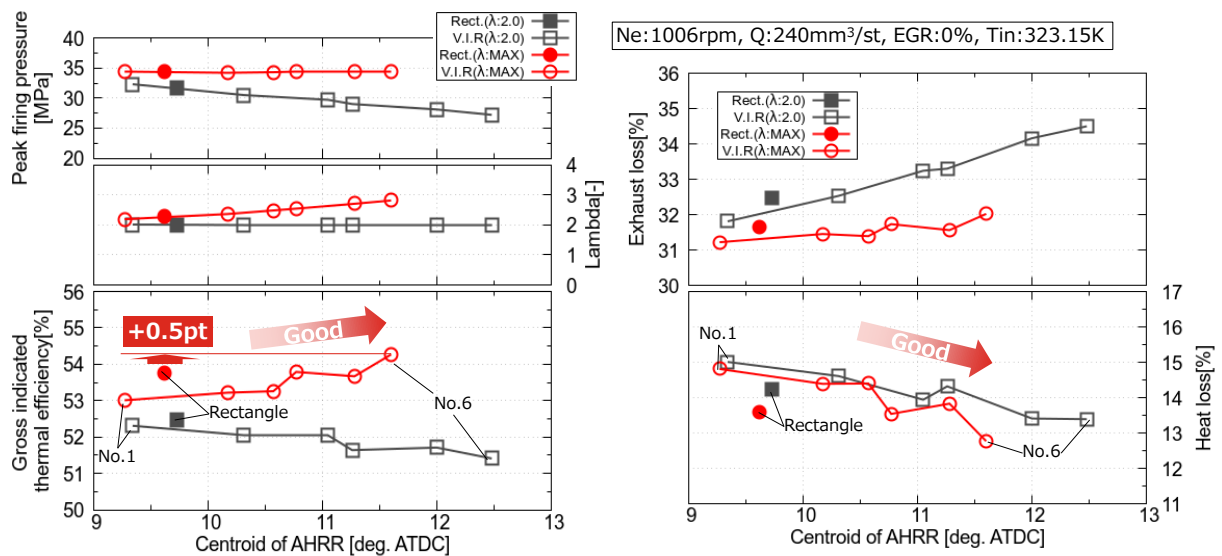
Fig. 10. Effect of injection rate modulation on thermal efficiency (V.I.R.: Variable Injection Rate shaping)

The other noticeable finding is that the thermal efficiency of the actual engines does not always improve with the increased η_{gl}, but with suppressed heat loss around TDC by modifying HRR profile even though η_{gl} was reduced. Figure 11 provides two opposed trends of ITE for η_{gl} with the same injection rates. The cause of phenomenon is the different trend of the cycle efficiency for the same injection

rates as described in Figure 12. Namely, it is essential to maintain or improve cycle efficiency, when HRR profile is modified for optimizing ITE.
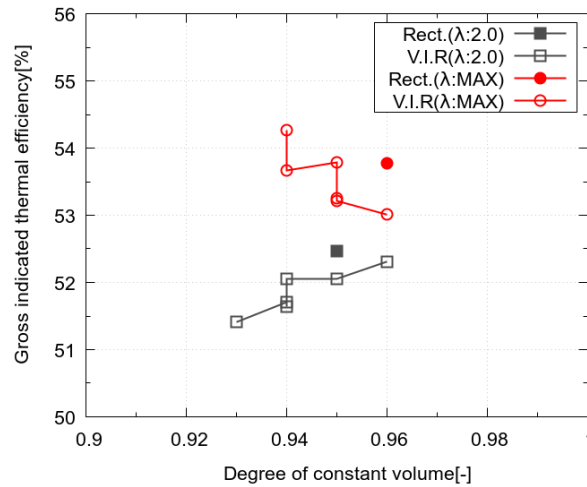
Fig. 11. Effect of η_{gl} on ITE
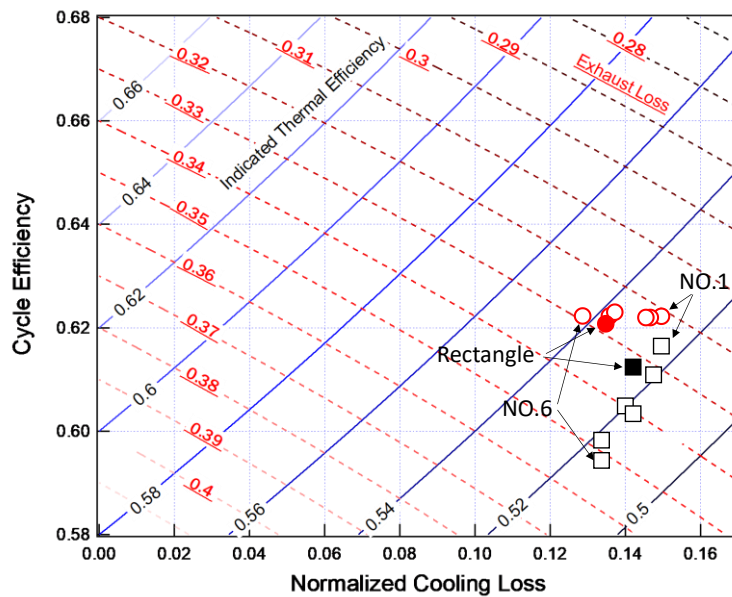
Fig. 12. Comparison of different λ conditions for various injection rates on C-C Chart [1] (same data with Fig. 9)

5. Novel combustion chamber

5.1 Design concept and numerical validation

A new concept intends to increase HRR in the late part of combustion without any further assistance of spray momentum with higher injection pressure, since TKE derived by fuel injection is almost attenuated just after finishing droplet evaporation with high compression ratio. Furthermore, in high compression ratio, sufficient fuel-air mixing is restricted not only by spray-to-spray and/or spray-to-wall interference with smaller volume for mixture formation, but also by shortened ignition delay resulting in the lack of air utilization. Therefore, base piston geometry was selected as 'open toroidal' type in lieu of toroidal type to reduce high temperature and equivalence ratio region in the late combustion period effectively, which was derived from the results of our previous studies [9]. Millo et al. proposed a new swirl-assisted combustion chamber design [10], which could have not only similar effects with WAVE piston bowl [11] to reduce spray-to-spray interaction by the radial bump, but to improve mixture formation by higher TKE generated at the bump with swirl flow dissipation during combustion period even with the common compression ratio of 16:1.

Numerical simulation was preliminary carried out to confirm the effect of 'bump' and to optimize the shape of 'bump' with the open toroidal combustion chamber geometry of higher compression ratio. Detailed calculation conditions are shown in Table 3.

Table 3. Numerical simulation setup

Software		Converge V3.0
Model	Turbulence	Standard k-ε
	Spray atomization	KH-RT
	Combustion	SAGE multizone: Detailed chemical reaction (Species:42 / Reaction:168)
	Wall heat transfer	O'Rouke-Amsden
Grid	Base size	2 mm
	Embedded	0.5 mm @Spray
	Adaptive mesh refinement	0.5 mm @Velocity / Temperature
Boundary conditions	Intake temperature	360 K
	Intake pressure	345 kPa abs.
	Intake oxygen content	21 %
	Fuel injection quantity	240 mm^3/st
	Fuel injection rate	High-heels HRR oriented as shown in Fig.4
	Nozzle specifications	Φ0.223 x 8-156°
	Compression ratio	27.8:1
	Swirl ratio	1.4, 2.8

The initial results for two different guide wall configurations named β and γ with higher swirl ratio: 2.8 as shown in Figure 13, however, did not show any significant increase of peak HRR in comparison with the simple toroidal shape: α. It could be suggested by the small difference in TKE and turbulent time scale. As shown in Figure 14, swirl with the guide wall was significantly decayed from before TDC without any spin-up like the baseline toroidal shape. Especially with β combustion chamber, swirl was significantly decayed before starting combustion even without injection. For γ combustion chamber, high swirl ratio was relatively kept around TDC, and significantly decayed with fuel injection. This phenomenon suggests that fuel spray and swirl are compensated each other by the interference. However, it will not have significant effect to enhance mixture formation from the TKE and HRR comparison. Improvement in HRR of late combustion in γ combustion chamber was exclusively caused by the reduction of spray-to-spray interference with the existence of the guide wall. In consequence, swirl momentum should be kept until combustion start and should be utilized for the better mixture formation by the modified interaction ways with fuel sprays, while the guide wall effect to reduce spray-to-spray interference in the late combustion period must be maintained.
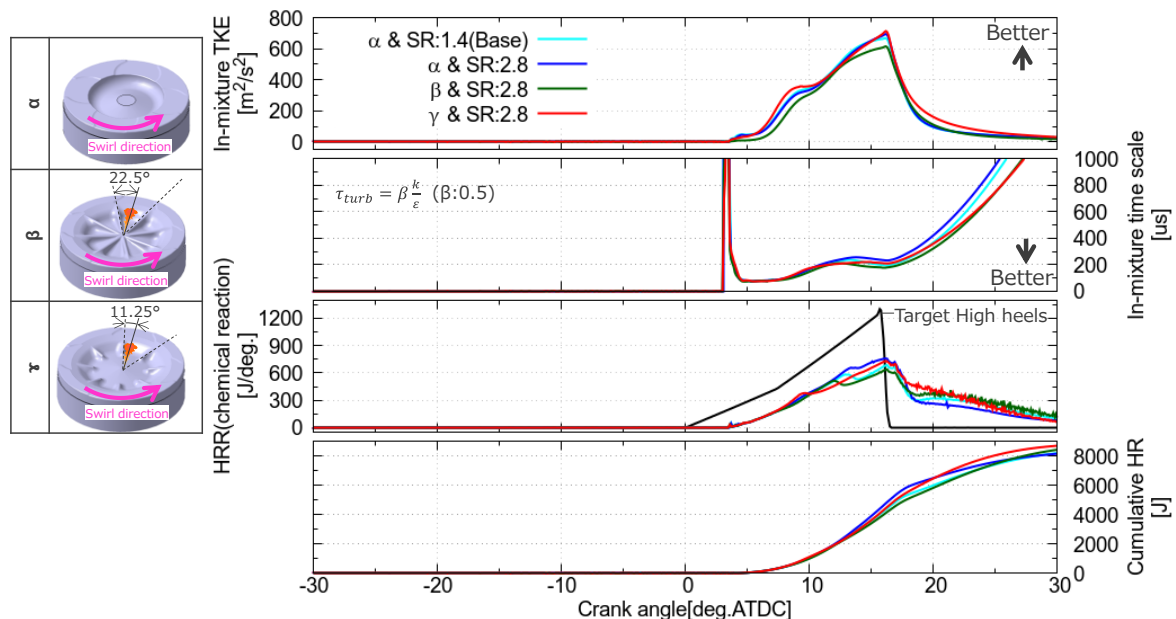
Fig. 13. Preliminary simulation results with baseline and two different chamber shape applying guide walls
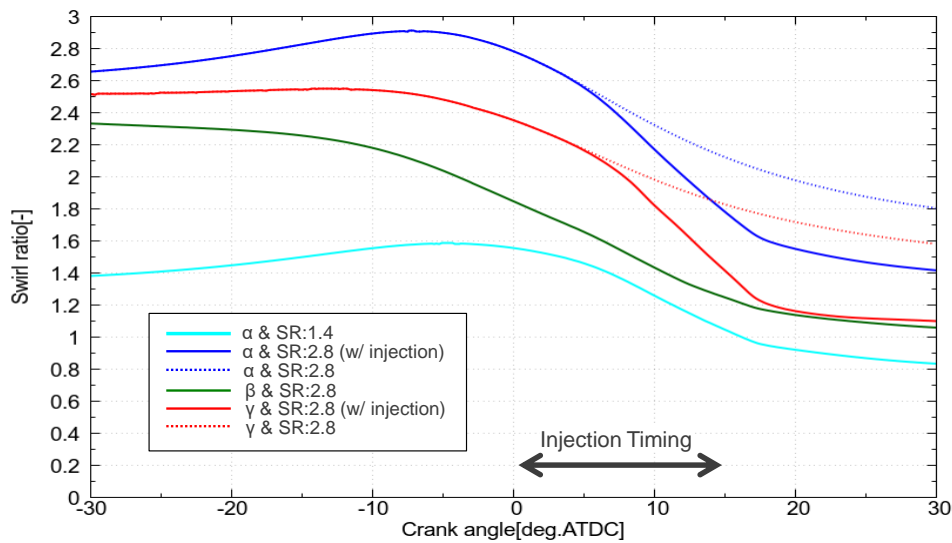
Fig. 14. Simulated time-varied swirl ratio for each set of combustion chamber and intake swirl ratio

A modified combustion chamber was then designed for satisfying the demands discussed above, which is named as δ combustion chamber (see the machined pistons in Figure 15). The inclined guide walls and the circular channel in the bottom of the δ combustion chamber aim to suppress early extinction of in-bowl swirl until the start of combustion and to enhance air entrainment by the air flow and spray interference at fuel rich portion; spray tip and spray contact area with the bottom surface of chamber. In recent years, a lot of combustion chambers with stepped-lip type have been proposed for not only light-duty but heavy-duty diesel engines with high compression ratio [12,13] aiming to increase in air utilization by splitting and enlarging spray direction mainly to the squish area. The open toroidal shape also has the similar effect to utilize the circumferential air with limiting radial spread of spray flame by the guide walls. On the other hand, the circular channel is intended to increase air entrainment at the stagnation region near the bottom of combustion chamber by the retained fresh air crossflow just below the spray.
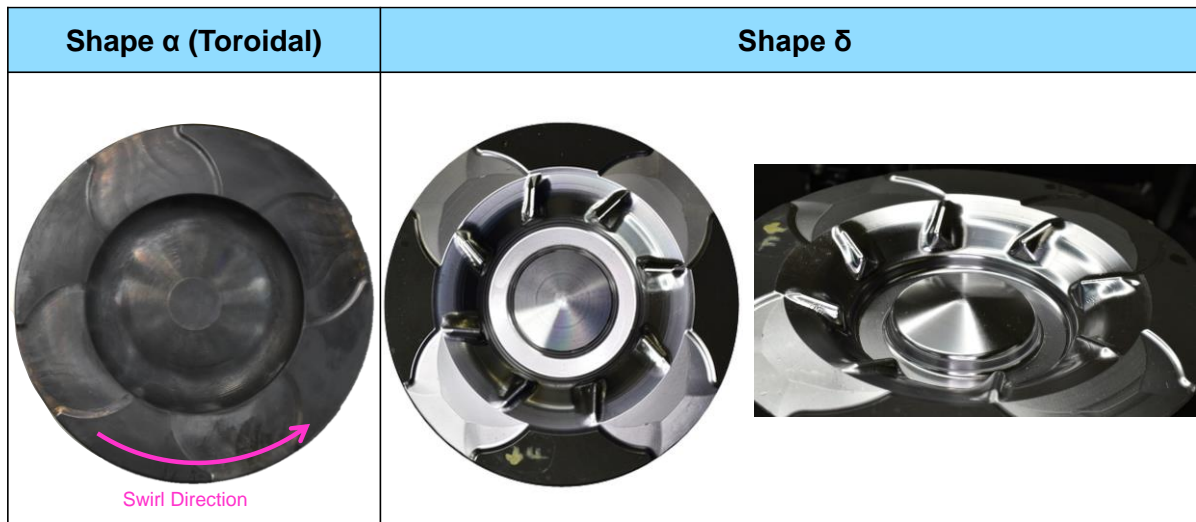
Fig. 15. Comparison of combustion chamber design (compression ratio are the same, 27.8:1)

As shown in the simulated local gas temperature results of Figure 16, adjacent spray flames are easily overlapped for the toroidal combustion chamber with higher compression ratio, which results in the deterioration of fresh air entrainment in the later combustion phase without the guide walls. The comparison of the local HRR for spatially divided regions as shown in Figure 17 also shows the effects of the circular channel and the guide walls along the spray growth. For the inner region (Region0), local HRR is the same for all conditions because of the same piston geometry and lower rotating speed regardless of the swirl ratio. At the circular channel region (Region1), local HRR is slightly improved, which is supposed by the increased air entrainment at the stagnated bottom of sprays. In the outer region (Region2), local HRR in the late combustion period is significantly increased, which could be

caused by not only the reduction of spray-to-spray interference as intended, but the more diluted mixture prepared in the upstream region. In summary, it is numerically expected that the δ combustion chamber could have a potential to increase in the overall HRR even though the simulated peak HRR is not significantly improved.
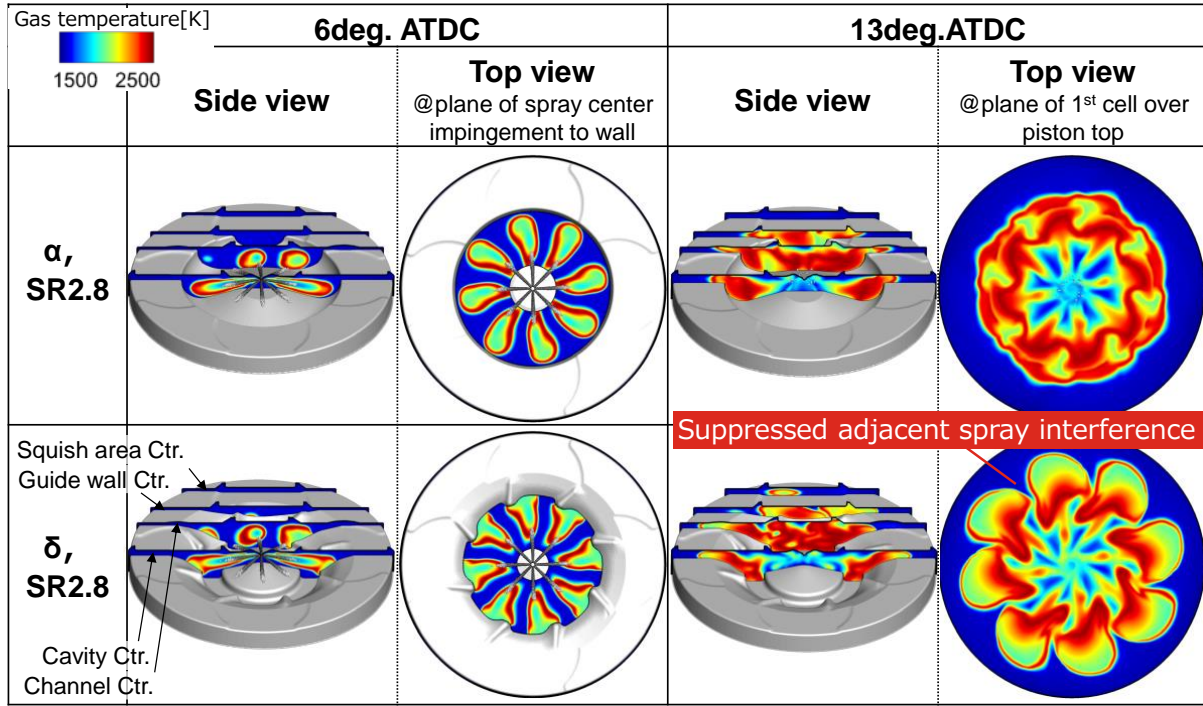
Fig. 16. Comparison of simulated local gas temperature with different combustion chamber designs
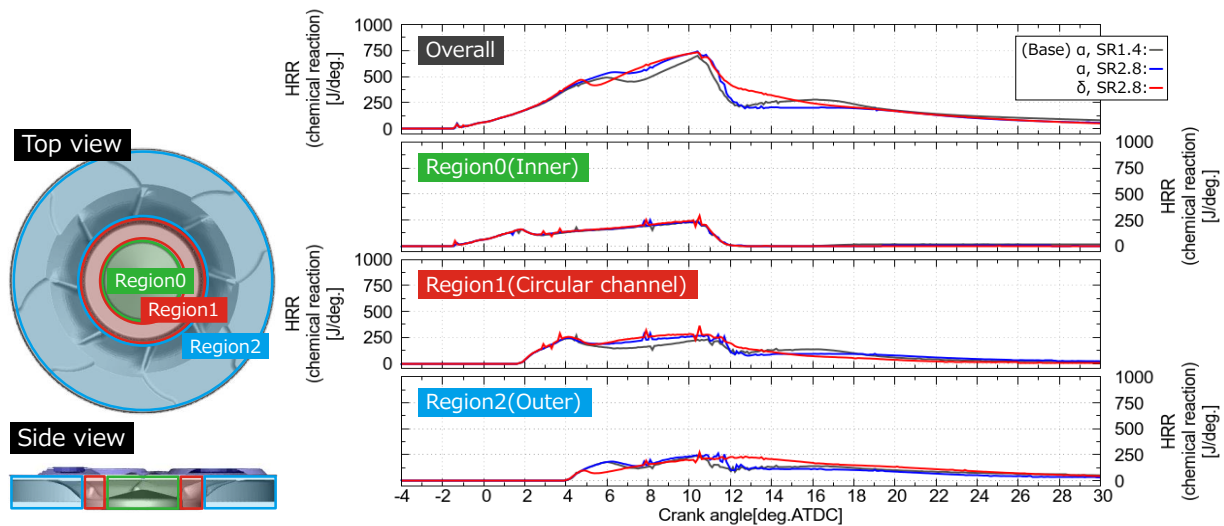
Fig. 17. Comparison of simulated local HRR for spatially divided regions

5.2 Engine experimental result

From the numerical simulation results, the combination of variable injection rate control aiming High-heels HRR and δ combustion chamber could have advantages in ITE in comparison with the baseline even though the achieved injection rate has not satisfied the optimum shape, so far.

Figure 18 shows the comparison of combustion characteristics and energy balance analysis acquired by the single cylinder engine experiments under fixed excess air ratio: 2.0 for the different set of injection rate shape and combustion chamber as described in it. The higher ITE has not achieved with modified injection rate and combustion chamber, whilst PFP was significantly reduced with maintaining ITE and cycle efficiency. Therefore, it could be validated that the effectiveness of the proposed HRR concept, even it is still relied on the engine hardware. Further improvements in the variable-rate-

shaping fuel injection system and the combined combustion strategy (combustion chamber geometry and air motion in the cylinder) further to increase peak HRR without any drawbacks in cooling loss are the next challenge.
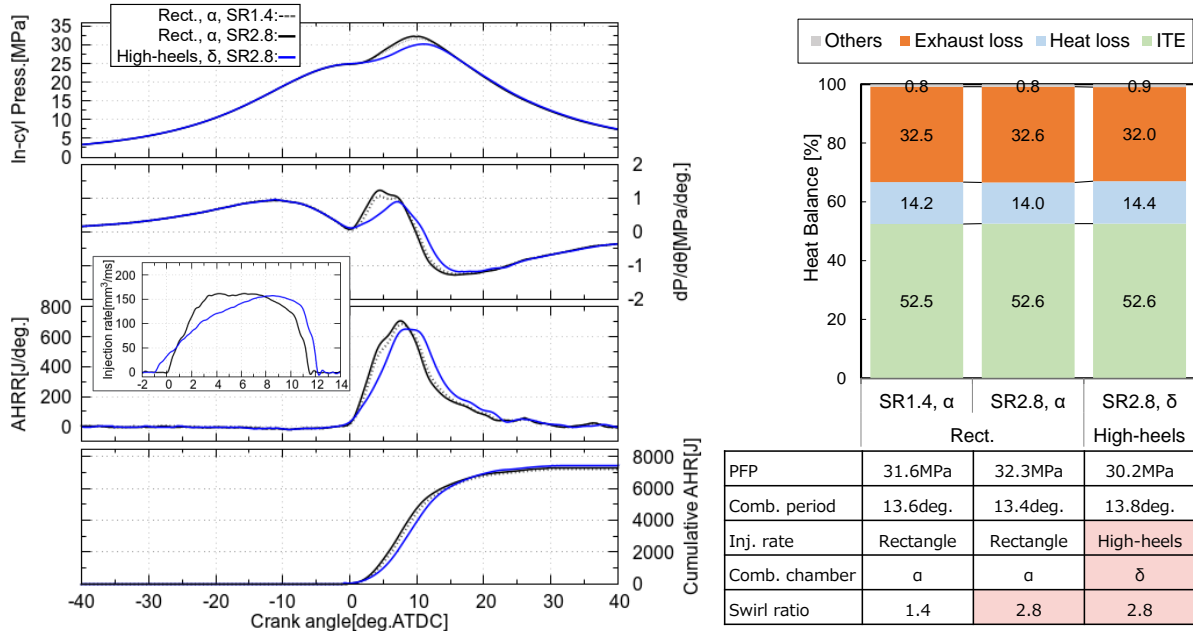
Fig. 18. Integrated effect of variable injection rate and new combustion chamber on combustion characteristics and heat balance analysis for the engine experiments at the constant excess air ratio: 2.0

Summary

A novel combustion control for the improvement in thermal efficiency was numerically and experimentally investigated. Especially for higher compression ratio, isochoric-like combustion is not effective by compensating the improvement with increased PFP and cooling loss. Instead of isochoric cycle, a new thermodynamic cycle with the 'High-heels' HRR was discussed as the prerequisite target for achieving higher thermal efficiency. The practical difficulty is to significantly increase in late part of HRR with diffusion combustion. Therefore, a variable-rate-shaping fuel injection system and a piston with a new combustion chamber design were developed. By means of these tools, effectiveness of the new concept was experimentally validated even though ITE improvement was little.

- Under the same PFP condition, ITE with High-heels HRR oriented injection rate control increased by 0.5 %pt. in comparison with the baseline rectangular injection rate
- Retarded centroid of AHRR combined with higher excess air ratio is more promising measure for further thermal efficiency improvement due to PFP and cooling loss reduction than increasing η_{gl}
- Suppressing the decrease of cycle efficiency is essential to increase ITE even with decreased η_{gl} by retarded centroid of AHRR
- The new combustion chamber can slightly increase HRR mainly in the late combustion caused by reducing adjoined spray interference and by increasing air utilization, whilst cooling loss was not decreased by its complex geometry and higher gas flow velocity

Acknowledgements

References

[1] Uchida N. A Novel Technology Assessment Chart for Thermal Efficiency Improvement of IC Engines. *Int J Engine Res.* Epub ahead of print April 2021. DOI: 10.1177/14680874211009671.

[2] Burger B and Bargende M. The Isochoric Engine. SAE paper 2020-01-0796, 2020.

[3] Uchida N, Galpin J, Watanabe K et al. Numerical and Experimental Investigation into Brake Thermal Efficiency Optimum Heat Release Rate for a Diesel Engine. SAE paper 2019-24-0109, 2019.

[4] Uchida N Watanabe K and Enya K. Achieving Higher Brake Thermal Efficiency under Existence of Peak Firing Pressure Constraint with a HD Diesel Engine. In: *THIESEL 2020 Conference on Thermo- and Fluid Dynamic Processes in Direct Injection Engines*, Virtual conference in Microsoft Teams, 8-11 September 2020, pp.207-219. CMT-Motores Térmicos.

[5] Lam N. Double Compression-Expansion Engine Concepts: Experimental and simulation study of a split cycle concept for improved brake efficiency. 2019. Energy Sciences, Lund University.

[6] Uchida N, Okamoto T and Watanabe H. A new concept of actively controlled rate of diesel combustion for improving brake thermal efficiency of diesel engines: Part 1 - verification of the concept. *Int J Engine Res* 2018; 19(4):474–487.

[7] Aizawa T, Akiyama S, Shimada T et al. TAIZAC -TAndem Injectors Zapping ACtivation- for Thermal Efficiency Improvement of Diesel Engine. *SAE Int J Adv. & Curr. Prac. in Mobility* 2020; 2(1):310-318.

[8] Tsurushima T, Harada A, Iwashiro Y et al. Thermodynamic characteristics of premixed compression ignition combustions. SAE Paper 2001-01-1891, 2001.

[9] Hashimoto M, Osada H, Murayama T et al. Study of Combustion Chamber Design for High Compression Ratio. *Transactions of Society of Automotive Engineers of Japan* 2014 (JSAE 20144148); 45(1):55-62 (Japanese).

[10] Millo F, Piano A, Roggio S et al. Numerical Investigation on Mixture Formation and Combustion Process of Innovative Piston Bowl Geometries in a Swirl-Supported Light-Duty Diesel Engine. *SAE Int J Engines* 2021; 14(2):247-262.

[11] Eismark J, Andersson M, Christensen M et al. Role of Piston Bowl Shape to Enhance Late-Cycle Soot Oxidation in Low-Swirl Diesel Combustion. *SAE Int J Engines* 2019; 12(3):233-249.

[12] Perini F, Busch S, Zha K et al. Piston Bowl Geometry Effects on Combustion Development in a High-Speed Light-Duty Diesel Engine. SAE Paper 2019-24-0167, 2019.

[13] Funayama Y, Yoshitomi K, Ishii M et al. Influence of Combustion Chamber Shape and In-Cylinder Density on Soot Formation in Diesel Combustion. *SAE Int J Adv & Curr Prac in Mobility* 2020; 2(1):415-425.

THIESEL 2022 Conference on Thermo- and Fluid Dynamics of Clean Propulsion Powerplants

Experimental Optimization of a Medium Speed Dual Fuel Engine towards RCCI Oeration

M. Merts[1,2], J. Hyvönen[3], M. Lundgren[1], P.A. Veenhuizen[2] and S. Verhelst[1]

[1] Department of Energy Sciences, Lund University, Ole Römers Väg 1, 22363 Lund, Sweden.

[2] HAN Automotive Research, HAN UAS, Ruitenberglaan 29, 6826CC Arnhem, The Netherlands.

[3] Wärtsilä Finland Oy, P.O. Box 244, Jarvikatu 2-4, 65101 Vaasa, Finland.

Abstract.

To reduce CO_2, NO_x, soot and sulphur emissions, methane (natural gas) is becoming increasingly relevant as marine fuel. In medium speed engines it is mainly applied in a Conventional Dual Fuel concept. In this concept the methane is indirectly injected, and ignited by a diesel pilot injection just before top dead centre. Closely related to dual fuel is the RCCI combustion concept. Also making use of two fuels, this concept aims at ultralow NO_x emissions by strongly premixing the pilot fuel. The concept is known for high efficiency and low NO_x emission, but also for limited controllability and completeness of the combustion. Similar to dual fuel, diesel and methane can be used as fuels for RCCI. Using the same fuels, the main difference between the concepts is the pilot injection timing, resulting in a different combustion profile, emissions, and efficiency.

In this work a 200mm bore medium speed engine is tested in the range from conventional dual fuel towards RCCI. The goal of this research was to better understand the combustion process and find engine operating conditions with lowest emissions and highest engine efficiency and controllability. Besides intake conditions and pilot mass, the main parameter to investigate was the timing (SOI) of the pilot injection. Over the range of SOI variation, areas with different behaviours were observed. With an SOI close to top dead centre, the typical diesel behaviour was seen. Here, advancing SOI results in higher NO_x. Next, a further advancing of the pilot into RCCI operation resulted in lower NO_x, caused by the strong premixing of pilot fuel. An even further advancing of the pilot still lowers NO_x but increases methane emissions and variance of IMEP. The best operating conditions were found with not too early RCCI timing, resulting in NO_x emissions below 2 g/kWh without aftertreatment.

Notations

aTDC	-	After Top Dead Centre	GHG	-	Green House Gas
bTDC	-	Before Top Dead Centre	IMEP	-	Indicated Mean Effective Pressure
CA50	-	Crank Angle at 50% heat release	IVO	-	Inlet Valve Opening
CAD	-	Crank Angle Degree	IVC	-	Inlet Valve Closing
CDC	-	Conventional Diesel Combustion	LTC	-	Low Temperature Combustion
CDF	-	Conventional Dual Fuel	NO_x	-	Nitrogen Oxides
CI	-	Compression Ignition	RCCI	-	Reactivity Controlled Compression Ignition
CO_2	-	Carbon dioxide	SOC	-	Start of Combustion
EHVA	-	Electro Hydraulic Valve Actuation	SOI	-	Start Of Injection
EVC	-	Exhaust Valve Closed	TDC	-	Top Dead Centre
EVO	-	Exhaust Valve Opened	uHC	-	Uncombusted HydroCarbons

1. Introduction

Partly driven by the recently proposed European Climate Law [1], the marine sector shows a strong interest in the application of renewable fuels [2], [3]. The usage of renewable fuels prevents the addition of new carbon, originating from fossil fuels, to the atmosphere. Instead the fuel has either no carbon at all, or carbon that was already part of the atmosphere. The GHG emission footprint of the sector can by reduced relatively fast by the usage of renewable fuels. At the same time a reduction of oxides of nitrogen (NO_x), soot and sulphur emissions seems feasible by running conventional engines on alternative fuels [4]. When making use of existing engines running on alternative fuels, the transition towards low carbon propulsion can be done with limited investments and at a pace needed to comply with the Paris Climate Accords. This applies not only to marine, but also to non-road, agricultural and industrial applications where high powers and high energy amounts are used.

Renewable fuels can originate from different sources. Most common are fuels from a biological source, and synthetic fuels based on renewable electricity. To rate the suitability of a renewable fuel as transport fuel, the Triple S criteria of Verhelst [5] are meaningful. The fuel should be sustainable, scalable, and storable. The first criterion emphasizes that the energy source should be renewable and resources should be used in a closed cycle on a realistic time scale. The second criterion calls for an abundant availability at reasonable prices. The third criterion demands a sufficient energy density. Looking at fuel candidates that fulfil these criteria to a greater or lesser extent, much research in academia and industry is ongoing on (bio)methane [6], hydrogen [7], methanol [8], and ammonia [9].

These fuels are all high-octane fuels, well suitable for spark ignition (SI) engines. The bulk of the engines in use in marine and industry are compression ignition (CI) engines, which make use of low octane fuels. As alternative to completely changing the engine or engine concept from compression ignition to spark ignition, a combination of high octane and low octane fuel can be applied in a compression ignition engine. In the Conventional Dual Fuel (CDF) concept, the low octane, high reactive diesel fuel acts as an ignition source for the high-octane fuel. This can be done by applying an injection close to Top Dead Centre (TDC), where the pilot diesel fuel mainly combusts as a diffusive flame [10]. Alternatively, in the Reactivity Controlled Compression Ignition (RCCI) concept, the pilot fuel is injected much earlier in the cycle which results in a premixed diesel combustion [11]. A recent overview of different fuel combinations and combustion concepts is given by Karczewski in [12].

Both methods have their pros and cons, and it is noteworthy that they originate from different research goals. The driver for RCCI research and development is the quest for low NO_x emissions and high efficiency, through the application of Low Temperature Combustion (LTC) [13]. In most CDF developments the main goal is to apply a high-octane fuel in a CI engine, while enabling lowered emissions. CDF is used in commercial applications, while RCCI powertrains are not yet applied in the market.

In CDF combustion the pilot injection close to top dead centre (TDC) results in a diesel combustion around the diesel jet. Although the amount of released heat in this phase is lower than in a conventional diesel engine, this rich and concentrated diffusive combustion still results in high local temperature and thus NO_x production. Belgiorno [14] shows how low NO_x can be achieved with very late combustion phasing. Another typical aspect of CDF operation is incomplete combustion resulting in high methane emissions [15]. As reported by Sharafian [16], the excessive methane emissions that can occur in medium speed dual fuel engines have an impact on their greenhouse gas (GHG) emissions, due to the high global warming potential of CH_4, meaning the advantage of applying a low carbon fuel could be nullified.

RCCI is a relatively new and promising combustion concept. An extensive review on RCCI combustion is given by Reitz in [17], covering simulations and experiments, both for light and heavy duty. An improved efficiency over conventional diesel engines was found, mainly caused by lower heat losses. Extremely low NO_x emissions were reported. On the other hand the concept is known for its high emissions of uncombusted fuel, increase of the Coefficient of Variation for the Indicated Mean Effective Pressure (COV-IMEP) [18] and challenging controllability [19].

Although much research on both combustion modes is available, the reported results and limitations do not lead to a conclusion on which mode is favourable for a certain engine application. Neither is it clear how to exactly define a mode. Martin [20] uses the moment where early injections are not ending inside the piston bowl as discriminator, since this can mark the point where traditional diesel-like combustion is not feasible anymore. For engines with a flat piston, as the engine in the current work, this cannot be used. Taritas [21] observes a transition in heat release when sweeping injection timing, which could be correlated to transitioning from CDF to RCCI operating mode. Klingbeil [22] shows how sensitive the

injection timing can be in relation to knock and misfiring, and explains the trade-off between NO_x emission and efficiency in a 250 mm bore engine. All in all, when doing research on a dual fuel engine in the range from CDF to RCCI, more clarity is desired on the behaviour of trade-offs and the results which are achievable.

At Lund University (Sweden) this research is performed on a 200mm bore medium speed dual-fuel marine engine. The research goal of this work is to create a better understanding of how the pilot injection ignites the premixed fuel under different conditions. Because of its market maturity this work focusses on methane as main fuel. The engine can be set up in 'optical' or 'metal' configuration. The optical configuration is done according to the Bowditch design [23], while in the metal configuration the engine is assembled conform the standard production setup. The optical work performed on this engine aims at investigating the ignition process of the pilot injection [24]. The optical measurements do not allow for emission measurements and are typically limited in testing time. For this reason, as preparation for a more extensive optical campaign, a metal campaign was performed. The current paper discusses the results from the metal campaign. This should give insight in the advantages and limitations of CDF combustion, RCCI combustion, and its transition range in a medium speed engine. In metal configuration extensive testing, including emission measurement, was possible. The question that will be answered with this research is: what are the most preferable operating conditions? The engine operation will be rated on NO_x emissions because of legislation, uncombusted methane because of its greenhouse gas impact, engine efficiency and cycle to cycle IMEP variation.

During the campaign the engine was run with an injection timing ranging from RCCI to Conventional Dual Fuel mode. In the next section the experimental setup used in this measurement campaign will be described. This will be followed by the testing procedure and the range of tested parameters. Next the results will be discussed. Finally, the conclusion and recommendations for follow up are given.

2. Experimental setup

2.1 The engine

The base engine on which the campaign was performed is a Wärtsilä W20DF 6-cylinder engine. Engine specifications are presented in Table 1. For research purposes the engine, shown in Figure 1, is converted to single cylinder operation. For this reason, the cylinder heads from the unused cylinders are

Figure 1 Warstsila W20DF research engine in single-cylinder configuration.

removed, and the cylinders are blocked off. To prevent undesired pumping or compression their piston crowns are removed leaving an open connection with the crankcase.

Table 1 Engine specifications

Engine identification	Wärtsilä W20DF
Displaced volume	8.8 liter / cylinder
Bore	200 mm
Stroke	280 mm
Compression ratio	12.7:1
Number of valves	4 / cylinder
IVO	-5 cad aTDC
EVO	-35 cad aBDC
IVC	-35 cad aBDC
EVC	10 cad aTDC
Valve lift	17 mm

The original turbocharger is omitted because it would not be sized appropriately for single cylinder operation. To create the desired cylinder charging, the remaining cylinder is supplied with air from a 2000 litre buffer, which is filled with air from the 10 bar workshop compressor over a control valve. To mimic realistic exhaust backpressure two butterfly valves are placed in the exhaust trajectory. By placing a large, coarsely controlled valve in parallel to a smaller, finely controlled valve in parallel, any desired backpressure can be created precisely.

The fuelling system contains a full-size diesel injector, centrally placed in the 4-valve head. The injector has enough capacity to run the dual fuel engine in diesel-only operation over the complete torque range. High pressure diesel is supplied through a common rail, from an externally driven XPI high pressure pump. The natural gas is injected into the intake port, at a pressure 2 bar higher than intake pressure. This pressure ensures sonic conditions, making the gas supply insensitive to pulsations in the intake port.

The engine is equipped with an experimental valve drive system. Both intake and exhaust valves are operated by hydraulic pistons which are electronically controlled. This Electro Hydraulic Valve Actuation (EHVA) [25] system gives freedom to choose any desired value for both valve timing and valve lift. Hydraulic supply is coming from an engine driven hydraulic pump and the control is performed by a dSpace MicroAutoBox. Besides the experimental freedom on valve operation, the lack of mechanical coupling of the valve train is a very strong practical advantage when converting the engine to optical operation.

2.2 Cylinder pressure analysis

For cylinder pressure analysis the engine is equipped with a water cooled Kistler 7061B pressure sensor in the cylinder and Kistler 4075A pressure sensors in the intake and exhaust port. Engine position was measured at a resolution of 0.2 CAD using a Kistler 2614CK crank angle encoder.

During-post processing the pressure is pegged making use of the fast intake pressure sensor. A TDC correction and the compression ratio are determined based on a motored cycle, and the polytropic coefficient is fitted during compression and expansion. With this data the apparent heat release analysis could be performed.

2.3 The fuels

All tests were performed with Swedish commercial diesel fuel, and natural gas coming from the south-Swedish natural gas net[26]. This is a high caloric gas, with a low nitrogen and carbon dioxide content. Specification of both fuels can be found in Table 2.

Table 2 Properties of the fuels used in dual fuel tests.

Diesel MK1	
Cetane number	51-54
H/C ratio [-]	1.87
Boiling point [˚C]	160-380
Density [kg/m^3]	810-820
LHV [MJ/kg]	43.15
Swedish Natural Gas	
Methane [mol-%]	88.91
Ethane [mol-%]	6.00
Propane [mol-%]	2.46
i-Butane [mol-%]	0.39
n-Butane [mol-%]	0.60
i-Pentane [mol-%]	0.13
n-Pentane [mol-%]	0.10
Hexane [mol-%]	0.05
Nitrogen [mol-%]	0.32
Carbon Dioxide [mol-%]	1.04
Methane Number [-]	71.70
LHV [MJ/kg]	47.90
Density [kg/m^3]	0.827

2.4 Emission analysis

Emissions were continuously sampled from the engine exhaust, downstream of the backpressure control valves. Emissions were measured with a Horiba Motor Exhaust Gas Analyser MEXA-9400 and the required appropriate exhaust cooling and drying equipment. Next to the main control module, the emission rack comprises an infrared analyser for CO and CO_2, a flame ionization analyser for uncombusted hydrocarbons, a chemiluminescent NO_x analyser and a magneto pneumatic O_2 analyser. The specifications can be found in Table 3 All data was continuously recorded, and after a stabilization time the data was averaged over the measurement duration of 300 cycles.

Table 3 Emission analyzer specifications.

Species	Range	Precision
CO / CO_2	0-1 / 16 %	±1% FS
NO_x	0-5000ppm	±1% FS
HC	0-10000ppm	±1% FS
O2	0-25%	±1% FS

3 Parameter variations and results

Parameter variations tests were performed with a constant natural gas energy input. This allowed a swift execution of tests, with good reproducibility. This was done with three different amounts, representing three different engine loads. The injected gas masses for the three load levels are given in Table 4.

Table 4 Injected gas mass per load case.

10 bar IMEP reference, low load	380 mg/cycle

14 bar IMEP reference, medium load	490 mg/cycle
18 bar IMEP reference, high load	610 mg/cycle

The pilot diesel injection parameters were chosen to match a not yet published optical research campaign in a spray chamber, for the same injector as used in the test engine.

In total 448 individual tests were performed, with variation on intake and exhaust pressure, gas amount, and diesel injection parameters, including SOI of the pilot diesel injection. A subset of the test matrix is reported in this paper. Every test was, after a stabilization period, recorded over 300 combustion cycles. Unless otherwise stated the presented results are the average values over such recording.

3.1 Lambda

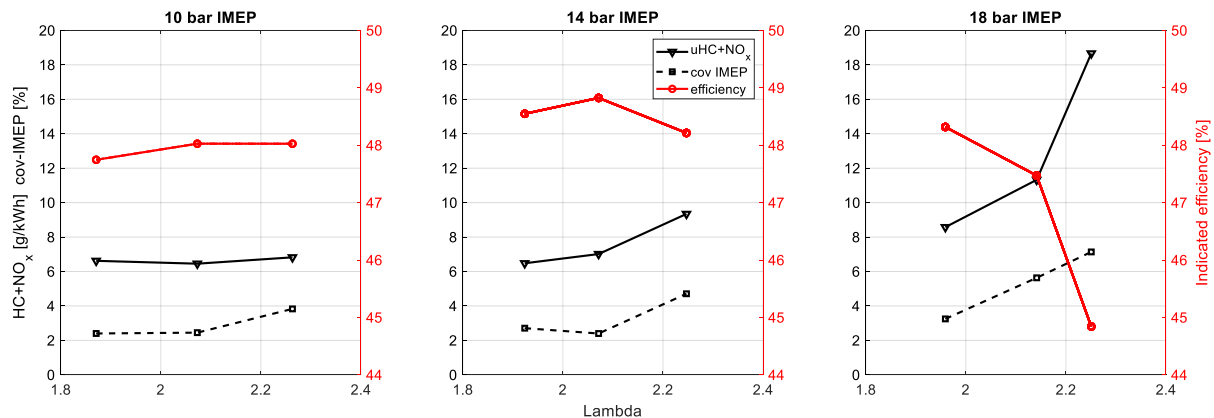A first investigation was done on desired global lambda value. This was calculated making use of the

Figure 2 Impact of lambda for three different load cases.

stoichiometry number of both fuels, weight-averaged on their masses. Tests with different lambda values were performed by changing the intake charge pressure. The air supply control valve in the intake system of the test cell was used for this.

It was shown that the lambda value has a significant impact on emissions, efficiency, and engine cycle to cycle stability. Besides the impact on the normal combustion behaviour, the global lambda value is also an important parameter for knock sensitivity. Richer conditions are increasing the likeliness of knocking combustion late in the cycle. Knocking combustion, observed through cylinder pressure analysis, was used as rich limit during testing.

Since the combustion speed is significantly influenced by lambda, the effect that injection timing has on the combustion phasing differs between different lambda test points. This makes it complex to separate the influence of chosen lambda value, irrespective of chosen SOI of the diesel injection. As a solution, a sweep of SOI timings was done for different lambda values. The initial rating is done on the optimal achievable result over this sweep of timings, per lambda value. A trade-off is seen between NO_x and uncombusted hydrocarbons (uHC), when varying injection timing. As a result, the minimum achievable NO_x emission and uHC emission cannot be achieved simultaneously. To come to a more realistic rating of results, at this stage the sum of NO_x and uHC is assessed, in the same way as done in various emission legislations [27]. The results can be seen in Figure 2.

Multiple observations can be made. The cycle to cycle variation, represented by the coefficient of variation on Indicated Mean Effective Pressure (cov-IMEP) according to equation (1), shows a clear trend; a leaner combustion leads to more variation. Some reasons for this are the lower temperature and lower combustion velocity for the air fuel mixture under these conditions [28]. The operated lambda values are on the edge of flammability for methane [29], which increases the risk of misfire. This can be recognized by a higher cov-IMEP under lean conditions.

$$cov_{IMEP} = \frac{\sigma_{IMEP}}{IMEP} * 100\%$$

The presented emissions are the result of two effects. Through the same mechanism that affected cov-IMEP, i.e. the lean flammability limit of methane; leaner conditions result in higher emission of uncombusted methane. At the same time, these leaner conditions result in a lower peak combustion temperature, lowering NO_x formation. Combining these two trends, Figure 2 shows an increase of the sum of uHC and NO_x for leaner conditions.

Finally, the indicated engine efficiency is investigated. It is calculated as the ratio between the indicated mechanical work and the sum of injected diesel and natural gas energy. Also here we see two separate effects, where the first is again related to the lean combustibility of methane. The methane that is not combusted under lean conditions is not creating useful work and thus directly reducing efficiency. On the other hand, leaner combustion in general has a higher efficiency than rich combustion, caused by lower heat losses and a higher heat capacity ratio. Which of the two effects prevails differs over the load cases shown in Figure 2. For the highest load the efficiency drop-off at leanest condition is clearly caused by uncombusted methane. At the lowest load the two effects almost balance out.

Taking efficiency, emissions and stability in consideration for all tested load conditions, it was concluded the best results were not found in the most lean tests. The results also indicated that a much richer mixture did not lead to better overall results. As a conclusion the available operating points with a lambda value slightly richer than two were selected for further testing. The core of the program was being run at the following conditions:

Table 5 Base operating conditions for testing.

Engine speed	900 rpm
Lambda	1.95
Diesel railpressure	1700 bar
Diesel injection duration	300 μs
Reference IMEP	10, 14, 18 bar

3.2 Emissions

Making use of the parameters listed in Table 5, an investigation was done on how the combustion process performs over the range from CDF to RCCI. A sweep over pilot diesel SOI timing was done accordingly. The emission results are shown in Figure 3.
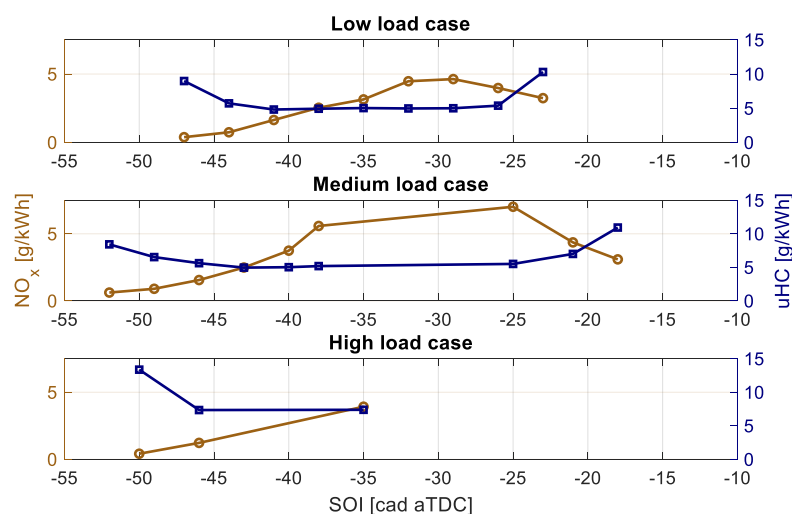
Figure 3 HC and NO_x emissions for all tested load cases, for a range of SOI timings.

As can be seen in Figure 3, the full timing range was not covered at all load ranges. At medium load a start of injection timing between -38 and -25 cad aTDC cannot be achieved, because of knocking combustion induced by high peak temperature and pressure inside the combustion chamber. The same limitation was seen for high load, for injections later than -35cad aTDC. The combustion phasing shown

in Figure 5 below, makes it clear that knock is related to very early combustion phasing, with the CA50 position before top dead centre.

Although the absolute SOI limit of this range is dependent on the applied conditions, the recorded NO$_x$ emissions show that in the range starting around 30 CAD bTDC until TDC the typical diesel behaviour is seen. Analogues to the term Convention Diesel Combustion (CDC), this area can be labelled as the Conventional Dual Fuel operation, where an earlier start of combustion is resulting in higher NO$_x$ production. The early combustion phasing created by this early timing results in a significant amount of combustion taking place before top dead centre. The increasing temperature and pressure in a decreasing volume result in high local combustion temperature. This peak temperature is the dominant parameter for NO$_x$ formation in combustion engines.

In this range an earlier combustion phasing leads to lower uHC emissions. This is also related to the same conditions as mentioned for NO$_x$ production: higher local temperature and pressure. Higher pressure and temperature promote the combustion of premixed methane under lean conditions. At a later combustion phasing incomplete combustion increases, caused by too much combustion that still has to take place during the tail of the combustion. The increased volume, lowering pressure and temperature, are conditions not favourable for reliable flame propagation. An increase in uncombusted methane is the result.

At the early side of the tested SOI range, a different relation between emissions and combustion timing is observed. This is the area where RCCI combustion behaviour is realized. In all three load cases the earliest applied injection leads to lowest NO$_x$ values. Values below 2gr/kWh can be achieved. The mechanism in this operating range leading to low NO$_x$ emissions is the stronger dilution of the diesel fuel, created by the early pilot injection [30]. The dilution leads to a leaner local lambda value, and thus lower combustion intensity. The resulting lower flame temperature results in lower NO$_x$ formation.

The mentioned difference in combustion behaviour between RCCI and CDF can be clearly seen on the heat releases plotted in Figure 4. Here, the heat release profiles for medium load at an SOI of 46 CA bTDC (RCCI) and 21 CA bTDC (CDF) are plotted. Although both cases have almost the same indicated load (RCCI 13.6 bar, CDF 13.3 bar), the heat release profile differs significantly. Although the RCCI case has the highest maximum heat release, it is the initial peak of hardly diluted diesel fuel combustion during CDF operation that results in an almost five times higher NO$_x$ emission (RCCI 0.9 g/kWh, CDF 4.4 g/kWh)
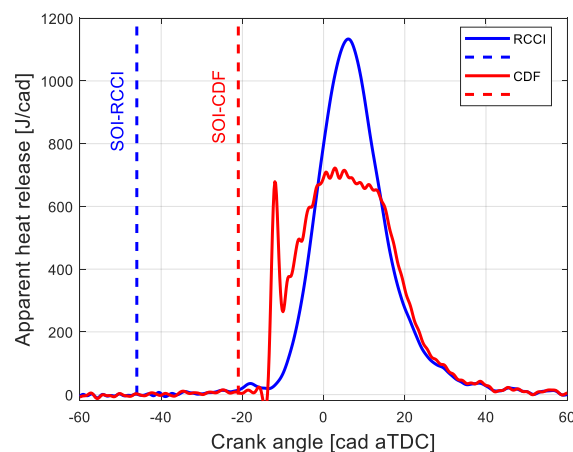
Figure 4 Heat release profile for medium load RCCI and CDF operating points.

Comparable to the CDF range, also in RCCI operation a trade-off between uHC and NO$_x$ emissions is seen. Advancing injection timing, which lowers NO$_x$ formation, results in an increase in uHC emissions. The early injection creates a long ignition delay during which a strong dilution of the pilot fuel can take place. Although the average mixture strength remains the same, the reduction of rich flame kernels acting as high intensity ignition sources for the premixed fuel restrict a proper flame propagation through the lean premixed fuel. The result is an increase in uHC emissions, when advancing start of injection in the RCCI range.

Although the range in between CDF and RCCI operation area could not be tested for all load cases in a safe way, a simple interpolation in Figure 3 indicates that in this third area the lowest uHC and the highest NO$_x$ emissions can be expected.

3.3 Efficiency

Not only does the injection timing have a significant impact on emissions, it also influences indicated engine efficiency which is represented in Figure 5. Two different mechanisms play a role in the resulting efficiency of a dual fuel engine when varying the SOI.

Figure 5 efficiency and combustion phasing.

3.3.1 Combustion phasing.

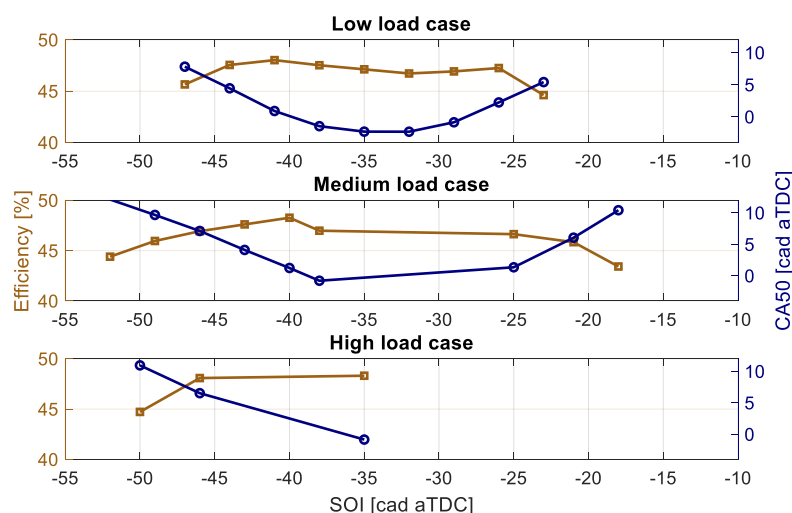The SOI timing is influencing the phasing of the combustion process. As with any engine there is a thermodynamic optimum for this. Too early combustion leads to high heat losses, while too late combustion leaves less of the engine stroke effectively available to generate mechanical work. As indicator for combustion phasing usually the CA50 angle is used; the engine position where 50% of the heat is released from combustion. For light duty engines a commonly accepted rule of thumb for optimal phasing is a position of CA50 between 8 and 10 cad aTDC [31]. With this value being dependent on heat release profile and engine speed it is not surprising that the results show a slightly different value [32]. On the tested low speed engine best efficiency was achieved with a CA50 position between 0 and 5cad aTDC, as can be inferred from Figure 5.

3.3.2 Completeness of combustion

The measured methane emissions in the exhaust gas indicate that not all gaseous fuel is combusted. On average an indicated specific fuel consumption around 160 g/kWh was seen during testing. That means that observed methane emissions in the range between 5 and 10 g/kWh are representing a significant amount of the total amount of metered gaseous fuel. A theoretical change from 10 to 5 g/kWh would lead to a relative engine efficiency increase of 3%. It can be concluded that for best efficiency a low emission of uHC is required.

3.4 Engine stability.

To ensure a constant power delivery at acceptable noise, vibration and harshness (NVH) conditions, a small cycle to cycle variation of engine torque is required. During the test campaign this behaviour was rated on cov-IMEP. The results over the applied range of SOI timings are presented in Figure 6. What is considered as acceptable maximum level depends on the application, brand, customer and engine type. Common threshold values are in the range from 3 to 5% maximum [33]. Considering this range, the measured data and observation of the engine running in the test cell, a maximum cov-IMEP of 4% was chosen as acceptable threshold. What can be seen is that this limit is crossed when going to very early or very late SOI timing. These are the same areas where uHC emissions start to increase. This can be explained by the fact that both cycle to cycle variations and high uHC emissions are caused by poor combustion quality. This correlation is substantiated in Figure 7, showing the combinations of uHC and cov-IMEP from the discussed operating points. The included regression line indicates that one parameter could be used to give an estimation of the other. In situations where methane emissions are not measured, or are difficult to measure (e.g. skip-fire operation in optical configuration), a qualitative prediction could be made based on trends in measured or analysed torque variations.
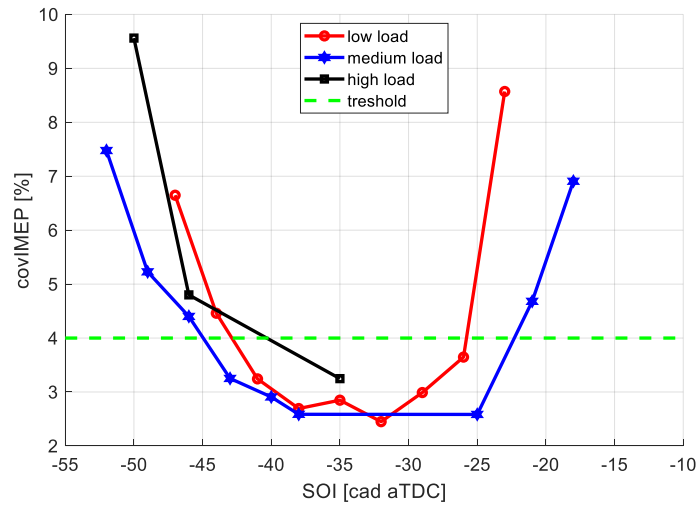
Figure 6 Cycle to cycle variation of IMEP for various start of injection timings.

In a situation where no torque, speed uniformity or IMEP analysis is possible, a uHC measurement could be used to estimate stability. A limitation for this approach is that other parameters should not vary too much. Whether other parameter variations are the cause of the wide spread around the shown regression in Figure 7 is open for future research.
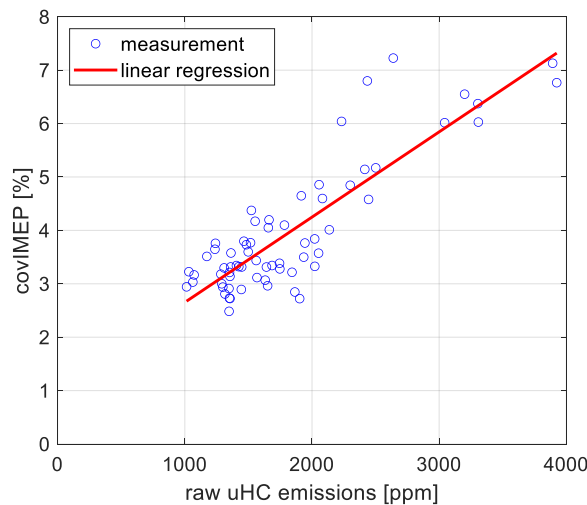
Figure 7 Correlation between incomplete combustion and variation in IMEP

3.5 Desired operating range.

When taking the measured emissions, engine efficiency and stable engine operation into account, it is clear that the optimal working point is strongly dictated by requirements. When the only requirement is on NO_x emissions, for example because of legislation, the earliest possible timing is preferred. When efficiency is key, timing should be retarded to the latest possible RCCI timing, at the cost of high NO_x emissions. Best engine stability, with the lowest cycle to cycle variation, can be achieved by running in the operating range in between RCCI and CDF mode.

When taking all requirements into account, a sound engineering optimum can be addressed. For the actual engine, under the tested conditions, an injection timing between -45 and -40 cad aTDC shows at the same time close to optimal NO_x, uHC, efficiency and cov-IMEP results. This timing is in the transition area towards RCCI combustion. From this area on the heat release profile starts to show the typical RCCI-type bell shape, like demonstrated in Figure 4.

4 Conclusions and future work

A measurement campaign was performed on a medium speed marine engine, running on natural gas using a pilot diesel injection for ignition. The engine was operated in the range from RCCI to CDF, defined by the timing of the pilot injection. The following observations were made:

- A preferred global lambda value for the analysed operating points, taking into account emissions, cov-IMEP and efficiency, is found just below Lambda=2.
- Lowest NO_x emissions can be achieved with either late CDF timing or early RCCI timing. The highest NO_x emissions are seen in between RCCI and CDF timing, where the earliest combustion phasing is achieved. An indicated value below 2g/kWh can be achieved.
- A correlation between increased NO_x emissions and an initial peak in heat release was observed.
- The emission of uncombusted methane is lowest with late RCCI timing or early CDF timing. The observed trends are inverse to those for the NO_x emissions.
- Highest engine efficiency was achieved with a ca50 combustion phasing between 0 and 5 CAD aTDC, in the RCCI regime.
- Engine stability was rated on cov-IMEP. The best values, below 4%, were achieved in the timing range between RCCI and CDF operation.
- An overall optimum of efficiency, emissions and stability can be achieved with a pilot timing in the range between -45 and -40 cad aTDC. This is the start of RCCI operation.

Until now all work was done with one pilot injection, and natural gas as main fuel. In a future campaign, experiments with a second pilot can be performed, to try to shift the trade-off between NO_x and uHC downwards. The timing experiments can also be very relevant for methanol as main fuel, which is currently getting high attention in the marine industry.

The currently found optima will be the operating points in a future optical campaign. Here a more in-depth explanation of the development of the combustion process should be found.

5 References

[1] REGULATION (EU) 2021/1119 OF THE EUROPEAN PARLIAMENT AND OF THE COUNCIL of 30 June 2021 establishing the framework for achieving climate neutrality and amending Regulations (EC) No 401/2009 and (EU) 2018/1999 ('European Climate Law'). 2021. doi: 10.5040/9781782258674.

[2] H. Kim, K. Y. Koo, and T.-H. Joung, "A study on the necessity of integrated evaluation of alternative marine fuels," Journal of International Maritime Safety, Environmental Affairs, and Shipping, vol. 4, no. 2, pp. 26–31, Apr. 2020, doi: 10.1080/25725084.2020.1779426.

[3] K. Andersson, S. Brynolf, J. Hansson, and M. Grahn, "Criteria and Decision Support for A Sustainable Choice of Alternative Marine Fuels," Sustainability, vol. 12, no. 9, p. 3623, Apr. 2020, doi: 10.3390/su12093623.

[4] A. G. Elkafas, M. Khalil, M. R. Shouman, and M. M. Elgohary, "Environmental protection and energy efficiency improvement by using natural gas fuel in maritime transportation," Environmental Science and Pollution Research, vol. 28, no. 43, pp. 60585–60596, Nov. 2021, doi: 10.1007/s11356-021-14859-6.

[5] S. Verhelst, "Future vehicles will be driven by electricity, but not as you think [Point of View]," Proc. IEEE, vol. 102, no. 10, pp. 1399–1403, Oct. 2014, doi: 10.1109/JPROC.2014.2351191.

[6] D. M. Wall, S. McDonagh, and J. D. Murphy, "Cascading biomethane energy systems for sustainable green gas production in a circular economy," Bioresource Technology, vol. 243, pp. 1207–1215, Nov. 2017, doi: 10.1016/j.biortech.2017.07.115.

[7] Y. Bicer and I. Dincer, "Clean fuel options with hydrogen for sea transportation: A life cycle approach," International Journal of Hydrogen Energy, vol. 43, no. 2, pp. 1179–1193, Jan. 2018, doi: 10.1016/j.ijhydene.2017.10.157.

[8] J. Dierickx et al., "Strategies for introducing methanol as an alternative fuel for shipping," in 7th Transport Research Arena TRA 2018 (TRA 2018), 2018, pp. 1–10. doi: 10.5281/ZENODO.1456425.

[9]   J. Hansson, S. Brynolf, E. Fridell, and M. Lehtveer, "The Potential Role of Ammonia as Marine Fuel—Based on Energy Systems Modeling and Multi-Criteria Decision Analysis," Sustainability, vol. 12, no. 8, p. 3265, Apr. 2020, doi: 10.3390/su12083265.

[10]   G. A. Karim, Dual-fuel diesel engines (1st ed.). CRC Press, 2015.

[11]   S. L. Kokjohn, R. M. Hanson, D. A. Splitter, and R. D. Reitz, "Fuel reactivity controlled compression ignition (RCCI): a pathway to controlled high-efficiency clean combustion," International Journal of Engine Research, vol. 12, no. 3, pp. 209–226, Jun. 2011, doi: 10.1177/1468087411401548.

[12]   M. Karczewski, J. Chojnowski, and G. Szamrej, "A Review of Low-CO2 Emission Fuels for a Dual-Fuel RCCI Engine," Energies, vol. 14, no. 16, p. 5067, Aug. 2021, doi: 10.3390/en14165067.

[13]   R. K. Maurya, Characteristics and Control of Low Temperature Combustion Engines. Cham: Springer International Publishing, 2018. doi: 10.1007/978-3-319-68508-3.

[14]   G. Belgiorno, G. Di Blasio, and C. Beatrice, "Parametric study and optimization of the main engine calibration parameters and compression ratio of a methane-diesel dual fuel engine," Fuel, vol. 222, pp. 821–840, Jun. 2018, doi: 10.1016/j.fuel.2018.02.038.

[15]   J. Liu, F. Yang, H. Wang, M. Ouyang, and S. Hao, "Effects of pilot fuel quantity on the emissions characteristics of a CNG/diesel dual fuel engine with optimized pilot injection timing," Applied Energy, vol. 110, pp. 201–206, Oct. 2013, doi: 10.1016/j.apenergy.2013.03.024.

[16]   A. Sharafian, P. Blomerus, and W. Mérida, "Natural gas as a ship fuel: Assessment of greenhouse gas and air pollutant reduction potential," Energy Policy, vol. 131, pp. 332–346, Aug. 2019, doi: 10.1016/j.enpol.2019.05.015.

[17]   R. D. Reitz and G. Duraisamy, "Review of high efficiency and clean reactivity controlled compression ignition (RCCI) combustion in internal combustion engines," Progress in Energy and Combustion Science, vol. 46, pp. 12–71, Feb. 2015, doi: 10.1016/j.pecs.2014.05.003.

[18]   T. Duy Nguyen et al., "An experimental evaluation of engine performance and emissions characteristics of a modified direct injection diesel engine operated in RCCI mode," AIMS Energy, vol. 8, no. 6, pp. 1069–1087, 2020, doi: 10.3934/energy.2020.6.1069.

[19]   J. Li, W. Yang, and D. Zhou, "Review on the management of RCCI engines," Renewable and Sustainable Energy Reviews, vol. 69, pp. 65–79, Mar. 2017, doi: 10.1016/j.rser.2016.11.159.

[20]   J. Martin and A. Boehman, "Mapping the combustion modes of a dual-fuel compression ignition engine," International Journal of Engine Research, p. 146808742110183, May 2021, doi: 10.1177/14680874211018376.

[21]   I. Taritaš, M. Sremec, D. Kozarac, M. Blažić, and Z. Lulić, "The Effect of Operating Parameters on Dual Fuel Engine Performance and Emissions – An Overview," T FAMENA, vol. 41, no. 1, pp. 1–14, Apr. 2017, doi: 10.21278/TOF.41101.

[22]   A. Klingbeil, S. Hong, and R. J. Primus, "Influence of Diesel Fuel Injection Characteristics on Dual-Fuel Combustion Modes in a Large-Bore, Medium-Speed Engine," Journal of Engineering for Gas Turbines and Power, vol. 142, no. 1, Nov. 2019, doi: 10.1115/1.4045344.

[23]   F. W. Bowditch, "A New Tool for Combustion Research A Quartz Piston Engine," 1961. doi: 10.4271/610002.

[24]   M. Merts, S. Derafshzan, J. Hyvönen, M. Richter, M. Lundgren, and S. Verhelst, "An optical investigation of dual fuel and RCCI pilot ignition in a medium speed engine," Fuel Communications, vol. 9, p. 100037, Dec. 2021, doi: 10.1016/j.jfueco.2021.100037.

[25]   M. Herranen, K. Huhtala, M. Vilenius, and G. Liljenfeldt, "The Electro-Hydraulic Valve Actuation (EHVA) for Medium Speed Diesel Engines - Development Steps with Simulations and Measurements," Apr. 2007, pp. 2007-01–1289. doi: 10.4271/2007-01-1289.

[26]   "Swedegas." https://www.swedegas.com/Gas_grid/gas_grid

[27]   "Emissions Standards - BorgWarner." https://www.borgwarner.com/technologies/emissions-standards

[28]   John B. Heywood, Internal Combustion Engine Fundamentals, Second Edition, 2nd edition. New York: McGraw-Hill Education, 2018.

[29]   J. J. Hernandez, M. Lapuerta, C. Serrano, and A. Melgar, "Estimation of the Laminar Flame Speed of Producer Gas from Biomass Gasification," Energy & Fuels, vol. 19, no. 5, pp. 2172–2178, Sep. 2005, doi: 10.1021/ef058002y.

[30]   M. Merts, "Conceptual model for the start of combustion timing in the range from RCCI to conventional dual fuel.," presented at the SAE WCX 2022, Detroit, Apr. 2022.

[31]   L. de O. Carvalho, T. C. C. de Melo, and R. M. de Azevedo Cruz Neto, "Investigation on the Fuel and Engine Parameters that Affect the Half Mass Fraction Burned (CA50) Optimum Crank Angle," Oct. 2012. doi: https://doi.org/10.4271/2012-36-0498.

[32]   J. A. Caton, "Combustion phasing for maximum efficiency for conventional and high efficiency engines," Energy Conversion and Management, vol. 77, pp. 564–576, Jan. 2014, doi: 10.1016/j.enconman.2013.09.060.

[33]   R. D. Atkins, An Introduction to Engine Testing and Development. Warrendale, PA: SAE International, 2009. doi: 10.4271/R-344.

THIESEL 2022 Conference on Thermo- and Fluid Dynamics of Clean Propulsion Powerplants

Advances in Pre-Chamber Combustion Technology for Fuel-Flexible High-Efficiency Engines

H.G. Im[1], M. Ben Houidi[1], P. Hlaing[1], F. Almatrafi[1], Q. Tang[1], M.M. Silva[1], H. Aljabri[1], X. Liu[1], K. Hakimov[1], W. Tang[1], I. Gorbatenko[1], J.W.G. Turner[1], G. Magnotti[1], A. Farooq[1], S.M. Sarathy[1], B. Mohan[2], A. AlRamadan[2], A. Nicolle[3], E. Cenker[2], A. Amer[2], W.L. Roberts[1]

[1] King Abdullah University of Science and Technology (KAUST), CCRC, PSE, Thuwal 23955-6900, Saudi Arabia.

E-mail: hong.im@kaust.edu.sa
Telephone: +(966) 544700186

[2] Saudi Aramco Research and Development Center, Transport Technologies Division, Dhahran, Saudi Arabia

E-mail: emre.cenker@aramco.com
Telephone: +(966) 547531173

[3] Aramco Fuel Research Center, Paris, France

Abstract. Internal combustion engines (ICE) remain important as a viable solution in various transport applications. Higher efficiency, lower emissions, and fuel flexibility are key enablers for the ICE to fulfill its mission toward the decarbonization of the transportation sector. The pre-chamber combustion concept shows great promise in achieving this goal by allowing stable lean or highly diluted combustion that utilizes conventional and renewable fuels. KAUST and Aramco have been collaborating under the FUELCOM project to improve the pre-chamber technology in a novel drop-in design for modern light- and heavy-duty engines in order to demonstrate ultra-efficient and near-zero-emission performance. This interdisciplinary project utilized state-of-the-art optical and metal engine facilities, high-pressure laser diagnostics, a well-controlled spray chamber, improved chemical kinetic description validated by experiment and theory, and high fidelity computational fluid dynamic simulations. This paper provides an overview of the recent and ongoing activities to showcase our synergistic effort to design and implement an active pre-chamber technology in heavy-duty engines. Various gaseous and liquid fuels are used, including methane, gasoline, and hydrogen. Extensive experiments and detailed in-cylinder investigations revealed the importance of the fuel-air mixing inside the pre-chamber and its link to the optimal ignition and subsequent main chamber combustion. Based on the fundamental insights gained from the studies, advanced machine learning techniques are also employed to identify optimal pre-chamber design. Key highlights of research methodologies, predictive tools, physical behavior of the pre- and main chamber interactions, and the resulting outcomes in practical engine performance are presented.

1 Introduction

The fuel combustion (FUELCOM) project is a long-term research collaboration program between the Clean Combustion Research Center at KAUST and the Transport Technologies Division at Saudi Aramco's Research and Development Center. The partnership aims to develop early-stage technology by improving the science and application of core ideas that pave the road for sustainable mobility. FUELCOM commenced with a number of projects centered around fundamentally characterizing a wide range of fuel components based on their combustion behavior. This was followed by an extensive investigation of emerging engine combustion concepts, including gasoline compression ignition and preventing preignition in spark ignited engines. In the third and current phase, future concepts are being explored to reach cost-effective, ultra-efficient, and near-zero-emission internal combustion engines (ICE). In recent years, FUELCOM has been undertaking a project to advance the pre-chamber concept to adapt it to lean-burn operations aiming to improve efficiency and reduce emissions. In this paper, we present a review focused on the FUELCOM pre-chamber-related works in which new drop-in solutions have been implemented and investigated in light-duty and heavy-duty configurations. In particular, the we have investigated pre-chamber designs that can be conveniently installed into a heavy-duty engine

with minor reconfiguration. The selected pre-chamber concepts aim to improve the engine's thermal efficiency while limiting NO_x emissions and allowing operation with a wide range of fuels. In general, the vehicle lifespan of heavy-duty trucks is considerably longer compared to the light-duty vehicles, and the project aims to propose a retrofit solution for current vehicles in service as the pre-chamber replaces the diesel injector without modifying the cylinder head. The project also explores alternative fuels that can be produced from renewable sources such as methane, hydrogen, methanol, and ethanol. In addition, this work shed light on the fundamental understanding of pre-chamber jet ignition and combustion while providing practical criteria for optimizing this concept. The main research objectives include:

- Understanding the effect of pre-chamber geometry on different engine operation modes (lean burn vs. EGR dilution at stoichiometry)
- Understanding the mixture formation process inside the pre-chamber and its effect on the ignition
- Understanding the fundamentals of the ignition process induced by the turbulent jets generated by the pre-chamber
- Adapting the pre-chamber operation with different fuels
- Optimizing the pre-chamber design and operation
- Identifying the key chemical kinetic pathways that influence the ignition and combustion propagation

The FUELCOM pre-chamber framework is composed of five workstreams interacting efficiently to achieve the ultimate targets of the project, as illustrated in Fig. 1. We started to design a first concept based on the geometry recommendations in the literature [2, 3]. The design is capable of active and passive operation and has been tested experimentally in a metal engine to evaluate the operating limits and performance. The results then fed the workstreams focused on CFD simulations and optical diagnostics. The relevant engine operating conditions have been reproduced in an optical engine to allow the application of various diagnostics and this has contributed to a better understanding of the engine behavior. Both metal and optical engine experiments were used to validate the CFD simulations. The simulation work has a central role in the project framework. On one hand, it allowed identifying the key improvements needed for a more predictive simulation. This was achieved in close collaboration with the chemical kinetics teams. On the other hand, the validated simulations provided insights into the details of pre-chamber mixture formation, ignition process, and turbulence chemistry interaction. The CFD tool has then served as a platform for applying machine learning to improve the concept geometry. The recommended modifications have been implemented and experimentally tested in engines.
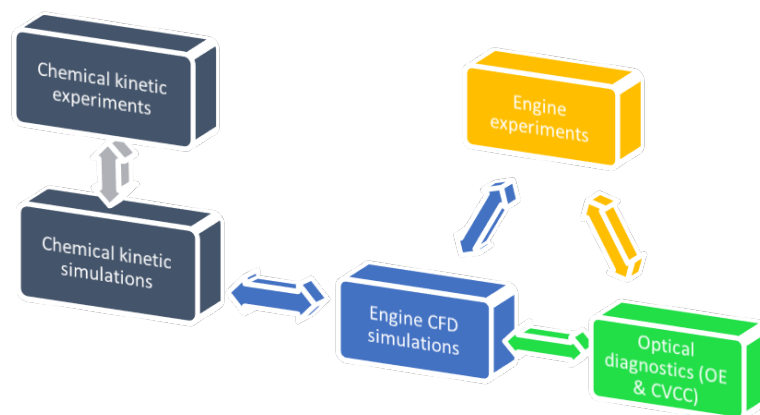
Fig. 1. Illustration of FUELCOM3 research model: interaction between the different work packages.

This review paper is structured into three main sections. First, the experimental work on metal and optical engines is reported to show the methodology and the main findings. Second, the CFD simulation work is presented similarly to show the modeling setup and validation, followed by an overview of the key understanding related to the mixture formation and turbulence chemistry interaction. The optimization of the pre-chamber geometry based on the simulation is also summarized. Third, the chemical kinetics experiment and simulation works are reviewed. The paper reports in its last section the ongoing studies in which our findings and the best CFD practices are used to explore pre-chamber operation in different engine configurations.

2 Pre-chamber design and experiments
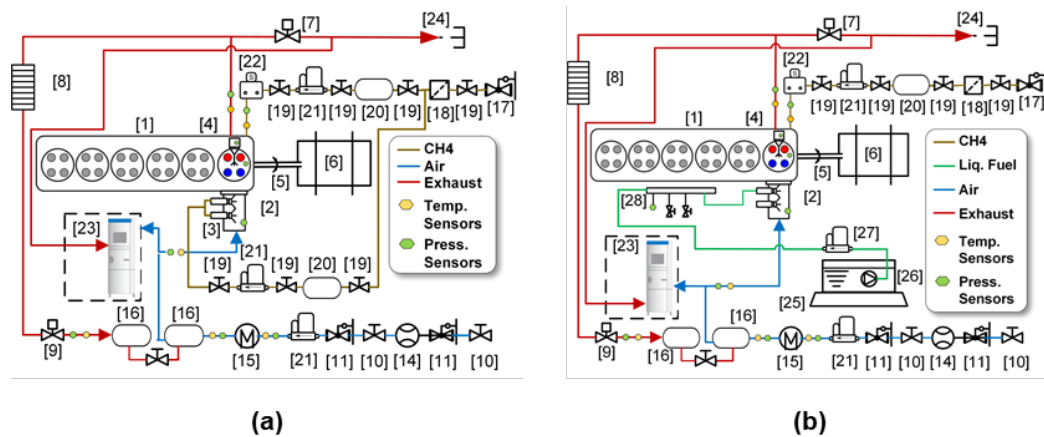
2.1 Experimental engine setup

2.1.1 Single-cylinder research engine

A six-cylinder heavy-duty Volvo truck engine was modified for pre-chamber combustion, including installing a modified intake manifold for port fuel injection and deactivating five of the cylinders for single-cylinder operation. An omega-shaped piston with a bowl volume larger than the standard piston was installed in the active unit to reduce the engine geometric compression ratio to 11.5 from the standard 17.0. The summary of the engine specifications is listed in Table 1. The engine control hardware is built around a National Instruments (NI) real-time controller (CompactRIO), equipped with a C-series module for dedicated control and data-acquisition functions. The control software was written in the NI LabVIEW environment. More details can be found in the previous publications [4-8].

Table 1. Engine Specifications

Engine model	Volvo D13C500	
Control system	NI LabVIEW	
Piston shape	Bowl-in-piston	
Valve mechanism	Single overhead cam	
Number of valves	2-Intake 2-Exhaust	
Bore	131	[mm]
Stroke	158	[mm]
Connecting rod length	255	[mm]
Compression ratio	11.5	[-]
Displacement (Single Cylinder)	2.1	[L]
Engine speed	1200	[rpm]
Intake pressure	1.5	[bar]
Intake valve timing	Open	-360 CAD aTDC
	Close	-170 CAD aTDC
Exhaust valve timing	Open	145 CAD aTDC
	Close	-360 CAD aTDC

The engine layout can be set up for gaseous and liquid fuel operation in the main chamber, as shown in Fig. 2 (a) and (b). A common feature between the two layouts was that the pre-chamber was fuelled with gaseous fuel (methane). The flow rate was controlled by a mass flow controller, and the injection duration was set by a solenoid valve downstream of the mass flow controller. Passive pre-chamber fuel operation, where no auxiliary fuel was added into the pre-chamber, can be achieved by deactivating the mass flow controller and the solenoid valve in the pre-chamber fuel line. In the main chamber gaseous fuel layout (Fig. 2 (a)), the fuel flow rate was metered by a mass flow controller. In contrast, the main chamber liquid fuel layout (Fig. 2 (b)) employed a gravimetric fuel balance system to measure the fuel flow rate. In addition, a Coriolis mass flow meter was also installed downstream of the fuel pump to cross-verify the mass balance readings.

Fig. 2. Schematic diagram of the experimental setup – (a) Gaseous fuel injection into the main chamber, and (b) Liquid fuel injection into the main chamber (1. Engine, 2. Intake manifold, 3. Port fuel injectors, 4. Pre-chamber, 5. Cardan shaft, 6. Dynamometer, 7. Back pressure valve, 8. EGR Cooler, 9. EGR valve, 10. Main air valve, 11. Pressure regulator, 12. Control air valve, 13. Intake throttle valve, 14. Air flowmeter, 15. Air heater, 16. Mixing Tank, 17. Main gas fuel valve, 18. Gas fuel filter, 19. Valve, 20. Pressure damping vessel, 21. Mass flow controllers, 22. Pre-chamber injector, 23. Horiba exhaust analyzer, 24. Vent to the atmosphere, 25. Mass balance, 26. Fuel tank and submerged pump assembly, and 27. Coriolis mass flow meter, and 28. Low-pressure common rail).

2.1.2 Single-cylinder optical engine

The optical engine was modified based on the metal engine mentioned in the previous section, maintaining similar geometric dimensions. Fig. 3 shows the optical engine setup [9]. A Bowditch extended piston with a flat optical piston crown provided optical access to the combustion chamber from the bottom view. Three optical windows allowed laser access and imaging from the side view. Self-lubricating PTFE piston rings were used for combustion chamber sealing. Metal or optical pre-chamber were adopted to investigate the combustion characteristic of the main chamber and pre-chamber, respectively. Optical diagnostic techniques, such as the high-speed imaging of the natural flame luminosity or OH* chemiluminescence, planar laser-induced fluorescence (PLIF) of acetone and formaldehyde were applied. More details about the optical engine and diagnostic methods can be found in [9-11].
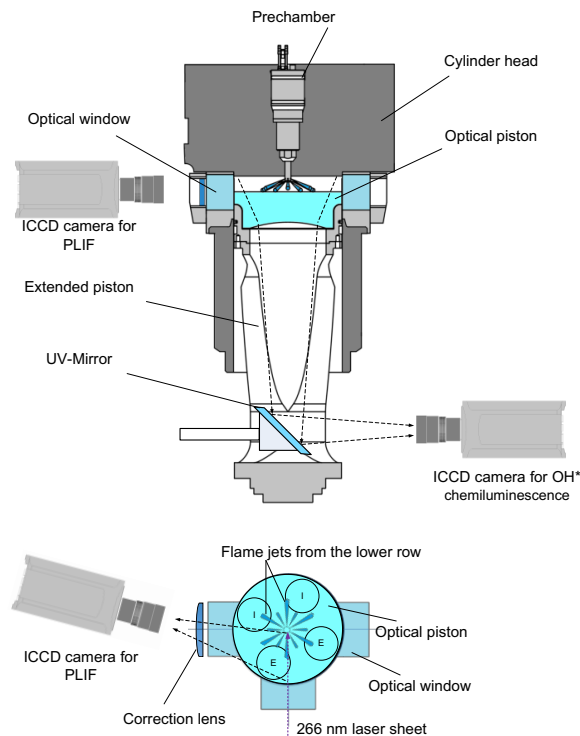
Fig. 3. Schematic of the optical engine and simultaneous PLIF (side view) and OH* chemiluminescence (bottom view) imaging system [9, 10, 12].

2.2 Pre-chamber Design and Parameterization Scheme

The selected pre-chamber concept has a geometry that makes it fit into the in-series Volvo D13 diesel engine. The engine's central injector is replaced with a pre-chamber assembly that fits inside the injector's pocket. Accordingly, the pre-chamber design has a relatively long and narrow shape compared to most pre-chamber designs found in the literature, as shown in Fig. 4. The prominent feature of the pre-chamber design is the long and narrow throat geometry; hence, the design was named the narrow-throat pre-chamber design.
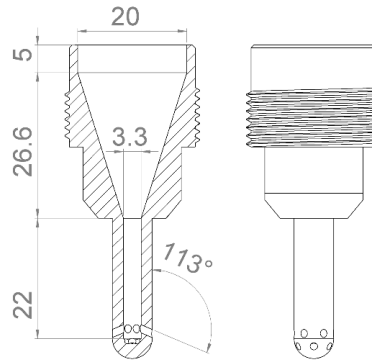

Fig. 4. The internal geometry of the narrow-throat pre-chamber.

In the base design, the pre-chamber (PC) volume and total nozzle opening area were selected based on the recommendations from Gussak et al. [2, 3], which are consistent with a later study by Shah et al. in a heavy-duty engine setting [13]. To understand the effect of pre-chamber geometry on engine combustion characteristics with this novel narrow-throat feature, the pre-chamber dimensions are parameterized following a scheme similar to the one used by Shah et al. [13], as shown in Table 2. Two characters denote the pre-chambers: the first letter represents the pre-chamber volume. The second number indicates the total nozzle opening area normalized by pre-chamber volume (e.g., PC-B2). The resulting pre-chambers with different volumes are presented in Fig. 5.

Table 2. Parameterization of pre-chamber geometrical parameters

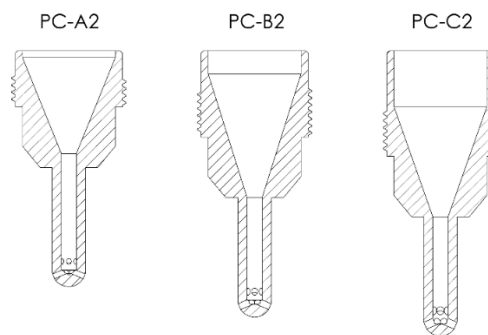|			Volume classification		
			A	B	C
	PC volume / Engine clearance volume [%]		1.6	2.5	3.4
	PC volume [cc]		3.25	5.07	6.90
	Total nozzle area / PC volume [cm⁻¹]		Nozzle hole diameter [mm]		
Nozzle class.	1	0.027		1.20	
	2	0.035	1.10	1.40	1.60
	3	0.047		1.60	

Fig. 5. The internal geometry of pre-chambers with different volumes.

Since the nozzle tip is too small to accommodate the desired total nozzle opening area, the number of nozzle holes was set to 12, arranged in two layers, each containing 6 holes. A 30-degree radial offset angle was introduced between the two nozzle layers. The nozzle umbrella angle is kept constant at 134 degrees for all the pre-chambers.

Given that the PC throat diameter was kept constant in all the pre-chambers, another generation of pre-chamber was designed with a larger throat diameter (5.3 mm), based on the pre-chamber volume and nozzle diameter setting of the base pre-chamber geometry (PC-B2 in Table 2). The previous pre-chamber set with a 3.3 mm diameter was denoted as the Generation 1 pre-chambers, while the larger throat diameter pre-chambers were denoted as Generation 2. The two pre-chamber generations are compared in Fig. 6.
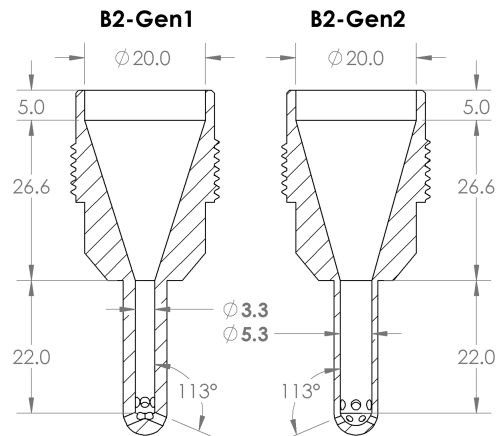
Fig. 6. Comparison of Generation 1 and 2 PC-B2 pre-chambers.

The PC body was installed into an adaptor part that houses a spark plug, a thermocouple, a piezo-lectric pressure sensor, and a gas supply channel for PC fueling. A check valve is installed into the gas supply channel to prevent backflow when the PC combustion occurs. The cross-section view of the pre-chamber assembly inside the cylinder head and the components are shown in Fig. 7.
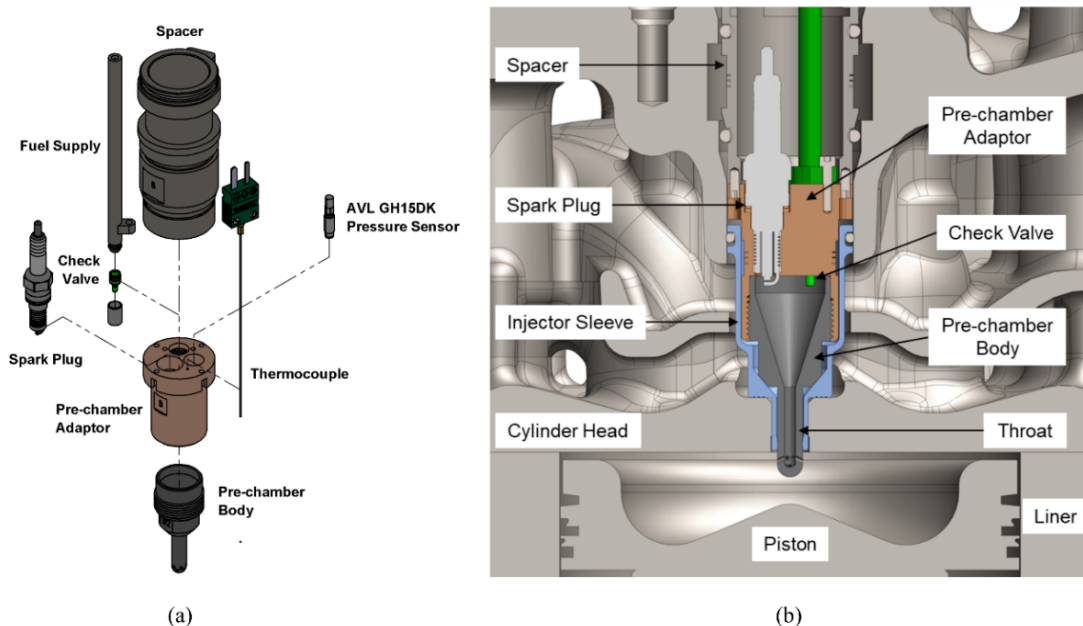
Fig. 7. Pre-chamber assembly: (a) Exploded view showing pre-chamber components, and (b) Cross-section view of the cylinder head.

The check valve on the fueling line allows the delivery of fuel into the PC only while the fuel line pressure is above the PC pressure. This mode of fuel supply hampered the precise control of the fuel quantity and timing in the pre-chamber. Depending on the PC mass flow controller settings, the amount of fuel line pressure was also different. To handle these complexities, a 1-D engine simulation model

was set up in GT-Power simulation software, mimicking all the important aspects of the pre-chamber fueling arrangement in the model, as shown in Fig. 8. The flow rates table through the check valve was acquired from the original manufacturer. Initial model parameters, such as PC fuel line pressure and fuel temperature, are measured from the experiments [6]. The discharge coefficient through the pre-chamber nozzle holes was determined by calibrating pre-chamber and main chamber pressure predictions from the 1-D model against the measured pressure traces. In addition to the GT-Power model, an in-house multi-chamber heat release analysis code was used to estimate the heat release rate in the pre-chamber and the main chamber separately.
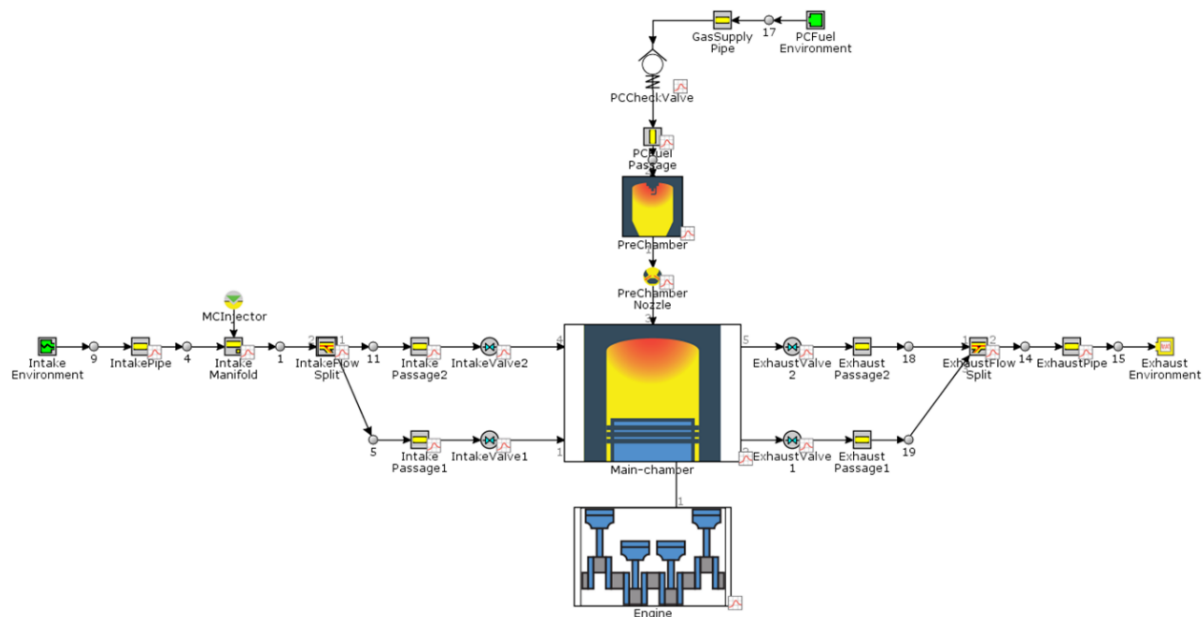

Fig. 8. 1-D GT-Power pre-chamber engine setup with pre-chamber fueling via a check valve.

## 2.3   Understanding pre-chamber combustion from engine experiments

2.3.1 Effects of different pre-chamber fueling strategies

Using methane (CH_4), a major research campaign was conducted to understand the mixture formation process in the pre-chamber [6]. The 1-D GT-Power model was used to analyze the mixture formation process in the pre-chamber, particularly during the intake stroke (where the pre-chamber fuel injection occurs) and the compression stroke (where the lean air-fuel mixture from the main chamber is pushed into the pre-chamber by the rising piston). The pre-chamber λ values that are estimated by the 1-D GT-Power model for different operating conditions (global-λ 1.6 to 2.0) were compared against the 3-D CONVERGE CFD simulations. This led to the following observations:

- A significant offset was observed between the 1-D and 3-D models, with the former showing richer air-fuel compositions. The pre-chamber λ values estimated by the CFD model are well-correlated to the measured pre-chamber pressure buildup. In contrast, the 1-D model predictions of pre-chamber λ failed to match the experimental observations.
- It was concluded that the 1-D model over-predicts the amount of fuel retained in the pre-chamber following the injection event. The CFD simulations showed that a significant fraction of the injected fuel is leaking into the main chamber during the fuel injection phase. The idealized 1-D model did not consider this leak, thus it over-predicted the fuel retention in the pre-chamber.
- Using Benson's trapping efficiency equation with short-circuiting, the trapped fuel in the pre-chamber is estimated. The coefficients required for Benson's equation are acquired by a curve fitting of trapping efficiency calculated from the CFD results. The applicability of Benson's equation is tested further at different operating conditions and showed similar estimations of pre-chamber λ predictions as compared to the CFD results.

The effects of different fueling strategies were also investigated in the optical version of the engine. The main chamber combustion characteristics of the active and passive pre-chamber were compared by Marquez et al. [14]. The global lambda of the two cases was maintained close to 1.3 and the active case added about 4% of the total fuel to the pre-chamber. The averaged flame probability distributions (AFPD) of the two cases are presented in Fig. 9 along with the pressure measurements in the pre- and main chamber of the optical engine. Note that the term Fuel Mean Effective Pressure of the PC (FuelMEP$_{PC}$) was used to represent the PC fueling mass. The AFPD was used to study the jet probability in the earliest part of the cycle for the reported passive case. It indicates that the peak PC pressure and main chamber heat release are higher in the active case due to the PC enrichment. The first two AFPD images of the active case present symmetric with six flame jets, indicating a stable main chamber combustion.

Sampath et al. [10] studied the effect of the pre-chamber fueling ratio (PCFR) on the main chamber combustion using simultaneous 10 Hz acetone PLIF and OH* chemiluminescence imaging. Two cases with global lambda of 2.0 and PCFR of 7% and 13% were compared, as shown in Fig. 10, which shows the ensemble-averaged PLIF and OH* fields. Based on GT-Power simulations, the pre-chamber air/fuel mixture of the PCFR 7% was close to stoichiometry and slightly richer in the PCFR 13% case. It showed that the over-enrichment of the pre-chamber results in a delay of the pre-chamber jet penetration and combustion phasing.
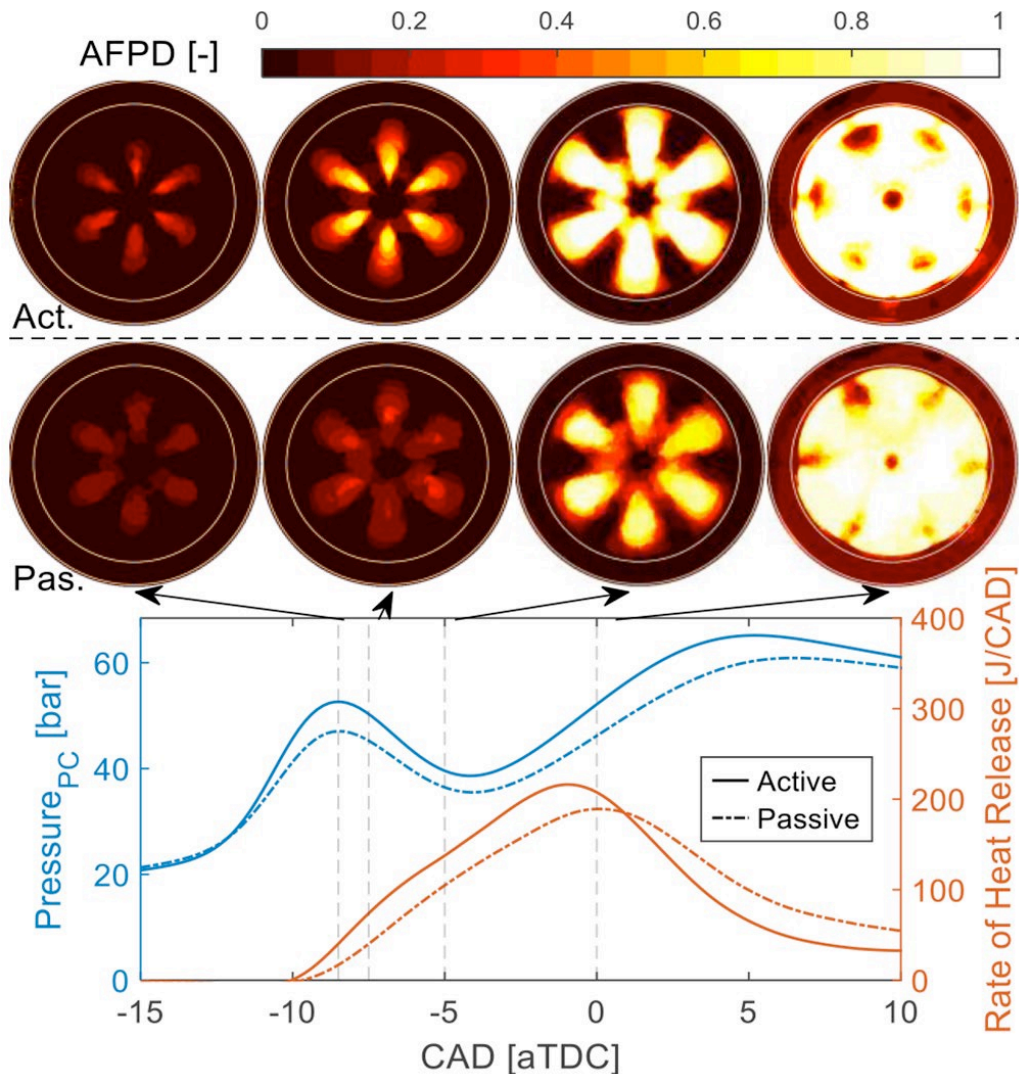
Fig. 9. The averaged flame probability distribution (AFPD), pre-chamber pressure, and the main chamber heat release rate of the active (FuelMEP$_{PC}$ of 0.84 bar, FuelMEP$_{MC}$ of 20.83 bar, and λ_{Global} of 1.3) and passive (FuelMEP$_{PC}$ of 0 bar, FuelMEP$_{MC}$ of 20.88 bar, and λ_{Global} of 1.26) pre-chamber cases [14].
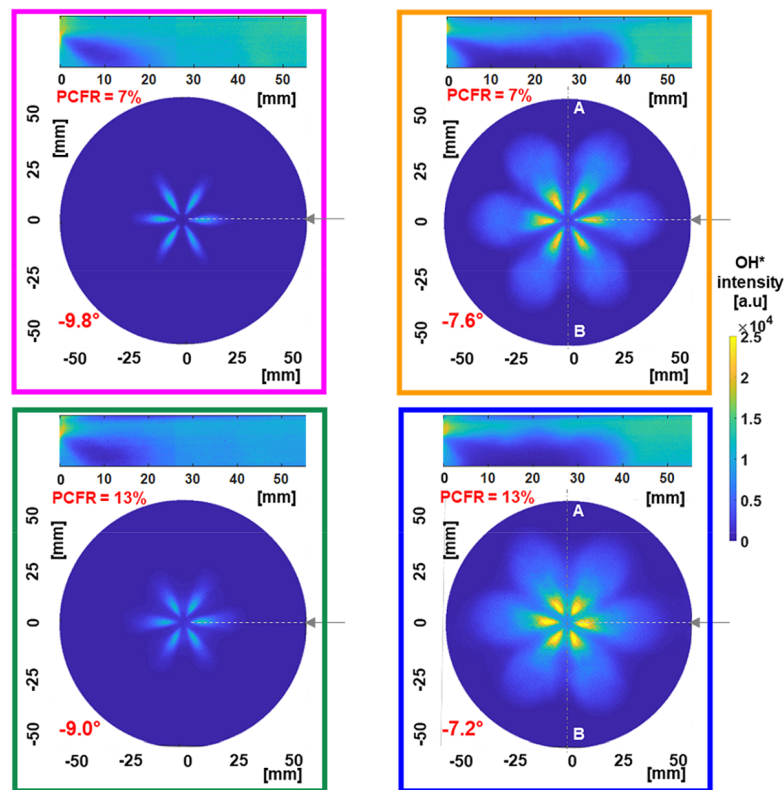
Fig. 10. (a) Ensemble-averaged PLIF and OH* chemiluminescence for the two cases with λ_{Global} of 1.3 and PCFR of 7% and 13% [10].

Tang et al. [12] investigated the effect of the main chamber fueling rate on the pre-chamber jet and flame jet penetration. The pre-chamber fueling was fixed at 7.2 mg/cycle and the main chamber fueling was varied to achieve global lambda of 1.8 (lean case) and 2.3 (ultra-lean case). The "post" pre-chamber jets were spotted by the PLIF imaging after the main jet discharge in the ultra-lean case, which explained the "post-combustion" phenomenon reported in the metal pre-chamber engines [5]. Two unburned hydrocarbon regions, one in the central part of the cylinder near the nozzle and the other among the pre-chamber jets, were elucidated by the PLIF imaging. Fig. 11 shows that the pre-chamber jet (PLIF) penetration length is always longer than that of the flame jet (OH*), indicating a layer of unburned or partially burned species surrounding the propagating flame jets. The over-enrichment from the main chamber to the pre-chamber in the lean case results in a decrease in the peak ΔP and a slower pre-chamber jet penetration, which is not in favor of faster main chamber combustion and higher engine efficiency. The pre-chamber velocity shown in Fig. 11 is obtained by calculating the change rate of the averaged jet penetration length from different cycles at the same crank angle. Due to the cycle-to-cycle variation of the engine, the speed at the beginning of the jet discharge can be significantly underestimated. A dual laser system like particle imaging velocimetry is required to measure the instantaneous jet velocity.

2.3.2 Effects of pre-chamber geometry

Based on the comparison of the five pre-chamber geometries presented in Table 2, the influence of the narrow-throat pre-chamber volume and nozzle hole diameter was studied at a constant engine speed of 1200 rpm for the global-$\lambda \geq 1.6$ until the lean limit using methane fuel [8]. The PC-λ values were estimated from the corrected 1D simulation scheme. Combustion visualization was also performed on the optical version of the engine where the same operating conditions were reproduced. This helped to explain the initial jet developments in the main chamber before the second or bulk heat release stage. In these studies, it was found that:

- With increasing pre-chamber volume, the combustion gas temperature in the pre-chamber increases, leading to hotter jet temperatures in the main chamber. At ultra-lean conditions (global-$\lambda > 1.8$), ultra-low NOx emissions were observed. The NOx emissions are more sensitive to PC jet temperature at these conditions, which scales with the pre-chamber volume.

In contrast, the higher jet temperatures can reduce unburned fuel species and thus, improve combustion efficiency.

- The gross indicated efficiency is highest for the smallest pre-chamber, likely due to the reduced heat transfer losses. With increasing pre-chamber volume, the pressure build-up inside the pre-chamber increases inducing a higher jet momentum and thus higher heat losses. The heat transfer losses inside the pre-chamber were calculated using the in-built flow heat transfer model. The gas temperature was estimated from the pre-chamber pressure, and the wall temperature was measured from the experiments [8].

- The trend of pre-chamber pressure buildup with increasing the nozzle opening area is non-monotonic due to the throat to nozzle opening area ratio, which is lower than unity in the narrow-throat pre-chamber design.

- The baseline pre-chamber, PC-B2, shows the shortest flame development angle and faster combustion rates compared to other pre-chambers. Although this pre-chamber does not show the best gross indicated efficiency, the combustion characteristics and emission performance are optimum with this pre-chamber.

- The throat opening area affects the pre-chamber pressure buildup significantly. The Generation 2 - PC-B2 pre-chamber has almost twice the throat opening area of its Generation 1 counterpart, and the pre-chamber pressure buildup in the former is half of the latter.

- The lower pressure buildup with the larger throat pre-chamber resulted in comparatively longer combustion duration compared to the narrow-throat pre-chamber results. As a result, the gross indicated efficiency diminishes when increasing the pre-chamber nozzle diameter.

(a) Ultra-lean case (PC7.2MC54, λ=2.3)

(b) Lean case (PC7.2MC72, λ=1.8)
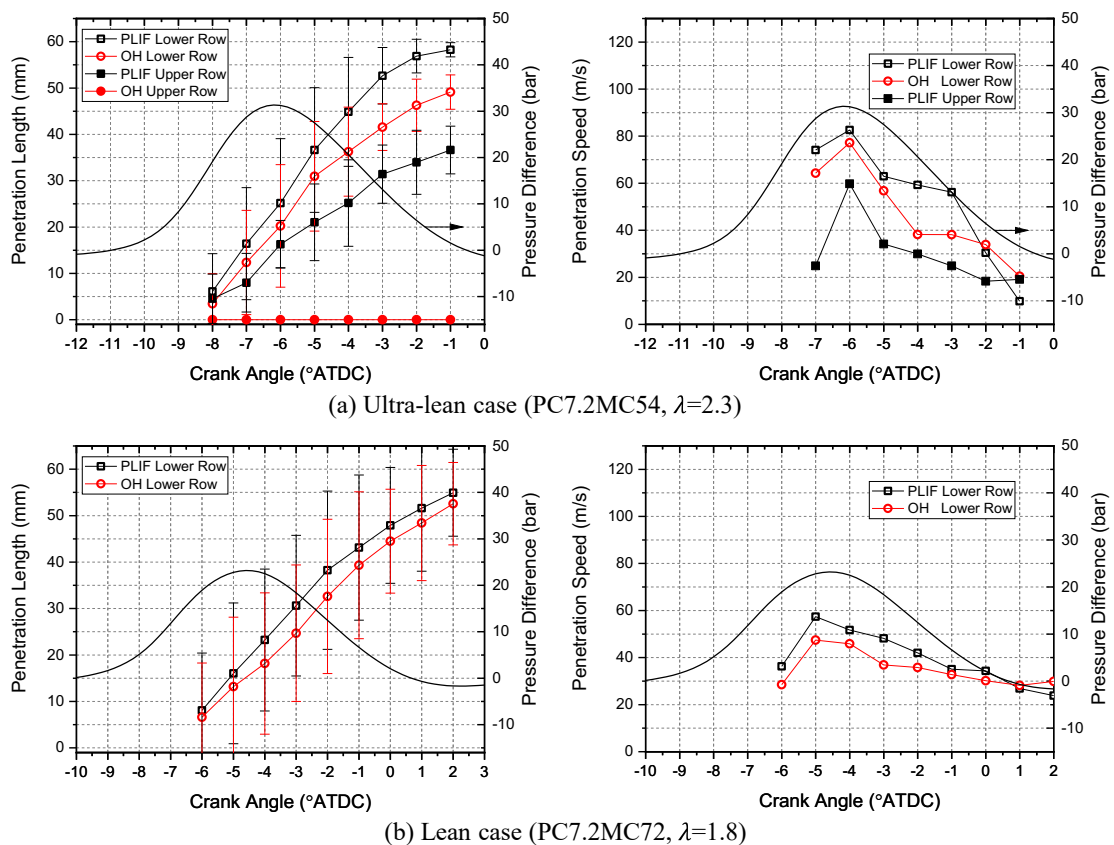
Fig. 11. The horizontal penetration length and mean horizontal penetration speed of the pre-chamber jet (PLIF) and reaction zone (OH*) from the lower row orifice: the ultra-lean case (PC fueling of 7.2 mg/cycle, MC fueling of 54 mg/cycle, and λ_{Global} of 2.3), and the lean case (PC fueling of 7.2 mg/cycle, MC fueling of 72 mg/cycle, and λ_{Global} of 1.8) [12].

Tang et al. [15] studied the effects of narrow-throat pre-chamber geometry on the pre-chamber jet velocity and main chamber combustion. The pre-chamber jet velocity was quantified using dual formaldehyde PLIF imaging for the first time, as shown in Fig. 12. The formaldehyde PLIF shows that the main

chamber combustion can be generally classified into two stages: the initial flame ignition and the following flame propagation. The maximum local formaldehyde jet boundary velocity of the narrow-throat pre-chamber with an inner throat diameter of 3.3 mm (C2G1) is up to about 280 m/s and it decreases dramatically when the inner throat diameter is increased to 5.3 mm (B2G2). The inner throat diameter is found to be the key dimension in the narrow-throat pre-chamber design.
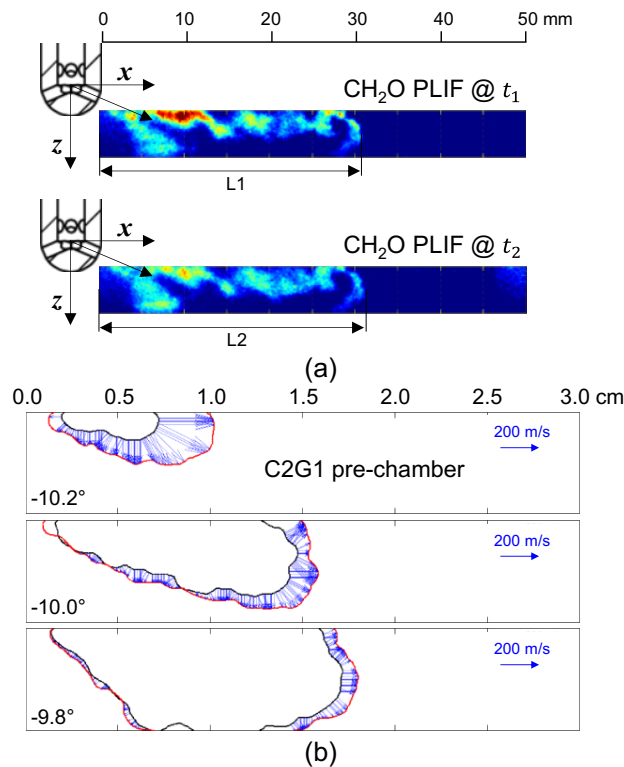
Fig. 12. (a) Single-shot CH$_2$O PLIF and (b) measured velocity distribution along the pre-chamber (C2G1) jet boundary is quantified by the dual formaldehyde PLIF imaging [15].

2.3.3 Effects of fuel property on combustion characteristics

Although the majority of the experiments were conducted with methane, gasoline surrogates (primary reference fuels) and alcohols were tested in the lean narrow-throat pre-chamber combustion mode in the latter part of the project [7]. To avoid complexities associated with the liquid fuel injection into the pre-chamber, these experiments were performed with methane injection into the pre-chamber while the main chamber is fueled with liquid fuels, injected via the air intake. Some remarkable observations are noted below:

- As shown previously, the mono fuel operation with methane has a lean limit around global-λ of 2.3 (see **Error! Reference source not found.** and Fig. 13). When the main chamber is fueled with liquid fuels, the lean limit is extended significantly, reaching a global-λ of 3.4 with methanol and 3.0 with ethanol and isooctane.
- From experiments with PRF 90, 95, and 100 fuels, the lean limit is marginally extended when the octane number decreases. However, the faster flame speed of the alcohol fuels appears to be beneficial in lean limit extension. The observation is most evident for ethanol and isooctane results. Although ethanol has a higher research octane number (RON), its faster flame speed resulted in a lean limit comparable to isooctane.
- The gasoline surrogates show significant end-gas auto-ignition (knock) even at global-λ 2.0, with the maximum amplitude of pressure oscillations (MAPO) values reaching 10 bar. The fast combustion characteristic of the narrow-throat pre-chamber combustion concept appears to be triggering auto-ignition prematurely.
- The effect of fuel property on the narrow-throat pre-chamber combustion concept is being investigated with Toluene primary reference fuels (TPRF) surrogates to explore the influence of sensitivity of fuel (S) on end-gas auto-ignition characteristics with the narrow-throat pre-chamber.
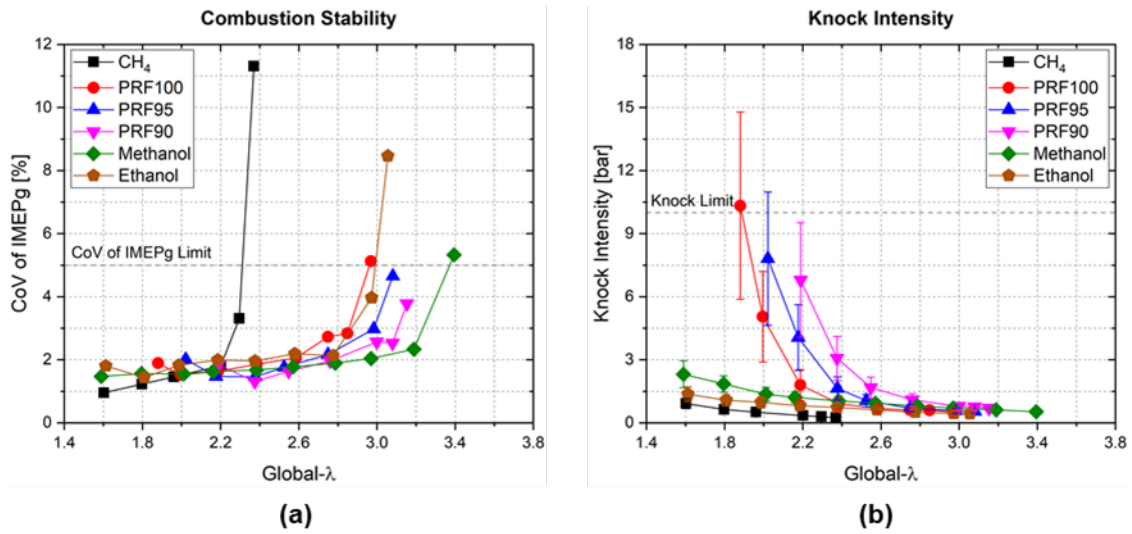
Fig. 13. Effect of fuel property on narrow-throat pre-chamber combustion: (a) combustion stability, and (b) end-gas auto-ignition (knock) characteristics at 1200 rpm, intake pressure 1.5 bar condition.
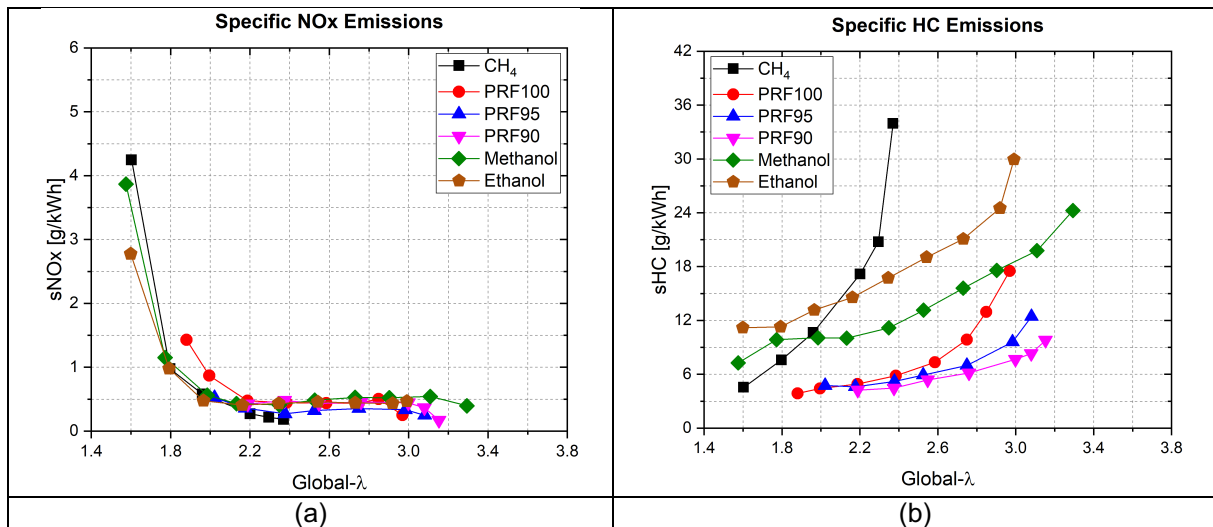
Fig. 14. Effect of fuel property on narrow-throat pre-chamber combustion: (a) specific NOx, and (b) specific unburned hydrocarbon emissions at 1200 rpm, intake pressure 1.5 bar condition.

- The specific NOx and unburned hydrocarbon emissions are plotted in Fig. 15. The NOx emissions are generally less sensitive to the fuel properties and are more sensitive to the global-λ. For all the fuels, the unburned hydrocarbon emission increases as the global-λ becomes leaner. Methane fuel shows the highest unburned hydrocarbon emissions, followed by ethanol and methanol. The PRFs typically show significantly lower unburned hydrocarbon emissions at all global-λ conditions, apart from the lean limit.

2.3.4 Ignition inside the pre-chamber

To investigate the ignition process inside the active pre-chamber, the fuel was only injected in the pre-chamber and the port fuel injection was interrupted. This is aiming to reduce the complexity of the pre-chamber combustion by decoupling the operation of the pre-chamber from the jet ignition in the main chamber.

Tang et al. [9] applied simultaneous 10 Hz negative PLIF and OH* chemiluminescence imaging in the main chamber. The pre-chamber was fueled with 14.2 mg/cycle of methane while the port fuel injection was deactivated. The acetone PLIF imaging from the cylinder side visualized the pre-chamber jet and the OH* imaging from the piston bottom view indicated the hot flame generated by the jet. The

probability distributions of the PLIF and OH* of the 14.2 mg/cycle case are shown in Fig. 15. It indicates that the pre-chamber jet discharge initiates when the ΔP is close to the peak and the pre-chamber jet is longer than the flame jet because some of the unburned charges in the pre-chamber are pushed out during the pre-chamber flame propagation and pressure buildup. The pre-chamber jet further penetrates after the peak ΔP when the flame jet (OH*) intensity decreases. An intense jet impingement on the piston top is presented after -8 CAD and the jet penetration decelerates. The pre-chamber jet manages to reach the cylinder liner at 0 CAD thanks to the high peak ΔP of about 30 bar of the current pre-chamber design.
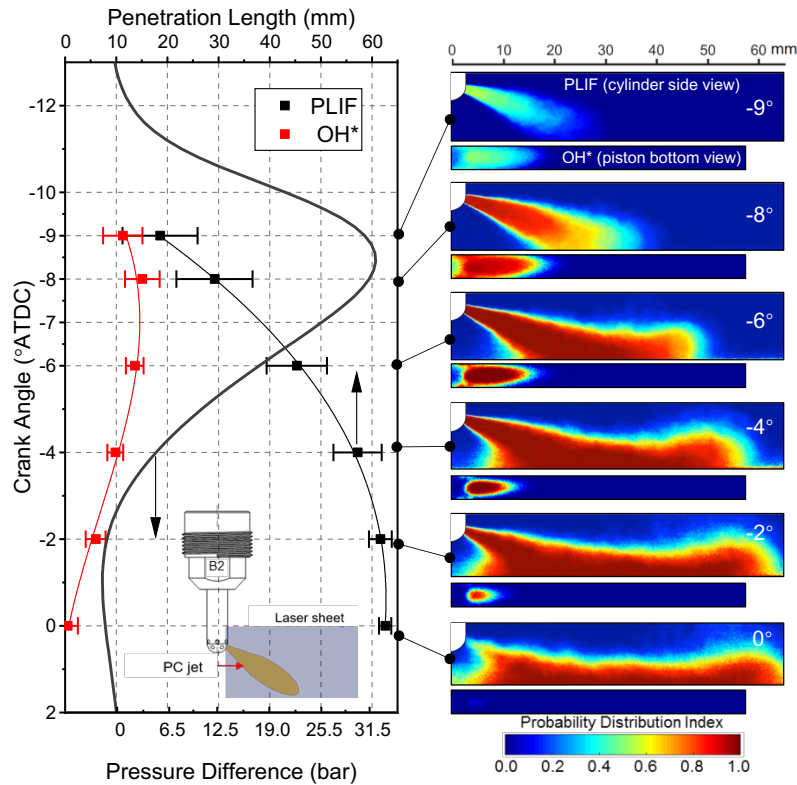
Fig. 15. Horizontal penetration length of the negative PLIF and OH* chemiluminescence and the probability distribution of the negative PLIF and OH*. Methane fueling to the pre-chamber of 14.2 mg/cycle and no main chamber fueling [9].
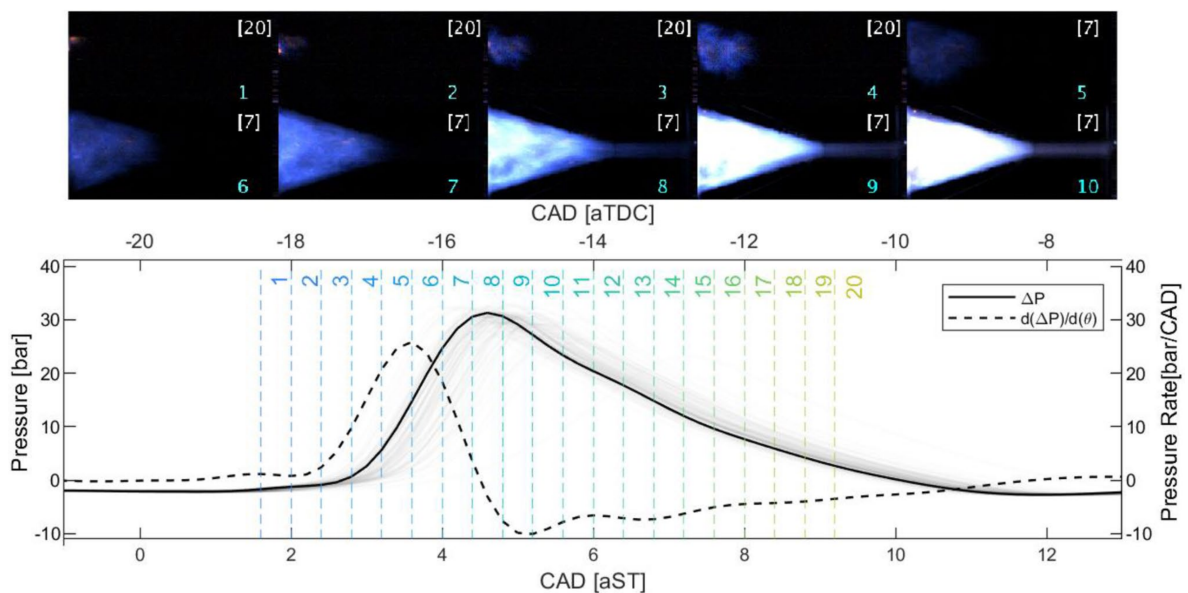
Fig. 16. Images of the combustion evolution inside the pre-chamber and the corresponding ΔP and $d(\Delta P)/d(\theta)$. [Image intensity magnification factor] is shown on the top right of each image. Methane fueling to the pre-chamber of 12 mg/cycle and no main chamber fueling [11].

The optical pre-chamber was tested in the same fueling configuration. High-speed natural flame imaging was acquired while only the pre-chamber is fueled with 12 mg/cycle of methane. The detailed results are reported in Marquez et al. [11] and an overview is shown in Fig. 16. The pre-chamber global lambda was estimated to be close to stoichiometry. It shows that the flame propagation inside the pre-chamber after spark ignition is accelerated due to the cone design of the pre-chamber. The pressure buildup between the pre-chamber and main chamber (ΔP) reaches its maximum and the flames occupy the pre-chamber throat zone from image 7 to image 8 when the estimated flame speed is higher than 300 m/s. The ΔP decreases thereafter during the following jet discharge process.

2.3.5 Jet combustion in the main chamber

In the active pre-chamber cases, the high-speed imaging of the natural flame luminosity of the flame discharge process in the main chamber indicates no flame quenching of the flame jet when passing through the orifice. Thus, the pre-chamber ignition is dominated by the "flame ignition" using the current narrow-throat pre-chamber design. The formaldehyde PLIF and the OH* imaging prove that there is a formaldehyde jet surrounding the flame jet during pre-chamber discharge. The formaldehyde jet starts to decelerate as soon as it penetrates the main chamber. The formaldehyde jet is thick during the initial flame ignition process and it becomes very thin when the later flame propagation process, the speed of which is lower than 50 m/s. In brief, the active pre-chamber combustion process is composed of the flame ignition and the following flame propagation [15].

3 Pre-chamber CFD simulation

3.1 Simulation setup and validation

3.1.1 Numerical setup

The density-based finite volume CFD solver CONVERGE^{TM} was utilized in the current investigation. The detailed numerical investigation of the KAUST narrow-throat pre-chamber is reported in [16-19]; details on the computational mesh and physical models can be found in [16, 17, 28]. The combustion was modeled using the G-equation to describe the flame propagation, combined with a multi-zone well-stirred reactor model (MZ-WSR) to determine the post-flame gas composition and to predict possible auto-ignition events in the upstream reactants.

The G-equation model (1) describes the turbulent flame brush as an iso-surface of a scalar variable, $\tilde{G} = 0$ [20], which propagates at the turbulent flame speed (S_T) following the correlation [21]:

$$\langle \rho \rangle \frac{\partial \tilde{G}}{\partial t} + \langle \rho \rangle \nabla \tilde{\vec{u}} \cdot \tilde{G} = \{\langle \rho S_T \rangle - \langle \rho \rangle \tilde{\kappa} D'_t\} |\nabla \tilde{G}| \qquad (1)$$

$$S_T = S_L + u' \left\{ -\frac{a_4 b_3^2}{2b_1} Da + \left[\left(\frac{a_4 b_3^2}{2b_1} Da\right)^2 + a_4 b_3^2 Da \right]^{1/2} \right\} \qquad (2)$$

where S_L is the laminar flame speed, u' is the fluctuating turbulent component, b_1, and b_3 are model constants representing the large and small-scale turbulence, respectively; a_4, b_1, and b_3 were set to 0.78, 2.0, and 1.0, respectively, following the original formulation [21]. The Damköhler number (*Da*) represents the ratio of the integral eddy turnover time $\left(\frac{l_T}{u'}\right)$ to the flame time $\left(\frac{\delta_L}{S_L}\right)$, where l_T is the integral length scale, and δ_L is the laminar flame thickness. S_L was tabulated from the 30-species skeletal chemical kinetic mechanism derived from GRI Mech 3.0 by Lu and Law [22]. For the flame development, the spark was modeled as a spherical source located in the spark plug gap as the initial flame kernel.

3.1.2 Validation and selection of suitable models

The experimental data used for the validation step is reported in [4]; further refinement of initial and boundary conditions, was performed using 1D GT-Power simulations; the schematic of the testbed and further specifics can be consulted in [4, 6, 8]. The geometric compression ratio of 11.5 and a bowl-in re-entrant piston design were used. The effective compression ratio was determined to be 11.1 against 11.5 of the geometrical value. The PC fueling was performed during the intake stroke. Details on injection strategy can be found in [6].

The ultimate confirmation of the aforementioned modeling approach was further confirmed by comparing the modeling against optical data. The preliminary results, shown in Fig. 17, are for global-λ 1.8

and active pre-chamber with PCFR 6%, with satisfactory similarities between CFD and the OH* chemi-luminescence data [23]. These results will be further investigated over a wider range of data points to ultimately generalize the modeling capabilities and fine-tune the models if needed.
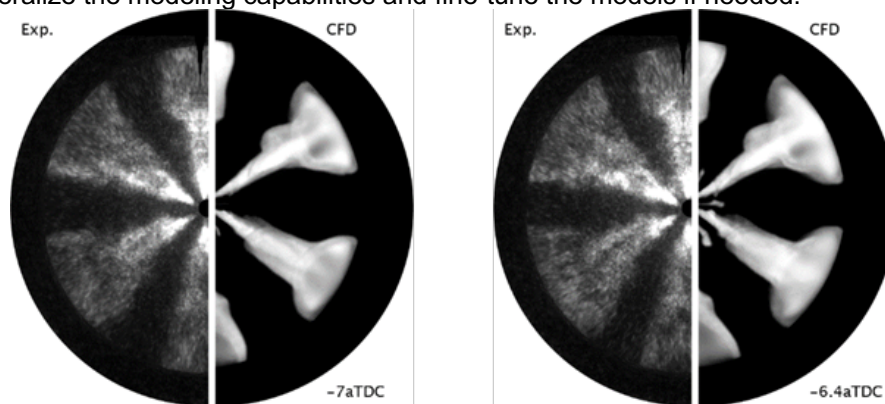

Fig. 17. Optical validation of pre-chamber jet evolution after it is issued into the main chamber at distinct engine times: OH* (experiments) and OH density (CFD) normalized by its maximum value.

Comprehensive validation of pressure curves and engine performance can be found in previous works [24,30]. A comparison of distinct combustion models was performed. It was verified that distinct combustion models are expected to yield acceptable results provided that the correct laminar flame and ignition delay times are well captured in the ultra-lean region. Minor differences are expected, while over a larger dataset the G-Equation has shown advantageous aspects since it accounts explicitly for the turbulence-chemistry interaction, and therefore should be the preferred method for modeling combustion in pre-chamber engines. An example of a comparison of simulation cases using G-equation and MZ-WSR is presented in Fig. 18 [24].
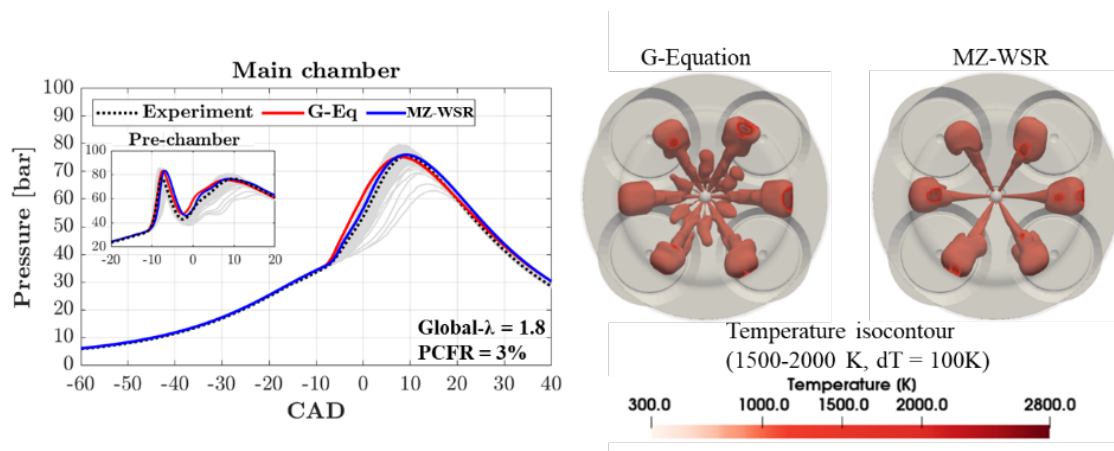
Fig. 18. Comparison of distinct combustion sub-models: (left) pre- and main chambers pressure build-up and (right) jet topology at the imminence of reaching the piston.

Predictive modeling of pre-chamber combustion engines relies primarily on the correct description of laminar and turbulent flame speeds, therefore prediction of correct composition within the pre-chamber is crucial. For engineering applications, the correlations of the flame speeds with physical variables involve empirical constants that are valid for a limited range of operating conditions [25]. The significance of laminar flame speed prediction on the simulation of ultra-lean pre-chamber engine combustion operated with methane was assessed in [25, 26]. Gülder's empirical correlation for laminar flame speed was chosen as a reference and was further modified for equivalence ratio, pressure and temperature ranges beyond what it was originally derived for; the changes were accommodated in the model constants where reside the primary source of uncertainties. Based on the computational results using the skeletal reaction mechanism, the correlation was modified to yield more accurate flame speeds at ultra-lean engine conditions. In all cases, Peters's turbulent flame speed correlation was used, and was found to have insignificant effect for the conditions under study, confirming the importance of the accurate determination of the laminar flame speed, while *ad hoc* correction of small and larger scale turbulence should be avoided and follow the original formulation. An illustration of the above models' validation is shown in Fig. 19.
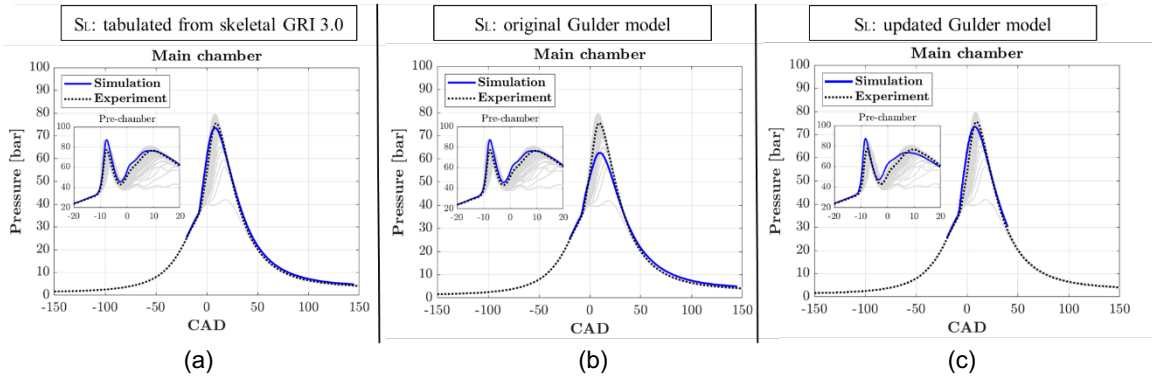
Fig. 19. Comparison of distinct laminar flame speeds: (a) tabulated values from the skeletal GRI, (b) Gülder's correlation, and (c) modified Gülder.

3.2 Understanding pre-chamber combustion from CFD simulations

3.2.1 Mixture formation inside the pre-chamber

Accuracy in estimating the pre-chamber excess air ratio (λ) is vital in the active pre-chamber concept before any additional model validation is performed. Experimental and numerical investigations were performed in [6] using a narrow-throat pre-chamber at various compositions (global-λ 1.6, 1.8, and 2.0), corresponding to different fractions of fuel energy injected in the pre-chamber (PCFR 3%, 7%, and 13%). Comparing with 1-D simulation software GT-Power and 3D CFD simulations, it was found that the 1-D results were unable to reproduce the experimental observations on the pre-chamber pressure buildup accurately. The CFD results revealed that the amount of fuel trapped in the pre-chamber at the inlet valve closing timing is over-predicted by the GT-Power simulations, due to the 1-D model formulation. The comparison of the estimated air/fuel excess ratio inside the pre-chamber is presented in Fig. 20.
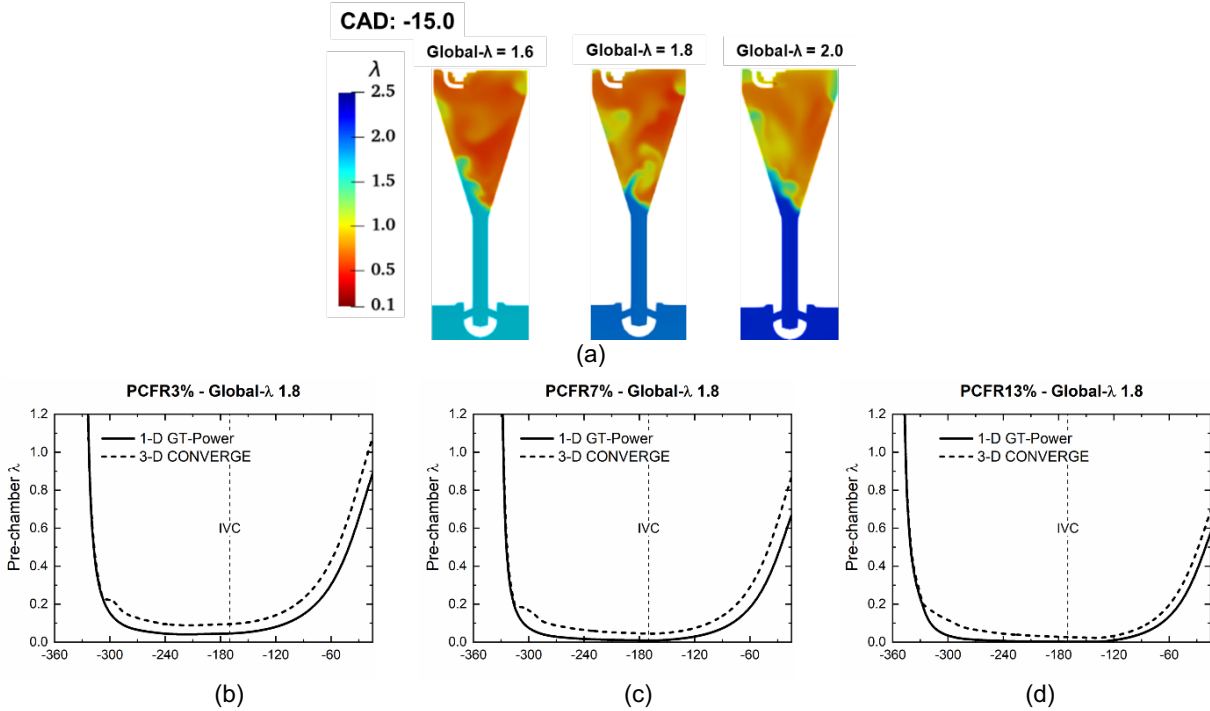
Fig. 20. Comparison of transient composition between 1D and 3D CFD modeling approaches [6] for distinct fueling conditions : (a) PC composition at spark timing, (b) global-λ 1.8 and PCFR 3%, (b) global-λ 1.8 and PCFR 7%, (c) global-λ 1.8 and PCFR 13% [6].

3.2.2 Turbulence chemistry interaction in pre-chamber combustion

Figure 21 shows the turbulence-chemistry-related parameters averaged across the flame front as dimensionless ratios of speed and length scale; the pre-chamber referred to as PC-1 was taken as an example. The computational cells located between 0.5 and 1.5 mm in front of the flame surface were for computation. The flame thermal thickness δ_L is defined as:

$$\delta_L = \frac{T_{ad} - T_u}{\max{(dT/dx)}} \qquad (1)$$

where T_{ad} and T_u represent the adiabatic and unburned temperatures, and the denominator is the maximum temperature gradient. The fluctuating component of the velocity, u', was obtained from the transport equation for the turbulent kinetic energy, k, under the assumption of homogeneous and isotropic turbulence, as follows:

$$u' = \sqrt{\frac{2}{3}k} \qquad (2)$$

The integral length scale l_T computation is determined by the following expression for RANS formulations:

$$l_T = C_\mu^{3/4}\frac{k^{3/2}}{\varepsilon} \qquad (3)$$

where the C_μ = 0.09, and ε is the rate of dissipation of k, which was also obtained from its transport equation.

The initial conditions inside the pre-chamber are highly turbulent and the trend of u'/S_L is dominated by the values of u' given it can reach values of one order of magnitude higher than for S_L, evidencing the high turbulent scenario encountered in pre-chamber ignited engines. As the flame enters the main chamber, there is a peak in u' resulting from the highly turbulent jets which naturally generate a strong shear layer within the main chamber. The turbulence is rapidly dissipated as the pressure difference diminishes, explaining the rapid drop in u, and the remaining level of fluctuation is bounded by the main chamber flow. Around TDC, it is observed that the flame is entering the squish region; therefore, one may rely on the turbulence effect of the jet solely during the jet issuing event [27].
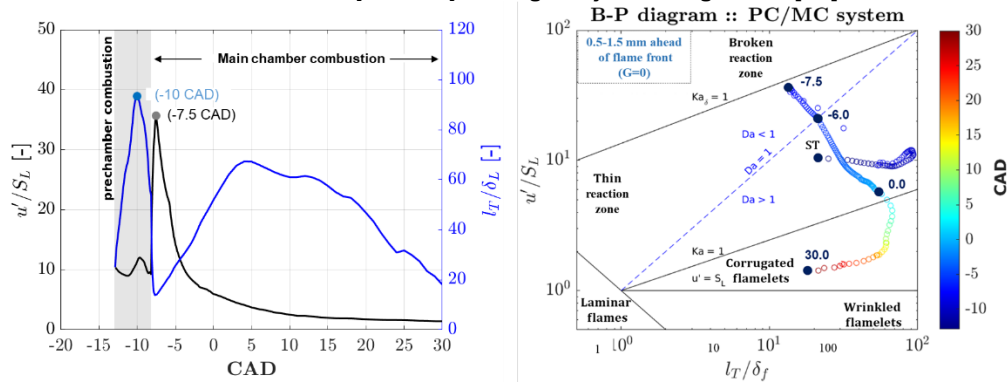
Fig. 21. Turbulence-chemistry quantities averaged near the flame surface and correspondent Borghi-Peters diagram.

The ratio, l_T/δ_f starts small near the initial flame; this is expected because the initial flame is located near the sparkplug wall, where eddies are entirely dissipated. As the flame moves away from the walls, it increases significantly until before entering the throat region, where high turbulence and smaller eddies are present. As the jets propagate into the main chamber, the ratio l_T/δ_f drastically drops. This is mainly due to two reasons: the small-scale turbulence induced by the nozzles, and the shear-driven mixing happening in the jets' viscous super-layer. At later times, as the jets' momentum dissipates, the flame front encounters larger eddies naturally occurring in the main chamber. Therefore, l_T values expectedly increase. Subsequently, it slowly decreases as the flame front enters the squish region; expectedly the squish region has smaller flow structures due to its confined space and near-wall combustion, justifying the decreasing trend.

The Borghi diagram and respective average Damkohler (Da) number contour are displayed in Fig. 21. Overall, the initial flame is located within the thin reaction zone regime, and at later crank angles, it enters the corrugated flamelet zone. On average, the pre-chamber combustion regime is marked by Da>1, while the early jet transients are characterized by Da<1. Later, the MC flame reaches Da>1 and subsequently lies in the corrugated flamelet regime nearly at the time it enters the squish region.

3.3 Optimization of the pre-chamber geometry

3.3.1 Effect of the pre-chamber throat diameter

While the majority of literature proves that the nozzle characteristics hugely impact the pre-chamber combustion, it was identified that the narrow throat is a key aspect in this type of pre-chamber; a comprehensive characterization was disused by Silva et al [28] and will briefly quote in the current work. Different pre-chamber designs yielded distinct flow and scalar fields at spark timing, resulting from the difference in narrow throat diameter. A large disparity between pre-chambers pressure build-up was observed, mainly caused by the distinct throat and nozzle flow dynamics, which culminated in substantially distinct jet topologies. For instance, in Fig. 22, the larger turbulence coming from PC-1 yield a minor advantage on the overall main chamber burning duration compared to PC-2 since the turbulence is quickly dissipated as the jets reach the piston walls. Even though, the results suggest that the turbulent aspect of the jet is as crucial as the number of jets, and indeed the former may overtake the latter when faster combustion is desired. The pre-chamber and main chamber combustion processes were found to develop with a sizable variation of turbulence-chemistry interaction. Thus, the results suggested that the G-equation combustion model coupled to MZ-WSR is adequate for modeling pre-chamber combustion engines [28].
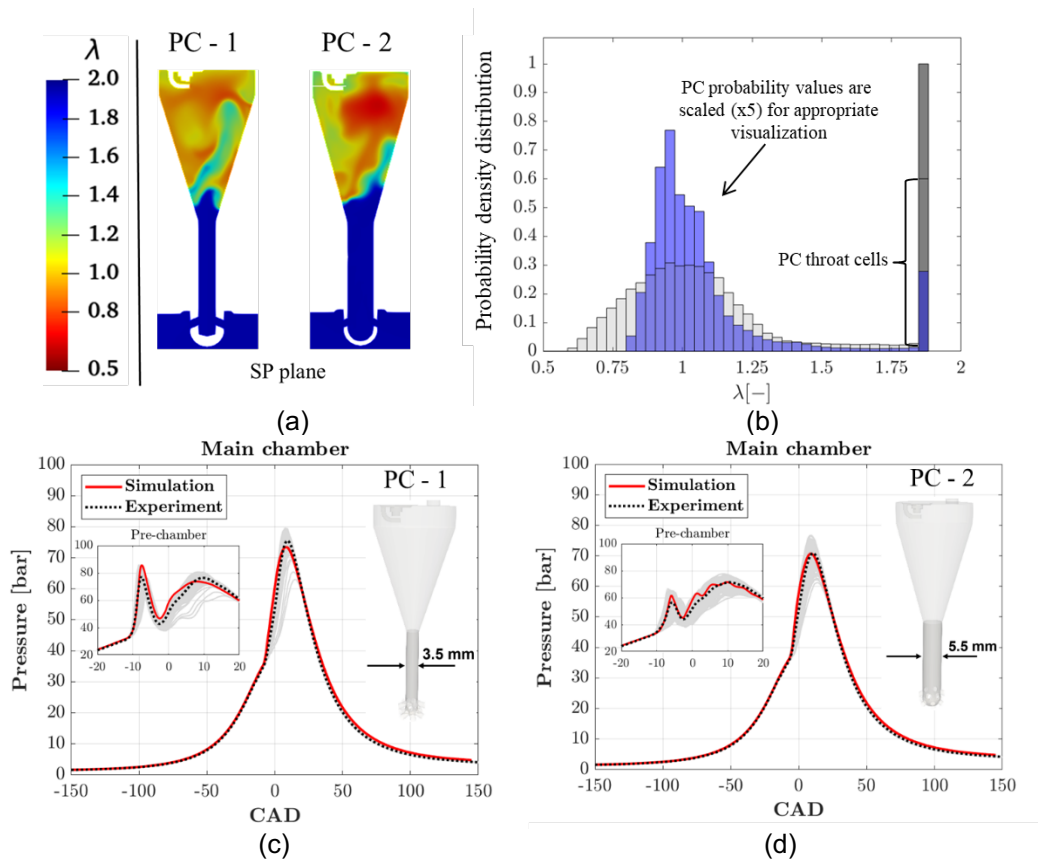
Fig. 22. Pre-chamber combustion characterization: (a) composition at spark timing, (b) pressure build-up for distinct pre-chambers, and (c) fluctuating velocity distribution within the pre-chamber at spark timing [28].

Despite both pre-chambers have 12 nozzles, PC-1, and PC-2 yield distinguishable pressure buildup and jet development (Fig. 23). Note that the large pre-chamber pressure build-up and flow dynamics within PC-1 due to the narrow and long throat cause its unexpected behavior. The pressure and Mach (Ma) number isocontours show that the narrower throat region of PC-1 experiences a sufficiently high-

speed flow, reaching transonic conditions such that the upper nozzle flow is choked, thus substantially diminished compared to the bottom nozzles.
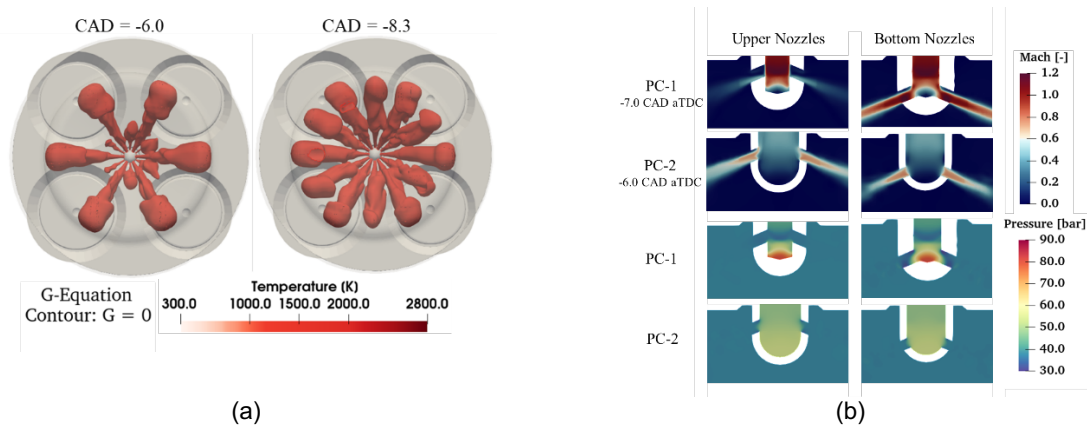
Fig. 23. Pre-chamber jet development for distinct throat diameters: (a) jet/flame topology at the imminence of reaching the piston, and (b) thermodynamic pressure and Mach number contours in the upper (left column) and bottom (right column) nozzles for both cases [28].

The bottom nozzles of PC-1 behave as expected; the flow coming from up and through the throat, when encountering the pre-chamber bottom tip, has to come to stop (thus increasing the pressure locally), while Ma falls to small values. This promotes a favorable pressure gradient between the nozzle entrance and the main chamber, thus driving the flow out of PC-1. This counterintuitive behavior for the PC-1 was confirmed via optical engine experiments [9,10,12,15]. The PC-2 works as expected, with all twelve nozzles functional. The lower speed due to the wider throat of PC-2 reflects the Ma<1, causing a moderate pressure gradient sufficient to eject the flame out of the pre-chamber through all 12 nozzles.

3.3.2 Co-optimization of piston and nozzle holes' axis

The investigation on the influence of piston designs suggested that the jet-wall interaction is an additional key feature that can influence overall performance in a PC engine. Three different pistons were selected for the current study, P1 (base piston), P2, and P3, respectively. The squish height was adjusted to maintain the constant effective compression ratio of 11.1. The initial composition and stratification inside the pre-chamber were observed to be comparable when only the piston shape is varied and the compression ratio is kept constant. This suggests that the pre-chamber design has a leading effect on the field variables within it. As a result, the pressure build-up inside the pre-chamber remained similar.

The combustion duration was found to be significantly increased when the piston has squish, provided that such a confined space has its combustion affected by the proximity to the walls. The premature jet reaching the walls was found to deprecate the turbulent enhancement brought by the jets. In Fig. 24, the l_T/δ_f values are mostly larger for the P3 flat piston case at later stages. For the other two cases (P1 and P2), due to the presence of squish and smaller turbulent structures occurring there, the l_T values tend to be smaller compared to P3. Nonetheless, the final trend for all the cases approaches smaller values as the flame is mostly closer to the walls. Therefore, the optimized PC-MC system should consider modifications on the pre-chamber and piston, while obeying constraints on engine-out quantities and key aspects of heat management per boundary. Further details on this study would be found in [29].
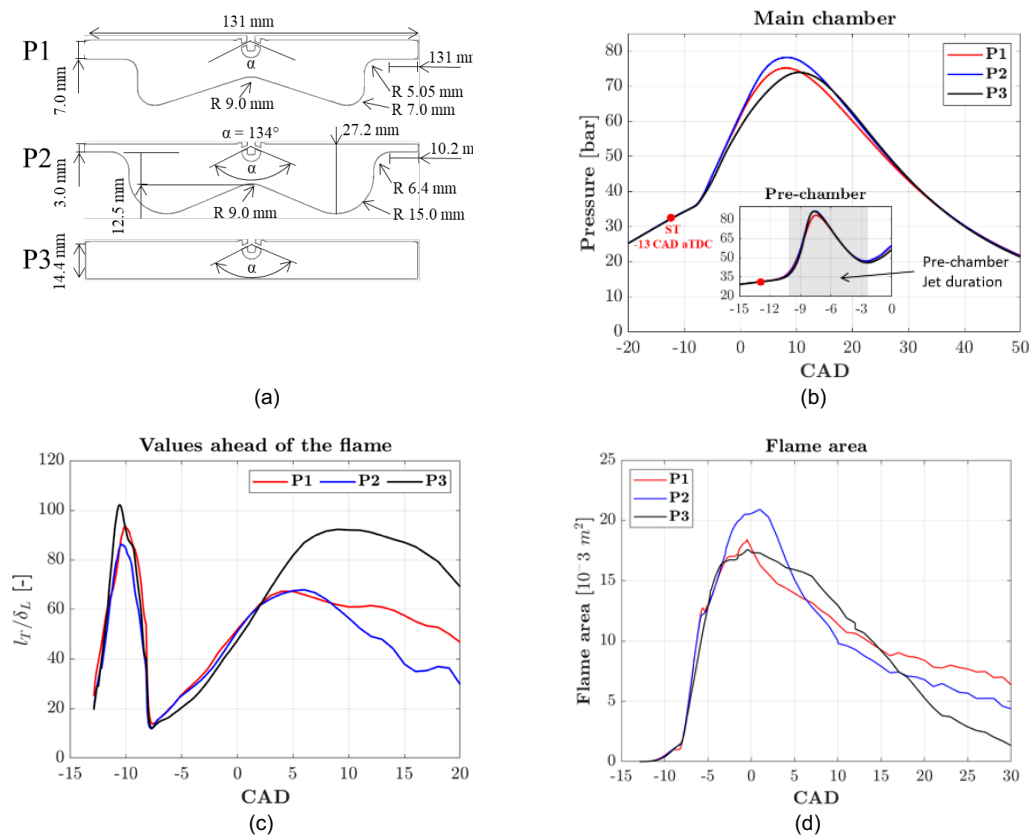
Fig. 24. Comparison of the pre-chamber combustion with three pistons shapes.

3.3.3 Optimization of the pre-chamber geometry using ML

The optimization of pre-chamber geometrical features was investigated in [30] using Machine Learning tools and CFD simulations. The pre-chamber was parametrized and six independent and two dependent variables were considered, over a design space of 300 samples (overlaid in gray in Fig. 25), while the volume was kept constant. A one-shot design of experiment (DoE) optimization was considered. A merit function was adopted; it considers the indicated specific fuel consumption (ISFC), emissions (NOx, sCO, sHC), safety (P_{max-PC}, P_{max-MC}, and maximum pressure rise rate). Secondly, machine learning algorithms were trained to utilize the DoE results aiming at finding a globally optimum geometry for the considered operating condition. Five 5 design iterations proposed by the ML framework were considered (<50 cases). ML was able to propose a new design with superior performance compared to the best DoE. The dataset was further analyzed to identify key features of PC geometry, such as throat diameter, nozzle count, and orientation.

Further details on parametrization and ML framework can be found in [30]. In summary, the DoE yielded considerable improvements; nearly 7% improvement in merit was observed with ~5 g/kW-h benefit in fuel consumption. Five sequential iterations were performed and the ML algorithms were capable of proposing a new design with superior performance compared to the best DoE; the best ML design resulted in improvement in sNOX, 10 % in sCO, 2% in sHC, 6% in MPRR, and 0.4% in merit, compared to the best DoE.
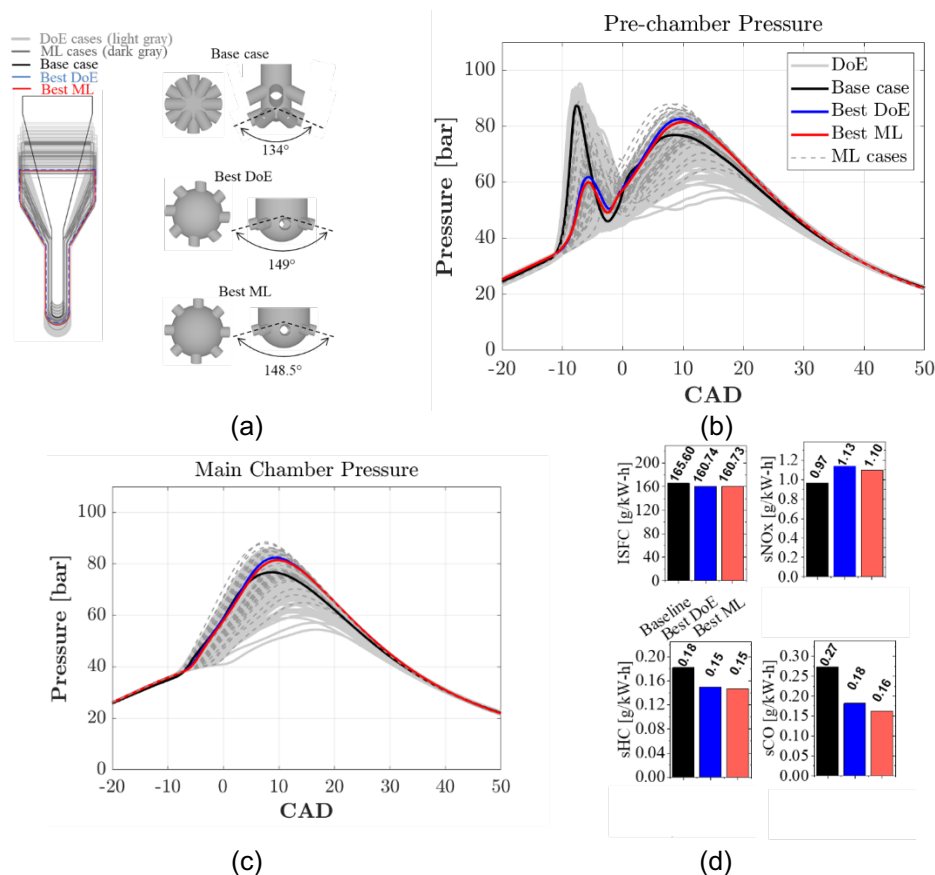
Fig. 25. Pre-chamber optimization: (a) Geometry, (b) pre-chamber and (c) main chamber pressure comparison, and (d) performance metrics comparison.

4 Chemical kinetics of pre-chamber combustion

Understanding the fundamental processes of mixing and turbulent/chemical interactions between hot jet and fresh gases is crucial to determining ignition [31]. Ignition is generally favored where thermo-chemical composition and temperature in the mixing layer advance rapid kinetic rates. The numerical studies [32, 33] showed that in addition to the thermal effects, the chemical effects of the turbulent jet issuing from the pre-chamber play an important role in defining the main chamber ignition processes. The chemical effect relates to the highly reactive radicals in the jet. The high-temperature turbulent jets containing chemically reactive radicals (O, H, and OH) are distinctive characteristics of the pre-chamber combustion. They create a rigorous vorticity field and stratified mixture in the main chamber. The reacting jet contains partially and fully burned combustion products, which govern the flow field evolution and mixing processes in the MC. This, subsequently, results in different ignition and combustion processes in the MC.

Tang et al. [34] used a zero-dimensional model (0D batch reactor simulations for both PC and MC) to obtain an improved understanding of the chemical effects imposed from the PC combustion on the MC combustion. This is important to assess the success of the ignition and combustion phenomenology of TJI. Simulation results of varying the equivalence ratio reactants in the PC indicated that the pre-chamber generated more chemically reactive radicals such as H and OH when burning around the stoichiometric condition, while more low-carbon species were produced when burning at rich conditions. The authors observed the rapid ignition performance in the ultra-lean mixture of the MC with the addition of combustion species from the PC burning in the stoichiometric condition. This was due to the transfer of highly active species injected from the pre-chamber into the main chamber [34].

Using a network of 0D-1D reactors (0D partially stirred reactor (PaSR) simulations and a 1D premixed laminar flame model), Gorbatenko et al. [35] conducted a thorough investigation of the initial fuel composition, micro-mixing time, and PC progress effects on the MC combustion in terms of combustion efficiency and pollutant formation characteristics. Full 3D computational fluid dynamics [29] were used to calibrate the proposed model in terms of predicting the pre-chamber throat conditions. Simulations varied in PC progress, micro-mixing time, and ethanol toluene primary reference fuel (ETPRF) composition (in terms of research octane number (RON) and octane sensitivities (OS)).

It was shown that high dissipation rates and fast mixing amplified reactant concentrations while reducing product concentrations and limiting reaction rates. Hence, under these conditions, the chemistry failed to maintain combustion resulting in smaller temperatures, and restricting fuel conversion. The results suggested that OH and NO had the highest chemical impact on MC reactivity, whereas the chemical effects of CO_2 and H_2O were small. After a detailed parametric study, a tailored merit function for evaluating PC engine optimal operating performance was proposed. It consisted of parameters to account for micro-mixing effects on reactivity, promoting the effects of PC jet on lower flammability and pollutant formation characteristics. The overall merit function showed the best performance at high RON and OS in the range of two to six, consistent with the requirements for Advanced Compression Ignition (ACI) and Spark-Induced Compression Ignition (SICI) operations.

A more comprehensive kinetic study of the PC combustion system facilitated the prediction of the PC combustion species including complete and incomplete combustion products from stoichiometric to rich conditions during the PC combustion, meanwhile, capturing the effects of PC combustion species on MC combustion under lean and ultra-lean conditions. Tang et al. [36, 37] are improving and validating the chemical kinetic models of the conventional gasoline surrogate fuel of iso-octane, the renewable biofuel of methanol, and the base natural gas composition of methane in PC and MC conditions. Thoroughly validated chemical kinetic models can provide accurate simulations of engine experiments in conditions not accessible otherwise and offer the imperative tool for obtaining quantitative knowledge into kinetic interactions that benefit the general understanding of TJI processes.

Iso-octane is one of the archetypal components of gasoline surrogates and fuels with high octane numbers. Although iso-octane autoignition has been studied extensively in the literature both theoretically and experimentally, there was a lack of experimental data obtained from shock tubes and rapid compression machines at lean and ultra-lean conditions. In the study by Hakimov et al. [38], the base iso-octane kinetic model from Atef et al. [39] was improved in the ignition performance under lean (Φ = 0.4 – 0.6) and ultra-lean (Φ = 0.2) conditions over a wide range of temperatures (630 – 1250 K) and high pressures (20 – 40 bar) relevant to MC operating conditions, as shown in Fig. 26.
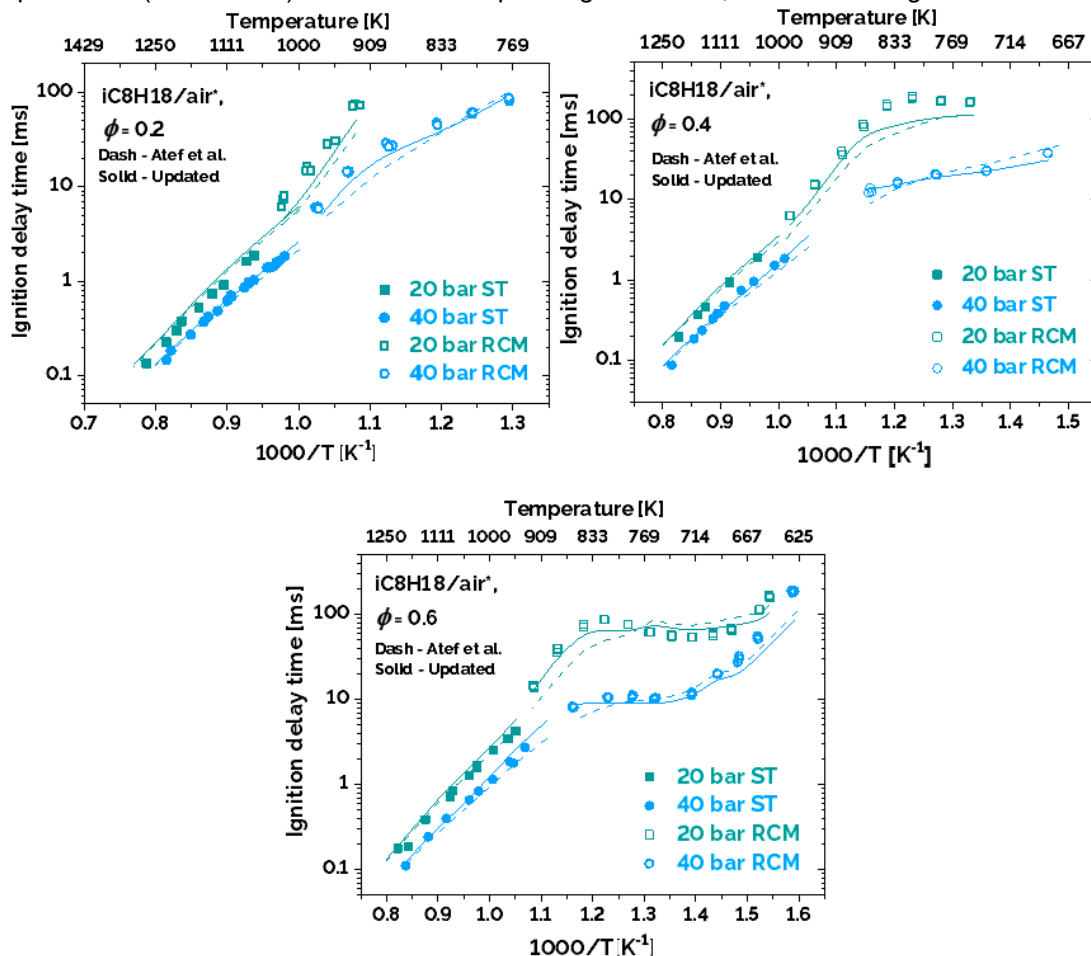
Fig. 26. Ignition Delay Times of iso-octane/air mixtures measured in the KAUST High-Pressure Shock Tube and Rapid Compression Machine compared to original [39] and updated [38] model predictions.

The newly obtained ignition delay times from the high-pressure shock tube and rapid compression machine in KAUST helped to enrich the iso-octane autoignition studies in lean and ultra-lean conditions. The improved iso-octane kinetic model from Hakimov et al. [38] also enabled computational fluid dynamic simulations with increased accuracy and optimization studies of PCC for their potential implementation in mainstream transport vehicles. Dedicated experiments and modeling work [36] are ongoing at KAUST to unravel the chemical effects of high NOx concentration on iso-octane combustion as a result of competing chain promotion/termination effects related to pressure-dependent HONO and RNO2 formation channels [40-42].

In collaboration with CFD simulations, skeletal methane, methanol, and associated NOx model were modified to be suitable for pressure predictions in both PC and MC combustion against engine experiments. These modifications are focusing on ignition delay time, speciation data, and laminar flame speed at high temperatures and pressures in lean and stoichiometric conditions. In addition to the gas phase model modifications, a detailed H2 surface kinetic model is being developed to investigate the effects of surface reactions on the radical pool during the PC combustion. The improved skeletal gas-phase mechanism, coupled with the newly developed surface kinetic model in CFD simulations helps to enhance the understanding of the PC combustion progress and the kinetic effects of PC combustion species on MC combustion in lean and ultra-lean conditions. These works are still in progress and have not been published yet.

5 Exploring different engines and configurations

5.1 Design of a passive pre-chamber for a light-duty single-cylinder engine

A parallel passive pre-chamber work was done on a single-cylinder gasoline direct injection (GDI) light-duty engine with a displacement volume of 454 cm^3. The light-duty part aimed to find a direct injection strategy that can enrich the passive pre-chamber more than the main chamber, increasing the lean limit and consequently improving the engine efficiency. Firstly, CFD work was done using CONVERGE to investigate the injector location, injection pressure, and piston shape effects on the pre-chamber air-fuel mixture. The simulation setup was guided by the best practices identified in the heavy-duty pre-chamber simulation work from the current FUELCOM project.

In this study [43], a split injection strategy was proposed. Approximately, 80% of the fuel would be introduced homogeneously early in the intake stroke, and the remaining amount will be injected during the compression stroke to enrich the passive pre-chamber aerodynamically. Moreover, six more pistons were designed, and eight pistons were simulated. In addition, the direct injector can be mounted either on the side or in the center of this particular light-duty cylinder head. It should be noted that neither injection location spray can be aimed at the passive pre-chamber, and the combustion chamber flow pattern must be utilized to introduce the fuel into the passive pre-chamber.
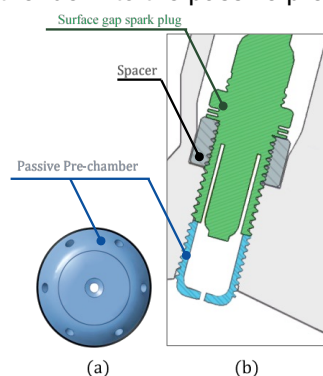
Fig. 27. (a) Bottom view of the passive pre-chamber. (b)Section view of the passive pre-chamber assembly.

Results from side injection simulations showed that the spray has a too high momentum. Thus, the injected fuel cannot be guided into the passive pre-chamber using the engine's internal aerodynamics. Reducing the injection pressure from 150 to 50 bar helped to decrease the excess-air ratio but not below the main chamber excess-air ratio value (λ_{MC}=1.6). On the other hand, the central injection was better in introducing the fuel to the passive pre-chamber by utilization of both flows- and wall-guided approaches. Of the six newly designed pistons, one piston effectively modified the main chamber flow to aid the spray from the central injector to be pushed into the passive pre-chamber. The piston (A4),

illustrated in Fig. 28, features an inclined converging bowl along with excess-air ratio values for different start of injection timing (SOI).
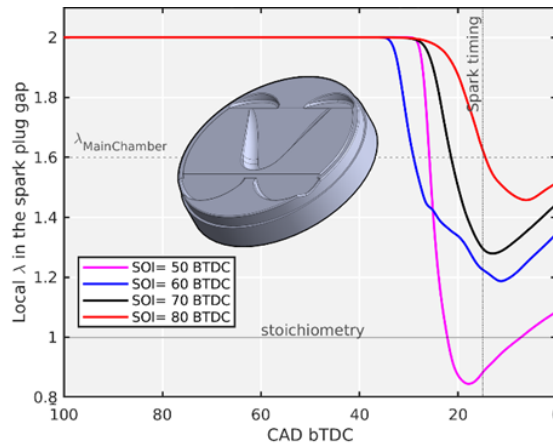
Fig. 28. Excess air ratio λ in the spark plug gap using different SOI values for the second injection (Piston: A4).

Then, the optimized piston (A4) was manufactured and fitted to the engine along with an eight-hole pre-chamber with a volume of 2.3% of the engine clearance volume (one cm^3). Experimental work was carried out using gasoline with a RON of 95. Several injection methods were tested for comparison against the split injection strategy proposed earlier; furthermore, a conventional spark plug was used for comparison. Typically, passive pre-chambers in light-duty engines are operated with PFI, which can produce a more homogenous air-fuel mixture inside the combustion chambers, and is used as a reference point. Moreover, a single early injection at IVO was tested and compared to the proposed split injection strategy. Please note that the split injection strategy in the experiments consisted of two central direct injections where the first injection was at IVO and contained more than 70% of the total fuel, while the remaining fuel was injected later in the compression stroke.

Defining the lean limit at 5% of COV_{IMEP} showed that the split injection increased the passive pre-chamber lean limit significantly when using the proposed split injection compared to port fuel injection (PFI). However, the passive pre-chamber lean limit with PFI was lower than its SI counterpart, indicating poor scavenging of residual gasses, which can be improved by a better design of the passive pre-chamber.
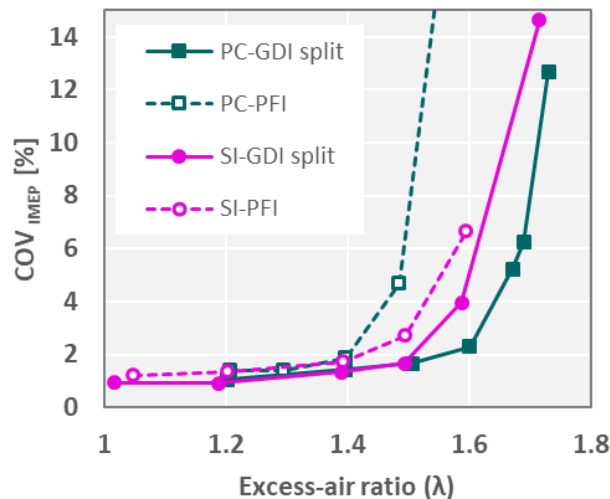
Fig. 29. COV_{IMEP} against λ when using PFI and split DI for passive PC and SI.

Single early injection performed better than PFI but worse than split injection for passive pre-chamber in the lean limit. Nevertheless, excessive soot emissions were observed inside the combustion chamber and attributed to the second injection impinging on the piston. It was concluded that the passive pre-chamber could be enriched indirectly through GDI and piston shape modification and improve its combustion stability at lean operating points, furthermore increasing its lean limit. Further details on this study can be found in [43].

5.2 Design of a pre-chamber for operation with H_2

An investigation of the combustion performance and NOx emissions for the H_2 pre-chamber combustion engine was conducted. One of the major obstacles faced is the high reactivity of H_2 at high temperatures – driven by its low ignition energy – which can easily induce pre-ignition and knock and – as a result – the engine efficiency limit was restricted. Thus, the main target was to inhibit pre-ignition and knocking and meanwhile extend the high-efficiency limit. To start with, the methane pre-chamber combustion case was adopted as the baseline case using a 7% pre-chamber fueling ratio (PCFR). The preliminary results indicated a high engine knocking tendency which was evidenced by the steep pressure rise rate due to the fast jet flame speed coming from the pre-chamber, as seen in Fig. 30 and Fig. 31. To refrain from the knocking tendency, the PCFR ratio should be adequately reduced and the spark-ignition timing should be postponed.
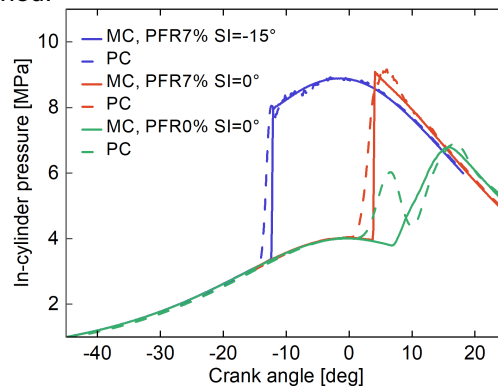
Fig. 30. Predicted pressure profiles for various H2 pre-chamber combustion cases.
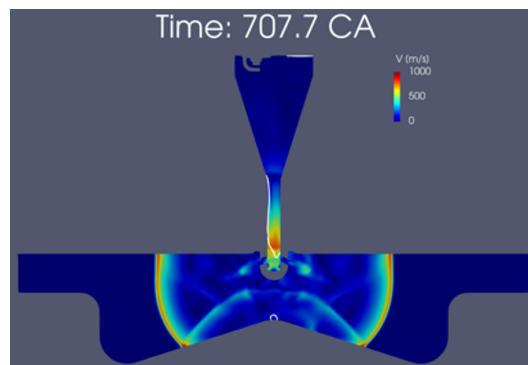
Fig. 31. Predicted velocity distribution for the case with PCFR = 7% and SI = -15°.
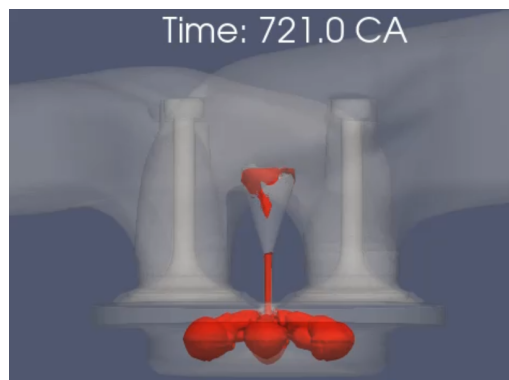
Fig. 32. Predicted iso-surface of T = 2200 K for the case with λ= 2.4, PCFR = 0% and SI = -5°.

To obtain a better control of the H_2 pre-chamber combustion process, different values of λ in the PC and MC were analyzed. In particular, even with a lean mixture within the PC ($\lambda > 2.0$), the PC combustion is still able to yield a high flame speed to burn out the ultra-lean mixture in the MC, as seen in Fig. 32. To effectively inhibit knocking, an ultra-lean mixture in the MC with $\lambda > 2.5$ should be employed. Note that at such a lean condition, the chemical properties are crucial in the prediction of flame speed. Thus, two different mechanisms were investigated namely the Burke mechanism [44] and the optimized Burke

mechanism developed by Park et al. [45] which was validated under similar engine conditions compared with the baseline case considered. The simulation results demonstrated that these two mechanisms predicted different combustion processes. Thereafter, two different combustion models were investigated, including the well-known MZ-WSR detailed chemical kinetic chemistry and the G-equation combustion model.

As an alternative method to reduce the engine knocking tendency in the MC, different PC designs were investigated and the results indicated the possibility of using high PCFR without facing the problem of high PRR. Afterward, the effect of different compression ratios was also assessed. It was found that at a high compression ratio it is preferable to use high values of λ in the MC. On the other hand, at low compression ratios, it was possible to use low values of λ but still considered to be very lean $2 < \lambda < 3$. In addition, the effect of exhaust gas recirculation (EGR) and water injection was also assessed as a method to reduce the engine knocking tendency.

6 Concluding remarks

In the FUELCOM3 project, different active pre-chambers were designed to operate with mostly gaseous fuels (methane). Experiments were performed on single-cylinder metal and optical engines. The extensive experiments demonstrated the importance of the fuel-air mixing inside the pre-chamber and its link to the optimal spark timing. These experiments supported the validation of CFD simulations, which were continually supported by the updated and optimized chemical kinetic models. The comprehensive investigations through the synergistic the project workstreams examined the effects of various key parameters such as the local equivalence ratio in the pre-chamber in controlling the engine performance by allowing operation at leaner conditions. The experimental and simulation results provided insights into the underlying physics related to jet ignition, turbulence chemistry interaction, jet-wall interaction, and its impact on the heat transfer losses. We used our best practices from the CFD work to optimize the pre-chamber and piston geometries and explore the suitability of pre-chamber concepts in different engine configurations.

The major conclusions are summarized as follows:

(1) The geometrical parameters of the pre-chamber, such as the volume, nozzle opening area, and throat diameter govern the combustion characteristics in the pre-chamber and the subsequent initial flame development in the main chamber.

(2) At a fixed throat diameter, the pre-chamber pressure build-up scales with the volume of the pre-chamber, and faster jet velocities are expected with larger volumes. For a fixed pre-chamber volume, increasing the throat diameter drastically reduces the pressure rise in the pre-chamber, and the delay between the spark timing and the start of heat release in the main chamber becomes prolonged.

(3) The fidelity of modeling of PC engines depends strongly on the correct prediction of the field variables at the time of spark. Distinct combustion submodels are capable to predict the combustion evolution in PC engines upon appropriate model calibration.

(4) The jet-wall interaction was found to influence the engine response. Therefore, the piston geometry is one additional design aspect to be considered in PC engines. In addition, with the help of DoE and ML, rapid engine prototyping was achieved.

(5) Chemical kinetic studies provided an improved understanding of the chemical effects imposed from the PC combustion products on the MC combustion. Simulation results suggested that OH and NO have the highest chemical impacts on MC reactivity.

(6) A comprehensive iso-octane kinetic model was developed. It achieved a more accurate prediction of PC combustion exhausts and their subsequent effects on MC ignition characteristics.

7 Acknowledgments

8 References

[1] D. Kumar, A.F. Abdul-Manan, G. Kalghatgi, A.K. Agarwal, Review of Life Cycle Analysis Studies of Less Processed Fuel for Gasoline Compression Ignition Engines, Gasoline Compression Ignition Technology, (2022) 245-273.

[2] L. Gussak, High chemical activity of incomplete combustion products and a method of prechamber torch ignition for avalanche activation of combustion in internal combustion engines, SAE transactions, (1975) 2421-2445.

[3] L. Gussak, V. Karpov, Y.V. Tikhonov, The application of lag-process in prechamber engines, SAE Transactions, (1979) 2355-2380.

[4] P. Hlaing, M. Echeverri Marquez, V. Shankar, E. Cenker, M. Ben Houidi, B. Johansson, A study of lean burn pre-chamber concept in a heavy duty engine, (2019).

[5] P. Hlaing, M.A. Echeverri Marquez, E. Singh, F.A. Almatrafi, E. Cenker, M. Ben Houidi, B. Johansson, Effect of pre-chamber enrichment on lean burn pre-chamber spark ignition combustion concept with a narrow-throat geometry, SAE 2020-01-0825 (2020).

[6] P. Hlaing, M. Silva, M.E. Marquez, E. Cenker, M. Ben Houidi, H.G. Im, J.W. Turner, B. Johansson, Estimates of the air-fuel ratio at the time of ignition in a pre-chamber using a narrow throat geometry, International Journal of Engine Research, (2021) 14680874211059148.

[7] P. Hlaing, M.E. Marquez, P. Burgos, E. Cenker, M.B. Houidi, B. Johansson, Analysis of Fuel Properties on Combustion Characteristics in a Narrow-Throat Pre-Chamber Engine, SAE International Journal of Advances and Current Practices in Mobility 3 (2021) 3020-3043.

[8] P. Hlaing, M.E. Marquez, E. Cenker, H.G. Im, B. Johansson, J.W. Turner, Effects of volume and nozzle area in narrow-throat spark-ignited pre-chamber combustion engines, Fuel 313 (2022) 123029.

[9] Q. Tang, R. Sampath, M.A. Echeverri Marquez, P. Hlaing, P. Sharma, M. Ben Houidi, E. Cenker, J. Chang, G. Magnotti, B. Johansson, Simultaneous negative PLIF and OH* chemiluminescence imaging of the gas exchange and flame jet from a narrow throat pre-chamber, SAE Technical Paper 2020-01-2080, (2020).

[10] R. Sampath, Q. Tang, M.E. Marquez, P. Sharma, P. Hlaing, M.B. Houidi, E. Cenker, J. Chang, B. Johansson, G. Magnotti, Study on the pre-chamber fueling ratio effect on the main chamber combustion using simultaneous PLIF and OH* chemiluminescence imaging, SAE International Journal of Advances and Current Practices in Mobility 3 (2020) 137-149.

[11] M.E. Marquez, P. Sharma, P. Hlaing, E. Cenker, G. Magnotti, B. Johansson, J. Turner, Visualization of the pre-chamber combustion and main-chamber jets of a narrow throat pre-chamber, Report No. 0148-7191, SAE Technical Paper, 2022.

[12] Q. Tang, R. Sampath, M.E. Marquez, P. Sharma, P. Hlaing, M.B. Houidi, E. Cenker, J. Chang, G. Magnotti, B. Johansson, Optical diagnostics on the pre-chamber jet and main chamber ignition in the active pre-chamber combustion (PCC), Combustion and Flame 228 (2021) 218-235.

[13] A. Shah, P. Tunestal, B. Johansson, Effect of pre-chamber volume and nozzle diameter on pre-chamber ignition in heavy duty natural gas engines, Report No. 0148-7191, SAE Technical Paper, 2015.

[14] M.E. Marquez, P. Hlaing, Q. Tang, R. Sampath, E. Cenker, M.B. Houidi, G. Magnotti, B. Johansson, High-Speed Imaging of Main-Chamber Combustion of a Narrow Throat Pre-Chamber under Lean Conditions, Report No. 0148-7191, SAE Technical Paper 2020-01-2081, 2020.

[15] Q. Tang, R. Sampath, P. Sharma, M.E. Marquez, E. Cenker, G. Magnotti, Study on the effects of narrow-throat pre-chamber geometry on the pre-chamber jet velocity using dual formaldehyde PLIF imaging, Combustion and Flame 240 (2022) 111987.

[16] M.M. Silva, A Numerical Investigation of Pre-chamber Combustion Engines, KAUST, 2020.

[17] S. Sanal, M. Silva, P. Hlaing, E. Cenker, B. Johansson, H.G. Im, A Numerical Study on the Ignition of Lean CH 4/Air Mixture by a Pre-Chamber-Initiated Turbulent Jet, Report No. 0148-7191, SAE Technical Paper, 2020.

[18] M. Silva, S. Sanal, P. Hlaing, E. Cenker, B. Johansson, H.G. Im, Effects of geometry on passive pre-chamber combustion characteristics, Report No. 0148-7191, SAE Technical Paper, 2020.

[19] M. Silva, S. Sanal, P. Hlaing, E. Cenker, B. Johansson, H.G. Im, A Computational Investigation of Fuel Enrichment in the Pre-Chamber on the Ignition of the Main Chamber Charge, Report No. 0148-7191, SAE Technical Paper, 2021.

[20] F. Williams, Combustion Theory: the Fundamental Theory of Chemically Reacting Flow Systems. Benjamin/Cummings Pub. Co, (1985).

[21] N. Peters, Turbulent Combustion, Cambridge University Press2000.

[22] T. Lu, C.K. Law, A criterion based on computational singular perturbation for the identification of quasi steady state species: A reduced mechanism for methane oxidation with NO chemistry, Combustion and Flame 154 (2008) 761-774.

[23] S. Sanal, M.E. Marquez, M. Silva, E. Cenker, H.G. Im, A numerical study on the effect of a pre-chamber initiated turbulent jet on main chamber combustion, Report No. 0148-7191, SAE Technical Paper, 2022.

[24] M. Silva, Liu, X,. Hlaing, P., Cenker, E., Turner, J., Im, H. G. , A Computational Assessment Of Combustion Submodels For Predictive Simulations Of Pre-Chamber Combustion, Proceedings of the

28   H.G. Im, et al.

ASME 2022 Internal Combustion Engine Division Fall Technical Conference, Indianapolis, Indiana. In press., (2022).

[25] M. Silva, Alkhamis G., Cenker E., Im H. G. , A Computational Assessment of Laminar Flame Speed Correlation in an Ultra-lean Pre-chamber Engine, International Journal of Engine Research In press (2022).

[26] G. Alkhamis, A Computational Assessment of Laminar Flame Speed Correlation in an Ultralean Prechamber Engine, KAUST, 2021.

[27] M. Silva, E. Cenker, X. Liu, H. G. Im, A Computational Investigation of the Combustion Behavior and Turbulence-Chemistry Interaction in a Narrow-Throat Prechamber Combustion Engine, 13th Asia-Pacific Conference on Combustion 2021, (2021).

[28] M. Silva, X. Liu, P. Hlaing, S. Sanal, E. Cenker, J. Chang, B. Johansson, H.G. Im, Computational assessment of effects of throat diameter on combustion andturbulence characteristics in a pre-chamber engine, Applied Thermal Engineering in press (2022,).

[29] M. Silva, M.B. Houidi, P. Hlaing, S. Sanal, E. Cenker, A. AlRamadan, J. Chang, J. Turner, H. Im, Computational analysis on piston shape and jet-wall interaction in an engine operated with a narrow-throat pre-chamber, SAE PFL, (2022).

[30] M. Silva et al., CFD-guided optimization of a scavenged pre-chamber geometry in a heavy-duty engine operated with methane, Applied Energy in press (2022).

[31] S. Biswas, L. Qiao, Ignition of ultra-lean premixed hydrogen/air by an impinging hot jet, Applied Energy 228 (2018) 954-964.

[32] H. Kahila, A. Wehrfritz, O. Kaario, V. Vuorinen, Large-eddy simulation of dual-fuel ignition: Diesel spray injection into a lean methane-air mixture, Combustion and Flame 199 (2019) 131-151.

[33] M. Feyz, V. Hasti, J. Gore, M. Nalim, Large eddy simulation of hot jet ignition in moderate and high-reactivity mixtures, Computers & Fluids 183 (2019) 28-37.

[34] W. Tang, M. Sarathy, Investigate Chemical Effects of Pre-Chamber Combustion Products on Main Chamber Ignition Performance under an Ultra-Lean Condition, Report No. 0148-7191, SAE Technical Paper, 2020.

[35] I. Gorbatenko, Nicolle A., Silva M., Im H. G., Sarathy S. M., The impact of gasoline formulation on turbulent jet ignition, Fuel In press (2022).

[36] Wenxian Tang, Khaiyom Hakimov, Andre Nicolle., Aamir Farooq., Manis S. Sarathy, Experimental and kinetic modeling study: NO and hydrogen effects in iso-octane oxidation, Combustion and Flame in press (2022).

[37] W.X. Tang, Hakimov K., Zhang X.Y., Nicolle A., Farooq A., Sarathy S.M., Experimental and kinetic modeling study of the skeletal methanol_NOx model, Energy and Fuel in preparation (2022).

[38] K. Hakimov;, Y. Li;, J. Badra;, E. Cenker;, S.M. Sarathy;, A. Farooq;, Autoignition of iso-Octane at Ultra-Lean and Lean Conditions, Combustion and Flame in press (2022).

[39] N. Atef, G. Kukkadapu, S.Y. Mohamed, M. Al Rashidi, C. Banyon, M. Mehl, K.A. Heufer, E.F. Nasir, A. Alfazazi, A.K. Das, A comprehensive iso-octane combustion model with improved thermochemistry and chemical kinetics, Combustion and Flame 178 (2017) 111-134.

[40] C. Saggese, R. Fang, S. Wagnon, C. Sung, W. Pitz, Kinetic modeling of NO and NO2 promotion/inhibition interactions with gasoline surrogate components, Lawrence Livermore National Lab.(LLNL), Livermore, CA (United States), 2021.

[41] G. Moréac, P. Dagaut, J. Roesler, M. Cathonnet, Nitric oxide interactions with hydrocarbon oxidation in a jet-stirred reactor at 10 atm, Combustion and Flame 145 (2006) 512-520.

[42] W.-T. Chan, S.M. Heck, H.O. Pritchard, Reaction of nitrogen dioxide with hydrocarbons and its influence on spontaneous ignition. A computational study, Physical Chemistry Chemical Physics 3 (2001) 56-62.

[43] F. Almatrafi, M. Silva, M. B. Houidi, E. Cenker, J. Badra, B. Mohan, H. G. Im, J. Turner, Injector and Piston co-optimization for a passive pre-chamber engine using CFD, SAE PFL (2022).

[44] M.P. Burke, M. Chaos, Y. Ju, F.L. Dryer, S.J. Klippenstein, Comprehensive H2/O2 kinetic model for high-pressure combustion, International Journal of Chemical Kinetics 44 (2012) 444-474.

[45] J.-W. Park, Y. Pei, Y. Zhang, A. Zhang, S. Som. Optimizing Hydrogen Kinetics for Zero-Carbon Emission Transport Technologies. In: editor^editors. International Petroleum Technology Conference; 2022: OnePetro. p.

THIESEL 2022 Conference on Thermo- and Fluid Dynamics of Clean Propulsion Powerplants

A Numerical Study of Fuel Stratification, Heat Transfer Loss, Combustion, and Emissions Characteristics of a Heavy-Duty RCCI Engine Fueled by E85/Diesel

A. Willems[1], P. Rahnama[1,2], B. Somers[1] and R. Novella[2]

[1] Power & Flow – Department of Mechanical Engineering. Technical University of Eindhoven. P.O. Box 513, 5600 MB Eindhoven, The Netherlands.

[2]CMT – Motores Térmicos. Universitat Politècnica de València. Camino de Vera s/n, E-46022 Valencia, Spain.

E-mail: pouryarahnama@gmail.com

Abstract. Reactivity-controlled compression ignition is a new advanced combustion strategy developed to reach cleaner and more efficient combustion by controlling fuel stratification inside the engine cylinder and reducing heat loss. While its potential to produce high efficiency and low emissions and to reach higher loads than other Low-Temperature Combustion strategies (LTC) has been confirmed numerous times, its operating range is still limited to moderate loads. One potential solution to increase the operating range is using E85 fuel as the premixed fuel due to the potential of providing a longer combustion duration. This work will focus on developing a computational fluid dynamics (CFD) model for a reactivity-controlled compression ignition (RCCI) engine fueled by E85/diesel with a double step piston bowl geometry. The model is used to investigate the effects of four different design parameters, namely injection timing, boost pressure, initial temperature, and spray included angle, to identify their impact on all crucial parameters describing combustion i.e. the stratification level, heat loss, and emissions characteristics. It has been found that the start of injection affects the fuel stratification levels inside the cylinder, with the optimum location for efficiency located in the moderate stratified region. The boost pressure mainly influences the mean gas temperature, the start of combustion, combustion duration, and the recession time of the Heat Release Rate (HRR) curve. It is found that the boost pressure does not have an influence on the heat loss of the engine and the heat loss is more correlated to flame temperature than the average temperature. It is also proven that the boost pressure could assist in the suppression of NOx, but when the intake pressure is too high, the thermal efficiency drops. Furthermore, the results show that the initial temperature is preferred to be as low as possible but sufficiently high enough to burn all the introduced fuel. Intake temperature alters the HRR shape and combustion duration significantly. Lastly, it is found that the combination of the spray included angle and piston bowl geometry can substantially determine the way the flame is formed and its location. The study on the effect of spray angle provides essential insights on the origin of unburned hydrocarbon emission, HRR shape, and heat loss.

Notation

AMR	*Adaptive mesh refinement*
ATDC	*After top dead centre*
BDC	*Bottom dead center*
CA50	*Crank angle of 50% cumulative heat release*
CAD	*Crank angle degree*
BDC	*Bottom dead center*
CDC	*Conventional diesel combustion*
CFD	*Computational fluid dynamics*
CO₂	*Carbon dioxide*
CO	*Carbon monoxide*
DI	*Direct Injection*
DTBP	*Di-tert-butyl peroxide*
E85	*Fuel blend of 85% ethanol to 15% gasoline volume-based*
EGR	*Exhaust gas recirculation*
EVO	*Exhaust valve opening*
GHG	*Greenhouse gas*
HCCI	*Homogeneous charge compression ignition*
HC	*Hydrocarbons*
HECC	*High-efficiency clean combustion*
HRF	*High reactivity fuel*
HRR	*Heat release rate*
IC	*Internal combustion*
IDT	*Ignition delay time*
IT	*Initial temperature*
IVC	*Intake valve closure*
LFS	*Laminar flame speed*
LHV	*Lower heating value*
LRF	*Low reactivity fuel*
LTC	*Low-temperature combustion*
NOx	*Oxides of nitrogen*
NTC	*No time counter*
PFI	*Port fuel injection*
PPCI	*Partially premixed compression ignition*
PPLTC	*Partially premixed low-temperature combustion*
PRF	*Primary reference fuel*
RANS	*Reynolds-Averaged Navier-Stokes*
RCCI	*Reactivity controlled compression ignition*
RNG	*Renormalization group*
SCCI	*Stratified charge compression ignition*
SOC	*Start of combustion*
SOI	*Start of injection*
TDC	*Top dead center*

1. Introduction

Internal combustion (IC) engines are heavily integrated into society with their primary purpose to produce mechanical power from the chemical energy contained in fuel by a chemical process called combustion, which burns or oxidizes the fuel inside the enclosed space of the engine [1]. The most common fuels used in this process are gasoline and diesel, also known as fossil fuels. IC engines operating on fossil fuels [2] produce about 10% of the world's greenhouse gas (GHG) emissions [3] and produce hazardous exhaust emissions such as carbon monoxide (CO), oxides of nitrogen (NOx) and soot. Concerns and regulations about the emission of GHG and dangerous exhaust emissions have guided research into internal combustion engines further towards cleaner and more efficient combustion to reduce these emissions [4, 5]. The application of alcoholic fuels in IC engines is under spotlight due to their high enthalpy of vaporization, octane number, flame speed, and low adiabatic flame temperature.

As a result, new advanced combustion strategies with renewable fuels are being developed, and most of these strategies can be categorized under low-temperature combustion (LTC) [6]. An LTC mode engine works at lower combustion temperatures compared to conventional diesel mode engines [7]. The benefit of having a lower combustion temperature is reducing NOx emission while simultaneously improving thermal efficiency [8, 9]. Various strategies can achieve LTC in combustion engines. Homogeneous charge compression ignition (HCCI) [10, 11], partially premixed compression ignition (PPCI) [12, 13], and reactivity controlled compression ignition (RCCI) [14]. The strategy that will be researched in this work is RCCI. RCCI has been introduced to overcome the disadvantages of HCCI and PPCI strategies in the direct control of the start of combustion and the combustion rate [15]. It is a dual fuel strategy in which one so-called Low Reactivity Fuel (LRF) and one High Reactivity Fuel (HRF) are used [16]. Utilizing the two fuels, the combustion phase, combustion duration, and magnitude of heat release rate can be controlled [17]. Researchers at the University of Wisconsin-Madison have proven that RCCI combustion can achieve high efficiency and clean combustion [18, 19]. For example, they have shown that RCCI has a better performance in terms of efficiency and emissions at mid-load conditions than conventional combustion [20].

Many researchers have used conventional fuels, gasoline as an LRF and diesel as an HRF, in their studies. E.g., Kokjohn and Benajes used these fuels in their studies [21, 22] to demonstrate the RCCI concept and its advantages. Although fossil fuels are the most convenient and affordable to use as fuel, they are neither renewable nor clean and will deplete in the future [23]. Combining both new advanced LTC strategies with alternative fuel sources has huge potential for cleaner and more efficient combustion. Some examples of alternative LRF possibilities are natural gas [24, 25], syngas [26, 27], alcoholic fuels like methanol [28], ethanol [8], and butanol [15]. Regarding an alternative HRF, biodiesel [29] and dimethyl ether [30] have been investigated. This fuel flexibility of the RCCI strategy is a huge benefit in the optimum design of the engine.

Although RCCI engines with alternative fuels provide significant advantages over other LTC strategies by controlling combustion phasing and maximum pressure rise rates (MPRR), these two factors still limit the RCCI operating range to moderate loads. Ethanol has high resistance to auto-ignition, which provides a large reactivity gradient inside the cylinder to extend the operating range of RCCI engines [31]. In addition, it has a high heat of vaporization and can improve the efficiency and lower NOx emission in RCCI engines [32]. Curran et al. [33] were among the first researchers who investigated the potential benefit of using E85 in a light-duty RCCI engine experimentally. They concluded that replacing gasoline with E85 could significantly extend the high load limit of the engine, and in general, the engine emissions were a little lower with E85. Benajes et al. [34] compared the use of E85 and gasoline as the premixed fuel in a light-duty RCCI engine experimentally and found that E85 can extend the high load limit of the engine by 2 bar at the expense of a little higher emissions. Willems et al. [35] studied the effect of using E85 in a heavy-duty RCCI engine experimentally. They defined a metric to correlate reactivity stratification inside the cylinder to HRR shape and heat loss, and its impacts on combustion efficiency, heat transfer, and NOx emission were explored.

Most of the research done on E85/Diesel engines focuses on experimental work on light duty engines. Achieving higher load operation in heavy-duty engines is more important, and the use of numerical modeling to investigate the effect of the most critical design parameters is missing. It has been shown that CFD modeling can give in depth analysis in the design process of the engine to understand the source of emissions and combustion characteristics by providing 3D visualization of flow parameters which is not possible with experiments. This work aims to numerically investigate the effect of design parameters on all essential parameters including fuel stratification, heat loss, combustion, and emission characteristics in a heavy-duty RCCI engine fueled by E85/diesel with double-step piston geometry.

Effects the start of injection, boost pressure, initial temperature, and spray included angle are investigated. A computational fluid dynamics (CFD) model with detailed kinetic chemistry is built. This CFD model is validated against experimental data obtained by researchers at the Technical University of Eindhoven. The validation is completed by comparing the numerical results of the pressure curve, the heat release rate (HRR), and the engine emissions to that of the experimental data. Following the validation of the CFD model, design parameters will be varied, after which the results are presented and discussed.

2. The computational fluid dynamics model

In this section, the detailed CFD model developed to numerically investigate the effect of design parameters in RCCI engines using E85 as the premixed fuel and diesel as the injected fuel is described. Important topics like CFD software, engine specifications, and numerical models for physical processes, including combustion, spray, turbulence, emissions, and heat transfer, are selected and explained.

2.1 Software description

Please note the following points: In this work the commercially available CFD software CONVERGE is used [36]. CONVERGE is a CFD software for simulating three-dimensional, incompressible, or compressible, chemically-reacting fluid flows in complex geometries with stationary or moving boundaries. CONVERGE features tools such as truly autonomous meshing, adaptive mesh refinement (AMR), fixed embedding, and advanced validated numerical models for physical processes including combustion, spray, turbulence, emissions, and heat transfer. The AMR feature can adapt the generated mesh during runtime, adding cells in areas with large gradients of flow variables to yield more accurate results. At the same time, fixed embedding technology gives the user the ability to define locations within the geometry and time segments to add grid resolution to more accurately resolve critical flow features. Combining AMR and fixed embedding will ensure that the generated mesh is refined when and where it is needed to deal with complex fluid flows.

2.2 Model Description

Experiments were conducted in previous research by Robbert Willems et al. [37] on a single-cylinder of 12.6 liters DAF XEC heavy-duty diesel engine equipped with a common rail system Delphi DFI21 injector and double-step piston at Technical University of Eindhoven. Detailed information of measurements and the experimental setup can be found in [35, 37]. The specifications of this engine are provided in Table 1. The engine rotational speed is maintained at a constant value of 1200 revolutions per minute, and it has a geometrical compression ratio of 15.85, which was lowered from its original value. E85 was injected by a low-pressure injector fitted into the intake port of the cylinder.

Table 1: The specifications of the heavy-duty DAF XEC

Specification	Value
Displaced volume	2097 cc
Bore	130 mm
Stroke	158 mm
Connecting rod length	266.7 mm
Piston bowl shape	Double-step
Number of valves	4
Intake valve closure (IVC)	-153 CAD ATDC
Exhaust valve opening (EVO)	128 CAD ATDC
Number of injector holes	7
Hole diameter	0.195 mm
Spray included angle	139°

The IC engine cylinder is axisymmetric. Combining this with the seven equally distributed holes of the high-pressure injector in the middle of the cylinder, the domain can be divided into seven identical portions of 51.4°. The model leverages a structured Cartesian grid with base size of 1.4 mm. Boundary embedding and adaptive mesh refinement were also used to assure the mesh independent solution. A fixed embed scale of one near the piston and cylinder head and a fixed embed scale of two in the vicinity of the injector nozzle, and an AMR embed scale of two for spatial gradients in velocity and temperature. In addition, the fluid flow from IVC to EVO is only simulated, resulting in a further reduction of computational resources needed. This approach reduces the complexity of the complete CFD model because it does not need to include the intake/exhaust valve's motion as they will remain closed. The initial mixture inside the cylinder is considered to be homogeneous. It has been shown that all these simplifications are rational for calculating the essential parameters describing combustion and emissions characteristics concerned in the current study [38]. The result is a simplified CFD model of the DAF XEC heavy-duty diesel engine running RCCI combustion. The visualization of the surface file used can be seen in Fig. 1.

(a)

(b)

(c)
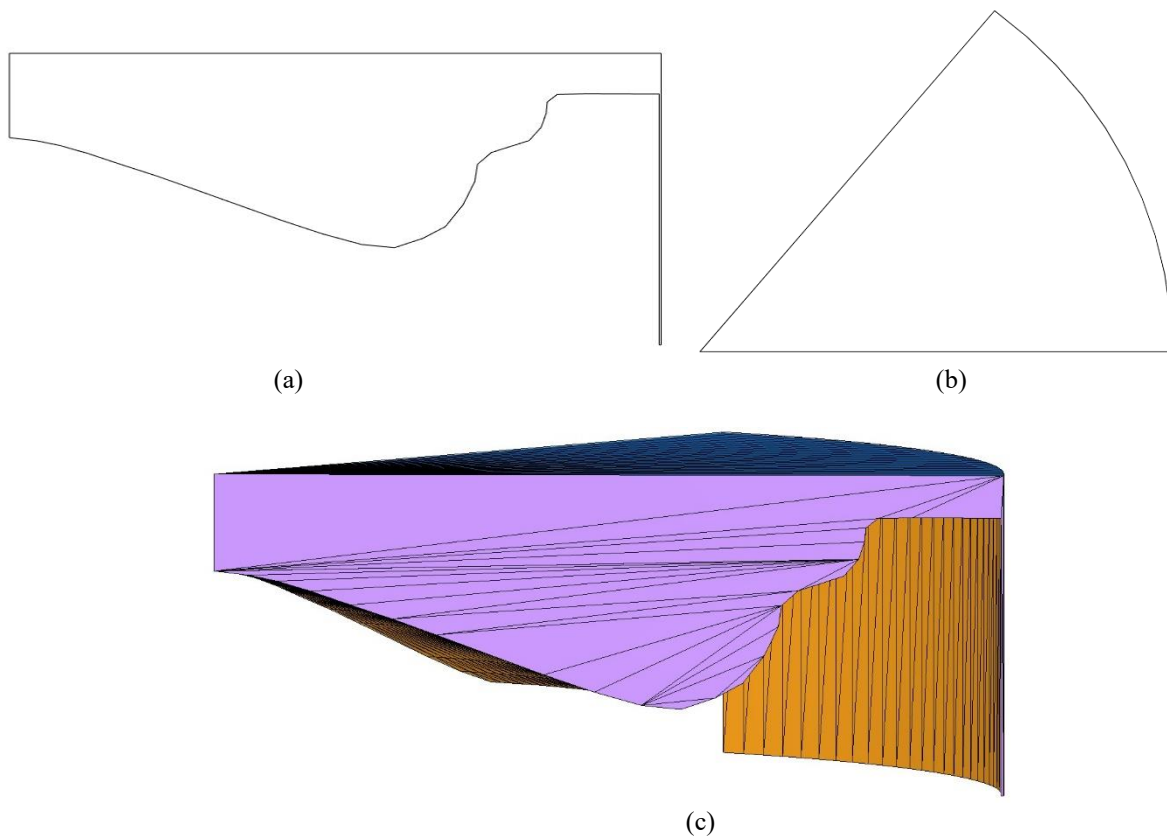
Fig. 1 Planar and upper view sketch of the piston bowl combined with the 3D visualization of the 51.4° surface file of the RCCI engine including the piston crevice region and double-step piston bowl at TDC

2.3 Numerical models

The simulation of the thermophysical and flow processes, including combustion, spray, turbulence, emissions, and heat transfer, requires corresponding models to be selected. There are numerous validated models for these processes implemented in CONVERGE. This section will address the chosen numerical models used in the CFD model. The overview of all the models selected in CONVERGE are presented in Table 2.

Table 2: Overview of the models used in the CFD model using CONVERGE CFD

Phenomenon	Model

Combustion model	SAGE
Combustion chemical kinetics	A reduced PRF-methanol-ethanol-DTBP mechanism [39]
Spray break up	KH-RT
Spray collision model	NTC
Spray wall interaction model	Wall film with O'Rourke splash model
Evaporation model	Frossling
Emission models	Extended Zeldovich NOx model and Hiroyasu-NSC soot model
Turbulence flow	RANS RNG $k - \varepsilon$
Heat transfer model	O'Rourke and Amsden

2.3.1 Combustion model

This work is investigating the combustion of E85 as the LRF and diesel as the HRF. E85 consists of 85% and 15% volume-based percentage of ethanol (C_2H_5OH) and gasoline, respectively. However, gasoline consists of hundreds of different hydrocarbons. Commonly gasoline is simplified to a single hydrocarbon with somewhat similar thermal and chemical properties, namely isooctane (C_8H_{18}), to reduce the computational cost. The lower heating value (LHV) of this blend was set to 29.1 MJ/kg to keep the fuel energy and mass input similar to the experiments of Willems et al. [35, 37]. The result is an LRF blend in the simulation that consists of 69.56 mass-percentage ethanol (C_2H_5OH) and 30.44 mass-percentage isooctane (C_8H_{18}), with the mixture having an LHV of 29.1 MJ/kg. The HRF of diesel consists of hundreds of different hydrocarbon molecules as well. In order to keep the computation cost of the CFD model low, the thermal and chemical properties of n-heptane (C_7H_{16}) are used as a substitute for the diesel fuel's properties in the CFD model. N-heptane is frequently used as a substitute for diesel in many numerical studies, and researchers have proven the combustion characteristics are very similar to diesel (e.g., Ra et al. [40]). Similarly, the LHV of n-heptane (C_7H_{16}) was set to 42.6 MJ/kg to keep the fuel energy and mass input similar to the experiments data.

CONVERGE provides many options for the non-premixed combustion. This work uses the SAGE model [41] for combustion modeling. SAGE detailed chemistry model uses local conditions to calculate reaction rates based on the principles of chemical kinetics [36]. This solver is fully coupled to the flow solver, but the chemistry and flow solvers parallelize independently, which speeds up the simulation [36]. The SAGE solver requires a chemical kinetic mechanism input file with all the species involved during combustion. The chemical kinetic mechanism consists of thermochemical data for 80 species and chemical rates coefficients for 349 reactions. It has the necessary fuel species which this work requires, i.e., ethanol (C_2H_5OH), isooctane (C_8H_{18}), and n-heptane (C_7H_{16}). The reaction mechanism is the reduced PRF-methanol-ethanol-DTBP mechanism developed by Wang et al. [39]. This mechanism has been proposed to simulate the HCCI combustion processes of PRF and alcohol-DTBP fuel mixtures and discover the reactivity enhancement of DTBP to alcohols. It is a frequently used kinetic model in studies with alcohol and isooctane. It has been validated extensively in prediction of IDT and LFS for a wide range of conditions for methanol, ethanol, isooctane, and n-heptane [42].

2.3.2 Spray model

In an RCCI engine, the HRF will be injected directly into the cylinder. This spray of liquid will eventually evaporate and mix with the existing gas mixture inside the cylinder. The spray modeling process introduces fuel droplet parcels into the domain at the specified injector location inside the cylinder. The droplets experiences break up, collision, and evaporation until all fuel droplet parcels are evaporated. For each sub-process, a model has to be selected. The hybrid KH-RT model [43] is commonly used to simulate the DI diesel fuel breakup process. The collision of fuel droplets is modeled using the no time counter (NTC) approach [44]. The Frossling model [45] has been selected to predict the spray evaporation process, and the interaction between the HRF and the wall is done with a wall film model with an O'Rourke splash model [46]. These models were selected based on performance in other studies [47, 48].

As introduced in Section 2.2, the current setup of the CFD model will only simulate a cylinder section. Hence the number of nozzles or injector holes needing to be configured is reduced to 1. The nozzle area is circular with a diameter of 0.195 mm. The nozzle is located in the middle of the cylinder and has the spray included angle of 139°. This angle is defined as an umbrella shape angle of the spray. The injection spray type is a solid cone that starts injecting the fuel at a specified injection rate into the combustion chamber at the SOI. Due to lack of experimental data on the injection rate shape, the default time-dependent profile of Converge CFD software is used.

2.3.3 Emission models

To examine the emissions by the effect of changing design parameters, two extra emission models are implemented in this CFD model. The extended Zeldovich model is used to calculate NO formation [1], and the Hiroyasu-NSC soot model [49] is used to simulate soot oxidation. The model constants are calibrated during the validation stage. CO emission is modeled automatically, since SAGE models detailed kinetic and information on the amount of emitted for these species is available.

2.3.4 Turbulence model

The modeling of turbulence is a critical aspect in predictive and precise combustion simulations. Turbulent motion inside the cylinder is responsible for most of the mixing of fuel and air. It is highly influential on the combustion output parameters and significantly influences the soot emission [50]. The RANS renormalization group (RNG) k-ε turbulence model [50] is chosen in this work. It has been shown in other studies that, the model is not only cost-effective in terms of computational cost but also good enough to predict that most critical engine output parameters [51, 52]. CONVERGE already has set a validated preset for this model, and in this work the values of the default RANS RNG k-ε turbulence model are used.

2.3.5 Heat transfer model

During combustion, the local temperature of up to 2500 Kelvin (K) and the average gas temperature above 1800 K depending on operating conditions are reached. The engine walls are cooled, which induces a temperature gradient between the walls and the charge, generating a heat flux and thus energy losses. These energy losses can be huge, and the heat transfer process must be simulated. Among several validated wall heat transfer models available in CONVERGE, the O'Rourke and Amsden [45] heat transfer model is selected to account for heat transfer through the walls because it is widely used in combustion engine simulation and based on the authors' experience will result in better prediction for the most important combustion characteristics. For simplicity, the piston, liner, and head temperature are set to have the fixed values of 500, 400, and 450 Kelvin, respectively. CONVERGE already has preset values for using this model in IC engines. Fig. 2 depicts a flowchart to show the simulation procedure.

2.3.6 Numerical Solution Procedure

the finite volume method is utilized to discretize the governing transport equation assuring full conservation of flow quantities in the domain. The pressure-velocity coupling is performed using a modified PISO algorithm [53]. The solution algorithm starts with the solution of the momentum equation, which acts as a predictor step. A pressure equation is solved to correct the momentum equation. After the first correction, other transport equations are solved. The procedure is repeated until reaching numerical convergence. In Fig. 2 a flowchart is presented showing all submodels and the numerical solver. More details can be found in the Converge CFD's manual [36].
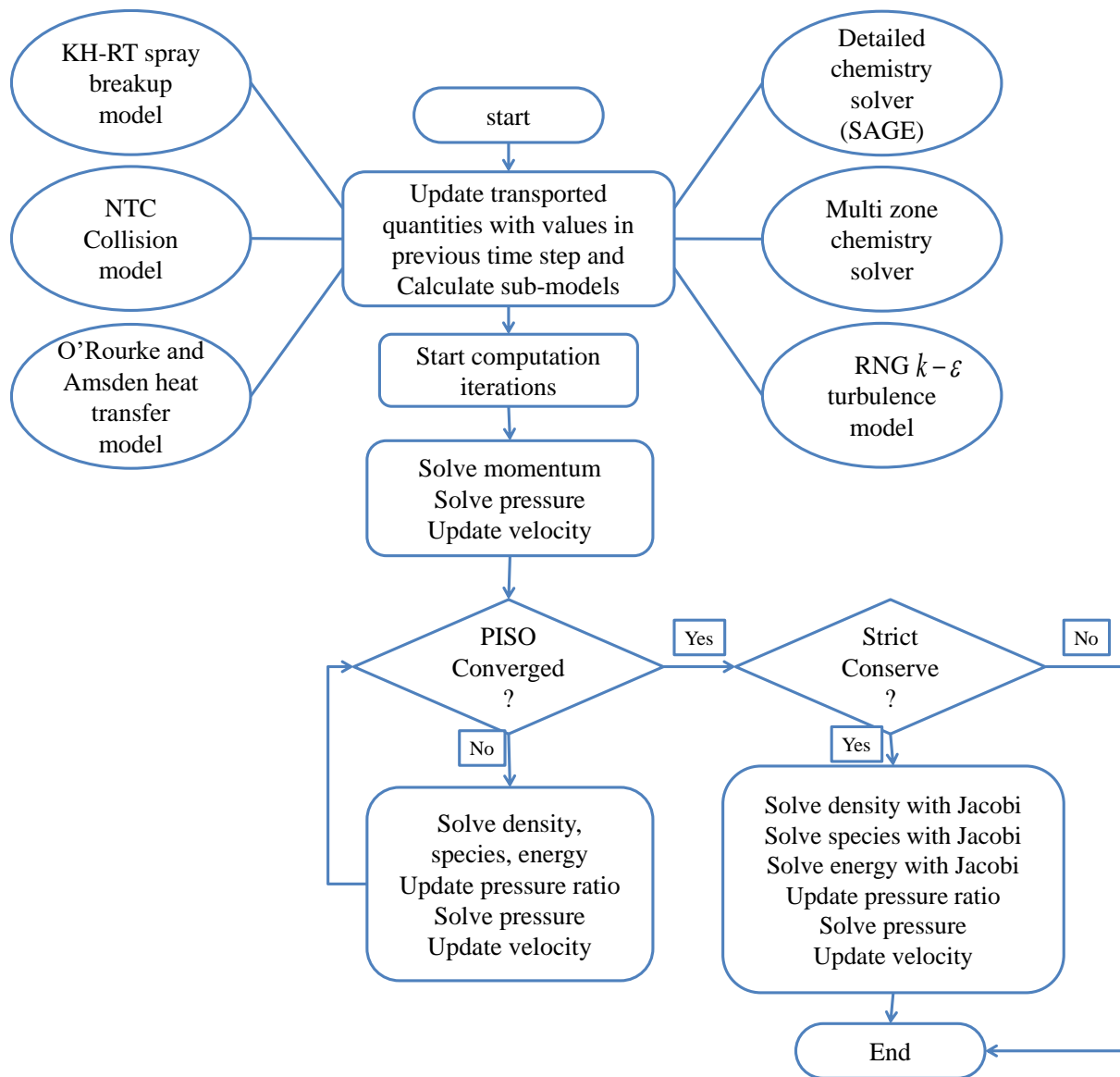
Fig. 2 Flowchart of CONVERGE simulation for a single time step

3. The validation of the CFD model

The CFD model has to be validated against experimental data to trust the results obtained by the numerical CFD model. Experimental data from Willem et al [35, 37] is used to evaluate the CFD model's precision in simulating an RCCI engine. Figure 3 schematically depicts the experimental setup. The complete description of experimental procedure, setup and data collection can be found in the previous research [37]. This section will present the results for combustion, emission, stratification level, and heat transfer characteristics.
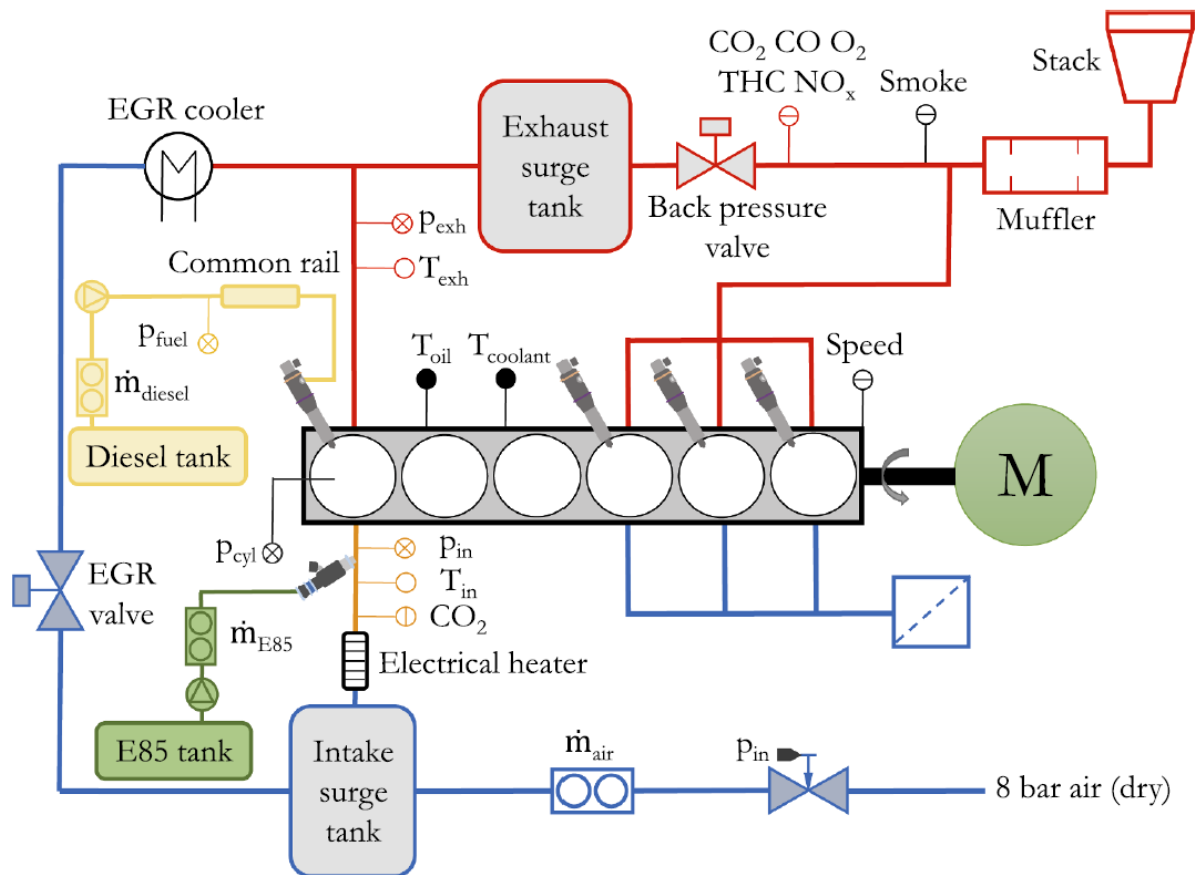
Fig. 3. The schematic diagram of the experimental setup. Blue line shows cold flow and red line shows hot flow.

3.1 The validation process

The validation process of the CFD model is iterative and is based on tuning the parameters which are difficult or impossible to measure during the experiments, and are commonly used in IC engine validation. For example there is no instrument to obtain the actual droplet size distribution of spray. Also, measuring temperature inside the cylinder is very difficult, since the sensor measuring the temperature should be made of special material to tolerate the high temperature during the combustion. According to the study of Senecal [54], the initial temperature at IVC timing should be a little bit higher than the intake temperature. Therefore, in this study, the initial temperature was considered to be higher as well and adjusted accordingly to reach the same combustion timing as we had in the experimental data. Small adjustment were also made the spray model constants which are used to determine the size distribution of droplets inside the domain to match the in-cylinder pressure, the heat release rate behavior, and combustion and emission characteristics, which are fundamental characteristics of IC engines. Only the final result of the validation process will be further discussed in this section.

3.2 The model validation

The experimental data from operating conditions listed in table 3 is selected to validate the CFD model. The operating conditions are chosen to be far away from misfiring and unstable conditions in the engine which have high unburned fuel and pressure rise rate respectively. The EGR value was used to calculate the initial concentration of species at IVC timing. The Combustion Products Calculator tool in Converge was used to calculate the initial mass fractions which leverages the chemical equilibrium solver to compute the initial mass fraction of species at equilibrium.

Table 3: the operating condition of the engine validation case

The engine speed (rpm)	1200
PFI ratio (% by vol)	75.0
SOI ($^{\circ}CA$ ATDC)	-42.5
Intake pressure (bar)	2.0
Intake Temperature (K)	353.0
EGR flow rate (%)	10.0
Air mass flow (g/s)	35.4
Diesel mass flow (g/s)	0.31
PFI fuel mass flow (g/s)	0.9
Common rail pressure (bar)	500
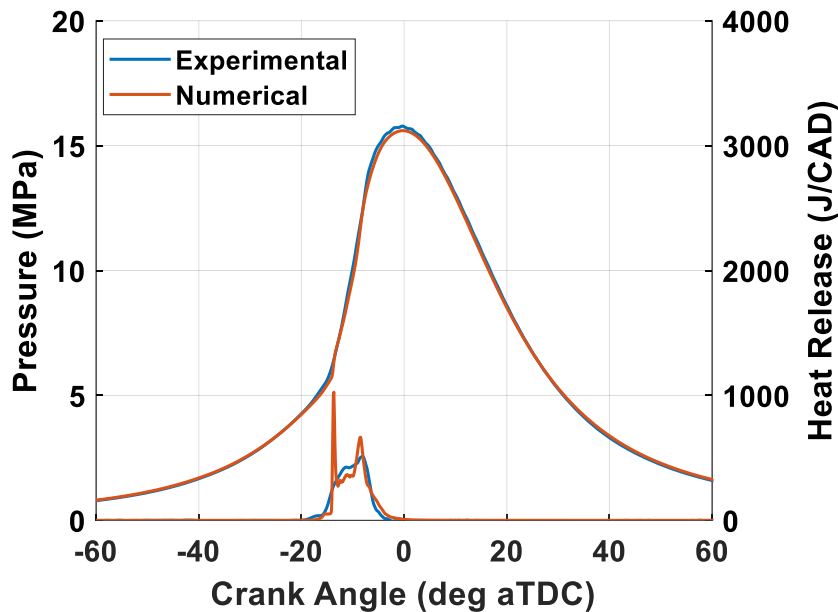
Fig. 4. In-cylinder pressure and heat release rate between -60 and 60 crank angle degrees after top dead center obtained from the experimental data in blue and CFD simulation in orange.

In Figure 4, the results for in-cylinder pressure and HRR of the numerical model and experimental model are presented. As visualized in Figure 4, the CFD model created in CONVERGE accurately predicts the pressure and HRR history of the RCCI engine. The in-cylinder pressure rise rate (the maximum value of the pressure gradient with respect to crank angle) and in-cylinder peak pressure match the experimental data with a maximum deviation of less than 5%. The HRR has a more difference. The HRR curve has a high initial spike because of the chemical mechanism, but it successfully captures dual-stage combustion, usually seen in late injection in RCCI engines [55].

The HRR was further investigated by comparing the combustion phasing and combustion duration. The combustion phasing indicated by the CA50 is in both cases (i.e., the experimental data and numerical simulation) very similar. The combustion duration deviates a bit more but is still within decent margins. To finalize the validation, the emission results are compared and can be seen in Table 4. The soot emissions do not seem to match well, but both values are extremely low and with only an order-of-

magnitude difference. The Hiroyasu soot model is oversimplified since it contains no dependence on the type, composition or structure of the fuel. However it is still sufficient to capture tendencies during the parametric study of the current research. The NOx emission results are different, but they are in the same order of magnitude. The CO emission deviate an order of magnitude from experimental data. And lastly, the CO_2 emissions are relatively good as they are in the same order of magnitude. Although the error between experimental data and simulation results for some of the emissions is high, the exact values for the current parametric study are not so relevant. The simulation values are only used to study how changing design parameters would affect how important output parameters vary.

Table 4: Comparison of CA50, combustion duration, and emissions result from values between the experiments and CFD simulation

	Experiment	**Simulation**	**Absolute Error**
CA50 (deg.ATDC)	-9.96	-9.87	0.0900
Combustion duration (deg)	8.19	7.55	0.6400
Soot emissions (gr/KW.hr)	0.0042	0.222	0.0180
NOx emissions (gr/KW.hr)	10.6	4.085	6.5150
CO emissions (gr/KW.hr)	2.2	0.935	1.2650
CO_2 emissions (gr/KW.hr)	559.1	635.0	75.9000
Efficiency (%)	47.5	44.93	2.57

The validation results indicate that the model developed in this study is able to be predict the in-cylinder pressure, HRR and other combustion characteristics such as combustion duration and phasing accurately. However the model prediction is not very accurate to reproduce the emission values. Nevertheless it is still sufficient to take the emissions trends. Investigating the effects of changing design parameters on the performance of an RCCI engine will be done in the next section. The final verdict of this validated CFD model is that it predicts the current case setup adequately, except for the exact values of the emissions results.

4. Results and discussion

In this section, the CFD results regarding the investigation into the effects of the changing design parameters including the SOI, spray included angle, boost pressure, and initial temperature (IT) on the performance and emissions of an RCCI engine fuelled by E85 and diesel are presented and discussed. The created and validated CFD model is the fundamental starting point for further parametric investigation with only the design parameter altering among simulations.

4.1 Effects of the start of injection

The first design parameter being investigated is the SOI (i.e., the moment this RCCI engine starts its single direct injection strategy). Figure 5 presents the in-cylinder pressure and HRR values between -40 and 40 CAD ATDC for injection timing of -65, -57.5, -50, -42.5, and -35. It is observed that the highest peak pressure occurs in an SOI of -35 CAD ATDC, and this slowly drops in correlation with an advancing SOI to the lowest peak pressure perceived in the SOI of -65 CAD ATDC.
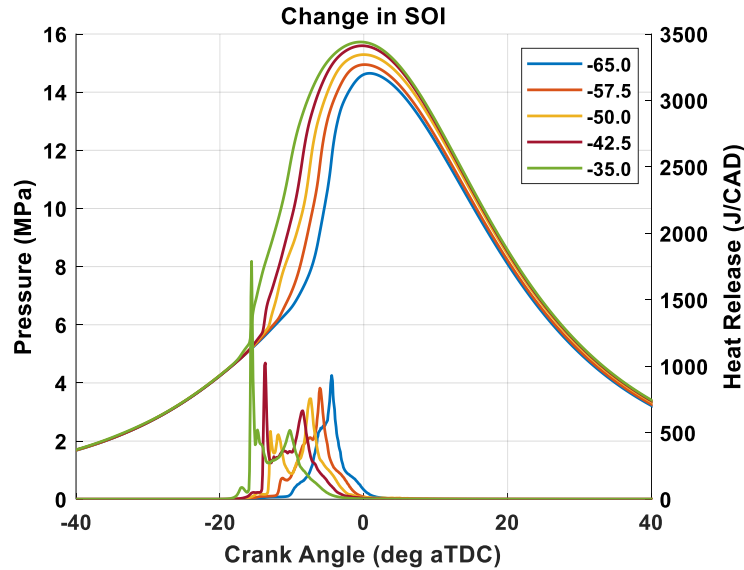
Fig. 5. In-cylinder pressure and heat release rate between -40 and 40 after top dead center obtained from the simulations with -65, -57.5, -50, -42.5, and -35 start of injection (SOI) parameters.

When examining the HRR, the transition towards a single-stage HRR can be seen clearly with the SOI of -65 CAD ATDC having only a single-stage HRR, and the SOI of -35 CAD ATDC having a distinguishable dual-stage HRR. The dual-stage HRR combustion starts in the heavily stratified region, and this region combusts in an intense first part of the combustion, after which the remaining LRF combusts, creating the second stage of the HRR. The single-stage HRR starts in a more centralized location inside the engine cylinder at lower reactivity stratification levels, making the single stage of HRR. The HRR curves also clearly show that the start of ignition retards as the SOI timing advanced away from TDC. Setting forward the SOI allowed the direct-injected diesel more time to distribute, creating a less stratified charge with less concentrated fuel-rich regions resulting in lower local ignitability. The total equivalence ratio inside the engine cylinder is visualized to indicate the level of fuel reactivity stratification. The total equivalence ratio of the E85/diesel dual-fuel engine can be calculated according to Equation 1 derived from the formula in the work of Zheng et al. [56].

$$\varphi = \frac{m_{C_2H_5OH}*9 + m_{C_8H_{18}}*15 + m_{C_7H_{16}}*15.2}{m_{O_2} + m_{N_2}} \tag{1}$$

In the numerator in the equation the mass of each fuel has been multiplied by its stoichiometric AFR (Air-Fuel ratio) value. This equivalence ratio is visualized on cut planes of three simulations at the start of combustion (SOC) presented in Figure 6, where the SOC is defined as the moment where the initial heat release occurs, and the combustion is in the first stage of the dual-stage combustion. The total equivalence ratio distributions on the cut planes of the engine at SOC are vastly different between

the simulations. In the case with SOI of -35 CAD ATDC combustion starts at a high fuel reactivity stratification (the flame location is located at low equivalence ratio, indicating all fuel is burned) as the DI spray is still visible. In comparison, the earlier SOI of -65 CAD ATDC clearly shows a lower level of fuel reactivity stratification.
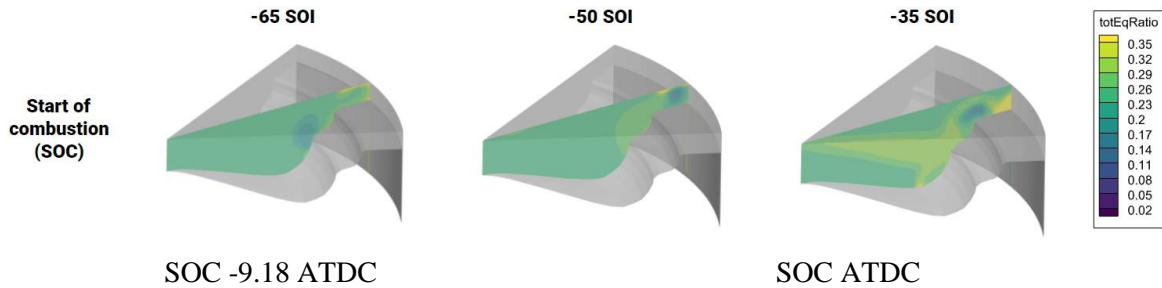
Fig. 6. Total equivalence ratio cut planes at start of combustion (SOC) for -65, -50, and -35 start of injection (SOI) simulations.

This lower level of fuel reactivity stratification produces a shorter single-stage HRR than a high level of fuel reactivity stratification, which creates a longer dual-stage HRR as already stated (see Fig. 5 and 8f). Reducing the fuel reactivity stratification also affects the temperature inside the cylinder considerably as lower equivalence ratio values mixture burns at lower temperatures. This fact can be observed from the contour plot in figure 7, where the local temperature is visualized on the cut planes of three simulations at CA10, CA50, and CA90. As expected, the identified locations with higher equivalence ratio values in Figure 8 result in higher local temperatures. This affect soot and NOx emissions. higher gas temperature increases the NOx emission as NOx formation rates are higher while simultaneously decreasing soot emission since more soot will be decomposed (see Figs. 9b and 9d).

Figure 8 compares six combustion and heat release output parameters of the five different SOI cases. In Figure 8a, the in-cylinder mean gas temperature is visualized. It is observed that by advancing the SOI and decreasing the fuel reactivity stratification, the mean gas temperature drops significantly. In Figure 8b, the heat transfer loss is presented which is calculated by adding up all of the heat transfer values from all boundaries, and the final value is divided by the total input energy that is calculated by the LHV of the fuels. By pulling the SOI away from TDC, the heat transfer loss decreases significantly. This fact correlates with the difference in mean gas temperature, as the advanced SOI simulations create lower in-cylinder temperatures than the delayed SOI simulations.
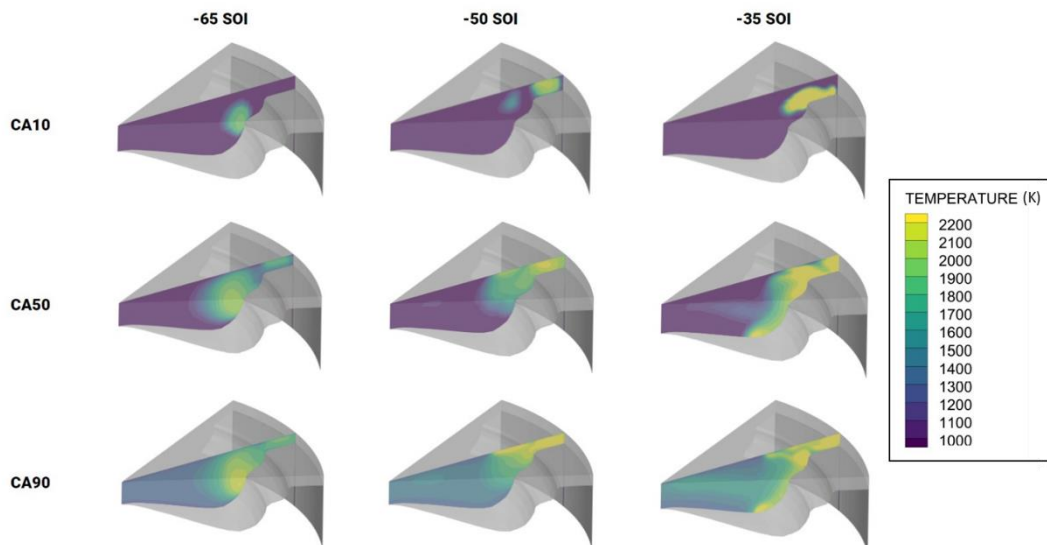

Fig. 7. Temperature cut planes at CA10, CA50, and CA90 for -65, -50, and -35 (ºCA ATDC) start of injection (SOI) simulations.
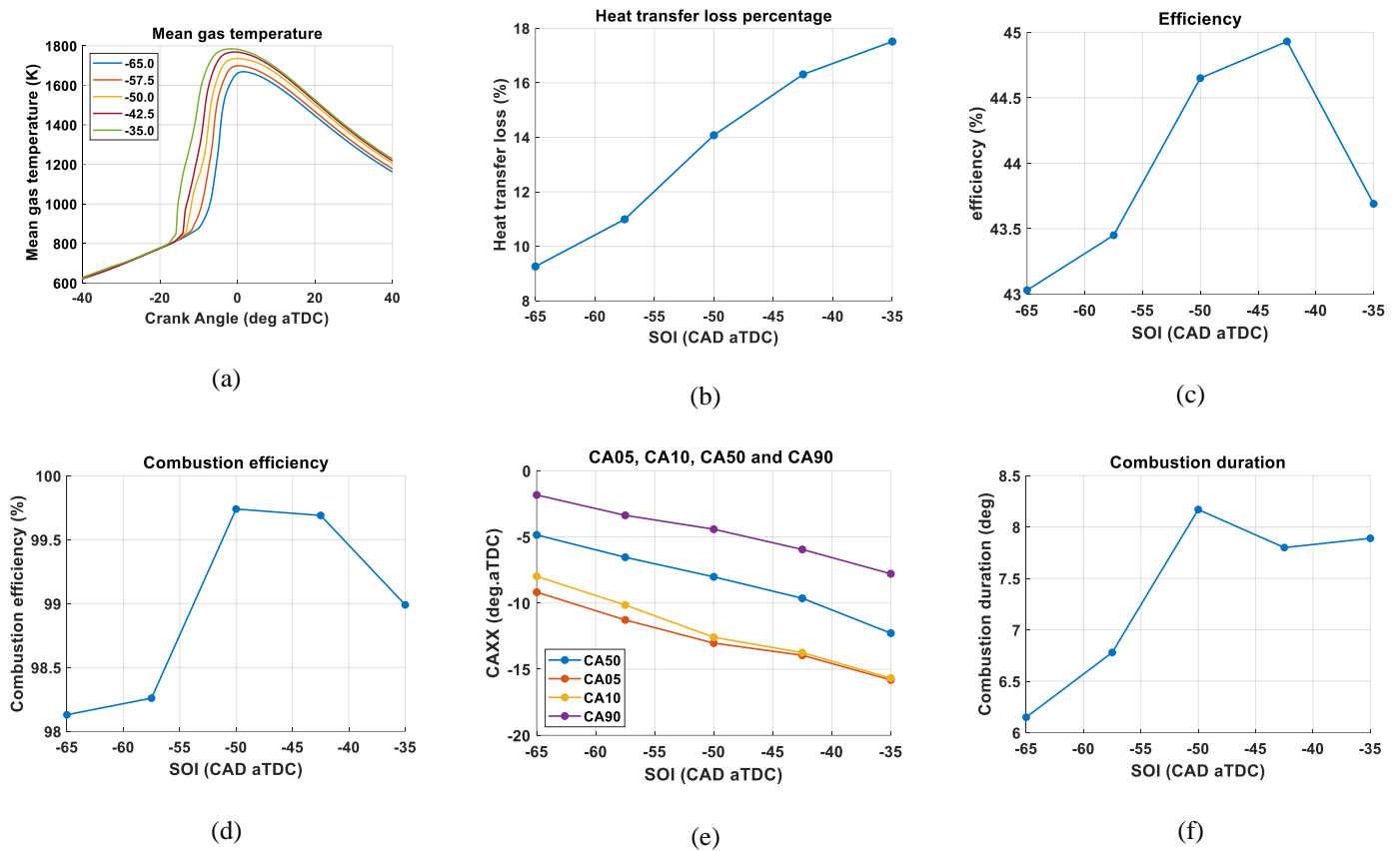
Fig. 8. Combustion and heat release characteristics when varying start of injection timings from -65 to -35 crank angle degrees ATDC with an interval of 7.5 crank angle degrees.

In Figure 8c, the engine's efficiency is presented. The engine efficiency is calculated through dividing the work of the in-cylinder gas mixture by the total input energy of the fuels. The efficiency seems to have an optimum efficiency somewhere in between the cases. This is caused by opposing losses. The gained energy in reducing heat transfer by advancing the SOI gets nullified by the decreased peak pressure due to delayed combustion start, creating less work. While for the case where SOI is -35 CAD ATDC, combustion and consequently the increase in pressure is way too early, and all of the amounts of heat release is during the compression stroke, which causes negative work, thereby significantly reducing thermal efficiency. In Figure 8d, the combustion efficiency is presented. The combustion efficiency is linked to the CO emission results as it represents the total amount of fuel converted to the final product of combustion. The combustion efficiency seems to have an optimum location between the simulations and is impacted by temperature and fuel reactivity stratification. Generally, with higher temperatures, the burning rate of the fuels will be increased, reducing the emissions. But in the case of the too much delayed SOI, the higher local equivalence ratio forms near the cylinder wall (see Fig. 6) causing incomplete combustion.

In figure 8e, crank angles for 5, 10, 50, and 90 percent mass of fuel burned can be seen (i.e., CA05, CA10, CA50, and CA90). The SOC identified with the CA05, CA10, CA50, and CA90 shifts towards TDC when injection happens earlier. Specifically looking at the combustion phasing (indicated by CA50), the trend is observed. The earlier the SOI is, the later the combustion phasing is. Additionally, the less intense first part of the combustion in the earlier SOI simulations is also observed as the offset between CA05 and CA10 increases with an advanced SOI timing. Meanwhile, in the last figure (8f), the combustion duration of the simulations is shown, and it is perceived that by delaying the SOI, the combustion duration increases. This comes from the fact that advancing the SOI produces less fuel reactivity stratification, making the combustion similar to HCCI engines in which the charge auto-ignites suddenly at the same time and closer to TDC.
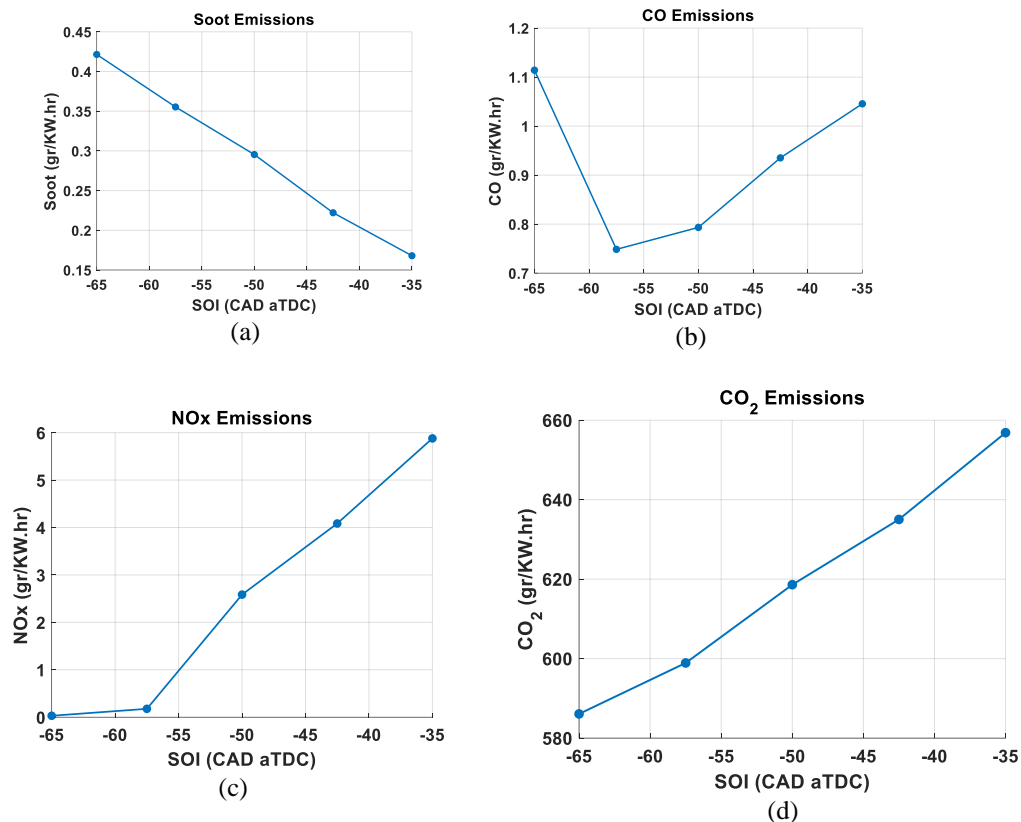
Fig. 9. Variation of emissions results with different start of injection (SOI) timings from -65 to -35 crank angle degree ATDC with an interval of 7.5 crank angle degrees

The final step in the investigation examines the emissions characteristics of the five different simulations. The results in gram per kWh can be seen in Figure 9. The CO emissions seem to have an optimum location where the lowest emissions results are found. It is established that the generated power (which is correlated to the efficiency) mainly determines the shape of the CO emission results. In the CO emission results, two opposing effects are present. Delaying the SOI too much towards TDC leads to more incomplete combustion due to the high fuel stratification (local equivalence ratio). In contrast, advancing the SOI too much results in lower combustion temperatures leading to more incomplete combustion due to too low temperature. The latter only happens in the SOI of -65 CAD ATDC. While CO emission drop and rise with a delayed SOI, the soot, NOx, and CO_2 emissions seem to have only a single response. Setting back the SOI results in the soot emission decrease and NOx and CO_2 emission increase. The soot emission decreases due to the higher combustion temperatures decomposing more soot. Although soot emission is related to the local equivalence ratio as well, it seems the effect of temperature is more prominent. The NOx emission increases with the higher combustion temperatures as NOx formation rates are more noticeable at higher temperatures. The CO_2 emission increases as higher temperatures lead to more complete combustion.

4.2 Effects of boost pressure

The second design parameter being investigated is the boost pressure (i.e., the intake pressure through the inlet manifold). Figure 10 presents the in-cylinder pressure and HRR history from -40 to 40 CAD ATDC for the cases where boost pressures are 1.6, 1.8, 2.0, 2.2, and 2.4 bar. The start of injection and the other operating conditions has been kept the same as table 3. It is observed that the highest peak pressure reached is 17.4 MPa in the simulation of 2.4 bar boost pressure, and this drops to the lowest peak pressure of 13.7 MPa while decreasing boost pressure to 1.6 bar as expected. With increasing pressure the concentration of the molecules in the intake charge elevates and the number of collision between molecules increases subsequently which finally leads the mixture to ignites earlier. Continuing the observations to the HRR, it is perceived that combustion duration in the higher boost pressure is significantly longer. With increasing boost pressure, flame speed decreases due to lower

average temperature. Most notably, the recession of the HRR curve takes longer as the remaining fuel fragments burn out later. This will be even clearer when the crank angles for 90 percent mass of fuel burned (i.e., CA90) are visualized in the second part of this section. Another effect perceived in the HRR is the advanced SOC with the increased boost pressure. The cause can be attributed to an increased mean gas temperature before SOC, causing the charge to reach the necessary ignition conditions earlier. Figure 13a visualized this effect as the mean gas temperature before combustion is indeed different, with the simulations with the higher boost pressure having the highest mean gas temperature before SOC. However, as Figure 11b visualizes, the peak temperature is reduced with increasing boost pressure because of the presence of cooler air [38]. Additionally, the decrease of peak global gas temperature reduces the heat transfer losses (see Fig. 12). Consequently, the NOx emission decreases as a result of the increased boost pressure.
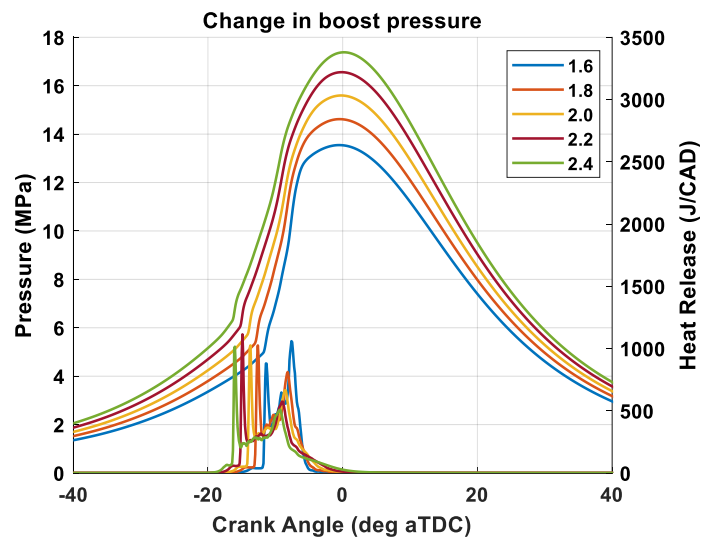
Fig. 10. In-cylinder pressure and heat release rate from -40 to 40 crank angle degrees ATDC obtained from the simulations with boost pressures of 1.6, 1.8, 2.0, 2.2, and 2.4 bar.
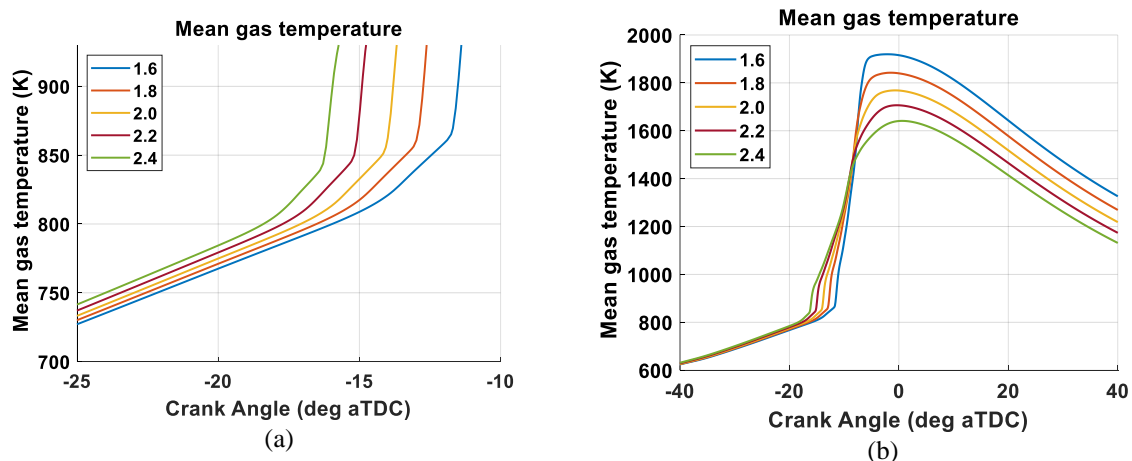
Fig. 11. Mean gas temperature between -25 and -10 (i.e., before SOC) and -40 and 40 crank angle degree ATDC obtained from the simulations with boost pressures of 1.6, 1.8, 2.0, 2.2, and 2.4.

Figure 12 compares five combustion and heat characteristics of the five different boost pressure simulations. In Figure 12a, the percentages of heat transfer loss to the total fuel energy input are presented. The heat loss does not change significantly by altering the boost pressure. Similar finding were also reported in [57] where the effect of boost pressure on heat transfer in an RCCI engine were investigated. Although the average temperature decreases by boosting pressure, as shown in Figure 11b, the heat loss seems to be influenced by combustion duration, maximum local temperature, and flame distance from the walls as well. The outputs of the model shows that increasing intake pressure raises the maximum local temperature slightly. In Figure 12b, the engine's efficiency is presented. The engine efficiency is the ratio of the useful work done to the heat provided by combustion. As visualized in the figure, the efficiency seems to have an optimum efficiency somewhere between the simulations. The

efficiency is affected by the amount of energy loss, combustion phasing, and peak pressure. In general, higher peak pressure and less heat loss contribute to improved efficiency; however, combustion phasing should not be too early, which produces negative work during the engine's compression stroke. In this case, the gained energy in increasing peak pressure by boosting intake pressure gets nullified by the advanced start of combustion, creating less work. The combustion and consequently the increase in pressure is way too early, and all of the heat released is not used to produce work, thereby reducing thermal efficiency.

In Figure 12c, the combustion efficiency is presented. The combustion efficiency is linked to the CO emission results as it represents the total amount of fuel converted to the final product of combustion. As perceived in the figure, the combustion efficiency decreases with increasing boost pressure. In Figure 12d, crank angles where 5, 10, 50, and 90 percent of fuel mass burned can be seen. It shows that CA05, CA10, CA50, and CA90 shift away from TDC with higher boost pressures. The higher the boost pressure is, the earlier the combustion phasing is. Additionally, the increased burning duration is noticeable, with the CA90 moving closer to TDC with increased boost pressure. And in the last Figure 12e, the combustion duration of the simulations is shown. By increasing the boost pressure, the combustion duration increases significantly.
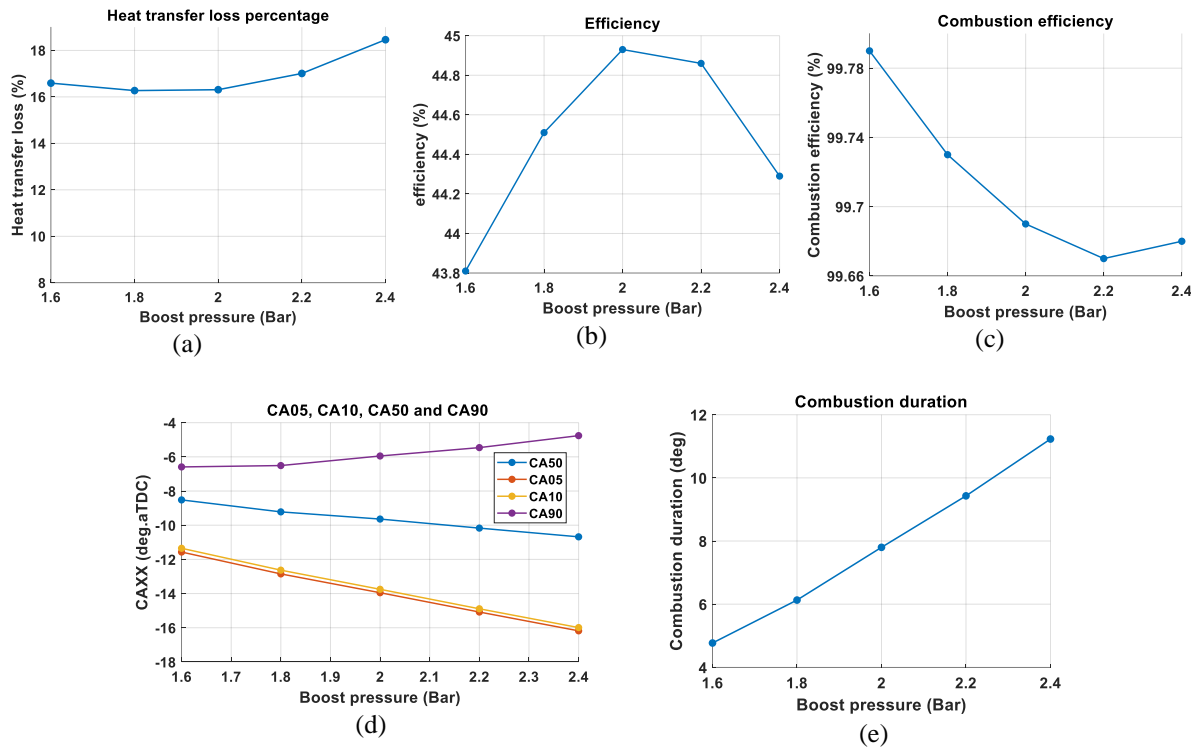
Fig. 12. Combustion and heat release characteristics with varying boost pressures between 1.6 and 2.4 bar with an interval of 0.2 bar.

The emission characteristics are presented in gram per kWh in Figure 13. Similar to the engine response with change in SOI, both the CO and CO_2 emissions seem to have an optimum location at which the lowest emission results are found. The CO emission results are determined, and two opposing effects are presented as an explanation. It is observed that increasing the boost pressure too much seemed to result in lower combustion temperatures leading to incomplete combustion. It also increase the amount of oxygen in the mixture and CO conversion to CO_2 is facilitated. This is seen in the highest boosted case. In contrast, decreasing the boost pressure leads to faster combustion because of the higher average temperature. Thus increasing the boost pressure reduces the CO emission, as long as the temperature is not too low.

While the CO, and CO_2 emissions drop and rise with increased boost pressure, the soot and NOx emissions seem to have monotonic behavior. The soot emissions are linked to the in-cylinder local equivalence ratio and temperature. in-cylinder local equivalence ratio is almost identical in all cases since the premixed equivalence ratio, injection timing, and amount of injected diesel fuel are the same. But the temperature decreases with increasing boost pressure, resulting in increased soot emissions

due to less oxidation. The NOx emission results are heavily linked to the in-cylinder temperature, which decreases with increasing boost pressure, resulting in reduced NOx emission.
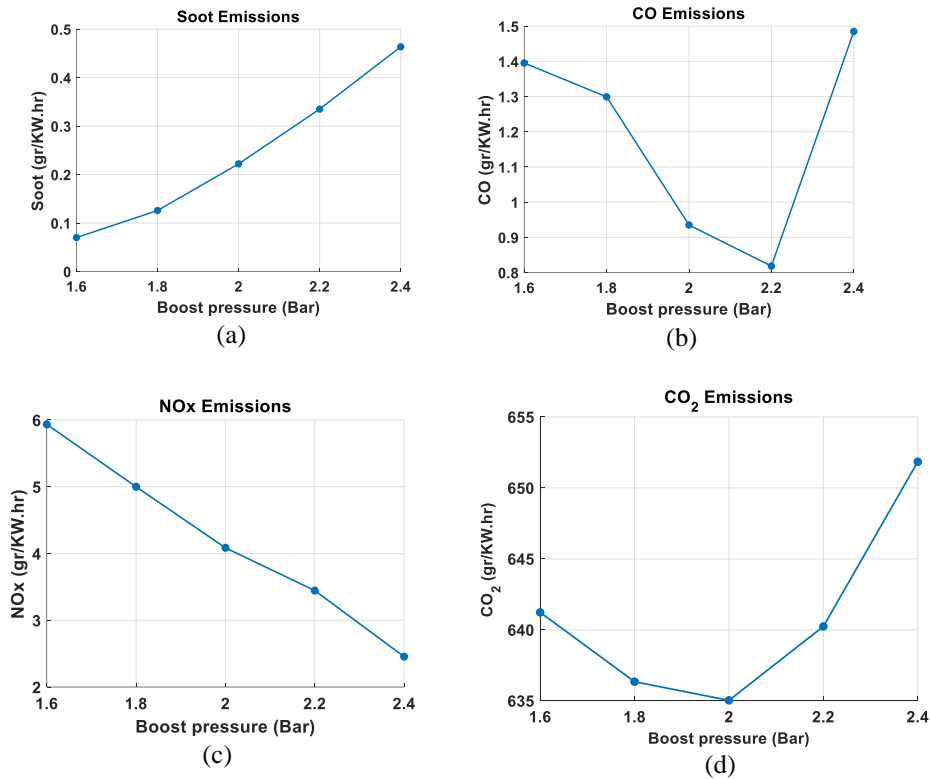
Fig. 13. Emissions results with varying boost pressures between 1.6 and 2.4 bar with an interval of 0.2 bar.

4.3 Effects of initial temperature

The initial temperature (i.e., the temperature of the premixed charge at the start of IVC) is another critical parameter that mainly affects the mixture's burning rate. Figure 14 demonstrates the in-cylinder pressure and HRR values between -40 and 40 CAD ATDC for different initial temperatures of 313, 333, 353, 373, and 393 kelvin. The start of injection and the other operating conditions has been kept the same as table 3. It is seen that the highest peak pressure reached is 15.6 MPa in the simulation, where the initial temperature is 353 kelvin. Generally higher initial temperature has two important effects. Firstly, It leads to more complete, faster combustion, and accordingly higher peak pressure due to less unburned fuel. However, it also alters the combustion phasing and the amount of air mass. Too advanced combustion timing results in more negative work and lower peak pressure. Thus peak pressure first elevates and then reduces. Regarding HRR, it is perceived that combustion duration in the higher initial temperature simulations is significantly shorter. Most notably, the shape of the HRR seems the same but compressed with a more intense HRR. The reason for this compressed and more intense HRR is that with an increased temperature, the necessary activation energy for the chemical reaction to occur is achieved easier, consequently increasing the reaction rates resulting in a quicker HRR. Another effect perceived in the HRR is the advanced SOC with raising the initial temperature. The observed cause is the increased mean gas temperature before SOC, causing the charge to reach the necessary temperature conditions for ignition earlier. Still the efficiency increasing with reducing the initial temperature because of the reduced heat loss (fig. 15b) and improved combustion phasing fig (15c).
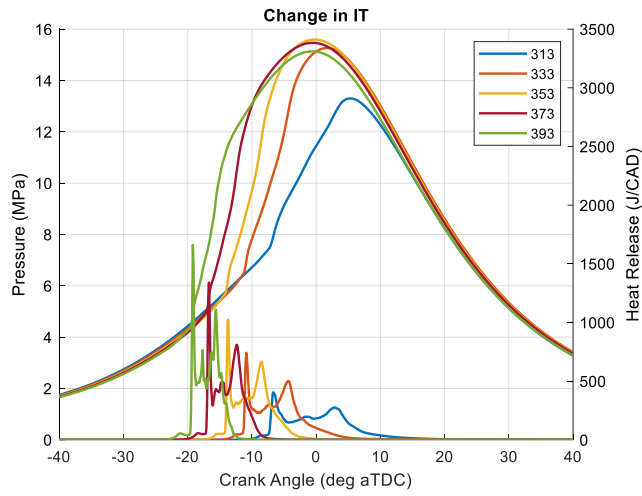
Fig. 14. In-cylinder pressure and heat release rate between -40 and 40 crank angle degree after top dead center obtained from the simulations with 313, 333, 353, 373, and 393 Kelvin initial temperature (IT)
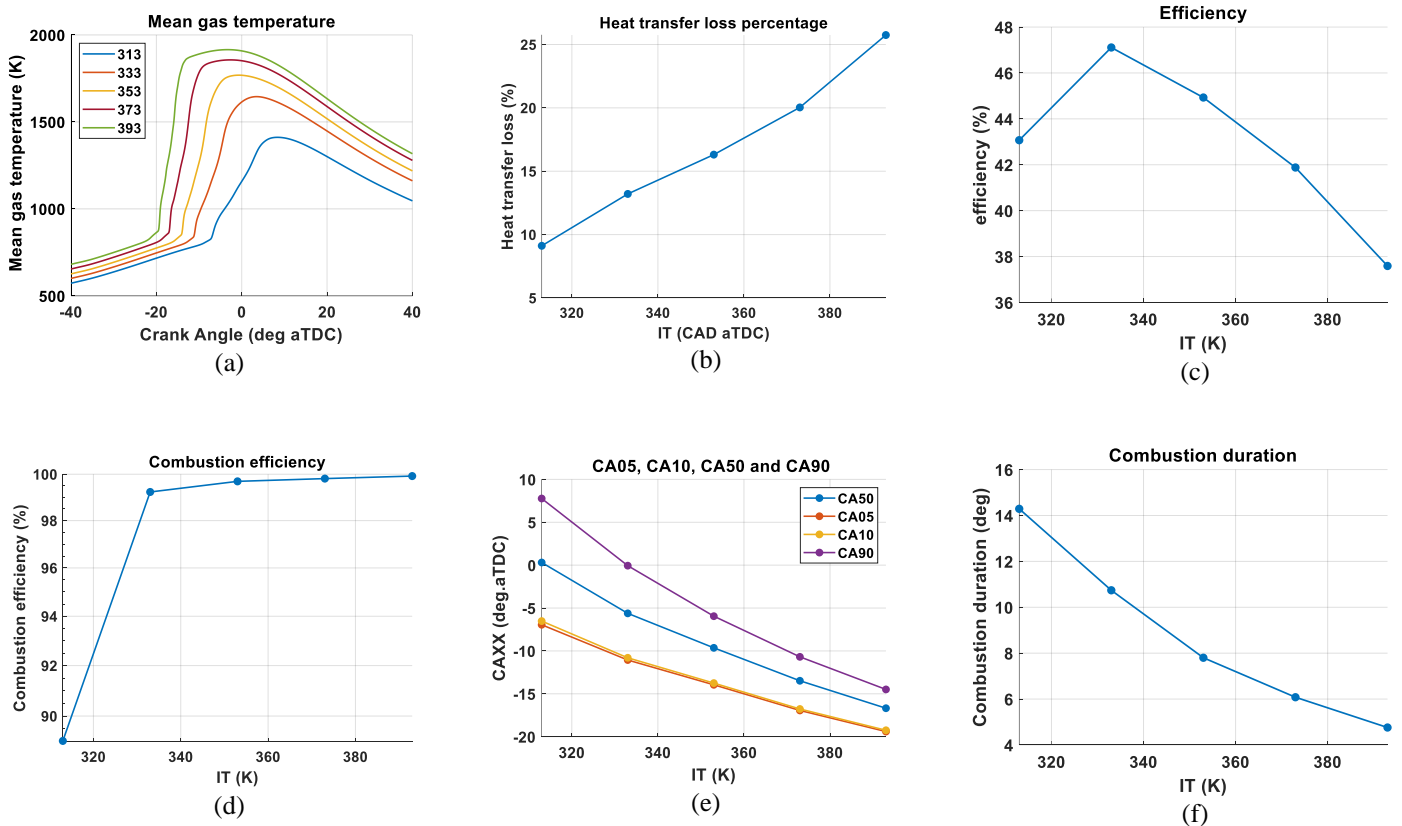
Fig. 15. Combustion and heat release characteristics with varying initial temperatures between 313 and 393 Kelvin with an interval of 20 Kelvin.

The global mean gas temperature of the charge is significantly higher with elevated initial temperatures (see Fig. 15a). Consequently, this would affect the heat transfer loss percentage as higher heat fluxes are present, as visible in Figure 15b. In Figure 15c, the engine's efficiency is presented. When the initial charge is too hot, the efficiency is decreased, for the gain in combustion efficiency is less than the energy percentage lost by heat transfer. Additionally, the work provided by the higher initial temperature is too early, consequently further reducing the thermal efficiency. Figure 15d visualizes the combustion efficiency. It is seen that the change in combustion efficiency rapidly increases by

decreasing initial temperature. This is, of course, caused by the increased incomplete combustion occurring at lower temperatures. In Figure 15e, the crank angles where 5, 10, 50, and 90 percent of fuel (by mass) is burned can be seen. With increasing initial temperature, SOC is advanced by going away from TDC, and the offset between CA10, CA50, and CA90 is reduced with more intense HRR. And lastly, Figure 15f visualized the decreased combustion duration, already discussed in the previous section.
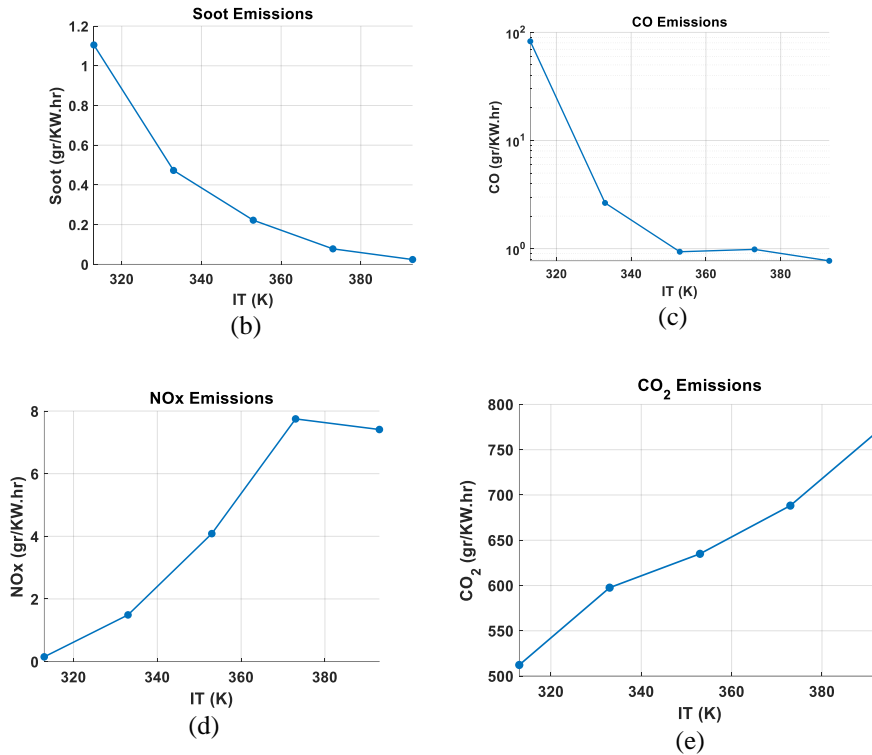

Fig. 16. Emissions results with varying initial temperatures between 313 and 393 kelvin with an interval of 20 kelvin.

The effect on emission characteristics is presented in Figure 16. As expected, soot, and CO emissions decrease with increasing initial temperature. The CO emission decrease because combustion will be more complete at higher temperatures. At higher temperature the amount of air mass also decrease. However, faster burning rate outweighs the effect of the air mass. The soot emissions decrease as the higher temperatures result in more soot being oxidized before EVO. The NOx emission is higher at higher initial temperatures as the increased temperature results in higher in-cylinder gas temperature resulting in higher NO formation rates.

4.4 Effects of spray included angle (Umbrella angle)

Umbrella angle (UA) in RCCI engines can determine where the combustion starts inside the engine's cylinder. Figure 17 represents the contour of the total equivalence ratio in cut planes for different Injection Angles (IAs) which are defined here to be the half of UA. In the case of the injection angle of 40 degrees, the geometry of the piston directs diesel fuel from the center of the cylinder to the bowl's double step location, and the fuel moves toward the liner. When the angle is 50 degrees, the spray more or less hits the lower step head-on. This keeps the fuel mostly inside the bowl and combustion occurs at the same location. But when the angle is 60 degrees, the fuel hits the edge of the lower step, and its path branches into two, which causes the flame to initialize in two different parts. Finally, in the case of the injection angle of 70 degrees, the fuel hits the wall of the cylinder and accumulates mostly above the piston squeeze area. The flame is initialized and moves from the liner into the bowl. Note that for this case, the flame starts near the cylinder wall and the crevice region, it burns all the fuel trapped in that area, and because these areas are the source of HC emission, it causes HC emissions to decrease.

Normally smaller injection angles cause the flame to start closer to the central axis inside the cylinder, and it does not reach the area near the crevice region, and as shown in the figure, some fuel remains unburned near the cylinder wall and crevice region.
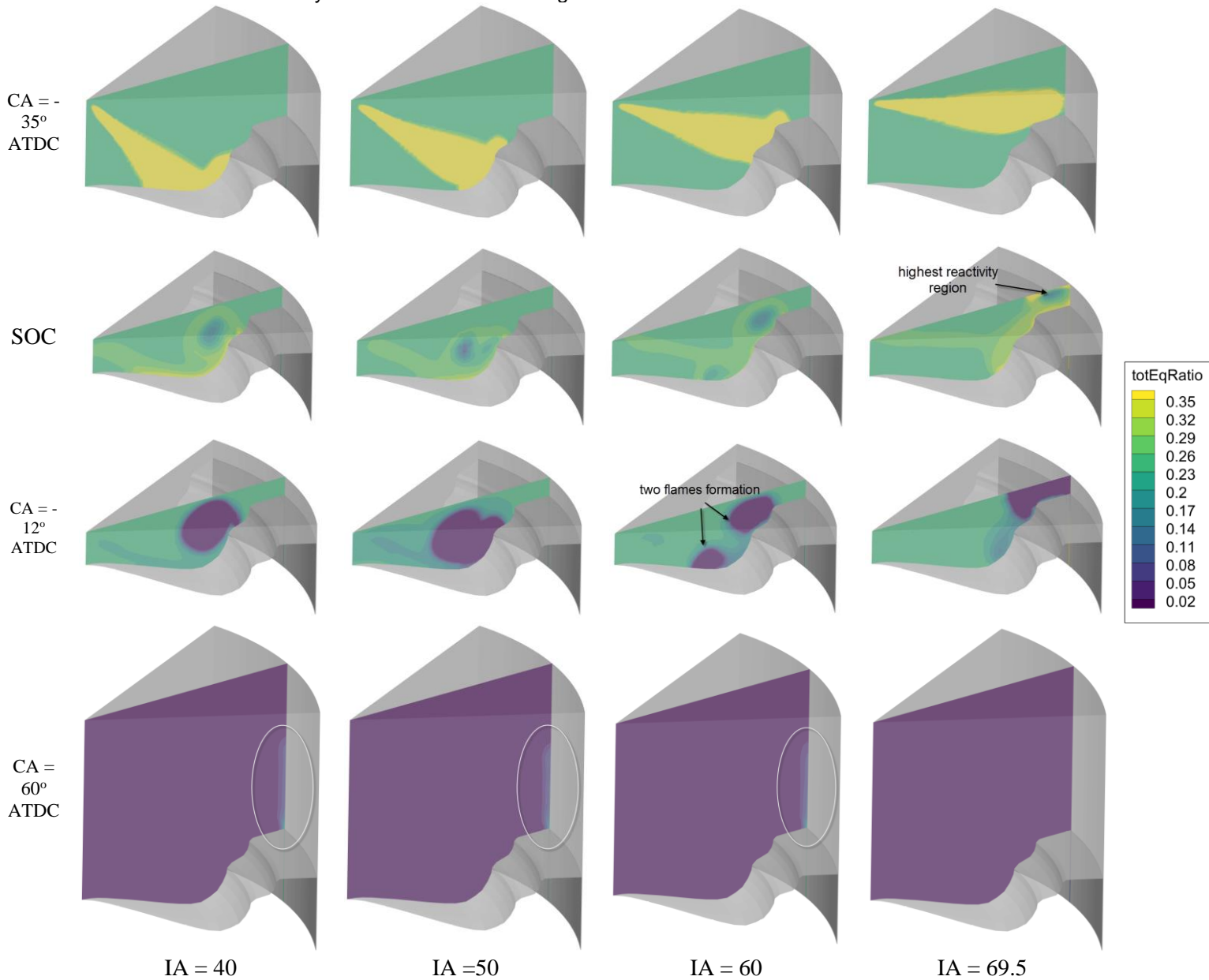
Fig. 17. Total equivalence ratio cut planes at -35 deg. ATDC, start of combustion (SOC), -12 deg. ATDC, and 60 deg. ATDC for different injection angles.

Figure 18 shows the in-cylinder pressure and HRR values for the different injection angles. The start of injection and the other operating conditions has been kept the same as table 3. As we can see, there is no significant difference among the results. The peak pressure in the case of injection angle of 69.5 degrees is a bit higher than other cases because there is less unburned fuel discussed in the contour plot of equivalence ratio. As a result, the combustion and thermal efficiency are improved with larger injection angles (See Figs. 19c, 19d). The HRR curves for the injection angles of 69.5 and 50 have a higher initial spike. The reason behind the initial spike can be attributed to the fact that in these two cases, the amount of fuel accumulation in one location is higher than in the other cases (as we discussed in the previous section). In the other two cases, fuel tends to mix better, resulting in less fuel accumulation in one place. One further important observation from the HRR curves is that the latest rise of the HRR curve corresponds to the case with the highest injection angle. This can be attributed to hitting fuel to the cylinder liner, which has a lower temperature than the piston crown resulting higher heat loss since the fuel hits the piston crown in all of the other cases. It can also be observed the case

with largest IA has two peaks. This can be due to the burning of the fuel trapped in the crevice region later on during the combustion process.

Figure 19 depicts the important output parameters. The average temperature inside the cylinder is a bit higher for the largest injection angle because of more complete combustion. The heat loss is also higher with a larger injection angle, considering that the flame is formed near the cylinder liner where the highest heat transfer occurs. Since the combustion phasing in all the cases is almost the same, thermal efficiency will be determined mainly by combustion efficiency and heat loss. The combustion efficiency is higher for the largest injection angle because of less incomplete combustion, and it seems its effect outweighs the heat loss on the thermal efficiency. Combustion phasing and duration do not change significantly, which was also found from HRR curves. However, there is a slight difference in the combustion duration results.
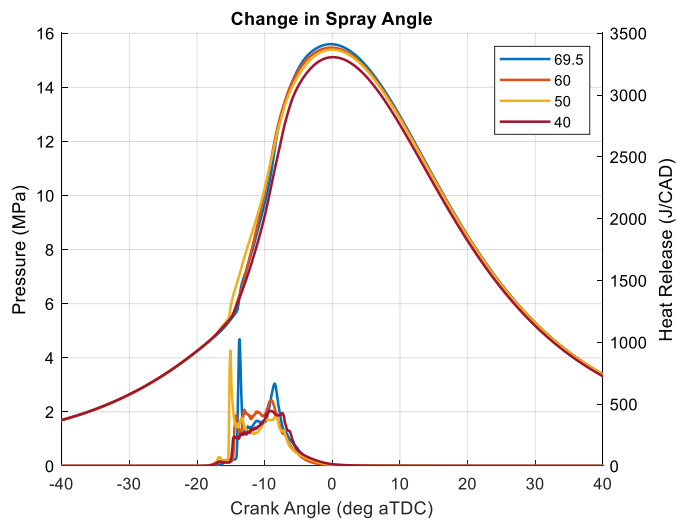

Fig. 18. In-cylinder pressure and heat release rate between -40 and 40 crank angle degree after top dead center obtained from the simulations with different injection angles
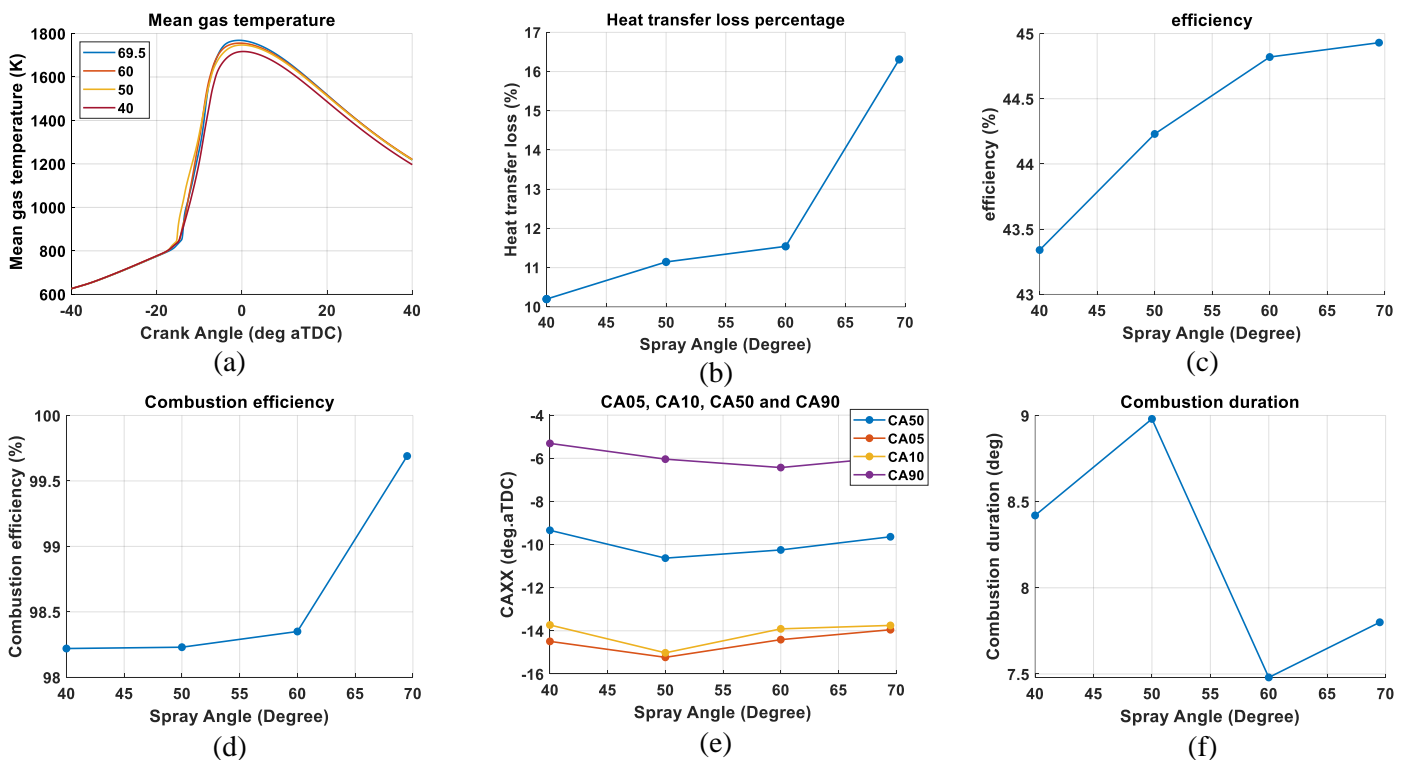

Fig. 19. Combustion and heat release characteristics with varying injection angle

The results of engine emissions can be perceived in Figure 20. As expected, the soot, and CO emissions decrease with injection angles because of more complete combustion and a bit higher temperature at higher injection angles. The soot emissions decrease marginally as the average temperature is a bit higher at larger angles, while the maximum local equivalence ratios are the same in all cases. As a consequence of fixed combustion phasing and the lower emission results of CO and soot, CO_2 emission increase because of the more complete combustion. Regarding the NOx emission, since the average temperature is almost the same among the cases, it is mainly determined by combustion duration and start of combustion. The combustion duration is most prolonged when the injection angle is 50 degrees resulting in higher NOx emission since NOx formation is slow process and when the charge is given more time NOx emission will be higher.
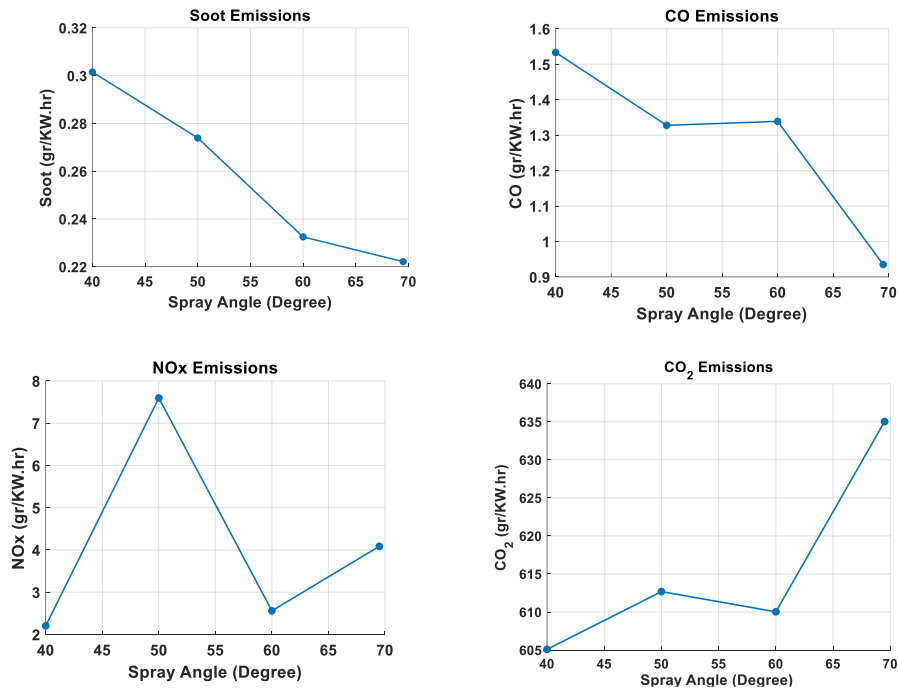
Fig. 20. Emissions results with varying injection angle

Conclusions

This work performed a parametric investigation on the effects of the SOI, boost pressure, initial temperature, and spray included angle in a heavy-duty RCCI engine fuelled by E85/diesel with double step piston bowl geometry. Their impacts on the stratification level, heat transfer, performance, and emission characteristics were studied. In the research on the effect of changing SOI, it became clear that fuel reactivity stratification, local equivalence ratio, and the shape of the HRR curve are influenced by a change in SOI. It was found that by keeping the stratification levels low with an early SOI, the total heat loss inside the combustion chamber can be reduced. However, the fuel reactivity stratification level should not become too low, as combustion efficiency and thermal efficiency will decrease. This concludes that the optimum timing corresponds to a moderate stratification level (in this work caused by an SOI around -46 CAD ATDC).

In the investigation into the effect of boost pressure, it became clear the boost pressure primarily influenced the global gas temperature, combustion duration, HRR shape. With higher boost pressure, the recession of the HRR curve takes longer as the remaining fuel fragments burn out later. Also, the mean gas temperature before SOC increased, causing the charge to ignite earlier. Nevertheless, peak average temperature reduced significantly with higher boost pressure. Besides, It was found that heat transfer losses does not change significantly with boost pressure, and it is more related to maximum local temperature (flame temperature) rather that maximum average temperature. Although increasing the boost pressure would, in most cases, considerably reduce NOx, and CO emissions by providing higher oxygen levels, the boost pressure cannot be increased indefinitely, as thermal and combustion efficiency decreases, not to mention the engine's lifetime because of elevated max pressure inside the cylinder.

Moreover, it became clear that the initial temperature massively impacts the global gas temperature. It was found that by decreasing the initial temperature, the overall global gas temperature was reduced. With the reduced overall gas temperature, heat transfer losses can be mitigated. The initial temperature is preferred to be as low as possible but sufficiently high enough to burn all the introduced fuel and keep most of the combustion period before TDC. Otherwise, thermal efficiency will decrease again. It was found that keeping the temperature low is at the cost of higher CO, and soot emissions. Finally, it realized that the injection angle (IA) and piston bowl geometry could substantially affect the flame formation location. Two flames could be formed at the same time by changing IA. The HRR shape, emission, and performance characteristics of the engine were influenced by IA as well. Preferably the flame should form near the cylinder liner and cylinder head rather than the piston bowl to reduce HC emission and increase combustion efficiency. Flame formation near the wall means higher heat loss. Additionally, IA could not alter the combustion phasing, but it could change fuel stratification inside the cylinder, and combustion duration is also affected. It was also found that the initial spike in HRR shape stems from fuel accumulation in one location inside the cylinder.

References

[1] Heywood JB. Internal combustion engine fundamentals: McGraw-Hill Education; 2018.

[2] Kakaee A-H, Rahnama P, Paykani A, Mashadi B. Combining artificial neural network and multi-objective optimization to reduce a heavy-duty diesel engine emissions and fuel consumption. Journal of Central South University. 2015;22:4235-45.

[3] Reitz RD, Ogawa H, Payri R, Fansler T, Kokjohn S, Moriyoshi Y, et al. IJER editorial: the future of the internal combustion engine. SAGE Publications Sage UK: London, England; 2020.

[4] Novella R, Bracho G, Gomez-Soriano J, Fernandes CS, Lucchini T. Combustion system optimization for the integration of e-fuels (Oxymethylene Ether) in compression ignition engines. Fuel. 2021;305:121580.

[5] Novella R, Gomez-Soriano J, Martinez-Hernandiz PJ, Libert C, Rampanarivo F. Improving the performance of the passive pre-chamber ignition concept for spark-ignition engines fueled with natural gas. Fuel. 2021;290:119971.

[6] Pan S, Cai K, Cai M, Du C, Li X, Han W, et al. Experimental study on the cyclic variations of ethanol/diesel reactivity controlled compression ignition (RCCI) combustion in a heavy-duty diesel engine. Energy. 2021;237:121614.

[7] Krishnamoorthi M, Malayalamurthi R, He Z, Kandasamy S. A review on low temperature combustion engines: Performance, combustion and emission characteristics. Renewable and Sustainable Energy Reviews. 2019;116:109404.

[8] Han J, Somers LMT, Cracknell R, Joedicke A, Wardle R, Mohan VRR. Experimental investigation of ethanol/diesel dual-fuel combustion in a heavy-duty diesel engine. Fuel. 2020;275:117867.

[9] Kakaee AH, Rahnama P, Paykani A. Numerical study of reactivity controlled compression ignition (RCCI) combustion in a heavy-duty diesel engine using 3D-CFD coupled with chemical kinetics. Automotive Science and Engineering. 2014;4:792-804.

[10] An Y, Jaasim M, Raman V, Pérez FEH, Sim J, Chang J, et al. Homogeneous charge compression ignition (HCCI) and partially premixed combustion (PPC) in compression ignition engine with low octane gasoline. Energy. 2018;158:181-91.

[11] Schröder D, Banke K, Kaiser SA, Atakan B. The kinetics of methane ignition in fuel-rich HCCI engines: DME replacement by ozone. Proceedings of the Combustion Institute. 2021;38:5567-74.

[12] Tanov S. Investigation of Partially Premixed Combustion in an Optical Engine: In-Cylinder Flow and Combustion Characterization. Ph.D. Thesis: Lund University; 2017.

[13] Zhang Y, Cho K, Sellnau M. Investigation on Combining Partially Premixed Compression Ignition and Diffusion Combustion for Gasoline Compression Ignition—Part 2: Compression Ratio and Piston Bowl Geometry Effects. SAE International Journal of Sustainable Transportation, Energy, Environment, & Policy. 2021;2.

[14] Kokjohn SL. Reactivity controlled compression ignition (RCCI) combustion. 2012.

[15] Han J, Somers B. Effects of Butanol Isomers on the Combustion and Emission Characteristics of a Heavy-Duty Engine in RCCI Mode. SAE Technical Paper; 2020.

[16] Paykani A, Garcia A, Shahbakhti M, Rahnama P, Reitz RD. Reactivity controlled compression ignition engine: Pathways towards commercial viability. Applied Energy. 2021;282:116174.

[17] Benajes J, García A, Monsalve-Serrano J, Sari RL. Experimental investigation on the efficiency of a diesel oxidation catalyst in a medium-duty multi-cylinder RCCI engine. Energy Conversion and Management. 2018;176:1-10.
[18] Splitter D, Hanson R, Kokjohn S, Reitz RD. Reactivity controlled compression ignition (RCCI) heavy-duty engine operation at mid-and high-loads with conventional and alternative fuels. SAE Technical Paper; 2011.
[19] Hanson R, Kokjohn S, Splitter D, Reitz R. Fuel effects on reactivity controlled compression ignition (RCCI) combustion at low load. SAE International Journal of Engines. 2011;4:394-411.
[20] Kavuri C, Kokjohn SL. Computational optimization of a reactivity controlled compression ignition (RCCI) combustion system considering performance at multiple modes simultaneously. Fuel. 2017;207:702-18.
[21] Benajes J, Molina S, García A, Belarte E, Vanvolsem M. An investigation on RCCI combustion in a heavy duty diesel engine using in-cylinder blending of diesel and gasoline fuels. Applied Thermal Engineering. 2014;63:66-76.
[22] Kokjohn SL, Hanson RM, Splitter DA, Reitz RD. Fuel reactivity controlled compression ignition (RCCI): a pathway to controlled high-efficiency clean combustion. International Journal of Engine Research. 2011;12:209-26.
[23] Han J. Alcohol applications in heavy-duty diesel engines. Ph.D. Thesis: Technische Universiteit Eindhoven; 2020.
[24] Bekdemir C, Baert R, Willems F, Somers B. Towards Control-Oriented Modeling of Natural Gas-Diesel RCCI Combustion. SAE Technical Papers. 2015;2015-April.
[25] Rahnama P, Paykani A, Reitz RD. A numerical study of the effects of using hydrogen, reformer gas and nitrogen on combustion, emissions and load limits of a heavy duty natural gas/diesel RCCI engine. Applied energy. 2017;193:182-98.
[26] Chuahy FDF, Kokjohn SL. Effects of reformed fuel composition in "single" fuel reactivity controlled compression ignition combustion. Applied energy. 2017;208:1-11.
[27] Rahnama P, Paykani A, Bordbar V, Reitz RD. A numerical study of the effects of reformer gas composition on the combustion and emission characteristics of a natural gas/diesel RCCI engine enriched with reformer gas. Fuel. 2017;209:742-53.
[28] Li Y, Jia M, Xu L, Bai X-S. Multiple-objective optimization of methanol/diesel dual-fuel engine at low loads: A comparison of reactivity controlled compression ignition (RCCI) and direct dual fuel stratification (DDFS) strategies. Fuel. 2020;262:116673.
[29] Hanson RM, Reitz RD. Effects of biofuel blends on transient reactivity-controlled compression ignition engine combustion. International Journal of Engine Research. 2016;17:857-65.
[30] Park SH, Shin D, Park J. Effect of ethanol fraction on the combustion and emission characteristics of a dimethyl ether-ethanol dual-fuel reactivity controlled compression ignition engine. Applied Energy. 2016;182:243-52.
[31] Dempsey AB, Walker NR, Reitz R. Effect of cetane improvers on gasoline, ethanol, and methanol reactivity and the implications for RCCI combustion. SAE International Journal of Fuels and Lubricants. 2013;6:170-87.
[32] Dempsey AB, Das Adhikary B, Viswanathan S, Reitz RD. Reactivity Controlled Compression Ignition Using Premixed Hydrated Ethanol and Direct Injection Diesel. Journal of Engineering for Gas Turbines and Power. 2012;134.
[33] Curran S, Hanson R, Wagner R. Effect of E85 on RCCI Performance and Emissions on a Multi-Cylinder Light-Duty Diesel Engine. SAE International; 2012.
[34] Benajes J, García A, Monsalve-Serrano J, Villalta D. Benefits of E85 versus gasoline as low reactivity fuel for an automotive diesel engine operating in reactivity controlled compression ignition combustion mode. Energy Conversion and Management. 2018;159:85-95.
[35] Willems R, Willems F, Deen N, Somers B. Heat release rate shaping for optimal gross indicated efficiency in a heavy-duty RCCI engine fueled with E85 and diesel. Fuel. 2021;288:119656.
[36] Richards KJ, Senecal, P.K., and Pomraning, E.,. CONVERGE 3.0, Convergent Science. Wisconsin Madison, 2021.
[37] Willems RC. Designed experiments for efficient engines. Ph.D. Thesis: Technical University of Eindhoven; 2020.
[38] Rahnama P, Arab M, Reitz RD. A Time-Saving Methodology for Optimizing a Compression Ignition Engine to Reduce Fuel Consumption through Machine Learning. SAE International Journal of Engines. 2020;13:267-88.
[39] Wang H, Dempsey AB, Yao M, Jia M, Reitz RD. Kinetic and Numerical Study on the Effects of Di-tert-butyl Peroxide Additive on the Reactivity of Methanol and Ethanol. Energy & Fuels. 2014;28:5480-8.

[40] Ra Y, Yun JE, Reitz RD. Numerical parametric study of diesel engine operation with gasoline. Combustion Science and Technology. 2009;181:350-78.
[41] Senecal PK, Richards KJ, Pomraning E, Yang T, Dai MZ, McDavid RM, et al. A new parallel cut-cell Cartesian CFD code for rapid grid generation applied to in-cylinder diesel engine simulations. SAE Technical Paper; 2007.
[42] Rahnama P, Bao H, Somers B, Paykani A, Novella R. A chemical kinetic study of low alcohol/iso-octane blends in both premixed and partially premixed combustion. 2021.
[43] Beale JC, Reitz RD. Modeling spray atomization with the Kelvin-Helmholtz/Rayleigh-Taylor hybrid model. Atomization and sprays. 1999;9.
[44] Schmidt DP, Rutland CJ. A new droplet collision algorithm. Journal of Computational Physics. 2000;164:62-80.
[45] Amsden AA, O'Rourke PJ, Butler TD. KIVA-II: A computer program for chemically reactive flows with sprays. Los Alamos National Lab.(LANL), Los Alamos, NM (United States); 1989.
[46] O'Rourke PJ, Amsden AA. A spray/wall interaction submodel for the KIVA-3 wall film model. SAE transactions. 2000:281-98.
[47] Meng X, Meng S, Cui J, Zhou Y, Long W, Bi M. Throttling effect study in the CDF/RCCI combustion with CNG ignited by diesel and diesel/biofuel blends. Fuel. 2020;279:118454.
[48] Hao C, Lu Z, Feng Y, Bai H, Wen M, Wang T. Optimization of fuel/air mixing and combustion process in a heavy-duty diesel engine using fuel split device. Applied Thermal Engineering. 2021;186:116458.
[49] Hiroyasu H, Kadota T. Models for Combustion and Formation of Nitric Oxide and Soot in Direct Injection Diesel Engines. SAE Transactions. 1976;85:513-26.
[50] Han Z, Reitz RD. Turbulence modeling of internal combustion engines using RNG κ-ε models. Combustion science and technology. 1995;106:267-95.
[51] Sener R, Yangaz MU, Gul MZ. Effects of injection strategy and combustion chamber modification on a single-cylinder diesel engine. Fuel. 2020;266:117122.
[52] Kumar A. A CFD study on DME/Methanol fuelled unconventional RCCI. M.Sc. Thesis: Technical University of Eindhoven; 2021.
[53] Issa RI. Solution of the implicitly discretised fluid flow equations by operator-splitting. Journal of computational physics. 1986;62:40-65.
[54] Senecal PK. Development of a methodology for internal combustion engine design using multi-dimensional modeling with validation through experiments: The University of Wisconsin-Madison; 2000.
[55] Guerry ES, Raihan MS, Srinivasan KK, Krishnan SR, Sohail A. Injection timing effects on partially premixed diesel–methane dual fuel low temperature combustion. Applied Energy. 2016;162:99-113.
[56] Zheng J, Wang J, Zhao Z, Wang D, Huang Z. Effect of equivalence ratio on combustion and emissions of a dual-fuel natural gas engine ignited with diesel. Applied Thermal Engineering. 2019;146:738-51.
[57] Hendricks TL, Splitter DA, Ghandhi JB. Experimental investigation of piston heat transfer under conventional diesel and reactivity-controlled compression ignition combustion regimes. International Journal of Engine Research. 2014;15:684-705.

Session S3.3 Advanced Powertrain Control

V2X-Based Engine Management and Transient Control in HEVs with Planetary Gear Unit

Zhenhui Xu[1], Bo Zhang[1], Shohei Narita[1], Fuguo Xu[2],Tielong Shen[1]

[1]Department of Engineering and Applied Sciences, Sophia University, Tokyo, Japan

[2]Advance Research Laboratories, Tokyo City University, Tokyo, Japan

E-mail: tetu-sin@sophia.ac.jp
Telephone: +(81) 332383308

Abstract. Focusing on improving the energy efficiency of the connected hybrid electric vehicles, this paper proposes an optimal management strategy of combustion engines in HEVs with planetary gear unit. It consists of two layers: the upper layer provides segment traffic-dependent thresholds and the lower layer manages the transient performance by learning-based control to reach the given optimal operation point. With the provided threshold, the engine on-off decision is made by comparing a short-term prediction of energy demand and the threshold, and once the engine is switched on with a set-value of operating point, the optimal control law designed by reinforcement learning will manage the throttle opening and generator torque (motor torque). The problem of finding the threshold is formulated as a statistic optimization of a cloud of vehicles. To demonstrate the proposed scheme, a case study result will be represented where the segment-depended threshold is found by the genetic algorithm based on a static data of traffic. The problem of finding the optimal control for improving the transient performance is formulated as an infinite-horizon optimal control problem for two dimensional continuous-time nonlinear system, and a model-free policy iteration algorithm is developed based on the reinforcement learning technique. Finally, simulations are conducted on a high-fidelity simulator of HEV with power-split powertrain provided by the Ministry of Economy, Trade, and Industry of Japan, and simulation validation is demonstrated.

1. Introduction

Under the pressure of carbon neuralization and sustainable development goals, hybrid electric vehicles (HEVs) are gaining increasingly attention due to the ability of improving the energy efficiency. As is well-known, the potential for saving energy in HEVs is not only from the regenerative braking but also managing the engine operating point such that the combustion engine is working at possible efficient condition [1-3]. The latter is enabled by the ability of storage energy when the combustion engine generate too much power in order to achieve a better fuel efficiency. Motivated by this knowledge, power splitting or distributing the total power demand of driver to the combustion engine and the electric motors has been the main issue attracted by the research community of HEV powertrain control. In the last three decades, developing energy management strategies relied on this research line.

At early stage, the power split problem is considered for the case when the driving route, the power demand profile such that the vehicle speed traces the given route, is previously known. This problem is usually formulated as a multi-step decision problem for the engine operating point coordinated by the engine torque and the rotational speed, and the given route serves as constraint for solving the optimal decision problem of the total power generation. For example, the Dynamic Programming-based optimal solution in [4,5], the Pontryagin's maximum principle based optimal energy strategy in [6]. Obviously, to know the driving route previously, especially the profile of vehicle speed along the route, is an impracticable assumption, since the behavior of the driver is always with uncertainties. In order to achieve minimizing energy consumption in the real-world practice, instead of the long-term optimal decision along a given route, on-line optimization problem with power demand prediction is addressed attention such as look-ahead horizon-based energy management strategy [2,7], driver's power prediction-based receding horizon optimization [8-10]. The key issue in these researches is how to predict the power demand for a look-ahead horizon. Very recently, using the connected information in prediction of real-world driver's power demand is attempted and real-time energy optimization with vehicle-to-everything (V2X)-based prediction has been investigated in a lot of the literature [11,12]. With utilization of big data from vehicle-to-vehicle (V2V) and vehicle-to-infrastructure (V2I), the future demand torques for model predictive control (MPC) in the predictive horizon was predicted by extreme learning machine and it was used to improve the total energy consumption in economical sense [13]. Meanwhile, the Gaussian process, as an effective tool in machine learning, was explored for driver demand torque prediction, where

the predicted results were used for the short-term energy consumption optimization in the acceleration scenario for a power-split HEV [14].

However, it should be noted that almost all researches paid attention on the torque splitting or operating point decision for the combustion engine, oblivious to caring the engine transient operation once the set-point is decided by the energy management strategy. Indeed, the influence of transient control of combustion engine to fuel consumption has been demonstrated by a few references [15,16], and the issue of transient control including combustion quality has been addressed by many literatures including the author's group publications [17,18]. In HEVs, engine control involves two issues, decision of ignition on/off mode and engine transient control. Due to the thermal inertia and intake-to-pawer delay, and the poor fuel performance during transient operating period, the former should be decided according to a longer period to avoid frequent on-off switching. The connected data including statistic profiles of a larger scale vehicle on the targeted route will provide most possible driving profile of current route. This observation gives as a hint to make the ignition on/off decision according to the statistic connected V2X data. Meanwhile, in HEVs, to control engine rotational performance is not only relying on the throttle operation. Adjusting generator's torque might contribute to improve the engine rotational transient performance by motoring and absorbing over power generation of the engine without energy losses. Benefited from this observation, this paper proposed an engine management strategy that involves two layers: statistic data-based decision of the threshold for engine ignition on/off switching, and engine transient control with the throttle operation and the generator's torque adjusting.

The contributions of this paper are summarized as follows. Firstly, the total demand power prediction in a traffic-dependent segment is predicted by extreme learning machine with utilization of the V2X information. Then, the real-time demand power threshold in each segment is optimized by a scenario-based approach to determine the engine on/off mode of HEV. Finally, considering the engine transient dynamics, to track the referred engine torque and engine speed that is determined by optimal operation line of engine, both engine's throttle and generator torque are optimized by reinforcement learning algorithm.

The other parts of this paper are organized as follows. The motivation and problem description are given in Section 2, which includes the background of this problem, modeling of HEV powertrain with consideration of engine transient model and the proposed layered framework of this paper. The transient engine control by reinforcement learning in the lower layer is given in Section 3. Furthermore, the segment traffic-depended threshold optimization in the upper layer, consisting of demand power prediction and operation mode switch strategy, is given in Section 4. The simulations conducted to show the effectiveness of the proposed algorithm are shown in Section 5. Section 6 concludes the paper finally.

2. Motivation and Problem

2.1 Background

2.1.1 Connected environment

Aiming at the connected hybrid electric vehicles, this paper investigates the engine management problem of ego vehicle to improve the energy efficiency. The engine management in hybrid electric vehicles involves ignition on/off switching and power split when the engine is switched on, i.e. the engine is operated at HEV mode. Considering the inertia of thermal dynamics and the intake dynamics of combustion engine, it is obviously undesirable to frequently switch the ignition on/off. Moreover, once the engine is switched on, caring the transient performance of the combustion engine to reach a given operating set-point decided by the energy management layer is also desired because the fuel efficiency of a combustion engine is usually not good enough. Indeed, it is desirable to make decision on ignition on/off as a longer horizon optimization problem if the power demand of the longer horizon is previously known. However, it is unfortunately unreachable in the real-world driving. In the real world, the power demand delivered by a human driver or a vehicle driving system is always with undetectable factor. Whereas, it must be satisfied by the actual total driving power generated by the powertrain. Benefited from the connected environment, most possible power demand profile is hinted at not only by current V2X information but also the statistic profiles of the vehicles running through the route. The basic idea of this paper is to utilize this potential to propose a traffic data-based ignition on/off decision and model-free learning-based engine transient control design approach.

In order to present our approach intuitively, through this paper a real route shown in Figure 2.1 is

used as a benchmark example, which has been served as benchmark challenging competition at IFAC E-COSM 2021 [3]. However, it should be noted that the presented approach is not constrained to this example. The design approach is a general methodology. It is supposed that the targeted route consists of several segments portioned by traffic signals or intersections. In the example, there are 26 segments and the total distance is 16 km. Also, we suppose that a statistic driving speed profile, simply say route, is previously known. Figure 2.2 shows a statistic record of the route driven by human drivers. The first layer in our presented approach is to provide a threshold valve for each segment of the route that will be used to make ignition on/off decision with online prediction of power demand based real-time V2X information. We will show that this issue can be solved by formulating a statistic optimization problem with the statistic traffic data. Once the on/off switching decision is made in the lower layer with the threshold, a transient control of engine is then performed by cooperative control of intake air mass flow rate and the generator torque.

Fig. 2.1: The location of the road from Google Maps.
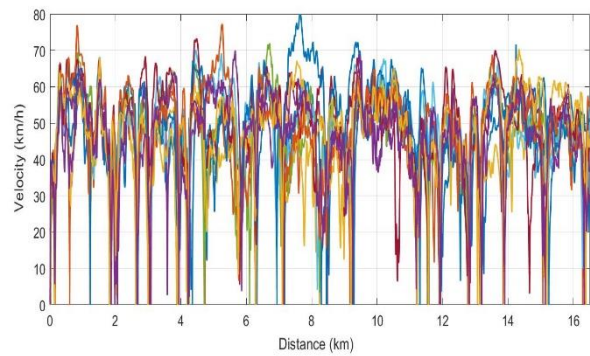
Fig. 2.2: The profiles of vehicle speed in 18 senarios.

2.1.2 Modeling powertrain system

In order to get the physics of the targeted hybrid electric powertrain, we begin with modeling of the powertrain system. It should be noted later that a model-free learning based transient control design scheme will be developed in the following section. Hence, the modeling is to show how the design objectives of engine control and the total driving torque generation are decoupled at the energy management and transient control.

A powertrain with planetary gear units is considered as sketched in Fig. 2.3. The powertrain system consists of an internal combustion engine, an electric motor, a generator, and planetary gears. The control inputs to be decided are the commands for the intake air mass flow rate $\dot{m}_{in}$ and the engine torque τ_e to the combustion engine, and the torque commands to the motor τ_m and the generator τ_g.
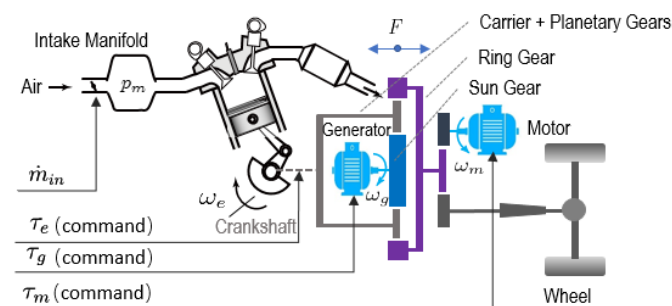
Fig. 2.3. Planetary gear-based HEV strcuture.

It is assumed that all the connections in the powertrain system are rigid, then the rotational speeds of the carrier gear, ring gear, and sun gear, simply referred to as engine speed ω_e, motor speed ω_m, and generator speed ω_g, must satisfy the following kinematic constraint

$$\omega_m R_r + \omega_g R_s = 2\omega_e (R_s + R_r), \tag{2.1}$$

where R_r and R_s are radii of the ring gear and sun gear, respectively.

Noting that the inertia of the carrier gear, ring gear, and sun gear are equivalent to the inertia of the engine crankshaft (J_e), motor crankshaft (J_m), and generator crankshaft (J_g), repectively. According to the Newton' s second law, the dynamics of the rotational motion are balanced by

$$\begin{cases} J_e \dot{\omega}_e = \tau_e - R_r F - R_s F, \\ J_g \dot{\omega}_g = \tau_g + R_s F, \\ J_m \dot{\omega}_m = \tau_m + R_r F - \tau_t, \end{cases} \tag{2.2}$$

where τ_t denotes the torque of the reduction gear. R_c represents the carrier gear radius, sun gear and carrier gear F is the interative force. Ingnoring the dynamics of the generator, we have

$$\tau_g = -R_s F. \tag{2.3}$$

By using (2.2) and (2.3), it gives

$$J_e \dot{\omega}_e = \tau_e + \frac{R_r + R_s}{R_s} \tau_g. \tag{2.4}$$

The above generated energy is converted to the final drive drift and used to enforce the vehicle motion, and the vehicle longitudinal dynamics is determinedd by the physical energy conservation law and Newton' s second law as follows

$$M\dot{v} = \frac{i_0}{R_{tire}} \tau_{dr} - F_v(v), \tag{2.5}$$

where F_v represents the road load and can be expressed by

$$F_v(v) = Mg(\mu_r \cos\theta + \sin\theta) + 1/2\rho A C_d v^2, \tag{2.6}$$

v is the vehicle speed. $i_0, R_{tire}, M, g, \mu_r,$ and θ represent the final gear ratio of the vehicle wheel, the wheel radius, the vehicle mass, the gravity acceleration, the coefficient of rolling resistance, and the road slop, respectively. ρ, A, and C_d denote the air density, the frontal area of the vehicle, and the drag coefficient, respectively.

It should be noted that in this modeling fashion, the driving torque, later called demanded torque is

$$\tau_{dr} = \frac{R_{cs}}{R_m} \tau_m - R_r R_{cs} F = a\tau_m - b\tau_g. \tag{2.7}$$

To sake of simplicity, τ_{dr} is also called as torque demand without of further explanation. Comparing with the electric dynamics of the motor and the generator, the inertia of the engine torque generation is much larger which is mainly dominated by the dynamics of the air intake-path and the mechanical rotational dynamics of the combustion engine. As is well-know, a mean value of the torque generation is modeled as follows [19]

$$\tau_e = \frac{\eta_f c_f Q}{4\pi} p_m, \tag{2.8}$$

where η_f, c_f are coefficients that depend on the operation point (p_m, ω_e), Q is the heat release from unit air mass of gas. And the intake manifold pressure p_m is modeled by

$$\dot{p}_m = \frac{RT}{V} \left(\dot{m}_{in} - \frac{\eta_f}{4\pi} p_m \omega_e \right). \tag{2.9}$$

As summary, it can be observed that the engine dynamics is dominated by the mean value model (2.4) and (2.9), where the external inputs $\dot{m}_{in}$ and τ_e can be chosen to improve the transient behavior.

This means that the generator could be used to motoring the engine and rejecting the over torque generation of the engine, since the generator torque effect to the driving torque τ_{dr} can be compensated by the electric motor τ_m. This enables us to decouple the power split between electric machines and the engine from the engine transient control loop.

2.2 Proposed framework

2.2.1 Overview

Focusing on mode switching decisions and improving the transient performance of engine operation, we propose an optimal engine management strategy. As shown in Fig. 2.4, it consists of two layers: the upper layer provides a segment traffic-depended thresholds, and the lower layer manages the transient performance by learning-based control to reach a given optimal operation point. With the provided threshold, the engine on-off decision is made by comparing a short-term prediction of energy demand with the thresholds. Once the engine is switched on with a set-value of operating point, the optimal control law designed by the reinforcement learning technique will manage the throttle operating and the generator torque compensation.
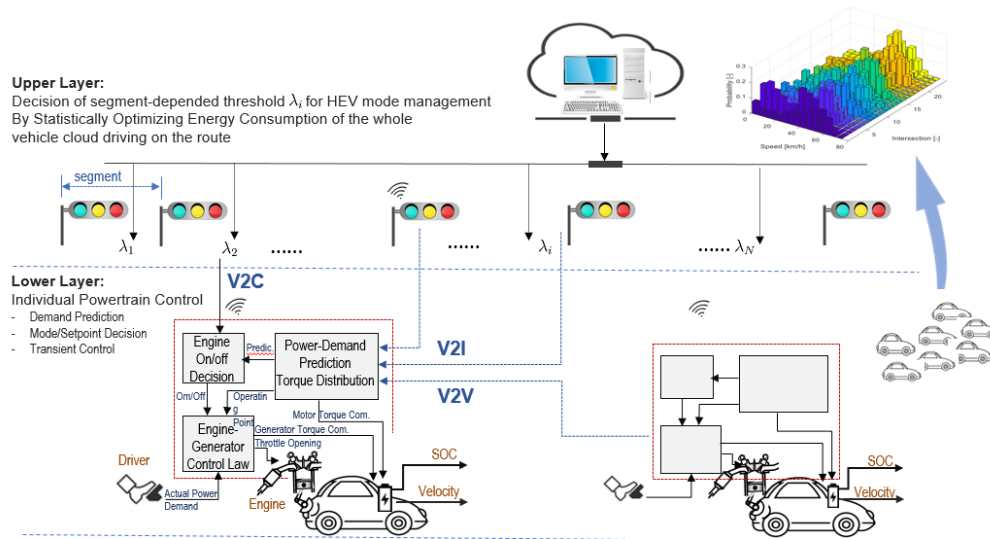
Fig. 2.4: The engine operation management system.

2.2.2 Control design problem in lower layer

By equations (2.4) and (2.9), the speed-related dynamics of an engine system in HEVs can be summarized in the following matrix form

$$
\begin{bmatrix} \dot{\omega}_e \\ \dot{p}_m \end{bmatrix} = \begin{bmatrix} \frac{\eta_f c_f Q}{4\pi J_e} p_m \\ -\frac{\eta_f R T}{4\pi V} p_m \omega_e \end{bmatrix} + \begin{bmatrix} \frac{R_r + R_s}{R_s J_e} & 0 \\ 0 & \frac{RT}{V} \end{bmatrix} \begin{bmatrix} \tau_g \\ \dot{m}_{in} \end{bmatrix}. \tag{2.10}
$$

It is worth pointing out that although (2.10) is a two-dimensional nonlinear affine system, the parameters exhibit strong uncertainties. In particular, $\eta_f, c_f,$ and Q are difficultly calibrated, η_f and c_f depend on the thermal environment, and Q is greatly influenced by the external conditions even if the air-fuel ratio is controlled to be constant and the ignition time is also well regulated. The strong uncertainty of model (2.10) is the motivation for developing a model-free control design scheme, which aims to regulate both the throttle and generator torque so that the engine speed ω_e and engine torque τ_e converge to a given set-point ω_{ed} and τ_{ed} without the requirement of model information.

In order to improve the transient performance, we introduce the following performance index

$$\mathbb{J}_1 = \int_0^\infty \left(q_1(\omega_e - \omega_{ed})^2 + q_2(p_m - p_{md})^2 + \|u - u_d\|_R^2 \right) \mathrm{d}t, \tag{2.11}$$

where $q_1, q_2 > 0$ are weighting factors and $R > 0$ is the weighting matrix. $u = [\tau_g, \dot{m}_{in}]^{\mathrm{T}}$ is referred as the control input and $u_d = [\tau_{gd}, \dot{m}_{ind}]^{\mathrm{T}}$ is the feedforward input. According to the given values ω_{ed} and τ_{ed}, the set-point p_{md} and the feedforward input u_d are calibrated. The proposed engine transient control system in the lower layer is depicted in Fig. 2.5.

Fig. 2.5: The engine transient control system.

2.2.3 Statistics-based optimization in upper layer

The demand power of targeted vehicle is determined by

$$P_{dr} = \tau_{dr} \frac{v}{R_{tire}} \frac{2\pi}{60}, \tag{2.12}$$

and a simplified battery model is

$$\dot{SoC} = \frac{-U_{oc} + \sqrt{U_{oc}^2 - 4RP_{batt}}}{2RQ_{batt}}, \tag{2.13}$$

where U_{oc}, R and Q_{batt} represent the open circle voltage, the internal resistance of the battery and the maximum battery capacity, respectively. P_{batt} is the battery power affected by the motor torque and the speed and is determined by $P_{batt} = \tau_m \omega_m + \tau_g \omega_g$.

It is aimed to design a sequence of power demand thresholds $\lambda = \{\lambda_i\}_1^N$, where N is the number of segments in the route, to make the engine on/off decision. Focusing on optimizing the total fuel consumption along the route and SoC reaching the set-value at the terminal time, we introduce the following cost function

$$\mathbb{J}_2(\lambda) = E\left[\int_0^T \dot{m}_{fuel}(\omega_e(t), \tau_e(t))\mathrm{d}t + \rho(SoC(T) - SoC_d)^2 \right], \tag{2.14}$$

where $T > 0$ is a time horizon and $\dot{m}_{fuel}$ is the fuel mass flow rate, $\rho > 0$ is the weighting factor.

3. Learning-based Transient Control Design

3.1 Problem reformulation for control design

It is assumed that the set-point $(\omega_{ed}, p_{md}, \tau_{ed}, \dot{m}_{ind}, \tau_{gd})$ for engine operation is given, let

$$x_1 = \frac{1}{k_1}(\omega_e - \omega_{ed}), \quad x_2 = \frac{1}{k_2}(p_m - p_{md}), \tag{3.1}$$

where $k_1 > 0$ and $k_2 > 0$ are used to normalize the engine speed error and the intake manifold error.

By using equation (2.10), the error system can be expressed by

$$\dot{x} = f(x) + g(x)\mu(x), \quad x(0) = x_0, \tag{3.2}$$

where $x = [x_1, x_2]^{\mathrm{T}} \in \mathbb{R}^2$ is the state, $\mu \in \mathbb{R}^2$ is the feedback control input, and

$$[\tau_g, \dot{m}_{in}]^{\mathrm{T}} = [\tau_{gd}, \dot{m}_{ind}]^{\mathrm{T}} + \mu, \quad f(x) = \begin{bmatrix} \frac{\eta_f c_f Q}{4\pi J_e}(k_2 x_2 + p_m) \\ -\frac{\eta_f RT}{4\pi V}(k_2 x_2 + p_{md})(k_1 x_1 + \omega_{ed}) \end{bmatrix}, \quad g(x) = \begin{bmatrix} \frac{R_r + R_s}{R_s J_e} & 0 \\ 0 & \frac{RT}{V} \end{bmatrix}.$$

Followed with Section 2.2.2, it is easy to see that the error system (3.2) is a continuous-time nonlinear affine system with unknown dynamics. For system (3.2), the cost function is defined as

$$V(x_0) = \int_0^\infty \left(\|x(\tau)\|_Q^2 + \|\mu(x(\tau))\|_R^2 \right) \mathrm{d}\tau, \quad x_0 \in \mathbb{R}^2, \tag{3.3}$$

where $Q = \mathrm{diag}(q_1 k_1, q_2 k_2), R > 0.$ It is equivalent to the performance index (2.11).

As is well known, the optimal cost function $V^*(x)$ can be obtained by solving the following HJB equation

$$\left(\frac{\partial V^*}{\partial x} \right)^{\mathrm{T}} f + \|x\|_Q^2 - \frac{1}{4} \left(\frac{\partial V^*}{\partial x} \right)^{\mathrm{T}} gg^{\mathrm{T}} \frac{\partial V^*}{\partial x} = 0 \tag{3.4}$$

and the optimal control input $\mu^*(x)$ is

$$\mu^*(x) = -\frac{1}{2} R^{-1} g^{\mathrm{T}} \frac{\partial V^*}{\partial x}. \tag{3.5}$$

Focusing on system (3.2) with unknown $f(x)$ and $g(x)$, the remaining task is solve the following optimal control problem (**P1**): for a given initial admissible control input $\mu_0(x)$, design a sequence $\{V_i(x), \mu_i(x)\}_1^\infty$ such that for any given $\varepsilon > 0$, there exists a $I_0 > 0$, we have for all $i > I_0$, the following results hold:

$$|V_i(x) - V^*(x)| < \varepsilon, \quad \forall x \in \mathbb{R}^2, \tag{3.6}$$

$$\|\mu_i((x) - \mu^*(x)\| < \varepsilon, \quad \forall x \in \mathbb{R}^2. \tag{3.7}$$

3.2 Model-free algorithm for engine operation

Next, we propose a completely model-free algorithm to solve the optimal control problem **P1**. To this end, an auxiliary trajectory $x_a(t)$ is generated by the following designed system

$$\dot{x}_a = A x_a, \tag{3.8}$$

where $x_a \in \mathbb{R}^2$ is the system state, and the state matrix A is Hurwitz and designed to generate an exciting signal.

We define an error $e(t) = x(t) - x_a(t)$ and assemble x_a and e together into an augmented state $X = [x_a^{\mathrm{T}}, e^{\mathrm{T}}]^{\mathrm{T}} \in \mathbb{R}^4$. By using (3.2) and (3.8), the augmented system can be obtained by

$$\dot{X} = F(X) + G(X)\tilde{\mu}(X), \quad X(0) = X_0, \tag{3.9}$$

where $\tilde{\mu} : \mathbb{R}^4 \to \mathbb{R}^2$ is the control input and $\tilde{\mu}(X) = \mu(e + x_a)$.

$$F(X) = \begin{bmatrix} Ax_a \\ \tilde{f}(X) - Ax_a \end{bmatrix}, \quad G(X) = \begin{bmatrix} 0_{2\times 2} \\ \tilde{g}(X) \end{bmatrix}, \quad \tilde{f}(X) = f(e + x_a), \quad \tilde{g}(X) = g(e + x_a).$$

For augmented system (3.9), a policy iteration (PI) algorithm is proposed as follows.

[Policy Evaluation]: Given an admissible control input $\tilde{\mu}_{i-1}(X)$, find $\tilde{V}(X) \in \mathcal{C}^1$ with $\tilde{V}_i(0) = 0$ by solving

$$\left(\frac{\partial \tilde{V}_i}{\partial X}\right)^{\mathrm{T}} \left(F + G\tilde{\mu}_{i-1}\right) + \|e + x_a\|_Q^2 + R\tilde{\mu}_{i-1}^2 = 0. \tag{3.10}$$

[Policy Improvement]: Update the control policy $\tilde{\mu}_i(X)$ by

$$\tilde{\mu}_i(X) = -\frac{1}{2}R^{-1}G^{\mathrm{T}}\frac{\partial \tilde{V}_i}{\partial X}. \tag{3.11}$$

It is noted that the convergence results of the iterative solutions of (3.10) and (3.11) has been given in [18]. The extended dimension of the augmented system is used to embed the auxiliary system dynamics into the iterative equations, which can provide flexibility to generate efficient data in the learning process while avoiding unnecessary oscillations of the system (3.2) caused by the probing noise.

Based on the above algorithm, we further propose a model-free PI algorithm. First, an external input $u_a(t)$ is added into system (3.9) as follows:

$$\dot{X} = F(X) + G(X)\big(\tilde{\mu}_{i-1}(X) + u_a(t)\big). \tag{3.12}$$

where u_a is T_1-periodic and determined by

$$u_a(\tau) = c_j, \quad \forall \tau \in [t_j, t_{j+1}), \tag{3.13}$$

where $\{c_j\}_{j=1}^{L}$ is sequence of constant vectors in $\mathbb{R}^2$, $t_j \in [t, t+T]$, $j = 0, \ldots, L$, $t = t_0 \lessgtr t_1 \lessgtr t_2 \leq \cdots t_L = t + T$, satisfying the following condition.

Assumption 3.1. *There exist $\kappa_1, \kappa_2 > 0$ such that*

$$\kappa_1 I_2 \sum_{j=1}^{L-1} \leq (c_j - c_{j+1})(c_j - c_{j+1})^{\mathrm{T}} \leq \kappa_2 I_2. \tag{3.14}$$

Then, adding $\left(\frac{\partial \tilde{V}_i}{\partial X}\right)^{\mathrm{T}} Gu_a(t)$ into both sides of equation (3.10) yields

$$\left(\frac{\partial \tilde{V}_i}{\partial X}\right)^{\mathrm{T}} \left(F + G(\tilde{\mu}_{i-1} + u_a)\right) + \|e + x_a\|_Q^2 + R\tilde{\mu}_{i-1}^2 = \left(\frac{\tilde{V}_i}{\partial X}\right)^{\mathrm{T}} Gu_a(t), \tag{3.15}$$

By using (3.11) and integrating (3.15) over the time interval $[t, t + T_1]$ along system (3.12) yields

$$\tilde{V}_i(X(t + T_1)) - \tilde{V}_i(X(t)) + \int_t^{t+T_1} 2\tilde{\mu}_i^{\mathrm{T}} R u_a \mathrm{d}\tau + \int_t^{t+T_1} \left(\|e + x_a\|_Q^2 + \|\tilde{\mu}_{i-1}\|_R^2 \right) \mathrm{d}\tau = 0. \tag{3.16}$$

Hereinafter, the auxiliary trajectory-embedded PI algorithm is established as follows.

[Policy Evaluation & Policy Improvement]: Given an admissible control input $\tilde{\mu}_{i-1}(X)$, find $\tilde{V}_i(X) \in \mathcal{C}^1$ with $\tilde{V}_i(0) = 0$ and $\tilde{\mu}_i(X) \in \mathcal{C}^0$ by solving equation (3.16).

The convergence of the above algorithm is shown in [18]. It is worth pointing out that equation (3.16) does not require the dynamics of system (3.12), instead, it requires the error trajectory $e(t)$ and the auxiliary trajectory $x_a(t)$. Moreover, the cost function $\tilde{V}_i(X)$ and the state feedback control input $\tilde{\mu}_i(X)$ can be updated simultaneously.

In the pratical implementation of the above model-free algorithm in the engine regulation, an actor-crtic structurer is used to solve (3.12). It is noted that the initial state set of system (3.2) depends on the operating region of interest. Therefore, suppose $x_0 \in \Omega_0$ and there exists a compact set $\Omega \supset \Omega_0$ such that the state trajectory always remains in Ω. Then, the augmented state trajectory $X(t)$ can remain in $\Omega \times \Omega$ by designing the auxiliary system (3.8).

Let $\phi_c(X) \in \mathcal{C}^1(\Omega \times \Omega)$ and $\phi_a(X) \in \mathcal{C}^0(\Omega \times \Omega)$ be the linearly independent and complete function sets on their respective function spaces. By the high-order Weierstrass approximation theorem ([20]), $\tilde{V}_i(X)$ and $\tilde{\mu}_i(X)$ can be represented by the actor-critic neural networks as follows

$$\tilde{V}_i(X) = \sum_{j=1}^{\infty} c_i^j \phi_c^j(X), \tag{3.17}$$

$$\tilde{\mu}_i(X) = \sum_{j=1}^{\infty} d_i^j \phi_a^j(X). \tag{3.18}$$

In the actor-critic structure, $\tilde{V}_i(X)$ and $\tilde{\mu}_i(X)$ are approximated by

$$\hat{\tilde{V}}_i(X) = \sum_{j=1}^{N_c} w_i^j \phi_c^j(X) = \mathrm{w}_i^{\mathrm{T}} \phi_c(X), \tag{3.19}$$

$$\hat{\tilde{\mu}}_i(X) = \sum_{j=1}^{N_a} v_i^j \phi_a^j(X) = \mathrm{v}_i^{\mathrm{T}} \phi_a(X), \tag{3.20}$$

where $\mathrm{w}_i \triangleq [w_i^1, \cdots, w_i^{N_c}]^{\mathrm{T}} \in \mathbb{R}^{N_c}$ is the weight vector of the critic NN with the number of neurons N_c. $\mathrm{v}_i \triangleq [v_i^1, \cdots, v_i^{N_a}]^{\mathrm{T}} \in \mathbb{R}^{N_a \times 2}$ is the weight vector of the actor NN with the number of neurons N_a.

Replacing $(\tilde{V}_i(X), \tilde{\mu}_i(X))$ with $(\hat{\tilde{V}}_i(X), \hat{\tilde{\mu}}_i(X))$, equation (3.16) generates the residual error

$$\delta_c(X(t), t, T_1) = \Psi^{\mathrm{T}}(X(t), t, T_1)\theta_i + P_i(X(t), t, T_1), \tag{3.21}$$

where $\theta_i := \begin{bmatrix} \mathrm{w}_i^{\mathrm{T}}, \mathrm{v}_i^{\mathrm{T}} \end{bmatrix}^{\mathrm{T}}$, $\Psi(X(t), t, T_1) := \begin{bmatrix} \Phi_c^{\mathrm{T}}(X(t), t, T_1), \Phi_a^{\mathrm{T}}(X(t), t, T_1) \end{bmatrix}^{\mathrm{T}}$,

$$\Phi_c(X(t), t, T_1) := \phi_c\big(X(t + T_1)\big) - \phi_c\big(X(t)\big),$$

$$\Phi_a(X(t), t, T_1) := \int_t^{t+T_1} \Big(2r u_a(\tau) \phi_a\big(X(\tau)\big) \Big) \mathrm{d}\tau,$$

$$P_i(X(t), t, T_1) := \int_t^{t+T_1} \Big(\|e + x_a\|_Q^2 + \|\tilde{\mu}_{i-1}\|_R^2 \Big) \mathrm{d}\tau.$$

Let $t_k = t + (k-1)T$, where $T > 0$ is a sampling time, and

$$\begin{cases} \Psi[k] = \Psi(X(t_k), t_k, T_1), \\ P_i[k] = P_i(X(t_k), t_k, T_1). \end{cases}$$

Then, the parameters θ_i are determined in the sense of least squares

$$\theta_i = \Big(\sum_{k=1}^{L} \Psi[k] \Psi^{\mathrm{T}}[k] \Big)^{-1} \Big(\sum_{k=1}^{L} \Psi[k] P_i[k] \Big), \tag{3.22}$$

where $L > (N_c + N_a)$ is the number of the efficient sample set. The flow chat of the NN-based algorithm is shown in Fig. 3.1.
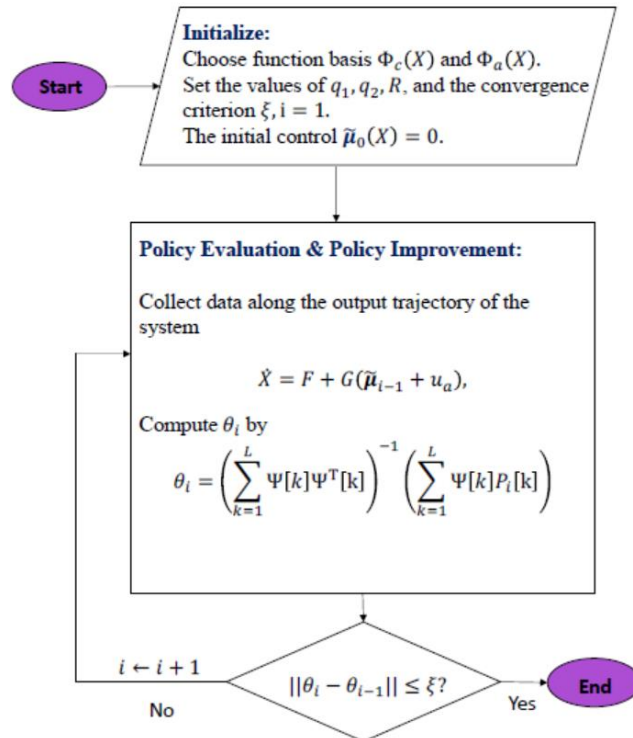
Fig. 3.1: The flowchart of NN-based algorithm.

Note that the auxiliary trajectory decomposes the original system state trajectory into two different oscillating trajectories, which can make the collected data cover the domain adequately to increase the sample size. On the other hand, excitation trajectories are directly injected into the input channel of the

original system and only serve as the inputs of two neural networks during the learning process, as shown in Figure 3.2. The learned state feedback control input combined with given feedforward input can improve the transient performance of engine operation.
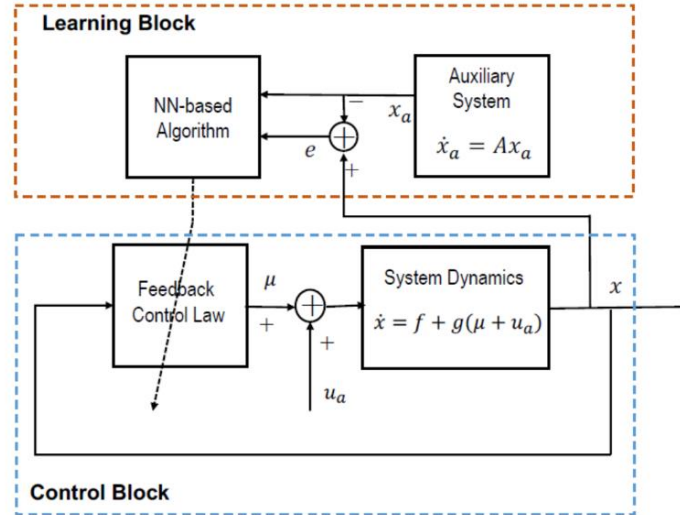

Fig. 3.2: The structure of the system with optimal adaptive control.

4. Segment Traffic-depended Threshold Optimization

4.1 Operation mode switching strategy

It is well known that one significant character for HEVs is the multimode operation provided by two power sources. Therefore, the determination of mode switching signals becomes one of the key factors to improve the real-time fuel economy efficiency of the energy management strategy in the actual driving cycle. Generally, a logical or rule-based algorithm is used to decide the operating mode, i.e., hybrid mode (HEV) or electrical mode (EV). However, this simple method usually leads to frequent start and stop operation of the engine. That not only results in the mechanical loss to the engine but also reduce the energy efficiency. Moreover, considering the real driving conditions, the traffic information influence the driver's action, especially in each road segment. It should be noted that the distribution of velocity possesses statistical characteristics. Motivated by this, a mode switching with segment traffic-depended threshold strategy is investigated for the long-term control. The threshold $\lambda_i, (i = 1, \cdots, N)$ at each road segment represents the baseline of power demand during a future horizon.
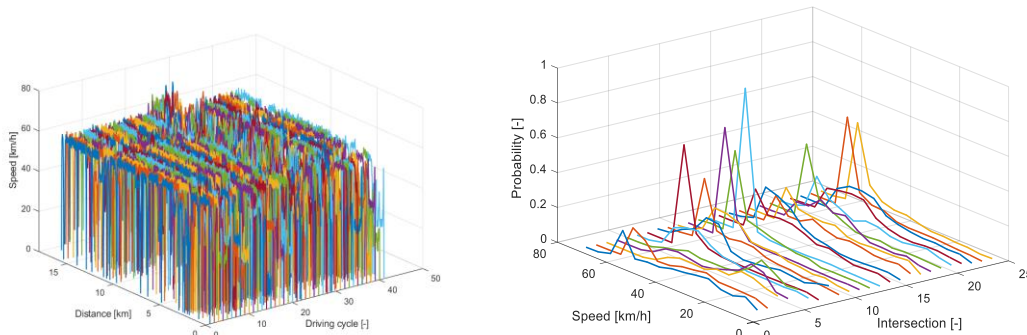

Fig.4.1: Static data of a vehicle cloud.

The used benchmark geographical map is shown in Fig.1, which is a 16[km] driving cycle with 26 signal segments. To clearly describe the optimization problem, the velocity distribution of the vehicles

during each segment is shown in Fig.4.1. The statistical result is extracted from 41 driving tests on the same route. The left subgraph shows the vehicle velocities in each driving cycle. The tests are realized in the same road but with different traffic environments, such as traffic density and the state of traffic lights. The right subgraph describes the probability of speed in each segment. From the statistical results, it is observed that the vehicle speeds in each segment usually exist distribution characteristics to some extent. Therefore, a segment traffic-depended threshold strategy is investigated to decide the mode switching of the powertrain system. Besides, the total power demand during the future horizon is considered as the threshold signal take into account the vehicle motion inertia. For the specific driving road, we aim to find the optimal power thresholds in each segment such that decide the engine operation mode (on or off). It means that 26 power demand thresholds should be optimized in this work. Under above conditions, the problem of the engine mode switching for statistically optimizing energy efficiency by utilizing big data is formulated as follows

$$\min_u \mathbb{E}\left\{\sum \dot{m}_f(k)\Delta t + \rho(SoC(T) - SoC_T)^2\right\}$$

$$\text{s.t.} \begin{cases} \hat{P}_k = \sum P_{dem} \\[4pt] Mode = \begin{cases} 1, & \hat{P}_k > \lambda_i, \\ 0, & \hat{P}_k < \lambda_i - \Delta\lambda, \end{cases} \\[10pt] \Delta\lambda = \begin{cases} \Delta\lambda, & Mode = 1, \\ 0, & Mode = 0, \end{cases} \\[10pt] \tau_e = \begin{cases} \text{Rule}(\tau_e), & Mode = 1, \\ 0, & Mode = 0, \end{cases} \\[10pt] \tau_m = \begin{cases} \text{Rule}(\tau_m), & Mode = 1, \\ f_1(\tau_d), & Mode = 0, \end{cases} \\[10pt] \tau_g = f_2(\tau_e), \\[4pt] SoC_{k+1} = SoC_k + \dfrac{-U_{oc} + \sqrt{U_{oc}^2 - 4RP_b}}{2RQ_b}\Delta t, \\[8pt] SoC_0 = 0.5, \quad SoC_T = 0.5, \\[4pt] SoC_{min} \leq SoC_k \leq SoC_{max}, \\[4pt] 0 \leq \tau_r \leq tau_{e,max}, \\[4pt] \tau_{g,min} \leq \tau_g \leq \tau_{g,max}. \end{cases}$$

where $u = [\lambda_1, \lambda_2, \cdots, \lambda_N]^{\mathrm{T}}$ is the input, in other words, the threshold signals, f_1 and f_2 represent the vehicle dynamic equations with related to the engine speed and vehicle velocity. To simplify the statistical expectations optimization problem, the scenario-based stochastic optimization method is used.

4.1.2 Scenario-based optimization method

It is difficult to solve the stochastic optimization problem. Therefore, we use the scenario-based optimization method in this work. Based on the experimental tests, 3 typical driving cases from 41 driving cycles are extracted, then the original optimization problem can be transformed into the following deterministic optimal problem.

$$\min_{\lambda_i} \mathbb{J}_E = \sum_{j=1}^{3} p_j \mathbb{J}_2^j(\lambda_i) \tag{4.1}$$

where $\mathbb{J}_2^j = \sum \dot{m}_f^j(k)\Delta t + \rho(SoC(T) - SoC_T)^2$, $\dot{m}_f^j(k), p_j, (j = 1, 2, 3)$ represent the fuel mass flow rate and the weighting coefficient of each scenario and the sum of the three probabilities is equal to 1, i.e., $\sum_{j=1}^{3} p_j = 1, \lambda_i[kW], (i = 1, \cdots, N)$ is the threshold at each segment, which is the input series to be optimized. The extracted 3 typical driving scenarios are shown in Fig. 4.3. For the whole driving tests, three scenarios with high similarity to the average speed scenario were selected, and the cost weight p_j for each scenario is determined from the velocity distribution.
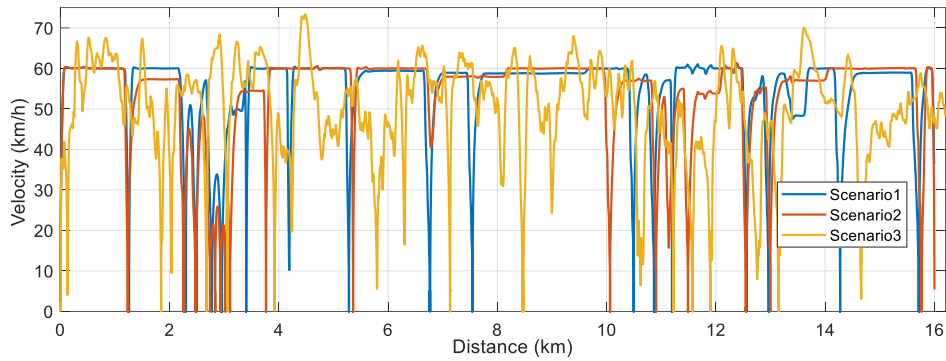
Fig.4.3 The used 3 typical driving scenarios.

In this work, a genetic algorithm (GA) technique is used to deal with above optimization problem such that minimize the total energy consumption during a driving cycle. As GA is considered as a search process to find an exact or an approximate solution for the optimization problem [21]. The initial population is randomly generated within a predefined range that includes a certain number of individuals. The objective function is calculated in each individual based on the vehicle dynamic functions and fuel map. The output is a value returned by an evaluation function such that estimate its performance for solving the optimization problem named fitness value.

While during the hybrid model, the power demand is provided by the internal combustion engine and electric machines together. It would be better to make the engine operate at nearby its best operating line for fuel efficiency. In this work, the engine is forced to work at the working operation $1800[rpm]/100[Nm]$ when the hybrid mode is activated. Furthermore, to evaluate the performance of the proposed scenario-based optimization method, a benchmark scenario is given for comparison. The velocity curve is shown in Fig.4.4, which is a representative driving scenario among the 41 test experiments. Then the obtained threshold of the driver's power demand λ_{bench} is considered as a benchmark to validate the fuel efficiency of the powertrain system.
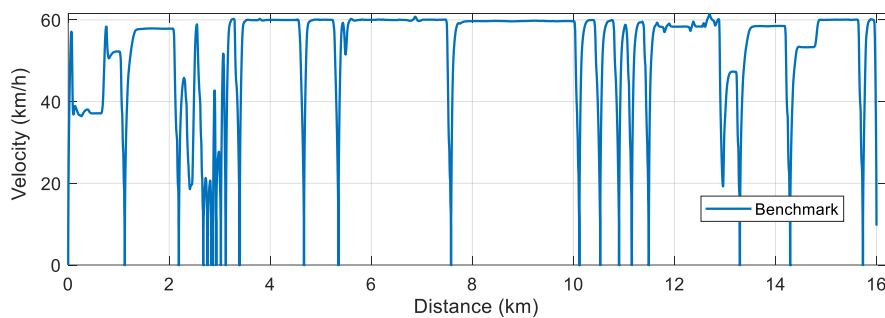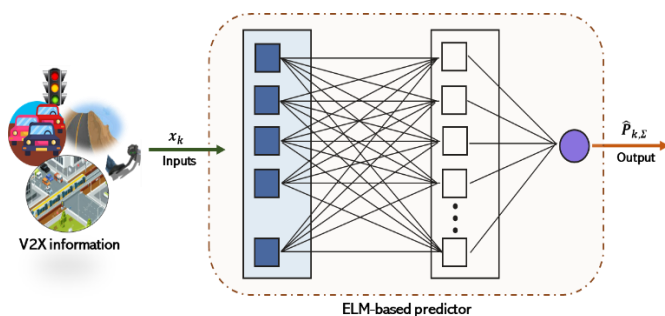

Fig.4.4: The benchmark driving scenario.

4.2 Power demand prediction

Fig.4.5: Structure of ELM-based power demand predictor.

Traffic information		x_k
Ego vehicle	Torque demand	$\tau_{dr,k}$; $\tau_{dr,k-1}$; $\tau_{dr,k-2}$
	Vehicle speed	v
V2V	Preceding vehicle speed	v_p
	Preceding vehicle acceleration	a_{vp}
	Preceding vehicle distance	s_{vp}
V2I	Traffic light state	l_s
	Traffic light remain time	l_t
	Distance to traffic light	s_l

Table 4.1: The used V2X information for ELM predictor.

To perform the proposed optimal engine management strategy with real-time traffic conditions, a key issue is to predict the accumulation of the future power demand. That's because the future power demand provides the possibility to describe the system behavior based on the dynamical model. Moreover, the hybrid powertrain system operates satisfied with the power demand. Contributing to the development of connected environment, it is possible to use the V2V and V2I information for driver's demand prediction. In this work, we will present an extreme learning machine (ELM) algorithm to estimate the driver's power demand with actively using traffic information, which will perform the short-term controller. ELM is a feedforward type neural network which generally includes three layers: input layer, feature mapping layer, and output layer. Both the input and output are considered as nodes or units. The learning process can be summarized to adjust the weights between nodes. Besides, the ELM possess one hidden layer. ELM is a method in which the weights of the nodes of the hidden layer are randomly given from the input layer, and only the weights of the output layer are learned from the hidden layer. It can be learned by finding the generalized inverse matrix by the least squares' method instead of learning. Therefore, it has the characteristic of improve the learning speed of feedforward neural networks.

The basic idea of ELM is that the input weights $a_j \in \mathbb{R}^{n_i \times 1}$ and feature mapping layer biases $b \in \mathbb{R}^{n_h \times 1}$ do not need to be adjusted, instead that they are randomly assigned, and the middle layer can be represented by a random hidden node or kernel. In such a setting, the model can simply be considered as a linear system, and the output weight $\omega \in \mathbb{R}^{n_h \times 1}$ of the model can be determined analytically by the simple generalized inverse of the middle layer output matrix. We consider the following data set for machine learning.

$$D = \{(x_1, y_1), (x_2, y_2), \cdots, (x_N, y_N)\}$$

here, N represents the number of training samples, x are the input signals and y is the output to be observed. Based on learning set D, ELM learning becomes the following optimization problem:

$$\min_{\omega} \|H\omega - Y\|^2$$

where $H = [h(x_1), h(x_2), \cdots, h(x_N)]$ and $Y = [y_1, y_2, \cdots, y_N]$ is the feature mapping function. And the least norm least squares of ω for the above linear system should be expressed as:

$$\omega^* = H^+ Y.$$

It should be noted that H^+ is the Moore–Penrose pseudoinverse of matrix H. More details about the basic idea of ELM can be found in paper [13]. In this work, we employ this issue for one-step-ahead power prediction. The structure of ELM-based power demand predictor is depicted in Fig.4.5. The prediction output is the power accumulation during a future horizon Δt. The input variables include 11-dimension vector that related with V2V and V2I information. When moving from the input layer to the hidden layer, a randomly determined weight a_j and b_j are given. In the hidden layer, the input is converted to output by the activation function $\Phi(s)$. The prediction output can be described as follows

$$\hat{y}_k = \hat{P}_{k,\sum} = \omega^{\mathrm{T}} \Phi(a_j x_k^i + b_j),$$

and the least squares model to minimize the error between the integral value of predicted power and actual power is summarized as follows

$$\omega = \arg\min \sum_i (P - \hat{P}_{k,\sum})^2$$

where $\hat{y}$ represents the prediction output, i.e., the integral of future power demand and x_t denotes the input variables at the current time t, which can be found in the Tab.4.1. The input signals include the vehicle torque demand, the speed, acceleration and driving distance of preceding vehicle, the phase state and remaining time of the traffic light and the velocity, acceleration, and the distance to the intersection of the ego vehicle. To evaluate the performance of the designed predictor, the predicted result in a random scenario is shown in Fig.4.6. The red line represents the predicted power demand sum during the future $3[sec]$, the blue one is the corresponding actual power demand.
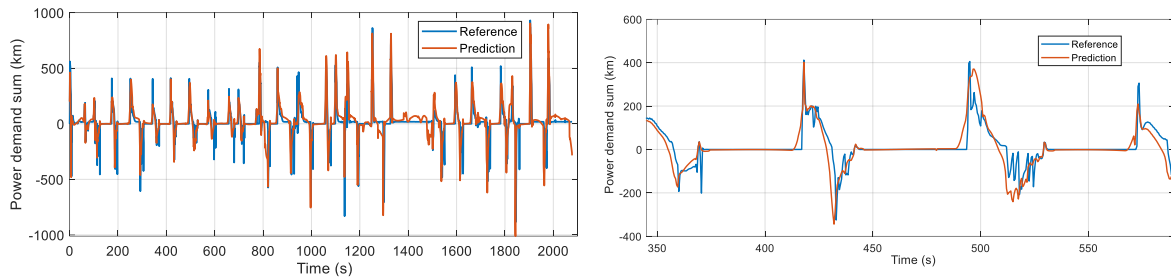
Fig.4.6 Power demand predictions during 3s.

5. Simulation Verification

5.1 Experiment platform setup

5.1.1 HEV simulator platform

To verify the effectiveness of the proposed algorithm, simulations are conducted in a high-fidelity simulator of HEV with power-split powertrain, which is provided by the Ministry of Economy, Trade and Industry (METI). This METI HEV model is built based on the physical mechanism so that it is also used a test platform for the Research association of Automotive Internal Combustion Engines (AICE) project to achieve the target of zero emission. The capture of the HEV simulator platform is shown in Fig. 5.1. The statistic data-based decision of the threshold in the upper layer, and the powertrain demand prediction, the real-time torque distribution strategy and the engine on/off decision in the lower layer run in the HV block in the HEV simulator platform shown in Fig. 5.1. Moreover, the engine-generator control law in the lower layer runs in the ENG block to replace the original engine controller shown in Fig. 5.1.
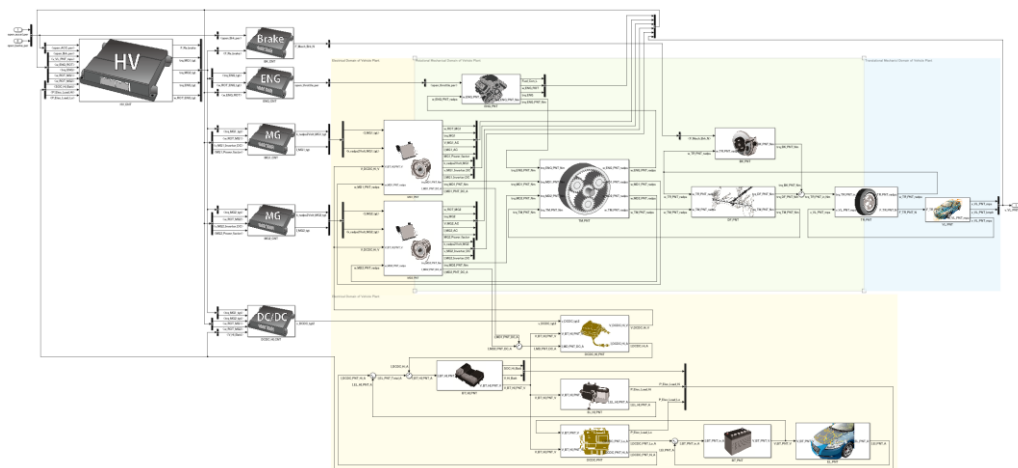

Fig.5.1: Capture of the HEV simulator platform.

On the other hand, to simulate the dynamic of engine, an engine model with consideration of dynamics of in-cylinder combustion pressure is built and replaced the original block of Engine. The parameter of the mean-value model of the engine dynamics is calibrated with a four-cylinder gasoline engine and testbench experiment. The specification of the engine is shown in Table 5.1.

Cylinder type	L-type 4 cylinders
Fuel injection	Port injection
Displacement	1.797 L
Max output power	72 kW
Max torque	142 N · m

Table 5.1: Specification of the engine test bench.

5.1.2 Data collection of connected environment

To collect data of connected environment, a simulated connected traffic environment is built in IPG CarMaker. The real-world road, as shown in Fig. 2.1, is located in Susono, Shizuoka, Japan. The geographic information of this road, including the slope, intersection position, departure point and destination point, is provided from Toyota engineers. Meanwhile, the traffic lights in the intersections along the route, consisting of start phase and time duration of each phase, are set in advance. The traffic density in each link of the route is also set in advance to simulate the different driving condition. The maximum speed along the route is given as 60 [km/h].

In this traffic simulator, it is possible to simulate the connected traffic environment. For example, the real-time communication between V2V and V2I are available to ego vehicle. The V2I communication, including the phase and reminding timing, the distance to the next 1st and 2nd intersections (traffic lights) is given to ego vehicle. Moreover, the preceding vehicle's information, such as the real-time speed and acceleration, is sent to ego vehicle. Since there are some sensors equipped in ego vehicle, the headway distance between ego vehicle and preceding vehicle and the relative speed are available to ego vehicle. Through GPS, when the departure and destination are given before the starting of a route, the slope and the total distance along the route can be known in advance.

To simulate the different traffic conditions, such as the congestion and normal traffic, the traffic densities in different links are set in different traffic scenarios, which generate different vehicles in the ahead traffics. Meanwhile, the initial positions of these vehicles are different. On the other hand, the starting phase and reminding time of traffic lights are set in different traffic scenarios. In summary, 18 traffic scenarios are generated through above settings and the data of V2V and V2I are collected for simulation.

5.2 Results of transient control of the engine operation

To learn the suboptimal state feedback control input, we chose the operating range of engine (ω_e, p_m, τ_e) from (125.6637 [rad/s], 0.711 [bar], 100 Nm) to (188.4956 [rad/s], 0.679 [bar], 100 Nm), and the corresponding feedforward inputs $(\tau_{gd}, \dot{m}_{ind})$ are given by (27.7778 [Nm], 8.6808 [g/s]) and (27.7778 [Nm], 11.7499 [g/s]), respectively. The auxiliary system is designed by

$$\dot{x}_a = \begin{bmatrix} -10^{-4} & 1000 \\ -1000 & -10^{-4} \end{bmatrix} x_a, \quad x_a(0) = [0,1]^{\mathrm{T}}, \tag{5.1}$$

and $T_1 = 0.1$ [sec], the additional input is chosen by

$$u_a(\tau) = \begin{cases} [0.9, 1.2]^{\mathrm{T}}, & t \leq \tau < t + 0.02, \\ [0.5, 1.1]^{\mathrm{T}}, & t + 0.02 \leq \tau < t + 0.04, \\ [2.2, 1.05]^{\mathrm{T}}, & t + 0.04 \leq \tau < t + 0.06, \\ [1.5, 1.15]^{\mathrm{T}}, & t + 0.06 \leq \tau < t + 0.08, \\ [1.1, 1.25]^{\mathrm{T}}, & t + 0.08 \leq \tau < t + 0.1. \end{cases} \tag{5.2}$$

Note that it satisfies Assumption 3.1. Let $X = [x_a^1, x_a^2, x_1 - x_a^1, x_2 - x_a^2]^{\mathrm{T}} = [X_1, X_2, X_3, X_4]^{\mathrm{T}}$, then the activation functions are selected as follows

$$
\begin{aligned}
\phi_c = [\,& X_1^2 + X_3^2, X_1 X_3, X_1 X_2 + X_3 X_4, X_1 X_4 + X_2 X_3, X_2 X_4, X_2^2 + X_4^2, X_1^4 + X_3^4 \\
& + 4(X_1^3 X_3 + X_1 X_3^3), 6 X_1^2 X_3^2, (X_1^3 + X_3^3) X_2 + 3(X_1^2 X_3 + X_1 X_3^2) X_4, (X_1^3 + X_3^3) X_4 \\
& + 3(X_1^2 X_3 + X_1 X_3^2) X_2, (X_2^3 + X_4^3) X_1 + 3(X_2^3 X_4 + X_2 X_4^2) X_3, (X_2^3 + X_4^3) X_3 \\
& + 3(X_2^2 X_4 + X_2 X_4^2) X_1, (X_1^2 + X_3^2)(X_2^2 + X_4^2) + 4 X_1 X_2 X_3 X_4, (X_1^2 + X_3^2) X_2 X_4 \\
& + X_1 X_3 (X_2^2 + X_4^2), X_2^4 + X_4^4 + 6 X_2^2 X_4^2, X_2^3 X_4 + X_2 X_4^3\,]^{\mathrm{T}},
\end{aligned}
\tag{5.3}
$$

$$
\begin{aligned}
\phi_a(X) = [\,& X_1, X_2, X_3, X_4, X_1^3 + X_3^3, 3(X_1^2 X_3 + X_1 X_3^2), X_1^2 X_2 + X_3^2 X_2 + X_1^2 X_4 + X_3^2 X_4, \\
& 2(X_1 X_2 X_3 + X_1 X_3 X_4), X_2^2 X_1 + X_4^2 X_1 + X_2^2 X_3 + X_4^2 X_3, \\
& 2(X_2 X_4 X_1 + X_2 X_4 X_1)\,]^{\mathrm{T}},
\end{aligned}
\tag{5.4}
$$

with $N_c = 16$ and $N_a = 10$. The weight vectors of both NNs are

$$
\mathrm{w}_i = \begin{bmatrix} w_i^1 & w_i^2 & w_i^3 & w_i^4 & w_i^5 & w_i^6 & w_i^7 & w_i^8 & w_i^9 & w_i^{10} & w_i^{11} & w_i^{12} & w_i^{13} & w_i^{14} & w_i^{15} & w_i^{16} \end{bmatrix}^{\mathrm{T}},
$$

$$
\mathrm{v}_i = \begin{bmatrix} v_i^{11} & v_i^{12} & v_i^{13} & v_i^{14} & v_i^{15} & v_i^{16} & v_i^{17} & v_i^{18} & v_i^{19} & v_i^{210} \\ v_i^{21} & v_i^{22} & v_i^{23} & v_i^{24} & v_i^{25} & v_i^{26} & v_i^{27} & v_i^{28} & v_i^{29} & v_i^{210} \end{bmatrix}^{\mathrm{T}}.
$$

The other designed parameters are $q_1 = 10, q_2 = 100, R = \mathrm{diag}([1, 1]), k_1 = 62.8319$, and $k_2 = 0.1358$.

Instead of setting convergence criterion, we fix the running time of simulator at 2000 [sec]. In order to collect the data along the trajectory, then engine is switched between the above operations during the learning process, and two flags are used to measure data, as shown in Fig 5.2
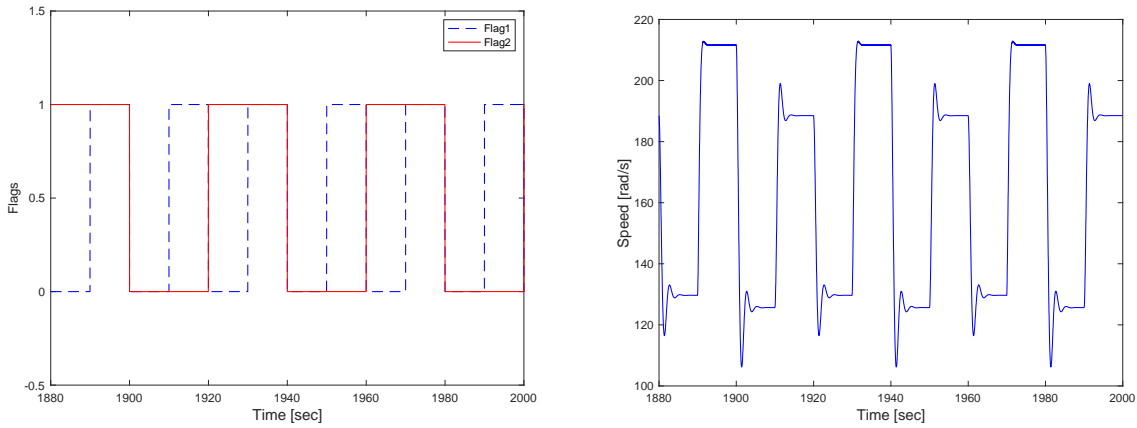

Fig 5.2: The trajectories of learning process.

Fig. 5.2 shows the engine speed trajectory and two flags during the last 120s of learning process When Flag1=Flag2=1, the engine is controlled by the learning state-feedback control input and feedback control input, and the real-time data is collected to implement the NN-based algorithm. When two flags are set to other value couples, the engine is only controlled by the feedforward control input. The simulation results are shown in Figs 5.3 and 5.4 for the convergence results of the weights of both NNs. From the simulation, the weights are convergent by both auxiliary trajectories. Moreover, in order to show the effectiveness of the learned control, we compare the results controlled by only feedforward control and feedforward control with learned state feedback control, as sketched in Fig. 5.5 for the profiles of engine speed, intake manifold pressure, and engine torque, and Fig. 5.6 for the profiles of two control inputs, generator torque and air mass flow rate. It can be seen that the transient performance of the engine operation are improved by the learned control input.
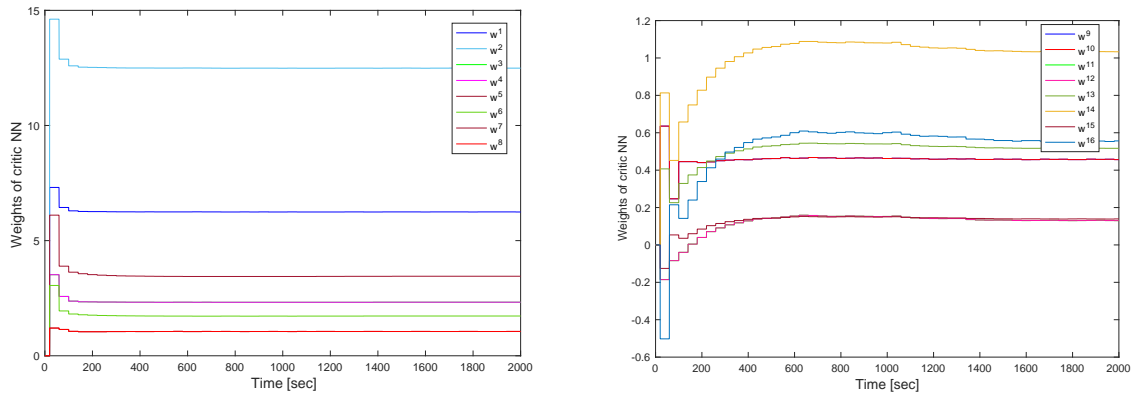
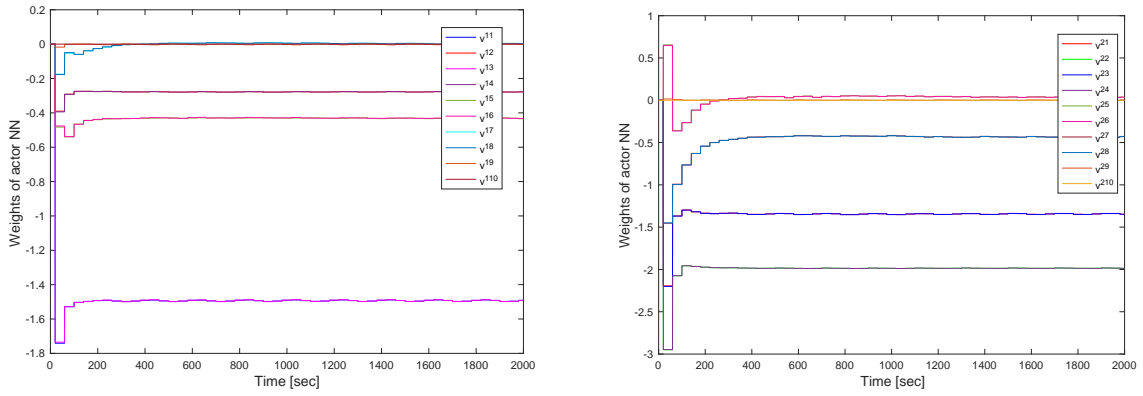Fig 5.3 Weights of the critic neural network.
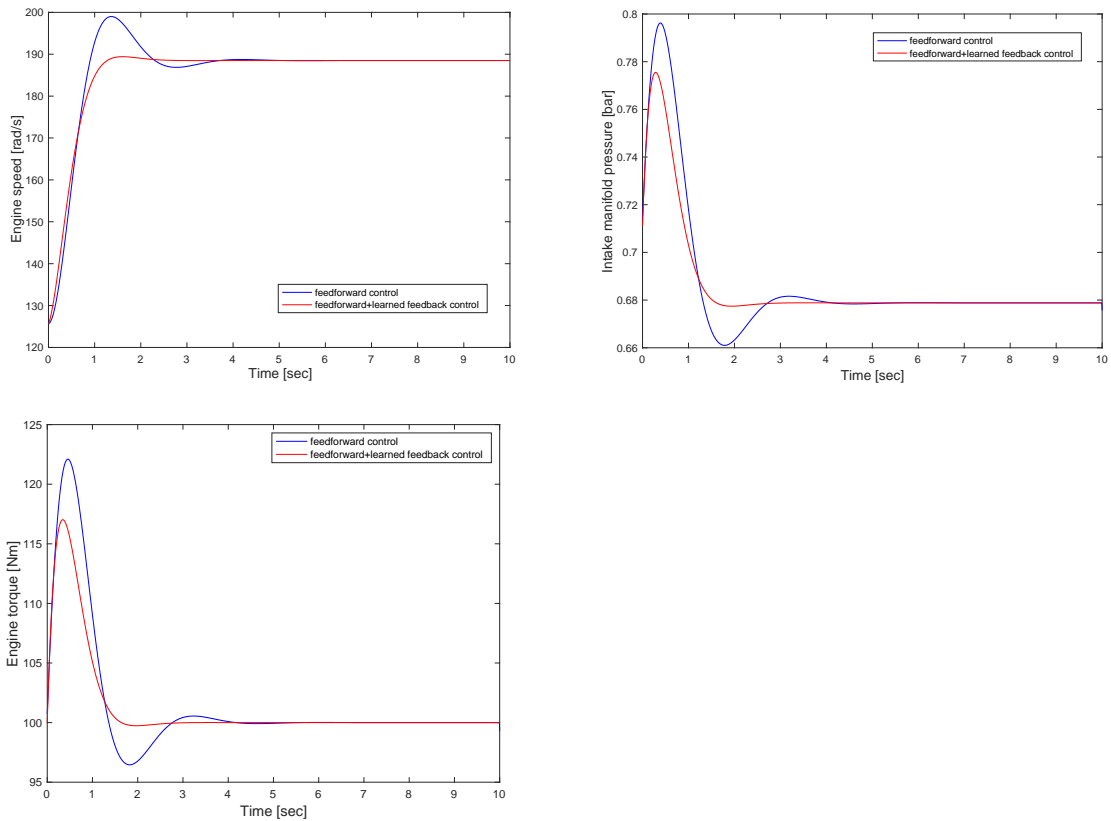

Fig 5.4 Weights of the actor neural network.
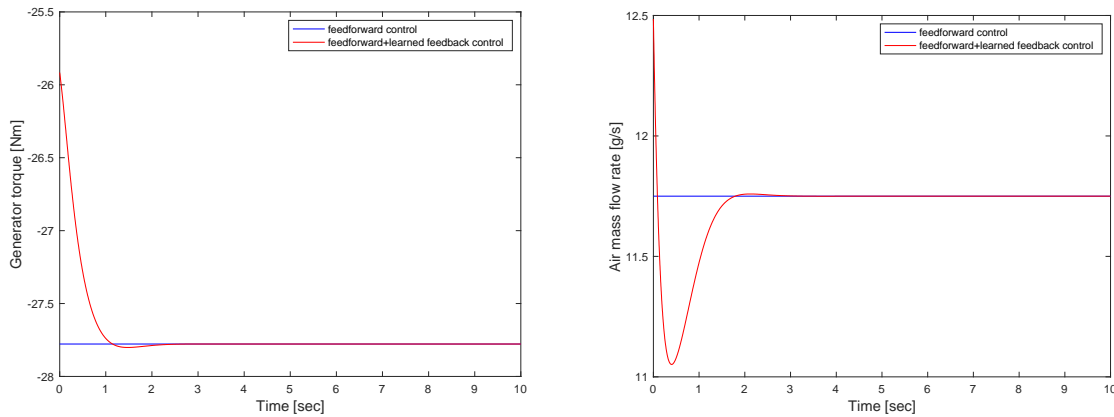

Fig 5.5: The profiles of engine operation.

Fig 5.6: The profiles of control inputs.

5.2 Results of segment traffic-depended threshold optimization

To evaluate the performance of the long-term control strategy, the control system is realized in the designed driving scenarios. To clearly observe the validation, the simulation results in one specific driving scenario is shown firstly. The real driving velocity of the ego vehicle is shown in Figure 5.7. To decide the driving mode, the sum of the power demand is a necessary signal. Therefore, the predicted power demand during the future 3 [s] based on ELM method is given in Figure 5.8. The threshold signals to decide the driving mode for the specific scenario is given in Figure 5.9. There are 26 threshold signals obtained from the GA scheme we designed. In other words, the engine is on when the predicted power demand is greater than the threshold λ_i in each segment.
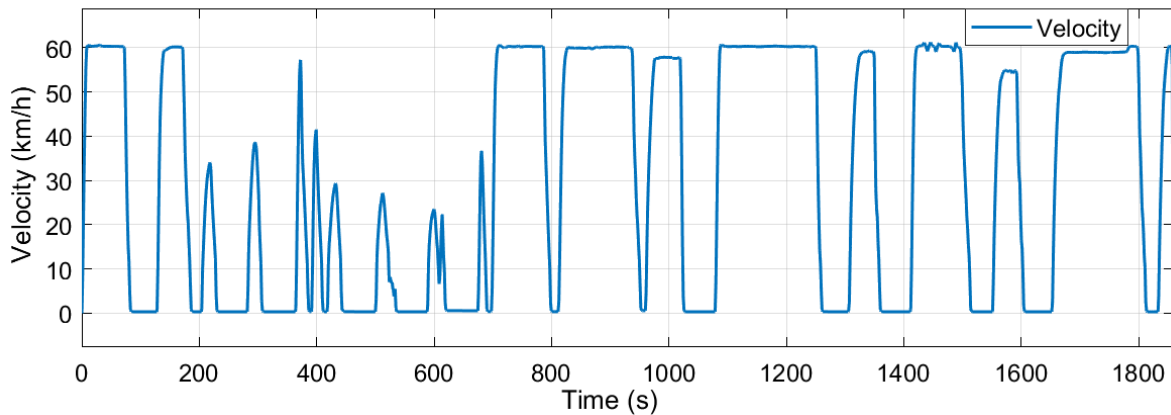

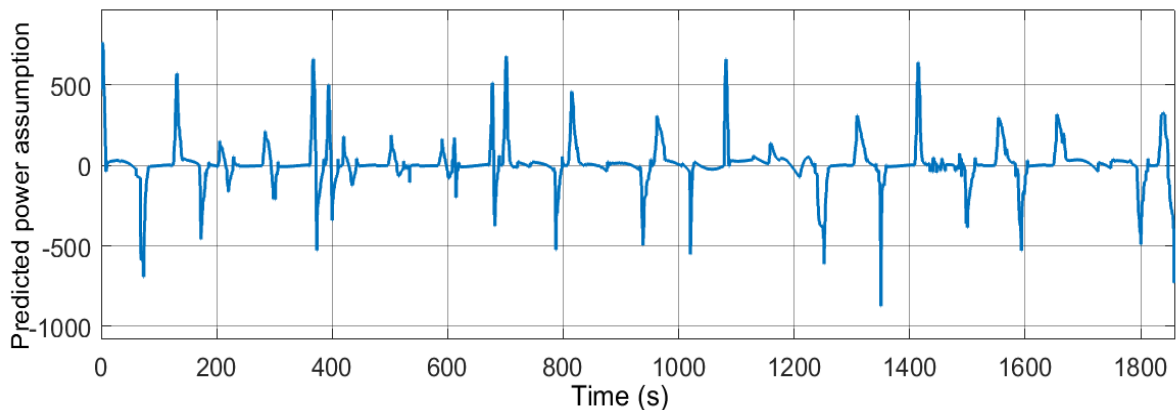Fig.5.7: The vehicle velocity for a specific scenario.

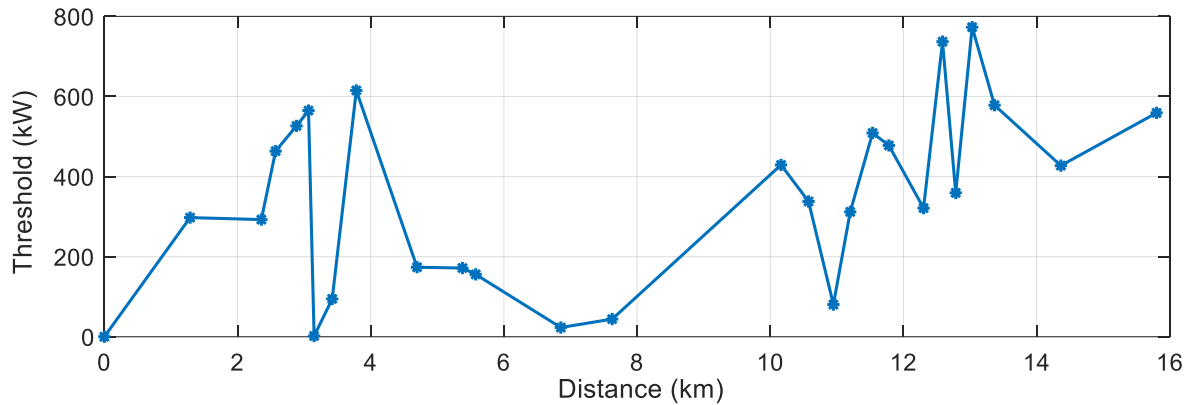Fig.5.8. The predicted power assumption using ELM-based predictor.

Fig.5.9. The threshold signals to decide the driving mode for a specific scenario

The torque split results directly affect the total fuel consumption. Therefore, the torque distribution results for the long-term control are shown in Figure 5.11, which is distributed based on the torque demand in Figure 5.10. In Figure 5.11, the top subgraph shows the engine torque, the middle one shows the generator torque, and the bottom one represents the motor torque. It is observed that the engine assists to work for 12 times during the whole driving cycle. When the engine starts to work, the generator assists the engine reach the desired operating point as soon as possible. Then the motor offsets the remaining torque demand. In such case, the HEV can drive smoothly. The speeds of the engine, generator, and motor for the hybrid powertrain system are drawn in Figure 5.12. The results show that the engine can reach the desired reference speed quickly and can maintain this speed. All the speeds are in a reasonable range.

Furthermore, to evaluate the total fuel consumption and battery state, the fuel consumption and SoC during the driving cycle are given in Figure 5.13 and Figure 4.14, respectively. It is shown that the total fuel consumption is 279 [g] and the terminal SoC can maintain at 52%, which is within a reasonable horizon.
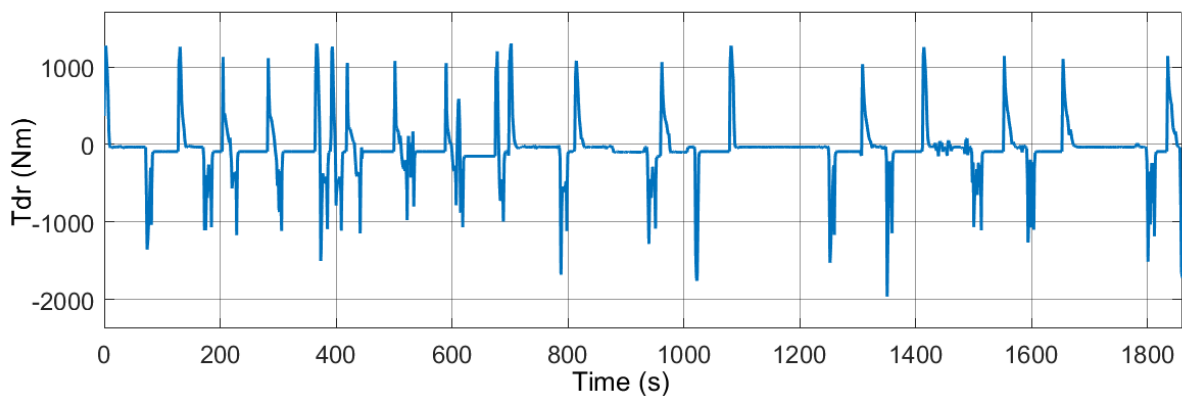

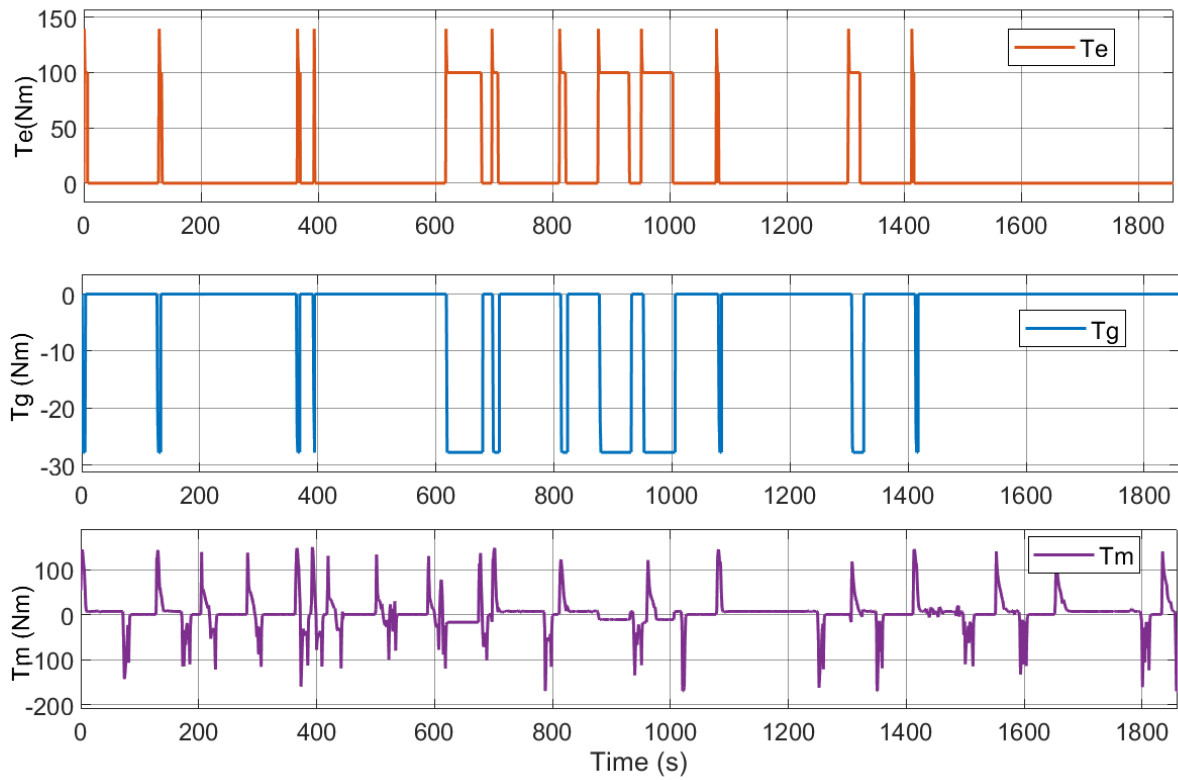Fig.5.10: The torque demand of the HEV for a specific scenario

Fig.5.11: The power split results for the hybrid powertrain system.
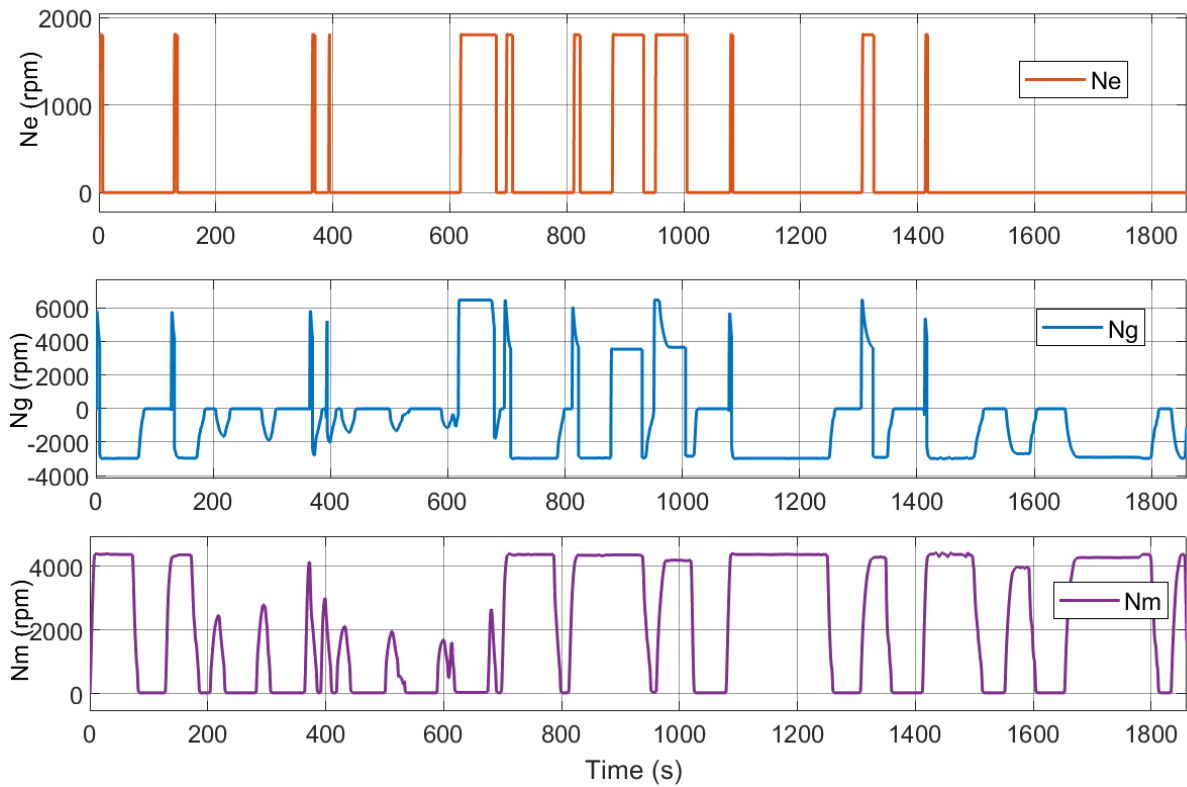

Fig.5.12: The speeds of the engine, generator, and motor for the hybrid powertrain system.
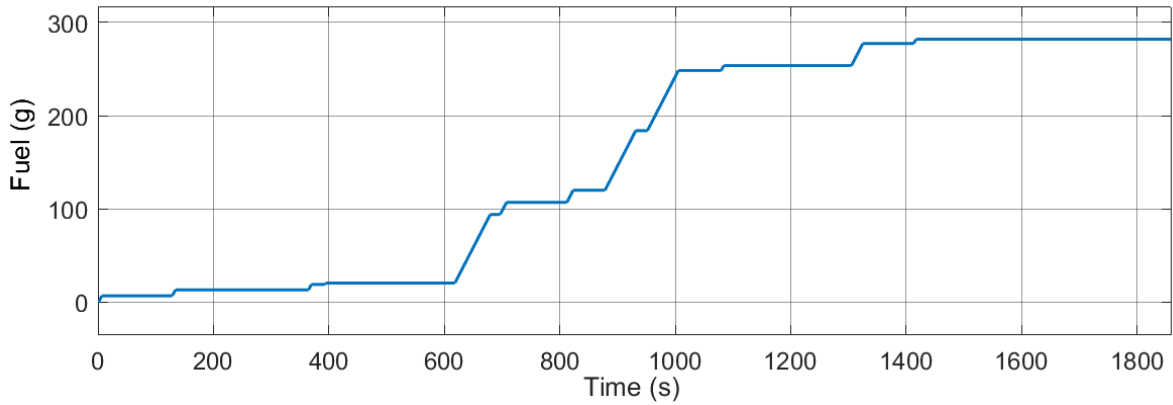
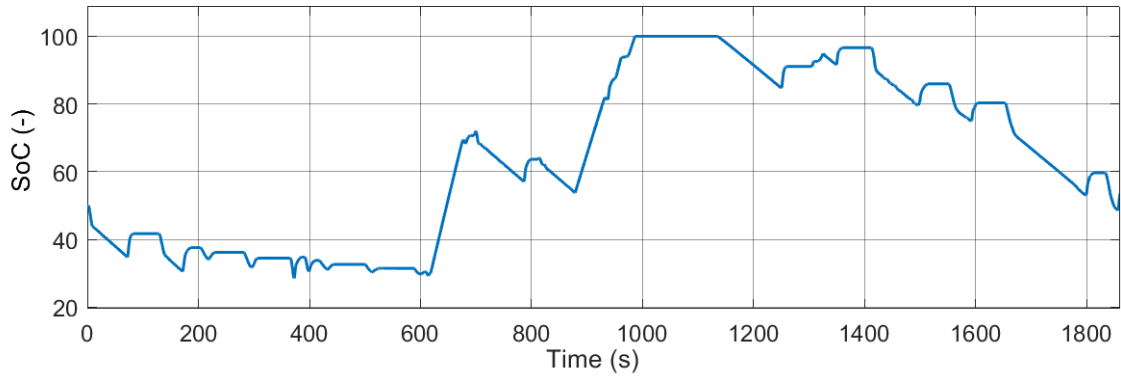Fig.5.13: The fuel consumption of the specific scenario.

Fig.5.14. The SoC of the specific scenario.

Table.5.2: The comparison results for 19 scenarios.

Fuel consumption [g]				Terminal SoC [-]				Switching times [-]		
	Scenario-based	Benchmark			Scenario-based	Benchmark			Scenario-based	Benchmark
Route 1	281.38	316.88		Route 1	42.99	62.87		Route 1	17	17
Route 2	253.63	224.23		Route 2	33.76	14.62		Route 2	12	14
Route 3	263.33	281.93		Route 3	32.40	40.67		Route 3	16	18
Route 4	266.94	205.47		Route 4	35.16	10.00		Route 4	16	16
Route 5	221.76	413.23		Route 5	10.55	100		Route 5	13	18
Route 6	253.93	341.41		Route 6	19.60	66.68		Route 6	15	17
Route 7	238.02	214.02		Route 7	21.35	6.05		Route 7	16	19
Route 8	238.62	301.66		Route 8	34.82	67.04		Route 8	12	17
Route 9	250.54	259.56		Route 9	18.25	21.97		Route 9	14	17
Route 10	297.46	299.67		Route 10	47.66	47.45		Route 10	20	19
Route 11	239.02	330.50		Route 11	6.50	58.23		Route 11	17	17
Route 12	286.72	230.23		Route 12	45.25	10.49		Route 12	10	19
Route 13	206.51	282.65		Route 13	13.10	55.83		Route 13	8	12
Route 14	262.55	342.13		Route 14	24.10	67.68		Route 14	13	19
Route 15	311.78	396.59		Route 15	71.49	100		Route 15	11	18
Route 16	269.62	380.59		Route 16	45.83	100		Route 16	8	15
Route 17	273.84	220.15		Route 17	49.66	17.19		Route 17	11	12
Route 18	262.58	307.86		Route 18	25.53	49.25		Route 18	17	23
Route 19	238.98	291.06		Route 19	32.04	60.05		Route 19	10	15

Finally, another comparison test results are given to evaluate the performance of the proposed strategy for long-term driving. A benchmark threshold result is given, which is obtained from one typical scenario. The results show that fuel economy improves in 15 scenarios among the total 19 scenarios. The engine switching times can be reduced in 17 scenarios among the total 19 scenarios. The results show the effectiveness of the proposed strategy.

Conclusions

Recently, the attention in automotive industry is focused on the potential for improving energy efficiency under the connected environment. For the connected hybrid electric vehicles, the efficiency improvement might be further improved by decision making of engine operating management not only depend on the real-time state of eco-vehicle but also the information of a cloud of vehicles on the traffic flow and the environment. In this paper, we challenged to develop a data-based scheme for managing the operation of combustion engine in HEVs. The proposed scheme involves two layers: statistic data-based decision of the threshold for engine ignition on/off switching, and engine transient control with the throttle operation and the generator's torque adjusting. Firstly, we predicted the total demand power prediction by extreme learning machine with utilization of the V2X information. Then, we applied a scenario-based approach to optimize the real-time demand power threshold in each segment to determine the engine on/off mode of HEV. Finally, we designed both engine's throttle and generator torque control schemes to improve the engine transient dynamics by using the reinforcement learning algorithm. The effectiveness is validated on a high-fidelity simulator of HEV with power-split powertrain provided by the METI.

Reference

[1] Zhang, F., Hu, X., Langari, R., & Cao, D. (2019). Energy management strategies of connected HEVs and PHEVs: Recent progress and outlook. Progress in Energy and Combustion Science, 73, 235-256.

[2] Xu, F., & Shen, T. (2020). Look-ahead prediction-based real-time optimal energy management for connected HEVs. IEEE Transactions on Vehicular Technology, 69(3), 2537-2551.

[3] Xu, F., Tsunogawa, H., Kako, J., Hu, X., Li, S. E., Shen, T., ... & Guardiola, C. (2022). Real-time energy optimization of HEVs under-connected environment: a benchmark problem and receding horizon-based solution. Control Theory and Technology, 1-16.

[4] Lin, C. C., Peng, H., Grizzle, J. W., & Kang, J. M. (2003). Power management strategy for a parallel hybrid electric truck. IEEE transactions on control systems technology, 11(6), 839-849.

[5] Larsson, V., Johannesson, L., & Egardt, B. (2014). Analytic solutions to the dynamic programming subproblem in hybrid vehicle energy management. IEEE Transactions on Vehicular Technology, 64(4), 1458-1467.

[6] Kim, N., Cha, S., & Peng, H. (2010). Optimal control of hybrid electric vehicles based on Pontryagin's minimum principle. IEEE Transactions on control systems technology, 19(5), 1279-1287.

[7] Bin, Y., Réama, A., Cela, A., & Hammar, A. (2010). Optimal power management for vehicle hybrid electric system using look-ahead route information. IFAC Proceedings Volumes, 43(1), 30-35.

[8] Moura, S. J., Stein, J. L., & Fathy, H. K. (2012). Battery-health conscious power management in plug-in hybrid electric vehicles via electrochemical modeling and stochastic control. IEEE Transactions on Control Systems Technology, 21(3), 679-694.

[9] Sun, C., Moura, S. J., Hu, X., Hedrick, J. K., & Sun, F. (2014). Dynamic traffic feedback data enabled energy management in plug-in hybrid electric vehicles. IEEE Transactions on Control Systems Technology, 23(3), 1075-1086.

[10] Shen, X., Zhang, J., & Shen, T. (2016, June). Real-time scenario-based stochastic optimal energy management strategy for HEVs. In 2016 European Control Conference (ECC) (pp. 631-636). IEEE.

[11] Guanetti, J., Kim, Y., & Borrelli, F. (2018). Control of connected and automated vehicles: State of the art and future challenges. Annual reviews in control, 45, 18-40.

24   Zhenhui Xu, Bo Zhang, Shohei Narita, Fuguo Xu, Tielong Shen

[12] Vahidi, A., & Sciarretta, A. (2018). Energy saving potentials of connected and automated vehicles. Transportation Research Part C: Emerging Technologies, 95, 822-843.

[13] Zhang, J., Xu, F., Zhang, Y., & Shen, T. (2020). ELM-based driver torque demand prediction and real-time optimal energy management strategy for HEVs. Neural Computing and Applications, 32(18), 14411-14429.

[14] Zhang, B., Zhang, J., Xu, F., & Shen, T. (2020). Optimal control of power-split hybrid electric power-trains with minimization of energy consumption. Applied Energy, 266, 114873.

[15] Yan, F., Wang, J., & Huang, K. (2012). Hybrid electric vehicle model predictive control torque-split strategy incorporating engine transient characteristics. IEEE transactions on vehicular technology, 61(6), 2458-2467.

[16] Kuchly, J., Nelson-Gruel, D., Charlet, A., Simon, A., Jaine, T., Nouillant, C., & Chamaillard, Y. (2021, June). Predictive energy management of a HEV considering engine torque dynamic. In 2021 European Control Conference (ECC) (pp. 1367-1372). IEEE.

[17] Zhang, J., Shen, T., & Marino, R. (2010). Model-based cold-start speed control scheme for spark ignition engines. Control Engineering Practice, 18(11), 1285–1294.

[18] Xu, Z., Pan, L., & Shen, T. (2021). Model-free reinforcement learning approach to optimal speed control of combustion engines in start-up mode. Control Engineering Practice, 111, 104791.

[19] Shen, T., Zhang, J., Jiao, X., Kang, M., Kako, J., & Ohata, A. (2015). Transient control of gasoline engines. CRC Press.

[20] Hornik, Kurt, Maxwell Stinchcombe, & Halbert White. (1990). Universal approximation of an un-known mapping and its derivatives using multilayer feedforward networks. Neural networks 3(5), 551-560.

 [21] Zhang B, Zhang J, Shen T. Optimal control design for comfortable-driving of hybrid electric vehicles in acceleration mode. Applied Energy, 2022, 305: 117885.

THIESEL 2022 Conference on Thermo- and Fluid Dynamics of Clean Propulsion Powerplants

Economical Predictive Cruise Control-based Real-time Energy Management Strategy for Connected HEVs

Yahui Zhang[1] [3], Xiongxiong You[1], Zeyi Wei[2], Xiaohong Jiao[1]

[1] School of Mechanical Engineering, Yanshan University, China.

E-mail: zhangyahui@ysu.edu.cn
Telephone: +(86) 18830453696

[2] Engineering Research Center of the Ministry of Education for Intelligent Control System and Intelligent Equipment, Yanshan University, China

E-mail: yxx@stumail.ysu.edu.cn; jiaoxh@ysu.edu.cn

[3] State Key Laboratory of Automotive Safety and Energy, Tsinghua University, China

Abstract. With the realization of vehicle interconnection in intelligent transportation systems (ITS), the co-optimzation of powertrain operation and vehicle dynamics has become a significant research problem. Due to this issue remains computationally challenging, research on energy-efficient operation typically prefers sequential optimization or eliminating some constraints. To this issue, this paper proposes a control strategy for hybrid electric vehicles (HEVs),including a predictive cruising control method considering economy (Eco-PCC) for vehicle speed planning and an energy management strategy based on approximation of the optimal cost-to-go values (ACG-EMS) for maintaining the continuous working ability of the battery. In this strategy, the host vehicle speed is planned by the preceding vehicle speed predicted by the conditional linear Gauss (CLG) model, and the economic cost (EC) estimated indirectly by the least absolute shrinkage and selection operator (LASSO). The designed ACG-EMS is comprised of the main item of real-time power allocation by the artificial neural network (ANN) model trained with the offline optimization results of dynamic programming (DP) and a PI correction item. The effectiveness of the control strategy is verified by the simulation comparisons with the existing results in the interconnected simulation environment established by MATLAB/Simulink and Car-Maker.

Notation

M	*Mass.*
A	*Frontal area.*
C_d	*Air drag coefficient.*
ρ	*Air density.*
R_{tire}	*Tire radius.*
v	*Vehicle speed.*
η	*Tansmission efficiency of differential gear ratio.*
θ	*Road slope.*
T_{trac}	*Traction torques.*
T_{br}	*Braking torques.*
ω	*Rotational speed.*
T	*Torque.*
e	*Engine.*
m	*Motor.*
g	*Generator.*
v_f	*Speed of the host vehicle.*
v_p	*Speed of the preceding vehicle.*
ΔL	*Distance between two vehicles.*
Δv	*Relative velocity.*

Δa *Relative acceleration.*
BSFC   *Fuel consumption rate of the engine.*
U_{OC} *Open circuit voltage.*
R_b *Battery equivalent resistance.*
P_b *Battery power.*
I_b *Battery current.*
P_{dem} *Required power of the vehicle.*
SOC_0 *Initial value of SOC.*
SOC_t *The value of SOC at time t.*
γ *Weighting factor.*
φ *Weighting factor.*
L_T *Distance from vehicle to traffic light.*
δ_T *Traffic light status.*

1. Introduction

HEVs can make the engine work in an efficient working area through energy management optimization technology to realize the high efficiency of the multi-power energy system [1]. Meanwhile, with the rapid development, vehicles can obtain road information and surrounding vehicles' states from vehicle-to-infrastructure (V2I) and vehicle-to-vehicle (V2V) [2]. As a result, intelligent energy-saving control of vehicles based on environmental information and optimization methods has gradually attracted widespread attention [3]. Intelligent energy-saving control relies on high-speed communication facilities with V2V and V2I to control vehicle speed, and powertrain [4].

While the increase in the number of state and control variables contributes to improve fuel efficiency, it also increases the complexity of optimal control problems [5]. Therefore, it is necessary to integrate environmental information and optimization algorithms to explore the optimization scheme of HEV eco-driving [8]. In general, two methods cataloged solve these problems [6]. One is so-called integrated optimization, in which the energy consumption of the propulsion system and the velocity planning are carried out in the design simultaneously. The other is sequence optimization, which first plans the velocity curve and then optimizes energy management.

Some papers discuss the method of integrated optimization. Literature [7] proposed an integrated and connected ecological driver assistance system that synergistically optimizes the vehicle dynamics and powertrain operation of the vehicle. In [8], the authors developed a co-optimization method for speed planning and energy management when passing multiple consecutive signalized intersections. The integrated optimization problem has high dimension and computational complexity, which is not conducive to real-time operation, but such methods provide specific ideas for the sequential optimization strategy. The speed planning of the HEV determines the total power demand for energy management. The energy management control strategy in the HEV operation, in turn, affects the HEV energy consumption model used for speed planning, which affects the speed planning of the HEV. That is, the speed planning and energy management strategies are coupled [9].

Based on the decoupling idea of speed planning and energy management, sequential optimization is adopted to reduce the computing time, and memory consumption [10]. In the first stage, the speed curve is optimized by a safe driving distance [11], or acceleration deviation [12]. The second stage achieves the minimum energy consumption through the optimal power distribution between the engine and the motor [13]. For example, in [14], the authors studied the effectiveness of sequential optimization methods. They adopted the strategies of model predictive control (MPC) and adaptive equivalent consumption minimization (ECMS) to solve the vehicle dynamics and energy management problems of HEVs.

It is worth mentioning that [15] compares the performance of the sequential and integrated optimization methods of HEVs. The integrated optimization and sequential optimization of energy-saving driving are comprehensively analyzed and compared from each powertrain component's energy consumption, operation mode, and overall cost. Literature [16] also compares the integrated optimization performance of the HEVs with the sequential optimization method and finds the trade-off between optimality and complexity in terms of fuel consumption, state of charge (SOC) trajectory, and calculation time and memory. Integrated optimization includes finding the optimal speed distribution and power distribution at the same time, which has better performance in fuel economy than the sequential optimization method [17]. In [18], the particle swarm optimization algorithm is used to optimize the speed profile and balance energy consumption and calculation time in the space domain. Then the EMS

based on DP is designed to reduce the complexity of calculation, which carries out boundary range calculation of the state variables in advance based on the analysis of the operating mode.
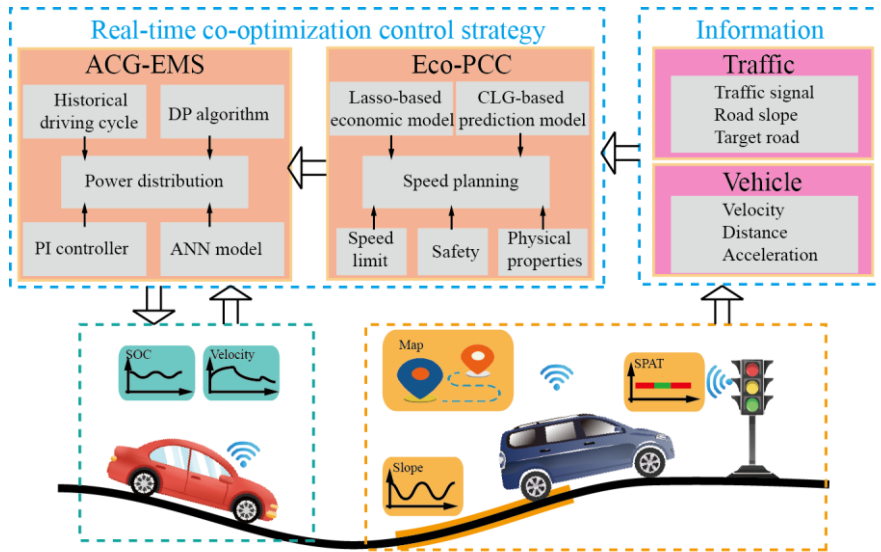
Fig. 1. Schematic diagram of real-time co-optimization control strategy.

Past research has shown that fuel economy can be improved from vehicle speed and powertrain levels. Co-optimization of these two levels for HEV will result in higher fuel efficiency. The integrated optimization performed better in fuel economy than the sequential optimization. However, due to the complex structure, many variables, and heavy computational burden, integrated optimization is generally used as a benchmark for comparison. Accordingly, more efforts focus on the design method development for achieving the effect of co-optimization of eco-driving and energy management.

In this regard, this paper proposes a novel real-time co-optimization control strategy that includes an Eco-PCC for vehicle speed planning and an ACG-EMS for allocation of required power, as shown in Fig. 1.

2. Connected HEV description

This section mainly introduces the mathematical model of non-plug-in HEV and the formation of optimal control problems, including the vehicle longitudinal dynamics model and power system model in the connected environment.

2.1 HEV powertrain mathematical model

This paper considers the model structure of HEV shown in Fig. 2 for designing and implementing the control strategy. Relevant parameters are the same as in reference [20].
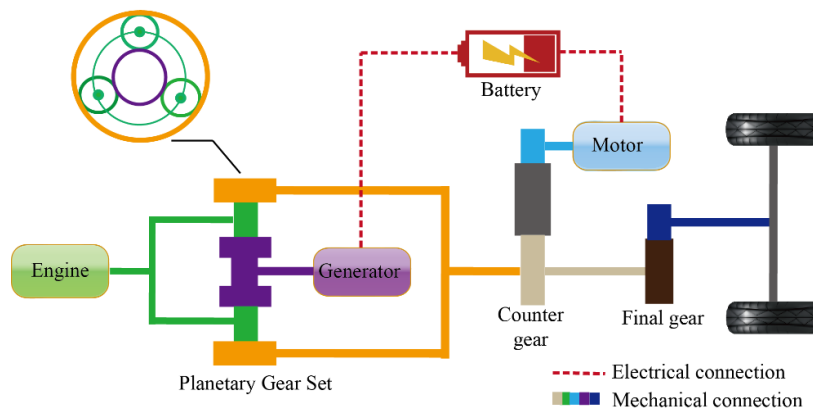
Fig. 2. Powertrain structure of hybrid electric vehicles.

The force analysis of the vehicle shows that the longitudinal dynamics equation of the vehicle is described as follows:

$$M\dot{v} = \frac{\eta T_{trac} - T_{br}}{R_{tire}} - Mg(\mu_r \cos\theta + \sin\theta) - \frac{1}{2}\rho A C_d v^2 \qquad (1)$$

The dynamic equation of battery SOC can be written as:

$$S\dot{O}C = -\frac{U_{oc} - \sqrt{U_{oc}^2 - 4R_b P_b}}{2Q_b R_b} \qquad (2)$$

Fuel consumption is a vital fuel economy indicator when designing a control strategy for HEVs, which is evaluated by the fuel mass flow rate described as:

$$\dot{m}_f = BSFC(T_e, \omega_e) \cdot T_e \cdot \omega_e \cdot 10^{-5} / 36 \qquad (3)$$

where BSFC represents the fuel consumption rate of the engine.

Making the engine work in the optimal working curve is essential for fuel economy. It is necessary to fit the best efficiency curve of the engine in advance, as shown in Fig. 3 The optimal curve represents the best efficiency curve of the engine.
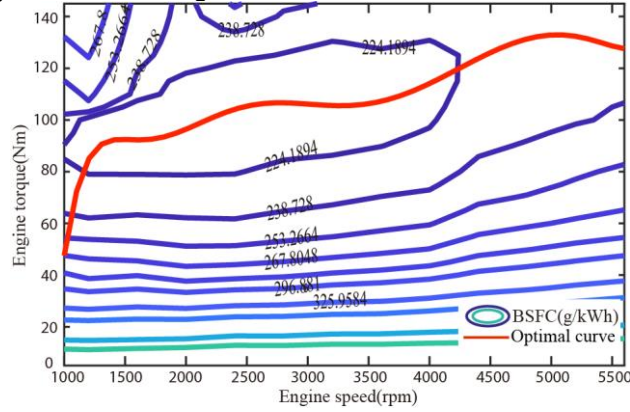

Fig. 3. Engine universal characteristic diagram.

2.2 Formation of the optimal control problem

The connected environment has complex and changeable characteristics. Under traffic rules and road conditions, special road sections may cause vehicles to start and stop frequently. In such a complex driving environment, the distance between the preceding vehicle and the host vehicle involved in traffic safety issues is crucial, which can be described as follows:

$$\Delta L = (v_p - v_f)\Delta t \qquad (4)$$

Moreover, according to the following safety, minimum distance and maximum distance between two vehicles can be defined as follows:

$$\begin{cases} \Delta L_{min} = \alpha_1 + \alpha_2 \cdot v_f + \alpha_3 \cdot v_f^2 \\ \Delta L_{max} = \beta_1 + \beta_2 \cdot v_f + \beta_3 \cdot v_f^2 \end{cases} \qquad (5)$$

The driving power of the HEV comes from two parts, and the power balance equation is as follows:

$$P_{dem} = T_e\omega_e + T_g\omega_g + T_m\omega_m \qquad (6)$$

The energy management strategy can issue commands for the power that each power source needs to provide according to the actual vehicle driving power demand. Before designing the control strategy, the objective function needs to be set, which will be used as the optimization objective and the evaluation basis for the effectiveness of the control strategy.

$$J_F = m_f + \gamma(SOC_0 - SOC_t) \qquad (7)$$

The specific inequality constraints are as follows:

$$
\begin{cases}
SOC_{\min} \leq SOC \leq SOC_{\max} \\
\omega_{e\_min} \leq \omega_e \leq \omega_{e\_max} \\
\omega_{m\_min} \leq \omega_m \leq \omega_{m\_max} \\
\omega_{g\_min} \leq \omega_g \leq \omega_{g\_max} \\
T_{e\_min}(\omega_e) \leq T_e \leq T_{e\_max}(\omega_e) \\
T_{m\_min}(\omega_m) \leq T_m \leq T_{m\_max}(\omega_m) \\
T_{g\_min}(\omega_g) \leq T_g \leq T_{g\_max}(\omega_g)
\end{cases} \tag{8}
$$

3. Real-time Energy Management Control Strategy

The structure of real-time EMS includes two parts: speed level optimization and powertrain level optimization. At the speed optimization level, based on integrating environment information, the speed planning and vehicle power transmission control are combined to establish a speed planning control scheme based on Eco-PCC. At the power system optimization level, an ACG-based EMS, composed of a PI correction controller and an ANN model, is designed based on the fusion of historical driving cycle information combined with the engine's dynamic characteristics.

3.1 Speed profile optimization

In the speed optimization part, the CLG-based speed prediction model predicts the preceding vehicle's speed, using the historical speed information of the preceding vehicle and the information of the traffic lights. The economic fuel consumption estimation model based on LASSO established by the optimal sample data can be used as an economical guide for speed planning. Combining with safety performance indicators and traffic rules, an Eco-PCC-based vehicle speed planning scheme is established.

3.1.1 CLG-based prediction model

In the connected environment, the vehicle can obtain information about the upcoming traffic light status and the state of the preceding vehicle through V2X communication, which makes the preceding vehicle speed prediction have low uncertainty and a long prediction range. As a result, a particular variant of the Bayesian network, namely the CLG model, is used to predict the preceding vehicle's longitudinal speed directly. The advantage of this model is that a joint distribution over all variables models the time series of the velocity. Additionally, the required amount of data for estimating the parameters is kept relatively low compared to Markov models due to the linear dependencies.

Generally, inference in probabilistic networks with continuous-valued variables is based on the algorithms of discrete Bayesian networks. By integrating the distribution function of the continuous-valued variables, the inference methods of discrete Bayesian networks are extended to work with continuous distributions. Observations [19] during an actual road test drive show that, in an urban traffic environment, the future speed of a vehicle mainly depends on the following variables. The preceding vehicle's speed, the distance to the next traffic light, and the traffic light status.

Design the structure of a directed acyclic graph, as shown in Fig. 4. The prediction nodes $v_{p,k+1}$ are CLG distributions. The continuous-valued parent node represented by $v_{p,k}$ and $L_{T,k}$ is the current speed of the preceding vehicle and the distance to the next traffic light. The speed prediction node $v_{p,k+i}$ is a continuous parent node and is connected to the previous moment $v_{p,k+i-1}$ to reflect the correlation of the predicted trajectory within the prediction range. Each prediction node has a discrete-valued parent node for the future traffic light signal state $\delta_{T,k+i}$, assuming that the traffic lights only have red and green lights.

Based on the assumptions mentioned earlier, the structure of the directed acyclic graph, as shown in Fig. 4.
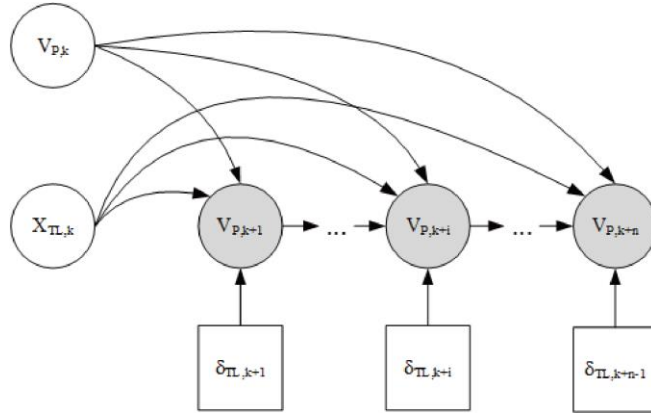
Fig. 4. CLG prediction model.

It is assumed that information about the preceding vehicle and traffic light obtained is entirely accurate. The input vector of the model is expressed as:

$$x_k = [\delta_{T,k}, L_{T,k}, v_{p,k-2}, v_{p,k-1}, v_{p,k}] \tag{9}$$

Note that the prediction model is based on the rolling time-domain method. The mean and variance of the entire future velocity trajectory are estimated at each sampling instant using actual input data. Hence, at time k the predicted trajectory $v_{p,k}$ can be stated as:

$$v_{p,k} = \{v_{p,k+i}\}, i \in \{1,2,\cdots n\} \tag{10}$$

where each element $v_{p,k+i}$ is a 1-D Gaussian distribution with mean and variance, that is:

$$v_{p,k+i} \sim GP(m(v_{p,k}), k(v_{p,k})) \tag{11}$$

3.1.2 LASSO-based fuel consumption estimation model

Optimizing the speed of HEVs in the connected environment is a basis for the high-performance operation of energy management strategies. In order to further improve the economy of HEV, an economical fuel consumption estimation model for HEV speed optimization is established. The optimal data samples are obtained by offline optimization of historical driving information through DP. The LASSO regression model established by the sample data set is used as an economic guide in the vehicle speed planning controller.

DP is used for offline optimization of historical driving conditions to form optimal data samples. To more accurately screen the input variables of the economic prediction model and reduce the calculation burden, the LASSO model is used to perform linear regression fitting on the sample data. The LASSO model can be used to estimate the economy of vehicle speed. Fig. 5 shows the schematic diagram of the offline fitting process of LASSO.
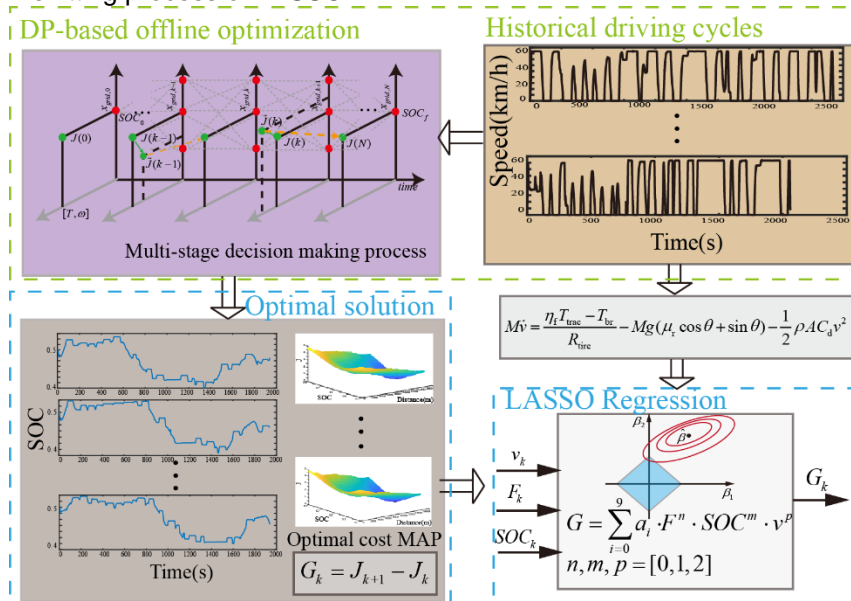

Fig. 5. Offline fitting process of LASSO model.

Specifically, the optimal cost function value and SOC curve are obtained by offline optimization of historical driving information using DP. In addition, considering that the speed information cannot fully reflect the traffic environment (slope information), the historical speed information is converted into traction force F through the longitudinal dynamics of the whole vehicle. A LASSO model with three inputs (traction force F, battery state SOC, speed v) and single-output (one-step EC value G) is formed. Among them, the optimal SOC trajectory and cost function value of historical driving information lay the foundation for the economic-guiding role of the LASSO model.

3.1.3 Speed planning based on Eco-PCC

With the realization of vehicle interconnection in intelligent transportation systems, the optimization of power system operation and vehicle dynamics has become an important research topic for energy efficiency improvement. The speed optimization level has excellent potential for improvement of fuel consumption. In this section, additional states and control variables resulting from the operation of the vehicle's powertrain are added to the optimization algorithm to determine the energy-efficient speed distribution during vehicle motion.

$$J_D = \sum_{i=0}^{t_p-1} (J_{\Delta v}(u(i\,|\,k)) + J_{\Delta a}(u(i\,|\,k)) + J_{\Delta L}(u(i\,|\,k)) + \varphi G(u(i\,|\,k), x(i\,|\,k))) \tag{12}$$

where G is the one-step EC value estimated by the LASSO model with multi-input and single-output.
The loss function for the inter-vehicle distance is as follows:

$$J_{\Delta L} = \begin{cases} +\infty, & \Delta L \le \Delta L_{\min} \\ \left| \Delta L - \dfrac{\Delta L_{\min} + \Delta L_{\max}}{2} \right|, & \Delta L_{\min} \le \Delta L \le \Delta L_{\max} \\ h_1(\Delta L - \Delta L_{\max})^2, & \Delta L_{\max} \le \Delta L \end{cases} \tag{13}$$

In the connected environment, relative speed and relative acceleration are also factors that affect the process of vehicle following. Thus, the index functions are as follows:

$$\begin{cases} J_{\Delta v} = h_2 \cdot \Delta v^2 \\ J_{\Delta a} = h_3 \cdot \Delta a^2 \end{cases} \tag{14}$$

When the vehicle approaches a traffic light intersection, it is necessary to redefine the speed limits of the host vehicle according to the corresponding traffic rules, distance L_T to the next traffic light, time sequence, and phase sequence of traffic lights. Suppose g_i is the start of the ith green of the next traffic light, and r_i is the start of the ith red of the next traffic light, the subsequent light broadcasts at regular intervals, a sequence

$$[g_1, r_1, g_2, r_2....] = [40, 100, 160, 220....]$$

To pass an intersection during the first green of the first light, the speed of the host vehicle should be in the interval $[L_T/r_1, L_T/g_1]$ It is only feasible if this interval has a set intersection with the possible speed interval of $[v_{min}, v_{max}]$ If this set intersection is empty, passing through the first green interval without stopping at the red interval is infeasible. In that event, the feasibility of passing during the next green interval is checked.

3.2 HEV energy management based on ACG-EMS

In the ACG-based EMS part, there are the pre-fitted optimal working curve of the engine, the ANN model, and the PI correction controller. The ANN model divides the required power into engine power and battery power. The engine power can combine with the optimal working curve of the engine to obtain the optimal torque and speed. The PI controller obtains the motor torque according to the target speed of the vehicle and the battery power, as well as generator speed and torque to meet the vehicle's power requirements.

The ANN model is trained offline, which process is shown in Fig. 6 Using the DP algorithm to optimize the historical driving data, set the state variable as x, and set the control variable as T. And then, the DP optimization result is a training set to form a four-input and single-output ANN model to

obtain the optimal data sample, including SOC, acceleration a, speed v, travel distance S and lookahead cost function value J. These will serve as the primary basis for power allocation. Here the function are obtained as the optimal or nearly optimal cost functions of a simplified optimization problem, which is more convenient for computation. Simplifications may include exploiting decomposable structures, ignoring types of uncertainties, and reducing state space size.
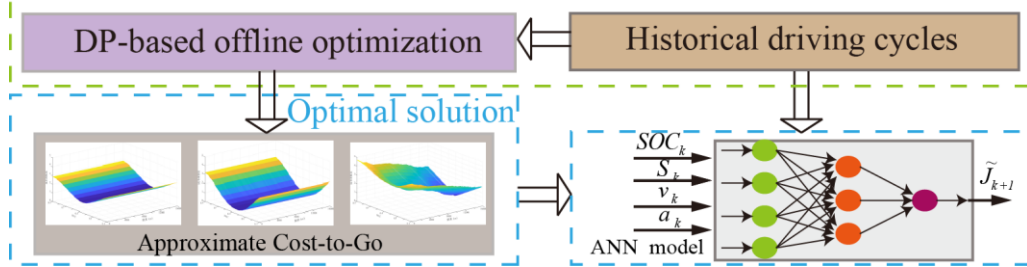

Fig. 6. Sketch of ANN offline training process.

The real-time instantaneous cost function is set as:

$$F_k = \dot{m}_{f,k}(u(k), x(k)) + \tilde{J}_{k+1}(S(k), v(k), a(k), x(k)) \tag{15}$$

Based on the predicted speed of the preceding vehicle, the Eco-PCC controller uses the loss function and combines the LASSO-based fuel consumption estimation model to plan the safe vehicle speed in real-time. According to the longitudinal dynamics of the vehicle, the desired vehicle speed is converted into the required power. Then the required power is divided into engine power and battery power by the ANN model. The minimum value of the above formula is taken as the target to determine the battery power and engine power. Consider that the engine is set to work at an optimal point located at the best operating line. In this case, according to the configuration of the considered HEV powertrain, the generator is used to regulate the engine speed to the desired working point, and the motor should do the work to realize the battery power. Based on the above analysis, the required vehicle acceleration can be realized.

$$\begin{cases} T_e = T_e^* \\ T_g = k_p(\omega_e^* - \omega_e) + k_i \int (\omega_e^* - \omega_e)dt \end{cases} \tag{16}$$
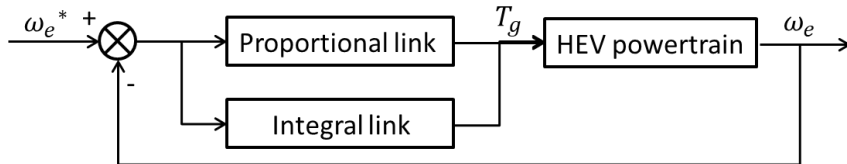

Fig. 7. Sketch of PI controller.

4. Simulation Results and Discussions

In this section, the HEV model based on MATLAB/Simulink and the connected environment of CarMaker is used to verify the effectiveness of the proposed EMS as shown in Fig. 8.
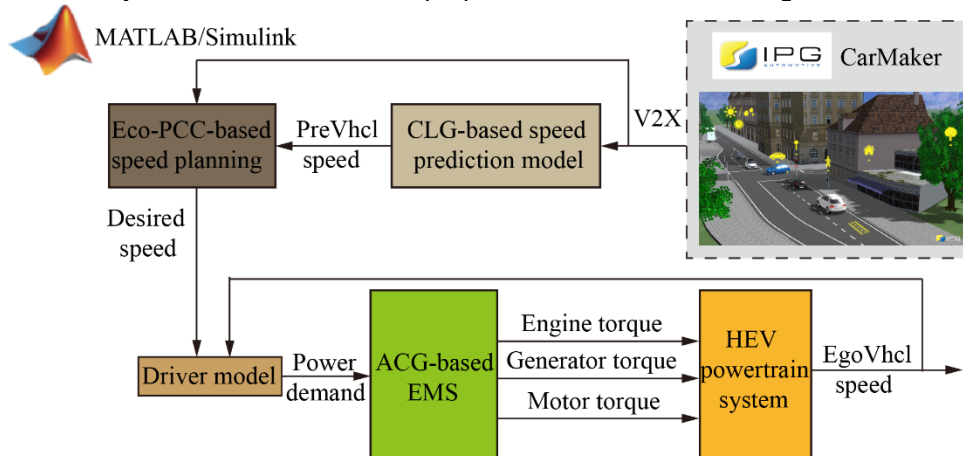

Fig. 8. Schematic of CarMaker and MATLAB/Simulink simulation test platform for HEV.

The targeted road shown in Fig. 9 is a montane town area, and a white line highlights the running route. Automotive road tests obtain the data of height and slope along the route. When the starting and ending points of vehicles on the road are determined, the slope and position of intersections along the road can be known in advance through GPS information.

Fig. 9. Map showing the location of the road obtained from Google Maps.

4.1 Validation of predictive and estimated models

A separate evaluation cycle is used to evaluate the prediction model. Noting that the model is in a receding horizon manner, the longer the prediction horizon is adopted, the more prediction error will accumulate. The resulting prediction performance for different horizons is shown in Fig. 10. Fig. 11 illustrates the predicted value and the accompanying inputs. As can be seen from the above, the prediction model is reasonable.
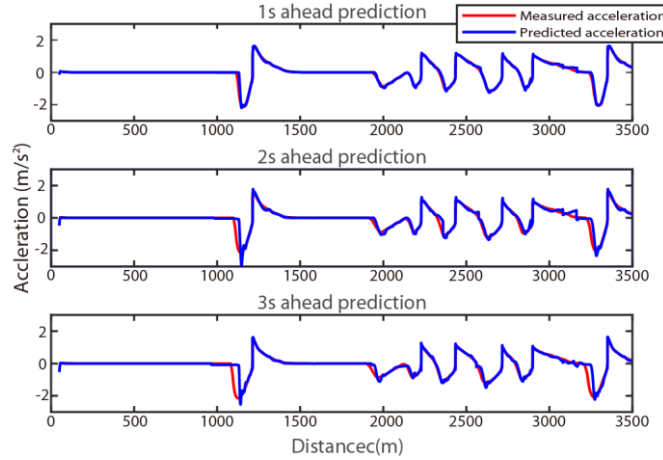

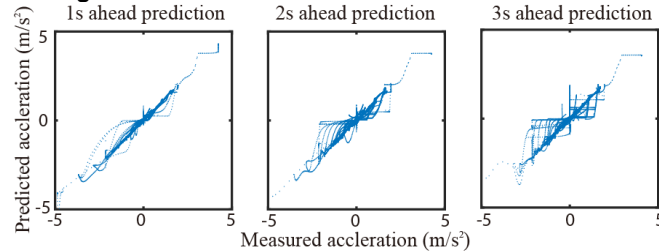**Fig. 10.** Predicted acceleration for different horizons.

Fig. 11. Predicted acceleration and measured acceleration.

It can be seen from Fig. 12 that when the λ value of the LASSO regression model is $4.84 * 10^{-5}$, it meets the fitting requirements, and the function polynomial of the model is

$$G(k) = a_0 + a_1 \cdot F(k) + a_2 \cdot v(k) + a_3 \cdot SOC(k) + a_4 \cdot F(k) \cdot v(k) + a_5 \cdot F(k) \cdot SOC(k)$$
$$+ a_6 \cdot SOC(k) \cdot v(k) + a_7 \cdot F(k)^2 + a_8 \cdot v(k)^2 + a_9 \cdot SOC(k)^2 \tag{17}$$

where the coefficients are: $a_0 = 0, a_1 = 0.18, a_2 = -0.0036, a_3 = 0.000014, a_4 = 0, a_5 = 0.00000317, a_6 = 0, a_7 = -0.133, a_8 = 0, a_9 = 0$.
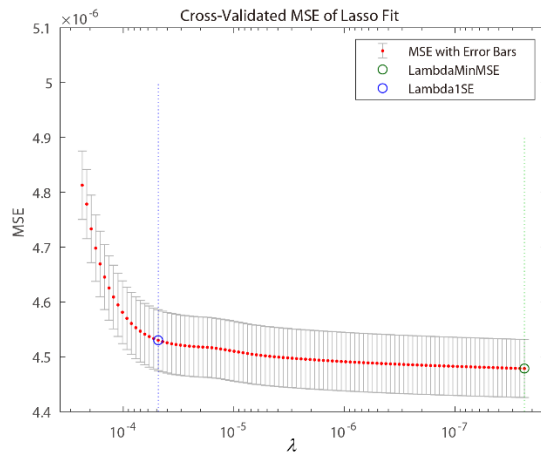
Fig. 12. Cross-validate MSE of LASSO fit.

It can be seen from Fig. 13 that the output value and numerical change trend of the artificial neural network model are consistent with the actual value, and the root mean square error is 0.14, which meets the accuracy requirements required by EMS.
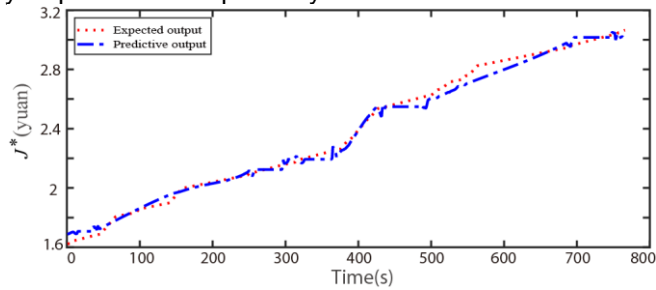

Fig. 13. ANN model expected output and predicted output.

4.2 Control strategy effectiveness verification and analysis

For the effectiveness of the proposed strategy, the CarMaker software is used to generate new operating condition information in this scenario. The simulation results are shown as below.
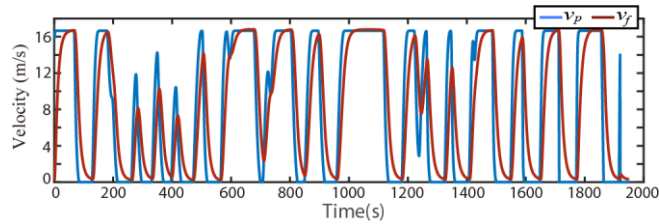

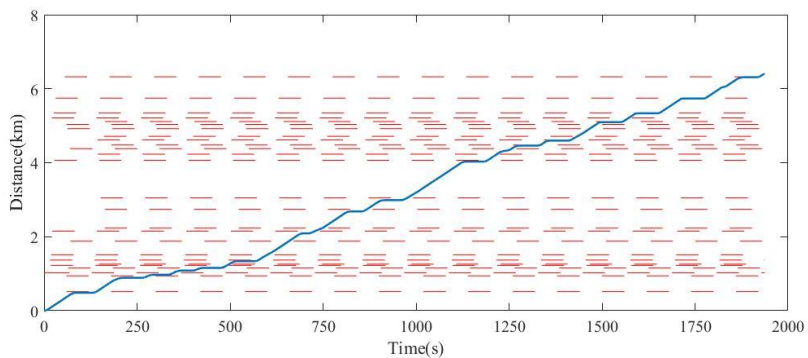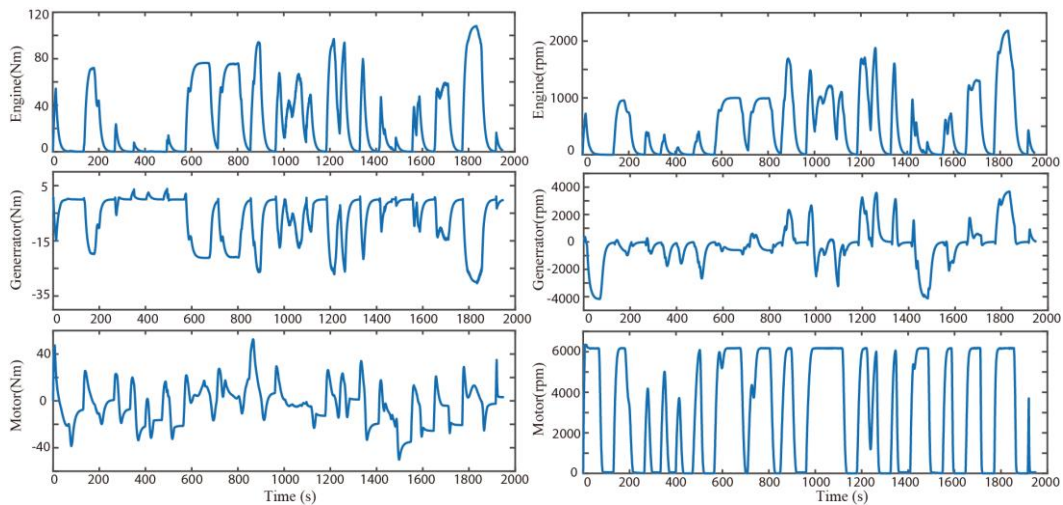**Fig. 14.** Velocity curve of vehicles under the random data.

Fig. 15. Schematic diagram of traffic light information and vehicle driving status.

Fig. 16. Torques and speeds of engine, generator and motor under the random data.

The simulation result Fig. 14 shows that the preceding vehicle and the host vehicle maintain a safe distance and a specific speed difference. The maximum speed difference between the preceding and host vehicles is 8.3 m/s, and the minimum is -0.7 m/s. It can be seen from Fig. 15 that the vehicle driven by this scheme does not pass through the traffic intersection when the traffic light is red. It can be seen that the speed planning scheme designed in this paper satisfies the requirements for safe driving and real-time operation under the condition of complying with the traffic light rules. From Fig. 16, it can be seen that the relationships between engine speed and torque and powers of the engine, generator, and motor are all matched. Therefore, it can be concluded that the proposed EMS can ensure vehicle following safety and comply with traffic rules while meeting the constraints of physical conditions.

A comparative analysis illustrates the improvement of the fuel economy of the proposed control strategy for the proposed ACG-EMS based on Eco-PCC, the ACG-EMS based on PCC, the ECMS based on Eco-PCC, and the DP based on Eco-PCC. The following figures show the simulation results of these strategies on the simulation test platform and the operation of the first set of driving cycles on a 16km fixed route.

The purpose of this scheme is to plan an energy-saving speed curve. The change range and rate of acceleration have a great impact on fuel consumption. Therefore, it can be seen from the figure that the speed change rate of the energy-saving speed curve is low. At the same time, in order to ensure the effect of following the car, the speed change range is wider. It can be seen from Fig. 17 that the proposed EMS based on Eco-PCC has a smoother change in vehicle speed than the EMS based on PCC. Under the control of the strategy designed in this paper, the change speed of the distance between the two vehicles is slower, but the range of change is larger.
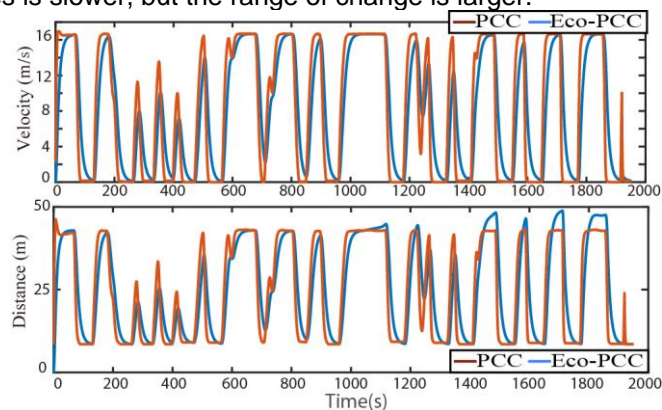
Fig. 17. HEV driving state comparison of the two strategies under the random data.
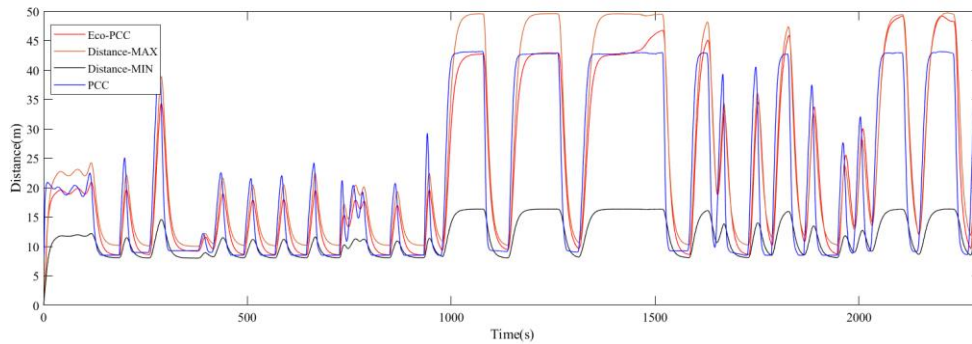
Fig. 19. Comparison of maximum and minimum distance between vehicles.

Analyzing Fig. 20 and Table. 1, we can see that when the initial value of SOC is the same, the final SOC value under these control strategies is roughly the same, but there is a big difference in fuel consumption. In the design of ECMS control strategy, because the setting of the equivalent factor has a great influence on the effect of the control strategy, the real-time calorific value relationship between oil and electricity prices is used to design the value of the equivalent factor. In the PCC+ACG control strategy simulation results and the Eco-PCC+ACG control strategy, the difference in the final SOC value is small. However, the fuel consumption of the latter is lower, indicating that the speed planning strategy of Eco-PCC is better than PCC in terms of energy-saving. From the simulation comparison results, it can be seen that the fuel consumption of Eco-PCC+ACG is higher than that of Eco-PCC+DP, but it is lower than that of Eco-PCC+ECMS. The ACG control strategy has stronger real-time performance than the globally optimized DP strategy and has a stronger fuel economy than the ECMS strategy. The cost is 5.59 yuan, 5.16 yuan, 5.54 yuan and 5.47 yuan, respectively. The control strategy designed in this paper uses the fuel consumption model to plan the energy-saving speed curve in real time under the condition of satisfying the traffic constraints and the physical dynamic constraints of the vehicle, and excavates the energy-saving space existing in the distance between vehicles, providing a certain decoupling for collaborative optimization and sequence optimization. ideas. Therefore, the HEV equipped with this control strategy can improve fuel consumption in the interconnected environment.

Table 1. Comparison of different control strategies in the random set of road conditions.

Method	SOC_0[%]	SOC_f[%]	Fuel[g]	Price[yuan]
PCC+ACG	50.00	49.50	623	5.59
Eco-PCC+ACG	50.00	49.90	576	5.16
Eco-PCC+DP	50.00	50.00	506	4.54
Eco-PCC+ECMS	50.00	49.96	610	5.47
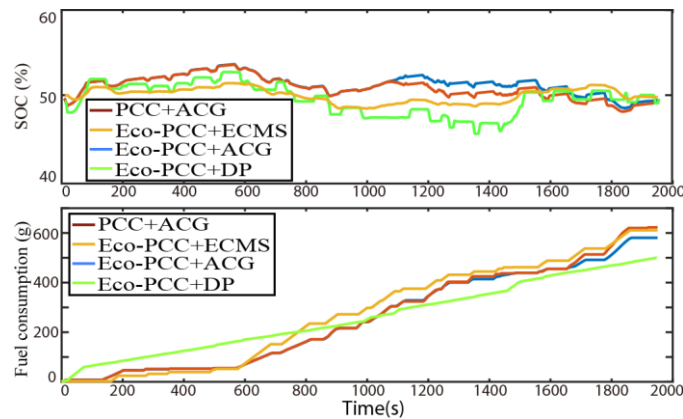
Fig. 20. Vehicle state comparison of the four strategies under the random set of data.

The analysis shows that the designed control strategy has tapped the energy-saving potential within the range of vehicle spacing changes. The fuel consumption of the designed control strategy is lower than other instantaneous optimization control strategies, which further illustrates the effectiveness of the proposed control strategy.

Conclusion

In order to improve the fuel economy of the online EMS in the connected environment, an optimization control strategy is proposed based on the speed prediction of the preceding vehicle, the Eco-PCC-based speed planning, and the ACG-based EMS. The HEV simulation system in the interconnected environment established on the Matlab/Simulink and CarMaker platforms verifies the effectiveness of the control strategy. The simulation results show that the designed EMS is practical and reasonable. At the same time, the simulation comparison results confirmed that the designed EMS could achieve better economy by adjusting the distance between vehicles in the connected environment. It also provides some ideas for the decoupling between energy management and vehicle speed planning.

Acknowledgments

References

[1] Shen C, Shan P, Gao T. A comprehensive overview of hybrid electric vehicles. International Journal of Vehicular Technology, 2011: 1-7.

[2] Nathaniel S, Hajo R. Review of research on V2X technologies, strategies, and operations. Renewable and Sustainable Energy Reviews, 2019, 105: 61-70.

[3] Guo L, Zhang X, Zou Y, et al. Co-optimization strategy of unmanned hybrid electric tracked vehicle combining eco-driving and simultaneous energy management. Energy, 2022, 246:0360-5442.

[4] Xu F, Shen T. Look-ahead prediction-based real-time optimal energy management for connected HEVs. IEEE Transactions on Vehicular Technology, 2020, 69: 2537-2551.

[5] Meng Z, Tang G, Zhou Q, et al. A review of hybrid electric vehicle energy management strategy based on road condition information. IOP Conference Series: Earth and Environmental Science, 2021, 831: 012031.

[6] Marina C, Hu X, Cao D. Energy management in plug-in hybrid electric vehicles: Recent progress and a connected vehicles perspective. IEEE Transactions on Vehicular Technology, 2017, 66(6): 4534-4549.

[7] Qi X, Wu G, Hao P, et al. Integrated-connected eco-driving system for PHEVs with co-optimization of vehicle dynamics and powertrain operations. IEEE Transactions on Intelligent Vehicles, 2017, 2: 2-13.

[8] Wei X, Leng J, Sun C, et al. Co-optimization method of speed planning and energy management for fuel cell vehicles through signalized intersections. Journal of Power Sources, 2022, 518: 230598.

[9] Nie Z, Jia Y, Wang W, et al. Co-optimization of speed planning and energy management for intelligent fuel cell hybrid vehicle considering complex traffic conditions. Energy, 2022, 247: 0360-5442.

[10] Li G, Gorges D. Ecological adaptive cruise control and energy management strategy for hybrid electric vehicles based on heuristic dynamic programming. IEEE Transactions on Intelligent Transportation Systems, 2019, 20: 3526-3535.

[11] Yang C, Wang M, Wang W, et al. An efficient vehicle-following predictive energy management strategy for PHEV based on improved sequential quadratic programming algorithm. Energy, 2021, 219:119595.

[12] Zhang J, Xu F, Zhang Y, et al. ELM-based driver torque demand prediction and real-time optimal energy management strategy for HEVs. Neural Computing and Applications, 2020, 32: 14411-14429.

[13] Min Q , Li J , Liu B , et al. Guided model predictive control for connected vehicles with hybrid energy systems. Energy, 2021, 230: 120780

[14] Zhang B, Zhang J, Xu F, et al. Optimal control of power-split hybrid electric powertrains with minimization of energy consumption. Applied Energy 2020, 266: 114873.

[15] Kim Y, Figueroa-Santos M, Prakash N, et al. Co-optimization of speed trajectory and power management for a fuel-cell/battery electric vehicle. Applied Energy, 2019, 260: 114254.

14   Y. Zhang, X. You, Z. Wei, X. Jiao

[17] He Y, Zhou Q, Makridis M, et al. Multiobjective co-optimization of cooperative adaptive cruise control and energy management strategy for PHEVs. IEEE Transactions on Transportation Electrification, 2020, 6: 346-355.

[18] Liu Y , Huang Z , Li J , et al. Cooperative optimization of velocity planning and energy management for connected plug-in hybrid electric vehicles. Applied Mathematical Modelling, 2021, 95: 715-733.

[19] Asadi B, Vahidi A. Predictive cruise control: Utilizing upcoming traffic signal information for improving fuel economy and reducing trip time. IEEE Transactions on Control Systems Technology, 2011: 707-714.

[20] Xu F, Tsunogawa H, Kako J, et al. Real-time Energy Optimization of HEVs under Connected Environment: ECOSM 2021 Benchmark Problem and a Case Study.

THIESEL 2022 Conference on Thermo- and Fluid Dynamics of Clean Propulsion Powerplants

Assessment of Driving Patterns Influence on a BEV Supercar Range using System Simulation

Manuel Montesinos, Manuel Rivas, Eduardo Elipe

AVL Ibérica. Paseo del Arco de Ladrillo 68, 5E, E-47007 Valladolid, Spain.

E-mail: iberica@avl.com
Telephone: +(34) 983548073

Abstract. Because of the new challenging targets set around the idea of net zero emissions for the future, BEVs will play a big role in this technology transition towards net zero emissions. In these BEVs, the battery pack is one of the most important components, mainly, because of its cost, energy density and thermal management; it has a big impact on the production costs, consumer and environment, making the development process key for achieving the desired targets and customer satisfaction. One of the principal concerns and biggest disadvantage of BEVs, when compared to HEVs, PHEVs or ICEVs, is its driving range, for this reason, the battery has become one of the most important components to help close the competitive gap with other powertrains.

In this paper, a system simulation study has been carried out to analyse the range variation of a BEV depending on the driving patterns. Before conducting the study, a validation of the BEV model, built in AVL CRUISE™ M, was performed using real data. The base BEV used for the study is a supercar, which will have to comply with broader driving pattern situations, as sporty driving in circuits and normal city driving, compared to an average application.

This paper provides a simulation and research method in order to understand the critical driving conditions for the battery range of a BEV. This methodology, used in combination with a battery thermal management model, could be used for the minimum capacity calculation of the battery in other BEV applications before building a prototype vehicle, the perfect example of frontloading.

Notation

HV   *High Voltage*
HVAC *Heating, Ventilation and Air Conditioning*
OEM   *Original Equipment Manufacturer*
KPI   *Key Performance Indicator*
DoE   *Design of Experiments*
SoC   *State of Charge*
RMS   *Root Mean Square*
HiL   *Hardware in the Loop*
SiL   *Software in the Loop*
MiL   *Model in the Loop*
BEV   *Battery Electric Vehicle*
HEV   *Hybrid Electric Vehicle*
PHEV *Plug-in Hybrid Electric Vehicle*
ICEV *Internal Combustion Engine Vehicle*
WLTC *Worldwide Harmonized Light Vehicle Test Cycles*
NEDC *New European Driving Cycle*
RDE   *Real Driving Emissions*
KPI   *Key Performance Indicator*
FLA   *Full Load Acceleration*

1. Introduction

CO_2 emissions have been one of the main focus of the industry since 1998 when Europe decided to give to diesel powered vehicles a competitive advantage against gasoline powered vehicles in order to reduce the CO_2 emissions of the European fleet (Helmes, 2013). After the *dieselgate* and with the target of net zero emissions by 2050, Europe is in the route to decide that Diesel powered vehicles, or even more radically, any vehicle powered by an ICE cannot be sold after 2035, because new cars usually stay on the road for 10-15 years (Pole, 2022). Therefore, BEVs are supposed to play a big role in this European roadmap towards net zero emissions by 2050.

BEVs are still in development and still have several important subjects to address in these upcoming years before being able to fully substitute their fellows HEVs, PHEVs and ICEV. A few of these topics are related to the battery, its range, durability, charging, etc. Several studies have been performed around these subjects such as, study of thermal effect on BEV range (Eisenstein, 2019) and study on driving range at high and low temperature (Jiang Yu, 2019) where it was observed that the BEV calculated range can be affected as much as 66% (from 240 km to 82 km) at low ambient temperatures (-30 ºC). Some of these subjects will interact in an opposite way among each other, like the development of aging prediction models to understand that increasing battery capacity is not the best solution against aging but an effective thermal management and setting electrical loads limits can be (YOUNGCHUL LIM, 2020). This also goes in the opposite direction as improving the range of the BEV by increasing the charge power limit to store more energy from the regenerative braking (Bryan, 2017). Therefore, a lot of challenges are appearing and will appear in the near future when BEVs start to be an important part of society's daily life, because it has other important limitations that until now ICE powered vehicles did not have.

One of the most challenging subjects to address is how to ensure the range of the BEV in any condition, as it was mentioned before, the durability (aging) of the battery depends on the electrical load limits and its thermal management but also this has a negative impact on the amount of regenerative braking that can be stored. This, plus the auxiliary components used to maintain the passenger compartment in a desired temperature (HVAC concerns), impacts directly the range of the BEV, reducing it. Analysis around this issues have been performed to determine the optimal range of the battery in the BEV, taking into account the travel patterns, charging behaviors and charging infrastructure (Yue Zhou, 2020) showing that for a private vehicle 300 miles will cover 90% of the drivers while 100 miles will cover 80% in a case study of Beijing. If this study is combined with the impact of the ambient temperature in the range of the BEV, explained before, it can be found that 880 miles (around 1400 km) of range would be needed in order to cover the worst case scenario in low temperature conditions (-30 ºC) and 410 miles (around 660 km) of range to cover the high temperature scenario (40 ºC).

The average range declared of the BEVs sold on the market is around 330 km, with a range from 95 km to 695 km, with an average price of 42.000 euros (Holding, 2021). In order to be able to replace their fellows HEVs, PHEVs and ICEV, BEVs need to get cheaper and increase their range but also the OEMs need to be more transparent about it, now it is not a matter of having 1 l/100 km of fuel consumption difference with the declared value, but it's a matter of the car not being able to fulfill the requirements of the user because of the real range that the car is able to offer.

As it has been mentioned the range of the BEVs is and will be an important part of the development, image of the product and a very important information for the client to make the decision of purchase. Therefore, new ways of evaluating driving patterns will represent an important part of the possible range that the vehicle can offer, as other topics already mentioned before. For this reason, in this paper, a methodology using simulation is developed in order to analyze the impact of different driving patterns in the range of a supercar BEV. The range of utilization of a supercar BEV in terms of driving patterns is much wider than a normal car, therefore a bigger difference and impact will be seen in the range of the vehicle.

The evaluation of the driving patterns is performed by simulation, using a 0D model developed in AVL CRUISE™ M. The methodology of validation, the chosen driven patterns and analysis of the results can be implemented in any other BEV in order to evaluate the possible range variation depending on the application. It would be interesting to cross the effect of driving patterns and ambient temperature impact, but this would be a next step for the simulation model in the future.

The results showed an important impact of the driving pattern on the range of the BEV as it was expected, in this case we can see very extreme situations as circuit sport driving and normal city driving,

and therefore results are in line with those corner cases. This work contributes to the understanding of this problematic around BEVs and demonstrates the possibility to use simulation in order to judge, analyze and right-size the capacity of the battery, promoting the front loading in the development of future BEVs.

2. Methodology and tools

The 0D simulation model was develop using AVL CRUISE™ M tool then adjusted and validated using real life data. The adjustment of the model was mainly performed in the vehicle coast-down and HV system, to be able to predict as well as possible real life energy consumption.

In this section, a brief description of the tool used for the simulation is presented and an explanation of the developed 0D model used for the study.

2.1 AVL CRUISE™ M Tool

AVL CRUISE™ M is a multi-disciplinary vehicle system simulation tool. Suitable to assist during the whole powertrain development cycle.

With AVL CRUISE™ M vehicle makers can predict energy efficiency and performance early in the concept phase. This can even be achieved when little vehicle data is available. It enables the modelling, among others, of the driveline, electric network and control strategies, while showing their impact upon energy consumption and emissions. The software's flexibility allows to switch easily between conventional, hybrid and electric powertrain concepts.

AVL CRUISE™ M includes the possibility to model different physical domains, including thermodynamics, mechanical and chemical systems, flow and electric. This allows for the detailed design layout and optimization of numerous sub-systems, such as engine gas exchange and combustion, exhaust gas after-treatment system, driveline, cooling circuit, hydraulic and pneumatic networks, electric network and HVAC systems.

Control unit development and calibration can be front-loaded, starting in the virtual environment. Individual office models can then be reused in environments such as MiL, SiL or a real-time HiL. Real time office models can be reused as plant models on virtualized engine, powertrain or chassis dyno testbeds. This is perfect for controller validation and component testing.

The AVL approach encapsulated in AVL CRUISE™ M is applicable over the entire engineering process and works well in combination with third party tools. This enables its integration on existing development environments, while saving cost and time.

2.2 0D Simulation Model

The base BEV used for the study is a supercar with 4 e-motors in the rear axle, two per side. The developed model using the tool AVL CRUISE™ M is a representation of a 0D BEV model without lateral dynamics. The 0D models are determined by an ordinary differential equation in function of time as independent variable. Even though AVL CRUISE™ M is capable of including lateral dynamics, it is not its main focus, and the evaluated vehicle does not use a differential.

In Figure 1 the EV model in an AVL CRUISE™ M environment is presented. The model is structured in different model zones such as the vehicle itself, evaluation and visualization, the driving maneuver, eBrake regeneration split and battery power limitation strategy.

In the vehicle model, a BEV with rear propulsion with two e-motors (as a simplification of the four identical motors in the actual vehicle) and a planetary transmission to the wheel is presented. The required components for the BEV model are seen outside the color boxes. The components required for evaluation and visualization of the plant, such as visualization monitors, KPIs for evaluation, real data time traces and calculation function, are presented in the yellow box. The blue one holds everything which refers to the driver and the driving profile definition. In the green box, the eBrake regeneration split strategy is defined including the eBrake control of the motors and the recuperation weight. The last color

box, in red, holds the open loop battery power limitation control, including the battery power limits, a drawn current estimation, the power control and a low pass filter for the derated load fed to the motors.
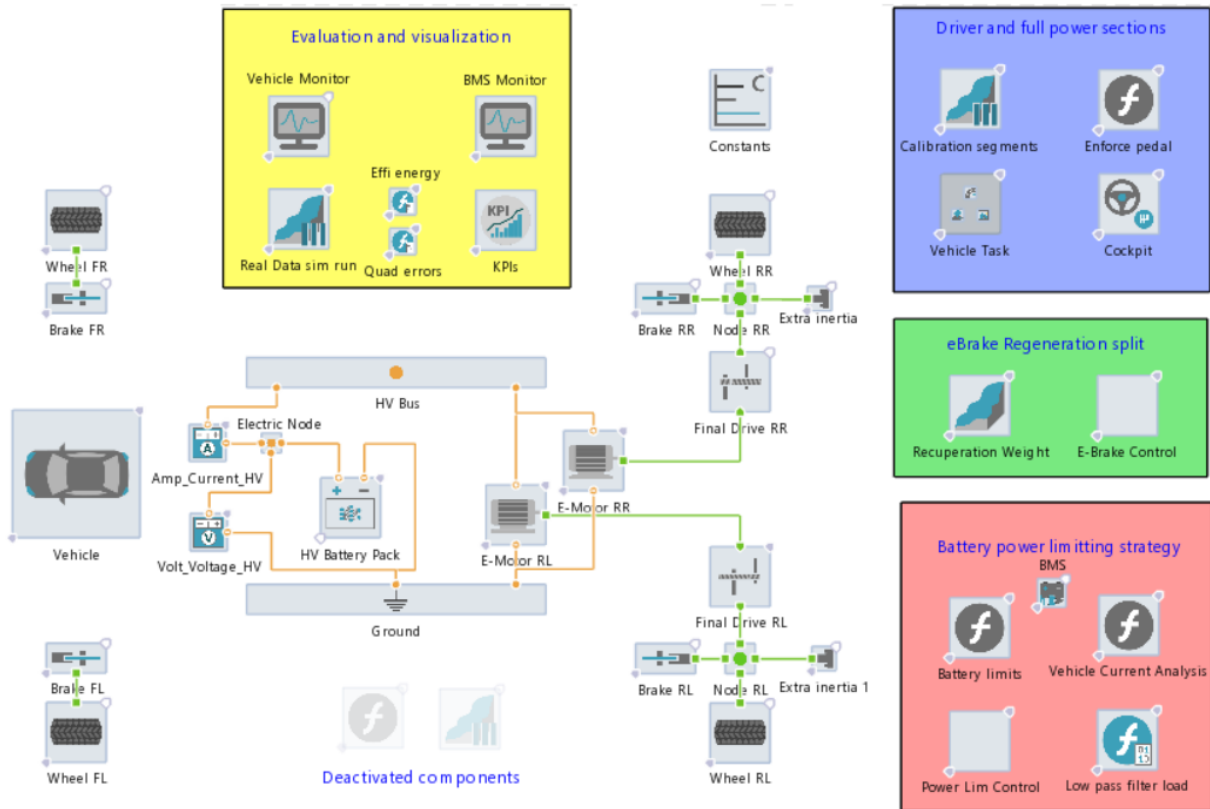

Fig. 1. Base BEV model in AVL CRUISE™ M

Focusing on the vehicle model and starting on left side of the Figure 1 It can be observed, the front wheels with their specific brake discs, the HV battery component modelling the whole pack, the vehicle block with general information and dimensions, the two e-motors connecting the electric to the mechanical networks, the rear wheels with their final drive and their specific brake discs. Important to mention that the green lines show a mechanical connection between the different components whilst the orange lines represent the electrical connections, other physic domains would be represented by other colors.

The available real dataset to adjust the model was a two-lap recording to a circuit where a battery SoC of almost full charge to 73% was observed. This will derivate in overestimation of the range in cycles where the SoC is near minimum values since the behavior of discharge is not lineal. Although, for this study it will not influence the final output.

First, the measured HV Battery voltage/current data was introduced into an ad-hoc battery testing model in AVL CRUISE™ M seen in Figure 2 in which the measured current was imposed into the battery. A series of DoE and optimizations runs (features native to AVL CRUISE™ M, though the normal procedure would have been fitting the model out of supplier information with the dedicated battery fitting wizard) were used to perform a parameter identification of the relevant battery semi-empirical model´s parameters.

Once the HV Battery subsystem was fitted, the whole BEV model was built around the recorded velocity trace. During the two laps of the data, the battery discharge was limited to 350 kW for the first and 500 kW for the second lap. This was replicated in the model with a simple open loop control derating the load signal to the traction machines. The implemented open loop control and the saturation strategy implemented is good enough as its control error, in open loop, is around 3% (aprox 515 kW of actual battery saturation for the intended 500 kW value)
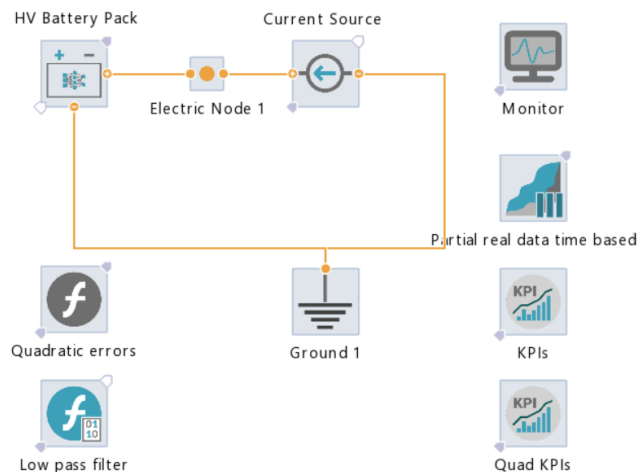
**Fig. 2.** Ad-hoc battery testing model in AVL CRUISE™ M

Once the derating control strategy was implemented, the sections of the two lap recordings in which it was observed that the battery was limited to the corresponding power were identified and brought into the simulation as part of the overall control strategy. When the simulated vehicle was within the segments of the lap in which the battery was limited to its full power, the virtual driver´s control output was overwritten with a 100% demanded load, later fed to the derating strategy. In this way it was expected for the simulated vehicle to achieve maximum performance figures in the lap segments in which the actual test used full power independent of the driver´s model.

The load overwriting strategy explained on the previous paragraph made possible to, having already calibrated the battery´s semiempirical model, perform another round of DoEs and optimization runs aimed at identifying the vehicles´ losses: the constant, linear and quadratic terms as well as the overall driveline efficiency. Being those the degrees of freedom to identify, the system responses used to calibrate them were the overall RMS error for the SoC time trace, the maximum velocity recorded as well as the RMS error of the velocity trace in the areas in which the battery was operated at its corresponding limit, in other words, under full allowed power ignoring the virtual driver´s output. This is the reason why both, the battery subsystem had to be calibrated, and a suitable derating strategy, were needed before proceeding to the vehicle´s losses characterization.
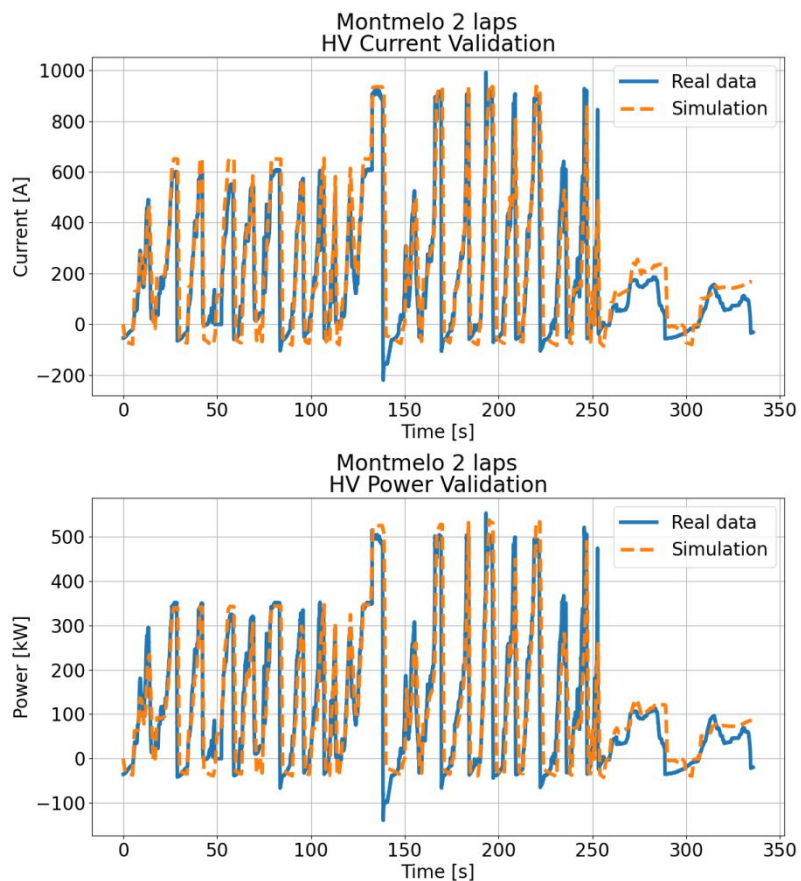
3. Model Validation

The HV SoC of the battery and velocity validation plots are presented in the top and bottom figures of Figure 3. In Figure 4 it is shown the real and simulated data of HV Current and HV Power. In Figure 5 the comparison between real and simulated data is performed with a parity plot in order to assess the R^2. To show the accuracy of the model, a R^2 of 0.99 can be observed for the SoC of the HV battery and a R^2 of 0.91 for the velocity. The error in the velocity profile comparison can be explained because of the control structure, the simulated velocity is the outcome, being the real velocity profile the system´s demand. Naturally having performed a forward-style simulation, the system´s response will be slightly delayed with respect to the system´s demand. Moreover, there is not enough information regarding the elevation profile of the track and this simplification of the model could explain small velocity errors in some local points of the track.

The validation performed, demonstrates the correct behavior of the model after adjusting the vehicle and powertrain parameters. This provides a model that can be used to predict the outcome of this vehicle with different driving patterns in a correct way.
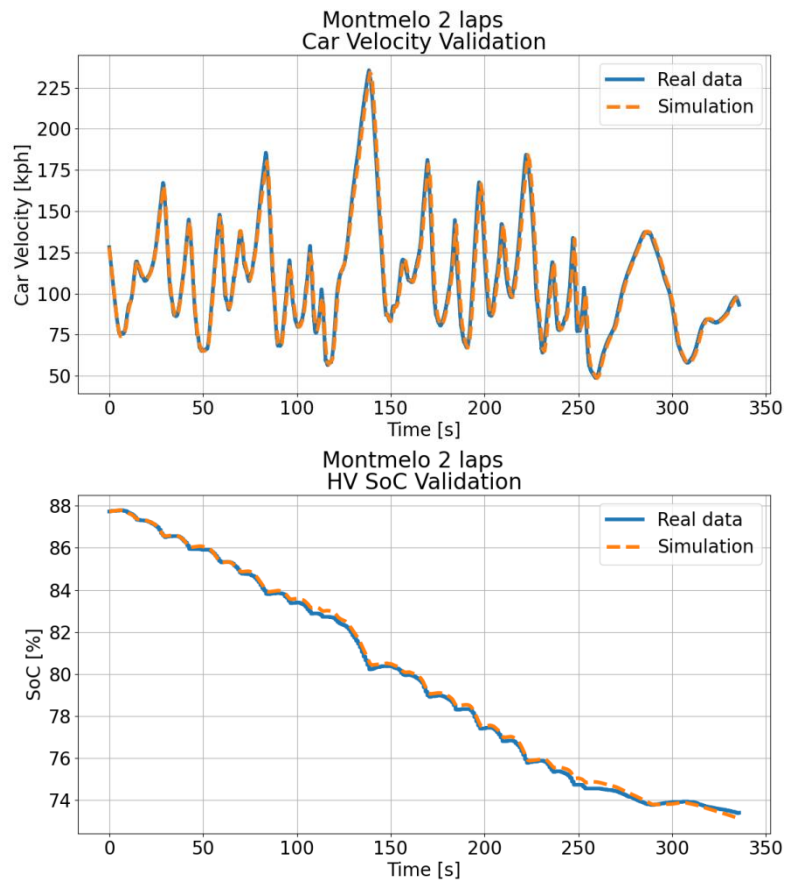
Fig. 3. Car velocity (top) and HV SoC (bottom) Validation

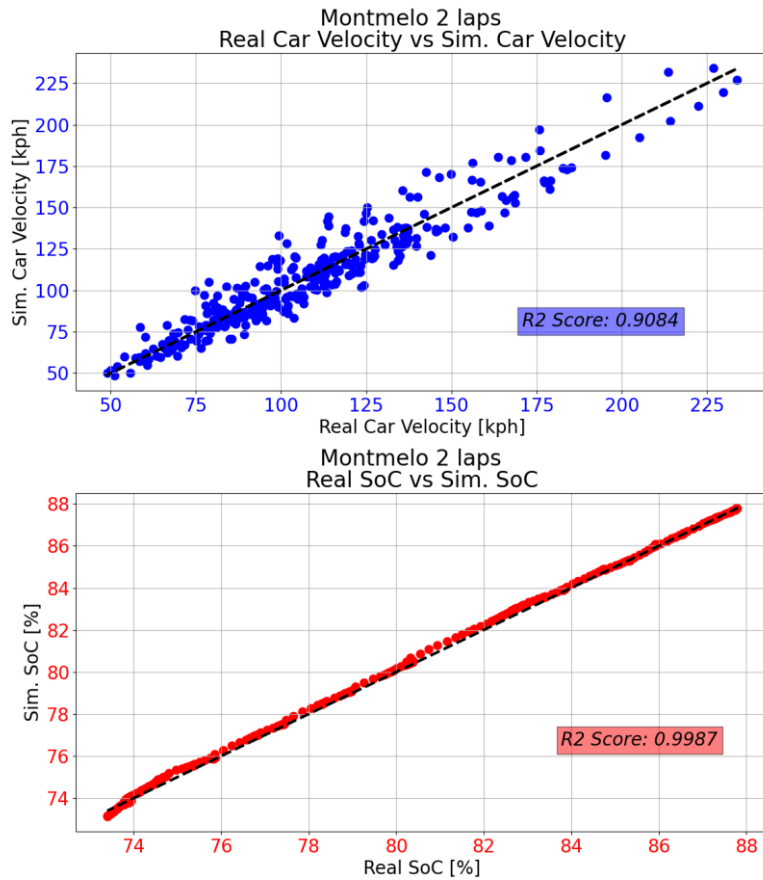**Fig. 4.** HV Current (top) and HV Power (bottom) validation

Fig. 5. Model accuracy - Car velocity (top) and HV SoC (bottom) Validation

4. Results and analysis

In this section the principal results of the simulations using different types of vehicle velocity profiles are going to be presented. In these results, the velocity profile of the simulated cycle, the HV battery SoC, voltage and current are going to be presented for evaluation. A part of these principal variables of the HV system, the range of the BEV, final SoC of the HV battery, %SoC/km, total regenerated power (HV Charge Battery) and total discharge power (HV Discharge Battery) are calculated for each cycle simulated in order to evaluate the impact of the different types of driving patterns. Please note, the initial SoC was chosen as 87.7% for all the cycles.

Table 1. Range of BEV model depending on the homologation cycle

Cycles	Final SOC [%]	Distance [km]	km / %SOC	HV Discharge Energy [kWh]	HV Charge Energy [kWh]	HV Energy In/Out Efficiency [%]	Range [km]
NEDC	76,15	10,99	0,97	54989,22	-359,13	0,65%	96,86
WLTC	63,09	23,31	0,96	118371,12	-1339,02	1,13%	95,53
RDE	10,03	68,27	0,88	376744,30	-5628,03	1,49%	88,12
Cycle 2	79,93	7,46	0,99	37308,09	-1092,70	2,93%	98,52
Cycle 3	64,23	22,50	0,97	114292,34	-2921,34	2,56%	96,69
Cycle 4	80,77	6,29	0,93	33060,40	-984,90	2,98%	93,45
Cycle 5	81,15	7,12	1,12	34506,70	-3916,88	11,35%	112,14
		Total AVG	0,97	109896,02	-2320,29	3,30%	97,33
FLA	80,60	3,10	0,45	32850,00	0,00	0,00%	44,93
Montmelo Data	73,20	9,99	0,70	75236,00	-5142,00	6,83%	68,60

In the next Figures 6, 7 and 8, the results for the principal and most important cycles will be presented as an example NEDC, WLTC and a typical hard RDE.

In Figure 6 the results for a NEDC can be seen, the SoC and the velocity profile represented in the top part of the figure and the HV current and voltage on the bottom part of the figure. In Figure 7 the results for a WLTC cycle can be seen, the SoC and the velocity profile are represented on the top part of the figure and the HV current and voltage on the bottom part of the figure. In Figure 8 the results for a RDE cycle can be seen, the SoC and the velocity profile are represented on the top part of the figure and the HV current and voltage on the bottom part of the figure.

When analyzing these three cycles, as it was expected, the highest SoC of the HV battery at the end of the cycle is for the shortest and less transient cycle, the NEDC. On the other hand, when the current is observed during the cycle, a similar peak can be seen in the NEDC, WLTC and RDE cycles, around 110 A in the last phase of the cycles.

A voltage drop is also observed during the cycles, being the RDE cycle the longest and where it can be seen the biggest voltage drop of the three cycles of the comparison. This of course goes in the same direction as the evolution of the HV battery SoC, as it was expected, more transient demand, higher acceleration rates will require more power and will impact in a more severe way the calculated BEV range under those conditions. The HV and motor efficiency are dependent of motor operational points which rely on motor rotational speed and torque demand, so at higher acceleration loads the motors efficiency slightly worsens This is true for some of the cycles simulated that can be seen in Table 1 but in the comparison of these three standard cycles, similar range can be observed.

Furthermore, the regenerative braking will be more efficient in the case of a moderate transient and moderate deceleration rate demand since it has been limited to around 50 kW. This limitation of regenerative power will have an optimal type of cycle, the one that can have the most regenerative events near the maximum or at the maximum capacity of the system and the less events with a high acceleration rate and lower velocity. In Table 1, it can be observed that in this case the RDE is where a higher amount of energy was accumulated during regeneration, but on the other hand is in cycle 5 where the best ratio of power deployed and recovered is observed and because of that is also the cycle with the highest range prediction. SoC lower limit has been set in 10% that is the reason why the RDE simulation stops abruptly.

Standard homologation cycles seemed to have similar impact in the range of the vehicle, as it was mentioned before. But when changing the driving pattern to a sporty driving, in comparison to these standard cycles, like the example of the two laps to the Montmelo circuit, this impacted directly in the predicted range of the vehicle as it was expected reaching a reduction of around 30%. On the other hand, when changing to a more "efficient" driving pattern compared to these standard cycles, like in the case of cycle 5 which favors the efficiency of the powertrain, an increase of 15% of the range can be observed. This can be explained due to the big amount of decelerations from 60 to 0 kph that increase the ratio between HV Power Charged and HV Power Discharged. The velocity / acceleration scatter plot of cycles 2, 3, 4 and 5 are shown in Figure 9 and Figure 10 in comparison to a standard WLTC cycle.
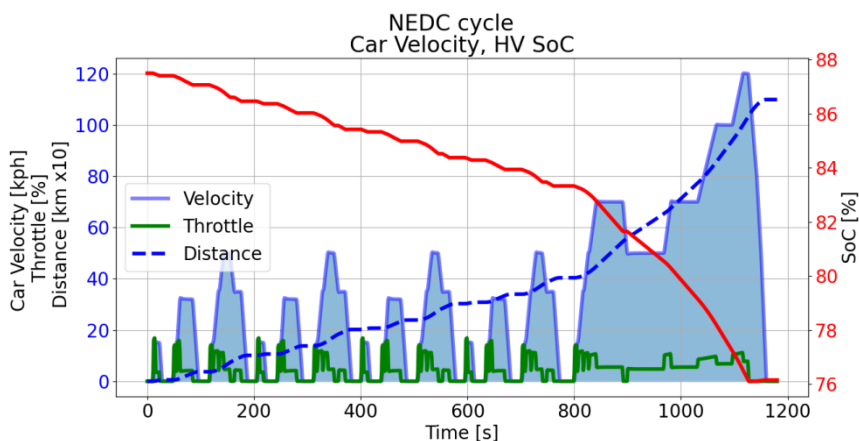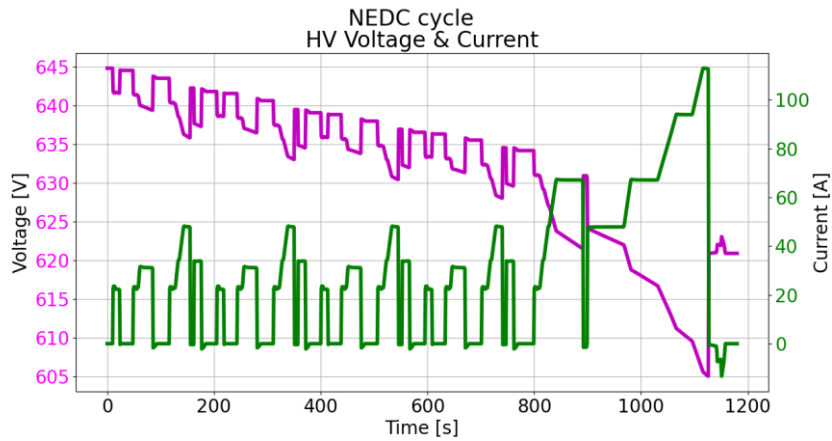
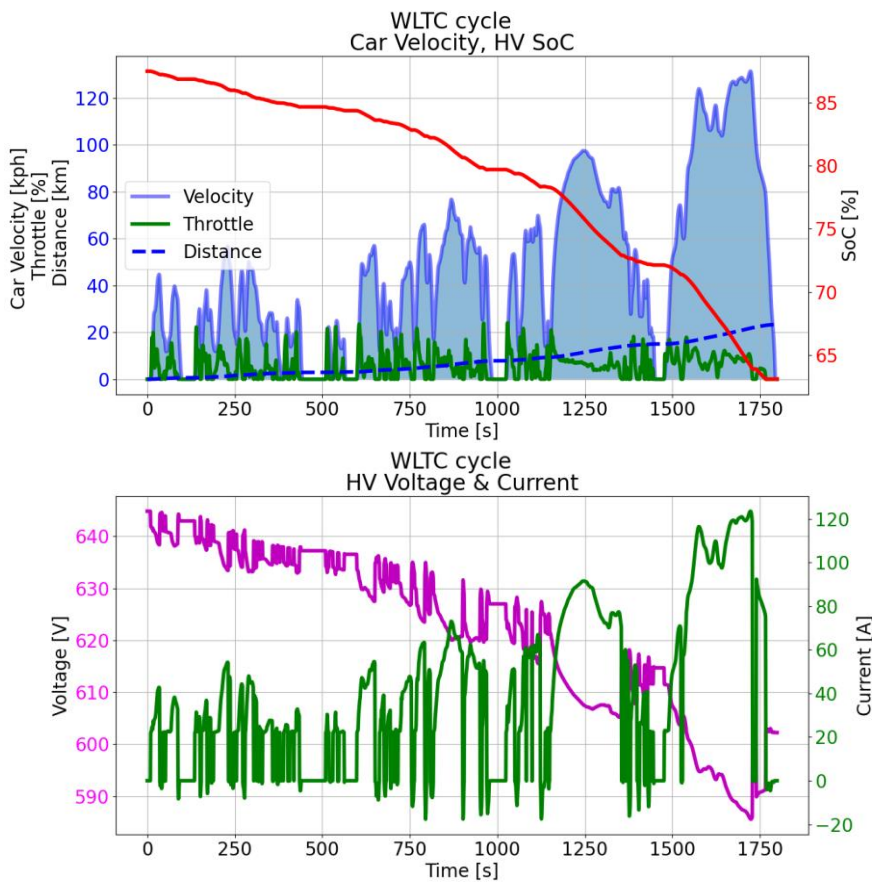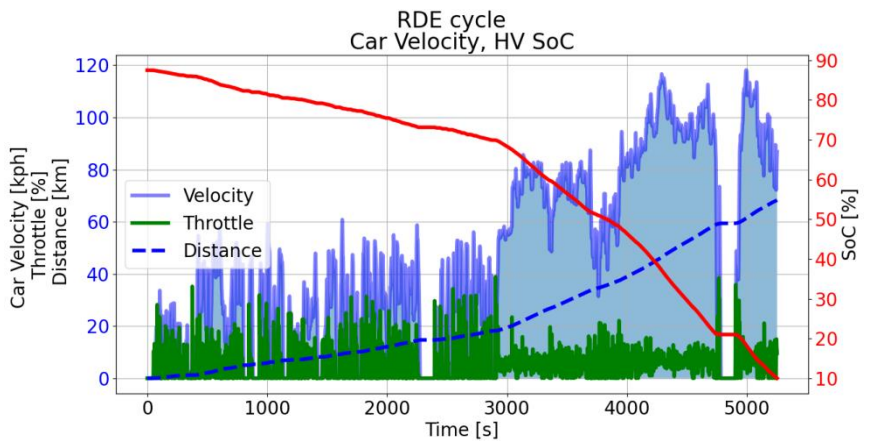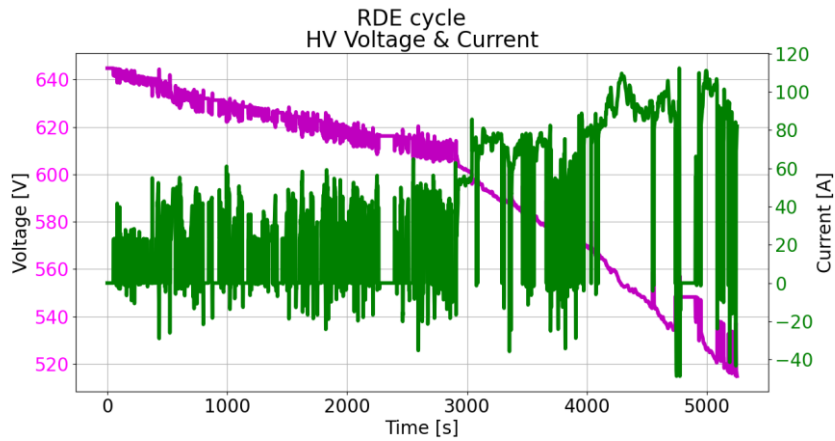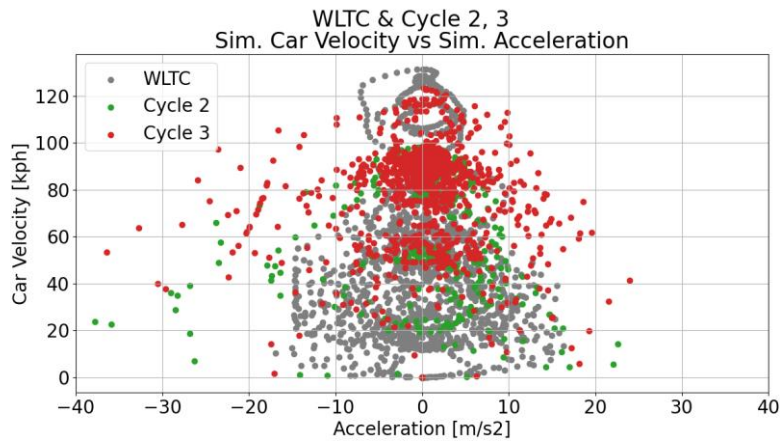**Fig. 6.** NEDC - Car velocity & HV SoC (top) and HV Current & Voltage (bottom)

Fig. 7. WLTC - Car velocity & HV SoC (top) and HV Current & Voltage (bottom)
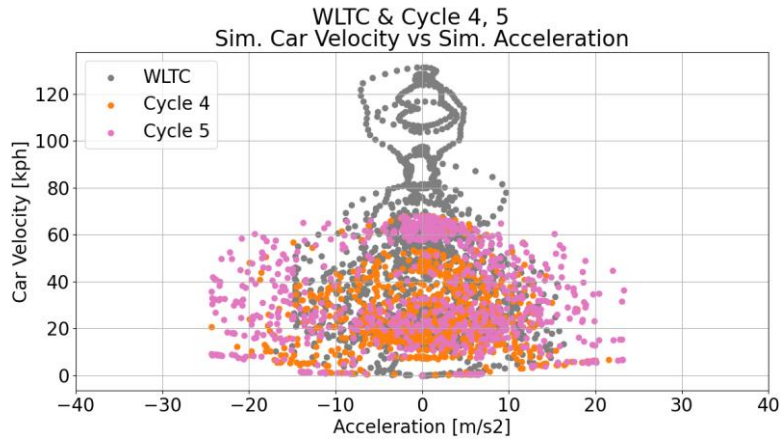
Fig. 8. RDE - Car velocity & HV SoC (top) and HV Current & Voltage (bottom)

Fig. 9. Comparison between Cycle 2, 3 and WLTC

Fig. 10. Comparison between Cycle 4, 5 and WLTC

Furthermore, to study in more detail the influence of the regeneration limit of the HV Battery in the final SoC, a series results simulation was performed. In that simulation, the cases are created changing the regeneration power limit of the HV control strategy that in the real data was set to 50 kW. The assessment is carried out from 25 kW to 200 kW analysing the HV final SoC and range. To be able to show in a better way the results, a comparison is observed in Figure 11 and 12, where the same plot is presented for a standardized driving type profile (WLTC) and a sporty circuit driving type profile, in which it is clearly observed that in the WLTC it is pointless to increase the regeneration power limit beyond a certain initial value as the cycle itself does not present braking events powerful enough to profit from higher regeneration powers. On the other hand, it is observed that for the circuit driving, the range and final SoC keeps rising until the máximum regeneration power (200 kW).
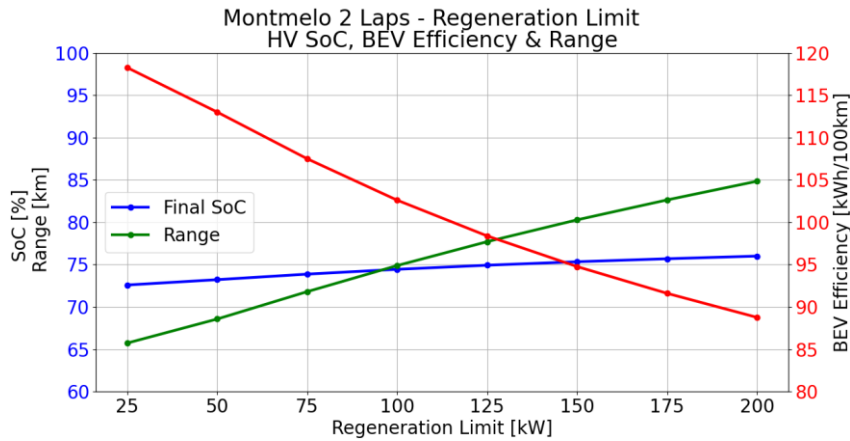
Fig. 11. Relationship between HV final SoC / Range in Montmelo 2 laps and HV regeneration limit
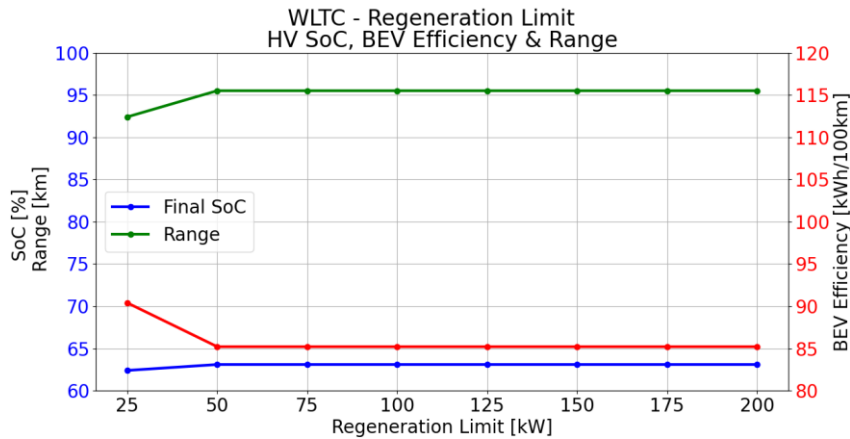

Fig. 12. Relationship between HV final SoC / Range in WLTC and HV regeneration limit

5. Conclusions

A simulation model of a supercar BEV was developed in order to evaluate the influence of the velocity profile into the calculated range of the BEV. A specific validation process was developed to warranty the correct behavior and accuracy of the model.

After the model was successfully validated with real data, the simulations were performed using different cycles that covered a wide range of acceleration rates and velocities. It was demonstrated how the driving pattern, transient acceleration rate variation and velocity ranges could impact the calculated range of the BEV. In this case, a much more specific situation, taking into account the high electric power of this BEV.

It was observed how an aggressive and circuit type driving can reduce as much as 30% the range of the BEV, whereas with a more standard type of velocity profile or type of conduction the range of the vehicle is more than 95 km. The recovered energy played a big role on the final efficiency ratio of energy recovered vs energy deployed per km, this means that depending on the vehicle specifications, recovery energy capacity, e-motors´ power and coast down characteristics, certain driving patterns will influence more or less the vehicle range. As it was observed the most beneficial cycle in this case, increased the range by 15% approximately when compared to standard homologation cycles.

This work demonstrates the big impact that the predicted BEV range can suffer when driving patterns are changed with a variation of -50% (in case of FLA) to +15% (in case of cycle 5), which means that more work is still necessary in order to adjust this predictions and how it is transmitted to the client.

In addition, this work also demonstrates the usage of simulation to evaluate challenging tasks during the development of a BEV, where a proper developed model can bring a proper analysis of different conditions supporting in the correct sizing of the battery pack for the application.

12   M. Montesinos, M. Rivas, E. Elipe

References

Bryan, S. G. (2017). Big Data Analysis of Battery Charge Power Limit Impact on Electric Vehicle Driving Range while Considering Driving Behavior . *WCX™ 17: SAE World Congress Experience*, 7.

Eisenstein, P. A. (2019, 03 18). AAA Studies Thermal Effects on EV Range. *SAE International*.

Helmes, M. C. (2013). Critical evaluation of the European diesel car boom - global comparison, environmental effects and various national strategies. *Environmental Sciences Europe volume 25*.

Holding, J. (2021, 08 19). *Autocar*. Retrieved from https://www.autocar.co.uk/car-news/electric-cars/ev-prices-rose-28-europe-yet-halved-china-past-decade

Jiang Yu, Y. N. (2019). Simulation Study on Driving Range at High and Low Temperature. *New Energy & Intelligent Connected Vehicle Technology Conference*, 5.

Pole, J. (2022, 05 12). *Euronews.green*. Retrieved from https://www.euronews.com/green/2022/05/12/eu-wide-ban-on-new-fossil-fuel-cars-to-kick-in-from-2035-as-lawmakers-back-proposal

YOUNGCHUL LIM, Z. E. (2020). A Development of Battery Aging Prediction Model Based on Actual Vehicle Driving Pattern. *WCX SAE World Congress Experience*, 11.

Yue Zhou, R. W. (2020). Optimal battery electric vehicles range: A study considering heterogeneous travel patterns, charging behaviors, and access to charging infrastructure. *Energy Journal.*

Poster Session

OH* and NL Measurements of Two HD Diesel Injectors with Identical Cetane Number Fuels, RME and Diesel

H. Fajri, S. Rieß, R. Clemente, M. Wensing

[1] Professorship for Fluid Systems Technology, Friedrich-Alexander-Universität Erlangen-Nürnberg FAU, Germany

E-mail:
Hamidreza.fajri@fau.de, Sebastian.riess@fau.de, Rafa.clemente@fau.de, Michael.wensing@fau.de
Telephone: +(49) 9131 85-29770

Abstract.

In the transition to sustainable mobility, drop-in biofuels are important both in the short- and medium-term transfer process and as a sustainable energy route in the long term. Rapeseed Oil Methyl Ester (RME), which is produced by esterification of the rapeseed oil is analysed along with reference diesel fuel with identical cetane numbers in a constant volume combustion chamber by utilizing two optical methodologies, OH* chemiluminescence and natural flame luminosity (soot). Excluding the influence of cetane number on ignition delay brought a chance to relate fuel volatility and oxygen content to start of the ignition and the lift-off length. Although the results illustrate RME has a higher liquid penetration and a visible delay regarding the liquid/vapour phase change, this biofuel nevertheless shows a shorter ignition delay when it compared to diesel - due to its chemical structure including 10% of oxygen.

In the current study, a high-speed camera with an intensifier and a band-pass filter (around 308 nm) is synchronized with a second high-speed camera which are simultaneously utilized to scrutinize the combustion behaviour of two large-scale heavy-duty marine injectors with an outlet diameter of 300 micrometres. The two injectors with a conicity factor of 0 and 4 demonstrate geometry effects and show visible diversity in flame initiation and propagation and connect spray cone angle and penetrations to the formation and location of soot and OH* signals. The results shed light upon the fact that more air entrained to the spray due to a wider cone angle in the cylindrical nozzle has a non-negligible influence as it causes faster ignition initiation. The ability to change the ambient properties in the combustion chamber means that ignition delay, the length of the lift-off process and soot formation can be correlated with the real conditions in the engine cylinder and influences of individual parameters can be analyzed in isolation.

1. Introduction

Natural flame luminosity (soot) and OH* chemiluminescence have been widely utilized to figure out soot formation and ignition incidence in CVCs and optical transparent engines.

Theoretically, OH* occurs during the second stage of the ignition process [1] results from near-stoichiometric high-temperature combustion [2]. Accordingly, the first OH* signal is referred to the pre-mixed phase initiation. The natural luminosity signal is initiated later at the premixed phase which is developed sharply due to fast flame expansion and fuel burning. It should be highlighted that the ignition time and lift-off length may have an impact on the combustion and soot processes during the mixing controlled phase of combustion [3].

2. Theory

According to [4, 5], the flame lift-off length could have the following relationship to different parameters:

$$H = CT_a^{-3.74}\rho_a^{-0.85}d^{0.34}U^1Z_{st}^{-1} \tag{1}$$

H (mm) represents lift-off length, C is a tuning constant, T_a (K) is ambient temperature, ρ_a (kg/m³) is ambient density, d (μm) is injector nozzle exit diameter, U (m/s) is injection velocity and Z_{st} is stoichiometric mixture fraction.

2. Fuel Specifications and Nozzles

The first generation of biodiesel, RME fuel, was assessed and compared to reference diesel fuel in this study. The fuel parameters are shown in Table 1 and nozzles specifications are depicted in Table 2.

Table 1. Fuels Specifications

Specifications	Diesel RF-06-03	RME
Density [kg/m3]	834	882.7
Lower Heating Value [MJ/kg]	43.2	37.2
Cetane Number	52.4	51
Stoichiometric air-fuel ratio	14.51	12.56
Kinetic viscosity in the temp. of 20°C [mm^2/s]	2.749	4.474

Table 2. Nozzles Specifications

Parameters / Nozzles	$\emptyset_{entrance}$ [μm]	$\emptyset_{exit}$ [μm]	Length [mm]	L/D [--]	K factor [--]
Conical	340	300	1.3	4.33	4
Cylindrical	300	300	0.65	2.16	0

3. Liquid Spray and OH* Signal

Figure 1 (left side) demonstrates a comparison between the cylindrical and the conical nozzles using both Diesel and RME fuels. The outcome begins to compare exactly 350 seconds after the injection begins, when there is no ignition signal at all. At least one or two shots (out of 32) with RME fuel are started to burn at the next recorded image (375 seconds after SoI), in this case, the exterior border of the OH* signal is depicted as a black line across the liquid phase of the spray. There are several reasons for RME ignition to occur more quickly, which can be classified as follows:

1- The RME oxygen-carbon bond is considerably easier to break than other fuel bonds such as carbon-carbon or carbon-hydrogen, which could speed up ignition and the first phase of combustion.

2-In comparison to Diesel, RME has a stoichiometric air-fuel ratio of 12.5 against 14.5. Consequently, RME is set to reach the stoichiometric region faster than diesel, resulting in faster mixture formation.

The flame lift-off length, as indicated by the left-written length, indicates that there is currently a discernible difference between two injectors.

The following time steps show how quickly flame propagates in both axial and radial directions. In theory, starting flame velocity is strongly influenced by how near a region comes to a stoichiometric state, which can be adjusted by nozzle designs. Due to the cavitation mechanism, the cylindrical nozzle is able to evaporate fuel faster and introduce significantly more air to the spray plume as a result of its broader cone angle. In the end, it is feasible that the initial ignition time of the cylindrical nozzle could be shorter. In general, the final time-averaged flame lift-off length is estimated during the quasi-steady phase of combustion (which in this case is after 500 seconds), therefore no reason other than the cylindrical nozzle faster fuel evaporation could explain why its LoL is placed under the conical nozzle.

4. OH* Signal and Natural Flame Luminosity

Natural luminosity refers to the broad band light emitted by high-temperature soot particles during combustion, which is mostly created in the rich zone when the flame is exposed to a mixture-controlled diffusion flame. When RME and Diesel fuels are compared from the time they begin to burn, Diesel produces much more soot and forms it much faster than RME due to two factors: first, diesel has higher aromatics compounds, which makes diesel fuel much sootier and facilitates soot formation, and second, RME has a high amount of oxygen, which causes it to produce less and delay soot formation. Although the start of soot formation is much sooner in RME (Figure 1 right side) when both compared from the start of injection because of high early ignition incidence of RME fuel. The right-written length illustrates

soot lift-off length. In comparison to diesel fuel, RME SLoL remains longer than its FLoL during the quasi-steady phase of combustion. The key reason is because RME contains 10% oxygen, which results in less soot production. Finally, because soot formation is directly connected to the time of ignition incidence, the cylindrical nozzle accelerates soot formation due to its shorter ignition delay.
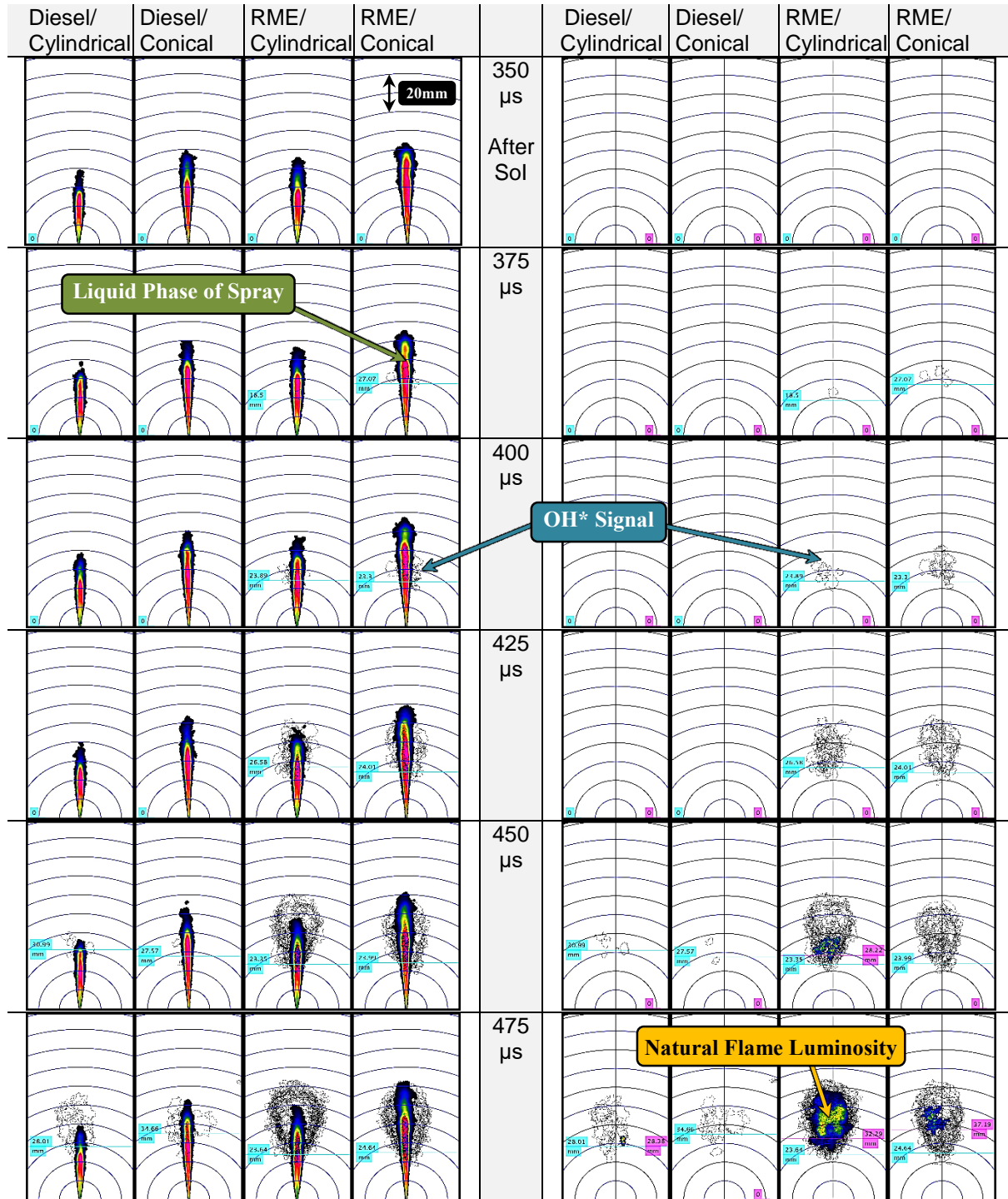

Fig. 1. Left Side: OH* Signal and Liquid Phase of Spray, Right Side: OH* Signal and Visible Natural Luminosity

5. Ignition Delay

The first appearance of OH* signal could not be taken into consideration as the ignition delay, therefore, a cumulative Gaussian distribution is passed through the first signal occurrences from the first point

4   H. Fajri, S. Rieß, R. Clemente, M. Wensing

before the initial OH* signal to the first point of time where all 32 injections have begun to burn. The ignition probability based on the number of ignition incidences per time for analysed points is depicted in Figure 2. Accordingly, Table 3 considers the final ignition delay time and indicates that the cylindrical nozzle and RME fuel have a tendency to reduce ignition time.
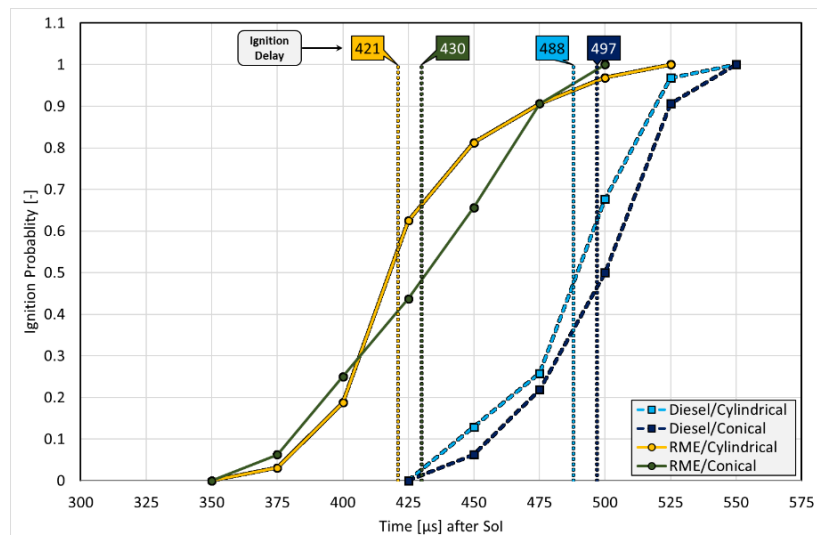

Fig. 2. The Number of Ignition Events per Time – Comparison of All Points

Table 3. Ignition Delay Time and Relevant Standard Deviation

	Ignition Delay [µs] after SoI	Standard Deviation [µs]
Diesel/Cylindrical	488	24
Diesel/Conical	497	25.5
RME/Cylindrical	421	28
RME/Conical	430	38

6. Conclusion

OH* chemiluminescence and natural flame luminosity measurements of two fuels, RME and reference Diesel have been carried out in the current study. The RME oxygen-carbon bond and its lower stoichiometric ratio makes ignition time shorter and delays and reduces soot formation. Apart from that, in comparison to diesel fuel, RME SLoL remains longer than its FLoL during the quasi-steady phase of combustion because of its 10% oxygen content. The cylindrical nozzle broader cone angle allows it to evaporate fuel faster and introduce substantially more air to the spray plume due to the cavitation mechanism. Therefore, it is plausible that the ignition time of the cylindrical nozzle might be reduced. In addition, because the time of ignition incidence is directly related to soot formation, the cylindrical nozzle promotes soot formation due to its shorter ignition delay.

7. References

1. Cárdenas, M., et al., "Investigations of Clustred Diesel Jets under Quiescent High-Pressure and High-Temperature Conditions using Mie, Schlieren and Chemiluminescence Imaging". *SAE International Journal of Engines*. 2(2): p. 272-286, 2010, DOI: 10.42712009-01-2771.
2. Kojima, J., Y. Ikeda, and T. Nakajima, "Spatially resolved measurement of OH*, CH*, and C2* chemiluminescence in the reaction zone of laminar methane/air premixed flames". *Proceedings of the Combustion institute*. 28(2): p. 1757-1764, 2000, DOI: 10.1016S0082-0784(00)80577-9.
3. Pickett, L.M. and D.L. Siebers, "Fuel effects on soot processes of fuel jets at DI diesel conditions". *SAE transactions*: p. 2044-2066, 2003, DOI: 10.42712003-01-3080.
4. Siebers, D. and B. Higgins, "Flame lift-off on direct-injection diesel sprays under quiescent conditions". *SAE Transactions*: p. 400-421, 2001, DOI: 10.42712001-01-0530.
5. Siebers, D., B. Higgins, and L. Pickett, "Flame lift-off on direct-injection diesel fuel jets: oxygen concentration effects". *Sae Transactions*: p. 1490-1509, 2002, DOI: 10.42712002-01-0890.

Very Low Soot Combustion with Modulated Liquid Length and Lift-off Length of Diesel Spray Flame

C. Zhai, K. Nishida, Y. Ogata

Department of Mechanical Engineering, University of Hiroshima, 1-4-1 Kagamiyama, Higashi-Hiroshima, 739-8527, Japan.

E-mail:　　　nishida@hiroshima-u.ac.jp
Telephone:　　+(81) 82 424 7694

Abstract. To further study the spray and combustion characteristics under ultra-high pressure, the liquid length and combustion characteristics of multi-hole injectors have been investigated under different injection pressures via an experimental method. The results show that the time for the liquid length to reach a stable stage reduces with the increase in injection pressure and decrease in hole diameter. When the liquid length is longer than the flame lift-off length, a large amount of soot is generated during combustion. Through the intersection of the liquid length and flame lift-off length trend line, it is estimated that the region of the liquid length is less than the lift-off length under different conditions.

1. Introduction

　　　　Owing to increasingly stringent emission standards, many efficient injection and combustion strategies have been proposed [1]. Higher injection pressures and smaller hole diameters are beneficial for improving fuel atomization [2]. Previous studies pertaining to ultra-high injection pressures or micro-hole primarily focused on single-hole injectors, whereas in actual engines, eight- or ten-hole multi-hole injectors are used. Meanwhile, an interaction occurs between spray and a spray during the injection of the multi-hole injector. In this study, we used the diffuse back-illumination imaging (DBI) method, two-color pyrometry, and the OH* chemiluminescence method to compare the effects of increasing the injection pressure and reducing the hole diameter on the spray and combustion characteristics. Finally, the relationship among LL, LOL, and KL value is discussed.

2. Liquid Length (LL)

　　　　The prediction model of spray liquid length has also been established by many researchers. Higgins et al. [3] established a prediction model of liquid length on the basis of experiments, which has been used or modified by many researchers [4], [5]

$$LL = D_n k A^\alpha B^\beta \tag{1}$$

$$A = \frac{\rho_f}{\rho_a} \tag{2}$$

$$B = \frac{C_{Pf}\left(T_b - T_f\right) + h_{vf}}{C_{Pa}\left(T - T_b\right)} \tag{3}$$

$$D_n = \sqrt{C_a} D \tag{4}$$

Where LL is the Liquid Length, D_n is the effective nozzle hole diameter, k,α,β is a model constant(k=18.4, α=0.51,β=0.37) [6], ρ_f is the fuel density, ρ_a is the ambient gas density, C_{Pf} is the specific heat of fuel, T_b is the fuel boiling temperature, T_f is the fuel temperature, h_{vf} is the latent heat of vaporization of the fuel, C_{Pa} is the specific heat of ambient gas, T is the ambient gas temperature, C_a is the coefficient of area contraction (C_a=0.9) [6], D is the nozzle hole diameter.

　　　　F. Dos Santos et al. proposed the following Liquid Length prediction model in 2011[7]. By modifying Chehroudi's model [8], Eq. (5) is obtained:

$$LL = C_1 \left(\frac{294}{T}\right)^{C_2} D \left(\frac{\rho_f}{\rho_a}\right)^{0.5} \tag{5}$$

Where C_1 and C_2 are two model constants.
Beale and Reitz et al. established the following Liquid Length prediction model in 1999 [9].

$$LL = 0.5B_1D\left(\frac{\rho_f}{\rho_a}\right)^{0.5} \tag{6}$$

Where B_1 is the breakup constant of the Kelvin Helmholtz model (B_1=60) [10].

Figure 1 shows that F. dos Santos' model can more accurately predict the change of liquid length under ultra-high injection pressure conditions. But requires accurate model constants as model input. Higgins' model can also better predict the change in liquid length.
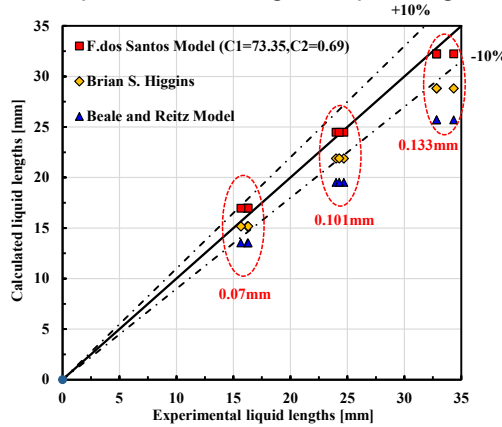

Fig. 1. Comparison of liquid length between current experimental and empirical equations from the literature

3. Lift-Off Length (LOL)

Many researchers have also established LOL prediction models. The regression model was established by Benajes et al [11]. is used by many researchers. The equation is as follows:

$$LOL = kT^a\rho_a^bU_{th}^cO_{2\%}^d \tag{7}$$

Where T refers to the chamber temperature, ρ_a to the chamber density, U_{th} to the theoretical velocity of the fuel at the nozzle exit, calculated by the equation [11]:

$$U_{th} = \sqrt{\frac{2\Delta P}{\rho_f}} \tag{8}$$

Where ΔP is the pressure drop through the nozzle orifice, and ρ_f is the desity of the fuel.

Table 1. Parameter for the lift-off length correlation.

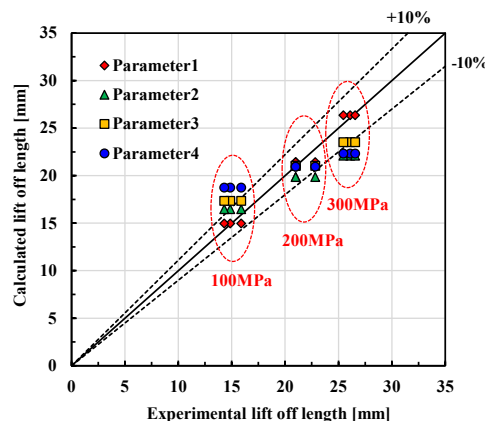| Parameter	a	b	c	d	k
1.Siebers et al. [13]	-3.74	-0.85	1	-1	6.03×106
2.Payri et al. [12]	-3.97	-0.93	0.52	--	3.61×109
3.Benajes et al. [11]	-3.89	-1	0.54	-1	5.10×108
4.Benajes et al. [11]	-5.10	-1.14	0.31	-0.86	1.40×1013

Fig. 2. Comparison of lift-off length between current experimental and empirical equations from literature

The table 1 contains the results obtained by Benajes et al. [11], Payri et al. [12], and Siebers and Higgins [13], for reference purposes. Fig.2 shows the comparison of the four parameters in Table 1 with the experimental results. From the figure, we can find that the results calculated using the parameters of Siebers et al (parameter 1) are most similar to the experimental data.

4. Flame-Area-Integrated KL / Injection Mass

Figure 3 shows the value of the integrated KL (IKL) divided by the integrated fuel mass (IFM). We can find that increasing the injection pressure and decreasing the hole diameter can efficiently reduce the soot mass per unit mass. Compared with reducing the hole diameter, increasing the injection pressure to 300MPa with the large hole diameter injector can obtain the smaller value of IKL/IFM, but the difference of IKL/IFM between these two ways is very small.
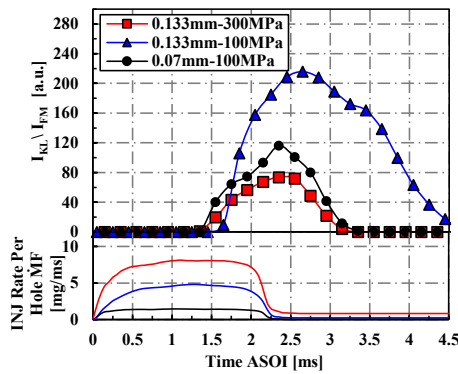

Fig. 3. Temporal Variations of Flame-Aria-Integrated KL (Soot) / Injection Mass

5. Correlation of Injection Pressure and Hole Diameter for Very Low Soot Flame with Modulating LL < LOL

Figure 4 shows a conceptual model of soot formation in the spray flame under modulated LL and LOL with injection pressure and hole diameter. We can find that decreasing the hole diameter will shorter the LL and make the value of LL/LOL less than 1. Increasing the injection pressure will longer the LOL and make the value of LL/LOL less than 1. When the value of LL/LOL is less than 1, the soot generation will be effectively suppressed. This is because the air is usually entrained into the fuel upstream of spray. The intersection of LL and LOL reduces the entrainment of upstream diesel spray. For more detail to analyze and confirm the relationship between the value of LL/LOL and the equivalent ratio at the LOL.
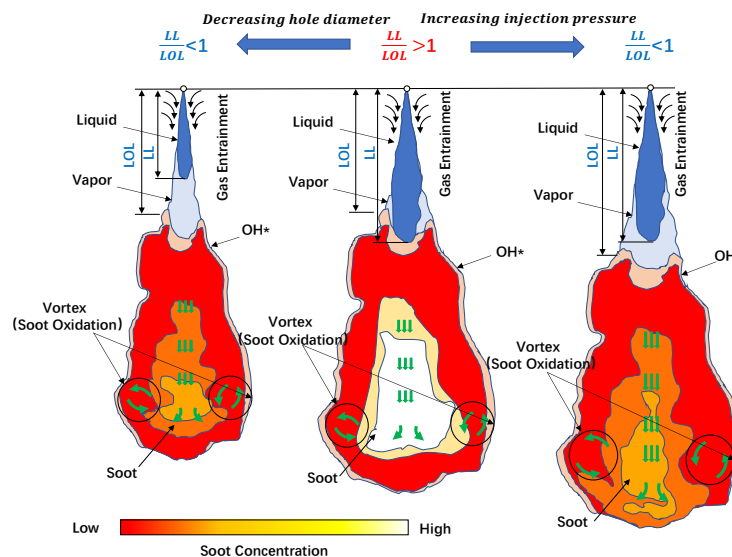

Fig. 4. Conceptual model of soot formation in spray flame, modulating LL with hole diameter and LOL with injection pressure

4   C. Zhai, K. Nishida, Y. Ogata

Figure.5 shows a comprehensive comparison of the liquid length, lift-off length, soot formation, and injection conditions. The size of the sphere in the figure represents the value of the KL divided by injection mass. Through Eq.7 and Eq.5, we can estimate the range of the liquid length less than the lift-off length under different conditions, as shown by the blue dotted line in Fig. 5. The black triangle is the intersection of the experimental LL and LOL. The left side of the blue dotted line is the area with LL/LOL less than one, namely, the liquid length in this area is less than the lift-off length, which helps reduce the formation of soot. The determination of this range provides guidance and suggestions for the selection of hole diameters for injectors and injection pressure for diesel engines.
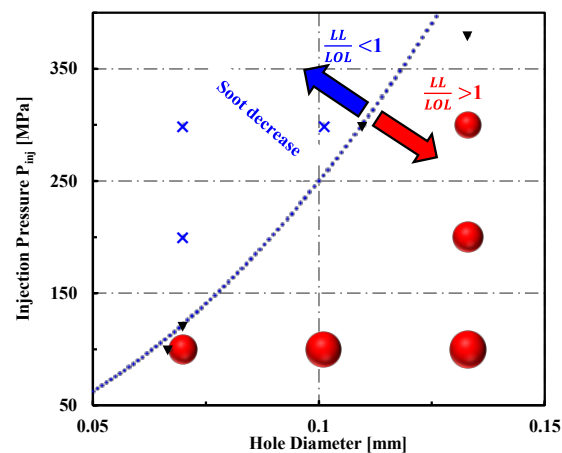

Fig. 5. Correlation of liquid length, lift-off length, and soot.

Conclusions

The F. Dos Santos' model and the parameters of Siebers et al (parameter 1) can better predict the LL and LOL under different conditions. When the liquid length is longer than the lift-off length, the formation of soot is increased. According to the intersection of the LL and LOL prediction model trend line, it is estimated that the range of the liquid length is less than the flame LOL under different conditions. The determination of this range provides guidance and suggestions for the selection of the hole diameters of injectors and injection pressure for diesel engines.

References

[1] Abedin MJ, Masjuki HH, Kalam MA, Sanjid A, Rahman SMA, Masum BM: Renewable and Sustainable Energy Reviews, Vol .26, p. 20-33 (2003).
[2] Johnson J, Naber J, Lee S-Y, Hunter G, Truemner R, Harcombe T: SAE Technical Paper; (2013).
[3] Higgins, Brian S., Charles J. Mueller, and Dennis L: SAE transactions p.630-643, (1999).
[4] Ma, Yinjie, et al: Energy Conversion and Management ,Vol. 130 p. 240-251 (2016).
[5] Payri, Raul, et al: Fuel Vol. 188 p.645-660 (2017).
[6] Payri, Raul, et al: Fuel Vol. 183 p. 20-33 (2016).
[7] Dos Santos, F., and L. Le Moyne:Oil & Gas Science and Technology–Revue d'IFP Energies nouvelles Vol. 66.5 p. 801-822 (2011).
[8] Chehroudi, Behrouz, et al: SAE transactions p.764-773 (1985).
[9] Beale, Jennifer C., and Rolf D. Reitz: Atomization and sprays (1999).
[10] Su, T. F., et al: SAE transactions p.1281-1292 (1996).
[11] Benajes, Jesús, et al: Applied thermal engineering. Vol. 58 p.554-563 (2013).
[12] R. Payri, J. Gimeno, M. Bardi, A.H. Plazas: Applied Energy, Vol. 106 pp. 152-162 (2013).
[13] Siebers D, et al: SAE transactions 2001:400-21.

THIESEL 2022 Conference on Thermo- and Fluid Dynamics of Clean Propulsion Powerplants

Numerical and Experimental Investigations on the Ignition Behavior of OME

Frederik Wiesmann[1], Lukas Strauss[2], Sebastian Riess[2] and Thomas Lauer[1]

[1]Institute of Powertrains and Automotive Technology, TU Wien, 1060 Vienna, Austria

E-mail: frederik.wiesmannl@ifa.tuwien.ac.at; thomas.lauer.tuwien.ac.at
Telephone: +(43) 1 58801 31560

[2]Institute of Engineering Thermodynamics, FAU Erlangen-Nuremberg, 91058 Erlangen, Germany

E-mail: lukas.strauss@fau.de; sebastian.riess@fau.de

Abstract.
On the path towards climate-neutral future mobility, the usage of synthetic fuels derived from renewable power sources, so-called e-fuels, will be necessary. Oxygenated e-fuels, which contain oxygen in their chemical structure, not only have the potential to realize a climate-neutral powertrain, but also to burn more cleanly in terms of soot formation. Polyoxymethylene dimethyl ethers (PODE or OMEs) are a frequently discussed representative of such combustibles.
However, to operate compression ignition engines with these fuels achieving maximum efficiency and minimum emissions, the physical-chemical behavior of OMEs needs to be understood and quantified. Especially the detailed characterization of physical and chemical properties of the spray is of utmost importance for the optimization of the injection and the mixture formation process.
The presented work aimed to develop a comprehensive model, to simulate the spray atomization, mixing and auto-ignition of OMEs and dodecane, which served as a reference diesel-like fuel, for single- and multi-injection patterns. The simulation results were validated against experimental data from a high-temperature and high-pressure combustion vessel. The sprays' liquid and vapor phase penetration were measured with Mie-scattering and Schlieren-imaging for both fuels. To characterize the ignition process and the flame propagation, measurements of the OH* chemiluminescence of the flame were carried out.
The CFD model captured the spray characteristics across different fuels, injection patterns, and ambient temperatures and showed a good correlation with the experiments. Significant differences in the auto-ignition behavior between OMEs and dodecane could be identified in both experiments and CFD simulations. Liquid penetration as well as flame-lift off length is consistently shown to be longer for OMEs. Additionally, the transient behavior of high temperature reactions for OME is predicted to be much faster.

1. Introduction

In order to achieve climate-neutrality, research into the applicability and behavior of CO2-neutral synthetic fuels is essential. Therefore, a steadily growing interest in academic research in this topic can be observed [1]. Oxygenated fuels in particular are of special interest as they provide beneficial combustion properties that can help solve the soot-NO_x trade-off [2]. Polyoxymethylene dimethyl ethers (PODEs), also known as oxymethylene ethers (OMEs), are a quite promising class of such synthetic and oxygenated fuels. Extensive research for various engine types has been done to confirm the potential of OMEs regarding the reduction of soot emissions [3]–[5] and even increased engine efficiency [6]. The lack of *C-C* bonds within the chemical structure of OMEs - $CH_3O(-CH_2O)_n-CH_3$ - together with the high oxygen content (42.1-49.5 wt. % for OME1-6 with $1 \le n \le 6$) is responsible for the nearly sootless combustion.

      Most academic research so far focused on OME_1 as higher grade OMEs have been difficult to synthesize [7]–[10]. However, in general terms, OME_{3-6} were determined to be of best suitability for diesel engine applications, considering their boiling point, lubricity and viscosity are close to diesel itself [9], [11], [12]. Therefore, recently the focus shifted towards higher OMEs. Previous findings for OME_1 regarding very low soot and particle emissions were also confirmed for OME_{3-6} [2], [4], [13].

      Special emphasis in this work is placed on the effects caused by multiple injection strategies. Choi and Reitz [14] investigated the effects of oxygenated fuel blends and multiple injections on DI diesel engines. The study concluded that oxygenated fuel blends reduced soot emissions at high engine

loads without increasing NO_x emissions. Furthermore, it was shown that a split injection pattern had an additional favorable effect on soot formation at high engine loads and was particularly effective at reducing particulate emissions at low engine loads. Therefore, the combination of oxygenated fuels and multiple injection strategies has the potential to significantly reduce particulate matter emissions over a wide range of engine operating conditions. The used injection pattern in this study consists of a short pilot (or pre) and a longer main injection, described in next section. Short pilot injections result in a ballistic injector operation regime, which strongly influences the spray propagation, mixture formation and ignition behavior. Previous studies emphasized the challenges to properly model highly transient ballistic working regimes of an injector [15] and to correctly specify the small quantities of fuel injected [16]. The authors in [17] found that multiple injection strategies using pilot injections result in a leaner in-cylinder charge yielding a more complete combustion. This reduces the fuel fraction reaching the cylinder wall and crevice regions and therefore leads to lower UHC and CO emissions in comparison with single injection strategies.

In order to fully leverage the potential of OMEs in combination with multi-injection events it is essential to study their physical-chemical behavior in depth. The primary aim of this study is to advance the understanding of OMEs in terms of spray atomization, mixture formation and auto-ignition for single and multiple injection strategies by developing a comprehensive 3D CFD model using the commercial software AVL FIRE®.

Detailed reaction mechanisms are used for an OME_{3-6} fuel and dodecane, which serves as a diesel surrogate fuel, to identify the differences in the combustion regimes before and after a stable flame lift-off is established. The spray and combustion models are validated with experimental data from a constant pressure combustion vessel.

2. Setup

The injector used in this work is the Continental 3 Hole injector (Conti3L) with a nominal exit diameter of 115 µm and an elevation angle of 45°. For the contraction coefficient a value of $C_A = 0.98$ was chosen.

The operating points studied in this work are ranging from 800 K to 1000 K chamber temperature and from 0% to 15% and 21% oxygen content at a reference density of 22.8 kg/m³. The injection duration for the single injection events are 1.5 ms. For the multi-injection a pattern of 0.3 ms pilot duration, followed by a 0.5 ms dwell phase and 1.2 ms main injection was chosen.

2.1   Used OME Fuel

Table 1 shows the composition of the used OME fuel for this study. It can be seen that the dominating molecules are OME_3 to OME_5.

Table 1: OME mix composition

Molecule	Content [wt. %]
OME_1	0.01
OME_2	<0.01
OME_3	57.90
OME_4	28.87
OME_5	10.07
OME_6	1.91

2.2   Experimental Setup

The experiments for the spray investigation are carried out at an optically accessible high-temperature and high-pressure constant volume injection chamber.

For all types of measurements, the optics are placed in such a way, that the fuel spray is shown in side view. The gaseous penetration is measured with a typical schlieren setup under inert conditions while the liquid phase is illuminated from three sides enabling the high-speed camera to detect the Mie-scattered light as well (Fig. 1, left). To characterize the ignition, the OH*-chemiluminescence is detected. For this, the OH*-signal is filtered out of the flame signal (Fig. 1, right).
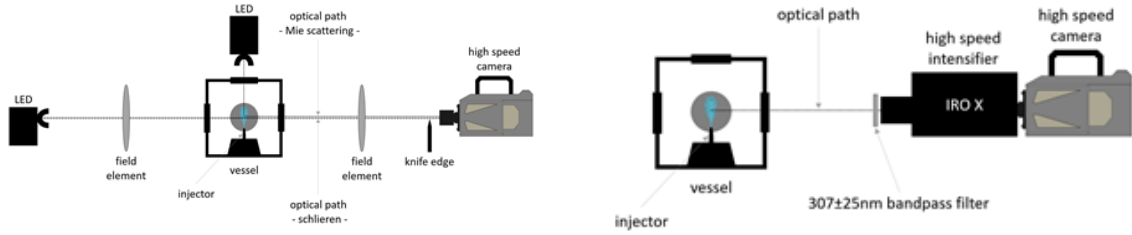
Fig. 1. Experimental setup: (left) Mie-scattering and Schlieren setup; (right) OH*-chemiluminescence setup

2.3   Numerical Setup

The CFD calculations were carried out using a simple spray-box mesh of 120 mm in length and 60 mm in width including several refinements reaching a maximum resolution of 125 µm.

The simulations were conducted using an Euler-Lagrange approach with a summary of the numerical setup given in Table 2. The combustion modeling is done using detailed reaction kinetics (Yao [18] for dodecane and Niu [19] for OME) and treating every cell as a well-mixed reactor.

Table 2: Numerical setup

Eulerian (gaseous) phase models	
Temporal discretization	0.5 µs
Turbulence modeling	RANS; k-ζ-f model
Wall treatment	Compound (hybrid)
Pressure-correction	SIMPLE (1st) / PISO (2nd)
Lagrangian (liquid) phase models	
Injection type	Blob
Breakup	KHRT
Turbulent dispersion	O'Rourke
Evaporation	Dukowicz (Dodecane); Multi-Component-Model (OME)
Drag Law	Schiller-Naumann

3. Results

The trends concerning the dependency on temperature and oxygen content for flame lift-off and ignition delay show a significant difference for OME compared to dodecane (Fig. 2). It can be seen that the lift-off for OME is consistently predicted to be longer by simulation and experiment. The trends for varying oxygen content show a steeper rise in flame lift-off length for OME with decreasing oxygen content. It is also noticeable that the gradient of the OME trends for experiments and simulations along lower chamber temperatures is higher than for dodecane between 800 K and 900 K. For 1000 K OME deviates from the linear behavior for simulation and experiment in contrast to dodecane, which shows a strictly linear dependence on temperature.

Fig. 3 compares the visual signal extracted from OH*-chemiluminescence experiments with the respective simulated OH mass fraction contour in the spray center plane for 900 K and a varying oxygen content of 15% O_2 (left side) and 21% O_2 (right side). The respective experimentally determined ignition delay ($t_{SOC,Exp}$) was chosen as reference point. From beginning to end of the combustion it can be seen that dodecane is forming a kidney-shaped or "V" contour with distinctive high-intensity regions at the shear boundary of the spray and the ambient air. In contrast the OME results show greater reaction activity in the spray center axis. Rather straight high-intensity regions emerge, which bend towards the spray tip as the combustion proceeds.

The left plot of Fig. 4 details the profiles of the maximum temperature and the respective ignition delay at their maximum gradients. The most obvious difference is the stark decline in maximum temperature for OME during the injector dwell phase, which results in a second ignition. The auto-ignition after the pilot injection at around 300 µs aSOI (pilot) cannot be validated. The maximum temperature profile for dodecane only yields one ignition delay timing after the pilot injection. The center plot of Fig. 4 underpins these observations as the mean mass fractions of OH during the dwell period remains on a higher plateau in case of dodecane.
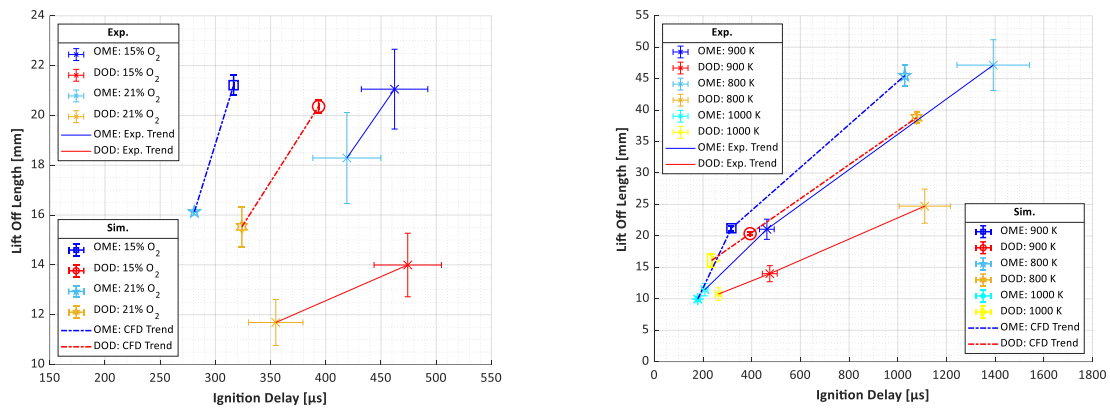
Fig. 2. Lift-off length vs ignition delay (T_{CC}=900 K): (left) O_2 content trend; (right) Temperature dependency
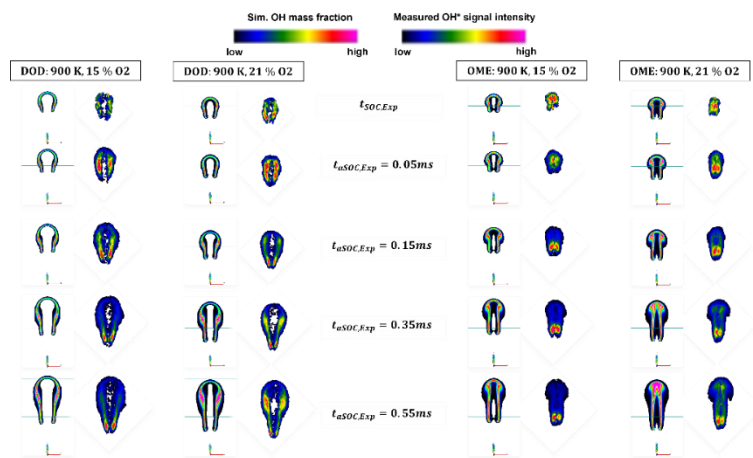

Fig. 3. OH flame shape in center plane: Simulation vs experiment: (left) Dodecane; (right) OME
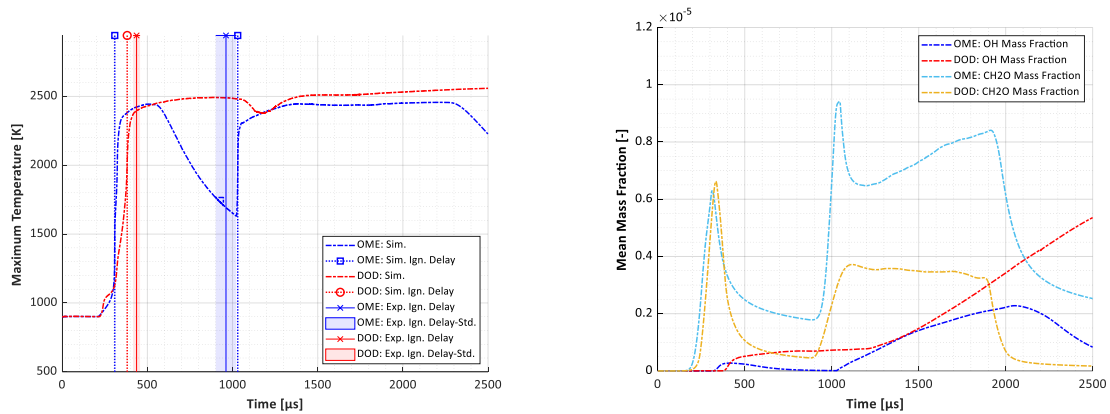

Fig. 4. Multi-injection profiles (T_{CC}=900 K): (left) Maximum temperature; (right) OH and CH_2O mass fractions

Conclusions

This study showed that OME has a flame that lifts-off further downstream compared to dodecane. Furthermore, the mixing regimes of the ignition zones are very different for the two fuels. OME combustion shows significant reaction activity in the spray center axis and the flame shape does not bend towards the shear boundary layer of fuel and ambient air in contrast to dodecane. The different flame shapes and ignition zones for OME are driven by the oxygen bound in the chemical formula of the fuel, delivering oxygen and therefore an ignitable mixture in regions where it is impossible for dodecane to ignite.

For the multi-injection the differences of OME and dodecane in the transient evolution of temperature and key species were determined. Especially the high-temperature reactions, signaled by the OH mass fractions, differ substantially for OME and dodecane. The high-temperature combustion of dodecane progresses longer in time after injection events ended.

References

[1] S. Deutz *et al.*, "Cleaner production of cleaner fuels: wind-to-wheel – environmental assessment of CO2-based oxymethylene ether as a drop-in fuel," *Energy Environ. Sci.*, vol. 11, no. 2, pp. 331–343, Feb. 2018, doi: 10.1039/C7EE01657C.

[2] A. Damyanov, P. Hofmann, B. Geringer, N. Schwaiger, T. Pichler, and M. Siebenhofer, "Biogenous ethers: production and operation in a diesel engine," *Automot. Engine Technol.*, vol. 3, no. 1, pp. 69–82, Aug. 2018, doi: 10.1007/s41104-018-0028-x.

[3] J. Liu *et al.*, "Effects of diesel/PODE (polyoxymethylene dimethyl ethers) blends on combustion and emission characteristics in a heavy duty diesel engine," *Fuel*, vol. 177, pp. 206–216, Aug. 2016, doi: 10.1016/j.fuel.2016.03.019.

[4] M. Härtl, K. Gaukel, D. Pélerin, and G. Wachtmeister, "Oxymethylene Ether as Potentially CO2-neutral Fuel for Clean Diesel Engines Part 1: Engine Testing," *MTZ Worldw*, vol. 78, no. 2, pp. 52–59, Feb. 2017, doi: 10.1007/s38313-016-0163-6.

[5] A. Omari, B. Heuser, and S. Pischinger, "Potential of oxymethylenether-diesel blends for ultra-low emission engines," *Fuel*, vol. 209, pp. 232–237, Dec. 2017, doi: 10.1016/j.fuel.2017.07.107.

[6] H. Liu, X. Ma, B. Li, L. Chen, Z. Wang, and J. Wang, "Combustion and emission characteristics of a direct injection diesel engine fueled with biodiesel and PODE/biodiesel fuel blends," *Fuel*, vol. 209, pp. 62–68, Dec. 2017, doi: 10.1016/j.fuel.2017.07.066.

[7] B. Lumpp, D. Rothe, C. Pastoetter, R. Laemmermann, and E. Jacob, "Oxymethylenether als Dieselkraftstoffzusaetze der Zukunft," *Motortechnische Zeitschrift*, vol. 72, no. 3, 2011, Accessed: Mar. 31, 2022. [Online]. Available: https://trid.trb.org/view/1123204

[8] M. Härtl, P. Seidenspinner, G. Wachtmeister, and E. Jacob, "Synthetischer Dieselkraftstoff OME1 — Lösungsansatz für den Zielkonflikt NOx-/Partikel-Emission," *MTZ Motortech Z*, vol. 75, no. 7, pp. 68–73, Jul. 2014, doi: 10.1007/s35146-014-0392-7.

[9] M. Härtl, P. Seidenspinner, E. Jacob, and G. Wachtmeister, "Oxygenate screening on a heavy-duty diesel engine and emission characteristics of highly oxygenated oxymethylene ether fuel OME1," *Fuel*, vol. 153, pp. 328–335, Aug. 2015, doi: 10.1016/j.fuel.2015.03.012.

[10] A. Feiling, M. Münz, and C. Beidl, "Potential of the Synthetic Fuel OME1b for the Soot-free Diesel Engine," *ATZextra Worldw*, vol. 21, no. 11, pp. 16–21, Jan. 2016, doi: 10.1007/s40111-015-0516-1.

[11] L. Pellegrini, M. Marchionna, R. Patrini, C. Beatrice, N. Del Giacomo, and C. Guido, "Combustion Behaviour and Emission Performance of Neat and Blended Polyoxymethylene Dimethyl Ethers in a Light-Duty Diesel Engine," Apr. 2012, pp. 2012-01–1053. doi: 10.4271/2012-01-1053.

[12] K. Gaukel *et al.*, "Der Kraftstoff OME2: Ein Beispiel für den Weg zu emissionsneutralen Fahrzeugen mit Verbrennungsmotor /The Fuel OME2: An Example to Pave the Way to Emission-Neutral Vehicles with Internal Combustion En...," Apr. 2016, p. II–223. doi: 10.51202/9783186799128-II-193.

[13] G. Richter and H. Zellbeck, "OME als Kraftstoffersatz im Pkw-Dieselmotor," *MTZ Motortech Z*, vol. 78, no. 12, pp. 66–73, Dec. 2017, doi: 10.1007/s35146-017-0131-y.

[14] C. Y. Choi and R. D. Reitz, "An experimental study on the effects of oxygenated fuel blends and multiple injection strategies on DI diesel engine emissions," p. 15, 1999.

[15] J. Frühhaber *et al.*, "Modeling the Pilot Injection and the Ignition Process of a Dual Fuel Injector with Experimental Data from a Combustion Chamber Using Detailed Reaction Kinetics," Sep. 2018, pp. 2018-01–1724. doi: 10.4271/2018-01-1724.

[16] C. H. Lee and R. D. Reitz, "CFD simulations of diesel spray tip penetration with multiple injections and with engine compression ratios up to 100:1," *Fuel*, vol. 111, pp. 289–297, Sep. 2013, doi: 10.1016/j.fuel.2013.04.058.

[17] K. Anand and R. D. Reitz, "Exploring the benefits of multiple injections in low temperature combustion using a diesel surrogate model," *Fuel*, vol. 165, pp. 341–350, Feb. 2016, doi: 10.1016/j.fuel.2015.10.087.

[18] T. Yao, Y. Pei, B.-J. Zhong, S. Som, T. Lu, and K. H. Luo, "A compact skeletal mechanism for n-dodecane with optimized semi-global low-temperature chemistry for diesel engine simulations," *Fuel*, vol. 191, pp. 339–349, Mar. 2017, doi: 10.1016/j.fuel.2016.11.083.

[19] B. Niu, M. Jia, Y. Chang, H. Duan, X. Dong, and P. Wang, "Construction of reduced oxidation mechanisms of polyoxymethylene dimethyl ethers (PODE1–6) with consistent structure using decoupling methodology and reaction rate rule," *Combustion and Flame*, vol. 232, p. 111534, Oct. 2021, doi: 10.1016/j.combustflame.2021.111534.

Effect of Split Injection Mass Ratio on Fuel Adhesion Characteristics of Flat-Wall Impinging Spray

F. Chang[1], H. Luo[1], Y. Hagino[1], T. Tashima[1], K. Nishida[1], Y. Ogata[1], R. Hara[2], K. Uchida[2], W. Zhang[2]

Graduate School of Advanced Science and Engineering, Hiroshima University,1-4-1 Kagamiyama, Higashi-Hiroshima, 739-8527, Japan

E-mail: d193153@hiroshima-u.ac.jp
Telephone: +(81) 070 4559 4854

[2]Mazda Motor Corporation, 3-1 Shinchi, Fuchu-cho, Aki-gun, Hiroshima 730-8670, Japan

E-mail: zhang.wu@mazda.co.jp
Telephone: +(81) 082 424 4324

Abstract. It is inevitable that spray/wall interaction phenomenon exist in direct-injection spark-ignition (DISI) engines. The interaction leads to the formation of fuel adhesion on the cylinder and piston wall. And fuel adhesion has an obvious effect on the combustion efficiency and the generation of unburned hydrocarbon. In this work, the aim is to investigate the effect of injection mass ratios (25%: 75%, 50%: 50%, 75%: 25%) on fuel adhesion characteristics by the refractive index matching (RIM) method under non-evaporation condition. Results show that injection mass ratios have a significant effect on the fuel adhesion. Especially, the fuel adhesion is the largest when injection mass is same of first and second injections. Two possible reasons can be concluded as "fuel adhesion thickness" and "momentum energy" effects, which both induce the splashing. However, the mechanism of two effects inducing splash is different.

Keywords: Mass ratio; Split injection; Fuel adhesion; Uniformity; Wall impingement

1. Introduction

Due to the pace of technological innovation, split injection strategy and direct-injection spark-ignition (DISI) system are widely applied to gasoline engines and bring about the benefits of high combustion efficiency and low emissions. However, because of engine miniaturization and high injection pressure, it is difficult to avoid spray/wall interaction in a DISI engine.

Comprehensive experiments have been conducted to study the effect of split injection strategy on spray characteristics in constant-volume chambers. Zhang et al. [1] investigated the spray characteristics of split injection and found that the spray development rate of the later injection was higher than that of the earlier injection under split injection. The penetration velocity of the later injection was higher than that under single injection. Li et al. [2] studied the effect of split injection on mixture formation in the engines. They found that the spray-induced ambient air motion under split injection promoted the formation of a more combustible mixture.

To date, the influence of different injection mass ratio on the deposited fuel during the spray impingement process have not been adequately investigated. The fuel adhesion characteristics of different injection mass ratios need to be compared under non-evaporation conditions.

2. Experimental system and calibration results

2.1 Experimental apparatus Imaging processing method

Fig. 1 depicts the optical apparatus for the fuel adhesion measurement. The external layout of the optical apparatus is described by Fig. 1(a).

The internal layout of optical arrangement is shown in Fig. 1(b). More details about experimental system can refer to [3]. Regarding the split injection schemes, the injection mass ratio of the first injection varied from 25 to 75 per cent with a fixed dwell time of 2.0 ms and a constant total fuel injection mass (8 mg). In the notation D25-75, "D" indicates double injection, the first number "25" denotes the injection mass ratio of the first injection in percentage, the last number "75" denotes the second injection. Three different injection mass ratios are 2 mg: 6 mg, 4 mg: 4 mg and 6 mg: 2 mg (namely D25-75, D50-50 and D75-25).
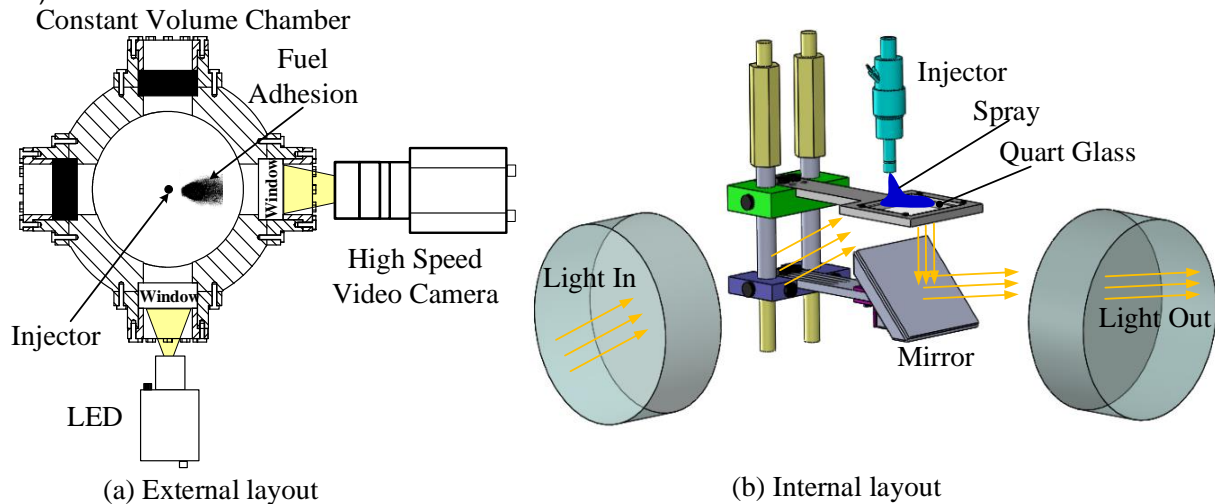

(a) External layout   (b) Internal layout

Fig. 1. Optical apparatuses for fuel adhesion measurement.
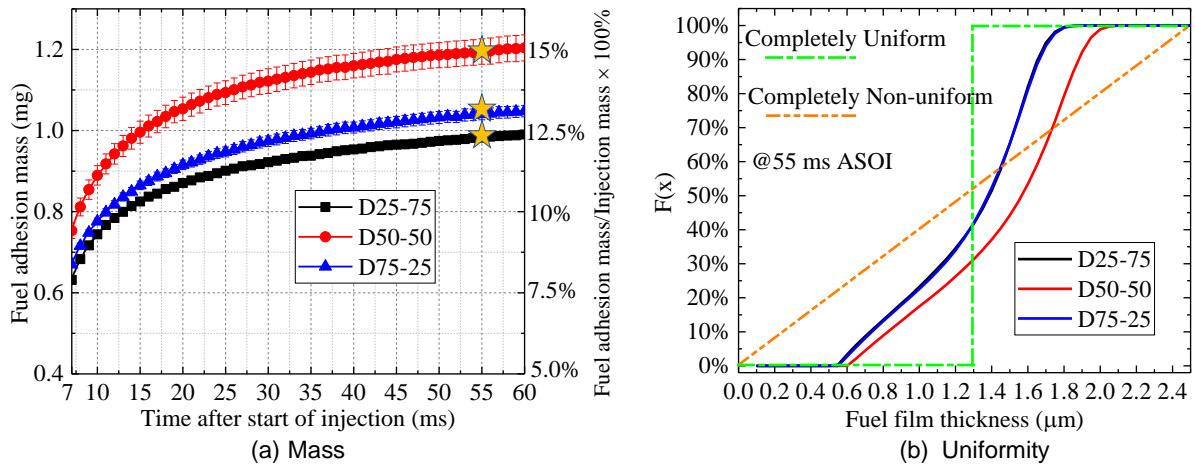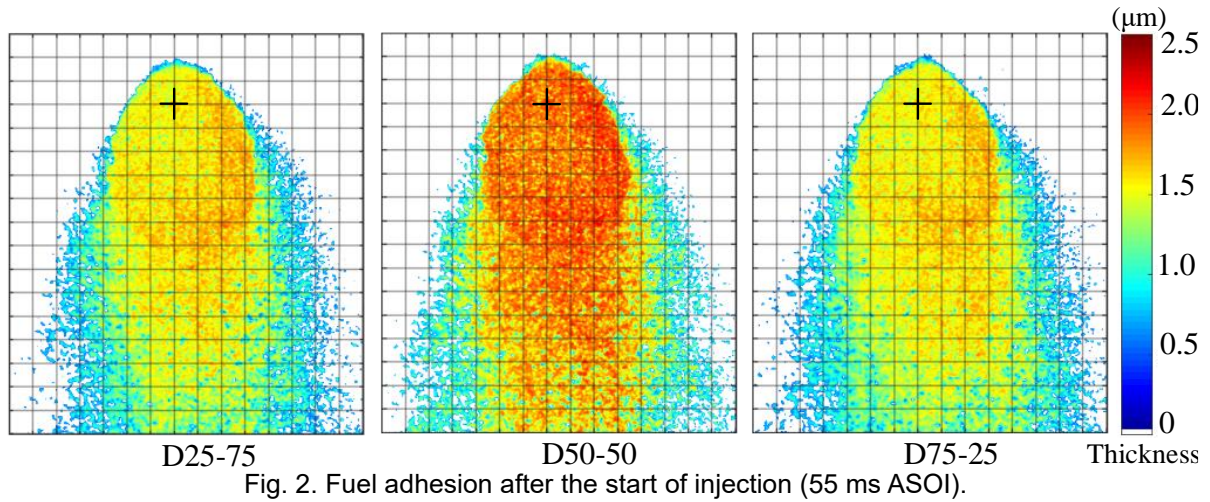
3. Results and discussion

3.1 Fuel adhesion mass and uniformity

Fig. 2 shows the fuel adhesion at 55 ms for the different injection mass ratios. Pseudocolor in the images are applied to represent the thickness, ranging from 0 to 2.5 μm. The fuel adhesion thickness of D50-50 is significantly larger than those of D25-75 and D75-25, which have similar fuel adhesion thicknesses.

The fuel adhesion mass under different injection mass ratios is depicted in Fig. 3 (a). The fuel adhesion mass increases obviously with time for different injection mass ratios. This increase may be related to the re-deposition of some droplets above the wall. It is particularly noteworthy that the fuel adhesion mass of D50-50 is larger than those of D25-75 and D75-25. According to the findings of Gong et al. [4], larger fuel adhesion thickness and momentum energy tend to promote "splashing", resulting in the fuel adhesion decreasing. These two factors are called "fuel adhesion thickness" and "momentum energy" effects.

Uniformity has a significant impact on the evaporation rate of fuel adhesion. Uniform adhesion is not easy to evaporate than the uneven adhesion under the high ambient temperature. This is because the uneven adhesion is easily to collapse and evaporate quickly. In Fig.3 (b), the vertical axis is F(x), and the horizontal axis is fuel adhesion thickness under non-evaporation condition. F(x) increases with fuel adhesion thickness. The black line represents D25-75, the red line represents D50-50 and the red line represents D75-25. The cumulative distribution function F(x) is a straight line parallel to the vertical axis, which indicates the fuel adhesion is completely uniform, which is depicted by a dashed dotted line. If the fuel adhesion is completely non-uniform, the cumulative distribution function F(x) is a straight line with a certain angle to the vertical axis, which is described by a dashed double-dotted line. For the injection mass of D25-75 and D75-25, the curves increase readily than that of D50-50. The curves of D25-75 and D75-25 reach to 100% at about 1.8 μm, whereas the curves of D50-50 reach to 100% at about 2.0 μm. Furthermore, the curves of D25-75 and D75-25 are closer to the curve of indicating completely uniform adhesion, whereas the curves of D50-50 are closer to the completely non-uniform curve, indicating that the fuel adhesion of D25-75 and D75-25 is significantly more uniform than that of D50-50.

Fig. 2. Fuel adhesion after the start of injection (55 ms ASOI).

(a) Mass

(b) Uniformity

Fig. 3. Fuel adhesion mass and uniformity.

3.2 Mechanism of fuel adhesion under different injection mass ratios

Fig. 4 is applied to clearly depict the mechanism of the fuel adhesion formation. Two main reasons are summarized for the difference of different injection mass ratios. One reason is the "fuel adhesion thickness" effect as shown in Fig. 4 (a). The black dot represents the adhered mass of 1st injection. As the first injection mass increases, fuel adhesion thickness increases, and the fuel adhesion thickness of D75-25 is the maximum. The thicker fuel adhesion is more likely to promote the splashing when the spray of second injection impinges on the wet wall, which is named "fuel adhesion thickness" induce the splashing. The red line depicts that the splashing ability created by the adhesion thickness of 1st injection. Another reason is that the penetration velocity of second injection increase with injection mass under different injection mass ratios as shown in Fig. 4 (b). Momentum is the main parameters to determine the splashing behavior. When momentum energy is large enough, spray tends to splash after impingement. The penetration velocity of 2nd injection around the 20 mm penetration distance is calculated from the studies of Zhang et al. [1]. They found the penetration velocity of 2nd injection of D25-75 is much larger than that of D50-50. The penetration velocity of D75-25 is estimated and represented by the white dot in Fig. 4 (b). Therefore, the higher penetration velocity of the 2nd injection promotes the splashing, which is called "momentum energy" induce the splashing. Fig. 4 (c) depicts the adhered and splashing mass ratios. Results shown that the adhered mass ratio of D50-50 is 14.5% and it is the maximum. The splashing mass ratios of D25-75 and D75-25 are much larger than that of D50-50 and similar. Reason for this difference is the combination of the two effects. The thicker fuel adhesion is more likely to promote the splashing, at the same time, the large momentum energy tends to splash after impingement. Two effects on the fuel adhesion of different injection mass ratios are opposite as Fig. 4 (d) shown, resulting in the maximum adhesion of D50-50.
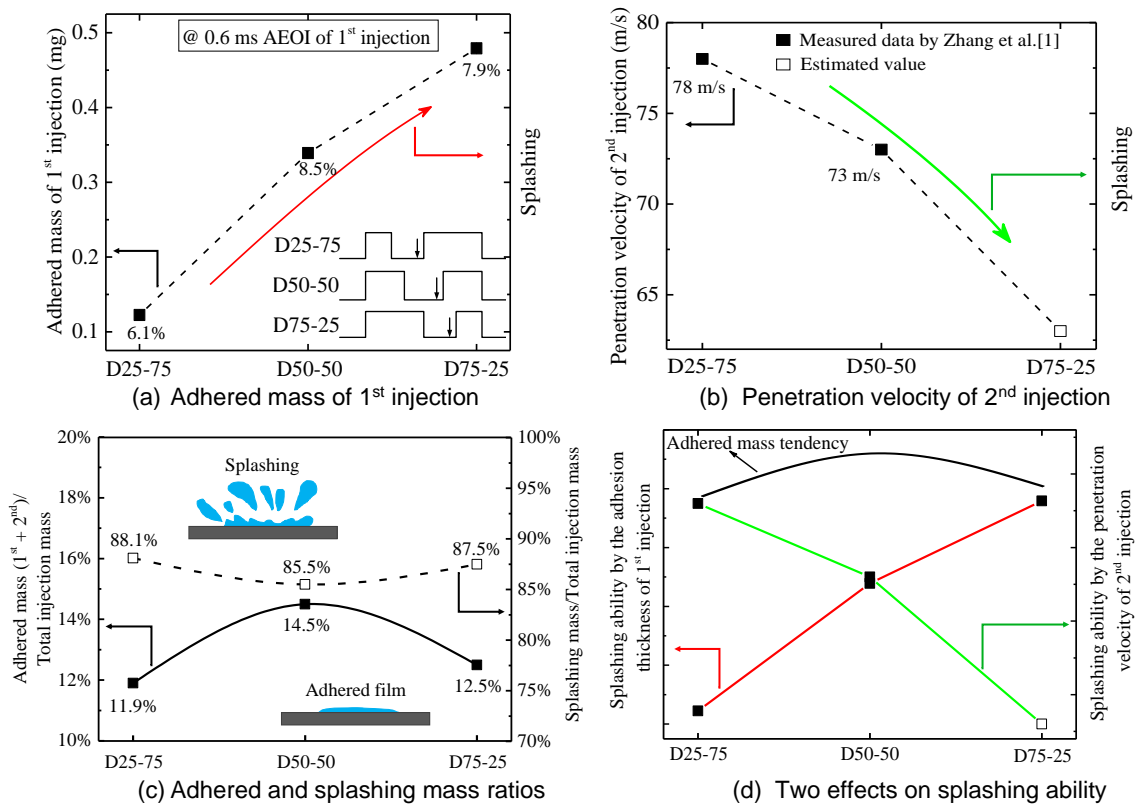
4   Feixiang Chang, Hongliang Luo et al.

Fig. 4. Mechanism of fuel adhesion under different mass ratios.

Conclusions

In this work, the fuel adhesion characteristics and the mechanism under different injection mass ratios in fuel adhesion under non-evaporation condition were analyzed. The main conclusions are as follows.

(1) Fuel adhesion mass of D50-50 increases obviously from 12.5% to 15% (At 60 ms ASOI) compared to that of D25-75 and D75-25 under non-evaporation condition. Two possible reasons are account for this difference. One is the effect of "fuel adhesion thickness", which is formed by the spray of first injection. The thicker fuel adhesion is more likely to promote the splashing when the spray of second injection impinges on the wet wall. The other reason is the effect of "momentum energy", which is on account of the larger penetration velocity of the later injection with larger injection mass. The two effects lead to the fuel adhesion mass of D50-50 is the maximum.

(2) The effects of different injection mass ratios on the uniformity of the fuel adhesion have a big difference under non-evaporation condition. The fuel adhesion uniformity of D50-50 is the worst compared to that of D25-75 and D75-25. However, the uniformity of D25-75 and D75-25 is similar.

References

[1] Zhang Z, Zhao F, Deng J, Li L, Shen Y. Characteristics of the multiple injection diesel spray employed common rail system. J Therm Sci Technol 2013; 8 (1): 106-119.
[2] Li T, Nishida K, Zhang Y, Yamakawa M. et al. An insight into effect of split injection on mixture formation and combustion of DI gasoline engines. SAE Technical Paper 2004; 01(1949).
[3] Chang F, Luo H, Hagino Y, Tashima T, Nishida K, Ogata Y. Effect of split injection on fuel adhesion characteristics under non-evaporation and evaporation conditions, Fuel, 317; 123465; 2022.
[4] Gong C., Luo H., Wu X., Nishida K. Experimental analysis in dynamics characteristics of impinging spray by a pfi injector: from spray atomization to fuel adhesion formation. 31(12) 77-96, 2021.

THIESEL 2022 Conference on Thermo- and Fluid Dynamics of Clean Propulsion Powerplants

A Simulation and Experimental Study of the Feasibility of a Hydrogen Fuelled Split Cycle Engine

R.E. Morgan[1], E. Wylie[1], A. Panesar[1], A. Atkins[2], N.J. Owen[2], R. Pickett[2], A. Harvey[2]

[1]Advanced Engineering Centre, University of Brighton, Lewes Road, Brighton BN24GJ, UK.
[2]Dolphin N2, Building 5, UTAC, Millbrook Proving Ground, Station Lane, Millbrook, MK452JQ, UK.

E-mail: r.morgan2@brigthon.ac.uk
Telephone: +(44) 1273641950

Abstract.

The recuperated split cycle engine is an ultra-efficient, clean internal combustion engine. The cycle has been developed on fossil diesel but must be proven on a sustainable fuel to have a future beyond the 2030's. In this paper, we apply the combustion focused design methodology to assess the feasibility of hydrogen in a split cycle engine. The research focused on the fundamental ignition and combustion characteristics of hydrogen to investigate the feasibility of use in a split cycle engine.

Kinetic analysis using CHEMKIN is presented to determine the optimal configuration of a split cycle engine operating on hydrogen. The analysis determined the available operating window between misfire and the formation of NOx where the engine can operate efficiently and at ultra-low emissions. From the analysis, a spark ignited high pressure late injection strategy was identified as the most promising solution. Early results from single cylinder engine testing using diesel pilot ignition and spark ignition are presented. The experimental results demonstrate the viability of hydrogen in this type of engine and demonstrated cold starting on hydrogen monofuel and the viability of diesel pilot and spark ignition.

1. Introduction

The recuperated split cycle engine (RSCE) represents a step change in efficiency at near zero emissions [1]. In a RSCE, the compression and expansion processes occur in different cylinders enabling both cool compression and interstage heat recovery via a recuperator. The cycle has been demonstrated on diesel fuel [2] but to meet the net zero target, the cycle must also work on a sustainable fuel. In this paper, we investigate the feasibility of using hydrogen in a RSCE. Of all the sustainable fuels proposed, hydrogen has the lowest production energy cost [3]. There are other implications of switching to hydrogen such as infrastructure on vehicle energy storage and safety but these have been covered by others and will not be discussed in this paper. In this paper, we apply a combustion focused design approach to a hydrogen fuelled RSCE. The CHEMKIN kinetics software was used to investigate the ideal operating conditions to achieve a stable and complete reaction of the air and fuel at near zero emissions. Preliminary test results from a single cylinder engine are presented to validate the approach.

2. Application of the Combustion Focused Design Approach

2.1 The combustion focused design methodology

With the combustion focused design approach the system is designed from the reaction chamber out. The ideal thermo-fluid conditions to achieve maximum efficiency whilst avoiding conditions where toxic emissions can form are identified and then the mechanical system is designed to achieve these parameters. This approach differs from conventional engine design, where the mechanical system is usually designed first and the combustion system then within the mechanical constraints of the hardware. Previous research on operation with diesel fuel showed the recuperated split cycle engine architecture matched the ideal thermo-fluid conditions for clean, efficient reaction of chemical fuels [4]. The key enabling features of the RCSE are (1) decoupling of compression ratio from ideal efficiency [1] (2) high charge air turbulence to promote mixing of reactants [5] (3) precise control of the temperature at the start of combustion [4] (4) reaction phasing during the expansion stroke, providing a 'brake' on the rate of temperature rise. Hydrogen has very different properties to diesel: (1) different mixing

characteristics, being a gas rather than liquid (2) high ignition energy (3) wide flammability range. The present research aims to assess the suitability of the RSCE combustion system for hydrogen.

2.2 Definition of Questions and Requirements

The fundamental requirements of the RSCE combustion system are high conversion efficiency and ultra-low NOx emissions. To achieve these requirements, the temperature range where both stable, complete reaction of the hydrogen is achieved and a peak temperature low enough to avoid the formation of NOx emissions must be determined. These requirements lead to a key design question; when to introduce the fuel – at low pressure before air induction or at high pressure during air induction? For a hydrogen RSCE this is a key question as it determines the nature of the hydrogen injection equipment. Low pressure injection technology is currently available whereas high pressure (c. 300bar) injection equipment is only in development.

3. Analysis and Definition of Combustion System

The CHEMKIN simulation code was used to explore performance in the area between stable ignition and NOx formation. A constant volume well stirred reactor model was built and simulations undertaken over a range of starting temperatures and equivalence ratios. The simulation set up was previously described in [4].
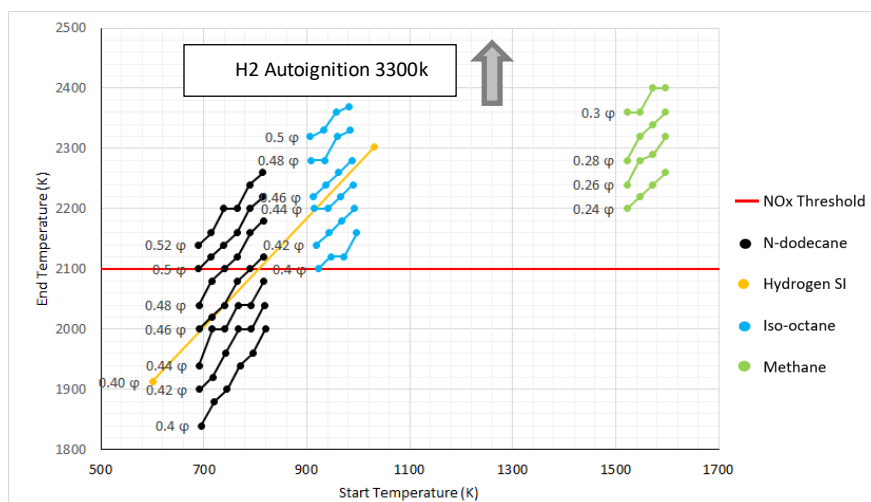
Fig 1: CHEMKIN simulation results from a well stirred reactor varying initial temperature and equivalence ratio. results for carbon-based fuels taken from [4]

From the simulation results shown in **Fig 1**, autoignition of hydrogen in a RSCE is possible, but a high initial temperature (1350K) is required and significant NOx emissions are likely to form. However, if a spark plug is included to ignite a lean mixture, the initial temperatures can be lowered significantly to the point where NOx formation can be avoided. The analysis indicated an operating 'window' of intake temperatures between 600K to 800K, which matches well the practical operating window of the diesel fuelled RSCE in development. However, it is widely reported in the literature that hydrogen has a high propensity to ignite from hot surfaces [6]. Given the combustion chamber of a

RSCE is insulated with ceramics, early injection of hydrogen before the induction of the hot inlet charge air could result in pre-ignition of the hydrogen. This is illustrated in **Fig. 2**.
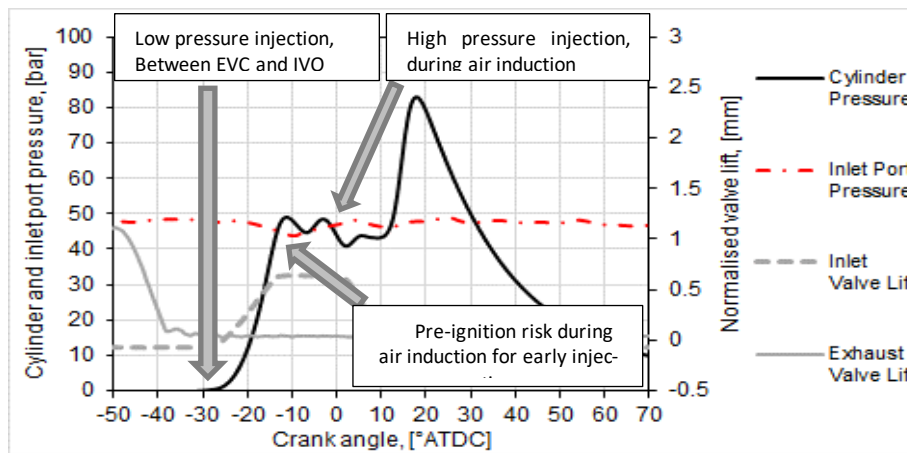
Fig 2: Schematic of cylinder pressure trace illustrating hydrogen injection options (cylinder pressure trace is from a diesel fuelled experiment from [2])

4. Results from Single Cylinder Engine

A Titan single cylinder engine (1.1ℓ capacity) was modified to accept a hydrogen gas injector and spark plug. The basic engine and test facility are described in [2]. The central diesel injector was maintained to allow the engine to be operated in diesel or diesel-hydrogen mode as well as hydrogen only mode. The hydrogen injector was restricted to 36bar maximum fuel pressure, which led to a maximum charge air pressure at injection of 20bar. It should be noted this specification was driven by available parts and meant the engine would be operated at very low induction pressure but would still enable the ignition and basic characteristics of the combustion system to be assessed.

4.1 Dual Diesel-Hydrogen Experiments

The engine was started on diesel and then hydrogen was introduced in the period between exhaust valve closure and when a chamber pressure of 18bar was reached during air induction. **Fig. 3** shows a series of cylinder pressure traces with increasing quantities of hydrogen substitution. As expected, the engine operating window was very constrained by pre-ignition of the hydrogen limiting the injection timing and quantities of injected hydrogen to 16% (by energy). The experiment did demonstrate that (1) hydrogen can be mixed and burn in a RSCE with diesel pilot ignition and (2) the ignition of hydrogen in a hot RSCE can be achieved even at charge air temperatures below the autoignition temperature of hydrogen. The results also indicate a late high pressure injection strategy is required to avoid pre-ignition.

4.2 Hydrogen Monofuel Experiments

Further experiments were undertaken to see if the engine could be operated on hydrogen alone without a diesel pilot. The engine was initially started with early inlet valve timings to generate a small compression stroke with the hydrogen introduced between exhaust valve closure and inlet valve opening. A spark plug was also fitted to the cylinder head to assist ignition. The engine was successfully started from cold, and the inlet valves were progressively retarded towards top dead centre to achieve split cycle operating conditions (with air induction over top dead centre). It was found with an early low-pressure injection (36bar), the inlet valve timing could not be fully retarded to split cycle conditions before pre-ignition was observed. It was also interesting to note that ignition was controlled largely by

4   R.E. Morgan, E. Wylie, A. Panasar, A. Atkins, N.J. Owen, R. Pickett, A. Harvey

autoignition and not by the spark plug at retarded conditions. This was verified by turning the spark off and observing no change in the cylinder pressure trace. However, this experiment does demonstrate (1) RSCE can be cold started on hydrogen with a spark plug (2) at split cycle operating conditions, autoignition can be readily achieved and a spark plug may only be required for starting and ignition assist at some parts of the operating map and (3) high pressure late direct injection of hydrogen is required to mitigate pre-ignition.
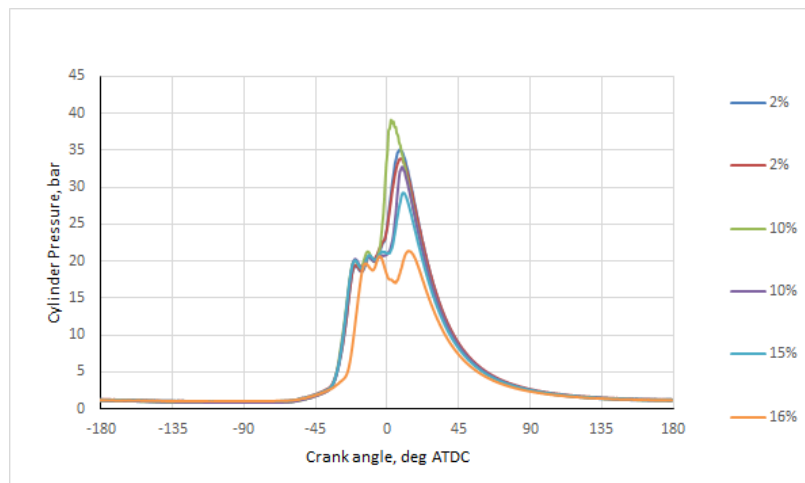
Fig 3: Single cylinder test results for hydrogen – diesel combustion at 38bar hydrogen injection pressure for different hydrogen – diesel concentrations (legend shows percentage of hydrogen injected by energy)

5. Conclusions

The CHEMKIN simulation study indicated the RSCE can be operated on hydrogen. The analysis indicated autoignition requires start of combustion temperatures that would produce significant quantities of NOx emissions. The inclusion of a spark plug significantly lowers the temperature range to a region where the hydrogen will react but not hot enough to produce significant NOx emissions. Diesel pilot ignition would also deliver a similar result. Single cylinder testing using a low pressure (36bar) injection system showed (1) the engine could be started from cold using hydrogen with a spark plug, (2) from hot conditions, hydrogen will ignite in an RSCE at temperatures below the autoignition temperature. It is suspected the hot combustion chamber surfaces promote pre-ignition. Early low-pressure injection of the fuel, before inlet valve opening is not feasible due to pre-ignition. High pressure injection, replicating the diesel RSCE combustion system is required and is the focus of our ongoing research.

References

1. Dong, G. *et. al.* (2016) Thermodynamic analysis and system design of a novel split cycle engine concept, *Energy,* vol. 102, pp. 576-585.
2. Morgan, R. *et. al.* The Ultra Low Emissions Potential of the Recuperated Split Cycle Combustion System. In Proceedings of the SAE Technical Paper Series 2019-24-0189; 2019; Vol. 1.
3. Hanggi, S. *et. al.* A review of synthetic fuels for passenger vehicles. 2019 Energy Reports Vol. 6 p 555-569.
4. Morgan, R. *et. al.* Towards zero emission engines through the adoption of combustion- lead engine design realised using a split cycle topology. *THIESEL* **2018**.
5. Harvey, S. *et. al.* Starting to unpick the unique air fuel mixing dynamics in the recuperated split cycle engine. Energies 2021 14(8) 2148.
6. Wang, L. *et. al.* Research on the hot surface ignition of hydrogen-air mixtures under different influencing factors. 2018 Int. J Energy Res. 42 p. 3966-3976.

THIESEL 2022 Conference on Thermo- and Fluid Dynamics of Clean Propulsion Powerplants

Modeling of Dual-Fuel Combustion under Different Fuel Ratios and Injection Timing Conditions

Sunyoung Moon, Kyoungdoug Min

Seoul National University, 1 Gwanak-ro Gwanak-gu, Seoul, South Korea.

E-mail: symoon10@snu.ac.kr
Telephone: +(82) 2-8808363

E-mail: kdmin@snu.ac.kr
Telephone: +(82) 2-8801661

Abstract.
Due to stricter emissions regulations, new advanced combustion concepts have emerged, especially in terms of the LTC concept. Dual-fuel combustion has advantages in high efficiency and emission reduction, so it is still widely investigated in the internal combustion engine field.
Dual-fuel combustion uses fuels of different reactivity together, so it shows very complex combustion phenomena. For a thorough investigation of dual-fuel combustion and further optimization, CFD analysis can assist to achieve the target. The objective of this paper is to find a relation between the operating strategies in dual-fuel combustion and the dominant combustion modes. The operating strategies chosen are the fuel ratio and the injection timing of a high-reactivity fuel. CFD simulations are used based on the experimental results. The combustion model used was developed by the authors, which consists of a combination of the RIF model and the G-equation model to better capture complex combustion modes occurring in dual-fuel combustion. The experiment was also conducted to provide the validation data for the model under a single-cylinder dual-fuel engine which was modified from a conventional diesel engine. The fuels used were diesel as a high-reactivity fuel and gasoline as a low-reactivity fuel. The model validation was conducted with the experimental results and showed a good agreement with the experimental data. Based on the validated results, the fuel ratio and the diesel injection timing were varied. These parameters were changed from the reference condition, and their effects on combustion modes were studied. It is expected from this study to give insight into dual-fuel combustion to form desired combustion modes by adjusting operating conditions.

Notation
CFD   *Computational Fluid Dynamics*
RIF   *Representative Interactive Flamelet*
KHRT   *Kelvin-Helmholtz Rayleigh-Taylor*

1. Introduction

Even though the vehicle industry and global society are being re-organized into the electric vehicle field, there is still a need for improvement of the internal combustion engine to prepare for this transition. Among many advanced combustion concepts, dual-fuel combustion has a possibility of drastic emissions reduction with achieving high efficiency. The disadvantage of dual-fuel combustion is that high pressure rise rate and higher CO, THC emissions hinder load expansion to high/low loads, which eventually leads to a limited operating range.

The dual-fuel combustion model was modified by the authors to further quantify combustion modes[1-3]. By assumptions, a gradual auto-ignition and flame propagation can occur simultaneously in dual-fuel combustion[4]. These two combustion modes can mainly appear as a dominant combustion mode depending on operating conditions, and their amount can be quantified by considering the proportion of each sub-combustion model. The modified combustion model[3] consists of a combination of the RIF, G-equation, and multi-zone models. These sub-models represent combustion modes of (gradual) auto-ignition, flame propagation (premixed flame), and chemical reactions from low-reactivity fuel only.

The objective of this paper is to find out the relationship between dominant combustion modes and the engine operating parameters by using the dual-fuel combustion model with a CFD. Injection

timing and fuel ratio were selected as the target operating parameters. An operating condition of 2000 rpm BMEP 10 bar was chosen as a reference condition and simulation results of in-cylinder pressure and heat release rate were matched with the experimental data. Based on these results, injection timing and fuel ratio were changed by simulation and compared. From the reference condition (injection timing bTDC 46CA), the injection timing was advanced to bTDC 36CA, 26CA, and 16CA. For fuel ratio, an additional simulation with a 3% reduced gasoline ratio from the reference condition was conducted (by energy ratio).

2. Experimental/Simulation setup

The reference condition was obtained from dual-fuel engine experiments[3]. The engine hardware was a single-cylinder diesel engine that was modified for dual-fuel combustion. Gasoline was supplied through the intake port to provide a premixed gasoline-air mixture inside the cylinder, and diesel was injected directly. The engine was 400cc with a compression ratio of 14 and a bathtub piston was installed. In the chosen reference condition (2000 rpm BMEP 10 bar), the injection timing was bTDC 46CA with a 62% gasoline fuel ratio (by energy). The AF ratio was about 15.5 with 36% of EGR added.

A commercial CFD software STAR-CD v4.22 (Siemens) was used with implemented user sub-routines. The computational mesh was generated to a 1/8 sector mesh with a 1mm base cell size. It had about 48,000 cells at IVC and 8000 cells at TDC. The temperature boundary was set to 440K for a piston, 430K for a head, and 420K for a liner. A k-e RNG turbulence model was used for a flow field and KHRT droplet breakup model was used with a lagrangian approach.

3. Simulation results

Figure 1-(a) shows the simulation and experimental results of in-cylinder pressure and heat release rate of the reference condition. The simulation results showed a good agreement with the experimental results. Figure 1-(b) shows the simulation results of varied injection timing. All simulation cases commonly showed low-temperature heat release before the main heat release rate, and ignition delay of the low-temperature heat release rate advanced as the injection timing did. The ignition delay of the main heat release rate also advanced, but at injection timing bTDC 46CA (reference case) the combustion phase was slightly delayed. Since the reference condition already had a higher gasoline ratio of 62%, the injection timing variation did not have much effect on the dominant combustion mode. As in figure 2, the flame propagation ratio of the total burned region was 61% in the reference condition. As the injection timing advanced, the maximum difference in the flame propagation fraction was 4% which was between cases "Injt 26CA" and "Injt 16CA".

Figure 1-(c) shows the fuel ratio variation results with an injection timing bTDC 26CA. The "3%" case had the same conditions as the case "Injt 26CA" with a 3% reduced gasoline ratio. The 3% value was calculated based on total fuel energy. Both conditions showed similar pressure and heat release rate shapes, but the result fractions of combustion modes were different. Since injection timing bTDC 26CA case retained the same gasoline fuel ratio, about 62% of the total burned area was by flame propagation due to premixed gasoline. However, in the "3% Injt 26CA" condition only 43% was burned by the premixed flame. Even though the heat release rates showed a similar shape, the dominant combustion mode changed from flame propagation to auto-ignition mode.
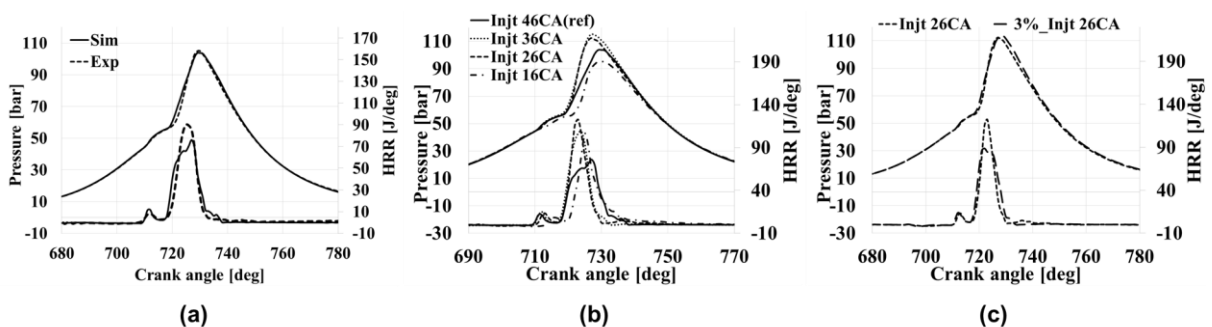
Fig. 1. In-cylinder pressure and heat release rate of (a) reference case with experimental results, (b) injection timing variation, and (c) fuel ratio change with the injection timing bTDC 26CA
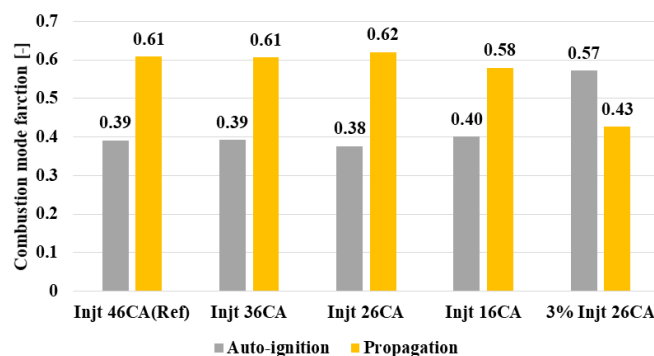
Fig. 2. The fractions of each combustion mode in the total burned area at aTDC 50CA

The dominant combustion mode was highly affected by the fuel ratio since a sufficient concentration of premixed fuel is required for flame propagation, especially under the EGR condition. In terms of injection timing, it did not much affect the combustion mode. Rather, it mostly determined the ignition delay.

Conclusions

The effects of injection timing and fuel ratio in dual-fuel combustion were studied using CFD simulation in this paper. The injected high-reactivity fuel was chosen to be diesel fuel, and the low-reactivity fuel that was supplied as a premixed state was gasoline. A reference condition 2000 rpm BMEP 10 bar was calculated and matched with the experimental results, and injection timing and fuel ratio were varied based on this condition.

Since the reference condition was favorable for the premixed flame that had a higher gasoline ratio (62%), the main dominant combustion mode appeared to be the flame propagation. In this condition, the injection timing variation had little effect on the combustion mode that the burned area fraction by flame propagation changed by 4% during 30CA injection timing change.

The fuel ratio directly affected the dominant combustion mode. When comparing the same conditions with a 3% difference in fuel ratio, the dominant combustion mode changed to auto-ignition when the gasoline ratio reduced by 3%. Even though these two cases showed different dominant combustion modes, the results of pressure or heat release curves were similar. From these results, it can be found that the main combustion mode in dual-fuel conditions was mainly affected by the premixed fuel ratio, and ignition delay timing can be adjusted by varying injection timing.

References

[1]   Moon, S., *et al.* "A Study of Flow Characteristics on the Diesel-Gasoline Dual-Fuel Combustion by 3-D CFD." SAE Technical Paper, 2019.
[2]   Moon, S., *et al.* "Numerical Analysis on the Effect of Piston Bowl Geometry in Gasoline-Diesel Dual-Fuel Combustion." SAE Technical Paper, 2019.
[3]   Moon, S. "Modeling of Dual-Fuel Combustion with Representative Interactive Flamelet, G equation, and Multi zone Models in Various Combustion Modes." Ph.D.Thesis, Seoul National University, 2022.
[4]   Lee, S. "Modeling of Combustion and Emission Characteristics in a Dual-fuel Engine by Combining Diffusion and Premixed Combustion." Ph.D.Thesis, Seoul National University, 2013.

THIESEL 2022 Conference on Thermo- and Fluid Dynamics of Clean Propulsion Powerplants

A Numerical Study of Hydrogen Combustion in Wankel Rotary Engines

K. Moreno-Cabezas, G. Vorraro, X. Liu, J. Turner, H. Im

CCRC – Clean Combustion Research Center. King Abdullah University of Science and Technology, Thuwal, Saudi Arabia.

E-mail: kevin.morenocabezas@kaust.edu.sa
Telephone: +(966) 54 410 8749

Abstract. To pursue compliance with the very strict modern emission regulations for automotive applications, there is a need for new and alternative fuels, technologies, and combustion modes that allow a reduction in emission and decarbonization of vehicles. Wankel rotary engines have been an interesting alternative option to replace conventional Spark Ignition (SI) reciprocating engines due to their most distinctive features as lightweight, small size and high-power density, and stronger fuel adaptability. Some of these characteristics make this engine concept suitable as a range extender in electric vehicles and to operate with alternative fuels such as hydrogen (H_2). This research presents a study that numerically explores the performance, emissions, and combustion characteristics of a H_2-fueled Wankel engine. The simulations were performed using CONVERGE CFD software. The results show the potential feasibility of H_2 as a substitute for conventional carbon-based fuels in alternative engine technologies such as the Wankel concept. To control the peak pressure and combustion duration and reduce nitrogen oxides (NO_x) emissions to acceptable levels a lean mixture of at least $\lambda = 1.9$ is required. Lean H_2 mixture combustion increases the combustion efficiency and reduces the heat transfer losses. Further improvements in the concept can be realized by implementing H_2 direct injection.

1. Introduction

The necessity of a better world with clean air for forthcoming generations is an alarming concern as human activities have resulted in emissions of NO_x, particulate matter (PM), and greenhouse gas (GHG) emissions. A great fraction of these emissions is generated by the engines in the automobile sector as more than 99% of transport is powered by combustion engines and more than 90% of transport energy comes from petroleum-based fuels [1]. The stringent regulations to reduce these emissions lead to electrification, the development of non-conventional fuels and technologies or engine concepts that allow increasing the efficiency of the power system in vehicles. One possible technology that can assist the actual vehicles is the Wankel rotary engine, and energy from renewable sources can be applied to produce alternative fuels like H_2 or sustainable liquid fuel such as are known as electro fuels [2] or e-fuels suitable for internal combustion engines. The so-called Wankel rotary engine was first built in 1957 by Felix Wankel as an alternative to the conventional reciprocating piston SI engines [3] with fewer components making it simpler, lighter, easier to maintain, compact and well-balanced. These characteristics make it suitable for applications such as aircraft or as a range extender in Hybrid Electric Vehicles. Among the greatest drawback of the Wankel engine is the reduced thermal efficiency due to the long, thin, and moving combustion chamber that increases the surface area to volume ratio and heat transfer and also generates flame quenching [4].

As part of the current alternative fuels proposed for internal combustion engines, H_2 is one of the most important, promising and considered the fuel of the future as it can be obtained from multiple green sources. H_2 would be expected to be an appropriate fuel to operate the Wankel engine as it has a low extinction distance allowing the flame to reach the crevices when the chamber becomes thin and improving the efficiency due to the high combustion rate [5] as one cycle in the Wankel concept is 1.5 times longer (in terms of angle of the shaft). This research makes a numerical study by using a Computational Fluid Dynamic (CFD) tool to investigate the performance and combustion characteristics such as pressure trace inside the combustion chamber, combustion efficiency, heat transfer, energy conversion efficiency, NO_x emissions and energy distribution of a Wankel rotary engine fuelled with H_2 in a premixed SI mode.

2. Experimental engine

The available experimental results [6] used to validate the proposed CFD model were previously obtained at the University of Bath with a 225 cm^3 Wankel rotary engine manufactured by Advanced Innovative Engineering UK (AIE) in the United Kingdom [7]. Some of the technical specifications of the engine are presented in Table 1. These experiments were run using gasoline as fuel under stoichiometric conditions.

Table 1. Engine specifications [7]

Engine Type	Wankel single rotor
Power output	40 hp / 30 kW
Weight	10 kg
Displacement	225 cm^3
Torque	27 lb/ft @ 8000 rpm
Compression ratio	9.6:1
Ignition system	Twin spark plug
Generating radius	69.5 mm
Eccentricity	11.6 mm
Width of the rotor housing	51.941 mm

3. Computational CFD model

The software used to model the engine was CONVERGE v3.0. One of the main characteristics of this CFD code is the automatic generation of a structured mesh of the geometry at each solved time step. The governing equations that CONVERGE solves correspond to the conservation of mass, momentum, and energy. Some of the implemented submodels are the Reynolds-Averaged Navier-Stokes (RANS) Re-Normalisation Group k-ε for turbulence, SAGE as a detailed transient chemistry solver, Redlich-Kwong as the equation of state and the extended Zeldovich for the thermal NO$_x$ emissions. The experimental results obtained at the University of Bath [8] were used to validate the computational model in CONVERGE using a chemical mechanism for Primary Reference Fuel (PRF) blends comprised of 48 species and 152 reactions. The gasoline surrogate implemented in the validation corresponds to a Research Octane Number (RON) of 98 (PRF98) composed of 98% iso-octane and 2% n-heptane according to the experiments. The validation was done by comparing the pressure trace for the model with the experiments corresponding to a Brake Mean Effective Pressure (BMEP) of 3 bar at 3000 rpm and Wide-Open Throttle (WOT). The validation showed that the model can predict the pressure rise during the compression stroke and the start of the combustion resulting in correct peak pressure and pressure rise among the cycle-to-cycle variation of the experiments. The good agreement between the experiments and simulation in the pressure as a sample of all the processes occurring in the engine concludes that the model will predict the behaviour and tendency of using H$_2$ as a fuel in a rotary Wankel engine.

4. Hydrogen combustion simulations

The H$_2$ simulations were conducted for the same conditions as the gasoline validated case but using the detailed H$_2$/O$_2$ kinetic mechanism by Burke [9]. In the standard engine configuration, the spark timing corresponds to -18 deg. bTDC and stoichiometric condition. The pressure trace of H$_2$ combustion under this configuration is expected to show fast combustion and results in an instantaneous pressure rise, knock conditions, and unfavourable peak pressure. For this reason, in Figure 1 the efficiency of the engine is shown for different spark timing and lean mixtures to keep the pressure under desirable conditions. In the figure can be seen that for leaner mixtures the operating range moves to early spark timings due to a decrease in burning rate and longer combustion. Additionally, it can be seen that the optimum operating condition is $\lambda = 1.9$ and with the spark timing at the TDC position. The efficiency and operating range of the reference PRF98 case is also shown for comparison. From this can be seen that the H$_2$ under the optimum conditions represents an absolute improvement of 2.2% in the efficiency of the engine compared to the reference case.
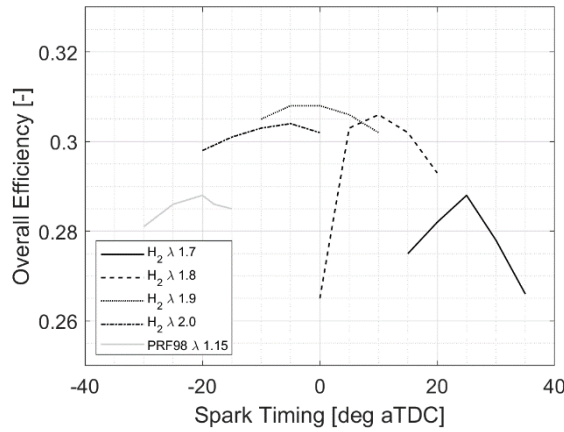
Figure 1. Overall engine efficiency under lean conditions

Figure 2 (a) shows a comparison of the energy distribution of H_2 combustion for $\lambda \geq 1.7$ and spark timing at TDC, and the PRF98 reference case. From the figure can be seen that increasing the air excess improves the combustion efficiency as there is more oxygen available to burn the injected fuel. Also shown is that the increase in lambda results in lower combustion temperature that reduces the heat transfer losses and will decrease the NO_x emissions. Also, when the mixture goes leaner the longer combustion compared to rich mixtures reduces the peak pressure but allows an increase in the generated work as is shown in Figure 2 (b).
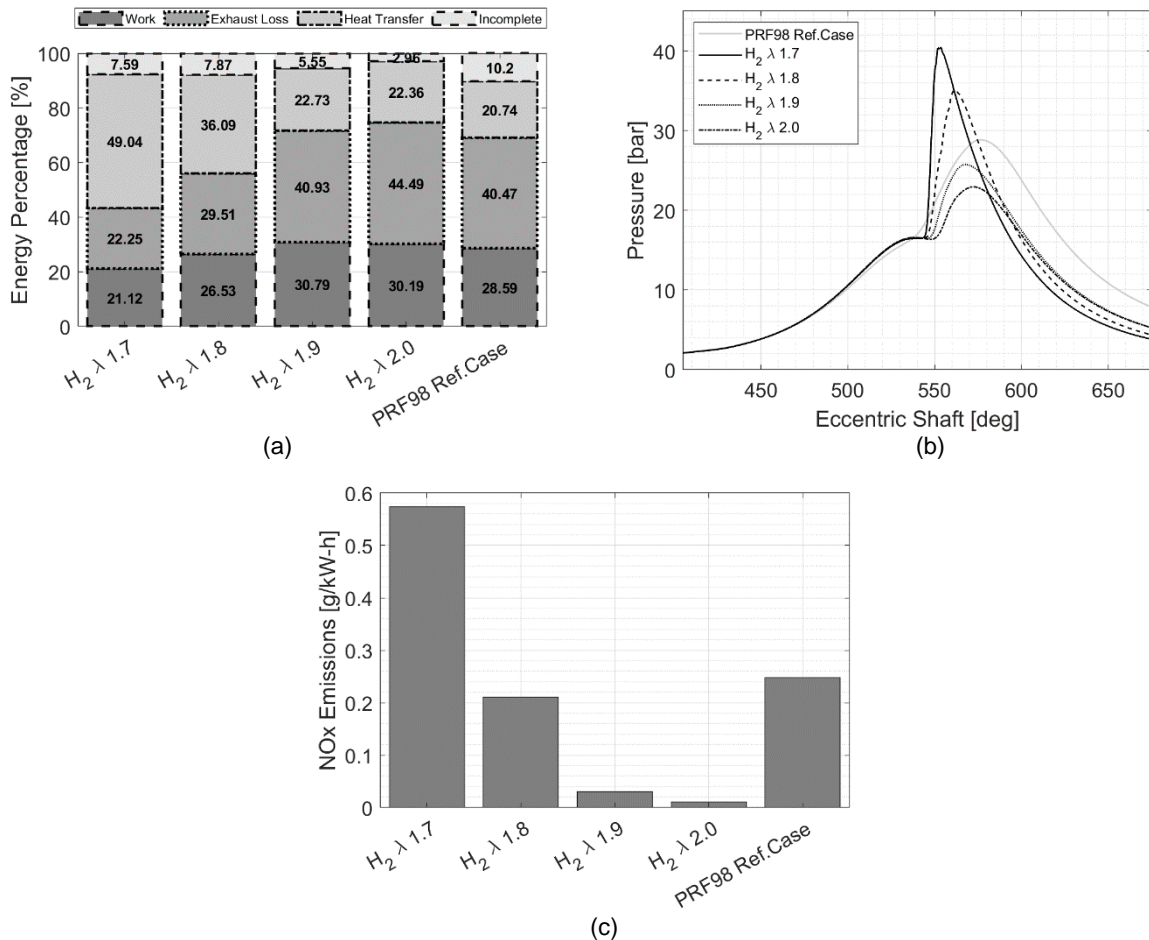

(a)

(b)

(c)

Figure 2. H_2 energy distribution (a), pressure trace (b), and NO_x emissions (c) comparison under optimum spark timing

4   K. Moreno-Cabezas, G. Vorraro, X. Liu, J. Turner, H. Im

Comparing the energy distribution of H_2 combustion against the gasoline reference case, we can see that H_2 combustion even at non-optimum conditions allows an increase in combustion efficiency improving the fuel economy and the shorter combustion allows increasing the generated work as is also shown in the pressure trace in Figure 2 (b). Even when the heat transfer losses are reduced for leaner mixtures, they are higher for H_2 compared with gasoline. This is something that can perhaps be improved by changing the fuel injection method from premixed to direct injection. This is a research subject for future study. Figure 2 (c) shows the NO_x emissions for the H_2 combustion cases compared to the reference gasoline case. From the figure the NO_x emissions reduction for lean H_2 mixtures can be seen and that even for the gasoline reference case the emissions are lower than 0.4 g/kWh, corresponding to the EURO VI diesel standard [10], but for H_2 combustion at $\lambda > 1.8$ emissions they are almost negligible.

5. Summary and conclusions

A preliminary study of the performance and combustion characteristics of a premixed SI Wankel rotary engine fueled with H_2 by using a CFD tool was presented. Some of the conclusions are:

- The H_2 combustion allows an improvement of up to 2.2% in efficiency compared to gasoline combustion under standard conditions.
- For H_2 combustion, lean mixtures are required to control the combustion and keep the peak pressure and NO_x emissions low.
- The optimum spark timing and operating range for H_2 are earlier for leaner mixtures due to lower burning rates and longer combustion.
- Increasing the air excess improves the combustion efficiency due to more oxygen availability.
- A reduction in combustion and heat transfer losses generates an increase in work output for lean H_2 combustion.
- An improvement in combustion efficiency and heat transfer losses might be achieved by direct injection of the fuel, which will be studied in the future.

6. References

1. Leach, F., Kalghatgi, G., Stone, R., and Miles, P., "The scope for improving the efficiency and environmental impact of internal combustion engines," *Transportation Engineering* 1:100005, 2020, doi:10.1016/J.TRENG.2020.100005.
2. Kalghatgi, G., "Is it really the end of internal combustion engines and petroleum in transport?," *Applied Energy* 225:965–974, 2018, doi:10.1016/J.APENERGY.2018.05.076.
3. General Information about Rotary Engines, https://www.wankelsupertec.de/en_rotary_engines.html, Feb. 2022.
4. Tartakovsky, L., Baibikov, V., Gutman, M., Veinblat, M., and Reif, J., "Simulation of Wankel engine performance using commercial software for piston engines," *SAE Technical Papers* 4, 2012, doi:10.4271/2012-32-0098.
5. Akal, D., Öztuna, S., and Büyükakın, M.K., "A review of hydrogen usage in internal combustion engines (gasoline-Lpg-diesel) from combustion performance aspect," *International Journal of Hydrogen Energy* 45(60):35257–35268, 2020, doi:10.1016/j.ijhydene.2020.02.001.
6. Vorraro, G., Turner, M., and Turner, J.W.G., "Testing of a Modern Wankel Rotary Engine - Part I: Experimental Plan, Development of the Software Tools and Measurement Systems," *SAE Technical Papers* 2019-Janua(January):1–16, 2019, doi:10.4271/2019-01-0075.
7. 225CS - 40BHP - Wankel Rotary Engine | Advanced Innovative Engineering (UK) Ltd, https://www.aieuk.com/225cs-40bhp-wankel-rotary-engine/, Feb. 2022.
8. Vorraro, G. and Turner, J., "Testing of a Modern Wankel Rotary Engine - Part III : firing condition analysis," 1–17, 2022, doi:10.4271/2022-01-0592.Received.
9. Burke, M.P., Chaos, M., Ju, Y., Dryer, F.L., and Klippenstein, S.J., "Comprehensive H 2/O 2 kinetic model for high-pressure combustion," *International Journal of Chemical Kinetics* 44(7):444–474, 2012, doi:10.1002/kin.20603.
10. Emission Standards: Europe: Heavy-Duty Truck and Bus Engines, https://dieselnet.com/standards/eu/hd.php, Jun. 2022.

Numerical Analysis of Emissions and Operating Range of Acetone Fuel in a Homogenous Charge Compression Ignition at Different Engine Speeds

J.M. Garcia-Guendulain[1], J.M. Riesco-Avila[2], J.P. Perez-Trujillo[1], A.E. Mendoza Rojas[1], O. Rodriguez-Abreo[1], R. Hernandez-Alvarado[1]

[1]UPQ – Universidad Politécnica de Querétaro. Carretera Estatal 420 SN, El Rosario, El Marques, Queretaro, Mexico

E-mail: manuel.garcia@upq.edu.mx
Telephone: +(52) 442 101 9000

[2]University of Guanajuato, Carretera Palo Blanco, Salamanca, Guanajuato, Mexico

E-mail: riesco@ugto.mx
Telephone: +(52) 464 650 4132

Abstract. In this work an evaluation of operating range in a HCCI engine fueled with acetone using an onion skin multizone model has been developed. The effect from physical and chemical processes for engines can be obtained from this model with a lower computational demand. Several consecutive cycles can be simulated in minutes compared with others, such as CFD models, which requires either hours or days.

A single cylinder HCCI engine fueled with PRF90 was simulated and compared with literature data. A good agreement with experimental data allowed to analyze the engine performance with acetone and iso-octane (50% by volume for each) as fuel at several engine speeds. The results show a comparison of pressure profiles and indicated mean pressure as a function of equivalence ratio and engine speeds. A mixture labelled as IAF50 (iso-octane 50% by volume and acetone 50% by volume) show a delayed start of combustion compared with IAF50 (iso-octane 100% by volume and acetone 0% by volume). This work is a start point to obtain operating region of HCCI engine fueled with of acetone-isooctane mixtures

1. Introduction

Nowadays, internal combustion engines (ICE) operating regimes promise to improve the efficiency vs. emissions of conventional engines (spark-ignited and compression ignited engines). Homogenous charge compression ignition (HCCI) engines has been widely studied due to (1) high efficiency resulting from high compression ratio, lean operation and unthrottled intake [1]–[5], and (2) low NOx and PM emissions due to high levels of dilution leading to low temperature, fuel lean combustion [6].

Unlike to conventional engines, a control mechanism for start of combustion is necessary in HCCI engines, due to HCCI engines require adequate conditions at intake valve closing (IVC) instead a spark plug or injector (which are used in conventional engines). The uncontrolled start of combustion can result in rapid heat release leading to high in-cylinder pressure and the ringing problem (also known as knock), it can produce severe engine damage. Therefore, a detailed analysis of HCCI combustion is necessary to guide engine designers toward practical solutions. In this way some models have emerged and can be classified as zero-dimensional (single zone), multi-dimensional (CFD), and quasi-dimensional (multizone).

Multizone models can consider thermal stratification and chemical kinetics at much reduced computational expense vs. CFD (which have more accuracy but require considerable most computacional resources [7]–[9], and therefore provide a versatile tool for accurate and computationally efficient analysis of HCCI combustion. This is especially true when the combustion process involves large molecules modeled with chemical kinetic mechanisms including thousands of species, or when hundreds of runs are necessary for determining optimum regions of operation. Improved methodologies can increase computational advantage even more, enabling rapid execution of hundreds of cases well within the computational capability of today's desktop or laptop computers rather than supercomputers.

2   J.M. Garcia-Guendulain[1], J.M. Riesco-Avila[2], J.P. Perez-Trujillo[1], A.E. Mendoza Rojas[1], O. Rodriguez-Abreo[1], R. Hernandez-Alvarado[1]

In this paper a multizone model has been programmed and used for simulation of engine at several operating conditions with less computational resources than multidimensional models (CFD models). With this model, operational points of operation for a HCCI engine can be generated for a mixture of conventional and unconventional fuel. In this case, due to physical and chemical properties [7], acetone is used as unconventional fuel in the mixture of 50% acetone and 50% iso-octane by volume at several engine speed (1200 rpm, 1600 rpm and 2000 rpm), and the effect on indicated mean pressure and pressure profiles were analyzed.

2. Multizone Model

In this study the multizone model with detailed chemical kinetics was used to solve species, temperature and pressure in transient conditions. The operation was simplified to closed cycle between inlet valve closing (IVC) and exhaust valve opening (EVO), for each incremental angle position between IVC and EVC.

The cylinder was split into a number of homogenous zones (see Fig. 1) in terms of temperature, pressure and species concentrations; however, these values can be stratified amongst zones. Heat transfer is obtained between zones by conduction heat transfer, and convection heat transfer is obtained at the first zone (near to walls).

Species evolution for each zone is calculated, and volume for each zone is calculated. The overall pressure is assumed to be constant. All the equations are solved numerically using CANTERA package for calculations of chemical kinetics and thermodynamic properties.
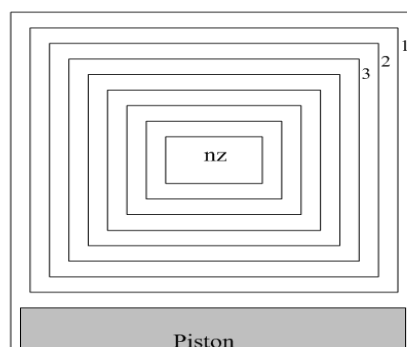

Fig. 1. Scheme of zone distribution for multizone onion-skin model

3. Results

3.1 Validation

Multizone model has been validated by comparison with CFD results obtained from a single cylinder HCCI engine fueled with iso-octane (iC_8H_{18}), 90% by mass and n-heptane (nC_7H_{16}) 10% by mass mixture (PRF90). Table 1 shows geometrical and operational conditions for the engine The multi-zone model is limited to closed cycle (from IVC to EVC), and a mechanism with 252 species and 1038 reactions were used [8].. The number of zones used here are agree with those shown in literature [9]–[11]. Validation is shown in Fig. 2, which good agreement with literature date is obtained.

Table 1. Engine specifications and operating conditions [12]

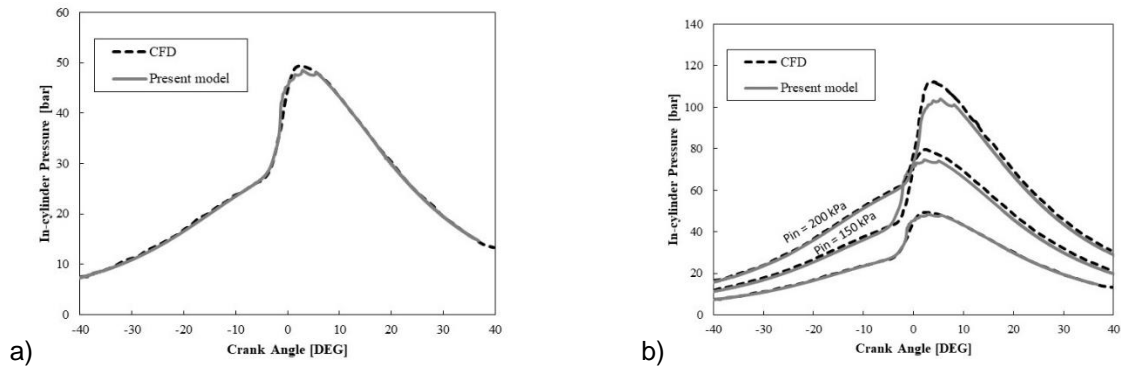| Displacement	0.540 liters
Bore	86 mm
Stroke	94.3 mm
Connecting rod length	152.2 mm
Compression ratio	12.25:1
Valves	4
Speed	2000 rpm
Intake pressure	100 kPa (absolute)
IVC	130° BTDC
EVO	148° ATDC

Fig. 2 Validation of present model with literature data [12] **at a) Pin=100 kPa and b) Different Pin**

3.2. Comparison with acetone fuel

In this work, simulations were carried on with iso-octane 100% by volume (represented by IAF0) and a mixture of 50% iso-octane and 50% acetone by volume (represented by IAF50). The in-cylinder pressure obtained for several equivalent ratios is shown in Fig. 3 and the indicated mean pressure (IMEP) for several engine speeds and equivalence ratios is shown in Fig. 4.
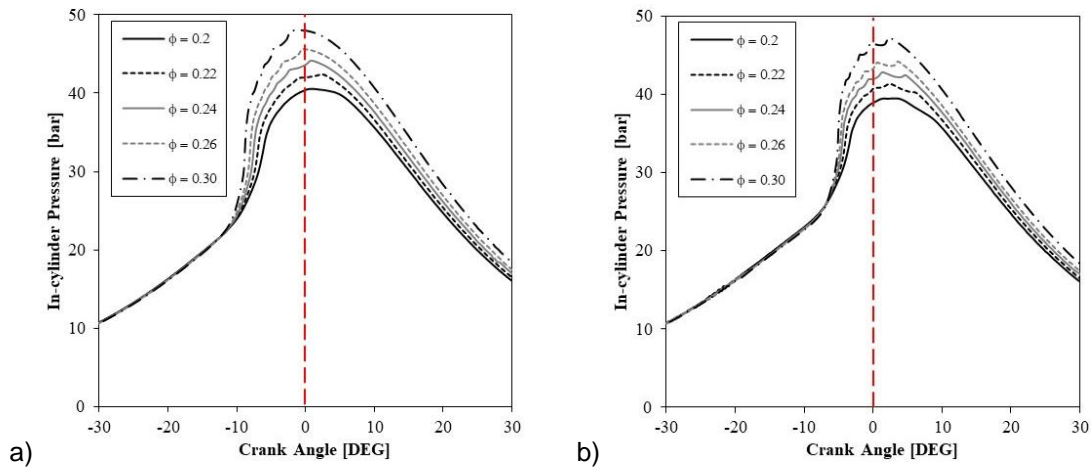

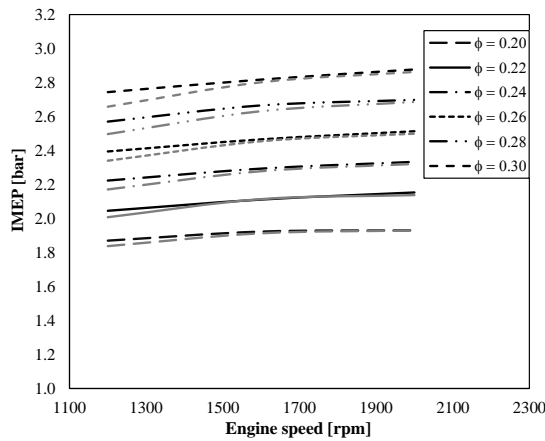**Fig. 3. In-cylinder pressure fueled with a) IAF0 and b) IAF50 mixtures at 1200 rpm**

Fig. 4. Indicated Mean Pressure comparison. Black lines represent IAF0 mixtures and gray lines IAF50 mixtures.

4   J.M. Garcia-Guendulain[1], J.M. Riesco-Avila[2], J.P. Perez-Trujillo[1], A.E. Mendoza Rojas[1], O. Rodriguez-Abreo[1] and R. Hernandez-Alvarado[1]

Conclusions

In this work a multizone onion-skin model has been programmed and used for simulation of several engine conditions. Comparison with literature data for three intake pressures show good agreement with present model and therefore, simulations of different operational conditions can be obtained. Analysis of several engine speeds with mixtures of iso-octane and acetone fuels were carried out.

Results show early combustion is obtained when the engine run with iso-octane 100% by volume (IAF0) compared with IAF50 for the same operational conditions, which is because of acetone can produce suitable conditions for HCCI combustion due to chemical and physical properties [7]. Delayed combustion also, can produce a slightly increase of IMEP when IAF50 is used instead IAF0. Acetone fuel could be used as an alternative fuel when it is mixed with conventional fuel and slightly even improvement of IMEP could be obtained. This work is a start point to obtain operating region of HCCI engine fueled with of acetone-isooctane mixtures.

[1]   J. E. Dec y M. Sjöberg, «A Parametric Study of HCCI Combustion - the Sources of Emissions at Low Loads and the Effects of GDI Fuel Injection», SAE International, Warrendale, PA, SAE Technical Paper 2003-01-0752, mar. 2003. doi: 10.4271/2003-01-0752.

[2]   J. E. Dec, «A Computational Study of the Effects of Low Fuel Loading and EGR on Heat Release Rates and Combustion Limits in HCCI Engines», SAE International, Warrendale, PA, SAE Technical Paper 2002-01-1309, mar. 2002. doi: 10.4271/2002-01-1309.

[3]   M. Sjöberg, J. E. Dec, y N. P. Cernansky, «Potential of Thermal Stratification and Combustion Retard for Reducing Pressure-Rise Rates in HCCI Engines, Based on Multi-Zone Modeling and Experiments», SAE International, Warrendale, PA, SAE Technical Paper 2005-01-0113, abr. 2005. doi: 10.4271/2005-01-0113.

[4]   H. Machrafi y S. Cavadiasa, «An experimental and numerical analysis of the influence of the inlet temperature, equivalence ratio and compression ratio on the HCCI auto-ignition process of Primary Reference Fuels in an engine», *Fuel Processing Technology*, vol. 89, n.º 11, pp. 1218-1226, nov. 2008, doi: 10.1016/j.fuproc.2008.05.019.

[5]   M. Yao, Z. Zheng, y H. Liu, «Progress and recent trends in homogeneous charge compression ignition (HCCI) engines», *Progress in Energy and Combustion Science*, vol. 35, n.º 5, pp. 398-437, oct. 2009, doi: 10.1016/j.pecs.2009.05.001.

[6]   P. Duret *et al.*, «Progress in Diesel HCCI Combustion Within the European SPACE LIGHT Project», SAE International, Warrendale, PA, SAE Technical Paper 2004-01-1904, jun. 2004. doi: 10.4271/2004-01-1904.

[7]   A. Calam, «Study on the combustion characteristics of acetone/n-heptane blend and RON50 reference fuels in an HCCI engine at different compression ratios», *Fuel*, vol. 271, p. 117646, jul. 2020, doi: 10.1016/j.fuel.2020.117646.

[8]   M. Mehl, J. Y. Chen, W. J. Pitz, S. M. Sarathy, y C. K. Westbrook, «An Approach for Formulating Surrogates for Gasoline with Application toward a Reduced Surrogate Mechanism for CFD Engine Modeling», *Energy Fuels*, vol. 25, n.º 11, pp. 5215-5223, nov. 2011, doi: 10.1021/ef201099y.

[9]   M. Bissoli, A. Frassoldati, A. Cuoci, E. Ranzi, M. Mehl, y T. Faravelli, «A new predictive multi-zone model for HCCI engine combustion», *Applied Energy*, vol. 178, n.º Supplement C, pp. 826-843, sep. 2016, doi: 10.1016/j.apenergy.2016.06.062.

[10]   S. Visakhamoorthy, J. Z. Wen, S. Sivoththaman, y C. R. Koch, «Numerical study of a butanol/heptane fuelled Homogeneous Charge Compression Ignition (HCCI) engine utilizing negative valve overlap», *Applied Energy*, vol. 94, pp. 166-173, jun. 2012, doi: 10.1016/j.apenergy.2012.01.047.

[11]   E. Neshat, R. K. Saray, y S. Parsa, «Numerical analysis of the effects of reformer gas on super-charged n-heptane HCCI combustion», *Fuel*, vol. 200, pp. 488-498, jul. 2017, doi: 10.1016/j.fuel.2017.04.005.

[12]   J. Kodavasal *et al.*, «An accelerated multi-zone model for engine cycle simulation of homogeneous charge compression ignition combustion», *International Journal of Engine Research*, vol. 14, n.º 5, pp. 416-433, 2013.

THIESEL 2022 Conference on Thermo- and Fluid Dynamics of Clean Propulsion Powerplants

Towards the Integration of Heavy-Duty Vehicles in the Hydrogen Sector: Development of a Spark Ignition Engine using Hydrogen as Fuel

J.M. Neveu[1], F. Foucher[2], R. Oung[2], D. Serrano[3], B. Walter[3], F. Duffour[3]

[1]Volvo Group Trucks Technology, 1 avenue Henri Germain, 69800 Saint-Priest, France.

E-mail: jean-marc.neveu@volvo.com
Telephone: +(33) 481932835

[2]Université d'Orléans, 8 Rue Léonard de Vinci, 45072 Orléans, France.

E-mail: fabrice.foucher@univ-orleans.fr
Telephone: +(33) 238494514

[3]IFP Energies nouvelles, Rond-point de l'echangeur de Solaize, 69360 Solaize, France.

E-mail: david.serrano@ifpen.fr
Telephone: +(33) 437702157

1. Introduction

In the crucial context of global warming, hydrogen is considered as an essential energy carrier to reduce greenhouse gases emissions. Its potential applications are numerous and present across all energy sectors. Particularly, our mobility needs are continually increasing, leading to an upsurge in the energy demand in the very next future. The diversification of the energy sources is urgently required. Hydrogen mobility has the potential to answer some of the key emission reduction challenges. Compared to batteries, it offers advantages concerning storage density and quick refuelling. Hydrogen may be used to feed a fuel cell, or directly used as a fuel in an internal combustion engine. This latter option offers the advantages of re-using current fossil fuel engines– existing and proven technology, long life-time, controlled cost of ownership, less dependence to rare materials, robustness against hydrogen and air quality – with a very low carbon footprint. Commercial vehicle manufacturers and equipment suppliers show continuing interest on hydrogen ICE considering them as a very competitive alternative.

In this context, Renault Trucks is leading the French consortium "PLH2" funded by ADEME, the French agency for energy transition to develop a demo-truck equipped with a spark-ignited hydrogen internal combustion engine. The project gathers Renault Trucks, Prisme Université d'Orléans, IFP Energies nouvelles, Hynamics, Plastic Omnium and Total Energies like described in figure 1. The main objective is the development of a hydrogen internal combustion engine (ICE) meeting some important requirements. The hydrogen ICE needs to be manufactured on the same industrial facilities as current Diesel engines for a short time to market. Moreover, this new engine should keep commonality with actual Diesel product as much as possible for cost reasons. The engine should also match equivalent performance as today Diesel product. This proof of concept will use the same Exhaust Aftertreatment System as the current Diesel engine. H_2 ICE need to fulfil EUVII target emission (Clove hypothesis) and Low Emission Vehicle capability ($CO_2 < 1$ g/kWh). CO_2 requirements impose a low NOx engine combustion to avoid too much CO_2 produced by urea injection and leave some room for CO_2 caused by oil consumption. Finally, hydrogen ICE should tolerate low purity hydrogen gas.

Fig. 1. MH8 consortium partnership

2. Simulation and design

Thanks to its low ignition energy and high speed and high temperature of combustion, hydrogen combustion needs to be controlled with dilution. Dilution decreases both temperature and flame speed allowing to lower NOx emissions, to mitigate knock and to decrease the risk of abnormal combustion like pre-ignition. For this project, dilution is obtained by air plus liquid water injection. This latter helps to decrease drastically compression and combustion temperature thanks to its high latent heat of vaporization. Injecting water in the intake port has a cooling effect, especially on remaining exhaust gases on cylinder and back flow to inlet. One other key point is the lower enthalpy on exhaust gases on a hydrogen ICE. Theoretical calculation shows the possibility, at same level of temperature, to maintain more exhaust energy for the turbine by increasing water content. For the air demand, a 1.7 factor with only air dilution is needed compared to the air for Diesel engine version at same power. This ratio is reduced to 1.2 with water injection. An attention must be paid on water in oil dilution and steel corrosion, that could be the drawback of this solution.
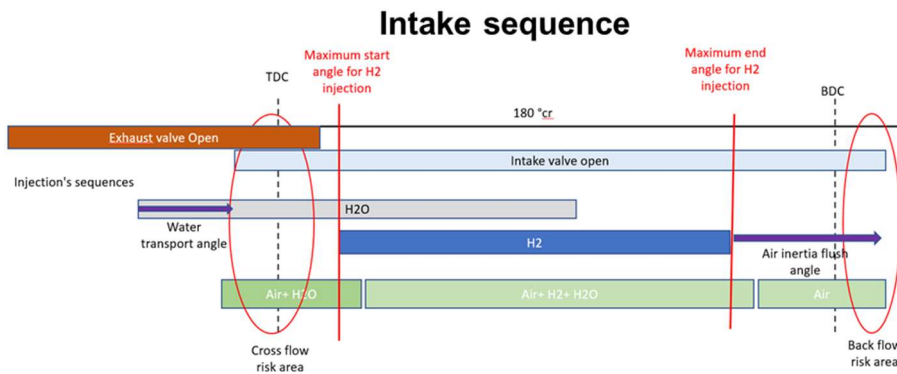
Fig. 2. Theoretical injection sequence during intake phase: cooling of back flow gases, scavenge of air and water, short H$_2$ injection

The engine concept was based on retrofitting an existing Diesel engine by keeping current Variable Geometrical Turbocharger and keeping the Diesel camshaft, thus determining the full load performance. Besides, in order not to deeply modify Diesel cylinder head, the hydrogen was port fuel injected. This choice induces a specific work to mitigate as much as possible backfire risk. The spark plug was mounted in place of Diesel injector. For the piston evolution, piston bowl was adapted to reduce compression ratio to 12:1 and to change air motion. Additionally, port water injection was implemented to enhance dilution. A principle of injection sequence was then determined and patented like described in figure 2. Main risks are around backflow of hot gases or at the end of intake. Backflow at valve overlap could be cooled thanks to water. Backflow at intake valve closing will be mitigated thanks to air flush effect with high-speed inertia.
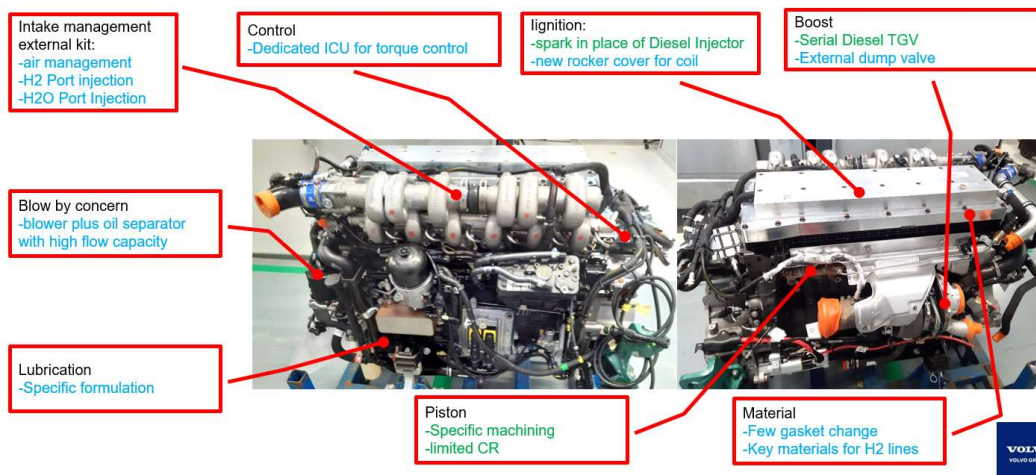
Fig. 3. Photo of the prototype engine built according to the retrofit spirit

For the air intake manifold design, air energy is used to scavenge the intake port and decrease risk of residual hydrogen. The runner was designed with a specific diameter to reach high air velocities and use air inertia. The length of individual runner was adjusted to get maximum volumetric efficiency according to the "average road engine speed" used on Medium Duty application. Intake design is motivated with a compromise between packaging and volumetric efficiency: coiled runner is one solution.

3. Single cylinder engine tests

A first test campaign has been carried out on a single cylinder engine (SCE) to validate the engine design. The engine has been implemented on a hydrogen dedicated engine test cell at PRISME Université d'Orléans, France. The SCE study was based on engine parameter sweeps to evaluate the impact of each setting on the engine efficiency and the pollutant emissions, specifically NOx. The SCE was tested at 900 rpm and 1400 rpm with a load range between 8 bar up to 22 bar IMEP.
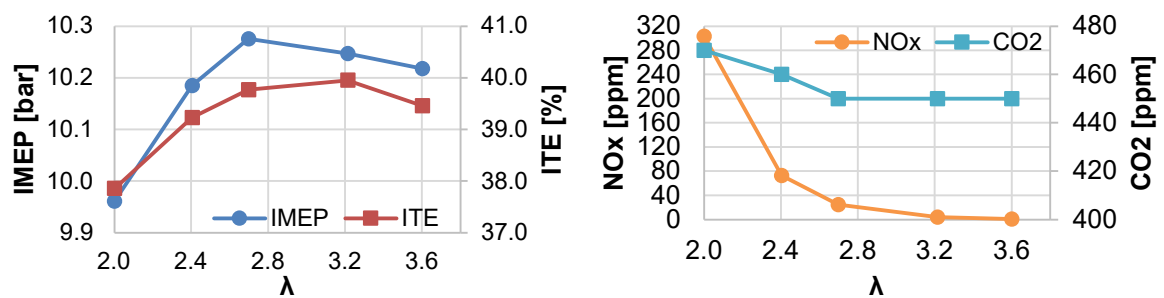

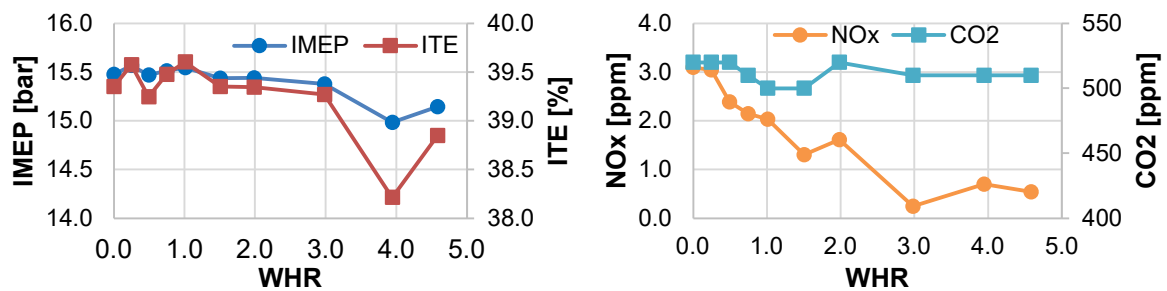**Fig. 4.** λ sweep - IMEP & ITE (left), NOx & CO2 (right) at 1400 rpm, IMEP=10 bar

Fig.5. Water/H2 Ratio (WHR) sweep – IMEP & ITE (left), NOx & CO2 (right) at 1400 rpm IMEP=15.5 bar & λ=3

The main following results have been highlighted:
- Lean conditions and water injection help to mitigate NOx emissions and prevent from backfire and knock occurrences as described in figures 4 and 5.
- Despite H_2 port fuel injection, which is presumed to form more homogeneous charge than H_2 direct injection, the mixing between air and H_2 is an issue that should be addressed to tend toward NOx free operation.
- Some parameters need to be addressed or tuned for optimal H_2 combustion like start of injection for H_2 or water, injector's location in the intake runner, multiple injections, piston shape, injection pressure.
- Comparison between λ and Water/H_2 Ratio (WHR) sweeps shows that air dilution is more effective to achieve NOx free operation.
- For achieving same power as Diesel operation, high boost level up to 3.5 bar is needed for the H_2 ICE. On a multicylinder engine, ensuring high boost level during transient or part load is limited by exhaust gases enthalpy. For those conditions, water injection will maintain low NOx emissions and mitigate abnormal combustion occurrences.
- NOx emissions can also be reduced by late spark timing but at the expense of indicated thermal efficiency (ITE).
- Lean conditions and a compression ratio of 12:1, allows to achieve a range of 41-42% ITE at medium and full load.

4   J.M. Neveu, F. Foucher, R. Oung, D. Serrano, B. Walter, F. Duffour

4. Multicylinder engine tests

The following stage of this project consisted in testing and calibrating the multicylinder prototype engine. Therefore, the multicylinder has been implemented on a hydrogen dedicated engine test cell at IFPEN in Solaize, France. The first round of the calibration test campaign was done to build engine settings maps in steady-state conditions. These tests were focused on the low and mid load without water injection. The figure 6 gives an example of spark timing variation at different λ at 1400rpm and keeping constant the injected H_2 mass flowrate. For example, the optimal BMEP is reached at 11bar for λ=2.1 as BTE reached its maximum at 40.5%. The optimal combustion phasing depicted by the parameter CA50 averaged on the 6 cylinders is in the area around 5 to 10 CAD ATDC. The best BTE is obtained for the lowest λ=2.1 but this latter led to high NOx emissions. Considering the trade-off BTE/engine-out NOx emissions, λ=3 was the optimal air/fuel ratio. Increasing λ over 3.5 led to a drastic drop in BTE (and consequently in BMEP at constant injected H_2 mass flowrate) caused by slow flame propagation. Besides, high λ created combustion instabilities.
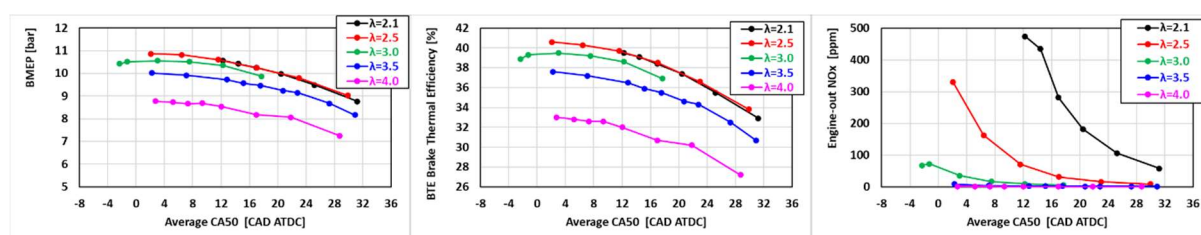
Fig. 6. Spark timing variation at 1400rpm at injected H_2 mass flowrate =7.2kg/h for λ = {2.1/2.5/3.0/3.5/4.0} without water injection – BMEP, Brake thermal efficiency, Engine-out NOx

One of the key challenges of the indirect injected hydrogen combustion is controlling abnormal combustions: single backfiring, double backfiring, knocking and even pre-ignition like described in figure 7. The backfiring was experienced at every engine speed at low load. Pre-ignition and knocking occurred at higher load. The backfiring can be described as a combustion starting in the combustion chamber during intake valve opening which flame propagates reversely inside the intake duct. A thin thermocouple placed in the intake duct can detect backfiring. Usually, the temperature will raise just after the backfiring.
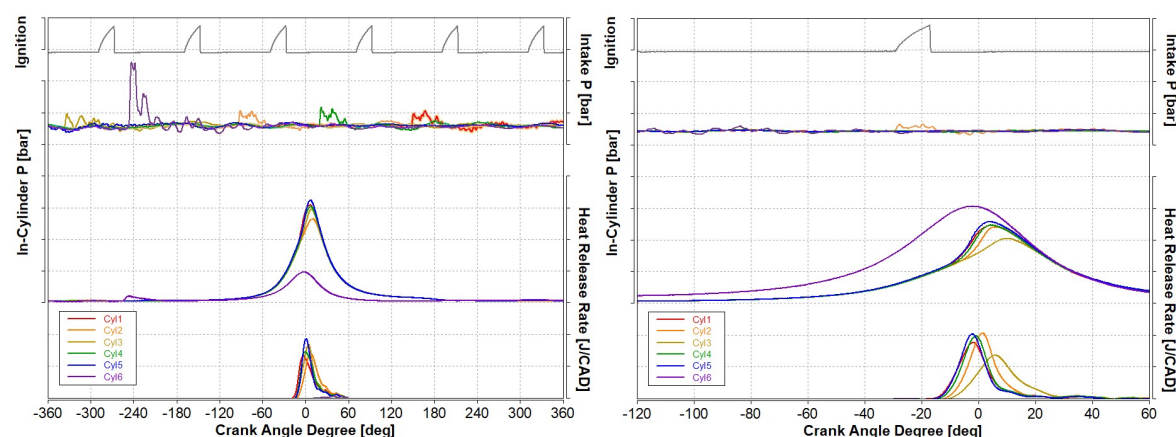
Fig. 7. Abnormal combustions experienced during engine calibration: single backfiring and pre-ignition occurrences.

The causes of backfiring are numerous and well-known in the literature. For instance, hot spots in the combustion chamber can lead to abnormal combustion like non adapted spark plugs or crevices in the combustion chamber. Moreover, the combination of hydrogen flowrate and its mixing process with fresh air can also be a major contributor to backfiring. A fine attention should be taken in the design of the intake ducts. Another cause can be the residual exhaust gases (internal EGR) caused by early intake valve opening. The discrepancies cylinder to cylinder can also cause backfiring. Finally, lubricant can also cause conditions for backfiring occurrence. Fortunately, in this study, it has been shown that fine tuning of hydrogen start of injection allows backfiring free operation.

High Performance and Near Zero Emissions H₂ Engine

S. Caprioli, F. Scrignoli, A. Volza, C.A. Rinaldini, E. Mattarelli

Dipartimento di Ingegneria "Enzo Ferrari" - Scuola di Ingegneria - Università degli studi di Modena e Reggio Emilia, Via Pietro Vivarelli 10, 41125 Modena

E-mail: stefano.caprioli@unimore.it
Telephone: +39 059 2056110

Abstract. The paper presents a study on a virtual 2-stroke 3-cylinder 0.9 L DI turbocharged engine running on Hydrogen, able to meet both high performance targets (max. specific power: 90 kW/l, max. specific low end torque: 260 Nm/l) and ultra-low emissions limits (NOx<20 ppm). The combustion system is directly imported from a similar 4-stroke prototype while the cylinder head and the actuation law of both intake and exhaust valves are specifically optimized for the 2-stroke cycle. In comparison to a more conventional 2-stroke loop scavenged engine, with piston-controlled ports, the use of poppet valves permits a free schedule of the gas exchange process and to maintain the same design of a 4-stroke engine for pistons, cylinders block, crankcase and lubrication system. On the other hand, it is more difficult to avoid the short-circuit of the fresh charge, while permeability of the valves becomes quite critical at high engine speed. Therefore, great care must be devoted to the optimization of the intake and exhaust ports geometry, as well as to the valves' actuation law. While the development of the scavenging system was mainly supported by CFD-3D simulation, the optimization of the supercharging system, made up of a VGT turbocharger, a volumetric compressor and two charge coolers, is driven by 1D analyses (by GT-Power). The 1D engine model of the 2-stroke engine is closely derived from the experimentally calibrated model of the 4-stroke H₂ prototype, at least for what concerns the combustion system. Finally, a numerical comparison between the 2 and the 4-stroke engine is presented.

1. Introduction

4-Stroke DI Hydrogen engines can achieve near zero NOx emissions and excellent Brake Thermal Efficiencies when working at relative air-fuel ratio around 2.5 [1], [2].Operations are also regular, without knocking. The main drawback is the need of very high air flow rates, penalizing the specific brake power and torque, as well as the transient performance (big turbochargers are generally characterized by high inertia). The double frequency of the 2-stroke cycle may be a solution to retain all the above mentioned advantages without any compromise on steady and dynamic performance [3], [4]. Among the different 2-stroke designs, a very interesting concept appears to be the one characterized by loop scavenging with intake and exhaust poppet valves, a solution already explored by Toyota in the '90s [5]. The main advantage of this solution is the minimum number of modifications required to build a prototype starting from a correspondent 4-stroke engine. Only the cylinder head, including the ports and the valves actuation system, must be designed from scratch, in order to optimize the scavenging process. While on 4-strokes Hydrogen direct injection is generally adopted to improve volumetric efficiency and to prevent backfire in the intake system, in the 2-stroke application it is mandatory, in order to avoid the short circuit of fuel during the scavenge process. For this purpose, Hydrogen should be injected when the valves are closing, or even better when they are already closed. The short time available for mixture formation between valves closing and ignition is not critical for two main reasons: hydrogen is a gas, so it can diffuse within the charge at a much faster rate than liquid gasoline; the turbulence (tumble vortex) generated by the scavenge process in the 2-stroke engine is typically much stronger than in a correspondent 4-stroke. However, the development of a 2-stroke Hydrogen engine, starting from a 4-stroke turbocharged prototype, is far from trivial. First of all, the turbocharger must be supported by a further compressor, in order to start the engine and guarantee a positive pressure differential across the cylinder at any operating condition (without the exhaust and intake strokes, air must be pumped into the cylinder when the piston is at bottom dead centre). In this study, a positive displacement compressor, driven by an electric motor, is inserted after the turbocharger compressor and the first intercooler. The reason for choosing an electric supercharger instead of a mechanical one is the high flexibility of engine control: the air flow rate delivered by the engine can be varied by modifying the compressor speed, without using a throttle valve. The electric drive of the compressor also enhances the engine response during transient operations. A cheaper and less complex alternative can be a mechanical supercharger featuring a bypass valve for load control. In terms of fuel efficiency, the electric supercharger is convenient only if using energy recovered from vehicle braking (supposing a hybrid powertrain).

The size of the turbocharger and of the electric supercharger must be carefully chosen, in order to reach the performance targets and to minimize fuel consumption. Due to the relatively low exhaust gas temperature, a VGT turbine can be selected: this choice has the advantage to further improve the flexibility of engine control and to reduce the turbine back-pressure at full load, high speed. Another fundamental issue to be addressed in 2-strokes with poppet valves is the tendency to short circuit during the scavenging process. Even if no fuel is lost, the work spent by the electric supercharger for compressing the by-passed charge penalizes the engine efficiency. This problem can be mitigated in many ways: optimization of the intake ports geometry; optimization of the valves actuation law and reduction of the overlapping period; tuned exhaust manifold, et cetera. The paper presents a study on a virtual 2-stroke 3-cylinder 0.9L DI turbocharged engine running on Hydrogen, designed to meet both high performance targets (max. specific power >80 kW/l, max. specific low-end torque: 200 Nm/l) and ultra-low emissions limits (NOx<20 ppm). The combustion system is imported from a similar 4-stroke prototype, described in literature [1]. Two types of CFD tools have been used in this study: 3-D simulation for the optimization of the scavenge system; 1-D simulation for the optimization of the main engine parameters, for providing initial and boundary conditions to the 3-D analyses, and for predicting final engine performance. A 1-D engine model was previously built and experimentally calibrated also for the reference 4-stroke Hydrogen engine [1].The 2-stroke model is closely derived from the 4-stroke, at least for what concerns the combustion system.

2. Scavenging process
2.1 Cylinder geometry
The main characteristics of the optimized 2-stroke cylinder are reported in Table *1*, while Figure 1 shows the geometry of the valve ports. Besides the specific valves actuation, the main differences from a conventional 4-stroke are: a) high bore-to-stroke ratio (2.0) for maximizing the dimensions of the valves; b) exhaust valves larger than the intake ones for reducing the exhaust back pressure; c) vertical orientation of the intake ports, for generating a reverse tumble within the cylinder and limiting the mixing between fresh charge and residuals; d) valves masking: a shroud along a portion of the intake valves orients the inlet flow through the curtain toward the cylinder liner, in an attempt to reduce the short-circuit and generate a stronger reverse tumble vortex; e) smooth path for the intake and exhaust flows, for limiting flow losses; f) "aggressive" valve actuation laws for maximizing permeability and reduce the parasitic work of the electric supercharger. The Hydrogen injector will be installed between the intake valves and the liner for speeding up the air-fuel mixing process.

Table 1: 2-stroke cylinder main parameters

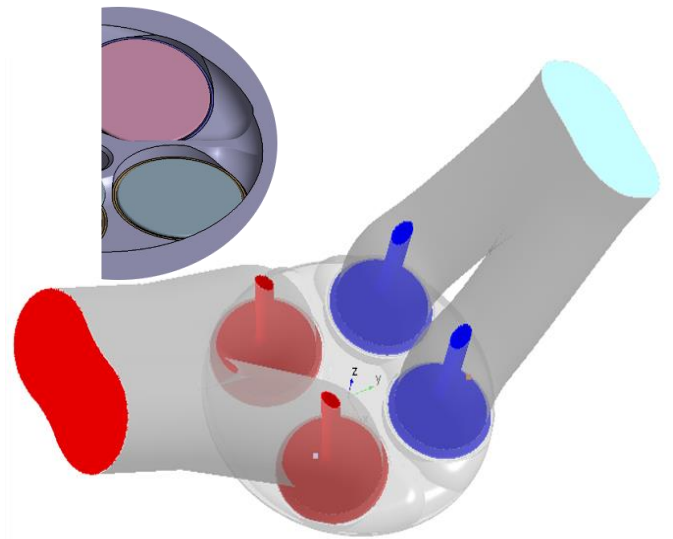| Bore	91.4 mm
Stroke	45.7 mm
Conrod length	115 mm
Compression ratio	16:1
Displacement	299.8 cm^3
Intake valves seat diam.	29.5 mm
Exhaust valves seat diam.	31.5 mm
IVO-IVC	126-258 @0.2mm
EVO-EVC	85-244 @0.2mm
Max. Intake lift	9.6 mm
Max. Exhaust lift	11.4 mm
Max. engine speed	7000 RPM

Figure 1: Optimized ports of the 2-S engine

2.2 Virtual development of the scavenge system
3D CFD multi-cycle scavenge simulations were performed at the most critical operating condition, i.e. WOT and maximum engine speed (7000 RPM), to support the design of the cylinder, as well as to provide information for the setup and calibration of the 1D 2-stroke engine model. The last one provides the initial and boundary conditions to the 3D analysis, with an iterative process. The simulation runs between 80 and 260 CAD after TDC, for at least 3 cycles. The computational grid is structured with cubic elements of average size of 2 mm, wall refinements with 2 layers of 1 mm. The number of cells varies from 246,000 to about 350,000. The fluid volume is initialized with O2 at the intake and N2 within the cylinder and the exhaust ports to facilitate the post-processing analysis. Figure *2* shows the trends of Charging Efficiency, CE (ratio of trapped air mass to the reference mass), Trapping Efficiency, TE (ratio of trapped air to delivered air) and Scavenge Efficiency, SE (ratio of trapped air to total cylinder

mass) as a function of Delivery Ratio, DR (ratio of delivered air mass to reference mass). The drop of TE at the beginning of the scavenge process is due to a short circuit, clearly visible in Figure 3. However, the tuned exhaust manifold and the optimized valve actuation laws permit an almost complete recovery of the lost air, as demonstrated by the high values of TE for DR>0.5. Figure 2 shows also the tendency of the cylinder to retain some residuals, even in presence of high DR (at DR=1.5, SE is 0.8, meaning that 20% of the trapped charge is composed by exhaust gas). The optimized valves actuation law and the tuned exhaust manifold enable a quite effective decoupling between intake and exhaust flows, as visible in Figure 4. At IVO, the exhaust valve is almost at maximum lift; moreover, IVC occurs after EVC.
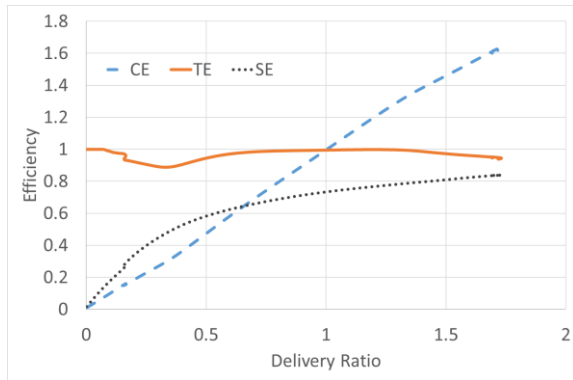

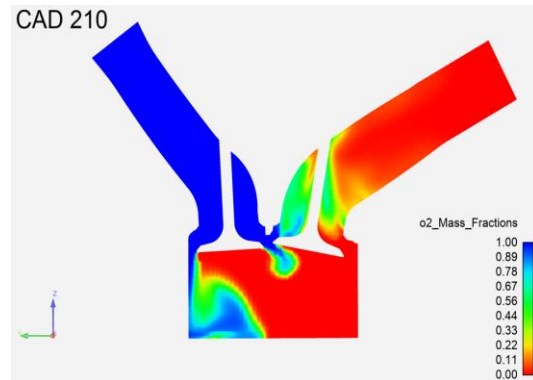Figure 2: CE, TE, SE, function of DR; CFD 3D results

Figure 3: CFD 3D results at 210 CAD shows the fresh air short-circuit
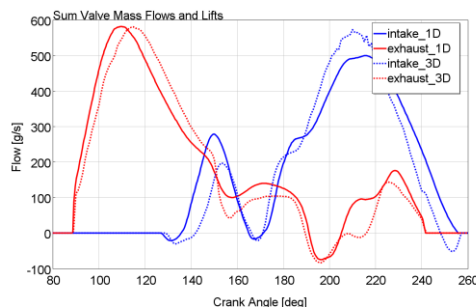
.

Figure 4: mass flow rates through the intake and exhaust valves: 1D vs 3D simulation

Figure 4 shows a comparison between the results provided by the calibrated 1D engine model and the 3D simulation. The gas flow rates through the valves are plotted as a function of crank angle, for the optimized cylinder design. The alignment of the curves is acceptable, considering the strong simplifications of the 1D engine model. Moreover, the difference on the total trapped mass in the cylinder is below 0.5%.

3. CFD-1D engine models

3.1 Calibration of the 4-stroke model

The GT-Power modelling of H_2 combustion is based on the study of a 4-stroke physical prototype, described in [2]. It's a 2L, turbocharged 4-cylinder engine, with a bore of 88 mm, operating from 1000 to 3500 rpm with ultra-lean combustion (λ=2.4) and producing "near-zero-emissions" with high values of BTE. A simple but accurate model of the engine was built and calibrated against experiments. Figure 5 shows the comparison between some numerical and experimental results, demonstrating the soundness of the simulation.
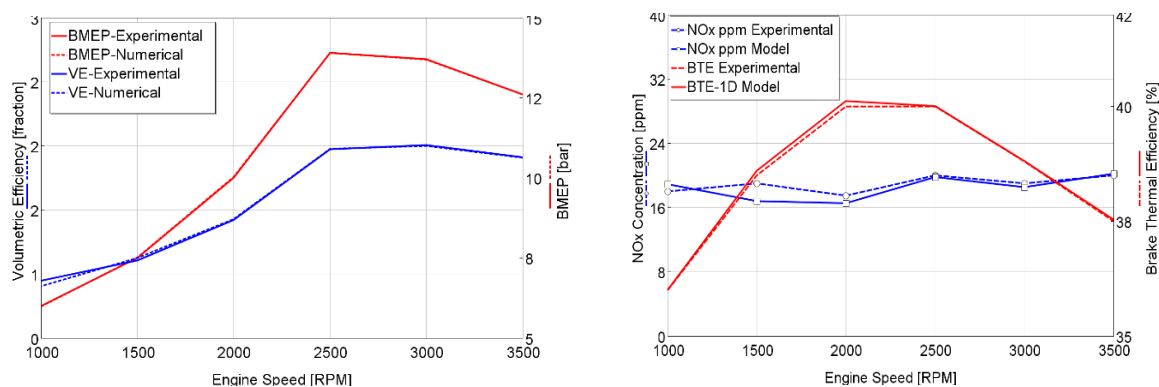

Figure 5: experimental validation of the 4-S H2 engine model

4   S. Caprioli, F. Scrignoli, A. Volza, E. Mattarelli, C.A. Rinaldini

3.2 2-Stroke model

For what concerns the combustion system, the 1D model of the 2-stroke engine is closely derived from the 4-stroke prototype. In particular, the air-fuel ratios and the burn rate curves are the same, corresponding to the values measured on the physical prototype. The engine layout, including the additional supercharger and the second intercooler, the dimensions of the pipes, the size of the turbocharger and the cylinder geometry are specifically designed for the 2-stroke application, on the basis of the CFD 1D and 3D calculations. The proposed engine has 3 cylinders (thus a total displacement of 0.9 L) and a maximum crankshaft speed of 7000 RPM. However, implementing a reduction gear of 2:1, as typically done on motorcycles, the maximum rotational speed at the engine outlet, before the gearbox, is the same.

3.3 2-Stroke vs. 4-Stroke

Figure *6* presents a comparison between the 2 and the 4-stroke engine in terms of specific torque and power (brake torque or power divided by total displacement). The specific performances of the 2-stroke engine are about 2.5 times higher, while maintaining the same near-zero emissions (NOx<10 ppm). Another clear advantage of the 2-stroke is the extremely flat torque curve, making this engine ideal for automotive applications

In Figure *7*, a slight worsening can be observed in terms of BTE, due to the energy spent to drive the supercharger and the mechanical losses associated to the additional reduction gear. Also peak cylinder pressure are higher, but always below the limit of 120 bar
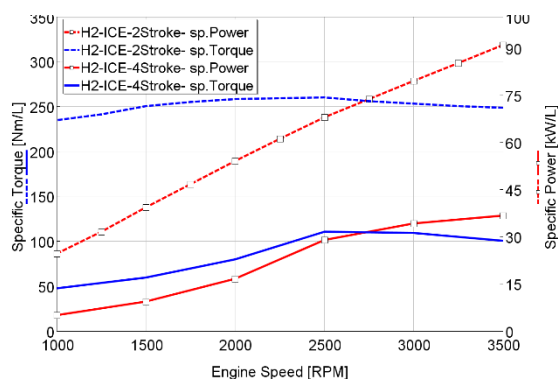

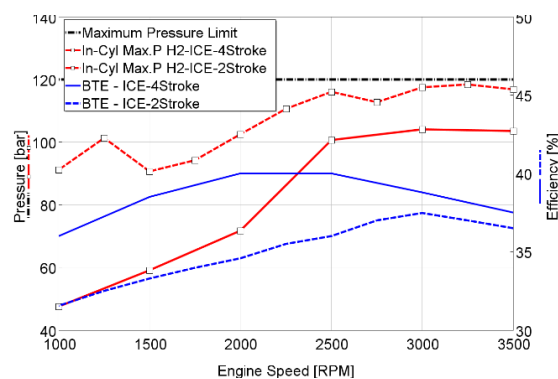Figure 6: comparisons in terms of specific Torque and Power

Figure 7: comparisons in terms of in-cyl maximum pressure and BTE

4. Conclusions

The paper explores, by means of a numerical study based on cfd 1D and 3D simulations, the potential of the 2-stroke DI Hydrogen engine with poppet valves. It is found that it can achieve much higher brake performance (2.5 time!) than its 4-stroke counterpart, while retaining all the advantages in terms of pollutant emissions (near zero). The development of this family of engines requires particular care in the design of the cylinder and of the valves assembly, while all the mechanical components can be derived from conventional 4-stroke engines.

References

[1]   «Optimal control strategy of the turbocharged direct-injection hydrogen engine to achieve near-zero emissions with large power and high brake thermal efficiency», *Fuel*, vol. 325, pag. 124913, ott. 2022, doi: 10.1016/j.fuel.2022.124913.

[2]   «Development of a turbocharged direct-injection hydrogen engine to achieve clean, efficient, and high-power performance», *Fuel*, vol. 324, pag. 124713, set. 2022, doi: 10.1016/j.fuel.2022.124713.

[3]   E. Mattarelli e C. A. Rinaldini, «Two-Stroke Gasoline Engines for Small-Medium Passenger Cars», apr. 2015, pagg. 2015-01–1284. doi: 10.4271/2015-01-1284.

[4]   E. Mattarelli, C. A. Rinaldini, e E. Agostinelli, «Comparison of Supercharging Concepts for SI Engine Downsizing», SAE Technical Paper, 2016-01–1032, apr. 2016. doi: 10.4271/2016-01-1032.

[5]   G. P. Blair, *Design and simulation of two-stroke engines*. Warrendale, PA: Society of Automotive Engineers, 1996.

THIESEL 2022 Conference on Thermo- and Fluid Dynamics of Clean Propulsion Powerplants

The Argon Power Cycle: Characterization of Hydrogen Injections

M.E.E. Peters[*], N.C.J. Maes, N.J. Dam, J.A. van Oijen

Eindhoven University of Technology (TU/e). Building 15, Groene Loper 5, 5612 AP Eindhoven

*E-mail: m.e.e.peters@tue.nl
Telephone: +(31) 40 247 2225

Abstract.
In order to solve the problem of intermittently available renewable energy sources in the future, the Argon Power Cycle is introduced. The Argon Power Cycle is expected to become an important enabler for the use of hydrogen as a chemical energy carrier in the future. The main drawbacks of using hydrogen in internal combustion engines, high NO_x emissions and low thermal efficiency are solved with the use of the noble gas Argon as a working fluid in a closed cycle.

To investigate different hydrogen and oxygen direct injection strategies, a new experimental setup has been developed. To investigate jet penetration and cone angle, Schlieren measurements are conducted, while the mass of injection and discharge coefficient are calculated with the use of pressure transducer measurements. The results clearly show which setup variables affect jet propagation, injected mass, and the discharge coefficient.

1. Introduction

As most renewable energy sources are intermittently available, hydrogen could successfully fill these gaps as a chemical energy carrier. In order to facilitate the use of hydrogen or other synthetic fuels, conversion of these chemicals needs to be efficient and clean. With use of the Argon Power Cycle, heat engines could maintain their significant role in the future sustainable energy landscape.

The major drawbacks of using heat engines are the relatively low thermal efficiency (<55%) and its polluting emissions. Hydrocarbon emission are 'obsolete' with the use of 100% renewable fuels, but the direct injection of hydrogen introduces locally rich and high-temperature diffusion flames leading to high NO_x emissions. When using argon as the compressible medium in heat engines, NO_x emissions can potentially be avoided.

Figure 1 shows that in order to feed and recirculate the engine with argon, a closed loop intake/exhaust is ideal. While this comes with additional challenges, thermal efficiency is expected to rise as a result of the higher ratio of specific heat. Due to the fact that the cycle is not using ambient air, oxygen needs to be added in the chamber. However it does raise the challenge; how to inject H_2 and O_2 easily in an argon engine such that they burn in a controlled way?
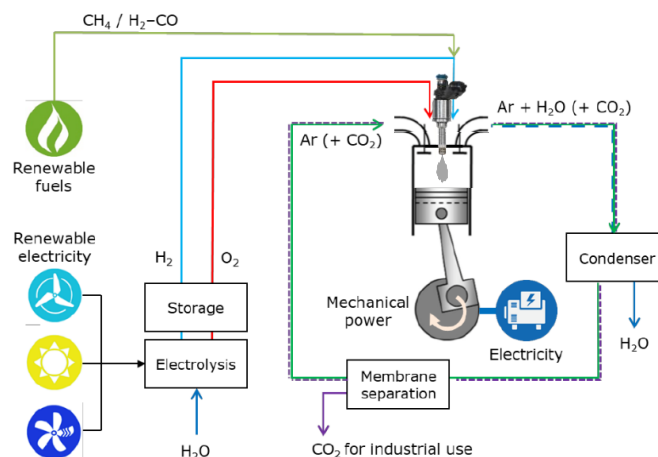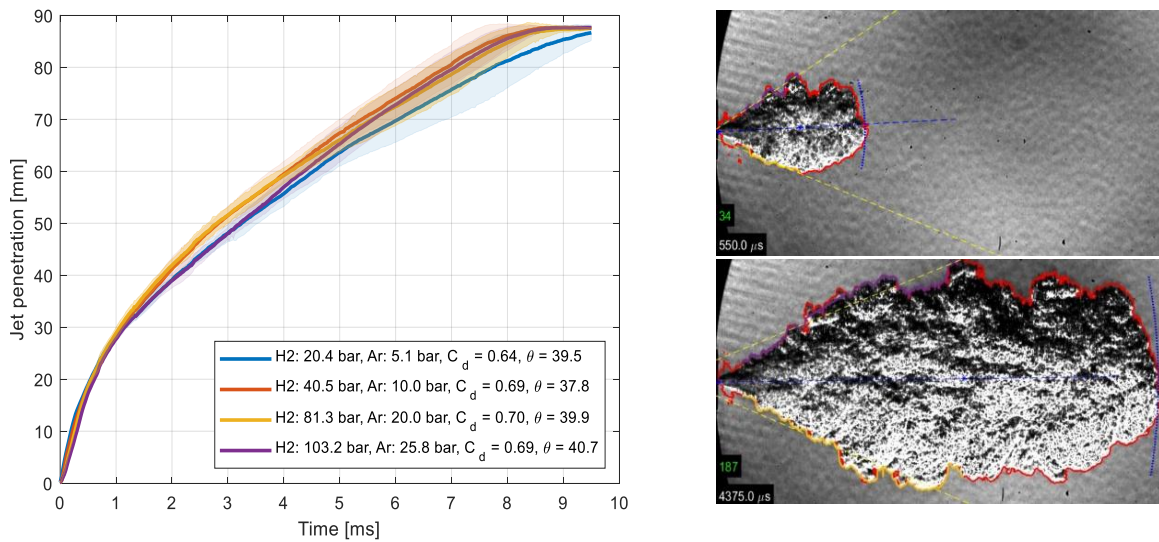

Fig. 1. Schematic layout of the Argon Power Cycle

Fig. 2. Jet penetration and post processing from measurements in the ELPC while nPR=4. Conditions are stated in the legend and the injection duration is fixed at 10 ms, with an ambient temperature of 291 K

2. Optical hydrogen injection experiments

Our current research comprises optical measurements of hydrogen injections using a Bosch HDEV1.2 in our newly developed Eindhoven Low-Pressure Cell (ELPC). For the validation of CFD simulations, cold flow hydrogen injections at high pressures are measured both optically (Schlieren) and with the use of high-speed pressure transducers.

Using Naber & Siebers post-processing method [1] as the basis, the far-field jet penetration is measured. The cone angle is measured using a fit with 95% confidence interval on the jet borders, between the start and the center of the identified jet area. In right panel of Figure 2 the penetration radius is visualized with the blue dotted segment perpendicular to the blue dashed centerline from the injector. The resulting cone angle is identified by the yellow dashed lines.

The pressure ratio (nPR) between fuel rail pressure (H_2) and chamber pressure (Ar) is kept at 4, while the injection pressure is varied. The left graph in Figure 2 shows a relatively similar jet penetration, discharge coefficient and cone angle for these highly turbulent jets.
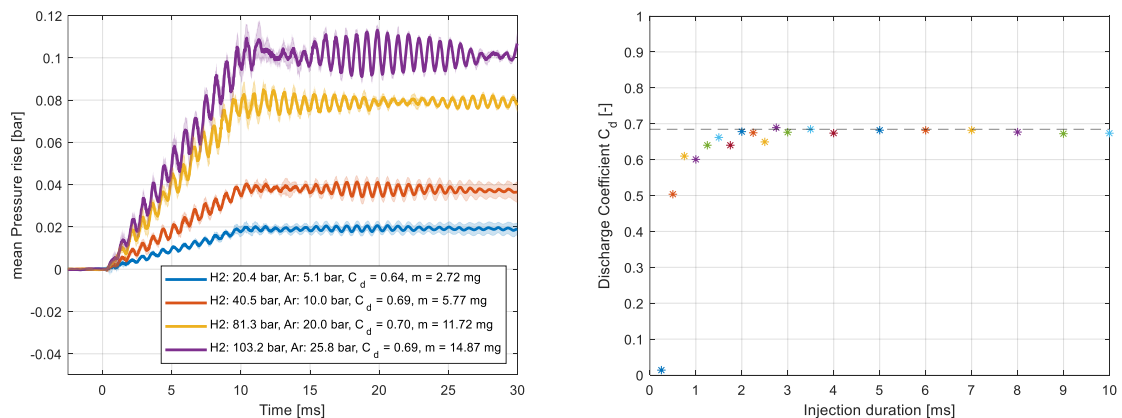
Fig. 3. The left graph shows the pressure rise (Δp) due to a 10 ms injection, including a 95% confidence interval. The graph on the right shows the discharge coefficient for different durations of injection

3. Injected mass and the discharge coefficient

The injected mass (m_{inj}) is calculated from the global pressure increase (Δp) with the use of the ideal gas law,

$$m_{inj} = \Delta p \frac{V}{RT} , \qquad \qquad \text{(eq. 1)}$$

with V the volume of the constant volume chamber, R the specific gas constant and T the temperature in the chamber. As the ideal mass flow for choked flow conditions ($\dot{m}_{ideal}$) is assumed not to be affected by downstream effects, it follows that [2]

$$\dot{m}_{ideal} = \frac{A \cdot p}{\sqrt{T}} \sqrt{\frac{\gamma}{R}} \left[\frac{\gamma+1}{2} \right]^{-\frac{\gamma+1}{2(\gamma-1)}}, \qquad \qquad \text{(eq. 2)}$$

with A the nozzle hole area and γ the specific heat ratio. Ultimately, using the injection duration (t_{inj}), the discharge coefficient (C_d) between the injected- and ideal mass can be calculated as

$$C_d = \frac{m_{inj}}{\dot{m}_{ideal} \cdot t_{inj}} . \qquad \qquad \text{(eq. 3)}$$

While the Schlieren measurements show comparable results for injections with equal pressure ratio's, the injected mass for these conditions (Figure 3) differs substantially because of the different rail pressure, which directly influences the mass flow (eq. 2). As the discharge coefficient remains quite similar, the actual injected mass also seems mostly unaffected by down-stream (chamber) conditions.
The right panel of Figure 3 illustrates the effect of opening and closure behaviour of the injector on the discharge coefficient. In this graph it becomes apparent that, starting from injection durations of 2 milliseconds or longer, the discharge coefficient remains constant at a value of around 0.69.

4. Future work

Future research will focus on 2D density fields with the use of planar Rayleigh scattering and line-of-sight Shadowgraphy measurements of the near field region of the jet with its shock barrel and Mach disk. Combustion experiments are planned on a high-pressure, high-temperature constant-volume vessel setup using various optical diagnostics for reacting hydrogen jets and different oxygen and hydrogen injection strategies.

Conclusions

The optical Schlieren experiments show that jet propagation and cone angle are mainly dependent on the ratio between rail and chamber pressure when injecting hydrogen in argon under choked flow conditions. However, the injected mass differs substantially for equal pressure ratio's and is strongly affected by rail pressure and injection duration, as expected with choked flow conditions. The injected mass (nPR=4, $t_{inj} = 10 \text{ ms}$) ranges from 2.72 mg to 14.87 mg, depending on the rail pressure. Lastly, the discharge coefficient remains constant at 0.69 for injection durations longer that 2 milliseconds.

References

[1] Naber, J. and Siebers D.L., Effects of gas density and vaporization on penetration and dispersion of diesel sprays, SAE Technical Paper 960034, 1996, https://doi.org/10.4271/960034

[2] Franquet E., Perrier V., Gibout S. and Bruel P., Free underexpanded jets in a quiescent medium: A review, Progress in Aerospace Sciences Volume 77, 2015, https://doi.org/10.1016/j.paerosci.2015.06.006

The Argon Power Cycle: Exploring DI-H2 and DI-O2 Injection Strategies using CFD

N. Diepstraten[*], L.M.T. Somers, J.A. van Oijen

Eindhoven University of Technology. Building 15, Groene Loper 5, 5612 AP, Eindhoven. The Netherlands

*E-mail: n.diepstraten@tue.nl

1. Introduction

In order to combat climate change, there is a shift from fossil fuels to renewable energy sources, such as solar and wind power. A disadvantage of these renewable energy sources is their intermittent nature. An internal combustion engine (ICE) can counteract this mismatch between energy demand and supply, thanks to their ability to dispatch power quickly when required. A drawback of ICEs is the relatively low thermal efficiency (<50%) compared to other technologies, such as fuel cells (~60%).

The Argon Power Cycle (APC) is a promising energy conversion system. It uses argon as work-ing fluid instead of nitrogen, which could increase the efficiency by approximately 25% due to its high specific heat ratio due to the low heat capacity of Ar. A low heat capacity in an ICE means higher in-cylinder pressure and temperature. This increases work on the piston and reduces exhaust losses.

One advantage of the APC is that there will be no NOx formation, thanks to the absence of nitrogen in the oxidizer. Moreover, when hydrogen is employed as fuel, there will be no carbonaceous emissions either! In case of stoichiometric and complete combustion, the exhaust only contains argon and water. When water is removed from the system by condensation, the argon can be led back to the intake to be reused. This is done by the closed-loop configuration, also understood as 100% exhaust gas recirculation, which is illustrated in figure 1.

Since both hydrogen and oxygen need to be injected separately, the APC has an extra degree of freedom compared to an air-breathing engine. This allows the APC to maintain its high efficiency throughout its range load. This project focuses on compression-ignition (CI) engines, which can operate at high compression ratios and thereby have the potential to reach much higher efficiencies than spark-ignition (SI) engines. The hydrogen and oxygen can either be injected in the intake port (PFI) or directly in the combustion chamber (DI). This project focuses on DI-H2 (and PFI-O2) and DI-O2 (and PFI-H2). Please note that other strategies are also possible, but they are not studied in the current work.

This work provides initial insights regarding the potential of and differences between the two injection strategies. It is looked at injection events, combustion characteristics and convective heat trans-fer to the walls. The next chapter will elaborate the approach. After that, the CFD simulation environment is elaborated. In the last two chapters, the results are presented and an outline on future work is provided.
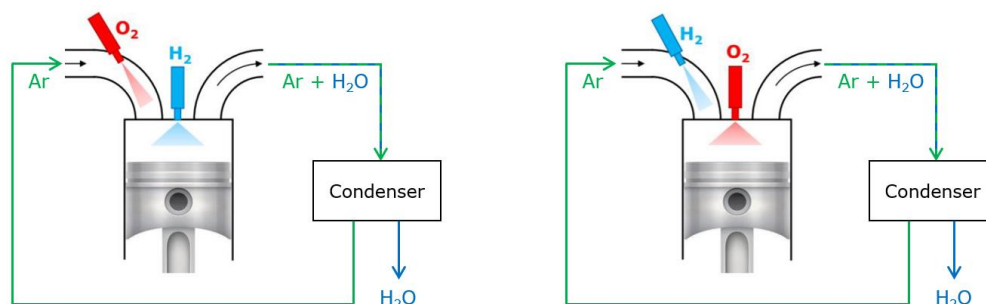

Fig. 1. Schematic representation of the APC with the DI-H2 (left) and DI-O2 (right) injection strategies

2. Approach

First, the setup of the DI-H2 simulation is elaborated. As a starting point, a target was set for the total amount of energy released by combustion: 2900 J, which can be translated to a medium to high load point (IMEP$_{gross}$ = 9 bar). Using a lower heating value of 120 MJ/kg for hydrogen, this comes down to 24.2 mg. The injection pressure was chosen to be 300 bar and the engine speed was set to 1800 RPM. Together with a nozzle diameter of 0.5 mm, the duration of injection becomes approximately 13 CAD. The start of injection was set to -2 CAD ATDC. The plenum is composed by 23 %mass oxygen -

comparable to oxygen content in air - and 77 %mass argon, atmospheric pressure and 373 K. This results in an overall lambda of 1.7. Please note that stoichiometric combustion would theoretically result in the highest efficiency. However, it is most likely that this will not be feasible in practice. A lambda of 1.7 is therefore chosen as initial value; studying the effect of lambda on the engine performance is left for consequent studies.

A similar approach is used for the DI-O2 simulation. Only this time, there has to be an excess of hydrogen in the system to ensure no oxygen will be left after combustion. When this is not the case, a hydrogen-oxygen will be present in the intake because of the closed-loop configuration. This could result in undesired, spontaneous ignition in the engine's intake or combustion chamber. Whereas the DI-H2 simulation uses a lambda of 1.7, the DI-O2 uses a lambda of 1/1.7, such that H2 remains in the exhaust. The stoichiometric oxygen-fuel-ratio of hydrogen combustion is 7.93. This means that the injected oxygen mass in DI-O2 must be 7.93 as much as the injected hydrogen mass in DI-H2. In order to compensate for the increased injected mass, the nozzle diameter is increased. This way, important injection properties for combustion, such as injection pressure and timing, can be held constant. Whereas the nozzle diameter for the DI of hydrogen is 0.5 mm, this value is increased to 0.67 mm for the DI of oxygen.

3. CFD simulation environment

This research explores the DI-H2 and DI-O2 injection strategies using the commercial software package CONVERGE CFD. To reduce computation time, only the closed valve cycle is simulated. The engine geometry is based on Caterpillar's C9 ACERT engine, with a compression ratio of 16.1 and a displacement of 1.47 liter per cylinder. Since there are no high-pressure direct-injection hydrogen injectors commercially available, a non-existent multi-hole injector geometry with 6 holes was designed. A sector mesh of 60º is simulated since the geometry is periodic around the injector.

**Table 1**. Numerical settings of the CFD environment

Combustion	SAGE detailed chemistry
Chemical mechanism	9 species, 25 reactions (Burke et al., 2011)
Turbulence	RANS, RNG, $\kappa - \epsilon$
Gas E.O.S.	Soave-Redlich-Kwong
Navier Stokes solver	PISO, density-based

4. Simulation results

Figure 2 shows that the DI-H2 ignites faster than the DI-O2 simulation. This can be caused by the higher in-cylinder temperature at SOI, but also by the highly diffusive nature of hydrogen. As a consequence of the longer ignition delay for the DI-O2, the premixed peak is much higher and a large pressure rise rate is observed around TDC in figure 3 (MPRR$_{DI-H2}$ = 4.7 bar/CA vs MPRR$_{DI-O2}$ = 10.6 bar/CA). Besides, the global mass burning rate is higher for the DI-O2.
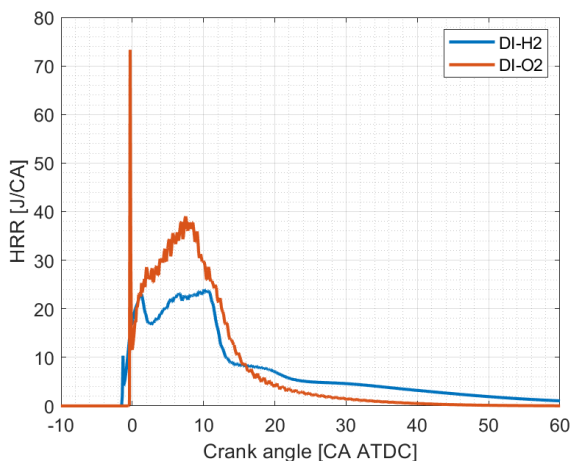

Fig. 2. Heat release rate
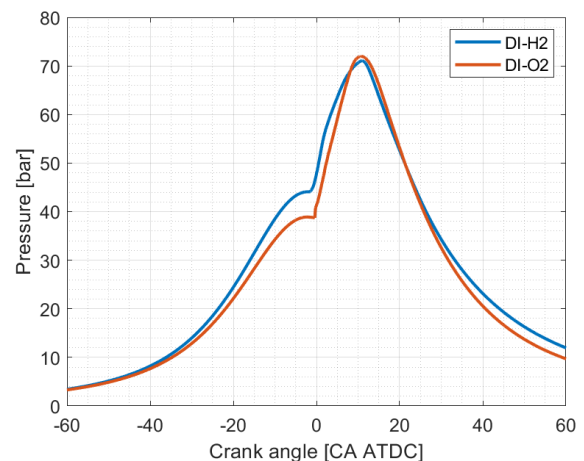
Fig. 3. In-cylinder pressure

Figure 4 shows temperature contour plots for a cross-section at two different time stamps. The black line indicates an iso-contour of 0.1 %mass of the injected species. It is observed that the oxygen jet penetrates much faster than the hydrogen jet, which can be attributed to the higher momentum rate. Consequently, the global mixing combustion phase (combustion occurring after the jet has impinged on the piston bowl) is much more intense for the DI-O2 simulation.

(a) DI-H2 at TDC   *(b) DI-O2 at TDC*

(c) DI-H2 at 3 CAD ATDC   *(d) DI-O2 at 3 CAD ATDC*
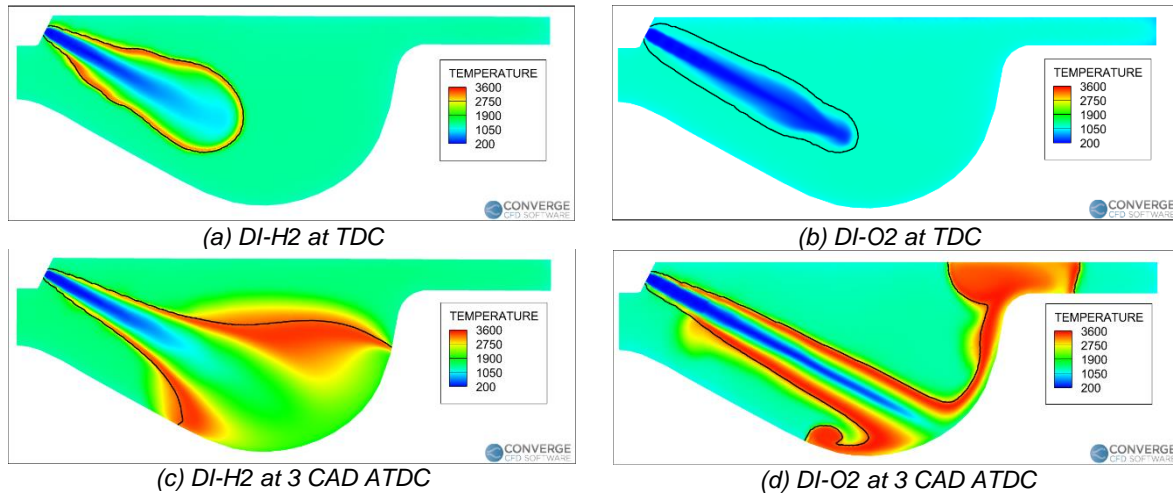
Fig. 4. Temperature contours and jet outline (0.1 %mass) for the two simulations at -0.5 and 3 CAD ATDC.

Since the in-cylinder temperature of an APC will reach higher values compared to an air-breathing engine, it is important to monitor heat losses. Figure 5 shows that the DI-O2 strategy has more heat loss compared to the DI-H2. The slightly higher heat loss rate before ignition (around TDC) can be attributed to the particular viscosity and conductivity of hydrogen. The higher heat loss rate after ignition is believed to be caused by the intense injection and combustion of the oxygen jet.
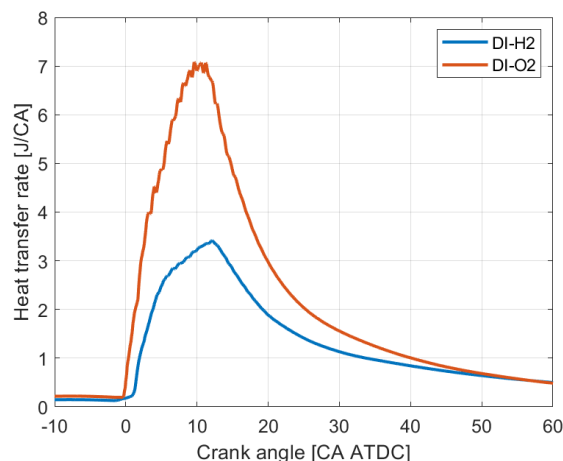
Fig. 5. Spatially averaged heat loss rate for the two simulations

Future work

This study shows the very early tries of the DI-H2 and DI-O2 strategies. Improvements on the engine's performance will be made in a subsequent study. Typical indicators such as energy budgets will be made to investigate and reduce losses. Also parameters such as injection timing will be optimized.
In order to gain more understanding on burning hydrogen and oxygen jets in an argon environment, parametric studies varying ambient conditions will be conducted. Besides, system analysis of the APC will be performed using 1D CFD to estimate system efficiencies and derive more realistic plenum conditions for 3D CFD engine simulations.

Spray Combustion of Fast Pyrolysis Bio-Oil in a Constant Volume Combustion Chamber

Y. Wang*, N. Maes, B. Somers

Department of Mechanical Engineering, Eindhoven University of Technology, P.O. Box 513, 5600 MB Eindhoven, the Netherlands.

E-mail: y.wang14@tue.nl
Telephone: +(31) 40 247 2135

Abstract. Fast-pyrolysis bio-oil (FPBO) and its blends with n-butanol are tested in a constant-volume combustion chamber setup under ambient temperature of 750 ºC and pressure of 50 bar. Pressure-based heat-release analysis and high-speed visualization of flame natural luminosity are adopted to investigate the spray combustion characteristics of tested fuels. Results show that FPBO spray flame has lower sooting tendency and alleviates the end-of-injection dribble compared with diesel. However, at low injection pressure, the worsened atomization results in the "grainy" spray flames and the severe nozzle clogging, both of which can be relieved by elevating the injection pressure. Adding 30% n-butanol could slightly improve the ignitability and reduce the flame natural luminosity.

1. Introduction

Using biomass-derived fuels to replace fossil-based fuels is a promising way to contribute to net-zero carbon dioxide emissions. Fast pyrolysis is an efficient process to convert solid biomass to liquid bio-oils. The EU funded SmartCHP project is aiming to develop a smart and flexible small-scale combined heat and power (CHP) system running on fast-pyrolysis bio-oil (FPBO). In SmartCHP system, FPBO is used in the stationary diesel engines for power generation.

The special physical and chemical properties of FPBO limit its direct application in diesel engines. Compared to diesel, the high viscosity and acidity of FPBO require modifications in engine fuel supply system. Moreover, its low chemical reactivity makes it necessary to either elevate engine compression ratio or preheat the intake air or both [1,2]

Fuel upgrade is also a realistic way to fuel diesel engines with FPBO. There are a number of upgrade methods: physically, chemically and catalytically [3]. Compared with other upgrading methods, blending the FPBO with a higher-quality base-fuel is a common solution to fuel an unmodified diesel engine with FPBO. Due to the polar properties of FPBO, low carbon alcohols, such as ethanol and n-butanol, are widely used to mix with FPBO [4,5]. Blending with alcohols brings many benefits for FPBO, such as reducing its viscosity as well as surface tension and curbing polymerization. All these effects could improve the stability and atomization quality of the fuel blends. However, due to the low chemical reactivity of both FPBO and alcohols, it is still necessary to make proper engine modification or to add high reactivity compositions [6,7].

Although it is promising to fuel diesel engine with FPBO, in most of existing experimental studies, the mass fraction of FPBO was limited lower than 30%. A few studies achieved using high FPBO content (>70%) in the modified diesel engine [1,2]. However, there is still a lack of optical diagnostics on FPBO spray flames. Hence, the fundamental spray combustion characteristics of FPBO and FPBO/n-butanol blends are experimentally investigated in this study.

2. Methodology

The combustion research unit (CRU) is employed to study the combustion processes of FPBO and FPBO/n-butanol blends. Figure 1 shows its schematic and more detailed description on CRU working principle can be found in Ref. 8. The constant-volume combustion chamber of CRU provides the well-defined initial ambient conditions. It also has a borescope port which accommodates to the high-speed diagnostics on fuel spray flames. A heavy-fuel oil (HFO) injection system is adopted to adapt for the high viscosity of FPBO. The HFO injection system employs the sophisticated dual-circuit design, using
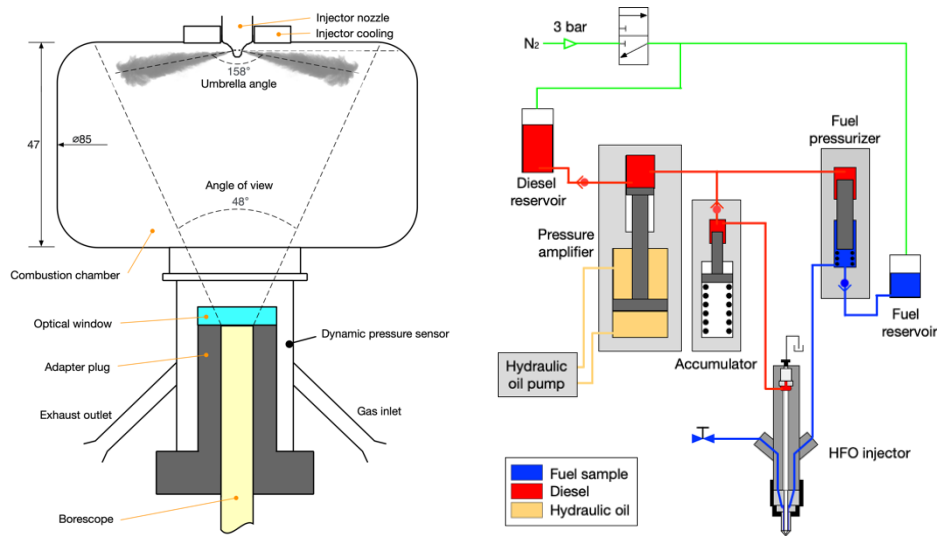
Fig. 1. Schematic overview of the CRU combustion chamber with borescope port (left) and the heavy-fuel oil injection system (right)

diesel as working medium to pressurize FPBO. The isolation of the FPBO sample and the more vulnerable pressure amplifier improves the stability and durability of the fuel supply system.

The wood-based FPBO and its blends with n-butanol blends (n-butanol mass fraction of 10% and 30%, respectively) are tested in CRU. The chamber wall temperature and initial chamber pressure are fixed at 750 °C and 50 bar, respectively. The influences of injection pressure on FPBO spray combustion are also investigated. The pressure-based heat release analysis is performed to obtain heat-release rate (HRR) and mass fraction burned (MFB) profiles, while the high-speed imaging technique is adopted to visualize flame natural luminosity (NL) during the fuel spray combustion processes and the cumulative NL is calculated to present the overall intensity of flame NL evolved with the time.

3. Results and discussion

3.1 Diesel vs. FPBO at low injection pressure

Pure FPBO is first tested at an injection pressure of 300 bar. Continuous 20 injections of FPBO are performed using the same nozzle. Figure 2 shows the heat-release analysis results of five out of a total of 20 injections (injection number 4, 7, 13, 16, and 20). The results of diesel at the same test condition are also presented as the reference. From the HRR profiles of FPBO, it becomes clear that the peak
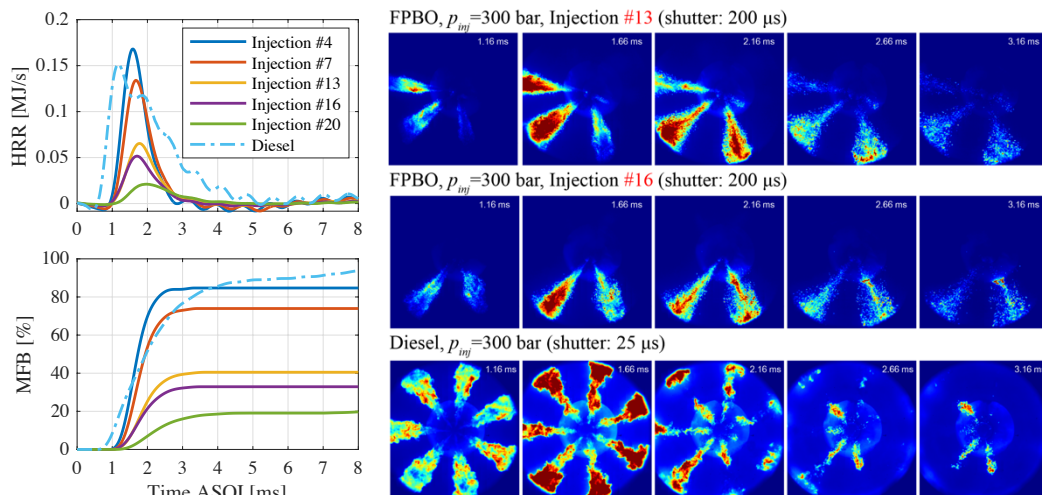
Fig. 2. The results of heat release analysis (left) and NL images (right) for FPBO and diesel spray combustion at low injection pressure (300 bar)

value reduces with the number of injections, while the phasing is gradually delayed. As illustrated by the accompanied natural luminosity images in the right-hand side of this figure, this is caused by severe nozzle clogging that happens within several injections. During the 13th injection, 3 out of 7 orifices are fully clogged, while one is partially clogged. The remaining spray plumes are not evenly distributed, meaning that in fact the original spray directions have been altered. In the 16th injection, the effective number of orifices is further reduced to only two. MFB results quantitatively denotes the influence of nozzle clogging on the effective injection volume, which is substantially reduced to only 20% within 20 injections. This is caused by the special properties of FPBO compared to diesel. On one hand, it has solid/ash contents which is prone to blocking nozzle orifice. On the other hand, in the sac of nozzle, the polymerization tendency of FPBO is aggravated due to the elevated temperature (above 150 ºC in estimation), leading to the precipitation of the large molecules from the liquid phase.

When compared to diesel, FPBO has a significantly reduced chemical reactivity, leading to a retarded ignition delay and peak HRR phasing (both on the order of 0.5 ms). As shown in the NL images, relatively severe fuel dribble is observed for diesel combustion at this injection pressure, which lasts for several milliseconds. Interestingly, the combustion reactions of FPBO end at around 3 ms after start of injection (ASOI) in the HRR panel, without obvious fuel dribble in the NL images. This could be because the fuel remaining in the nozzle sac after the end of injection is less prone to cause fuel dribbling because of the high viscosity as and high surface tension of FPBO.

The flame natural luminosity of FPBO is much lower than diesel, meaning that the lower sooting tendency (notice that different shutters are used for diesel and FPBO in Figure 2). Different from diesel combustion, there are many bright, distinct parcels observed in the FPBO spray flames at the injection pressure of 300 bar, which is referred to as a "grainy spray flame structure" in this study. The grainy structure could indicate that the atomization quality of FPBO at lower injection pressures is much poorer than diesel. The parcels in these structures need longer time to be oxidized after the end of injection.

3.2 Diesel vs. FPBO at high injection pressure

The results of FPBO and diesel spray flames at injection pressure of 900 bar are shown in Figure 3. The nozzle clogging problem of FPBO is alleviated, none of the nozzle orifices clogged within 30 injections. Moreover, the fuel atomization is apparently improved at higher injection pressure, and hence the appearance of FPBO spray flame looks much more similar to the benchmark diesel cases. This means that they appear much smoother than the grainy spray flames at low injection pressure, discussed previously. Compared to diesel, the ignition delay of FPBO is longer, while the lift-off length seems to be shorter.
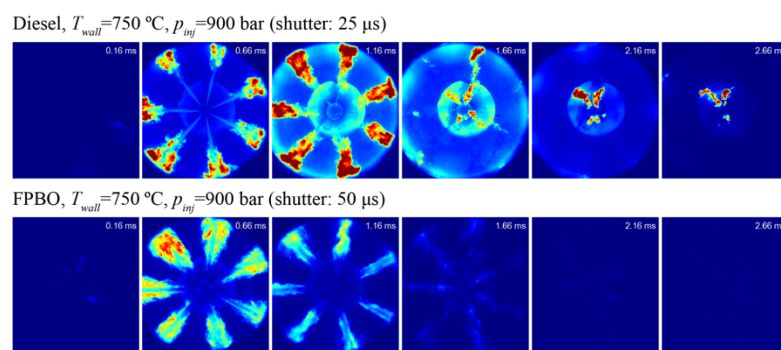

Fig. 3. Development of diesel (top) and FPBO (bottom) spray flames at high injection pressure (900 bar)

3.3 FPBO with addition of n-butanol

Figure 4 shows the heat-release analysis (HRR and MFB profiles) and cumulative NL results of FPBO with addition of 0 – 30% n-butanol. As shown in HRR and cumulative NL pannels, 30% n-butanol addition slightly shortens the ignition delay of FPBO. There are two possible reasons. On one hand, n-butanol addition could improve the physical atomization characteristics of FPBO, which facilities fuel autoignition. On the other hands, it is reported that the chemical reactivity of n-butanol seems to be higher than FPBO [5].

4   Y. Wang, N. Maes, B. Somers
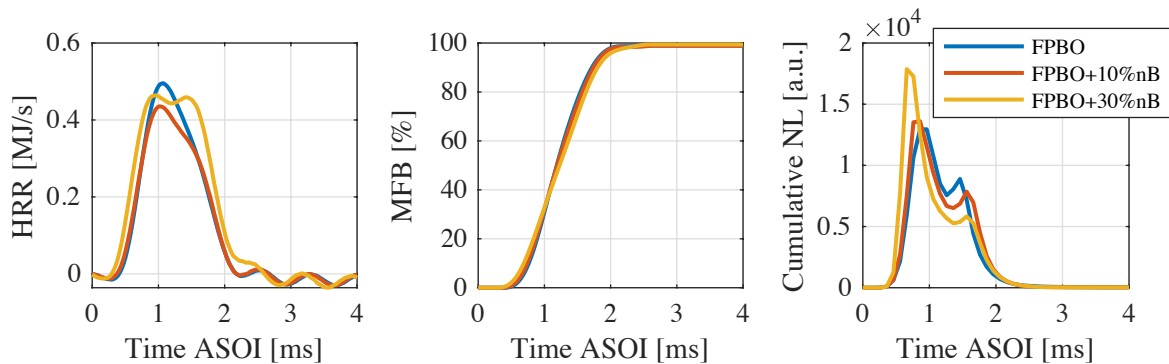
Fig. 4. HRR, MFB, and cumulative NL results of FPBO with addition
of 0 – 30% n-butanol

4. Conclusion

Compared to diesel, FPBO sprays has lower sooting tendency and is able to alleviate end-of-injection dribble. However, its atomization quality at the injection pressure of 300 bar is quite poorer, leading to the "grainy" spray flames and the severe nozzle clogging, both of which can be relieved by elevating the injection pressure. Adding 30% n-butanol could improve the ignitability and slightly reduce the flame natural luminosity.

5. References

[1]   van de Beld B, Holle E, Florijn J. The use of pyrolysis oil and pyrolysis oil derived fuels in diesel engines for CHP applications. Appl Energy 2013;102:190–7. https://doi.org/10.1016/j.apenergy.2012.05.047.

[2]   van de Beld B, Holle E, Florijn J. The use of a fast pyrolysis oil – Ethanol blend in diesel engines for chp applications. Biomass and Bioenergy 2018;110:114–22. https://doi.org/10.1016/j.biombioe.2018.01.023.

[3]   Bridgwater A V. Review of fast pyrolysis of biomass and product upgrading. Biomass and Bioenergy 2012;38:68–94. https://doi.org/10.1016/j.biombioe.2011.01.048.

[4]   Lee S, Kim TY. Feasibility study of using wood pyrolysis oil-ethanol blended fuel with diesel pilot injection in a diesel engine. Fuel 2015;162:65–73. https://doi.org/10.1016/j.fuel.2015.08.049.

[5]   Wang Y, Han J, Maes N, Cuijpers M, Somers B. Ignition and Combustion Characteristics of N-Butanol and FPBO/N-Butanol Blends With Addition of Ignition Improver. Front Energy Res 2022;10:1–13. https://doi.org/10.3389/fenrg.2022.832509.

[6]   Lee S, Kim TY, Kang KY. A Feasibility Study of Using Pyrolysis Oil/Butanol Blended Fuel in a di Diesel Engine. SAE Tech Pap 2015;2015. https://doi.org/10.4271/2015-24-2437.

[7]   Kim TY, Lee S, Kang K. Performance and emission characteristics of a high-compression-ratio diesel engine fueled with wood pyrolysis oil-butanol blended fuels. Energy 2015;93:2241–50. https://doi.org/10.1016/j.energy.2015.10.119.

The Influence of Hydrogen Direct Injection on the Combustion Characteristics of a Compression Ignition Engine

Mahdi Aghahasani[1], Ayat Gharehghani[1*], Amin Mahmoudzadeh Andwari[2*], Juho Könnö[2]

[1]School of Mechanical Engineering, Iran University of Science and Technology, Tehran, Iran

[2]Machine and Vehicle Design (MVD), Materials and Mechanical Engineering, University of Oulu, P.O. Box 4200, FI-90014 Oulu, Finland

Ayat_Gharehghani@iust.ac.ir, Ayat Gharehghani
Amin.Mahmoudzadehandwari@oulu.fi, Amin Mahmoudzadeh Andwari, Tel: +358 29 448 1621

Abstract. Hydrogen, as a clean and sustainable energy carrier, has been widely considered by many researchers in internal combustion engine (ICE) application as a primary fuel or in combination with other conventional fuels such as diesel and gasoline. To date, several studies have focused on investigation on premixed PFI (port fuel injection) hydrogen internal combustion engine (H_2ICE) which suffers from lower power output and combustion efficiency, due to low density of hydrogen. In this study, computational fluid dynamics (CFD) using Converge software is utilized to evaluate the combustion performance of a hydrogen-diesel dual fuel compression ignition (CI) engine considering direct injection strategy of hydrogen which enhances the volumetric efficiency of the engine cycle. The combustion characteristics of the engine for five different hydrogen energy shares (HES) from 10 % to 50 % and three different hydrogen injection timings have been investigated. The results revealed that the addition of hydrogen increases the acceleration of heat release rate (HRR) and the combustion peak pressure (P_{max}) by 43 % for 50 % HES. Since hydrogen addition accelerates the combustion speed, the combustion duration is reduced by 90 %, leading to a nearly constant volume combustion, therefore the thermal efficiency of the hydrogen-diesel CI engine is comparable to or higher than diesel-only fueled mode. Having increased HES resulted in lower carbon monoxide (CO), carbon dioxide (CO_2) and soot, however, hydrogen deteriorated NOx concentration as a matter of higher combustion average temperature.

Keywords. Hydrogen; Direct Injection; Dual Fuel; Diesel; Emission; CFD

Introduction

Recently, due to the negative environmental effects of diesel engine, the pressure to emissions reduction in this sector has progressively increased [1]. European Union aims to reduce greenhouse gas emissions in all sectors ,including transportation, by 60 % until 2050 [2]. Development of H_2ICEs offering emissions reduction together with improved thermodynamic efficiency, has been highly regarded by many researchers recently [3,4]. To performing the H_2 application in the ICEs, several types them are extensively studied, such as homogeneous charge compression ignition (HCCI), spark ignition (SI) [7-9] and dual-fuel engines. Recent studies have focused on the effect of hydrogen combustion on SI engines in order to increase the laminar flame speed and to achieve higher efficiency along with greater combustion stability [8], which have reached significant improvements in the engine performance as well [9,10]. To date, the most of H_2ICE studies are associated with the premixed hydrogen fuel strategy namely, hydrogen port fuel injection (PFI) engine which suffers from low power output and efficiency, due to hydrogen very low density [15-18]. In hydrogen PFI engine, a higher boost is used to compensate the low energy density of hydrogen as well as to increase the engine output power. Furthermore, at high HES, engine heat-losses increase, which can rich up to 45 % of the total fuel heating value therefore it limits both the engine efficiency and durability [19,20]. Limitations of hydrogen PFI technology promote the development of boosted hydrogen engines with stratified charge features and hydrogen direct injection (DI) engines. Recent work has proven increasing up to 42 % in thermal efficiency for a particular size of engine [13]. By hydrogen DI and stratified charge away from the cylinder and piston wall, heat losses can be significantly prevented [9,10,14]. However, despite the many advantages offered from this concept compared to PFI combustion, research on compression engines (CI) cycle with non-premixed hydrogen combustion has recently been severely limited.

This study aims to investigate the effect of hydrogen substitution rate on a hydrogen-diesel dual-fuel engine. A numerical study on the effects of injection timing and HES on the in-cylinder pressure and engine-out emissions including NO_x, PM, and CO of hydrogen-diesel CI engine are presented. Three different injection timings, -120, -130 and -140 aTDC (after top dead center) of hydrogen, along with five different HES (10 %, 20 %, 30 %, 40 % and 50 %) were investigated in conjunction with a conventional diesel-only fueled mode.

Engine model and validation

Simulations were conducted on four-stroke diesel engine, single-cylinder, naturally aspirated, water-cooled variable compression ratio engine test rig (shown in figure 1) [15]. The engine is equipped with a diesel fuel injector nozzle and hydrogen direct nozzle which pressurizes the H_2 and injects at a constant pressure of 14 bar. The engine operates at a constant speed of 1500 rpm and full-load. The study includes a comparison of conventional diesel-only operation with different HES including 10 %, 20 %, 30 %, 40 %, and 50 % hydrogen. The start of injection (SOI) has been selected for hydrogen direct injection at -120, -130, and -140 CA aTDC. The technical specifications of this engine are presented in Table 1. All settings of the modeling were performed in CONVERGE software solution (Table 2). A set of 168 reactions and 42 species in the CONVERGE solvent was used to model combustion for a hydrogen-diesel engine. Diagnostic modeling of nitrogen and soot was performed from CONVERGE software solvent. Extended Zeldovich thermal NOx model with mass scaling factor converting NO to NOx equal to 1.533 and Hiroyasu-NSC soot model were used for modeling NOx and soot. In all cases, the total input energy is kept constant. The simulation was performed for full-load and the injection pressure of hydrogen was 14 bar for all cases and injection duration of hydrogen for 50 % HES was 20 CA. The results of simulation are compared with previous experimental study [15] as shown in figure 2 to validate the numerical results obtained from the CFD code. However, a slight difference in peak pressure is observed. The experimental pressure appeared lower as compared with the simulation, since in the compression stroke the gases escape from the crevice region (Blow-by effect).
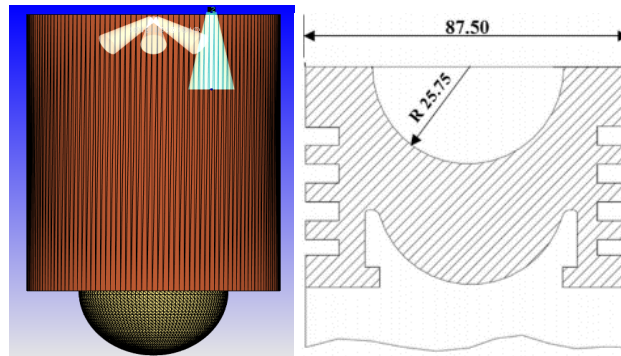

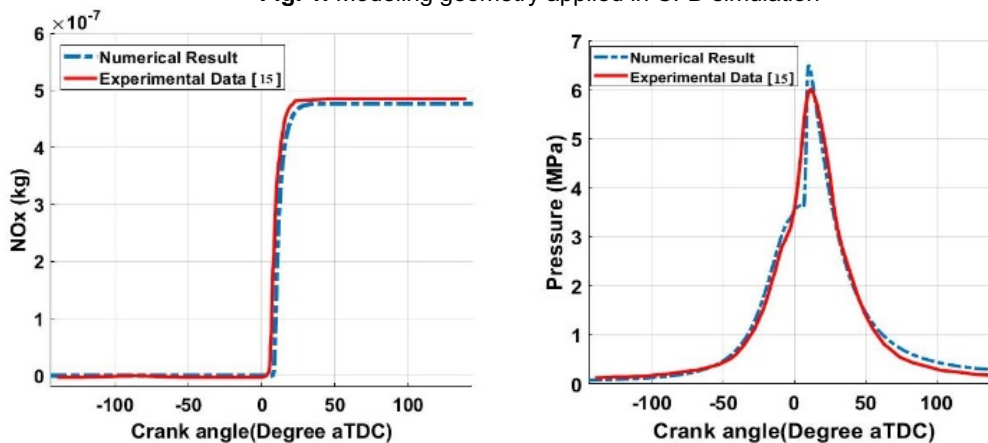
Fig. 1. Modeling geometry applied in CFD simulation

Fig. 2. Pressure and NOx validation for diesel-only combustion

Table 1. Geometry and operating condition of engine

Bore (mm)	87.5
Stroke (mm)	110
Connecting rod length (mm)	243
Speed (R.P.M)	1500
Injected mass of fuel (kg/cycle)	2.57778e-05
Compression ratio	17.5
Inlet valve timings (aTDC)	IVO -184.5; IVC -144.5
Exhaust valve timings (aTDC)	EVO 144.5; EVC 184.5
Piston, cylinder, and head temp. (K)	523, 443 and 523
No of nozzle holes (diesel)	3
No of nozzle holes (diesel)	0.255 mm

Table 2. Sub-model group

Turbulence model	RNG k-e
Injection drop distribution	Chi squared distribution
Drop drag	Dynamic drag model
Droplet collision model	NTC model
Collision outcomes model	Post collision outcomes
Drop turbulent dispersion	O'Rourke model
Evaporation model	Chiang drop correlations
Combustion modeling/chemical	SAGE
Spray breakup	KH-RT

Effects of hydrogen DI on combustion characteristics and emission outputs

Figure 3 explains the effects of the hydrogen DI timing and HES on the P_{max} and indicated mean effective pressure (IMEP). Hydrogen addition has two different effects on IMEP. Firstly, addition of H_2 advances the start of combustion (SOC) resulting higher negative work which reduces IMEP. Secondly, on the other hand, H_2 addition increases the P_{max} which leads to higher IMEP. For 10% HES, the effect H_2 addition on the advancement of SOC is more dominant comparing to P_{max} therefore, the IMEP became lower than diesel-only fueled mode. Contrarily, by increasing the HES up to 30%, the effect of P_{max} will be dominated thus the IMEP is increased as much as the same value for diesel-only fueled mode. In addition, by following more HES percentage, again effect of SOC advancement (i.e., negative work) will be more effective accordingly, the IMEP is decreased. P_{max} is raised when HES increased. Two main reasons can be given explaining these variations. Firstly, hydrogen has a higher flame propagation speed than diesel, leading a near constant volume combustion mode which effectively increases the P_{max}. Secondly, hydrogen has a wider combustion limit making the combustion more complete. P_{max} for HES from 10 % to 50 % is increased almost 15.6 %, 16.7 %, 26.5 %, 35.8 % and 37.4 %, respectively compared to diesel-only fueled mode. The addition of H_2 up to 30 % HES increases the IMEP, while further hydrogen addition (i.e., 40 % and 50 % HES) results in IMEP decline due to the low energy density of hydrogen. As illustrated in Figure 3, the IMEP peaks at 30 % HES. Figure 4 demonstrates the effect of the hydrogen DI timing and HES on NOx, PM, and CO emissions. NOx emission behaves similarly to P_{max}. The most important factor affecting NOx emission is temperature. The addition of hydrogen clearly raises the in-cylinder temperature therefore, the NOx concentration increases with hydrogen addition. Since hydrogen can make combustion more complete and reduce the wall quenching distance, the PM and CO emissions are both reduced noticeably. PM emissions for HES from 10 % to 50 % decrease by average of 72.6 %, 76.4 %, 91.4 %, 96.8 % and 98.6 %, respectively compared to diesel-only. At the SOI of -140 CA aTDC, due to longer available mixing time for hydrogen forming a well homogeneous mixture, a more complete combustion takes place therefore, PM emissions reduction trends is more considerable from HES more than 20 %.
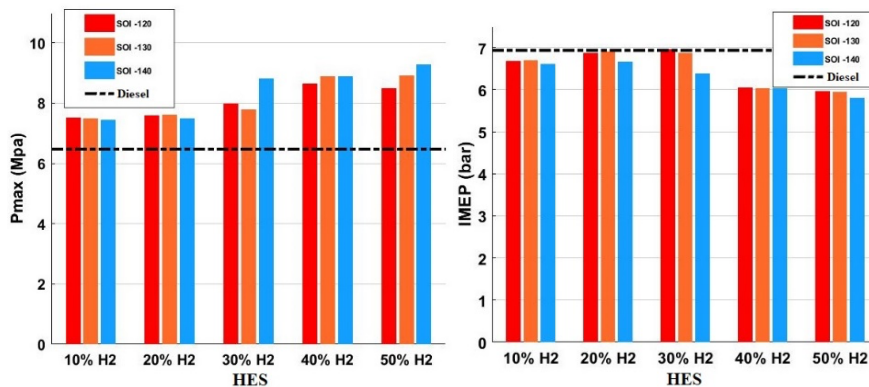

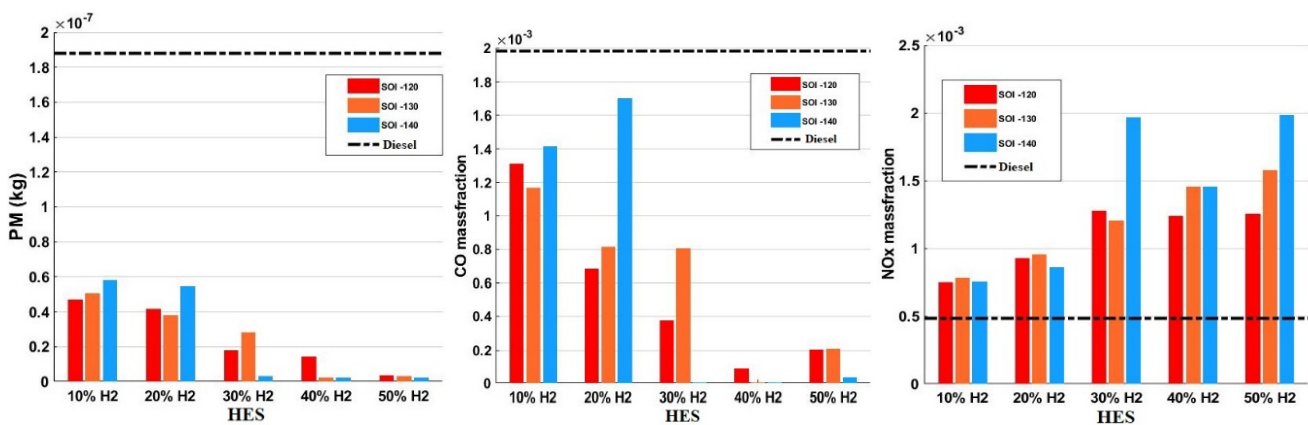**Fig. 3.** Effect of hydrogen DI timing and HES on P_{max} and IMEP

Fig. 4. Effect of hydrogen DI timing and HES on PM, CO and NOx emissions

4   Mahdi Aghahasani, Ayat Gharehghani, Amin Mahmoudzadeh Andwari, Juho Könnö

Conclusions

A numerical study was conducted to investigate the effect of hydrogen injection timing and substitution rate on the in-cylinder pressure and engine-out emissions. In general, hydrogen DI improves volumetric efficiency and speeds up the combustion process. P_{max} for HES from 10% to 50% increase by average of 15.6 %, 16.7 %, 26.5 %, 35.8 % and 37.4 %, respectively compared to diesel-only fueled mode. Hydrogen DI reduces CO and PM emissions by average of 34.6 %, 46.3 %, 80.1 %, 98.4 %, 92.6 %, and for CO emission followed by 72.6 %, 76.4 %, 91.4 %, 96.8 %, 98.6 % respectively for HES from 10 % to 50 % compared to diesel-only fueled mode. Hydrogen DI increases the combustion average temperature leading to higher concentration of NOx emission.

References

[1]   Directive 2009/28/EC on the promotion of the use of energy from renewable sources and amending and subsequently repealing Directives 2001/77/EC and 2003/30/EC (Text with EEA relevance. 2009).

[2]   Trends and projections in Europe 2019 - tracking progress towards EuroHES climate and energy targets d European Environment Agency n.d. https://www.eea.europa.eu/ publications/trends-and-projections-in-europe-1 (accessed March 6, 2020).

[3]   Verhelst S, Wallner T. Hydrogen-fueled internal combustion engines. Prog Energy Combust Sci 2009;35:490e527. https:// doi.org/10.1016/j.pecs.2009.08.001.

[4]   Yip HL, Srna A, Yuen ACY, Kook S, Taylor RA, Yeoh GH, et al. A review of hydrogen direct injection for internal combustion engines: towards carbon-free combustion. Appl Sci 2019;9:1e30. https://doi.org/10.3390/app9224842.

[5]   Verhelst S, Wallner T. Hydrogen-fueled internal combustion engines. Prog Energy Combust Sci 2009;35:490–527.

[6]   Mohammadi A, Shioji M, Nakai Y, Ishikura W, Tabo E. Performance and combustion characteristics of a direct injection SI hydrogen engine. Int J Hydrogen Energy 2007;32:296–304.

[7]   Antunes JMG, Mikalsen R, Roskilly AP. An investigation of hydrogen-fuelled HCCI engine performance and operation. Int J Hydrogen Energy 2008;33:5823–8.

[8]   Das LM. Hydrogen-oxygen reaction mechanism and its implication to hydrogen engine combustion. Int J Hydrogen Energy 1996;21:703e15. https://doi.org/10.1016/0360-3199(95)00138-7.

[9]   Takagi Y, Mori H, Mihara Y, Kawahara N, Tomita E. Improvement of thermal efficiency and reduction of NOx emissions by burning a controlled jet plume in high-pressure direct-injection hydrogen engines. Int J Hydrogen Energy 2017;42:26114e22. https://doi.or.

[10]   Tanno S, Ito Y, Michikawauchi R, Nakamura M, Tomita H. High-efficiency and Low-NOx hydrogen combustion by high pressure direct injection. SAE Int J Engines 2010;3:259e68. https://doi.org/10.4271/2010-01-2173. [24] Naganuma K, Honda T, Yamane K, Takagi Y, .

[11]   Rahman MM, Hamada KI, Aziz A A. Characterization of the time-averaged overall heat transfer in a direct-injection hydrogen-fueled engine. Int J Hydrogen Energy 2013;38:4816e30. https://doi.org/10.1016/ j.ijhydene.2013.01.136.

[12]   A. M. Andwari, A. Pesiridis, V. Esfahanian, M. F. Muhamad Said. "Combustion and Emission Enhancement of a Spark Ignition Two-Stroke Cycle Engine Utilizing Internal and External Exhaust Gas Recirculation Approach at Low-Load Operation", Energies, 2019, 12 (4), 609; doi:10.3390/en12040609

[13]   A. M. Andwari, M. F. Muhamad Said, Azhar Abdul Aziz, V. Esfahanian, M. A. Idris, M. R. Mohd Perang, H. M. Jamil. "Design, Modeling and Simulation of a High-Pressure Gasoline Direct Injection (GDI) Pump for Engine Applications", Journal of Mechanical Engineering (JMechE) Vol. S1 6 (1) (2018) pp 107-120 (ISSN: 1823-5514)

[14]   A. M. Andwari, Azhar Abdul Aziz, M .F. Muhamad Said and Z. A. Latiff, A. Ghanaati. "Influence of Hot Burned Gas Utilization on The Exhaust Emission Characteristics of A Controlled Auto-Ignition Two-Stroke Cycle Engine", International Journal of Automotive and Mechanical Eng., Vol 11 (2015), pp 2396-2404, DOI:http://dx.doi.org/10.15282/ijame.11.2015.20.0201

[15]   "Shudo T, Nabetani S. Analysis of degree of constant volume and cooling loss in a hydrogen fuelled SI engine. SAE Tech Pap 2001. https://doi.org/10.4271/2001-01-3561."

Numerical Analysis of the Effect of Pre-Injection Strategy on Performance and Emissions of an Opposed-Piston Two-Stroke Engine

Rafael Menaca, Giovanni Vorraro, Mickael Silva, Hong G. Im, James W. G. Turner

King Abdullah University of Science and Technology (KAUST). Thuwal 23955-6900, Saudi Arabia.

E-mail: rafael.menaca@kaust.edu.sa
Telephone: +(966) 565072780

Abstract. The current work explores the pre-injection strategy and its effect in engine performance for a medium-duty opposed piston two-stroke (OP2S) diesel engine via computational fluid dynamics (CFD) simulations using CONVERGE™. OP2S engines have remarkable high thermal efficiencies and fundamental advantages over conventional four-stroke diesel engines. Towards ultra-efficient thermal engines, these are potential aspirants for the next generation of highly-efficiency internal combustion engines for range-extender applications in hybrid vehicles. OP2S engines attract further attention due to the ease of manufacture, proper balance, and competitive performance compared with regular four-stroke engines. Pre-injection strategy is common in diesel engines and aims to reduce harmful and soot emissions simultaneously, with compromise in thermal efficiencies. This strategy has been poorly explored in OP2S engines, where further improvements may reside for which, the current work provides further research directions. It is encountered that pre-injection affects the NO_x and soot emissions, increasing the former and decreasing the latter, mainly because of an increasing in the in-cylinder temperature.

1. Introduction

To comply with the stringent emission regulations for internal combustion engines (ICE), their development and optimization is needed while they are dominant in the car park. Opposed-piston two-stroke (OP2S) engines can circumvent multiple drawbacks and arises as a bridging technology for the next high-efficiency engines generation. This engine concept is ultra-efficient and has multiple advantages over conventional diesel engines, as reduced heat losses due to the high stroke/bore ratio and the elimination of the cylinder head substituted by the opposed piston and better combustion characteristics [1,2]. In addition, the OP2S engines become attractive whether as a range extender or powertrains. In macro aspects, compared with conventional four-stroke (4S) diesel engines, the OP2S engine delivers higher power because of its two-stroke engine architecture, thus it is more efficient [3], its harmful emissions are reduced, the engine has fewer elements, and attractive production cost [4]. In conventional 4S diesel engines, the pilot injection technique has shown engine noise reduction [5] with a possible reduction of soot [6], while maintaining similar levels of nitrogen oxides (NO_x) emissions [7]. The pilot injection technique for the OP2S diesel engine has been tested limitedly [8], hence this work provides a wider analysis of the pilot injection application technique in this engine. In this work, a sensitivity analysis on the start of pre-injection (SOPI) and the pre-injection duration (PID) numerically verified by employing computational fluid dynamics (CFD), while the engine performance is compared. To build upon previous work based on simplified 1D simulations [13,14], the work unravels 3D features of the main field evolution and flame development.

2. Methodology

2.1 Computational setup

The CFD solver CONVERGE™ is utilized in the current work; a medium-duty OP2S engine is used and its geometrical details can be found in [11]. The simulations are initialized 136.5 ºCA before the intake and exhaust ducts opening; the initial field variables were mapped from a priori simulation, thus miming effects of field initialization. The simulation lasts until the end of one cycle (180 ºCA after minimum volume (aMV)); the engine speed is 1500 RPM. The fuel quantity is conserved for all simulations and the pilot injection mass is selected as 10% of the total mass, as similar values recommended in other works [8, 9]. The main injection starts at -10 ºCA aMV and its duration is 17.1 ºCA. The mass injection

rate for the pilot is approximated as a triangular shape due to the short period of injection [7]. The mass injection rate for the main injection is scaled from previous works [12]. SOPI and the PID were varied (SOPI was varied from -12 until -18 ºCA aMV sweeping each -2 ºCA; for all the previous SOPI, PID of 1 and 2 ºCA was employed). For instance, the case SOPI-12 PID1 corresponds to an engine operation with pre-injection at -12 ºCA aMV, with a duration of 1 ºCA.

SAGE model is used for the combustion modeling with a reaction mechanism for diesel as the fuel [13]. RNG $\kappa - \epsilon$ turbulence model is selected. Adaptive mesh refinement is focalized on velocity and temperature gradients. For the spray atomization and break-up modeling, the KH-RT hybrid model is implemented. Wall-film and No time counter models are utilized to compute drop-wall interaction and droplet collision/coalescence, respectively. Pressure-implicit with splitting of operator (PISO) algorithm is executed for coupling pressure and velocity. Redlich-Kwong equation of state is used, with real gas properties as a function of temperature with single-species diffusion tabulated data. Boundary conditions are adopted from a computational investigation with a similar engine [14]. NO_x and soot emissions are modeled with the Zeldovich procedure and Hiroyasu model, respectively.

2.2 Validation

The results were validated against 1D GT-Suite models previously developed [10], and the validation stage can be observed in Table I. The 3D-CFD results satisfactorily predict those obtained with the 1D model with marginal, yet acceptable, deviations.

Table I. Model validation stage

|	Results from [10]	Numerical results	Relative error (%)
IMEP [bar]	14	14.1	0.7
CA50 [ºCA aMV]	10.4	10.9	4.6
MPRR [bar/ºCA]	7.1	7.4	4.1
Peak Pressure [bar]	124	116	-6.9

3. Results and discussion

3.1 Start of pre-injection

Fig. 1 (a) shows the heat release rate when pre-injection is applied (with a PID of 1 ºCA). With the implementation of pre-injection, the ignition delay is shortened mainly because of the pilot fuel mixing, which promotes earlier susceptible locations for the combustion process. Furthermore, the curves collapse as the timing passes the minimum volume (MV), so the pilot injection mostly affects the early combustion stage; the latter combustion stage is governed by the main injection combustion. When the pilot is injected near to the main injection (SOPI-12) and consequently near to the MV, compared with more advanced pre-injections, the pilot injection burns in diffusion combustion mode promoting higher in-cylinder temperature and pressure at the main injection timing. For the early pre-injections (SOPI-16 and SOPI-18), the pilot fuel has more time to be mixed before the main injection and the premixed combustion phase is elevated.

As shown in Table II, soot emissions are decreased with the pre-injection strategy implementation, because the quantity of fuel burning in diffusion combustion mode is reduced, although the SOPI-12 operating point maintains the soot emissions levels compared with the non-pre-injection case, due to the short time for the pilot mass mixing. Soot levels are also reduced due to the combustion of the pilot injection, which arranges appropriate conditions for the soot oxidation at elevated temperatures. Table II also presents that maximum pressure rise rate (MPRR) is first increased for the SOPI-12 and SOPI-14, and then it decreases for earlier pre-injections, because it arranges conditions for the main injection fuel combustion, which combusts as it is injected, reducing peaks in the pressure rise rate. The NO_x emissions are increased for all the SOPI points, because of the prolonged elevated temperatures achieved in the combustion process. Fig. 2 illustrates the in-cylinder locations where the temperatures achieved are higher than 2000 K, where can be perceived reduced locations of high temperature when there is no pre-injection. Additionally, the high temperatures when a pilot injection is implemented, arise earlier and last longer, provoking higher NO_x levels. End-gas auto-ignition occurs for early SOPI (as shown in Fig. 2 in the second row at -5 ºCA aMV) due to the extended time for the pilot mixing, although strong/high pressure rise rates are not observed.

3.2 Pre-injection duration

Fig. 1 (b) shows the heat release rate for two pre-injection operating points (one advanced and one near the main injection), emphasizing the effect of the PID (1 ºCA and 2 ºCA) over it. The release of heat starts earlier when the PID is shorter and achieves higher rates in the pilot phase. With the aim of an injection with the same quantity of fuel in a shorter period, the pilot injection must be executed at higher pressures (considering constant the rest of the injection and injector variables), hence it suggests that the fuel atomization is much stronger, with a faster rate of evaporation leading to a better mixing and faster combustion.

(a)   (b)
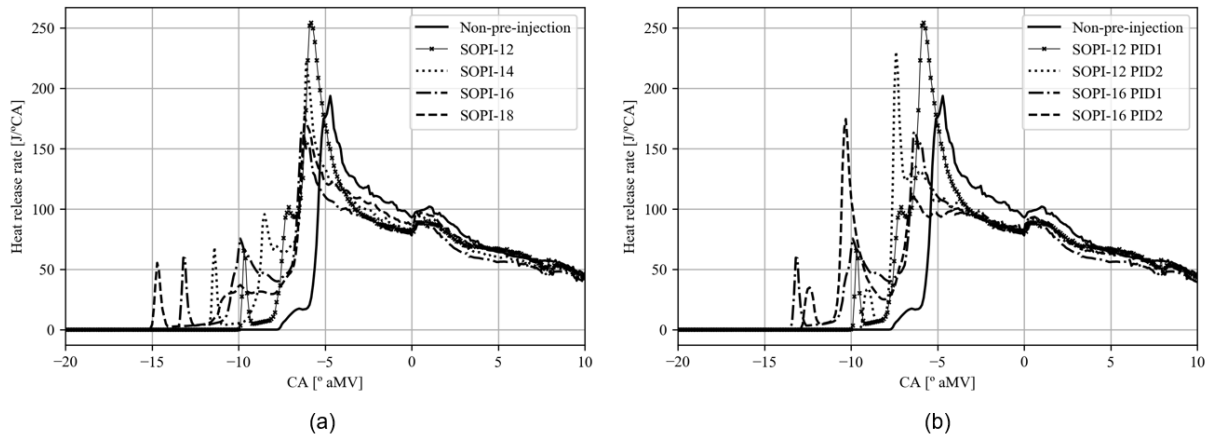
Fig. 1. The heat release rate for the different pre-injection operating points with focus on (a) SOPI and (b) PID

Table II. Performance and emissions of the OP2S engine with the variation of the SOPI

	Non-PI	SOPI-12	SOPI-14	SOPI-16	SOPI-18
Power [kW]	25,86	25,29	25,6	25,65	25,75
MPRR [bar\ºCA]	7,4	8,95	8,39	6,41	6,8
NO$_x$ [g/kW-h]	4,22	4,73	4,91	4,52	4,96
Soot [g/kW-h]	2,15	2,16	1,82	2,02	1,67
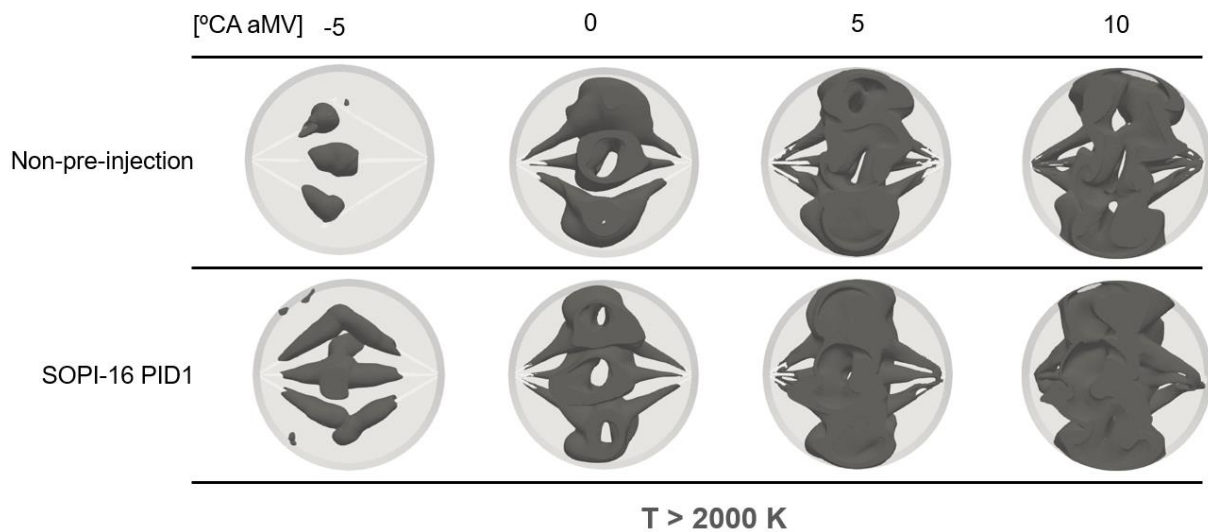
Fig. 2. Locations of high temperature in the jet combustion for two operation conditions at different timings

Table III presents the effect of the PID over performance and emissions of the OP2S engine. Due to the small quantity of fuel as pilot, the power output minorly varies as consequence of the change in the

combustion mode. When PID is elongated, the MPRR is reduced due to a slower mixing and longer combustion. The NO_x and soot emissions do not follow an appreciative trend when the PID is varied.

Table III. Performance and emissions of the OP2S engine with the variation of the PID

	Non-PI	SOPI-12 PID1	SOPI-12 PID2	SOPI-16 PID1	SOPI-16 PID2
Power [kW]	25,86	25,29	25,4	25,65	25,32
MPRR [bar\ºCA]	7,4	8,95	7,47	6,41	6,01
NO_x [g/kW-h]	4,22	4,73	4,48	4,52	5,03
Soot [g/kW-h]	2,15	2,16	2,02	2,02	2,15

Conclusions

The effect of the pre-injection application in an OP2S engine was investigated numerically. It was found that early pilot injections enhanced premixing since the pilot fuel had sufficient time to mix with air. Additionally, the soot emissions were minimized owing to a reduced fuel amount burned in diffusion combustion mode. Furthermore, advancing pre-injection, the MPRR decreased due to prolonged combustion promoted by the pilot. Despite the benefits of pre-injection, a compromise in NOx emission was observed relative to non-pre-injection cases; this was mainly caused by prolonged high in-cylinder temperature promoted by the early pilot combustion. Ultimately, for a longer PID, the rate of heat release was decreased in the pilot combustion phase, with marginal changes in NOx and considerable decrease in MPRR.

References

[1]   G. Regner, D. Johnson, J. Koszewnik, E. Dion, and F. Redon, "Modernizing the Opposed Piston , Two Stroke Engine for Clean , Effi cient Transportation Two-Stroke Operation," 2021.

[2]   R. E. Herold, M. H. Wahl, G. Regner, J. U. Lemke, and D. E. Foster, "Thermodynamic Benefits of Opposed-Piston Two- Stroke Engines," 2011, doi: 10.4271/2011-01-2216.

[3]   S. Naik *et al.*, "Practical applications of opposed-piston engine technology to reduce fuel consumption and emissions," *SAE Tech. Pap.*, vol. 12, 2013, doi: 10.4271/2013-01-2754.

[4]   J. Pirault and M. Flint, "Opposed-Piston Engine Renaissance Power for the Future," 2010.

[5]   L. Zhang, "A Study of Pilot Injection in a DI Diesel Engine," no. 724, 2018.

[6]   P. Carlucci, A. Ficarella, and D. Laforgia, "Effects of pilot injection parameters on combustion for common rail diesel engines," *SAE Tech. Pap.*, no. x, 2003, doi: 10.4271/2003-01-0700.

[7]   K. Pfonts, "DE3-1 Evaluation of Pilot Injections Large Two-Stroke Marine Diesel Engine , Using CFD and T-rp Mapping," pp. 181–188, 2008.

[8]   S. Shirvani, S. Shirvani, and A. H. Shamekhi, "Effects of injection parameters and injection strategy on emissions and performance of a two-stroke opposed-piston diesel engine," SAE Technical Paper, 2020.

[9]   J. W. G. Turner *et al.*, "2-Stroke Engine Options for Automotive Use: A Fundamental Comparison of Different Potential Scavenging Arrangements for Medium-Duty Truck Applications," *SAE Tech. Pap.*, vol. 2019-Janua, no. January, pp. 1–21, 2019, doi: 10.4271/2019-01-0071.

[10]   A. Young, J. Turner, and R. Head, "Turbocompounding the Opposed-Piston 2-Stroke Engine," *SAE Tech. Pap.*, no. 2021, pp. 1–16, 2021, doi: 10.4271/2021-01-0636.

[11]   A. G. Young, A. W. Costall, D. Coren, and J. W. G. Turner, "The effect of crankshaft phasing and port timing asymmetry on opposed-piston engine thermal efficiency," *Energies*, vol. 14, no. 20, 2021, doi: 10.3390/en14206696.

[12]   J. A. Badra *et al.*, "Numerical Simulations of Hollow-Cone Injection and Gasoline Compression Ignition Combustion With Naphtha Fuels," *J. Energy Resour. Technol. Trans. ASME*, vol. 138, no. 5, pp. 1–11, 2016, doi: 10.1115/1.4032622.

[13]   N. Nordin, "Numerical simulations of non-steady spray combustion using a detailed chemistry approach," *Licent. Eng. thesis, Dep. Thermo Fluid Dyn. Chalmers Univ. Technol. Goteborg, Sweden*, 1998.

[14]   J. Gandolfo *et al.*, "Effects of Port Angle on Scavenging of an Opposed Piston Two-Stroke Engine," pp. 1–18, 2022, doi: 10.4271/2022-01-0590.Received.

Large Eddy Simulations (LES) towards a Comprehensive Understanding of Ducted Fuel Injection Concept in Non-Reacting Conditions

F. Millo[1], C. Segatori[1], A. Piano[1], B. Peiretti Paradisi[1] and A. Bianco[2]

[1]Energy Department, Politecnico di Torino, Italy.

E-mail   federico.millo@polito.it

Telephone: +(39) 011 0904517

[2]POWERTECH Engineering, Italy.

Abstract. The diesel combustion research is increasingly focused on Ducted Fuel Injection (DFI), a promising concept to abate engine-out soot emissions in Compression-Ignition engines. A large set of experiments and numerical simulations, at medium-low computational cost, showed that the duct adoption in front of the injector nozzle activates several soot mitigation mechanisms, leading to quasi-zero soot formation in several engine-like operating conditions. However, although the simplified CFD modelling so far played a crucial role for the preliminary understanding of DFI technology, a more accurate turbulence description approach, combined with a large set of numerical experiments for statistical purposes, is of paramount importance for a robust knowledge on the DFI physical behavior.

In this context, the present work exploits the potential of Large Eddy Simulations (LES) to analyze the non-reacting spray of DFI configuration compared with the unconstrained spray. For this purpose, a previously developed spray model, calibrated and validated in the RANS framework against an extensive amount of experimental data related to both free spray and DFI, has been employed. This high-fidelity simulation model has been adapted for LES, firstly selecting the best grid settings, and then carrying out several numerical experiments for both spray configurations until achieving a satisfying statistical convergence. With this aim, the number of independent samples for the averaging procedure has been increased exploiting the axial symmetry characteristics of the present case study. The reliability of this methodology has been herein proven, highlighting an impressive runtime saving without any remarkable worsening of the accuracy level.

Thanks to this approach, a detailed description of the main DFI-enabled soot mitigation mechanisms has been achieved, bridging the still open knowledge gap in the physical understanding of the impact of spray-duct interaction.

1. Introduction

The urgency of keeping air quality under control and limiting the global warming due to the anthropogenic greenhouse gas emissions are pushing a substantial portion of the internal combustion engines research to find new strategies to abate soot (i.e., black carbon) emissions from diesel combustion.

A particularly interesting solution is Ducted Fuel Injection (DFI), a hardware-related concept currently under investigation in several research groups across the world. The DFI, conceived by Mueller et al. [1], means assembling a small cylindrical pipe coaxially, some distance downstream, to the injector nozzle, aiming at improving the mixture preparation upstream of the autoignition zone. A dramatic soot reduction through DFI, compared to the conventional free spray, has been demonstrated in combustion studies, performed both in Constant-Volume Vessel (CVV) [1,2] and in optically accessible Compression-Ignition (CI) engine [3]. However, a clear and generally accepted explanation of the DFI soot mitigation mechanisms still misses, despite the large number of physics-oriented studies available in literature in both non-reacting and reacting conditions, using experiments and CFD. This comprehensive understanding is of paramount importance in making DFI technology suitable for a large and complex range of operating conditions, such as the one characterizing a typical CI engine map, as well as in supporting from a geometry optimization and assembly perspective.

In light of this, the purpose of the herein work is to analyze the non-reacting spray of DFI configuration compared with the unconstrained spray to a deeper level, involving 3D-CFD with a high-fidelity spray model and an accurate turbulence modelling approach like Large Eddy Simulation (LES), adopting a grid size able to capture very small turbulent eddies and performing several numerical experiments until achieving a satisfying statistical convergence. The large computational cost associated with this approach has been significantly reduced though the method suggested in [4],

thus increasing the number of independent samples by exploiting the axial symmetry characteristics of the present case study. The reliability of this methodology has been herein proven for the DFI case, before its employment for the detailed physical analysis, which is the main object of this research.

2. Methodology

2.1. Case Study

The case study considered for this LES analysis was presented in [5,6], where a free spray configuration was compared with DFI concept in CVV, in both non-reacting and reacting conditions, using a prototype single-hole Common Rail injector with a 0.180 mm nozzle diameter. Both spray configurations are herein considered, under the non-reacting operating conditions summarized in Table 1.

Table 1. Operating conditions

Rail pressure	1200 bar
Injection duration	1.5 ms
Vessel pressure	20 bar
Vessel temperature	773 K

As far as the DFI configuration is concerned, the duct features a diameter of 2 mm, a length of 14 mm and a stand-off distance (i.e., the gap between duct inlet and injector nozzle) of 2 mm.

2.2. 3D-CFD Simulation Setup

The 3D-CFD analysis was carried out by means of the commercially available software CONVERGE CFD V3.0.14 [7]. The spray model was developed in the RANS framework [5,6,8], extensively validated against experimental data in both free spray and DFI configuration. For the turbulence modelling, the LES approach was employed, allowing for direct resolution of the largest turbulent scales. The one-equation dynamic structure model was used for the sub-grid scale [9].

The computational domain was meshed with a cartesian grid by means of the CONVERGE CFD patented cut-cell technique, reaching a minimum grid size of 31.25 μm in the most critical areas through the Adaptive Mesh Refinement (AMR) tool. This final value was the result of a grid sensitivity analysis, aiming at a high-quality LES resolution in the whole domain of interest for both configurations. In particular, a minimum target of 80% of resolved turbulent structures was achieved, as suggested by [10,11]. This minimum grid size, relatively low if compared with most of the LES spray simulations available in literature, was especially required for the DFI case, to obtain a good description of the inflow at the duct inlet and outflow at duct outlet, where the flow detachment plays a key role. At the duct wall, a Near Wall Modelling (NWM) approach was used, adopting the wall function developed by Werner and Wengle [12] and adopting a 1-layer inlaid mesh at the inner wall, whose extrusion dimension (62.5 μm) was accurately calibrated in order to match the y+ criteria. The choice of a NWM approach was determined by the prohibitive computational cost needed to resolve the boundary layer with a LES turbulence model at high Reynolds number conditions.

2.3. Ensemble Average Method

For the herein study, a runtime saving methodology to ensemble average several axial symmetric LES spray simulations was employed. As stated by Farrace et al. [4], considering a cylindrical test vessel equipped by a single-hole injector coaxial to the cylinder axis, the conventional approach (herein named *standard approach*) is to obtain a certain number of statical samples (N) by running S=N simulations, varying either initial conditions or random seed parameters. Nevertheless, considering a certain number (M) of semi-slices parallel to the spray axis, and by assuming that each semi-slice behaves as a different numerical experiment, if statistical independency is ensured by a sufficient angular distance among semi-slices, the same number of statistical samples (N) can be achieved by S=N/M simulations. This approach (herein named *multi-slice approach*) enables a M-fold reduction in computational costs with the drawback of limiting results to a 2D representation. For the sake of clarity, a schematic representing the two considered ensemble average methods is reported in Fig. 1, considering M=4 for the multi-slice approach.
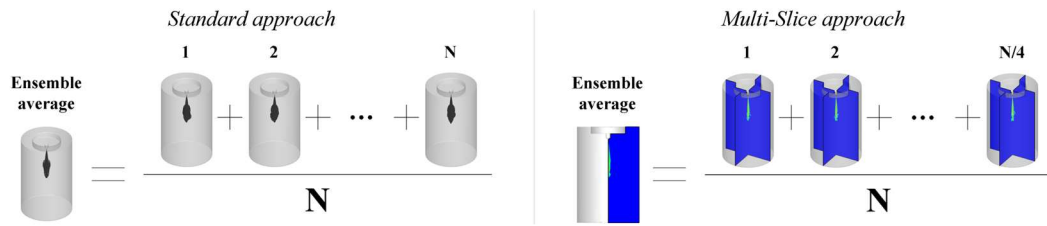
Fig. 1. Sketch of the ensemble average methods at equal number of samples

The first step of this analysis was the assessment of the abovementioned multi-slice approach, especially for the DFI configuration, considering the ensemble average among 20 different samples. However, it is not herein reported for the sake of brevity. Since this methodology resulted to be reliable and the number of samples sufficient, the multi-slice approach was adopted, and the same settings were maintained for the subsequent physical analysis.

3. Results

In Fig. 2, the resolved Turbulent Kinetic Energy (TKE) distribution on a longitudinal semi-slice is reported for both free spray and DFI configurations at four different time instants during the injection event. The resolved TKE, computed starting from the root mean square of the average velocity fluctuations component [10], can be used as turbulent mixing index, as carried out in [5,6,8].

At each time step, it can be observed that the high turbulence values for the free spray case are strongly localized in the spray tip, while for the DFI are widely distributed on the whole spray plume after the duct outlet. Hence, starting from the duct outlet, a larger and longer area (up to the spray tip) characterized by high TKE values is present for the DFI. This is caused by the flow detachment at the duct outlet, where the spray is suddenly no more guided by the duct wall and strong velocity, density and concentration gradients appear. Focusing on the duct wall, a small high-mixing region can be detected, which was identified as a first stage turbulent mixing in previous studies [6].

More in general, the energy cascade seems spatially more advanced due to the duct adoption, shifting back TKE values higher than 2000 m2/s2 of 10-20 mm. Even though the maximum value in the domain at equal time step can be higher for the free spray, it is more important that DFI enables a wider and more advanced turbulent mixing, especially considering the limited dimension of a combustion chamber and the necessity to reduce the fuel-to-air ratio before the Lift-Off Length (which is even extended by the duct adoption [1,2]).
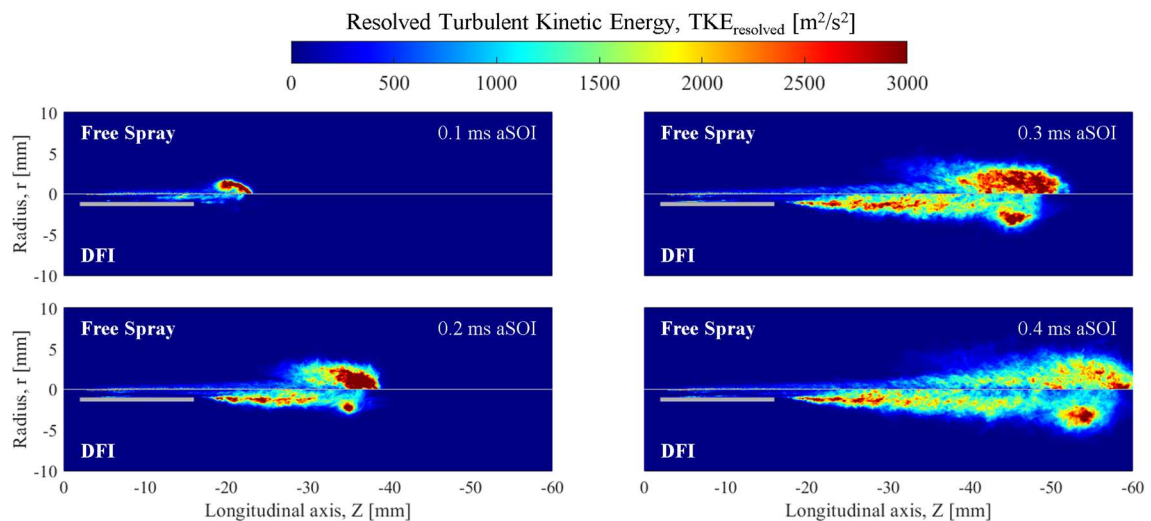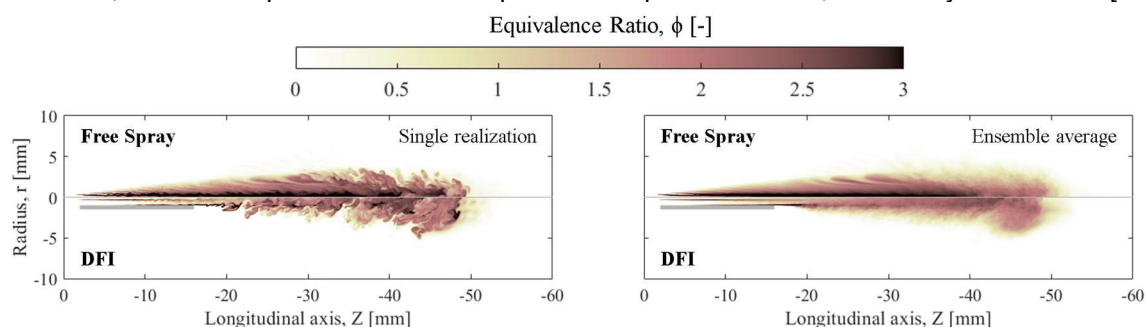

Fig. 2. Resolved Turbulent Kinetic Energy distribution on a longitudinal semi-slice for both free spray (top side) and DFI (bottom side) at four time instants during the injection event

In Fig. 3, the equivalence ratio (ϕ) distribution on a longitudinal semi-slice is reported for both free spray and DFI configurations at 0.3 ms after Start of Injection (aSOI). In this case, for a better visualization of the formation of vortices, also the outcome from a randomly selected realization is reported (left) together with the ensemble average (right).

4   F. Millo, C. Segatori, A. Piano, B. Peiretti Paradisi, A. Bianco

The free spray is characterized by a rich central core which is broken and mixed with the available air at about 40 mm from the injector nozzle on average; namely, when the high turbulent mixing is present according to Fig. 2. In the DFI case, no central rich core is present, while a high ϕ region exits the duct close to the wall, due to the inhibited contact with air. This region is rapidly broken by the high second stage turbulent mixing (Fig. 2), leading to a leaner mixture about 20 mm in advance with respect to the free spray on average. Focusing on the single realization, this rich core breakage is associated to the formation of small vortices immediately after the duct outlet. To reach similar turbulent eddy dimensions in the free spray case, additional 15-20 mm distance is needed.

It is noteworthy that also the shape of the spray plume is drastically changed by the duct adoption. In fact, a more compact mushroom shaped head is present for DFI, as already observed in [13].

Fig. 3. Equivalence ratio distribution on a longitudinal semi-slice for both free spray (top side) and DFI (bottom side) at 0.3 ms aSOI. Results for both a randomly selected realization (left) and the ensemble average (right).

Conclusions

A 3D-CFD analysis was carried out to analyze Ducted Fuel Injection (DFI) physical behavior compared to the free spray case in non-reacting condition. The Large Eddy Simulation (LES) turbulence model, a highly refined computational grid, and a large set of numerical experiments enabling statistical analysis have been employed to bridge the still open knowledge gap about the impact of spray-duct interaction. The computation of resolved Turbulent Kinetic Energy (TKE), the definition of high turbulent mixing regions in terms of values and location, the observation of the rich cores, and the study of small and large vortices formation allowed improving the understanding on this promising technology for low-soot diesel combustion.

References

1.   Mueller, C.J., Nilsen, C.W., Ruth, D.J., Gehmlich, R.K. et al., "Ducted fuel injection: A new approach for lowering soot emissions from direct-injection engines," *Appl. Energy* (2017), doi:10.1016/j.apenergy.2017.07.001.
2.   Gehmlich, R.K., Mueller, C.J., Ruth, D.J., Nilsen, C.W. et al., "Using ducted fuel injection to attenuate or prevent soot formation in mixing-controlled combustion strategies for engine applications," *Appl. Energy* (2018), doi:10.1016/j.apenergy.2018.05.078.
3.   Nilsen, C.W., Biles, D.E., and Mueller, C.J., "Using Ducted Fuel Injection to Attenuate Soot Formation in a Mixing-Controlled Compression Ignition Engine," *SAE Int. J. Engines* (2019), doi:10.4271/03-12-03-0021.
4.   Farrace, D., Panier, R., Schmitt, M., Boulouchos, K. et al., "Analysis of Averaging Methods for Large Eddy Simulations of Diesel Sprays," *SAE Int. J. Fuels Lubr.* (2015), doi:10.4271/2015-24-2464.
5.   Millo, F., Piano, A., Peiretti Paradisi, B., Postrioti, L. et al., "Ducted Fuel Injection: Experimental and numerical investigation on fuel spray characteristics, air/fuel mixing and soot mitigation potential," *Fuel* (2021), doi:10.1016/j.fuel.2020.119835.
6.   Millo, F., Piano, A., Peiretti Paradisi, B., Segatori, C. et al., "Ducted Fuel Injection: A Numerical Soot-Targeted Duct Geometry Optimization," *SAE Int. J. Engines* (2021), doi:10.4271/03-15-02-0014.
7.   Richards, K.J., Senecal, P.K., and Pomraning, E., *CONVERGE 3.0.14*, 2022.
8.   Millo, F., Segatori, C., Piano, A., Peiretti Paradisi, B. et al., "An engine parameters sensitivity analysis on ducted fuel injection in constant volume vessel using numerical modeling," *SAE Technical Paper 2021-24-0015* (2021), doi:10.4271/2021-24-0015.
9.   Pomraning, E. and Rutland, C.J., "Dynamic one-equation nonviscosity large-eddy simulation model," *AIAA J.* (2002), doi:10.2514/2.1701.
10.   Pope, S.B., *Turbulent Flows*, Cambridge University Press, 2000.
11.   Pope, S.B., "Ten questions concerning the large-eddy simulation of turbulent flows," *New J. Phys* (2004), doi:10.1088/1367-2630/6/1/035.
12.   Werner, H., Wengle, H., "Large eddy simulation of turbulent flow over and around a cube in plane channel," *Proceedings of the Eighth Symposium on Turbulent Shear Flows* (1991), doi:10.1007/978-3-642-77674-8_12.
13.   Li, F., Lee, C. fon, Wang, Z., Liu, F. et al., "Optical investigation on impacts of ambient pressure on macroscopic spray characteristics of ducted fuel injection under non-vaporizing conditions," *Fuel* (2020), doi:10.1016/j.fuel.2020.117192.